ADA 274798

TITANIUM '92

SCIENCE AND TECHNOLOGY

VOLUME I

94-00280



94 1 5 036

Best
Available
Copy

TITANIUM '92

SCIENCE AND TECHNOLOGY

VOLUME I

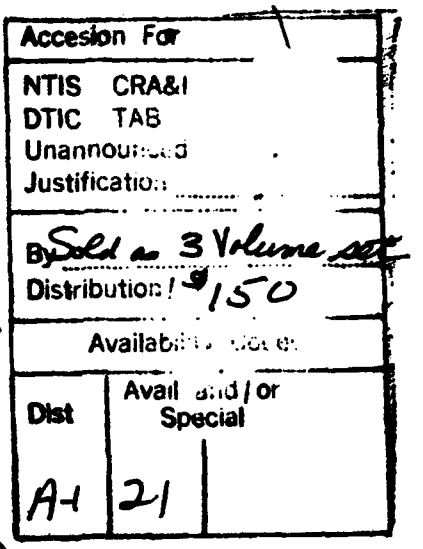
Proceedings of a Symposium sponsored
by the Titanium Committee of the Minerals, Metals & Materials
Structural Metals Division

Held at the Seventh World Titanium Conference
June 29 - July 2, 1992
in San Diego, California

Edited by
F.H. FROES and I.L. CAPLAN

A Publication of
TMS
Minerals • Metals • Materials

DTIC QUALITY INSPECTED 5



A Publication of The Minerals, Metals & Materials Society
420 Commonwealth Drive
Warrendale, Pennsylvania 15086
(412) 776-9000

The Minerals, Metals & Materials Society is not responsible for statements or opinions and is absolved of liability due to misuse of information contained in this publication.

Printed in the United States of America
Library of Congress Catalog Number 93-78482
ISBN Number 0-87339-222-1

Authorization to photocopy items for internal or personal use, or the internal or personal use of specific clients, is granted by The Minerals, Metals & Materials Society for users registered with the Copyright Clearance Center (CCC) Transactional Reporting Service, provided that the base fee of $3.00 per copy is paid directly to Copyright Clearance Center, 27 Congress Street, Salem, Massachusetts 01970. For those organizations that have been granted a photocopy license by Copyright Clearance Center, a separate system of payment has been arranged.

TMS
Minerals • Metals • Materials

© 1993

If you are interested in purchasing a copy of this book, or if you would like to receive the latest TMS publications catalog, please telephone 1-800-759-4867.

PREFACE

It is with a mixed sense of relief, accomplishment and pride that we open this final prologue to the Seventh World Titanium Conference. Relief that the uncountable hours spent in organizing the conference and compiling these proceedings are behind us. Accomplishment and pride that the conference went so well, including riding out the strongest earthquake that mother nature has served up to Southern California in quite some time. We thank the numerous people who verbally and in writing complemented us on both the technical program and social events -- it makes the hours spent worthwhile.

We want to take this opportunity to thank the other members of the U.S. Organizing Committee for their hard work, the International Organizing Committee (IOC) representatives for their support and outstanding coordination, The Minerals, Metals & Materials Society staff for their superb management of the conference, and the Titanium Development Association for their efficient handling of the Exhibition. Furthermore, a special thanks is extended to the plenary and keynote speakers for their conscientious preparation and participation. Finally, the Executive Committee deeply appreciates the much needed financial support generously provided by each of the sponsoring organizatiors and companies in these difficult economic times.

Of course these proceedings would not have been possible without the generally excellent manuscripts submitted by authors from around the world -- thank you all! We also want to mention the behind-the-scenes contributions of Debkumar Mukhopadhyay, graduate student at the University of Idaho, in compiling these proceedings. His diligent efforts were invaluable.

This conference marked 20 years since the last international titanium conference was held in the United States in Boston, Massachusetts. At that time, only four countries made up the IOC and less than 200 papers were presented. Since then, the IOC has grown to sever countries, with the admittance of China in 1992. Conference attendance in San Diego exceeded 700 persons, representing 26 nations, presenting more than 400 papers.

And so on to Birmingham, England in October 1995 for the Eighth World Titanium Conference. We wish Paul Blenkinsop and his "team" the best of luck, and hope that everything goes as well for them as it did for us.

Francis H. (Sam) Froes
University of Idaho
Moscow, ID

Ivan L. Caplan
Naval Surface Warfare Center
Annapolis, MD

Conference Co-Chairmen and Proceedings Editors - March 1993

DOMESTIC ORGANIZING COMMITTEE

Ivan L. Caplan	Co-chairman
F.H. Froes	Co-chairman
Neil E. Paton	Finance
F.H. Froes, Ivan L. Caplan	Technical Program/Proceedings
James A. Hall	Poster Sessions
Harold D. Kessler	Activities
Rodney R. Boyer	Secretary
Neville R. Moody	Student Activities
Paul Bania	Promotions
Barbara J. Kamperman	Conference Management
Titanium Development Association	Exhibition Management

INTERNATIONAL ORGANIZING COMMITTEE

F.H. Froes	The Minerals, Metals & Materials Society
G. Beranger	Société Française de Métalurgie et de Matériaux
T. Suzuki	The Japan Institute of Metals
S. Seagle	ASM International
I.V. Gorynin	The Academy of Sciences
G. Luetjering	Deutsche Gesellschaft für Materialkunde
P. Blenkinsop	The Institute of Metals



PROCEEDINGS DEDICATION

Robert I. Jaffee

1 1 July 1917 - 28 November 1991

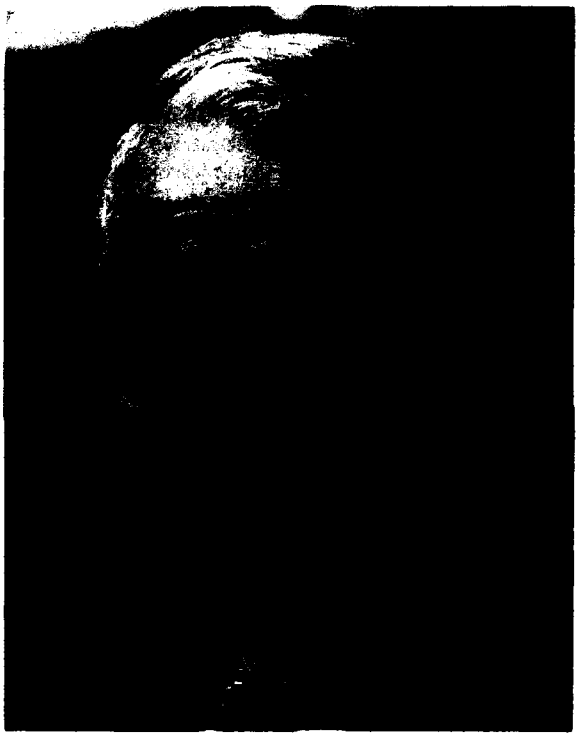
Mentor, colleague, co-worker, friend. Bob Jaffee was some or all of these to the titanium community in general, and to many of us individually.

For thirty-two years at Battelle, he was a major contributor to, and stimulator of, the rapidly growing field of materials, creating a materials science group around himself that was second to none in the world. His seminal work on the physical metallurgy of titanium still undergirds much of the technology which permits its effective use. As young men in the 50's, we did not hesitate to bring him our ideas, however tentative. He listened, was always objective, and responded with useful commentary. Later, I well remember working closely with him to co-edit the Proceedings of the Second International Titanium Conference - the previous time it was held in the United States in Boston, 1972. In particular, developing an index with him provided a window into his mind, a measure of what he considered to be important. He was precise, logical, and had a visionary perspective of the future.

After Battelle, he did not rest on his laurels but undertook a second career -- 17 years beyond his first retirement and active until his death -- at the Electric Power Research Institute. Here his focus shifted from aerospace to power generation, and he provided international leadership. Bob's precision and logic have been experienced by many. His famous "NONSENSE" when sloppy thinking or parochial motives intruded upon technical judgments, often led the way back to rationality. His energy and irrepressible enthusiasm were legendary, from his golf game to his membership or leadership of many advisory committees; early on I learned about "joy through work" -- another Jaffee'ism that enriched us. He was both a scientist and an engineer, fostering the development of science-based technology in the service of man.

Bob received numerous honors, from the Presidency of the Metallurgical Society to membership in the National Academy of Engineering. I have tried to emphasize how he enriched so many of us, particularly in the titanium community, and in the tradition started with Dr. Wilhelm Kroll after the first conference. It is entirely appropriate to dedicate these Proceedings of the Seventh World Titanium Conference to Dr. Robert I. Jaffee—mentor, colleague, co-worker, and friend.

Dr. Harris M. Burte
Chief Scientist, Materials Laboratory
Wright Laboratories
Dayton, OH.
May 1992



Robert I. Jaffee
11 July 1917 - 28 November 1991

TABLE OF CONTENTS

VOLUME I

VOLUME II 957-1,968
VOLUME III 1,969-2,982

PLENARIES

Titanium Process Modelling 3
F.H. Froes, H.L. Gegel, C.H. Hamilton, G.W. Kuhlman, and J.H. Moll

Advanced Alloys and Processes 15
P.A. Blenkinsop

Alloy Theory and Phase Transformations in Titanium Alloys 27
R. Penelle and C. Servant

Surfaces and Elevated Temperature Effects 41
M.A. Daeubler and D. Helm

Present Features in Production of Titanium Sponge and Ingot 53
S. Tamamoto

Material Science and Ti-Production Problems in View of New Horizons of the Application 65
I. Gorynin

MICROSTRUCTURE AND PROPERTIES

Microstructure - Property Relationships in Titanium Alloys (Critical Review) 77
R.R. Boyer and J.A. Hall

Hot Deformation Microstructure Study in Ti-6Al-4V and in β-Cez Alloys 89
C. Servant, C. Quesne, T. Baudin, and R. Penelle

Structural Stability of β-Cez Alloy 97
A. Henri and A. Vassel

Deformation and Fracture Mechanisms in the β Metastable β-Cez Alloy 105
C. Combres, G. Dumas, A.-M. Chaze, and B. Champin

Fatigue and Fracture Toughness Properties of Ti-6Al-4V with Acicular Alpha Microstructures 113
T. Matsumoto, T. Nishimura, S. Muranaka, and S. Ishigai

The Effect of Thermal Treatment on the Cryogenic Mechanical Properties of Cast 5Al-2.5Sn ELI Titanium 121
D.P. Dennies and J.C. Gibeling

Optimization of Service Properties for Titanium Forgings with Bimodal Microstructure 131
H. Puschnik, J. Fladischer, G. Lütjering, and R.S. Jaffee

Microstructure and Mechanical Properties Relationship of β-Rich α-β Titanium Alloy: SP-700 141
M. Ishikawa, O. Kuboyama, M. Niikura, and C. Ouchi

Development of Titanium OT4-1 Alloy 149
S.C. Sharma, R.K. Bannadi, R. Ganesh, and S.A. Badami

Oxygen Effects on the Mechanical Properties of Timetal·21S 153
W.M. Parris and P.J. Bania

Microstructural Stability of Beta 21S 161
M.W. Mahoney, P.L. Martin, and D.A. Hardwick

Effect of Heating-Rate on the Formation of (α+β) Microduplex Structure in a Ti-15V-3Cr-3Sn-3Al Alloy 169
K. Ameyama, T. Inaba, K. Hirota, K. Hirai, and M. Tokizane

Effect of Cold Work and Heat Treatment in Alpha Region on Mechanical Properties of Ti-15-3 Alloy 177
M.A. Imam, P.K. Poulose, and B.B. Rath

Deformation Behavior of an Age Hardenable Beta + Alpha-Two Titanium Alloy 185
L.S. Quattrocchi and D.A. Koss

Correlation of Mechanical Properties and Microstructures of Ti-6Al-2Sn-2Zr-2Mo-2Cr-0.25Si Titanium Alloy 193
H.R. Phelps and J.R. Wood

Evaluation of Ti-6Al-2Sn-2Zr-2Cr-2Mo-.23Si Sheet 201
R.C. Bliss

TMP Conditions - Microstructure - Mechanical Property Relationships in Ti-6-22-22S Alloy 209
A.K. Chakrabarti, R. Pishko, V.M. Sample, and G.W. Kuhlman

Theoretical Design of β-Type Titanium Alloys 217
M. Morinaga, M. Kato, T. Kamimura, M. Fukumoto, I. Harada, and K. Kubo

Omega Phase Formation in Titanium and Titanium Alloys 225
G.T. Gray, III, C.E. Morris, and A.C. Lawson

Role of Composition and Microstructure in Dynamic and Static Fracture of Alpha-Beta Titanium Alloys 233
R.W. Judy, Jr. and I.L. Caplan

An Investigation on Strengthening Process and Its Strengthening Mechanism for TC_4 Titanium Alloy 241
X.K. Meng, Y.G. Zhou, and H.Q. Yu

Improvement of Structure and Properties of (α+β)-Titanium Alloys Using the Rapid Heating and Accelerated Cooling 247
O.M. Ivasishin and P.E. Markovsky

Void Nucleation, Void Growth and Tensile Behavior of Ti-10V-2Fe-3Al 255
H. Margolin and S.J. Pak

Effects of Hydrogen on the Structure and Properties of Beta-C™ (Ti-3Al-8V-6Cr-4Mo-4Zr) Sheet 263
J.R. Wood and M.L. Bogensperger

Quantitative Texture Analysis of α-Based Titanium and Titanium Alloys—A Two Stage Approach 271
A.W. Bowen

The Effect of Process Route and Rare Earth Content on the Microstructure and Properties of a PM Titanium Alloy 279
A.P. Woodfield, M.F.X. Gigliotti, and R.A. Amato

The Influence of Silicon and Silicides on the Properties of Near-Alpha Titanium Alloys 287
D.F. Neal and S.P. Fox

The Influence of Thermal Exposure on Properties and Microstructure of Elevated Temperature Titanium Alloys 295
W.T. Donlon, J.E. Allison, and J.V. Lasecki

Room and Elevated Temperature Properties of Ti-1100 303
M. Peters, V. Bachmann, K.-H. Trautmann, H. Schurmann, Y.T. Lee, and C.H. Ward

Correlation Between Microstructure and Creep Behavior of the High-Temperature Ti-Alloy IMI 834 311
C. Andres, A. Gysler, and G. Lütjering

Creep and High Temperature Low Cycle Fatigue of Cast Ti-6Al-2Sn-4Zr-2Mo Alloy 319
S. Bashir and M.C. Thomas

On Crack Mechanism of Ti-6.5Al-3.5Mo-1.5Zr-0.35Si Alloy Under Fatigue-Creep-Environment Interaction 327
Y.G. Zhou, Y. Zhou, and H.Q. Yu

Thermodynamics Aided Design of $\alpha+\alpha_2$ High Temperature Titanium Alloys (Ti-Al-Sn-Zr-Nb-Si System) 335
H. Onodera, S. Nakazawa, K. Ohno, T. Yamagata, and M. Yamazaki

The Mechanical Properties of Ternary and Quarternary Ti_2NbAl-Based Titanium Aluminide Alloys 343
R.G. Rowe

Study of Creep Crack Growth Behavior of Ti-24Al-11Nb 351
M. Khobaib

An Investigation of the Effects of Heat Treatment on the Microstructure and Mechanical Behavior of $(\alpha_2+\beta)$ Forged Ti-24Al-11Nb 359
W.O. Soboyejo

Microstructure/Property Relationships for the Alpha-2 Titanium Aluminide Alloy Ti-24.5Al-12.5Nb-1.5Mo 367
B.J. Marquardt

Effects of Microstructure on Tensile Properties in the Alloy Ti-25Al-10Nb-3V-1Mo 375
F.C. Dary and A.W. Thompson

The Effect of Deformation and Heat Treatment Conditions on Structure and Mechanical Properties of γ-Alloys 383
B.I. Bondarev, N.F. Anoshkin, A.B. Notkin, D.V. Elagin, and A.V. Molotkov

The Influence of Microstructure on the Creep Behavior of the Near-γ Alloy Ti-48Al-1V-0.2C 391
B.D. Worth, J.W. Jones, J.E. Allison, and W.E. Dowling

Microstructure and Mechanical Properties of Refractory Metal Modified Ti-48 at% Al-2 at% Nb-2 at% Cr 399
P.L. Martin and C.G. Rhodes

In-Situ Strengthening in Titanium 407
A.M. Russell, J.A. Jensen, L.S. Chumbley, D.G. Konitzer, and T.W. Ellis

Effect of Oxygen Content on Microstructure and Properties of Beta-C™ (Ti-3Al-8V-6Cr-4Mo-4Zr) Investment Castings 415
J.R. Wood, D.P. Barbis, and D. Eylon

The Effect of Microstructure and Carbon on the Tensile Behavior of the $\gamma+\alpha_2$ Alloy Ti-48Al-1V-0.2C (at %) 423
W.E. Dowling, Jr., B.D. Worth, W.T. Donlon, and J.E. Allison

The Role of Input Powder Microstructure and Extrusion Conditions on Properties of PM Titanium-Rare Earth Alloys 431
M.F.X. Gigliotti, A.P. Woodfield, R.A. Amato, J.R. Hughes, and L.C. Perocchi

Creep Behavior of Ti-24Al-11Nb 439
M. Khobaib

Microstructure and Mechanical Properties of β-21S Titanium Alloy 447
D. Upadhyaya, D.M. Blackketter, C. Suryanarayana, and F.H. Froes

Microstructural Modification and Analysis of an IMI 685 Titanium Alloy 455
Z.X. Guo and T.N. Baker

Thermomechanical Treatment of Various Beta Processed Titanium Alloys 463
J.F. Uginet

Microstructure and Texture Control of Hexagonal Sheet Alloys - Role of Alloying Elements on Mechanical Properties and Formability 473
M.J. Philippe, C. Esling, M. Serghat, A. Molinari, G. Canova, A.W. Bowen, H.S. Ubhi, K. Barnes, J. Driver, N. Cheneau, R. Schwarzer, M.J. Bunge, S. Zefferer, P. Van Houtte, L.S. Toth, J.G. Sevillano, and J.A. Medina-Perilla

Effects of Deformation Temperature on As-Deformed and Post-Aging Microstructures, and Tensile Properties After Aging in Ti-15V-3Cr-3Sn-3Al 481
H. Ohyama, A. Takemura, and T. Nishimura

Thermomechanical Treatment to Diminish β Flecks in Ti-6Al-6V-2Sn Plate 489
H.G. Suzuki, S. Ishikawa, N. Noda, K. Kaku, Y. Kako, and N. Yamada

Fatigue Fracture of Cold-Rolled Titanium in Vacuum 497
M. Sugano, T. Satake, and S. Inoue

Effect of Heat Treatments on the Fatigue Behavior of the Beta-C Titanium Alloy 505
D. Buttinelli, F. Felli, and G.B. Festa

On Effects of Beta Fleck on the Properties of Ti-10V-2Fe-3Al Alloy 513
Y.G. Zhou, J.L. Tang, H.Q. Yu, and W.D. Zeng

The Effect of Texture on Impact Energy and Fracture of Ti-4Al Alloy 523
C. Xuezhang, L. Chenggang, and W. Hua

Structure/Property Relationships in Near Beta Ti-V-Fe-Al Based Alloys 531
A.I.P. Nwobu, H.M. Flower, and D.R.F. West

Structural Strengthening of the High Concentration Titanium Alloys with Transition Metals 539
L.K. Kondratenko and V.F. Shamray

ALLOY THEORY AND PHASE TRANSFORMATIONS

Theory of Alloys and Phase Transitions (Critical Review) 547
I.S. Polkin, S.G. Glazunov, and A.A. Ilyn

Phase Equilibria in the Titanium-Aluminum System 563
J.H. Perepezko and J.C. Mishurda

Phase Selection During Solidification Processing of Ti-40 at% Al Powder 571
E.M. Clevenger and J.H. Perepezko

Estimation of Recrystallized Grain Size Under Continuous Annealing of Cold-Rolled β Titanium Alloy Strips 579
H. Ohyama, A. Takemura, and T. Nishimura

High Temperature Phase Stability of XD™ TiB_2 Reinforced Near-Gamma Ti-48Al-2Nb-2Mn 587
S. Guillard, H.J. Rack, and D.E. Larsen

Elevated Temperature Phase Stability of Ti-25Al-11Nb 595
M. Long, P.K. Chaudhury, and H.J. Rack

Texture in Rolled Rods of Alpha-and (Alpha+Beta) Titanium Alloys 603
A.S. Shihmakov and R.A. Adamesku

Determination of the Recovery Properties of a Ti45.5-Ni54.5 (wt%) Shape Memory Alloy in Tension 611
P. Roumagnac, M. Clavel, Y. Barbaux, and M.H. Campagnac

Effect of Stress on the Hydride Formation Behavior of Ti-6Al-4V Alloy 619
K. Nakasa and J. Liu

Effect of Thermomechanical Treatments on TA6Zr5D β Grain Size Evolution 627
J.M. Kempf, E. Gautier, A. Simon, J.F. Uginet, and A. Gavart

Grain Growth of Titanium and its Grain Size Distribution 635
Y. Takayama, N. Furushiro, T. Tozawa, H. Kato, and Y. Umakushi

Phase Transformations in a Near β-Ti Alloy: Microstructure and Mechanical Properties 643
J. Bechet, C. Angelier, B. Cormier, O. Lacagne, and M. Lhermitte

Precipitation and Hardening in Titanium-Magnesium and Titanium-Calcium Alloys 651
C.M. Ward-Close, P.G. Partridge, and C.J. Gilmore

An X-Ray Diffraction Study of Vapour Quenched Titanium-Magnesium Alloys 659
C.M. Ward-Close, P.G. Partridge, P. Holdway, and A.W. Bowen

Grain Growth of TA6V β Phase After Thermomechanical Treatments 667
N. Côme-Dingremont, E. Gautier, and A. Simon

Phase Equilibria in the Systems Ti-N, Ti-Zr-N and Ti-Hf-N and Properties of δ-TiN_{1-x} δ-$(Ti,Zr)N_{1-x}$ and δ-$(Ti,Hf)N_{1-x}$ 675
W. Lengauer, R. Täubler, J. Bauer, J. Debuigne, and P. Ettmayer

The Regularities of Structure Formation in Pseudo-Alpha-Ti Alloys During Hot Plastic Deformation 683
S. Ushkov, B. Krivitskiy, I.N. Rasuvaeva, and V.N. Kopylov

The Ti-C-N System and Properties of Ti(C,N) 689
S. Binder, W. Lengauer, and P. Ettmayer

Relation Between Electrical Resistivity and Phase Constitution in Metastable β Ti-Nb Alloys 697
M. Ikeda, S.-Y. Komatsu, T. Sugimoto, and K. Kamei

The Effect of Aluminum on the Phase Transformations in Ti-19V and 23V Alloys 705
T. Maeda and H.M. Flower

High Temperature Phase Equilibria in the Ti-Al-Ta Ternary System 713
T.J. Jewett, S. Das, and J.H. Perpezko

On the Nature of Orthorhombic Symmetry of Martensite in Titanium Alloys 721
O.M. Ivasishin and N.S. Kosenko

Phase Transformations in Combined Alloyed α-Ti Alloys and Their Effect on Thermal Embrittlement and Corrosion Mechanical Properties 729
S. Ushkov, V. Rybin, I. Rasuvaeva, E. Nesterova, and O. Gunbina

Transformation Kinetics of Titanium and Equi-Atomic Titanium-Zirconium Solid-Solution by Means of Isothermal Dilatometry 739
J. Debuigne and E. Etchessahar

On the Ternary System Ti-V-N 747
A. Guillou, J. Bauer, and J. Debuigne

The Effect of the β-Stabilizing Elements and Heating/Cooling Rate on Phase Transformations on Multicomponent Ti-Alloys with Constant Al Content 755
J. Sieniawski and F. Grosman

Phase Transformation in Ti-15V-3Cr-3Sn-3Al Alloy 761
S.H. Wang, G.Q. Shen, and Y.M. Liang

A Study of Grain Growth Behaviour in Titanium Alloys 769
S.P. Fox

Grain Growth Kinetics in Beta Phase of Ti-6Al-4V Alloy 777
F.J. Gil, P. Tarín, and J.A. Planell

On the Ordering Transformations in Ti_3Al-Nb Alloy 785
L. Dong, Z. Jing, C. Xin, and G. Shaoxuan

POWDER METALLURGY, THERMOCHEMICAL PROCESSING, AND NANOSTRUCTURES

Synthesis of Ti Alloys by Powder Metallurgy, Nanostructured Materials, and Thermomechanical Processing 793
A. Vassel and F.H. Froes

A Spray-Reaction Process for Production of Titanium Powder 805
H. Kametani and H. Sakai

Y_2O_3 Dispersed α+β and Near-α Titanium Alloys Prepared by P/M Processing 813
T. Khan, D.F. Neal, M.J. Hill, M.J. Weaver, F. Schwartz, B. Champin, and S. Naka

Tensile and Fracture Toughness Properties of P/M Ti-1.3Al-8V-5Fe and Derivatives 821
C.F. Yolton and J.M. Oraboni

Synthesis of Titanium Aluminides Using a Combined Mechanical Alloying and Thermochemical Processing Approach 829
D.K. Mukhopadhyay, C. Suryanarayana, and F.H. Froes

Effect of Hydrogen on Microstructure and Phase Stability of Alpha-2 Base Titanium Aluminide Castings 837
M. Saqib, L.S. Apgar, D. Eylon, and I. Weiss

Changes in Microstructure and Phase Morphology During Vacuum Annealing of Ti-25Al-10Nb-3V-1Mo-H Alloy 845
M. Saqib, L.S. Apgar, D. Eylon, and I. Weiss

Improvement in Mechanical Properties of α+β Type Titanium Alloys by Microstructural Control Using Thermochemical Processing 853
M. Niinomi, B. Gong, T. Kobayashi, and Y. Ohyabu

The Effect of Hydrogen Alloying on Workability of Titanium Alloys 861
B.A. Kolatchev, A.V. Malkov, I.A. Vornbyov, V.A. Volodin, and A.V. Mitin

Study on Effects of HVC Treatments on Improvement of Superplastic Behavior of Ti-10V-2Fe-3Al 871
D. Zhongquan, W. Gaochao, C. Yuxio, W. Clunlei, and Z. Zhifang

High Pressure Hydrogenation for Ti-6Al-4V Castings 879
S.E. Hsu, C.P. Chang, S.G. Kao, W.P. Sun, and S.T. Thun

Property Enhancement of α-β Titanium Alloys by Blended Elemental P/M Method 887
M. Hagiwara, Y. Kaieda, Y. Kawabe, and S. Miura

Fabrication of Ti-Ni-Cu Shape Memory Alloys by Spontaneous Reaction Synthesis and Directed Hot Extrusion Forming 895
M.T. Yeh, H.P. Kao, and S.E. Hsu

Nanostructure Formation in a Mechanically Alloyed Ti-24Al-11Nb Alloy 903
G.-H. Chen, C. Suryanarayana, and F.H. Froes

Complex Processing of Low-Grade Spongy Titanium into High Effective Powdery Products 911
V.S. Ustinov, V.M. Anokhin, V.V. Voleinik, V.A. Drozdenko, and V.M. Prozorov

Characteristics of High Purity Titanium Powder by HDH Process 919
E. Fukasawa, R. Murayama, and W. Kagohashi

Fabrication and Study of an ODS β Titanium Alloy by Mechanical Alloying 927
R. Baccino, D. Brenet, and F. Moret

Synthesis of γ-TiAl by Mechanical Alloying of Elemental Powders 933
A. Frefer, C. Suryanarayana, and F.H. Froes

Phase and Structure Transformations in Titanium Alloys Under Thermohydrogenous Treatment 941
A.A. Ilyn, B.A. Kolachev, and A.M. Mamonov

The Effect of Porosity on the Viscoplastic Response of Sintered Ti-6Al-4V 949
M. Da Silva and K.T. Ramesh

TABLE OF CONTENTS

VOLUME II

VOLUME I 1-956
VOLUME III 1,969-2,982

INTERMETALLICS

Microstructures and Mechanical Behavior of Gamma Titanium Aluminides (Critical Review) 959
M. Yamaguchi

Environmental Effects on Fatigue Properties of Alpha-2 Titanium Aluminides 971
P.S. Godavarti, M.D. Lipschutz, J.G. Snow, and J.A. Hall

The Isothermal Forging of the Ti_3Al Based Alloy, Superalpha 2 979
J.C.F. Millett, J.W. Brooks, and I.P. Jones

Spray Forming of Ti-Aluminide-Based Alloys 987
J.W. Sears, G. Itoh, and M.H. Loretto

Microstructural and Textural Changes During Rolling of Alpha-2 Titanium Aluminide Foils 995
R. Verma and A.K. Ghosh

The Role of Silicon in a Ti_3Al Based Alloy 1,003
D.J. Arrell, H.M. Flower, and S. Kerry

The Influence of Deviation from Stoichiometry on Microstructure and Tensile Properties of a Ti_3Al Base Alloy 1,009
I. Ehrhart and A. Vassel

Transformation Kinetics in $\gamma+\alpha_2$ TiAl Based Alloys 1,017
A. Denquin, S. Naka, and T. Khan

A Novel Inert Gas Atomization Facility for the Production of Intermetallic Titanium-Based Alloy Powders 1,025
R. Gerling, F.P. Schimansky, and R. Wagner

Microstructural Development in Ingot and Forged XD™ Ti-48Al-2Mn-2Nb (+2% TiB_2) Near-Gamma Titanium Aluminide 1,033
M. Jezioro, S. Moorhouse, M. Cope, and P. Postans

The Effect of Chromium on the Kinetics of Alpha Decomposition in Gamma TiAl Alloys 1,041
P.A. McQuay, D.M. Dimiduk, H.A. Lipsitt, and S.L. Semiatin

An Investigation of the Effects of Heat Treatment on Microstructure and Fracture Behavior of Extruded Ti-48Al-1.5Cr 1,049
W.O. Soboyejo and S.M.L. Sastry

Effect of Refining Grains on Mechanical Properties in Ti-Rich TiAl 1,057
T. Maeda, M. Okada, and Y. Shida

The Effects of Al, Cr, Nb and Ta on the Tensile Properties of Cast Gamma Titanium Aluminide 1,065
C.M. Austin, T.J. Kelly, and S.C. Huang

Processing and Properties of Ductile Phase Reinforced Gamma Titanium Aluminide Alloys 1,073
M.S. Dadkhah and J.A. Graves

Effects of Processing and Heat Treatment on Microstructure and Mechanical Properties of Gamma Titanium Aluminide Powder Compacts ... 1,083
C.F. Yolton and D. Eylon

α/γ Peritectic Oscillations in Directionally Solidified Ti-52at%Al 1,091
D.B. Snow, C.T. Burilla, and B.F. Oliver

Wrought Processing of a Gamma Titanium Alloy Ti-48Al-2Cr-2Nb 1,099
J.C. Chesnutt and D.S. Shih

The Influence of Forging on the Microstructure of Plasma-Melted γ-Based Titanium Aluminides 1,107
X.D. Zhang, R.V. Ramanujan, T.A. Dean, R. Dewes, M.H. Jacobs, and M.L.H. Wise

Gas Tungsten-Arc Welding of a Ti-48Al-2Cr-2Nb Gamma Titanium Aluminide 1,115
L.C. Mallory, W.A. Baeslack, III, D. Phillips, and T.J. Kelly

Creep Behavior of Ti-27 mol%Al Intermetallics 1,123
M. Ohtsuka and H. Oikawa

Thermal Strains in Titanium Aluminide and Nickel Aluminide Composites 1,131
A. Saigal and D.S. Kupperman

Fracture and Fatigue of TiAl Based Aluminides 1,139
A.W. James and P. Bowen

Deformation of the Orthorhombic Phase in Ti-Al-Nb Alloys at High Temperatures 1,147
D. Banerjee and R.G. Rowe

Micromechanisms of Fracture in Titanium Aluminides 1,155
A.W. Thompson

Influence of Strain Rate on the Structure/Property Behavior of the Alpha-2 Alloy Ti-24.5Al-10.5Nb-1.5Mo 1,163
G.T. Gray, III, S.I. Hong, and B.J. Marquardt

Microstructure, Tensile Ductility, and Fracture Toughness of Ti-25Al-10Nb-3V-1Mo 1,171
C.H. Ward, I. Roman, J.C. Williams, and A.W. Thompson

Micromechanisms of Fracture in Alpha-Two Based Titanium Aluminides 1,179
R.A. Chave, S. Kerry, C.J. Beevers, and P. Bowen

On the Influence of the Phase Morphology on the Mechanical Properties of the Two-Phase Intermetallic Compound Super Alpha-2 1,187
G. Proske, G. Lütjering, J. Albrecht, M.A. Däubler, and D. Helm

Effects of Microstructure on Fatigue Crack Growth in a Ti_3Al Based Aluminide at Ambient and Elevated Temperatures 1,195
R.J.T. Penton, M.T. Cope, and P. Bowen

Recrystallization and Its Effect on the Flow Behaviour of TiAl 1,203
N.K. Park, Y.T. Hyun, Y.T. Lee, and A.K. Ghosh

Deoxidation of TiAl Intermetallic Compounds 1,211
T.H. Okabe, K. Fujiwara, T. Oishi, and K. Ono

Effects of Environment on Fatigue Crack Growth in a Ti_3Al Based Aluminide 1,219
R.J.T. Penton, M.T. Cope, and P. Bowen

Crack Growth Resistance of Alpha-Two Based Titanium Aluminides Under Cyclic Loading at Ambient and Elevated Temperatures 1,227
R.A. Chave, S. Kerry, C.J. Beevers, and P. Bowen

Microstructure and Properties of Forged Plasma Arc Melted and Vacuum Arc Remelted Titanium Aluminides 1,235
C.L. Huang, Z. Chen, T.A. Dean, and M.H. Loretto

Phase Stability in Ti_3Al+X Base (X = Nb, Mo, V, Ta, Fe) Alloys 1,243
M. Thomas, S. Naka, and T. Khan

Creep of Ti-24Al-11Nb 1,251
D.E. Albert and A.W. Thompson

Phase Equilibria in Ti-Al-Nb Alloys Near Ti_2NbAl 1,259
R.G. Rowe, D. Banerjee, K. Muraleedharan, M. Larsen, E.L. Hall, D.G. Konitzer, and A.P. Woodfield

Structure-Property Relationships of Investment Cast Gamma Titanium Aluminides 1,267
D.A. Wheeler, B. London, and D.E. Larsen, Jr.

The Effect of Processing on the Microstructure and Tensile Properties of a γ-TiAl Alloy 1,275
G.E. Fuchs

Effects of Microstructure in Hydrogen Embrittlement of Titanium Aluminide Alloys 1,283
A.W. Thompson

A Re-Examination of the Ti-Al Equilibrium Diagram in the Range 33-54 A/O Aluminum 1,291
A. Bartz, L. Rothenflue, M. Saqib, R. Omlor, and H.A. Lipsitt

Microstructure and Mechanical Properties of Ti-Al-(CrSi) Alloys 1,299
G. Frommeyer, T. Kremser, and W. Wunderlich

The Chemistry and Structure of Plasma-Melted γ-Based Titanium Aluminides 1,309
R.V. Ramanujan, X.D. Zhang, I.P. Jones, J.M. Young, and J.W. Sears

FORGING, FORMING, JOINING, AND CASTING

Titanium—A Review of Current Forming and Fabrication Techniques (Critical Review) 1,319
J.W. Brooks, P.J. Bridges, and D. Stephen

Microstructure and Property Modification of Cast Alpha-2 Titanium Alloys by Thermochemical Processing with Hydrogen 1,331
L.S. Apgar, C.F. Yolton, M. Saqib, T. Weiss, and D. Eylon

Thermomechanical β-Processing of High Strength Medium Temperature Ti Alloys: Comparison of Ti-17 and β-Cez 1,339
P.E. Mosser, N. Marnier, and Y. Honnorat

Hot Deformation of the High Strength Beta-Cez Titanium Alloy 1,347
F. Montheillet, D. Dajno, N. Côme, E. Gautier, A. Simon, P. Audrerie, A.-M. Chaze, and C. Levaillant

Manufacture and Properties of Heavy Open-Die Forgings from Low-Alloy Ti-0.3Mo-0.8Ni for Chemical Processing Equipment 1,355
D. Fischer and K. Hülse

A Study on the Trans-Beta Hot Die Forging of Ti-10V-2Fe-3Al Alloy 1,363
W. Jinyou and Y. Bin

Characterization of Ti-6-22-22S: A High Strength Alpha-Beta Titanium Alloy for Fracture Critical Applications 1,371
G.W. Khulman, K.A. Rohde, and A.K. Chakrabarti

High Temperature Flow Localization in Coarse Grain Widmanstätten Ti-6Al-4V 1,379
H.J. Rack and A. Wang

Computer Simulation of Changes in Temperature and Stresses in Titanium Alloy Forgings During Heat Treatment 1,387
M.Y. Brun, V.M. Olshansky, G.Z. Malkin, A.N. Lozhko, and L.A. Bykova

Laser Forming of Near Shapes 1,395
F.G. Arcella

Superplastic Forming of Industrial Parts: A Numerical Simulation 1,403
C. Corsini, M. Bellet, and J. Pora

Superplasticity and Post-Forming Room Temperature Tensile Properties of Ti-2.5% Cu Alloy 1,413
M.A. Hassan and C. Hammond

Superplastic Behavior of Ti-6Al-4V and β-Enhanced Iron-Modified Ti-6Al-4V 1,421
M. Meier and A.K. Mukherjee

Seamless Thin-Walled TiAl6V4 Tubes Manufactured by Flow-Forming Process 1,429
M. Koch, H. Sibum, H. Jelenak, and E. Plänker

Effect of Interfacial Microvoid Geometry During Diffusion Bonding of Ti 6-4 Alloy 1,437
H.A. Nied

Some Aspects of Formation of Joints of Various Configurations During Diffusion Bonding of Two-Phase Titanium Alloys 1,445
N.F. Anoshkin, A.A. Gelman, and V.M. Pavlov

Interface Characteristics of Solid-Phase Welds Between Ti-6Al-2Sn-4Zr-2Mo-0.1 Si and Ti-14Al-21Nb Titanium Aluminide 1,453
M.C. Juhas, W.A. Baeslack, III, H.L. Fraser, P. Threadgill, P. Phillips, and T.F. Broderick

Pressure Welding Process Window for Ti-6Al-4V (Addendum) 2,941
R.E. Sundell, M.F.X. Gigliotti, and L. Hellemann

Plasma Arc Welding of TA6V Titanium Alloy 1,461
C. Boucher, F. Messager, F. Gaillard, and J.L. Heuze
Postweld Heat Treatment of GTA Welds in a High-Strength, Metastable-Beta Titanium Alloy--Beta-C™ 1,469
W.A. Baeslack, III, P.S. Liu, D.P. Barbis, J.R. Schley, and J.R. Wood
Laser Welding of an Oxidation Resistant, Metastable-Beta Titanium Alloy--Beta-21S 1,477
P.S. Liu, K.H. Hou, W.A. Baeslack, III, and J. Hurley
Near-Net Shape Processing of Gamma & XD™ Gamma Titanium Aluminides by Investment Casting 1,487
D.E. Larsen, Jr., D.A. Wheeler, and B. London
Recent Advances in Titanium Investment Casting 1,495
M.S. Cianci, R.G. Vogt, and G.N. Colvin
Effects of HIP and Heat Treatment on the Microstructure and Room Temperature Properties of Near-γ Titanium Aluminide Castings 1,503
P.E. Jones, M. Saqib, T.J. Kelly, W.J. Porter, I. Weiss, and D. Eylon
Effects of Microstructure on the Mechanical Properties of Ti-15V-3Cr-3Al-3Sn Castings 1,511
W.J. Porter, R.R. Boyer, and D. Eylon
A New Calcia Technology for Investment Casting of Titanium Alloys with the Lost Wax Process 1,519
S. Prigent and J. Debuigne
Superplastic Deformation Behaviour of Ti-4Al-4Mo-2Sn-0.5Si (IMI 550) 1,527
L.B. Duffy and N. Ridley
Superplastic Deformation Properties of As-Received, Rolled and Beta Transformed Ti-2% Al-2% Mn Alloy 1,535
M.A. Hassan and C. Hammond
Hot Bar Rolling of Ti-6Al-4V in a Continuous Mill 1,543
M. Moriga, Y. Takahashi, and M. Shigenaga
Strengthening and Toughening of Alpha-Beta Titanium Alloys by Thermomechanical Processing 1,551
M. Okada
High Strength α+β or β-Titanium Alloys for Fasteners and Technology of Their Production 1,559
I.S. Polkin, I.A. Vorobyev, V.A. Sheenkov, and V.V. Dolgov
Structure and Mechanical Properties of VT22 (α+β) High Strength Titanium Alloy Semiproducts 1,569
I.S. Polkin, V.L. Rodinov, A.N. Stroshkov, T.V. Ishunkina, V.G. Kudryashov, and O.S. Korobov
Effects of Strain Path Changes on Work Hardening in Titanium Sheet 1,579
W.T. Roberts and R.A. Chamberlain
Manufacturing of Large Turbine Blades of Titanium Alloy 1,587
T. Satoh, S. Ishigai, and T. Matsumoto

Effects of Processing on Tensile and Creep Properties of Two Cast α_2 Titanium Aluminide Alloys 1,593
D. Eylon, L.S. Apgar, D.J. Evans M. Saqib, W.J. Porter and I. Weiss

Effect of Contamination by Air on the TIG Welding of Commercially Pure Titanium Sheet 1,601
M.F. Gittos and M.M. Scott

An Investigation of the Characteristics of Bonding Strength in Titanium Clad Steel 1,609
T. Kawanami, S. Shirasuna, S. Shirogane, and A. Segawa

Effect of Diamond Wheel Grain Size on the Grindability of Ti-6Al-4V 1,617
N. Kumagai, K. Kamei, and Y. Tanaka

Isostatic Diffusion Bonding of Superplastic Ti-6Al-4V and Super Alpha-2 Intermetallic Alloy 1,625
N. Ridley, M.F. Islam, and J. Pilling

PHYSICAL AND MECHANICAL PROPERTIES

Mechanical Properties of Titanium Alloys (Critical Review) 1,635
G. Lütjering, J. Albrecht, and A. Gysler

The Properties of Ti-6Al-2Sn-2Zr-2Mo-2Cr Sheet 1,647
R.R. Boyer and A.F. Caddey

Tension Creep of a Single Phase γ TiAl Alloy 1,653
R.W. Hayes and P.L. Martin

Strain-Rate and Temperature Effects on the Deformation and Crack Initiation Behavior of Ti-48Al-1V 1,661
L.S. Harbison, D.A. Koss, and R.J. Bourcier

Mechanical Behaviour of Extruded I/M and P/M Super α_2 Alloys 1,669
M. Thomas, S. Naka, M. Marty, W.G. Smarsly, and T. Khan

The Deformation and Fracture Behaviors of Ti-25Al-10Nb-3V-10Mo Alloy at Different Temperatures 1,677
F. Sun, C. Li, and C. Cao

Improvement of Ductility and Strength of Ti-25Al-10Nb-3V-1Mo by TMT 1,685
J. Kumpfert, C.H. Ward, Y.T. Lee, and M. Peters

The Role of Hydrogen in Cyclic and Dwell Sensitive Fatigue of a Near Alpha Titanium Alloy 1,693
W.J. Evans and M.R. Bache

Hot Strength of Ti and Ti Alloys Deformed in Axial Compression 1,701
R.A.N.M. Barbosa, H.C. Braga, and J. Breme

The Effect of Boron and Cerium on the Creep Behavior of a High Temperature Titanium Alloy 1,709
Z. Jinxu, X. Jialong, C. Guoliang, C. Kexiu, and G. Honglin

Some Factors Affecting the Creep Properties of Ti-6242 1,717
K.E. Thiehsen, M.E. Kassner, D.R. Hiatt, and B.M. Bristow

Microstructure and Mechanical Properties for PREP/PM IMI 829-1Gd and IMI 829-1Er Alloys 1,725
L. Guozhen, D. Ju, L. Tao, Z. Yueqin, and Y. Guanjun

High Temperature Deformation Behavior of α, α-β and β Titanium Alloys 1,733
M.N. Vijayshankar and S. Ankem

The Microstructural Features Associated with the Growth of Short Fatigue Cracks in a Near-Alpha Ti Alloy 1,741
A.L. Dowson, C.J. Beevers, and L. Grabowski

Small Crack Growth at Elevated Temperatures in a Near Alpha Titanium Alloy 1,749
S.H. Spence, W.J. Evans, and A. Goulding

Low Cycle Fatigue Behavior of Ti 6246 1,757
A.S. Beranger, X. Feaugas, D. Lai, and M. Clavel

Fatigue Under Tension/Torsion Loading in IMI 685 1,765
W.J. Evans and M.R. Bache

Creep Behavior and Thermal Stability of a Novel High Temperature Titanium Alloy 1,773
H. Chuanxi and Z. Renqi

Deformation of Beta Titanium Solid Solution Alloys at Elevated Temperatures 1,779
H. Oikawa, Y. Ishikawa, and M. Seki

Strengthening Mechanisms in Undermatched Titanium Welds 1,787
M.E. Wells

Modelling of Texture Evolution During Thermomechanical Treatments for Different Titanium Alloys 1,795
M.J. Philippe, F. Wagner, M. Serghat, A. Bowen, and C. Esling

Fatigue Crack Growth Mechanisms of Two Titanium Alloys at Room and Elevated Temperatures 1,803
Y. Dai, N. Marchand, M. Hongoh, and J.I. Dickson

The Monitoring of Anisotropy of Physico-Mechanical Properties of Flat Semiproducts of α+β Titanium Alloys 1,811
I.V. Gorynin, A. Kudrjavtsev, and R.A. Adamesku

Fatigue Crack Growth Behavior of Ti-6Al-4V at Elevated Temperature 1,819
J. Petit, W. Berata, and B. Bouchet

High Cycle Fatigue Properties of Ti-6Al-4V Alloys at Cryogenic Temperatures 1,827
K. Nagai, T. Yuri, O. Umezawa, T. Ogata, K. Ishikawa, Y. Ito, and T. Nishimura

Fatigue Crack Propagation in Ti-6Al-4V Alloys Containing Retained Metastable β Phase 1,835
M. Niinomi, T. Kobayashi, and A. Shimokawa

Effect of Heat Treatment on the Cyclic Softening of Ti-6Al-4V Alloy 1,843
F.J. Gil, J.M. Manero, and J.A. Planell

Effect of Heat Treatment on the Mechanical Properties of Ti-10V-2Fe-3Al for Dynamically Critical Helicopter Components 1,851
D.P. Davies

Plastic Behavior of Ti-15-3 Alloy During Tensile and Deep Drawing Deformation 1,859
L. Guozhen, Z. Shuqi, X. Liying, W. Yiqing, and H. Quan

Improvement of Hydrogen Embrittlement of Beta Ti Alloy 1,867
A. Nozue, T. Okubo, Y. Saita, and H. Sakamaki

Fracture Characteristics of Solution-Treated Ti-15V-3Cr-3Sn-3Al Alloys 1,875
K. Nagai, K. Ishikawa, T. Horiya, and H. Suzuki

Effect of Duplex-Aging After Cold-Working on the Mechanical Properties of Ti-15V-3Cr-3Sn-3Al 1,883
N. Niwa and H. Takatori

Effects of Nb and W on Mechanical Properties and Oxidation Resistance of High Temperaure Titanium Alloys 1,891
H. Chuanxi and L. Bingnan

The Tensile Properties of Post-Superplastically Formed Ti-6Al-4V Fine Grain Sheet 1,899
B.-Q. Han and Z.-R. Lin

A State Variable Material Model for Superplastic Titanium-6Al-4V 1,907
D.A. Mosher and P.R. Dawson

Small Crack Growth at Stress Concentrations in a Near Alpha Titanium Alloy 1,915
W.J. Evans, S.H. Spence, and A. Goulding

Influence of Processing Variables on the Mechanical Properties of Ti-15V-3Cr-3Al-3Sn Sheet for Helicopter Erosion Shield Applications 1,923
D.P. Davies

Influence of Thermomechanical Processing on the Mechanical Properties of Ti-6Al-4V for Helicopter Dynamic Components 1,931
D.P. Davies

Adiabatic Shear Failure of the Titanium Alloy Ti6Al4V Under Biaxial Dynamic Compression/Shear Loading 1,939
L.W. Meyer and E. Staskewitsch

Effect of Zr, Sn and Al Addition on Mechanical Properties of Metastable β Titanium Alloys 1,947
S. Isiyama and S. Hanada

Creep-Fatigue Interaction in Titanium Alloy Ti-6Al-1.6Zr-3.3Mo-0.3Si at Room Temperature 1,955
M. Tavafoghi, C. Ramachandra, A.K. Singh and V. Singh

The Behaviors of Fretting and Fretting Fatigue of Ti-10V-2Fe-3Al Alloy 1,963
S.H. Wang, Y.M. Liang, and G.Q. Shen

TABLE OF CONTENTS

VOLUME III

VOLUME I 1-956
VOLUME II 957-1,968

SURFACES, ENVIRONMENTAL EFFECTS, PROTECTION

Protective Coatings for Titanium Aluminide Intermetallics 1,971
R.L. McCarron, J.C. Schaeffer, G.H. Meier, D. Berztiss, R.A. Perkins, and J. Cullinan

Results on Nitriding Titanium and TiAl6V4 with a New Thermochemical Treatment Under High Gas Pressure 1,979
F. Preisser and P. Minarski

Metallurgy of the Ti-N System: Heat-Treatment of Titanium Mono-Nitride ... 1,989
Y.-U. Sohn, J.P. Bars, and E. Etchessahar

The Electroplating of Titanium From NaCl-KCl Fused Salt 1,997
S. Duan, Y. Kong, Z. Qiao, and X. Gu

The Strengthening of Friction Unit Parts Produced of Titanium Alloys by Explosive Coatings 2,005
V. Goldfine, I. Galeev, V. Ignatov, and S. Ushkov

Surface Hardening of Ti-6Al-4V Alloy by Electrochemical Hydrogenation 2,009
T.I. Wu

Sputter Ion Plating on Ti6Al4V and Ti(CP) - Preparation and Properties of Oxidation and Resistant Wear Coatings 2,017
M. Meyer, R. Suchentrunk, H. Franz, W. Herr, and E. Broszeit

Reliable Operation and Environmental Compatibility in Cold Forming Process with Adapted Ceramic Coatings 2,027
D.A. Keller, R. Hauert, and J. Reissner

The Oxidation of High Temperature Titanium Alloys 2,035
T.J. Johnson, M.H. Loretto, and M.W. Kearns

Environmental Influence on Fatigue Crack Growth Performance of Ti-1100 at Elevated Temperatures 2,043
R. Foerch, A. Madsen, and H. Ghonem

Investigation of Properties of α-Titanium Alloys in a Gaseous Hydrogen Medium 2,049
V.I. Sytshikov, L. Rtitsheva, S. Ushkov, V. Durjagin, and A. Repechenko

Hydrogen Assisted Stress Cracking of Titanium Alloys 2,055
I. Azkarate, A. Recio, and A. Del Barrio

Microstructure Transformation and Cracking of Titanium Alloys Under Contact Loading 2,065
P. Blanchard, S. Fayeulle, A.B. Vannes, and L. Vincent

Effects of Oxygen and Iron on the Environmental and Mechanical Properties of Unalloyed Titanium 2,073
R.W. Judy, Jr., I.L. Caplan, and F.D. Bogar

Same Regularities of Alloying Elements Effect on α-Base Titanium Alloys Embrittlement in Air and Corrosive Environment 2,081
S. Ushkov and A. Igolkin

Hydrogen Absorption of Titanium in Offshore Related Environments Under Cathodic Charging 2,087
L. Lunde, R. Nyborg, and W. Wilhelmsen

Enhancing Corrosion Resistance of the Ti-3Al-8V-6Cr-4Zr-4Mo (Beta-C™) Alloy for Industrial Applications 2,095
R.W. Schutz and M. Xiao

Electrochemical Behavior of Titanium Implanted with Molybdenum and Tantalum Ions 2,103
Y. Sugizaki, T. Yasunaga, and H. Satoh

The Effect of Beta-Stabilizers on Low Cycle Life Sensitivity of α-Base Titanium Alloys to Chloride Solutions 2,111
S. Ushkov, A. Igolkin, Y. Hesin, and L.A. Ivanova

Electrochemical Behavior of TiN Coated Titanium in a Hydrochloric Acid Solution 2,119
T. Yashiki, Y. Sugizaki, H. Tomari, and H. Satoh

Structural Characterization of Plasma Nitrided Titanium Alloys 2,127
M. Salehi, T. Bell, and P.H. Morton

Properties of Surface Oxides on Titanium and Some Titanium Alloys 2,135
N. Frey, T. Buchillier, V.-D. Lê, and S.G. Steinemann

A New Corrosion-Resistant Titanium Alloy Ti-3AR with Higher Strength 2,143
Y.J. Hu, X.Z. Cai, and G.Z. Liu

The Optimization of Descaling Oxide Skin of Ti-2.5 Cu Alloy 2,149
X.Z. Cai, Y.Q. Zhang, P.Q. Li, and H.H. Zheng

Corrosion Behavior of Ti-Ni-(Pd, Ru)-Cr Alloys in Hydrochloric Acid 2,157
K. Ueda, Y. Sugizaki, and H. Satoh

Thin N_2^+/H_2O Ion Beam Treated Titanium Layers as Diffusion Barrier for Hydrogen 2,163
B. Kempf

Ripple Load Degradation in Titanium Alloys 2,169
P.S. Pao, R.A. Bayles, S.J. Gill, D.A. Meyn, and G.R. Yoder

Oxidation Characteristics of Beta-21S in Air in the Temperature Range 600 to 800° C 2,177
T.A. Wallace, K.E. Wiedemann, and R.K. Clark

Mechanical Properties of Coated Beta-21S After Exposures to Air at 700 and 800° C 2,185
K.E. Wiedemann, R.K. Bird, T.A. Wallace, and R.K. Clark

The Detection of Crevice Corrosion in Titanium and Its Alloys Through the Use of Potential Monitoring 2,193
D.D. Bergman and J.S. Grauman

The Influence of Hydrogen on the Mechanical Properties of Timetal 21S 2,201
G.A. Young, Jr. and J.R. Scully

Hydrogen Environment Embrittlement of Beta Titanium Alloys 2,209
L.M. Young and R.P. Gangloff

A Study on the Anodic Behavior of Titanium and Some Ti Alloys in Hot Acid NaCl Solution 2,217
Y.X. Zhao, F.X. Gan, and L.-A. Yao

RAW MATERIALS, MELTING, RECYCLING AND PRIMARY PROCESSING

Raw Materials, Melting, Recycling and Primary Processing (Critical Review) 2,227
P.J. Bania

Estimating Domestic Titanium Requirements for the 90's 2,239
R.L. Fisher

Leaching of Ilmenite with Sulfuric Acid-Thiourea Solutions 2,247
F.J. Tavera, S.L. Bribiesca, and E.S. Contreras

HID and HDI Dissolution During Titanium Melting Processes 2,257
A. Mitchell and D.W. Tripp

DOSS, an Industrial Process for Removing Oxygen from Titanium Turnings Scrap 2,265
R.L. Fisher and S.R. Seagle

Preparation and Characterization of Extra-Low Oxygen Titanium 2,273
T.H. Okabe, M. Nakamura, T. Ueki, T. Oishi, and K. Ono

High Intensity Magnetic Removal of Paramagnetic Material from Recycle Titanium Turnings 2,281
R. Young

Titanium Sponge Automatic Sorting 2,287
A.N. Petrunko, V.M. Malshin, A.D. Kulkov, U.S. Levin, E.D. Samusik, and A.A. Golubev

The Effects of Plasma Cold-Hearth Melting on the Production of Titanium Alloy Ingots 2,293
J.W. Sears, J.M. Young, and M. Kearns

Recent Improvements in the Economics of Plasma Melting 2,301
R.C. Eschenbach, M.E. Schlienger, and R.E. Haun

Thermochemical Analysis of Kroll Process for Titanium Sponge Production 2,309
R.V.S. Nagesh, K.V. Rama Rao, and S. Rao

A New Method to Produce Segregation-Free Ingot of Ti-6Al-6V-2Sn by VAR 2,317
H. Hayakawa, N. Fukada, M. Koizumi, and H.G. Suzuki

Large Scale Statistically Based Exception Reporting in Vacuum Arc Melting 2,325
W. George

Electroslag Remelting of Titanium 2,331
A. Choudhury, H. Scholz, and N. Ludwig

State of the Art in Electron Beam Melting of Titanium 2,339
C.H. Entrekin and H.R. Harker
Thermal Modelling of Solidification and Cooling of an Electron Beam Melted Titanium Ingot 2,347
J.P. Bellot, A. Jardy, and D. Ablitzer
Investigation of Heat-Exchange in the Electrode Tip of the Non-Consumable Electrode Vacuum Arc Furnace for Melting Titanium 2,355
K. Rüdinger, K.-E. Piper, H. Schnecke, and P. Schüler
Production Titanium Plasma Cold Hearth Melting 2,363
W.R. Chinnis and W.H. Buttrill
Electrorefining Titanium - The Process Capability 2,371
H.W. Rosenberg and J.E. Green
Potentialities of Electroslag Remelting as Applied for Production of High-Quality Titanium Ingots 2,377
V.N. Radchenko, O.V. Tarlov, A.P. Maksimov, I.N. Dubinsky, and S.Y. Andrienko
Developing a New Continuous Process for Making Titanium 2,385
R. Winand, A. Fontana, L. Segers, P. Vernin, C. Rome, P. Dassargues, and B. Leurquin
Induction Slag Process for Producing Titanium by Reduction of Calcium Fluorotitanate 2,393
G.T. Fisher and D.E. Traut
Industrial Production of Spongy Titanium of Low Hardness and Prevention of Gas-Saturated Inclusions 2,401
A.E. Andreev, A.I. Guliakin, V.M. Malshin, V.S. Lobanov, and V.E. Lugovoy
Temperature Measurements of Surface and Evaporated Species of Molten Titanium in Thermal Plasma 2,407
A. Tomita, T. Nagane, M. Susa, and K. Nagata
Five-Tonne Titanium Ingots Produced by Skull Melting 2,415
M.I. Musatov, A.S. Freedman, and B.N. Sukhorosov
Oxygen Contamination of Titanium Sponge in the Kroll-Process 2,423
S.V. Aleksandrovsky, A.A. Zakharevich, and A.I. Guliakin
Arc-Slag Remelting of Titanium and Titanium Alloys 2,429
B.E. Paton, B.I. Medovar, V.Y. Saenko, B.B. Fedorovskii, L.B. Medovar, V.V. Shepelev, V.A. Riabinin, and J.J. Shutey
Electrowinning of Titanium from Sulfuric Acid Titanium Solutions 2,439
S.L. Briblesca, E.S. Contreras, and F.J. Tavera
Characteristics of Niobium-Aluminum Master Alloy for Production of Advanced Titanium Alloys 2,445
E.A. Loria
Titanium Alloy Hearth Melt Technology 2,451
C.E. Shamblen, W.H. Buttrill, and G.B. Hunter
Industrial Production of High Purity Titanium by the Improved Iodide Process 2,459
Y. Yoshimura, Y. Shimizu, and Z. Imamura

METAL MATRIX COMPOSITES

Titanium Based Composites (Critical Review) 2,467
T.W. Clyne and H.M. Flower

Continuously Reinforced Titanium Based MMC's Produced by the Matrix Coated Fibre Process 2,479
C.M. Ward-Close and P.G. Partridge

Microstructures and Tensile Properties of Titanium-Based Composites Produced by Powder Metallurgy 2,487
M. Hagiwara, S. Emura, J. Takahashi, Y. Kawabe, and N. Arimoto

Selective Reinforcement of Investment Cast Titanium Components Via Bicasting 2,495
S.J. Veeck and G.N. Colvin

Titanium/Ceramic Composites Produced by Laser Processing 2,503
J.H. Abboud and D.R.F. West

Advanced Powder Metal Titanium Alloy Matrix Composites Reinforced with Ceramic and Intermetallic Particles 2,511
S. Abkowitz and P. Weihrauch

Combustion Synthesis of TiC-Al_2O_3-Ti Ceramic-Metal Copmosite Materials: An Initial Phenomenological Examination 2,519
K.R. Hunter, J.J. Moore, and D. Wirth

Micromodelling and Methodology of Assessment of Fibre Reinforced Titanium Metal Matrix Composites Using Fracture Mechanics Parameters 2,529
D.C. Cardona and P. Bowen

Micromechanical Prediction of the Thermal Stresses in Sigma Fiber (SiC)/β-21S Titanium Composite: Effect of Coefficient of Thermal Expansion of the Coating 2,537
D. Upadhyaya, D.M. Blackketter, and F.H. Froes

Fiber-Matrix Interfacial Behavior in SiC-Titanium Alloy Composites 2,545
I. Roman, S. Krishnamurthy, and D.B. Miracle

Fiber/Matrix Interface Structure and Fracture Behavior in Continuous SCS-6™ Reinforced Ti-15-3-3-3 2,553
D.E. Morel

Interfacial Reaction Kinetics in α- and β- Titanium Based Metal Matrix Composites 2,561
E.N.T. Jong, H.M. Flower, and D.R.F. West

The Use of Pushout Testing to Investigate the Interfacial Mechanical Properties in Ti-SiC Monofilament Composites 2,569
M.C. Watson and T.W. Clyne

Micromechanisms of Damage in Fibre Reinforced Titanium Based Metal Matrix Composites 2,577
A.R. Ibbotson, M.V. Hartley, C.J. Beevers, and P. Bowen

The Forging Characteristics of Two Ti-6Al-4V-Based Particulate Composites 2,585
T.P. Johnson, M.H. Loretto, M.J. Walker, and M.W. Kearns

Longitudinal Creep Behavior and Damage in SCS-6/Ti-6Al-4V Metal Matrix Composites 2,593
S.W. Schwenker, D.J. Evans, and D. Eylon

Cyclic Fatigue Resistance of Fibre Reinforced Titanium Metal Matrix Composites at Ambient and Elevated Temperatures 2,601
A.R. Ibbotson, P. Bowen, and C.J. Beevers

Deformation Mechanisms in a Ti-Alloy/SiC Metal Matrix Composite 2,609
B.S. Majumdar, G.M. Newaz, F.W. Brust, and J.R. Ellis

Microstructural Property Correlation in a Unidirectional SiC (SCS-6) Fiber-Reinforced Ti-24Al-11Nb Composite 2,617
G. Das

Microstructure of Unidirectional SiC/Ti-24Al-11Nb Composite Deformed in Tension, Fatigue and Creep 2,625
G. Das, S.M. Russ, and M. Khobaib

SiC Fibre/Ti-Based Composites: Processing, Microstructure and Interface Properties 2,633
Z.X. Guo and B. Derby

Metal-Ceramic Composite Layer Formation on Titanium Surfaces Through Laser Treatment 2,641
S. Mridha, H.S. Ubhi, P. Holdway, T.N. Baker, and A.W. Bowen

Interfacial Properties and Fatigue Crack Propagation in Continuously Reinforced Ti/SiC Metal Matrix Composites 2,649
K.M. Fox, P.J. Cotterill, M. Strangwood, and P. Bowen

NON-AEROSPACE APPLICATIONS

New Development in Application of Titanium as an Ecological Metal: Non-Aerospace Application/Environment and Development 2,659
K. Sakai

Application of Near Beta Titanium Alloys for Turbine Blades 2,673
A. Takemura, Y. Ashida, H. Ohyama, A. Morita, S. Hattori, K. Tani, A. Hasegawa, and T. Matsumoto

The Development of γ/α_2 Titanium Aluminides for Exhaust Valves 2,681
W.E. Dowling, Jr., J.E. Allison, and A.M. Sherman

Beta-Titanium Alloy for Surgical Implants 2,689
S.G. Steinemann, P.-A. Mäusli, S. Szmukler-Moncler, M. Semlitsch, O. Pohler, H.-E. Hintermann, and S.M. Perren

Low Modulus, High Strength, Biocompatible Titanium Alloy for Medical Implants 2,697
K. Wang, L. Gustavson, and J. Dumbleton

The Electrochemical Behavior of a New Titanium Alloy with Superior Biocompatibility 2,705
P. Kovacs and J.A. Davidson

The Dynamic Interaction Between Titanium and Snow 2,713
M. Abe, H. Ito, K. Ueda, H. Aoyagi, and T. Nishimura

Beta Titanium in the United States Surface Navy
Improved Water Brake 2,721
S.L. Opet, Jr., and D.F. Peters
Production of Titanium 6Al-4V ELI Electronic Bottles
for the Curv III Submersible 2,729
M.E. Wells and J.A. Sasse
Corrosion Behavior of Timetal-21S for Non-Aerospace Applications 2,737
J.S. Grauman
Anodizing Mechanisms in High Purity Titanium 2,743
H.W. Rosenberg and M.S. Cooper
A Ti-5%Ni Alloy Electrode for Production of Electrolytic
Manganese Dioxide 2,751
K. Taki, Y. Mitsuyoshi, and H. Sakuyama
Development of Endosseous Implants on the Base of Titanium Alloys
with Improved Functionality 2,757
J. Breme, W. Schulte, and K. Donath
Development of a new Casting Technology for Dental Applications
Using Titanium 2,765
H. Brauner, U. Holzwarth, and U. Zwicker
Superplastic Forming of Ti-6Al-4V Denture Base 2,773
M. Okada, H. Mitsuya, and I. Katoh
The Use of Titanium Chelate in Agriculture 2,779
M.-L. Huang, X.-D. Tang, and L. Liu
A New Low Cost Titanium Alloy 2,787
P.J. Bania, A.J. Hutt, R.E. Adams, and W.M. Parris
Titanium Tubing Experience in Utility Condensers 2,795
P.L. Moore and M.J. Nugent

INSPECTION, NDE, QUALITY ASSURANCE, DEFECTS

Quality Assurance for Titanium Critical Applications 2,805
P. Martin and J.P. Herteman
Laser Ultrasonics for Large Metal Structures 2,819
C. Calder, H. Park, and D. Hiatt
Ultrasonic Noise and Its Influence on Flaw Detection
in Aircraft Engine Alloys 2,827
R.B. Thompson, J. Rose, F.J. Margetan, and Y.K.H. Han
Confirmation Test Methods for Titanium Tube Damage
of Steam Surface Condenser 2,835
M. Goto and Y. Itabashi
Analyzing High Purity Titanium 2,843
H.W. Rosenberg and J.E. Green
Radioautography Investigation of the Distribution Regularities (Carbon)
in Ingots as Well as Forgings of Pseudo-Alpha-Titanium Alloys 2,851
*E. Karasev, A. Kudrjavtsev, V. Kurapov, V. Tetjukhin, S. Ushkov,
V. Urtjev, and A. Trubin*

Ultrasonic Inspection of Titanium Billets 2,859
J. Vinot, C. Moisson, and Y. Combres
The Role of Melt Related Defects in Fatigue Failures of Ti-Al-4V 2,867
K.R. Clark, A.B. Dillard, B.C. Hendrix, J.K. Tien, and T. Denda

AEROSPACE APPLICATIONS

Application of Ti Alloys in the European Aerospace Industry 2,877
P.-J. Winkler, M.A. Däubler, and M. Peters
Titanium Application in Aviation Industry of China 2,891
C. Li and J. Ma
Ultra High Strength Titanium Alloy for Fasteners 2,899
P.J. Bania, A.J. Hutt, and R.E. Adams
Applications of Titanium Aluminides in Gas Turbine Engine Components 2,907
P.J. Postans, M.T. Cope, S. Moorhouse, and A.B. Thakker
The Titanium Investment Casting Technology 2,915
K.-D. Folkers
Timetal·1100 Sheet Properties 2,923
A.J. Hutt and W.M. Parris
Rolls-Royce's Wide Chord Fan Blade - The Next Generation 2,931
G.A. Fitzpatrick and J.M. Cundy

ADDENDUM

Pressure Welding Process Window for Ti-6Al-4V 2,941
R.E. Sundell, M.F.X. Gigliotti, and L. Hellemann

Subject Index 2,949
Author Index 2,973

PLENARIES

TITANIUM PROCESS MODELLING

F. H. Froes[1], H. L. Gegel[2], C. H. Hamilton[3],
G. W. Kuhlman[4], and J. H. Moll[5]

1. Director and Professor, Institute for Materials and Advanced Processes (IMAP) College of Mines, University of Idaho, Moscow, ID., 83843.
2. Director, Materials Processing and Manufacturing Division, UES, Inc., Dayton, OH., 45432-1894.
3. Professor, Materials Science and Engineering, Department of Mechanical and Materials Engineering, Washington State University, Pullman, WA., 99164.
4. Director of Technology, Alcoa Forged Products, 1600 Harvard Av., Cleveland, OH., 44105.
5. Technical Director, P/M and Titanium, Crucible Research, 6003 Campbells Run Road, Pittsburgh, PA., 15205-1022.

ABSTRACT

Wide-spread use of titanium alloys in demanding aerospace and terrestrial applications is often stymied by the high cost of fabrication of titanium components. The present paper discusses the application of process modelling to four titanium fabrication methods: forging, superplastic forming, powder metallurgy, and casting. It is demonstrated that this allows lower cost processing due to greatly reduced pre-production trial-and-error, and more reproducible and closer to final shape production parts. In addition process modelling allows greater control over microstructure of fabricated parts, leading to a tighter scatter-band in mechanical properties, and therefore an increase in minimum specification mechanical property levels.

Introduction

Because of the attractive combination of mechanical properties exhibited by titanium alloys - a fact well documented in the papers which follow in these proceedings - titanium is the designers choice in many demanding aerospace and terrestrial structural applications. However often the inherently high cost of titanium components results in titanium being used when it is the only material which can perform adequately. Thus over the years there have been many attempts to reduce the cost of titanium components, with an emphasis on near net shape approaches(1,2).

Essentially a different segment of the titanium community has spent considerable time defining, and refining, chemistry - processing (synthesis) - mechanical property relationships (1). This has led to a large data bank of information (3,4) which allows careful control of the chemistry and microstructure to lead to increased levels of specification minimum mechanical properties for a given titanium alloy (4). That is by reducing variations in

Titanium '92
Science and Technology
Edited by F.H. Froes and I. Caplan
The Minerals, Metals & Materials Society, 1993

chemistry and microstructure the spread of mechanical property values is also reduced.

The present paper brings together the cost and performance aspects of titanium technology. Processing modelling is a science-based technique which allows reduced cost near net shape processing by (a) cutting down on expensive trial and error pre-production shape-making activities, and (b) resulting in more reproducible closer to net shape production components. At the same time process modelling also allows greatly improved prediction/control of the metal movement during processing (5,6), which directly relates to the amount of deformation occurring in specific locations of a component, and in turn the microstructure and mechanical properties (1).

The application of process modelling to four component fabrication techniques will be addressed in this paper: forging, superplastic forming, powder metallurgy and casting.

Forging

Background

Many forged parts ranging from small simple shapes to large complex configurations are produced from titanium alloys particularly for use in the aerospace industry. The forging industry is as a capital intensive business, where success necessitates effective and efficient utilization of critical capital resources. However, historically, the forging industry has used empirical technologies and a great deal of know-how and experience has accumulated, largely through costly and time consuming trial-and-error methods.

In the late 1970's CAD (Computer Aided Design) and CAM (Computer Aided Manufacturing) technologies were explored and resulted in the emergence of two powerful Finite Element Analysis (FEA) codes, specifically in 1983 ALPID (Analysis of Large Plastic Inelastic Deformation) (7) and in 1990, a significant enhancement called DEFORM (Design Environment for FORMing)(8,9). The development of these two codes, along with major advances in the efficiency, speed and cost of mini-computer hardware revolutionized use of FEA in forging process modelling (10-16).

Because FEA is a costly process in terms of manpower and computer expense that must be carefully managed in the cost build-up of a given part, it is very efficient to use with difficult to fabricate alloys such as titanium. The critical design, processing and manufacturing areas that a forging engineer must attempt to answer in the forging of titanium parts using FEA are:

* Die design, die stresses and die compatibility particularly with multiple die sets
* Preform shape, blocker shape and/or finished part design and compatibility
* Defect prediction and/or adequacy of die fill
* Total effective strain and/or strain rate optimization
* Unit pressure optimization
* Die and part temperature interactions, prediction and/or optimization
* Forging grain flow and strain distributions
* Thermal history and/or thermal treatment optimization
* Final product microstructure and mechanical properties optimization

Major reductions in the cost of developing new forging shapes and in flow times from design to successful part manufacture and/or enhanced final product uniformity and conformance to geometry and mechanical property specifications using FEA have occurred (11-13, 16). For example, some workers (10-13) have reported flow time reductions by as

much as 50 to 75%.

Process Modelling

The advantages to be gained by modelling a very large Ti-6Al-4V dome closed-die forging (Fig.1a) used in a power generation application with the DEFORM code is shown in Fig.1. Fig.1b illustrates temperature profiles predicted in the finished conventionally forged part using the appropriate constitutive law for the material; variables include preform geometry, material and die temperature, strain rate, and strain. Combining temperature data and total effective strain contour predictions (Fig.1c) allows prediction of the final microstructure and hence mechanical properties.

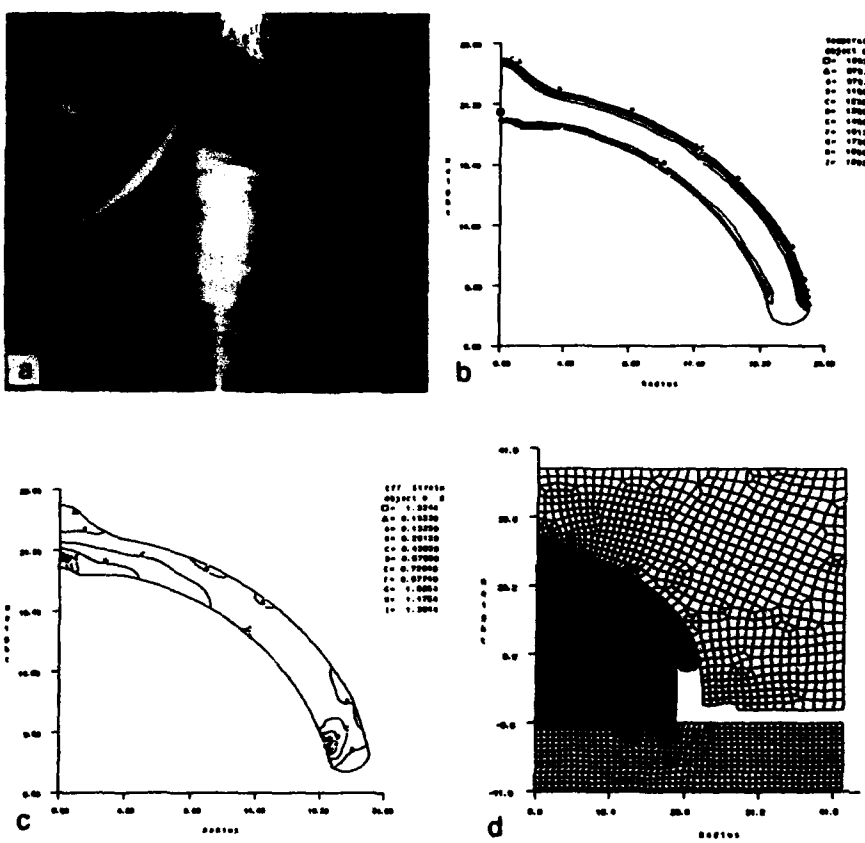


Fig. 1. (a) Ti-6Al-4V Dome Close-Die Forging, (b) Predicted Temperature Profiles, (c) Predicted Total Effective Strain, and (d) Simulation of Partial Die Fill.

In the future, with Artificial Intelligence and Expert Systems approaches, microstructure development in forging may be physically coupled with the FEA modelling process, but this needs further fundamental work and correlation with experimental data.

The Ti-6Al-4V closed-die forging can also be used to demonstrate die and/or part design and geometry problems successfully managed through FEA. Fig.1d illustrates a partially complete simulation of die fill which, using computer animation techniques, allows the forging sequence to be presented in real time. This program in combination with predictions of die stresses and stress vectors, allows prediction of factors such as die design/manufacture, degree of fill, defect generation, and die life before committing to the actual forging operation.

ALPID and DEFORM are excellent 2D FEA models handling forging geometries best represented by surfaces of revolution very well. However they are very numerically and computer intensive for complex parts, a significant time and cost factor. For very complex forgings, such as airframe web-rib shapes, 2D solutions with these codes can result in significant inaccuracies. Development of 3D FEA codes is embryonic and will probably require at least five years for wide-spread use to occur. However, significant advances have been made in the process modelling of titanium forgings and use is increasing steadily.

Superplastic Forming

Background

Superplastic forming (SPF) of titanium alloys has matured in the past 20 years to the point where it is widely used for sheet forming in the aerospace industry (17,18). The cost of forming presses is quite high, thus there is a large incentive to maximize production rates including minimization of time spent on trial-and-error work. Improvements in productivity can be achieved through alloy development, but the cost and lead time for this are high. A more effective approach is better understanding of the mechanics of the process and the material being formed which requires both a good representation of the material flow properties, expressed through a constitutive relationship, and a mechanical model.

Process Modelling

Mechanical Modelling of SPF: Early solid mechanics models using specific relatively simple geometries (19,20) led later to representation of complex stress/strain-rate relationships with fourth order polynomial functions (21,22). This early work provided valuable insight into the effects of forming parameters, and was of value in guiding the rate of pressure application to keep strain rates in the superplastic region, while processing at a higher rate than would otherwise be possible. More recently, the emergence of FEA methods has lead to development of models which are more adaptive to complex configurations, albeit more computer-time intensive (23-27). The material deformation properties and characteristics are represented by a constitutive relationship and related flow rule, and are incorporated intrinsically into the FEA model.

By assuming that the macroscopic behavior of the material is isotropic and obeys the von Mises flow rule, and by neglecting elasticity and assuming quasi-static deformation, a viscous flow model which proves to be very efficient for large deformation problems has been developed (26). The solution requires an iterative scheme, often incorporating grain size evolution.

To date most FEA models efforts have generally been limited to prediction of thicknesses in a forming sheet, but very recently efforts have been made to establish control algorithms to predict forming pressure profiles (28).

Constitutive Relations: Constitutive relations based on microstructural modelling invoke dislocation motion and diffusional accommodation (26,29). The strain rate sensitivity, m, for alpha-beta titanium alloys of 0.6 to 0.75 (30) can be accounted for by a grain size distribution and diffusional accommodation. To represent real behavior a microstructure-based constitutive model must be formulated allowing the m parameter to be set from experimental results.

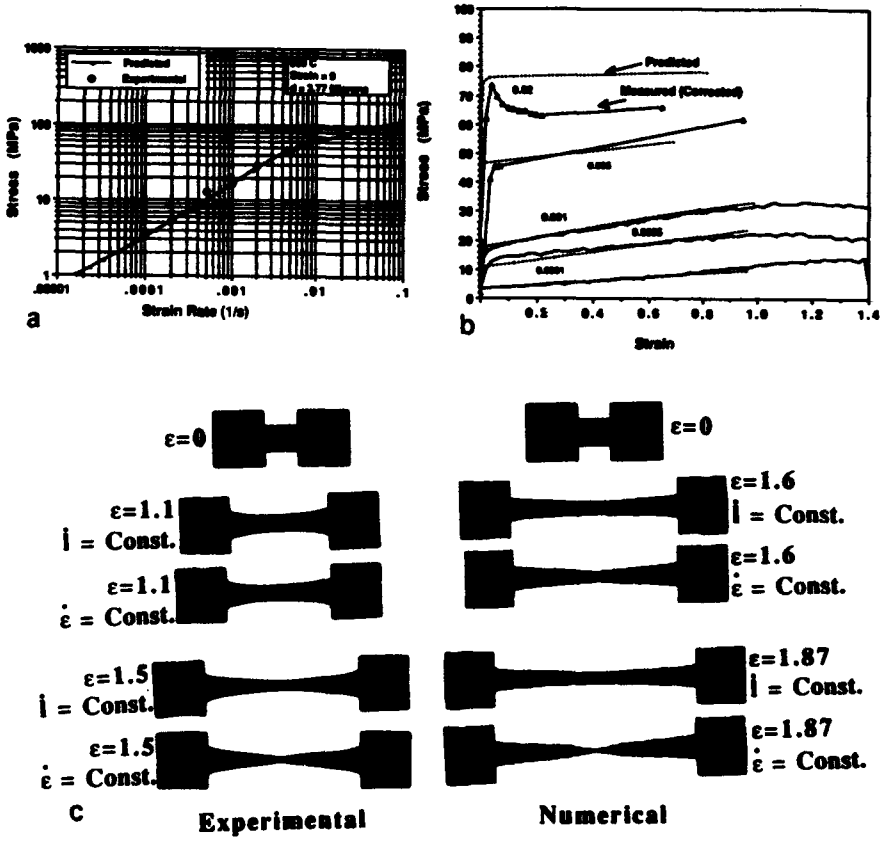


Fig. 2. (a) Stress vs. Strain Rate Curves from Constitutive Relationship (Solid Curve) and Experimental Data (Solid Points) for Ti-6Al-4V at 900°C, Stress for Strain =0 and Grain Size Present at Initiation of Test, (b) Correlation of Stress vs. Strain Characteristics for Ti-6Al-4V at 900°C Measured Experimentally and Predicted Using a Constitutive Relationship Incorporating Static and Deformation-Enhanced Grain Growth, at the High Strain Rate, above the Superplastic Strain Rate Region Dynamic Recrystallization Occurs which is not Accommodated in the Grain Growth Model, and (c) Thinning in Ti-6Al-4V Tensile Test Specimens at 900°C, Experimental and Computed, $\dot{\epsilon}$ is Strain Rate and $\dot{l}$ is Extension Rate.

Grain size, which can vary in different parts of the sheet, has a strong influence on the stress; therefore it must be specified continuously during deformation. The diffusivity

must also be specified for example in terms of a combined grain boundary diffusivity and lattice diffusivity. The characteristic log (σ) vs. log ($\dot{\epsilon}$) curve resulting from this approach (26) is sigmoidal in shape and consistent with that observed for the Ti-6Al-4V alloy, as shown in the representative Fig.2a for the onset of deformation; i.e., strain = 0.

Dynamic Grain Growth: The grain growth during superplastic deformation is accelerated above that for static grain growth due to an increase in grain boundary vacancy concentration (30-32). Incorporation of the appropriate grain size into the constitutive relation leads to a good prediction of the actual flow hardening, for example, for the Ti-6Al-4V alloy at 900°C Fig.2b.

Model Computations: Grain growth rate varies with strain rate, and m varies with grain size, thus the rate of necking is affected by the strain rate path imposed (26). Experimental studies using the Ti-6Al-4V alloy, and FEA model computations using the microstructure-based constitutive relation, indicate neck development for different deformation paths (Fig. 2c).

By bringing the constitutive relation into the FEA numerical model prediction of SPF characteristics, including prediction of optimum pressure cycles, are possible for complex thin sheet components where a balance between computational time and precision in thinning predictions is desired.(28, 33, 34)

Powder Metallurgy

Background

In recent years, considerable work has been conducted to develop powder metallurgy processes for titanium alloys as a lower cost approach to part fabrication (35-38). A number of techniques have been developed including prealloyed, blended elemental, rapid solidification, and mechanical alloying; only the first will be considered here.

The prealloyed approach has matured to the point that virtually any titanium alloy can be produced as powder, consolidated to form simple or complex shapes (Fig.3a), and exhibits mechanical properties equal or superior to castings or forging (39). Implementation has been slow however, due to designer conservatism. (36)

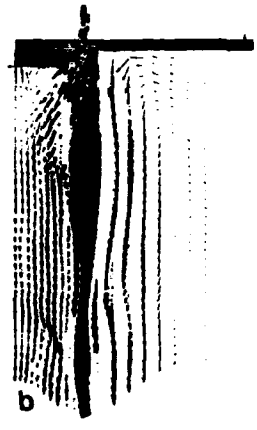
Process Modelling

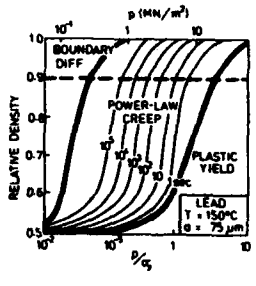
Atomization: Gas atomization has been recently developed to produce titanium based prealloyed powder with a range of particle sizes (40). However, many current potential applications require a specific particle size: for example, plasma spray deposition used for making metal matrix composites, or powder with a particular solidification rate (38). Thus sophisticated techniques including Schlieren photography, pulsed laser holography, high speed cinematography, in situ particle size measurement via laser interferometry, and invasive fluid dynamic measurement of the gas flow field have been used to model and control particle size (41). Recently a Computational Fluid Dynamic (CFD) program for modelling the gas-only flow field of gas atomization dies has been developed which is useful for defining the effects that factors such as die geometry and gas parameters (e.g., gas species, pressure, temperature, etc.) have on the gas flow field, and hence powder particle size. Fig. 3b shows an example of the predicted gas flow velocity field produced for an elementary die geometry, where the lengths of the arrow are proportional to velocity. Similar plots can be made for gas density, mach number, and energy. This work should lead to optimization of the operation of existing atomization dies.

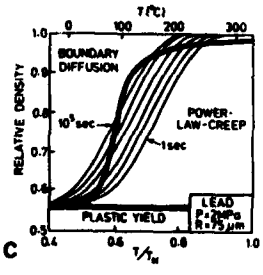
Densification and Shape Making: The precise prediction of large complex shapes by hot-isostating pressing (HIP) (e.g. Fig.3a), is difficult because the densification process results in non-uniform shrinkage leading to a distorted part. The problem is particularly difficult because it results from a large number of interacting factors including:

* Powder density/shape
* Powder mechanical properties
* Geometry of the part
* Mechanical properties of container
* Fabrication of container
* Consolidation conditions









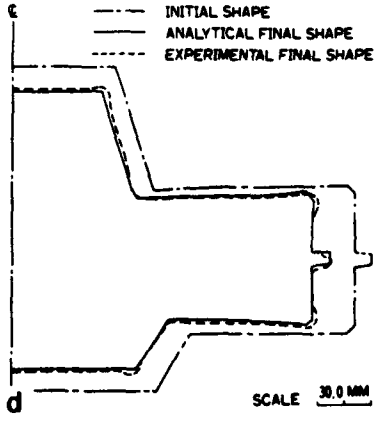


Fig. 3. (a) Complex PM Airframe Part Produced Using the Ceramic Mold Process, (b) Predicted Velocity in the Gas Flow Field for an Elementary Atomization Die Geometry, (c) HIP Diagrams Showing the Interrelationship between Time, Temperature, Pressure and Density, and (d) Comparison of the Final Predicted Shape and Actual Final Shape.

Modelling and prediction of densification/shape change during HIP has resulted in HIP diagrams (42) which are useful in selecting conditions to achieve desired density in a specified time at a certain pressure (Fig.3c). These can be used to trade off temperature for pressure where high temperature exposure is undesirable due to microstructural coarsening.

Modelling of the shape making aspect of the HIP densification process has been improved by the recent development of a technique to monitor dimensional changes in real time using a eddy current sensor technique to measure cross-sectional area during HIP (43). Using this technique a phase transformation during heating of as-atomized powder during HIP was shown to result in an unexpected increase in densification rate around 800°C; the effect was removed with a subsequent anneal.

Good agreement between predicted and actual final shape have been attained in modelling the HIP process using FEA, for example for turbine disc parts (Fig.3d) (44).

Castings

Background

Titanium alloy castings are seeing increased use in the aerospace industries because of their low cost and improving mechanical properties (45, 46); only the high integrity investment casting approach will be addressed in this paper.

Advancements in the investment casting industries have made it possible to cast complex net shapes which previously required multiple parts followed by joining to form a single component (Fig.4). Stringent quality requirements for aerospace structural castings demand precise processing parameters to produce high quality castings on a repeatable basis; with product characteristics such as alpha case depth, optimum filling rate, and casting dimensions major challenges which modelling should help to solve (47).

The quality of a titanium investment casting, its microstructure and mechanical properties, and development time and cost depend on the process parameters (48) including:

* Processing materials selection
* Equipment selection
* Processing parameters
* Post processing parameters
* Mold design
  - shell
  - rigging system

Although the quality of a casting is primarily set during the filling and solidification stage, certain casting defects and microstructures can be altered by post processing, including chemical milling, HIP and weld repair, and heat treatment.

The single most important factor in titanium investment casting is the design of the molds. The mold design includes the selection of casting orientation for pouring, the number of castings in a cluster, the gating and risering system design, shell thickness design, insulation and chill design, pouring rate and selection of allowances for operations such as chemical milling, casting dimensional and wax pattern shrinkage.

Process Modelling

Casting involves simultaneous heat flow, fluid flow, stress analysis, and phase transformations presenting a difficult challenge to process modelling. Currently number of simulation tools employing FEA and finite difference techniques are available to the casting industry.

Shell Generation Tool: The building of the casting and mold geometry has been enhanced by making use of an automatic tool to build the shell around the casting geometry. This tool

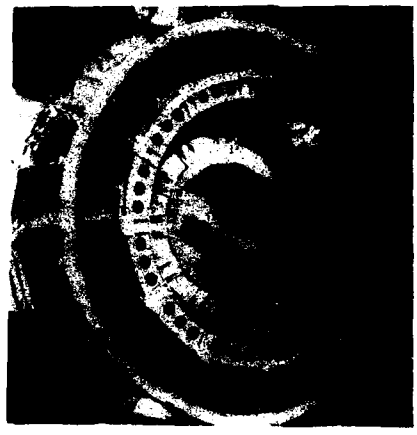


Fig. 4. Large Complex Investment Casting, Ti-6Al-4V Fan Frame for General Electric CF6-80C Gas Turbine Engine Case (Courtesy PCC).

enables the user to build different shell thicknesses and to apply suitable boundary and initial processing conditions, such as shell temperature and pour atmosphere, for modelling.

Solidification Modelling: The radiation effect of the mold on the adjacent cast part in a clustered casting or even in a single casting has a strong influence on the solidification pattern. Therefore, the solidification analysis tool should take this factor into account in FEA calculations, and tools are available to do this job efficiently.

Modelling Mold Filling: Titanium alloys generally have a short freezing range and therefore, in casting thin walled structural castings, the shell temperature, pouring rate and pouring temperature must be carefully selected or the casting will solidify prematurely and develop a cold-shut. Process modelling, which can model combined mold filling and solidification is thus highly desirable. Using such an analysis tool, the process designer can optimize the pouring temperature, shell temperature and pouring rate. The modelling of mold filling also helps the process designer to develop an efficient rigging system.

Alpha Case Depth Prediction Tool: The brittle alpha case (45,46) removal is a problem for foundries, especially on castings with varying section thicknesses. Thus a tool which will predict the case depth is highly desirable, allowing appropriate chemical milling allowances.

Dimensional Contraction Prediction by Simulation: The final dimensions of any investment casting depend on the allowances provided for wax pattern contraction, shell mold expansion, casting material contraction and the often non-uniform chemical milling. Tightly coupled FEA thermal, fluid, and stress analysis, combined with the alpha case formation model allow appropriate allowances to be defined leading to close dimensional tolerances on the final casting.

The most important and time consuming element of process design is the building of a casting geometry and generation of a finite element mesh. Fig.5a shows the finite element

mesh on a (quarter) investment casting cluster with down sprue, runners, and ingates without the shell. Fig.5b illustrates the automatically generated shell mold for the test piece casting cluster. Fig.5c shows the metal flowing into the three dimensional mold. In producing thin wall castings of titanium alloys, this feature is highly useful in designing an optimum rigging system. Fig.5d shows an example of an isochron diagram, that is a schematic of the temperature at various locations in the casting, in this case at the solidus temperature. Such plots help to predict alpha case and casting shrinkage defects.

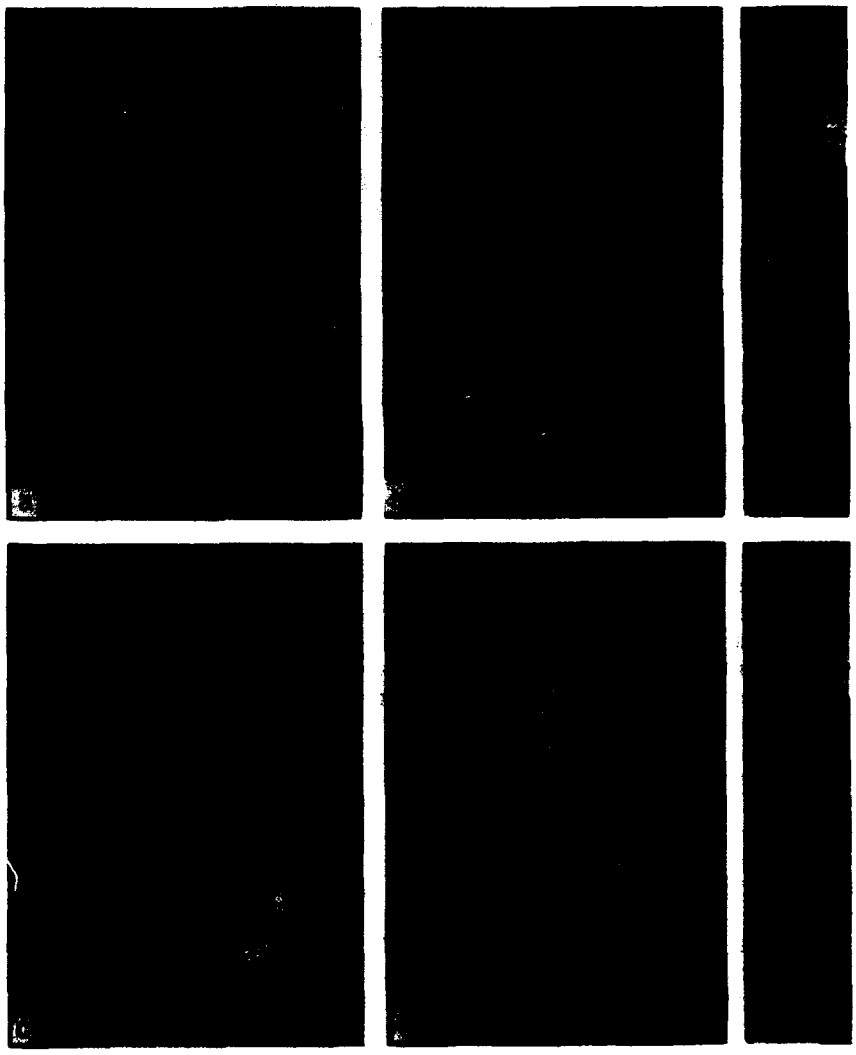


Fig. 5. (a) Casting Cluster with Finite Element Mesh, Quarter Shown, (b) Automatically Generated Shell Over Casting Cluster, (c) Metal Flow into the Mold and (d) Predicted Ischron in Casting at Solidus Temperature (originals in color).

Concluding Remarks

The application of process modelling to fabrication of titanium components has been presented. Four fabrication techniques have been discussed: forging, superplastic forming, powder metallurgy and casting. Both cost reduction and enhancement in mechanical property specification levels can result from use of process modelling in association with these processing methods. While advances have been made it is clear that more wide-spread use will result in the future with development of more realistic models, including three dimensional concepts.

Acknowledgements

The authors would like to acknowledge the assistance of D. F. Carbaugh, M. D. Crowley, C. F. Yolton and T. Veerabadran in paper preparation. We also recognize Miss Aimee Keller and Mrs. Kandy Nelson for formatting and typing the manuscript.

References

1. F. H. Froes, D. Eylon and H. B. Bomberger, eds., Titanium Technology: Present Status and Future Trends, (1985), TDA, Dayton, OH.
2. F.H. Froes and D. Eylon, eds., Titanium Net Shape Technologies, (1982), TMS, Warrendale, PA.
3. R. R. Boyer and J. A. Hall, "Microstructure - Properties Relationships in Titanium Alloys - A Critical Review", this conference.
4. P. A. Blenkinsop, "Advanced Alloys and Processes",this conference.
5. T. Altan, S. I. Oh and H. Gegel, Metal Forming Fundamentals and Application, ASM Int., Materials Park, OH., (1983) 5.
6. John Walters, J. of Mat. Proc. Tech. 27 (1991) 43.
7. W. T. Wu and S. I. Oh, of NAMRC-XIII Conference, Berkely, California, (1985) 449.
8. S. I. Oh, W. T. Wu, J. P. Tang and A. Vedhanayagam, J. Mat. Proc. Tech., 27 (1991) 25.
9. W. T. Wu, S. I. Oh, T. Altan, and R. A. Miller, 1990 ASME Inter. Computers in Engineering Conf., ASME Aug. 1990, Boston, 283.
10. H. E. Delgado, 1990 Trans. of NAMRI/SME, 84.
11. T. E. Howson and H. E. Delgado, JOM, (3), (1989) 32.
12. J. Walters, J. Mat. Proc. Tech., 27 (1991) 43.
13. S. N. Dwivedi and R. Shankar, Ad. Mats. and Proc., Feb. 1990, 23.
14. M. Rebela and C. R. Boer, "A Process Modelling Study of the Influence of Friction During Rib Forging", BBC Brown Boveri Company, Ltd., Research Center, KLR, Baden, Switzerland, (1989).
15. S. P. Dudra and Y. T. Im, J. Mat. Proc. Tech., 21 (1990) 143.
16. H. E. Delgado, Proceedings of Complas II, Second Int. Conf. on Computational Plasticity, Barcelona, Spain, Sept. 1989, 121
17. C. H.Hamilton, and N. E. Paton, eds. Superplasticity and Superplastic Forming, (1988), TMS, Warrendale, PA.
18. S. Hori, M. Tokizane, and N. Furushiro, eds. Superplasticity in Advanced Materials, (1991), Japan Society for Research on Superplasticity.
19. G. E. Cornfield, and R. H. Johnson, Int. J. Mech. Sci., 12 (1970) 479.

20. F. Jovane, Int. J. Mech. Sci., 10 (1968) 403.
21. A. K. Ghosh, and C. H. Hamilton, Process Modelling: Fundamentals and Applications to Metals, ASM Int., Materials Park, OH.,(1979) 331.
22. A. K. Ghosh, and C. H. Hamilton, Metall. Trans., 13A (1982) 733.
23. N. Chandra, and K. Chandy, J. Mater. Shaping Technol., 9(1), (1991) 27.
24. N. Chandra, S. C. Rama, and R. E. Goforth, in Advanced Materials, Osaka, Japan: The Japan Society for Research on Superplasticity, (1991) 837.
25. J.S. Doltsinis, J. Luginsland, and S. Nolting, Eng. Comput., 4 (4), (1987) 266.
26. C. H. Hamilton, et al., in Second Japan International SAMPE Symposium and Exhibition, Chiba, Japan, (1991) 272.
27. M. U. Polat, and M. A. Dokainish, Comp. and Struct. 36 (2), (1990) 251.
28. J. Bonet, A. H. S. Wargadipura, and R. D. Wood, Commun. Appl. Numer. Meth., 5 (1989) 121.
29. B. P. Kashyap, and A. K. Mukherjee, "On the Models for Superplastic Deformation in Superplasticity", Grenoble, France: Centre National de la Recherche Scientifique, Paris, (1985) 4.1.
30. A. K. Ghosh, and C. H. Hamilton, Metall. Trans., 10A (1979) 699.
31. M. A. Clark, and T. H. Alden, Acta Metall. 21 (1973) 1195.
32. K. Holm, J. D. Embury, and G. R. Purdy, Acta Metall., 25 (1977) 1191.
33. J. Bonet, R. D. Wood and Zienkiewicz, Ref. 17, 291.
34. J. Bonet, R. D. Wood, and Wargadipura, Int. J. Num. Meth. Eng., 30 (1990) 1719.
35. F. H. Froes and J. E. Smugeresky eds., Powder Metallurgy of Titanium Alloys, (1980) TMS, Warrendale, PA.
36 F. H. Froes and D. Eylon, Int. Mat. Reviews 35 (3), (1990) 162.
37. A. Vassel and F.H. Froes, "Synthesis of Titanium Alloys by Powder Metallurgy, Nanostructured Materials, and Thermochemical Processing", this conference.
38. F.H. Froes and C. Suryanarayana, "Powder Processing of Titanium Alloys", in Reviews of Particulate Materials, eds. A. Bose, R. German and A. Lawley, (1993), Pub. by MPIF, Princeton, NJ.
39. J. H. Moll and C. F. Yolton, Modern Developments in Powder Metallurgy, 19 (1988) 709.
40. C. F. Yolton, P/M in Aerospace and Defense Technologies ed. F. H. Froes MPIF, N. J.,(1990) 123.
41. S. D. Ridder, S. A. Osella, P. I. Espina and F. S. Biancaniello, Int. J. of PM, 28 (2), (1992) 133.
4`. M. F. Ashby, Proc. Int. HIP Conf. - Lulea/15-17 June 1987, Centek, Sweden, (1988) 29.
43. R. J. Schaefer, G. M. Janowski, and A. H. Kahn, Industrial Heating, December (1990) 34.
44. T. Soh, A. Nohara, and T. Nakagawa, as Ref. 42, 81.
45. D Eylon, F. H. Froes and R. W. Gardiner, Ref.1, 35.
46. C. V. White, D. Eylon and F. H. Froes, eds., High Integrity Castings, ASM Int., Metals Park, OH. (1988).
47. Vijay Shende, Thiru Veerabadran, Mark Samonds and Sokka Doraivelu, "Knowledge Integration Design Systems (KIDS)", Int. Rpt., WL-TR-91-4107, Wright Laboratories, WPAFB, OH., (1992).
48. J. Schadlich-Stubenrauch, P.R. Sahm and H. Linn, Sixth World Conference on Titanium, Société Française de Métallurgie, eds. P. Lacombe, R. Tricot and G. Béranger, (1989) 649.

ADVANCED ALLOYS AND PROCESSES

P. A. Blenkinsop*

Interdisciplinary Research Centre in Materials
For High Performance Applications
University of Birmingham, B15 2TT
United Kingdom

Abstract

The four years since the last World Titanium Conference have been a period of consolidation of existing alloys and processes. While the aerospace industry remains the principal driving force for alloy development, the paper illustrates examples of new markets being established in 'older' alloys, by a combination of product/process development and a re-examination of engineering design parameters.

Considerable attention is still being directed towards the titanium aluminide systems, but other more conventional alloy developments are underway aimed at specific engineering and process requirements, both in the aerospace and non-aerospace sectors. Both the advanced high temperature and conventional alloy developments are considered, before the paper goes on to assess some of the new processes and products, like metal matrix composites and shaped-plate rolling.

* Formerly at IMI Titanium Ltd, Birmingham, UK.

Titanium '92
Science and Technology
Edited by F.H. Froes and I. Caplan
The Minerals, Metals & Materials Society, 1993

Introduction

While the title of this paper may imply that it will only address alloys of the future, as all titanium alloys are regarded as advanced in many fields outside the aerospace industry, it is appropriate in this overview presentation to assess the whole spectrum of titanium alloys. The four years since the last World Conference have been a period of review and consolidation. While new alloys have been developed, the commercial difficulties the industry has faced have prompted a re-examination of existing alloys against potential new markets. This decade will see the 50th anniversary of the onset of titanium alloy development. Over most of that period the driving force behind the alloys has been the demands of the aerospace industry. The 1960's and '70's saw considerable strides in alloy development aimed at higher temperatures and strengths. Many of the alloys developed in that period failed to make a technical and commercial impact, not because they were metallurgical failures, but because the aerospace programmes, for which they were developed, were terminated for either political or commercial reasons. One example is the RMI alloy Ti-5-6-2-1S, which was effectively lost when the US cancelled the development of the SST aircraft in the late 1960's and there are many more examples in both to USA and Europe [1].

A combination of the need to establish new markets, a relaxation of the engineering design constraints (i.e. a better understanding of the relationship of mechanical properties in terms of component lifing), and process developments, have all prompted a re-examination of the older alloys. This paper will attempt to address the developments in the older and recently introduced alloys, before considering present alloy research, and process and products developments. It is not the intention here to present detailed technical data, but rather to highlight the developments, many of which are the subject of presentations to be given during the Conference.

Alloys

Existing 'Older' Alloys

The titanium alloy developers have achieved significant strides over the last 40 years. Strengths have risen from 300-400MPa to over 1500MPa, while temperature capabilities have increased from a modest 200°C to over 600°C. The need to establish new markets, allied to process/product developments, has resulted in the re-examination of older alloys. It is significant, that many of the alloys that were originally produced in billet and bar for forged components, such as discs, blades and struts, have seen extensions of their potential applications through product developments in plate, sheet and castings. Table I lists the alloys which have attracted renewed interest and have either seen extended applications, or in some instances, are likely to secure major use in aerospace for the first time.

Table I. Existing Alloys Attracting New Applications

Alloy	Composition (wt%)
Ti-6-22-22	Ti-6Al-2Sn-2Zr-2Cr-2Mo-0.23Si
Ti-10-2-3	Ti-10V-2Fe-3Al
Ti-15-3-3	Ti-15V-3Cr-3Sn-3Al
Beta C	Ti-3Al-8V-6Cr-4Mo-4Zr
IMI 550	Ti-4Al-2Sn-4Mo-0.5Si

It is significant that the alloys have high strength, rather than high temperature capabilities. Ti-6-22-22 is an alloy that was first publicised at the 2nd World Titanium Conference in 1972. The alloy shows a good combination of strength and fracture toughness, with room temperature strengths of typically 1200MPa and fracture toughness in the range 50 to 60MPa$\sqrt{m}$. It has now been specified for the two-thirds of the titanium airframe structure for the F-22 Advanced Tactical Fighter. The largest usage is in thick plate and forgings, where the alloy's attractive strength/toughness properties give it a design advantage over Ti-6-4 [2]. Like other alloys of its type the product range of Ti-6-22-22 has been extended, particularly into sheet, where it has displayed good superplastic forming (SPF) capabilities, with advantages of lower SPF forming temperatures and higher post-forming strengths compared to Ti-6-4 [2].

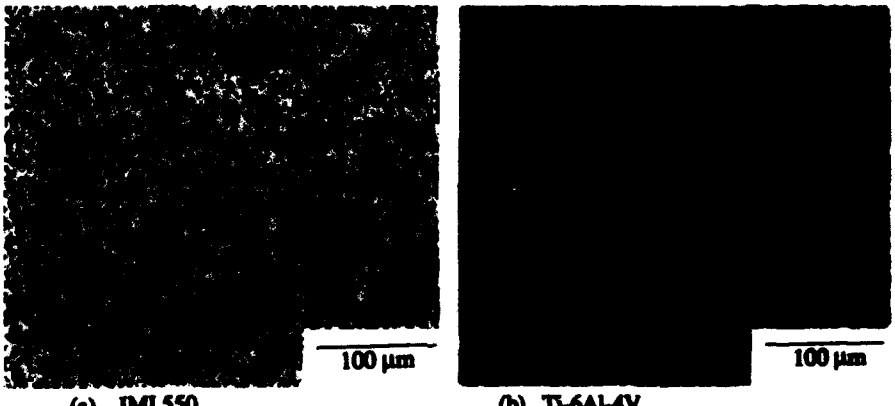
Meta-stable beta titanium alloys Ti-10-2-3, Ti-15-3-3 and Beta C were all developed ten to twenty years ago. While over the years the alloys have found limited applications, it is only recently that significant applications have been identified.

Like all meta-stable beta titanium alloys they can be heat treated to give high strength in combination with high fracture toughness. Ti-10-2-3 was originally developed as a forging alloy, aimed at replacing steel components in airframes, while Ti-15-3-3 was designed as a cold rollable strip alloy. However, the developments in near-to-net shape extrusions and castings have allowed applications to be identified for both alloys in the airframe of the Boeing 777 [3]. Ti-10-2-3 will be used as forged components in the landing gear and net-shape extrusions for seat track crowns, while Ti-15-3-3 high strength castings (~ 1140MPa UTS) have been specified for landing gear components.

Although Beta C has attracted the attention of the airframe manufacturers, particularly as castings and fasteners, the alloy's major applications, because of its combination of high strength and good corrosion resistance, have been in industrial components. The alloy is being considered for use in sour gas and geothermal wells. Though the alloy has good mechanical properties and corrosion resistance for most environments, for hot sour brines a modified version of Beta C, with low levels of precious metal additions (~0.05% Pd), has been developed. This modification expands the useful temperature range and still provides for adequate crevice and stress corrosion resistance [2].

The final alloy in Table I, IMI 550, is the oldest, being developed in the UK in the late 1950's. It is different from the other alloys in the sense that, since its introduction, it has always found applications in the European aerospace industry. Over 4000 tonnes have been produced in the last 10 years, as components for both aero-engines and airframes. It was originally developed as a medium/high strength creep resistant alloy for the Rolls Royce Pegasus and Olympus engines, which power the Harrier (AV8B) and Concorde, respectively. Since its introduction into engines as discs, more recent applications have been centred on airframe components in both European military and civil aircraft e.g. Jaguar, Tornado and Airbus.

From an alloy development view-point IMI 550 is significant in that it was the first commercial alloy to exploit the benefits of silicon in terms of creep strength and grain refinement. Figure 1 illustrates the comparison in microstructure between similarly processed IMI 550 and Ti-6-4 plate. The refinement seen in the microstructure is also reflected in the macrostruture of the alloy. The alloy has seen extended interest following its development into a variety of product forms. The introduction of extrusions, castings and thin SPF quality sheet and plate have all increased its potential; all products have maintained the alloy's significant grain size and tensile, fatigue and creep strength advantages over Ti-6-4. In SPF quality sheet the typical grain size of IMI 550 is 2-3 μm compared to 4-8 μm in Ti-6-4.



(a) IMI 550 (b) Ti-6Al-4V

Figure 1 Comparison of the microstructure in IMI 550 and Ti 6-4 plate.

One perceived disadvantage of the alloy, like others of its type, has been the question of joining. While sound welds can be produced in the alloy, either full heat treatment, or a modified electron beam welding process, were found necessary to give optimum properties. However, recent studies[4] have shown its ready applicability to joining by solid state diffusion bonding, even when using low bonding pressures.

Table II details some of the results from the programme.

Table II Comparison of properties of diffusion bonded IMI 550 and Ti-6-4.

Alloy/Condition	Room Temperature Tensile				Charpy Impact
	0.2% P S	UTS	Elong ($5.65\sqrt{S_o}$)	R of A	J
	MPa	MPa	%	%	
Ti-6-4/As bonded	844	940	18	44	30.5
IMI 550/As bonded	872	976	16	50	20
IMI 550/As bonded+STA	960	1125	15.5	44	19.5

Diffusion bonding cycle - 945^{0}C / 2.07MPa / 3hour

Solution treatment + age (STA) - 900^{0}C 1hr AC + 500^{0}C 24hr AC.

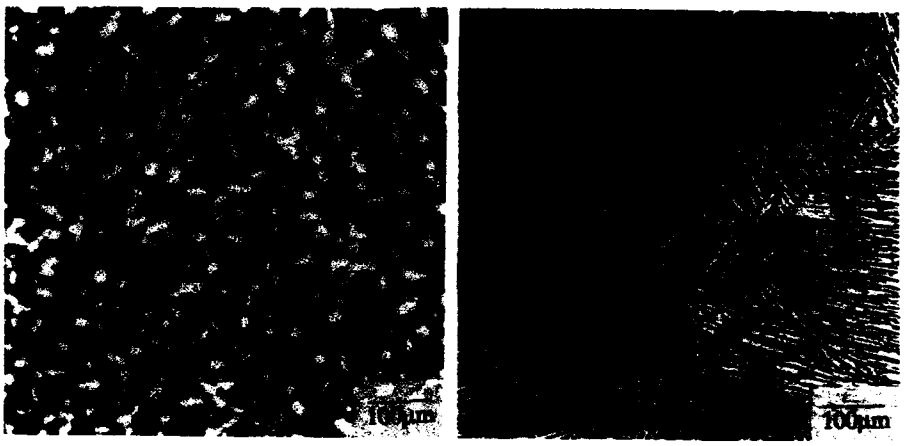
High Temperature Titanium Alloys.

a) Conventional alloys.

Over the last few years the alloys that have attracted the most attention have been those targetted towards high temperature aero-engine applications. The area splits into two distinct groups. The immediate and medium-term requirements, which are addressed by conventional alloys like IMI 834 and Ti-1100, and the longer-term aspirations, which are principally concerned with intermetallic systems based on titanium aluminides.

In first considering the conventional alloys, both IMI 834 (Ti-5.8Al-4Sn-3.5Zr-0.7Nb-0.5Mo-0.35Si-0.06C) and Ti 1100 (Ti-6Al-2.75Sn-4Zr-0.4Mo-0.45Si) have been well-documented in the literature [5,6], where extensive property data is detailed. It is not the intention of this paper to table any comparative mechanical property data, however, it is appropriate to consider the philosophy behind the alloys, for while their compositions would suggest that they are similar, in reality their metallurgical concepts are entirely different.

The significant difference between the alloys is that IMI 834 is processed as an $\alpha+\beta$ alloy, the heat treatment being specifically designed to produce a lean primary α+ transformed β microstructure (Figure 2a). The structure of Ti-1100 is derived, either from β forging, or from a full β heat treatment, thereby producing a fully transformed acicular α microstructure in the final product, similar to that shown in Figure 2b. Structures of this type are known to maximise creep at the expense of fatigue strength. Similarly processed alloys, such as IMI 685 and IMI 829, have been used successfully for over 20 years in the compressor stages of both military and civil aircraft. The composition of Ti-1100 has been optimised to take maximum advantage of its creep potential, while at the same time minimising the mechanical property short-comings seen in earlier alloys of the same type.



(a) (b)

Figure 2 Comparison of α+β microstructure of IMI 834 (a) with a β heat treated alloy (b).

The α+β microstructure associated with IMI 834 is aimed at optimising the balance of properties, particularly those of fatigue and creep strengths. The use of an α+β heat treatment to produce a low level of primary α, typically 7 to15%, is only possible because of the alloy's composition, in particular the presence of carbon, and the advances that have occurred over the last decade in production melting, forging and heat treatment technologies and practices. Twenty years ago an alloy of this type would not have been possible as a production reality. Figure 3 shows the significant difference in the shape of the β approach curve, between IMI 834 and other titanium alloys. It is the shallow form of the curve, resulting from the presence of carbon in the alloy, which allows IMI 834 to be successfully heat treated high in the α+β phase field. Some reservations were expressed at the out-set that in production the alloy could not be melted and processed to give a reproducible heat treatment window. Now after the production of over 500 tonnes of ingot the reproducibility and consistency of the alloy, and the viability of the heat treatment, are no longer in question.

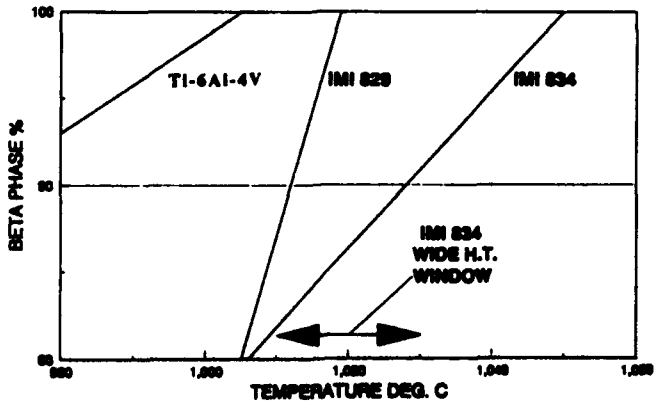


Figure 3 Beta approach curve for IMI 834 in comparison with Ti-6-4 and IMI829

As has been the recent trend, the product range of both IMI 834 and Ti-1100 has been extended to include sheet, foil and castings. The optimum $\alpha+\beta$ structure of IMI 834 is ideally suited to SPF sheet applications [4].

b) Titanium Aluminides.

Given the extensive literature on the alloys, only a few general points will be covered in the following section. The potential of the aluminides can be seen in Table V, which compares them with conventional titanium alloys and superalloys.

Table V Properties of Titanium Aluminides, Titanium - Based Conventional Alloys and Superalloys.

Property	Ti Base	Ti_3Al	TiAl	Superalloys
Density Mgm^{-3}	4.5	4.15-4.7	3.8	8.3
Creep Limit T max^{0}C	650	700	1000	1100
Oxidation (long-term T max^{0}C)	600	650	900	1100
Ductility % at RT	8-25	2-10	1-4	3-5

The aluminide systems are still the subject of considerable study. Within Europe a number of programmes are underway, some funded by national governments, while others have cross-border collaboration, and are funded by the European Community within the BRITE-EURAM initiative.

While interest still remains in the Ti_3Al-based systems, particularly those based on Super α_2 (Ti - 25Al - 10Nb - 3V - 1Mo at%), the major emphasis has shifted to exploring the gamma aluminides, where the potential in terms of high temperature performance and density could threaten the supremacy of the superalloys. Though Ti_3Al-based alloys can be processed like conventional titanium alloys, there is a growing view that in their present state of development their advantages over titanium alloys, such as IMI 834 and Ti 1100, are insufficiently attractive to justify widespread applications in aerospace projects. The window of opportunity has decreased significantly over the years, as conventional titanium alloys have pushed their temperature ceiling higher and confidence has grown over the potential for success in developing the gamma aluminides. For instance, Figure 4 illustrates the oxidation behaviour of titanium alloys Grade 2 and IMI 834 compared to Ti_3Al and gamma-based alloys at 900^{0}C [7]. The potential advantages of the gamma-based systems are apparent, but the graph also illustrates the lack of any benefits accruing to Super α_2 against IMI 834.

The engineering limitations of the Ti_3Al-based alloys are widely recognised and in an effort to over-come the alloys' short-comings detailed studies of the Ti-Al-Nb alloy system have led to the discovery of an ordered orthorhombic Ti_2AlNb phase (O phase) [8].

Preliminary assessment of alloys based on the O phase plus ordered beta (β_o) has shown them to have higher strength to density ratio and better room temperature ductility and fracture toughness than Ti_3Al-based alloys, with no loss in high temperature properties. The two Ti_2AlNb-based compositions showing particular promise are Ti-24.5Al-23.5Nb and Ti-22Al-27Nb (at%), whose properties are not only attractive when compared with Ti_3Al-based alloys, but also show specific strength advantages over the superalloy IN718.

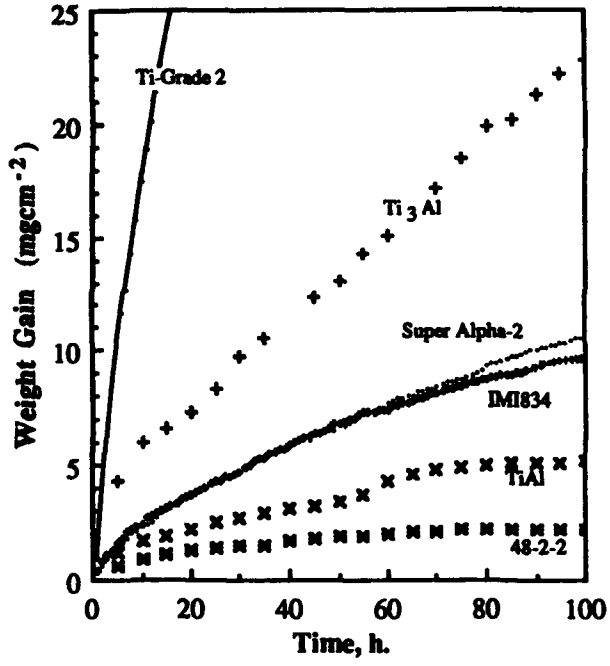


Figure 4 Comparison of Oxidation behaviour at 900°C.

One of the most interesting developments recently launched in the field of gamma aluminides is the XD™ process developed by Martin Marietta [9], where the addition of up to 7 volume % of TiB_2 has resulted in significant improvements in strength, modulus and structural refinement.

Table VI compares the effect of the addition of 7 volume % of TiB_2 on the room temperature properties of cast Ti - 48Al - 2V - 2Mn (at %).

Table VI. Room Temperature Properties of Investment Cast Ti - 48Al - 2V - 2Mn Alloy With and Without 7 vol% TiB_2.

Alloy	Yield Strength MPa	UTS MPa	Elongation %(4D)	Young's Modulus GPa
Base Composition	400 - 428	538 - 573	1.1 - 1.2	159
XD™ 7vol% TiB_2	573 - 587	704 - 731	0.9 - 1.1	180

Within the more general field of gamma aluminide research, considerable world-wide effort is being directed to the questions of composition and the effect of thermo-mechanical processing on properties, as well as addressing the basic problems of manufacture, which embrace

conventional ingot metallurgy, casting and powder production. Realistically the development of such systems must be regarded as long-term, given the problems they present, and the time that will be required to scale-up the development stage and fully validate aerospace components. Given a typical gestation period of ten years from the inception to full-scale application of a conventional titanium alloy, a realistic date for significant applications of gamma aluminides is likely to be beyond the turn of the century.

New Conventional Alloy Developments.

While the preceding section dealt with high temperature alloys, there have been a number of quite varied alloy developments reported recently, ranging from high strength alloys to non-burning alloys, to alloys for medical applications. Though these programmes do not have a common thread, apart from the fact that they are predominantly based on conventional alloy metallurgy, they do indicate an increasing awareness of the need to solve problems in existing applications, as well as showing how significant efforts are being made to expand the applications for titanium alloys.

Table VII lists the alloys in question and indicates the reason for their development.

Table VII New Conventional Alloy Developments.

Alloy	Composition (wt%)	Target
Beta Cez	Ti-5Al-2Sn-4Zr-4Mo-2Cr-1Fe	High strength/medium temperature
Beta 21S	Ti-15Mo-2.7Nb-3Al-0.2Si	Cold rolling/MMC's
Protosul 100 (IMI 367)	Ti-6Al-7Nb	Medical/lower toxicity
Ti-Zr-Nb	Ti-13Zr-13Nb	Medical/lower toxicity/modulus
Ti-Mo-Zr-Al	Ti-15Mo-5Zr-3Al	Medical/lower toxicity/modulus
SP 700	Ti-4.5Al-3V-2Mo-2Fe	Lower SPF temperature
DAT 52F	Ti-3Al-2V-0.2S-0.47Ce-0.27La	Improved machinability
BTT-1	Ti-Al-Cu	Fire resistant
BTT-3	Ti-Al-Cu	Fire resistant
Alloy C	Ti-(22-40)V-(13-36)Cr	Fire resistant

Beta Cez [10] is aimed at high strength aero-engine applications with a maximum operating temperature of 450^{0}C. The alloy is a result of a collaborative programme between Snecma, Onera and Cezus and is a potential rival to Ti-17 and Ti-6-2-4-6, having room temperature tensile strength of the order of 1200MPa and fracture toughness levels of 60MPa$\sqrt{m}$.

Beta 21S [10] is a cold rollable alloy developed by Timet to address the specific problems of high temperature reactivity that have been encountered in the use of Ti-15-3-3 in the manufacture of MMC's.

The next three alloys in Table VII, starting with Protosul 100 (IMI 367) [12], have been designed to address specific problems associated with medical applications. Protosul 100 (IMI 367) was developed in Switzerland by Sulzer Bros as an alternative to Ti-6-4. The alloy design set out to overcome the perceived harmful biological effects of vanadium, by its replacement with the non-toxic element niobium. In mechanical property terms the alloy is similar to Ti-6-4. After extensive trials, components, particularly hip joint implants, are now full-scale production.

The other two alloys [13,14] listed in Table VII are also being developed to address potential problems of biocompatibility, in addition the engineering targets are to develop alloys with properties compatible with either the modulus, or the yield strength/modulus ratio of bone. This latter parameter is known as the admissible strain and has a value of 0.67% for human cortical bone [14]. The higher values obtained in titanium alloys make them 'more forgiving' in clinic than competitive materials.

The field of alloy development for prostheses is one that has become increasingly active recently following the claims, and counter-claims, of the medical profession of the potential toxic nature of certain elements. There is scope for future market exploitation of titanium in the field, but such developments must be undertaken in parallel with sound medical objectives and experiments.

Alloy developments aimed at addressing specific manufacturing problems are highlighted by SP 700 [15] and DAT52F[16]. Both are targetted to reducing production costs, the former by lowering superplastic forming temperatures and the latter by improving machinability.

By adding beta stabilising elements, the SPF forming temperature of SP 700 has been reduced to 750^{0}C, compared to a nominal 930^{0}C for Ti-6-4. SP 700 continues a development started over 10 years ago [17], where up to 2% of Fe, Cr and Ni were added to Ti-6-4 to reduce its forming temperature. Unlike this earlier work on Ti-6-4, that on SP 700 has used large amounts of beta stabiliser to achieve the desired effect and thereby produced a significantly different alloy. The second important parameter is the diffusion bonding temperature, for any alloy to be successful it must be possible to combine the SPF and DB cycles, as there are more limited applications for an alloy based solely on its SPF behaviour.

The other alloy, DAT 52F, is an interesting development specifically aimed at reducing machining costs of valve manufacture for the automobile industry. The industry is already evaluating existing alloys Ti-6-4, Ti-6-2-4-2, IMI 834 and Ti-1100 for potential inlet and outlet valve applications. In DAT 52F the addition of sulphur and rare earth elements have been shown to increase the machining speeds, in comparison with the established alloys. However, the presence of particles within the alloy, which aid machining, could, depending on their size and distribution, significantly reduce component life by causing premature fatigue failure.

The final alloys in Table VII are aimed at a particular problem in the aero-engine, that of titanium component fires. At the present time the use of titanium alloy components is limited because of fire risks. If the problem could be overcome then more titanium components could be used in engines with the corresponding weight reductions. The alloys BTT-1 and BTT-3 are Russian developments [18], where the fire threshold has been increased to 650^{0}C and > 850^{0}C, respectively. The last alloy in Table VII has been developed by Pratt and Whitney[19], and is a fully beta stabilised one. Under the condition of test the alloy does not burn and has good overall mechanical properties up to about 650^{0}C.

Processes and Products

Near to Net Shape Processing.

a). Casting - The casting industry continues to make developments in terms of quality and size. With greater demands from users for thinner-walled components, studies of the problems of metal flow, porosity, repair, surface finish and mould-surface reactions have resulted in significant improvements in all areas. One somewhat surprising omission from the area is the apparent lack of alloy development specifically aimed at cast components. The industry is still dominated by alloys that were developed for their wrought properties. While clearly the difficult-to-fabricate new materials, particularly those based on gamma aluminide, have used the casting processes, no significant attempts have been made to develop new alloys which address the metallurgical short-comings of the present ones. There is scope to develop a range of castable alloys which could produce properties in cast components beyond those attainable in existing alloys. Titanium alloys must be one of the few engineering materials where alloys have not been specifically developed for the foundry industry.

a). Roll Forming - One of the most striking recent engineering/metallurgical developments in UK has been that at IMI Titanium Ltd [4] in its work on taper rolling. The process is extremely versatile. By the use of specially profiled rolls a wide range of shaped plate geometries can be produced in stepped and tapered forms to an extremely high level of dimensional accuracy in combination with a consistent degree of microstructural development. In the first instance near-to-net shape stepped and tapered plates are in production for large aero-engine fan blades. The process is well-established and components are in volume production. Figure 5 shows an example of a profile rolled plate product. The technology, originally developed using Ti-6-4, is not alloy-limited and has been extended to other titanium alloys. For example, for some wide-chord hollow fan blade applications where IMI 550 profile rolled plate has been shown to exhibit finer microstructure and superior fatigue properties than the corresponding Ti-6-4 product.

Further developments of the process are in-hand to extend the size and complexity of components that can be produced. The technique is seen as having significant potential applications beyond the existing aerospace products and alloys.

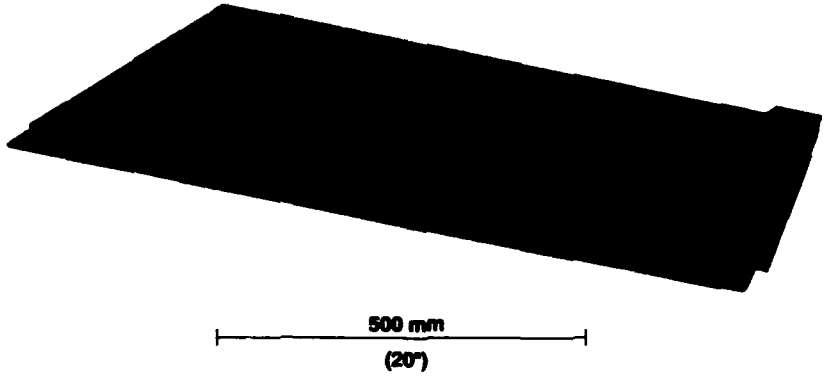


Figure 5 Near-to-net Shape Profiled Rolled Plate-(courtesy of IMI Titanium Ltd.)

Metal Matrix Composites

The development of metal matrix composites straddles the boundaries between alloy, process and product developments. All three technologies interact, but particularly those of process and product development. The driving force behind the technology is higher strength and modulus with lower density and hence reduced component weight. In the ultimate, weight reductions of the order of 75% have been claimed, when comparing an existing titanium compressor assembly with one designed using composite rings.

Considerable effort has been directed towards the process of production of the titanium matrix with continuous SiC fibre reinforcement and the study of the interactions between the fibre and different alloys. While a number of processes are being evaluated for the production of the titanium matrix, at the present time most of the development thrust is still centred on the use of titanium alloy foil as the starting matrix. Developments have taken place to produce foil in a range of alloys from Ti-6-4 to aluminides. Processes have been developed to manufacture, on a production basis, panels of Ti-6-4, 100μm thick up to 1m by 0.5m in area [4]. Other alloys, such as IMI 834, Ti 1100 and super α_2, have been successfully produced on a development

scale, while cold rollable alloys, such as Ti-15-3-3 and Beta 21S, are readily available in foil. Typical tensile and Young's modulus values of a number of MMC, using foil and BP Composite's Sigma SiC fibre, are shown in Figure 6 [20].

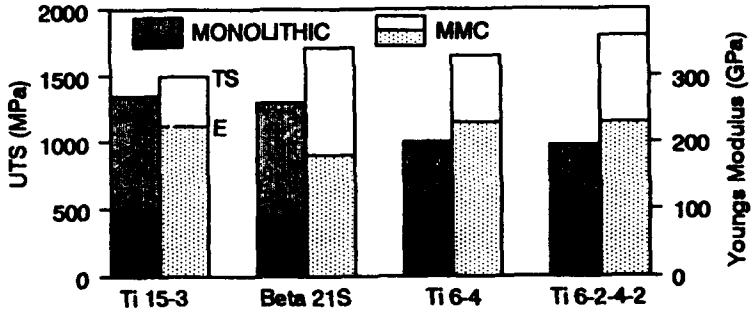


Figure 6 Comparison of Tensile and Young's Modulus of SiC reinforced MMC's with Monolithic Materials

A particularly exciting development in the UK is being undertaken at DRA Farnborough [21], using a physical vapour deposition process to coat SiC fibres with titanium alloys. Technically, the process has many attractions. In the first instance, there is no restriction on alloy matrix composition, matrix thickness around the fibre can be varied without difficulty and on consolidation, the problems often encountered in the foil route, in terms of spacing and fibre movement, are eliminated. Figure 7 shows a consolidated, coated SiC fibre MMC with 80 vol % fibre. The process which, until recently was only operating on a small scale, is being scaled-up to produce continuous lengths of coated fibre.

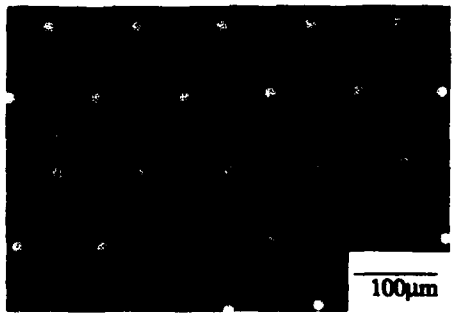


Figure 7 MMC - Ti-Al-V alloy / 80% vol fraction of SiC fibre

Conclusions

The paper has had to be restricted in its content and there are a number of topics, like RSR powder, spray-forming and mechanical alloying, that it has been necessary to omit. However,

the message to the alloy/process developer should be clear, that there are still many opportunities to develop new alloys and processes and establish new markets, while at same time extending opportunities for existing alloys.

Acknowledgements.

The author would like to thank IMI Titanium Ltd for its technical and financial support in preparing and presenting this paper, in particular J Tamberlin, A Barber, D Bretherton, D Neal, M Kearns, D Rugg, Mrs M Finglass and Mrs J Robinson. Technical contributions are gratefully acknowledged from P Partridge and M Ward-Close, DRA Farnborough, D Young, BP Metal Composites Ltd, J Wood, RMI Titanium Co, R Boyer, Boeing Materials Technology, Prof S Steinemann, University of Lausanne, Prof I Polkin, VILS Moscow, and from colleagues at the IRC in Materials, University of Birmingham.

References

1. P A Blenkinsop. Titanium Science and Technology (Oberursel Germany, DGM 1985), 2322-2338.
2. J R Wood. Private communication with author, RMI Ti Co, November 1991.
3. R R Boyer. Private communication with author, Boeing Materials Tech, Aug 1991.
4. M W Kearns. Private communication with author, IMI Ti Ltd, February 1992.
5. M A Daubler,D Helm and D F Neal, Titanium 1990 Products and Applications , (Dayton TDA 1990) 78-87.
6. T E O'Connell and P J Bania, ibid. 794-803.
7. T Johnson. Private communication with author IRC in Materials University of Birmingham, February 1992.
8. R G Rowe. Microstructure/property Relationships in Titanium Aluminides and Alloys. (Warrendale, TMS, 1991), 387-398.
9. J D Bryant, L Christodoulou and J R Maisano, Scripta Metall. 1990, 24, 33-38.
10. B Prandi et al. Titanium 1990 Products and Applications,(Dayton TDA, 1990),150-159.
11. P J Bania and W M Parris. ibid. 784-793.
12. M Semlitsch, Designing with Titanium, (London, Institute of Metals,1986), 292-304.
13. Smith and Nephew Richards Inc. European Patent Application 0437079A1, 1990.
14. S Steinemann et al. Beta-Titanium Alloy for Surgical Implants. To be published in Proceedings of the Seventh World Titanium Conference, San Diego 1992.
15. N K K Corporation, Tokyo Japan, Technical Brochure, May 1991.
16. S Nakamura,Proceedings of Sixth World Ti Conference,(Cannes,Soc. Fran.Met. 1988), 1415-1420.
17. J Wert and N E Paton, Metallurical Transactions, 1983, 14A, 2335-2344.
18. V V Tetyukhin, Titanium 1990 Products and Applications, (Dayton,TDA,1990), 56-65.
19. United Technologies Corp. UK Patent Application 2238057A, 1991.
20. D Young. Private communication with author, BP Metal Composites Ltd, Feb. 1992.
21. P G Partridge and C M Ward-Close. To be published in International Materials Review.

ALLOY THEORY AND PHASE TRANSFORMATIONS IN TITANIUM ALLOYS

R. PENELLE and C. SERVANT

Laboratoire de Métallurgie Structurale, U.R.A. C.N.R.S. n°1107, Bât. 413, Université de Paris Sud, 91405 Orsay Cedex, France.

Abstract

The predictions of thermomechanical and thermal treatments to carry out on multicomponent alloys in order to obtain the microstructure giving rise to the best combination of mechanical properties for given applications can be made from assessments of phase diagrams either by the thermodynamic approach or the electronic one.

Introduction

This paper is divided into two parts dealing with the thermodynamic and electronic assessment of phase diagrams including phase transformations. The development of titanium alloys is mainly related to needs in new materials with high performances for aeronautical and space industry. Improvement of mechanical properties of these alloys in severe use conditions involves research of new compositions and new thermal and thermomechanical treatments. These treatments are based on the existence of two phases, the first so called β, crystallizes during cooling of the alloy after melting, the second α forms at low temperature. A key step for the control of thermal and thermomechanical treatments in titanium alloys is the knowledge of the proportion and the composition of the α and β phases as a function of temperature for the complex alloys (with 5 to 7 elements) and of the β transus temperature (1, 2). The number of experimental informations necessary to the knowledge of the thermodynamic system of these alloys increases rapidly with the number of alloying elements.
Such a thermodynamic approach can be very powerful both planing and reducing considerably the number of costly experiments (3).
For a multinary system $\underline{n}$, the systems of lower order have to be firstly computed by combination analysis (4). For instance, in the case of the β CEZ alloy which contains 7 elements (5) in wt % : Ti bal. - 5 Al - 4 Mo - 4 Zr - 2Cr - 1Fe - 2Sn, the possible number of ternary systems is equal to 35 .
So it is of capital importance to have means of analysis allowing on one hand to predict the evolution of the phase limits in the multinary systems and on the other hand to extrapolate punctual experimental results.

Thermodynamic approach

The thermodynamic approach of a system begins generally by a list and a knowledge of the phases in equilibrium.

Titanium '92
Science and Technology
Edited by F.H. Froes and I. Caplan
The Minerals, Metals & Materials Society, 1993

Brief recall of the thermodynamic descriptions

If for a given temperature and at a constant pressure the Gibbs energies of all the phases forming the system are known, their composition at equilibrium corresponds to the minimum Gibbs energy G of the system (6, 7).G is a function of the temperature T and of the molar fraction $x_i(j)$ of the different components i in the coexisting phases j:

$$G = f(T, x_i(j))P$$

and $$G = Hj - TSj$$

where H_j and S_j are respectively the enthalpy and the entropy of the phase j.

In order to plot a phase diagram, G is transformed into :

$$T = g\ (x_i(j))P$$

In fact, absolute values for the Gibbs energies are not measurable and the Gibbs energy of a phase (j) is related to the Gibbs energy change ΔG_j of mixing by considering the Gibbs energy ${}^\circ G_i^x$ of the pure components x, in general, in the same structural and physical state as that for the solution phase :

$$\Delta G_j = G_j - \sum_{i=1}^{n} x_i\ {}^\circ G_i^x$$

So : * For a stoichiometric compound

$$G_{\text{compound}} = G_{\text{reference}} + \Delta G_f$$

where ΔG_f is the Gibbs energy of formation of the compound.

* For a solution

$$G = G_{\text{reference}} + G_{\text{ideal}} + G_{\text{excess}}$$

a) $G_{\text{reference}}$: the term $G_{\text{reference}}$ defines a level of reference (a line, a plane, a surface) according to the order (binary, ternary or quaternary) of the system and can be expressed as :

$$G_{\text{reference}} = \sum_{i=1}^{n} x_i\ {}^\circ G_i^x$$

The Gibbs energy of formation of the pure components according to their different physical and structural state has been determined by the Scientific Group Thermodata Europe (S.G.T.E.) (8) and expressed as a power series :

$${}^\circ G_i^x = \sum_{k=-1}^{4} a_k T_k + b\ T\ Ln\ T + cT^7 + d\ T^{-9}$$

The coefficients of the terms of the series are indicated in a given temperature range and several intervals are in general necessary to describe the function ${}^\circ G_i^x$

b) G_{ideal} : The term G_{ideal} expresses the Gibbs energy of a solution where the elements -whatever their nature- can substitute one another according to a random distribution on the same sublattice.

G ideal can be written as :

$$G_{ideal} = RT\sum_{i=1}^{n} x_i \, Ln x_i$$

c) G excess : The excess Gibbs energy of the solution which expresses the deviation to the ideality can be expressed according to the Redlich-Kister equation (9) as :

* For a binary system AB

$$G_{(A,B)\ excess} = x_A \, x_B \sum_{\nu=0}^{n} (x_A - x_B)^{\nu}$$

* For a ternary system ABC

$$G_{(A,B,C)\ excess} = [G_{(A,B)\ excess} + G_{(A,C)\ excess} + G_{(B,C)\ excess} + G^{ter}_{(A,B,C)}]$$

with: $G_{(A,B,C)ter\ excess} = x_A \, x_B \, x_C \, (L_A \, x_A + L_B \, x_B + L_C x_C)$

The L_i coefficients vary with the temperature according to the relation :

$$L_i = a_{i0} + a_{i1} \, T + ... + a_{in} \, T^n + b_i \, T^{-1} + c_i T \, Ln \, T$$

where a_i is a constant.

In the expression of G excess, the terms L_i are calculated by means of an optimization procedure developed by LUKAS et al (10), where experimental and thermodynamic data as well as phase diagram data are taken into account.

The description of the different phases has been made using two different models :

* An ideal substitution solution characterized by a random distribution of atoms on only one sub-lattice with an interchange energy of zero. This first model is used in particular for the liquid phase.

* A combination of sub-lattice : (Harvig, Hillert) (11, 12)
In fact, for special reasons (size effect, electro-negativity, charge...), atoms prefer certain sites of the sub-lattices. Stoichiometric compounds can thus be described and it has been considered that each kind of atom is situated on a different sub-lattice. So the number of sub-lattices is equal to the number of type of sites and the mixing entropy is equal to zero.
In order to approach the phase diagram of an alloy such as the ß CEZ, first we will consider the case of the ternary system Ti-Al-Mo and as a preliminary step that of the three binary systems :

Ti-Al , Al-Mo and Ti-Mo.

Binary systems

Ti-Al
The Ti-Al diagram is characterized by a liquid phase, two solid solutions BCC and HCP in the titanium rich corner as a function of decreasing temperature and by a FCC solid solution near aluminium rich corner. The main phases of this system with their crystalline structure are summarized in Table I.

Phases	Crystalline structure	Phases	Crystalline structure
Ti_3Al	DO_{19}	$TiAl_2$	
TiAl	$L1_0$	$TiAl_3$	DO_{22}
$Ti_{3+x}Al_{5-x}$		$Ti_{1+x}Al_{3+x}$	

TABLE I

Two phase diagrams have been recently published. The first established by LOISEAU (13) from T.E.M. observations and the second due to MURRAY (14) from experimental data compilation. As it can be seen on Figure 1, there is a disagreement about the representation of the existence domain of the ordered phase Ti3Al.

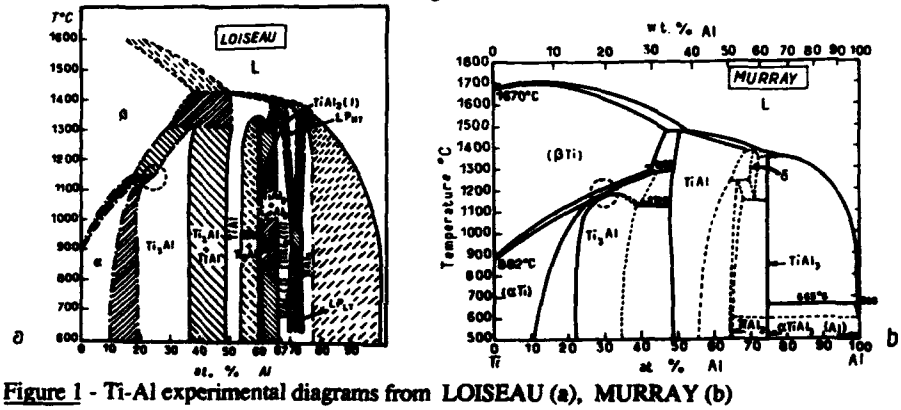


Figure 1 - Ti-Al experimental diagrams from LOISEAU (a), MURRAY (b)

For our part, we have studied by dilatometry in the case of the Ti3Al compound, the structural transformations occurring during continuous heating and cooling with an average rate of 300°C h^{-1} (15), Figure 2.

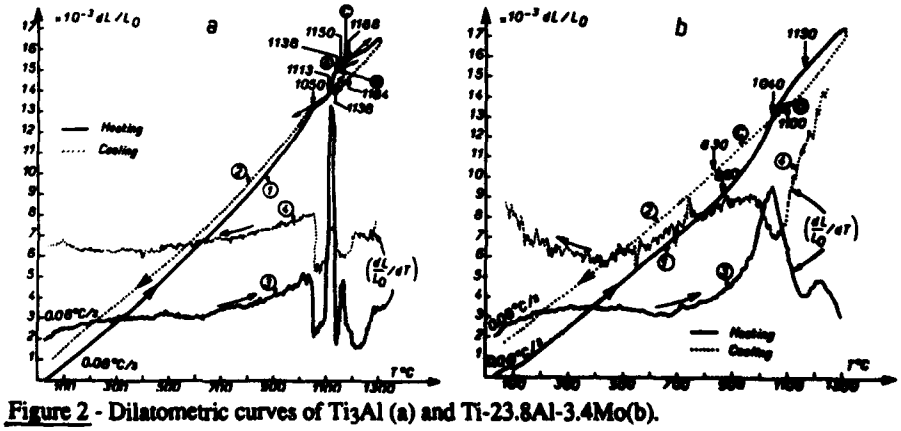


Figure 2 - Dilatometric curves of Ti3Al (a) and Ti-23.8Al-3.4Mo(b).

This figure shows dilatometric curves:

$\frac{dL}{Lo} = f(T)$ and $\frac{dL/Lo}{dT} = f(T)$ between 20 and 1300°C.

From the heating curves, we can distinguish four transformation ranges :

Range A : 1050 → 1138 °C

It is characterized by a slight contraction from 1050°C followed by a strong dilatation between 1113°C and 1138°C due to the formation of the α phase according to the reaction :

$\alpha 2 \rightarrow \alpha + \alpha 2$

Range B : 1138 → 1150°C

The α phase is only present

Range C : 1150°C

$\alpha \rightarrow \alpha + \beta$ disord

The β transus : 1188°C

$\alpha + \beta$ disord → β disord

These results are in good agreement with the phase diagram of MURRAY (14) and that calculated by GROS (16), Figure 3. The experimental diagram previously established by LOISEAU does not include the ($\alpha + \alpha 2$) domain.

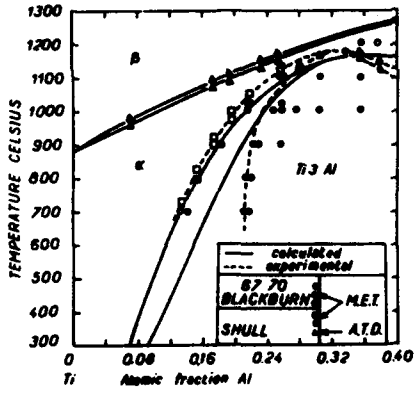


Figure 3 - Ti-Al phase diagram calculated by GROS compared to the experimental one.

Ti -Mo and Al-Mo systems

The Ti-Mo diagram which presents a miscibility gap is quite simple unlike the Mo-Al system (17), Figure 4. In this last case, GROS and ANSARA only considered the aluminium rich corner; moreover as the enthalpies of formation of all the Al-Mo compounds are not known , GROS only considered the β transus temperature calculation.

As the Mo Al system was optimized by KAUFMAN (18), GROS only optimized the Ti-Al and Ti-Mo systems. For the Ti-Al system, GROS described the thermodynamic behaviour of the ordered phase Ti_3Al using the sub-lattice model developed by HILLERT (12) and generalized to the multicomponent systems by HARVIG (11) and SUNDMAN (19).

The liquid and BCC phases are described by a substitution model. The behaviour of the hexagonal phase whatever its structure, ordered or disordered is described by the two sub-lattice model.

To optimize the Ti-Mo system, the BCC, the HCP and the liquid phases are described as regular solutions (16).

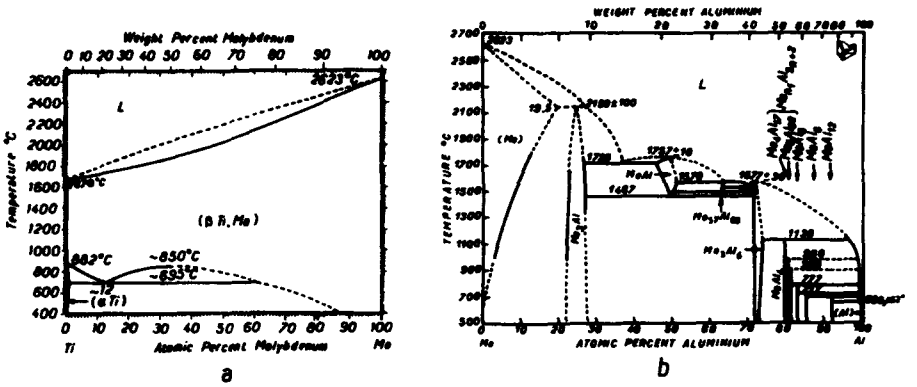


Figure 4 - Phase diagrams of the Ti-Mo (a) and Mo-Al (b) systems.

Ternary system

Ti-Al-Mo at equilibrium

The isothermal sections at 900 and 800°C have been calculated by GROS (16) without ternary interaction parameter. It can be seen that the phase limit ($\alpha + \beta$) /β is between the experimental points determined by electron microprobe analysis of the β phase, which shows a satisfactory agreement between experimental and calculated data, Figure 5. Furthermore, HAMAJIMA (20) experimentally established isothermal sections of the ternary system Ti-Al-Mo; he found that from about 400°C the ordered phase β_2 begins to disorder.

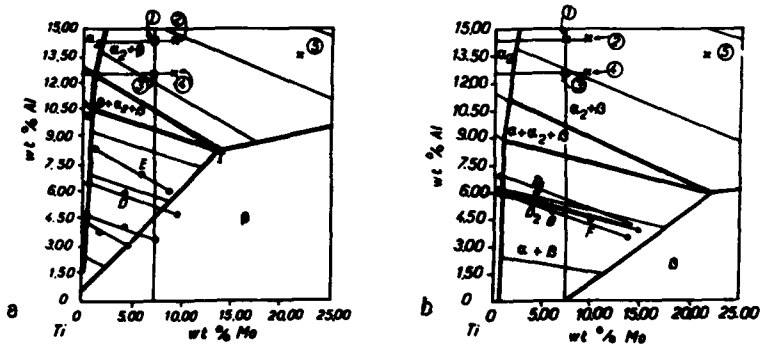


Figure 5 - Isothermal sections calculated by GROS at 900°C (a) and 800°C (b)

For our part, we have studied four Ti_3 Al-Mo alloys having the following compositions in at %:

- Ti - 23.8 Al - 3.4 Mo
- Ti - 24 Al - 4.4 Mo
- Ti - 21 Al - 3.5 Mo
- Ti - 21 Al - 4.5 Mo

Analysis of dilatometric curves of these alloys points out a continuous expansion between 650 and 1160°C which can be related to the successive transformations

$\alpha_2 + \beta_2 \rightarrow \alpha_2 + \beta$ (disordering of β_2)

$\alpha_2 + \beta \rightarrow \alpha + \beta$ (" α_2)

$\alpha + \beta \rightarrow \beta$

In conclusion there is a disagreement between first GROS and HAMAJIMA because GROS did not consider the ordering of the β phase, and HAMAJIMA and ourselves as for the temperatures of disordering of the β phase.

Ti-Al-Mo out of equilibrium

Structural transformations have been studied during continuous cooling transformations by dilatometry.

1) For the Ti_3Al compound as shown on Figure 6a, three fields of phase formation can be characterized as a function of the decreasing cooling rate, that is :

$\beta \rightarrow \alpha'_2$

$\beta \rightarrow \alpha'_2 + \alpha_2$

$\beta \rightarrow \alpha_2$

The ordering reaction for Ti_3Al is very rapid, indeed it is observed for a cooling rate of about 80 $°Cs^{-1}$

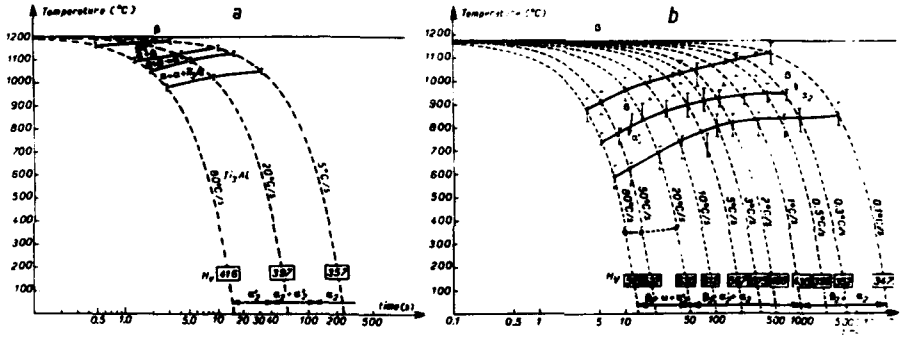


Figure 6 - CCT diagrams of Ti_3Al (a) and Ti-23.8Al-3.4Mo (b)

2) For the Ti_3Al-Mo aluminides

Three fields of phase formation have been defined, they lead at 20°C to the phases, Figure 6b, as follows :

* For rapid cooling rates R_C (80-20°Cs^{-1}), we observe :

- $\beta_2 + \alpha'_2$: the ordering of the β phase occurs before the formation of α'_2 which forms by displacive mechanism.

*For intermediate cooling rates (10-1°Cs^{-1}), $\beta_2 + \alpha'_2 + \alpha_2$ appear. The β phase transforms by a mechanism of displacive transition in α'_2 and α_2, growth of which occurs by diffusion phenomena.

* For low cooling rate, β_2 and α_2 are observed.

It can concluded that addition of Mo toTi_3Al :

- stabilizes at room temperature a microstructure essentially with two phases (α'_2 and/or α_2)+ β_2
- is favourable to the formation of the athermal ω phase into β_2 for the fastest cooling rates.
- decreases the transformation temperatures

- refines the microstructure

3) Ti bal.-5Al-4Mo-4Zr-2Cr alloy (wt %) :

GROS and ANSARA (16, 21) calculated the β transus temperature of such an alloy and they found β_T = 894.4°C. The composition of this alloy is very close to that of the β CEZ which contains two extra alloying elements that is : 1% Fe and 2% Sn. In this last case, the β transus experimentally found is within 890-895°, which is near that of the previous alloy (5). It can be concluded that the thermodynamic simulation gives a good approach of the different phase fields. Results on TiZrX alloys (X = Hf, Nb, Ta, Mo, W) have been recently presented by DELAY team (22) in Belgium.

It must be underlined that the phase diagram activity is well coordinated :

- At the world scale through A P D I C which is the Alloy Phase Diagram International Commission. The correspondant in France is ANSARA.
- In Europe through S G T E Scientific group Thermodata Europe.
- Through journals.
  - * CALPHAD : Calculation of Phase Diagrams.
  - * Bulletin of Alloy Phase Diagrams.

Electronic approach

During these last years, the assessment of the formation energy ΔE of alloys has been widely studied (1, 23). According to the level of approximation, the different microscopic theories divide into two groups : the ab-initio and the semi-empirical methods.

In the formers, no parameter is introduced in the calculation and they give results considered as exact. Among these methods, it is convenient to distinguish the approaches based on pseudopotentials and those based on linearized methods of calculation of band structures. For transition metals because of tightly bound character of the electrons in the valence band, calculations of the total energy are performed with methods such as Linear Muffin Tin Orbital, L.M.T.O. or Linear Augmented Plane Wave, L.A.P.W.

About the semi-empirical methods, the tight binding method is relatively simple and it is used to study the energitical properties of the transition metals and their alloys either in the ordered or disordered atomic structure, Figure 7a. The chemically disordered systems are treated by the Coherent Potential Approximation, C.P.A., which is a mean field theory which consists in replacing the real level of energy of all the atomic sites by an average medium except that of the central atom which is exactly treated.

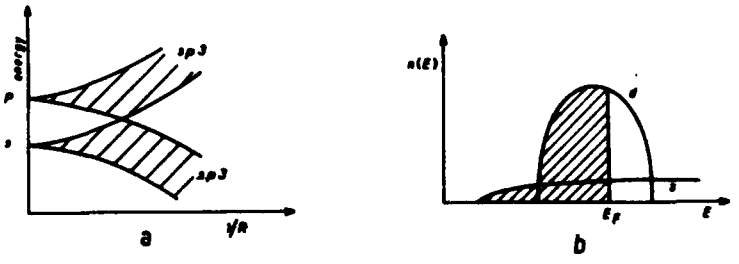


Figure 7 - (a) In the covalent limit the s- and p-bands of tetrahedrally coordinated semiconductors transform into bonding and antibonding sp^3 bands.
(b) Schematic density of states n(E) of a transition metal with overlapping s-and d- bands

Contrary to the C.P.A. method, the Cluster Bethe Lattice Method, C.B.L.M., takes into account the short range order. For solid solutions, the Generalized Perturbation Method, (G.P.M.), proposed by GAUTHIER and DUCASTELLE (24) is also able to reach the order energy. BESSOUD (25) pointed out that these last both methods are equivalent.

LE (26), in France, studied the Ti-Ni system; Ti and Ni are transition metals, their properties are related to the d character of the valence states. This can be explained by the nature of the two electronic populations : the weak overlapping of the d atomic orbitals gives rise to a narrow band with a high density of states, inside of which is the Fermi level. This d band overlaps the s band which is wide because of the important overlapping of the corresponding atomic orbitals and which presents a low density of states (two s states per atom), Figure 7b. Because of the strong d character, the electronic structure of transition metals and of their alloys can be described using the tight binding approximation.

Calculation of thermodynamic parameters and phase diagrams

Calculation of the formation energy of an alloy

Let us consider a binary alloy $A_x B_{1-x}$ characterized by a short range order σ and by a composition x for the element A (26).

The formation energy ΔE of the alloy is defined by :

$$\Delta E(x,\sigma) = E(x,\sigma) - xE_A - (1-x)E_B$$

where $E(x,\sigma)$ is the total energy of the alloy and E_A, E_B the total energy of the pure metals A and B. Let us recall that the total energy E_I of a pure element I is given by the relation.

$$E_I = f(\int^{EF} En(E)\,dE)$$

where n(E) is the density of state of the element I. The total energy of the alloy is in a similar way :

$$E(x,\sigma) = f(\int^{EF} E\rho_{all}(E)\,dE)$$

where $\rho_{all}(E)$ is the state density of the alloy with :

$$\rho_{all}(E) = x\rho_A(E) + (1-x)\rho_B(E).$$

The formation energy of an alloy can be expressed as the sum of two terms

$$\Delta E(x,\sigma) = \Delta E_{dis}(x) + \Delta E_{ord}(x,\sigma)$$

- The first term $\Delta E_{dis}(x)$ represents the contribution of the alloy completely disordered and it only depends on the composition of the system.
- The second term is the order energy of the system which depends on the composition and the short range order : $\Delta E_{ord} = f(V_k)$ where V_k is the pair interaction energy

If $V > 0$ there is a tendency to ordering
If $V < 0$ there is a tendency to segregation

Configurational entropy

1) Stoichiometric compounds

As the order is assumed to be perfect the configurational entropy of an alloy is equal to zero.

2) Solid solution

The configurational entropy of an alloy is calculated using the Cluster Variational Method, (C.V.M.). For a FCC alloy the cluster is a regular tetrahedron., for a BCC alloy the cluster is a non regular tetrahedron, Figure 8.

3) Liquid phase

Several models are possible to calculate the entropy. A simple way consists in neglecting the short range order so : $S_{conf} = -N k_B (x_A \, Lnx_A + x_B \, Lnx_B)$ where N is the number of Avogadro.

Free energy and calculation of phase diagram

The total free energy of a binary alloy AB in the α phase based on a crystalline lattice I is given by

$$F^{\alpha}{}_{I} = x_A F^{I}_{A} + x_B F^{I}_{B} + \Delta E^{\alpha I} - TS^{\alpha I}{}_{conf.}$$

where F^{I}_{A}, F^{I}_{B} are the free energies of thepure elements A and B in the structure I. The formation energy of the alloy ΔE is obtained from calculation of electronic structure and the configuration entropy is calculated by the CVM method. In practice, the free energies are calculated relative to a common reference state and to calculate the thermodynamic paramaters of mixing at equilibrium, the free energy function is minimized for a given composition. For the calculation of a phase diagram, it is necessary to introduce the grand potential Ω defined by :

$$\Omega = \frac{1}{2} (\mu^{\alpha}{}_{A} + \mu^{\alpha}{}_{B})$$

where $\mu^{\alpha}{}_{I}$ is the chemical potential of the component i in the α phase. The compositions of phases at equilibrium are obtained by minimization of the grand potential at a given chemical potential.

Application to the Ni-Ti system

From a technological point of view, this system is specially interesting for the development of "shape memory alloys" the composition of which is close to the equiatomic composition.
The experimental diagram shows presence of two stoichiometric compounds : $NiTi_2$ with a complex FCC structure and Ni_3Ti with an hexagonal structure and an intermetallic phase based on the composition Ni Ti with the B2 structure.
Moreover it will be noted the presence of a solid solution in the nickel corner with a FCC structure A1 and a solid solution with a BCC structure A2 in the titanium rich corner; at low temperature, the solubility of the nickel in titanium α is very low.
The Figure 9 represents the diagram calculated by LE (a)(26), the experimental diagram (b) (17) and three diagrams calculated by KAUFMAN (c) (27), SANCHEZ (d) (28) and SAUNDERS (e) (29).
Relative to the experimental diagram, that of LE presents some differences about the temperature and the composition of the phase transformation points but these results are encouraging.
It will be recalled that in this system the cohesion is due to a strong hybridation of the d bands of titanium and nickel.

Others systems

It must be mentioned some systems under investigation, for example :
In France, at ONERA, RUBIN, FINEL and DUCASTELLE are working on the ternary systems Ti-Al-Mo, Ti-Al-Nb and Ti-Al-W (30, 31).
J.M. SANCHEZ has results on the systems : ti-Al and Ti-Al-Ni.
Let us recall that MORINAGA (32, 33) from Japan goes on to publish results in the theory design of β type titanium alloys.

ACKNOWLEDGEMENTS

The authors wish to thank : Prof. J.M. SANCHEZ, AND M. R. RUBIN, A. FINEL and F. DUCASTELLE for helpful discussions.

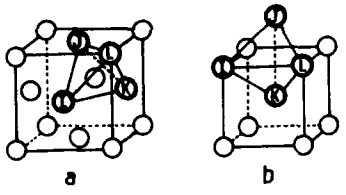


Figure 8 : Tetrahedrons for structures : FCC (a) BCC (b).

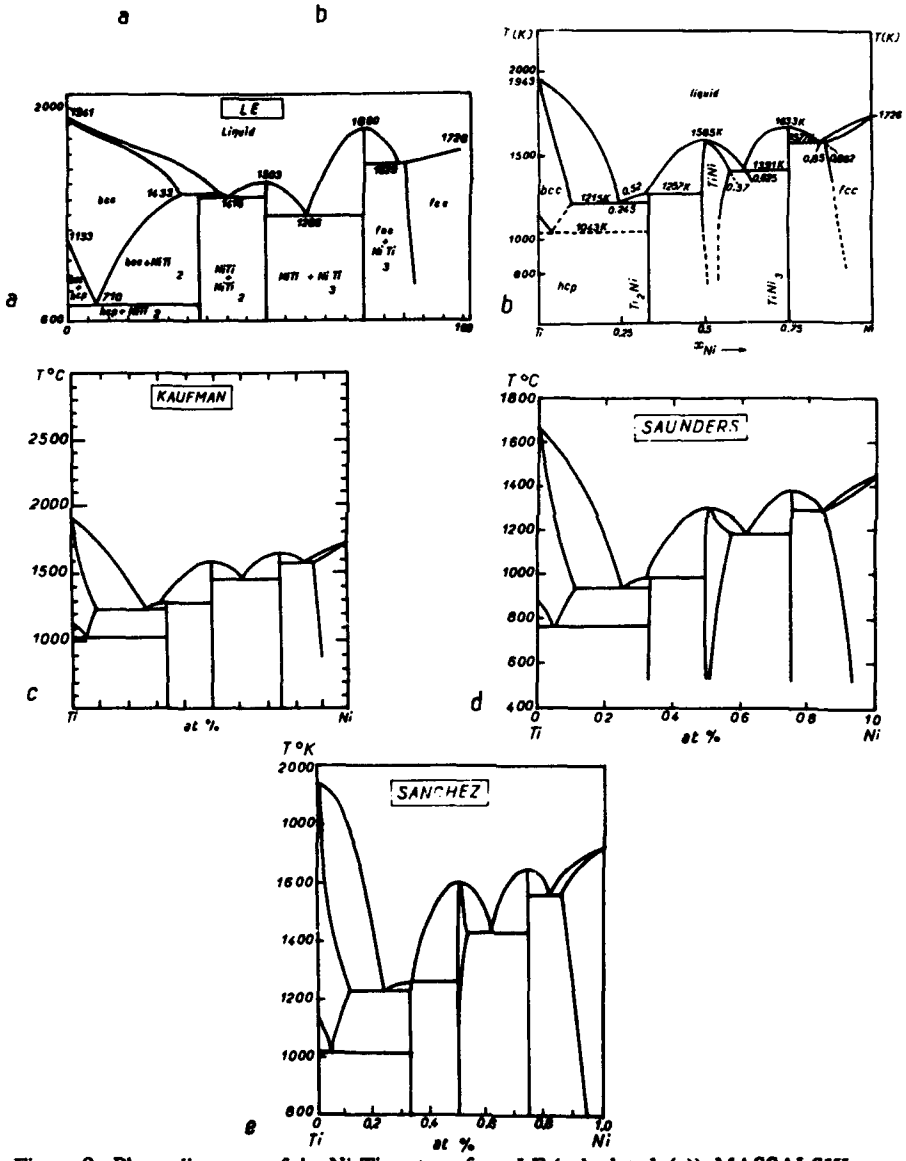


Figure 9 : Phase diagrams of the Ni-Ti system, from LE (calculated, (a)), MASSALSKI (experimental, (b)), KAUFMAN (calculated, (c)), SAUNDERS (calculated, (d)), SANCHEZ (calculated, (e)).

REFERENCES

1. R. TRICOT, Matériaux et Techniques, Fév, (1988), 47-64.

2. Y. COMBRES et B. CHAMPIN, Matériaux et Techniques, Mai-Juin, (1991), 31.

3. I. ANSARA, Thermodynamics of Alloys, Nancy, France, April 28-29-30, May 1st (1992), 26.

4. T. MASSALSAKI, Met. Trans B, vol 20B, (1988), 445-473.

5. E. ALHERITIERE, F. SCHWARTZ, M. THOMAS and B. PRANDI, Sixth World Conference on Titanium, Cannes, FRANCE, (les Editions de Physique, vol II, June 1988), 811-818.

6. I. ANSARA, International Metal Reviews, (Review 238, N°1), (1979), 20-53.

7. J. C. ANGLEZIO, C. SERVANT and I. ANSARA, Calphad, *to* be published.

8. I. ANSARA and B. SUNDMAN,S.G.T.E. Scientific Group Thermodata Europe, Proc. Conf. Codata, Ottawa, (1986).

9. O. REDLICH and A. KISTER, Indust. Eng Chem, 40, (1948), 345-348.

10. H. L. LUKAS, E. Th. HENIG and B. ZIMMERMANN, Calphad, 1, (1977), 225.

11. H. HARVIG, Acta Chemica Scand. 25, (1971), 3199.

12. M. HILLERT and L. I. STAFFANSON, Acta Chemica Scand., 24, (1970, 3618.

13. A. LOISEAU, "Contribution à l'étude du diagramme de phases Ti-Al par microscopie électronique conventionnelle et haute résolution", (Thèse de Doctorat ès Sciences Physiques, 13 Juin 1985), Université de Paris VI.

14. J. L. MURRAY, Phase Diagrams of Binary Titanium Alloys, vol. 1, (edit. T. B. MASSALSKI, Metals Park, OHIO, ASM, 1987), 13.

15. S.DJANARTHANY, C. SERVANT and R. PENELLE, Jal of Materials Research, vol 6, n°5, (May 1991), 969-986.

16. J. P. GROS, "Prévision Thermodynamique de la transformation α / β dans les alliages de titane", (Thèse de Docteur Ingénieur, INPG, 4 Mai 1987).

17. T. B. MASSALSKI, Binary Alloy Phase Diagrams, (Edit.J. L .MURRAY, L. H. BENETT and H. BAKER, vol 2, Second Printing, August 1987).

18. L. KAUFMAN and H. NESOR, Calphad, 2(4), (1978), 325.

19. B. SUNDMAN and J. AGREN, J. Chem..Solids, 42, (1981) 297.

20 T. HAMAJIMA, G. LUTJERING and S. WEISSMANN, Metal. Trans, vol 3, (1972), 2805-2810.

21. J. P. GROS, M. ALLIBERT and I. ANSARA, Sixth World International Conference on Titanium, Cannes, FRANCE, (les Editions de Physique, vol III, June 1988), 1553-1559.

22. L. LIN, L. DELAEY, P. WOLLANTS and O. VAN DER BIEST, Thermodynamics of Alloys, Nancy, FRANCE, (April 28-29-30, May 1st 1992).

23. F. DUCASTELLE, "Order, and Phase Stability in Alloys, Cohesion and Structure", vol 3, (Edit. F.R. de BOER and D.G. PETTIFOR, 1991).

24. F. GAUTIER and F. DUCASTELLE, (1971), Ecole d'Eté de Royan.

25. A. BESSOUD, "Analyse des interactions dans des alliages à base de métaux de transition", (Thèse INPG, 1989).

26. Duc Hiep LE, "Structure Electronique et Stabilité des Composés à Base de Métaux de Transition", (Thèse de Doctorat en Sciences, INPG, 26 Avril 1990).

27 L. KAUFMAN and H. NESOR, Calphad, vol 2, n°1, (1978), 81.

28. N. C. TSO and J.M. SANCHEZ, Mat. Res. Society Symposium Proceedings, 133, (1989), 63.

29. N. SAUNDERS, Thèse de LE, (1990), 98.

30. R. RUBIN, A. FINEL and F. DUCASTELLE, private communication.

31. S. NAKA, M. THOMAS and T. KHAN, Conference "High Temperature Intermetallics" (The Royal Society, London, (G.B.), April 30, May 2, 1991).

32. M. MORINAGA, M. KATO, T. KAMIMURA, M. FUKUMOTO, I. HARADA and K. KUBO, this book.

33. M. MORINAGA, N. YUKAWA, T.MAYER and K. SONE, Sixth World Conference on Titanium, Cannes, FRANCE, (Les Editions de Physique, Juin 1988),.1601.

SURFACES AND ELEVATED TEMPERATURE EFFECTS

M.A. Daeubler, D. Helm

MTU Motoren- und Turbinen-Union München/
Deutsche Aerospace, P.O. Box 50 06 40,
8000 München 50, FR Germany

Abstract

The need for improving the performance of aeroengines requires increasing the application temperature for titanium above 450° C. Titanium alloys developed to operate at high temperatures up to 600° C are generally sensitive to surface conditions. A major challenge is long term oxidation resistance at operating temperatures around 600° C combined with maximum exploitation of applied loading. Surface treatments e.g. mechanical machining, electrochemical machining (ECM), shot peening, or surface finishing have a great impact on fatigue life. Detrimental effects must be accounted for if contaminants such as nickel or steel particles and lubricants cannot be avoided. The need for coatings as protection against oxidation, corrosion, fretting and titanium fire is obvious. This paper discusses the influence of surface treatments and protection on mechanical properties relevant to jet engine applications.

Titanium '92
Science and Technology
Edited by F.H. Froes and I. Caplan
The Minerals, Metals & Materials Society, 1993

Introduction

Improved aeroengine performance often can be achieved only by increasing service temperatures and specific strength. The latest developments in high temperature titanium alloys are designed for operating temperatures up to 600° C. The more the temperature capability in terms of strength and bulk stability of titanium alloys is increased, the higher is the penalty which has to be paid with respect to surface stability and integrity. The steadily increased service temperature accompanied with enhanced surface sensibility has possibly reached or exceeded the temperature limits even of the newest high temperature titanium alloys. Surface effects are becoming more and more critical and therefore urgently need to be addressed; oxidation, corrosion, erosion, fretting, contamination, fire resistance, surface treatments and finishing are of major importance. The influence of heat treatments, surface conditions and treatments or surface protection on mechanical properties relevant to jet engine applications will be discussed in the following sections.

Surface Oxidation

The influence of long time exposure at elevated temperatures in air on the mechanical properties of IMI 834 has been reported recently [1]. In this section differences in surface oxidation sensitivity between IMI 834 and Ti-6242 will be discussed. The influence of long term exposure in air on IMI 834 tensile properties at room temperature and 650° C is shown in Fig.1. The yield stress of exposed material, either with the oxidized surface removed or retained was 50 MPa above the reference material aged 2 hrs at 700° C only. The increase in strength is an indication for additional aging during long term exposure at 650° C. Looking at tensile elongation (A_5) two effects can be recognized. Firstly, there is a ductility loss of some 3 percent over the whole temperature region due to age hardening (compare triangles against solid dots). If the oxidized surface is not removed a drastic drop in elongation at room temperature (open circles) is experienced. With increasing test temperature the influence of increased plastic deformation reduces the differences in tensile ductility. Isochronal exposure tests for IMI 834 (Fig. 2) revealed a strength increase at and above 450° C and simultaneously only a slightly reduced ductility was observed for specimens with surface removed. After exposure of 100 hrs in air and 2 hrs in vacuum respectively the ductility loss is more pronounced, when the surface is retained. For IMI 834 life reduction by oxidized surfaces on low cycle fatigue (LCF) at room and elevated temperatures has also been reported earlier [1, 2]. Fig.3 gives an example at 550 °C test

temperature. For smooth specimens oxidized 500 hours at 600° C in air the life cycles are lowest when the oxidized surface is retained. Note that the life time is longest for a specimen after long term exposure and removal of the oxidized surface. This is due to aging by additional precipitation of Ti_3Al.

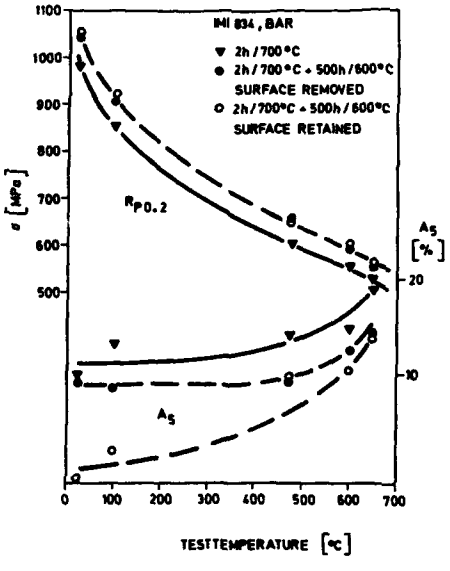


Fig. 1 Influence of long time exposure in air on IMI 834 tensile properties.

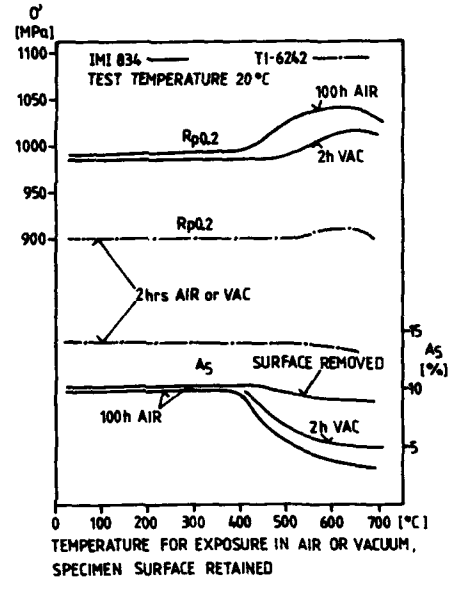


Fig. 2 Isochronal exposure of IMI 834 and Ti 6242 tensile specimens.

In contrast to IMI 834 the Ti-6242 does not show any remarkable tensile ductility loss after 2 hrs exposure at temperatures between 550 and 650° C in air or vacuum, respectively. Fig. 2 illustrates a slight increase in yield stress with increasing exposure temperatures whereas the elongation remains almost constant. Tensile tests are not, however, always sensitive enough to reveal surface embrittlement effects. It can be seen in Fig. 4 for strain controlled LCF tests of smooth specimens that at both test temperatures (20° C and 400° C) exposure in air at 590° C for 2 hrs reduces the number of cycles to failure remarkably. These LCF results clearly demonstrate that exposure in air at temperatures above 450 °C should be avoided for both titanium alloys IMI 834 and Ti-6242, or a reduction in fatigue life must be counteracted by oxidation protective coatings. Desired heat treatments during fabrication, even in technical vacuum, e.g. post weld heat treatment or stress relieving, should subsequently be followed by surface removal.

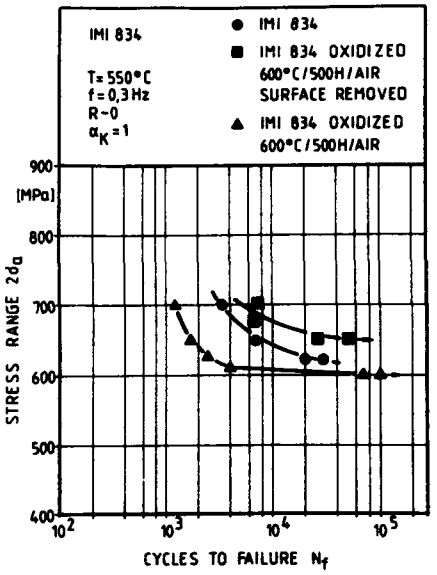


Fig. 3 Influence of oxidation on load controlled LCF.

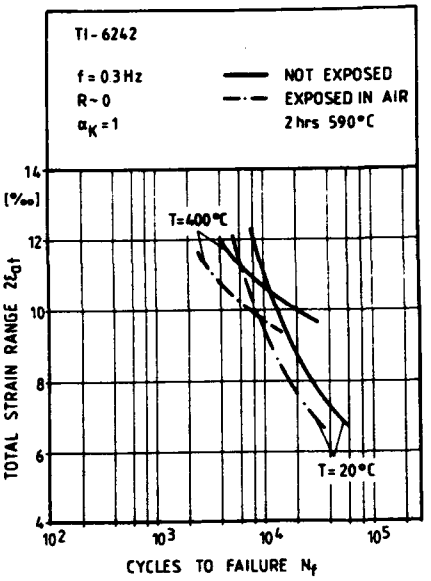


Fig. 4 Influence of oxidation on total strain controlled LCF.

Surface Treatments

Surface treatments have a great impact on fatigue properties of titanium alloys. The high cycle fatigue (HCF) behavior of cylindrical smooth specimens for IMI 834 is plotted in Fig. 5. At room temperature, a surprisingly low fatigue strength for 10^7 cycles of about 400 MPa was measured for as turned and mechanically polished (MP) specimens. Assuming that residual stresses due to distortion of the surface during specimen machining caused this effect, the surfaces of some specimens were additionally electrolytically polished (EP) or stress relieved (SR). For the EP condition about 100 μm surface was removed. Stress relieving was conducted at 600 °C for 24 hrs. In both cases the fatigue strength increased to almost 600 MPa at 10^7 cycles. This example indicates that machining even combined with post mechanical polishing can cause significant fatigue strength reduction at least for HCF under tension-tension loading. Due to the residual stress distribution, surface layers are under compressive stresses whereas subsurface regions (some 100 μm depth) are in tension which leads to early subsurface crack initiation resulting in reduced fatigue life. Shot peening does not improve the fatigue life of the MP specimens in tension-tension testing. On the other hand an improvement is observed for tension-tension tests on circumferentially notched HCF specimens, Fig. 6, as well as for rotating beam tests on smooth specimens. The reason is that

shot peening is only effective, when it results in a total stress gradient with the maximum stress on the surface, which is the case for the latter two testing situations. In Fig. 6 it can be seen that shot peening increases the 10^7 fatigue strength at 600 °C from 675 MPa to 900 MPa ($\sigma_{max}.K_t$). The reference curve is EP, i.e. the surface was electrolytically polished. In order to provide a proper comparison, the shot peened (SP) specimens were mechanically polished before testing to eliminate possible surface roughness effects.

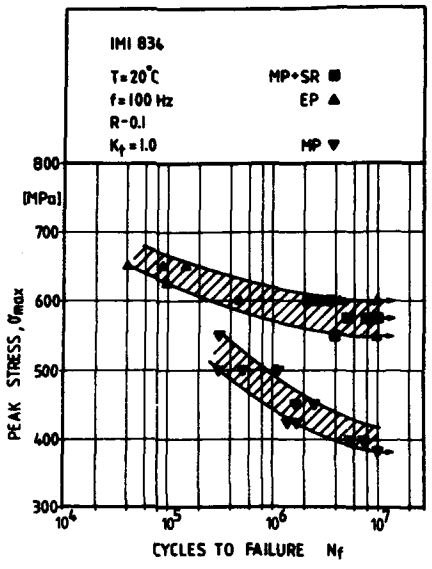


Fig. 5 Influence of stress relieving on room temperature HCF

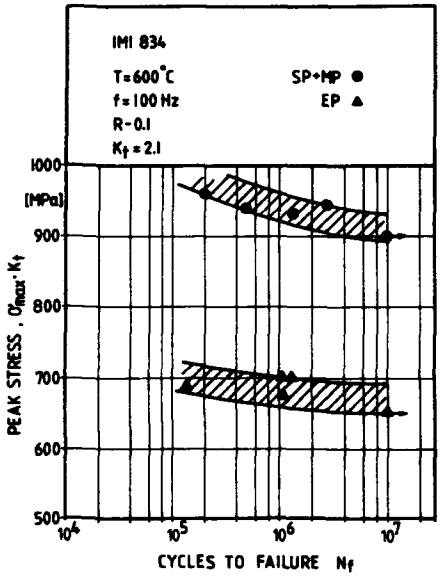


Fig. 6 Influence of shot peening on elevated temperature HCF. (notched specimens)

Low cycle fatigue (LCF) behavior is also influenced by surface condition as can be seen from Fig. 7 for the alloy IMI 834. The tests were performed on flat specimens with a center hole (dia. = 4.5 mm) and notch factor K_t = 2.5; stress relieving was 2 hrs at 700 °C. Fatigue life is lowest for stress relieving (SR) after prior machining (drilling) and highest in the as drilled condition. Life time was only intermediate for drilled and shot peened center holes possibly due to its higher surface roughness compared to the drilled surface. Residual stress profiles were comparable for both drilled only and drilled and finally shot peened holes exhibiting maximum compressive stresses of around 700 MPa. Additional LCF tests were performed on Ti-6242 using flat specimens with milled double edge notches, K_t = 2.2, tested at room temperature (RT) and 300 °C. Fig. 8 reveals that specimens at both testing temperatures with machined only (milled) and machined plus shot peened notches show

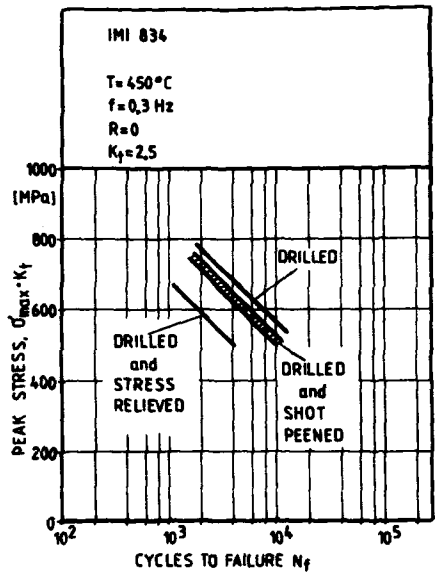


Fig. 7 Influence of surface conditions on LCF. Flat specimens with center hole.

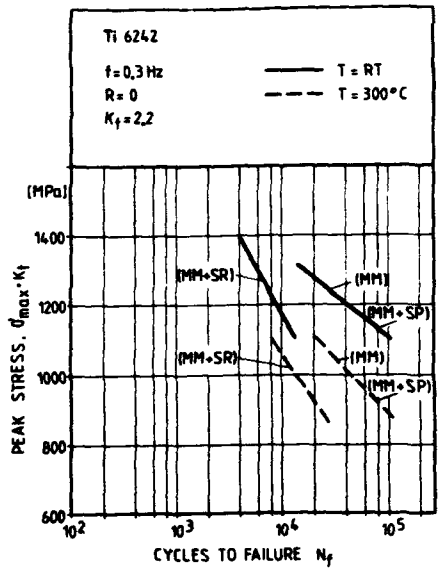


Fig. 8 Influence of surface conditions on LCF. Flat specimens with double edge notches.

identical fatigue life cycles within a typical scatterband. Final stress relieving (2 hrs 590 °C) again leads to lowest life. As a consequence for the production of components with holes or notches, shot peening should be performed after the last stress relieving (e.g. post weld heat treatment) whenever possible.

Contaminants

During fabrication completely machined parts often need to be heat treated mostly for stress relieving without subsequent surface cleaning. Contaminants sticking on the surface often cause detrimental surface attack during heat treatments even in vacuum and especially during exposure in air. The latter is the worst case and can occur in faulty technical vacuum or for applications in a jet engine compressor. The influence of a lubricant, different Ni-containing powders, and steel after 50 hrs exposure at different temperatures in air is listed in Table 1. Extreme testing conditions have been chosen for demonstrative purposes. Taking IMI 834 as an example, it was found that up to 425° C exposure most contaminants caused only weak attack, between 450 and 550° C a remarkable pitting corrosion appeared, while at 600° C and above, deep cor-

	"Never Seez" Lubricant	Nickel, pure 5/µm Powder	*Udimet 700* 45/µm Powder	*Inconel 718* 50/µm Powder	*Steel balls* S110 (350 µm)
Metallic Contamination Components	Ni Al	Ni pure	Ni, Cr, Co some Mo, Ti, Al	Ni, Cr, Fe some Mo, Nb	Fe some C, Mn
IMI 834					
350 °C	-	-	-	n.e.	n.e.
400 °C	-	-	-	n.e.	n.e.
425 °C	-	-	-	-	*
450 °C	++	+	-	-	n.e.
500 °C	++	+	-	-	n.e.
550 °C	++	+	+	-	*
600 °C	0	+	0	0	n.e.
650 °C	0	0	0	0	*
Ti 6-2-4-2 550 °	0	0	-	-	*
IMI 685 600 °C	0	0	0	0	*
Ti 6-4 600 °C	0	0	0	0	*

Pit Depth

0 1-2 µm
++ .5 µm (with reaction zone)
+ .5 µm
- weak attack of oxide layers
* sub surface embrittlement
N.e. not evaluated

Table 1: *Influence of contaminations after 50 hrs exposure in air for different Ti-Alloys at elevated temperatures*

rosion pits were observed. It is recalled that previously mentioned effects, in particular oxidation (see Fig. 2), also fall in the above temperature classification. Additional penetration due to diffusion into the subsurface layers was not evaluated. The results for Ti-6-4, Ti-6-2-4-2 and IMI 685 at 550° C and 600° C support the results for IMI 834. This leads to the conclusion that heat treatments in air or low quality vacuum and applications above circa 425° C for long times must be regarded with care and a corresponding life reduction has to be taken into account depending on the extent of surface degradation. The above mentioned results also emphasize the need for careful cleaning of machined parts before heat treatment even in technically high quality vacuum.

Coatings

Titanium fire is a very fast surface combustion/oxidation process resulting in temperatures as high as 3200° C. It is a very short event of less than 10 seconds and applies mainly to military jet engines due to excessive temperature, pressure, and aerodynamic conditions. Measures against titanium fire include avoiding wear of titanium against titanium, blade tip platings, coatings (e.g. Pt/Cu/Ni, ZrO_2, C/C), or fire resistant Ti-alloys. The burning velocity for conventional Ti-alloys (IMI 834, Ti-6-4, $TiCu_2$) and titanium-aluminides (Super Alpha Two) on Ti_3Al base and Ti-48Al-2Nb on TiAl (Gamma base) is shown in Fig. 9. The results suggest the use of Al-rich alloys or coatings against titanium fire due to their ignition and burning resistance.

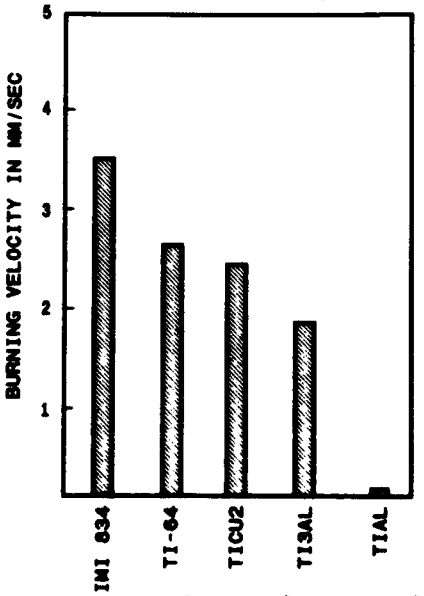


Fig. 9 Burning velocity of different titanium alloys

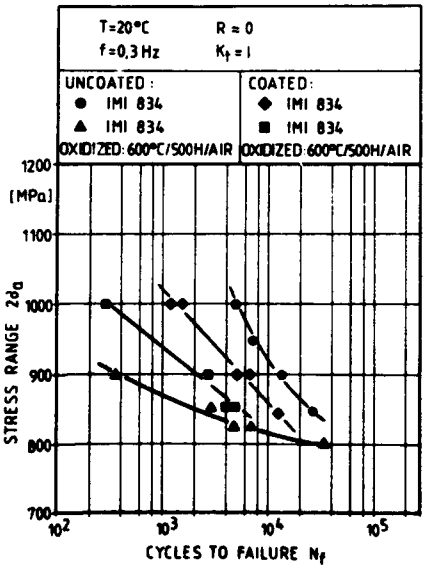


Fig. 10 LCF of coated and uncoated IMI 834 unexposed and after exposure

Oxidation resistant coatings will play a key role when applying Ti alloys at temperatures as high as 600° C. General reports about surface engineering [3] and oxidation resistant coatings for Ti-alloys [4] were presented at the last Ti-Conference in 1988. Both papers suggested that almost all coatings resulted in reduced fatigue strength or, at best, little change. Oxidation resistant coatings, e.g. NiCr coating on IMI 829 [4] showed good oxidation protection but still reduced fatigue life in LCF tests when comparing coated and unexposed with coated and exposed specimens. For an Al diffusion coating similar results were evaluated for IMI 834 at room temperature LCF tests (Fig. 10). Comparing unexposed material (solid dots) a loss in fatigue life due to coating (diamonds) is obvious. A further life reduction was measured for coated and exposed condition (squares), worst was exposed and surface oxidized material (triangles). For high cycle fatigue at room temperature (Fig. 11) the unexposed and exposed specimens showed, within some scatter, the highest HCF strength whereas the coated and coated plus exposed conditions showed the lowest HCF strength. At 600° C the differences diminished with the tendency for lowest HCF strength of the exposed and surface retained condition (Fig. 12) marked by solid triangles. For IMI 834 Al-diffusion on coatings revealed detrimental effects on LCF and HCF at room temperature and at best, little improvement on HCF at 600° C.

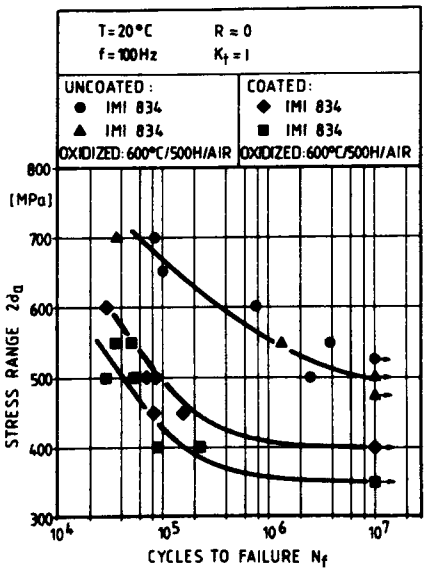


Fig. 11 Room temperature HCF of coated and uncoated IMI 834 with and without exposure.

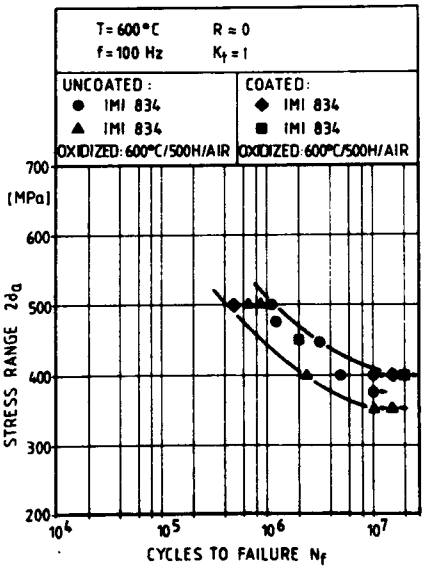


Fig. 12 Elevated temperature HCF of coated and uncoated IMI 834 with and without exposure.

Fretting Fatigue

Recently the influence of several coatings on fretting fatigue behavior of Ti-6Al-4V has been tested [5] using flat specimens with fretting pads. It could be demonstrated that besides shot peening and a $Co+Cr_2O_2$ coating a copper plating was the most effective coating. The efficiency depends on the thickness of the copper layers. The fatigue strength at 20° C dropped from 600 MPa stress range (R=0.1) down to 200 MPa under fretting without coating. A variety of increasing copper layer thicknesses up to 60 μm was tested. Fretting fatigue strength increases back up to 450 MPa. Additional HCF fretting fatigue tests on Ti-6242 at 300° C have been performed [6]. Specimens were either laser gas nitrided or ion implanted using nitrogen or boron. Ion implantation produces relatively thin layers (0,1 to 1 μm) and therefore are not fretting fatigue resistant. Laser gas alloying produces TiN or TiC in the subsurface material on the order of 50 to 500 μm thickness. The TiN or TiC layers are generally wear resistant, but superimposed with fatigue loading early crack initiation reduces fretting fatigue life remarkably.

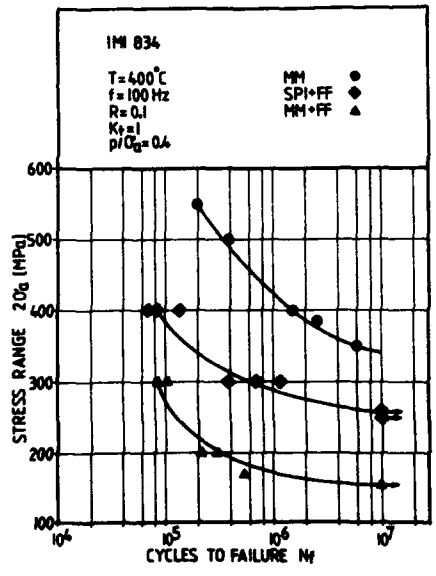


Fig. 13 Fretting fatigue for material combination IMI 834 flat specimens and IMI 834 pads.

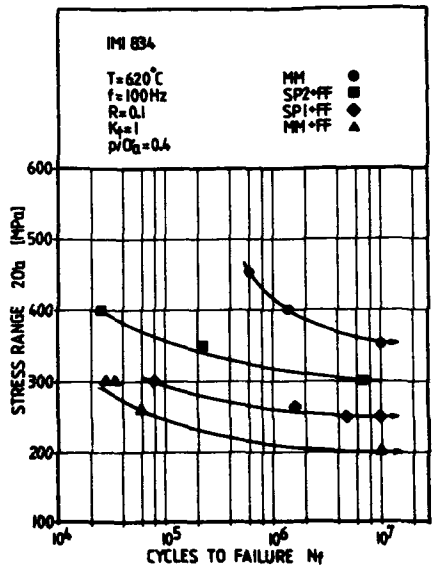


Fig. 14 Fretting fatigue for material combination IMI 834 flat specimens and IN 718 pads.

Shot peening is a very effective alternative to coatings against fretting fatigue. For Ti-6Al-4V shot peening increased the stress range (maximum stress for R=0.1 at 10^7 cycles) from 200 MPa up to 400 MPa under HCF-fretting at room

temperature [5]. An example of fretting fatigue behavior of IMI 834 is given in Fig. 13. The material combination IMI 834 specimen/ IMI 834 fretting pads simulates IMI 834 disc/IMI 834 blade component tests at 400° C. Specimens and pads were milled (MM) or shot peened (SP). Fretting fatigue tests were designated as FF, reference curves without designation are regular HCF tests without fretting. HCF strength at 450° C is 360 MPa, drops under fretting fatigue down to 160 MPa and increases after shot peening to 250 MPa. Comparable tendencies were measured at 620° C for a simulation of IMI 834 disc combined with a superalloy IN 718 blade (Fig. 14). HCF strength is 350 MPa, fretting reduces fatigue strength to 200 MPa. Shot peening (SP1 refers to small ball sizes, SP2 refers to bigger sizes) enhances fretting strength to 250 MPa for (SP1) and 300 MPa for (SP2). Both examples demonstrate that most of the fatigue strength lost under fretting fatigue can be regained by shot peening which is effective even at temperatures up to 620° C.

Summary and Conclusions

The results of investigations of the effect of surface treatments and protection on the high temperature mechanical properties of titanium alloys can be summarized as follows:

- Exposure in air at or above 450° C results in surface degradation, reducing ductility and low cycle fatigue strength.

- Nickel containing lubricants and powders as well as steel particles have to be avoided at or above 450° C.

- High cycle fatigue strength of smooth IMI 834 specimens can be enhanced by stress relieving or electrolytical surface removing. Shot peening is effective on notched specimens even at 600° C testing temperature.

- LCF of specimens having as machined notches or holes exhibited life times not different from machined and shot peened condition.

- Titanium fire can be opposed by aluminium-rich coatings or alloys. However oxidation resistant coatings that do not reduce fatigue life still have to be developed.

- Shot peening is a sufficient alternative to coatings against fretting fatigue and is effective even at temperatures up to 620° C.

- For envisaged application temperatures above 450° C surface protection for titanium alloys has therefore become of increasing importance.

Acknowledgment

The authors would like to acknowledge the helpful discussions and support of G. Luetjering regarding surface treatments. We also wish to express our appreciation to W. Wei, J. Specht, T. Uihlein and R. Grunke for their assistance and supplementary results. A. Axtner and R. Lackermeier are also gratefully acknowledged for their technical support.

Literature

[1] M.A. Daeubler, D. Helm, "Influence of Long Time Exposure at Elevated Temperatures in Air on Mechanical Properties of the High Temperature Titanium Alloy IMI 834" in Titanium 1990 - Products and Applications, Proc. of 1990 Int. Conf. Orlando, FL, USA, published by TDA Titanium Development Association, Dayton, Ohio 45401, 1990, PP 244-255.

[2] B. Borchert, M.A. Daeubler, "Influence of Microstructure of IMI 834 on Mechanical Properties Relevant to Jet Engines" in Proc., 6th World Conf. on Titanium, Cannes 1988, Eds. P. Lacombe, R. Tricot, G. Beranger, Les Editions de Physique, 1989, pp 467-472.

[3] P.H. Morton, T. Bell, "Surface Engineering of Titanium", ibid., pp 1705 - 1712.

[4] N.W. Kearns, J.E. Restall, "Oxidation Resistant Coatings For Titanium Alloys", ibid., pp 1753 - 1758.

[5] M. Thoma, "Influence on Fretting Fatigue of Ti-6Al-4V by Coatings" ibid., pp 1877 - 1881.

[6] K. Dittmar, "Fretting Fatigue Behavior of Ion Implanted and Laser Alloyed Ti-6242", Diploma Thesis (in German) 1991, MTU-Munich

PRESENT FEATURES IN PRODUCTION OF TITANIUM SPONGE AND INGOT

Shigeru Tamamoto

Osaka Titanium Co., Ltd.

Higashihama-cho 1, Amagasaki, Japan 660

Abstract

With the production of titanium sponge growing steadily, worldwide annual production capacity reached 136,000 tons this year. Nearly 96% is produced by the Kroll process, and the remainder by the Hunter process. Remarkable advancements in technological development were made in the 1950s through the mid 1980s. Although a number of research efforts to find a new method of production have been made, none have reached the industrial application stage. On the other hand, rapid progress has been made in the technology for producing small quantities of high purity titanium for use as a semiconductor material.

Consumable electrode vacuum arc remelting (VAR) is still by far the major process, while cold hearth melting by electron beam or plasma arc is attracting increased attention for melting critical aircraft engine material, since it effectively removes HDIs and LDIs. However, VAR furnaces will remain the major means of melting the material for general use. A new cold crucible melting process using induction heating has advanced to the stage of practical use. Melting of large size ingots has not, however, been realized. Hopefully its practical application will be realized in various fields by taking advantage of its features as the technology is perfected.

Introduction

Rapid progress has been made in titanium production for almost half a century since its industrialization. The status of development was reported in detail at two preceding conferences held in Munich and Canne (1, 2). This report outlines the present status of production and the technology relating to titanium sponge production and its melting.

Titanium '92
Science and Technology
Edited by F.H. Froes and I. Caplan
The Minerals, Metals & Materials Society, 1993

Titanium Sponge

1. Production of Titanium Sponge by Conventional Process

1-1 Quantity and Capacity of Production

The worldwide capacity and the titanium sponge production processes are tabulated in Table I. Surprisingly CIS is said to have a capacity of 80,000 tons per year. The Kroll magnesium reduction and Hunter sodium reduction processes represent the current production processes, with the Kroll process accounting for nearly 96% of the total capacity.

Table I Ti Sponge Production Capacity and Processes Worldwide (1992)

Company/Country	Production (tons/year)	Process	Number of Reduction Furnaces	Furnace Productivity (tons/year)
TIMET	12,700	Mg-Leach	NA	NA
OREMET	6,800	Mg-He Sweep	10	680
U.S. Total	19,500			
Osaka	15,000	Mg-Vac. Distil.	40	380
Toho	10,800	Mg-Vac. Distil.	32	340
Showa	3,000	Mg-Vac. Distil.	10	300
Japan Total	28,800			
Deeside	5,000	Na-Leach	30	170
Total Free World	53,300			
CIS (USSR)	(80,000)	Mg-Vac. Distil.	NA	130 - 350
China	(2,700)	Mg-Vac. Distil.	NA	NA
Total World	(136,000)			

Note: NA: Not available
The capacity is based on TDA reference (3) partly ammended by recent information.

The number of reduction furnaces and their productivity are also shown in Table I within the scope of available information. Among other moves to date, TIMET, which uses the Kroll process and removes chlorides by leaching, has introduced vacuum distillation technology from Toho Titanium and commenced construction of a 10,000-ton/year facility. It is reported that Toho Titanium will enlarge its reduction and distillation furnaces and develop automation in order to increase productivity.

1-2 Progress in Kroll Process

The productivity achieved by the main facilities at Osaka Titanium over the past 30 years is shown in Figure 1. Chlorinator productivity increased 12 times due to changing from the fixed bed to the fluidized bed process, while that of magnesium electrolytic cells rose ten times through the advent of multipolar cells. The increase in productivity, however, remains at no more than fourfold despite the process change and enlargement of the reduction and distillation furnace. However, an increase in productivity due to enlargement of the batch size is very important in terms of reducing the cost of titanium sponge. This is still being pursued in the US and Japan. In this regard, credit must go on OREMET who took the initiative back in 1965. A remarkable reduction in electric power consumption through the use of multipolar cells has been attained in magnesium electrolysis which consumes more than 70% of the power required for titanium production.

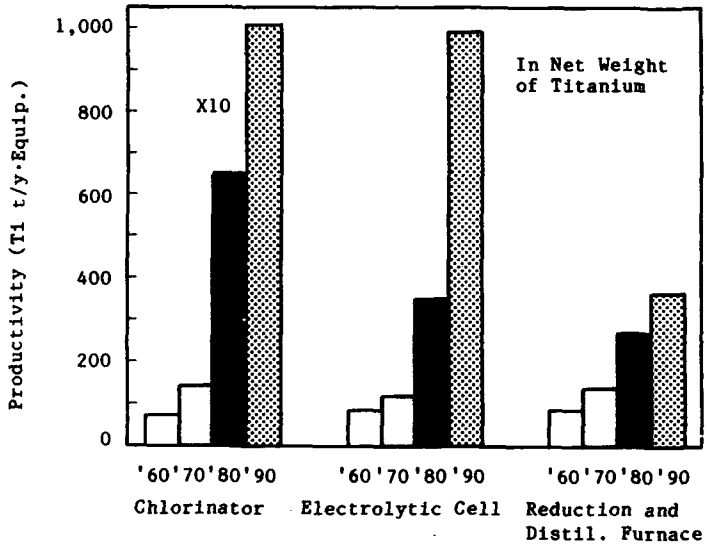


Figure 1 Equipment Productivity Using Kroll Process

1-3 Radioactivity Problems in Japan

Beginning with the detection of radioactivity in the waste from the sulfuric acid leaching of titanium ore at the titanium pigment producers in July 1990 in Japan, the problem was passed on to the sponge producers. The maximum level of radioactivity detected in the waste from the titanium pigment producers was 1.8 μGy/hr, and that from the sponge producers was 0.7 μGy/hr. Radioactivity of the waste was reduced to below 0.14 μGy/hr by selecting titanium ore and improving process, and the problem was solved in June 1991.

2. Production of Titanium by New Processes

A number of efforts have been made to develop new processes. Although many reports (4, 5, 6, 7, 8) have appeared concerning the method of direct electrolysis, none has been presented on its practical utilization because of potential difficulties and cost. Since there are certain research

activities in this field, some of the new processes currently being developed are mentioned below.

2-1 GTT Process

Ginatta has developed the electrolytic process (9, 10, 11), and has set up a 30-ton/year pilot plant where a product containing O<600, N<20 and Al, Fe, Si<10 in ppm is obtained (12). A 140-ton/year pilot plant went into operation in 1989 at RMI (10,13).

2-2 Thermal Plasma Process

The Colorado School of Mines researched disproportionation of TiI_4 by means of high temperature plasma based on the free energy data. However, no metallic titanium was obtained due to insufficient control of the temperature in the plasma reactor (14).

2-3 Vapor Phase Reaction of $TiCl_4$ and Mg

A group in Japan is experimenting vapor phase reaction between titanium tetrachloride and magnesium as a part of the Minerva Project. The project was named after the Goddess of Wisdom in Roman mythlogy.

2-4 Reduction of Calcium Fluorotitanate

Research is being carried out by the U.S. Bureau of Mines, where titanium ore such as ilmenite is reacted with fluorosilicate acid to obtain TiF_4. After purifying TiF_4, $CaTiF_6$ is precipitated through its reaction with $CaCO_3$ and HF. Metallic titanium is obtained by Ca reduction of $CaTiF_6$ continuously fed into the induction slag furnace (15).

3. Production of High Purity Titanium

3-1 Uses of High Purity Titanium

The titanium target is sputtered to form low resistivity gates, interconnectors and diffusion barrier in Si-LSIs. Titanium with a minimum level of impurities listed below is required in order to obtain semiconductor devices of stable characteristics:

. Fe, Cr, Al etc: Metallic elements cause junction leaks and lower the high voltage barrier.

. Na, K etc: Alkaline metals are mobile and cause deterioration of the interface characters.

. U, Th etc: α-radioactive elements cause soft errors.

3-2 Production of High Purity Titanium by the Conventional Process

High purity titanium of 4N (four nine) grade is being produced using the current Kroll process. In this process, impurities tend to be positively segregated toward the bottom and the sides of the sponge cake. Therefore, enlarging the batch size will reduce both their average values and the deviation. Osaka Titanium has made it possible to supply 4N titanium with Fe<30, alkaline metals<0.1, U & Th<0.001 and other metals<10 in ppm on the basis of a 10-ton batch and the selection of its core with less impurities (16). Recently, it has become possible to produce 4N5 titanium using the Kroll process under strict quality control.

3-3 Production of High Purity Titanium by Novel Processes

Typical processes employed and the degree of purity obtained by each producer are shown in Table II. ALTA and Nippon Mining electrorefine crude titanium sponge, while Osaka Titanium uses the Iodide process.

In the case of electrorefining by Nippon Mining, an electrolytic bath containing a mixture of Na, K and Li chlorides is used. The cathode is placed in the center of the cell vertically, and the anode is in the form of a cylindrical basket surrounding it. The titanium sponge is contained in the basket anode. The titanium electrodeposited on the cathode is extracted and leached, and subsequently electron beam melted to produce 6N titanium. The concentration of metallic impurities is Fe<0.05, Na & K<0.02 and U & Th<0.001 in ppm (17, 18, 19).

Table II Processes and Purity of High Purity Titanium (Example)

Company	Process	Purity	Oxygen (ppm)	Nitrogen (ppm)
ALTA (USA)	Electrorefining	4N8 - 5N	50 - 300	5 - 15
Nippon Mining (Japan)	Electrorefining	6N	120	NA
Osaka (Japan)	Iodide Process	5N	50 - 80	10
	Kroll Process	4N5	250	10

Note: NA: Not available

In the Iodide process used by Osaka Titanium, crude titanium is reacted with TiI_4 vapor to form TiI_2, which is then thermally decomposed to deposit high purity titanium. High purity titanium with Fe, Ni and Cr<1 in ppm can be obtained by this process (20).

Melting

1. Comparison of Melting Furnaces and Their Capacity

Consumable electrode arc remelting (VAR) accounts for more than 90% of the titanium melting capacity. Electron beam and plasma arc melting methods have entered practical use and are being widely used. Table III lists the estimated melting capacities worldwide.

Table III Melting Capacity Worldwide (1991)
Estimated (tons/year)

Country	All Funaces	Other than VAR
USA Japan Europe	75,300 21,200 12,800	[13,600] [900] [500]
Total Free World	109,300	[15,000]
CIS China	(55,000) (4,000)	
Total World	(168,300)	

The melting rate and the power consumption reported on the currently used titanium melting furnaces are summarized in Figure 2. The furnace capacity and the kind of the melt stock or the alloy results in a vast difference in the data obtained for the same type of furnace, however, a general trend is shown.

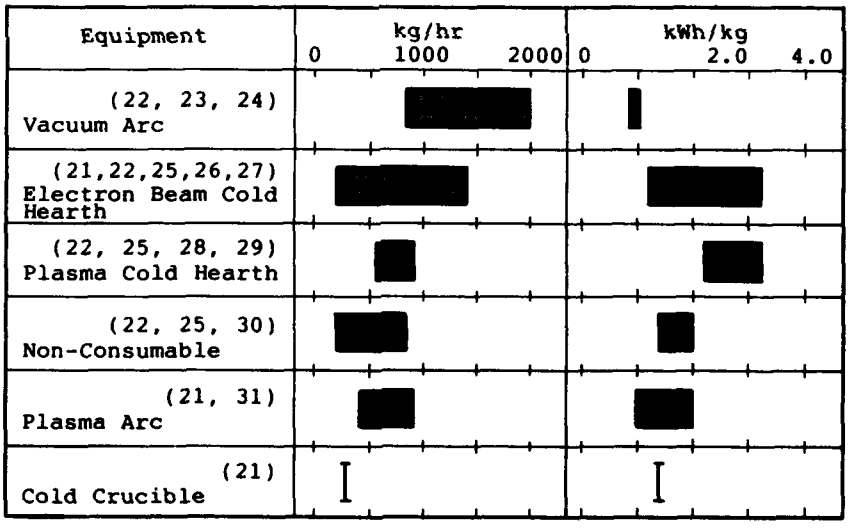


Figure 2 Comparison of the melting rate and the electric power consumption of various furnaces

The furnaces listed in Figure 2 have a number of merits and demerits, and the representative features appear in Table IV.

Table IV Features of Titanium Melting Furnaces

Equipment	Features	Weak Point
Consumable Arc (VAR)	. Simple . Economical	. Difficult to Eliminate Inclusions
Electron Beam Cold Hearth (EBCHR)	. Elimination of Inclusions . Variable Ingot Shape	. Evaporation of Al
Plasma Cold Hearth (PCHM)	. Elimination of Inclusions . Variety of Feed Stocks	. Low Power Efficiency
Non-Consumable Electrode (NCE)	. Compacting not Necessary . Variety of Feed Stocks	. Primary Melting Only
Cold Crucible (CCM)	. Stirring Pool . Held in superheat	. Difficult to Make Large Ingots

2. Present Status of Melting Furnaces of Different Types

2-1 VAR Furnace

This type still constitutes the mainstream for titanium melting, although no remarkable progress has been made in either the equipment or the melting technology since the last conference was held (2). A coaxial type electric power supply and computer-controlled melting have become common practice. It is said that melting furnaces in RMI can produce the world's largest 23 ton ingot.

Taking advantage of its economy brought about by low electric power consumption and high melting rate, VAR will continue to play the leading role in melting materials of standard quality for aircraft engine parts and those for non-aircraft use.

One problem associated with the VAR process is bursts caused by damage to the mold. The Japan Titanium Society holds a study group for the purpose of ensuring safety during melting.

2-2 Cold Hearth Melting Furnace

Electron beam or plasma is the source of thermal energy. It is characterized by the local separability of melting, refining and solidification. Low-density inclusions (LDIs) such as nitrides and oxides, and high-density inclusions (HDIs) such as high-melting heavy metals are prevented from entering into the ingot pool by dissolution or precipitation on the skull, while the molten metal flows through the cold hearth (32, 33, 34, 35). This feature of cold hearth melting has been noted lately. It will be prevailing in the production of premium quality parts for aircraft engines (36, 37).

(1) Electron Beam Cold Hearth Refining Furnace (EBCHR)

Axel Johnson used to own a 2,000 kW EBCHR furnace, and has completed a new one with a power output of 3,300 kW (38, 39). As a result, its melting capacity was increased from 2,300 tons/year to 6,800 tons/year.

Most recent advances in EBCHR include measurement and control of the melting rate, measurement of temperature distribution on the melt surface, monitoring of the melt components by means of energy dispersion X-ray analysis, automation of the hot top process, and improved stability and reproducibility by means of position determination with the electron beam (28). It is now also possible to make a hollow ingot or perform multistrand casting by EBCHR (40).

(2) Plasma Cold Hearth Melting Furnace (PCHM)

The plasma furnace features little vaporization loss of the alloying elements compared with the electron beam furnace. While Wyman-Gordon has a 2,250 kW PCHM furnace (41), Teledyne Allvac installed a 750 kW furnace equipped with four plasma torches which has been in operation since 1990 (42).

Ar or He is chosen for the torch gas in the inert gas atmosphere in the plasma furnace, and it is now feasible to use He for the torch gas though it is expensive, since gas recycling equipment was brought into practical use (22). He is more efficient than Ar, hence, it is said that twice the melting rate can be realized under normal melting conditions (43).

Other novel technology includes: Determination and control of the melting rate in terms of the ingot withdrawal and feeding rate, determination of the melt surface temperature distribution using two-color pyrometric devices or thermal imaging, monitoring of the melt composition (or concentration of certain elements) by means of emission spectroscopy, and analysis and monitoring of the off gas from the melt surface using a mass spectrometer (28).

2-3 Cold Crucible Melting Furnace (CCM)

CCM is a process for melting metal having a high melting point in a water-cooled copper crucible that is split into a number of segments and placed inside the induction coil instead of a refractory crucible. CCM is in practical use for casting small products taking advantage of the feasibility of obtaining cleaner metal compared with the induction melting process using a refractory crucible, and the melt can be brought to an appropriate superheat in comparison with VAR.

A process of manufacturing a billet by directly withdrawing the ingot has been developed (44, 45). It was thought that the diameter was limited to between 150 and 200 mm, and it was not feasible to make ingots of larger diameter. However, it is reported that in the former Soviet Union, CCM of various dimensions ranging up to 1,000 mm in diameter and 2,000 mm in length have been completed and are in use for melting, refining and reducing titanium and other metals (46). In any case, since CCM is still in the development stage, equipment in a higher degree of completion will be brought into practical use to find applications for which it is best suited.

3. Scrap Recycling

Titanium scrap was first recycled in the 1950s. Assisted by improvements in scrap treating technology and its qualification for use in aircraft components, its blending ratio has increased yearly, reaching 40% of ingot material in the US recently (47). As for other countries in 1987, it was 35% to 40% in Germany, 25% to 30% in other European countries, and about 15% in Japan (48). The low figure for Japan is attributed to the relative small size of the aircraft industry.

Recycling of more scrap is necessary so that titanium usage may be extended, reducing costs, absorbing yearly increasing energy costs, and further coping with the problems of environmental preservation. Although removing HDIs and LDIs has become possible through the use of cold hearth melting, concerns over inclusion of foreign metals and composition (49) still remain. To this end, a better understanding of scrap control at the source is required.

4. Casting

Casting of titanium as the near-net-shape has been steadily increasing in the US from 200 tons in 1981 to 608 tons in 1991 (50). Application to large, complicated shapes or to critical parts is being extended supported by large part size capability, preformed cores, HIP, precision chemical milling and other advanced technologies as well as by strict quality and process control (51).

Since the aircraft industry is relatively young in Japan, the scale of production is still small, being limited to making a small number of struts and flanges for V2500 engines. Other than that, 10 to 20 tons/year of pumps and valves for the chemical industry are produced and tens of thousands of titanium-made golf club heads are shipped yearly.

Conclusion

An overview has been presented on the present situation regarding titanium and its melting technology. The findings may be summarized as follows:

1. The Kroll process is responsible for the overwhelming majority of titanium sponge production. While the basic technology will remain as it is, further efforts to reduce cost should be made by increasing productivity, advancing automation and simplifying design.

2. Development of a number of novel refining methods is progressing. So far, however, none superior to conventional methods in terms of production cost or equipment productivity have appeared. Thus, emergence of a new refining process at less cost is awaited.

3. Titanium of up to 6N purity is now available, thanks to technological developments in response to demand for higher purity for use as an electronics material.

4. As for melting furnaces, the VAR furnace holds an overwhelmingly superior position from the aspect of economy. Further efforts will be needed to improve ingot cleanness and homogeneity, as well as to ensure operational safety to keep its present superiority over other types of furnaces.

5. Use of cold hearth furnaces using electron beam or plasma as the energy source will grow for melting material for use in making premium quality aircraft engine parts in the future, taking advantage of its ability to remove HDIs and LDIs. Pursuit of better economy, on the other hand, is necessary.

6. The CCM furnace is still in the development stage. However, melting large diameter ingots will enter practical application in the near future, and uses will be found taking advantage of its features to stir large amounts of melt and superheat it.

7. Intensive scrap recycling is indispensable from the stand point of global environmental preservation and cost reduction.

Acknowledgment

A great deal of cooperation in the way of responding to questions and providing references and other information was offered by titanium sponge producers, melters, equipment manufacturers, and other organizations around the world during the preparation of this article. My sincere and warmest thanks go out to all of them. Due to space limitations, not all the information provided could be used.

References

1. T. Ikeshima, (the 5th Int. Conf. Titanium, FRG, 1984), 3-
2. T. Tanaka, (the 6th World Conf. Titanium, France, 1988), 11-
3. Titanium 1990, Statistical Review 1981-1990, ed. by T.D.A, (1991)
4. G. Cobel et al., (the 4th Int. Conf. Titanium, Japan, 1980), 1969-
5. J. C. Priscu, The Extractive Metallurgy Symposium
6. A. J. Meyren, J. Metals, 20 (5) (1968), 38-
7. S. Tokumoto, J. Metals, 27 (11) (1975), 18-
8. B. Champin et al., Mémoires et Etudes Scientifiques Revue Métallurgie, 77 (5) (1980), 681-
9. M. V. Ginatta and G. Orsello, US Patent PN 4,670,121, 1987
10. M. V. Ginatta et al., (the 6th World Conf. Titanium, France, 1988), 753-
11. M. V. Ginatta et al., (Int. Symp. Production and Electrolysis of Light Metals, Halifax), (1989), 201-
12. M. V. Ginatta, Private Communication, Ginatta Torino Titanium, 1991
13. L. E. Lynd and R. A. Hough, Titanium Minerals Yearbook - 1989, (US Department of the Interior, Bu of Mines), (1991)
14. F. K. Ojebuoboh and G. P. Martins, Refractory Metals: Extr., Processing Appl., (The Materials, Metals & Minerals Society), (1990), 101-
15. D. E. Traut, Private Communication, US Department of the Interior, Bu of Mines, 1992
16. J. Iseki et al., (1986 Int. Conf. Titanium Products and Appl.), 2 (1987), 948-
17. Y. Shindou et al., Rare Metals '90, (1990), 191-
18. M. Kuroki et al., Japan Patent Application, Laid-Open 3-177594, 1991
19. E. Nishimura et al., Japan Patent Application, Laid-Open 2-213490, 1990
20. Y. Yoshimura, Japan Patent Application, Laid-Open 3-215633, 1991
21. S. R. Seagle and R. L. Fisher, (the 6th World Conf. Titanium, France, 1988), 565-
22. J. W. Sears, J. Metals, 42 (3) (1990), 17-
23. H. Kusamichi et al., (the 7th ICVM, Japan, 1982), 1275-
24. N. Fukuda et al., (the 6th World Conf. Titanium, France, 1988), 631-
25. P. M. Mergeanian, (Int. Light Metals Conf., USA, 1986), 19-
26. H. R. Harker and C. H. Entrekin, Titan 1986, 2 (1987), 939-
27. H. R. Harker and C. H. Entrekin, (the 2nd Int. SAMPE Met. Conf., Ohio, 1988), 128-
28. H. Stumpp et al., (the 2nd Int. SAMPE Met. Conf., Ohio, 1988), 144-
29. H. Pannen et al., (the 6th World Conf. Titanium, France, 1988), 597-
30. K. Rüdinger et al., (the 5th Int. Conf. Titanium, FRG, 1984), 115-
31. S. C. Stocks and F. Caputo, (the 6th World Conf. Titanium, France, 1988), 573-
32. R. N. Jarrett et al., (the 6th World Conf. Titanium, France, 1988), 593-

33. R. N. Jarrett, Electron Beam Melting and Refining State of the Art 1986, (Englewood, NJ: Bakish Materials Corp.), 332-
34. W. R. Chinnins and R. C. Eschenback, (the 9th Int. Vacuum Met. Conf., CA, 1988)
35. C. H. Entrekin, Electron Beam Melting and Refining State of the Art 1985, (Englewood, NJ: Bakish Materials Corp.), 40-
36. R. J. Koenig et al., (USA Federal Aviation Administration), (1990)
37. C. E. Shamblen, Electron Beam Melting and Refining State of the Art 1990, (Englewood, NJ: Bakish Materials Corp.), 49-
38. H. R. Harker, Electron Beam Melting and Refining State of the Art 1989 Part 2, (Englewood, NJ: Bakish Materials Corp.), 185-
39. S. M. Tilmont and H. R. Harker, Electron Beam Melting and Refining State of the Art 1990, (Englewood, NJ: Bakish Materials Corp.), 135-
40. C. H. Entrekin and H. R. Harker, (the 6th World Conf. Titanium, France, 1988), 615-
41. M. P. Schlienger, (the 2nd Int. SAMPE Met. Conf., Ohio, 1988), 437-
42. W. R. Chinnis, Electron Beam Melting and Refining State of the Art 1990, (Englewood, NJ: Bakish Materials Corp.), 128-
43. J. W. Sears and R. C. Eschenbach, Electron Beam Melting and Refining State of the Art 1989 Part 1, (Englewood, NJ: Bakish Materials Corp.), 185-
44. P. Paillere et al., (the 6th World Conf. Titanium, France, 1988), 583-
45. M. Garnier and P. Paillere, Journal Français de l'Electrothermie, no. 38 (1989), 35-
46. A. P. Gubchenko et al., (the 6th Int. Iron and Steel Congr., Japan, 1990), 275-
47. Metal Statistics 1990-91, (NY: American Metal Market)
48. K. Rudinger, (the 8th Int. Light Met. Congr., 1987), 392-
49. J. P. Laughlin, (the 6th World Conf. Titanium, France, 1988), 627-
50. Mineral Industry Surveys Titanium, (US Department of the Interior, Bu of Mines), (1991)
51. J. K. Thorne, W. J. Barice and G. Broihanne, (the 6th World Conf. Titanium, France, 1988), 643-

MATERIAL SCIENCE AND TI-PRODUCTION PROBLEMS

IN VIEW OF NEW HORIZONS OF THE APPLICATION

Igor Gorynin

The Central Research Institute of Structural Materials "Prometey"
Sankt-Petersburg, Russia, 193167

Abstract

The report analises the metallurgical material science and technological problems which are solving in the Russian Federation and is relating to the conversion of the titanium alloys application and expansion of its application in the national economy and domestic techniques. The special attention is paid to the problems relating to the reduction of prices of the metallurgical production and methods for the production of different structures.The examples of the effective application of the titanium alloys in the shipbuilding,pulp and paper industry and the shape castings in the municipal economy and medicine are given.

Introduction

It is possible to point out the several periods of titanium production with respect ot application areas. The first period - is titanium application for space, rocket and military equipment. The second period - is when titanium was partly applied (apart from space) for priority trends of modern equipment where it gives extremely high technical and economical effect (civil aviation, chemical industry, marine technique and shipbuilding power engineering and some other areas of shipbuilding). And at last titanium introduction in various industries up to domestic equipment, medicine devices and decoration things where titanium may be very useful and efficient. The diagram (Figure 1) shows approximate consumption of titanium in the USSR in various fields and according to periods given above.
Each period puts up specific tasks before titanium metallurgy. It requires material science investigations, special technological solutions. Thus, the first period had priority trends to work out perfect metallurgy of titanium, to develop series of refractory alloys and to produce their semifinished products in accordance with the areas of application. The second period was distingished mainly by the development of structural alloys and high corrosion-resistant alloys. It required to wide the scope of nomenclature in order to produce heavy-sized sheets and plates, heavy forgings, a wide range of pipes and welding wires. That period was characterized by the detailed investigations of Ti-alloys serviceability in various external media and loading conditions. The first two periods of titanium alloys application have been fully presented at the international seminars on titanium alloys. It seems that currently the third period is going on. It is the development

Titanium '92
Science and Technology
Edited by F.H. Froes and I. Caplan
The Minerals, Metals & Materials Society, 1993

of titanium application for general national economy, for people everyday needs. It became possible only after considerable relax of international tension in the world and sequently reduction in arnament expences. In essence, titanium conversion pwriod has come while until recently Ti had been

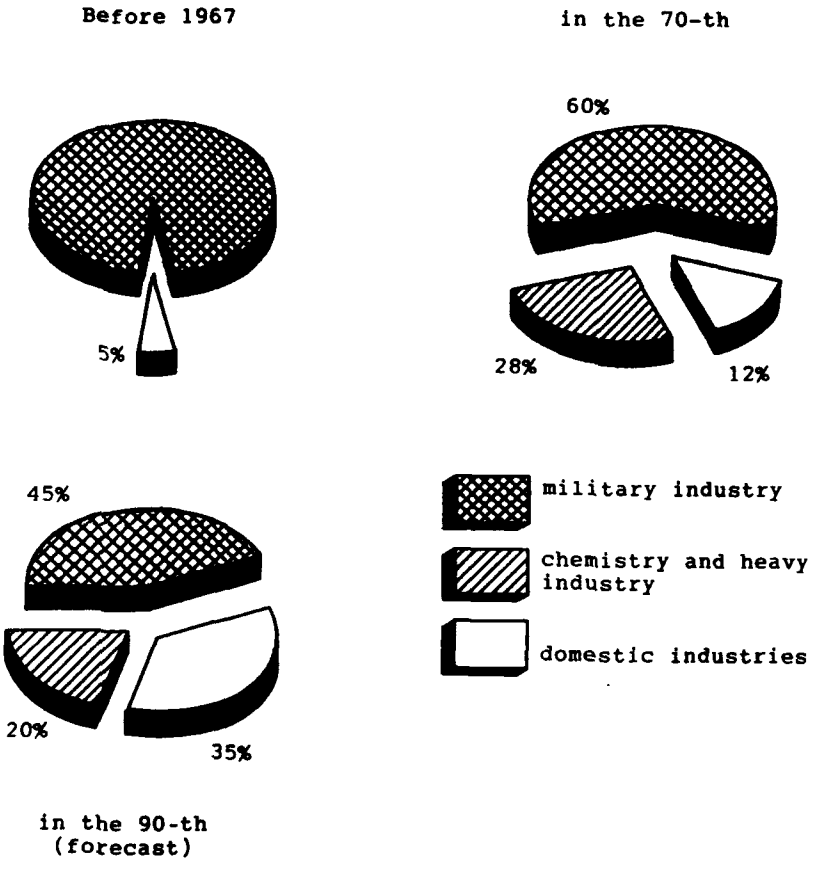


Fig. 1 Approximate shares of titanium consumption in our country in respect to different areas.

mostly applied for military equipment. The present paper is devoted to the third period and correspondently to the problems the titanium industry is facing with.

The following areas of titanium alloys application can be regarded as the new ones: oil-production offshore drilling rigs /1/, members of hyll equipment and propellers for civil and fishing vessels /2/ (foil devices for sea-

swift passenger ships, propellers and shaft lines etc), for bleaching and boiling towers for cellulose-paper industry (Figure 2), pumps, tanks and other equipment for chemical /3/, food and wine industries, everyday equipment (plates and dishes, accessories, decorations), power and finishing units in civil engineering /4/, sport equipment, public services (sanitary technique), inpantants and surgical instruments for medicine, gas-cleaning

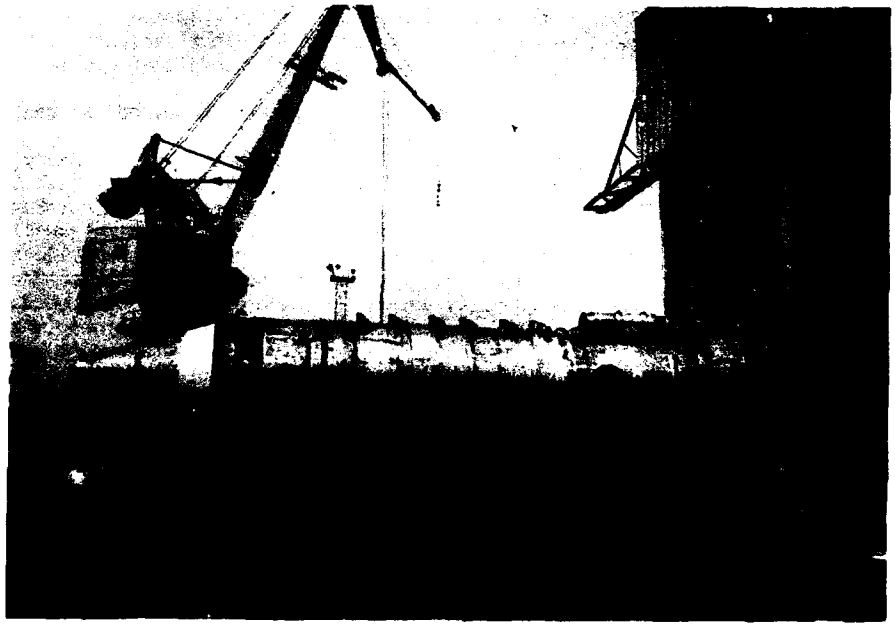


Figure 2 Cellulose bleaching tower in the process of manufacture.

(on the request of Ahlstrom company /Finland/)

devices for smoke desulphyrization in steam power plants /5/ etc.
The main problem of above mentioned areas of titanium application is the competitiveness of titanium with materials traditionally applied in these areas and primarily the price of applied alloys and efficiency of products fabrication. The latter needs special investigations and requires to solve the problems in metallurgy and titanium material science as well as the problems of titanium treatment.

Metallurgical tasks

Manufacturing cost of production may be governed by the composition of charge for titanium alloys melt, different technologies of ingots melt and semi-finished products. For this reason in the conditions of military orders conversion and in the course of transfer to national industry production one should reconsider the quality requirements and melting methods. One of the ways to reduce the titanium semifinished products manufacturing cost is to make good use of the low grades of sponge and metal wastes like scrap

and chip in ingots melting. Introduction of a large quantity of various wastes requires to use special melting methods and corresponding melting equipment. In the USSR in the majority of cases the first remelt at serial ingots melt from sponge is accomplished by vacuum-arc melting of consumable electrode (with the exception of shape castings manufacture). In the USSR the garnisage consumble electrode melting (GCE method) is under development at wastes remelt. This promising method allows to introduce a large quantity of wastes at melting, but is not widely applied in serial production though it gives a good quality of metal. It is necessary to consider the economical efficiency of other melting methods application (plasma-arc, electron-beam, induction melting etc.) in order to find optimum varients with the aim at considerable reduction of titanium alloys ingots cost due to wastes application.
The development and introduction of special equipment is required as well as new standards and requirements to metal quality.
The second important problem in metallurgy is the production of secondary titanium alloys (alloys produced from production scrap). There is a task to select the composition of secondary alloys and correspondently the development of several technically pure titanium grades. One must identify the limits of alloying elements and impurities content for one or several alloys in order to use the whole range of secondary alloys to be put into production taking into account the quantity aspect for each alloy. It is necessary to adopt the acceptable limits of technological impurities content (mainly, oxygen) for every grade of secondary technically pure titanium. At production of secondary titanium alloys the problem of possible requirements on mechanical properties is to be solved. Some grades of secondary titanium may be produced according to "customers request", for example, currently titanium is widely used for bells production (Figure 3), where shaped castings with a wide range of chemical composition are applied. The same situation is with domestic things of decoration and art purposes (statuettes, decorative patterns etc.).Shaped castings melting is very important due to universal method to obtain parts of various configuration.
In our country the centrifugal casting in metal and ceramic moulds with protective coatings is of wide use as well as investment casting where cheap castings may be used for different purposes, in particular for tanks and members of pumps (Figure 4).
There is no doubt that much attention is to be given to powder metallurgy which allows to produce pseudoalloys with unique properties efficiently used in instrument making industry, friction joints etc. Besides, there are wide possibilities for titanium application for long-term filters of various purposes./5/.

Material science problems

The most developed Ti-alloy produced on an industrial scale are the heat-resistant (more accurately, thermal-resistant) alloys applied for the aerospace equipment. In general these alloys are alloyed by expensive in short supply materials such as vanadium, molybdenum, sometimes by zirconium, niobium and tantalum. These alloying elements not only make the alloy noble, but make them more expensive. Because of this the commercially pure titannium is more technological for wide and various application. Some grades of the commercially pure titanium of a different strength level as a function of a procedure impurity contents (oxygen, nitrogen, carbon, iron) are required to provide its wider application for the domestic equipment. It is necessary to expand activities aiminig the development of economically alloyed titanium alloy of the widest application meeting the high requirements of the safety and the procedure in metallurgical and job production. The best properties can be provided by the multicomponent alloying, not by high content of alloying elements. To provide good procedure the strentth requi-

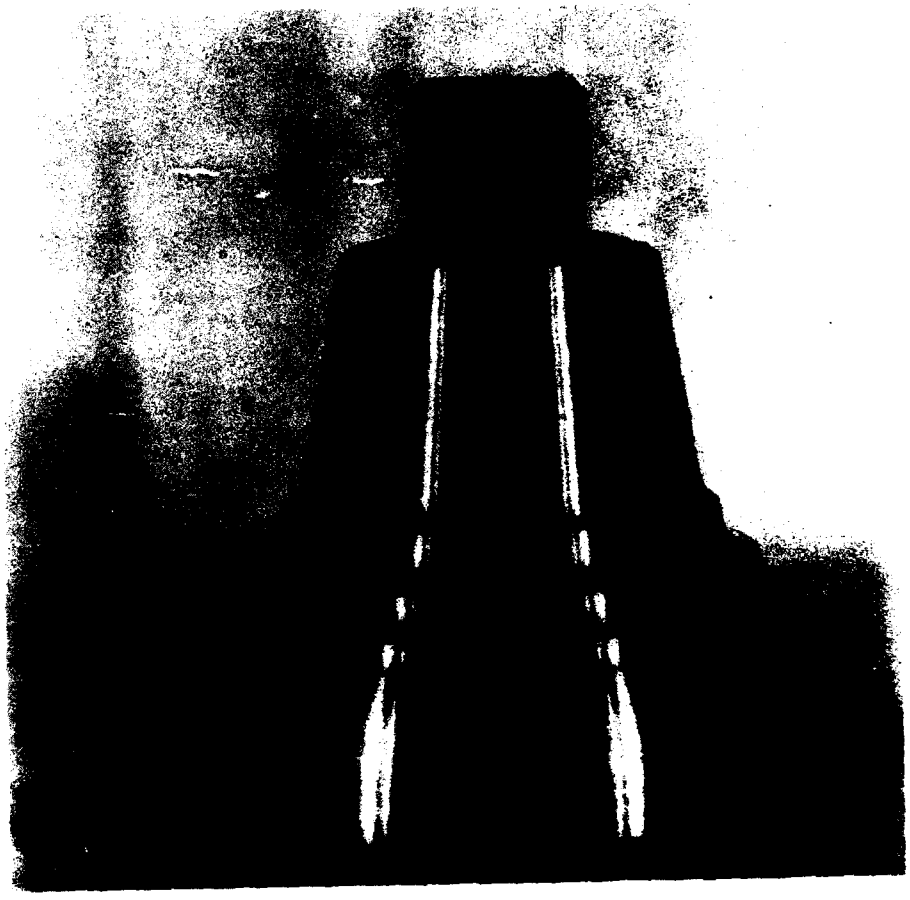
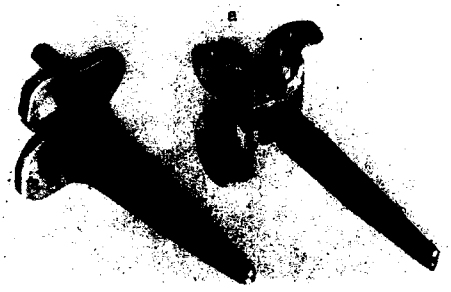


Figure 3 Ship's bell.



a) Pump bodies 620 kg in mass.



b) Endodentures elements for surgery.

Applied alloy TL5 (Ti 4Al 2V)

Technical characteristics:

$\sigma_{0,2} \geqslant 588$ MPa ; $\sigma_B \geqslant 637$ MPa

$\delta > 8$ % ; KCV > 392 kj/m²

Figure 4 Titanium shaped castings.

rement can't exceed 550-600 MPa. In view of the fact that the application of the titanium in consumation fields is based on the high corrosion resistance and the satisfactory biological compatibility the corrosion resistance and the corrosion cracking resistance of a new unified alloy is to be studied. The performance and the safety of the secondary alloys for the critical products (turbines, inner combustion engines) is to be thoroughly investigated as the increased contents of impurities can result in appreciable reduction of structural strength parameters of metals (fatigue resistance, crack resistance, corrosion cracking resistance etc)/6/. During further Ti investigations the surface properties of the titanium decorative coating or chemical heat treatment, especially, to obtain the desired surface properties is also to be paid an immense attention. Among the new methods of the decorative coating application the microarc oxidation resulting in the uniform stable colour of the surface: from white to black is of note. The methods of the stable colouring and its natural wear resistance is to be studied. The possibility of the titanium decorative colouring by defferent types of the gas thermal coating has been studied in a limited extent (only the decorative plasma spraying by the titanium nitrides and blackening have been investigated). Some obscure phenomena can be observed when the titnaium is applied for the utensiles and the table covers (blackening by spoons and knives on china, tarneshing of dishes and plates etc.). The investigation of these phenomena must result in precision of efficiency of the titanium application in this field.

Procedure problems

The wide application of the titanium in many new fields is related to the various methods of welding and brazing. First of all it relates to the large structures: celulose bleaching columns, the foil devices for the ships (Figure 5) ship machinebuilding etc. where automatization of the welding, multilayer welding, precision welding of small thickness of fine parts (if apparatus, utensiles, adornment are in mind) are required. The titanium can be welded by different methods. The selection of a welding method can be argued by economical reasons and technical feasability of the particular structure and features of the welded joints itself. The most applicable process is an argon arc welding and its modifications. The application of the high concentrated heat sources allows to weld the titnaium alloys of a large thickness range and to obtain the relatively low residual stresses and small buckling of the structures. Sometimes it allows to give up the following heat treatment as undesired. Among the welding methods,in spite of the expensive equipment, the most reasonable are electron beam welding and laser welding. The former is widely used for the military equipment and the laser welding is applied for the precision welding of domestic structures and jewelry when the powerful energy sources are not required.
The simple welding methods: contact welding (point and seam welding including), the diffusion welding and the friction welding were hardly used. The ample application of the titanium for a domestic use can undoubtely evaluate the efficiency of these welding methods.
Along with welding the brazing can provide either similar joints where welding is not reasonable or dissimilar joints of the titanium and other metals (steels, copper, aluminium alloys). The available solders for brazing the titanium are characterized by high procedure parameters as compared to generally used silver solders and are less expensive (the cost of the solders amounts about 70-80% of the titanium cost). The surface chemico-thermal treatment of the titanium alloys, the gas thermal coating of the surface and different local deposits allow to manufacture friction units and seals of the required working capacity (tube fittings and systems, for example).

THE FOIL DEVICES OF SEA - SWIFT WALKING S[illegible]'A"

PRODUCED OF PT3V THE TITANIUM ALLOY

THE TECHNICAL DATA OF PT3V ALLOY:

The yield strength, MPa.....585 not less

The tensile strength,MPa.....880 not more

The endurance limit in sea water .....0,4 - 0,5σ_B



The ships with foil devices of the titanium alloys are navigating on all latituds of the World Ocean.

The foil devices of the PT3V titanium alloy are characterized by unlimited actual service life, can withstand the load twice as high as the foils of the austenitic steels.

Figure 5 Titanium foil devices for the sea swift pleasure ship "Cometa" (made by "Prometey")

Issue of the standard guide documentation

When the titanium alloys were used for the aerospace and other type of military equipment some procedure developments and standards were made. However, in many cases the documentation is of special nature and is not always available for a wide range of the scientists, technologists and designers. It is necessary to extend the documentation relating to the delivery of the titanium semiproducts, all the feasability of the material production including, in accordance with the simplified requirements concerning with dimensions of the product up to pieces and standard scrap, which must result in the reduction of their cost. It implies a considerable increase of finished product yield and of efficiency of the titanium application.
The appropriate technical documentation of non-confedential type must represent the newest achievements in the procedure of production of different semi-products expanding their range (for tubes, bands and foils, especially).
The retreatment and conversion of the technical documentation is very important as it makes easier to develop scillful production of the titanium goods of people consumption for a wide range of the manufactures, small enterprizes including. Of note is the specificity of the procedure properties of the titanium alloys relating to the heating and welding, especially.
It is undenyable that the expansion of the scientific and popular publications and the technical literature edition are required and not only in the aerospace field. The leading research and development institutes and organizations of the USSR are ready to resolve the discussed problems with a large scale cooperation with foreign countries.

References

1. R.D.Tems,"Selection and use of large diameter titanium pipe in a condeep off shore oil production platform."Titanium 1990,Products and Applications, Published by Titanium Development Association,vol.1,p.368.
2.R.W.Schuts,"Anoverview of current and candidate titanium alloy applications on U.S.Navy surface ships", Titanium 1990,Products and Applications, Published by Titanium Development Association, vol.1, p.394.
3. A.N.Petrunko,V.E.Lugovoy, V.A.Alexandrov, V.V.Volinsky,Titanium 1990, Products and Applications, Published by Titanium Development Association, vol.1, p.345.
4. Y.Fuduhara,"Non-aerospace application of Titanium",Sixth World Conference on Titanium, Cannes, June 6-9, 1988,Ed.P.Lacombe, R.Tricot, G.Beranger,vol.1 p.381.
5.V.V.Tetyukhin, Titanium alloys in the USSR, Proceedings of the Technical Programme from the 1990 International Conference, Published by Titanium Development Association, vol.1,p.56.
6. I.V.Gorynin, B.B.Chechulin,Titanium in Machinebuilding, (Moscow, Machinostroenie, 1990)400.

MICROSTRUCTURE AND PROPERTIES

MICROSTRUCTURE - PROPERTY RELATIONSHIPS IN TITANIUM ALLOYS (CRITICAL REVIEW)

R.R. Boyer[1] and J.A. Hall[2]

[1] Boeing Commercial Airplane Group
Seattle, WA 98124 USA

[2] Allied-Signal Aerospace Company
Phoenix, AZ 85010-5217 USA

Abstract

Considering, primarily, the engineering properties of commercially available Titanium alloys, the critical issues associating these properties with the alloy microstructure are reviewed. Interpretation of the micromechanisms are made and related to the features which dominate a material's behavior and which might be the focus of process control. Selected examples from each of the α, near α, α/ß and metastable ß alloy classes are made to illustrate the current state of understanding of how and why microstructure influences engineering properties.

Introduction

This review summarizes the important findings with respect to the correlation of effects of microstructure on key properties of Titanium alloys published since the 6th World Conference, held in Cannes, France, in 1988. In order to be concise, discussion is restricted to conventional Titanium alloys used for aerospace applications. The properties considered include tensile strength, creep, fatigue and fracture related properties. Microstructure variables include the size, morphology and distribution of various phases, texture, and chemistry. The reader is encouraged to obtain greater detail from the references.

Strength, Ductility and Toughness of Metastable Beta Alloys

Metastable beta alloys have been studied rather extensively in recent years because of their high strength and relative ease of fabrication. The most common microstructural features studied have been ß grain size, grain boundary α and the size and distribution of any primary and aged α resulting from thermomechanical treatments.

Grain Boundary and Grain Size Effects

Studying Ti-15V-3Cr-3Sn-3Al (Ti-15-3) alloy with 35 and 120 micron grain sizes, Breslauer and Rosen (1) found that the solution treated version of the alloy showed the classical grain size effect on strengthening. However, after giving the material a common age, the larger grained material was stronger and had a higher fracture toughness, Figure 1. Concomitant with the improved fracture toughness, the larger grained material exhibited lower ductility. They concluded that the Hall-Petch strengthening effect was countered by the change in α phase nucleation and growth products, particularly at grain boundaries. They considered the overall strength to be a combination of: (1) Hall-Petch strengthening, which accounts for the strength of the solution treated material, and (2) the contribution of the grain interior, attributed to α precipitation. This contribution can be calculated using a modified Orowan equation. Using the α precipitate size measured in their study and the strengths observed, the interparticle spacing was back calculated and was in reasonable agreement with their observations. The greater grain boundary area in the small grain material provided more nucleation sites for the formation of a larger amount of coarse, grain boundary α, which does not contribute to strengthening. The higher volume fraction of α at the grain

Titanium '92
Science and Technology
Edited by F.H. Froes and I. Caplan
The Minerals, Metals & Materials Society, 1993

boundaries in the smaller grain material reduces the potential amount of secondary α which can form within the grains upon aging, particularly in the near grain boundary area due to partitioning of ß stabilizers into this region. This explains the lower strength for the fine grained material.

According to (1), grain boundary α participates in the toughening mechanisms of aged microstructures in different ways, depending on the strength of the surrounding matrix and the grain boundary α thickness. Due to the presence of relatively soft α phase, cracks tend to find grain boundaries to be the path of least resistance. The crack tip plastic zone is restricted to this grain boundary region when the matrix is significantly harder, as in the case of aged small grain material, resulting in predominantly intergranular fracture. Thus, lower energy is consumed propagating the crack than when the matrix strength adjacent to the grain boundaries is closer to that of the grain boundary α. In this case the plastic zone occupies a greater volume, i.e., extends into the matrix, and a greater amount of transgranular fracture occurs because there is less of a barrier for cracks to leave the grain boundary zone.

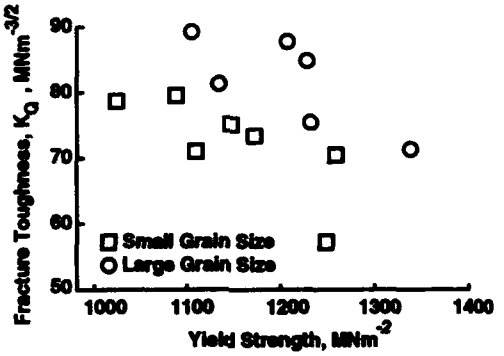


Figure 1. Variation of Fracture Toughness K_Q, With Yield Strength for All Large Grain Size and Small Grain Size of Aged Ti-15V-3Cr-3Al-3Sn Specimens (After Ref. 1)

We feel that the above rationale is not totally self-consistent. Their explanation for the toughness behavior has overlooked some factors: (1) they state that the hardness differential between the matrix and grain boundaries must be greater in fine grain material; yet, their data showed that the large grain material had the higher strength, and the highest intragranular micro-hardness, and (2) along the same line, it is inferred that the density of α precipitates must be greater in the region of the grain boundaries in the small grained material. However, earlier in the paper they stated that early grain boundary α formation in the small grained material would cause the adjacent material to be the least favorable sites for initiation, which would imply the opposite conclusion.

The fracture behavior, more intergranular for fine grained material and transgranular for the larger grained material, must be influenced by the above factors. However, it is difficult to provide one microstructural model which provides all the correct correlations. Furthermore, another contribution to the observed fracture behavior could be a "geometry" factor. As illustrated in Figure 2, the crack can follow the grain boundaries in smaller grained material without deviating greatly from a plane normal to the tensile axis. Crack deviations required to follow the grain boundaries would be more difficult to achieve in the larger grained material. In any case the void nucleation step remains associated with the grain boundary α.

The results of Parris and Bania (2) on Beta-21S (Ti-15Mo-2.7Nb-3Al-0.2Si), Table I, clearly demonstrate the effect on ductility of the strength differential between the α and ß phases. When tested at two strength levels, with a constant grain size, a much more devastating effect of grain boundary α was found if the material was aged to higher strengths. Bella, et al. (3) report data on Ti-3Al-8V-6Cr-4Mo-4Zr (Ti-3-8-6-4-4 or ß-C) that can be rationalized in the same manner. Boyer et al. (4) also found that thicker grain boundary α in Ti-15-3 castings resulted in reduced ductility.

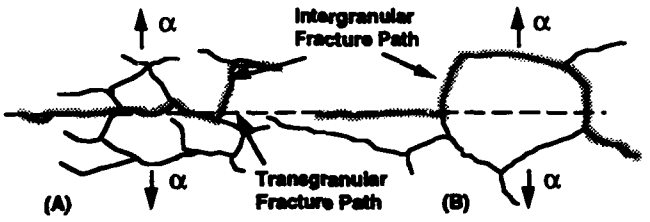


Figure 2. Schematic Illustration of Why It Is Geometrically Easier for Intergranular Crack Propagation to Occur In (A) Small Grained Material Than It Is In (B) Larger Grained Material

The influence of the strength differential, between the intragranular α phase and aged ß matrix on fracture behavior, was studied by Margolin and Pak (5) in Ti-10V-2Fe-3Al (Ti-10-2-3) with two microstructures and at two strength levels. They found that as the difference in the hardness between the two phases increased void formation at the beginning of tensile failure occurred more readily. Conversely, as the strength of the α and ß phases become more nearly equal, the α phase offers little resistance to propagation of slip in the ß phase. In this case, α phase spacing has no important influence on ductility and void nucleation becomes more difficult. Because of the importance of grain boundary α in determining the fracture and ductility properties of ß alloys, considerable work has been done to control this microstructural feature (6-10).

Table I. Tensile Properties of Beta-21S at Two Strength Levels, Before and After Thermal Exposure at 593° C (After Ref. 2)

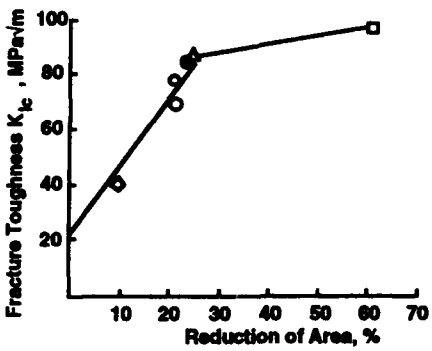
Condition	Exposure Time hours	UTS MPa	TYS MPa	Elongation %
Low Strength	0	908	836	16.5
	960	924	877	12.0
	2000	951	855	6.0
High Strength	0	1186	1096	10.0
	1500	1007	951	1.0
	3500	*	945	0

* The specimen failed just beyond yield with no ductility

Thermomechanical Treatments

The classical low plus high temperature two-step aging process typically is used to produce uniformly dispersed intragranular α precipitation for maximum strength and ductility. Using this approach on Ti-3-8-6-4-4 Gregory and Wagner (11) reported a direct correlation between ductility and toughness (Figure 3). In this case variations were intrinsic, not dependent upon a crack tip deflection mechanism. These results are counter to the usual inverse relationship between toughness and ductility in Titanium alloys as exemplified by the work of Boyer and Kuhlman (12). In their work on Ti-10-2-3 primary α morphology was an important variable which influenced crack tip deflection and the resultant extrinsic influence on toughness. This clearly illustrates the need to consider both intrinsic and extrinsic effects on fracture toughness. Gregory and Wagner showed improvements in both toughness and ductility at a given strength level using a double-age as opposed to a single-step age.

In contrast to approaches using low temperature initial aging to provide nucleation sites, Niwa et al. (9), supported by Ito (13), demonstrated improvements in ductility of Ti-15-3 by first performing a high temperature age on heavily deformed material to affect a state of partial recovery and then using the resultant dislocation network as nucleation sites for further α precipitation to strengthen the matrix. Figure 4 shows Niwa's results, indicating improved ductility over a range of strength levels, by high, then low temperature aging of initially cold worked material, as compared to single step aging.



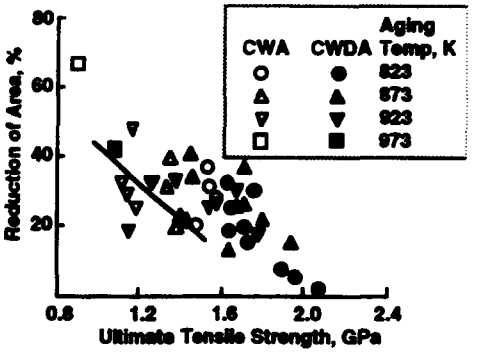


Figure 3 (Left). Relationship Between Fracture Toughness (K_{Ic}) and Ductility as Assessed By Reduction of Area of ß-C (After Ref. 11)

Figure 4 (Right). Variation of the Relationship In Ti-15V-3Cr-3Al-3Sn Between Reduction of Area (RA) and Ultimate Tensile Strength With Aging Conditions (CWA: Aged Between 973 and 823°K After Cold Swaging. CWDA: Re-aged at 673°K After CWA). The Straight Line Indicates the Relationship Between Reduction of Area and Ultimate Tensile Strength Obtained By Aging After Solution Treatment (After Ref. 9)

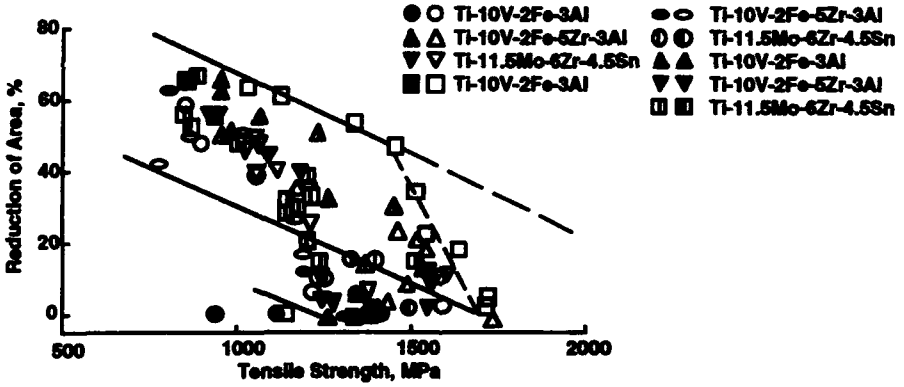


Figure 5. Relationship Between Ductility (RA) and Yield Strength (YS) for Various ß Alloys. Open Circles Indicate Samples Aged From 723 to 923°K and Closed Circles Indicate Samples Aged From 573 to 673°K and YS for Various ß Alloys (After Ref. 14)

In the latter case of double aging to attain optimum combinations of ductility and toughness, the material must start with heavily cold worked microstructures, which are easily accomplished for sheet products but heavier articles such as plate and forgings offer significant challenges. The work of Gregory and Wagner (11) showed advantages for low-high duplex aging treatments in ß-C which represents a greater opportunity for heavier section sizes. Unfortunately, it too has drawbacks. Following ß recrystallization, the cooling rate must be sufficiently rapid to avoid formation of significant grain boundary α. This critical cooling rate is a section size issue as well as an alloy stability issue.

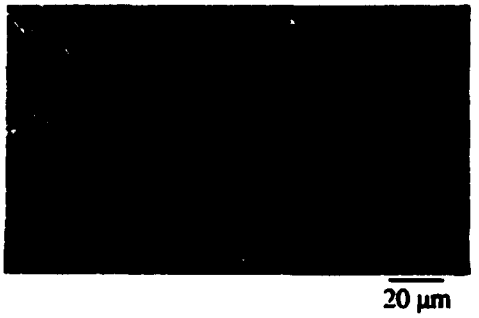
Typically, for Titanium alloys, as strength is increased, ductility decreases as long as other variables are held constant. Niwa et al.(9) show this in Figure 4 for Ti-15-3 and demonstrated ways to enhance the relationship by thermomechanical working. Kawabe and Muneki (14), working with a number of metastable ß alloys, show that there is both a grain size effect and an

intragranular aging precipitate effect on the strength-ductility relationship. Figure 5 summarizes this work where the upper bound of the plot is formed by data from fine grain material and the lower bound is from large grain material. Data points under the lower boundary (Figure 5) come from large grain material aged to form very fine precipitates of α or ω. The authors contend that the upper bound could be extended, as indicated by the dashed line, if the ß grain size were made even finer. This offers a large potential advantage with microstructural refinement. They proposed a model which contends that as the grain size is reduced, the mode of tensile failure tends to become transgranular. Conversely, as the grain size is increased, lower energy intergranular failure becomes dominant. This logic is in conflict with Breslauer and Rosen (1), who showed that finer grain sizes result in a greater propensity for intergranular fracture. The differences between these two sets of observations may be related to the means used for obtaining the grain size variation. The latter (1) achieved grain size differences by different anneals or solution treatments, which impart grain growth. The former (14) modified grain size using different thermomechanical treatments to reduce the grain size. Precipitation kinetics, affected by obvious factors such as differences in dislocation substructures, will be quite different between these two techniques. More subtle differences such as grain boundary impurity distribution, which could be important in determining the nature of the grain boundary precipitates, could also differ between these two methods, which could affect the properties. The degree and sense of the grain size effect on properties appears to be highly dependent upon aging conditions, the presence of grain boundary α and perhaps on other features derived from the specific thermomechanical processing applied.

Strength, Ductility and Toughness of Alpha-Beta Alloys

Microstructural control of α/ß alloys has been practiced for many years and proceedings of the previous six International Titanium Conferences contain many exemplary reports on these activities. A recent review by Kuhlman (15) provides an excellent compilation of the effects of microstructure on strength, ductility and toughness of α/ß and ß alloys, emphasizing effects of uniform microstructures. More recent work by Combres and Champin (16) has shown benefits by the use of an inhomogeneous microstructure. By introducing a "necklace" (Figure 6) microstructure in lieu of monolithic α at prior ß grain boundaries, the authors report increases in strength and possibly ductility while maintaining the same toughness. Results for Corona 5 (Ti-4.5Al-5Mo-1.5Cr), and a new age hardenable alloy, ß-CEZ (Ti-5Al-2Sn-4Zr-4Mo-2Cr-1Fe), are shown in Table II. This necklace structure is accomplished by three steps: 1) refine ß grain size in the usual way by recrystallizing a highly worked structure, 2) induce nucleation of α, and 3) deform and break up the α phase as it precipitates at the ß grain boundaries.

Nagai et al.(17) studied composition effects on cryogenic and room temperature properties of Ti-6Al-4V forgings and rolled plate. Their findings lead to the conclusion that oxygen, at very low levels, down to 0.054% oxygen, provides the alloy with reasonable ductility at temperatures as low as 4°K, while maintaining high fracture toughness. Higher temperature tests show little effect of oxygen on toughness at levels up to 0.135% oxygen (Figure 7).



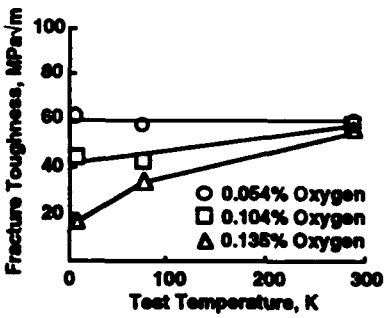


Figure 6 (Left). ß-CEZ Microstructure Exhibiting a Fine α Phase Necklace at the Prior ß Grains Boundaries (After Ref 16)
Figure 7 (Right). Temperature and Oxygen Content Dependence of Fracture Toughness K_{Ic}(J) of Ti-6Al-4V (After Ref. 17)

Table II. Advantage for ß-CEZ and Corona 5, of the Necklace Microstructure (After Ref. 16)

Alloy	Processing	0.2% YS MPa	UTS MPa	Elongation %	K_{Ic} MPa $\sqrt{m}$
ß-CEZ	Conventional	1111	1215	8.4	74
	Necklace Micro	1287	1346	10	73
Corona 5	Conventional	761	854	19.5	145
	Necklace Micro	860	935	20	144

Tensile and Creep Properties of Near Alpha Alloys

Strength and Ductility

In a recent series of papers, (18-20) Sridhar and Sarma worked with IMI 829 (Ti-6.1Al-3.2Zr-3.3Sn-1Nb-0.5Mo-0.32Si) to identify the mechanisms for reduced ductility occurring with certain heat treatments. All of their work featured ß heat treated microstructures cooled at various rates, followed by aging for 24 hours at temperatures between 625 and 959°C. They found that aging of more rapidly quenched structures produced a dramatic reduction in room temperature ductility; the debit diminishes with reduction in the severity of quenching and/or an increase in aging temperature. Although this reduced ductility is accompanied by higher strength, the authors attribute the lower ductility to the precipitation of silicides which, in turn, foster planar slip concentrations, resulting in faceted brittle fracture. They imply that the presence of ß phase, with which the silicides are associated, reduces the detrimental effect of the planar slip on the resultant ductility. Photomicrographs reveal coarser silicides occurring concomitantly with growth of the ß phase, both of which are associated with ductility increases.

Table III comes from their work (19), and shows the influence of the silicide size on properties. It is not clear how the authors rationalize the effects of silicide size on ductility without making some attempt to explain the independent effects of yield strength (aged α or α'), the presence of some ß phase and the size of the silicide precipitates.

Table III. Age Temperature Effects on Room Temperature Ductility In Beta Heat Treated and Water Quenched IMI 829. (After Ref. 19)

24 Hr Age Temp, °C	0.2% YS MPa	RA %	Silicide Size (microns)*	
25	886	19	None	*The silicides are lenticular
625	1005	1	0.02 X .2	in shape after the 625 and
700	973	1	0.02 X .2	the 700°C age but ellipsodal
800	950	3	0.3 X 0.3	after higher age temperatures.
950	903	5	0.7 X 0.7	

Summarizing these results in Table IV, the authors reported that silicides provide void initiation sites at α'/α' boundaries and α/ß boundaries and they are most detrimental in the absence of ß phase. The presence of ß phase somehow makes microvoid formation/coalescence more difficult.

Table IV Microstructural Interaction With Fracture In Aged IMI 829 With Different Cooling Rates - Summary of Ref. 18-20

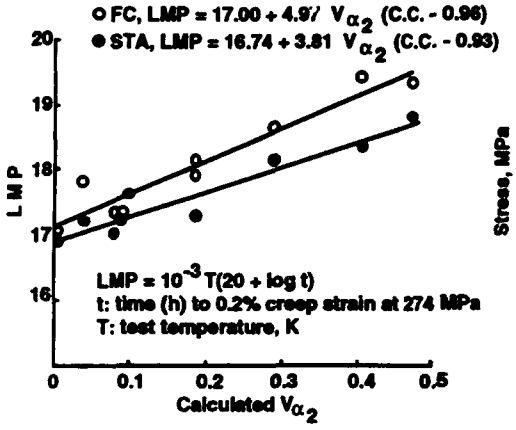
Treatment	Fracture Site/Origin Observations
WQ + Age	Brittle fracture on α'/α' interfaces with very fine silicide precipitates
OQ + Age	Brittle fracture on prior ß grain boundaries associated with silicides as void nucleation sites.
AC + Age	α/ß boundaries and prior ß grain boundaries, with classical void formation.
FC + Age	Mostly dimpled, transgranular fracture

WQ = water quench, OQ = oil quench, AC = air cool, FC = furnace cool

We would suggest that the improvement in ductility is probably more related to the presence of the ß associated with the silicides than with the size of the silicides. The ductile ß associated with the silicides would result in providing more strain accommodation between the matrix and the silicide, which would improve the ductility.

High Temperature Properties, α and α + ß Alloys

Onodera et al. (21) have studied the thermodynamics of the formation of ordered α_2 in the Ti-Al-Sn-Zr system and found that the creep properties seem to correlate very well with the calculated volume fraction of α_2 ($V\alpha_2$) in the alpha phase of this alloy system (Figure 8). ß grain size and solid solution strengthening play a lesser role, at least at 550° and 600°C. Room temperature ductility appeared to be dramatically affected by the $V\alpha_2$, with a drastic drop occurring when $V\alpha_2$ exceeds about 0.1% for the furnace cooled samples. For more rapidly quenched and unexposed or unaged material, the authors' data suggest that higher $V\alpha_2$'s could be tolerated.



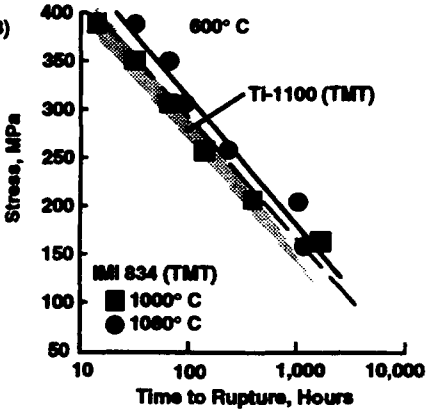


Figure 8 (Left). Correlations Between Larson-Miller Parameter (LMP) for Time (Hour) to 0.2% Creep Strain and the Calculated $V\alpha_2$ (at 873 K) for Ti-Al-Sn-Zr Alloys With a Range of Compositions (After Ref. 21)

Figure 9 (Right). Stress/Rupture Curves Comparing Ti-1100 and IMI 834 Which Have Been Swaged, Solution Treated at 40°C Above and Below the ß Transus, and Aged at 600°C for 4 Hours (After Ref. 22)

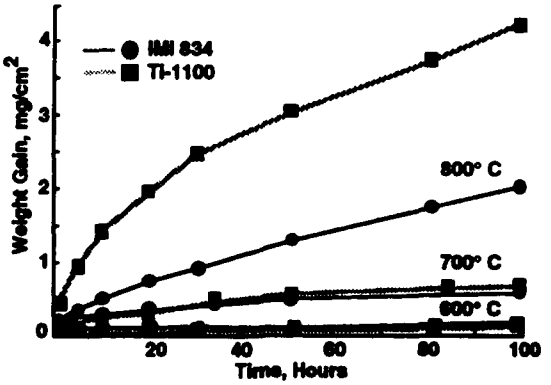


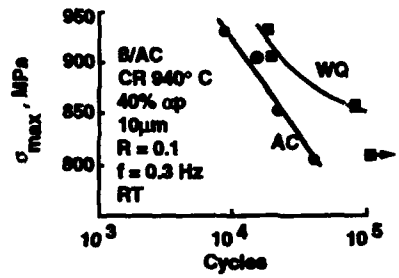
Figure 10. Oxidation Weight Gain Curves of Ti-1100 and IMI 834 Determined at 600°C, 700°C and 800°C in Laboratory Air (After Ref. 22)

Peters et al. (22), as part of their studies on two emerging high temperature Titanium alloys, Ti-1100 (Ti-6Al-2.7Sn-4Zr-.4Mo-.45Si) and IMI 834 (Ti-5.8Al-4Sn-3.5Zr-.7Nb-.5Mo-.35Si-.06C), tried to achieve a wide range of microstructures in both alloys. They were partially

successful, and, after rationalizing the differences in the starting material conditions, they reported little to separate the two alloys from the standpoint of 600°C creep behavior (Figure 9), but the oxidation behavior of the IMI 834 alloy at 800°C appeared to be significantly better, as shown in Figure 10. Hence, when considering the use of a conventional Titanium alloy with occasional temperature excursions above 700°C, IMI 834 alloy may be preferred over Ti-1100 on this basis. Basically, they found that sub-transus solution treatments lead to lower room and elevated temperature strength, higher ductility and lower creep resistance in comparison to supra-transus heat treatments. Thermomechanical treatments (swaging), which provide microstructural refinement, improved the strength and ductility, while reducing creep resistance.

Fatigue

The relative role of microstructure and texture on fatigue behavior of Ti-6Al-4V has been well documented by Wagner et al. (23). They used a 40 volume percent (v/o) primary α bi-modal microstructure as a baseline with variations in primary α size and in secondary α characteristics by virtue of cooling rate from a lower, second solution treatment temperature. Included also was a ß heat treated and annealed microstructure for comparison. In addition, they incorporated unidirectionally rolled and cross rolled alloy plate with quite different textures. Key to their findings was that so long as the primary α was small, variations in it's size had little effect on low cycle fatigue (LCF). Similarly, moderate variations in texture had little effect on LCF. They did, however, find a large effect of quench rate, which affects the fineness of the secondary α, on the LCF behavior of the bi-modal microstructures, Figure 11. It was also shown, that the lamellar ß heat treated microstructure results in an LCF debit relative to the bi-modal microstructures (Figure 12). Tests in the low crack growth rate region, using small cracks in electropolished specimens, resulted in a significantly lower growth rate for the bi-modal microstructures, Figure 13. This is in contrast to the conventional wisdom that fatigue cracks grow less rapidly in coarse lamellar microstructures. This observation is likely to be an example of the differences in behavior between small and large cracks pointed out by several investigators and recently summarized in Ref. 24.



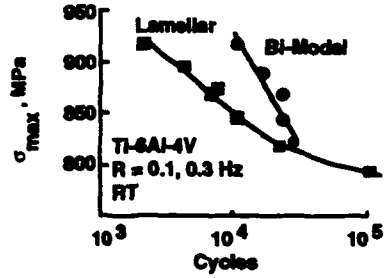


Figure 11 (Left). Effect of Cooling Rate on the LCF Behavior of the Bi-Modal Microstructures of Ti-6Al-4V (After Ref. 23)

Figure 12 (Right). Effect of Microstructure on the LCF Behavior of Ti-6Al-4V (After Ref. 23)

Ref. 23 also demonstrated that high cycle fatigue (HCF) performance, as with LCF, exhibited differences associated with cooling rate; the more rapidly cooled structures having greater lives (Ref. 23). While the finer secondary α seemed to have a significant effect, the range of primary α size between 10 and 40 microns appears to have little effect, just as in the LCF case. All this leads to the conclusion that finer secondary α either makes crack initiation more difficult or it is more effective at inhibiting the growth of small cracks. There appears to be a strong effect of texture on HCF, more so than for LCF, leading to the conclusion that the primary α (which is the primary source of the texture) contribution to HCF life comes from its influence on crack nucleation. The secondary α, not being strongly textured, contributes less to the crack nucleation in HCF, but its coarseness, related to the aging temperature and cooling rate from the solution treatment, does influence the early crack propagation between the nucleated sites on primary α particles. Hence small-crack propagation, a major portion of HCF life, is greatly influenced by the secondary α characteristics. Their fatigue results are summarized in Figures 14 and 15. Unidirectional rolling provided slightly better HCF properties regardless of cooling rate in their study.

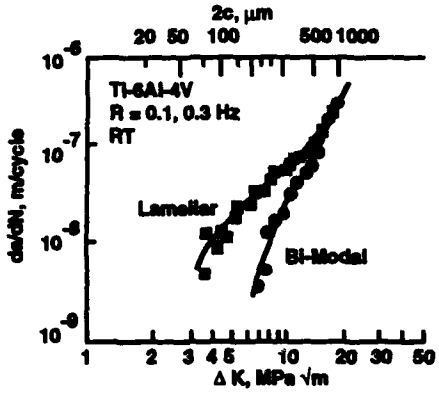


Figure 13. da/dN-ΔK Curves of Microcracks In Ti-6Al-4V (Effect of Microstructure) (After Ref. 23)

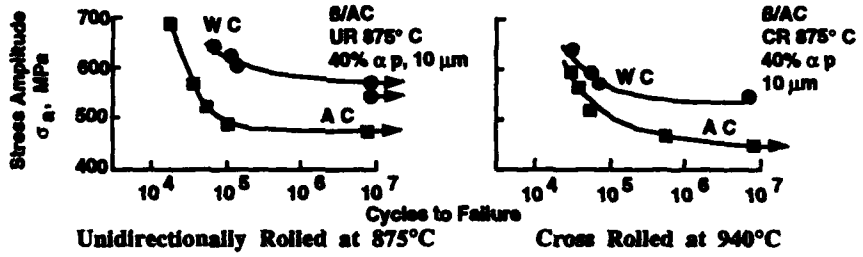


Figure 14. Effect of Cooling Rate on the HCF Behavior of the Bi-Modal Microstructures of Ti-6Al-4V (R= -1, f=80 Hz, RT) (After Ref. 23)

Near threshold large crack fatigue crack growth behavior of Ti-6Al-4V as a function of the variants or orientations of transformed ß microstructures was reported by Ravichadran (25). His primary conclusion was that the controlling microstructural unit is the α colony in rapidly cooled structures, while it is the α lath width in relatively slowly cooled microstructures. He further extended this argument to say that the near threshold fatigue crack growth parameters, ΔK_{th} and $\Delta K_{eff,th}$ increase with the size of the microstructural unit and attributes this observation to its interaction with the crack tip plastic zone, Figure 16. This interaction is most effective as the size of the controlling microstructural unit approaches the plastic zone size. Note that as the crack grows in the same microstructure, the controlling microstructural element may change as the crack tip plastic zone increases. Hence, interpretation of crack growth properties by microstructural relationships must be done with this in mind.

Nagai et al. (17) demonstrated in Ti-6Al-4V with bi-modal and lamellar microstructures, that the fineness of the microstructure must be looked at carefully. Their very fine microstructure was associated with a micro-texture. This micro-texture resulted in an increased slip length as the similarly aligned, but separate, small, equiaxed α presented a common slip path within a "texture zone". In this case the controlling microstructural unit is likely to be the micro-texture zone.

Peters et al. (22) observed in their study of IMI 834 and Ti-1100 that, to maximize HCF performance, one wants to obtain an optimum amount of equiaxed primary α (a study of their photomicrographs indicated the optimum amount was in the range of 40-50%, in agreement with the results of Ref. 23 for Ti-6Al-4V). The effect of ß versus α/ß heat treatments is dramatically demonstrated at 400°C in Figure 17 for Ti-1100. In the higher stress region of the HCF curve, where crack growth is an increasing portion of the total life, lamellar microstructures were seen to be slightly superior. The benefits of thermomechanical treatment are also obvious in the same figure and are more significant for HCF.

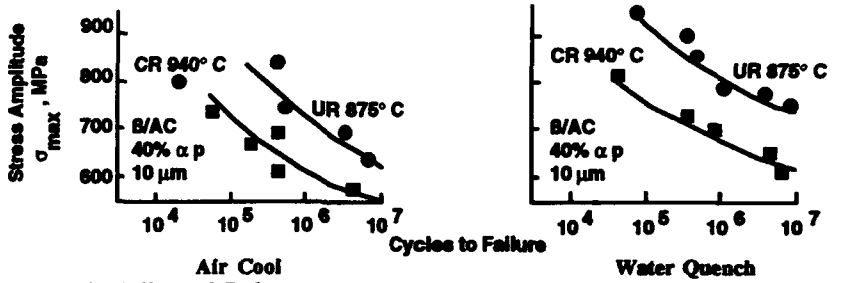


Figure 15. Effect of Deformation Treatment on the HCF Behavior of the Bi-Modal Microstructures of Ti-6Al-4V (R= 0.1, f=80 Hz, RT) (After Ref. 23)

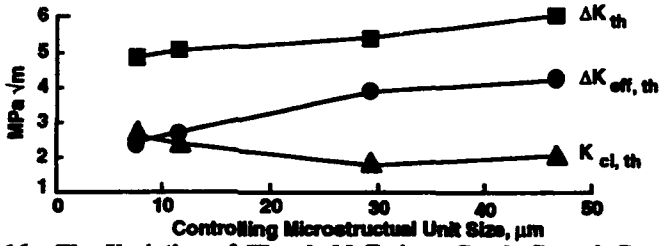
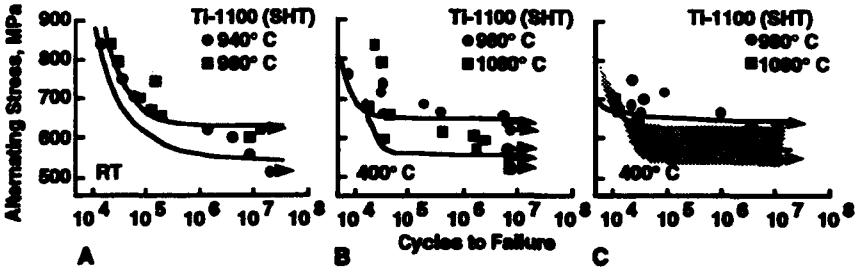


Figure 16. The Variation of Threshold Fatigue Crack Growth Parameters of Ti-6Al-4V as a Function of the Controlling Microstructural Units (After Ref. 25)

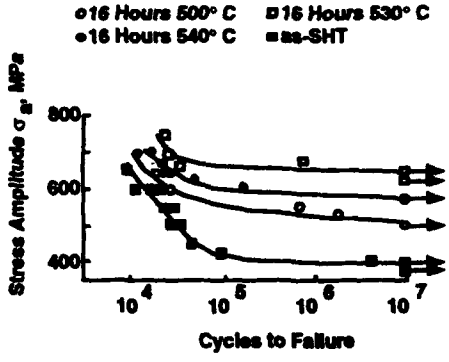


Test conditions for each curve: R = -1, f = 100± 10 Hz, laboratory air

Figure 17. HCF Properties of Ti-1100 as a Function of (A) Variation of Primary α Content, (B) β vs α/β Heat Treatment (β_t = 1020°C) and (C) Effect of Swaging Prior to Heat Treatment. Shaded Band Indicates No TMT. (All Specimens Aged 8 Hours at 600°C) (After Ref. 22)

Gregory and Wagner (11) studied the fatigue behavior of the Ti-3-8-6-4-4 as a function of strength of solution treated, single-step and duplex-aged conditions. In the solution treated and single-aged conditions, the endurance limit was about one half of the UTS, Figure 18. Duplex-aging provided a fatigue benefit as seen in Figure 19. Despite the higher strength of the single-step aged material, the run-out stress is higher for the duplex-aged material. The single-aged material aged inhomogeneously, resulting in intragranular precipitate free zones. The authors felt that these "soft" regions provided easier crack nucleation sites than the aged matrix, detracting from the fatigue strength.

Gregory and Wagner (11) and Krugmann and Gregory (26) showed that there is very little influence of α aged microstructures on fatigue crack growth rates in Ti-3-8-6-4-4. However, the α aged structure, which is otherwise of little interest, exhibits significantly lower crack growth rates (11). Figure 20 illustrates these effects which are in qualitative agreement with earlier work on Ti-10-2-3 (7).



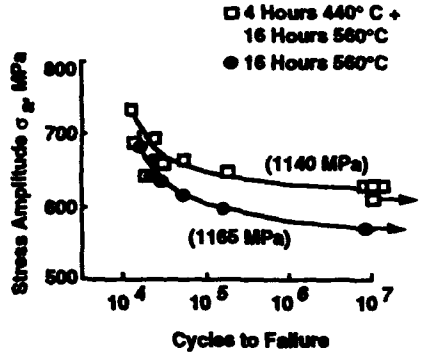


Figure 18 (Left). S-N Curves at RT of ß-C at R= -1, f=50 Hz, Comparing as-SHT and Single Aged Conditions (After Ref. 11)
Figure 19 (Right). S-N Curves of ß-C at R= -1, f=50 Hz, Comparing Single and Two Step Aging Treatments. Numbers In Parentheses Are Tensile Strengths (After Ref. 11)

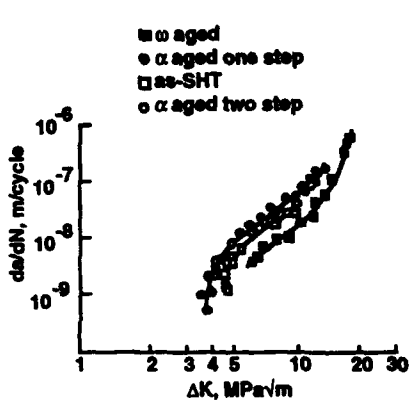




Figure 20 (Left). da/dN-ΔK Curves for for as-SHT, α Aged, and ω Aged ß-C Tested In Air at 10 Hz, Load Ratio = 0.1 (After Ref. 11)
Figure 21 (Right). SEM Fractograph of Grain Boundary α Initiation of HCF Specimen of Cast Ti-15-3 (After Ref. 4)

Boyer et al. (4) studied fatigue of cast Ti-15-3 heat treated to about 1170 MPa tensile strength. A significant variation in ductility was observed as a function of cast section thickness. The cooling rate from the HIP cycle or a solution treatment would be slower with heavy sections, increasing the grain size and width of the grain boundary α, which in turn reduces ductility. Ductility varied from about 1 to 12% elongation. Neither the smooth nor the notched high cycle fatigue performance, despite the large range of tensile ductility, was affected by the range of beta grain sizes and grain boundary α thicknesses investigated. In most cases the fatigue crack initiation site was associated with grain boundary α as shown in Figure 21, implying that this phase is less resistant to deformation than the aged matrix. Grain boundary α therefore suffers a disproportionate share of the plastic strain imposed during the fatigue cycle causing it to be an initiation site. The range of structures investigated was evidently insufficient to promote alternate initiation mechanisms. Because the load controlled fatigue test induced less strain/cycle than the tensile failure strain for any of the microstructures studied, the HCF strength of the material was not affected by those features which influence tensile ductility such as grain boundary α thickness.

Summary

The increased interest in metastable β Titanium alloys has spawned a number of detailed studies relating processing, microstructure and properties. This class of alloys offers a wide variety of static property combinations by control of microstructure through thermal and thermomechanical processing. However, control of dynamic properties, primarily crack growth rate,by microstructural manipulation remains elusive. It can be said, however, that because of this insensitivity, the crack growth rate of defect free metastable β alloys are more predictable, not as subject to variations in processing as are the other classes of Titanium alloys.

Properties of near-α and α/β Titanium alloys, on the other hand, are very sensitive to microstructural variations. Progress has been made towards an improved understanding of the specific role played by the various microstructural features in determining both static and dynamic properties. In concert with this, methods of reliably controlling microstructures are rapidly evolving into feasible production practices with a solid foundation of understanding.

References

1. E. Breslauer and A. Rosen, "Relationship Between Microstructure and Mechanical Properties in Metastable β Titanium 15-3 Alloy," Material. Sci. & Tech., 7 (1991), 441-446
2. W.M. Parris and P. J. Bania, "Oxygen Effects on the Mechanical Properties of TIMETAL-21S," Proceedings of this Conference
3. G. A. Bella, et al., Microstructure Property Relationships in Titanium Aluminide and Alloys, (Warrendale, PA: TMS, 1991), 493
4. R. R. Boyer et al., ibid., 511
5. H.A. Margolin and Sung Pak, "Void Formation and Void Growth in Ti-10V-2Fe-3Al," Proceedings of This Conference
6. M. Ninomi and T. Kobayashi, "Toughness and Strength of Microstructurally Controlled Titanium Alloys (Review)", ISIJ International., 31 (1991), 848-85
7. T.W. Duerig and J.C. Williams, Beta Titanium Alloys in the 1980's, (Warrendale, PA: TMS 1983) 19
8. M. Okada, "Strengthening of Ti-15V-3Cr-3Al-3Sn by Thermo-Mechanical Treatments," ISIJ International, 31 (1991), 834-839
9. N. Niwa, et al., "Mechanical Properties of Cold-Worked and High-Low Temperature Duplex Aged Ti-15V-3Cr-3Al-3Sn Alloy", Ibid.,856-862
10. G. T. Terlinde, T. W. Duerig and J. C. Williams, Titanium '80 Science and Technology, (Warrendale, PA; TMS,1983) 1571
11. J. K. Gregory and L. Wagner, "Heat Treatment and Mechanical Behavior in Beta-C," Proceedings of the Seventh International Meeting on Titanium, Turin, Italy, In Print
12. R. R. Boyer and G. W. Kuhlman, "Processing Properties Relationships of Ti-10V-2Fe-3Al," Met. Trans. A, 18A (1987), 2095-2103
13. K. Ito, Private Communication with the Author, University of Tokyo, Japan, June 23, 1991
14. Y. Kawabe and S. Muneki, "Strengthening and Toughening of Titanium Alloys (Review)," ISIJ International., 31 (1991), 785-791
15. G. W. Kuhlman, Microstructure Property Relationships in Titanium Aluminides and Alloys, (Warrendale, PA:TMS, 1991) 465
16. Y. Combres and B. Champin, "Titanium Alloys Processing: State of Art and Perspectives," Mat et Tech., (1991) 31-41
17. K. Nagai, et al., "Cryogenic Mechanical Properties of Ti-6Al-4V With Three Levels of Oxygen Content," ISIJ International., 31 (1991), 882-889
18. G. Sridhar and D.S. Sarma, "Structure and Properties of a Near-α Titanium Alloy after β Solution Treatment and Aging at 625°C," Met Trans A,19A, (1988), 3025-3033
19. G. Sridhar and D.S. Sarma, "Structure and Properties of a β Solution Treated, Quenched, and Aged Si-Bearing Near α Titanium Alloy," Met Trans A, (1989), 55-62
20. G. Sridhar and D.S. Sarma, "On the Influence of Microstructure on the Room Temperature Deformation Behavior of a Near-α Titanium Alloy," Met Trans A, 22A (1991), 1122-1125
21. H. Onodera, et al., "Creep Properties of $\alpha + \alpha_2$ High Temperature Titanium Alloys Designed by the Aid of Thermodynamics," ISIJ International., 31 (1991), 875-881
22. Peters, et al., Microstructure Property Relationships in Titanium Aluminides and Alloys, (Warrendale, PA:TMS, 1991), 533-548
23. L. Wagner, G. Lutjering and R.I. Jaffee, Ibid., 521-531
24. J.A. Hall, "Fatigue Crack Initiation in Titanium Alloys," (Paper presented Sixth China National Titanium Conference, Xian, Shaanxi, China, 17-21 Sept., 1987)
25. K.S. Ravichandran, "Near Threshold Fatigue Crack Growth Behavior of a Titanium Alloy: Ti-6Al-4V," Acta Met., 39 (1991), 401-410
26. H.-E. Kruegmann and J.K. Gregory, "Microstructure and Crack Propagation in Ti-3Al-8V-6Cr-4Mo-4Zr," Microstructure Property Relationships in Titanium Aluminides and Alloys, (Warrendale, PA:TMS, 1991) 549-561

HOT DEFORMATION MICROSTRUCTURE STUDY IN Ti-6Al-4V AND IN β–CEZ ALLOYS

C. SERVANT, C. QUESNE, T. BAUDIN and R. PENELLE

Laboratoire de Métallurgie Structurale
ISMA - URA CNRS 1107 - Université de Paris Sud - Bât 413, 91405
ORSAY Cedex., FRANCE

Abstract

Hot deformation microstructures in compression were studied in the Ti-6Al-4V and β–Cez alloys by optical and transmission electron microscopy. In the Ti-6Al-4V alloy, the compression tests were performed in the (α+β) field on two initial microstructures, equiaxed and acicular. Texture determination by neutron diffraction confirmed the microstructural evolution. In the deformed samples of the β-Cez alloy, dislocation bands were observed as a function of the strain amount, within a modulated b.c.c. microstructure.

INTRODUCTION

Hot deformation experiments in compression were performed on Ti-6Al-4V and β–Cez alloys. The knowledge of the microstructures developed during these tests simulating some thermomechanical treatments (TMT) and the description of the different mechanisms of hot deformation which control these microstructures are necessary to optimize the TMT and the subsequent thermal treatments and therefore to obtain the best combination of mechanical properties for the chosen application. In the case of the new French alloy β–Cez, developed by Cezus Company (1), a sharp initial peak was observed on the stress-strain curves during compression tests as a function of temperature and strain rate by (2). Samples weakly and strongly deformed were investigated by TEM in order to try to relate this anomaly to the microstructure. In the literature different hypotheses are suggested to explain the initial flow stress increase and subsequent drop: in the β-Cez alloy, anchoring of dislocations by solute atoms and breakaway of dislocations from their atmospheres (2) or in other β-Ti alloys, a low initial mobile dislocation density and subsequent rapid multiplication (3)

EXPERIMENTAL

In the case of the Ti-6Al-4V alloy, the compression tests were carried out in the (α+β) field at 935°C and at a strain rate $\dot{\varepsilon}$ of 10^{-3} s^{-1} and for a deformation $\bar{\varepsilon}$ =0.75 amount. In order to reach the stabilization of the chosen temperature, 30 min were necessary. Two types of initial microstructures were studied: the former, equiaxed, was obtained after an annealing performed at 940°C for one hour followed by a 300°C h^{-1} cooling to 700°C then an air cooling to 20°C; the latter was acicular: it resulted from an annealing at 1030°C for half an hour followed by an

Titanium '92
Science and Technology
Edited by F.H. Froes and I. Caplan
The Minerals, Metals & Materials Society, 1993

air cooling in order to go slowly through the β transus. Concerning the β-Cez alloy, the compression tests were carried out at 920°C as follows:

A treatment: to the deformation-peak (about 1%) at $\dot{\varepsilon} = 10^{-3}\ s^{-1}$;

B treatment: 65% deformation at $\dot{\varepsilon} = 10^{-2}\ s^{-1}$;

C treatment: 65% deformation at $\dot{\varepsilon} = 10^{-2}\ s^{-1}$, followed by an annealing for 50 min at 920°C.

For the A, B and C treatments, the cooling was uniformly performed at 200°C s^{-1} from 920 to 20°C.

The TEM experiments were carried out with a JEOL 2000 EX operating at 200 kV. The thin foils were obtained by electropolishing at -45°C using the two-jet technique with the Blackburn solution (4).

The texture determinations were carried out by neutron diffraction in transmission (at the Laboratoire Léon Brillouin, in Saclay, France) from orthocylinders of about 12 mm.

RESULTS AND DISCUSSION

Compressive curves of the Ti-6Al-4V

As shown in Fig 1, a yield point is observed at the elastoplastic transition on the stress-strain curve. The value of the upper yield point is slightly higher when the initial microstructure is treated in the β field relative to that treated in the (α+β) field.

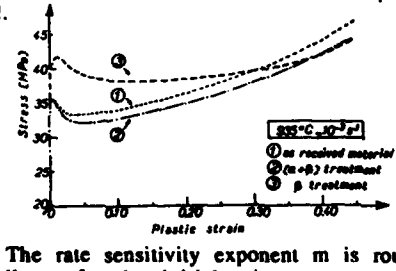


Fig 1 - Compressive stress-strain curves obtained at 935°C and with $\dot{\varepsilon} = 10^{-3} s^{-1}$ for three different Ti-6Al-4V microstructures

The rate sensitivity exponent m is roughly equal to 0.15 in the range 800-930°C regardless of the initial microstructure. Just under the β transus, m increases up to 0.32. These results are in good agreement with those of Chen (5).

It will be noted that the final forging performed by Cézus Company in the (α+β) field at 940°C in the case of the as-received material was followed by an annealing at 720°C for two hours in order to provoke a partial recovery of the Ti-6Al-4V alloy which was two-phase (α+β).

Microstructures

The deformed structures were compared to undeformed baseline microstructures as follows: the Ti-6Al-4V standard was annealed for 30 min at 935°C then cooled at 300°C h^{-1} to 20°C and the β-Cez standard was annealed for 50 min at 920°C then quenched at 200°C s^{-1} to 20°C

Ti-6Al-4V: initial equiaxed microstructure

By TEM, in the *Ti-6Al-4V undeformed standard*, both α and β phases are observed. In each phase, two types of areas are distinguished.

In fact, α appears both as equiaxed primary regions, α_p (about 50% vol.) and lamellar regions, α_l (about 45% vol); this latter morphology results of the β phase

transformation : $\beta \rightarrow \alpha_l + \beta_{lr}$ during cooling, where l and r are used respectively for lamellar and residual. The β_{lr} phase is enriched in beta-stabilizing elements (V, Fe) compared to the α_l phase (6). It appears as thin layers along the α_l lamellae and contains tangles of dislocations but neither dislocation cells nor recovery grains are evidenced. Moreover, the f.c.c. interface phase referred to as the L phase (6) is observed at the α_l/β_{lr} interface. Secondly, the beta phase appears locally as patches at triple points of α_p grains, it is referred to as β_r. At the α_p/β_r interface, the L phase is never detected. Inside the β_r phase, which does not contain dislocations, thin platelets of α'_a martensite are clearly detected, Fig 2a, the lateral growth of which can be explained in terms of the model developed by (7). In addition at the α'_a/β_r interface, the L phase is never revealed. The α'_a and β_r phases result of the transformation: $\beta \rightarrow \alpha'_a + \beta_r$.

The two morphologies of the beta phase (β_{lr} and β_r) observed may express a difference of composition in beta stabilizing elements resulting of a local inhomogeneity of composition in the beta phase at 935°C.

Moreover, two areas of α_p phase are revealed. They can be distinguished by their defect arrangements. In one, a high dislocation density is noted, Fig. 2b. They can result of the initial forging, or of the cooling (phase transformation, difference between the thermal coefficients of α and β phases). The dislocations appear either isolated or as long parallel sets of dislocations with $\vec{b} = 1/3\langle 11\bar{2}0\rangle$. . Some dislocation cells are observed. In the other areas, only a few isolated dislocations are noted while a lot of subboundaries revealed a well developed recovery stage, Fig. 2c. Twist subboundaries are very much numerous than the tilt ones.

In the α_l areas, only a few isolated dislocations are observed at 20°C: in fact, during the beta phase transformation on cooling, the dislocations which are not eliminated during the annealing for 30 min at 935°C, are more probably swept out or incorporated in the α/β interfaces.

In the α_p areas of the *deformed microstructures*, a very high dislocation density is observed with planar arrangements, Fig. 3a. No dislocation cells and a few faceted subboundaries are noted. The slip is intragranular and recovery subboundaries showing strain induced boundary migration (SIBM) are simultaneoustly observed, Fig. 3b. This result is in agreement with the in-situ TEM observations of Naka et al (8) on commercial purity titanium. Furthermore, neither recrystallization nor twinning were detected.

In the α_l areas, only a few unarranged dislocations exist.

Ti-6Al-4V: initial acicular microtructure

Inside the *acicular undeformed standard*, two phases are observed, referred to as α_l and β_{lr}; inside the α_l phase, the dislocation density is lower than the one in the α_l *phase of the equiaxed undeformed standard. Some* $\vec{c}+\vec{a}$ dislocation arrangements are observed as well as twist boundaries. Inside the lamellae of the β_{lr} phase, a few short and unarranged dislocations are revealed.

.After the *compressive tests*, the α lamellae appear larger and shorter than in the undeformed standard. They fragment into misoriented subgrains, Fig. 4.

β-Cez alloy

The *undeformed thermal standard* is single phase consisting of disordered body centered cubic beta phase with large grains. Inside these latter, the presence of elongated subgrains is noted as well as a very high dislocation density in the subgrains with $\vec{b} = a/2\langle 111\rangle\beta$, Fig. 5a. These very mobile dislocations appear as long

Ti-6Al-4V



Fig 2. - *Thermal undeformed standard of the Ti-6Al-4V* initial equiaxed microtructure showing:

a) βr phase with thin platelets of the α'_a phase,
b) α_p phase areas with a high dislocation density;
c) α_p phase areas where subboundaries reveal a well developed recovery stage.

Ti-6Al-4V



Fig 3 - *Deformed sample of the Ti-6Al-4V* initial equiaxed structure showing:
a) a very high dislocation density with planar arrangements;
b) strain induced boundary migration (arrow);



Fig 4 - *Deformed sample of the Ti-6Al-4V* initial acicular structure showing a fragmentation of the α_I lamellae.

screw segments with small edge. They may result from the fast cooling or from a non sufficient homogenization duration at 920°C. Inside the β grains, a modulated structure is revealed by very thin parallel lines (Fig. 5b) related to premartensitic phenomena (9) such as weak maxima at 1/2<110>*β, 1/2<112>*β..., and diffuse streaks along <110>*β, <112>*β ....The athermal ω phase is also revealed, Fig 5c.

The *deformed microstructures* of the β-Cez alloy also appears as modulated and contains athermal ω phase.

After the A treatment, dislocation bands more or less well formed appear in some areas of the thin foil, Fig. 6a; they are parallel and their average width is 10 nm. Their direction is near <113>β; these bands are similar to the slip bands observed by Banerjee et al (10) in titanium aluminides. In a few other places, larger bands referred to as "superbands" of about 500 nm wide are observed; they contain a lot of individual dislocation bands. Finally, some areas without bands exist, they contain a high density of screw dislocations with $\vec{b}$ = a/2<111>β. In addition, tilt and twist subboundaries are observed.

After the B treatment, the dislocation bands are more numerous and consist of tangled dislocations, Fig. 6b. Neither dislocation cells nor twinning were observed. Moreover, the subboundaries are more numerous: a dynamic recovery has taken place.

After the C treatment, "superbands" and individual dislocation bands are yet observed. The average distance between the individual dislocation bands is however increased as compared to the B treatment, Fig. 6c They have begun to disappear during the annealing at 920°C for 50min performed after the compressive tests. So, during this thermal treatment, a static recovery has occurred. Cross slip is also observed and some bands are formed with very thin twins, the twinning elements are classical : {121}β <111>β.

The TEM observations did not provide any information between the occurrence of the sharp initial peak on the stress-strain curves and the dislocation structure evolution.

Textures

In the initial equiaxed microstructure of the Ti-6Al-4V alloy, subsequently deformed in the (α+β) field at 935°C, neither static nor dynamic recrystallization were observed. Only a strain induced boundary migration (SIBM) was shown. This fact was confirmed by a retention of the initial texture in the deformed samples characterized by a partial fiber <10$\bar{1}$0> + <11$\bar{2}$0> parallel to the bar axis of the Ti-6Al-4V material, referred to as B.A., Fig. 7. In the case of the initial acicular microstructure, a partial <10$\bar{1}$1> texture appears.

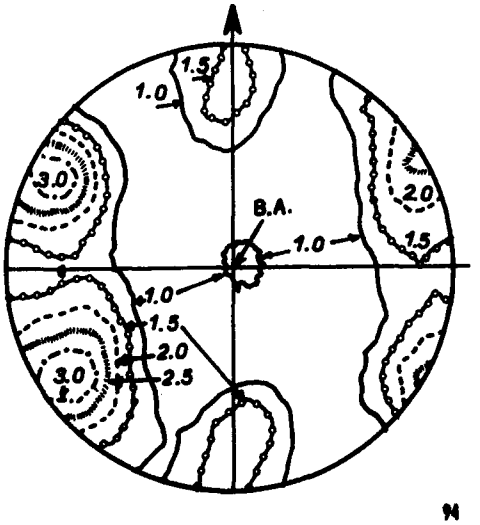


Fig. 7 - (0002) pole figure (Ti-6Al-4V)

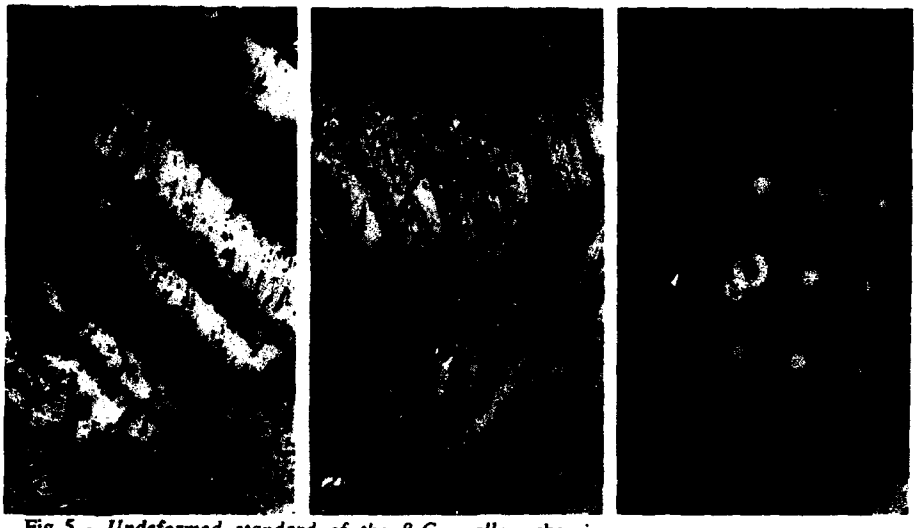


Fig 5 - *Undeformed standard of the β-Cez alloy* showing:
a) elongated subgrains with a high dislocation density;
b) the modulated structure;
c) <110>β electron diffraction pattern with the athermal ω phase spots.

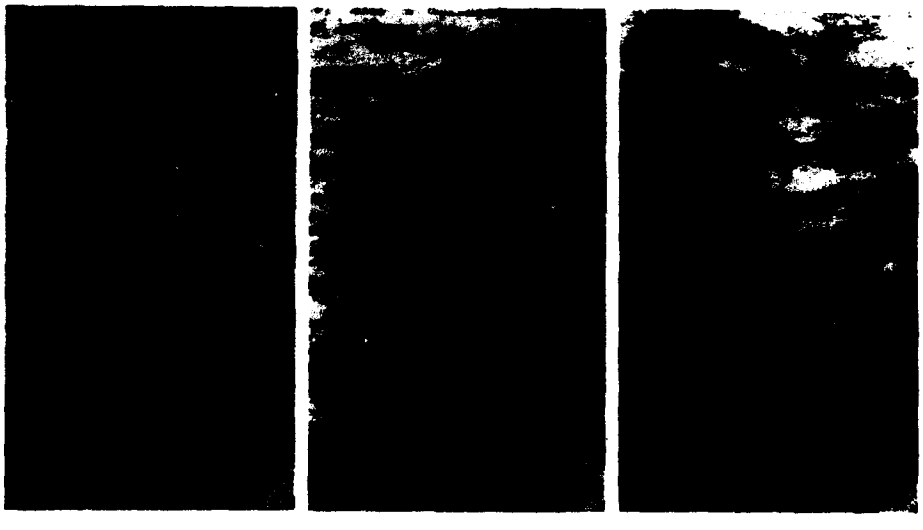


Fig. 6 - *Deformed samples of the β-Cez alloy* showing:
a) more or less well defined dislocations bands (A treatment);
b) more numerous dislocation bands (B treatment);
c) that during the post deformation thermal treatment (50min at 920°C), the dislocation bands begin to disappear (C treatment).

CONCLUSION

In the Ti-6Al-4V equiaxed ($\alpha+\beta$) microstructure deformed in compression at 935°C only dynamic recovery and SIBM were observed. No recrystallization occurred as confirmed by the retention of the initial texture revealed by neutron diffraction experiments. In the β-Cez alloy, the room temperature initial structure is modulated and contains athermal ω phase. After compressive deformation, at the TEM scale, some dislocation bands are already observed for a low strain (<1%); when the strain reaches 65%, they are very numerous : they show that the deformation is inhomogeneous. During a consecutive post deformation thermal treatment of 50 min at 920°C, these bands partially disappear.

REFERENCES

1. B. Prandi et al,"β-Cez, a High Performance Titanium Alloy for Aerospace Engines", International Conference on Titanium 88, ed. P. LACOMBE, R. TRICOT and G. Béranger (Paris, Société Française de Métallurgie, 1988),pp. 811-818.
2. F. Montheillet et al, "Hot deformation of a new high strength titanium alloy" in the Proceedings of the Seventh World Conference on Titanium,, San Diego, U.S.A., 1992.
3. M.N. Vijayshankar and S. Ankem, "High Temperature Tensile Deformation Behavior of β-Ti Alloys", Materials Sc. and Eng., A129, 1990, pp. 229-237.
4. M.J. Blackburn and J.C. Williams, "The preparation of thin foils of titanium alloys", Trans AIME, 1967, vol. 239, pp. 287-288.
5. C.C. Chen, "Influence of initial microstructures on the forgeability and microstructure of isothermally forged Ti-6Al-4V alloy", Titanium and titanium alloys, Proceedings of the Third International Conference on Titanium, Moscow 1976, (edited by J.C. Williams and A.F. Belov, Plenum Press 1982), pp. 397-411.
6. C. Servant et al, "Contribution to the analysis of the α/β interface in some titanium alloys", J. Mater. Res., 1991, vol. 6, No. 5, pp 987-998.
7. H.K. Bhadeshia, M. Dechamps and L.M. Brown, Acta Met., 1981, vol.29, pp. 1473-1474.
8. S. Naka et al., Titanium'80, Science and Technology, Proceedings of the Fourth International Conference on titanium (edit. H. Kimura and O. Izumi, 1980), vol. 2, pp. 955-963.
9. I.M. Robertson and C.M. Wayman, Philosophical Magazine, 1983, vol. 48, No. 3, pp 421-442.
10. D. Banerjee, A.K. Gogia and T.K. Nandy, " Deformation structure in a Ti-24Al-11Nb alloy", Met. Trans. A, 1990, vol. 21, pp 627-639.

STRUCTURAL STABILITY OF "β-CEZ" ALLOY

Agnès Henri, Alain Vassel

ONERA, BP 72, 92322 Chatillon Cedex, France

Abstract

The "β-CEZ" alloy (Ti-5Al-2Sn-4Zr-4Mo-2Cr-1Fe) developed by CEZUS in France is designed for use in advanced aeroengines compressors up to 450°C. It is recognized that in this class of titanium alloys, the isothermal ω phase or titanium compounds may precipitate during ageing treatments or service conditions. The presence of these phases has been looked for to detect potential embrittlement of the alloy. Microstructural investigations revealed the good stability of the alloy ; no harmful phase precipitates under usual conditions.

Introduction

The high strength mid-temperature "β-CEZ" alloy (Ti-5Al-2Sn-4Zr-4Mo-2Cr-1Fe) recently developed by CEZUS in connection with SNECMA is designed for use in aeroengines compressor disks. As compared with alloys of the same class, it offers attractive characteristics up to 450°C. A good balance of mechanical properties is obtained after forging in the β field and heat treatment in α+β [1].

In all α+β and near-β titanium alloys which contain large additions of β-isomorphous and β-eutectoid stabilizers, the precipitation of isothermal ω phase or titanium compounds may occur during ageing treatments or service conditions. As the presence of these phases has an adverse effect on ductility, the conditions of their precipitation in "β-CEZ" alloy have been investigated.

Experimental

The study was carried out on two kinds of forged products, a pancake and a cylindrical bar, coming from different heats which compositions are listed in Table I. Considering the pancake (diameter 250mm, thickness 60mm), the last forging operation was performed under hot die conditions ; the starting temperature was 920°C, i.e. 30°C above the beta transus, and it steadily decreased during processing. The microstructure in the as-forged condition is illustrated in Fig. 1 ; it is of lamellar type with α

Titanium '92
Science and Technology
Edited by F.H. Froes and I. Caplan
The Minerals, Metals & Materials Society, 1993

phase decorating prior β grain boundaries.

Similarly, the final forging step on the cylindrical bar (diameter 80mm) started at 920°C, in the β field, and finished at about 750°C. Due to an increased amount of deformation in the α+β field, a recrystallized equiaxed structure develops at β grain boundaries (Fig. 2).

Table I Chemical composition of forged materials (wt.%)

	Al	Sn	Zr	Mo	Cr	Fe	O
Pancake	4.92	2.01	4.13	3.99	2.17	1.02	0.087
Bar	4.98	1.91	3.88	3.86	2.09	0.98	0.070

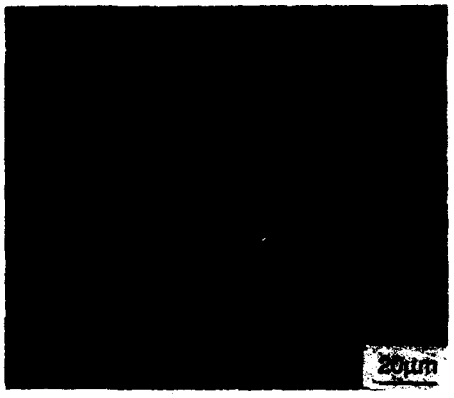


Figure 1 Microstructure of the pancake.

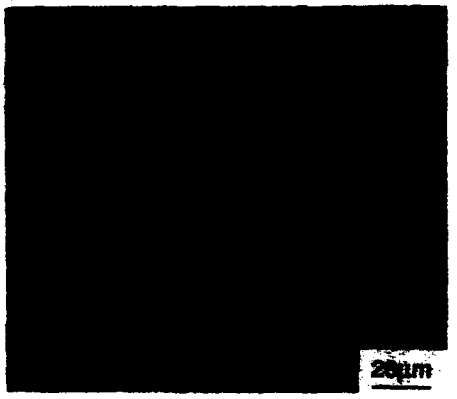


Figure 2 Microstructure of the bar.

Phase transformations during heat treatments and prolonged exposures at operating temperatures were investigated by examination of thin foils in a JEOL 200CX electron microscope. Tensile properties at room temperature were determined from cylindrical specimens 4mm in diameter and 30mm in calibrated length.

Results and discussion

Influence of heat treating parameters

The alloy is designed to be used in a solution treated plus aged condition. The solution treatment is carried out at 800°C or 830°C, in the α+β field, and the ageing temperature is chosen between 580°C and 620°C. Due to the thick section of forged disks, the cooling rate after solution treatment and the heating rate to the ageing temperature may be very different between the core and the surface. Also, these two parameters vary with the quenching medium (water, oil) and the type of furnace employed for ageing treatments (air furnace, salt bath). The transformation mechanism of the high temperature β phase depends on the quenching rate and a transient precipitation of ω phase may appear on slow heating to the ageing temperature [2,3,4]. Further, the presence of ω particles controls the subsequent precipitation of α phase the-

reby affecting the hardening response.

Microstructural studies were performed on samples 10mm in diameter cut in the pancake. They were either water quenched or air cooled after a solution treatment of 4 hours at 830°C ; the corresponding cooling rates are 50°C.s^{-1} and 5°C.s^{-1} approximately. It is to be noted that the second case is representative of a water quenching on a 70mm thick titanium alloy pancake. The ageing treatments were performed in a salt bath or in a progammed air furnace. The heating rates that have been selected (~200°C.min^{-1} and 1°C.min^{-1}) correspond to extreme values encountered in industrial conditions. In both cases, an ageing treatment of 8 hours at 580°C is applied to the samples once the temperature has been reached.

A cooling rate of 5°C.s^{-1} after solution treatment induces a decomposition of the high temperature β phase ; dark field transmission electron micrographs reveal the presence of needle like secondary α phase in the β matrix (Fig. 3). On the other hand,



Figure 3 TEM micrograph of transformed β phase in solution treated material (830°C 4h, cooling rate 5°C.s^{-1}) : dark field image showing secondary α phase.

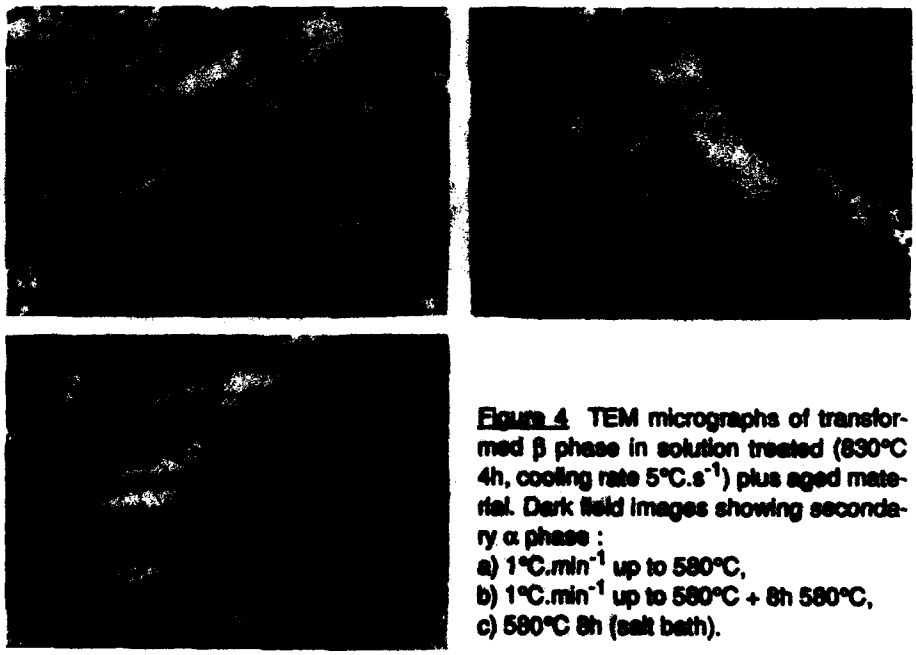


Figure 4 TEM micrographs of transformed β phase in solution treated (830°C 4h, cooling rate 5°C.s^{-1}) plus aged material. Dark field images showing secondary α phase :
a) 1°C.min^{-1} up to 580°C,
b) 1°C.min^{-1} up to 580°C + 8h 580°C,
c) 580°C 8h (salt bath).

the β phase is retained upon rapid quenching to room temperature ($50°C.s^{-1}$). Selected area diffraction patterns on $<110>_\beta$ zone exhibit streakings and diffuse athermal ω reflections. These microstructures will behave differently during ageing.

In the case of the lower cooling rate, the secondary α phase slightly grows when it is slowly heated to the ageing temperature (Fig. 4a) then it coarsens after 8 hours at 580°C (Fig. 4b). There is almost no influence on the final microstructure when the ageing treatment is carried out in salt bath (Fig. 4c). No other phase apart from α and β has been detected.

As far as the rapid quenching is concerned, weak reflections that may be attributed to isothermal ω phase appear on $<110>_\beta$ zone patterns in a sample slowly heated at $1°C.min^{-1}$ up to 300°C. The precipitation of that phase is confirmed at 350°C and 375°C (Fig. 5). The size and the volume fraction of ω particles seem to be maximum at 375°C. The ω phase morphology is controlled by the misfit between the precipitate and the β matrix : it is elliptic in Ti-Nb and Ti-Mo alloys and cubic in Ti-Cr, Ti-Fe and



Figure 5 TEM micrograph of transformed β phase in solution treated plus aged material (830°C 4h, cooling rate $50°C.s^{-1}$ + $1°C.min^{-1}$ up to 375°C). Dark field image showing isothermal ω phase.

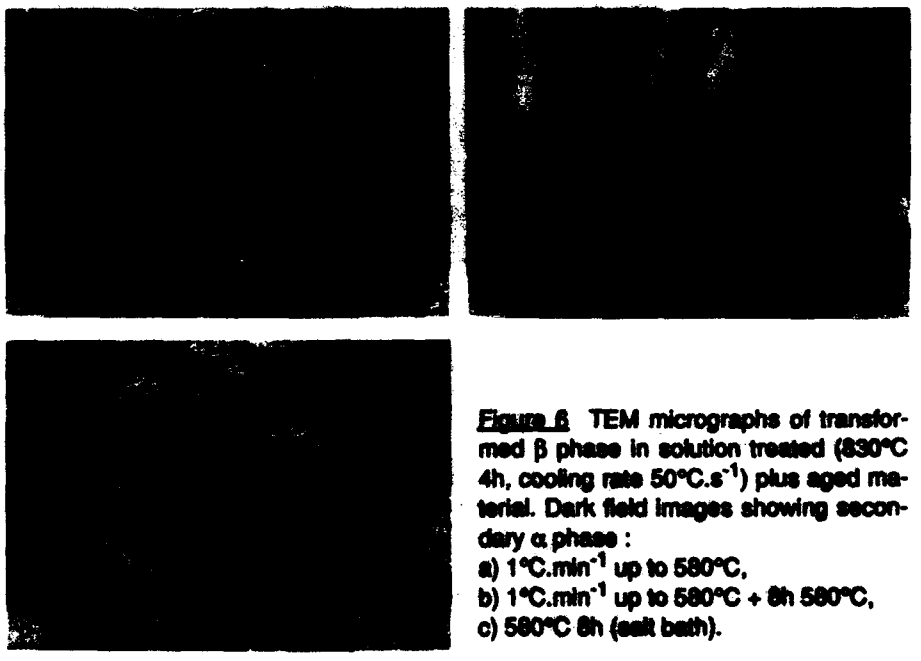


Figure 6 TEM micrographs of transformed β phase in solution treated (830°C 4h, cooling rate $50°C.s^{-1}$) plus aged material. Dark field images showing secondary α phase :
a) $1°C.min^{-1}$ up to 580°C,
b) $1°C.min^{-1}$ up to 580°C + 8h 580°C,
c) 580°C 8h (salt bath).

Ti-V systems [5]. Here, it is difficult to determine the exact morphology due to the small size of the particles. The secondary α phase begins to precipitate at 400°C ; at that temperature, isothermal ω and secondary α phases coexist and dark field images reveal that ω particles act as nucleation sites for the α phase. When a sample is slowly heated up to 450°C, the ω phase disappears and fine needles of secondary α phase are only observed.

It is interesting to compare the morphology and the distribution of secondary α phase after a slow heating up to 580°C when the alloy has been subjected to different cooling rates after solution treatment (Fig. 4a and 6a). It appears that the α phase is much finer and more uniformly distributed when it precipitates from isothermal ω phase than from the β matrix. The same tendency, although less pronounced, can be observed after 8 hours at 580°C (Fig. 4b and 6b). In the case of ageing in salt bath, i.e. a fast heating rate, the α phase directly precipitates from β and its aspect does not depend on the cooling rate after solution treatment (Fig. 4c and 6c).

Following microstructural investigations, tensile tests at room temperature were carried out on the pancake in some selected conditions (Table II). A high strength and a very low ductility have been measured when the alloy is rapidly quenched after solution treatment and slowly heated up to 580°C. This result is attributed to the extremely fine size and strong strengthening effect of secondary α phase grown from isothermal ω particles (Fig. 6a). The subsequent ageing treatment induces a coarsening of α platelets and leads to a decrease in strength and an improvement in ductility. The optimum properties are obtained with a cooling rate of $5°C.s^{-1}$ after solution treatment. In that condition, the heating rate to the ageing temperature has hardly no influence on tensile properties and this result is consistent with microstructural observations.

Table II Influence of heat treating parameters on tensile behaviour at 20°C

Solution treatment	Ageing treatment	Y.S. (MPa)	U.T.S. (MPa)	El. (%)	R.A. (%)
830°C 4h	$1°C.min^{-1}$ ↗ 580°C	1407	1545	0.7	3
↘ $50°C.s^{-1}$	$1°C.min^{-1}$ ↗ 580°C + 8h 580°C	1302	1389	4.3	6
	580°C 8h (salt bath)	1302	1363	4.8	9
830°C 4h	$1°C.min^{-1}$ ↗ 580°C	1230	1368	4	9
↘ $5°C.s^{-1}$	$1°C.min^{-1}$ ↗ 580°C + 8h 580°C	1185	1261	6	16
	580°C 8h (salt bath)	1253	1316	6.3	14

All values represent the average of two tests

Effect of prolonged exposures at operating temperatures

An important property for all materials used in aeroengines is the stability over time of their microstructure and mechanical characteristics. In particular, the "β-CEZ" alloy contains two β-eutectoid stabilizers, chromium and iron, which may induce the precipitation of $TiCr_2$ and TiFe compounds with a consequent decrease in ductility. For instance, $TiCr_2$ precipitates have been identified in Ti-3Al-8V-6Cr-4Zr-4Mo alloy after

long periods at 500°C [6]. Also, we have looked for a possible ordering reaction of the α phase, bearing in mind that the percentage of α-stabilizing elements in "β-CEZ" is low enough so that an extensive precipitation of Ti_3Al is unlikely to occur.

Microstructural studies and tensile tests were performed on the cylindrical bar supplied in a fully heat treated condition (830°C 1h, cooling rate $2°C.s^{-1}$ + 580°C 8h) (Fig. 2). The following exposures which correspond to service conditions were considered :

- 425°C up to 5000 hours,
- 475°C up to 500 hours.

Tensile tests at room temperature were carried out after these exposures and compared to the initial condition. In order to separate the influence of structural instability and surface oxidation, the specimens were tested with the surface removed or retained, respectively. Also, some creep tests (250MPa) were performed under similar conditions of temperature and time to detect a possible stress assisted precipitation.

All tensile tests results are listed in Table III. With no applied stress, it appears that there is no change in properties when specimens are machined after exposure. Examination on thin foils was unsuccessful to show the existence of an heterogeneous precipitation of a titanium compound like $TiCr_2$ or TiFe. Taking into account the very low solubility of chromium and iron in the α phase, 0.3 and 0.05 wt% at 500°C respectively [7], and the concentration of these elements in the alloy, the preceding observation suggests that the stabilization of the β phase by molybdenum, a β-isomorphous

Table III Effect of various exposures on tensile behaviour at 20°C

			Y.S. (MPA)	U.T.S. (MPa)	El. (%)	R.A. (%)
Initial condition			1195	1270	15	23
σ=0 (1)	425°C	300h	1208	1285	15	23
		1000h	1230	1301	15.2	22
		5000h	1233	1277	13.5	25
	475°C	100h	1203	1257	15.1	29
		500h	1226	1274	13.5	25
σ=0 (2)	425°C	300h	1222	1274	13.2	20
		1000h	1227	1304	11.2	11
		5000h	1241	1294	10.2	14
	475°C	100h	1216	1279	13	24
		500h	1241	1275	10.3	13.5
σ=250MPa (2)	425°C	1000h	1185	1264	12.3	19
	475°C	100h	1197	1260	10.5	17

(1) surface removed
(2) surface retained
All values represent the average of two tests

element, allows chromium and iron to remain in solid solution in β. The only minor microstructural change occurs after 5000 hours at 425°C ; diffuse superlattice spots can be seen on diffraction patterns of the α phase indicating the very beginning of Ti_3Al formation.

When specimens are tensile tested with the surface retained, a slight decrease in ductility is obeserved after prolonged exposures and this is attributed to a superficial oxygen contamination.

Finally, the application of a stress does not lead to a measurable damage. No stress assisted precipitation was detected by TEM.

Conclusions

The phase transformation generally observed when the "β-CEZ" alloy is solution treated and aged is β→β+α. It has been shown that the transient precipitation of isothermal ω phase only occurs after a rapid quenching ($50°C.s^{-1}$) followed by a very low heating rate to the ageing temperature ($1°C.min^{-1}$), condition not encountered in the industrial practice.

Prolonged exposures at operating temperatures, with and without an applied stress, have no adverse effect on microstructure and tensile properties. No harmful precipitation was detected by TEM ($TiCr_2$, TiFe, Ti_3Al,...).

These results highlight the good structural stability of "β-CEZ" alloy. No brittle phase appears during usual heat treatments or service conditions.

Acknowledgements

The authors acknowledge SNECMA for financial support. They are also grateful to B. Champin (CEZUS) and A. Lasalmonie (SNECMA) for technical discussions.

References

[1] B. Prandi, J.F. Wadier, F. Schwartz, P.E. Mosser, A. Vassel, 1990 International Conference on Titanium Products and Applications, vol.1 (T.D.A., Dayton, 1990), 150.

[2] G.M. Pennock, H. M. Flower, D.R.F. West, Titanium'80 Science and Technology, vol.2 (The Metallurgical Society of AIME, 1980), 1343.

[3] R.W. Coode, T.W. Duerig, G.H. Gessinger, ICSMA 6 (Pergamon Press, 1983), 263.

[4] M.H. Campagnac, A. Vassel, Designing with Titanium (The Institute of Metals, London, 1986), 261.

[5] J.C. Williams, M.J. Blackburn, Trans. AIME, 245 (1969) 2352.

[6] T.J. Headley, H.J. Rack, Met. Trans. A, 10A (1979) 909.

[7] J.L. Murray, Phase Diagrams of Binary Titanium Alloys (ASM, Metals Park, 1987).

DEFORMATION AND FRACTURE MECHANISMS IN THE ß METASTABLE ß-CEZ ALLOY

Y. Combres, G. Dumas, A.-M. Chaze* and B. Champin

Centre de Recherches de CEZUS
BP 33
73400 Ugine Cedex France
* Ecole des Mines de Paris-Cemef
Sophia-Antipolis
06565 Valbonne Cedex France

Abstract

The relationships between the deformation mechanisms and the fracture process in the ß metastable ß-CEZ alloy (Ti-5%Al-2%Sn-4%Zr-4%Mo-2%Cr-1%Fe) have been investigated to correlate the microstructure influence to the mechanical properties. Two series of samples have been tested in tension and toughness at room temperature: as Solution Treated (ST) specimens, consisting, after water quenching, in primary α (αI) and ß metastable (ßm) phases, and Solution Treated and Aged (ST+A) samples, for which, ßm transforms into secondary α (αII) and stable ß (ßs).There is a change in the deformation mechanisms in the ß phase, from dislocation for low ST temperatures, to dislocation + twinning for high ST temperatures. This evolution is related to ßm stability. For ST temperatures below the ß transus, the ductility is governed by the αI/ßm interface cracking, and the strength, by the the αI-αI interspacing which is related to the dislocations mean free path or twins length. For the ST+A samples, when the ageing temperature increases, αII particles coarsen, and the αII+ßs matrix is softer. The strength is then related to the αII average size in a Hall-Petch fashion. Toughness is controlled by the crack path tortuosity through the αII precipitates, and increases when they coarsen.

Introduction

Over the last past five years, the development of ß metastable titanium alloys has been stressed by the need of ever improved materials, either on the viewpoint of strength, toughness, creep resistance, formability, or corrosion resistance. Some of the newly designed ß metastable alloys are refered to as ß-CEZ [1,2], a high strength-high toughness-medium temperatures creep resistant grade, or SP 700 [3,4], a high strength-low temperature superplastic material, or TIMETAL 21S [5], a high strength-corrosion resistant alloy.

The authors acknowledge with gratitude the DGA/DRET/STPAé financial supports, for the ß-CEZ alloy development. Most of this work has been carried out during the training period of G.Dumas in his course of engineering degree at the Ecole des Mines de Paris. The authors are endebted to Prof. A. Pineau who organized this period.

Titanium '92
Science and Technology
Edited by F.H. Froes and I. Caplan
The Minerals, Metals & Materials Society, 1993

However, for all these materials, the final use lies in the adequate microstructure control (obtained through their large window processing) and which is targeted towards either designing or limiting properties. For this purpose, some basic knowledge of the deformation mechanisms and fracture processes is required to figure out the influence of the microstructure on the properties.

Therefore, the objectives of this paper are, at first, to characterize the deformation modes and fracture mechanisms, then, by a qualitative observation, to determine the relevant parameters controlling both the deformation and the fracture, and, finally, provided that the microstructure is well quantified, to propose some relationships between a property and a microstructural parameter. For such a study, the ß-CEZ alloy, patented by CEZUS at the end of the 80's, has been chosen. It is assumed that this material is representative of ß metastable titanium alloys.

Material and experimental procedures

ß-CEZ is the registered commercial name of the Ti-5%Al-2%Sn-4%Mo-4%Zr-2%Cr-1%Fe (wt %) grade [6]. The material comes from a triple VAR Ø 530 mm ingot, the actual composition of which is given in table I.

Table I: Chemical composition of the ß-CEZ used in this study (wt %)

Al	Sn	Zr	Mo	Cr	Fe	O	N
4.94	2.01	4.16	4.00	2.20	1.02	895*	55*

(* ppm by weight)

The ß transus temperature of this material, Tß, is 890 °C. Ø 150 mm bars have been prepared by forging in the α+ß range. To start with, the microstructure displays an equiaxed primary α phase (labeled αI in the following), with transformed ß in between. In order to separate the role of αI from the others phases, samples solution treated for 2 hrs and water quenched (WQ) have been used, which retain amounts of ß metastable phase (refered to as ßm), taking advantage of the high hardenability of the grade. A typical microstructure is presented in figure 1 (a). Upon a 8 hrs long ageing treatment (see figure 1 (b)), ßm transforms into a fine lamellar secondary α (named αII) and stable ß (labeled ßs). The solution treatment temperature was varying in the 830-910 °C range, whereas the ageing temperature was in the 550-650 °C range (followed by air cooling: AC).

The mechanical properties have been determined in tension, to characterize strength, ductility, deformation mechanisms with damage nucleation, and toughness tests for crack propagation. Creep and fatigue (da/dN and S-N curves) have also been characterized but will not be detailed here. The microstructures or fracture surfaces have been observed by means of optical microscopy, with sometimes polarized light, SEM, STEM and TEM. They have been quantified for both αI and αII by Image Analysis coupled to SEM or STEM.

Results

The results are gathered in the table II. They present at first the tensile properties and the toughness level as a function of heat treatment. For each treatment, the particles size as well as the volume fraction are indicated. For αI, direct measurement is made by Image Analysis, but due to their very small size, special techniques have been developped to get an estimate of

the αII size. The techniques will be not presented here; they are based upon mathematic morphology.

Table II: Selection of tensile properties, toughness and microstructure quantification

Treatment	0.2%YS (MPa)	UTS (MPa)	El (%)	K_{Ic} $MPam^{1/2}$	αI size (μm)	αII size (μm)	%αI	% ß
830 °C/2h/WQ	842	951	16	87	3.2	-	25	75
830 °C/2h/WQ + 550 °C/8H/AC	1518	1601	2	-	3.2	0.03	25	19
830 °C/2h/WQ + 600 °C/8H/AC	1211	1282	7	48	3.2	0.08	25	27
830 °C/2h/WQ + 650 °C/8H/AC	1070	1112	13	51	3.2	0.16	25	36
860 °C/2h/WQ	755	969	19	82	3.1	-	4	96
860 °C/2h/WQ + 550 °C/8H/AC	1478	1557	2	29	3.1	0.04	4	21
860 °C/2h/WQ + 600 °C/8H/AC	1304	1370	4	39	3.1	0.07	4	31
860 °C/2h/WQ + 650 °C/8H/AC	1109	1161	9	59	3.1	0.19	4	45
910 °C/2h/WQ	723	927	10	64	-	-	0	100
910 °C/2h/WQ + 650 °C/8H/AC	1036	1159	3	67	-	0.18	0	32

As solution treated (as ST'ed) specimens

As it has been published elsewhere [7,8], when the solution treatment temperature increases:

→ the number of αI particles decreases, whereas their size remains somehow constant,

→ the strength and toughness decrease too, but the ductility grows in the α+ß range, and is reduced in the ß field,

→ the ßm phase deforms by dislocations but more and more by twinning as shown in figure 2; αI always deforms very uniformly by dislocations,

→ ω phase precipitation is enhanced as shown by TEM selected area diffraction patterns in figure 3; the ω particles are so small, however, that dark field technique fails to reveal them; deformed specimens exhibit traces of α" orthombic phase precipitation,

→ fracture surfaces are always covered by equiaxed dimples, which become sometimes elongated in the 100% ßm sample (figure 4),

→ side views of toughness specimens show that crack propagation takes place in ßm and at the αI/ßm interface (figure 5).

Solution treated and aged (ST+A) specimens

αII phase precipitates out very finely and special techniques have been developped to observe and quantify the structures [7-9]. When the ageing temperature is raised, αII lamellae

coarsen and their number is reduced; the ßs phase proportion grows. Strength decreases, and both ductility and toughness increase. αI and αII deform only by dislocations. Contrary to what was observed in the as ST'ed specimens, the dislocations are often arranged into intense shear bands in αI which create steps at the boundary, as shown in figure 6. In all the specimens, the fracture is ductile in nature and consists of very small equiaxed dimples. Some of them are elongated, and are relevant of αII lamellae disbonding. Quite often, microcracks nucleate at the αI grain boundary (figure 7).

Discussion

Deformation mechanisms and fracture process

In the as ST'ed specimens, as ßm is more metastable, i.e. as the ST temperature is raised, athermal ω phase precipitation is enhanced (water quenching from temperatures below 860 °C does not reveal it), and the ω particles are very fine. Simultaneously, deformation by twinning becomes prominent. These results on twinning are consistent with those of literature concerning Ti-15%Mo-5%Zr [10], Ti-Fe [11] or Ti-Cr [12] alloys. Probably, as suggested in the case of ßIII single crystals [13], the presence of ω phase suppresses the normal movement of dislocations in the b.c.c. lattice, and thereby, promotes the occurence of other modes of deformation, such as twinning.

On the other hand, the corresponding fracture surfaces exhibit ductile dimples some of them being elongated. In the case of α type titanium alloys, the occurence of twinning-elongated dimples has also been reported, as in the case of Ti-5%Al-2.5%Sn [14] at cryogenic temperatures, or ASTM grade 2 containing hydrides [15]. In the last two studies, the restriction in the dislocation motion is due to the lack of thermal activation or hydrides presence, and the elongated dimples have been related to twins intersections or twin-grain boundary interactions. The same seems to apply in the case of ß-CEZ alloy in the ß phase, and the presence of the ditch in figure 4, looks very similar to those reported [14,15]. Dislocation pile ups or twins at the ß grain boundaries or αI/ßm interface lead to very high local stress concentrations. Especially, crack nucleation occurs at these points [9]. In toughness tests, αI/ßm interface breaks easily and deviates crack path.

In the ST+A samples, which are representative of industrial treatments, it is confirmed that isothermal ω phase is not found. But, as shown elsewhere [16], the athermal ω phase precipitates act, at the begining of the ageing process, as nucleation sites for αII. The αII precipitation is therefore very fine, and the particle size is sub-microscopic. When the ageing temperature is raised, this size increases too, as for the Ti-15-3 [17]. The αII/ßs interface is a very efficient barrier to dislocation slip. This results in a very high strengthening effect, and the αII+ßs matrix is very hard, as shown by micro hardness measurements [9]. The deformation is accomodated by the softer regions of the material, i.e. the αI grains. This is consistent with the presence of intense shear bands in the αI phase. Then, cracking occurs very easily at the αI boundary.

Mechanical properties-microstructure relationships

In both the as ST'ed and ST+A specimens, α and ß phase deform extensively. In the as ST'ed samples, dislocation pile ups or twin length reductions should increase the ductility.

Especially, below Tß, reducing the ST temperature would lead to a more ductile alloy, because, if the αI grain size does not vary significantly, αI-αI interspacing decreases. Nevertheless, the contrary applies here, and this suggests that the αI/ßm interface is controling the damage nucleation. When the ST temperature is lowered, the total αI/ßm interface length grows, and the possibility of microcracking is greater.

In the ST+A specimens, the material consists of approximately 70-80 % α phase. The properties can be explained only by it, and more specifically by αII, since αI size does not vary that much. The finer are the αII particles, the larger is the strength, and the lower is the toughness. In particular, it has been found that 0.2% YS obeys a Hall-Petch relationship, the consistency of which is given in figure 8. On the other hand, when the αII coarsen, the toughnes is enhanced as shown in figure 9. The relationships can be established independantly on the heat treatment conditions, which justifies the choice of αII size as the pertinent microstructural parameter.

Conclusions

ß-CEZ precipitation characteristics, deformation mechanisms and fracture processes exhibit all the features already encountered in the ß metastable titanium alloys. The fracture process has been related to the deformation mechanisms, and especially, for the ST'ed specimens, the occurrence of elongated dimples is probably related to damage induced by twinning. Based on the observations made on ST+A samples, strength and toughness are both a function of the αII grain size; it is a remarkably good fit to the Hall-Petch relationship for strength.

References

[1] B. Prandi et al., "The ß-CEZ: a high performance titanium alloy for aerospace engines", Proc. 1990 TDA Int. Conf., TDA Ed. Dayton, OH, (1990) 150-159.
[2] B. Champin et al., " The ß-CEZ, a new high performance titanium alloy for aerospace engines", Proc. 1990 AAAF Meeting, (1991) .
[3] K. Takahashi, A. Ogawa and K. Minakawa, "Microstructures and mechanical properties of high strength beta-rich alpha+beta titanium alloy: SP-700", Proc. 1990 TDA Int. Conf., TDA Ed. Dayton, OH, (1990) 755-769.
[4] C. Ouchi, "High performance new a+ß type titanium alloy and new surface hardening process developed in NKK", Titanium to Zirconium, vol. 39, (1991) 134-137.
[5] J.S. Grauman, "821S: A new high strength, corrosion resistant titanium alloy", Proc. 1990 TDA Int. Conf., TDA Ed. Dayton, OH, (1990) 290-299.
[6] B. Prandi et al., "ß-CEZ, a high performance titanium alloy for aerospace engines", Proc. 6th World Conf. on Titanium, Lacombe et al. Eds., Ed. Phys. Les Ulis, (1989) 811-816.
[7] G. Dumas et al., "Quantification des microstructures de l'alliage de titane ß-CEZ" Proc. GS Ti, Pennelle Ed., to be published.
[8] G. Dumas, Ecole des Mines Training Period Report, (1991).
[10] S. Hanada and O. Izumi, Metall. Trans., vol 11A, (1980) 1447-1452.
[11] S. Hanada, T. Yoshio and O. Izumi, J. Mater. Sci., vol 21, (1986) 866-870.
[12] S. Hanada and O. Izumi, J. Mater. Sci., vol 21, (1986) 4131-4139.
[13] J.A. Roberson et al., Metall. Trans., vol 5, (1974) 2317-2322.
[14] R.H. Van Stone, J.R. Low and J.L. Shannon, Metall. Trans., vol. 9A, (1978) 539-552.
[15] Y. Combres et al., to be published
[16] A. Henry and A. Vassel, incl. in these proceedings.
[17] E. Breslauer and A. Rosen, J. Mater. Sci. And Technol., vol 7, (1991) 441-446.

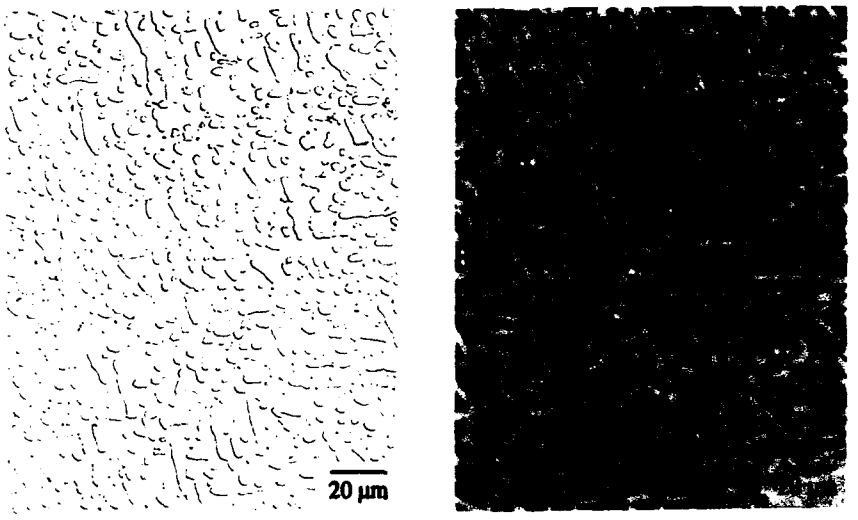


Figure 1: Typical microstructures of equiaxed ß-CEZ alloy: (a) as ST at 830 °C, (b) after ST (at 830 °C) +A (at 600 °C).

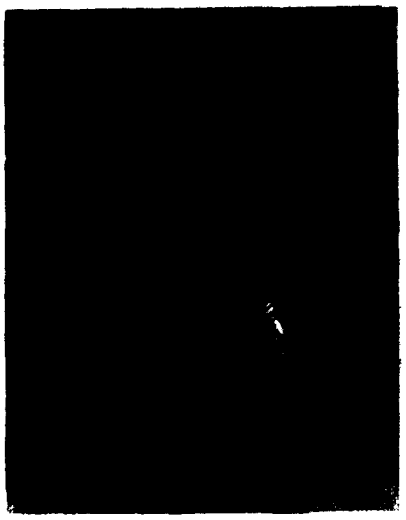


Figure 2: Polarized light in optical microscopy for the 100 % ß metastable sample, i.e. ST'ed at 910 °C.

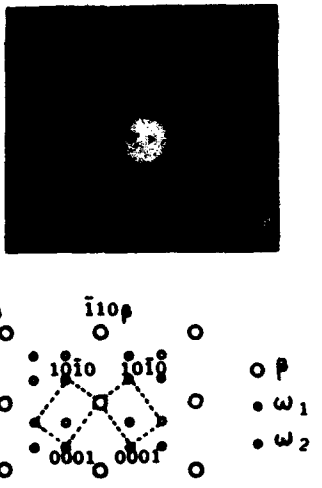


Figure 3: Selected Area Diffraction Pattern showing ω traces; ST at 860 °C, zone axis B = [110].

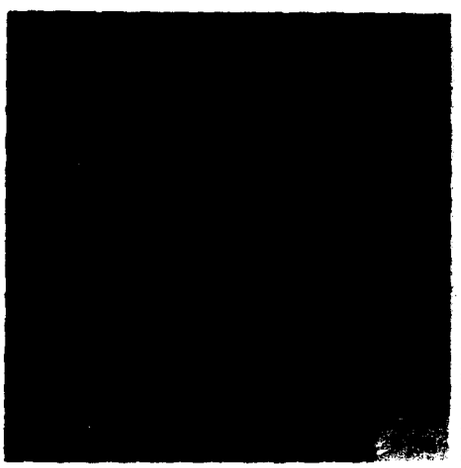


Figure 4: Elongated dimple in the fractography for the sample ST'ed at 860 °C.

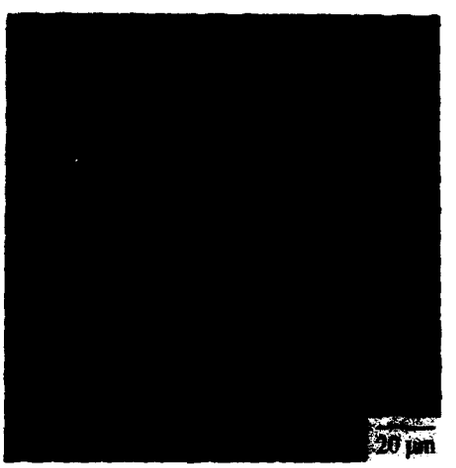


Figure 5: Crack propagation in the sample ST'ed at 830 °C.



Figure 6: TEM bright field of the specimen ST'ed at 860 °C and aged at 650 °C; αI exhibiting intense shear bands and steps at the boundary.

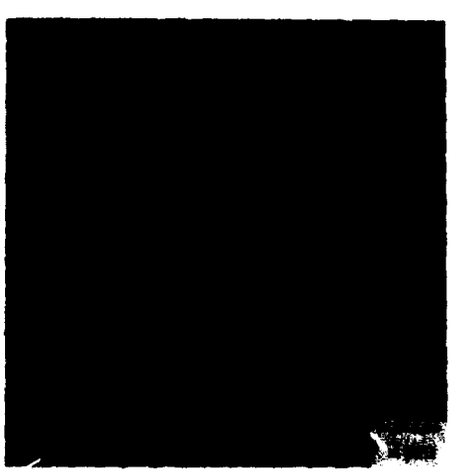


Figure 7: Damage occurring at the αI interface in a specimen ST'ed at 860 °C and aged at 550 °C.

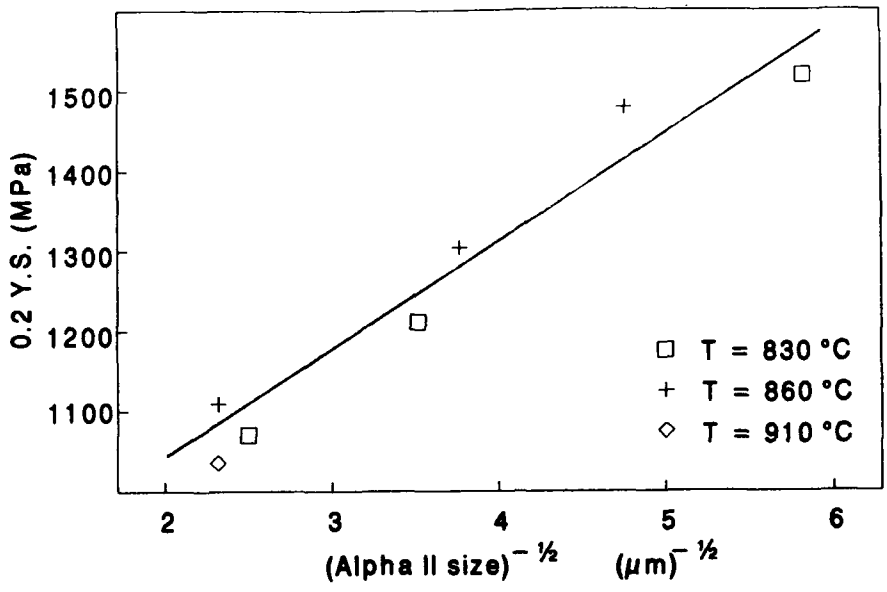


Figure 8: After ST+A; Hall-Petch relationhip 0.2% YS vs. the inverse square root of the αII size.

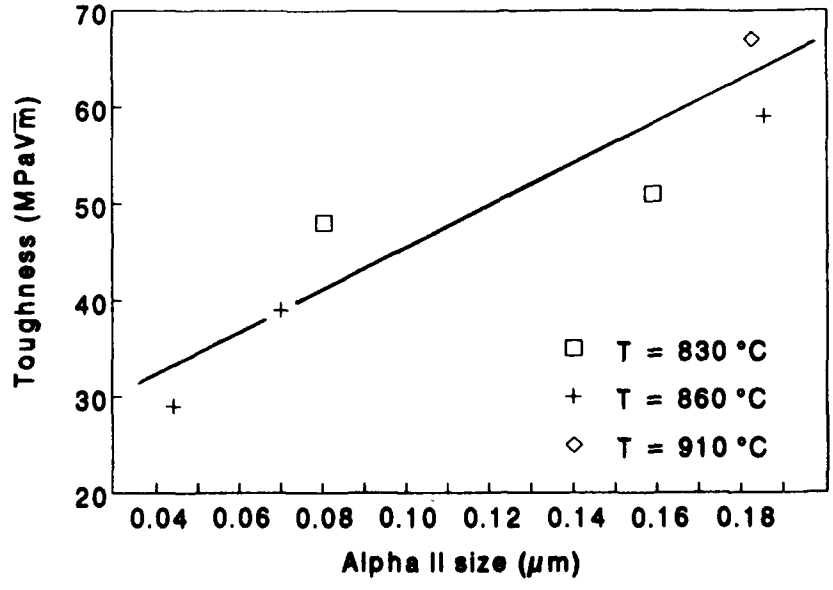


Figure 9: Toughness variations for ST+A samples, as a function of αII size.

FATIGUE AND FRACTURE TOUGHNESS PROPERTIES OF Ti-6Aℓ-4V WITH ACICULAR ALPHA MICROSTRUCTURES

* ** * *

T. Matsumoto, T. Nishimura, S. Muranaka, and S. Ishigai

*Engineering Department, Steel Casting & Forging Plant,
Takasago, Kobe Steel, Std.
Arai-cho, Takasago 676, Japan.

**Iron & Steel Research Labs., Kobe Steel, Ltd.
Kanazawa-cho, Kakogawa 675-01, Japan.

Abstract

High cycle fatigue and fracture toughness properties of large size Ti-6Al-4V forgings with acicular α microstructures were studied. According to forging and heat-treatment conditions, acicular α microstructures showed higher fatigue strengths than equiaxed α microstructures. The thinner the thickness of an α phase in the β grain boundary, or the finer the acicular α microstructures became, both the fatigue strength and fracture toughness were improved.

Introduction

Most of the titanium alloys including Ti-6Aℓ-4V tested here are used with equiaxed α microstructures. In the case of a relatively small product, the α grain can be worked into a fine granular equiaxed α grain, since finish hot forging in the $\alpha+\beta$ phase under β transus is sufficiently applicable. By making an α grain fine and equiaxed, it becomes possible to improve fatigue strength and ductility of an alloy. However, especially in the manufacture of large sized products, the percentage of the finish hot working under β transus is not sufficiently high owing to the dimensional limitations in ingots, which imposes not only restrictions on the extent of obtainable fine and equiaxed α microstructure but also brings a fall in fatigue strength. For this reason, in the manufacture of such large sized products, there have been some cases of practical use of acicular α microstructure instead of obtaining an elongated α grain in virtue of the finding that high cycle fatigue strength of acicular α microstructure is better than that of the elongated α garain [1].

But it does not seem to be widely acknowledged yet which morphologies of acicular α microstructures have superior fatigue strength, in particular, to equiaxed α microstructures.

Here in this paper, results of a experiment carried out on Ti-6Aℓ-4V with acicular α microstructures under a variety of forging and heat treatment conditions and of a study as to the relationship between high cycle fatigue, fracture toughness and microstructural characteristics, are reported.

Titanium '92
Science and Technology
Edited by F.H. Froes and I. Caplan
The Minerals, Metals & Materials Society, 1993

Experimental

Table I describes the chemical compositions of the Ti-6Aℓ-4V tested, and Table II indicates forging / heat treatment conditions after the fabrication of a billet. A billet of a 180 mm diameter, subjected to 20% forging ratio after β heat treatment, was used. The billets cut were subjected into a partial compression upsetting process in their longitudinal direction so that they were worked into panacake-like test pieces having a 125 mm thickness with predetermined forging ratios. The pancakes with a 125 mm thickness and a 200 mm diameter after machined were heat treated. However, in the cases of test pieces Nos. 12 and 13 of Table II, they were subjected to heat treatments after having been machined, following the upset forge, into rings having a 160 mm outer diameter, a 30 mm thickness, and a 125 mm height.

Table I Chemical compositions tested. (wt %)

Aℓ	V	Fe	C	N	O	H
6.16	4.25	0.200	0.008	0.0039	0.168	0.0036*

* The hydrogen content is in the case of No. 9.

Table II Forging and heat treatment conditions.

*1 No.	βHT *2 (℃)	$\alpha+\beta$ *3 Up-Set (%)	β *4 Up-Set (%)	HT *5
1	——	70	——	$\alpha+\beta$ STOA
2	——	20	——	$\alpha+\beta$ STOA
3	——	〃	——	β STOA
4	——	——	20	β STOA
5	——	——	〃	OA
6	——	——	50	β STOA
7	——	——	〃	OA
8	——	——	50	β STOA
9	1180	30	50	β STOA
10	〃	〃	〃	OA
11	1180	——	50	OA
12	——	20	——	β STOA
13	——	〃	——	OA
14	——	〃	——	β STOA

Round billets used in this study are finish-forged to 180mm diameter bars at the reduction rate of 20% at 960℃ after β quench treatment, 1050 ℃, 2hr, WQ.

*1 Test piece size when heat treated ——— 125mm thick × 200mm dia except Nos. 12 and 13 where rings with outer-diameter 160mm, thickness 30mm, and height 125mm are cut out after up-set forged.

*2 β heat treatment ——— 1180℃, 2hr, AC, (β transus temp =988℃)

*3 $\alpha+\beta$ up-set forge ——— 960℃

*4 β up-set forge ——— 1040℃ except No.8 conducted at 1150℃

*5 β STOA ——— 1040℃, 2hr, WQ + 705℃, 2hr, AC except No.14 where keeping time at 1040℃ is 1/2hr.

*5 $\alpha+\beta$ STOA ——— 955℃, 2hr, WQ + 705℃, 2hr, AC

*5 OA ——— 705℃, 2hr, AC

Test pieces for tensile and fatigue testing were cut out at a 1/2 radius and in the longitudinal direction in the case of the pancakes, and at a mid-thickness and in the direction of the height in the case of the rings. Thus, the tensile and fatigue test pieces were machined with a 6.25 mm and 8.0 mm diameter, respectively, at their parallel portion. The latter test pieces were polished up longitudinally with Emery Paper # 1200. Fracture toughness and fatigue crack growth test pieces: ASTM type CT specimens having a 25.4 mm and 12.7 mm thickness respectively, were machined so that cracking might be on the plane of a 1/2 thickness of a pancake and propagate to its radial direction.
The summary of forging / heat treatment conditions shown in Table II is as follows: As comparative material, provision was made for Nos: 1 and 2 test pieces forged in the $\alpha+\beta$ field with varied percentages of finish hot working, followed by a solution heat treatment in the $\alpha+\beta$ field and annealing (STOA) or just an annealing process. Nos, 3 to 7 are test pieces which were given finish hot working under or over β transus with a variety of working ratios, and then a solution heat treatment at 1040 ℃ over β transus followed by annealing (β STOA) or only annealing as indicated in the Table. No. 8 is a test piece subjected to β STOA after forged at a higher temperature of 1150℃ in the β field. Nos. 9 to 11 are cases when the billet of 180 mm in diameter were, before final forge, heated up at 1180 ℃ in the β field followed by air cool in order to make their microstructures coarse. / Nos. 12 and 13 were from the above-mentioned rings. No. 12 was sujected to the same condition of the finish forging and heat treatment as No. 3, but cooled at higher rate after holding the solution temperature than No. 3. No. 13 was just annealed. In the case of No. 14, its solution holding time was shortened from 2 hours for No. 3 to a 1/2 hou
The purpose of a series of the tests carried out under many kinds of forging and heat treatment conditions as above mentioned is to search for a guide line to manufacturing conditions for improving high cycle fatigue and fracture toughness properties.

Results and discussion

Fig. 1 shows some examples of microstructures obtained after final heat treatments.
As for the equiaxed microstructures of Nos. 1 and 2, it could be expected that No. 1 with he higher finish forging ratio would have a finer α garain than No. 2. The fact, however, was that there was no big difference in the α grain size between them. This can be attributed to heating times difference: twice for No. 1 and once for No. 2. Speaking of the equiaxed α microstructures of Nos. 2 and 13, the former STOA'ed revealed somewhat a finer α grain than the latter just annealed. In the case of acicular α microstructures, it has become clear that, with respect to the degree of fineass of a acicular α phase in a β grain and that of thickness of a α phase in a β grain boundary, those materials such as Nos. 12, 13, and 14 which were subjected to finish hot working in the $\alpha+\beta$ field and then to a β STOA process showed the finest and thinnest α Phase in a β grain and in a β grain boundary, respectively. Furthermore, in the case of acicular microstructures, there was a trend that the thinner the α phase along a β grain boundary became, the finer the acicular α in a β grain. Among them, the test piece which showed the most refined microstructure in the above-

mentioned sense was the β STOA'ed ring-shape material No.12. Materials Nos.3 and 4, which were assigned 2 hours and a 1/2 hour of a solution holding time, respectively, did not show any remarkable difference in their microstructures. Materials which showed the second finest microstructures were Nos.4 and 8, made of a billet subjected to water-cooled β treatment and to forging in the β field and then to β STOA heat treatment, followed by Nos.9 and 6 subjected to additional air-cooled β treatment to a billet and to forging in the β field and finally to β STOA heat treatment. Test pieces which revealed the coarsest microstructures were a group of Nos.5, 7, 10, and 11, made of materials subjected to final forging in the β field and to an annealing process; Among them, Nos.10 and 11 subjected to additional air-cooled β treatment showed the coarsest microstructures. Furthermore, the β STOA'ed materials showed clearly observable β grain boundaries, while the just annealed materials revealed imperfectly recrystallized microstructures featuring discontinuous α phases along β grain boundaries. As for the relationships between forging / heat treatment conditions and microstructures, further detailed experiments and their analyses are needed.

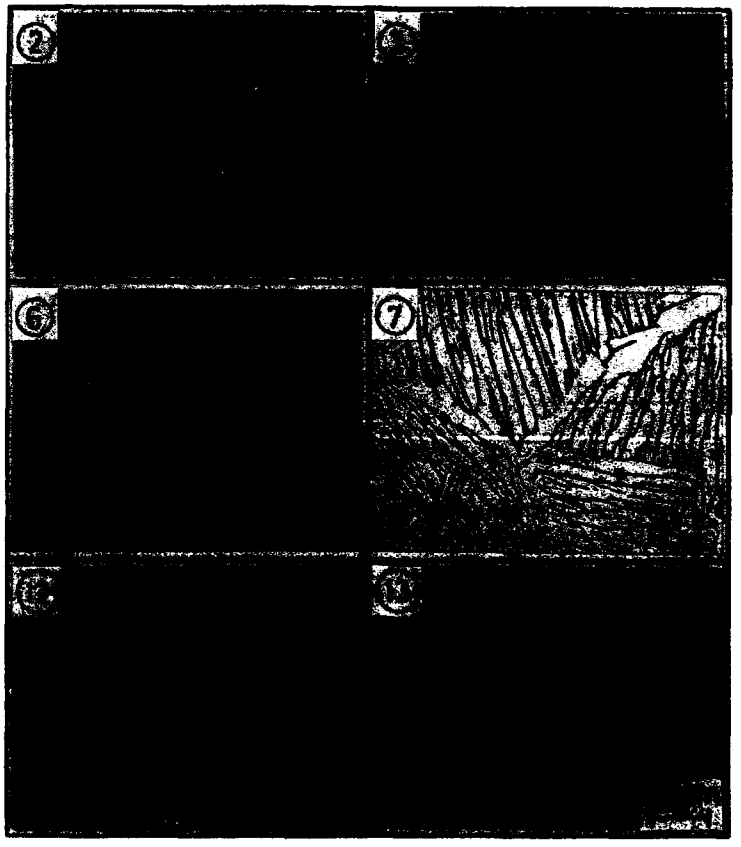


Fig. 1 Some examples of microstructures obtained.

The whole tensile test results at room temperature are shown in Table Ⅲ. Equiaxed α and fine acicular α microstructures showed somewhat higher strength than coarse acicular α microstructures. As for ductility, equiaxed α microstructures showed higher values. In the case of the acicular α microstructures, the finer the microstructures were, the better the ductilities became. Among the acicular α microstructures No. 12, of which cooling rate after holding solution temperature was higher, and No. 14 subjected to the shortened solution holding time, demonstrated higher ductilities for their high strength values. It was ascertained that even though it was an acicular α microstructure, the ductility could vary remarkably according to its microstructural fineness.

Table Ⅲ Tensile properties at RT.

No.	1	2	3	4	5	6	7	8	9	10	11	12	13	14
0.2YS(Mpa)	850	851	885	867	834	842	782	841	836	786	780	936	912	866
TS (Mpa)	997	939	973	957	916	940	902	935	924	897	901	1030	1011	964
El (%)	13	8	7	6	7	9	10	7	7	9	8	8	9	9
RA (%)	28	22	12	13	20	19	22	14	18	18	19	11	18	13

Table Ⅳ shows the summary of fatigue strengths at 10^7 cycles on all of the cases tested. The test results confirmed that even though it was an acicular α microstructure, its fatigue strength could be superior, according to the manufacturing conditions, to that of an equiaxed α microstructure. The material No. 12, which was finish forged in the $\alpha+\beta$ field and then β STOA'ed, of which cooling rate after holding at the solution temperature was higher, showed the best fatigue strength. Also, the fine acicular α materials subjected to a β STOA process such as Nos. 3, 4, 14, etc. showed higher fatigue strengths than thoes of the equiaxed α materials. However, those test pieces which were finish forged in the β field and then just annealed showed generally deteriorated fatigue strengths. A series of relationships between the fatigue strengths and other mechanical / metallurgical properties such as the tensile strengths, the reduction of area, β grain sizes obtainable when fully recrystallized, and α phase thicknesses along a β grain boundary, were plotted so as to study the extent of their correlativity to the fatigue strengths. A relatively good correlation was obtained from the relation with respect to the α phase thickness of a β grain boundary and to the tensile strength as well. Fig. 2 shows the relationship of the fatigue strength to the α phase thickness along a β grain boundary, plotted in the order of the thickness. Considering from the fact, in the case of acicular microstructures, that the fine acicular α microstructure of β STOA'ed material had a trend of having both higher tensile and fatigue strength, while the coarse acicular α microstructure tended to have a lower value of them, the considerably close correlation of the fatigue strength to the tensile strength may safely be affirmed to be another way of view of Fig. 2, showing the good correlativity of the fatigue strength to the α phase thickness.

Table Ⅳ Summary of fatigue strengths at 10^7 cycles.

(MPa)

No.	1	2	3	4	5	6	7	8	9	10	11	12	13	14
	470	480	520	540	480	500	430	430	480	410	490	580	490	510

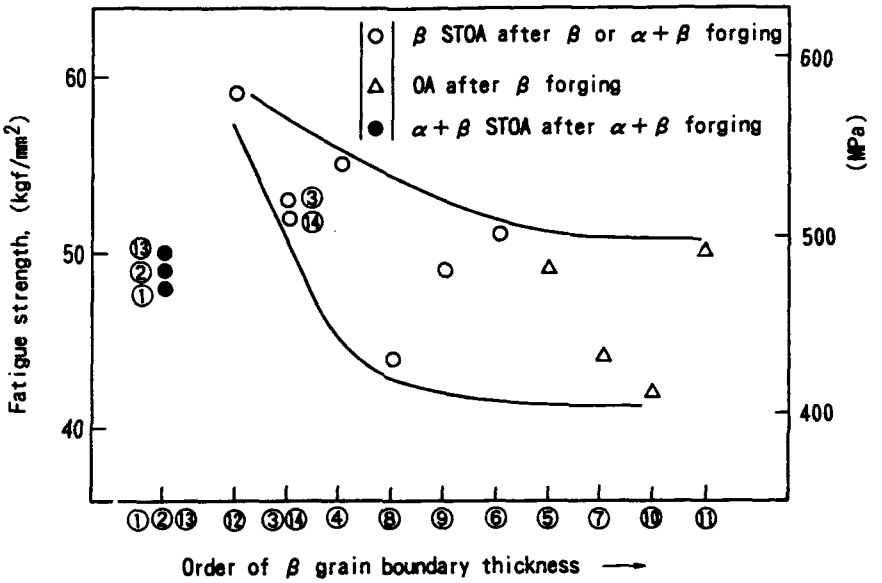


Fig. 2 Graph of fatigue strengths against β grain boundary α phase thickness.

Here, an additional fatigue test for a Ti-6Aℓ-4V small diameter bar of 20mm, which was sufficiently hot rolled from 130mm to 20mm in diameter in the $\alpha+\beta$ field after β treatment, was conducted. One group of the bar was STOA'ed in the $\alpha+\beta$ field, and the other group was β STOA'ed. Fatigue strengths at 10^7 cycles were 600 and 630 MPa, respectively as shown in Fig.3. It has become clear that the fatigue strength of the acicular α microstructure was excellent, even in the case of a small product like the bar.

Also, a series of fatigue crack growth tests were concordant for some pancake-like materials in Table Ⅱ, obtaining a result concordant with the commonly known information, that is to say, acicular α materials is superior to equiaxed α materials in the fatigue crack propagation characteristics.

Table Ⅴ shows the summary of fracture toughness test results. Values of the fracture toughness were also relatively well arranged using the same parameter as used for the aforementioned fatigue test results. The well known result is obtained that the fracture toughness of an acicular α microstructure is better

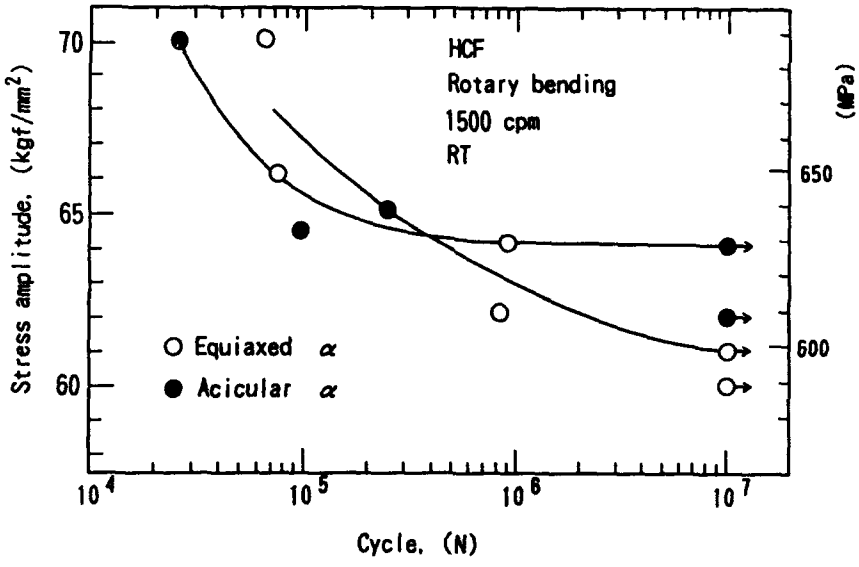


Fig. 3 Graph of fatigue test results on small diameter bars.

than that of an equiaxed α microstructure. From Fig.4, it can be seen that the perfectly and imperfectly recrystallized materials are considerably well arranged under a respective band, of which result will contribute positively to further understanding of fracture toughness dependency on microstructures. As for the former microstructures, the thinner the thikness of the α phase becomes, the more the fracture toughness is improved.
This indicates there is a microstructure which simultaneously gives superior fatigue strength and fracture toughness, of which fact is considered significant from the viewpoint of practical application of the results obtained here.

Table V Summary of fracture toughness values

														(MPa$\sqrt{m}$)
No.	1	2	3	4	5	6	7	8	9	10	11	12	13	14
	*1 75.6	*1 80.9	94.2	91.7	98.9	86.8	89.6	89.2	*1 83.4	85.2	93.6	—	—	102.0

Each mark *1 is valid K_{Ic}, and the others are invalid.

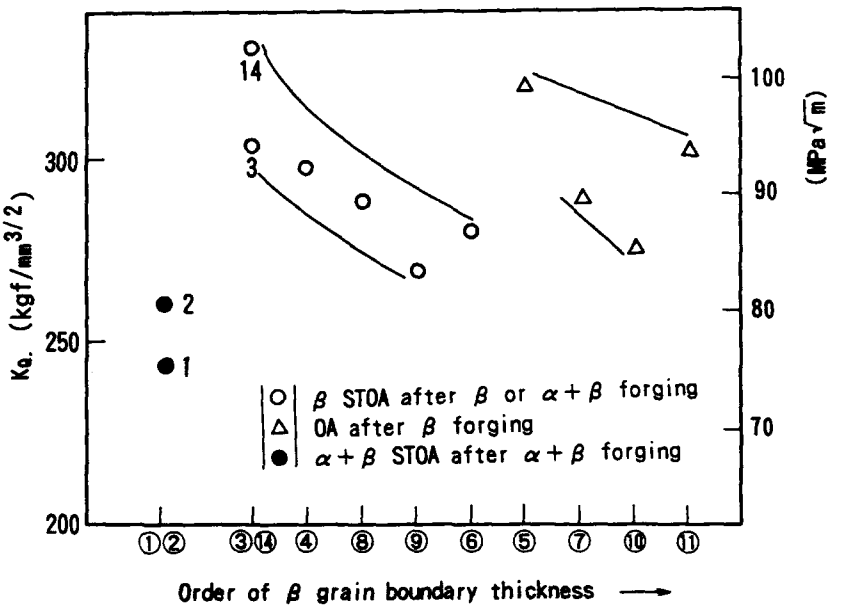


Fig. 4 Graph of fracture toughness values against β grain boundary α phase thickness.

Summary

1. When a forging and heat trreatment condition is selected appropriately, an acicular α microstructure can simultaneously afford a superior high cycle fatigue strength and fracture toughness value.

2. A high cycle fatigue strength and fracture toughness value of acicular α microstrucrtures can be improved by a single microsturctural parameter, thinning of α phase along a β grain boundary or refining microstructure within the grain.

References

[1] J. J. Lucas : Titanium Science and Technology, 1973, pp. 2081-2095.

The Effect of Thermal Treatment on the Cryogenic Mechanical Properties of Cast 5Al-2.5Sn ELI Titanium

Daniel P. Dennies
Materials and Processes Dept.
Aerojet Propulsion Division
Sacramento, California

Jeffery C. Gibeling
Dept. of Mechanical, Aeronautical and Materials Engineering
University of California
Davis, California

PRA-SA-APD 17 June 1992

ABSTRACT

The objective of this study was to determine the effect of thermal treatment on cryogenic mechanical properties for the cast form of 5Al-2.5Sn ELI titanium. The study consisted of a two by three thermal treatment matrix in which the hot isostatic press (HIP) and anneal temperatures were varied. The samples of the matrix were then subjected to tests at room temperature, 172 K, 77 K (LN_2), and 4 K (LHe) cryogenic temperatures. The tests included smooth tensile tests and fracture toughness tests.

The results reveal that a 1227 K HIP process in combination with a 1116 K anneal cycle produces the optimum combination of ductility and fracture toughness. Further, the properties of the cast 5Al-2.5Sn ELI titanium alloy are comparable to the properties of the wrought alloy at all temperatures. The results demonstrate that cast 5Al-2.5Sn ELI titanium is an acceptable alternative material for cryogenic applications.

INTRODUCTION

The 5Al-2.5Sn titanium alloy is an all-alpha alloy with good weldability and elevated temperature strength. The extra low interstitial (ELI) grade of the 5Al-2.5Sn titanium alloy has demonstrated an excellent history as the material of choice for cryogenic applications where toughness and ductility are required.

5Al-2.5Sn ELI titanium is currently used almost exclusively in the wrought form, especially for rotating hardware. However, because of the reduced cost and manufacturing complexity associated with casting, the cast form of this alloy is of interest for fabrication of rocket engine cryogenic turbopump rotating hardware such as impellers.

Titanium '92
Science and Technology
Edited by F.H. Froes and I. Caplan
The Minerals, Metals & Materials Society, 1993

EXPERIMENTAL APPROACH

The experimental goal of the present program was to alter the microstructure of cast 5Al-2.5Sn ELI titanium for improved cryogenic mechanical properties, especially fracture toughness. Theoretically, the optimum microstructure for fracture toughness would be one which produced the most tortuous path for the crack. For titanium, this would be a microstructure consisting of large platelet colonies containing coarse platelets.

A thorough review of the literature revealed that no information on the effect of thermal treatment on the microstructure or properties of cast 5Al-2.5Sn ELI titanium was available. Therefore, the literature for wrought 5Al-2.5Sn ELI titanium, wrought and cast 6Al-4V ELI titanium, and other titanium alloys was reviewed to determine thermal treatments [1]. However, the information from 6Al-4V ELI titanium studies must be applied to 5Al-2.5Sn ELI titanium with caution because the former is a two-phase alloy, whereas the latter is a single phase alloy.

The thermal treatment of cast titanium alloys normally consists of a hot isostatic press (HIP) followed by a heat treatment. For cryogenic applications, the heat treatment is an anneal cycle designed to produce optimum cryogenic ductility.

The two HIP processes selected were:
(1) 1172 K / 103.5 MPa / 2 hours
(2) 1227 K / 103.5 MPa / 2 hours

These are the two most common HIP processes for titanium alloys. Both have demonstrated the capability to close internal defects in titanium castings. Both HIP processes were evaluated to determine the effect on the thermal history of the material.

The three anneal cycles selected were:
(1) 1116 K / 2 hours
(2) 1255 K / 2 hours
(3) 1339 K / 2 hours

The 1116 K cycle is a common anneal for 6Al-4V ELI titanium, which represents approximately 50-60% of the titanium market. All titanium heat treaters must have furnaces operating at this temperature. However, the normal anneal for wrought 5Al-2.5Sn ELI titanium, which represents less than 1% of the titanium market, is 1033 K. Therefore, the 1033 K anneal for the 5Al-2.5Sn ELI titanium represents an unusual anneal temperature for titanium alloys in general. The 1116 K anneal cycle was selected as a low cost approach for annealing the material by eliminating the cost and schedule problems of a special annealing cycle at 1033 K.

The 1255 K and 1339 K anneal cycles were selected to fall within 60 K below and above, respectively, the published beta transus temperature of 1283 K for the 5Al-2.5Sn ELI titanium alloy [2]. Annealing just below and above this temperature was expected to introduce some variation in the microstructure.

Previous work has shown that the cooling rate from the anneal cycle is also critical due to the effects of ordering in the alpha phase [3-6]. The cooling rate for the present program was dictated by the normal casting process and HIP process cycles of the casting vendor, which were both furnace cools to approximately 811 K followed by air or fan cooling. The cooling rate from the anneal cycles at the testing supplier was also selected to be an air cool.

TEST PROCEDURE

Test blanks were fabricated from one heat of material. The material chemistry requirement was AMS 4924 with the following exceptions:

Hydrogen	< 90 ppm	Iron	< 0.20 weight percent
Yttrium	< 100 ppm	Oxygen	< 0.010 weight percent

The iron and yttrium are beta phase stabilizers and were controlled to the noted levels to promote good cryogenic behavior by avoiding beta formation [7-9]. The hydrogen and oxygen contents were also controlled to provide increased ductility of the material [6, 7, 9]. A thermal analysis of the 5Al-2.5Sn ELI titanium material was performed and revealed the beta transus temperature to be 1286 K ± 10 K.

The test bar blanks were 1.91 cm in diameter by approximately 16.51 cm long and were cast in molds of 32-36 test bar blanks. This yielded test bar blanks that were 1.65 cm in diameter by 15.25 cm long after chem milling. The compact tension blanks were cast in plates 26 x 33 x 6.35 cm. These plates were processed and then sectioned into 7.62 x 7.62 x 5.08 cm blocks prior to the NDT examinations.

The intent of the testing was to generate smooth bar tensile data per ASTM E8 and fracture toughness data per ASTM 399 and 813 for cast 5Al-2.5Sn ELI titanium material in the different thermal conditions at four temperatures, from room temperature to LHe temperature (298 K, 172 K, 77 K, and 4 K). The samples used were 0.64 cm diameter and 2.54 x 7.62 x 7.62 cm, respectively.

RESULTS AND DISCUSSION

The results of the mechanical tests are presented in graphs to compare the yield strength, tensile strength, elongation, reduction in area, and fracture toughness (Figures 1-5). The tensile data reveal no influence of HIP temperature or anneal temperature on yield strength or tensile strength (Figures 1 & 2). The elongation data indicate little effect of the anneal cycles for the 1172 K HIP temperature, although there is a trend of decreasing ductility with increasing anneal temperature for the 1227 K HIP temperature (Figures 3 & 4). The reduction in area data are consistent for both HIP temperatures and the 1116 K and 1255 K anneal temperatures, but the data for the 1339 K anneal exhibit greater variability (Figures 3 & 4).

Valid fracture toughness testing of the cast titanium samples was difficult due to the combination of the cast form and the inherent toughness of the titanium material. As a consequence, the fracture toughness test data for the following samples failed some validity requirements of the ASTM testing specification and can only be reported as K_Q and not K_{IC}.

1227 K HIP / 1339 K anneal / 298 K test	$K_Q = 124$ MPa - $\sqrt{m}$
1227 K HIP / 1255 K anneal / 4 K test	$K_Q = 82$ MPa - $\sqrt{m}$
1172 K HIP / 1116 K anneal / 172 K test	$K_Q = 107$ MPa - $\sqrt{m}$

The valid data indicate that the 1227 K HIP temperature produces higher fracture toughness than the 1172 K HIP temperature at all test temperatures except 172 K (Figure 5). The graph also indicates that the material HIP'ed at 1227 K exhibits little effect of the annealing temperature at all test temperatures except 298 K, while the material HIP'ed at 1172 K shows varying effects of the anneal temperature at

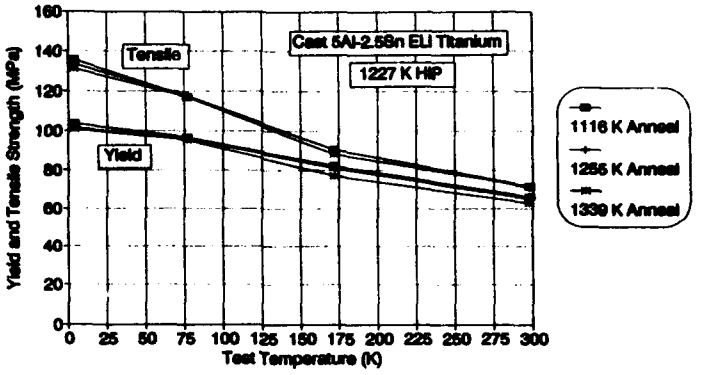


FIGURE 1: Yield And Tensile Strength vs. Temperature - 1227 K HIP

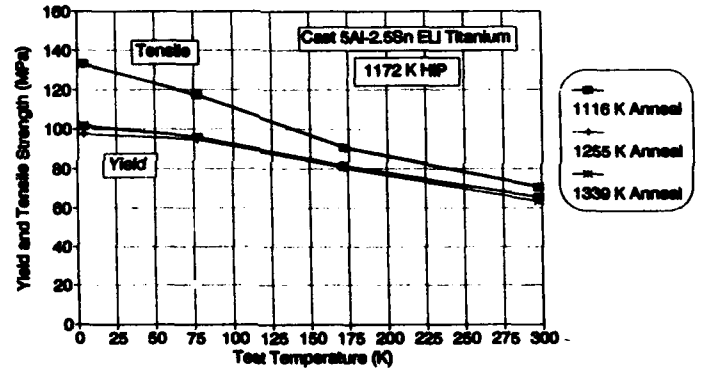


FIGURE 2: Yield And Tensile Strength vs. Temperature - 1172 K HIP

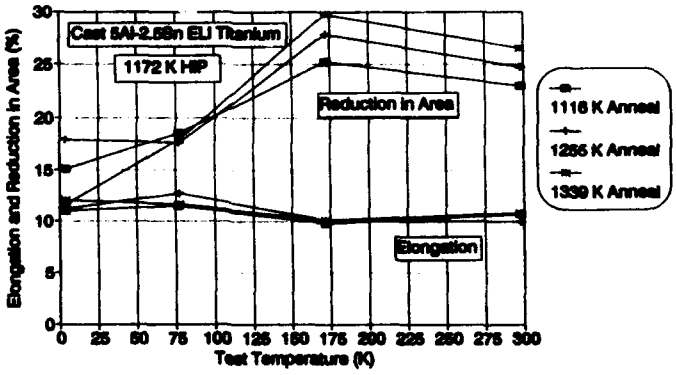


FIGURE 3: Elongation And Reduction In Area vs. Temperature - 1172 K HIP

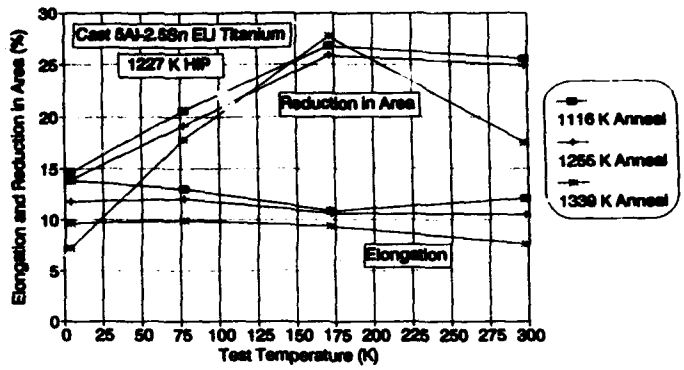


FIGURE 4: Elongation And Reduction In Area vs. Temperature - 1227 K HIP

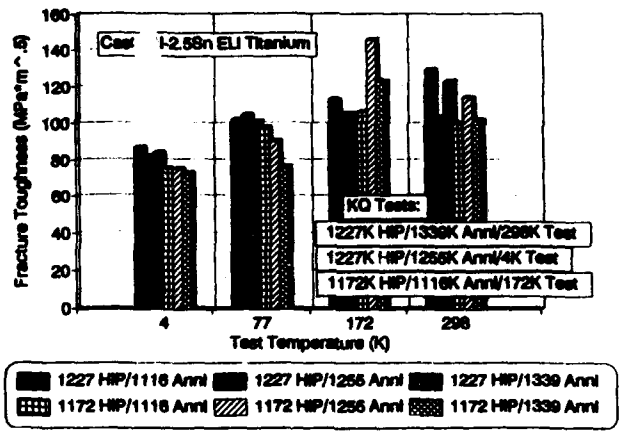


FIGURE 5: Fracture Toughness vs. Temperature

all test temperatures except 4 K. Finally, we note that two of the three data points with only K_Q values appear to fit in with the balance of the data and were, therefore, close to being actual K_{IC} values.

Based on the tensile and fracture toughness data, the optimum heat treatment for the cast form of 5Al-2.5Sn ELI titanium is a 1227 K HIP in combination with a 1116 K anneal cycle. Since the yield and tensile strengths are similar, the heat treatment selection is based on an optimum combination of fracture toughness, elongation, and reduction in area. The 1227 K HIP produces higher fracture toughness (except at 172 K) and less variation in properties with annealing temperatures than the 1172 K HIP. The 1116 K anneal temperature showed the highest fracture toughness, elongation, and reduction in area levels at all test temperatures when combined with the 1227 K HIP.

MATERIALS COMPARISON

The mechanical properties of the 1227 K HIP combined with the 1116 K anneal for the cast 5Al-2.5Sn ELI titanium were compared to the mechanical properties of the wrought form of 5Al-2.5Sn ELI titanium (Table I). The cast material demonstrates the same excellent cryogenic ductility and fracture toughness as the wrought material. The strength and fracture toughness are approximately 10% lower in the cast form, except for the 4 K yield strength , which is 25% lower. These same mechanical properties were also compared to the data for the wrought and cast forms of 6Al-4V ELI titanium (Table I). The cast 5Al-2.5Sn ELI titanium behavior, as a function of temperature, is virtually identical to wrought 5Al-2.5Sn ELI titanium. Both forms of 5Al-2.5Sn ELI titanium demonstrate lower strengths, higher ductility, and higher fracture toughness than either form of 6Al-4V ELI titanium, particularly at cryogenic temperatures.

TABLE I
Cast Titanium Properties Compared To Wrought Properties - Average Typical Data

		5Al-2.5Sn ELI (Cast)*		5Al-2.5Sn ELI [14] (Wrought)		6Al-4V ELI [11] (Cast)		6Al-4V ELI [12] (Wrought)	
		R.T.	LHe (4°K)	R.T.	LHe (4°K)	R.T.	LHe (4°K)	R.T.	LHe (4°K)
Smooth Tensile	F_{TU} (MPa)	717	1359	772	1483	883	1572	1000	1708
	F_{TY} (MPa)	662	1034	705	1405	807	1421	917	1708
	% El	12.1	13.8	14.6	10	9.7	6.4	11	1.5
	% RA	25.6	14.6	27.5	20	19.7	13.3	42	27
Fracture Toughness	K_{IC} (MPa$\sqrt{m}$)	130	88	149 K_Q	90	103	59	65	45

* 1227°K HIP + 1116°K Anneal

METALLOGRAPHY AND FRACTOGRAPHY

One tensile and one fracture toughness sample from each thermal treatment were selected for metallographic and fractographic examination. The metallographic examination was performed on longitudinal and transverse views and revealed large colonies of plate-like alpha phase. There is no discernable difference in the microstructure of the samples (Figure 6). This microstructure results from a nucleation and growth transformation mechanism during cooling from the casting and annealing processes, rather than a martensitic transformation. In addition, the microstructure appears to be controlled by the cooling rate from the anneal, but not by the anneal temperature. However, since the microstructure of 5Al-2.5Sn ELI titanium dictates the mechanical properties of the alloy, the property variations noted in the test results must be due to some microstructural variation not detected. A possible explanation could be the amount of ordering produced during the different anneal cycles [3-6].

Fractography was performed using scanning electron microscopy. Once again, there are no discernable differences between fracture surfaces of the samples subjected to the various HIP and annealing treatments. The fracture surfaces are all dominated by the cast structure and reveal ductile tear ridges on the crystallographic facets (Figure 7).

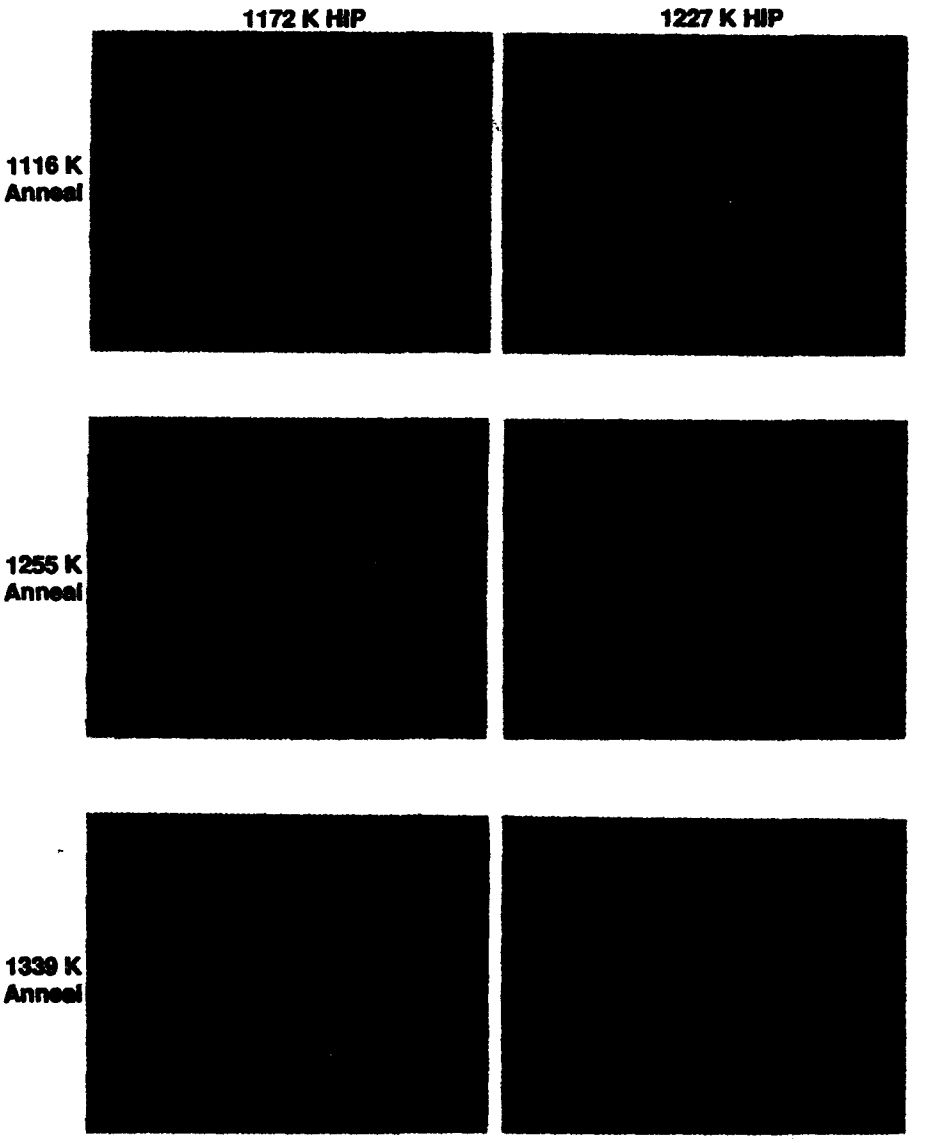


FIGURE 6:

Microstructure of Fracture Toughness Samples - 298 K Test/Mid Sample Position (50x)

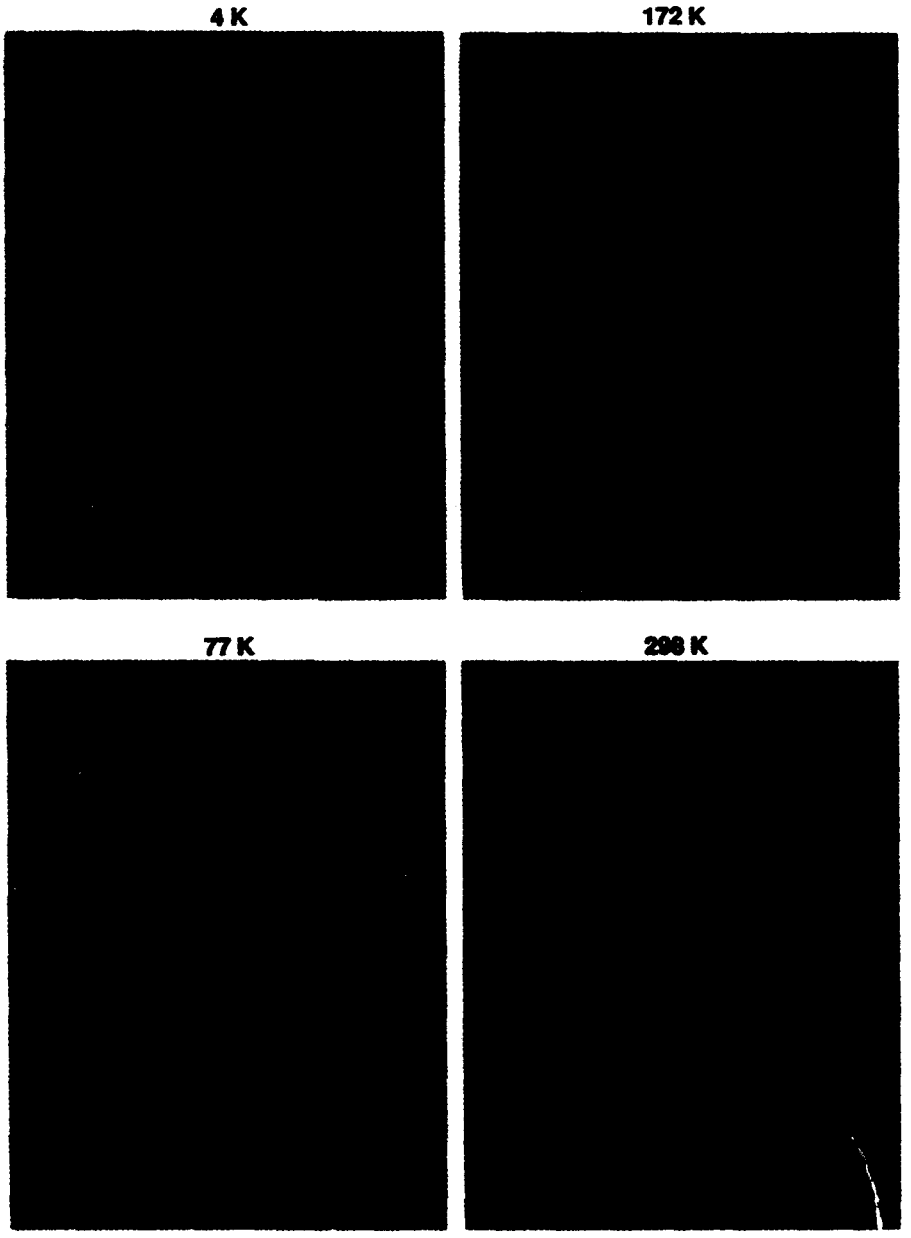


FIGURE 7:

Fracture Surface of 1227 K HIP/1116K Anneal Tensile Samples (100x)

CONCLUSIONS

1) For the cast form of 5Al-2.5 ELI titanium, a 1227 K HIP combined with the 1116 K anneal thermal treatment provides the best combination of tensile strength, fracture toughness, and ductility at all test temperatures.

2) The metallographic and fractographic examinations did not reveal any discernable differences in the microstructures created by the various thermal treatments.

3) The cast form of 5Al-2.5Sn ELI titanium has adequate mechanical properties for use as a potential substitute for wrought 5Al-2.5Sn ELI titanium and both forms of 6Al-4V ELI titanium in cryogenic applications.

REFERENCES

1. D.P. Dennies and J.C. Gibeling, "Cast 5Al-2.5Sn ELI Titanium Heat Treatment Study for Low Cost Cryogenic Turbopump Rotating Hardware", AIAA/SAE/ASME 27th Joint Propulsion Conference, AIAA Paper #91-1997, (24-26 June 1991)

2. "Quality Production and Services", Technical Bulletin,T/S-5000-9/89, (Timet, Toronto, Ohio, 1989)

3. R.H. Van Stone, J.R. Low, Jr., and J.L. Shannon, Jr., "The Effect of Microstructure on the Fracture Toughness of Titanium Alloys", NASA Technical Report #2-TI, NASA Research Grant NRG 39-087-047 (Dec. 1974)

4. R.H. Van Stone, J.R. Low, Jr., and J.L. Shannon, Jr., "Investigation of the Fracture Mechanism of Ti-5Al-2.5Sn at Cryogenic Temperatures", Metallurgical Transactions A, Vol. 9A (April 1978) pp. 539-552

5. T.K.G. Namboodhiri, C.J. McMahon, and H.Herman, "Decomposition of the Alpha-Phase in Titanium-Rich Ti-Al Alloys', Metallurgical Transactions, Vol. 4 (May 1973) pp. 1323-1331

6. Z. Liu and G. Welsch, "Effects of Oxygen and Heat Treatment on the Mechanical Properties of Alpha and Beta Titanium Alloys", Metallurgical Transactions A, Vol. 19A (March 1988) pp. 527-542

7. M.J. Donachie, Jr., editor, Titanium: A Technical Guide, (ASM International 1988)

8. E.F. Erbin, discussion on "Effects of Several Production and Fabrication Variables on Sharp Notch Properties of 5Al-2.5Sn Titanium Alloy Sheet at Liquid Hydrogen Temperature", Proc. ASTM, Vol. 62 (1963) pp 826-827

9. Aerospace Structural Metals Handbook, Code 3706 [Ti 5Al-2.5Sn], Code 3707 [Ti-6Al-4V], Code 3801 [Ti 6Al-4V Cast] (1965-1970)

10. K. Nagai, K. Ishikawa, T. Mizoguchi, and Y. Ito, "Strength and Fracture Toughness of Ti-5Al-2.5Sn ELI Alloy at Cryogenic Temperatures" Cryogenics, Vol. 26 (Jan. 1986) pp. 19-23

11. D.P. Dennies, Aerojet Propulsion Division, "Cast Titanium Heat Treatment Optimization and Alternate Material Evaluation", MA-91-128 (November 1991)

12. Y. Ito, T. Nishimura, K. Nagai, and K. Ishikawa, "Cryogenic Properties of Extra-Low Oxygen Ti-6Al-4V Alloy", Proc of the Sixth World Conference on Titanium (France 1988) pp. 87-92

Optimization of service properties for titanium forgings with bimodal microstructure

H.Puschnik [1], J.Fladischer [1]
G.Lütjering [2], R.I.Jaffee [3]

[1] Böhler Schmiedetechnik, Austria
[2] Technische Universität Hamburg-Harburg, Germany
[3] Electric Power Research Institute, USA

Abstract

In the present work the application of large last stage blades in Ti-6Al-4V for steam turbines is described. The increase in exhaust area permitted by titanium blades results either in an improvement in thermal efficiency or in a reduction in turbine capital cost due to the possibility of reducing the number of steam flows. The processing technology for bimodal and bimodal textured 40 inch blades is outlined and microstructure and properties are compared with those of conventional produced forgings. The bimodal structure is characterized by a reduced scatterband in the Young's modulus and improved LCF and HCF properties. With a sharper texture in the bimodal forging or by an optimization of the bimodal heat treatment another substantial enhancement of LCF and HCF properties can be achieved.

Introduction

Although titanium and titanium alloys are relatively expensive, they have established themselves during the last three decades as structural materials in the aircraft and aerospace industry because of their high specific strength but have also gained acceptance for terrestrial applications, particularly because of their excellent corrosion resistance in a great variety of aggressive media (1-3).

Fan and compressor blades in jet engines have been made from Ti-6Al-4V for years and the use of titanium alloy blades in the last two rows of stationary steam turbines replacing steel blades is continuously growing (3,4).

The better corrosion resistance of the titanium alloy compared to the hitherto commonly used 12%Cr- and precipitation hardening steels, especially in contaminated vapour phases, offers longer service life of the blades in the L-1 row and compensates thus for the considerably higher cost of titanium blades compared to those made of steel.

Titanium '92
Science and Technology
Edited by F.H. Froes and I. Caplan
The Minerals, Metals & Materials Society, 1993

The use of titanium for large last row blades offers besides the previously mentioned improved corrosion resistance a number of additional advantages, such as improved fatigue properties and a lower specific weight, which permits to use larger blades without increasing rotor loading (4).

The use of such large blades, namely with airfoils of 40 inches or more in length, allows to double the steam exhaust area and thus either to increase the thermal efficiency of the turbine or to reduce the number of rotor flows while maintaining the same efficiency. This allows a more compact and economical turbine design.

Manufacture of large last stage blades in Ti-6Al-4V

The experience of Böhler with forgings of this type dates back to the late seventies, when 48 inch blades were made for an European customer. Since then more than 1000 last stage blades for steam turbine application have been produced by Böhler in the form of precision or envelope forgings.

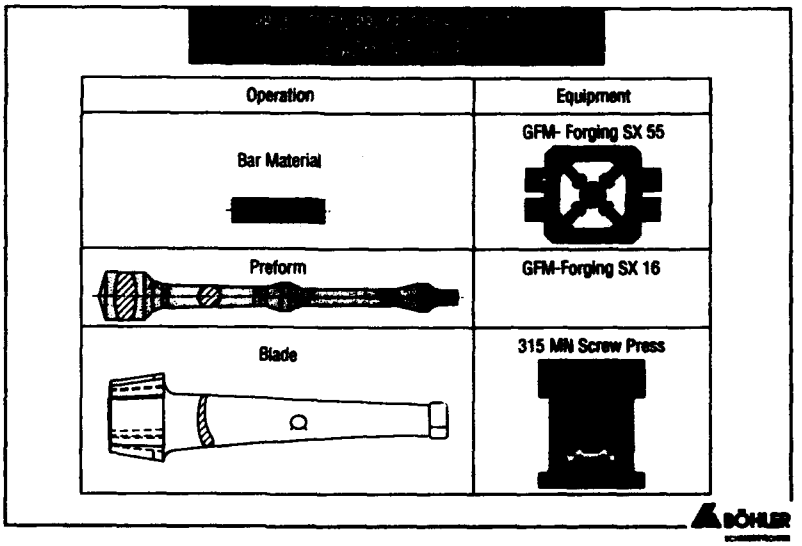


Figure 1

Fig.1 shows the manufacturing process in detail. Bars of defined dimensions are shaped into preforms on a four hammer GFM forging machine. The individual cross sections of the preform at that time corresponds in terms of volume to the relevant cross sections of the airfoil area of the finished blade. The second production step includes local upsetting of the root area in a hydraulic press. It is of course possible to use bars of larger starting diameter in order to eliminate this production step. However, beneath a better ultrasonic inspectability of the smaller bar, the additional deformation guarantees improved properties in the final product also in that area.

Die forging is performed on the world´s largest screw press having a maximum press force of 31.500 tons or 315 MN. The high deformation energy of this unit coupled with a relatively slow deformation speed permits to achieve tightest tolerances, even in case of complex blade geometries and blade lenthgs of up to 65 inches.
Several dies are used in order to keep the level of internal stresses as low as possible and to reduce the risk of distortion in case of complex geometrical configurations.
All relevant forging parameters are computer controlled and thus guarantees a fully reproducible forging process from blade to blade and from batch to batch.

Optimization of the microstructure - bimodal structure

Investigations made by EPRI, the Technical University of Hamburg-Harburg and Böhler revealed that an optimization of the mill-annealed $\alpha+\beta$-structure to a so called bimodal one has a significant influence on important service properties (5,6).
This includes the scatterband of the Young´s modulus, an important criterion for the design engineer, as well as the LCF and HCF behaviour which may considerably be improved by the optimized microstructure and has decisive influence on the service life, especially in the case of large last stage blades.

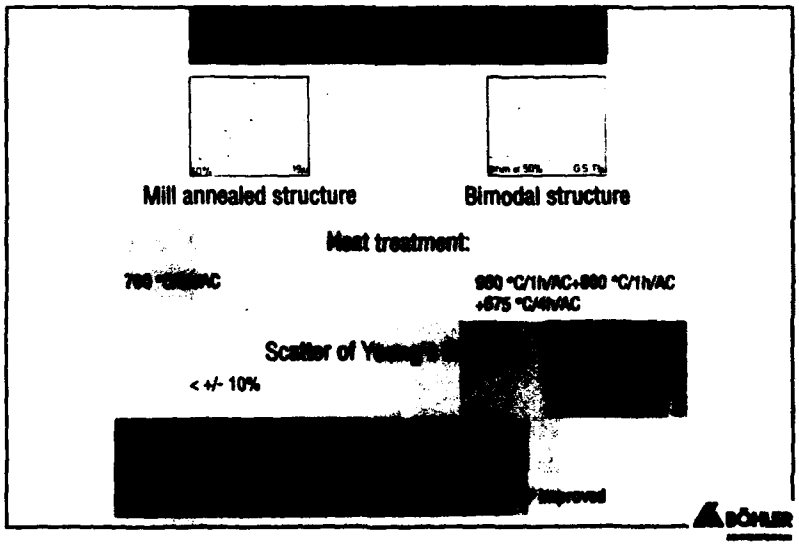


Figure 2

In Fig.2 the obtainable microstructure is compared to the conventional mill-annealed one. The photographs were taken from the root sections of 40 inch turbine blades. The improved, so called bimodal structure itself is characterized by a fine lamellar matrix surrounding globular primary α-grains of less than 15μm in size.
The production process includes rapid quenching from the β-range, followed by shaping operations below the transus temperature. A high amount of deformation is necessary to obtain a dislocation density in the material which is sufficiently high to

give a uniform finely recrystallized structure during subsequent heat treatment. All these operations were already described in detail in previous publications (6,7).

Investigations of the Young´s Modulus revealed that the scatterband of the different specimen locations (root, blade/root transition, airfoil) and directions (longitudinal, transverse and short transverse) are below 3% for the bimodal structure as compared to up to 10% for the mill annealed condition.
The decisive factors for this are on the one hand the elimination of the crystallographic texture by quenching from the β-range at the bar material stage and thus to achieve a defined starting structure and on the other hand the final bimodal heat treatment including annealing at a temperature of about 950°C leading to a homogeneous structure with a high degree of reproducibility.

While there are no differences in the results of the tensile test, the bimodal microstructure entails a considerable improvement of LCF and HCF properties.
With the Ti-6Al-4V alloy the fatigue properties are largely determined by the formation of cracks, which, in turn, depend on the resistance of the structure to the movement of dislocations. Therefore the finer bimodal structure with its reduced effective dislocation glide length as compared to the mill-annealed condition leads to improved fatigue behaviour.

Improvement of fatigue strength of bimodal structures

Laboratory tests conducted by Lütjering et al on bimodal specimens (5,7,8) revealed that fatigue cracks may occur either in the lamellar matrix or in the primary α-phase, depending on which structural constituent is the weaker one. The resistance of both, lamellar matrix and globular particles to cracking under fatigue load may be increased by special measures, which permits to achieve a further improvement of LCF and HCF properties. In the α+β-matrix this may be achieved by a finer lamellar thickness through a more rapid quenching operation in the final heat treatment, while the fatigue strength of the primary α-grains is mainly determined by grain size and crystallographic texture. Sharper textures as well as finer α-grains prove advantageous.

Influence of α-grain size

Tests on bimodal material with differently large primary α-grains (Fig.3) confirmed that the fatigue strength of the microstructure increases with the α-particles getting smaller and smaller, however only to a certain value which is in the range of 10 - 15μm. Even finer primary α-grains do not improve the fatigue properties considerably.
In commercial scale production a primary α-phase of this size can be achieved, a fact which has already been taken into account in the first specification requirements for bimodal forgings, which permit a grain size of up to 15μm.

Influence of texture

Because of the production technology of large blades, which means longitudinal deformation of the bar material and transverse deformation during the proper blade forging process in the die, the forged blades possess a weak texture with a 90°

symmetry corresponding to that of cross-rolled sheet. By introducing a strong longitudinal texture it was possible in laboratory rolling tests to increase especially HCF values as compared to the weakly textured material (5,7).

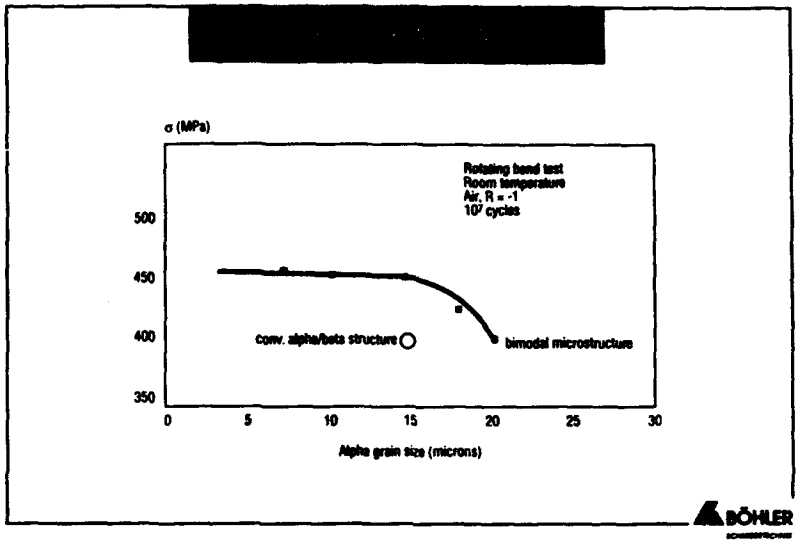


Figure 3

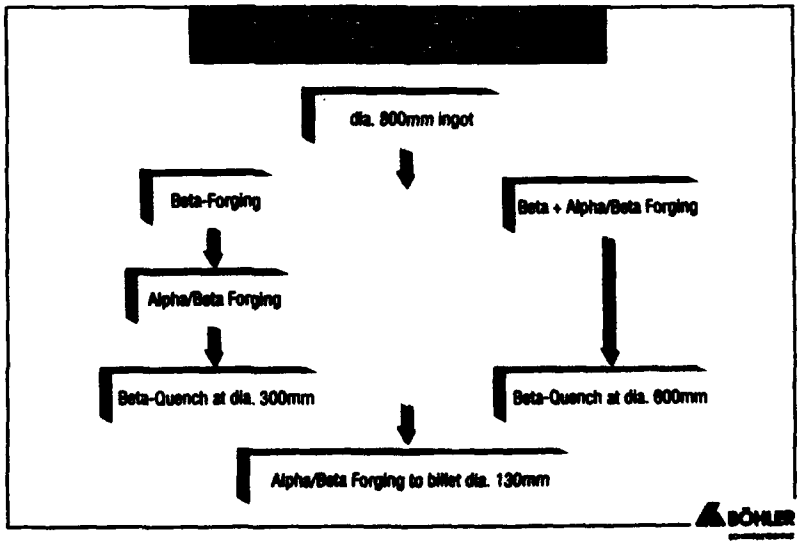


Figure 4

The difference is due to to the presence of basal slip planes in the weakly textured material, running under 45° to the load direction and facilitating an easier formation of fatigue cracks.

To obtain a stronger textured microstructure in the bimodal blade, β-quenching was already done at a bar diameter of 600mm (as compared to 300mm with the bimodal condition). The purpose of this was to achieve a pronounced longitudinal texture in the bar and finally in the finished blade due to a high degree of deformation in the $\alpha+\beta$-range in the direction of the longitudinal axis of the ingot (Fig.4).

After heat treatment, i.e. 960°C/1h/AC + 800°C/1h/AC + 675°C/4h/AC, the crystallographic texture was studied on specimens taken from the root and the blade/root transition area.
The 0002-pole figures are shown on the left hand side in Fig.5. The material from the transition area shows intensities of 2-3 in longitudinal and transverse directions with the viewing direction corresponding to the blade normal line. In the material taken from the root area the transverse directions showed no intensities greater than those in longitudinal direction.

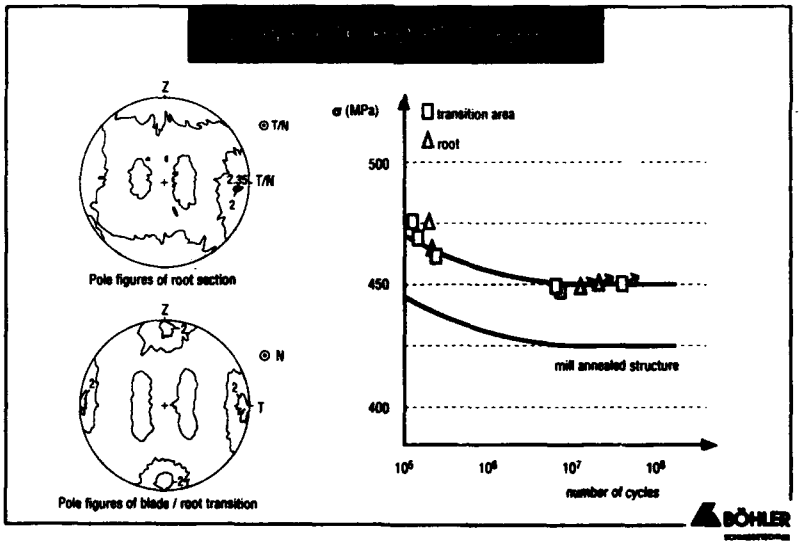


Figure 5

The corresponding results of the fatigue tests at room temperature are also shown in Fig.5.
The 10^7 fatigue strength for the bimodal textured material was 450 MPa in the root area and even somewhat lower for the transition area. The values obtained correspond practically to those of bimodal material without pronounced texture. For the purpose of comparison the relevant curve for mill-annealed material is also listed in that graph.

While the results for bimodal textured material are quite understandable in the root section with its usually weaker texture, the LCF and HCF values for the transition area were unexpected low. However, the structural investigations (see also Fig.6) revealed clearly the reasons for this.
The fact, that β-quenching was already performed on large bar dimensions only permitted to achieve primary α-grain sizes of around 20μm in the final product.
Based on the previously mentioned results of rotating bar fatigue tests with particle sizes of 20μm, a 10^7 fatigue strength of 400 MPa would have to be expected. The positive influence of the texture on the fatigue strength however compensates for the disadvantage of the larger hexagonal α particles and gives results which correspond in the bimodal material to a particle size of 10 - 15μm without pronounced texture.

For large bimodal forgings this means however that even with a longitudinal texture no improvement of the fatigue strength as compared to the bimodal condition can be achieved. This effect can only be utilized for forgings which permit the use of smaller bar diameters (< 100mm), where β-quenching can be performed on smaller bar dimensions so that an average α-grain size of below 15μm can be realized and nevertheless sufficient deformation is achieved in the direction of the longitudinal axis of the ingot to produce a strong texture.

Influence of heat treatment on fatigue and mechanical properties

The fatigue strength of the lamellar α+β-phase is mainly determined by the lamellae thicknesss, which itself may be adjusted by specific annealing and cooling operations. Therefore the bimodal heat treatment with air or water cooling, i.e. 960°C/1h/AC or WQ + 800°C/1h/AC + 675°C/4h/AC, was compared with a two step heat treatment, including annealing at 960°C/1h/WQ and ageing at 550°C/24H/AC.

The specimens were taken from the blade area of the previously mentioned 40" blade with a bimodal textured microstructure. Significant differences between the three conditions in term of fineness of lamellar constituents can be seen even in the light-optical microscope at a small magnification (Fig.6). The results of the electron-microscopical investigation are shown below.

The lamella width is about 1,5μm for the air-cooled condition and about 0,8μm for the comparable water quenched condition. The condition achieved after water quenching and direct ageing at a temperature of 550°C presents however a maximum lamella width of 0,3μm only. It can be clearly seen that there is a transformed martensitic structure. The heavy coarsening of the water quenched structure because of the heat treatment step at 800°C with the three step heat treatments is a big surprise and therefore the necessity of this second step should be rethought.

The LCF and HCF values determined in the rotating bar fatigue test (Fig.7) show the influence of the lamella configuration on the fatigue strength. By water quenching an increase of about 5% can be achieved, with water quenching and direct ageing (to avoid growth of lamellar constituents during annealing at 800°C) 10^7 fatigue strength of more than 500 MPa is achievable.

But it should also be mentioned that in case of long blades rapid quenching causes problems regarding distortion which can only be eliminated by additional and costly measures during the manufacturing process.

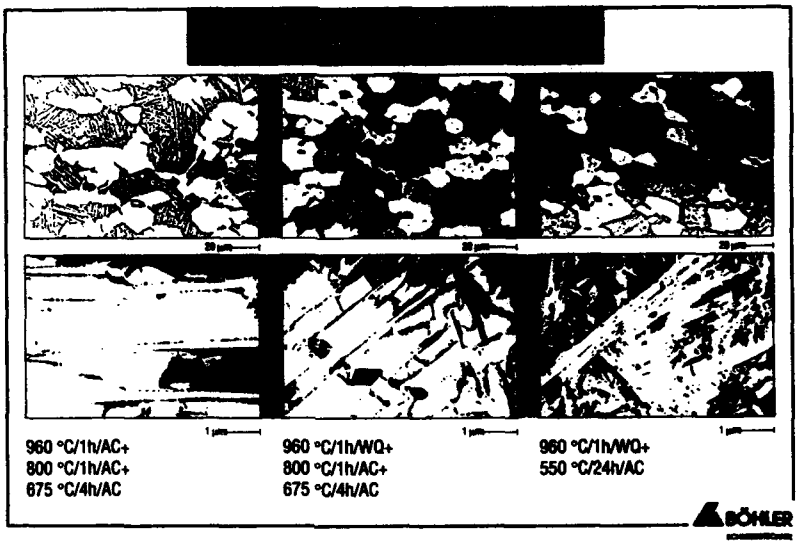


Figure 6

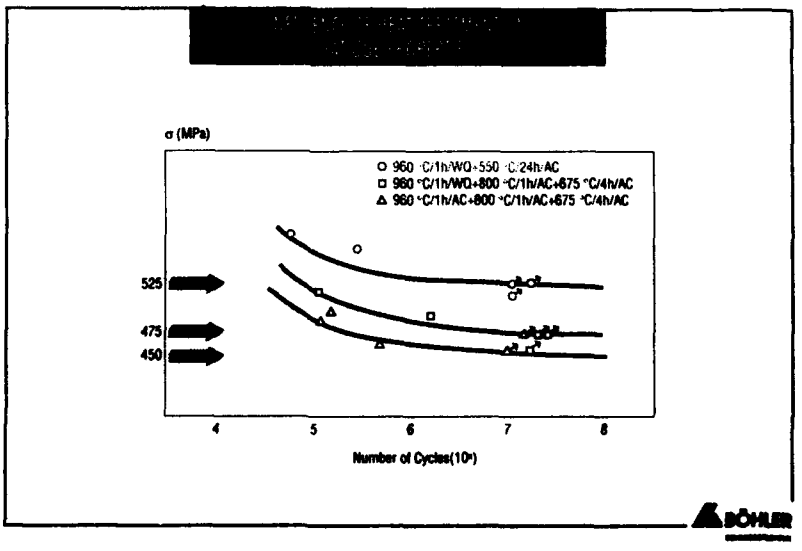


Figure 7

The mechanical properties (average values of specimens of root, blade/root transition and airfoil area) at room temperature (Fig.8) are hardly affected by the different cooling rates of the three step heat treatments. While mechanical strength and

toughness properties remain unchanged in the tensile test, the values of the water quenched specimens are slightly falling in the Charpy-V-impact test.
Direct ageing generally leads to an increase of mechanical strength coupled with a decrease of toughness in both tensile and impact testing.

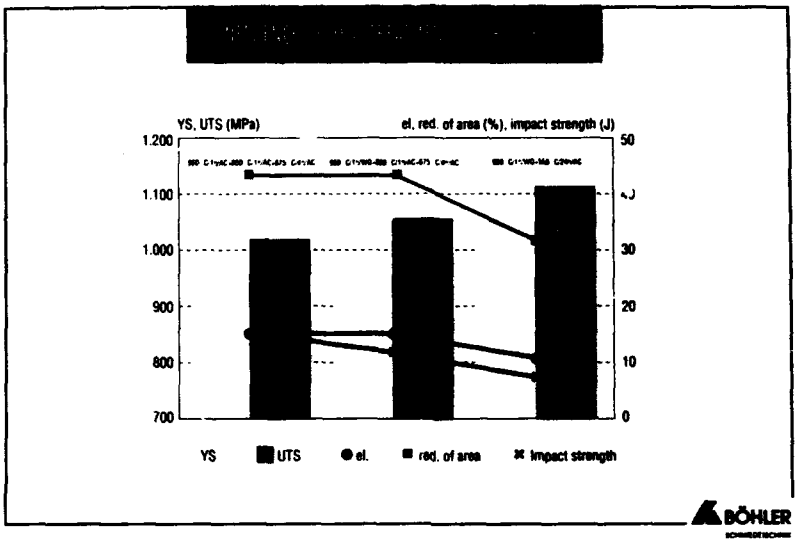


Figure 8

Conclusions

The experiences gained hitherto with bimodal structures as compared to the mill annealed $\alpha+\beta$-condition have shown that an optimization of certain properties (fatigue strength), as well as achievement of a better reproducible structure (variation of Young's Modulus, homogeneity) is possible.

The positive influence of the texture on the fatigue strength cannot be utilized in case of large forgings, because it is not possible to obtain sufficiently fine α particle sizes.

However, a further optimization of the fatigue strength of the bimodal microstrucutre can be achieved by modified heat treatment. In this respect a two step heat treatment seems to be very promising, because it permits to improve both the fatigue and mechanical properties. Complementary tests are carried out at the moment with two step heat treatments, with the temperature of the second step being in the range of 650°C up to 750°C, with the goal of avoiding the decrease of toughness properties by avoiding the coarsening of the lamellar constituents while retaining the same fatigue and strength values.

The results shall be available end of the year and will be published at that time.

Literature

1) Y.Honnorat; "Titanium alloy use in turbojet engines", Proc.of Sixth World Conference on Titanium, Société Francaise de Metallurgie, June 1988
2) Y.Fukuhura; "Nonaerospace applications of titanium", Proc.of Sixth World Conference on Titanium, Société Francaise de Metallurgie, June 1988
3) P.A.Coulon; "Development and trends in metallurgy of titanium", Titanium and Aluminium, IITT-International, Febr. 1990
4) R.I.Jaffee; "Titanium steam turbine blading", Workshop Proc., EPRI, Nov. 1988
5) L.Wagner, G.Lütjering, R.I.Jaffee; "Fatigue behaviour of bimodal microstructures in Ti-6Al-4V", Fatigue '90, July 1990
6) J.Mayerhofer, H.Jäger, H.Puschnik, J.Fladischer; " Last stage titanium blades with bimodal microstructure", Int. Conf.on Advances in Material Technology for Fossil Power Plants, ASM, Sept. 1987
7) H.Puschnik, J.Fladischer, G.Lütjering, L.Wagner, R.I.Jaffee; " Advanced structures for large Ti-6Al-4V turbine blades", Titanium and Aluminium, IITT-International, Febr. 1990
8) L.Wagner, G.Lütjering; " Propagation of small cracks in Ti alloys", Proc.of Sixth World Conference on Titanium, Société Francaise de Metallurgie, June 1988

Microstructure and Mechanical Properties Relationship of β-rich α-β Titanium Alloy; SP-700

M. Ishikawa, O. Kuboyama, M. Niikura and C.Ouchi

Advanced Technology Research Center, NKK Corporation
Kawasaki-ku, Kawasaki 210, Japan

Abstract

The newly developed β-rich α+β titanium alloy, SP-700, has two distinct characteristics compared with Ti-6Al-4V alloy. One is very great strength obtained by solution treated and aged as well as very high age-hardenability. The other is excellent superplasticity with a low forming temperature below 1027K. Microstructural development in SP-700 has a close relationship with such characteristics. Very fine α+β microstructure is obtained and stable β phase is retained after solution treating. α" martensite is produced after quenching. Aging causes decomposition of the retained β phase and transformation of α" martensite, resulting in a very fine dispersion of precipitated α and it produces a significant increase in strength with adequate ductility.

Introduction

The newly developed β-rich α-β titanium alloy, SP-700, is designed to decrease the peak superplastic temperature and improve superplastic formability as compared with Ti-6Al-4V. Based on the preliminary study [1] which examined the effects of alloying elements of Ti-6Al-4V on superplasticity , Fe and Mo were selected as alloying elements of SP-700 for the purpose of lowering the stress during superplastic deformation and refining duplex microstructure, respectively, and the contents of Al and V were modified to control β transus temperature which affects the superplastic temperature. The nominal composition of SP-700 is Ti-4.5%Al-3%V-2%Fe-2%Mo and the β transus temperature is about 1173K. SP-700 has extremely fine α+β duplex microstructure and shows excellent superplasticity at a low forming temperature below 1073K [2].

The microstructure of α-β titanium alloys such as Ti-6Al-4V can be significantly varied by alloying elements, processing parameters and heat treatment conditions. Mechanical properties are sensitive to such microstructural variations [3]. Solution heat treating and aging (STA) is applied in α-β titanium alloys to obtain high strength which is influenced by the cooling rate (section size effect) and quench delay [4]. Microstructural changes by this heat treatment occur mainly in prior β phase, and the strength depends on transformed β structure such as acicular α, α', α" martensite and retained β. Low cooling rate and the extension of quench delay time promote diffusional transformation and cause the nucleation and growth of acicular α which decreases the strength of Ti-6Al-4V [4,5]. SP-700 has higher β-stabilizer contents(Fe, Mo) which modify transformation of the β phase [6-14], and overall microstructural development in this new alloy is different from that of Ti-6Al-4V.

The present investigation was performed to examine the microstructural development of SP-700 and its effect on mechanical properties, especially strength of solution treated and aged SP-700.

Titanium '92
Science and Technology
Edited by F.H. Froes and I. Caplan
The Minerals, Metals & Materials Society, 1993

Materials and Experimental Procedure

40kg ingots of SP-700 and Ti-6Al-4V for comparison were melted in a laboratory VAR furnace. The chemical composition is shown in Table I. The ingots were forged into 80 mm slabs in the β phase region, and then rolled into 15mm thickness plates in the α-β field. Blanks were sampled from the plates for the subsequent heat treatment.

Microstructural development of SP-700 and Ti-6Al-4V was studied on the materials reheated at several temperatures in the α-β field and subsequently cooled in either water or air. The cooling rate was 150K/s for water cooling and 3K/s for air cooling respectively. Metallography samples were taken from the longitudinal-short transverse plane. The microstructures were observed with SEM and TEM, and constituent phases were analysed with an X-ray diffractometer. The volume fraction of the primary α phase was determined on scanning electron micrographs with the help of an image analyzer. The volume fraction of the retained β phase was determined using the results of the diffractometric investigations [15,16]. Phase decomposition was also studied for the material aged at 783K.

Mechanical properties were examined on the solution-treated and aged materials for both alloys. The solution treatment temperature was 1123K for SP-700 and 1223K for Ti-6Al-4V, and the aging temperature was 783K for SP-700 and 811K for Ti-6Al-4V, respectively. The aging time was 6hr for both alloys. Tensile tests were conducted according to ASTM E8 and the samples were 6.25 mm in gage diameter and 25 mm in gage length.

Table I . Chemical composition (wt%) and β transus temperature

	Al	V	Fe	Mo	O	C	N	H	Tβ (K)
SP-700	4.38	2.86	1.86	1.87	0.09	0.008	0.004	0.007	1173
Ti-6Al-4V	6.47	4.09	0.14	-	0.17	0.028	0.015	0.015	1269

Results

Microstructural development

Scanning electron micrographs for SP-700 and Ti-6Al-4V are shown in Fig.1. With the temperature increase, the primary α phase volume fraction decreases for SP-700 and a morphological change to equiaxed microstructure is observed. The grain size of recrystallized annealed SP-700 (Fig.1(b)) was extremely fine around 2μm as compared with that of Ti-6Al-4V around 8μm (Fig.1(e)). X-ray diffractometric analysis revealed that the β phase region, at the heating temperatures of 1073K and below, remained as retained β on the subsequent cooling, while the β phase at the heating temperature above 1073K partially transformed to α" phase on the cooling. As shown in Fig.1, the scanning electron micrograph did not reveal any difference between air cooling and water quenching conditions. However, in Ti-6Al-4V, relatively massive aciculer α grows in air cooling conditions. Fig. 2 shows transmission electron micrographs for the transformed prior β region. Transformed microstructures were influenced by the cooling rate, and the α" phase which contains internal twins was observed in the water-cooled material (Fig.2(a,b)). The slower cooling rate obtained by the air cooling still contains some retained β and α", but the slower cooling rate also permitted some diffusional decomposition of the β, resulting in fine acicular α precipitation.(Fig.2(c,d)).

The volume fraction of each phase constituent at room temperature is determined by image analysis and X-ray diffractometry and summarized in Fig.3. The highest volume fraction of the β phase was retained for the solution treatment at 1073K. It reached 50% for the water cooling condition and 40% for the air cooling condition. Above 1073K, the α" phase appeared in the water cooling and an increase in its volume fraction with the increase of the solution temperature. In air cooling conditions the acicular α phase appeared and increased its volume fraction. A distinct microstructural feature for SP-700 shown in Fig.3 was that a substantial retention of the β phase more than 30% was persistent in a wide range of solution conditions.

Fig.4 shows transmission electron micrographs of the solution treated and aged SP-700 and Ti-6Al-4V. The extremely thin lamellar α phase about 50nm in width precipitates in the retained β for water quenched and aged SP-700 is shown in Fig.4(b). Such lamellar microstructure is also observed between massive acicular α phases for air cooled and aged SP-700 (Fig.4(d)). Aging caused the decomposition of the retained β and α" martensite resulting in a very fine dispersion of precipitated α in the β phase [17]. The transformed β structure of water quenched and aged Ti-6Al-4V (Fig.4(e)) is coarser than that of air cooled and aged SP-700.

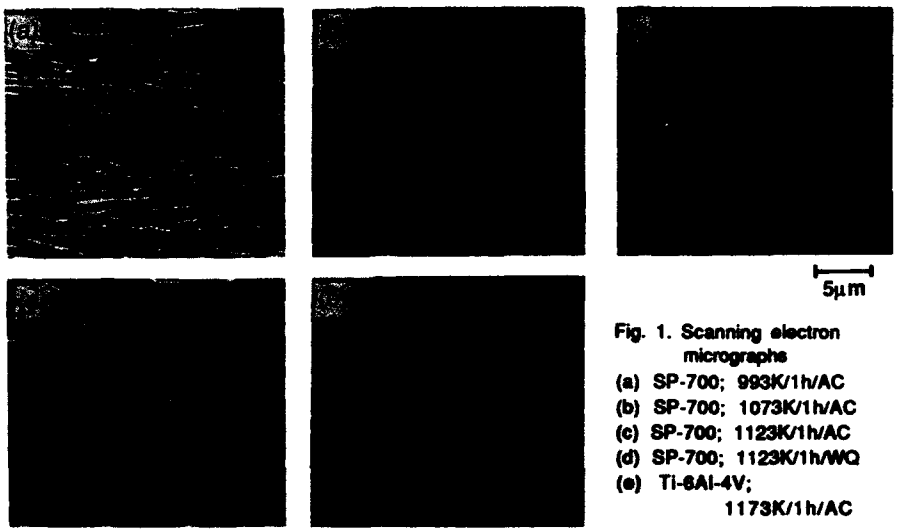


Fig. 1. Scanning electron micrographs
(a) SP-700; 993K/1h/AC
(b) SP-700; 1073K/1h/AC
(c) SP-700; 1123K/1h/AC
(d) SP-700; 1123K/1h/WQ
(e) Ti-6Al-4V; 1173K/1h/AC

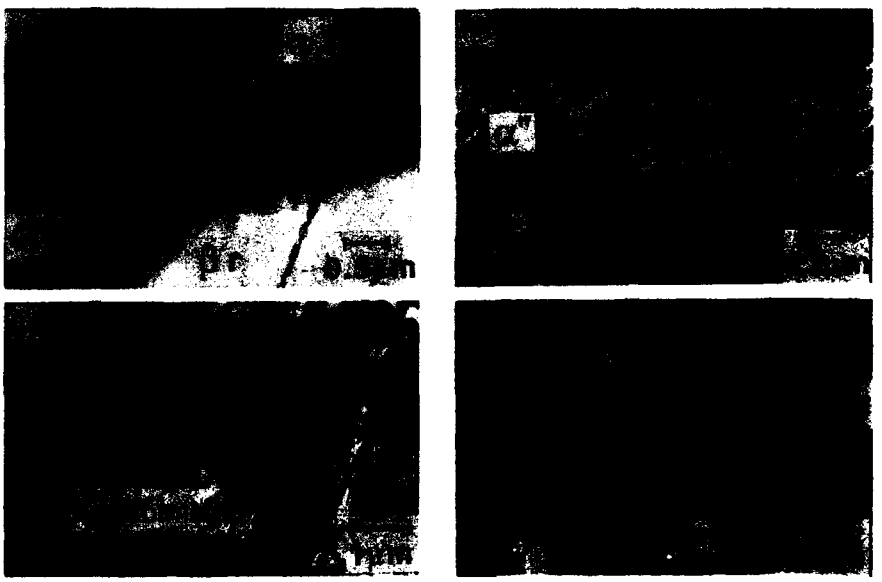


Fig. 2. Transmission electron micrographs of SP-700
(a), (b) water quenched from 1123K
(c), (d) air cooled from 1123K

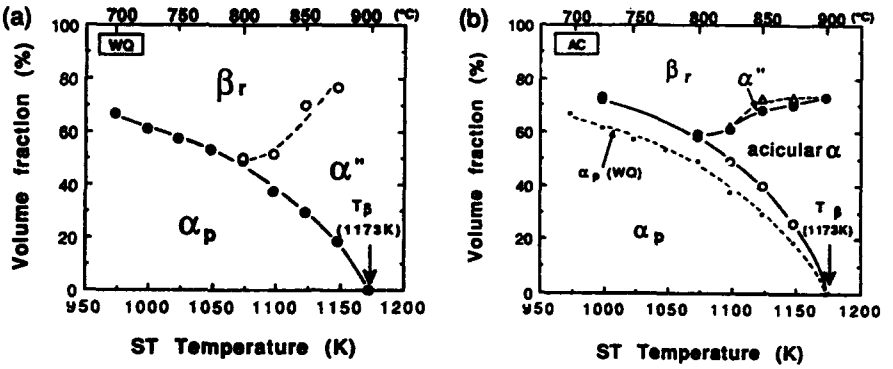


Fig. 3. Phase map of SP-700 showing the volume fraction of each phase at room temperature
(a) for water quenched SP-700, (b) for air cooled SP-700

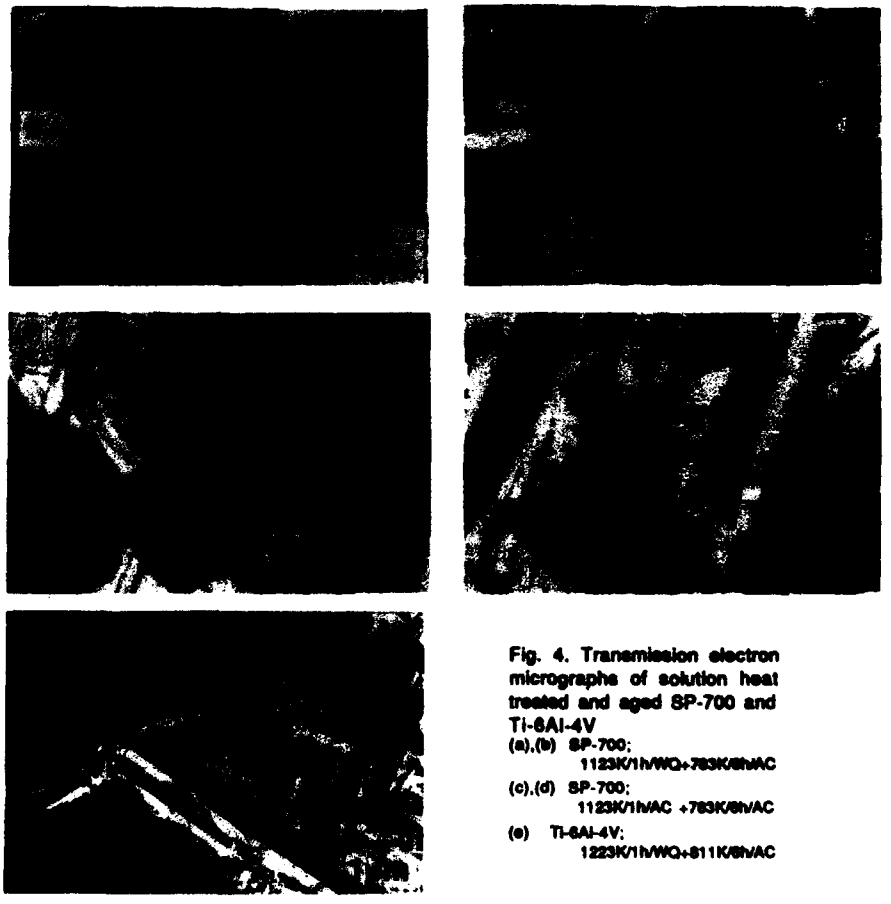


Fig. 4. Transmission electron micrographs of solution heat treated and aged SP-700 and Ti-6Al-4V
(a),(b) SP-700:
1123K/1h/WQ+783K/8h/AC
(c),(d) SP-700:
1123K/1h/AC +783K/8h/AC
(e) Ti-6Al-4V:
1223K/1h/WQ+811K/8h/AC

Tensile Properties

Fig.5 shows the effect of the cooling rate after solution treating on strength of solution treated and aged SP-700 as compared with Ti-6Al-4V. The strength of Ti-6Al-4V showed a high dependence on the cooling rate and decreases by as much as 250 MPa with the cooling rate decrease from 150K/s to 1K/s. On the other hand, the dependence in SP-700 is moderate, and high strength could be maintained in the low cooling rate range. For instance, tensile strength 1400MPa and elongation 8% were obtained at 150K/s and tensile strength 1250MPa and elongation 14% were obtained even at 1K/s.

Fig.6 shows the effect of quench delay on strength of solution treated and aged SP-700 and Ti-6Al-4V. The strength of Ti-6Al-4V decreases very rapidly with the increase in delay time which corresponds to the time elapsing from the extraction out of a furnace to the start of quenching. With a delay time of 10s, yield strength for Ti-6Al-4V is reduced to below 1000MPa. On the other hand, SP-700 shows little reduction in strength with a delay time of 30s, still providing tensile strength higher than 1300MPa.

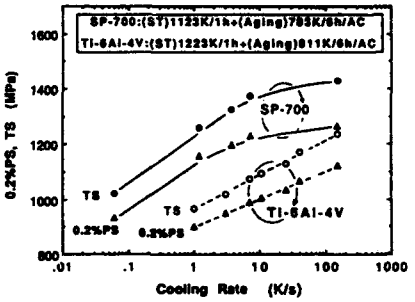


Fig. 5. Effects of cooling rate after solution treating on tensile strength in solution heat treatment and aging condition

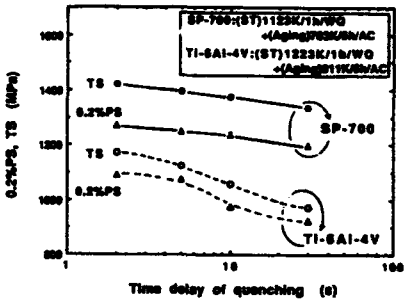


Fig. 6. Effects of quench delay on tensile strength in solution treating and aging condition

Discussion

As shown in Fig.4, aging after solution treating in SP-700 causes the decomposition of the retained β phase and the transformation of the α" martensite to α resulting in an extremely fine dispersion of α precipitate in the β phase. This microstructural feature provides very high strength of up to 1400 MPa and good elongation. The persistent retention of the β phase, more than 30% even for the air cooling as shown in Fig. 3, prevents the significant loss in strength in the low cooling rate for SP-700. On the other hand, relatively massive acicular α formation observed in the air-cooled Ti-6Al-4V in Fig.7 (a) is regarded as deteriorating the strengthening potential very drastically in the low cooling rate region, and such a diffusional transformed β phase may not provide effective strengthening during aging.

Fig.7 (b) shows that the prior β phase remains almost unchanged except for moderate growth in the primary α phase in quenched SP-700, while Fig.7 (c) shows grain growth of the primary α phase as well as nucleation and growth of acicular α phase in the Ti-6Al-4V during quench delay. Fig. 8 summarizes the hardness change in the primary α and the transformed β as well as the volume fraction change in solution treated and aged condition with delay time. In Ti-6Al-4V, the hardness of transformed β drastically dropped with the delay time due to the nucleation and growth of the acicular α rapidly increasing. On the contrary, in SP-700, the decrease in hardness in prior β and the volume fraction increase of primary α were insignificant with a delay time of up to around 30s. The β phase in SP-700 heated at solution temperature is so stable that diffusional transformation is suppressed during quench delay, and aging results in very high hardness of transformed β. The volume fraction of transformed β shows very little change during quench delay because of the low growth rate of primary α. These two factors, phase stability of prior β and stability of its volume fraction, give rise to less sensitivity to delayed quenching in SP-700.

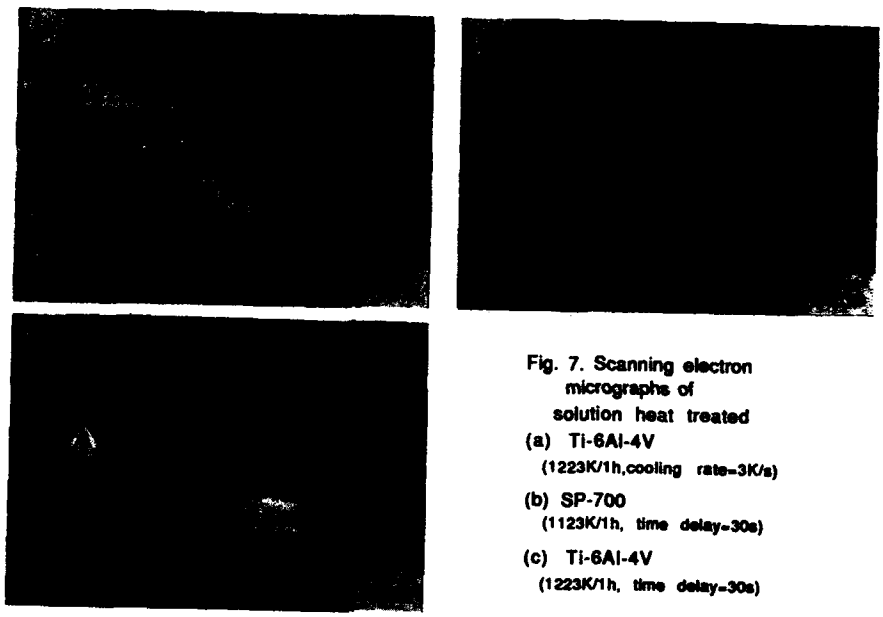


Fig. 7. Scanning electron micrographs of solution heat treated
(a) Ti-6Al-4V
(1223K/1h,cooling rate=3K/s)
(b) SP-700
(1123K/1h, time delay=30s)
(c) Ti-6Al-4V
(1223K/1h, time delay=30s)

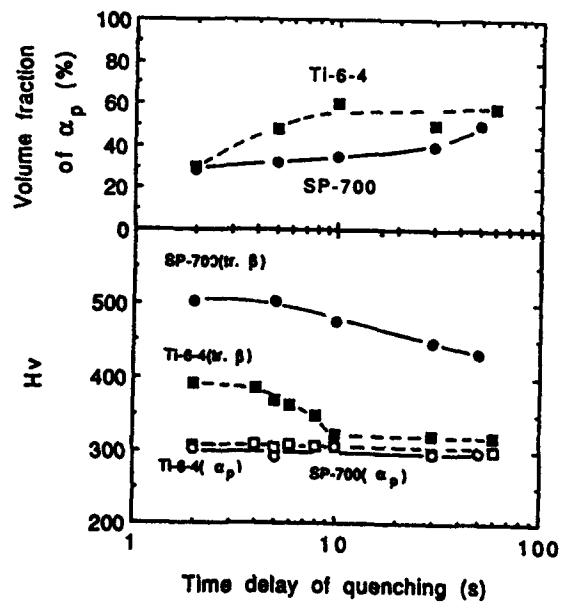


Fig.8. Effects of quench delay on the volume fraction of primary α and the microhardness of primary α and transformed β after aging

Phase stability of prior β is closely related to alloy partitioning on each phase constituent [3,5,18]. Table II exhibits alloy partitioning in the solution condition, which were determined through EDS analysis on thin foil. Most of the β-stabilizers such as V, Fe and Mo were concentrated in the prior β phase according to the partitioning of phases at heating temperatures, while concentration of V in the β phase was relatively moderate in Ti-6Al-4V. It is found that enrichment of β-stabilizers was much higher in SP-700 than in Ti-6Al-4V. The β transus temperatures of prior β in SP-700 were well below 1123K, this roughly matches those of β and near β type titanium alloys. This explains a high phase stability of prior β. The β transus temperature of prior β in Ti-6Al-4V was 1215K, which is not low enough for the suppression of acicular α nucleation.

Distinct microstructural characteristics described above improve markedly other mechanical properties such as cold-workability and superplasticity. Table III compares cold-workability of SP-700 3mmt sheet with that of Ti-6Al-4V 3mmt sheet in an annealing condition. SP-700 showed a lower bend factor than Ti-6Al-4V. This is regarded to be due to (a) a refined microstructure, (b) the substantial retention of the β phase which is highly formable because of the stable b.c.c. crystallographic structure and (c) the reduction of Al content to 4.5% [19].

Table IV compares the superplasticity of SP-700 with that of Ti-6Al-4V. They are the same materials shown in Table III. SP-700 shows higher superplastic elongation at the lower peak temperature than Ti-6Al-4V. The extremely fine grain size enhances superplastic elongation and reduces flow stress [20] at the temperatures around 1048K which is 100K lower than Ti-6Al-4V.

Table II. Microchemical analysis of the phases at selected heating temperature

	SP-700 alloy								
Temp.	α phase (wt%)				β phase (wt%)				calculated T_β
(K)	Al	V	Fe	Mb	Al	V	Fe	Mb	of β phase (K)
1023	5.05	0.28	0.14	0.24	3.09	6.52	4.52	4.35	1017
1073	5.26	0.16	0.10	0.19	3.83	6.07	3.87	3.63	1058
1123	4.96	0.21	0.06	0.34	3.93	4.87	2.74	3.09	1104
	Ti-6Al-4V alloy								
Temp.	α phase (wt%)				β phase (wt%)				calculated T_β
(K)	Al	V	Fe	Mb	Al	V	Fe	Mb	of β phase (K)
1223	6.82	2.24	0.02	-	5.53	5.44	0.17	-	1219

Table III. Comparison of cold-workability, microstructure and tensile properties with SP-700 and Ti-6Al-4V sheet (3mmt)

Alloy	Heat treatment	Grain size (μm)	Volume fraction of retained β (%)	Tensile properties			Bend factor
				0.2%PS (MPa)	TS (MPa)	El (%)	(R/t)
SP-700	993K/1hr/AC	-	30	958	1041	15	2.5
	1073/1hr/AC	2.1	40	893	963	19	2.1
Ti-6Al-4V	993K/1hr/AC	-	3	943	995	14	4.5
	1173/1hr/AC	5.2	4	906	991	15	4.0

Table IV. Comparison of superplasticity with SP-700 and Ti-6Al-4V sheet (3mmt)

	Test temp. (K)	Initial strain rate (s^{-1})	Stress (MPa)	Superplastic elongation (%)
SP-700	1048	3.3×10^{-3}	21	796
Ti-6Al-4V	1173	3.3×10^{-3}	20	660

Conclusions

(1) Microstructural features in SP-700 are summarized as follows; i) Primary α and shows an extremely fine mean grain size of less than 3μm. ii) the β phase at the solution treating temperature is very stable, and substantial retention of the β phase more than 30% is persistent in a wide range of the solution treating conditions. iii) Solution treated microstructure is much less sensitive to the cooling rate and quench delay. iv) Aging following solution treatment gives rise to the decomposition of the retained β and α" martensite resulting in a very fine dispersion of precipitated α of about 50nm thickness in the β phase.

(2) Very high strength with adequate ductility is obtained in solution treated and aged SP-700. An extremely fine dispersion of precipitate α in the β phase provides strength of up to 1400MPa with 8% elongation.

(3) Strength of solution treated and aged SP-700 is relatively insensitive to cooling rate and quench delay because nucleation of acicular α is suppressed and the volume fractions of retained β and α" martensite are large enough to provide high hardness in transformed β by aging.

(4) Most of the β-stabilizers such as V, Fe and Mo are concentrated in the β phase of the SP-700 heated at solution treating temperature, and stability of the β phase arises owing to the enrichment of such alloying elements.

(5) SP-700 shows excellent cold workability and superplasticity because of the very fine α+β microstructure.

References

1. A. Ogawa et al., Proc. First Japan Int. SAMPE (Japan, 1989), 75-80.
2. K. Takahashi, A. Ogawa, and K. Minakawa, Proc. TDA Int. of Conf. (TDA,1990), 755-769.
3. H. Suenaga, Y. Kohsaka, and C. Ouchi, Trans. ISIJ, 26(1986), 148-155.
4. M. J. Donachie,Jr., ed., Titanium A Technical Guide (Metals Park, OH: ASM Int., 1988), 62-68.
5. H. Suenaga and C. Ouchi, Tetsu-to-Hagane, 72 (1) (1986), 131-137.
6. E. W. Collings, The Physical Metallurgy of Titanium Alloys (Metals Park, OH: ASM,1984),75-101.
7. Y. Murakami et al., Proc. Fifth Int. Conf. of Titanium (Germany , 1985), 1403-1422.
8. O. P. Nazimov et al., ibid, 1451-1458.
9. V. N. Gvidnev, O. M. Ivasishin, S. P. Oshkaderov, ibid, 1635-1641.
10. J. Bechet and B. Hocheid, ibid, 1613-1619.
11. H. Sasano et al., Proc. Fourth Int. Conf. of Titanium(Japan, 1980), 717-724.
12. R. Davis, H.M.Flower, and D.R.F.West, J.Mater Sci., 14(1979), 712.
13. I. Maeda and H. M. Flower, Proc. Sixth World Conference of Titanium (France, 1989), 1589-1594
14. I. Maeda and H. M. Flower, ibid, 1629-1634.
15. R. D.Arnell, J. Iron and Steel Inst., 206 (1968), 1035.
16. R. Gullberg and R. Langneborg, Trans. AIME, 206(1968), 1482-1485.
17. H. M. Flower et al., Proc. Fifth Int. Conf. of Titanium (Germany , 1985), 1567-1574.
18. J. P. Gros et al., Proc. Sixth World Conference of Titanium (France, 1989), 1553-1564.
19. J. C. Williams and G. Luetjering, Proc. Fourth Int. Conf. of Titanium(Japan, 1980), 672
20. A. K. Ghosh and C. H. Hamilton, Met. Trans., 10A (1979), 699.

DEVELOPMENT OF TITANIUM OT4-1 ALLOY

Dr.S.C.Sharma, Rathnakar Kamath Bannadi,
R. Ganesh, Sandeep A. Badami

Research & Development Cell, Dept. of Mech.Engg.,
R.V. College of Engineering, Mysore Road,
Bangalore - 560 059, India.

Good fatigue and creep properties of Titanium alloys nesseciates its usage in todays Aircraft and Spacecraft Industries. Here we are dealing with only OT4-1 alloy with composition of 1.0% to 3.0% wt. of Aluminium and 0.5 to 2.0 weight percentage of Manganese which is used for sheet metal fabricated components of Aircraft and Spacecraft vehicles. Of these Two Aluminium stabilizers the phase and Ti-Al system exhibits peritectoid reaction. Mn is the stabiliser and a sluggish eutectoid reaction is exhibited by Ti-Mn system at around 560°C and it shows the behaviour of isomorphous system.

Titanium '92
Science and Technology
Edited by F.H. Froes and I. Caplan
The Minerals, Metals & Materials Society, 1993

INTRODUCTION

On the frontiers of technology Titanium and its alloys are a moving force. The synthesis of Titanium with other materials to produce composites have been tested with regard to their mechanical behaviour involving such factors as fracture strength and its relationship to alloy interface, yield strength, tensile modulii, response to para and ortho load applications and load transformation. The results reported being very encouraging, they gave the impetus to launch several forays in the field of composites containing dispersions of Tio_2 and other material particles with cast alloys. The present paper that deals with "Development of TIOT4-1 alloy" is a part of this ongoing effort designed to contribute to the understanding of this class of composites. Much work has been done relating to characterisation by experimental and analytic methods which includes amongst others an investigation of the elastic-/ inelastic properties fatigue and fracture, creep and environmental sensitivity(1).

The OT4-1 composition lies in two phase of the region in Ti-Al-Mn phase diagram at room temperature, and there is a strong partitioning of Al to the phase and Mn to the phase in the OT4-1 alloy which stabilises small amount of phase in the microstructure results in improvement of workability and streng*h pressure build-up near the melt surface is because of the evaporation of volatile matters from molten metal.

The strength of the OT4-1 alloys remains almost constant upto 2% and increases as the percentage of Aluminium increases. Tensile properties at different annealing temperature shows that a slight decrease in strength will be observed when annealed 610°C and 690°C. The strength of the alloy which is controlled by grain size shows a linear relation with yield strength.

Mechinability studies of OT4-1 alloy was carried out for different speeds, feeds and depth of cut. chip strain analysis was carried out by Scanning Electron Microscopy. By evaluating various forces Merchant Circle Diagram was drawn to know the detailed characteristic for its purpose and use.

PROCESS

The Titanium OT4-1 alloy is an ideal link up of several important properties such as, for instance, good fatigue and creep characteristics, that qualifies it as a promising candidate for structural applications in air craft, and space craft industries. With the phenomenal development of Ti-alloys which match up not only with todays needs, but also with the tougher demands projected for the 90's, it was decided to confine the present investigation to the somewhat neglected area of the Titanium OT4-1 alloy with composition of 1% to 3% by weight of the Aluminium and 0.5 to 2% by weight of Manganese which are often used for steel metal fabricated components of air craft and spacecraft structures (2). With Tianium alloys right on target for a vast range of aircraft and space craft applications, composites involving Titanium have been rates a winner in the race for cost/performance benefits.

The investigation provided encouraging results for outstanding toughness and strength to weight ratio, high heat resistance, and superior dimensional stability. Machanability and processing characteristics are expected to add up to its reputation as a great winning combination for highly demanding applications in the relevant industries (3). It is expected to deliver performance and properties approaching those required for aeronautics and aerospace applications (4,5).

In much as the conference is dedicated to the task of providing a forum that would cover all aspects of science and technology and applications of Titanium and its alloys, there are certain frontier technologies and applications, principally in the areas of aeronautics and aerospace engineering the benefits and spinoffs which can be widely used for diverse applications. This paper is initially presented in a compact from covering the first phase of a prolonged investigation. Thus it scope is intended to be multidimensional and consequently, has to be extended, to include the degree of suitability of Ti01-1 alloy to crucial applications as aircraft and aerospace structures that takes into account its response to loads stability, damage tolerance and durability analysis (6). If required the investigation will explore other thrust areas involving the use of advanced metal and composite materials principally biased in favour of Titanium metal matrix composites. It is suggested to incorporate and use the mathematical tools of analysis to concepts of linear and non-linear finite element modelling, variational principles, optimization and fracture mechanics (7).

Since aircraft and spacecraft are the target areas for application of Tibased MMMc's due emphais must be place on the need for indepth investigation relating to the response of these composites to the impact of structural dynamics. In this context adequate tools to deal with analytical and experimental methods for evaluation of the effects of resonance and forced to vibration and the dual response of Tibased MMMc's in transient and steady state conditions to excitation because of gust acoustics, impact and shock unsteady aerodynamics, aero elastic stability, and dynamic interactions with a board flight controls and propulsion systems and finaly its response to transient thermal environment needs a thorough evaluation (8).

As far as design engineering is concerned one should not loose sight of the fact that since future aircraft will be built with a very high percentage of components made from Ti composite materials and the road to this goal can be perilous. No option should be tied to a losing gambles on development of composites to aerospace applications.

CONCLUSION

The best way to ensure the realisation of specific goals in the development and application of composites is to utilise in their search on modern tools of design engineering, which should include any other, advanced analysis and optimization methods in the development of the materials, and to steer the path dedicated to the task of implementing the synthesis and evaluation of specific composites by utilising CAD & CAM that will lead to advance design concepts incorporating Finite Element Techniques to be utilized for construction purposes through the various stages of Geometric Modelling, Automatic generation of Finite Element Mesh, display of the complete model showing the stress contours and zoom capabilities that will magnify the high stress areas for closer examination (9).

REFERENCES

1. J.Y. Rossignol, J.M. Quenisset, R.Naslain "Mechanical bevaiour of 2D-C-C/Tic composites made from a 2 D-C-C perform densified with Tic by CVI" Composites Vol.18 No.2, Page 135-143.

2. Naslain R., Hagenmuller P, Christian F, Heraud L, Chousy J.J. "Advances in composite material" Proc-ICCM3 Pergamon Press Inc. Paris, France 1980 Page 596.

3. D. Mahulikar, HL Marcus "Environmentally influenced mixed mode fatigue crack propagation of Titanium MMC's" Metallurgical transactions, Vol.15, Jan-1984 Page - 209.

4. V. Bahman, D. Munz "Engineering Fracture Mechanics 1979 Vol.5, Page-23.

5. W.J. Coracs, C.J. London, "Synthesis and Material Characterisation of Beryllium/Ti-6AL-4V Composites. Matallurgical transactions Vol.8A, Jan. 1977, Page 179.

6. A Kelly, W. Tyson "High Strength Materials" Wiley, New York 1965, Page 578.

7. A. Banerji, P.K. Rohatgi "Cast Aluminium alloy containing dispersoids of Ti02 and Zn02 particles" Journal of Material Science 17 (1982) Pages 335-342.

8. W.A. Dean "Aluminium" Vol.1, American Society of Metals, Ohio, 1967, Page 163.

9. A Kelly, Strong solids Clasendon Press, Oxford-1966 Page 144.

OXYGEN EFFECTS ON THE MECHANICAL PROPERTIES

OF TIMETAL·21S

W. M. Parris and P. J. Bania

TIMET
P.O. Box 2128
Henderson, Nevada 89009

Abstract

TIMETAL·21S (Ti-15Mo-2.7Nb-3Al-.2Si) is a metastable beta alloy which is being considered for a variety of aerospace and industrial applications. In most cases, it would be used in an aged condition. Recent studies have shown that oxygen can have a pronounced effect on tensile strength and ductility after a given aging treatment. At a given strength level, however, oxygen up to 0.25% had no significant effect on ductility. Oxygen levels below 0.12% resulted in a large decrease in strength level after a given aging treatment. This can be compensated for by lowering the aging temperature or using a preaging heat treatment. Surface oxygen absorption during long-time exposures at 510°C to 615°C reduced tensile ductility. The alloy remained metallurgically stable however.

Introduction

The TIMETAL·21S alloy (formerly Beta-21S) is a metastable beta titanium alloy having a nominal composition of Ti-15Mo-2.7Nb-3Al-0.2Si. It was originally developed as a strip producible, oxidation resistant material for metal matrix composites.[1] Its unique set of properties, however, have led to its being considered for a variety of aerospace and industrial applications. Among these properties are, besides good oxidation resistance, good creep strength up to 450°C (840°F) and a combination of high strength with outstanding corrosion resistance.[2]

In many of the potential applications the alloy will be used in a high strength aged condition. Early work on this alloy as well as experience with other metastable beta compositions indicated that oxygen content could have a significant effect on the strength-ductility relationships attained with various aging cycles. There is also the more basic question of whether oxygen content affects ductility at a given strength level. To better define these effects a study was undertaken on laboratory and semi-commercial heats with oxygen contents ranging from 0.09 to 0.33%.

Titanium '92
Science and Technology
Edited by F.H. Froes and I. Caplan
The Minerals, Metals & Materials Society, 1993

In addition to bulk oxygen effects there was also the question of the effects of oxygen penetration of the surface of the alloy during extended exposures at elevated temperatures. This was also investigated at temperatures up to 615°C.

Materials and Procedures

Bulk Oxygen Effects. This study involved material from seven (7) 27 Kg (60-lb) laboratory heats and one 818 Kg (1800-lb) semi-commercial heat. Starting material for this study was obtained from the latter heat in the form of 76-mm (3-in) x 456-mm (14-in) forged slab. Chemical analyses of all heats are given in Table I. Sheet 1.3-mm (0.050-in) thick x 127-mm (5-in) wide was produced from all heats by a process simulating continuous strip production. The final operations on all sheet consisted of cold rolling 50% to final gage followed by annealing for 10 minutes 28°C (50°F) to 42°C (75°F) above the beta transus of each heat to produce an essentially fully recrystallized material. Hot rolled 13-mm (0.5-in) diameter bar stock was also produced from six of the heats for testing. Final operations for the bar consisted of rolling from 38-mm (1.5-in) square bar to final size from a temperature of 788°C (1450°F). Following rolling the bar was annealed for one hour at the same temperatures as sheet from the same heat.

TABLE I - Chemical Compositions of Heats

Heat No.	Mo	Nb	Al	Si	Fe	O	N
V-6966	16.0	2.54	3.02	0.21	0.110	0.26	0.002
V-7074	15.4	2.54	2.95	0.19	0.090	0.14	0.004
V-7297	15.1	2.85	3.07	0.18	0.081	0.09	0.003
V-7503	14.8	2.73	3.07	0.23	0.085	0.12	0.008
V-7504	14.5	2.68	3.05	0.23	0.082	0.13	0.010
V-7505	14.4	2.67	3.09	0.23	0.088	0.18	0.009
V-7506	14.7	2.69	3.08	0.23	0.086	0.23	0.008
V-7518	15.2	2.88	3.14	0.20	0.052	0.33	0.004
G-1664	15.0	2.84	2.97	0.20	0.127	0.13	0.004

The initial evaluation, early in the development program of the alloy, was carried out on sheet material only from Heats V-7074 and V-6966 containing 0.14% and 0.25% oxygen, respectively. Specimen blanks from each heat were aged for periods of 4, 8, 16 and 24 hours at temperatures of 482°C (900°F), 538°C (100C°F), and 593°C (1100°F) followed by air cooling. The later evaluation, carried out on Heats V-7297 thru V-7518 covered a wider range of oxygen contents (0.09% to 0.33%) and involved, in addition to cold rolled and recrystallized sheet, hot rolled and annealed bar. In this part of the investigation only three aged conditions were evaluated; 482°C (900°F) for 24 hours, 538°C (1000°F) for 8 hours, and 593°C (1100°F) for 8 hours. These treatments were selected because they represented a fully aged condition at each temperature and provided a range of strength levels covering those likely to be used in commercial applications.

Prior to tensile testing all sheet specimens were descaled and pickled to remove 0.05-mm (0.002-in) from each surface to remove any material contaminated by oxygen and/or nitrogen during heat treatment. Tensile testing was carried out according to ASTM E8. Gage section for the sheet specimens was 6-mm (0.25-in) x 25-mm (1-in) and for the bar specimens 6-mm (0.25-in) diameter x 25-mm (1-in).

In addition to the tensile tests some indication of sheet formability in the annealed condition was obtained by bend testing 25-mm (1-in) wide strips. These specimens were bent 105 degrees around successively smaller radii either until cracking visible at 20X magnification occurred or until the minimum radius of 0.76-mm (0.030-in) was reached.

Surface Oxygen Effects. This study involved two gages of sheet, 0.58-mm (0.023-in) and 1.3-mm (0.052-in) thick, produced by standard strip processing methods from commercial Heat G-1664. The chemical composition of this heat is also given in Table I. Prior to testing, specimen blanks of each gage were given an overaging type of heat treatment consisting of:

690°C (1275°F), 8 Hrs AC + 649°C (1200°F), 8 Hrs AC

Fully machined tensile specimens were then exposed in air for 1000 hours at temperatures of 510°C (950°F), 565°C (1050°F) and 615°C (1140°F). During exposure the specimens were so arranged that air had free access to all surfaces.

Following exposure the specimens were tensile tested both with the oxide scale intact and after descaling and removal of air contaminated surface metal by acid pickling. Thickness of the surface layer removed ranged from 0.05 to 0.1-mm (0.002 to 0.004-in) depending on the exposure temperature.

Results and Discussion

Bulk Oxygen Effects. With regard to bend ductility sheet in the annealed condition from all heats sustained a 105 degree bend around an 0.050-in (1.27-mm) radius without cracking. This translates to a bend ductility of 1T or less for sheet at all oxygen levels. Thus, oxygen contents up to 0.33% had no significant effect on this criterion for formability. However, as will be shown later, the tensile data indicated a possible oxygen effect on some other aspects of sheet formability.

Results of the tensile tests on sheet from the first two heats containing 0.14% and 0.25% oxygen are presented in Table II. It is immediately apparent that the higher oxygen level generally resulted in higher strength and lower ductility after a given aging treatment. The deleterious effect on ductility is particularly noticeable in the series aged at 593°C. The significant question, however, was whether the increased oxygen reduced ductility at a given strength level. Subjecting the data of Table II to linear regression analyses using elongation as the dependent variable gave the following equations:

0.14% O_2	Elong = 28.9 - 0.0177 UTS (MPa)
	Elong = 32.5 - 0.0222 YS (MPa)
0.25% O_2	Elong = 29.2 - 0.0181 UTS (MPa)
	Elong = 30.3 - 0.0200 YS (MPa)

Regression coefficients ranged from 0.85 to 0.90 indicating reasonably good adherence to a linear relationship. It is evident that the equations relating tensile elongation to either ultimate tensile or yield strength were virtually the same for the two oxygen levels. Thus, the tensile ductility, expressed as elongation, was essentially the same at a given strength level for both heats indicating that oxygen, per se, had no significant effect.

Table II Tensile Properties of TIMETAL•21S Sheet at Two Oxygen Levels[1]

Aging Temp, C	Aging Time, Hrs	Oxygen Content, %	UTS MPa	YS MPa	El, %
None	--	0.14	880.5	860.5	12.0
		0.25	931.5	914.3	15.0
482	4	0.14	1093.8	983.9	11.5
		0.25	1011.5	975.0	14.0
	8	0.14	1257.0	1145.3	4.0
		0.25	1143.9	1114.9	5.0
	16	0.14	1383.2	1276.9	5.0
		0.25	1473.5	1373.5	4.5
	24	0.14	1428.6	1319.7	3.5
		0.25	1529.3	1454.8	3.0
538	4	0.14	1297.0	1199.7	8.0
		0.25	1381.8	1297.6	5.5
	8	0.14	1269.4	1185.3	5.0
		0.25	1388.7	1303.2	3.5
	16	0.14	1289.4	1205.3	6.0
		0.25	1409.3	1341.1	3.5
	24	0.14	1268.0	1192.2	6.0
		0.25	1388.7	1336.9	3.5
593	4	0.14	1103.8	1024.6	11.0
		0.25	1180.4	1108.7	6.0
	8	0.14	1063.9	996.3	11.0
		0.25	1172.2	1103.9	7.5
	16	0.14	1074.2	999.8	10.0
		0.25	1194.2	1128.7	5.0
	24	0.14	1116.3	1059.1	8.0
		0.25	1199.7	1128.7	6.5

[1]Cold rolled 50% prior to annealing.
0.14 oxygen annealed 816°C(5 Min)AC. 0.25 oxygen annealed 857°C(5Min)AC.
All values are the average of two L and two T specimens.

Tensile test results for both sheet and bar stock of the second group of heats are presented in Table III. These heats were made to confirm the results of the earlier investigation and to extend the range of oxygen contents both above and below the two previous levels. In the annealed condition strength increased with oxygen content for both sheet and bar product. The magnitude of the increase over the full oxygen range was somewhat greater for sheet (159 MPa) than for bar (80 MPa). Ductility, however, remained essentially constant over the full range of oxygen for both product forms.

The picture changed somewhat for the aged specimens. As in the earlier work, for a given aging treatment strength increased with increasing oxygen and ductility decreased. Again, to determine whether the strength-ductility relationship was affected by oxygen the data for each aging treatment and each oxygen level were subjected to linear regression analyses. For the sheet, elongation was the dependent variable; for bar both elongation and reduction of area. In all cases, the data fitted a linear regression reasonably well, showing regression coefficients rangi.1 from 0.79 to 0.94 for the sheet specimens and 0.87 to 0.99 for the bar. The results of this work are presented in Table IV in the form of calculated elongation and reduction of area values for bar and sheet specimens at two strength levels, 1380 MPa (200 ksi) and 1034 MPa (150 ksi) ultimate tensile strength. For the sheet specimens no trend is evident for

Table III Effect of Oxygen Content on the Tensile Properties of Beta-21S Sheet and Bar

		Simulated Strip[2]			Hot Rolled Bar			
Heat Treatment[1]	Content, %	UTS MPa	YS MPa	El %	UTS MPa	YS MPa	RA, %	El, %
843°C(10 Min)AC	0.090	813.6	771.6	19.8	837.1	795.7	66.8	22.5
	0.120	859.8	819.8	20.1	847.4	815.7	66.2	24.0
	0.130	874.3	847.4	17.3	874.3	843.9	61.8	23.0
	0.183[3]	900.5	888.8	18.4	882.6	853.6	63.6	23.3
	0.229[4]	930.8	912.9	17.4	899.1	890.1	66.1	27.0
	0.334[5]	970.8	958.4	21.5	917.0	913.6	61.4	26.5
843°C(10 Min)AC + 481°C(14 Hr)AC	0.090	1336.9	1258.3	6.8	-	-	-	-
	0.120	1443.1	1341.8	4.1	1431.4	1352.1	15.8	7.0
	0.130	1391.4	1306.6	3.0	1434.2	1346.6	15.9	6.5
	0.183[3]	1447.3	1375.6	2.8	1494.8	1415.5	12.5	4.5
	0.229[4]	1541.7	1470.7	2.3	1583.1	1501.7	10.4	4.5
	0.334[5]	1579.6	1462.4	3.0	1540.3	1443.1	5.0	2.0
843°C(10 Min)AC + 538°C(8 Hr)AC	0.090	1157.0	1024.6	9.6	1202.5	1037.0	47.6	10.9
	0.120	1314.2	1232.8	5.8	1325.2	1253.5	24.3	8.3
	0.130	1320.4	1243.2	5.8	1326.6	1254.9	24.4	8.5
	0.183[3]	1421.7	1319.7	1.4	1395.5	1329.4	19.0	7.0
	0.229[4]	1434.8	1377.6	4.3	1467.3	1388.0	19.2	7.8
	0.334[5]	1461.1	1359.7	3.4	1425.2	1332.8	8.0	4.0
843°C(10 Min)AC + 593°C(8 Hr)AC	0.090	937.0	822.6	16.8	1045.3	947.4	44.2	11.5
	0.120	1068.0	986.0	12.5	1103.2	1010.1	35.5	14.0
	0.130	1060.5	987.4	9.0	1099.8	1011.5	35.2	13.5
	0.183[3]	1152.8	1081.8	7.9	1166.6	1084.6	26.9	12.0
	0.229[4]	1223.2	1148.0	8.0	1232.1	1146.6	22.5	10.3
	0.334[5]	1289.4	1194.2	6.5	1259.0	1180.4	16.0	8.3

[1]Annealing time for sheet was 10 min., for bar 1 hour.
[2]Cold rolled 50% prior to annealing.
[3]Annealed 857°C.
[4]Annealed 871°C.
[5]Annealed 885°C.

elongation values vs. oxygen content at either strength level. However, the bar material showed a distinct decrease in both elongation and RA at the high strength level (1380 MPa). This trend is not as evident at the lower strength level (1034 MPa) although there is some indication of a decrease in RA at the 0.33% oxygen level.

Although oxygen levels below 0.33 do not appear to significantly affect the strength-ductility relationship, the data of Table III show a strong effect of oxygen contents below 0.12% on strength level after a given aging treatment. For example, both sheet and bar of the 0.09% oxygen heat had yield strengths more than 200 MPa lower than the 0.12% oxygen heat after aging at 538°C for 8 hours. Strength of the low oxygen heat may be increased to that of the 0.12% oxygen material either by using the 482°C (24 hr) age or by using a duplex aging treatment. The latter involves a preaging treatment at 427°C for 4 hours followed by the standard 538°C (8 hr) age. The duplex age applied to bar stock of the 0.09% oxygen heat gave the following tensile properties:

UTS - 1311 MPa
YS - 1218 MPa
% RA - 30.4
% El - 11

These properties are very close to those of the 0.12% oxygen alloy after the standard 538°C (8 Hr) age.

There is another effect of oxygen shown in the data of Table III which could be important in certain types of forming operations. Note that in

Table IV Calculated[1] Tensile Ductility Values at Two Strength Levels as a Function of Oxygen Content

Oxygen Content, %	1380 MPa (200 ksi) UTS Elong, %	RA %	1034 MPa (150 ksi) UTS Elong, %	RA %
	Sheet Material			
0.09	5.0	-	13.9	-
0.13[2]	4.4	-	11.1	-
0.18	4.8	-	9.8	-
0.23	5.3	-	11.2	
0.33	5.0		9.5	
	Bar Material			
0.13[2]	7.7	19.8	15.1	39.6
0.18	7.3	18.2	15.1	32.8
0.23	8.3	18.9	13.7	29.8
0.33	5.5	10.7	13.2	24.7

[1]Calculated from linear regression equations obtained from the data of Table III.

[2]Data for both 0.13 and 0.14% oxygen heats are included.

the annealed condition the difference between yield and ultimate tensile strengths decreased as the oxygen level increased from a value of 42 MPa at 0.09% oxygen to a value of 12 MPa at 0.33% oxygen.

This behavior implies a decrease in work hardening capability with increasing oxygen and, concomitantly, an increase in the tendency to neck locally and fail during stretching or drawing operations.

All in all, the above data indicate that oxygen levels up to at least 0.25% can be tolerated in the TIMETAL•21S alloy where good strength-ductility relationships are the prime consideration. Other properties, such as fracture toughness or crack propagation, may revise this maximum figure when appropriate data become available. Lower oxygen contents are also indicated for applications requiring severe forming operations. The current aim of 0.13% oxygen for the alloy provides a compromise between adequate formability and high strength capabilities.

Surface Oxygen Effects. The effects of oxygen build-up in the surface layers of TIMETAL•21S sheet during exposure at elevated temperature for 1000 hours in air are shown in Table V. Prior to exposure the specimens were heat treated to provide a high degree of metallurgical stability. It is apparent that oxygen absorption by the surface layers reduced tensile ductility with the magnitude of the reduction depending on both exposure temperature and sheet thickness. Exposure temperature, of course, determined the depth beneath the surface to which the oxygen penetrated. The sheet thickness effect was associated with the higher percentage of sheet thickness remaining uncontaminated in the thicker sheet. In all cases the original ductility was restored after exposure by removing the oxygen contaminated surface layers by descaling and pickling. This confirmed the metallurgical (bulk) stability of the alloy under these conditions of exposure.

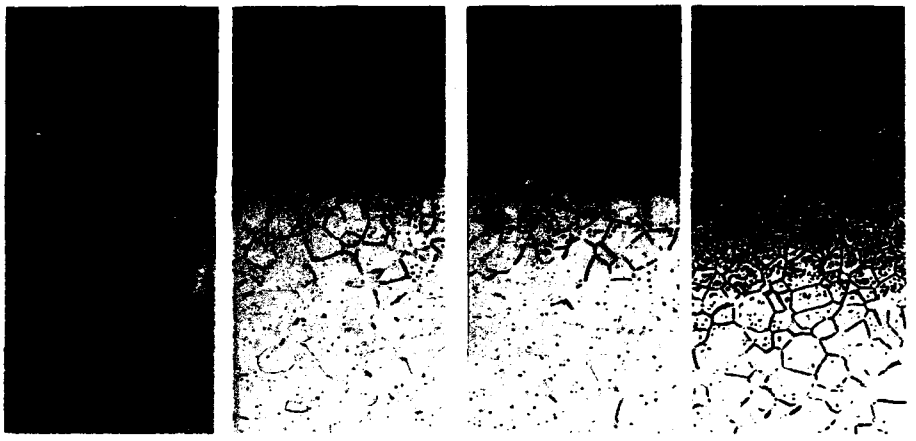
Table V Effect of Surface Oxygen Absorption on the Tensile Ductility of TIMETAL•21S Sheet[1]

Sheet Thickness, mm	Exposure[2] Temp, C	Surface	UTS MPa	YS MPa	Elong, %
1.32	None	-	917	848	19.0
	510	As Exposed	1015	941	13.0
		Pickled[3]	1010	927	14.0
	566	As Exposed	947	893	10.0
		Pickled[3]	949	877	17.0
	616	As Exposed	911	874	2.5
		Pickled[4]	941	838	15.0
0.58	None	-	977	905	13.5
	510	As Exposed	994	945	5.5
		Pickled[3]	1041	958	12.0
	566	As Exposed	985	940	5.5
		Pickled[3]	1003	919	13.5
	616	As Exposed	972	944	2.5
		Pickled[4]	960	862	13.5

[1]Prior heat treatment 691°C(8 Hrs)AC + 649°C(8 Hrs)AC.
[2]Exposure time = 1000 hours.
[3]Descaled and pickled to remove 0.05-mm from surface.
[4]Descaled and pickled to remove 0.075-mm from surface.

The actual depth of penetration of the oxygen normally can be determined by a relatively simple procedure in metastable beta titanium alloys. Oxygen increases the beta transus of the alloy about 3°C per 0.01% oxygen. Therefore, if the exposed sample is heated to a temperature just above the beta transus of the substrate for a short time only the uncontaminated metal of the substrate will completely transform to beta. The depth of oxygen penetration then is denoted by the presence of an alpha-beta structure. Care must be taken during this heat treatment to prevent additional oxygen pickup by using vacuum or an inert atmosphere or by encapsulating the specimen in a welded titanium pack.

In the case of specimens exposed for long periods of time at temperatures in the range 450°C to 650°C, however, the pre-existing alpha particles coarsen and become more stable. The enhanced stability is probably the result of attaining near equilibrium composition throughout the volume of the alpha particle. Thus, when the long exposure specimens are heated for short periods of time at a temperature just above the beta transus the alpha phase in the uncontaminated substrate does not completely transform. This is illustrated in Figure 1(a) which is a micrograph of the specimen exposed for 1000 hours at 538°C and solution treated at 815°C for 10 minutes. Note the alpha particles and particularly the grain boundary alpha still present in the substrate below the air contaminated surface. Increasing the solution treating time to one hour at 815°C results in the transformation of essentially all of the alpha in the substrate of the specimens exposed at 482°C and 566°C as shown in Figures 1(b) and 1(c). Some grain boundary alpha still remained in the specimen exposed at 615°C as shown in Figure 1(d).



(a) (b) (c) (d)

Figure 1(a) - 566°C for 1000 hrs + 815°C for 10 min.; (b) 510°C for 1000 hrs + 815°C for 1 hr.; (c) 566°C for 1000 hrs + 815°C for 1 hr.; (d) 615°C for 1000 hrs + 815°C for 1 hr.

From these micrographs it would appear that the overall oxygen penetration (intragranular and grain boundary) was very similar at 482°C and 566°C - about 0.13-mm. After the exposure at 615°C the penetration sharply increased to a value of about 0.25-mm.

Conclusions

1. Oxygen levels up 0.25% had no significant effect on the strength-ductility relationship of aged TIMETAL•21S. Higher oxygen levels degrade ductility.

2. Increasing oxygen decreases the work hardening capability of annealed sheet material of the alloy. This could adversely effect some aspects of formability.

3. Oxygen absorption at the surface during exposure in air at elevated temperature degrades tensile ductility. The magnitude of the effect in sheet is dependent on the exposure time and temperature and on sheet thickness.

4. After a suitable heat treatment TIMETAL•21S is metallurgically stable for at least 1000 hours at temperatures up to 615°C.

Reference

1. P. J. Bania and W. M. Parris, "Beta-21S: A High Temperature Metastable Beta Titanium Alloy", Proceedings, 1991 TDA Conference, p. 784.

2. J. S. Grauman, "Corrosion Behavior of TIMETAL•21S for Non-Aerospace Applications", 7th World Conference.

MICROSTRUCTURAL STABILITY OF BETA 21S

M.W. Mahoney, P.L. Martin and D.A. Hardwick

Rockwell International Science Center
1049 Camino Dos Rios
Thousand Oaks, CA 91360

Abstract

The relatively new titanium alloy Beta 21S (Ti-15Mo-3Nb-3Al-0.2Si w/o) has found application as a high temperature matrix material for composite development. The complex response of metal matrix composite (MMC) structures during excursions into creep and thermal mechanical fatigue regimes requires knowledge of the microstructure/property relationships of the monolithic matrix material. Precipitation processes leading to significant property changes can occur in titanium alloys containing large amounts of the retained high temperature β phase. Beta-21S is a metastable beta alloy and thus an understanding of microstructural development as a function of thermal exposure below the beta transus temperature is essential for understanding the mechanical response of any MMC based on this alloy. This study was undertaken to examine the microstructure of β-21S following exposure to temperatures in the range 430°C to 700°C as a function of time following solution treatment at 815°C.

Metallographic results illustrate the metastable nature of β-21S on exposure at temperatures below the beta transus. This is reflected in the morphology and volume fraction of the alpha phase in the beta matrix. Following heat treatments at 430°C, homogeneously nucleated, very fine alpha phase was observed and upon further aging the development of grain boundary precipitates and precipitate-free zones resulted in a nonuniform distribution of alpha. At the intermediate temperatures of 538°C and 650°C, a heterogeneous nucleation occurs but with continued growth resulted in a more uniform distribution of alpha phase. At the highest aging temperature of 705°C, precipitation of alpha phase again resulted in a nonuniform distribution of this phase. These precipitate distributions can be understood through consideration of the relationships between alpha phase nucleation sites, precipitation kinetics, and the driving force for precipitation.

Introduction

Beta 21S (Ti-15Mo-3Nb-3Al-0.2Si w/o) was developed to be roughly equivalent to Ti-15V-3Cr-3Sn-3Al (Ti-15-3) in terms of processing and properties but with

Titanium '92
Science and Technology
Edited by F.H. Froes and I. Caplan
The Minerals, Metals & Materials Society, 1993

significantly improved oxidation resistance (1). The high refractory metal content of the alloy results in a relatively high density compared to an alloy such as conventional Ti-6Al-4V, 4.94 g/cc vs. 4.45 g/cc. However, its exceptional oxidation resistance makes the β-21S alloy particularly suitable for use as the matrix alloy in a metal matrix composite designed for exposure to elevated temperatures. The maximum temperature of usage for any composite material will be a function of a number of variables including alloy stability at temperature, which is the subject of this paper.

Strengthening during the aging of titanium alloys is due to alpha phase precipitation, with the strength level controlled by the size, shape, and volume fraction of these precipitates (2). In addition, early work on Ti alloy development revealed that, for long-term, elevated-temperature applications, alloys with little or no beta phase performed better than alpha + beta alloys. This conclusion was a direct consequence of the thermal instabilities exhibited by the beta phase; thermal decomposition of the beta during long-term exposures resulted in changes in mechanical properties (3). An understanding of the microstructural stability of the monolithic β-21S matrix alloy subjected to elevated temperature long-term exposures will provide a fundamental basis for interpreting the behavioral response of composites based on this alloy.

Experimental Approach

The alloy was obtained from Timet Corp., Henderson, NV, as a 0.5 mm thick sheet in the mill annealed condition. The sheet had been rolled from an ingot (Heat G-1664) that had the average chemistry given in Table 1. All samples were first solution treated at 815°C/15 min. in a flowing argon environment and then water quenched. Subsequent high temperature aging treatments were also performed in an inert environment followed by a water quench. This rapid cooling normalized the influence of cooling rate effects, which could be an additional important issue for some heat treatments. The inert environment prevented the ingress of oxygen and its possible influence on the microstructural stability. To further remove any question of environmental effects, all micrographs were taken from the center of the through thickness orientation.

Table I Chemical Composition (in wt%) of Beta 21S

Ti	Mo	Nb	Al	Si	Fe	C	O	N	H
bal	15.0	2.94	3.07	0.20	0.104	0.22	0.121	0.005	0.0023

A sequence of high temperature aging treatments was performed to determine alpha phase precipitation and morphology as a function of temperature (430°C, 538°C, 650°C, and 705°C) and time (1,8,48, and 96 hours). Obviously, all microstructures observed cannot be presented within the confines of this paper, but representative illustrations are presented. Due to the extreme differences in the alpha phase morphologies, sample preparation and etching procedures were not constant. Where necessary, different metallographic procedures were developed to highlight the alpha phase precipitation. Corresponding Knoop hardness values (500 gm load) help to quantitatively illustrate the effects on gross mechanical response.

Results and Discussions

The β–21S solution treated (815°C) microstructure is shown in three dimensions in Fig. 1a with the TS orientation under Nomarski illumination shown in Fig. 1b. The TS orientation was the standard adopted for metallurgical examination. The fine apparent precipitate is an etch pitting artifact associated with sample preparation. The material has a relatively equiaxed microstructure with an average grain size of 20-30 μm. All samples were heat treated to this condition prior to aging. Knoop hardness for this annealed condition averaged 270.

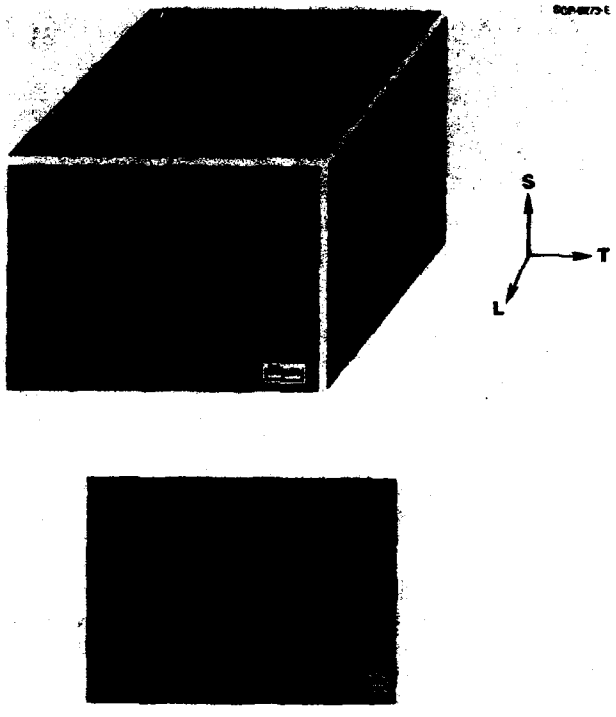


Figure 1 Solution treated (810°C/15 min) microstructure of β–21S a) illustrating the equiaxed geometry of the starting microstructure and b) Nomarski illumination of the TS orientation.

Figure 2 is a sequence of micrographs for β–21S aged at 430°C for times from 1 hour to 96 hours. After 1 hour at temperature, there is some evidence of alpha phase within grains. After 8 hours, precipitate nucleation becomes more evident as the grain interiors etch to a gray appearance indicating the presence of very fine alpha precipitates. After 48 hours, it is clear that alpha precipitation has also been proceeding along the grain boundaries. Presumably, the alpha phase had been precipitating at grain boundaries from the onset of aging but the very fine precipitate was masked by etching of the boundary itself. This is a classical example of homogeneous nucleation of precipitates at lattice defect sites within grain interiors and heterogeneously at grain boundaries. Adjacent to the grain

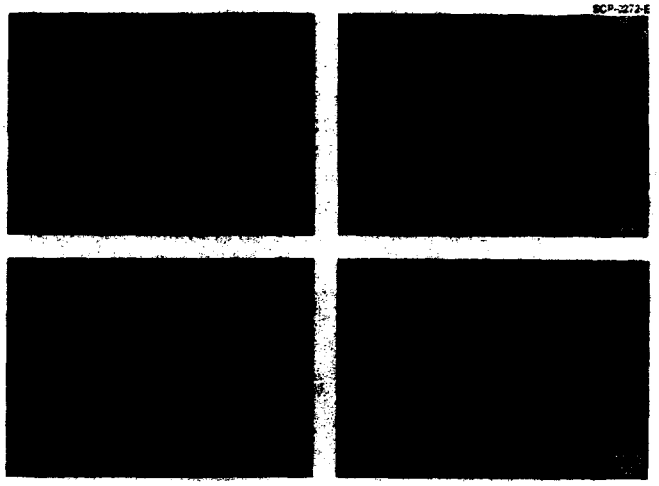


Fig. 2 Metallography illustrating the alpha phase precipitate morphology in β-21S at 430°C for times of a)1 hour, b) 8 hours, c) 48 hours, and d) 96 hours.

boundaries a precipitate free zone exists. It is postulated that within this zone, lattice defects (such as vacancies) diffuse to the boundaries, effectively eliminating precipitate nucleation sites. Therefore, the nucleation of alpha is either sluggish or nonexistent within this region, as evidenced by the presence of precipitate free zones even after 96 hours at 430°C.

Knoop hardness values are plotted in Fig. 3 as a function of temperature and aging time. Precipitation kinetics at 430°C are slow resulting in long times prior to achieving peak hardness. In this case, atomic motion is so slow that appreciable precipitation occurs only after extended aging times but to quite high hardness values. The lack of α precipitates near the β grain boundaries will lead to a locally softer region and potentially strain localization. Lower ductilities and "intergranular" fracture might be expected As pointed out by Williams et al. (2), numerous investigators have noted the formation of omega phase with aging of Ti-Mo alloys and the $\beta \leftrightarrow \omega + \beta$ reaction has been shown to occur rapidly during aging at temperatures between 315°C and 455°C. X-ray diffraction failed to detect ω in β-21S following aging at 430°C, but electron diffraction experiments in the TEM may be necessary to rule out its presence.

Figure 4 illustrates microstructures following aging at 538°C for times from 1 to 96 hours. Initially, alpha phase precipitation occurs predominantly at grain boundaries with additional nucleation in the grain interiors. At shorter times, grain boundary precipitation would be anticipated to dominate as the boundary provides a pre-existing surface for nucleation. With this higher temperature resulting in coarser alpha phase, the early nucleation at grain boundaries was more evident than at 430°C. With increasing time at temperature, a gray fine alpha phase develops throughout the grains. There is no evidence of a grain boundary precipitate-free zone. Although the under cooling for alpha phase stability is less at 538°C than at 430°C, the higher diffusivities at 538°C facilitate a more uniform distribution of the alpha phase.

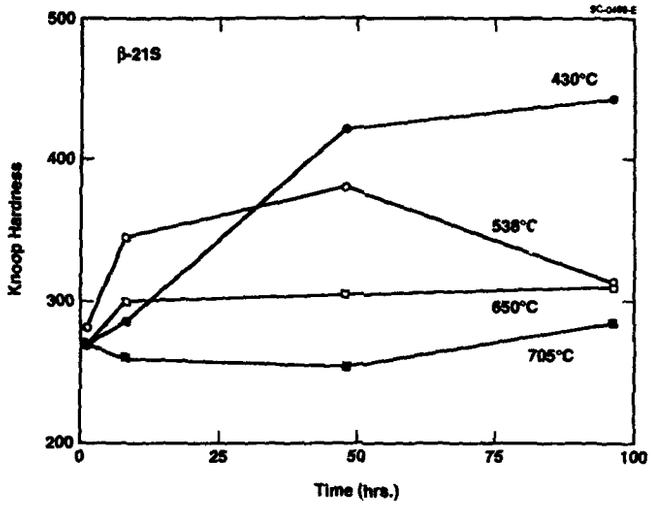


Fig. 3 Knoop hardness for β-21S as a function of aging time and temperature.

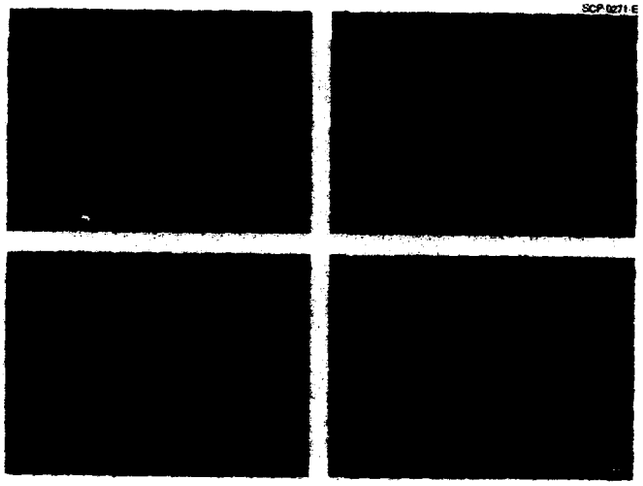


Fig. 4 Metallography illustrating the alpha phase precipitate morphology in β-21S at 538°C for a)1 hour, b) 8 hours, c) 48 hours, and d) 96 hours.

Hardness values as a function of time at 538°C are presented in Fig. 3. The more rapid increase in alpha phase precipitation as the temperature is raised is evident by comparing hardness results after 8 hours exposure at 430°C and 538°C. This is attributed to the increased kinetics of diffusion at the higher temperature. With increasing time, the curves overlap and the coarser alpha phase developed at 538°C results in a lower peak hardness value. At 538°C, the decline in the hardness between 48 and 96 hours is indicative of overaging. There is, however,

no microstructural evidence for this decrease in hardness. At magnifications up to 10,000X in the SEM, there is no apparent microstructural change such as alpha phase coarsening, to account for the hardness decrease. In addition, x-ray diffraction analysis does not illustrate the addition or deletion of any phases. The reason for this hardness decrease is therefore unexplained.

Metallography of samples aged at 650°C for 1 to 96 hours is shown in Fig. 5. Heterogeneous nucleation of the alpha phase is evident after one hour with significant growth at selected grain boundaries. With sufficient undercooling below the beta transus but at high enough temperature for rapid diffusion, a relatively uniform distribution of coarse acicular alpha phase develops quite rapidly. The volume fraction of alpha phase increases with aging time beyond 8 hours but clearly a relatively stable microstructure is developed between 8 and 48 hours. Hardness results confirm these observations (Fig. 3) with an initial increase in hardness up to 8 hours followed by essentially steady state conditions with only slight increases in hardness up to 96 hours at 650°C. For β–21S to be considered for use as a matrix alloy in a composite system, the matrix microstructure should be stabilized by aging at a temperature near 650°C for a period of time less than 48 hours. To further evaluate this hypothesis, samples aged at 650°C for 48 hours were further aged at a sequence of lower temperatures and the microstructure remained unchanged, at least at the scale of optical metallography.

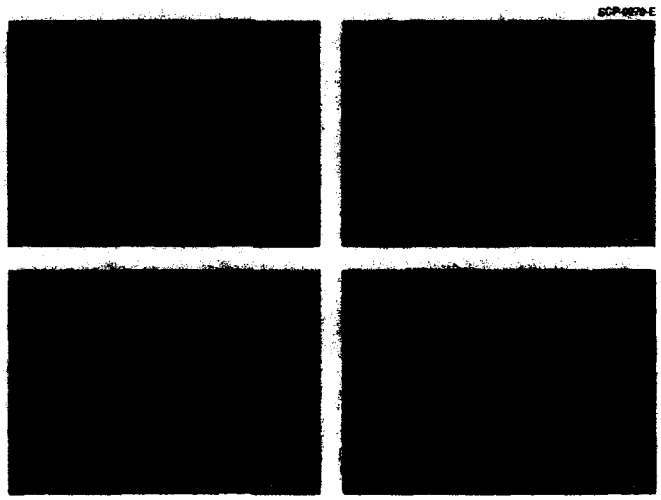


Fig. 5 Metallography illustrating the alpha phase precipitate morphology in β-21S at 650°C for a)1 hour, b) 8 hours, c) 48 hours, and d) 96 hours.

At the highest temperature of investigation, 705°C, a heavy, continuous grain boundary alpha phase formed, Fig. 6. After only 8 hours, almost all grain boundaries are covered by a continuous alpha film. The development of this heavy grain boundary phase created a solute depletion region near grain boundaries and a precipitate-free zone was again established as was observed at lower temperatures. In this case, the precipitate free zone resulted from the

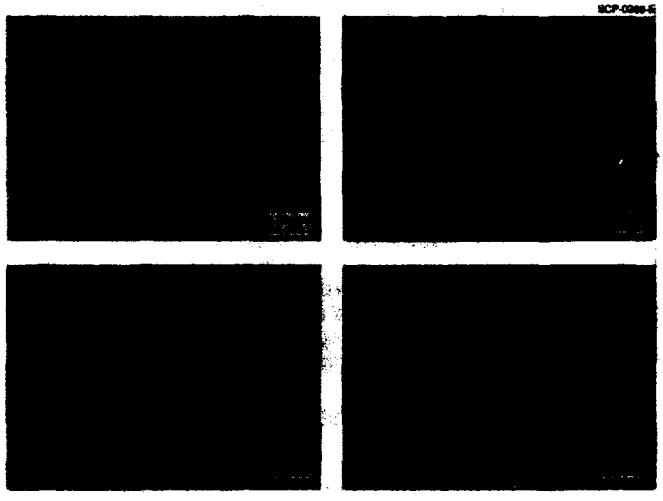


Fig. 6 Metallography illustrating the alpha phase precipitate morphology in β~21S at 705°C for a)1 hour, b) 8 hours, c) 48 hours, and d) 96 hours.

nucleation of α along the grain boundaries and the depletion of the solutes stabilizing the α phase or conversely rejection of the solutes stabilizing the β phase and a corresponding decrease in the chemical potential driving force for alpha nucleation. The precipitate free zones are clearly visible after 48 hours at 705°C; within the grains, a fine alpha phase contrasting with the light colored PFZ's has developed. With additional time at temperature, the intergranular alpha phase coarsens resulting in an acicular alpha after 96 hours. Hardness results for these different microstructures exhibited little variation, Fig. 3. The alpha phase precipitate is presumably too coarse to influence the hardness of the material.

Conclusions

The alpha phase precipitation behavior in β-21S titanium has been demonstrated. Homogeneous nucleation of alpha occurs at 430°C resulting in a very fine alpha phase at grain boundaries and within grains with a precipitate free zone near the grain boundaries. Extended aging at 430°C results in a very high hardness relative to other microstructures. Aging at 538°C produces a more uniform distribution of the alpha phase, as nucleation occurs first at grain boundaries followed by precipitation within grain interiors. The higher diffusion rates at 538°C result in both a more rapid precipitation and growth of alpha and consequently the appearance of a more uniform alpha distribution. Increasing the aging temperature to 650°C reduces the driving force for alpha precipitation with less undercooling below the beta transus. Alpha precipitation at 650°C again initiates at grain boundaries followed by nucleation and growth within grains but at 650°C a coarse acicular alpha results. Aging at 650°C produces a relatively stable microstructure with little additional microstructural change with longer time aging at lower temperatures. At 705°C, the driving force for alpha

precipitation is further reduced. A continuous alpha phase develops rapidly at grain boundaries but alpha precipitation within grains becomes more sluggish. Due to differences in solute concentration, a precipitate free zone is again evident. Hardness measurements show a classical response for strengthening by a nucleation and growth dominated reaction. The highest hardnesses are seen following low temperature aging with overaging noted at intermediate temperatures. High temperature aging results in little strengthening due to the coarseness of the alpha phase.

Acknowledgments

The metallographic specimens for the variety of micrographs presented in this paper were prepared by Mike Calabrese and Mark Wang. The authors are also grateful to Cecil Rhodes for helpful discussions. This work was supported by Rockwell International Science Center IR&D funding.

References

1. P.J. Bania and W.M. Parris, Beta 21S: "A High Temperature Metastable Beta Alloy," Presented at the 119th TMS Annual Meeting, Anaheim, CA, Feb. 1990.

2. J.C. Williams, F.H. Froes, and C.F. Yolton, "Some Observations on the Structure of Ti-11.5 Mo-6 Zr-4.5 Sn (Beta III) as Affected by Processing History," Met. Trans., Vol. 11A, Feb. 7, 1980, pp 356-358.

3. C.G. Rhodes, "Microscopy and Titanium Alloy Development," Applied Metallography, Ed. George F. Vander Voort, Van Nostrand Reinhold Co., New York, 1986, pp. 237-249.

EFFECT OF HEATING-RATE ON THE FORMATION OF (α+β) MICRODUPLEX STRUCTURE IN A Ti-15V-3Cr-3Sn-3Al ALLOY

Kei Ameyama* , Teruhiko Inaba** , Kenji Hirota***, Koichi Hirai**** and Masaharu Tokizane*

* Department of Mechanical Engineering, Ritsumeikan University, Kita-ku, Kyoto, 603 Japan.
** Hyogo Prefectural Institute of Industrial Research, Miki, Hyogo, 673-04 Japan.
*** Miki Netsuren Ind. Co. Ltd., Miki, Hyogo, 673-04 Japan.
**** Graduate Student, Ritsumeikan University, Kita-ku, Kyoto, 603 Japan.

Abstract

The cold rolling and heating-rate effects of β single-phase on α precipitation behavior and the mechanical properties were studied using a Ti-15%V-3%Cr-3%Sn-3%Al (wt%) metastable β alloy. Without cold rolling, preferential α precipitation occurred at the β grain boundaries, and then lath-shaped (heating-rate > $1Ks^{-1}$) or triangular-shaped (heating-rate < $0.1Ks^{-1}$) α precipitated in the β grains. The three dimensional shape of the triangular-α phase was a triangular pyramid consisting of three α precipitates with unique orientation relationships. Cold rolling of the β single-phase had a considerable effect on the resulting (α+β) structures. When the amount of cold rolling was less than 50%, preferential precipitation of α occurred at dislocations in the β grains, as well as at the β grain boundaries. With an increase in the amount of cold rolling, α precipitation took place predominantly at β subgrain boundary nodes which were formed through recovery of the deformed β phase during heating to the aging temperature or in the early stage of aging. In heavily cold rolled materials, an (α+β) microduplex structure, which consisted of very fine equiaxed α particles and β subgrains, was obtained. The heating-rate of cold rolled β phase to the aging temperature influenced on morphology of α precipitates and mechanical properties, such as tensile strength and elongation. The mechanical properties were improved by the formation of the (α+β) microduplex structure.

Introduction

In Ti-15V-3Cr-3Sn-3Al alloy the mechanical properties and age-hardenability have been the subject of many research papers [1-9]. It is well known that cold rolling and aging provide conditions for very fine precipitation of the α (hcp) phase in β (bcc) grains and improve mechanical properties, such as tensile strength. Recently, the authors reported that formation of (α+β) microduplex structure improves the mechanical properties, such as tensile strength and elongation, in metastable β alloys [8,9]. However, the effect of heating-rate on the microstructure and the mechanical properties are not clear yet. The objective of the present paper is to elucidate the formation process of the (α+β) two-phase structure and to examine mechanical properties with emphasis on changes in the microstructure under various heating-rates.

Experimental procedure

The chemical composition of the material is shown in Table 1. The material was solution treated in an Ar gas atmosphere at 1073K (above the β transus temperature) for 1.8ks and then water quenched to produce β single-phase structure. The average β grain size was approximately 80μm. The

Titanium '92
Science and Technology
Edited by F.H. Froes and I. Caplan
The Minerals, Metals & Materials Society, 1993

materials were then cold rolled by 0% to 90% and aged for time periods ranging from 0.6 to 86.4 ks, in Ar gas atmospheres, mainly at 873K under various heating-rates.

Thin foils for TEM were prepared using an ion milling machine. The foils were examined at 200kV. Materials for tensile testing were spark cut from 1 mm thick plate to 2mm in gauge width and 6mm in gauge length, after aging. Tensile tests were done on an Instron universal testing machine with a cross head speed of 8.3μm s^{-1} (0.5mm min^{-1}).

Table 1. Chemical composition. (mass%)

V	Cr	Sn	Al	Fe	O	N	H	Ti
15.27	3.05	3.03	3.06	0.165	0.112	0.0055	<0.001	bal.

Results and discussion

Undeformed materials

Figure 1(a) and (b) show a SEM micrograph (a) and an optical micrograph (b) of the materials aged at 873K for (a):0.6ks (heating-rate, 0.05Ks^{-1}) and (b): 50.4ks (3Ks^{-1}). Triangular-shaped α precipitates were observed in (a) while well known lath-shaped α in (b). The triangular-shaped α precipitates appeared when the heating-rate was less than 0.1Ks^{-1} or when the material was heat treated by two step aging at 573K and 813K. Figure 2(a) shows a TEM micrograph of a triangular-shaped α precipitate observed in a material heat treated by two step aging; i.e., aged at 573K for 180ks and then quenched to R.T. and again heated to 813K under the heating-rate of 0.1Ks^{-1} and held for 3.6ks. As can be seen, the triangular-shaped α is consisted of three α parts. Each α segments hold not only Burgers orientation relationship, i.e., $(110)_\beta/(0001)_\alpha$, $[\bar{1}11]_\beta/[\bar{2}110]_\alpha$, with matrix β phase but also near twin relationship with the adjoining α segments. Only the limited Burgers variants of the α phase are able to satisfy such a crystallographic rule [10]. Fig.2(b) shows a schematic drawing of three dimensional shape of the triangular-shape α phase. It is a triangular pyramid with the axis parallel to a common closed-packed parallel direction (e.g. $[\bar{1}11]_\beta/[\bar{2}110]_\alpha$) in the three α segments and the habit planes close to $\{11\ 11\ 13\}_\beta$. The triangular-shaped α precipitates were observed only in the materials without cold rolling.

Cold rolled materials

Precipitation of α from the cold rolled β matrix was observed to be extremely rapid [9]. The fast kinetics of α precipitation in the present alloy has been observed, as well, in other (α+β) titanium alloys. It has been explained in terms of heterogeneous nucleation on the pre-existing ω phase and/or on the dislocations [4,8,14-16]. Figure 3 shows SEM micrographs of materials cold rolled by 25% and 80% and aged at 873K for 7.2ks under the heating-rate of 3Ks^{-1}. Preferential α precipitation along β grain boundaries was observed in 25% pre-deformed materials. In addition, the 25% pre-deformed material had finely dispersed α precipitates within the β grains. In the present alloy system, the deformation mechanism is known to be mainly by slip deformation and partly by mechanical twinning [11-13]. Therefore, the wavy lines of α precipitates shown in Fig.3(a) are presumed to be predominant α precipitation at slip bands and a few mechanical twins. On the other hand, grain boundary α precipitation was not observed clearly and very fine α precipitates dispersed homogeneously in the 80% pre-deformed material (Fig.3(b)). Figure 4 shows a bright field TEM micrograph and Micro-Beam diffraction patterns of a material cold rolled by 80% and aged at 873K for 7.2ks under the heating rate of 3Ks^{-1}. The Micro-Beam diffraction patterns were taken from β subgrains marked a to e in the micrograph. The micrograph shows fine (α+β) microduplex structure of equiaxed grains of α and β. From the Micro-Beam diffraction patterns, it is obvious that the matrix β grains had almost the same orientation. Thus, the β matrix was subgrain structure, and no evidence for recrystallization (i.e., high angle β grain boundaries) was found.

During heating to the aging temperature and in the early stages of aging, recovery of the deformed structure proceeded and formed a recovered dislocation structure. The (α+β) microduplex



Fig.1 (a):SEM micrograph and (b): Optical micrograph of the materials aged at 873K for (a):0.6ks (heating-rate, $0.05Ks^{-1}$) and (b): 50.4ks ($3Ks^{-1}$).

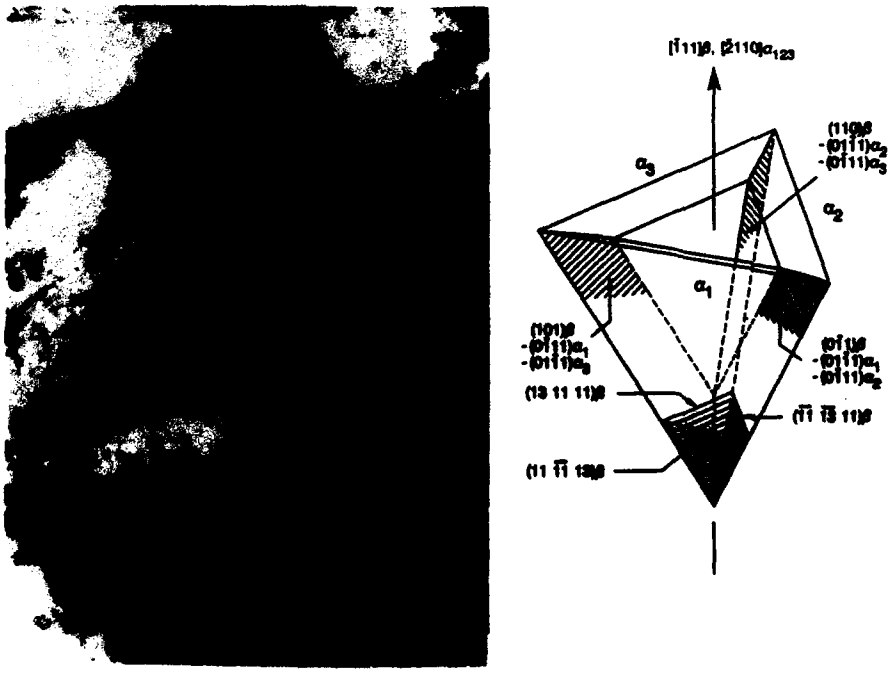


Fig.2 (a):TEM micrograph of a triangular-shaped α precipitate obeserved in a material heat treated by two step aging. Aged at 573K for 180ks and then quenched to R.T. and again heated to 813K under the heating-rate of $0.1Ks^{-1}$ and held for 3.6ks. (b):Schematic drawing of three dimensional shape of the triangular-shape α phase.

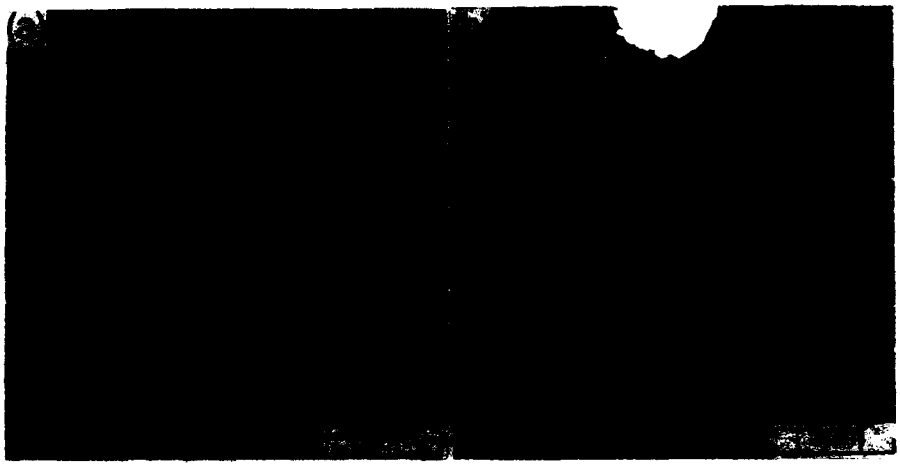


Fig.3 SEM micrographs of materials cold rolled by (a):25% and (b):80% and aged at 873K for 7.2ks under the heating-rate of $3Ks^{-1}$.



Fig.4 A bright field TEM micrograph and Micro-Beam diffraction patterns from grains marked a to e in the TEM micrograph of a material cold rolled by 80% and aged at 873K for 7.2ks under the heating rate of $3Ks^{-1}$.

structure is considered to be formed by α nucleation at subgrain boundary nodes in the subgrain structure. Equiaxed α and β grains observed in the microduplex structure shown in Fig.4 strongly supports α nucleation at β subgrain boundary nodes but not at any isolated dislocations, because α particles which nucleate at re-arranged dislocation arrays have lath-shaped morphology. A schematic illustration of the formation process of (α+β) microduplex structure is shown in Figure 5. Since the (α+β) microduplex structure in the present alloy is quite similar to the (α+γ) microduplex structure in two-phase stainless steels [18,19], the (α+β) microduplex structure may be accomplished in the manner of two-phase stainless steels, which has been confirmed. Hence, it can be concluded that microstructures, such as (α+β) microduplex structure or (lath α +β) two-phase structure, depend strongly on the recovering process of the deformed β matrix. When deformation of the matrix is limited, slow progress of β matrix recovery leads to preferential α nucleation at re-arranged dislocation arrays; however, when the deformation is significant, β subgrain formation precedes α precipitation and α particles nucleate subsequently at β subgrain boundary nodes. This formation process for the microduplex structure has also been reported for (α+γ) two-phase stainless steels [18-20], Ti-15Mo-5Zr-3Al and Ti-12Mo-6Zr-5Sn alloys [8].

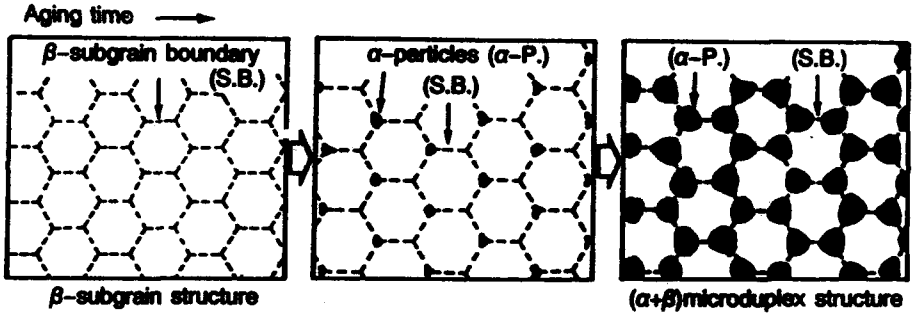


Fig.5 A schematic illustration of the formation process of (α+β) microduplex structure.

Figure 6 shows the effect of heating-rate on the microstructure of the materials cold rolled by 5, 50 and 90%, and aged at 873K for 3.6ks. When the heating-rate increased, the α precipitates in cold rolled materials changed to coarse. The effect of heating-rate on the α precipitation is more remarkable in slightly deformed materials. Only a few scattered α particles were observed in the 5% cold rolled material heated by $10Ks^{-1}$. In the 90% cold rolled material, although the (α+β) microduplex structure was formed in all materials examined, a small amount of (lath α+β) two-phase structure was also observed in materials heated by low heating-rates. The amount of the (lath α+β) two-phase structure was decreased with increasing heating-rate, and disappeared in the material heated by $10Ks^{-1}$. Figure 7 shows the change in α and β grain size of the (α+β) microduplex structure as a function of the heating-rate in the 90% cold rolled materials aged at 873K for 3.6ks. The size of (α+β) microduplex structure increases with increasing heating-rate. Figure 8 shows the tensile strength and elongation of materials deformed and aged at 873K for 3.6 ks under various heating-rates as a function of deformation. Microstructural difference shown in Fig.6 resulted in change in the mechanical properties. The tensile strength increased with increasing cold rolling, while the elongation dropped sharply with slight deformation. Coarser (α+β) microduplex structure in the 90% cold rolled materials improved the elongation a little.

It is worthy of note that heavy deformation such as 90% cold rolling gave highest tensile strength but did not spoil elongation. In addition, the elongation was improved a little by higher heating-rate due to the formation of coarse (α+β) microduplex structure in the 90% cold rolled material. In the slightly deformed materials, the mechanical properties were very sensitive to the heating-rate since the heating-rate produced a great effect on the microstructure, as shown in Fig.6.

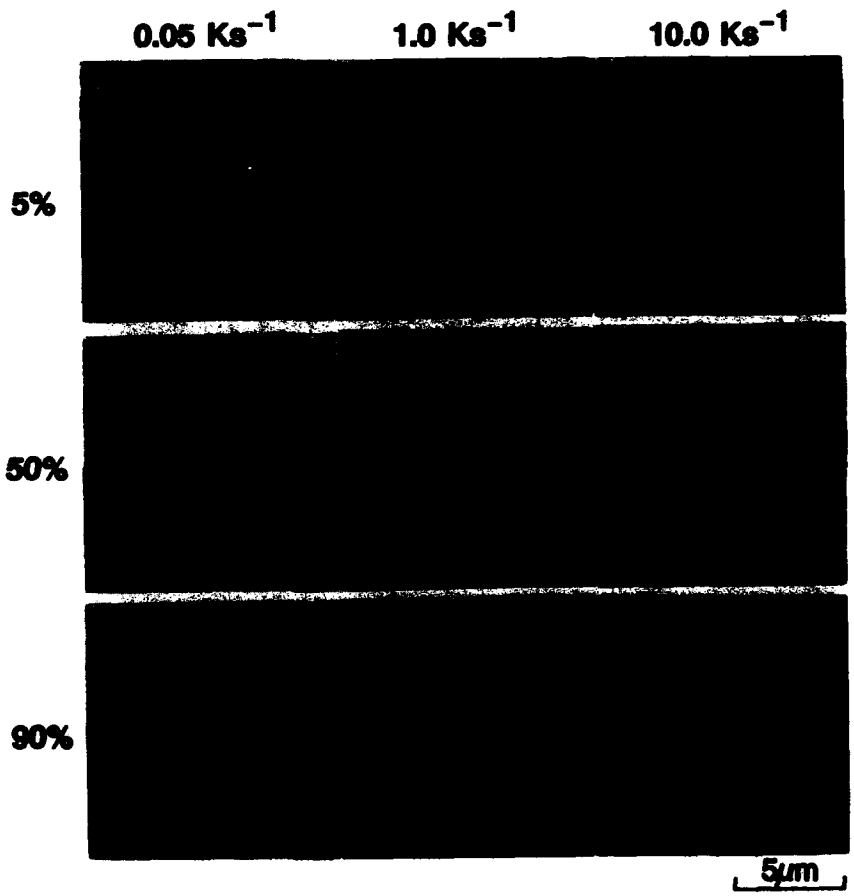


Fig.6 The effect of heating-rate on the microstructure of the materials aged at 873K for 3.6ks. (a), (b), (c): 5% cold rolled and heated by 0.05, 1.0 and 10 Ks^{-1}, respectively. (d), (e), (f): 50% cold rolled and heated by 0.05, 1.0 and 10 Ks^{-1}, respectively. (g), (h), (i): 90% cold rolled and heated by 0.05, 1.0 and 10 Ks^{-1}, respectively.

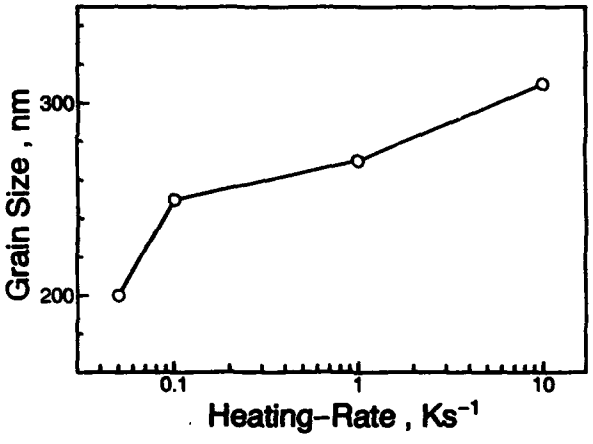


Fig.7 Change in α and β grain size of the (α+β) microduplex structure as a function of the heating-rate in the 90% cold rolled materials aged at 873K for 3.6ks.

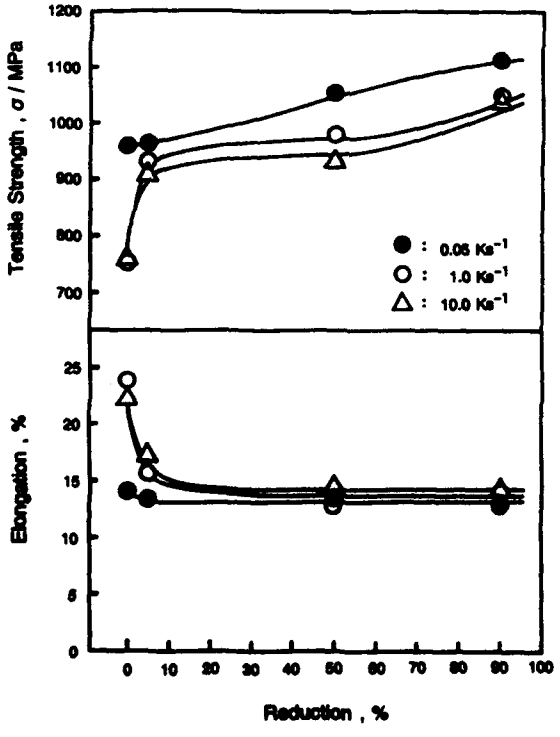


Fig.8 Changes in tensile strength and elongation as a function of deformation. Materials were aged at 873K for 3.6 ks under the heating-rates of 0.05, 1.0 and 10 Ks^{-1}.

In conclusion, (α+β) microduplex structure is considered to be quite important in improving both the tensile strength and ductility of the present alloy. The heating-rate has effects on both microstructure and mechanical property. In addition, the microduplex structure is known to generate superplastic deformation behavior in two-phase materials, such as (α+γ) two-phase stainless steels. Thus, future studies on superplastic deformation and wider application are anticipated for the present alloy.

References

1) H.W.Rosenberg: J.Metals, 35(1983), 30.
2) M.Okada, D.Banerjee and J.C.Williams: *Titanium Science and Technology*, Ed.by G.Lutjering, U.Zwicker and W.Bunk, D.G.M, Oberusel, FRG(1985), 1835.
3) M.A.Iman and B.B.Rath: *Sixth World Conference on Titanium*, Ed.by P.Lacombe, R.Tricot and G.Beranger, Cannes(1988), 1513.
4) H.W.Rosenberg: *Beta Titanium Alloys in 80's*, Ed.by R.R.Boyer and H.R.Rosenberg, AIME(1984), 409.
5) T.Horiya, H.G.Suzuki and T.Kishi: *Tetsu-to-Hagane*, 76(1990), 932.
6) N.Niwa, T.Demura and K.Ito: *Tetsu-to-Hagane*, 76(1990), 910.
7) C.Ouchi, H.Suenaga and Y.Kohsaka: *Sixth World Conference on Titanium*, Ed.by P.Lacombe, R.Tricot and G.Beranger, Cannes(1988), 819.
8) K.Ameyama, K.Yamashita, T.Inaba and M.Tokizane: J.Jpn.Inst.Met., 53 (1989), 1098.
9) T.Inaba, K.Ameyama and M.Tokizane: ISIJ International, 31(1991), 792.
10) T.Inaba, K.Ameyama and M.Tokizane: to be published in J.Jpn.Inst.Met., 56(1992).
11) H.Ohyama, H.Nakamori, Y.Ashida and T.Maki:ISIJ International, 32(1992),222.
12) M.Morinaga, N.Yukawa, T.Maya, K.Sone and H.Adachi: *Sixth World Conference on Titanium*, Ed.by P.Lacombe, R.Tricot and G.Beranger, Cannes(1988), 1601.
13) M.Niinomi, T.Kobayashi, I.Inagaki and A.W.Thompson: Met.Trans., 21A(1990), 1733.
14) T.Inaba, K.Ameyama, M.Tokizane, Y.Hayashi and G.Hashizume : ELECTRON-MICROSCOPY, 24(1989), 171.
15) T.Inaba, K.Ameyama and M.Tokizane: J.Jpn.Inst.Met.,53 (1989), 1188.
16) F.H.Froes, C.F.Yolton, J.M.Capanos, M.G.H.Wells and J.C. Williams: Met.Trans.,11A (1980), 21.
17) W.G.Burgers: Physica, 1(1934), 561.
18) K.Ameyama, K.Murakami, T.Maki and I.Tamura: J.Jpn.Inst.Met., 49(1985), 1045.
19) K.Ameyama, H.Matsuoka, A.Miyazaki and M.Tokizane: J.Jpn.Inst.Met., 53(1989), 991.
20) K.Tsuzaki, H.Matsuyama, M.Nagao and T.Maki: Mat.Trans.JIM, 31 (1990), 983.

EFFECT OF COLD WORK AND HEAT TREATMENT IN ALPHA REGION ON MECHANICAL PROPERTIES OF Ti-15-3 ALLOY

M. A. Imam, P. K. Poulose*, and B. B. Rath

Naval Research Laboratory
Washington, DC 20375-5000

*University of the District of Columbia
Department of Mechanical Engineering
Washington, DC 20008

Abstract

The beta titanium alloys such as Ti-15-3 have great potential for developing higher strength and fracture toughness by introducing suitable microstructures through controlled transformation of beta phase. The structure and distribution of transformed beta such as alpha precipitates depend on the alloy composition, aging time and temperature, and prior history of the alloy. The present study shows the effect of cold workings on subsequent transformation characteristics and mechanical properties of the alloy. The test results show that the vacancies and dislocation structures produced by cold working provide nucleation sites, and hence the precipitation is relatively homogeneous. At any given temperature the transformation rate is increased by cold working due to faster nucleation and thus strengthening can be achieved in a shorter period of time.

Introduction

Titanium alloys have come to prominence as aircraft structural materials because of their high strength-to-weight ratio and excellent corrosion resistance. Based on the microstructures that can be produced by alloy additions, titanium alloys are grouped as alpha, alpha-beta and beta alloys. Among the titanium alloys, beta titanium alloys are considered more favorably as candidate for aerospace application in thin sheet form because of their good cold formability in spite of high cost of these alloys. Beta alloys can be heat treated to attain wide range of strength and ductility in thin as well as in thick sections.

The transformation characteristics of the beta phase (metastable) determine the variations of the mechanical properties of these alloys. Although the stable phase at room temperature is alpha, the metastable beta is retained even after slow cooling from above the beta transus temperature. The beta

Titanium '92
Science and Technology
Edited by F.H. Froes and I. Caplan
The Minerals, Metals & Materials Society, 1993

phase, having body centered cubic structure, is very ductile compared to the hexagonal closed packed alpha phase. The transformation of beta phase is sluggish and can be controlled to produce desired properties. The structure of the transformed products and their distribution depend on the composition of the alloy and the aging conditions. During aging at high temperature, alpha is precipitated directly from beta by heterogeneous nucleation along grain boundaries and dislocations. At low temperature the transformation product is beta prime in solute-rich alloys similar to Ti-15-3, but in less rich alloys it has been found to be omega phase [1,2]. The precipitation of beta prime as well as omega is homogeneous. The low temperature precipitate particles are fine and the precipitation is intense; hence, the alloy hardens rapidly and it becomes brittle. Control of precipitation at the early stages of low temperature aging to achieve acceptable strength and toughness is difficult. Several studies have indicated that two step aging processes yield desirable properties [3-5]. A step aging involving a low temperature aging followed by high temperature aging produces homogeneous low temperature precipitation initially, which dissolves at high temperature giving rise to in situ precipitation of alpha homogeneously. A high temperature aging followed by a low temperature aging produces coarse alpha precipitation initially, but subsequent low temperature treatment yields finer alpha around larger alpha particles. Both types of step aging treatments yield good strength and toughness characteristics [3,5].

Another possible method of achieving desirable properties with lower aging time periods would be combinations of cold work and high temperature aging. The initial cold work would provide some strengthening and also provide additional nucleation sites at the dislocations produced on cold working, reducing the propensity for formation of alpha along the grain boundaries and avoiding the formation of low temperature brittle phases. Although some studies on this aspect has been attempted [6,7], further investigation of this approach is needed to realize full potential of the alloy.

For the present study, the solute rich Ti-15-3 alloy was chosen to investigate the effect of thermomechanical treatments on the strength and ductility of beta titanium alloys. Its cold formability is excellent, and its mechanical properties are quite sensitive to heat treatments. The effects of various combinations of cold work and heat treatments are discussed.

Experimental Procedure

The material for this study was furnished by Timet corporation in the form of 1.5 in thick hot rolled plates. The chemical composition of the alloy in weight percent was: V=14.79, Al=2.91, Cr=3.06, Sn=3.03, Fe=0.128, O=0.122 and N=0.009. Heat treatments were performed on the material in (a) as-received (hot rolled), (b) 25% cold-worked, and (c) 50% cold-worked conditions. Aging treatments were performed in a salt bath furnace at 480, 540 and 565°C. The progress of aging was studied by hardness measurement using Knoop hardness tester. Tension tests were performed on cylindrical specimens of gauge

length 1 in and diameter of 0.25 in on a screw driven Instron machine. Light, scanning electron and transmission electron microscopic studies were also conducted. Thin films were produced by electrolytic thinning using solution composed of 62.5% methanol, 31% butanol and 6.5% of 70% perchloric acid at 13.9 volts and -40 to -50°C.

Results and Discussion

The progress of hardening for different combinations of cold working and temperature are shown in Fig. 1. Although the

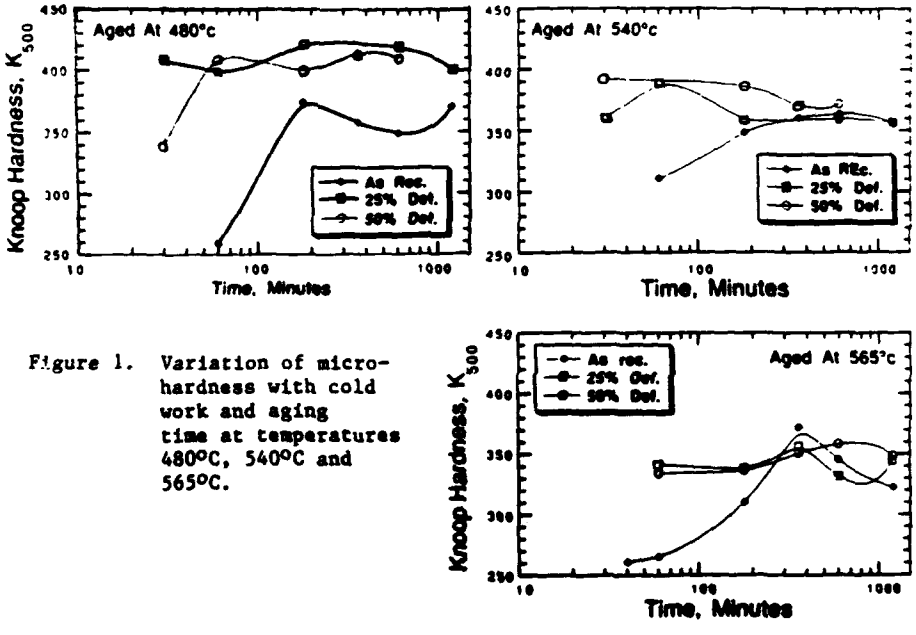


Figure 1. Variation of microhardness with cold work and aging time at temperatures 480°C, 540°C and 565°C.

initial hardness is increased by cold working, the peak hardness is essentially the same for a given temperature. However, cold working increased the rate of hardening, as seen by the earlier peak in cold worked conditions. The difference in the hardening rates between 25% and 50% cold worked alloys is not significant during aging at 540 and 560°C. Most of the hardening seems to have taken place at a very early stage due to high diffusivity at these temperatures. The peak hardness is higher at lower temperature, as expected.

The results of tension tests are given in Table 1. The specimens cold worked 25% and 50%, and aged at 480°C failed at the grip and appeared to be very brittle. The strength and ductility values of hot worked (as received) specimen after heat treatment conform to the results of earlier studies [3]. The increase in strength due to cold working and increase in hardening rate is also evidenced by the tension test results. All aging conditions exhibited low strain hardening, indicated by the small differences between yield strength and tensile

strength values. For a given strength the ductility values were comparable, and no one treatment could be considered superior to another. The hardness values are not very sensitive to changes in tensile properties. At 540°C the 50% cold worked alloy exhibits a higher strength than the 25% cold worked alloy after 3 hours of aging although the hardness values are essentially the same. This difference is observed after aging at 565°C as well.

Table 1. Tensile Properties of Ti-15-3 After Aging.

Cold Work %	Temp. °C	Time hrs.	Yield Strength MPa	Tensile Strength MPa	Elongation %
0	480	20	1306	1363	7.0
0	540	3	929	1053	10.3
25	540	3	1215	1299	6.1
50	540	3	1264	1349	4.9
0	565	3	850	899	19.7
25	565	3	1075	1152	8.3
50	565	3	1145	1222	6.0

The light micrograph of the alloy in hot rolled condition (Fig. 2) indicates that the material was completely recrystallized. Microstructures of hot rolled alloy after aging at 540°C and 565°C show preferred precipitation along grain boundaries. The transmission micrograph of hot rolled unaged alloy shows that

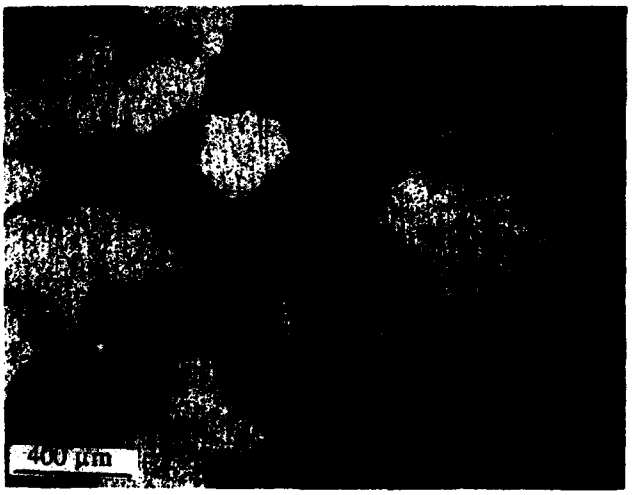


Figure 2. Recrystallized grain structure of the alloy in as received condition.

the rate of cooling after hot working did not produce any precipitation. However, some specimens showed a mottled appearance indicating beginning of nucleation of the low temperature phase (Fig. 3). Aging did not result in recrystallization at any temperature. This is evident from the

electron micrograph, which shows that the dense dislocation structures are retained in the aged alloys (Fig. 4). The grain

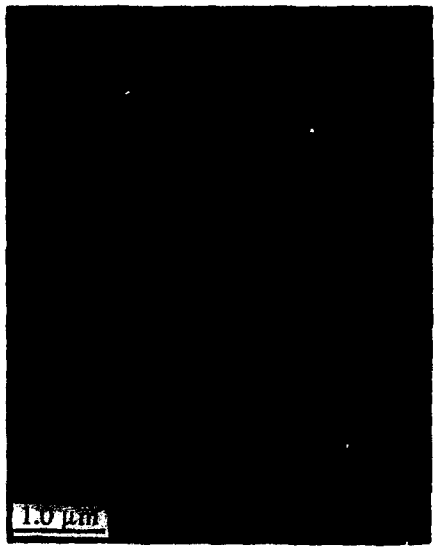


Figure 3. TEM showing mottled structure in the as received condition.



Figure 4. Dislocation structure in 50% C·R sample after aging for 1 hr. at 565°C.

boundaries were blurred in the cold worked structures. The precipitation appeared to be uniform. At any given temperature and time the precipitates were finer in the cold worked alloys, and as expected higher temperature aging resulted in larger particles in cold worked structures as well. Fig. 5 compares the effect of cold work on the microstructures. After aging at 565°C the precipitation on the hot rolled alloy is very coarse (Fig. 5a). After 25% cold work (Fig. 5b) the precipitates are smaller and homogeneous, and the dislocations are retained. After 50% cold work the precipitates are finer and homogeneous (Fig. 5c). This compares with the 50% cold worked alloy aged at 480°C (Fig. 5d) where the precipitates are homogeneous and very fine due to lower aging temperature.

Scanning electron microscopic examination of fracture surfaces of tensile specimens showed mixed transgranular and intergranular fracture. A typical fracture surface of an aged alloy is shown in Fig. 6. Fig. 6a shows regions of cleavage and shear. A magnified fractograph of the sheared region showing dimples is given in Fig. 6b. As expected, transgranular dimpled fracture was found to increase with increased dultility.

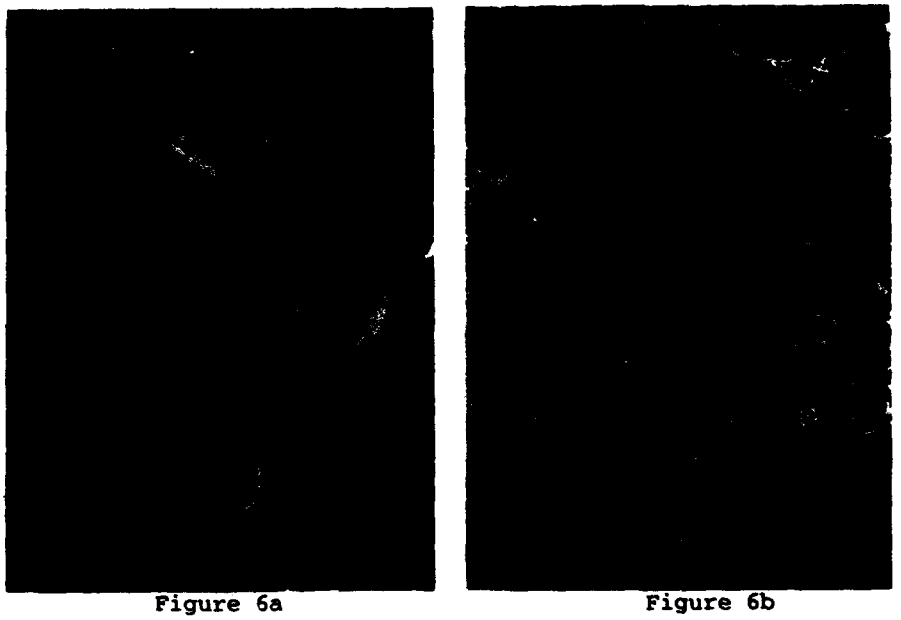


Figure 6a Figure 6b

Figure 6. Scanning electron fractograph of a typical tensile specimen (480°C/20 hrs., 0% C·R). a. Cleavage and shear fracture, b. Magnified region of shear fracture.

The present study shows the effect of cold working on subsequent precipitation characteristics and mechanical properties of the alloy. This approach may be used as an alternative to duplex aging to obtain homogeneous precipitation without precipitating brittle low temperature phases. The test results show that the vacancies and dislocation structures produced by cold working provide nucleation sites, and hence the precipitation is homogeneous. At any given temperature the transformation rate is increased by cold working due to faster nucleation; hence strengthening can be achieved in a shorter period of time. However, an increase in peak strength was not observed due to cold work. No enhancement of ductility was seen either. Duplex aged alloys have shown higher fracture toughness than single-step aged alloys at comparable strength values, even though improvement in ductility was not observed [3,4]. Possible similar effects in cold worked alloys are being investigated. An optimum amount of cold work, if there is any, also has not been established. Additional experiments are being performed using varying amounts of cold reduction.

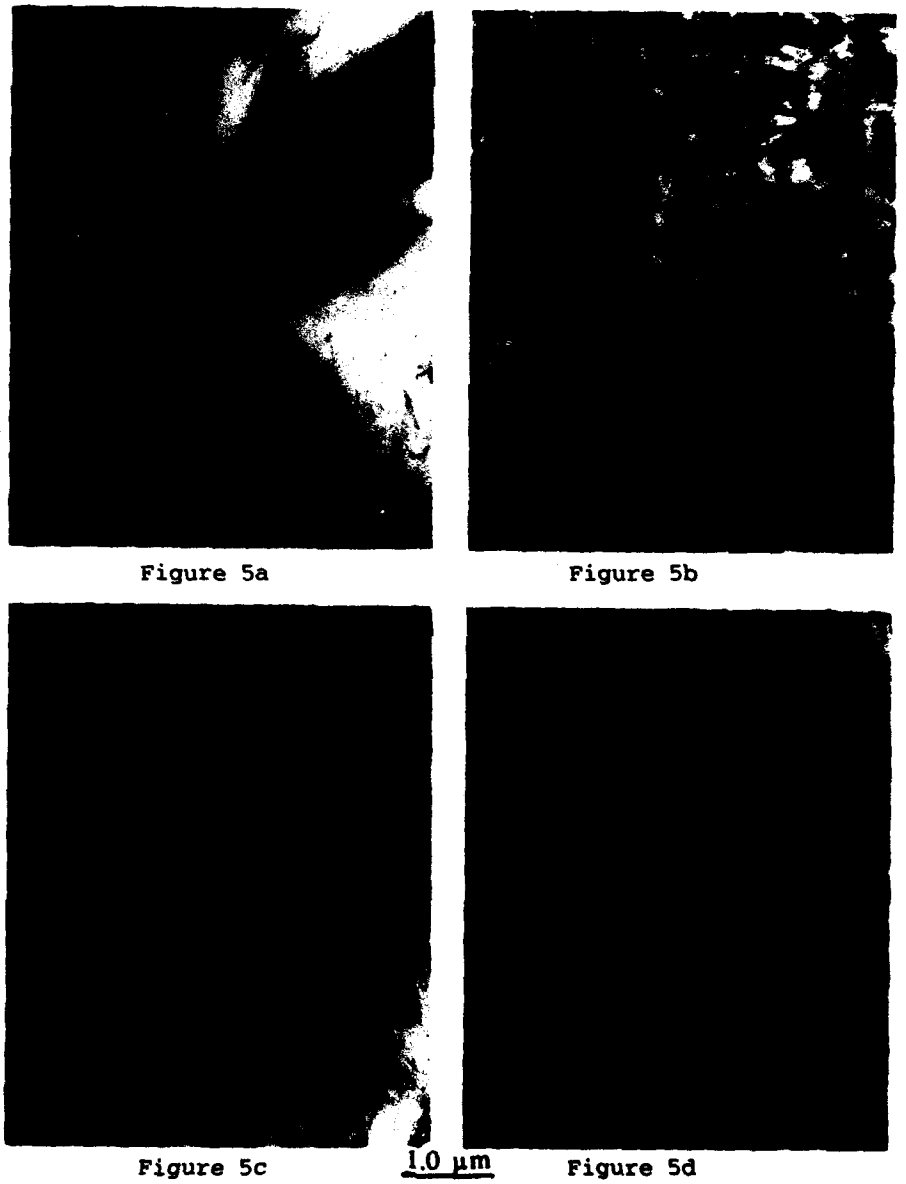


Figure 5a

Figure 5b

Figure 5c

Figure 5d

Figure 5. Alpha phase formation in samples cold rolled (C·R) and aged

a. 20 hrs. at 565°C, 0% C·R
b. 10 hrs. at 565°C, 25% C·R
c. 10 hrs. at 565°C, 50% C·R
d. 10 hrs. at 480°C, 50% C·R

Conclusions

The strengthening of Ti-15-3 alloy by direct aging and aging after cold work was investigated. The results show that:

1. Cold working increases the rate of strengthening, and hence, the aging time can be reduced by prior cold work.
2. The peak strength attained by the aged alloy is unaffected by prior cold work.
3. Perceivable difference does not exist between the ductility of the annealed and cold worked alloy in the peak aged condition.
4. Cold working reduces the tendency for formation of the grain boundary alpha. Cold working produces finer and homogeneous precipitation of alpha.
5. No recrystallization takes place below beta transus temperature.

References

1. F. H. Froes and H. B. Bomberger, The Beta Titanium Alloys, Journal of Metals, (July 1985), 28.

2. T. W. Duerig and J. C. Williams, Microstructure and Properties of Beta Titanium Alloys, (Proc. Sym. on Beta Titanium Alloys in the 80's, AIME, Atlanta, Georgia, March 8, 1983), 19.

3. P. K. Poulose and H. Liebowitz, Improvement of Fracture Toughness in High Strength Beta Titanium Alloys, (Final Technical Report, NAVAIR Contract Number N00019-83-C-0177, 1985).

4. N. Niwa, K. Ito, H. Takatori and H. Sukayama, Influence of Heat Treatment on Microstructure and Mechanical Properties of Ti-15-3 Alloy, (Proc. of the VI Internat. Conf. on Titanium, France, 1988), 1507.

5. M. Okada, Strengthening of Ti-15-3 by Two-Step Aging, ibid, 1625.

6. M. Okada, The Effect of Cold Work and Heat Treatment Conditions on Microstructure and Mechanical Properties of Ti-15V-3al-3Sn-3Cr Alloy, ibid, 205.

7. O. Ouchi, H. Suenaga and Y. Kohsaka, Strengthening Mechanism of Ultra-High Strength Achieved by New Processing in Ti-15%V-3%Cr-3%Sn-3%Al Alloy, ibid, 819.

DEFORMATION BEHAVIOR OF AN AGE-HARDENABLE BETA + ALPHA-TWO TITANIUM ALLOY

L. S. Quattrocchi* and D. A. Koss

Dept. of Materials Science and Engineering
The Pennsylvania State University
University Park, PA 16802

Abstract

The beta Ti alloy Ti-23Nb-11Al (at. pct.) differs from other beta Ti alloys in that it is age-hardenable due to the formation of lath-like, alpha-two precipitates based on Ti_3Al. This study reports the room temperature deformation and slip behavior of the Ti-23Nb-11Al alloy as a function of heat treatment. The results indicate that the formation of the alpha-two precipitates results in not only a large increase in yield stress but also can induce a change in slip mode from *inhomogeneous to uniform slip.*

Introduction

Existing age-hardenable beta Ti alloys depend on the formation of hcp alpha-phase precipitates during the aging of solution-treated material in the 450°-500°C range; see ref. 1, for example. While a range of phase transformations are possible in metastable beta Ti alloys [2], most result in limited ductility or embrittlement, usually due to extremely non-uniform slip. An exception is the behavior of a Ti-7Mo-16Al (at. pct.) alloy aged at ≅ 900°C in which case coarse alpha-two particles in a disordered beta matrix cause a transition to wavy, uniform slip accompanied by an increase in ductility [3]. However, aging at lower temperatures resulted in multiphase microstructures in which ordered B2 and, in some cases, alpha-phase particles were present and embrittlement occurred due to inhomogeneous, planar slip [3,4].

In the present study, we report results on the deformation behavior of a new age-hardenable beta Ti alloy Ti-23Nb-11Al (at.pct.), hereafter referred to as Ti-23-11. This alloy remains disordered upon quenching and readily forms alpha-two particles upon aging at 575°C [5]. The result is pronounced age hardening from temperatures as low as 375°C to as high as 675°C, where an increase of hardness of ≈120kg/mm^2 still occurs [5]. The present study reports the room temperature stress-strain as well as slip behavior of Ti-23-11 compression specimens deformed after the following heat treatments: (1) solution-treated (ST) obtained by quenching from 1000°C, (2) underaged in which ST material was aged at 375°C for 6 hrs., (2) peak-aged which consisted of ST+ 575°C/6 hrs, and (4) an overaged condition resulting from ST + 675°C/6 hrs.

---

* Currently at Pratt and Whitney, East Hartford, CT 06108

Titanium '92
Science and Technology
Edited by F.H. Froes and I. Caplan
The Minerals, Metals & Materials Society, 1993

Experimental

The Ti-23-11 alloy had a composition of Ti-22.8Nb-11.1 Al in at. pct. or Ti-38Nb-5Al in wt. pct. The material contained about 1580 wt. ppm oxygen, 160 wt. ppm nitrogen, and 11 wt. ppm hydrogen. Test specimens were machined from bar stock which was extruded at 1038°C using a 22:1 extrusion ratio. All heat treatments were performed by encapsulating Ta-wrapped specimens in quartz under a partial pressure of high purity argon. The compression specimens were electropolished at -40°C in a methanol, ethylene glycol, perchloric mixture [6] prior to aging.

Mechanical tests were performed at room temperature in compression on cylindrical specimens 6.35 mm in diameter and length at an engineering strain rate of 2×10^{-4}/s. Molydisilicide lubricant was used on the end faces to reduce friction; recent results indicate that this technique effectively produces accurate stress-strain data in compression to strains ≥ 0.5 [7].

Transmission electron microscopy (TEM) examinations were performed on foils thinned by milling using a gun angle of 15° for 10 hours, followed by 2 hours of milling at 5°. Ion milling was performed using a voltage of 3.5 kV and a current of 1mA.

Results and Discussion

Microstructure

The general features of the microstructures of the solution-treated (ST) condition as well as after aging at 575°C for 6 hours are described elsewhere [5]. The observations include the following: (1) upon quenching from 1000°C, TEM indicates that the Ti-23-11 retains a disordered bcc lattice; neither athermal omega or B2 phase were detected [5], (2) upon aging at 575°C, lath-like alpha-two precipitates form with a zig-zag morphology; the precipitates are crystollographically related to the matrix with the Burger's orientation relationship and have an average length of ≅ 170 nm.

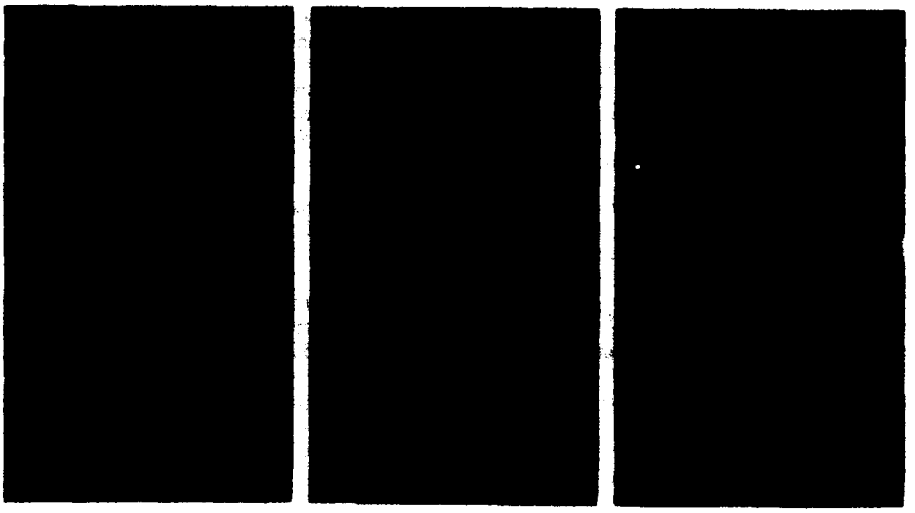


Figure 1 - Centered dark-field image of precipitates in the Ti-23 Nb-11Al alloy quenched from 1000°C and aged at (a) 375°C for 100 hrs, (b) 575°C for 6 hrs, and (c) 675°C for 100 hrs. At 575° and 675°C, the precipitates have been identified as the alpha-two phase.

Figure 1 illustrates the contrast in precipitate size after aging at 375°, 575°, and 675°C; the differences in magnifications should be noted. After aging at 375°C for 100 hrs, a uniform distribution of very *fine*, 5-10 *nm* long precipitates is evident. Bright field imaging of the alloy in this condition suggests that the precipitates appear to have a distinct alignment with each other, probably consistent with the zig-zag morphology seen at 575°C. Although the selected area diffraction patterns (SADP) after aging at 375°C precluded proper indexing, those data are consistent with SADP's obtained after aging at 575°C, where the alpha-two structure is *confirmed*.

After aging at 675°C for 100 hrs, the lath-like precipitates have coarsened to a maximum dimension of about 500 nm with a minor dimension in the 50-100 nm range; see Figure 1c. While they still retain a zig-zag morphology, the interparticle spacings have increased significantly, suggesting a considerably lower strength. On the other hand, growth of the precipitates from approx. 170 nm after 575°C/6 hrs aging to roughly 500 *nm* after 675°C/100 hrs. suggests coarsening is relatively slow in this system.

Precipitation Hardening: Yield Strength

The microstructures shown in Figure 1 suggest that the Ti-23-11 alloy should be age hardenable. As shown in Figure 2, there is a large precipitation hardening response upon aging in the temperature range of 375°C-675°C. It should be noted that, given the six-hour heat treatment, the alloy is underaged at 375°C and overaged at 675°C. The 575°C/6 hr. represents peak hardness, and the yield stress value of ~1270 MPa is about 700 MPa greater than that in the solution-treated condition.

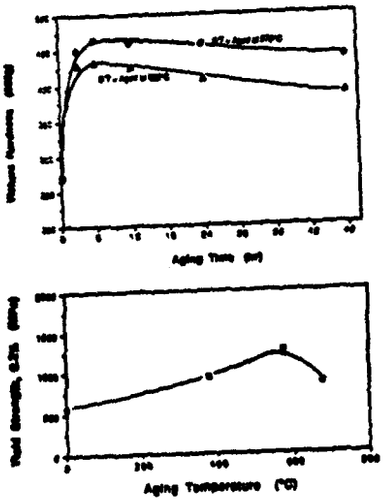


Figure 2 - The age-hardening response of the Ti-23Nb-11Al after quenching from 1100°C.

While we were not able to determine the volume fractions and interparticle spacings of alpha-two particles, the large age-hardening response shown in Figure 2 indicates the effectiveness of alpha-two precipitates in hindering dislocation motion. In the case of "conventional" beta Ti alloys, age hardened by alpha-phase precipitates, the alpha phase is known to be initially softer than the matrix; upon deformation, small alpha-phase particles work harden very rapidly [3,8]. As a result, particle hardening is achieved in large part by relying on the strain hardening of individual alpha-phase particles. In contrast, particle hardening based on alpha-two precipitates introduces an additional strengthening component due the long range order present in the alpha-

two particles. Given the Burgers orientation relationships between the beta matrix and the alpha-two precipitates [5] and the presence of Nb in the precipitates,* we expect that, at small particle sizes, the alpha-two particles will be sheared by slip on the basal planes. Because of the ordered structure, basal slip within Ti_3Al-Nb alpha-two phase should occur by the motion of coupled pairs of $\frac{a}{6}$ <11$\bar{2}$0> dislocations [9,10]. Thus, under conditions where shearing of precipitates is likely [underaged as well as peak-aged conditions], the particle shear process must either preserve long range order by superlattice dislocation motion or create an anti-phase boundary (which would have very high energy [10]) within the alpha-two precipitates. In short, strengthening due to ordered precipitates occurs. Alpha-two precipitates should thus be more effective in strengthening beta Ti alloys than disordered alpha-phase particles.

The Effect of Age-Hardening on Slip Mode

The fine scale of the precipitates, especially after aging at 375°C ($\leq$ 10 nm) suggests that upon yielding, dislocations should shear the precipitate particles, despite their ordered structure. Inhomogeneous (usually) planar slip is characteristic of precipitation-hardened beta Ti alloys when particle shearing occurs (see ref 3, for example). As Figure 3 shows, the Ti-23-11 alloy is no exception. Coarse, inhomogeneous slip is evident in the solution-treated condition as well as after aging at either 375°C or 575°C.

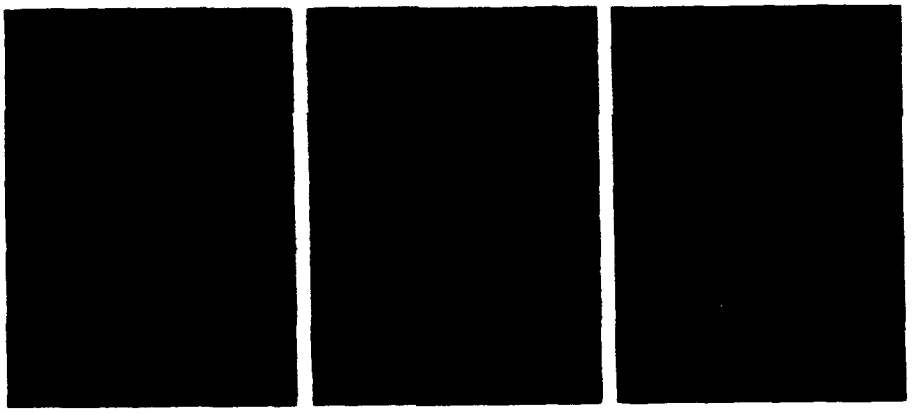


Figure 3 - Optical micrographs showing slip lines on the surface of compression specimens after 0.03 strain and which have been solution-treated and aged for 6 hrs at (a) 375°C, (b) 575°C, (c) 675°C.

The slip lines in Fig. 3 tend to be planar although some cross slip is evident; furthermore, no significant change in slip line spacing was detected between the ST, ST + 375°C, and ST + 575°C conditions. Bcc alloys with large levels of solid solution hardening elements, such as in the solution-treated Ti-23-11, are known to exhibit coarse, planar slip [11]. Furthermore, the addition of shearable precipitates is also known to favor inhomogeneous deformation in the form of continued slip on the same plane, given the slip-induced reduced-cross section area of the precipitate which intersects a particular slip plane. Thus, like most metastable beta Ti alloys in a hardened condition [2,12,13], Ti-23-11 is susceptible to coarse, inhomogeneous slip so long as particle shearing occurs. As expected, this is the case in the Ti-23-11 alloy from underaged to peak-age conditions; see Figure 3a to 3c.

* The presence of Nb in Ti_3Al is known to promote basal slip at room temperature in Ti_3Al-base alloys [9].

In contrast to conventional beta Ti alloys, the Ti-23-11 alloy can be heat treated such that slip is so uniform and on such a fine scale as to be unresolvable even at 5 k in a SEM. This is shown in Figure 3c. Given the previous discussion regarding the difficulty of shearing the ordered alpha-two particles, it is reasonable to expect that, given the particle growth that occurs in the overaged condition, such as at 675°C, the particle size should increase to a level where the dislocations bypass the particles by looping. In the present study, TEM of the 675°C/6 hr condition was not performed. However, after 100 hrs at 675°C, the alpha-two particles grew to ≅ 50-100 nm compared to ≅ 30 nm after 6 hrs at 575°C (the dimensions quoted are the minor dimensions along which particle shearing is likely). As is well known, changing the dislocation glide mechanism from shear to by-pass of the precipitate particles can cause a dramatic change in slip distribution at low temperatures. This was demonstrated in Ti-Al alloys [14], in which homogeneously distributed fine slip occurs when large Ti_3Al precipitates (≅ 70 nm diam.) are looped but inhomogeneous, coarse slip results when smaller particles, 25-50 nm diameter, are sheared. In the present case, we conclude looping occurs when the alpha-two particles grow to 50-100 nm but that particle shearing persists for the ≅ 30 nm particles. Thus, the observations for the two alloy systems, both hardened by alpha-two particles but with much different matrixes, are remarkably similar.

Strain-Hardening Behavior

A consequence of the above dislocation-particle interactions is that, under those conditions where dislocation bypass of the particles occurs, a rapid rate of initial work hardening is expected from the accumulation of dislocations at the particles as geometrically necessary dislocations [15]. The extra work hardening $\Delta\sigma$ due to the accumulation of dislocations at particles may be expressed as [15]

$$\Delta\sigma = M^{3/2} C G \left(\frac{bf}{d}\right)^{1/2} \sqrt{\varepsilon} \qquad (1)$$

where M is the Taylor factor which for bcc Ti is about 3, G is the shear modulus of beta Ti, b its Burger's vector, f is the volume fraction of precipitate particles, d is the average particle diameter, and ε is the strain. The term C is a constant whose predicted value is 0.24 [15].

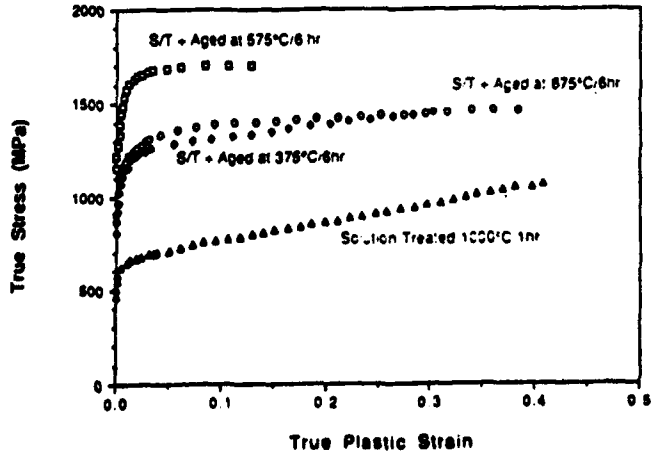


Figure 4 - True stress - true strain behavior of Ti-23Nb-11Al specimens deformed in compression at 25°C.

Figure 4 shows that all of the alloys exhibit stress-strain behavior which is characterized by a short period of rapid initial hardening followed by extended linear work hardening in all conditions except the peak-aged (575°C/6hr). The transition to linear "Stage IV" work hardening occurs at very small strains ($\varepsilon \cong 0.03$) in the solution-treated (S/T) as well as the underaged (375°C/6 hr) conditions but is delayed to $\varepsilon \cong 0.08$ in the overaged case (675°C/6hr).

If, as we expect, particle looping occurs in the overaged condition, Eq. 1 indicates that parabolic work hardening should occur such that $\Delta\sigma \propto \sqrt{\varepsilon}$. Fig. 5 shows this in fact occurs over the strain range $0.005 \leq \varepsilon 0.03$. A value of the constant C may be estimated assuming a volume fraction of precipitate at 675°C after 6 hrs, f ~0.1 [16]* and a particle diameter, ~75 nm, intersecting the slip plane. In the term $\Delta\sigma$, we also take into account the intrinsic work hardening of the matrix. Such a calculation yields $C \simeq 0.31$, which is consistent with other observations for particle-hardened bcc alloys (C = 0.30 to 0.52 [17-19]) as well as being very close to the predicted value of 0.24 [15]. Thus we conclude that in the overaged condition, the rapid initial work hardening behavior is quite consistent with expectations based on dislocation bypass and the accumulation of geometrically necessary dislocations.

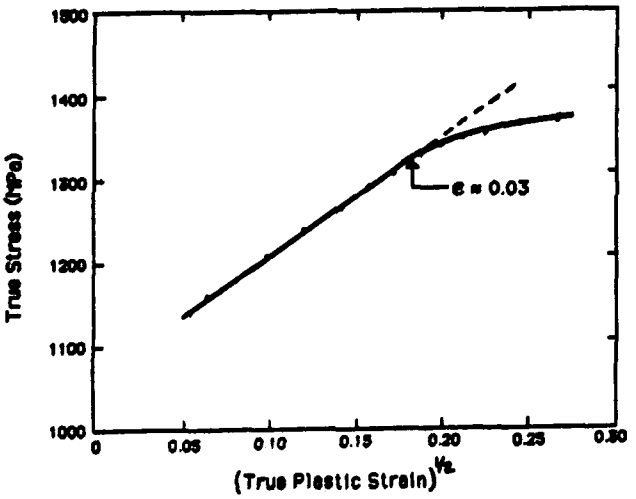


Figure 5 - The dependence of the flow stress σ on the square root of plastic strain ε, as predicted by Eq. 1.

Linear strain hardening, usually denoted Stage IV, has been observed in both fcc and bcc metals [20-22]. However, significant differences exist between those observations and the present data in Fig. 4. Typically, Stage IV occurs at much larger strains ($\varepsilon \gtrsim 0.5$) than those ($\varepsilon \simeq 0.1$) observed here. This may be a consequence of the high flow stress of the Ti-23-11 alloy and the suggestion that the onset of Stage IV occurs at smaller strains with increasing flow stresses [23]. The same analysis also predicts the magnitude of the linear work hardening $(d\sigma/d\varepsilon)_{IV}$ to increase with increasing flow stress [23]. However, Fig. 4 indicates $(d\sigma/d\varepsilon)_{IV}$ decreases with increasing flow stress; this has also been observed in Al alloys. In that case, the amount of solute in solution was believed to hinder the dislocation recovery and cell formation process, causing an increase in $(d\sigma/d\varepsilon)_{IV}$ under conditions where substitutional solute content is high, such as in the ST condition [24]. This may occur in the present case as well, especially in view of the

* This value of f was determined for an overaged condition of 850°C/180 hrs. Given the greater driving force for precipitat but decreased kinetics at 675°C, it should also be a reasonable estimate for the 675°C/6 hr condition.

inhomogeneous slip in Ti-23-11 in all but the overaged condition. Finally, the typically observed values of Stage IV work hardening, $(\delta\sigma/d\varepsilon)_{IV} \simeq 1\text{-}2\times10^{-3}G$ [20,25]. The current data in Fig. 4 indicate $(d\sigma/d\varepsilon)_{IV} = 5$ to $25\times10^{-3}G$ or much higher than is commonly observed for Stage IV linear hardening. Some of this may be due to the inhomogeneous nature of slip and its influence on the recovery processes which should decrease the linear hardening rate. However, it is worth noting that both the peak-aged and overaged conditions exhibit similar $(d\tau/d\gamma)_{IV}$ values but much different slip characteristics. Thus, the slip mode cannot be a controlling factor in determining the linear hardening behavior of this beta Ti alloy. We conclude that, while this beta Ti alloy exhibits linear strain hardening at relatively small strains, it is not clear whether or not it is Stage IV work hardening, as is often observed in fcc metals.

Summary

A strong age-hardening response has been identified in the beta Ti alloy Ti-23-11. The hardening, which depends on solution-treating and aging heat treatments, is caused by the formation of fine-scale, lath-like alpha-two precipitates based on Ti_3Al. We propose that the ordered structure of the precipitate particles makes them more effective than disordered alpha phase precipitates in strengthening the matrix. Furthermore, it is possible to grow the alpha-two precipitate to a size (~75 nm, minor dimension) wherein dislocation looping occurs. This results in a transition in slip mode from inhomogeneous to extremely uniform slip accompanied by rapid initial work hardening due to the accumulation of geometrically necessary dislocation. Linear strain hardening is observed at larger strains ($\varepsilon > 0.03$ to 0.10) but is not well understood.

Acknowledgments

The authors wish to acknowledge discussions with Professor P. Howell. This research was supported by the Office of Naval Research.

References

1. Beta Titanium Alloys in the 1980's, R. R. Boyer and H. W. Rosenberg, eds. (Warrendale, PA: TMS, 1984).

2. T. W. Duerig and J. C. Williams in Beta Titanium Alloys in the 1980's, R. R. Boyer and H. W. Rosenberg, eds. (Warrendale, PA: TMS, 1984), p. 19.

3. T. Hamajima, G. Lutjering and S. Weismann, Metall. Trans., 4 (1973) 847.

4. T. Hamajima, G. Lutjering, and S. Weismann, Metall. Trans., 3 (1972) 2805.

5. L. S. Quattrocchi, D. A. Koss and G. Scarr, Scripta Met et Mat. 26 (1992) 267.

6. L. S. Quattrocchi, M. S. Thesis, The Pennsylvania State University, 1991.

7. M. Lovato and M. G. Stout, to be published in Metall. Trans. A.

8. H. Margolin, E. Levine, and S. Hayden, Metall. Trans. 4 (1973) 2001.

9. S. A. Court, J. P. A. Lofvander, M. H. Loretto, and H. L. Fraser, Phil. Mag A 61 (1990) 109.

10. J. P. A. Lofvander, S. A. Court, P. Kurath, and H. L. Fraser, Phil. Mag Lett. 59 (1989) 289.

11. D. A. Koss and J. C. Chesnutt in Titanium Science and Technology, R. Jaffee and H. Burte, eds. (New York: Plenum Press, 1973) p. 1097.

12. A. Gysler, G. Lutjering, and V. Gerold, Acta Metall. 22 (1974) 901.

13. G. Terlinde, T. W. Duerig, and J. C. Williams, Metall. Trans. A, 14A (1983) 2101.

14. G. Lutjering and S. Weismann, Acta Metall. 18 (1970) 785.

15. M. F. Ashby in Strengthening Methods in Crystals, A. Kelly and R. B. Nicholson, eds., (New York: Elsevier, 1971), p. 137.

16. D. Goto, unpublished research, Penn State University, 1991.

17. R. H. Jones, Metall. Trans., 4(1973) 2799.

18. R. H. Jones, Metall. Trans., 5 (1974) 970.

19. J. B. Kosco and D. A. Koss, unpublished research, 1991.

20. J. Gil Sevillano, P. van Houtte, and E. Aernoudt, Prog. Mat. Science, 25 (1981) 65.

21. G. Langford and M. Cohen, Trans ASM, 62 (1969) 623.

22. H. J. Rack and M. Cohen, Mat. Sci. and Eng., 6 (1970) 320.

23. J. D. Embury and H. Mecking quoted in A. D. Rollett, U. F. Kocks, and R. D. Doherty in Formability and Metallurgical Structure (Warrendale, PA: TMS, 1987) p. 211.

24. D. J. Loyd and D. Kenny, Metall. Trans. A, 13A (1982) 1445.

25. A. D. Rollett, U. F. Kocks, and R. D. Doherty in Formability and Metallurgical Structure (Warrendale, PA: TMS, 1987) p. 211.

CORRELATION OF MECHANICAL PROPERTIES AND MICROSTRUCTURES

OF Ti-6Al-2Sn-2Zr-2Mo-2Cr-0.25S TITANIUM ALLOY

Henry R. Phelps* and J. R. Wood**

*Lockheed Aeronautical Systems Co.
Marietta, GA 30063

**RMI Titanium Company
Niles, OH 44446

Abstract

This paper details thermomechanical processing development work conducted on Ti-6Al-2Sn-2Zr-2Mo-2Cr-0.25Si (Ti-6-22-22S) titanium alloy. This alloy is deep hardenable and has high strength, creep resistance, and moderate toughness in the conventional alpha-beta processed and heat treated condition. Initially developed in the early 1970's, lack of production applications precluded additional development at the time.

Based on work conducted with similar alpha-beta alloys, it was anticipated that beta processing could be used to improve the Durability and Damage Tolerance (DADT) characteristics of Ti-6-22-22S for Advanced Tactical Fighter (ATF) applications, while maintaining a strength advantage over Ti-6Al-4V.

This paper describes the development efforts that established a baseline beta thermomechanical processing (TMP) route for the alloy. Beta processing of Ti-6-22-22S produced a superior combination of strength and DADT properties compared to damage tolerant grades of Ti-6-4 in the beta annealed condition. As a result of this effort, Ti-6-22-22S was selected as the baseline titanium alloy for the F-22 fighter aircraft.

Introduction

Titanium alloy Ti-6Al-2Sn-2Zr-2Mo-2Cr-0.25Si (Ti-6-22-22S) is an alpha-beta alloy developed by the RMI Titanium Company. This alloy was developed to be deep hardenable, have high strength, intermediate temperature creep resistance and moderate toughness. Conventional production melt and conversion practices were developed in 1973.(1)(2) Though initial alloy development occurred in the early 1970's, lack of production applications precluded further development work.

As Lockheed's ATF design matured, it became apparent that titanium would be used in a large number of thick section, fracture critical applications. Current state-of-the-art for such applications was the extra low interstitial (ELI) grade of Ti-6Al-4V (Ti-6-4) titanium alloy, in the beta annealed (BA) condition. This alloy has excellent fracture toughness and fatigue crack growth characteristics, but has low static and fatigue strength.

After an industry review of similar titanium alloys, it was concluded that beta processing of Ti-6-22-22S held the greatest potential for producing a

Titanium '92
Science and Technology
Edited by F.H. Froes and I. Caplan
The Minerals, Metals & Materials Society, 1993

superior mixture of DADT and strength properties over Ti-6-4. Goals established for the beta processed alloy are shown in Figure 1.

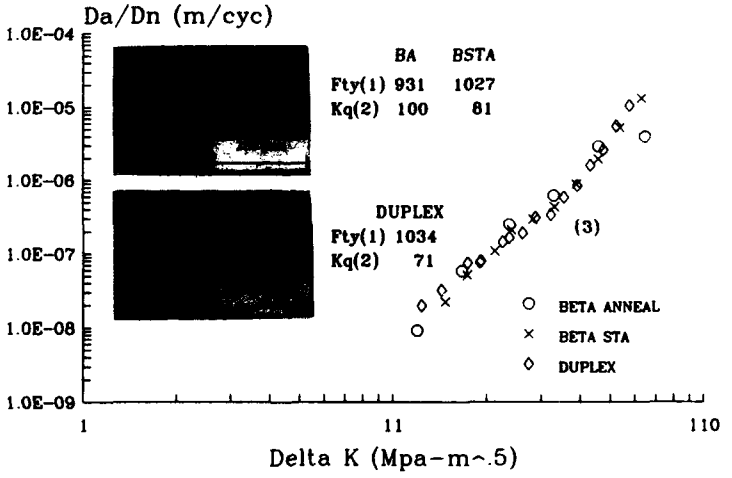
Figure 1. Property Goals for Beta Processed Ti-6-22-22S

Ftu = 160 ksi (1103 MPa)
Fty = 145 ksi (1000 MPa)
K_{Ic} = 80 ksi $\sqrt{in.}$ (88 MPa-$\sqrt{m}$)
Da/Dn ≤ Ti-6Al-4V (ELI, Beta Anneal)

Preliminary Beta Process Evaluation

Initial verification of the potential of beta processing Ti-6-22-22S utilized .58 inch (14.7 cm), alpha-beta rolled plate converted from a lab scale ingot. Several beta solution heat treatment and age sequences were evaluated on this material. All materials were still air cooled (AC) from the solution heat treat temperature. Figure 2 shows the correlation between strength, toughness, crack growth and microstructure for the heat treat schedules evaluated. The BA condition (Beta Transus [βT] + 65°F [36°C]-1Hr-AC) and Beta Solution Treat and Age (BSTA) (BA+ 1000°F [538°C]-8Hrs-AC) heat treatments produced a microstructure of fine acicular Widmanstätten alpha in a transformed beta matrix. Figure 2 shows that aging increases the yield strength by 10% with an associated 19% drop in toughness.

Figure 2. Mechanical Properties of Beta Solution Treated, Alpha-Beta Rolled, .58 Inch, Ti-6-22-22S Plate



1)Mpa 2)Mpa-m^.5, 3) R=0.1, LAB AIR

A duplex heat treatment consisted of BA + alpha-beta solution treatment followed by an age. The intermediate alpha-beta treatment consisted of βT - 50°F (28°C)-1Hr-AC. This produced a coarsening of the fine Widmanstätten alpha structure developed during the beta anneal. The duplex material exhibited yield strengths comparable to those developed with the BSTA heat treatment, but with typical fracture toughness values 12% lower. The figure shows that crack growth rates did not vary significantly for any of the heat treat schedules evaluated This work demonstrated that, when compared to conventional alpha-beta processed materials (Ref. 1), beta solution heat

treatments produced strengths that were lowered by 10 to 20 percent, with up to a 40 percent increase in fracture toughness.

Thermal Mechanical Processing Route Optimization

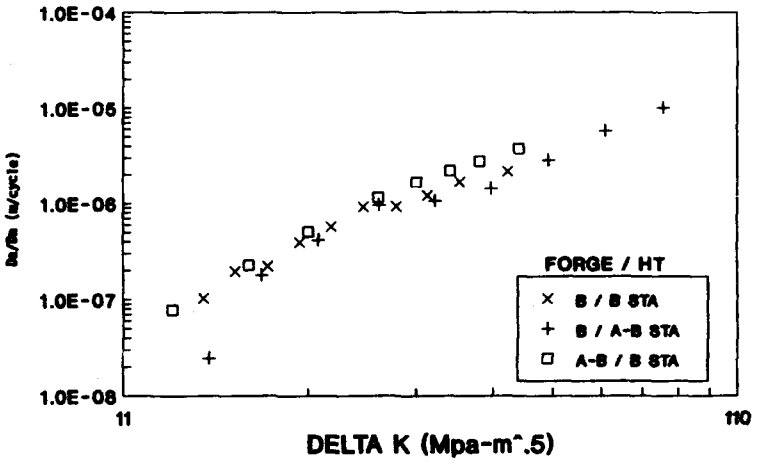
The next step in this development effort was to optimize the TMP route and insure that the goal properties could be achieved in production scale materials. A production scale ingot (30 inch [76 cm] diameter, 8,000 pounds [3,636 kg]) was cast and converted into several product forms including 4 to 6 inch (10.2 to 15.2 cm) thick hand forgings. Two conversion practices were evaluated, conventional alpha-beta finish forging and beta finish forging. The beta forging practice included a recrystallization step for grain refinement and produced a worked beta structure (i.e., through transus forging). Figure 3 shows the microstructure developed from the various TMP routes after heat treatment in a 3 inch (7.6 cm) section thickness. In order to retain some metastable beta phase to enhance aging response, fan air cooling (FAC) was used in all cases after the solution heat treatment. Similar microstructures were developed by both conversion practices when followed by a beta solution heat treatment. This produced an acicular basket weave structure, similar to that developed in the .58 (14.7 cm) inch alpha-beta rolled plate. The slower cooling rates in these forgings produced broader alpha platelets and thicker grain boundary alpha.

Figure 3 also shows that alpha-beta solution heat treatment produced a coarse basket weave structure with a fine acicular intergranular transformation product. Figure 4 shows that fatigue crack growth rates, even in a very corrosive environment (3.5% NaCl solution), were similar for all the TMP routes evaluated. Little or no sensitivity was evidenced in the mechanical properties between 1 and 3 inch (2.5 cm and 7.6 cm) section thicknesses. Based on these results, the TMP sequence of beta forged plus alpha-beta STA was selected as the baseline for additional property development work.

Figure 3. Correlation of Microstructure and Mechanical Properties for TMP Routes Evaluated Using Scaled Up Materials Heat Treated as 3-Inch (7.6 cm) Section Thickness

FINISH FORGE	ALPHA-BETA	BETA	BETA
HEAT TREATMENT	BETA STA	BETA STA	ALPHA-BETA STA
			
F_{tu} ksi (MPa)	159.8 (1102)	153.8 (1060)	159.5 (1100)
F_{ty} ksi (MPa)	141.0 (972)	133.9 (923)	143.4 (989)
e %	6.7	7.2	9.8
E MSI (GPa)	16.5 (114)	16.4 (113)	16.1 (111)
K_{1c} ksi $\sqrt{in}$ (MPa·$m^{1/2}$)	65.2 (71.6)	67.2 (73.8)	87.2 (95.8)

Figure 4. Comparison of 3.5% NaCl, Fatigue Crack Growth Rates for the TMP Routes Evaluated on Scaled Up Materials



L-T, R=0.1, 2 Hz, 3.5% NaCl

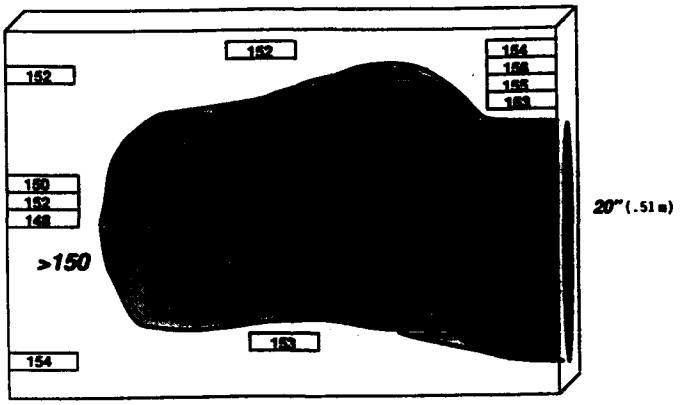
Cooling Rate Effects

A second production scale ingot was cast and converted to hand forgings for data base expansion. Evaluation of ATF applications indicated a large number of frames and bulkheads would be under 4 inch (10.2 cm) section thickness. The insensitivity to section thickness between 1 and 3 inches (2.5 and 7.6 cm) was anticipated to hold for 4 inch (10.2 cm) section thicknesses. This offered a potential to produce components with a single machining operation instead of the rough and post heat treat, finish machine operations normally required. A 6 inch (15.2 cm) beta forged billet was machined down to a 4 inch (10.2 cm) section thickness and alpha-beta solution heat treated and aged by RMI. A thermocouple was installed at the mid-thickness (t/2) position in one corner of the billet. This was monitored continuously during the heat treatment, even during fan cooling. Lot acceptance specimens taken adjacent to the thermocouple indicated the forging had adequate toughness but was marginally low on strength. After machining specimen blanks from several regions of the billet, a significant strength variation was discovered as illustrated in Figure 5. Ultimate tensile strength ranged from 156 to 143 ksi (1075 to 985 MPa). Re-solution heat treatment of select specimens, followed by a slow cool down and age under vacuum, uniformly lowered strengths. This indicated that the FAC employed by RMI was insufficient to adequately cool the center of the 4 inch (10.2 cm) section thickness.

Heat Transfer Coefficient Determination

The mechanical properties from the thermocoupled corner of the billet were marginal. A thermal analysis was conducted to model the cooling process. The effective heat transfer coefficient of the air moving over the billet surface was calculated by using the recorded temperatures at mid thickness (t/2) and adjusting the heat transfer coefficient until the model closely approximated the actual temperature response. This indicated that the FAC produced an effective heat transfer coefficient (H) of roughly five times the cooling rate of still air. Once the H coefficient for FAC was established, it was used to predict material cooling responses for various billet section thicknesses.

Figure 5. Variations in Mechanical Properties as a Function of Location for Billet Solution Heat Treated in a 4-Inch Section (102 cm) Units Shown are UTS in ksi.

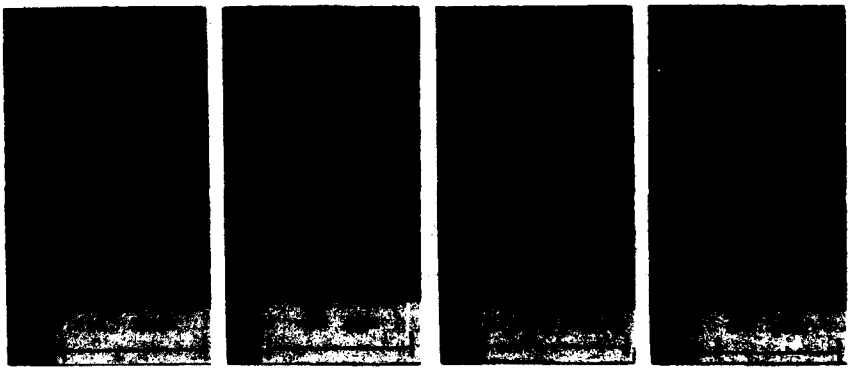


Ti-6-2-2-2-2 4" Plate, F_{tu} Properties

Cooling Rate Study

To quantify the effects of cooling rate, test blocks were instrumented and cooling rates monitored during cool down from the solution heat treat temperature. Post solution heat treat quenches evaluated included: oil, FAC, AC, and a slow furnace cool. Tensile strength and microstructure were determined. Figure 6 shows the correlation between microstructure and cooling rate. The cooling rate parameter used in this study was the time to half temperature (T_h), which is the time to cool the block mid-plane to half way between the solution heat treat and room temperature. The figure shows that as the cooling rate decreases, the acicular alpha platelets broaden and the tensile strength decreases.

Figure 6. Microstructure/Mechanical Property/Cooling Rate Correlation

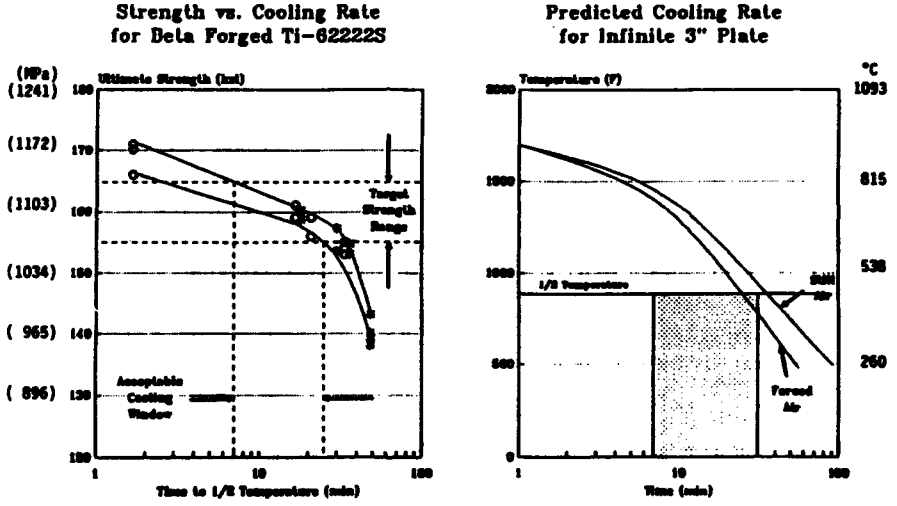


TIME TO HALF TEMP. (SEC)	100	1000	2000	2880
UTS-KSI (MPa)	169 (1165)	160 (1103)	154 (1062)	140 (965)

Process Window Definition

The cooling rate study data, with scatter bands, is plotted versus the time to half temperature on the left side of Figure 7. Acceptable fracture toughness values of $K_{Ic} \geq$ 80 ksi-√in. (88 MPa-√m) were associated with strength levels ranging from 155 to 165 ksi (1069 to 1138 MPa). Using upper and lower bounds of the data scatter, this indicated the acceptable time window to cool to T_β ranged from 7 to 23 minutes. Combining these data with the predicted mid-plane temperature response for FAC materials yielded the acceptable processing window for beta forged and alpha-beta STA Ti-6-22-22S (right side of Figure 7). This indicates that FAC of a 3 inch (7.6 cm) section can develop adequate properties while still air cooling will not. The results of this evaluation were incorporated into material heat treating specifications for the Ti-6-22-22S, limiting the heat treat section thickness. Larger section thicknesses are possible, providing a higher effective cooling rate can be achieved.

Figure 7. Determination of Acceptable Processing Window for Ti-6-22-22S



Conclusions

Beta processing of Ti-6-22-22S titanium alloy has been successfully used to improve fracture and crack growth characteristics. This study identified through-transus beta forging followed by an alpha-beta STA as the optimum TMP route. The heat treat section thickness of this alloy, however, is currently limited by the mid-plane cooling rates following solution heat treatment. Current heat treat practices have consistently produced an optimum combination of mechanical properties such as fracture toughness and fatigue crack growth rates.

Acknowledgments

The authors would like to thank several key personnel that contributed to the success of this research program. These include: Dr. Sharon Langenbeck, Mr. Richard Rainen and Ms. Charlotte Belsick (all formerly with Lockheed Aeronautical Systems Co., Burbank, CA), Mr. George Bella (formerly with RMI

Titanium Co.), and Mr. Pat Russo of RMI Titanium Co. Thanks are also due to the authors' respective organizations for permission to publish this paper.

References

1. L. J. Bartlo, H. B. Bomberger, S. R. Seagle, "Deep-Hardenable Titanium Alloy," (Report AFML-TR-73-122), May 1973. Work conducted under Air Force Contract F33615-72-C1152.

2. S. R. Seagle, G. S. Hall and H. B. Bomberger, "Development of a Deep-Hardenable Alloy for Intermediate-Temperature Applications." Proceedings of the Second International Conference, 1972, published as Titanium Science and Technology, Vol. 3, 1973.

EVALUATION OF Ti-6Al-2Sn-2Zr-2Cr-2Mo-.23Si SHEET

R. C. Bliss

RMI Titanium Company, Niles, OH, USA

Abstract

Ti-6Al-2Sn-2Zr-2Cr-2Mo-.25Si is an alpha-beta alloy which has good hardenability and a good combination of strength, ductility, and fracture toughness for structural applications. This alloy has been selected for use in advanced aircraft structural parts and was evaluated for those applications. Sheet produced from production ingots was evaluated for microstructure, mechanical properties, oxidation resistance, thermal stability properties and superplastic forming characteristics. The mechanical properties were evaluated from cross-rolled material in the mill annealed, solution treated, and solution treated + aged condition. The thermal stability and oxidation resistance properties were evaluated in both mill annealed and solution treated and aged conditions. Additionally, due to the fine grain size observed, superplastic forming evaluations were conducted on standard mill annealed material. Ti-6-22-22S sheet displays good strength and cold forming characteristics in the mill annealed condition. High strengths with good ductility can be achieved in the solution treat and aged condition. Thermal stability and oxidation results indicate that Ti-6-22-22S is equivalent to Ti-6Al-4V and under some conditions superior in this area.

Introduction

Ti-6-22-22S was originally developed as an alloy for large section applications. This meant achieving good toughness and ductility throughout the section. These properties and others such as fine grain size indicated that this alloy may also be suitable for thin sheet applications including superplastic forming (SPF). Accordingly, a study was performed to evaluate the characteristics of Ti-6-22-22S sheet. This study involved testing production sheet in several ways. These methods included standard mechanical tests, superplastic forming evaluations and tests for assessing effects of elevated temperature exposure.

Procedure

The material used in this study was taken from standard production material. The chemical composition is shown in Table I. The beta transus temperature is also given and was determined using differential thermal analysis methods.

Titanium '92
Science and Technology
Edited by F.H. Froes and I. Caplan
The Minerals, Metals & Materials Society, 1993

Sheet was produced from ingot utilizing a practice similar to that used on Ti-6-4. A variety of gauges were produced. The majority of the material used in this study was .063" (1.6 mm)thick, while some of the SPF tests were conducted on thicker material, up to .100" (2.54 mm). Three kinds of testing was performed on this material. All tensile tests were performed in accordance with the appropriate ASTM specifications. The superplastic forming tests were run on a tensile testing machine which has been equipped with a controlled atmosphere, resistance heated furnace. The furnace was evacuated before each test and the test itself run under a slight flow of argon. The testing was computer controlled, with the crosshead speed varied through three different levels and the load constantly recorded.

Table 1. Ingot Chemistry (wt. %) for Ti-6-22-22S Heat Used in Current Study

C	N	O	Fe	Al	Sn	Zr	Cr	Mo	β_t
.01	.007	.102	.05	5.64	1.90	1.91	1.98	1.86	1755°F

Mechanical Testing

The sheet was tested in several different heat treated conditions including solution treated and solution treated and aged conditions. Mill annealed properties for both Ti-6-22-22S and Ti-6-4 are shown in Table II for comparison. The mechanical testing consisted primarily of tensile tests.

Table II. Typical As-Annealed Tensile Properties

ALLOY	UTS ksi (MPa)	YS ksi (MPa)	El, %
Ti-6-22-22S	163 (1123)	158 (1089)	10.0
Ti-6Al-4V	140 (965)	130 (896)	15.0

These tests evaluated the effects of various solution treatment and aging temperatures on the properties of the alloy. The results are shown graphically in Figures 1-3. The data show that Ti-6-22-22S is susceptible to a strength drop caused by the formation of mechanically unstable beta-phase. This phenomenon is commonly seen in Ti-6-4 (Fig. 1). Additionally, mill annealed material was subjected to room temperature bend testing. Both longitudinal and transverse samples are able to make a 3X thickness radius bend of up to 105°. Microstructures of selected conditions are presented in Figures 4 and 5.

Elevated Temperature Testing

In an effort to evaluate the effects of long term elevated temperature exposure, samples of flat rolled, as-annealed Ti-6-22-22S were held for 100 hours at a variety of temperatures. For comparison purposes, samples of Ti-6-4 were exposed simultaneously. After exposure, the samples weight change was measured for the determination of relative oxidation resistance. Tensile tests were performed

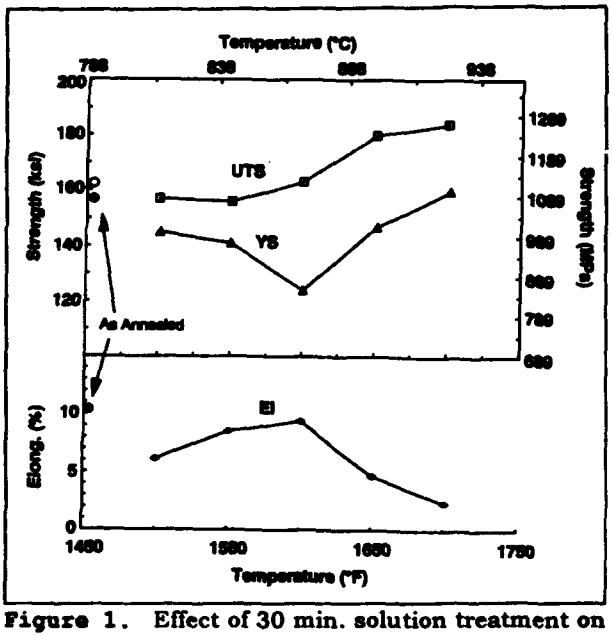


Figure 1. Effect of 30 min. solution treatment on tensile properties of Ti-6-22-22S .100 thick sheet.

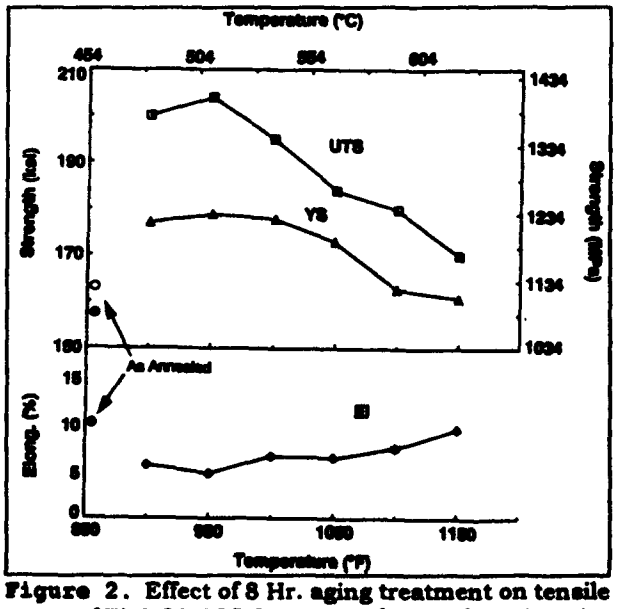


Figure 2. Effect of 8 Hr. aging treatment on tensile props of Ti-6-22-22S ST at 1600°F (871°C) - 30 Min.

similarly exposed as-annealed samples to determine thermal stability. Weight change was negligible in all cases except exposure at 1100°F (593°C) where Ti-6-4 showed some slight weight gain. The tensile results are plotted in Figure 6 which shows that Ti-6-22-22S undergoes a strengthening reaction with maximum strength occurring at approximately 900°F (482°C). Ti-6-4 undergoes a similar change with the maximum strength occurring around 600°F (316°C). In each case the ductility demonstrates the expected trend of decreasing elongation with increasing strength.

Superplastic Forming Evaluation

Samples of Ti-6-22-22S were subjected to a variety of superplastic forming (SPF) tests. These included high temperature, slow strain rate tensile tests; biaxial dome forming tests; production scale forming; and evaluation of as-formed mechanical properties. All results indicate that Ti-6-22-22S is readily superplastically formed. This is expected due to its alpha-beta structure and extremely fine grain size (ASTM #11 or finer).

The m-values are calculated from these results with the assumption

that elongation is uniform and necking is negligible. The results are shown in Figure 7. For comparison purposes, it should be noted that m-values for Ti-6-4 are generally in the range of .65-.85 at comparable strain rates. Ti-6-22-22S m-values reach a maximum between 1550°F (843°C) and 1650°F (899°C) but are above .5 (generally accepted as the minimum necessary for SPF) at slower strain rates for the entire temperature range investigated. In terms of flow stress, Ti-6-22-22S shows lower flow stresses then Ti-6-4 at similar temperatures.

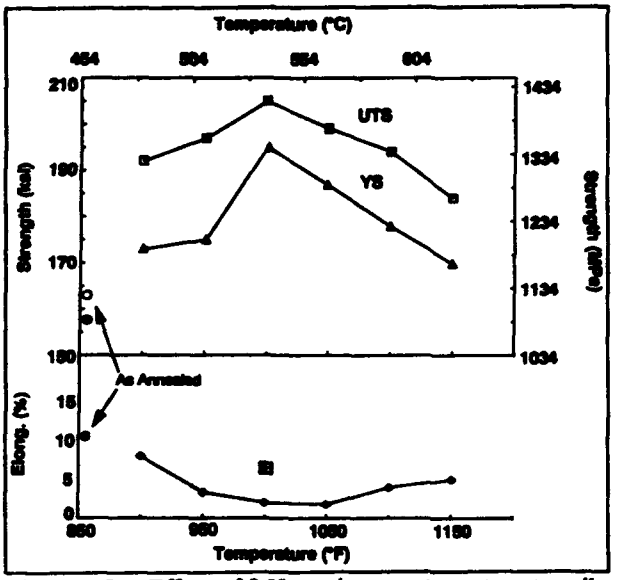


Figure 3. Effect of 8 Hr. aging treatment on tensile props of Ti-6-22-22S ST at 1700°F (927°C)- 30 Min.

Production scale trials were performed to evaluate biaxial formability of Ti-6-22-22S. Typically, this was implemented by using Ti-6-22-22S in place of Ti-6-4 on actual production parts. The forming parameters used were identical to those used for Ti-6-4 including temperature and forming pressure. A photograph of one such part is shown in Figure 8. No problems have been reported in forming Ti-6-22-22S in any production scale part and in some cases it was indicated that Ti-6-22-22S seemed to be better able to form around sharp corner radii.

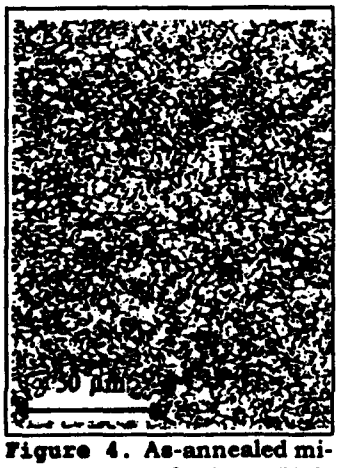


Figure 4. As-annealed microstructure of 1.6 mm Ti-6-22-22S sheet (ASTM Grain size 13).

As-formed mechanical properties were evaluated from both the uniaxial tensile tests and the production scale tests. This was done by machining sub-size tensile blanks from the material and testing them as standard room temperature tensile tests. In the case of the uniaxial tests, the blanks were taken from the reduced section, while the blanks from the production parts were machined from various locations throughout the parts. The results are shown in Figure 9 and Table III for the production part. The tensile tests taken from the production parts indicate that amount of strain does not affect the as-formed mechanical properties, as specimens taken from various locations have approximately the same properties. The results from the uniaxial tensile tests display a temperature

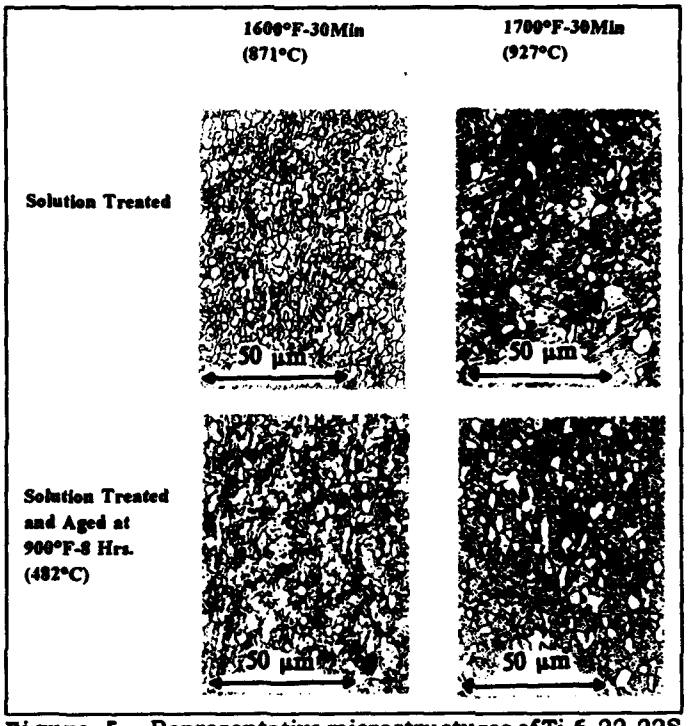


Figure 5. Representative microstructures of Ti-6-22-22S in ST and STA conditions.

dependence with two distinct strength levels. The lower level results from forming at lower temperatures [1450°F-1550°F (788°C-843°C)], while the higher strength level occurs after straining at 1600°F (871°C) and above. The yield strength and elongation show much less variation than the ultimate tensile strength. These facts are explained by the phase balance of the alloy which shifts away from alpha to beta and the transformation products formed on cooling. Even though larger grains result from the higher forming temperatures, the material is, in effect, being solution treated while being formed, resulting in higher strengths. As-annealed properties are shown for comparison purposes. Of particular importance is that, at the higher forming temperatures, the Ti-6-22-22S shows no appreciable drop in strength after forming. This is in contrast to Ti-6-4 which traditionally has displayed a decrease in strength after forming.

Table III. As-formed Properties of Production Scale Ti-6-22-22S Part Formed at 1650°F

LOCATION	UTS ksi (MPa)	YS ksi (MPa)	El, %
Flange	153 (1054)	148 (1020)	15.0
Side Wall	151 (1040)	141 (972)	14.0
Side Wall	155 (1068)	147 (1013)	14.0
Bottom	154 (1061)	146 (1006)	14.0
As-Annealed	167 (1151)	157 (1082)	18.6

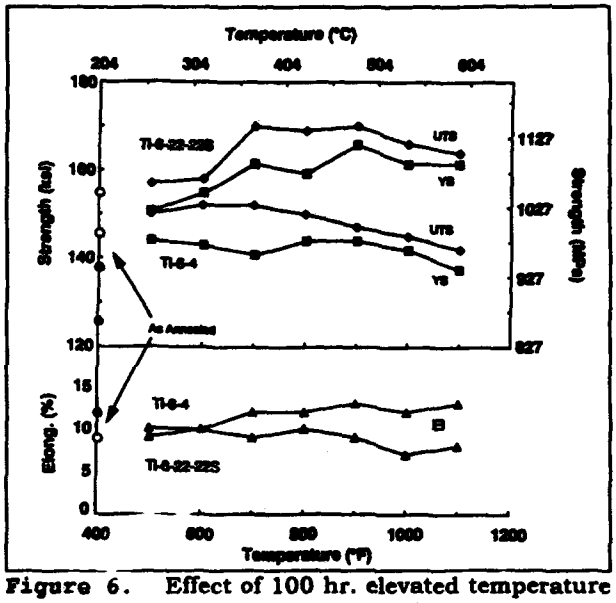


Figure 6. Effect of 100 hr. elevated temperature exposure on tensile properties of mill annealed Ti-6-22-22S.

Conclusions

Ti-6-22-22S, while originally developed as a deep-hardenable alpha/beta alloy for thick section applications, is well suited for use as sheet. It has higher strength than Ti-6-4, better ductility, and equivalent or better thermal stability and oxidation resistance. Additionally, Ti-6-22-22S is capable of being superplastically formed with the same ease as Ti-6-4. The forming may be accomplished at lower temperatures or, if better mechanical properties are desired, at identical temperatures as those used for Ti-6-4.

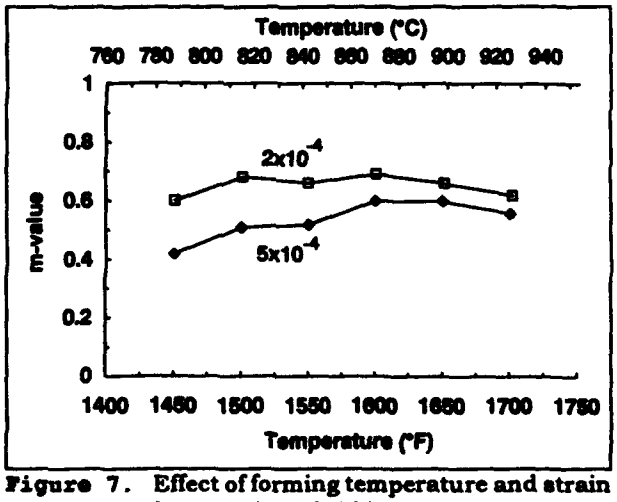


Figure 7. Effect of forming temperature and strain rate on m-values of Ti-6-22-22S.

Acknowledgements

The author would like to express his gratitude for the assistance given by Mr. Lou Bartlo and Ms. Kathy Leonard in the execution of this study.

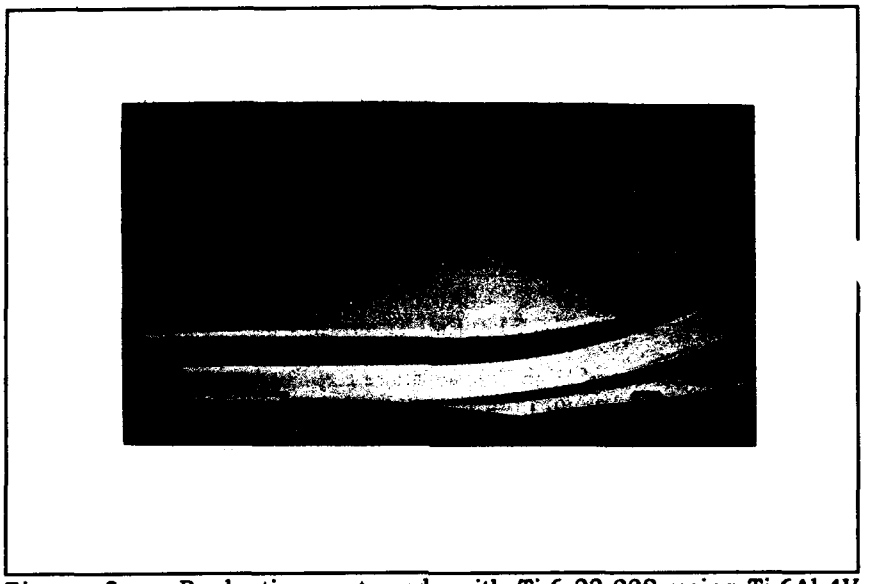


Figure 8. Production part made with Ti-6-22-22S using Ti-6Al-4V forming parameters.

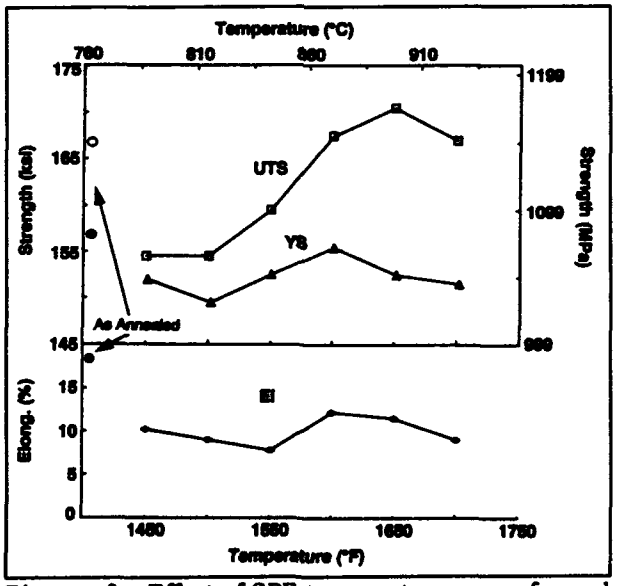


Figure 9. Effect of SPF temperature on as-formed tensile properties of Ti-6-22-22S (75% strain).

References

1. S.R. Seagle, G.S. Hall and H.B. Bomberger, "Development of a Deep-Hardenable Alloy for Intermediate-Temperature Applications," paper presented at 2nd International Conference, 1972. Published as Titanium Science and Technology (New York NY: Plenum Press, 1973).

2. G.A. Bella, "Properties of Ti-6Al-2Sn-2Cr-2Mo-2Zr-.23Si" (Internal Report, RMI Titanium Co, 1991).

3. G.A. Bella, "Evaluation of Ti-6Al-2Sn-2Zr-2Cr-2Mo Sheet" (Research and Development Report No. 712, RMI Titanium Co., 1990).

4. R.C. Bliss, "Effect of High Temperature Exposure on Ti-6Al-2Sn-2Zr-2Cr-2Mo" (Technical Memorandum 91-33, RMI Titanium Co., 1991).

5. C.D. Inglebrecht, "Tensile Properties of Titanium Alloys After Superplastic Strain" from Institute of Metals, Bristol Proceedings, July 1986, published as Designing with Titanium (London: The Institute of Metals, 1986).

TMP CONDITIONS–MICROSTRUCTURE–MECHANICAL PROPERTY RELATION IN Ti-6-22-22 S ALLOY

A. K. Chakrabarti, R. Pishko, V. M. Sample and G. W. Kuhlman*
Aluminum Company of America, Alcoa Technical Center
Alcoa Center, PA 15069 USA
*Aluminum Company of America, Forging Division
Cleveland, OH 44106 USA

Abstract

Thermomechanical processing history and the resulting microstructure have a significant effect on the mechanical properties of alpha-beta titanium alloys. The alpha-beta (primary alpha *in aged beta) microstructure* is generally characterized with high tensile properties and superior low cycle fatigue life whereas the beta (transformed beta) microstructure is characterized with a high fracture toughness and fatigue crack growth resistance. A duplex microstructure containing equiaxed primary alpha and elongated (acicular to plate type) transformed beta provides a desirable combination of strength, toughness, fatigue and fatigue crack growth resistance.

In order to meet a challenging combination of tensile strength (TYS > 1034 MPa, UTA > 1138 MPa), ductility (%El > 6, %RA > 12), fracture toughness ($\geq$ 88 MPa$\sqrt{m}$) and fatigue crack growth resistance (da/dN $\leq$ that of beta annealed Ti-64), development of transformed beta type microstructures was attempted. A beta finish forging and a through transus forging followed by α/β solution and an α/β forging followed by a β-solution were adapted to develop transformed beta type microstructures. Several variants of this microstructure were developed through designed variation of the TMP conditions. Desirable properties were achieved through two specific TMP conditions; however, the best property combination was achieved through an α/β fabrication followed by a beta solution, an α/β stabilization and an aging. Microstructure and mechanical property evaluations and fractographic analysis rationalize the observed results. Beta grain size and crack branching are observed to play significant roles in the fatigue crack growth resistance and fracture toughness in specimens having a transformed beta type microstructure.

Introduction

A major drive for the modern aircraft design is to reduce the overall weight of the aircraft. This weight reduction improves the thrust-to-weight ratio for quicker takeoff and landing and reduces the specific fuel consumption. The overall weight saving in an aircraft also increases the flight distance without the critical need of frequent refueling. A major weight saving can be achieved by reducing the weight of the airframe components through substitution of higher strength to density ratio material. However, to maintain a high design life and to adapt a damage tolerant design approach, the substitute materials must also exhibit a high fracture toughness and a high fatigue crack growth resistance. Based upon these general premises, attempts were made to develop a combination of mechanical properties in a titanium alloy which could result in a 10% or more weight savings in several critical aircraft components. One such combination of properties included: a tensile yield and ultimate strength greater than 1034 and 1138 MPa, respectively, % elongation and reduction in area at failure greater than 6 and 12, respectively, fracture toughness greater than 88 MPa$\sqrt{m}$ and fatigue crack growth resistance equivalent to that of beta-annealed Ti-6Al-4V alloy.

Titanium '92
Science and Technology
Edited by F.H. Froes and I. Caplan
The Minerals, Metals & Materials Society, 1993

The alloy selected was Ti-6Al-2Sn-2Zr-2Mo-2Cr-0.25Si, developed by Reactive Metals, Inc. (RMI) in the early 1970s on a U.S. Air Force Contract.[1] A review of the mechanical property data available in literatures[2,3] on all commercial titanium alloys indicated that the selection of Ti-6-22-22S was most appropriate in attempting to develop the selected combination of mechanical properties through innovative TMP (thermomechanical process) development. Most other commercial alloys through appropriate processing may either develop the strength or the toughness but would not develop the combination of high strength and high toughness. Moreover, even if the combination of strength and toughness is achieved, the fatigue crack growth resistance may not be adequate especially in variable 51 to 152 mm section size forgings.

A literature review was conducted to gather the background information on TMP-microstructure-mechanical property relations in Ti-6-22-22S alloy.[1,4-8] The review indicated that an α/β fabrication processing followed by α/β solution treatment and aging may develop the highest strength. However, the fracture toughness associated with these processes is significantly lower than the goal property (88 MPa$\sqrt{m}$). Strength gradients of more than 138 MPa were observed between the center and the edge locations in a 102 mm diameter solution treated, water quenched and aged bar. A double aging treatment within a temperature range of 482°-649°C reduces the strength gradient between the center and the edge of a billet; however, this treatment tends to reduce the fracture toughness. Best aging condition was determined to be 538°C/8 hr, followed by air cooling.

Beta upset forging with a 4:1 reduction ratio followed by an α/β solution treatment and aging develops tensile yield strength of the order of 960 to 1090 MPa with fracture toughness ranging from 110 to 81 MPa$\sqrt{m}$, respectively, depending on the α/β solution temperature and the post solution cooling rate. However, it is observed that the β-forged plus α/β solution treated materials also exhibited an inverse strength-toughness relation. Fatigue crack growth resistance of most of these experimental forgings was either not evaluated or was not reported in the literature.[1,4-8]

From a general review and understanding of microstructure–mechanical property relation[9] in titanium alloys and from the present review of microstructure-mechanical property relation in Ti-6-22-22S alloy, it was clear that a fracture toughness of the order of 88 MPa$\sqrt{m}$ can only be achieved in a transformed beta-type microstructure with or without a very small amount of equiaxed primary alpha. Whether or not the tensile strength and fatigue crack growth resistance goals would be met through such microstructures in variable section size thick forgings (51 to 152 mm thickness) could only be determined through experimental evaluations. Three major processing (TMP) routes, outlined in the next section, were adapted to develop the desired transformed beta (with or without primary alpha) type microstructure.

Experimental Procedure

Thermomechanical Processing

Three major TMP routes consisting of two variations in each were adapted to develop a transformed beta-type microstructure. The first group consists of α/β preform forging followed by a beta finish forging with an α/β solution treatment and aging (Table I, Processes 1 and 2). The second group consists of a beta preform forging followed by an α/β finish forging with an α/β solution treatment and aging (Table I, Processes 3 and 4). The third group consists of α/β preform forging followed by α/β finish forging with a β-solution treatment and aging. Approximately 152 mm diameter by 43 mm thick pancakes were fabricated through these processes. Alpha-beta processed billet stocks with 75 mm diameter by 180 mm length were applied for all TMP conditions. The chemical composition of the billet stock is shown in Table II.

Microstructure and Mechanical Properties

A typical macrostructure and microstructure at center mid-height location from a diametral section of these pancakes are shown in Figure 1. Room temperature tensile tests with chordal specimens, fracture toughness tests with 25 mm thick C-R specimens, strain controlled low cycle fatigue (LCF) tests with chordal specimens and fatigue crack growth tests with 6.4 mm thick C-R specimens were conducted using appropriate ASTM standard procedure. LCF tests were conducted at R-ratio = 0.1, using a triangular wave form at a frequency of 30 cycles per minute. The fatigue crack growth rate tests were conducted in ambient air (56% relative

humidity) at R-ratio = 0.1 and at a frequency of 10 Hz using a sinusoidal waveform. Tensile and fracture toughness test results are shown in Table I. The low cycle fatigue (LCF) results are shown in Table III and Figure 2 and fatigue crack growth rate (FCGR) test results are shown in Figure 3.

Results and Discussion

Macro- and Microstructures

A typical macrostructure of a quarter segment from a diametral section of a pancake (Process No. 6) is shown in Figure 1 (top). The macrostructure exhibits some nonuniformity of plastic deformation near the center section of the pancake due to friction and die-chill effects. Plastic flow lines are readily visible in this macrograph (Figure 1, top).

As expected from the TMP design, β-finish forging plus α/β solution treatment and aging (Group I, Processes 1 and 2) developed a lamellar transformed beta type microstructure (Figure 1A, B). A higher β-finish forging temperature (T_B + 50°C) in Process 2 did not create any significant difference in microstructures compared to those for the Process 1 which was finish forged at (T_B + 28°C) except that a higher beta finish forging temperature in Process 2 developed a coarser β-grain size (Figure 1B). Processes 3 and 4 where a β-preform forging was followed by an α/β finish forging, α/β-solution treatment and aging developed a broken up lamellar microstructure with some fine equiaxed primary alpha (Figure 1C, D). The volume fraction of fine equiaxed alpha did not vary significantly with 25% and 50% α/β deformation in Processes 3 and 4, respectively. Processes 5 and 6 where α/β preform forging plus α/β finish forging was followed by either a one-step β-solution for Process 5, or a two step β solution and α/β stabilization treatment for Process 6 (all followed by aging) developed an acicular transformed beta microstructure (Figure 1E, F). It is observed that the two-step β solution plus α/β stabilization in Process 6 did not develop a significantly coarser acicular structure (Figure 1E) compared to that in Process 5 where a one-step β-solution was adapted (Figure 1F). This two-step solution plus stabilization treatments, however, might have developed a more stable (equilibrium) transformed beta retained (aged) beta interfaces in the microstructure.

Mechanical Properties

Room temperature tensile properties of the pancakes processed via Processes 1 through 6 are shown in Table I. It is observed from Table I that the tensile goal properties of 1034 MPa offset yield strength and 1138 MPa ultimate tensile strength were not met through any of these processing routes. The highest tensile strength (both TYS and UTS) were achieved through Processes 3 and 4 where a mixed fine primary alpha plus broken up lamellar type microstructure was created through controlled (25% to 50% deformation) α/β finish forgings. It may be observed from Table II that the oxygen level (0.076 w/o) in the Ti-6-22-22S bar stock used in this study was lower than the desired 0.10 to 0.12 w/o. Based on the analysis of earlier results[4] it may be observed (Figure 4) that yield and ultimate tensile strength of Ti-6-22-22S increase significantly with increasing oxygen content in the alloy. From Figure 4, it is predicted that a 69 MPa increase in yield and ultimate tensile strength could be achieved through proper level of oxygen (0.12 w/o) in the alloy. However, this higher level of oxygen (0.12 w/o compared to 0.076 w/o) may also decrease the fracture toughness. Tensile property results indicate that TYS and UTS did not vary significantly between the surface and the center thickness locations within these forgings (not shown in Table I).

Room temperature fracture toughness of the pancake forgings is also shown in Table I. Process 1 clearly meets the fracture toughness goal property (88 MPa$\sqrt{m}$), whereas, Process 2 barely missed it. The mixed fine primary alpha-lamellar transformed beta microstructure developed through Processes 3 and 4 exhibits lower fracture toughness compared to those observed from the other processes. This lower fracture toughness can be rationalized in terms of two observations: 1) the lamellar alpha-fine equiaxed primary alpha microstructure would not be as effective as lamellar alpha only (100% lamellar alpha) microstructure in terms of developing crack path tortuosity; 2) the higher TYS associated with Processes 3 and 4 would develop a smaller plastic zone ahead of the crack tip and, thereby, would exhibit lower fracture toughness. Processes 5 and 6 which developed a Widmanstatten type transformed beta microstructure exhibit lower toughness than those exhibited by Processes 1 and 2 which developed a lamellar alpha type microstructure. Why the lamellar alpha (transformed beta)

microstructure developed via through transus beta finish forging plus α/β solution treatment and aging would exhibit higher toughness than those with a Widmanstatten type transformed beta microstructure developed through Processes 5 and 6 is not clearly understood.

Strain controlled room temperature LCF test results for Process 1, 4 and 6 are shown in Table III and Figure 2. It is observed from Table III that the number of cycles to fatigue crack initiation (N_i) and the number of cycles to fatigue failure (N_f) at three total strain ranges ($\Delta\varepsilon_t$ = 1.2, 0.9 and 0.75) are not significantly different for the different types of microstructure. Process 1 exhibits the best overall LCF properties followed by Process 4. This result is somewhat similar to those observed in Ti-6Al-4V alloy[10] in which the high cycle fatigue life of equiaxed primary alpha-lamellar alpha microstructure was observed to be inferior to that of fine lamellar only microstructure. The Widmanstatten (acicular) transformed beta microstructure (Process 6) exhibited the lowest LCF life. The LCF lives (number of cycles to failure) of beta-forged plus annealed Ti-6Al-4V have been compared to that of the α/β forged plus two-step solution plus stabilization treated (β-solution treated plus α/β stabilized and aged, Process 6) Ti-6-22-22S in Figure 2. It is observed that the LCF properties of Ti-6-22-22S (Process 6) are nearly identical to those of beta-forged plus annealed Ti-64.

Fatigue crack growth rate test results for selected processes (Processes 1, 3, 4 and 6) are shown in Figure 3 where the fatigue crack growth rate (da/dN) as a function of the applied ΔK (stress-intensity range) is displayed. It is observed that at any given ΔK (within the range of 22-61 MPa$\sqrt{m}$), the slowest crack growth rate (da/dN in meter per cycle) is associated with the specimen from Process 6. The fastest crack growth rate is associated with the specimen from Process 4. The specimen from Process 1 exhibits a crack growth rate intermediate to those from Processes 4 and 6. In other words, the Widmanstatten transformed beta microstructure (Process 6) exhibits the highest crack growth resistance, followed by the lamellar transformed beta (Process 1) and mixed primary alpha-lamellar alpha microstructures (Process 4).

The fatigue crack growth rate of two selected processes (Processes 1 and 6) are compared to that of other alloys and processing conditions in Figure 5. It is observed that the fatigue crack growth rate of the beta-solution treated plus α/β stabilized and aged (Process 6) Ti-6-22-22S specimen is comparable to that of the βMA Ti-64 (beta mill annealed Ti-6Al-4V). The through transus β-forged plus α/β-solution treated and aged specimen with lamellar alpha microstructure (Process 1) exhibits lower fatigue crack growth resistance compared to that of the βMA Ti-64. Thus, only one processing condition (Process 6) meets the fatigue crack growth resistance goal. Fatigue crack growth resistance of Ti-6-22-22S reported by Boyer[11] appears to be superior to that of βMA Ti-64. However, the details of the processing condition for this Ti-6-22-22S specimen and its other mechanical properties are not available.

Fractrographic observations on fatigue crack growth rate tested specimens from Processes 1, 4 and 6, representing the three major microstructural groups, are shown in Figure 6. SEM fractrographs taken on the FCGR-tested area exhibit: (i) a mixed striated plus dimpled appearance for the lamellar type microstructure (Process 1, Figure 6A1-A3); (ii) a relatively flat patchy mixed striated plus dimpled (shallow) appearance for the mixed fine primary alpha with lamellar alpha microstructure (Specimen 4, Figure 6B1-B3); and (iii) a mixed striated, heavily dimpled with intergranularly cracked area (Process 6, Figure 6C1-C3) for the acicular Widmanstatten transformed beta-type microstructure. Some crack branching (extensive secondary cracking) and secondary cracking due to splitting of the lamellar alpha-aged beta interfaces (marked as C's) are observed in the lamellar alpha-type microstructure (Figure 6A); little or no crack branching and secondary cracking due to interface splitting is observed in the mixed fine primary alpha-lamellar alpha type microstructure (Figure 6B); and extensive grain boundary cracking (marked as SC's) with minor secondary cracking due to interface splitting is observed in the acicular Widmanstatten type microstructure (Figure 6C).

Within these three microstructural groups, the highest fatigue crack growth resistance in the acicular Widmanstatten transformed beta microstructure is rationalized by extensive crack branching along the transformed beta grain boundaries leading to deflection of the main crack front, intermittent crack arrest and accumulation of further damage followed by propagation. This process of crack branching, intermittent crack arrest and further damage accumulation prior to renewed growth would require high energy or work leading to overall slow crack growth rate. A slightly faster crack growth rate in the lamellar alpha microstructure is rationalized by formation of numerous but shallow secondary cracks due to splitting of the lamellar alpha aged beta boundaries. This splitting at the interfaces seldom develops a situation which can be called as crack branching leading to a temporary crack arrest. However, formation of such numerous

shallow secondary cracks are associated with extra work or energy, thereby leads to a relatively slow crack growth. The fastest crack growth rate in the fine primary alpha-lamellar alpha microstructure is rationalized by the virtual absence of crack branching and secondary crack formation at the lamellar alpha-aged beta interfaces. A relatively smooth (with some dimples and fragmented striations) and flat fracture surface (Figure 6B) indicates the virtual absence of extra work or energy requirement besides that for propagation of the main crack front.

Summary and Conclusions

The original combination of goal properties were not met by any one of the six TMP schemes. However, Process 6 with α/β preform and finish forging followed by β-solution and α/β stabilization treatments plus aging developed a Widmanstatten transformed beta microstructure and best combination of tensile, fracture toughness and fatigue crack growth resistance properties. Process 1 with α/β preform and through transus β-finish forging followed by an α/β-solution treatment plus aging developed a lamellar transformed beta microstructure and second best combination of mechanical properties with the highest fracture toughness and a slightly lower fatigue crack growth resistance (compared to that of the Widmanstatten transformed beta microstructure). The mixed fine equiaxed alpha-lamellar alpha microstructure exhibited the highest tensile strength but lowest fracture toughness and fatigue growth resistance.

It was anticipated that with proper alloy chemistry having 0.10 to 0.12 w/o oxygen and Cr + Mo = 4 w/o, the tensile property goal could be achieved. In view of superior fatigue crack growth resistance and high fracture toughness, Process 6 (with Widmanstatten transformed beta microstructure) was selected as the best process with Process 1 (with lamellar transformed beta microstructure) as a close alternate. Even at the current property levels these processes are expected to develop a 10% higher specific strength compared to the incumbent β-annealed Ti-64 alloy.[12] Further details of prototype fabrication, tensile, fracture toughness, fatigue crack growth rate and other second tier mechanical properties are outlined in a separate paper in the conference.[12]

Acknowledgements

The authors would like to thank their colleagues at Alcoa, Boeing Commercial Airplane Company, Lockheed Corporation and RMI Company for their contributions to the work presented. In particular they would like to thank R. R. Boyer of Boeing Commercial Airplane Company, R. E. Lewis and J. J. Pengra of Lockheed Corporation, and S. R. Seagel and D. E. Thomas of RMI Company for their valuable discussions and suggestions.

References

1. "Mechanical Property Data–Ti-6-22-22S Alloy, Solution Treated and Aged Plate" (Report F33615-72-C-1280, Battelle Columbus Labs, 505 King Avenue, Columbus, OH 43204, 1973).

2. M. J. Donachie, Jr., ed., Titanium and Titanium Alloys (Metals Park, OH 44073: Am. Soc. for Metals, 1982), 12-308.

3. M. J. Donachie, Jr., ed., Titanium–A Technical Guide (Metals Park, OH 44073: Am. Soc. for Metals, 1988), 157-206.

4. P. A. Russo et al., "Development of a 900°F Titanium Alloy" (Technical Report AFML-TR-70-125, Air Force Materials Lab, Wright Patterson Air Force Base, 1970).

5. L. J. Bartlo et al., "Deep Hardenable Titanium Alloy" (Technical Report AFML-TR-73-122, Air Force Materials Lab, Wright Patterson Air Force Base, 1973).

6. R. A. Wood, "Titanium and Titanium Alloys–A Review of Selected Developments" (Technical Report, Battelle Columbus Labs, 1972).

7. "Mechanical Property Data–Ti-6-22-22S Alloy, Duplex Annealed Forged Billet" (Report F33615-73-C-5073, Battelle Columbus Labs, 1973).

8. "Allison Fan Disk Forging–Ti-6-22-22S, Grade 484" (Internal Memorandum, RMI Company, Niles, OH, 1974).

9. A. K. Chakrabarti, "Thermomechanical Process Development for Turbomeca Ti-6Al-4V Impaller Forgings" (Report Alcoa No. 12-88-FFT-001-25, Alcoa Laboratories, Alcoa Center, PA 15069, 1988).

10. G. Lutjering et al., eds., Titanium Science and Technology, (Proc. Fifth Intl. Conf. on Titanium, Munich, FRG, 1984), 2065-2083.
11. R. R. Boyer, private communication with author, Boeing Commercial Airplane Group, Seattle, WA, 1988-02-17.
12. "Characterization of Ti-6-22-22S: A High Strength Alpha-Beta Titanium Alloy for Fracture Critical Applications," F. H. Froes et al., eds., Titanium Science and Technology, (Proc. Seventh Intl. Conf. on Titanium, San Diego, CA, 1992).

Table I. Ti-6-22-22S Forging TMP Conditions and Mechanical Properties

				Tensile Properties				
Group No./ Process No.	Preform Forging	Finish Forging	Heat Treatments	TYS (MPa)	UTS (MPa)	% El	% RA	Fracture Toughness K_{IC} MPa$\sqrt{m}$
I/1	αβ	β-finish T_β+28	T_β-22°C/1, FAC+ 538°C/8, AC	993	1110	11	21	90.4
I/2	αβ	β-finish T_β+50	T_β-22°C/1, FAC+ 538°C/8, AC	1000	1117	12	21	87.6
II/3	β-preform	αβ-finish (25%)	T_β-22°C/1, FAC+ 538°C/8, AC	1033	1123	12	25	68.0
II/4	β-preform	αβ-finish (50%)	T_β-22°C/1, FAC+ 538°C/8, AC	1027	1117	12	25	58.4
III/5	αβ-preform	αβ-finish (50%)	T_β-28°C/1/2, FAC+ 538°C/8, AC	958	1110	10	15	75.1
III/6	αβ-preform	αβ-finish (50%)	T_β-28°C/1/2, FAC+ Tb-50°C/1, AC+ 538°C/8, AC	972	1096	10	17	85.1

Note: Heat treatment sequence temperature/time-cooling method. FAC - Fan Air Cool, AC - Air Cool.

Table II. Chemical Composition of Ti-6-22-22S Alloy

	Weight Percent									
	Al	Sn	Zr	Cr	Mo	Si	O	N	C	Fe
Spec.	6.25	2.25	2.25	2.25	2.25	0.27	0.14	0.03	0.04	0.25
Range	5.25	1.75	1.75	1.75	1.75	0.20				
Bar Stock	6.0	2.2	1.8	2.1	1.9	0.16	0.076	0.01	0.02	0.06

Table III. Room Temperature LCF Test Results

Process No.	Specimen No.	Total Strain Range (%)	No. of Cycles to Initiation (Ni)	No. of Cycles to Fracture (Nf)
1	1A	1.2	6,077	6,542
1	1B	0.9	18,240	19,215
1	1C	0.75	34,990	35,490
4	4A	1.2	6,800	6,903
4	4B	0.90	20,760	21,641
4	4C	0.75	22,412	24,400
6	6A	1.20	6,125	6,409
6	6B	0.90	13,445	13,707
6	6C	0.75	16,086	19,791

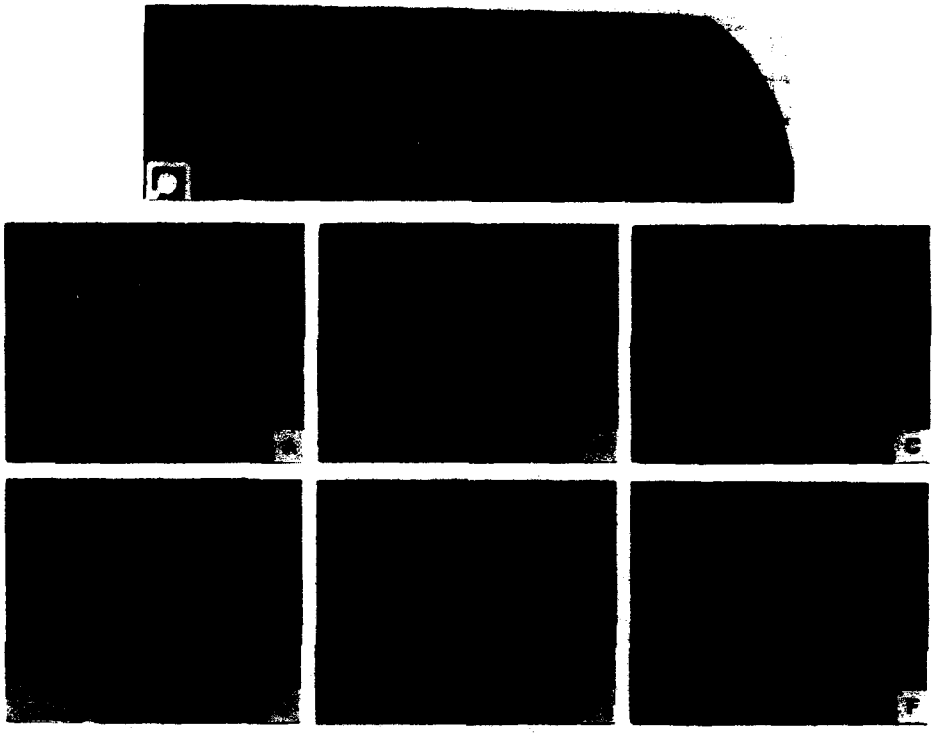


Figure 1. A Typical Macrostructure (Top, 1•5x) and Microstructures at Center-Mid-Height Locations in Pancake Forgings Fabricated Via Process Nos. 1 Through 6 (100X) Showing Lamellar Alpha (A and B) Mixed Equiaxed Primary Alpha-Lamellar Alpha (C and D) and WidmanstattenType Transformed Beta (E and F) Structure.

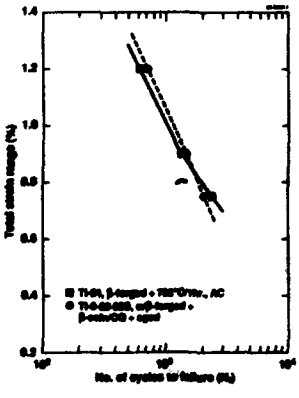


Figure 2. Comparison of Strain Controlled LCF Properties between Ti-64 and Ti-6-22-22S Material

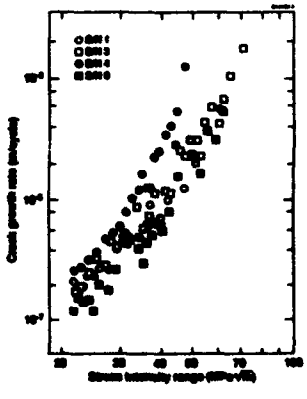


Figure 3. Fatigue Crack Growth Rate (da/dN) as a Function of the Applied Stress Intensity Range (ΔK) for Ti-6-22-22S Alloy

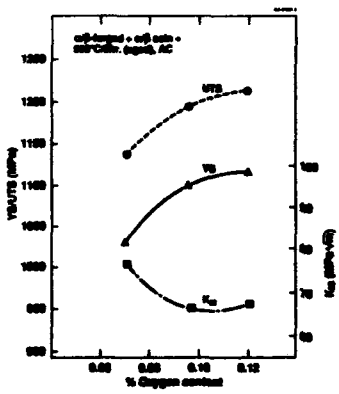


Figure 4. Effect of Oxygen Content on Tensile Yield, Ultimate Strength and Fracture Toughness in Ti-6-22-22S Alloy

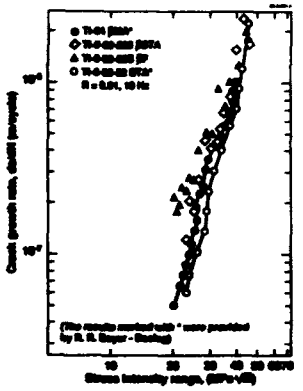


Figure 5. Comparison of Fatigue Crack Growth Rates in Ti-64 and Ti-6-22-22S Alloy

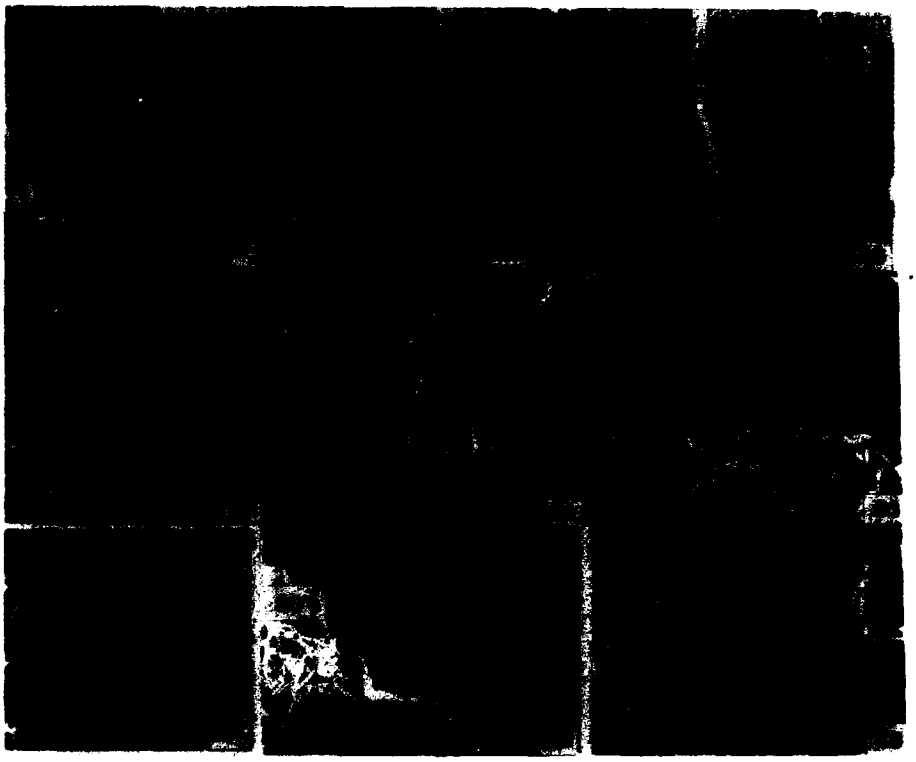


Figure 6. Fractographs of Fatigue Crack Growth Rate Tested Specimens from Process Nos. 1 (Top), 4 (Middle) and 6 (Bottom). The Direction of Crack Propagation in Each Specimen is Shown by Thick Arrow Marks. Selected Areas, Marked by Circles in A1, B1 and C1 are Shown at Higher Magnifications in Fractorgraphs A2, B2 and C2. Selected Areas from these Fractographs, Marked by Squares, are Shown at Higher Magnification in A3, B3 and C3.

THEORETICAL DESIGN OF β-TYPE TITANIUM ALLOYS

M. MORINAGA, M. KATO, T. KAMINURA, M. FUKUMOTO,
I. HARADA and K. KUBO

Department of Production Systems Engineering,
Toyohashi University of Technology,
Toyohashi, Aichi 441, Japan

Abstract

A theoretical alloy design was carried out on the β-type titanium alloys on the basis of the molecular orbital calculation of electronic structures. Employing two calculated parameters, the bond order (Bo) and the d-orbital energy level (Md), plastic deformation mode of β-type alloys was predicted correctly. With this prediction method a high performance alloy, Ti-13%V-3%Cr-2%Nb-(2-3)%Al, was designed successfully without doing any trial-and-error experiments. The twin mechanism as well as the slip mechanism was operating in the alloy. This new alloy was found to be superior in tensile strength and fracture toughness to a commercial Ti-15%V-3%Cr-3%Sn-3%Al (Ti-15-3-3-3) alloy. In addition, it was shown that there is a possibility for further increase in the strength of this alloy, since the microstructure could be modified readily by a proper thermomechanical treatment. The density was also lower than that of Ti-15-3-3-3.

Introduction

Recently great attention has been directed towards the β-type titanium alloys because of the excellent deformability and achievable high tensile strength. The development has been accelerated owing to much demand for these alloys for aerospace applications. However, the method used for development is still old-fashioned, depending on many trial-and-error experiments and several empirical rules. Recently we have proposed a new method for alloy design on the basis of the molecular orbital calculation of electronic structures [1-3]. In this paper this method has been applied practically to the development of new β-type titanium alloys.

Titanium '92
Science and Technology
Edited by F.H. Froes and I. Caplan
The Minerals, Metals & Materials Society, 1993

A method for theoretical alloy design

Employing a molecular orbital method (DV-$X\alpha$ cluster method [4]), electronic structures were calculated for bcc Ti alloyed with a variety of elements, and two alloying parameters were determined theoretically [2]. The one is the bond order (hereafter referred to as Bo), which is a measure of the covalent bond strength between Ti and an alloying element. The other is the metal d-orbital energy level (Md) which correlates with the electronegativity and the metallic radius of elements. These parameters are listed in Table I for various alloying elements in β Ti. For alloy, the average values of Bo and Md are defined by taking the compositional average of the parameter, and denoted $\overline{Bo}$ and $\overline{Md}$ respectively. Further detailed explanation on the parameters is described in ref.[2].

With these parameters the phase stability is well understood for titanium alloys. For example, Figure 1 is a phase stability map (called the $\overline{Bo}$-$\overline{Md}$ map) in which α, α+β and β type alloys separate clearly. The stability region of the β-type alloys extends to the high $\overline{Bo}$ and the low $\overline{Md}$ region. The β-type alloys are known to deform by either the slip or the twin mechanism, depending largely on the phase stability of alloys [5]. Namely, the plastic deformation mode changes from twin to slip mechanism as the stability of β-phase increases. In response to this change the β region in the $\overline{Bo}$-$\overline{Md}$ map is possibly separated into the either slip or twin dominant subregion as is shown in the map. In addition, the map includes another subregion of the martensite where the martensite forms in alloys upon quenching from high temperatures to room temperature. It is further noted that the boundary where an athermal omega phase forms in quenched alloys is close to the slip/twin boundary. Thus the phase stability is related closely to the plastic deformation mode of β-type alloys.

As shown in Figure 2, alloy position moves in the $\overline{Bo}$-$\overline{Md}$ map as the alloy composition varies. For example, for a Ti-V binary alloy it moves to the left (the lower $\overline{Md}$ region) with increasing V content. The vector drawn on the Ti-V line represents the position of a Ti-10 mol%V alloy in the map. Such a vector varies in direction and magnitude, depending on alloying elements, as is shown in the map. Therefore, once a specific $\overline{Bo}$-$\overline{Md}$ region and a specific alloy system are set in the map, the corresponding alloy composition is simply determined following the rule of the vector sum. The trial-and-error experiments are no longer needed in order to optimize the alloy composition. It is very interesting to note here that most practical β-type alloys are located along the slip/twin boundary or the martensite boundary in the $\overline{Bo}$-$\overline{Md}$ map (see Figure 1). For example, Ti-15-3-3-3 (Ti-15%V-3%Cr-3%Sn-3%Al) lies on the slip/twin boundary, and Ti-10-2-3 (Ti-10%V-2%Fe-3%Al) lies on the martensite boundary.

Table I List of Bo and Md values for bcc Ti

3d Elements	Bo	Md(eV)	4d Elements	Bo	Md(eV)	5d Elements	Bo	Md(eV)	Non-transition elements	Bo	Md(eV)
Ti	2.790	2.447	Zr	3.086	2.934	Hf	3.110	2.975	Al	2.426	2.200
V	2.805	1.872	Nb	3.099	2.424	Ta	3.144	2.531	Si	2.561	2.200
Cr	2.779	1.478	Mo	3.063	1.961	W	3.125	2.072	Sn	2.283	2.100
Mn	2.723	1.194	Tc	3.026	1.294	Re	3.061	1.490			
Fe	2.651	0.969	Ru	2.704	0.859	Os	2.980	1.018			
Co	2.529	0.807	Rh	2.736	0.561	Ir	3.168	0.677			
Ni	2.412	0.724	Pd	2.208	0.347	Pt	2.252	0.146			
Cu	2.114	0.567	Ag	2.094	0.196	Au	1.953	0.258			

Application to the design of β-type alloys

Ti-15-3-3-3 and Ti-10-2-3 are well-known β-type alloys with superior mechanical properties. Ti-15-3-3-3 deforms by the slip mechanism, but Ti-10-2-3 deforms by the twin mechanism. In general, the longer fracture elongation and the lower yield strength are expected in the alloy deformed by the twin mechanism than the slip mechanism. This means that the twin deformation enhances the cold-workability, whereas the slip deformation yields the high strength of alloys. In order to meet this opposite nature, the present study was purposed to design those alloys in which the twin mechanism works to some extent in the solution-treated state, but the slip mechanism works dominantly in the aged state. We supposed that it is convenient to keep a large elongation while the alloy is cold-rolled in the solution-treated state, but to have high strength in the final aged state.

The alloy compositions of the designed alloys are given in Table II. The alloy system selected in this study was Ti-V-Al-Cr-X (X=Zr, Sn, Nb). Here, V and Al were chosen, because these elements have high values of the (bond order/atomic weight) ratio [2] and hence the specific strength of alloys may be expected to be high. Needless to say, Al is the main strengthening element of the α phase which precipitates in the β matrix by proper aging treatments. From a preliminary experiment the Cr addition is known to be effective in improving the ductility of alloys. The last elements, X, were chosen to distribute alloy positions in a proper region in the $\bar{B}o$-$\bar{M}d$ map. As is shown in Figure 1, most of the alloys are located inside the twin region, indicating that the twin deformation will take place to some extent in the solution-treated state. However, the subsequent aging treatment will change the matrix composition toward the more β stabilized region, and hence the slip deformation may be expected to occur in the aged state.

Mechanical properties of designed alloys

Specimen preparation

The designed alloys were prepared by tri-arc melting from appropriate

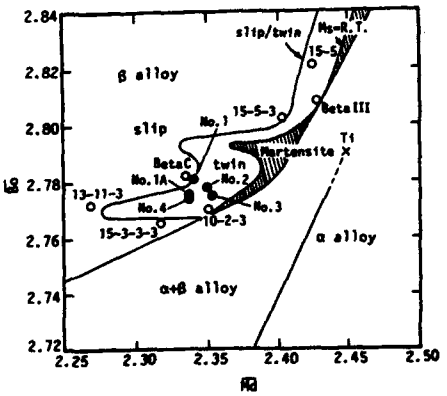


Figure 1 Phase stability index diagram based on $\bar{B}o$ and $\bar{M}d$ parameters. The designed alloys are shown by the solid circles.

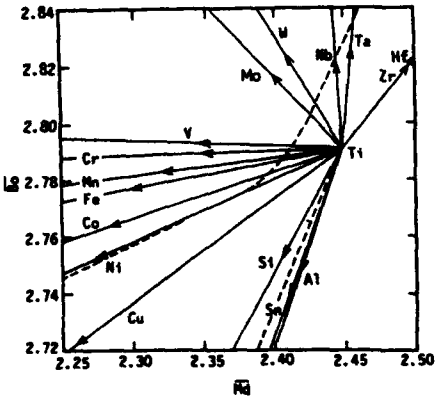


Figure 2 Phase stability change with alloying elements. The vector represents the location of Ti-10 mol% M.

Table II Alloy compositions and results of tensile test for designed alloys (No.1-4) and Ti-15-3-3-3 prepared by the process (A)

Alloy No.	Chemical composition (mass%)	Heat treatment	Yield strength (MPa)	Ultimate Tensile strength (MPa)	Elongation (%)
1	Ti-13V-2Al-3Cr- 2Nb	S.T.	532	661	26.6
2	Ti-12V-2.5Al- 3Cr-2Zr	S.T.	560	676	30.3
3	Ti-11V-3Al-3Cr- 2Zr	S.T.	552	651	28.0
4	Ti-13V-2Al-3Cr- 2Sn	S.T.	616	711	17.8
Ti-15-3-3	Ti-15V-3Al-3Cr- 3Sn	S.T.	749	761	20.8

* S.T. : solution-treatment

mixtures of sponge Ti and alloying metals. The button-shaped specimens were then hot or cold rolled and heat-treated in three different processes (A), (B) and (C) as shown in Figure 3. The thermomechanical treatments [6] are effective in reducing the β grain size, about 100 μm for the process (A) and about 40 μm for the process (B). A series of mechanical tests was carried out with both the solution-treated and the aged specimens. Also, oxygen and nitrogen contents in the No.1 specimen after aging were measured to be 0.25% and 0.019%, respectively.

Tensile test

Solution-treated state With small specimens shown in Figure 4(a) the stress-strain curves were obtained at a constant strain rate of 3×10^{-4}/s. The results are shown in Figure 5 for the alloys prepared by the process (A). Compared to Ti-15-3-3-3, every alloy in particular No.1, No.2 and No.3 alloys had lower yield strength and higher elongation. This was interpreted as due to the twin deformation, even though the slip deformation also took place in part in these alloys. As shown in Figure 6 many twins were observable near the fracture surface of No.1 alloy, whereas only the fine slip bands were seen in Ti-15-3-3-3, in reasonable agreement with the prediction from the slip/twin region in the $\bar{B}o$-$\bar{M}d$ map. However, it is noted here that the work hardening which is characteristic of the twin deformation was not so remarkable as that of Ti-10-2-3.

The cold workability was examined by measuring the cold-rolling pressure and also by observing the appearance of cold-rolled surface. The rolling pressure of No.1 alloy was comparable to that of Ti-15-3-3-3. However, the

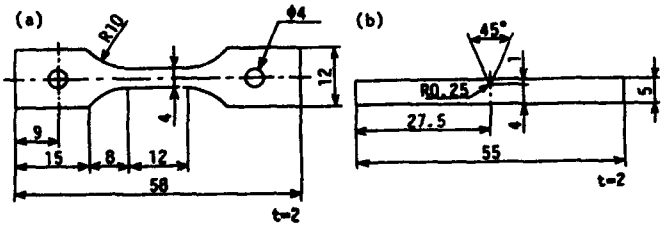


Figure 4 Specimens used for (a) tensile test and (b) Charpy impact test

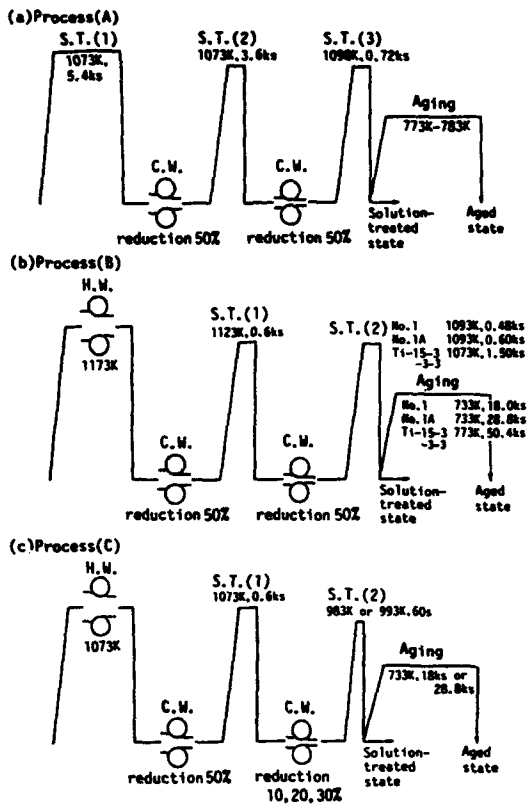


Figure 3 Thermomechanical processes of alloy production, S.T.: solution-treatment, C.W.: cold-working, H.W.: Hot-working

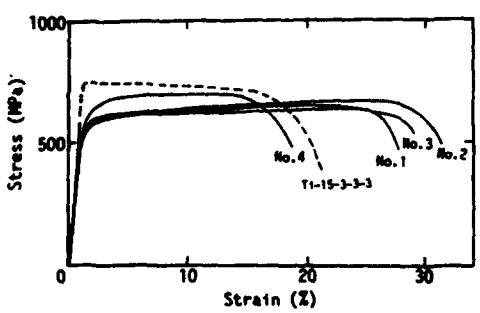


Figure 5 Stress-strain curves for the solution-treated state of alloys prepared by the process (A)



Figure 6 Microstructure near the fracture surface of (a) No.1 and (b) Ti-15-3-3-3

cold-rolled surface was very smooth in No.1 alloy, whereas it was rough, sometimes having small creases in Ti-15-3-3-3 and the other alloys. From this reason further study was concentrated mainly on No.1 alloy (Ti-13%V-2%Al-3%Cr-2%Nb). Another alloy containing 3%Al, No.1A (Ti-13%V-3%Al-3%Cr-2%Nb), was also investigated in order to examine an aluminium effect on the mechanical properties.

Aged state The aging curves are shown in Figure 7. The aging conditions of No.1 and No.1A alloys were determined to be 733 K for 18 ks and 733 K for 28.8 ks, respectively. It is apparent that the Al addition retarded the precipitation of the α phase in the alloys. The aging temperature was lower than 773 K for Ti-15-3-3-3, but the Vickers hardness was almost the same among them.

In Table III the results of tensile test are given for the aged state of No.1, No.1A and Ti-15-3-3-3 alloys, all prepared by the process (B). Compared to the results of the solution-treated state, both the yield strength (YS) and the ultimate tensile strength (UTS) were remarkably high in the aged state. For example, for No.1 alloy the UTS was as high as 1500 MPa. As shown in Figure 8 this was attributable to the precipitation of very fine α phase. The size of the α phase dispersed in the No.1 and No.1A alloys was about 60 nm and much finer than the size of the needle-like α phase in Ti-15-3-3-3, about 0.35 μm in length and 0.05 μm in width.

Charpy impact test

The Charpy impact test was carried out with a small V-notch specimen shown in Figure 4(b). The results for the aged alloys prepared by the process (B) are shown in Figure 9, where the total absorbed energy is plotted together with the yield strength. It is evident that the designed alloys, No.1 and No.1A, are superior in the fracture toughness to Ti-15-3-3-3.

Discussion

β transus and alloy density

The β transus was determined to be 1005 K for No.1 alloy and 1008 K for No.1A alloy by measuring electrical resistivities. These temperatures were comparable to 1003 K for Ti-15-3-3-3. The alloy density was also measured employing a conventional method. It was determined to be 4.684 (g/cm^3) for

Table III Results of tensile test for both the solution-treated state and the aged state of alloys prepared by the process (B)

Alloy No.	Chemical composition (mass%)	Heat treatment	Yield strength (MPa)	Ultimate Tensile strength (MPa)	Elongation (%)
1	Ti-13V-2Al-3Cr- 2Nb	S.T.	685	799	29.5
		S.T.A.	1464	1507	7.0
1A	Ti-13V-3Al-3Cr- 2Nb	S.T.	719	800	30.0
		S.T.A.	1321	1446	6.0
Ti-15-3-3-3	Ti-15V-3Al-3Cr- 3Sn	S.T.	804	813	15.0
		S.T.A.	1161	1242	11.0

* S.T. : solution-treatment, S.T.A. : aging after solution-treatment

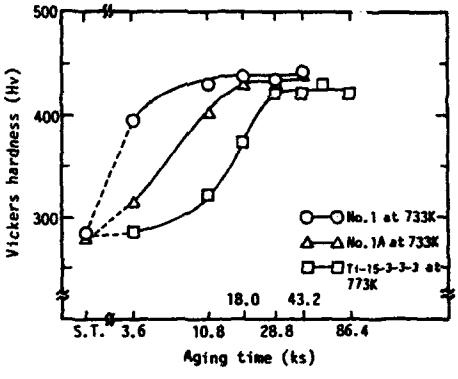


Figure 7 Aging curves for No.1, No.1A and Ti-15-3-3-3



Figure 8 Morphology of the α precipitates in (a) No.1 and (b) Ti-15-3-3-3

No.1 alloy, 4.660 (g/cm³) for No.1A alloy and 4.718 (g/cm³) for Ti-15-3-3-3 alloy. Compared to 4.650 (g/cm³) for Ti-10-2-3 alloy, the designed alloys had the density intermediate between Ti-10-2-3 and Ti-15-3-3-3 alloys.

Thermomechanical treatment

It is well-known that grain refinement by the thermomechanical treatment could improve the mechanical properties of alloys [6]. This was also confirmed in the present experiment. For example, as shown in Tables II and III, the solution-treated No.1 alloy exhibited the higher YS and UTS for the process (B) than for the process (A). This difference will be attributable to the difference in the β grain size, since it was about 40 μm for the process (B), much smaller than the size of about 100 μm for the process (A). In addition, for the aged No.1 alloy the total absorbed energy was about 40% larger for the process (B) than for the process (A). A similar result was also obtained in Ti-15-3-3-3, which agreed with a previous report [7]. The microstructure could be modified further by the process (C). This modification is probably associated with the

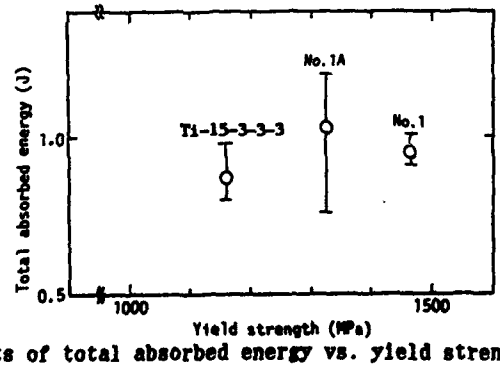


Figure 9 Plots of total absorbed energy vs. yield strength of alloys

deformation twins introduced to the alloys by the 2nd cold-rolling shown in Figure 3(c). Even for the subsequent annealing at 983-993 K for 60 s, the deformation twin did not recover completely, but still remained and behaved as if it is a sort of grain. The mechanical test of the alloys prepared by the process (C) are still in progress. But according to a preliminary experimental result, the process (C) seemed to increase the UTS of the designed alloys by about 200 MPa more than the process (B).

Conclusion

Employing a theoretical alloy design method, a new β-type titanium alloy, Ti-13%V-3%Cr-2%Nb-(2-3)%Al, was developed successfully. This alloy was superior in many aspects to Ti-15-3-3-3 alloy. It is concluded that the theoretical design is so useful for the development of high performance β-type titanium alloys.

Acknowledgments

We would like to express our thanks to Dr. M. Morishita of Himeji Institute of Technology for his assistance in the molecular orbital calculations of electronic structures. We also acknowledge the staff of the Computer Center, Institute for Molecular Science, Okazaki National Research Institute, for the use of the HITAC M-680H and S-820 computers. This research was supported in part by the Grant-in-Aid for Scientific Research from the Ministry of Education, Science and Culture of Japan and also by the Miyashita Research Foundation for Materials Science.

References

1. M. Morinaga et al.," New PHACOMP and Its Application to Alloy Design," Superalloys 1984, ed. M. Gell et al. (Warrendale, PA : The Metallurgical Society of AIME, 1984), 523-532.

2. M. Morinaga et al.," Theoretical Design of Titanium Alloys," Sixth World Conference on Titanium, vol.III (Les Ulis Cedex, France : Societe Francaise de Metallurgie, 1988), 1601-1606.

3. M. Morinaga and N. Yukawa," Alloy Design Based on Molecular Orbital Method," Computer Aided Innovation of New Materials, ed. M. Doyama et al. (Amsterdam : North-Holland, 1991), 803-808.

4. J. C. Slater, Quantum Theory of Molecules and Solids, vol.4 (New York, NY : McGraw-Hill).

5. S. Hanada et al.,"Tensile Properties and Plastic Deformation in β Phase Titanium Alloys," Sixth World Conference on Titanium, vol.I (Les Ulis Cedex, France : Societe Francaise de Metallurgie, 1988), 105-110.

6. R. Tricot, "Thermomechanical Processing of Titanium Alloys," Sixth World Conference on Titanium, vol.1 (Les Ulis Cedex, France : Societe Francaise de Metallurgie, 1988), 23-35.

7. M. Niinomi, T. Kobayashi and H. Honda, "Microstructure, Strength and Toughness in β Type Titanium Alloys," Current Advances in Materials and Processes, 3 (1990), 1600-1603 (in Japanese).

OMEGA PHASE FORMATION IN TITANIUM AND TITANIUM ALLOYS*

G.T. Gray III, C.E. Morris, and A.C. Lawson

Los Alamos National Laboratory
Los Alamos, NM 87545

Abstract

In this study, preliminary results concerning the influence of alloy chemistry on the propensity of omega-phase formation and its structure in three titanium alloys are presented. The influence of shock-wave deformation on the phase stability and substructure evolution of high-purity (low-interstitial) titanium, A-70 (3700 ppm oxygen) titanium, and Ti-6Al-4V were probed utilizing real-time velocity interferometry (VISAR) and "soft" shock-recovery techniques. Wave profiles of shock-loaded high-purity titanium revealed the omega-phase pressure-induced transition to occur at approximately 10.4 GPa. Wave profile measurements on A-70 Ti shocked to pressures up to 35 GPa and Ti-6Al-4V shocked to pressures up to 25 GPa exhibited no evidence of a three-wave structure indicative of a pressure-induced phase transition. Neutron and X-ray diffractometry and TEM analysis confirmed the presence of retained ω-phase in the electrolytic-Ti and the absence of ω-phase in the shock-recovered A-70 Ti and Ti-6Al-4V. Suppression of the α–ω phase transition in A-70 Ti, containing a high interstitial oxygen content, is seen to simultaneously correlate with suppression of deformation twinning. A volume fraction of ~28% ω-phase with lattice parameters a=0.4614 nm and c=0.2832 nm was measured in a sample shock-recovered to 11 GPa. The influence of alloy content on the kinetics of formation / retention of ω-phase and substructure evolution is discussed and contrasted in light of previous literature studies.

*Work performed under the auspices of the U.S. Department of Energy

Introduction

Although the response of titanium alloys to dynamic loading and instabilities continues to be examined, no self-consistent set of experimental data exists concerning the influence of chemistry on the detailed structure/property relationships of titanium alloys subjected to shock loading. These studies, in particular those focused on the polymorphic omega-phase transition at high pressure, are complicated by the known sensitivity of the deformation response of titanium to alloying additions, especially interstitials[1]. The ω-phase transformation in α-Ti under shock or hydrostatic soaking conditions exhibits a large hysteresis that is responsible for retention of the high-pressure ω-phase to atmospheric pressure[2,3]. The ω-phase induced in pure Ti is morphologically similar to ω-phase formed

Titanium '92
Science and Technology
Edited by F.H. Froes and I. Caplan
The Minerals, Metals & Materials Society, 1993

in as-quenched β-phase alloys based on Zr, Ti, and Hf[4]. Crystallographically, the phase transformation is believed to be a diffusionless displacive transition[3,4]. It has been proposed that the transition results from an ordered atomic displacement (shift) of close-packed atoms in a <1$\bar{2}$10> direction lying in the (0001) plane resulting from the propagation of a lattice-displacement wave through the crystal involving atomic shuffles[4]. The movement of these linear defects shift the close-packed hexagonal rows of the structure into the ω-phase in response to softening of select phonon modes. Under high pressure the stability of the alpha lattice to <1$\bar{2}$10> slip decreases leading to the α–ω transition[4]. This phonon softening is a precursor to a first-order martensitic-type transition[2,4].

The object of the present study was to investigate the α–ω shock-induced transition in titanium using "real-time" Velocity Interferometer for Any Reflector (VISAR) and shock recovery techniques. Experiments were conducted on three titanium alloys to probe the influence of alloy chemistry on the high-pressure phase stability of titanium under shock conditions. Characterization of the structure of retained ω–phase in shock-loaded titanium was done utilizing neutron diffraction and transmission electron microscopy.

Experimental Procedures

This investigation was performed on electrolytic alpha titanium(hereafter referred to as high-purity Ti), supplied by the Alta Group as 38mm x 100mm x 254-mm-bar stock, Ti-6Al-4V(hereafter Ti-6-4) in the form of 120-mm-dia-bar stock, and on A-70 AMS 4921 Titanium(hereafter A-70 Ti) in the form of 50-mm-dia-bar stock. The analyzed chemical compositions (in wt. %) of the titanium materials studied are listed in Table I. The high-purity Ti was cross-rolled in multiple passes at room temperature from 38 mm to 12.5 mm with intermediate anneals, (600°C for 30 minutes followed by a water quench) at 75 and 50 % rolling reductions. The high-purity Ti was recrystallized at 600°C for 4 hours, followed by a water quench, yielding an equiaxed grain structure with a 20 μm grain size. The Ti-6-4 was studied in the as-received condition; the starting microstructure possessing a duplex microstructure, sometimes called a bimodal microstructure, comprised of lamellar areas of α and β and equiaxed α grains of nominally 3 μm. The A-70 Ti was also studied in the as-received condition; the starting microstructure possessing an equiaxed microstructure with an α grain size of nominally 30 μm. Ultrasonic shear and longitudinal wave measurements of the titanium studied revealed the average sound speed to be 4.92, 4.95, and 4.87 km/sec for the high-purity Ti, Ti-6-4, and the A-70 Ti, respectively.

To investigate the influence of alloy content on ω-phase formation, wave profile (VISAR) and shock recovery experiments were conducted on the three titanium alloys as a function of shock pressure. Shock recovery experiments were performed on an 80-mm single-stage launcher utilizing a shock assembly consisting solely of titanium[5,6]. The wave profiles were measured with a VISAR built at Los Alamos using the design developed by Willard Hemsing[7]. Precision of the wave velocity measurements is believed to be approximately 1% in particle velocity. Specially designed photomultiplier circuits were utilized that had 1 ns risetimes. Symmetric impacts were performed in all VISAR shots. The VISAR wave profile experiments had tilts at impact of the order of 1 mrad for gas shots and 3 mrad for powder shots. Samples for optical metallography and transmission electron microscopy (TEM) were sectioned from the heat-treated and deformed samples. TEM foils were jet-polished with a solution of 84 % methanol, 10% butanol, and 6% perchloric acid at -40°C and 10 volts using a Struer's Electropolisher. Observation of the foils was made using a JEOL 2000EX at 200kV, equipped with a double-tilt stage. Neutron diffraction experiments were done on the High Intensity Powder Diffraction (HIPD) at the Los Alamos Neutron Scattering Center (LANSCE). Bulk specimens were examined without special preparation because the neutron penetration is large enough to sample the entire specimen.

TABLE I - Titanium Alloys Chemical Compositions (wt.%)

ELEMENT	High-Purity Ti	Ti-6Al-4V	A-70 Ti
O	360 ppm	0.18 wt%	0.37 wt%
C	60 ppm	200 ppm	170 ppm
N	10 ppm	110 ppm	240 ppm
H	14 ppm	7 ppm	8 ppm
Al	4 ppm	6.33 wt%	-
V	3 ppm	4.23 wt%	-
Fe	5 ppm	0.2 wt%	0.18 wt%
Ti	BAL	BAL	BAL

Results and Discussion

VISAR wave profile measurements were made on high-purity Ti from 6 to 22 GPa. Below 10 GPa a classic elastic-plastic two-wave structure was observed. At 15 GPa impact stress a three-wave structure (elastic plus two bulk waves) was observed (Figure 1), characteristic of a high pressure first-order phase transition. The best estimate of the transition pressure is 10.4 GPa. Several shots were fired at 15 GPa. All shots reproduced this three-wave structure although there was some variation in the transition pressure and shape of the transition wave. Shots were fired on 4.5-mm and 9-mm-thick samples to see if the transition pressures were comparable in samples with this range of thickness. Both samples exhibited approximately the same transition pressure. At 22 GPa only a two-wave elastic-plastic structure was observed, indicating the bulk transition wave had already overtaken the initial bulk shock in the α-phase. In other words, the high-purity Ti wave profiles are consistent with a material undergoing a first-order phase transition at 10.4 GPa with a small volume change.

VISAR wave profiles were made on A-70 Ti to study the α–ω transformation and the "apparent" phase transformation at 17.5 GPa reported by McQueen et al.[8]. The observed wave profiles up to 35 GPa consisted of a large elastic wave (1.8 GPa) followed by a bulk wave with a few nanosecond risetime. This elastic wave is over a factor of two larger than the elastic wave observed in the high-purity Ti. No evidence of a phase transition was observed over this pressure range. The VISAR U_s - U_p points, where U_s =shock velocity and U_p = particle velocity, smoothly extrapolated into the higher pressure flash-gap data above the kink in the U_s - U_p curve. The titanium used by McQueen et al. [8] in their Hugoniot measurements was very similar in chemical composition to the A-70 Ti used in this study. The VISAR data conclusively showed the kink in the U_s - U_p curve was an artifact of the flash-gap instrumentation. It is postulated that the kink in the previous flash-gap Hugoniot data was in fact the large elastic wave which prematurely closed the flash gaps rather than a phase transition. This interpretation is consistent with the shape of the low-pressure portion of the U_s - U_p curve. One would expect the greatest departure from linear extrapolation at low pressure and gradually diminishing to zero at a velocity slightly greater than the measured longitudinal velocity at zero pressure. Two-stage light gas gun data was used to extend the pressure range from 110 GPa to 260 GPa. The high pressure gun data fell on a linear extrapolation to high pressure of the VISAR / flash-gap Hugoniot data.

VISAR wave profile measurements were also made up to 25 GPa on Ti-6-4 to investigate the possible α–ω transition in this material [9]. Similar to A-70 Ti a classic elastic-plastic two-wave structure was observed over the entire pressure range investigated. The elastic precursor had an amplitude of 2.8 GPa, which was significantly larger than either the high-purity Ti or the A-70 Ti elastic waves. The VISAR data was positioned on a linear extrapolation to lower pressure of the flash-gap Hugoniot data. No evidence of a three-wave structure characteristic of a first-order phase transition was present. A qualification is in order about using loading-wave profiles to observe shock-induced phase transformations, because some types of transitions cannot be detected using this technique. The transitions that cannot

be observed are transitions with small volume changes or have sluggish transformation kinetics. In these cases monitoring the sound velocities in the shock state[10] would be the appropriate tool to study these transitions.

Samples of the three titanium materials were also shock loaded to 11 GPa at room temperature and soft recovered to assess the post-shock substructure and phases present. Neutron and X-ray diffractometry and TEM selected area diffraction (SAD) analysis confirmed the presence of retained ω-phase in the electrolytic-Ti and absence of ω-phase in the shock-recovered A-70 Ti and Ti-6-4. Bulk x-ray identification of the ω-phase was found to be very sensitive to the sample surface preparation with careful polishing required to avoid mechanical reversion of the ω at the surface. The substructure of the shock-loaded titanium was observed to consist of a high density of deformation twins, interspersed with areas containing retained ω-phase.(Figure 2a) The deformation twins in the high-purity titanium were found to be (1121) type twins that are similar to those observed previously in shock-loaded Ti-6-4[5]. SADP analysis confirmed the orientation relationship $(0001)_\alpha // (1\bar{2}10)_\omega$ and $<11\bar{2}0>_\alpha // <0001>_\omega$ between the α and ω-phase previously determined for titanium[2] and for Zr by Rabinkin et al.[4]. The SADP (Figure 2b) additionally shows streaking of the ω-phase pattern parallel to $(11\bar{2}0)_\omega$ planes. These streaks are thought be related to either: 1) the morphology of the ω-phase, 2) internal stacking faults within the ω formed during the transition, or 3) elastic distortion of the ω producing diffuse scattering in the direction of the distortion.

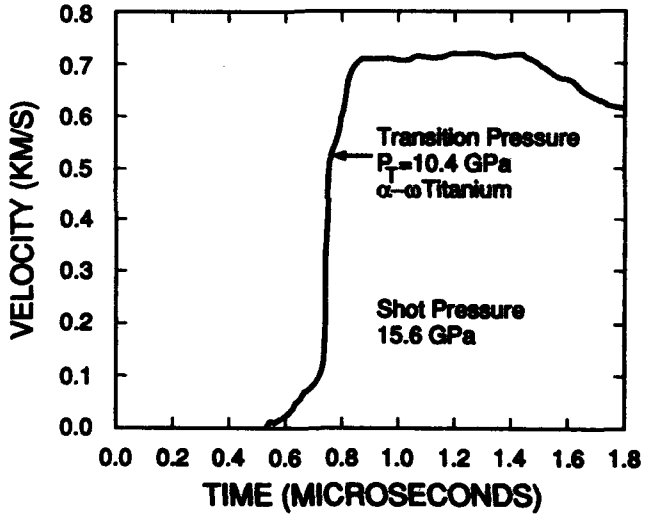


Figure 1 - VISAR wave profile showing the α–ω pressure-induced phase transition in high-purity titanium

The substructures of Ti-6-4 and A-70 Ti were both found to consist of primarily planar dislocation debris and in addition some isolated deformation twins in the case of Ti-6-4[5]. The planar nature of the substructure in these alloys is consistent with the aluminum and oxygen contents in the Ti-6-4 and A-70 Ti, respectively[1,11]. The coincident suppression of deformation twinning and ω-phase in the A-70 Ti is consistent with the influence of interstitial oxygen on the elastic constants, "c" lattice parameter, and dislocation mobility[1,11-13]. It has been postulated that oxygen may suppress the α–ω transition in titanium due to phase equilibrium considerations[2,14]. The results of the current study suggest that geometric constraint effects, related to interstitial effects, on lattice resistance to shear, rather than direct chemical effects on phase equilibrium may be controlling the transformation kinetics. Solid solution strengthening of the α-phase by oxygen has shown that the

concentration dependence of the yield stress varies approximately by $c^{1/2}$ [1]. While increasing oxygen and impurity content suppresses the α–ω transition in titanium[14], increasing oxygen content is also known to suppress deformation twinning in titanium under quasi-static loading[11,13]. In polycrystalline titanium samples oriented so as to be stressed along their c-axes tended to deform largely by twinning in low oxygen (<0.15 wt.%) alloys and to deform by c+a slip in high oxygen (> 0.20 wt.%) alloys[13].

The concurrent absence of both twins and ω-phase in the A-70 Ti alloy therefore suggest a potential link between both shear processes. In iron alloys it has been shown that deformation twins are suppressed with increasing interstitial carbon content[15]. This observation was shown to be consistent with the fact that the lattice shear accompanying twinning in iron carries two-thirds of the interstitial carbon atoms to improper octahedral interstitial lattice sites requiring a large number of atomic shuffles[15]. This lack of lattice registry leads to a crystallographic restraint causing a change in the twinning stress of iron with carbon content, and eventually a total suppression of twinning. It is postulated that the relatively large scatter in the α–ω transition pressure[2] due to interstitial or impurity content is caused by increased lattice shear resistance, similar to the previously mentioned case of deformation twinning, leading to different α–ω transition pressures. While the interaction between the dislocations and interstitial oxygen is no doubt largely elastic in nature, potential interstitial ordering at high oxygen contents may also be responsible for suppression of twinning and the α–ω transition[13].

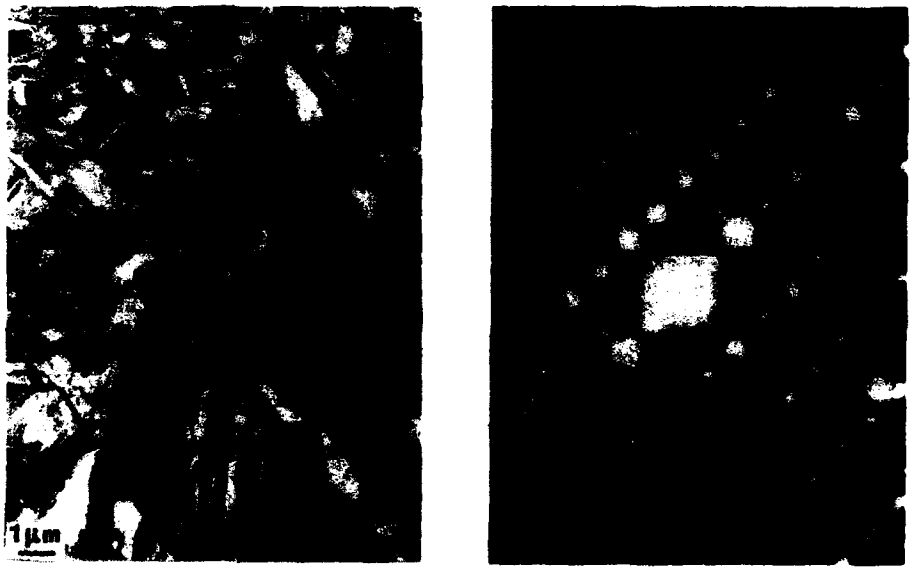


Figure 2 - a) Brightfield micrograph, and b) SADP showing retained omega phase and {1121} deformation twins in high-purity titanium shock loaded to 11 GPa.

Neutron diffraction was used to measure the in-situ bulk lattice constants and volume fractions of the α and ω phases in the recovered samples that were shock loaded. These results are given in Table II. A volume fraction of ~28% ω-phase with lattice parameters a=0.4614 nm and c=0.2832 nm was measured in the 11 GPa shock-recovered high-purity titanium sample. The lattice parameters measured in the current study differ from those quoted in the literature[2]. Unit cell constants for ω-phase have previously given values for "c" ranging

from 0.2813 to 0.2819 nm and "a" ranging from 0.4625 to 0.4643 nm[2]. Significant macrostrains are caused by the lattice mismatch between the α and ω-phases; the "a" of the α-phase tries to match the "c" of the ω-phase, and visa versa. These lattice values represent the global average lattice produced strains referenced to the lattice constants of pure titanium. This lattice mismatch is also seen to result in strains within both lattices which shows up as microstrain. The microstrains represent the distribution of the lattice constants in the sample.

TABLE II - Strains and Lattice Constants for α- and ω-Titanium

	High-Purity Ti	A-70 Ti
volume fraction ω (%)	28	0
lattice constants (nm):		
a(α)	0.29506(2)	0.29520(1)
c(α)	0.46795(4)	0.46884(4)
a(ω)	0.4614(1)	-
c(ω)	0.2832(1)	-
micro-strain from peak widths (%):		
strain (α)	0.68	0.52
strain (ω)	0.74	-
macro-strain from lattice constants (%):		
$(a(\alpha) - a_0) / a(\alpha)$	0.05	-
$(c(\alpha) - c_0) / c(\alpha)$	0.19	-
$(a(\alpha) - c(\omega)) / a(\alpha)$	-4.02	-
$(c(\alpha) - a(\omega)) / c(\alpha)$	-1.40	-

The current shock-recovery findings are contrary to a previous study where shock loading pure Ti at room temperature to pressures of 12 to 50 GPa yielded no retained ω while finding retained ω if shock loading was conducted at 120K[3]. Shock recovery experiments in this study were conducted by shock loading the Ti in steel containers which may have influenced the ε_{res} and thermal history in the recovered samples[3]. Even in the 120K Ti shots[3], measurement of the phase distribution through the recovered sample thickness revealed the absence of ω at the near impact and rear sample surfaces while showing a uniform amount of retained phase in the sample interior. Due to the mechanical and thermal metastability of the ω-phase, it is believed that the ε_{res} in the sample, surface contact stresses, and thermal history recovery effects caused in the steel container resulted in reversion of the ω during release and deceleration at room temperature in the previous study. The variations in the phase-retention results graphically illustrate the importance of utilizing soft recovery techniques to accurately assess shock-induced structure/property relationships and thereby provide post-mortem physical data for comparison with real-time wave profile data.

Summary and Conclusions

Based on a study of the influence of shock-loading and alloy chemistry on the α–ω pressure-induced phase transition in titanium, the following conclusions can be drawn:

1. VISAR wave profiles of shock-loaded high-purity titanium revealed the omega-phase pressure induced transition to occur at approximately 10.4 GPa.

2. Wave profile measurements on A-70Ti and Ti-6Al-4V shocked up to pressures of respectively 35 and 25 GPa exhibited no evidence of a three-wave structure indicative of a phase transition.

3. Neutron diffraction characterization of high-purity titanium shock loaded to 11 GPa and "soft" recovered displayed a 28% volume fraction of retained ω-phase with in-situ bulk lattice parameters of a=0.4614 nm, c=0.2832 nm, and c/a=0.6137.

4. Suppression of the α–ω in A-70Ti, containing a high interstitial oxygen content, is seen to simultaneously correlate with suppression of deformation twinning. It is postulated that the suppression of the α–ω phase transition in titanium is related to increased lattice shear resistance due to interstitial oxygen. This is considered to be a significant new observation which is believed to be basic to the mechanism of the α–ω pressure-induced transition.

Acknowledgments

The authors gratefully acknowledge the assistance of M.F. Lopez, C.E. Frantz, M.A. Winkler, and A.C. Mitchell. This work was performed under the auspices of the U.S. Department of Energy. The Manuel Lujan Jr., Neutron Scattering Center is a national user facility funded by the United States Department of Energy, Office of Basic Energy Science.

References

1. H. Conrad, "Effect of Interstitial Solutes on the Strength and Ductility of Titanium," Prog. Matls. Sci., 26 (1981), 123-403.

2. S.K. Sikka, Y.K. Vohra, and R. Chidambaram, "Omega Phase in Materials," Prog. Matls. Sci., 27 (1982) 245.

3. A.R. Kutsar and V.N. German, Titanium and Titanium Alloys, ed. J.C. Williams and A.F. Belov (New York: Plenum Press, 1982), 1633.

4. A. Rabinkin, M. Taliankar, and O. Botstein, "Crystallography and a Model of the α–ω Phase Transformation in Zirconium," Acta. Metall., 29 (1981) 691-698.

5. G.T. Gray III and C.E. Morris, Sixth World Conference on Titanium, ed. P. Lacombe, R. Tricot, and G. Beranger, (Paris, France: Les Editions de Physique, 1989), 269-274.

6. G.T. Gray III, High Pressure Compression of Solids, ed. J.R. Asay and M. Shahinpoor, (New York: Springer-Verlag, 1992), in press.

7. W.F. Hemsing, "Velocity Sensing Interferometer (VISAR) Modification,' Rev. Sci. Instrum., 50, #1 (1979) 73.

8. R.G. McQueen, S.P. Marsh, J.W. Taylor, J.N. Fritz, and W.J. Carter, "The Equation of State of Solids from Shock Wave Studies," in High Pressure Impact Phenomena, ed. R. Kinslow, (Academic Press, New York, 1970), 293.

9. C.E. Morris, M.A. Winkler, and A.C. Mitchell, "Ti-6Al-4V Alloy Wave Profile Measurements in the Shadow Region," in Shock Waves in Condensed Matter-1987, ed. S.C. Schmidt and N.C. Holmes, (Elsevier Science Publications, B.V., 1988) 265-268.

10. J.M. Brown and R.G. McQueen, "Melting of Iron Under Core Conditions," Geophys. Res. Lett., 7 (1980) 533.

11. J.C. Williams, A.W. Sommer, and P.P. Tung, "The Influence of Oxygen Concentration on the Internal Stress and Dislocation Arrangements in α Titanium," Metall.

Trans., 3 (1972) 2979-2984.

12. J.C. Williams, A.W. Thompson, C.G. Rhodes, and J.C. Chesnutt, "Strengthening and Fracture Mechanisms in Titanium Alloys Critical Review," in Titanium and Titanium Alloys, eds. J.C. Williams and A.F. Belov, (Plenum Press, New York, 1982) 467-496.

13. N.E. Paton, J.C. Williams, and G.P. Rauscher, "The Deformation of α-phase Titanium," in Titanium Science and Technology, eds. R.I. Jaffee and H.M. Burte, (Plenum Press, New York, 1973) 1049-1069.

14. Y.K. Vohra, S.K. Sikka, S.N. Vaidya, and R. Chidambaram, "Impurity Effects and Reaction Kinetics of the Pressure-Induced α–ω Transformation in Ti," J. Phys. Chem. Solids, 38 (1977) 1293-1296.

15. C.L. Magee, D.W. Hoffman, and R.G. Davies, "The Effect of Interstitial Solutes on the Twinning Stress of B.C.C. Metals," Philos. Mag., 23 (1971) 1531-1540.

ROLE OF COMPOSITION AND MICROSTRUCTURE IN DYNAMIC AND STATIC FRACTURE OF ALPHA-BETA TITANIUM ALLOYS

R. W. Judy, Jr.* and I. L. Caplan**

*Naval Research Laboratory, Washington, DC 20375-5000
**Naval Surface Warfare Center-Annapolis Detachment, Annapolis, MD 21402-1198

Abstract

In analysis of fracture properties of metals for structural applications, resistance to crack extension is usually considered to be a single-valued property of the material, and influences of metallurgical factors such as microstructure and composition are often ignored or underestimated. The thermomechanical processing used to reduce the material from ingot to plate or sheet can impart residual stresses, can result in pickup of impurities, can cause anisotropy and can result in other undesirable effects. This is particularly true of titanium alloys, which can have distinctly different grain structures for a single composition and which are extraordinarily sensitive to contamination by interstitial oxygen and hydrogen. To illustrate these effects, we present comparisons of fracture properties measured under dynamic and static loading conditions for two titanium alloys. The alloys were similar in composition, and each was processed by thermomechanical schedules that resulted in distinctly different microstructures.

Methods used to evaluate the materials included the tensile test, the dynamic tear test, the J Integral test and stress-corrosion cracking tests using fracture mechanics specimens. Comparisons of the static fracture properties showed that the effects of a variety of heat-treatments resulting in different microstructures in a Ti-Al-Mo-Zr alloy were dramatically different from those in a Ti-Al-V-Zr alloy. The dynamic fracture properties of both were nearly unaffected by variations in microstructure, and as a result, the two measures of fracture resistance did not correlate well.

Introduction

The great majority of engineering structures do not require sophisticated analysis and careful control of materials and fabrication processes because the consequences of fracture are not of dominant importance to the design. Detailed analyses of fracture, and steps to control fracture, are necessary where structural failure threatens human life, where major ecological damage is possible or where weight/performance tradeoffs necessitate the use of fracture sensitive materials. When materials are considered for such applications, it is important to have a complete knowledge of their resistance to fracture under both static and dynamic loading conditions. In analysis of fracture properties of metals for structural applications, resistance to crack extension is often considered to be a single-valued property of the material, and influences of metallurgical factors such as microstructure and composition are often ignored or underestimated. The thermomechanical processing used to reduce the material from ingot to plate or sheet can impart residual stresses, can result in pickup of impurities, can cause anisotropic effects, etc. This is particularly true of titanium alloys, wherein the final fracture properties are a function of the chemistry, the microstructure and the method used to evaluate fracture resistance. To illustrate

Titanium '92
Science and Technology
Edited by F.H. Froes and I. Caplan
The Minerals, Metals & Materials Society, 1993

the problem described above, we present comparisons of a variety of fracture properties measured on two similar alpha-beta titanium alloys, similar in composition and processed in parallel so that four distinctly different microstructural conditions were obtained for each material.

Materials

The materials were two alpha-beta titanium alloys of nominal compositions Ti-5.5Al-2V-2Zr and Ti-5.5Al-1Mo-2Zr. These alloys were part of a study to determine the efficacy of V and Mo as a beta stabilizer to produce alloys having optimal resistance to crack growth and fracture under a variety of service conditions. The interstitial oxygen content in each alloy was held at 0.09%. Both were produced as 450 kg (1000 pound) ingots and were reduced to 25 mm thick plate by forging and rolling operations as follows:

- Half of each ingot was processed to plate at temperatures starting in the beta field (1040 C); the other half was processed at temperatures starting in the alpha-beta field (960 C). This processing schedule resulted in two plates for each composition.
- Beta processing produced a fine widmanstatten structure with a fine transformed beta grain structure, while the alpha beta processing produced a lamellar structure.
- To complete the matrix of materials, a post processing heat treatment was applied to half of each of plate of each alloy.
- Beta worked materials were heat-treated at 945 C, which was just below the beta transus, for one hour; this produced a coarsening of the lath structure with no change in size of the prior beta grains.
- Alpha-beta worked materials were solution treated for one hour at 1025 C (above the beta transus) and were then heat-treated at 945 C. This produced a coarse colony structure with larger prior beta grains than were present in the beta worked materials. Another effect was the elimination of local residual stresses induced by hot working.

These final heat treatments were performed in a vacuum furnace on sawed test specimen blanks prior to final machining. The result of all of the above was to produce each of the materials in four distinctly different conditions shown for both alloys in figure 1 and generally described in the following table:

Table I. Microstructures Resulting from Processing Schedules.

	BETA WORKED	ALPHA BETA WORKED
AS ROLLED	FW (Fine Widmanstatten) Condition A	L (Lamellar) Condition C
AR + HT	CW (Coarse Widmanstatten) Condition B	C (Colony) Condition D

In each alloy, the final conditions included three transformed beta structures, each derived from different processing routes, as well as an alpha-beta structure.

Measurements

The tests used to evaluate the materials included the standard tensile test, the dynamic tear (DT) test, the J Integral test (J_{Ic}) and stress-corrosion cracking (SCC) tests using fracture mechanics specimens. All except the DT tests were performed with duplicate specimens. The following is a brief description of each test and its intended purpose. The standard (1) tensile test is used universally to measure strength and ductility; a 13 mm diameter specimen was used for this work. The dynamic tear (DT) test (2) was developed as a low cost method to indicate the resistance to crack extension under dynamic loading conditions. The DT energy, the energy to fracture the specimen, is taken as an index of merit for resistance to dynamic fracture. By itself, DT energy is not an absolute measure of fracture resistance that can be applied analytically, but it must be correlated to other measures and verified analyses to be most useful (3-6). Ratio Analysis Diagrams (RADs) developed for titanium alloys and for steels and aluminum alloys (6),

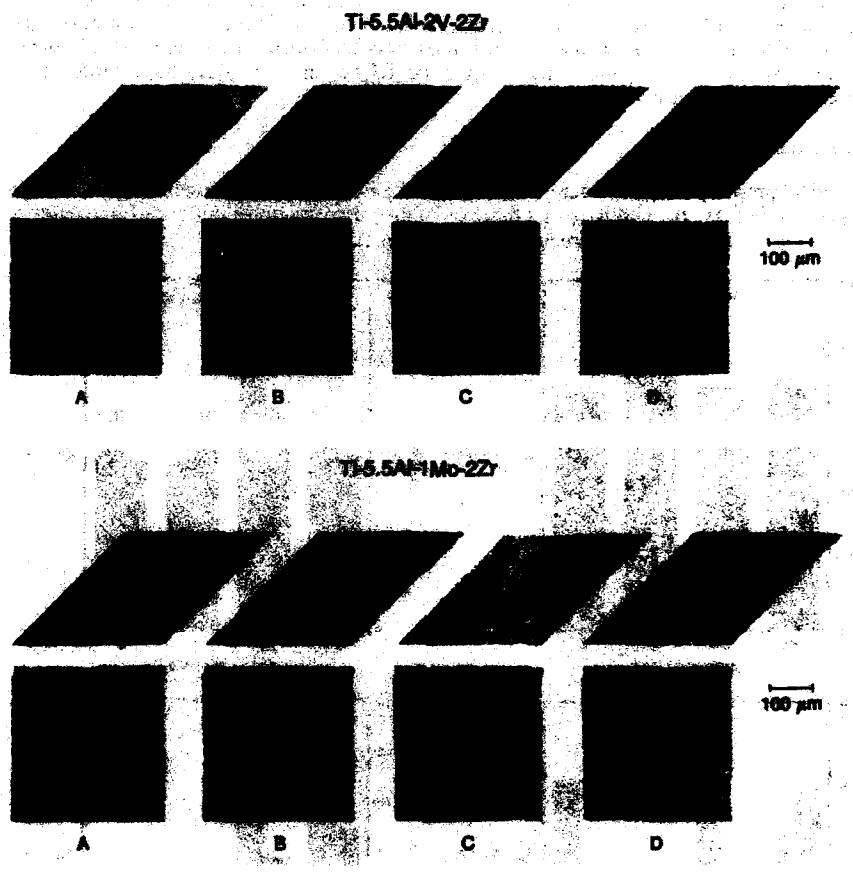


Figure 1 - Microstructures for Ti-5.5Al-2V-2Zr (top) and Ti-5.5Al-1Mo-2Zr (bottom) illustrating the four conditions discussed in this paper.

as well, were based on correlations between DT energy and K_{Ic}, the critical stress intensity factor for fracture under plane strain conditions.

The J Integral test (7) is widely used to measure the resistance of materials to crack extension under static or slowly applied loading conditions. The J_{Ic} parameter is used to measure resistance to crack initiation. Crack extension or tearing resistance is described by the J-R Curve, which depicts energy per unit crack extension. For these evaluations, standard 1T compact specimens were used to record the J-R Curve for each material, and the methods described in (7) were used to compute the values of J_{Ic}.

Stress-corrosion cracking (SCC) tests were conducted as a part of this investigation to determine the sensitivity of the materials to a seawater environment. The SCC tests are considered because the methods and parameters are based on linear elastic fracture mechanics and, in the absence of crack growth because of the salt water environment, the values measured in the test reflect static fracture properties. In these SCC tests, values of stress-intensity were measured using 25 mm WOL specimens in static loading frames by techniques reported in (8). The environment was 3.5% NaCl in distilled water. Bracketing techniques between loadings of no-crack-growth and specimen failure were used to identify the threshold value of stress-intensity (K_{sw}) for specimen

fracture. There was no identifiable crack growth due to SCC for any of the specimens, so that the values are really stress-intensity values measured for the 150 hour test duration, using specimens that in most cases would fail the thickness requirement for fracture tests. In the case of crack growth by SCC, the values would be KIscc, the threshold stress intensity for environmental crack growth.

Discussion of Results

Mechanical property data and fracture data for the titanium alloys are presented in plots of yield strength, DT Energy, J_{Ic}, and K_{Sw} as a function of the microstructures in figure 2; the letter code in this figure refers to the microstructures, as shown in Table 1.

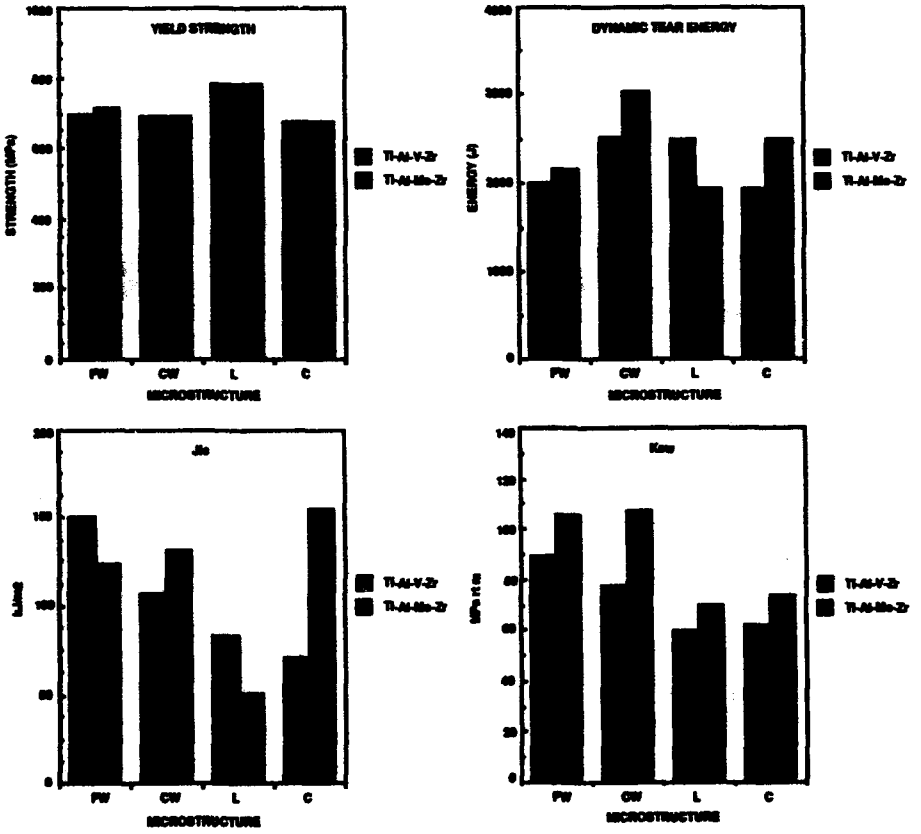


Figure 2 - Trends of property behavior with microstructural condition for two titanium alloys.

Yield strength was highest in the lamellar structure for both alloys, and no difference in the responses of the alloys to the thermal cycle was apparent. Dynamic fracture data show that coarsening the lath structure by heat-treating a beta structure (CW) improved the DT energy in both alloys. On the other hand, coarse lath colony structures obtained by heat-treating the lamellar alpha beta structures caused an unexplainable reduction of the DT energy in the Ti-Al-V-Zr alloy and an increase of DT energy in the Ti-Al-Mo-Zr alloy. The Al-Mo-Zr alloy exhibited higher values of DT energy in all of the beta structures, while the Al-V-Zr alloy had higher DT energy in the lamellar structure. It is cautioned that all of the values, when combined on the

RAD, indicate a level of fracture resistance that would require significant plasticity for fracture, so that the differences in predicted performance of the two are not as significant as one might infer from the values alone.

The remaining two bar graphs in figure 2 show static fracture resistance measured in terms of J_{Ic} and K_{sw}. In both of these measures, trends opposite to those shown for dynamic fracture are observed. Coarsening the beta structure, i.e., heat-treating FW to produce CW structure causes a reduction of the apparent fracture resistance in the Ti-Al-V-Zr alloy and has nearly no effect in the Ti-Al-Mo-Zr alloy, while heat-treating the lamellar structure had little effect on the Ti-Al-V-Zr alloy. The Ti-Al-Mo-Zr is clearly superior to the Ti-Al-V-Zr alloy in comparisons of K_{sw} values at all conditions, and in the coarser colony condition for J_{Ic} as well. The difference between the K_{sw} values and the J_{Ic} values is only in the loading rate; K_{sw} represents the applied stress intensity that can be maintained for a period of 150 hours or more, while J_{Ic} is measured under rising load conditions. Note that both widmanstatten structures give very high values of K_{sw} for both alloys, and the lamellar and colony structures give the lowest values.

The effects of microstructural variations on the measured J-R curves for each alloy are shown in figures 3A and 3B. In both alloys, the tearing resistance and J_{Ic} values for materials having lamellar microstructures were quite low. Transformation of lamellar to a colony structure dramatically improved the properties for the Ti-Al-Mo-Zr alloy and to a much smaller extent in the Ti-Al-V-Zr alloy . Coarsening of the widmanstatten structures caused only a small change of the J-R curve for each alloy. A strong influence of composition is also apparent. With the exception of the lamellar structure, all microstructure conditions for the Mo-containing alloy produced tearing resistance performance superior to the same condition for the V-containing alloy.

Past work to develop correlations of static fracture parameters K_{Ic} and G_{Ic} with DT energy led to standardized Ratio Analysis Diagrams (RAD's) that combined strength, fracture resistance and size factors for a simplified presentation of the problem (6). The correlation approach applied in a strict sense only where K_{Ic} could be measured and used; most structural materials, including titanium alloys, are used in the mixed-mode fracture or fully plastic fracture regime where now J_{Ic} and CTOD are applied. It is the authors' opinion that a similar correlation approach will be used when widely accepted analyses based on J Integral or another elastic plastic parameter are established and confirmed experimentally. One major point in all this is that tight correlations between various fracture parameters should not be expected, when such different responses of fracture properties to microstructure are evident. To illustrate this point, values of J_{Ic} vs DT energy are plotted in figure 4. Also shown in figure 4 are values of G_{Ic} and DT energy for titanium alloys taken from reference (4); the line in this figure is a best fit to the G_{Ic}-DT data set. The alloys in the G_{Ic} data set were near-alpha and alpha-beta compositions, and the data met ASTM criteria for validity in K_{Ic} testing. The alloys were tested in the as-received condition (beta rolled) or in the beta rolled and alpha-beta heat-treated condition. For comparison, the microstructures of most of those alloys would be close to the fine-widmanstatten condition of the present alloys. One contention is that the quantities G_{Ic} and J_{Ic} are equivalent. From the data of figure 4 it is abundantly clear that the J_{Ic} and DT Energy do not correlate, although G_{Ic} and DT Energy clearly do correlate. One possible explanation is that J_{Ic} and G_{Ic} are not equivalent, though this is unlikely given the conditions of the tests. A more likely explanation is that the local response of the materials is governed by the rate sensitivity of the microstructures. In the coarser widmanstatten, colony and lamellar structures, the DT test greatly underestimates the J_{Ic} values. Since the purpose of the correlation was to enable use of the DT test to predict K_{Ic} (or G_{Ic}) and by extension, J_{Ic}, the data illustrate that correlations between fracture parameters must be applied with some caution.

Several investigators have observed that increasing the strain rate or loading rate causes an increase in the fracture resistance in titanium alloys. For example, Bryant, Wilsdorf, et al (9), observed a trend of elevation of the tensile flow curve, as well as increasing K_{Ic}, in Ti-10V-2Fe-3Al with increasing strain rate; in their work they showed that several factors contributed to the increase in fracture resistance, including local adiabatic heating and a reduction in secondary

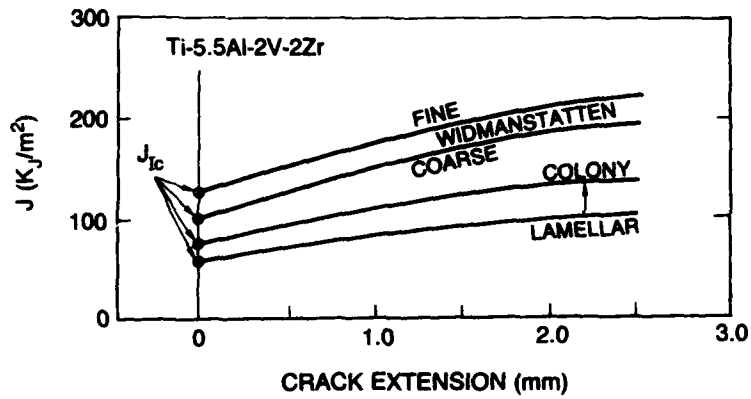


Figure 3A - J-R curves for Ti-5.5Al-2V-2Zr. Effects of microstructure are similar to those observed for the other alloy, though they are less dramatic.

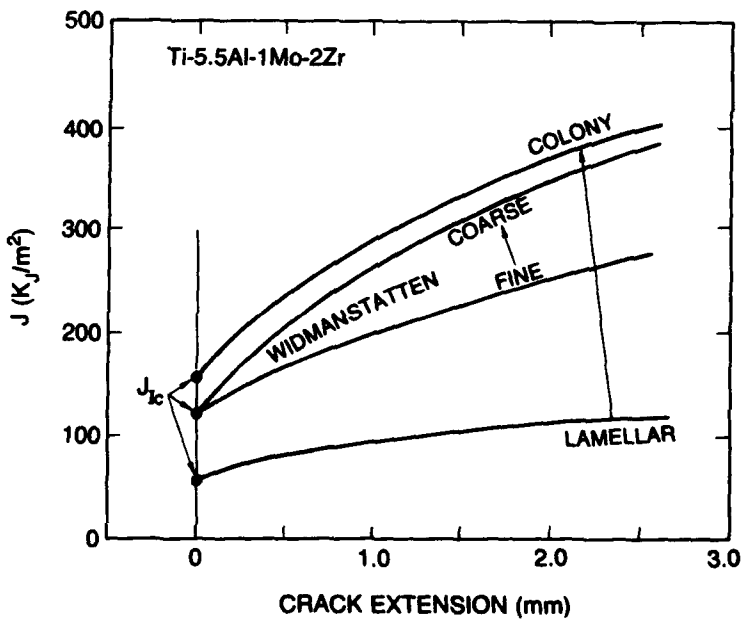


Figure 3B - J-R curves for Ti-5.5Al-1Mo-2Zr, showing the strong effect of microstructure. Note that changing the structure from lamellar to colony increases both J_{Ic} and the R-curve.

cracking (normal to the main fracture plane), with increasing strain rate. The effects of these events were a reduction of crack path tortuosity and a simultaneous increase in energy given to crack tip plastic flow. Most investigators who have studied the effects of microstructure on fracture in titanium (e.g. 10,11,12) have noted that the predominant mode of fracture is void

formation at grain boundary alpha and between the alpha laths, given time for such voids to form, as in static fracture. A strong contribution of the void formation process is also known to be the slip systems favored by the hexagonal structure of alpha titanium. In strongly textured structures, the properties vary with the orientation of the test specimen. The ease of void formation depends on both the thickness of the grain boundary alpha and the tortuosity of the lath structure, either colony or widmanstatten. Hence an increase in structural complexity or tortuosity going from the lamellar to colony or widmanstatten structure results in improved fracture initiation resistance at static loading rates.

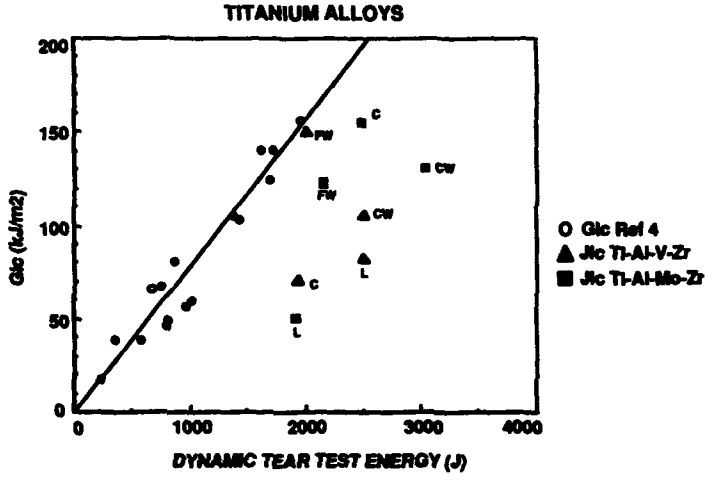


Figure 4 - Comparison of J_{Ic}-DT data for two titanium alloys with trends established for other titanium alloys. This plot illustrates the necessity of confining correlation data to a single microstructure for titanium.

Summary

Several conclusions can be drawn on the basis of the preceding discussion:

- There is little difference in the effectiveness of V or Mo as a beta stabilizing element with regard to tensile properties. The lamellar structure produced by rolling through the alpha-beta temperature range produces the highest yield strength; widmanstatten and colony structures resulted in materials with essentially the same yield strengths.
- Both alloys, in the metallurgical conditions examined, were insensitive to salt water SCC.
- Observations made concerning fracture resistance under dynamic loading conditions showed that there were no consistent trends relatable to microstructure. Available evidence indicates that in titanium alloys, secondary cracking is minimal at high loading rates in the formation stage of the crack tip plastic zone, and would be expected to be *minimal as the* plastic zone travels through the test section of the DT specimen. This being the case, the size of the plastic zone, and hence the energy expended in fracture, should not depend on the arrangement of microstructural components and therefore should not be strongly affected by the structure. With regard to chemistry, the Ti-Al-Mo-Zr alloy displayed higher dynamic toughness than the Ti-Al-V-Zr alloy in all microstructures except the lamellar.
- Observations made concerning crack initiation measures of fracture resistance made under static loading conditions, i.e. J_{Ic} and K_{sw}, are strongly influenced by both chemistry and microstructure. In particular, the lamellar structures produced the lowest resistance to crack initiation. Furthermore the response of J_{Ic} to heat treatment was dramatically different for the two alloys tested. With regard to chemistry effects, the Al-Mo-Zr system had consistently higher values of K_{sw} than did the Al-V-Zr system, for all microstructural conditions.

- In the alloys investigated in this work, there was very poor correlation between static fracture performance (J_{Ic} and Ksw) and dynamic fracture performance (DT Energy).
- For titanium alloys, wide ranges of properties can be expected for a single composition as a function of the microstructure. For this reason, efforts to predict the properties of titanium alloys by statistical analysis of the effects of various alloying elements must also include effects of microstructure, or better, must be applied to a single microstructural condition produced by a fixed processing schedule. Unless this is done, the predictions can only be correct in a general sense and cannot be used with any degree of accuracy to isolate effects of individual elements in complex alloys. This is amply demonstrated by the variation in single properties, such as J_{Ic} or yield strength, measured in the alloys discussed above.

References

1. ASTM Standard E8 81, 1983 Annual Book of ASTM Standards, Vol 03.01, American Society for Testing and Materials, Philadelphia, PA (1983)

2. P.P. Puzak and E.E. Lange, "Standard Method for the 1 Inch Dynamic Tear Test". NRL Report 6851, February 13, 1968

3. R. W. Judy, Jr. C. N. Freed and R. J. Goode, "A Characterization of the Fracture Resistance of Thick-Section Titanium Alloys" TITANIUM SCIENCE AND TECHNOLOGY, R. I. Jaffee and H. M. Burte, eds., The Metallurgical Society of AIME, Conference Proceedings, Plenum Press, 1973

4. R. W. Judy, Jr., B. B. Rath and R. J. Goode, "Fracture of Titanium Alloys" Invited Critical Review TITANIUM SCIENCE AND TECHNOLOGY, Proceedings of the Fifth International Conference on Titanium, Munich, West Germany,10-14 September 1984; , pp 1925-1944

5. R. W. Judy, Jr., and R. P. Mikesell, "Comparison of Fracture Resistance Characterizations of Titanium Alloys by Small-Specimen Methods" TITANIUM SCIENCE AND TECHNOLOGY, Proceedings of the Fifth International Conference on Titanium, Munich, West Germany,10-14 September 1984; pp 2055-2064

6. W.S. Pellini, PRINCIPLES OF STRUCTURAL INTEGRITY TECHNOLOGY, Office of Naval Research, Arlington VA, 1976

7. ASTM Standard E813-81, 1983 Annual Book of ASTM Standards, Vol 03.01, American Society for Testing and Materials, Philadelphia, PA (1983), 762

8. R. W. Judy, Jr., B. B. Rath and I. L. Caplan, "Stress Corrosion Cracking of Pure Titanium as Influenced by Oxygen Content" SIXTH WORLD CONFERENCE ON TITANIUM, P. Lacombe, R. Tricot and G. Beranger, eds. ,Societe Francaise de Metallurgie, Les Editions de Physique, Paris, pp 1747-1754

9. J.D. Bryant, "Deformational Heating at the Crack Tip and its Role in Fracture of Ti-10V-2Fe-3Al", Ph. D. Thesis, University of Virginia, January 1987

10. G. Lutjering, A. Gysler, and L. Wagner, "Crack Propagation in Titanium Alloys" SIXTH WORLD CONFERENCE ON TITANIUM, P. Lacombe, R. Tricot and G. Beranger, eds., Societe Francaise de Metallurgie, Les Editions de Physique, Paris, 1989, pp 71-80

11. J.C. Williams, J.C. Chesnutt and A.W. Thompson, "The Effects of Microstructure on Ductility and Fracture Toughness of Alpha+Beta Titanium Alloys", MICROSTRUCTURE, FRACTURE TOUGHNESS AND FATIGUE CRACK GROWTH RATE IN TITANIUM ALLOYS, A.K. Chakrabarti and J.C. Chesnutt, eds, The Metallurgical Society, Warrendale PA, pp 255-271

12. G. Terlinde and K.-H. Schwalbe, "The Role of Alpha Phase in the Fracture Toughness and Tensile Fracture of an Aged, Metastable Beta Titanium Alloy". Ibid, pp 97-109

AN INVESTIGATION ON STRENGTHENING PROCESS AND ITS STRENGTHENING MECHANISM FOR TC_4 TITANIUM ALLOY

X. K. Meng, Y. G. Zhou, and H. Q. Yu

Department of Materials Science and Engineering
Northwestern Polytechnical University
Xi' an, Shaanxi, P. R. China 710072

Abstract

A strengthening process for a TC_4(Ti-6Al-4V) titanium alloy is presented, consisting of "High Temperature Forging + High Temperature Solution Treatment + Conventional Annealing", and the mechanism of strengthening is discussed. Experimental results indicate that this new process can increase the room and high temperature strengths strikingly without reducing the ductility and thermal stability. Based on microstructural analyses, it is concluded that the most effective strengthening for TC_4 alloy is a "boundary layer" strengthening rather than the more commonly considered dispersion and/or solution strengthening.

Introduction

The conventional hot-working process for TC_4 titanium alloy is to forge at 30~40℃ below the transformation temperature and to anneal subsequently. Under this process the ductility and thermal stability of the alloy are usually quite good. Unfortunately the strength is relatively low and as a result the titanium forgings are often scrapped.

For the above reason, some technical standards for astronautical materials, such as those made in United States, now permit changes of heat treatment to strengthen this alloy. The authors' research[1,2], in which the process of strengthening heat treatment for TC_4 alloy is presented, has verified its feasibility. In resent years, near-β forging process[3] developed in the Chinese titanium industry has made dramatic success in raising hot-strength and improving mechanical properties. It may be expected that by combining the near-β forging with

X. K. Meng, Ph. D. Candidate, Y. G. Zhou, Professor, and H. Q. Yu, Associate Professor, are with the Department of Materials Science and Engineering, Northwestern Polytechnical University, Xi' an, Shaanxi, 710072, P. R. China.
This is a "student paper" accepted as an oral presentation for the Seventh World Conference on Titanium (No. 11-5).

Titanium '92
Science and Technology
Edited by F.H. Froes and I. Caplan
The Minerals, Metals & Materials Society, 1993

the strengthening heat treatment, the strength of the alloy will be raised effectively while maintaining its ductility and thermal stability. With this consideration, authors develop the strengthening process "High Temperature Forging + High Temperature Solution Treatment + Conventional Annealing".

Experiment Procedure

The material used in this investigation is prepared from 150mm diameter rolled bar of TC_4 titanium alloy, with a β transus (T_β) of 995℃ and the chemical composition shown in Table I.

Table I Chemical Composition of Material (mass%)

Material	Ti	Al	V	Si	Fe	C	H	O	N
TC_4	bal.	6.16	3.90	0.03	0.09	0.015	0.0046	0.112	0.019

The rolled bar is cut into samples 50 mm thick. After covered with FR_5 lubricant, the samples are upset 50% by 3T die-forging-hammer. The hot-working processes are as follows:

Convenional Process

The as-rolled samples are forged at 40℃ and 30℃ below T_β respectively, and air-cooled. Then the as-forged samples are annealed at 800℃ for 3 hours and air-cooled.

Strengthening Process

The as-rolled samples are forged at 10℃ and 5℃ below T_β respectively and cooled in water (High Temperature Forging). A two-step heat treatment is used to strengthen the as-forged samples. At first, they are processed with a solution heat treatment at 30℃ below T_β for 1 hour and quenched in water (High Temperature Solution Treatment), then annealed at 800℃ for 3 hours and air-cooled (Conventional Annealing).

Results and Discussion

Microstructure and Properties

Fig. 1 Shows the typical microphotographs of TC_4 alloy after processing per the conventional process. Fig. 1a was forged 40℃ below T_β and then air cooled. The content of equiaxed α in Fig. 1a is 31 percent. It is increased to 45 percent after conventional annealing, as shown in Fig. 1b. It can be seen that the microstruc-

ture after conventional processing produces an equiaxed structure.

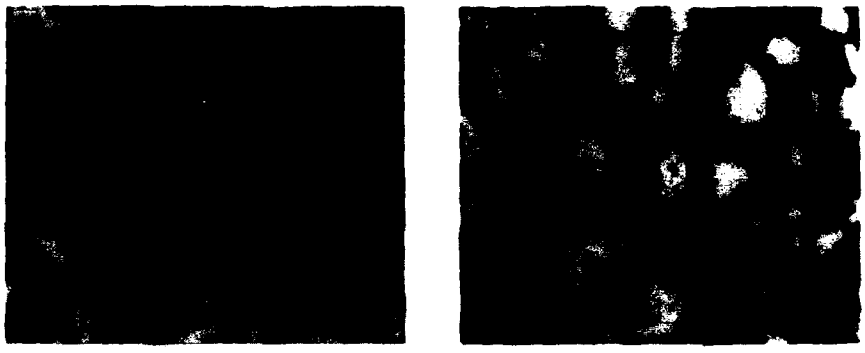


Fig. 1-Microstructure of TC_4 alloy processsed via conventional process.
a-Forging at 40℃ below T_0 followed by air cooling.
b- a+ Annealing at 800℃ for 3 hours followed by air cooling.

Differing from above, the microstructure after processing via the strengthening process is a bi-modal structure in which equiaxed α is accompanied by α-plate, as shown in Fig. 2, though the contrast of α-plates in Fig. 2a is not quite clear. The contents of equiaxed α in Fig. 2 a and b are 12 and 23 percent respectively.

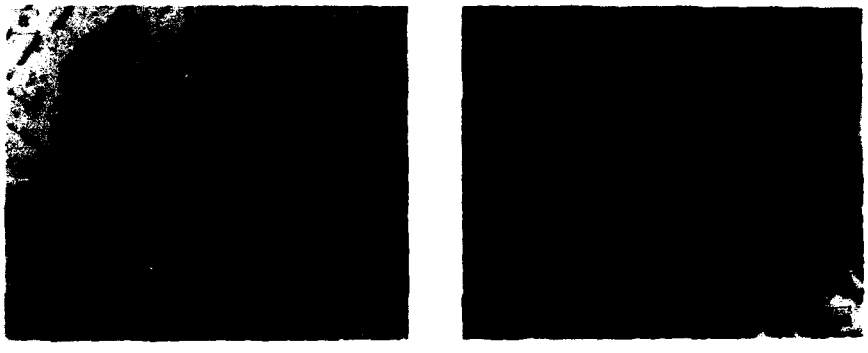


Fig. 2-Microstructure of TC_4 alloy processing via the strengthening process.
a-Forging at 5℃ below T_0 followed by water cooling.
b- a + Processing with solution treatment at 30℃ below T_0 for 1 hour followed by water cooling and then annealing at 800℃ for 3 hours followed by air cooling.

The metallurgical properties under the above processes are tabulated in Table 1.

Table I The Metallurgical Properties of TC_4 Alloy under the Different Hot-working Methods

Hot-working Methods	Forging Temperature (℃)	Mechanical Properties at Room Temperature				Mechanical Properties at High Temperature (400℃)			Thermal Stability (400℃-100 hours)			
		UTS σ_b (MPa)	YS $\sigma_{0.2}$ (MPa)	Elon. δ_5 (%)	ROA ψ (%)	UTS σ_b (MPa)	Elon. δ (%)	ROA ψ (%)	UTS σ_b (MPa)	YS $\sigma_{0.2}$ (MPa)	Elon. δ_5 (%)	ROA ψ (%)
Conventional Process	T_β-40	875	852	15.0	46.7	600	14.8	62.8	887	872	15.2	44.0
	T_β-30	881	874	14.8	45.5	602	14.2	61.0	893	887	14.8	43.5
Strengthening process	T_β-10	965	940	12.0	42.0	680	12.2	60.5	980	954	11.6	36.8
	T_β-5	978	941	12.2	43.0	689	12.7	57.0	984	955	12.0	40.0

Forging on Microstructure

During the heating process of forging, the $\alpha \rightarrow \beta$ transformation occurs, so α phase is transformed into β phase gradually. The higher the heating temperature becomes, the less equiaxed primary α is retained. Moreover, at a higher temperature, acicular Widmanstätten α in retained β is partially broken into pieces. If forging is followed by air cooling, the pieces will be trapped by α precipitated from retained β and hence be equiaxed (Fig. 1a). On the contrary, when water cooling follows forging, transformed β will be transformed into metastable martensite. Therefore, α can not be precitated from transformed β and the pieces can not be equiaxed. On this condition, a bi-moldal structure occurs, in which equiaxed primary α and α-piece (Fig. 2a) which would grow into α-plate (Fig. 2b) during solution treatment and annealing process are contained. The large amount of the β phase and the ultra-refinement of the equiaxed primary α (and α-piece), obtained by high temperature forging with quenching in water subsequently, can improve the strength of the two-phase alloy, according to the conclusion made lately by Kawabe and Muneki[4].

Boundary Layer Strengthening

It is generally accepted that the mechanism of strengthening for an equiaxed structure obtained with convertional process of TC_4 alloy is mainly based on solution and /or dispersion strengthening. Nevertheless, from strengthening process presented by authors, it seems that the striking strengthening should be attributed to a "boundary layer" strengthening resulted from bi-modal structure between equiaxed α and α-plate.

Transformed β, which is defined as a boundary layer between equiaxed α phases or between equiaxed α and α-plate[5], consists of acicular Widmanstätten α and retained β. As for conventional process, a little Widmanstätten α which is not broken and equiaxed grows into long-acicular α and no subgrain β occurs at the boundary, as shown in Fig. 3a and b.

Fig. 4 Shows a boundary layer between equiaxed α and an α-plate in the strengthening process sample. Fig. 4a is in a forged and water cooled state, in which Widmanstätten α is randomly distributed at the boundary and a large amount of subgrain β is formed. Due to the subsequent processing, with solution heat treatment at higher temperature followed by water cooling, the morphology of subgrain β is almost constant, even after conventional annealing, as shown in Fig. 4b. It can also be observed that Widmanstätten α in Fig. 4b is distributed at the boundary more randomly than that of in Fig. 4a, and the secondary α precipitates from the boundary layer in the form of particles.



Fig. 3-EM microphotographs of a boundary layer between equiaxed α phases under conventional process.
a-Forging at 40℃ below T_θ followed by air cooling.
b- a + Annealing at 800℃ for 3 hours followed by air cooling.



Fig. 4- EM microphotograghs of a boundary layer between equiaxed α and α-plate under strengthening process.
a-Forging at 5℃ below T_θ and water cooling.
b- a+Solution treating at 30℃ below T_θ for 1 hour and water cooling + Annealing at 800℃ for 3 hours and air cooling.

As for strengthening process, forging at a higher temperature near T_θ followed by rapid cooling and solution treatment processing is the main reason why subgrain β could be formed at the boundary layer, and its morphology and structure could be controlled even during conventional annealing process. Therefore, a striking effect of boundary strengthening is obtained. In the meantime, the ductility is not reduced due to the fact that a little equiaxed primary α is reserved. In the first process of heat treatment, i. e. , high temperature solution treatment, dislocation in a pile-up slip or climb again[5] and hence the differential energy of distortion between subgrains is reduced. Thus, the tendancy for subgrains growth is suppressed. The second process of heat treatment is conventional annealing during which the equiaxed primary α, acicular Widmanstätten α and subgrain β may grow or nodulize. As a result, bi-modal structure, in which transformed β (a boundary layer) segregates α-plate from equiaxed α, is formed completely (Fig. 2b) and the effect of boundary strengthening becomes more effective. Further-

more, equiaxed α grains in this structure make the plastic deformation cooperate harmoniously[2]. Hence crack or void initiation or propagation is delayed, even suppressed, and a satisfactory ductility as well as thermal stability is obtained simultaneously.

Summary and Conclusions

This paper shows that the most effective mechanism of strengthening for TC_4 alloy is "boundary layer" strengthening rather than solution and/or dispersion strengthening.

In comparison with conventional process, the strengthening process raises room-temperature strength up to 978 MPa, high-temperature strength (400℃) up to 689 MPa, while ductility and thermal stability are not reduced appreciably.

References

1. X. K. Meng et al., Titanium Science and Engineering (Changsha, China: Publishing House of Central South University, 1991), 537-539.
2. X. K. Meng et al., "The Heat Treatment Process Improving the Mechanical Properties of TC_4 Forgings," Chinese Journal of Heat Treatment of Metals, 34(1) (1991), 46-49.
3. *Y. G. Zhou, B. C. Zhang*, "*An Investigation on Near-Beta Forging of Titanium Alloys*," Acta Aeronautica et Astronautica Sinica, 10(1) (1989), 60-66.
4. Y. Kawabe, S. Muneki, "Strengthening and Toughening of Titanium Alloys," ISIJ Int., 31(8)(1991), 785-791.
5. X. K. Meng, "On Strengthening Technology of Titanium Alloys" (Paper presented at 1991 SSM Annual Meeting, Xi'an, 18-19 Feburary 1992), 67.

IMPROVEMENT OF STRUCTURE AND PROPERTIES OF (α+β)-TITANIUM ALLOYS USING THE RAPID HEATING AND ACCELERATED COOLING

O.M.Ivasishin and P.E.Markovsky
Institute for Metal Physics,
36 Vernadsky str., Kiev-142,
252680, Ukraine.

ABSTRACT

The possibility of transformation lamellar type of α-phase in high-alloyed (α+β)-titanium alloys into globular one without deforamation by means of rapid heating to β-region temperatures, accelerated cooling and further annealing has been shown. Such a treatment can be successfully used to improve mechanical properties of alloys. Possible application to heat treatment of weldments is given.

Introduction

Rapid heat treatment of (α+β)-titanium alloys gives rise to the peculiar structures [1,2] with the fine β-graines and high-dispersive intragraine α-phase. The structures of such kind are not attainable by conventional furnace heat treatment. The chemical inhomogeneity of β-solid solution plays an important role and its optimisation allows to achive one-of-a-kind combination of strength and plasticity. For example, for martensitic class alloy VT23 treatment including rapid heating into β-field, quenching and aging gives rise to UTS=1950 MPa at elongation δ=7% [2]. Besides that, the rapid heat treatment pereits high values of fatique characteristics. For example, the HCF strength of Ti-6Al-4V alloy becomes equal to 700...750 MPa after this treatment [3].

However, the positive influence of rapid heat treatment is perfectly pronounced only for the alloys with fine-grained initial structure. Alternatively, the properties improvement is much lower in the case of coarse-grained

Titanium '92
Science and Technology
Edited by F.H. Froes and I. Caplan
The Minerals, Metals & Materials Society, 1993

lamellar-type structures, because the morphology of initial phases is inherited by the metastable phases and their decomposition products on the quenching and ageing. Hereditary morphologic correlation between the final and initial structures may be avoided by means of special treatment, which includes the rapid heating up to the temperatures of β-field and accelerated cooling with rates of 30...80°C/s when martensitic transformation of inhomogeneous β-phase is accompanied by the complex diffusional redistribution of alloing elements [4].

Present work deals with the investigation of structure transformations in ($\alpha+\beta$)-titanium alloy VT23 that take place on above-mentioned treatment (rapid heating and accelerated cooling - RHAC) and further annealing in ($\alpha+\beta$)--field and their influence on mechanical properties.

Material and Experimental Procedure

High-strength titanium alloy VT23 (Ti-4.8(wt)%Al-1.6%Mo-4.2%V-0.5%Fe-1.1%Cr) with initial globular structure was investigated. The material was taken as a sheet of 1.5 mm thickness. The coarse-grained structure with lamellar α-phase was formed by the β-annealing in the part of specimens (Fig.1,a). The specimens were rapidly heated by direct resistance method using 50 Hz current. Formation of optimal chemical inhomogeneity of high temperature β-solid solution on $\alpha+\beta_0 \rightarrow \beta$ transformation [2] have been achieved by means of appropriate choise of rapid heating regime (the shift of β-transus temperature, being the function of heating rate, was taken into account for every specific initial structure [6]). The heating rate of 50°C/s was used as providing the necessary concentration parameters of β-solid solution after heating to temperatures of 920°C and 980°C for globular and lamellar structures, correspondingly. Then, the cooling to M_s point was carried out with rate of 50°C/s. Microstructures were investigated after different treatments by light (LM) and transmission electron (TEM) microscopy. Mechanical testing was carried out using the specimens and techniques described in [5].

Results and Discussion

As a result of RHAC, the dispersive homogeneous structure is formed in all specimens (Fig.1,b). The main feature of such structure described in details in previous paper [4] consists in highly uniform distribution of very fine martensite crystals in β-matrix. In accordance with the theory, proposed in [7], this may result from the noticeable internal stresses which accompany

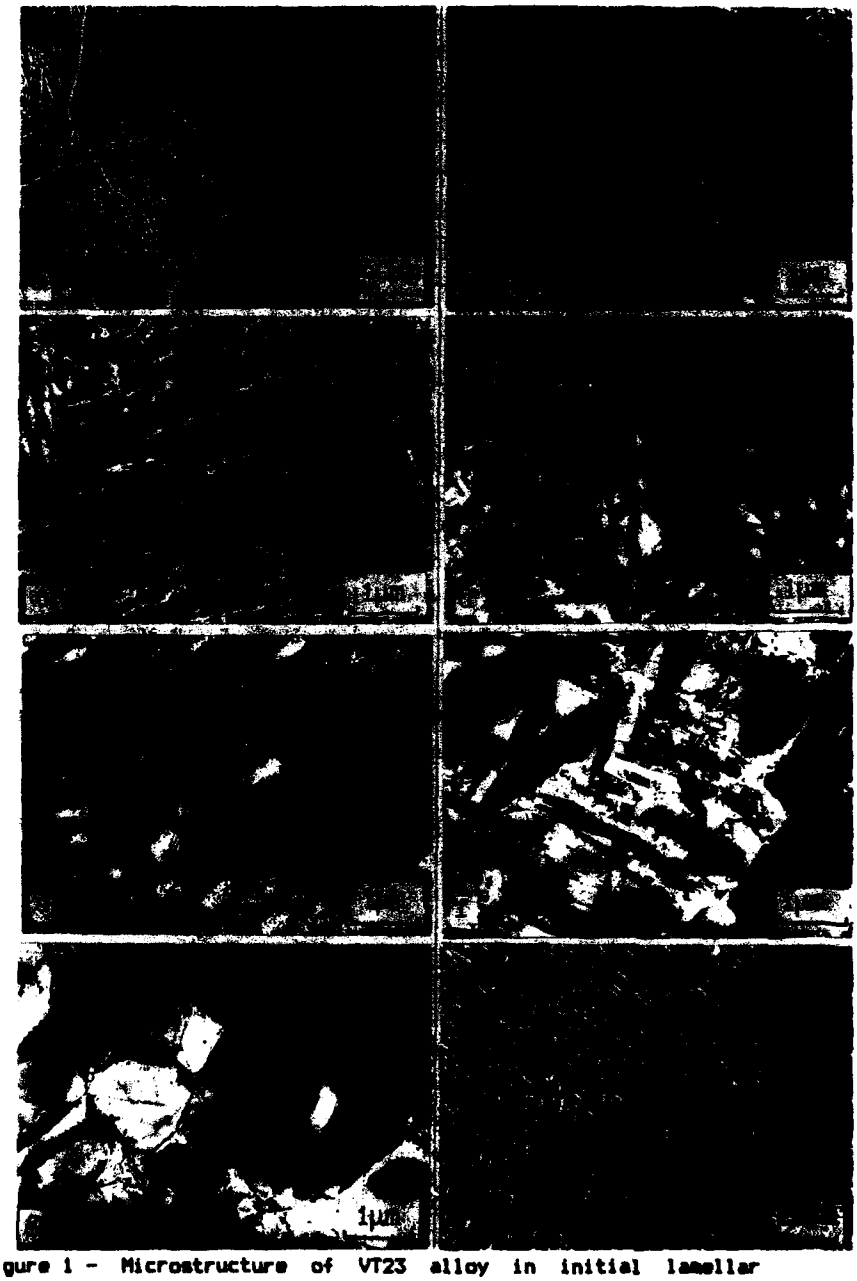


Figure 1 - Microstructure of VT23 alloy in initial lamellar state (a), after RHAC (b) and further annealing 600°C, 1 h (c); 650°C, 1 h (d,e); 650°C, 4 h (f); 650°C, 8 h (g); 750°C, 6 h (h). a,h-LM, b-g -TEM, e-dark field.

the decomposition of high-temperature β-phase. The similar high-dispersive martensite phase was observed, for example, in unalloyed titanium [8] quenched from β-field with rates of $10^4...10^5$ °C/s.

If the temperature of subsequent annealing is lower to 650°C, the decomposition of martensite and metastable β-phase as well as coagulation of decomposition products take place (Fig.1,c).The final geometry of α-particles has pronounced lamellar character. While the increasing the annealing temperatures up to 650...700°C individual α-globules appear in the structure side by side with the lamellar particles (Fig.1,d).The orientation of these globules differs from that of the neighbouring crystals (Fig.1,e). The last permits to suppose that the α-globule initiation goes through the recrystallization of fine lamellar α-phase. The prolongation of annealing leads to the progressive coarsening of both globular and lamellar types of α-phase (Fig.1,f), but growth of α-globules becomes preferable in what follows. As a result, the completely recrystallized globular structure (Fig.1,g) forms after 7...9 hours. The α-phase globules can be coarsened by additional annealing at higher temperatures. But, if annealing at once at temperatures over 700°C, the intensive coagulational growth of lamellar α-phase dominate over the initiation and growth of α-globules. The low aspect ratio and high dispersity of α-plates (Fig.1,h) are peculiar to resulting structure.

It may be deduced, that either of competing processes taking place on the annealing - formation of globules and coagulation of lamellars - is preferable in the certain temperature range. The formation of globules dominates only at 650...700°C. The recrystallization of α-phase, caused by the phase transformation of inhomogeneous β-solid solution on accelerated cooling, is not so uniform as that of after the plastic deformation and takes place within the rather restricted annealing temperature interval.

Another feature of RHAC-treated structures consists in the fact, that only part of the β-grain boundaries (roughly 70...80%) are enveloped by the α-phase in both globular and lamellar structures (Fig.2,a). When the globularization of the intragrain α-phase takes place the grain-boundary α-phase also forms as the chaines of α-globules (fig.2,b). The double annealing (550°C,8h + 750°C,4h)decreases the enveloped boundary part to 50...60%.

On the base of structural investigation the specimens for mechanical testing were chosen (table 1). Results of testing point to the fact that the optimal combination of mechanical properties is inherent to the specimens under the positions 3 and 8, which were exposed to the RHAC+annealing 650°C,8 h.

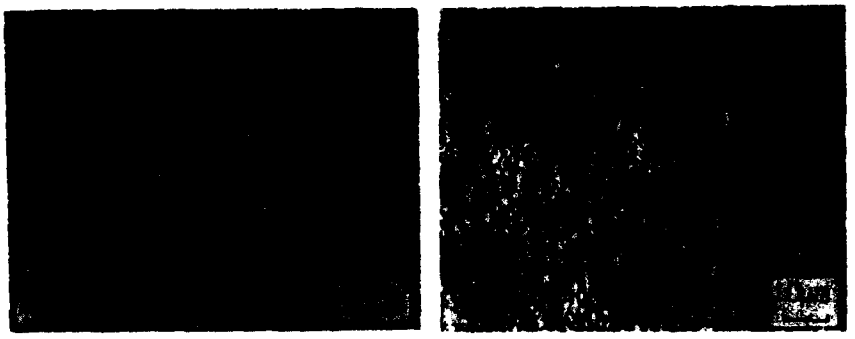


Figure 2. - Microstructure of VT23 alloy after RHAC + annealing 750°C,6 h (a) and 650°C,8 h (b).

High level of the properties after such treatment in the case of initially coarse-grained lamellar structure (position 8) should be stressed especially. As it may be deduced from the comparison of the properties of structures obtained by direct annealing at 750°C and double annealing, the decrease of the part of enveloped boundaries results in considerable improvement in plasticity, especially pronounced in the case of initialy corse-grained structure.

To check the possibility of practical applications of the proposed treatment, the VT23 alloy welds obtained by the electron beam welding were examined. Three regions with pronounced difference in the phase composition and structure occur in the weld: melted zone, heat affected zone (HAZ) and base metal. The melted zone and base metal are rather homogeneous and have the α''- and $(\alpha+\beta)$- structures correspondingly (Fig.3,a,b). HAZ structure includes whole spectrum of metastable phases, depending on the heating temperature on welding (Fig.3,c,d). Notwithstanding of the initial microstructure, the homogeneous high-dispersive structure, similar to that of shown on Fig.1,b, was obtained in all three zones as a result of RHAC, and fine equiaxed α-phase was formed after the annealing at 650°C (Fig.3,e,f).

The VT23 alloy welds exposed to above treatment have higher valuesof plasticity and impact toughness and similar values of strength (table 2) in comparison with the welds conventionally treated (800°C,1 h /water quenching/ aging 550°C,8 h).

Table 1. Mechanical Properties of VT23 Alloy

No	Treatments	Intragrain α-phase type	α-phase enveloped boundaries %	$\sigma_{0,2}$ MPa	UTS MPa	Elongation %	Cycles to failure at ε=1,5% N
1	Initial structure	globular	-	983	1058	8.0	9720
2	1+CT$	globular+ secondary lamellar	-	1095	1240	5.8	12263
3	1+RHAC+ 650°C,8 h	globular	80	1108	1270	9.1	19651
4	1+RHAC+ 750°C,6 h	lamellar	80	960	1080	7.8	3729
5	1+RHAC+ 550°C,8 h +750°C,4 h	lamellar	50	956	1020	11.4	3913
6	β-annealing	lamellar	100	896	950	5.5	4836
7	6+CT	lamellar	100	980	1072	3.6	4325
8	6+RHAC+ 650°C,8 h	globular	70	1190	1335	5.4	9846
9	6+RHAC+ 750°C,6 h	lamellar	70	987	1180	5.9	4968
10	6+RHAC+ 550°C,8 h+ 750°C,4 h	lamellar	60	975	1157	9.5	4258

$CT- conventional heat treatment (800 C°, 1 h / water quenching / aging 550°C,10 h).

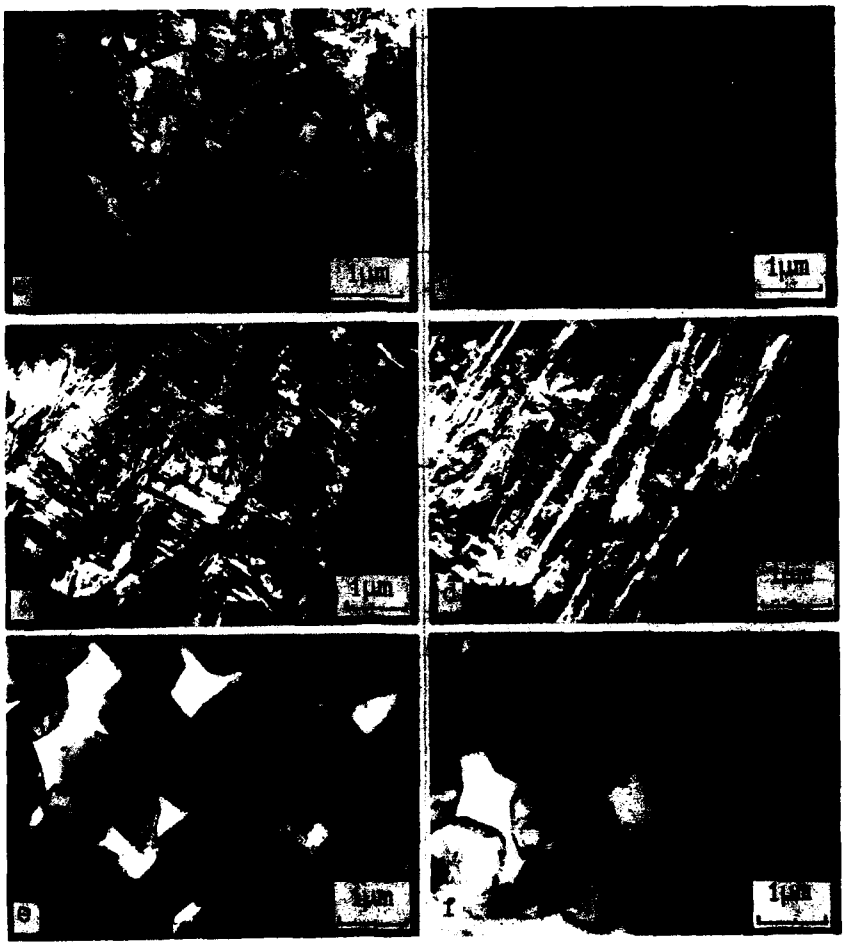


Figure 3 - Microstructure of VT23 alloy weldment in initial state (a-d) and after RHAC with annealing 650°C,8 h (e,f).
a,e - melted zone, c,d,f - HAZ, b - base metal.

Table 2. Mechanical Properties of VT23 Weldments

No	Treatment	$\sigma_{0,2}$ *MPa*	UTS *MPa*	Banding angle *degree*	Impact toughnes $kH \cdot m/mm^2$
1	CT	982	1070	28	2.6
2	RHAC+650°C 8 h	995	1058	59	4.02

References

1.Gridnev V. N., Ivasishin O. M., Oshkadyorov S. P., Proc. 5-th International Conf. "Titanium-84", New York, 1985, v.3, p.1635.

2.Ivasishin O.M., Markovsky P.E., Oshkadyorov S.P. Metalloved. i teraicheskaya obrabotka metallov (Rus.),1991, No 1, p.32.

3.Ivasishin O. M. et al. Proc. International Conf."Titanium 1990. Products and Applications", TDA Publ.,1990, p.99.

4.Gridnev V.N. et al.Physics of Metals, 1987, v.7, No 3, p.508.

5.Maksimovich G.G.et al.Preprint of PMI Ac Sc.of Ukr.SSR,1977,(Rus.) No 6, 36 p.

6.Gridnev V. N., Ivasishin O. M., Markovsky P. E. Metalovad. i Teraoobrabotka Metallov (Rus.), 1985, No 1, p.35.

7.Roitburd A.L., Kurdjumov G.V. Mat. Sci. and Eng.,1979,v.39, No 2, p.142.

8.Mirzaev D.A. et al. Fizika met. i metallovedenie (Rus.), 1984, v.58, No 1, p.69.

Void Nucleation, Void Growth and Tensile Behavior of Ti-10V-2Fe-3Al*

Harold Margolin and Sung Jun Pak

Polytechnic University
333 Jay Street
Brooklyn, NY 11201

Abstract

An incubation strain ε_n, for void nucleation was found in equiaxed (E) α alloys. Consistent with previous observations (8), ε_n increased as the strain hardening rate prior to void nucleation decreased. Evidence indicated that higher Al contents tended to reduce ε_n. Void nucleation took place at α/aged β interfaces. In Widmanstatten plus grain boundary (W+GB) α structures void nucleation took place at both GB and W α, but void growth was predominantly along prior β grain boundaries. Void growth in E α structures was both linear and non-linear. Non-linear void growth began when void coalescence commenced. For E α structures fracture strain, ε_f, was found to increase as ε_n increased. When the fracture stress corrected for necking, σ_{fc}, was plotted against $L_f^{-\frac{1}{2}}$, where L_f is the longest void at fracture, a linear relationship was found. When extrapolated to $L_f^{-\frac{1}{2}}=0$, the stress obtained was 1325MPa, which was above the yield strength of all the E α structures and thus consistent with the presence of ε_n.

Introduction

There have been a number of investigations of the relationship between void nucleation, void growth and tensile behavior (1-5). These studies have shown a relationship between microstructure, void nucleation and void growth. Generally voids nucleate more readily the coarser is the α in both equiaxed (E) α and Widmanstatten plus grain boundary (W+GB) α structures. Void nucleation takes place more readily and void growth is more rapid in W+GB α structures than in E α structures. For E α structures the larger is the interalpha particle spacing, λ, the more rapid is void growth (1,2). These observations on void growth and λ were questioned by Terlinde et al (6) as a result of work which they had carried out on Ti-10V-2Fe-3Al. These authors noted that interparticle spacings of W α were smaller than interparticle spacings of E α, yet the ductility of W+GB α structures was lower than that of E α. This study was undertaken to examine this question. As will be seen, the spacing between W α particles does not affect void growth because void growth in W+GB α structures takes place primarily along grain boundary α and to some extent along W α.

* This work was supported in part by the Boeing Airplane Co. through the efforts of Mr. Rodney Boyer. The authors are grateful for this assistance.

Experimental Procedure

The β transus was determined to be 800±3°C. Tensile bars, 3 inches long and 1/2" dia. were heat treated to produce E and W+GB α structures. W+GB α structures were produced by heating to 820°C, holding for 1 hr. then cooling to 730°C at rates of 2 and 10°C/hr. and holding for 1 week. E α structures were produced by heating as received material directly to 730°C for periods of 2 hrs., 1 day and 3 weeks to obtain various E α particle sizes. All specimens were aged at 500°C for 1 hr. For E α structures yield strengths from 1068 to 1275MPa were obtained. For W+GB α structures the yield strengths varied considerably less, Table I.

Button head tensile specimens with a 25mm gage length and a 6.25mm diameter were strained to fracture, and true stress-true strain curves were determined. Up to 10 serial sections were made on fractured specimens to determine longest void dimensions. The strain corresponding to a given void was determined from the chord diameter. The techniques used for these measurements have been described previously (1,2,4). Since the reported longest void at fracture was measured below the fracture surface, this void is actually the next to the largest void which caused fracture. The practice, however, is to report the longest measured void as the longest void at fracture. Microstructure dimensions were determined by linear traverse measurements.

Results and Discussions

Characteristic microstructures of E and W+GB α structures are given in Figs. 1 and 2. Microstructural measurements and tensile data are presented in Table I and true stress-true strain curves for E α and W+GB α structures are given in Fig. 3. The true stress-true strain curves for W+GB α structures follow the 3W curve of Fig. 3 up to the fracture strains given in Table I. Fig. 4 reveals a long void in a set 10W sample after true strain of 0.26.

Figs. 5 and 6 reveal the longest void-true strain curves for E and W+GB α structures. For the E structures, Fig. 5, void growth was linear for the unaged material, U1D, and for the 2 hr. hold at 730°C, 2H. For the 1 day, 1D, and 3 week, 3W, hold at 730°C, void growth was initially linear and later became non-linear at higher strains. Fig. 6 reveals non-linear growth for W+GB α structures.

Void Nucleation and Growth

As was noted in our earlier studies (1-5), voids nucleated at E α/β interfaces and at grain boundaries and occasionally at W α/β interfaces in W+GB α structures. Fig. 4 shows a typical void growth path in a W+GB α structure. The void lies primarily along grain boundaries of two adjacent grains at the left at A. A shorter portion of the void traverses W α in one grain and tends to follow W α in the adjacent grain at the right at B. The circular regions in the part of the void passing across W α suggests that voids had nucleated along W α and that the main void joined them.

In earlier work on the Ti-5.25Al-5.5V-0.9Fe-0.5Cu alloy aged to a yield stress of 1137MPa (1), voids did not form at W α interfaces. In that case slip was able to pass from the α to the β phase because of the Burgers orientation relationship between α and β phases, $(0001)\alpha//\{110\}\beta//\langle 11\bar{2}0\rangle\alpha//\langle 111\rangle\beta$. Here both planes and directions in each phase constitute slip systems which are parallel to one another, and slip, starting in α can readily transfer to β.

It is suggested that, in the present case, during aging α of a different orientation than that of the original W α platelet formed adjacent to the platelet. This would destroy the Burgers orientation relationship and replace the α/β interface with α/α interfaces. It has been shown earlier (2,7) that voids can readily form at α/α boundaries. This proposed explanation remains to be verified.

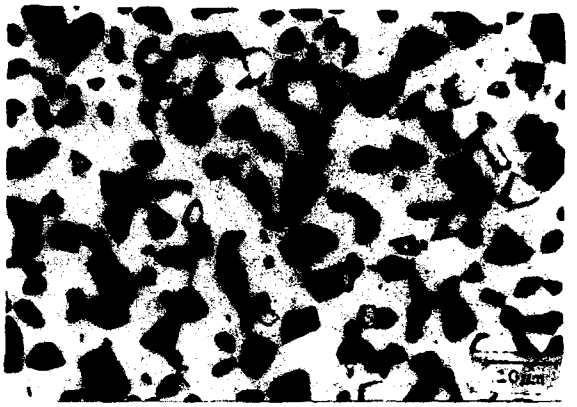


Fig. 1: Microstructure of set 3W sample, heated 3 weeks at 730°C, W.Q. aged 500°C, 1 hr.



Fig. 2: Microstructure of set 1CW. Sample heated 1 hr. 820°C, cooled to 730°C @ 10°C/hr., held 1 wk, W.Q. Aged 1 hr. 500°C.

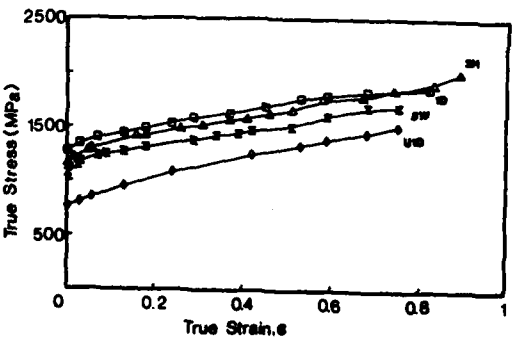


Fig. 3: True stress-true strain curves for E α structures.



Fig. 4: Void in set 10W sample, true strain C.26. Note largest portion of voids lies along α at prior β grain boundaries.

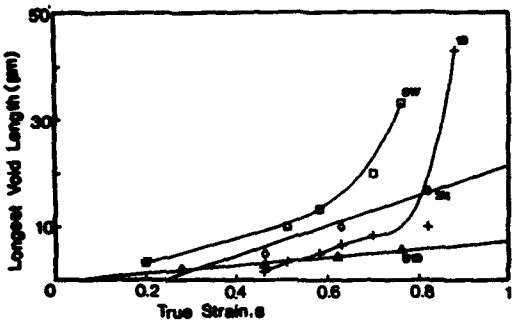


Fig. 5: Longest void, L_V, versus true strain, ε, for E α structures.

Table I Microstructural Parameter Measurements and Yield Strength Values for the Different Microstructures and Heat Treatments

Equiaxed α

Set Number	2H	1D	3W	U1D
Pct α	24	27	32	27
Dβ (μm)	5.5	7.5	26	7.5
d_α (μm)	2.5	3.7	5.5	3.7
Y.S. (MPa)	1275	1158	1068	792
U.T.S. (MPa)	1302	1350	1239	820
σ_{fc} (MPa)	2082	2285	1900	1675
Pct. R.A.	55.6	59	52.7	53
ϵ_f	0.82	0.89	0.75	0.76
λ	5.7	6.9	14	6.9

L_f (μm)	16.5	42.9	33	5.6

D_β - β Grain Size, d_α - α Particle Size
σ_{fc} - Fracture Stress Corrected for Necking
ε_f - Fracture Strain, λ - Spacing Between α Particles
L_f - Longest Void at Fracture

Heat Treating

2H - 2 hrs. at 730°C
1D - 1 day at 730°C
3W - 3 weeks at 730°C
U1D - Held 1 day at 730°C and Water Quenched

Widmanstatten Plus Grain Boundary α

Set Number	2W	10W
Pct α	19.5	21.1
D_β (μm)	244	132
l_α (μm)	9	6
d_w (μm)	9	4.7
Y.S. (MPa)	1068	1089
U.T.S. (MPa)	1137	1147
σ_{fc} (MPa)	1356	1433
Pct R.A.	23.3	21.9
ε_f	0.18	0.26
L_f (μm)	477	600

l_α - Grain Boundary α Thickness
d_w - Widmanstatten α Thickness

Heat Treating

2W - Cooling at 2°C/hr. from 820°C
10W - Cooling at 10°C/hr. from 820°C

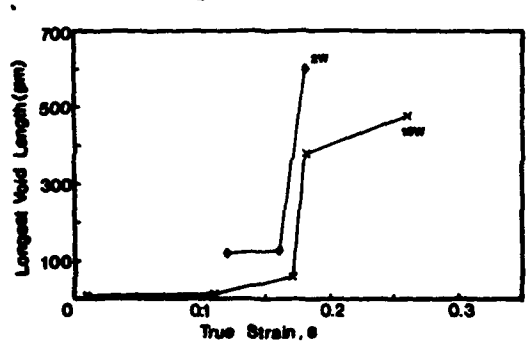


Fig. 6: Longest void, L_v, versus true strain, ε, for W+GB α structures.

In an earlier study (8) it had been shown that void nucleation depended on strain hardening prior to void nucleation. The higher the rate of strain hardening, the lower was the void nucleation strain. Fig. 7 is a plot of $\frac{\sigma_n - \sigma_{ys}}{\varepsilon_n}$ vs ε_n where σ_n is the true stress at which void nucleation took place, σ_{ys} is the 0.2% yield stress and ε_n is the true strain at which void nucleation took place. ε_n was obtained by extrapolating the data for Fig. 5 to zero void length. The data of Fig. 7 are consistent with the earlier results (8), where it was suggested that the lower the strain hardening rate, the lower would be the latent hardening. The lower the latent hardening rate, the more likely it would be that sufficient slip systems would be available to maintain compatibility between the matrix and the α phase.

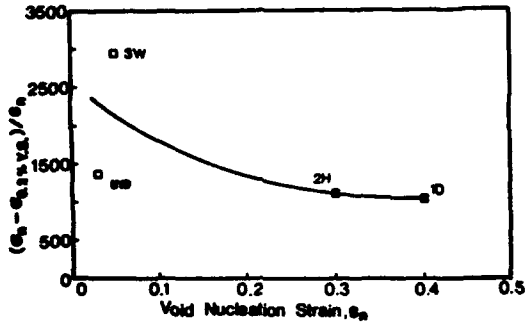


Fig. 7: Average strain hardening rate prior to void nucleation as a function of nucleation strain.

Examination of the data available on void nucleation (1,2,4,5,8) suggests that as the Al content of α increases, ε_n decreases, Table II. The comparison in Table II is made at a constant strain hardening rate of 1200MPa and for E α structures. As the Al content of the alloy increases, it is reasonable to assume that the Al content of the α will increase. A direct comparison of α Al content and ε_n, however, is not possible, since the composition of the α in the various alloys is unknown.

Table II Al Content and Void Nucleation Strains

Alloy	Alloy Al Content	ε_n for $\frac{\Delta\sigma}{\Delta E} = 1200$
Ti-Mn	0	>>0.3
Ti-10V-2Fe-3Al	3	0.3
Ti-4.5Al-5Mo-1.5Cr	4.5	0.038
Ti-5.25Al-5.5V-0.9Fe-0.5Cu	5.25	0.0*

*void nucleates near the yield strain

Williams and Luetjering (9) have shown that, as the Al content of α increases, the planarity of slip increases. Consequently, at higher Al contents slip concentrates at the head of the slip band, and, as a result, void nucleation occurs more readily.

In Fig. 6 specimens U1D and 2H reveal linear void growth over the entire range of void growth, while specimens 1D and 3W demonstrate linear void growth for only a portion of the void growth curve. No void coalescence was observed for specimens U1D and 2H, while void coalescence was seen in specimens 1D and 3W at the end of the linear void growth stage. Linear void

growth accompanying the absence of void coalescence was seen earlier (1), and the onset of non-linear void growth with the onset of coalescence was observed in CORONA 5 (4).

Fracture Strain, ε_f, Fracture Stress and Longest Void at Fracture, L_f

It is of interest to note for the E α structures that ε_f increases as ε_n increases, Fig. 8, that is, the longer void nucleation can be postponed, the larger will be the strain to fracture.

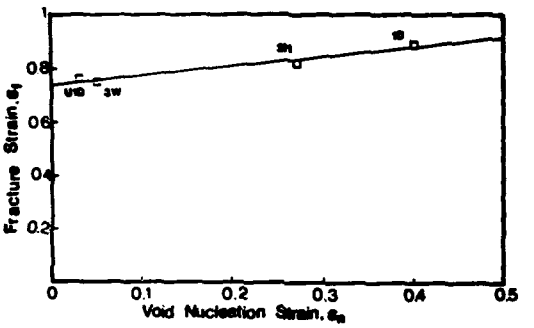


Fig. 8: Fracture Strain ε_f, as a Fracture of Nucleation Strain, ε_n.

Fig. 9 is a plot of the fracture stress corrected for necking, σ_{fc} as a function of $L_f^{-\frac{1}{2}}$. It will be recalled that L_f is the next to the longest

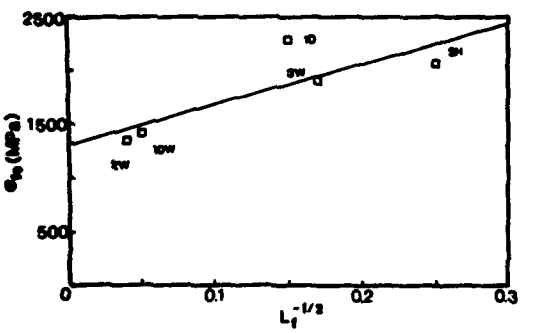


Fig. 9: Fracture Stress Corrected for Necking, σ_{fc}, as a Function of $L_f^{-\frac{1}{2}}$

void at fracture. It is found quite close to the fracture surface and, consequently, there is little difference between the stress of the fracture surface and the position at which L_f is found. A linear relationship is evident between σ_{fc} and $L_f^{-\frac{1}{2}}$ as was found earlier (1). The data include results from both E and W+GB α structures. As noted earlier, the true stress-true strain curves for the w α structures follow the 3W curves. The slopes of the curves do not differ greatly and it is probably for this reason that the data lie on a single curve.

The data of Fig. 9 extrapolate at $L_f^{-\frac{1}{2}}=0$ to 1325MPa, a stress which lies above the yield stress of any of the structures. The stress level is consistent with the observation that there is an incubation strain for E α structures. The void growth curves of W+GB α structures do not allow a determination of whether or not an incubation strain exists. Fig. 9 suggests that an incubation strain does exist for the W+GB α structures. No other physical significance can be attached to the value of 1325MPa.

References

1. M.A. Greenfield and H. Margolin: "The Mechanism of Void Formation, Void Growth and Tensile Fracture in an Alloy Consisting of Two Ductile Phases", Met. Trans. 3, 1972, 2649-2659.

2. H. Margolin and Y. Mahajan: "Void Formation, Void Growth and Tensile Fracture in Ti-6Al-4V", Met. Trans. A, 9A, 1978, 781-791.

3. H. Margolin and T.V. Vijayaraghavan: "A Rationalization of Tensile Ductility and Fracture in Alpha-Beta Ti-Mn Alloys", Met. Trans. A, 14A, 1983, 2043-2053.

4. T.V. Vijayaraghavan and H. Margolin: "The Effect of Matrix Strength on Void Nucleation and Growth in an Alpha-Beta Titanium Alloy, CORONA-5", Met. Trans. A, 19A, 1988, 591-601.

5. K.R. Narendrnath and H. Margolin: "The Effect of Matrix Strength on Void Nucleation and Growth in a Widmanstatten Alpha-Beta Titanium Alloy, CORONA 5", Met. Trans. A, 19A, 1988, 1163-1171.

6. G. Terlinde, H.-J. Rathjen and K.-H. Schwalbe: "Microstructure and Fracture Toughness of the Aged β-Ti Alloy Ti-10V-2Fe-3Al", Met. Trans. A, 19A, 1988, 1037-1049.

7. H. Margolin and J. Kene: "The Influence of Grain Size and Prior Cold Work on Void Nucleation and Growth and Tensile Fracture of Alpha Titanium", Titanium Science and Technology, Eds. G. Leutjering, U. Zwicker, W. Bunk (Deutsche Gesellschaft fur Metallkunde, Germany), 3, 1985, 1945-1951.

8. T.V. Vijayaraghavan and H. Margolin: "Void Nucleation and Strain Hardening", Scripta Met. 23, 1989, 703-704.

9. J.C. Williams and G. Luetjering: "The Effect of Slip Length and Slip Character on the Properties of Titanium Alloys", Titanium '80 Science and Technology, Eds. H. Kimura and O. Izumi (The Metallurgical Society, Warrendale, PA 15086), 1, 1985, 671-681.

Correction: Note in Fig. 3 the designations 2H and 1D have been interchanged. The triangular symbols refers to 1D and the square symbols to 2H.

EFFECTS OF HYDROGEN ON THE STRUCTURE AND PROPERTIES OF BETA-C™ (Ti-3Al-8V-6Cr-4Mo-4Zr) SHEET

J. R. Wood and M. L. Bogensperger

RMI Titanium Company
1000 Warren Avenue
Niles, Ohio 44446

Abstract

Beta-C™ is a metastable beta titanium alloy which is heat treatable to achieve good combinations of strength, ductility, and notch toughness. Although beta-titanium alloys have a high tolerance for hydrogen, it is not clear whether hydrogen affects the properties of Beta-C™ in the heat treated condition which contains a high volume fraction of alpha phase. This study explores the effects of hydrogen on the structure and properties of Beta-C™ in both the solution treated and solution treated and aged conditions. Tensile and bend properties and notch strength were evaluated at several hydrogen levels. In the solution treated condition, it was found that hydrogen levels up to 900 ppm had relatively minor effects on tensile and bend properties, but had significant effects on aging response. In the fully aged condition, hydrogen had no detrimental effects on tensile and notch stress rupture properties.

Introduction

Beta-C™ (Ti-3Al-8V-6Cr-4Mo-4Zr) is a metastable beta titanium alloy which is heat treatable to achieve good combinations of strength, ductility and notch toughness. In general, beta titanium alloys have a high tolerance for hydrogen due to high solubility of hydrogen in the beta phase which also acts as a beta stabilizing element. Hydrogen solubility on the order of 4000 ppm (parts per million by weight) has been reported in several beta titanium alloys, whereas the solubility in alpha and alpha-beta alloys is on the order of 200 ppm at room temperature.[1]

Some limited data on Beta-C™ in the solution treated condition (all beta phase) showed that up to 3600 ppm hydrogen increased strength modestly, but the effects on ductility were not reported.[2] It is not clear whether increased hydrogen affects Beta-C™ mechanical properties in the fully heat treated (aged) condition which contains a high volume fraction of alpha phase in the beta matrix. There is limited data on beta alloys which suggests that increasing hydrogen content decreases the rate of alpha phase precipitation during aging.[3] There also is some evidence that the morphology and distribution of alpha phase changes with increasing hydrogen content.[3]

The effects of hydrogen on aging kinetics in Beta-C™ have not been reported and the purpose of the present study was to explore the effects of increased

Titanium '92
Science and Technology
Edited by F.H. Froes and I. Caplan
The Minerals, Metals & Materials Society, 1993

hydrogen on Beta-C™ in both solution treated and solution treated and aged conditions. Sheet was chosen for this study because of the greater tendency for sheet products to pick up hydrogen during thermomechanical processing, heat treating and pickling. Current specification requirements allow 200 ppm max hydrogen and it was decided to explore levels well above this limit.

Procedure

Beta-C™ sheet, 0.060 inch (1.5 mm) thick, was solution treated at 1500°F(815°C)-30Min-Air Cool and analyzed for hydrogen at 124 ppm. The full chemistry for this heat is shown in Table I. This material was used for the low hydrogen level. Additional solution treated sheet samples were pickled in a solution of 20 vol% HF - 10 vol% H_3PO_4 - 70 vol% H_2O for 7 1/2 min. and 15 min. to achieve target levels of 500 ppm and 1000 ppm hydrogen, respectively. Pickled samples were re-solution heat treated at 1450°F(788°C)-30Min-AC to achieve hydrogen uniformity throughout the section thickness. Tensile and bend properties were measured.

Additional solution treated and hydrogen charged sheet material was aged at 900°F (482°C), 1000°F (538°C) and 1100°F (593°C) from 2 to 48 hrs. to determine effects of hydrogen content on aging response. Based upon aged hardness results, additional samples were aged at 900°F (482°C) for various times at the three hydrogen levels for the determination of tensile and notch stress rupture properties and aged microstructures.

To determine the effects of hydrogen in the aged condition, samples were solution treated and aged at 950°F (510°C) for 18 hrs. followed by pickling to achieve high hydrogen levels. Tensile properties were evaluated.

Table I. Composition of Beta-C™ Heat in the Present Study (wt%)

Al	V	Cr	Mo	Zr	Fe	O_2	H_2
3.3	7.9	6.1	4.1	3.9	.08	.096	.0124

Results and Discussion

Solution treated tensile tests versus hydrogen level after pickling are shown in Figure 1. There was a slight increase in tensile strength of about 10 ksi (68.9 MPa) in going from 124 ppm H_2 in the base condition to 900 ppm H_2 at the highest level. Interestingly, the yield strength dropped approximately 12 ksi (82.7 MPa) from low to high H_2 levels. Tensile elongation also dropped about 3% between low and high H_2 levels. Bend properties shown in Table II indicated no adverse effects of hydrogen and samples at all H_2 levels successfully passed a radius/thickness bend ratio of 3.5, which is satisfactory for sheet material.

FIGURE 1.

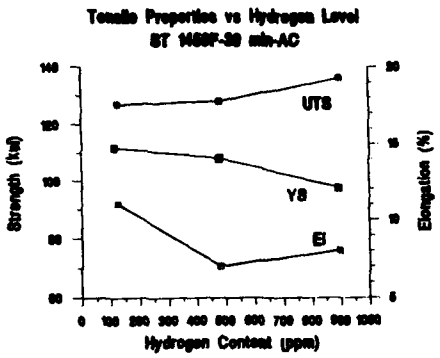


Table II.
Beta-C[TM] Sheet .060-Inch (1.5 mm) - Bend Test Results
S.T. Condition Only

Material Condition	R/T Factor	
	3.5	2.5
Low H_2 - L&T	Pass	Pass
Med H_2 - L&T	Pass	Pass
High H_2 - L&T	Pass	Pass

The effects of hydrogen on aging response are shown in Figure 2. For all three aging temperatures (900°F (482°C), 1000°F (538°C), and 1100°F (593°C)) at 16 hours, there was a significant reduction in the aged hardness indicating that hydrogen's beta stabilizing effect retarded the formation of alpha. Additional aging treatments were conducted at 900°F (482°C) for up to 48 hrs. and the hardness results shown in Figure 3 indicate that for medium and high H_2 content (322 ppm and 834 ppm, respectively), maximum aged hardness (Rc 40) was achieved in 32 and 48 hours, respectively.

FIGURE 2.

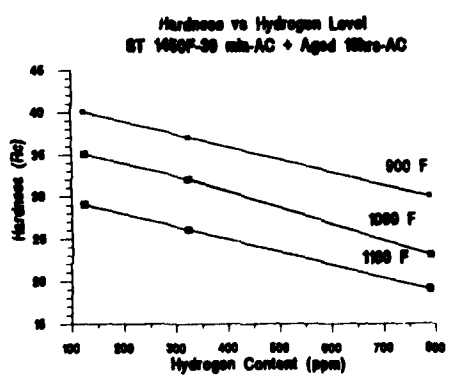
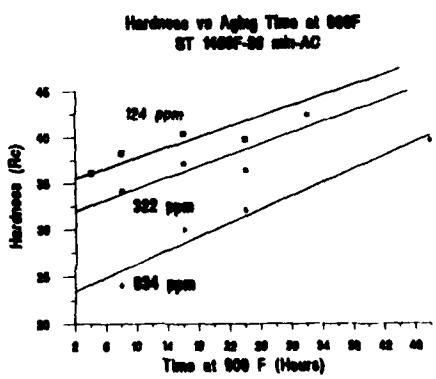


FIGURE 3.



Based upon hardness results, various aging treatments were established for each hydrogen level to aim for low (150 ksi (1034 MPa)) and high (190 ksi (1310 MPa)) strength conditions as shown in Table III. Tensile results for the low strength condition are shown in Figure 4. It is seen that the medium and high H_2 levels well exceeded the 150 ksi (1034 MPa) tensile strength goal whereas the low H_2 base material was below the goal at 139 ksi (958 MPa) tensile strength. Tensile ductility appeared to decrease with increasing hydrogen, however, this may be due to the higher strength levels rather than to hydrogen per se.

Table III.
Beta-C™ Sheet .060-Inch (1.5 mm)
900°F (482°C) Age Study vs. Hardness & Strength

	Low H_2	Med H_2	Hi H_2
Low Strength 150 ksi (1034 MPa) Rc 32	900°F 2 hrs.	900°F 6 hrs.	900°F 24 hrs.
Hi Strength 190 ksi (1310 MPa) Rc 40	900°F 16 hrs.	900°F 32 hrs.	900°F 48 hrs.

FIGURE 4.

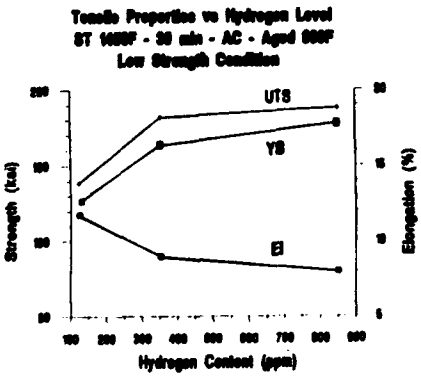
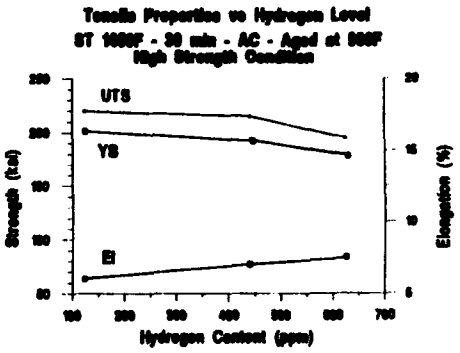


FIGURE 5.



Tensile results for the high strength aged condition are shown in Figure 5. In this case, all three hydrogen levels met the goal of 190 ksi (1310 MPa) tensile strength with a slight decrease in strength noted with increased hydrogen content. Tensile ductility showed an increase at higher hydrogen levels, reflecting the lower strength trend noted above.

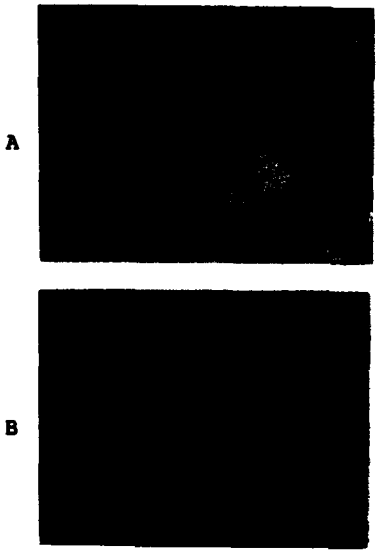
Notch stress rupture tests were conducted at room temperature for both low and high strength aged conditions. Samples were loaded at stresses equivalent to the ultimate tensile strength and, in some cases, at a stress level 25% greater than the tensile strength. Tests were held for 24 hours or until failure as noted in Table IV. All hydrogen levels passed the notch embrittlement test at the equivalent tensile strength levels except for one low hydrogen sample which broke through the holding pin hole during loading. The results indicate that hydrogen embrittlement as measured by this type of test is not apparent at hydrogen levels up to about 800 ppm.

Table IV.
Beta-C™ Sheet .060-Inch (1.5 mm)
Notch Stress Rupture Test - K_t = 4.5
Solution Treated at 1450°F (788°C)
Pickled
Aged at 900°F (482°C) for Selected Times

Material Condition	UTS ksi (MPa)	Static Stress ksi (MPa)	Test Duration Hours
Low H_2	137 (945)	137 (945)	24+
Low H_2	140 (965)	176 (1213)	<0.1
Low H_2	213 (1469)	213 (1469)	<0.1*
Low H_2	219 (1510)	276 (1903)	<0.1
Med H_2	205 (1413)	205 (1413)	24+
Med H_2	220 (1517)	220 (1517)	24+
Hi H_2	182 (1255)	182 (1255)	24+
Hi H_2	207 (1427)	207 (1427)	24+

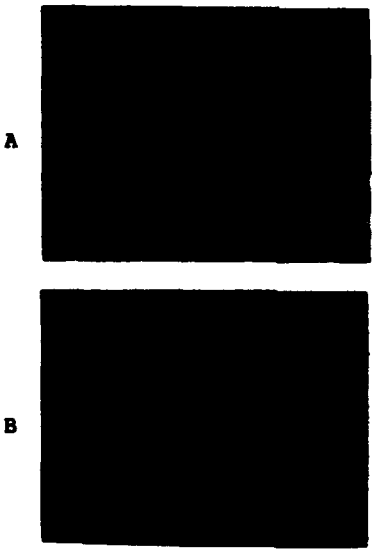
*Broke through hole upon loading

Microstructures for low, medium and high H_2 levels in the low strength aged condition are shown in Figures 6, 7, and 8, respectively, and in the high strength aged condition in Figures 9, 10, and 11, respectively. Incomplete aging is evident (Figure 6) for the low H_2 - low strength material which accounts for the low tensile strength observed. A fairly uniform fine needlelike alpha precipitate is observed for the medium and high H_2 - low strength materials (Figures 7 and 8). Some grain boundary denudation is apparent for both samples and the higher H_2 material has a coarser, less dense alpha structure which may be related to the longer aging time, to inherently higher H_2 content, or both.



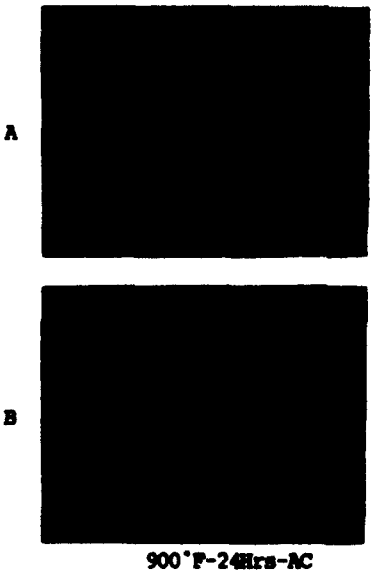
900°F-2Hrs-AC
Low Hydrogen

Figure 6.



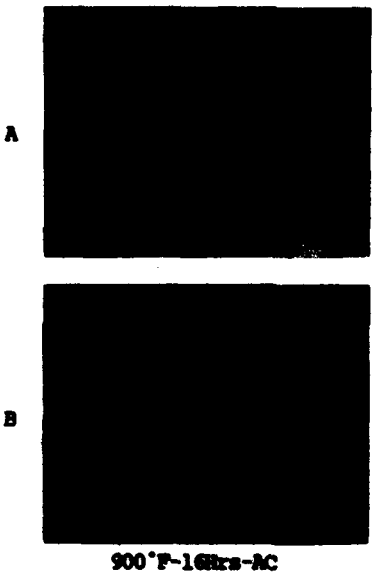
900°F-6Hrs-AC
Med Hydrogen

Figure 7.



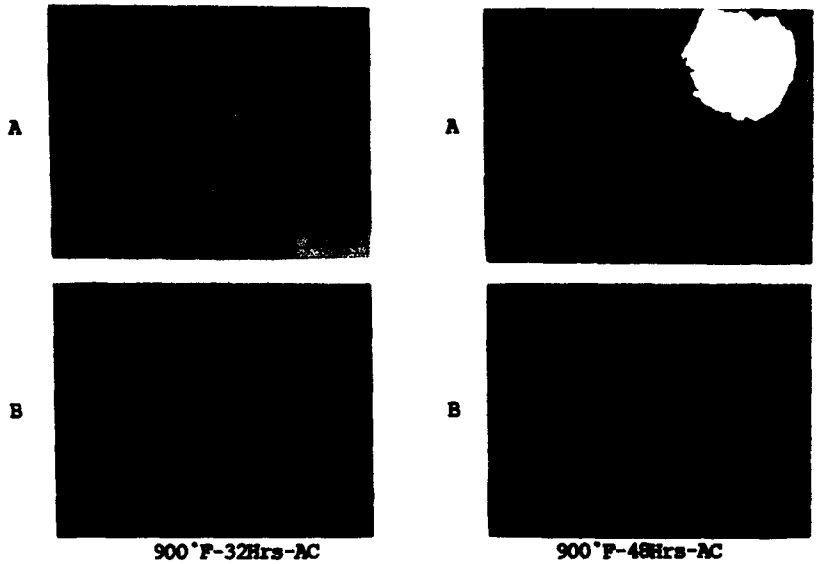
900°F-24Hrs-AC
Hi Hydrogen

Figure 8.



900°F-16Hrs-AC
Low Hydrogen

Figure 9.



900°F-32Hrs-AC
Med Hydrogen

Figure 10.

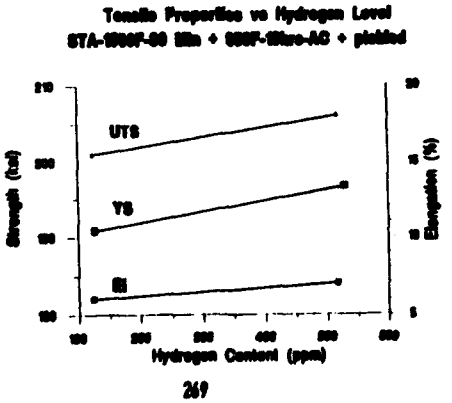
900°F-48Hrs-AC
Hi Hydrogen

Figure 11.

For the high strength condition, microstructures were similar for all three hydrogen levels with some alpha coarsening observed at longer aging times. These structures correspond to the observed tensile strength data which showed a drop off in strength at the higher hydrogen levels which appear related to the coarsening of the alpha platelets. It is not clear from this study whether hydrogen changes the alpha phase morphology during aging since aging times were not constant. Additional work is needed to better understand the effects of hydrogen on alpha phase morphology.

Adding hydrogen after aging increased tensile and yield strength slightly with no change in tensile elongation as shown in Figure 12. It appears that hydrogen pickup from pickling or chem milling after aging is not detrimental to ductility. Additional testing is probably warranted to better assess the effects of post-age hydrogen exposure.

FIGURE 12.



Conclusions

Hydrogen levels up to 900 ppm had relatively minor effects on solution treated tensile and bend properties. Hydrogen pickup before aging had significant effects on aging response at 900°F (482°C), 1000°F (538°C), and 1100°F (593°C). To achieve comparable aged hardness levels, aging times at 900°F (482°C) had to be extended to 48 hours for high hydrogen material compared to 16 hours for low hydrogen material. Hydrogen levels up to 800 ppm had no detrimental effect on tensile ductility or notch rupture strength in the aged condition. Hydrogen pickup of 500 ppm after aging had negligible effect on tensile strength and ductility. Hydrogen levels up to 900 ppm did not appear to significantly change alpha phase morphology during aging treatments, however, observations were confounded by differences in aging times and more work is needed to fully characterize alpha phase morphology during aging. Also needed is data on the effect of hydrogen pickup on beta transus and the relationship of beta transus to aging kinetics.

Acknowledgments

The authors would like to thank R. A. Raschilla, Jr. for coordinating the testing program, M. J. Jaros for metallography, and RMI for permission to publish this paper.

References

1. N. E. Paton and J. C Williams, "Effect of Hydrogen on Titanium and Its Alloys", in Hydrogen in Metals; Proceedings of the International Conference on the Effects of Hydrogen on Materials Properties and Selection and Structural Design, Champion, PA, September 23-27, 1973, (Metals Park, OH: American Society for Metals, 1974), 409-431.

2. N. E. Paton and O. Buck, "The Effect of Hydrogen and Temperature on the Strength and Modulus of Beta Phase Ti Alloys", in Effect of Hydrogen Behavior of Materials; Proceedings of International Conference, Moran, WY, September 7-11, 1975 (New York: Metallurgical Society of AIME, 1976), 83-89.

3. J. E. Costa, D. Banerjee, and J. C. Williams, "Hydrogen Effects in β-Titanium Alloys", Beta Titanium Alloys in the 80's, eds. R. R. Boyer and H. W. Rosenberg (AIME, 1984), 69-84.

QUANTITATIVE TEXTURE ANALYSIS OF α-BASED TITANIUM AND TITANIUM ALLOYS - A TWO STAGE APPROACH

A W Bowen

Materials and Structures Dept
Defence Research Agency Aerospace Division
Royal Aerospace Establishment
Farnborough, Hants GU14 6TD UK

Abstract

A two-stage approach is proposed as a means of quantifying the textures of α-based titanium and titanium alloys. In the first instance, where there are only one or two pole figures available, it is argued that, of the available methods, the calculation of the (Kearns) f-factor is the most appropriate. Examples are then given of the f-factors for three sets of experimental pole figures. In the second approach, when there are three or more pole figures available, it is advisable to use the Orientation Distribution Function. Some of the ways of presenting this information and the parameters and information that can be extracted from the Function are given using, in order to link the two approaches, an example one of the data sets for which f-factors were calculated.

Introduction

Historically, the textures of titanium alloys, as well other metals and alloys, have been represented by pole figures, and many examples of such figures, usually for (0002) and possibly (10$\bar{1}$0), can be found in the literature. However, the major disadvantage with these pole figures is their qualitative nature and hence the difficulty in comparing them and in relating them to mechanical and physical properties. This paper will address the two means of overcoming this disadvantage by proposing a two stage approach to the texture evaluation of α-based titanium alloys.

In the first instance, quantitative data from individual pole figures may suffice and it is suggested strongly that the method proposed by Kearns [1] for zirconium alloys, to calculate what are termed f-factors, be adopted for this purpose. The basis of the calculation of (Kearns) f-factors will be given, together with some examples of the types of f-factors for a number of experimental pole figures. Other parameters that have been proposed to quantify individual pole figures will also be considered.

In other instances, such information from individual pole figures will be insufficient. In these cases it is necessary to pool the information from a number of pole figures in order to extract precise crystallographic data in terms of the Orientation Distribution Function (ODF) [2]. The paper will provide a brief introduction to ODF's to illustrate some of the types of information that can be extracted from the ODF, using as an example the further processing of one of the data sets used for f-factor calculations in order to provide a read-across between the two approaches.

Titanium '92
Science and Technology
Edited by F.H. Froes and I. Caplan
The Minerals, Metals & Materials Society, 1993

Quantitative data from individual pole figures

The simplest means of quantifying an individual pole figure is to make use of the parameter proposed by Kearns [1], namely the f-factor, which represents the effective volume fraction of poles lying along a reference direction. Usually one defines an orthogonal set of axes, conveniently taken to be the rolling, transverse and short transverse directions (NLT in Figure 1a), and calculates

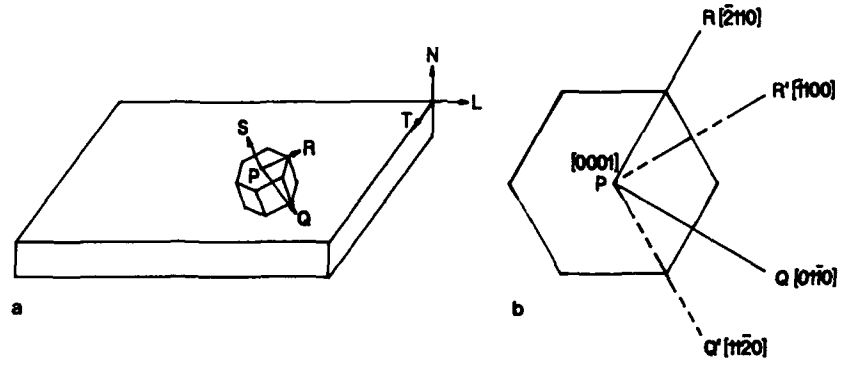


Figure 1. (a) orientation of unit cell axis (PQRS) in relation to sample axis (NLT); (b) choice of reference axis system (PQR or PQ'R') within unit cell.

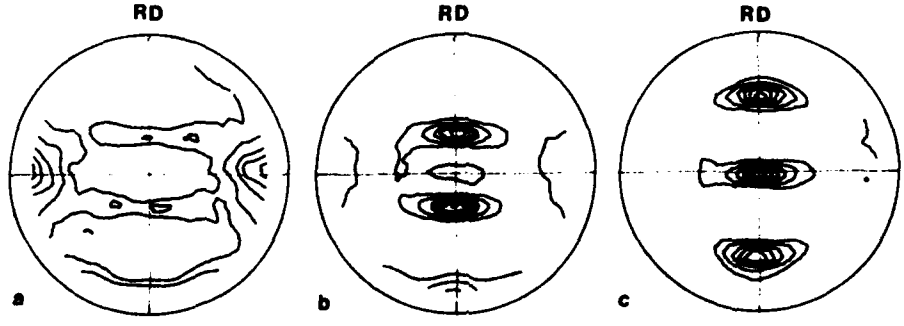


Figure 2. Pole figures for a 12.5mm thick Ti-6Al-4V rolled plate (a) (0002); (b) (10$\bar{1}$0); (c) (11$\bar{2}$0). Contours: 1,2,4,6,8,10,12 (xrandom).

the f-factor in each of these directions. This f-factor is defined by the equation:

$$f_i = \int_0^{\pi/2} I_\phi \sin\phi \cos^2\phi \, d\phi$$

where i = can be the N, L or T direction, ϕ is the angle between the [0001] and reference directions and I_ϕ is the average pole density. Values of f will vary from 0 to 1.

It can be shown that the sum of the f-factors for these three directions must be unity and that f=0.333 will represent the isotropic (random) case. Note that Kearns [1] only considered the [0001] direction but subsequent researchers have extended this to include prism poles as well; with the result that Kelly and

Watson [3] proposed that the empirical equation $f_{0002}+2f_{10\bar{1}0}=1$ should hold.

Examples of f-factors for a titanium specimen, in this case a Ti-6Al-4V plate whose pole figures are shown in Figure 2, are listed in Table I. These data show that:

(i) f_{n+l+t} is indeed equal to unity for the [0001], [$10\bar{1}0$] and [$11\bar{2}0$] poles; and (ii) $\Sigma f_p=f_{0002}+2f_{10\bar{1}0}=1$ is also true.

Table I Values of f-factors calculated for the Ti-6Al-4V plate shown in Figure 2.

Pole	f_n	f_l	f_t	Σf_{n+l+t}
0002	0.211	0.274	0.514	0.999
$10\bar{1}0$	0.369	0.335	0.296	1.000
$11\bar{2}0$	0.401	0.356	0.243	1.000
Σf_p	0.949	0.944	1.106	
Σf_s	0.981	0.965	1.053	

However, if a convenient crystallographic orthogonal axis is chosen viz [0001], [$10\bar{1}0$] and [$11\bar{2}0$] (PQRS in Figure 1a), then it is argued that the sum of f-factors in these three directions (for any given sample direction) must also be unity ie $\Sigma f_s=f_{0002}+f_{10\bar{1}0}+f_{11\bar{2}0}=1$. Examination of the Σf_s data in Table I shows that this is indeed the case to within ~5% (whereas the agreement for Σf_p is ~10%). Note that if one considers pole figures re-calculated from the ODF, then this agreement becomes exact (A W Bowen unpublished work). It is clear therefore that this latter, more rigorous, Σf_s equation should be preferred to the Σf_p equation proposed by Kelly and Watson [3]. The accuracy of these, and other, f-factors is about ±0.02 or less, which is the level of repeatability observed by the author for many other specimens and also reported in round-robin tests [eg 465].

Knorr and Pelloux [6] list a number of other parameters that have been proposed as a means of representing pole figures. None of these appears to offer any clear advantage over f-factors; for instance, none provides data for three orthogonal directions in a sample. Nevertheless, for the sake of completeness, Table II lists some of these parameters for the same Ti-6Al-4V plate in Figure 2, together with a representation of the severity of the basal pole figure (expressed as the root mean square deviation of the (0002) pole figure from random (which is assigned a value of zero)). Although Knorr and Pelloux [6] claim some virtues in using their parameters, there is no clear evidence for

Table II Quantitative data for the (0002) pole figure shown in Figure 2, according to the parameters listed.

Parameter (minimum and maximum values indicated where known)	Longitudinal direction	Transverse direction
Kallstrom et al [7]		
F (-1 to 1)	-0.263	-0.747
Dahl et al [8]		
1st moment	0.994	1.273
2nd "	1.228	1.700
std deviation (SD)	0.490	0.282
Knorr and Pelloux [6]		
F_r (-1 to 1)	0.743	0.922
F_A "	0.632	0.873
SD (0 to 0.308 (not 0.303 [9]))	0.282	0.152
ratio of integrations S (0 to 1)	0.322	
basal plane severity parameter [9]	1.096	

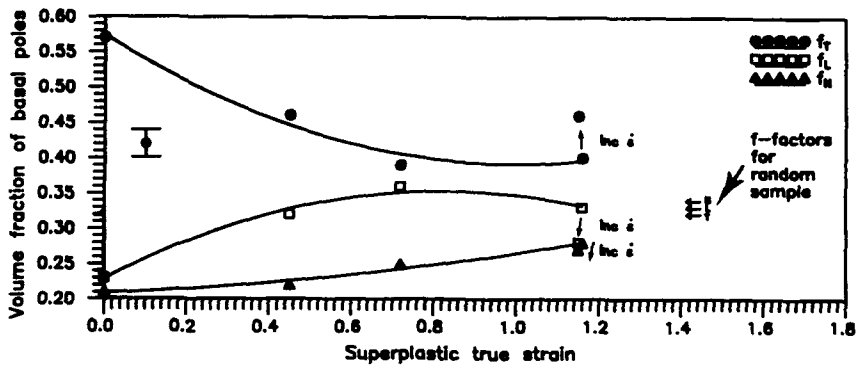


Figure 3. Volume fraction of basal poles as a function of superplastic true strain for test pieces of the Ti-6Al-4V alloy stressed in the transverse direction. Note increased divergence of f-factors (ie more anisotropy) if strain rate ($\dot{\varepsilon}$) is increased.

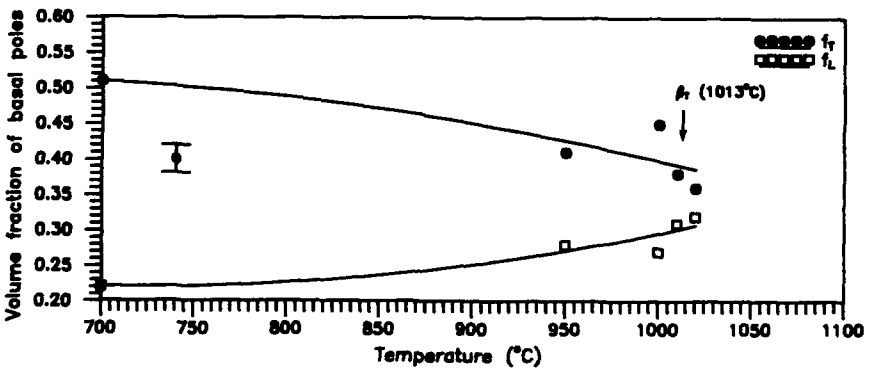


Figure 4. Volume fraction of basal poles as a function of heat treatment temperature for Ti-6Al-4V alloy samples.

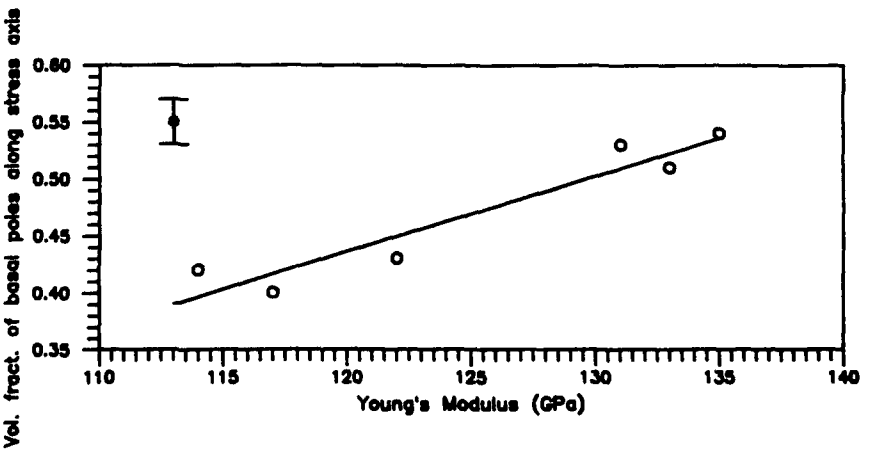


Figure 5. Volume fraction of basal poles along the axis of an IMI 829 titanium alloy bar in relation to measured values of Young's Modulus.

doing so. Moreover, too much emphasis on the further analysis of individual pole figures is likely to detract from the more important task of quantifying multiple pole figures and building up a reliable ODF database.

Applications of f-factor calculations. There follows three examples to illustrate how, from individual pole figures, it is possible to obtain quantitative data that permits more definitive conclusions to be drawn than just from a qualitative description of these figures (I = error bar in Figs 3-5):

(i) Superplastically deformed Ti-6Al-4V [10] - This paper showed that with increasing superplastic strain, an initially anisotropic plate of titanium became almost isotropic. Re-analysis of the pole figures generated during this investigation, to calculate f-factors, gave the results in Figure 3. It can be seen that the initially wide spread in f-factors is progressively reduced by superplastic deformation but, even after a strain of 1.15, the values have clearly not reached those of a random HIPed sample (f=0.32-0.34). Furthermore, the changes in texture are such that considerably more strain would be required to achieve a truly random texture.

(ii) Heat-treated Ti-6Al-4V [11] - Heat treatment at increasingly higher temperatures resulted in a weakening of an initially anisotropic texture, but it is clear from the f-factors calculated from representative pole figures for these heat treatments (Figure 4), that it is not until the β-transus is exceeded is a random texture (ie $f_1 \sim f_t \sim 0.33$) likely to be achieved. In addition, this transition is likely to occur rapidly over a relatively short temperature range close to the β-transus.

(iii) Rolled IMI829 [12] - Processing of this round bar produced significant changes in Young's Modulus (E). Re-analysis of the original pole figures to calculate f-factors, which produced the data plotted in figure 5, showed a consistent trend between the proportion of basal poles in the stress axis and E. Clearly, such a figure could be used as a means of predicting E and would be of use in quality control during processing, obviating the need for test piece machining and testing.

Quantitative data from multiple pole figures

The interpretation of pole figures in terms of ideal orientations is prone to uncertainty in all but the simplest of cases, with the consequence that the more rigorous ODF method was devised some years ago [2]. In this method an unambiguous means of representing ideal orientations (which are what we are trying to identify) was devised, into which is fitted the pole figure data. Here, two orthogonal reference axes are chosen, one for the crystal (PQRS in Figure 1a) and the other for the specimen (NLT in Figure 1a), and each ideal orientation is represented by the degree of mis-match between these two sets of axes. The mis-match is represented by what are termed the Euler angles, which are the three angles through which one must systematically, and consistently, rotate to get coincidence. These angles are represented by either the Bunge (ϕ_1,Φ,ϕ_2, as in this paper) or Roe (θ,Φ,Ψ) notations, which have a simple relationship to each other [2]. Unlike cubic crystals, however, where the standard cube projection presents no ambiguity, there are two options in the choice of crystal reference system for hexagonal crystals, viz the X-direction can either be parallel to <10$\bar{1}$0> or <11$\bar{2}$0> (ie the systems PQR or PQ'R' in Figure 1b). Examples of both systems can be found in the literature. In addition, exact values of the Euler angle will depend on the c/a ratio. In the first instance, it is possible to present a section through Euler space, where there is an immediate similarity to a pole figure. However, unlike a pole figure, each position (peak) in the ODF corresponds to a unique combination of (hkil)<uvtw> with the result that the texture components can be identified.

It should be noted, however, that a potentially powerful addition to this conventional (macro) approach to texture analysis using X-ray (or neutron) diffraction is to calculate the ODF from the Euler angles of grains whose orientations have been determined in the scanning electron microscope from their electron back-scattered diffraction patterns (EBSP) [13]. Because of the very selective nature of this technique, it should be possible to study very local changes in texture; for instance, recrystallisation nucleii. To avoid confusion with data generated from conventional (macro) ODF, it might be appropriate to refer to the information from EBSP as micro-ODF data.

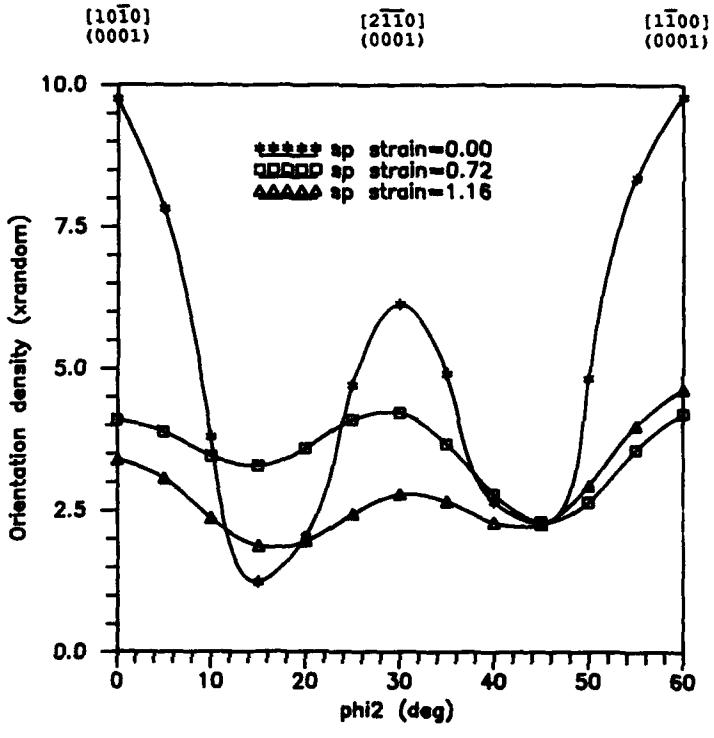


Figure 6. Orientation density along the [10$\bar{1}$0](0001)-[2$\bar{1}\bar{1}$0](0001)-[1$\bar{1}$00](0001) fibre axis of the ODF for the Ti-6Al-4V alloy superpastically deformed in the transverse direction to the strains indicated.

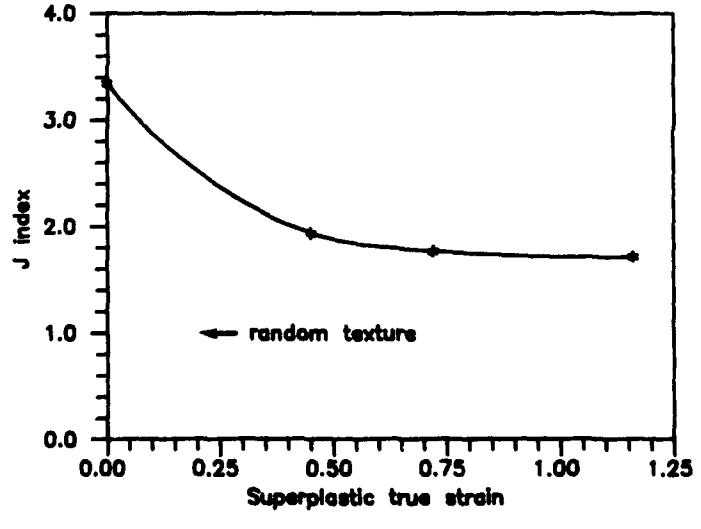


Figure 7. Texture severity, J, as a function of superplastic true strain for transversely stressed test pieces of the Ti-6Al-4V alloy. J=1 for a random texture.

Application of ODF analysis. To illustrate some of the additional information that can be extracted from the quantitative analysis of multiple (usually 3 or 4) pole figures, the ODFs of the superplastically deformed samples in Figure 3 have been determined. To show how the texture changes as a function of applied strain it is possible to plot the density variation along a fibre through the ODF. These curves, in Figure 6, illustrate how the original texture just 'melts' away with increasing applied superplastic strain, as the strain is accommodated by flow in the β-phase [10,14], and no other texture components are produced. Such information cannot be extracted from the individual pole figures. A further useful parameter that can be extracted from the ODF is the overall severity of the texture, represented by the J-index [2]. This parameter reveals how the overall texture intensity weakens rapidly at low strains and then decreases more gradually (Figure 7). In fact, this figure, on a log strain scale, shows that the weakening in the texture is linearly dependent on the applied stain. From such a figure it could be argued that a fully random texture will never be produced under these conditions [10,13], because no significant texture changes occur at strains greater than ~0.75. Similar trends are apparent in Figure 3 but they are not so clearly defined.

Recommendations

Textures in α-based titanium alloys should be quantified in either of two ways:

1. If there are only one or two pole figures, these should be quantified using the (Kearns) f-factor approach, making use of the equation $\Sigma f_o = f_{0002} + f_{10\bar{1}0} + f_{11\bar{2}0} = 1$.

2. If there are three or four pole figures the ODF approach should be used, where it is possible to uniquely identify texture components and to determine the overall and detailed changes in texture in a quantitative manner. Additionally, micro-ODF data can be generated by the EBSP technique.

Acknowledgements

The author would like to thank his colleagues on Brite/EuRam contact 0117C, particularly Dr L Toth, for providing the stimulating environment in which this paper was written; Dr M R Winstone for providing the modulus values for Figure 5; and Mrs S M Goodwin for the care in data processing and figure preparation.
© Copyright HMSO London 1992.

References

1. J. J. Kearns, Thermal Expansion and Preferred Orientation in Zircaloy, WAPD-TM-472, Westinghouse Elec Corp. Pittsburgh, Pa USA, 1965.

2. H. J. Bunge, Texture Analysis in Materials Science London:Butterworths, 1982.

3. P. M. Kelly and K. G. Watson, A Simple Method for Determining the Pole Figure of Zirconium Alloy Tubing, J Nucl Mat 44 (1972), 71-8.

4. J. E. Lewis, G Schoenberger and R B Adamson, Texture Measurement Techniques for Zircaloy Cladding: A Round-Robin Study, ASTM STP 754, (1982), 39-62.

5. J. L. Baron et al, Interlaboratories Tests of Textures of Zircaloy-4 Tubes. Part 1: Pole Figure Measurements and Calculation of Kearns Coefficients, Textures and Microstructures, 12, (1990) 125-40.

6. D. B. Knorr and R. M. Pelloux, Quantitative Characterisation of Crystallographic Textures in Zirconium Alloys, J Nucl Mat, 71 (1977), 1-13.

7. K. Kallstrom, T Anderson and A. Hofvenstam ASTM 551 (1974) 160.

8. J. M. Dahl, R. W. Mckenzie and J. H. Schemel, ASTM 551 (1974) 147.

9. P. I. Welsch, Personal communication, 1988.

10. A. W. Bowen, D. S. McDarmaid and P. G. Partridge, Superplastic Deformation of Strongly textured Ti-6Al-4V part 2, J Mat Sci 20 (1985) 1976-84.

11. A. W. Bowen, Texture Stability in Heat-treated Ti-6Al-4V, Mat Sci & Eng 29 (1977), 19-28.

12. M. R. Winstone, Effect of Texture on the Dwell Fatigue Properties of a Near-Alpha Titanium Alloy, 6th World Cong on Ti, Ed P Lacombe et al, Les Ed de Phys 1 (1988) 169-73.

13. D. J. Dingley, Backscattering in the scanning electron microscope, Inst of Phys Conf Ser No. 119 (1991) 551-8.

14. A. W. Bowen, D. S. McDarmaid and P. G. Partridge, Effect of high temperature deformation on the texture of a two-phase titanium alloy, J Mater Sci 26 (1991) 3457-62.

THE EFFECT OF PROCESS ROUTE AND RARE EARTH CONTENT ON THE MICROSTRUCTURE AND PROPERTIES OF A PM TITANIUM ALLOY

A.P.Woodfield, M.F.X.Gigliotti* and R.A.Amato

General Electric Aircraft Engines,
1 Neumann Way, Cincinnati, OH 45215.
*General Electric Corporate Research and Development,
1 River Road, Schenectady, NY 12301.

Abstract

A powder metallurgy titanium alloy, with and without erbium, was evaluated after HIP, extrusion, rolling and forging. Processing was performed in the beta phase field and all materials were given a direct age heat treatment. The beta HIP microstructures consisted of equiaxed prior beta grains containing aligned alpha colonies. The erbium-containing alloy had a significantly reduced prior beta grain size compared to the erbium-free alloy. The beta processed microstructures for the erbium-free alloy showed large elongated prior beta grains containing a mixture of basketweave and aligned alpha. The beta processed microstructures of the erbium-containing alloy consisted of very fine elongated prior beta grains with aligned alpha colonies.

Tensile, creep and fracture toughness properties of the beta processed and direct aged alloys were measured. Tensile properties showed the highest strengths were achieved in extruded materials. The high strengths were related to c-axis alignment of the alpha plates in the extrusion direction. Dispersion strengthening from the erbium-rich particles was not observed, since considerable coarsening occurred during beta consolidation and processing. The erbium addition generally resulted in decreased ductilities. Extruded materials had the best creep strengths due to their highly elongated prior beta grain structures. The creep strengths were generally lower for the erbium-containing alloy due to its more refined microstructure. The fracture toughness appeared to be independent of both processing route and erbium content.

This work was funded by NAWC, Contract N00140-88-R-1834.

Titanium '92
Science and Technology
Edited by F.H. Froes and I. Caplan
The Minerals, Metals & Materials Society, 1993

Introduction

Rapid solidification processing has been identified as a way of increasing the temperature capability of titanium alloys [1]. Following the development of rapid solidification techniques [1], rare earth-containing alloy compositions were developed that had increased high temperature tensile and creep strengths [2]. In one such study, a powder alloy was developed that had significantly higher tensile and creep strengths at 650°C than current commercially available titanium alloys [2]. The material was produced by gas atomization, HIP consolidated, extruded and given either a direct age or beta solution and age heat treatment.

Recently, a program was initiated between the General Electric Company and the Naval Air Warfare Center (NAWC) to investigate a wide range of process routes and rare earth levels on the microstructure and properties of powder titanium alloys [3]. The work reported in this paper describes the effects of beta processing on the microstructural development and mechanical properties of a near-alpha powder titanium alloy with and without erbium.

Experimental Procedure

Alloy Selection and Powder Production

The nominal compositions of two alloys used in this study, designated AF2-0Er and AF2-0.5Er are listed in Table 1. The AF2-0Er base is a near alpha alloy containing aluminum, tin and zirconium for alpha phase strengthening, hafnium, niobium and ruthenium for beta phase strengthening, and silicon and germanium for strain age strengthening. AF2-0.5Er contains a 0.5 atom percent erbium addition to form a dispersoid. The alloy powders were atomized in a gas atomizing unit consisting of an induction heated crucible and a heated tundish with an inert nozzle above the atomizing chamber [4]. Interstitial analysis of the powder indicated approximately 1200 wppm oxygen, less than 150 wppm carbon and nitrogen, and approximately 30 wppm hydrogen.

Table 1 Nominal AF2-0Er and AF2-0.5Er Compositions (Atom Percent)

Alloy	Ti	Al	Sn	Zr	Hf	Nb	Ru	Si	Ge	Er
AF2-0Er	bal.	11.5	1.3	1.6	0.7	0.5	0.15	0.25	0.22	-
AF2-0.5Er	bal	11.5	1.3	1.6	0.7	0.5	0.15	0.25	0.22	0.5

Thermomechanical Processing

All powders were sieved to -35 mesh (<500μm) and HIPped at 1200°C and 210 MPa for 3 hours either in cylindrical or rectangular HIP cans. Following consolidation, HIPped cans of each alloy were extruded 8:1 at 1200°C, hot die forged at 1200°C with an 80% height reduction, or rolled at 1200°C with a 75% reduction in thickness. A single HIP can of each alloy was retained for evaluating as-HIP microstructures and properties. A direct age heat treatment of 600°C for 8 hours was given to each alloy/process condition.

Texture Procedure

Texture measurements were made on the HIP plus extruded, HIP plus forged and HIP plus rolled material. Previous texture measurements on as-HIP material indicated that no significant texture existed [5]. Three pole figures were measured, (0002), $\{10\bar{1}1\}$ and $\{10\bar{1}0\}$, and recalculated according to the WIMV analysis [6]. Inverse pole figures were also generated. Data were collected at 5° intervals.

Mechanical Testing

Round tensile and creep specimens, and rectangular three point bend fracture toughness samples were machined from as-HIP, forged, and extruded materials. Sheet tensile, creep and fracture toughness specimens (center notched) were machined from the rolled plates. Test specimens from the rolled plates were taken from the transverse and longitudinal directions, while specimens from the forged pancakes were machined in the plane of the pancake. Extruded specimens were taken in the axial direction. The machining and testing procedures were in accordance with ASTM standards, and all testing was conducted in air. Young's modulus measurements were made on the cylindrical test specimen blanks using sound velocity measurements [7].

Results

Microstructural Characterization

The gas atomized powders of both compositions were examined metallographically. Powders of both compositions sometimes contained large ~100 μm dendrites [8]. The other powder particles appeared to be very homogeneous with fine prior beta grains. There was evidence of erbium segregation to dendrite and beta boundaries in both types of AF2-0.5Er alloy powder. Powder produced from a small research gas atomization unit [9] did not contain the large dendrites found in the powder used in this present study. The effects of starting powder microstructure on the final processed microstructure and mechanical properties are described in reference [8].

The microstructures of the two alloys after HIP, HIP plus extrusion, HIP plus forging and HIP plus rolling are shown in Figure 1. After a beta HIP consolidation, the microstructures consisted of prior beta grains with aligned alpha colonies, Figure 1(a,b). The microstructures following a beta HIP plus beta extrusion, beta forging and beta rolling appeared to be similar. The AF2-0Er alloy consisted of coarse elongated prior beta grains containing a mixture of basketweave alpha plates and aligned alpha colonies, Figure 1(c,e,g). The AF2-0.5Er alloy consisted of fine aligned alpha colonies; distinct prior beta grain boundaries were not evident, Figure 1(d,f,h). Thus, the erbium addition resulted in significant beta grain refinement during processing; the fine beta grains subsequently transformed to aligned alpha colonies. The much larger prior beta grains in the AF2-0Er alloy allowed some basketweave alpha to form during the transformation. After beta processing, the erbium-rich particles were typically less than 1 μm in size. Following the direct age heat treatment of 650°C for 8 hours, there was no obvious change in the microstructure.

Texture Measurements

The textures measured for the AF2-0Er and AF2-0.5Er alloys were similar. Examples of the as-extruded, as-forged and as-rolled textures are shown in Figure 2 for the AF2-0.5Er alloy. The inverse pole figure for the AF2-0.5Er HIP plus extrusion shows a high degree of (0002) alignment at 0°, at ~60° and at 90° to the bar axis, Figure 2(a). This is the expected texture for beta extruded material [10]. The intensity for the (0002) along the bar axis varied between 30 and 100 times random depending on the exact mounting of the sample in the specimen holder. A comparison of (0002) intensities between the two alloys could not be made due to the sensitivity of sample mounting on measured intensity.

The (0002) pole figure for HIP plus rolled AF2-0.5Er alloy shows a significantly lower intensity compared to the HIP plus extruded sample, Figure 2(b). There is some intensity of (0002) along the rolling direction and the transverse direction, in addition to a third component inclined at ~30° to the sheet normal toward the rolling direction. The intensity is slightly higher along the rolling direction compared to the transverse direction. This texture is similar to that found for beta rolled titanium alloys [11]. The (0002) pole figure for HIP plus forged AF2-0.5Er material was axisymmetric, with two rings of (0002) intensity, at approximately 45° and at 90° to the plane of the forging, Figure 2(c). The level of (0002) intensity was slightly lower for the HIP plus forged material compared to the HIP plus extruded material.

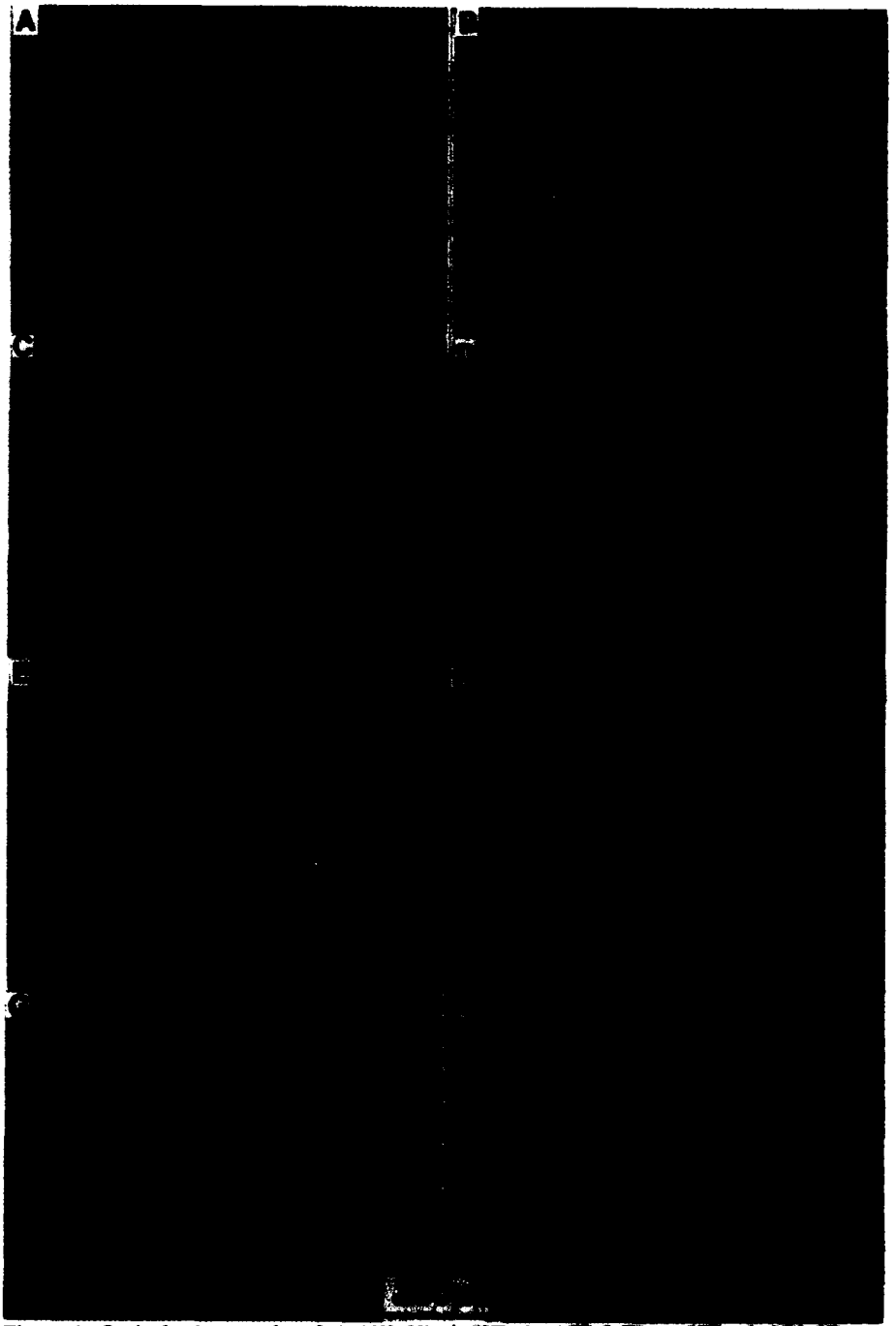


Figure 1 Optical micrographs of a) AF2-0Er as-HIP, b) AF2-0.5Er as-HIP, c) AF2-0Er as-extruded, d) AF2-0.5Er as-extruded, e) AF2-0Er as-forged, f) AF2-0.5Er as-forged, g) AF2-0Er as-rolled and h) AF2-0.5Er as-rolled.

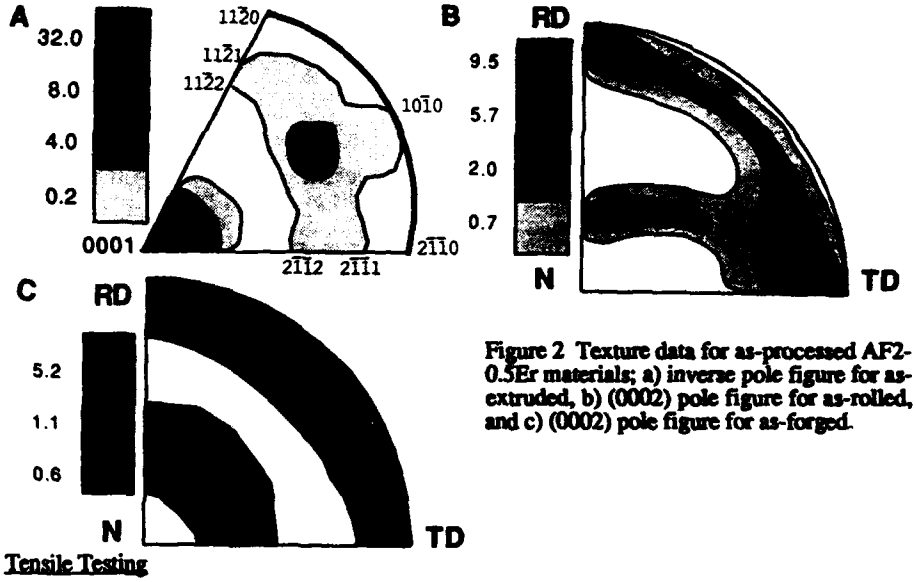


Figure 2 Texture data for as-processed AF2-0.5Er materials; a) inverse pole figure for as-extruded, b) (0002) pole figure for as-rolled, and c) (0002) pole figure for as-forged.

Tensile Testing

The tensile data for AF2-0Er and AF2-0.5Er in the four process conditions are shown in Table 2. Processing route had a significant effect on room temperature yield strength, ultimate tensile strength, ductility and modulus for both alloys. HIP plus extruded material had the highest yield strength, followed by *HIP plus rolled*, *HIP plus forged* and as-HIP. The yield strength of the HIP plus rolled material was slightly higher in the longitudinal direction compared to the transverse direction. Ultimate tensile strength, modulus and plastic elongation to failure also followed the same trend with the highest values observed for HIP plus extruded material and the lowest values for as-HIP material. At 650°C, HIP plus extruded material had the highest strength, while as-HIP had the lowest strength and ductility. HIP plus forged and HIP plus rolled material had the highest ductility at 650°C.

Table 2 Tensile and Modulus Data for AF2-0Er and AF2-0.5Er

	As-HIP						HIP Plus Extrude				
Alloy	Temp (°C)	Mod. (Msi)	YS (ksi)	UTS (ksi)	El_p %	Alloy	Temp (°C)	Mod (Msi)	YS (ksi)	UTS (ksi)	El_p %
AF2-0Er	RT	17.5	121.5	132.4	0.8	AF2-0Er	RT	18.9	158.6	177.7	5.4
AF2-0.5Er	RT	17.6	124.1	124.4	0.2	AF2-0.5Er	RT	19.2	169.0	175.4	2.1
AF2-0Er	650	-	61.9	77.8	6.1	AF2-0Er	650	-	90.8	114.8	8.6
AF2-0.5Er	650	-	62.9	80.7	5.6	AF2-0.5Er	650	-	99.0	124.2	2.1
	HIP Plus Roll						HIP Plus Forge				
AF2-0Er -L	RT	15.8	167.5	169.1	7.0	AF2-0Er	RT	18.0	136.4	148.9	2.6
AF2-0Er -T	RT	16.7	134.3	134.5	0.4*						
AF2-0.5Er -L	RT	16.2	145.5	152.1	1.2	AF2-0.5Er	RT	18.0	131.3	137.9	0.9
AF2-0.5Er -T	RT	16.5	141.8	146.5	0.6						
AF2-0Er -L	650	-	75.3	96.1	17.6	AF2-0Er	650	-	70.7	94.1	10.6
AF2-0Er -T	650	-	74.6	99.1	10.1						
AF2-0.5Er -L	650	-	78.4	107.7	10.1	AF2-0.5Er	650	-	74.4	91.8	8.7
AF2-0.5Er -T	650	-	75.8	104.7	8.3						

L Longitudinal, T Transverse, * Failed at extensometer attachment.

The erbium addition also affected tensile properties as shown in Table 2. The erbium addition had a mixed effect on yield strength at room temperature, however, the yield strengths were higher for the erbium containing alloy at 650°C. At room temperature and 650°C, the erbium addition resulted in a lower ductility.

Creep Testing

The creep data for the two alloys in the four process conditions are shown in Table 3. The process route had a significant effect on the creep strengths of the two alloys. The HIP plus extruded material had the highest creep strength, followed by HIP plus forged, as-HIP and HIP plus rolled material as shown by the time to 0.5 percent strain, and the strain developed in 100 hours at 650°C/25 ksi. The erbium addition in all process conditions reduced creep strength with the exception of the longitudinal HIP plus rolled AF2-0Er.

Table 3 Creep and Fracture Toughness Data for AF2-0Er and AF2-0.5Er

Alloy	Process	Orien.	Hours to % strain at 650°C/25ksi					Strain in 100 Hours	Kq (ksi√in.)
			0.1	0.2	0.3	0.4	0.5		
AF2-0Er	HIP	-	2.3	9.0	20.6	39.0	63.5	0.615	34.8
AF2-0.5Er	HIP	-	1.2	5.0	11.7	23.0	39.0	0.748	32.3
AF2-0Er	Extrude	L	3.0	13.6	39.5	91.8	181.5	0.414	32.4
AF2-0.5Er	Extrude	L	3.0	17.5	43.5	73.9	115.0	0.465	39.7
AF2-0Er	Roll	L	0.4	2.5	5.5	11.0	21.0	0.861	51.0
AF2-0Er	Roll	T	1.5	5.0	10.0	20.0	35.5	0.720	56.4
AF2-0.5Er	Roll	L	0.9	3.5	8.5	17.5	31.0	0.830	57.0
AF2-0.5Er	Roll	T	1.0	3.0	7.5	13.9	26.0	0.840	46.0
AF2-0Er	Forge	-	2.0	8.0	19.3	49.0	91.2	0.528	40.9
AF2-0.5Er	Forge	-	1.0	4.8	12.5	26.7	57.2	0.649	34.7

Fracture Toughness Testing

The fracture toughness data for the two alloys in the four process conditions are shown in Table 3. There was no obvious effect of process route or erbium content on the fracture toughness values shown in Table 3. (Note the toughness values for the HIP plus rolled materials are significantly higher as would be expected from the reduced section thickness tested).

Discussion

The tensile properties measured as a function of processing route and erbium content are directly related to the texture developed during processing. The highest texture, defined by intensity of (0002) aligned along the testing axis, was produced in the extruded material. This corresponded with high modulus values and yield strengths, which is consistent with other workers who have demonstrated the relationship between alignment of basal poles with increasing modulus and yield strength [11,12]. Although no difference in texture between the HIP plus extruded AF2-0Er and AF2-0.5Er alloys could be found, (a consequence of the intense texture and sensitivity to mounting in the specimen holder), the modulus data indicate a higher level of texture in the AF2-0.5Er alloy. This resulted in increased strength for the HIP plus extruded AF2-0.5Er alloy.

The HIP plus rolled texture showed a much lower degree of alignment of (0002) along the rolling and transverse directions. The intensity is slightly higher for the rolling direction compared to the transverse direction. The yield strength follows the same trend, being much lower than the HIP plus extruded material, with the rolling direction slightly higher in strength compared to the transverse direction. The intensity of (0002) for the HIP plus forged material is lower than the HIP plus rolled material and correspondingly has a slightly reduced strength. The as-HIP material which had a random texture [5] had the lowest yield strength of all the materials.

The creep properties measured as a function of processing route and erbium content appear to be related to the microstructure developed during processing. The HIP plus extruded materials have a significantly higher creep strength than the as-HIP materials. This is probably a result of the elongated prior beta grains and not the high modulus in the HIP plus extruded materials. If the dominating effect was modulus, then the as-HIP materials would be expected to have the lowest creep strengths as a consequence of their random texture. However, the as-HIP materials had higher creep strengths than the HIP plus rolled materials.

The effect of the rare earth addition was to reduce the creep strength (time to 0.5% strain and % strain in 100 hours) for each process condition. It is clear that the erbium addition refined the microstructure, resulting in reduced creep strengths. It should be noted that for HIP plus extruded materials, the erbium addition resulted in a lower creep strength compared to the erbium-free alloy. The erbium-containing alloy had a higher modulus, but a much refined microstructure, thus providing further evidence that microstructure and not modulus is the dominating effect in determining creep strength.

The fracture toughness data for the two alloys in the four process conditions could not be related to any microstructural features. The fracture surfaces of specimens with high toughness were macroscopically rough, however, no correlation between crack path and microstructural features was observed in test specimen cross-sections. It is possible that there may be a subtle relationship between beta grain size and shape, alpha plate morphology and possibly modulus, however, more data would be needed to confirm such a relationship.

The erbium addition resulted in significant grain refinement during beta processing; similar effects have been observed for yttrium additions to titanium alloys [13]. For the extruded materials, the erbium addition caused a sharpening of the texture which led to an increase in modulus and yield strength. There was no evidence of increased creep strengths by a dispersion strengthening mechanism in the beta processed AF2-0.5Er materials. This was anticipated since the particle sizes were relatively large (~ 0.5 to 1.0 μm) following beta processing. In fact the high temperature creep strengths of AF2-0.5Er materials were lower than for AF2-0Er due to the refined grain sizes found in erbium-containing alloy.

Conclusions

The effects of process route and erbium level on the microstructure and texture development of two advanced powder titanium alloys were investigated. The process route dominated the development of (0002) texture in the work direction leading to the highest modulus and yield strengths in HIP plus extruded materials. The erbium addition was less influential in the texture development for the various process routes, although some enhancement of texture was observed in the AF2-0.5Er extruded material. The process route and erbium level affected creep strength. Improved creep strengths were achieved by increasing the size and aspect ratio of the prior beta grains during processing with HIP plus extruded materials having the highest creep strengths. The erbium addition led to a refinement of the prior beta grain size which resulted in reduced creep strengths. Fracture toughness data could not be obviously related to process route or texture development.

Acknowledgements

The authors wish to acknowledge funding by NAWC, Contract N00140-88R-1834 and A. Culbertson from NAWC for useful discussions concerning the overall program. Dr. A. Rollett from Los Alamos National Laboratories provided helpful comments concerning the texture analysis. Powder production was performed by F. Yolton at Crucible Research Center and thermomechanical processing was carried out by J. Hughes, R. Laing, T. Douglas and R. Auer. Coordination of material characterization and testing was supervised by K. Kitchen. Their care and diligence is gratefully acknowledged.

References

1. F.H.Froes and R.G.Rowe, "Rapidly Solidified Titanium", in *Rapidly Solidified Alloys and their Mechanical and Magnetic Properties*, ed. B.C.Giessen, D.E.Polk and A.I.Taub, (Pittsburgh, PA: MRS, 1986), 309-334.

2. R.A.Amato, G.E.Wasielewski, M.F.X.Gigliotti and R.G.Rowe, "Properties of Advanced Rapidly Solidified Titanium Alloys" in *1989 Advances in Powder Metallurgy*, (Metal Powder Industries Federation, 1989), 189-201.

3. A.P.Woodfield, M.F.X.Gigliotti and R.A.Amato, "Processing Advanced High Temperature RS/PM Titanium", (Navy Contract N00140-88-R-1834, Phase I Report, 1991).

4. C.F.Yolton, "Gas Atomized Titanium and Titanium Aluminide Alloys", in *Aerospace and Defense Technologies*, (Princeton, NJ: Metal Powder Industries Federation, 1990), 1, 123-131.

5. A.P Woodfield, GE Aircraft Engines IR&D, 1991.

6. S.Matthies, "On the Basic Elements of and Practical Experience with the WIMV Algorithm; an ODF Reproduction Method with Additional Ghost Correction", in *International Conference on Textures of Materials*, ed. J.S.Kallend and G.Gottstein, (Warrendale, PA: TMS-AIME, 1988), 37.

7. E.Schreiber, O.L.Anderson and N.Soga, *Elastic Constants and Their Measurement*, (New York, NY: McGraw-Hill, 1973).

8. M.F.X.Gigliotti, A.P.Woodfield, R.A.Amato, J.R.Hughes and L.C.Perocchi, "The Role of Input Powder Microstructure and Extrusion Conditions on Properties of PM Titanium-Rare Earth Alloys", To be published in this conference proceedings.

9. J.H.Moll and C.F.Yolton, "Production and Characterization of Rapidly Solidified Titanium and other Alloy Powders Made by Gas Atomization", in *Titanium, Rapid Solidification Technology*, ed. F.H.Froes and D.Eylon, (Warrendale, PA: The Metallurgical Society of AIME, 1986), 45-56.

10. A.W.Bowen, D.V.Dunford, and P.G.Partridge, "Texture Analysis of Anisotropic Superplastic Deformation in a Ti-6Al-4V Extrusion", in *Proceedings of the Sixth World Conference on Titanium*, ed. P.Lacombe, R.Tricot and G.Beranger, (Cedex, France: Les Editions de Physique, 1988), 1367-1372.

11. F.Larson and A.Zarkades, "Properties of Textured Titanium Alloys" (Report MCIC-74-20, Metals and Ceramics Information Center, Batelle, Columbus OH, 1974).

12. M.R.Winstone "Effect of Texture on the Dwell Fatigue Properties of a Near-Alpha Titanium Alloy", in *Proceedings of the Sixth World Conference on Titanium*, ed. P.Lacombe, R.Tricot and G.Beranger, (Cedex, France: Les Editions de Physique, 1988), 169-173.

13. S.Naka, H.Octor, M.Marty and T.Khan, "Control of ß-Grain Size and Shape by Yttria or Other Particles in a Powder Metallurgy Processed Ti-6Al-4V Alloy" in *Proceedings of the Sixth World Conference on Titanium*, ed. P.Lacombe, R.Tricot and G.Beranger, (Cedex, France: Les Editions de Physique, 1988), 831-836.

THE INFLUENCE OF SILICON AND SILICIDES ON THE PROPERTIES OF NEAR-ALPHA TITANIUM ALLOYS

D.F. Neal and S.P. Fox

IMI Titanium Limited, P O Box 704, Witton, Birmingham, England.

Abstract

Silicon is an extremely effective and generally beneficial addition to titanium, particularly for high temperature tensile and creep strength. IMI Titanium has led the industry in exploiting the benefits of silicon, especially in near-alpha alloys such as IMI 679, IMI 685, IMI 829 and IMI 834, where the amount of silicon has been increased steadily. The aim, in terms of maximising high temperature properties in these alloys, is to achieve full solubility of silicon in the alpha phase. In practice, because of the natural segregation pattern in ingots and due to precipitation during service, silicides may come out of solution. There are therefore, two important aspects involved in the understanding of the effects of silicon on properties:-

1). the influence of silicon in solution.
2). the structure and morphology of silicides

Electron optical and analytical techniques have shown that silicides are generally of the Ti_5Si_3 type, but modifications to this have been observed.

The paper reviews these analytical results and describes the influence of silicon and silicides on mechanical properties.

Introduction

On a percentage basis, silicon is the most effective addition to titanium for high temperature tensile and creep strength. It has been used extensively in alloys developed in the UK and to a more limited extent in the USA and in the former Soviet Union.

This paper reviews established and new data, and is presented in two parts relating to:-

1). the effects of silicon in solution
2). the influence of silicides

The way these factors influence properties, alloy design and production is considered.

Titanium '92
Science and Technology
Edited by F.H. Froes and I. Caplan
The Minerals, Metals & Materials Society, 1993

The solubility of silicon in titanium is low; a maximum of 0.8 atomic percent (0.47wt%) in alpha phase is normally quoted, Figure 1[1]. Solubility decreases with decreasing temperature in alpha titanium and this, plus the amount of beta stabiliser in the alloy, has the strongest influence on the structure and properties of silicon containing alloys.

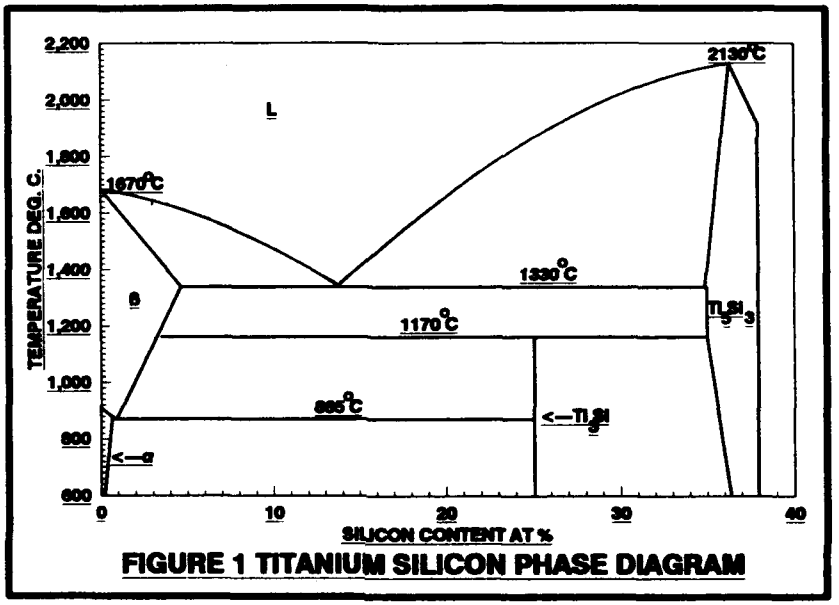


FIGURE 1 TITANIUM SILICON PHASE DIAGRAM

Silicon in Solution

Whether silicon is in solution (or remains in solution), is governed by:-

- Alloy composition
- Solution treatment temperature
- Ageing/stabilisation treatment
- Service conditions

Alloys with relatively high beta stabiliser content, such as IMI 550 (4%Al-4%Mo-2%Sn-0.5%Si), can in theory accomodate a relatively high silicon content, since beta phase has a higher solubility for silicon than does alpha phase (Figure 1). However, in practice, alloys like IMI 550 tend to be solution heat treated in the alpha plus beta plus silicide phase field and therefore free silicides are present. Near-alpha alloys such as IMI 834 (5.8%Al-4%Sn-3.5%Zr-0.7%Nb-0.5%Mo-0.35%Si-0.06%C) and Ti 1100 (6%Al-2.8%Sn-4%Zr-0.4%Mo-0.45%Si) which have low beta stabiliser content and relatively high silicon content, would normally be expected to contain free silicides. However, these near-alpha alloys are usually heat treated above the silicide solvus temperature for maximum silicon solubility and consequently good creep performance. Their microstructures consist of alpha plus transformed beta or of fully transformed beta, with silicon retained in solution.
In most near-alpha, creep resistant titanium alloys, zirconium is also

present up to around 5wt%. This element interacts with titanium and silicon to form mixed (TiZr) silicides. These aspects are considered in more detail later.

The effect of silicon on mechanical properties is quite significant. An example of it's influence on tensile strength is given in Figure 2 for near-alpha alloys. Over the range 0 to 0.5%Si, an increase of almost 15% on tensile strength can be achieved and these improvements are maintained to high temperatures (~800°C). An even more dramatic improvement can be seen in creep performance even at temperatures up to 800°C. An illustration of the benefit to creep performance in IMI 834 type alloys at 600°C is presented in Figure 3.

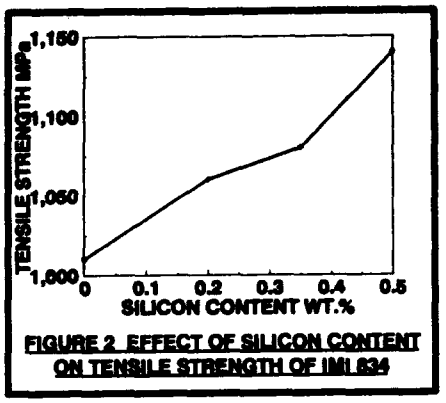


FIGURE 2 EFFECT OF SILICON CONTENT ON TENSILE STRENGTH OF IMI 834

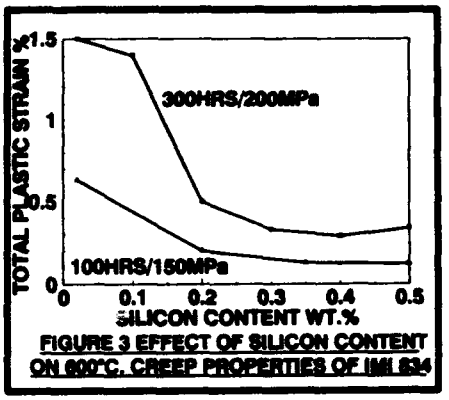


FIGURE 3 EFFECT OF SILICON CONTENT ON 600°C. CREEP PROPERTIES OF IMI 834

The strengthening mechanisms involved with silicon in solution are solid solution strengthening and solute drag. These effects are reasonably well understood and if service temperatures do not exceed~450°C then silicon normally stays in solution with little if any change in properties[2,3]. However, in practice, either due to precipitation and transformation effects or due to non-equilibrium conditions, silicides are present in all silicon containing alloys. In virtually all near-alpha alloys the service temperature may exceed 450°C and silicides precipitate either heterogenously on dislocations in the alpha phase or are produced by transformation of the residual beta phase to alpha plus silicide. The composition, formation and influence of silicides provides the most interesting area for study.

Silicon out of Solution (Silicides)

Microstructure

In typical near-alpha Ti alloys, three forms of silicide can be observed, as shown in Figures 4 and 5:-

1). Very fine (~0.01μm diameter), precipitation from alpha phase during service exposure (see A in Figure 4).
2). Fine (~ 0.1μm diameter), precipitation resulting from decomposition of residual beta phase during service exposure (see B in Figure 4).
3). Particles (~ 1 to 5μm diameter) resulting from solution treatment in a "silicide" phase field (see C in Figure 5).



FIGURE 4 SILICIDE PRECIPITATION DURING SERVICE EXPOSURE



FIGURE 5 SILICIDE PRECIPITATION DURING SOLUTION TREATMENT

Composition and Phase Fields

The two fine precipitates (Types 1 and 2) are generally regarded as being based on Ti_5Si_3 with, in alloys containing zirconium, a mixed $(TiZr)_5Si_3$ composition. In McIntosh's[4] review of silicide compositions, typical values of 37.5At%Si, 37.5At%Ti, 25At%Zr are quoted. However, if Sn was present in the alloy, some of the Si could be replaced by up to 5At%Sn (typically $\sim$ 1At%). In the case of the larger particles (Type 3), the present work suggests a composition of 31.8At%Si, 40.5At%Ti, 27At%Zr, 0.7At%Sn determined by energy dispersive X-ray analysis. This would suggest a composition of the type $(TiZr)_2(SiSn)$.

However, in one case,a composition of 25At%Si, 50At%Ti, 25At%Zr was measured, which would correspond to $(TiZr)_3Si$. Such a high level of titanium might suggest that there was contribution from the matrix, i.e. that the electron beam was irradiating some of the matrix rather than irradiating only the silicide particle. In an attempt to "remove" this factor, the data obtained from particle analysis (ZAF corrected energy dispersive) has been examined in more detail. In all of the analyses, small but measurable quantities of Al, Sn and Nb were always detected. It was assumed that the "presence" of Al was due to slight irradiation of the matrix and that analyses which showed the lowest level of Al had a composition nearest to the actual silicide composition. The Al content was therefore plotted against Ti, Zr, Si, Sn and Nb and the line was extrapolated to zero Al content, Figures 6, 7, 8 and 9.

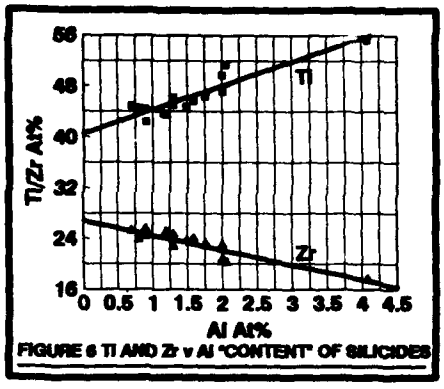


FIGURE 6 Ti AND Zr v Al "CONTENT" OF SILICIDES

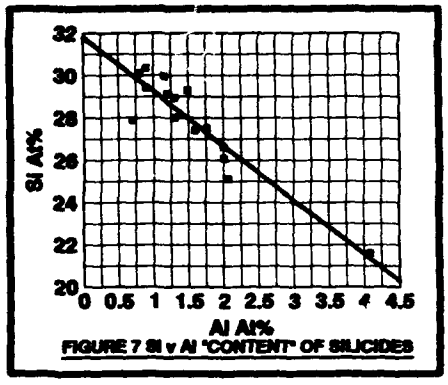


FIGURE 7 Si v Al "CONTENT" OF SILICIDES

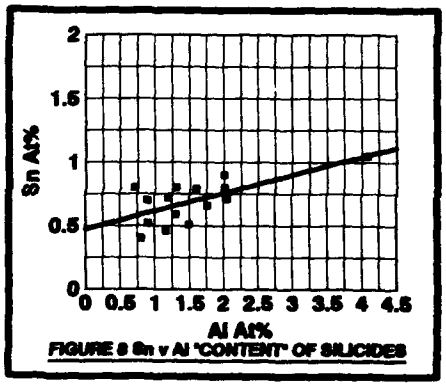


FIGURE 8 Sn v Al "CONTENT" OF SILICIDES

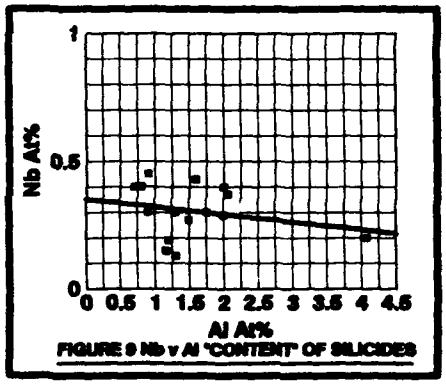


FIGURE 9 Nb v Al "CONTENT" OF SILICIDES

This indicates a composition of 31.79At%Si, 40.52At%Ti, 26.79At%Zr, 0.5At%Sn. (The correlation coefficient for Nb against Al suggested no relationship). Whether there is a genuine difference in composition between these silicides is not clear. It is possible that there is no basic difference between them, but that they simply represent the composition range of the nominal $(TiZr)_xSi$ field, where x may vary between 1.67 and 3. Silicide compositions have been determined by the authors in IMI 834 type alloys heat treated in phase fields containing silicide. No difference in silicide composition was detected over the temperature range 990°C to 1160°C. This temperature range covered the silicide solvus temperature for IMI 834 (990°C) and a similar alloy containing 0.8wt% silicon (1160°C). From this work, a schematic Ti-Si phase diagram for IMI 834 type alloys was constructed - Figure 10.

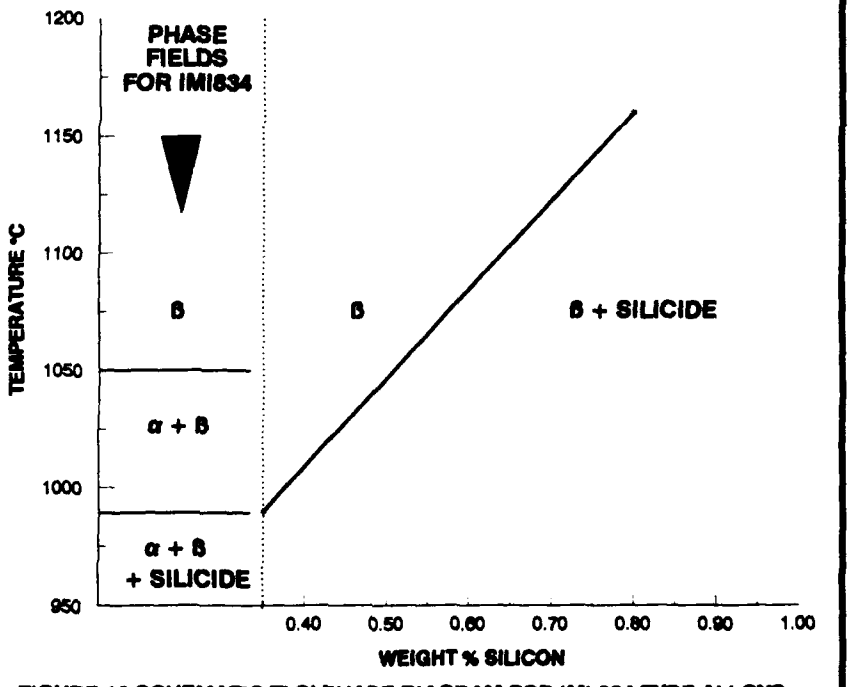


FIGURE 10 SCHEMATIC Ti-Si PHASE DIAGRAM FOR IMI 834 TYPE ALLOYS

The Influence of Silicon and Silicides on Properties

In IMI 834, mechanical properties are optimised at a silicon content of 0.35wt% i.e. significant strengthening is achieved and creep performance is at maximum. In Ti-1100 the chosen level of Si is 0.45%. However, this level of silicon cannot be retained in solution during ageing or during service exposure at temperatures up to around 600°C. The major microstructural change that occurs is that beta transforms to alpha plus fine silicide. In addition, some silicide is precipitated on dislocations within the alpha phase. Although some silicon comes out of solution during ageing or exposure, creep performance generally improves. (However, there is a complicating factor in that a small degree of ordering also occurs, which may improve creep performance).

The influence of ageing temperature on creep performance is also interesting. Work by the authors has shown that in IMI 834, creep performance at temperatures below ~ 565°C is superior if ageing is carried out at low temperature e.g. 625°C where little silicon is lost from solution. At creep test temperature above ~565°C, higher ageing temperatures (e.g. 700°C) are beneficial. This may suggest a change in the rate controlling creep mechanism away from solute drag.

The influences of silicon and silicides on tensile properties after exposure are somewhat more complicated. The major influence is that tensile ductility is reduced, particularly if the oxidised surface is retained. Figure 11 shows how silicon affects room temperature tensile ductility of IMI 834 before and after exposure, over a silicon range of 0 to 0.5wt%. There is a progressive loss of ductility as silicon content is increased and transmission electron microscopy at IMI Ti has revealed:-

- less dislocation mobility because of fine heterogenous silicide precipitation [5].
- void formation induced when planar slip bands intersect silicide particles [6].

both of which reduce tensile ductility.

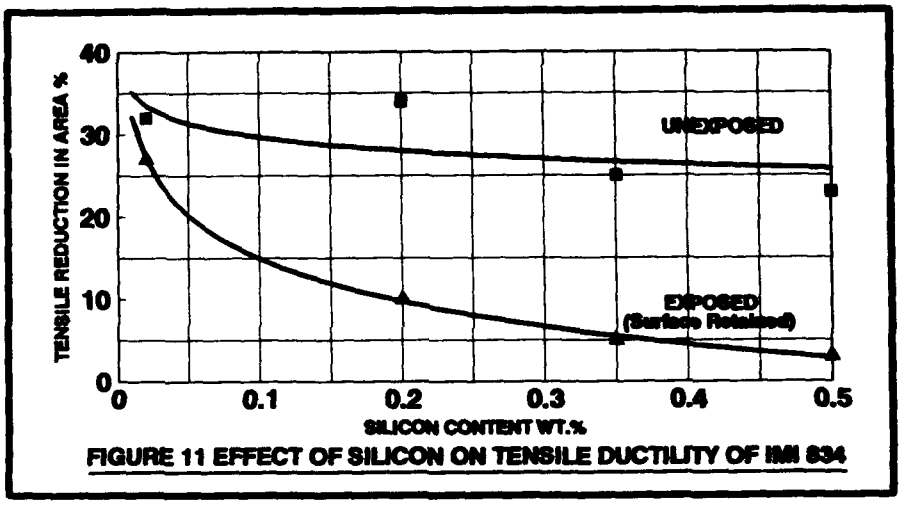


FIGURE 11 EFFECT OF SILICON ON TENSILE DUCTILITY OF IMI 834

The latter effect is also influenced by the alpha stabiliser content and its influence on ordering and hence on planar slip. If aluminium content is reduced to a level where more cross slip is possible, then no effect of silicon (silicides) on ductility is seen after exposure. Although silicon does influence exposed ductility, it has no apparent influence on surface oxidation during exposure or on the degree to which this oxidised layer (α-case) behaves under tensile loading.



FIGURE 12 CRACKING OF α-CASE DURING TENSILE TESTING

Figure 12 illustrates the surface crack initiation which occurs in exposed materials when tensile tested. This is an example of an alloy containing zero silicon content and is typical of alloys containing up to 0.5wt%Si. Any reduction in ductility (as assessed by a post creep, surface retained tensile test), appears to be due to a small reduction in matrix "toughness". During tensile testing of exposed specimens the α-case cracks and alloys containing high silicon content are less able to sustain such cracks when yielding occurs. However, if tensile tests of exposed specimens are carried out above $\sim$150°C, no effect of α-case is seen. After exposure at higher temperature e.g. $\sim$700°C, the alloys tend to soften and become tougher. There is therefore little further loss in ductility after such exposure despite the increasing alpha case thickness.

In alloys where solution treatment has been carried out in the alpha plus beta plus silicide phase field, free silicides typically of up to $\sim$ 5μm diameter, can be present. No influence of these silicides on mechanical properties has been seen. In tensile or fatigue testing of typical silicon containing alloys, fracture is initiated from planar slip bands in either the primary alpha or acicular alpha phases. (The authors have shown that this mechanism also occurs in Ti 6Al 4V.) Because silicide particles appear to play no part in fracture initiation, they have no measurable influence on properties such as tensile or fatigue performance.

Conclusions

1. On a percentage basis, silicon is the most effective addition to titanium for high temperature strength and creep resistance.

2. Because of the low solubility of silicon in alpha titanium, properties are influenced both by silicon in solution and by silicides in near-alpha alloys.

3. In near-alpha alloys where zirconium is present, the composition of the silicide is based on $(TiZr)_xSi$. The present work indicates that x may vary from between 1.67 and 3.

4. The larger silicides appear to have a composition close to $(TiZr)_2Si$.

References

1. J.L. Murray. Phase Diagrams of Binary Titanium Alloys. ASM Int. 1987, 289
2. M. Kehoe and R.W. Broomfield. Titanium Conference Proceedings 1972, 2167-2178.
3. V.J. Erdeman and E.W. Ross. Titanium Conference Proceedings 1968, 829-837.
4. G. McIntosh and T.N. Baker. Phase Transformation. 187. The Institute of Metals.
5. A.P. Woodfield, M.H. Loretto and R.E. Smallman. Titanium Conference Proceedings 1984, 1527-1534.
6. A.P. Woodfield, A.W. Wardle and M.H. Loretto. Titanium Conference Proceedings 1988, 357-362.

THE INFLUENCE OF THERMAL EXPOSURE ON PROPERTIES AND MICROSTRUCTURE OF ELEVATED TEMPERATURE TITANIUM ALLOYS

W. T. Donlon, J. E. Allison, and J. V. Lasecki

Ford Motor Company
Scientific Research Laboratory
Dearborn, MI 48212-2053

Abstract

The tensile ductilities of three near-α titanium alloys (Ti-1100, Ti-6242S and IMI-834) were measured after thermal exposures at temperatures between 450 and 760°C. For β processed microstructures, all alloys exhibited a minimum in ductility of approximately 1% elongation after aging at 600°C. α/β processed IMI-834 displayed higher ductilities in both the as-processed and thermally exposed conditions. Transmission electron microscopy (TEM) combined with energy dispersive x-ray (EDX) spectroscopy was used to determine the presence of silicides and α_2. Silicides were observed in unexposed Ti-1100 and IMI-834 alloys, while aging at 650°C for 8 hours was required to precipitate silicides in the Ti-6242S alloy. Weak diffuse scattering due to α_2 was observed in all alloys following β processing; with strong discreet α_2 reflections only visible after agings of 24 hours at 600°C. Solvus temperatures for α_2 and silicides were determined by reversion experiments. These results show that α_2 precipitates significantly decrease the ductility in titanium alloys, and this effect is further exacerbated by the precipitation of silicides.

Introduction

Titanium alloys designed for elevated temperature usage have long been known to experience microstructural "instabilities" which can lead to a reduction in ductility [1]. This loss of ductility has been attributed to precipitation of coherent α_2 [e.g. 1,2], silicides [e.g. 3-5] or a combination of both [6]. Recent efforts to stretch the operational limits of titanium include low stress applications at temperatures in excess of 550°C [7]. Such applications require an improved understanding of the effects of thermal exposure on microstructure and ductility. This study examines the influence of thermal exposure in the temperature regime of 450 to 760°C, on microstructure and tensile ductility of Ti-1100, Ti-6242S, and IMI-834.

Titanium '92
Science and Technology
Edited by F.H. Froes and I. Caplan
The Minerals, Metals & Materials Society, 1993

Experimental Procedure

Materials

The Ti-1100 alloy was obtained from Timet Corp, as β-forged 19.05 mm square rods. The Ti-6242S and the IMI-834 alloys were obtained from RMI Corp, and IMI LTD, respectively. These two alloys were procured in the α/β annealed condition in the form of 15.875 mm dia. rods. Table I shows the β-transus temperatures and compositions of these materials as provided by the manufacturers for these particular heats of material.

Table I β Transus and Composition (wt.%) of Alloys

Alloy	β-Transus	Al	Sn	Zr	Mo	Si	Nb	C	Fe	O
Ti6242S	996°C	5.7	1.9	3.7	1.9	.09	___	.02	.03	.11
Ti-1100	1014°C	5.9	2.6	4.0	0.4	.42	___	.02	.02	.08
IMI-834	1045°C	5.8	4.0	3.5	0.5	.34	.71	.06	.02	.12

Heat treatments to produce β and α/β microstructures are shown in Table II. Plastic elongations to fracture at room temperature for these solution treatments are also listed in the Table. Figures 1a-c show the three β-processed microstructures which consist of colonies of aligned α plates within prior β grains. Figure 1d shows the α/β processed IMI-834 alloy, consisting of equiaxed primary α grains in a transformed β matrix.

Table II Heat-Treatments & Room Temperature Ductilities for Alloys

Alloy	Solution Treatment Temperature & Time	Cooling Rate	Post-solution Heat-treatment	Elong. (R.T.)
β Ti-1100	1070°C for 1 hr	0.5-0.7°C/s	NONE	9.4%
β Ti-6242S	1070°C for 1 hr	0.5-0.7°C/s	NONE	10.0%
β IMI-834	1070°C for 1 hr	0.5-0.7°C/s	700°C/2hr/air cool (10°C/s)	5.0%
α/β IMI-834	1020°C for 2 hr	OIL QUENCH	700°C/2hr/air cool (10°C/s)	12.0%

Samples for tensile tests were aged for 300, 1000 and 2000 hours at temperatures in the range of $450° \leq T \leq 760°C$ and air cooled (AC) prior to machining. Samples exposed for shorter times to investigate precipitation kinetics via TEM, were water quenched (WQ) from the β-processing temperature, or oil quenched (OQ) from the α/β processing temperature to minimize precipitation during cooling.



Figure 1 - Microstructures of unexposed alloys. (a) β Ti-1100, (b) β Ti-6242S, (c) β (plus 2hr at 700°C) IMI834, (d) α/β (plus 2hr at 700°C) IMI834.

Mechanical Testing

Room temperature tensile tests were conducted to determine the ductilities (plastic elongations at fracture) before and following thermal exposure. These tests were conducted according to ASTM, E-8 standards using an Instron screw machine with a 25.4 mm extensometer at a strain rate of $\dot{\epsilon}$~8.3 x 10^{-4}/s. Sample geometry was a uniform-gauge test section type of 6.40 mm diameter x 31.75 mm gauge length.

Electron Microscopy

TEM was performed using a JEOL 2000FX microscope, a Gatan low background double tilt stage and a LINK AN10000 analyzer. Specimens were cut 0.25±0.05 mm thick using a low speed saw, and punched into 3mm disks. Electropolishing was performed using 10% perchloric, 90% methanol at -40°C and 10 volts. α_2 (Ti_3Al) precipitates were identified by electron diffraction, and dark-field microscopy. Silicide precipitates $(Ti,Zr)_5(Si,Sn)_3$ were identified by both EDX analysis and electron diffraction. Imaging of silicides, especially when only a few where present, required that the specimen be tilted to an orientation in which the silicides were strongly diffracting.

Results

Tensile Tests

Figure 2 shows the room temperature plastic elongation at fracture versus exposure temperature for the three alloys thermally exposed for 300, 1000 and 2000 hr. Thermal exposure to temperatures in the range of 450 to 500°C for 300 hr for the β-processed microstructures yields minimal losses of ductility. More obvious for these same microstructures is the minimum in ductility observed after 600°C exposures (Figures 2a-c). This behavior is not seen in Figure 2d for α/β IMI-834. It must be noted however that compared to the "unexposed" α/β condition (Table II), thermal exposure to temperatures between 500-600°C reduces the ductility 3-6% for this microstructure.

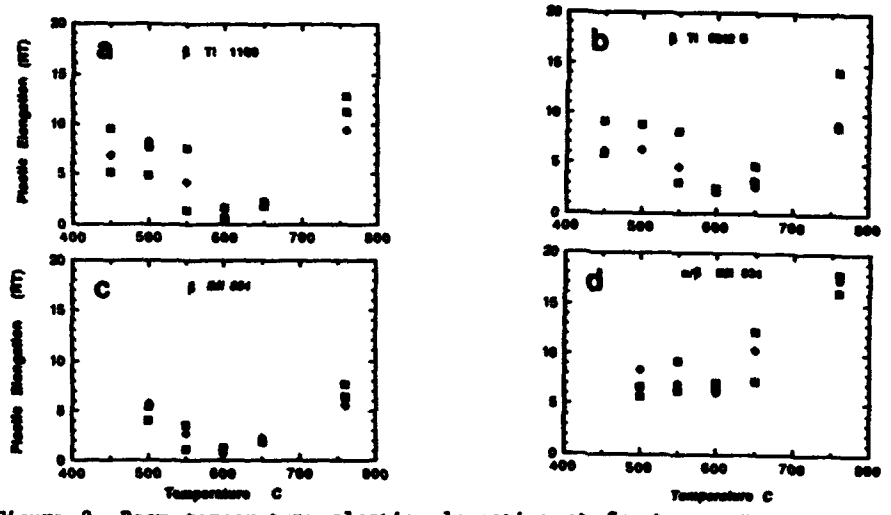


Figure 2. Room temperature plastic elongation at fracture versus exposure temperature for β processed; (a)Ti-1100, (b)Ti-6242S, (c)IMI-834, and (d) α/β processed IMI-834. Time at temperature is represented by: ⊡ for 300 hr, ♦ for 1000 hr, and ■ for 2000 hr.

TEM analysis of "unexposed" titanium alloys.

Diffraction patterns in Ti-1100 and Ti-6242S after control cooling exhibited weak and diffuse α_2 reflections (Figure 3a). Water quenching from the β processing temperature significantly reduced the intensity of the α_2 reflections. Identical results were observed for the IMI-834 alloy following oil quenching from the α/β processing temperature. The effect of the 2 hr at 700°C heat treatments performed on IMI-834 was most pronounced on the primary α grains in the α/β processed material (Figure 3b), while the intensity and sharpness of the α_2 reflections for α lathes was also affected (Figure 3c).

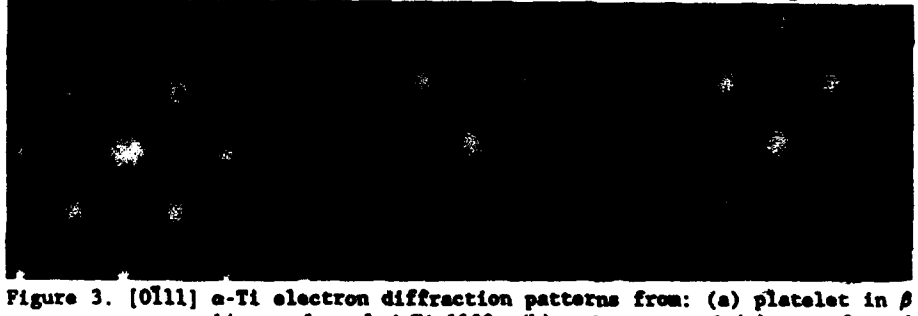


Figure 3. [0$\bar{1}$11] α-Ti electron diffraction patterns from: (a) platelet in β processed/control cooled Ti-1100; (b) primary α and (c) transformed α grains, in α/β processed (plus 700°C for 2 hours) IMI-834.

Precipitation of silicides was observed in both water quenched and control cooled samples of Ti-1100 (Figure 4a). No silicides were observed in β processed water quenched samples of Ti-6242S or IMI-834. Likewise control cooled samples of the Ti-6242S alloy did not exhibit silicides. Silicides were also observed after the 2 hour at 700°C post processing heat treatment in the β and α/β processed IMI-834 alloy (Figure 4b). No silicides were observed in samples from the IMI-834 alloy that were only α/β processed and oil quenched.

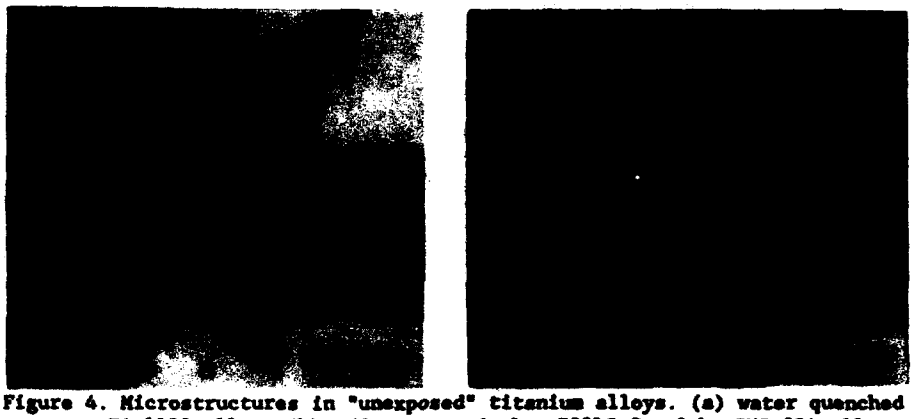


Figure 4. Microstructures in "unexposed" titanium alloys. (a) water quenched Ti-1100 alloy, (b) α/β processed plus 700°C for 2 hr IMI-834 alloy.

Determination of Solvus Temperatures for α_2 and Silicides.

In order to determined the solvus temperatures for α_2 and silicides for the four conditions listed in Table II, samples were given long term agings (≥300 hrs) at 600°C and 760°C to produce a high densities of α_2 and silicides. Subsequent series of one hour heat treatments at temperatures believed to be close to the solvus were performed at 20 or 30°C intervals followed by water quenching. TEM examination of these samples determined which one hour heat treatment dissolved the α_2 or silicides back into solution. The results of this part of the study are summarized in Table III.

Table III Effect Composition on α_2 and Silicide Solvus Temperatures

Alloy	α_2 solvus	silicide solvus
β proc. Ti-1100	740±10°C	1030±10°C
β proc. Ti-6242S	715±15°C	945±15°C
β proc. IMI-834	745±5°C	990±10°C
α/β proc. IMI-834	795±15°C (primary α) 735±15°C (transformed α)	990±10°C

Effect of Thermal Exposure on Formation of α_2 and Silicides

TEM samples obtained from the grip ends of tensile samples exposed for 2000 hours were used to determine the effect of temperature on microstructure. The results shown here are for the Ti-1100 alloy, but are representative for all four conditions. Figures 5a-c, show the [0$\bar{1}$11] α-Ti zone axis obtained from β processed and control cooled Ti-1100 aged for 2000 hours at 450, 600 and 760°C. In the sample aged at 450°C the α_2 reflections are weak and diffuse. At 600°C (minimal ductility) the α_2 reflections become sharp and exhibit their maximum intensity. Samples aged at 760°C exhibit minimal α_2 reflections.

The extent of silicide precipitation in β processed and control cooled Ti-1100 aged for 2000 hours is shown in figures 6a-c. Samples aged at 450°C contain silicides that are generally 0.1μm in diameter (Figure 6a). The density of silicides and their size is observed to increase when samples are thermally exposed to 600°C (Figure 6b). In the 760°C condition, the silicides continue to coarsen, while their density decreases (Figure 6c).

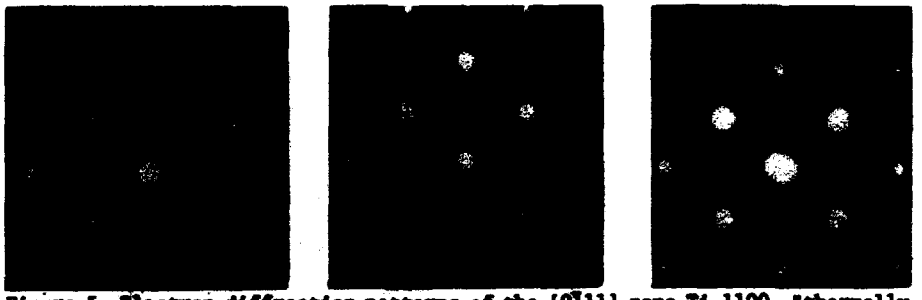


Figure 5. Electron diffraction patterns of the [0$\bar{1}$11] zone Ti-1100, "thermally exposed" for 2000 hours at: (a) 450°C, (b) 600°C, (c) 760°C.

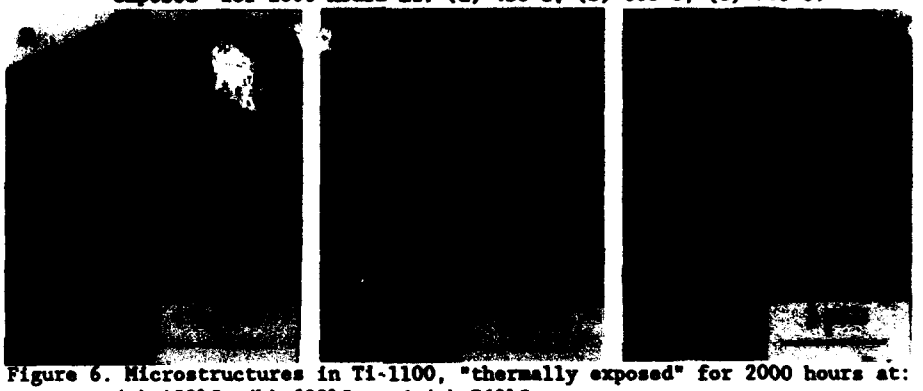


Figure 6. Microstructures in Ti-1100, "thermally exposed" for 2000 hours at: (a) 450°C, (b) 600°C, and (c) 760°C.

In addition to TEM examination of the samples that were given long time exposures (for mechanical testing), samples were also examined at shorter times to understand the kinetics of precipitation. These samples were either β processed and water quenched or, for the IMI-834 α/β processed condition, oil quenched prior to exposure. At least 30 hours in the temperature regime of 550° to 650°C was required to produce moderately intense and discreet α_2 reflections in the β processed microstructures. For the α/β processed IMI-834 alloy intense α_2 reflections were observed in the primary α grains after only 1 hr at 750°C. For all the conditions it was found that silicide precipitation occurred rapidly near 700°C with numerous silicides present after only several hours of aging. The results of these observations along with observations of the samples that were thermally exposed for the long times are summarized in Figure 7 for β processed microstructures.

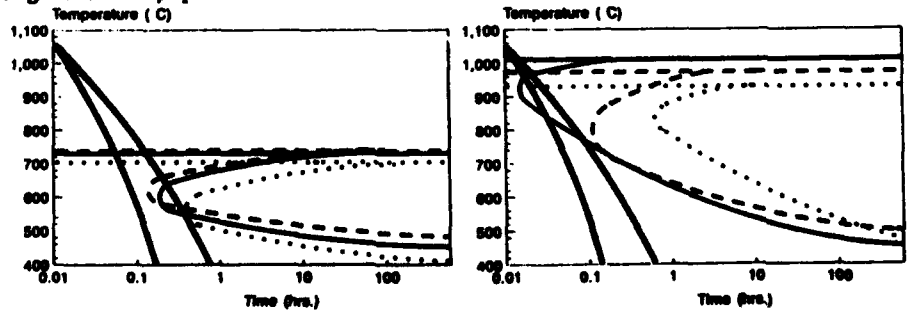


Figure 7. Precipitation curves for (a) the formation of α_2, and (b) silicides in β processed Ti-1100 (——), Ti-6242S (·····), and IMI-834 (-----).

Discussion

Comparing the three alloys in the β processed condition, the effect of increasing aluminum equivalent [2], has the anticipated effect on the stability of α_2 [8]. The alloy with the highest aluminum equivalent (IMI-834) exhibited the highest α_2 solvus, while the alloy with the lowest aluminum equivalent (Ti-6242S) exhibited the lowest α_2 solvus. However these differences were not extreme and in fact detailed TEM analysis after short term exposures at intermediate temperatures revealed no major differences in the kinetics of α_2 formation. In the α/β processed IMI-834 alloy, a marked increase was observed in the propensity of α_2 formation in the primary α grains. Similarly, the influence of silicon followed anticipated trends [8-11] with the alloy having the highest silicon content (Ti-1100) possessing the highest silicide solvus and that with the lowest silicon content (Ti-6242S) exhibiting the lowest silicide solvus. In contrast to the results on α_2 formation, however, the kinetics of silicide formation were strongly alloy dependent. Thus for the "as β processed" condition, silicides were formed upon control cooling in Ti-1100, but not IMI-834 or Ti-6242S.

The formation of α_2 and silicide precipitates combine to have a dramatic effect on tensile ductilities of all three alloys. The effect of thermal exposure is most pronounced at temperatures which correspond to the formation of α_2. The formation of α_2 leads to planar deformation characteristics and thus reduced tensile ductilities. This effect is particularly pronounced in the β processed condition due to the larger slip length present in the colony microstructure [12]. Although the presence of α_2 is critical to this decrease in ductility, silicides also play a role. Exposures at temperatures above the α_2 solvus result in no decrease of ductility and in some cases increases of ductility. However, in the β processed microstructures, the ductility minimum appears to be most pronounced in the alloys containing high silicon contents. Moreover, previous investigations [5], have shown that when the silicon content of Ti-6242S is reduced to 0.04w/o, no appreciable influence of thermal exposure on tensile ductility is observed. Thus it appears that the major factors influencing the reduction in tensile ductility are increased strain localization due to the presence of α_2 precipitates and a reduced critical void nucleation strain due to the presence of silicides at the α/β lath boundaries.

The ductility minimum observed between 550-600°C in the β processed microstructures is quite significant, with ductilities in the range of 1 to 2%. In contrast, the tensile ductilities over this temperature regime in α/β IMI-834 are fairly constant in the range of 6 to 8% (compared to a 12% for the as α/β solution treated condition). Thus although the presence of α_2 in the β microstructures appears to lead to increased strain localization, the refined α/β microstructure tends to limit the slip length and thus leads to increased ductilities. This microstructure, and potentially others such as those produced by β forging [13], offers the best potential for extending the use of titanium alloys to temperatures in excess of 550°C in applications where tensile ductility is important.

Summary

Long term thermal exposure in the temperature regime of 550 to 600°C can lead to a significant reduction in the tensile ductilities of β processed Ti-6242S, Ti-1100 and IMI-834. The decrease in ductility is primarily attributed to increase strain localization due to the formation of coherent α_2 precipitates, however, the presence of silicides further compounds this effect. The time-temperature response of both α_2 and silicide formation has been determined for these three alloys which should be helpful in selecting both heat treatments and application temperature limitations. Means such as α/β processing, which mitigate the influence of these precipitates on tensile ductility have been identified.

References

1. C. E. Shamblen, "Embrittlement of Titanium Alloys by Long Time, High Temperature Exposure," Met. Trans., 2, (1971), 277-280.

2. H. W. Rosenberg, "Discussion of Alloying of Titanium," The Science, Technology and Application of Titanium, ed. R.I. Jaffe and N.E. Promisel, (New York, NY: Pergamon Press, 1970), 1001.

3. C. Ramachandra and V. Singh, "Effect of Silicide Precipitation on Tensile Properties and Fracture of Alloy Ti-6Al-5Zr-0.5Mo-0.25Si," Metall. Trans, 16A, 1985, 227.

4. C. Ramachandra and V. Singh, "Effect of Silicide Precipitation on the Low Cycle Fatigue Behavior of Alloy Ti-6Al-5Zr-.05Mo-0.25Si," Scripta Met., 21, 1987, 633-636.

5. J. E. Allison, W. Cho, J. W. Jones, and J. V. Lasecki, "The Influence of Elevated Temperature on the Mechanical Behavior of α/β-Titanium Alloys," Sixth World Conference on Titanium, ed. P. Lacombe, R. Tricot, and G. Beranger, (Paris, France, Les Editions de Physique, 1989), 293-298.

6. A. P. Woodfield, P. J. Postans, M. H. Loretto, and R. E. Smallman, "The Effect of Long-Term High Temperature Exposure on the Structure and Properties of the Titanium Alloy Ti-5331S," Acta Metall., 36, (1988), 507-515.

7. J.E. Allison, A.M. Sherman, M.R. Bapna, "Titanium in Engine Valve Systems," Jour. Metals, 39, 2, (1987), 14-17.

8. M.J. Blackburn and J.C. Williams, "Strength, Deformation Modes and Fracture in Titanium-Aluminum Alloys," Trans. Am. Soc. Metals, 62, 1969, 398.

9. H. M. Flower, K. Lipscombe, and D.R. F. West, " The Effect of Silicon on the Structure and Mechanical Properties of a $\alpha+\beta$ Titanium Alloy," J. Mat. Sci., 17, (1982), 1221.

10. D. Banerjee, D. Mukerjee, R. L. Saha, and K. Bose, "Microstructure and Tensile Ductility in a β Heat Treated Titanium Alloy," Met. Trans., 14A, (1983), 413.

11. D. Banerjee, J. E. Allison F. H. Froes, and J. C. Williams, "The Effect of Silicon on the Microstructure of High Temperature Titanium Alloys," Titanium Science and Technology, ed. G. Lutjering, U. Zwicker, and W. Bunk, (Deutsche Gesellshaft Fur Metallkunde E.V., 1985), 1519.

12. J. C. Williams, G. Lutjering, "The Effect of Slip Length and Character on the Properties of Titanium Alloys," Titanium '80: Science and Technology, ed. H. Kimura and O. Izumi, (Warrendale, PA: AIME, 1980), 671.

13. P. J. Bania, "An Advanced Alloy for Elevated Temperatures," J. of Metals, 40, (1988), 20-22.

ROOM AND ELEVATED TEMPERATURE PROPERTIES OF TI-1100

M. Peters, V. Bachmann, K.-H. Trautmann, H. Schurmann

Y.T. Lee* and C.H. Ward**

DLR
German Aerospace Research Establishment
Institute for Materials Research
D-5000 Cologne 90, Germany

Abstract

To investigate the influence of the two most often used microstructures for elevated temperature Ti alloys on a variety of engineering properties, the latest of these conventional near alpha type alloys - Ti-1100 - was solution heat treated to achieve bi-modal and lamellar microstructures. Heat treatment below the ß-transus temperature led to lower room and elevated temperature strength, higher ductility, and improved high cycle fatigue strength at room and elevated temperatures; super-transus heat treatments improved low cycle fatigue and fatigue crack growth behavior as well as fracture toughness and creep rupture strength.

* now with KIMM, High Temperature Materials Department, Changwon, Korea

** on leave from Wright Laboratory, Materials Directorate, Wright-Patterson AFB, OH, USA

Titanium '92
Science and Technology
Edited by F.H. Froes and I. Caplan
The Minerals, Metals & Materials Society, 1993

Introduction

At the upper use temperature end of conventional ingot metallurgy two new Ti alloys were announced in the eighties (1), the most recent being Ti-1100. This near-alpha type alloy developed by Timet, Henderson, NV is aimed at pushing the maximum application temperature close to 600 °C (2). Contrary to the latest British near-alpha alloy IMI 834, where a primary alpha / transformed beta, i.e., a bi-modal microstructure, is recommended (3), Ti-1100 is suggested to be used in a fully lamellar alpha+beta structure. This microstructure is generated by forging in the beta-phase field with subsequent air cool (4).

In an attempt to evaluate the potential of Ti-1100, a program was initiated where the alloy was processed to a wide range of microstructures through sub- and super-transus heat treatments. Extensive thermomechanical treatments were applied to evaluate the strength potential of this alloy as well as its behavior at elevated temperatures (5). The present study will focus on now the two most typical microstructures for elevated temperature Ti alloys - bi-modal and lamellar - influence a wide range of engineering properties of Ti-1100, including strength, ductility, high- and low-cycle fatigue, fracture toughness, fatigue crack growth and creep.

Experimental

The alloy was supplied by Timet, Henderson, NV, USA as 206 mm bar material which had been given a final forge at 980 °C then air-cooled to room temperature (RT) without any further heat treatment. The nominal chemical composition of Ti-1100 is Ti-6Al-4Zr-2.75Sn-0.4Mo-0.45Si-0.07O_2-0.02Fe (4); the ß-transus temperature ($T_ß$) was determined by optical microscopy and dilatometry to be 1020 ± 5 °C.

Solution-heat treatments (SHT) were carried out for 20 minutes at 980 °C (40 °C below the ß transus) and 1060 °C (40 °C above the ß transus), then water quenched (WQ). Aging for 4 hours at 600 °C was chosen after the aging response had been evaluated by hardness measurements.
The microstructure of the alloys was investigated by optical and transmission electron microscopy.

Tensile tests were performed at RT and 600 °C on cylindrical specimens with a gauge length of 30 mm and a diameter of 6 mm at a strain rate of 5.6×10^{-4} s^{-1}. Strain gages were used to determine the 0.2% yield strength (YS).
Two fracture toughness test for each condition were performed on fatigue pre-cracked compact tension specimens (W = 25 mm; B = 12.5 mm) according to ASTM specifications.
Load controlled low cycle fatigue tests were performed on cylindrical specimens in tension mode (R = 0) at RT and 600 °C by employing triangular waveform at a frequency of 0.3 Hz.
High cycle fatigue tests were performed at RT and at 400 °C on a resonance machine in push-pull mode (R = -1). Cylindrical, smooth, hour-glass shaped, electrolytically polished specimens with a minimum diameter of 4 mm were tested at a frequency of 100 ± 10 Hz in laboratory air.
Fatigue crack growth tests were performed on a closed loop servohydraulic testing machine at RT and 600 °C in laboratory air with a frequency of 50 Hz at an R-ratio of 0.1. Compact tension specimens (W = 25 mm; B = 12.5 mm) were used; the crack growth was monitored optically and by DC potential drop technique.
Creep tests were performed at 600 °C in laboratory air on cylindrical specimens with a gauge length of 50 mm and a diameter of 5 mm. Constant tensile loads were applied while creep strain was continuously monitored.

Results and Discussion

Microstructure

The as-received material (AR) reveals an equiaxed structure with an α grain size of about 15 to 20 µm (Figure 1a). The equiaxed structure allowed the generation of both lamellar and bi-modal microstructures simply by heat treatment. SHT for 20 minutes at 980 °C plus quench led to a bi-modal microstructure with a primary α volume fraction of about 40 % in a transformed α/ß matrix (Figure 1b). SHT at 1060 °C in the ß phase field led to a martensitically transformed ß structure after quenching with ß grain sizes exceeding 1 mm (Figure 1c). In the following these two microstructures will be referred to as bi-modal and lamellar.

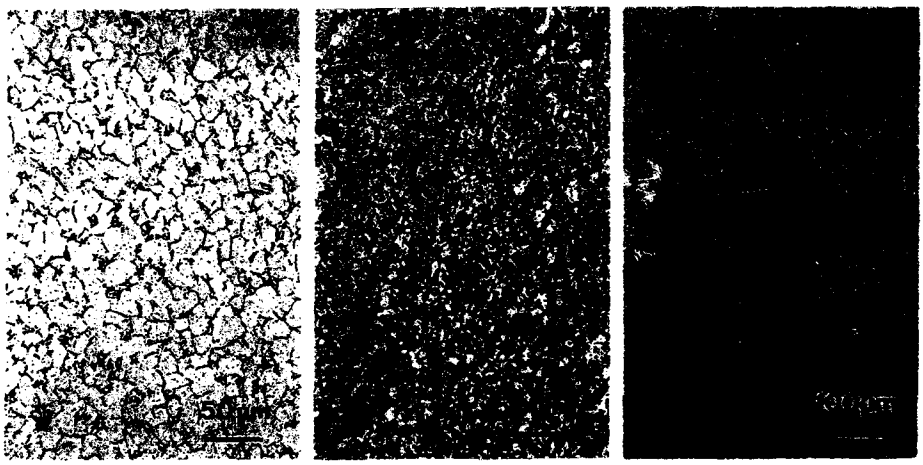


Figure 1: Optical micrographs of as-received material (a), SHT at 980°C (b) and 1060°C (c)

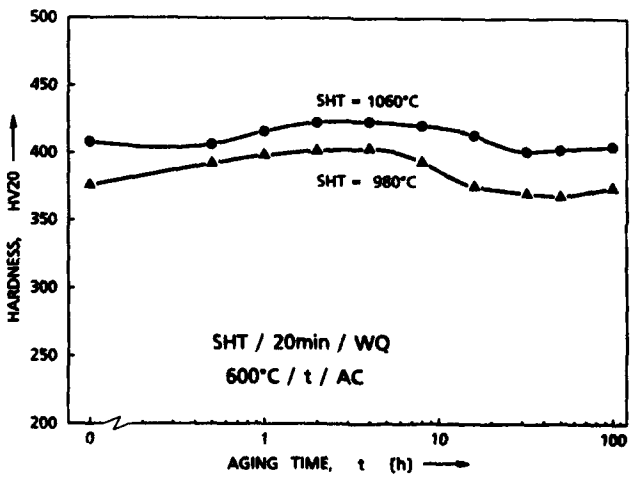


Figure 2: Aging behavior at 600°C after SHT at 980 and 1060°C, then quenched

Hardness

The age-hardening behavior was characterized by hardness measurements after aging at 600 °C. Figure 2 shows that for both SHT temperatures the hardness first increased slightly before it then moderately dropped after 5 to 10 hours of aging.

The hardness tests confirmed that - contrary to IMI 834 (6) - Ti-1100 is not a strong age-hardenable alloy. Therefore, a stabilization of 4 hours at 600 °C was chosen for all specimens being subjected to further mechanical testing.

Tensile Properties

The results of the tensile properties are given in Table 1. Compared to the AR material, both the yield (YS) and ultimate tensile strengths (UTS) increased after SHT, quenching and aging, whereas the elongation values decreased. The lamellar structure showed the highest strength values but also the lowest ductility. At 600 °C this trend was maintained, of course at lower strength and higher ductility values.

Table 1 - Tensile properties and fracture toughness at RT and 600°C of as-received material and after SHT 40°C below and above T_β, quenched and aged 4h 600°C

Test at	SHT	Structure	YS, MPa	UTS, MPa	El, %	K_{Ic}, MPa·m$^{0.5}$
20°C	AR	equiaxed	902	965	11.9	-
	980°C	bi-modal	989	1070	9.0	37* / --
	1060°C	lamellar	1065	1171	6.2	49.6 / 55*
600°C	980°C	bi-modal	553	701	22.7	-
	1060°C	lamellar	622	794	17.1	-

(*not valid according to ASTM specification)

The strengths of the β-treated material with a martensitic quenched microstructure are higher than for the bi-modal structure. The large prior β-grain size and thus the increased slip length is primarily responsible for the lower ductility of this structure in addition to a reduced work-hardening capability of the higher strength β-transformed material.

Fracture Toughness

The fracture toughness results are also given in Table 1. The limited data generated at RT indicates that the lamellar microstructure has a higher fracture toughness than the bi-modal structure.

These observations are consistent with results found for other Ti alloys, where "finer" microstructures show lower toughness than "coarser" ones (7). The improved toughness of lamellar structures is related to increased energy absorption as a result of crack deviation, crack bifurcation and a more tortuous crack path compared to equiaxed-type structures.

High-Cycle Fatigue Properties

The results of the high-cycle fatigue (HCF) tests at RT and 400 °C are plotted as S-N curves in Figure 3. For both temperatures the bi-modal structure shows superior fatigue strength which is more pronounced at 400 °C, there at lower stress levels.

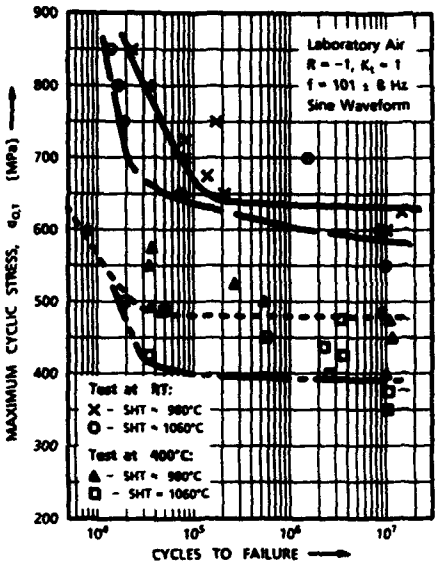


Fig. 3: High cycle fatigue properties at RT and 400°C after SHT at 980 and 1060°C, quenched and aged for 4h 600°C

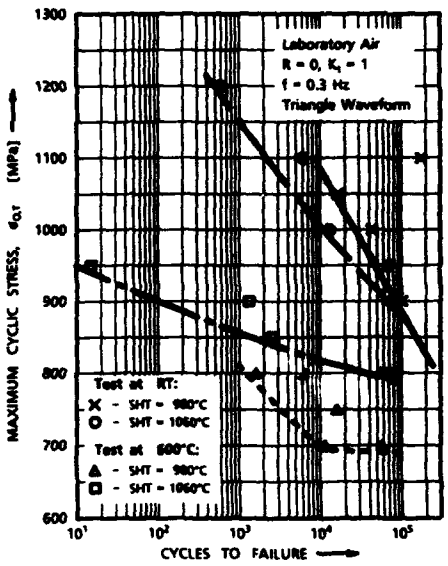


Fig. 4: Low cycle fatigue properties at RT and 600°C after SHT at 980 and 1060°C, quenched and aged for 4h 600°C

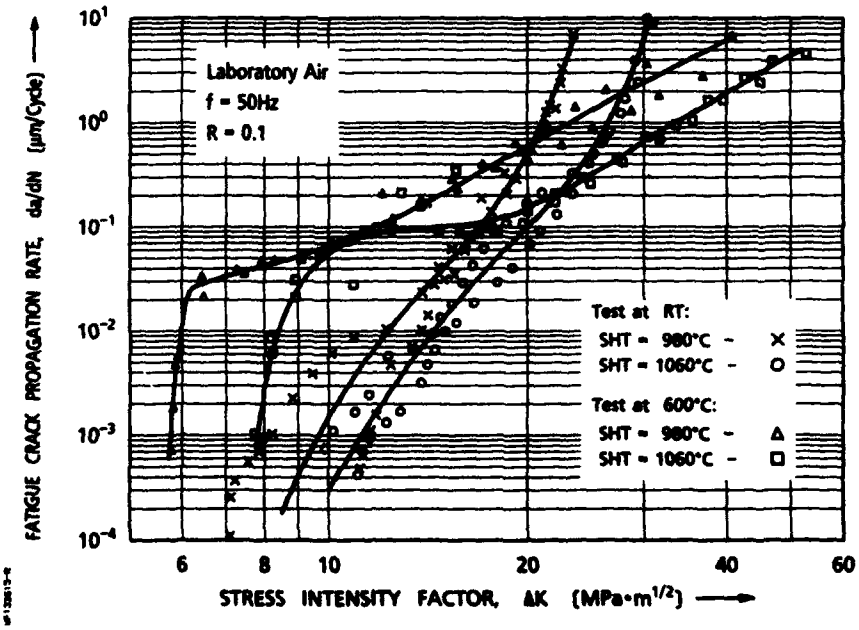


Figure 5: Fatigue crack growth behavior at RT and 600°C after SHT at 980 and 1060°C, quenched and aged for 4h 600°C

Fatigue strength is largely controlled by the resistance of an alloy to nucleate cracks. Therefore, coarse microstructures which usually contain origins for a potentially large slip length, like lamellar packet size, prior ß-grain size, or grain-boundary α, tend to form cracks early at these locations, thus reducing fatigue strength. Contrary, reducing the slip length of transformed ß structures, due to the presence of primary α as is the case in bi-modal structures, can increase the fatigue strength (8). In the present investigation, the slip-length reduction in the bi-modal structure is significantly increasing the fatigue strength since it must also compensate for the lower yield strength of this structure compared to the lamellar material. (As a rule of thumb, fatigue strength is closely related to yield strength if microstructure is constant).

Low-Cycle Fatigue

RT and 600 °C low-cycle fatigue (LCF) results generated for the two microstructures are plotted in Figure 4. At RT the bi-modal structure is slightly superior over the lamellar structure while at 600 °C the ranking changes and the lamellar structure shows improved fatigue life.
Contrary to HCF, LCF is dominated by crack propagation since at the much higher stress levels cracks nucleate early. Therefore, specimen life is dominated by crack propagation. Coarser structures are usually superior since crack closure effects, crack branching and bifurcation effectively reduce propagation rates, especially when the R ratio is low as is the case in the present investigation. At high temperatures the lamellar structure has the extra benifit of being more creep resistant. Therefore its improved behavior at 600 °C can partly be attributed to the creep portion during LCF.

Fatigue Crack Growth

The results of the fatigue crack propagation tests are plotted in Figure 5. In the threshold area the propagation rates are higher at RT than at 600 °C. There is, however, a cross over at intermediate delta K values so that for high stress intensities propagation rates are faster at 600 °C compared to RT. For the entire test range the lamellar structure shows improved fatigue crack growth resistance both at RT and 600 °C.
Since life during LCF is primarily dominated by crack propagation the microstructural influences observed there should be even more pronounced in a pure fatigue crack propagation test. This is confirmed by the results in Figure 5. Furthermore, the lamellar structure leads to a much coarser fatigued fracture surface than the bi-modal structure. Therefore, the energy needed to generate this larger surface is higher; additionally, on a microscale the effective stress intensity is lover due to the more strongly inclined fracture planes - both are arguments for the reduced crack propagation rates of the coarser lamellar structure (9). The sharp drop in elevated temperature fatigue crack propagation behavior at low growth rates is very likely a result of increased crack closure effects, mainly due to higher plasticity (10) and oxide build-up (11).

Creep Behavior

The results of the creep tests at 600 °C are shown in Fig. 6. The times to 0.1% creep strain as well as stress-rupture are plotted versus the initially applied stresses. The influence of SHT on creep reveals a superiority of the super-transus versus the sub-transus microstructure. The difference is more pronounced at 0.1% strain and particularly at high stresses than at final fracture, where the two conditions come closer together.
Creep behavior is usually superior for coarser structures since deformation occurs predominantly at grain or phase boundaries which have a higher density in finer structures, thus raising the propensity for creep. This argument can explain why the lamellar structure is more creep resistant than the finer bi-modal structure. This is in agreement with investigations on a near-α

alloy where the steady-state creep rate was much lower after a super-transus heat treatment (12).

Table 2 - Evaluation of bi-modal and lamellar microstructures on the mechanical behavior of Ti-1100

		bi-modal	lamellar
Yield and ultimate tensile strength	RT	-	+
	600 °C	-	+
Tensile ductility	RT	+	-
	600 °C	+	-
Fracture toughness	RT	-	+
High cycle fatigue strength	RT	+	-
	400 °C	+	-
Low cycle fatigue strength	RT	+	-
	600 °C	-	+
Fatigue crack propagation resistance	RT	-	+
	600 °C	-	+
Creep behavior	600 °C	-	+

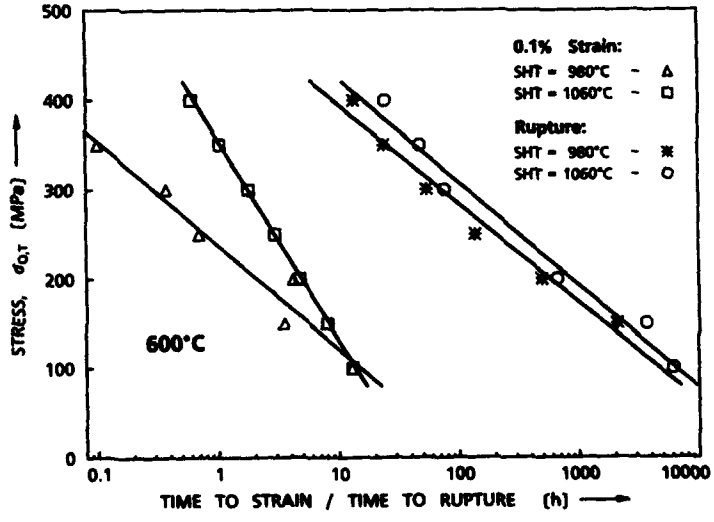


Figure 6: 0.1% creep strain and stress rupture at 600°C after SHT at 980 and 1060°C, quenched and aged for 4h 600°C

Summary and Conclusions

An attempt was made to evaluate the influence of the two preferred microstructures of near-alpha titanium alloys - bi-modal and lamellar - for a range of aerospace-relevant mechanical properties. Room and elevated temperature tests performed on Ti-1100 revealed that lamellar structures prove to be superior in terms of yield and tensile strengths, fracture toughness, fatigue crack growth and creep resistance, while finer bi-modal structures yield superior ductility and high-cycle fatigue strength. For low cycle fatigue tests bi-modal structures show slightly improved life at room temperature while lamellar structures are superior at elevated temperature (Table 2).

Acknowledgements

The authors highly appreciate the experimental support given by M. Alperth, J. Brien, J. Eschweiler, H. Hinderlich, K. Mull and W.-D. Zimmermann. They are grateful to Timet for kindly supplying the material.

References

(1) J.A. Hall: Recent Advances in Titanium Processes, Alloys and Production. In: P. Lacombe, R. Tricot and G. Béranger (eds.): Sixth World Conference on Titanium, part I. Les Ulis Cedex, France: Les Editions de Physique 1989, 1-10

(2) T.E. O'Connell and P.J. Bania: The Wide Processing Window of Ti-1100. In: Titanium 1990 - Products and Applications, Vol. 2, 794-803, TDA, Dayton, OH, 1990

(3) D.F. Neal: Development and Evaluation of High Temperature Titanium Alloy IMI 834. In: P. Lacombe, R. Tricot and G. Béranger (eds.): Sixth World Conference on Titanium, part I. Les Ulis Cedex, France: Les Editions de Physique 1989, 253-258

(4) P.J. Bania: Ti-1100: A New High Temperature Titanium Alloy. In: P. Lacombe, R. Tricot and G. Béranger (eds.): Sixth World Conference on Titanium, part II. Les Ulis Cedex, France: Les Editions de Physique 1989, 825-830

(5) M. Peters, Y.T. Lee, K.-J. Grundhoff, H. Schurmann, G. Welsch: Influence of Processing on Microstructure and Mechanical Properties of Ti-1100 and IMI 834. In: R. Boyer and Y.-W. Kim (eds): Microstructure/Property Relationships in Titanium Aluminides and Alloys. Warrendale, PA: TMS-AIME 1991, 533-548

(6) M.T. Cope and M.J. Hill: The Influence of Ageing on the Mechanical Properties of IMI 834. In: P. Lacombe, R. Tricot and G. Béranger (eds.): Sixth World Conference on Titanium, part I. Les Ulis Cedex, France: Les Editions de Physique 1989, 153-158

(7) J.C. Chesnutt, C.C. Rhodes and J.C. Williams: Relationship Between Mechanical Properties, Microstructure, and Fracture Topography in α+β Titanium Alloys. ASTM STP 600, 1976, 99-138

(8) M. Peters, A. Gysler and G. Lütjering: Influence of Microstructure and Texture in Ti-6Al-4V. In: H. Kimura and O. Izumi (eds.): Titanium '80, Science and Technology, Vol. 2. Warrendale, PA: TMS-AIME 1980, 929-935

(9) M. Peters, K. Welpmann and H. Döker: Fatigue Crack Growth Behavior of two Extreme Microstructures of Ti-6Al-4V. In: G. Lütjering, U. Zwicker and W. Bunk (eds.): Titanium Science and Technology, Vol. 4. Oberursel, FRG: DGM 1985, 2267-2274

(10) H. Ghonem, R. Foerch: Frequency effects on fatigue crack growth behavior in a near-alpha titanium alloy. Mat. Sci. and Engg. A138 (1991) 69-81

(11) J.E. Allison and J.C. Williams: The Role of Crack Closure in Rationalizing the Variations in Fatigue Crack Growth Behavior in Titanium Alloys. In: G. Lütjering, U. Zwicker and W. Bunk (eds.): Titanium Science and Technology, Vol. 4. Oberursel, FRG: DGM 1985, 2243-2250

(12) P.J. Bania and J.A. Hall: Creep Studies of Ti-6242-Si Alloy. In: G. Lütjering, U. Zwicker and W. Bunk (eds.): Titanium Science and Technology, Vol. 4. Oberursel, FRG: DGM 1985, 2371-2378

CORRELATION BETWEEN MICROSTRUCTURE AND CREEP BEHAVIOR OF THE HIGH-TEMPERATURE TI-ALLOY IMI 834

C. Andres, A. Gysler, and G. Lütjering

Technical University Hamburg-Harburg
Eissendorfer Str. 42
2100 Hamburg 90, Germany

Abstract

The creep and tensile properties at 600° C of the near α Ti-alloy IMI 834 with lamellar and bi-modal microstructures (equiaxed primary α in a lamellar matrix) were studied. The effects of variations in cooling rate from the recrystallization temperature (90 to 4000° C/min) and in volume fraction of primary α for bi-modal structures (4 to 40 %) on the creep behavior were of main interest.

The results showed that the creep resistance of all microstructures increased with increasing cooling rate, passed through a maximum and then decreased drastically. While the increase in creep resistance can be described with the observed decreasing α lamellae sizes with increasing cooling rates, the subsequent decrease is thought to result from increasing contributions of interface sliding, a hypothesis which is supported by the observed change in orientation differences between adjacent α-lamellae (nucleation and growth vs. martensitic transformation). Increasing volume fractions of primary α resulted in decreasing creep resistance, regardless of cooling rate.

Introduction

The high temperature Ti-alloy IMI 834 was developed for applications as disks and blades in the high pressure part of compressors for advanced gas turbine engines. The main requirements therefore are optimizations of fatigue and creep properties at intended service temperatures of around 600° C. For maximum fatigue strength the microstructure would have to consist of a fine equiaxed (α + β) structure, while a high creep resistance would require a lamellar microstructure. The alloy IMI 834 was designed to optimize these opposing requirements by adjusting the alloy composition and the processing route to result in a fine bi-modal microstructure consisting of about 15 vol.% equiaxed primary α within a fine grained matrix of transformed β (1).

The creep resistance of near α Ti-alloys, such as IMI 834, depends, besides for example on phase morphology, phase dimensions, and degree of age-hardening, strongly on the cooling rate with which these alloys are cooled from the recrystallization temperature through the β to α transformation regime. With increasing cooling rate the creep resistance normally increases, passes through a maximum and then drastically decreases (2-5). However, a satisfactory explanation for this behavior still seems to be missing so far.

The purpose of the present investigation therefore was to contribute to the further understanding of the effect of cooling rate on microstructure and in turn on the creep behavior of Ti-alloys.

Titanium '92
Science and Technology
Edited by F.H. Froes and I. Caplan
The Minerals, Metals & Materials Society, 1993

Experimental Procedure

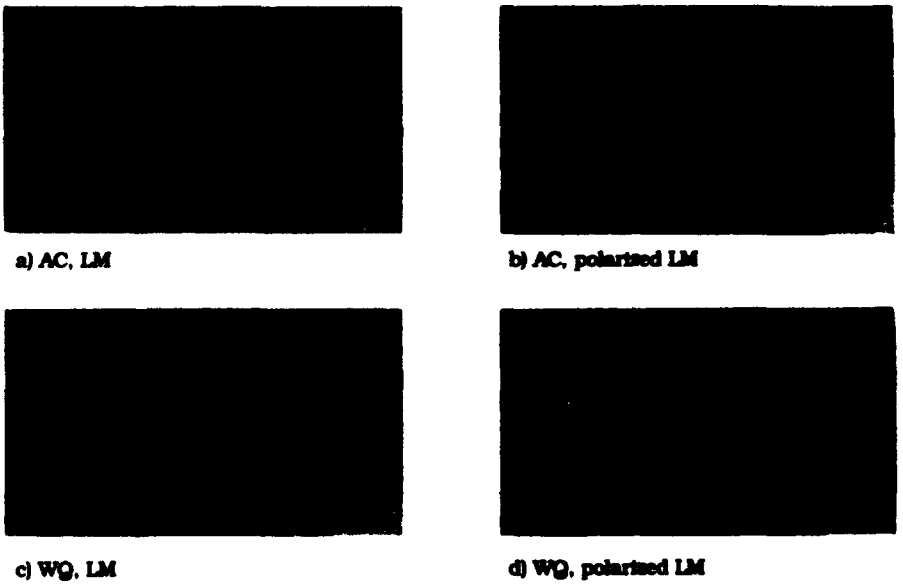
The IMI 834 alloy had the following composition: Ti-5.8Al-4Sn-3.5Zr-0.5Mo-0.7Nb-0.35Si-0.06C (wt.%). Blanks for hot rolling (45 x 45 x 35 mm) were heat treated in the β phase field (1h 1080°C/AC) to start with a defined lamellar microstructure, subsequently cross-rolled in multiple passes at 1020° C (deformation degree $\varphi = -1.6$) followed by air cooling (AC). The microstructures were controlled by recrystallization treatments of specimen blanks for mechanical testing (7 x 7 x 60 mm) under argon atmosphere and by controlling the cooling rate $\dot{T}$ through the β to α transformation regime. Lamellar structures were obtained by a β treatment of 1h 1080°C, and various bi-modal structures by (α + β) treatments: 2h 1027°C (~ 4 vol.% primary α),4h 1010°C (~ 15 vol.% primary α), and 8h 990°C (~ 40 vol.% primary α). The cooling rates were varied between 90 and 4000° C/min, with for example air cooling (AC) resulting in 300° C/min and water quenching (WQ) in 4000° C/min average cooling rates. Some of the recrystallized blanks were additionally heat treated for 2h at 830° C/AC. The final aging treatment for all specimen blanks was 2h 700° C/AC.

Tensile and creep specimens (gage dimensions: 3 mm diameter, 15 mm length) were tested in air at 600° C. The initial tensile strain rate was $8 \times 10^{-4} s^{-1}$. The creep tests were performed under constant load (initial stress $\sigma = 210$ MPa) and the plastic creep strain was determined by LVDT up to 100 h testing time.

For comparison purposes a few tensile and creep tests were also carried out on a Ti-6Al-4V alloy in air at 480° C. This alloy was tested in a lamellar condition (recrystallization: 1h 1050°C, $\dot{T}$: AC, WQ, age-hardening: 24h 500°C/AC).

Experimental Results

Pertinent examples of the various microstructures are shown in Figs. 1 and 2 by light micrographs (LM) and in Figs. 3 and 4 by transmission electron micrographs (TEM). Recrystallization of IMI 834 in the β phase field (1h 1080°C) and subsequent air cooling resulted



a) AC, LM

b) AC, polarized LM

c) WQ, LM

d) WQ, polarized LM

Figure 1 - IMI 834, lamellar microstructures: a) and b) slow cooling (AC), c) and d) fast cooling (WQ).

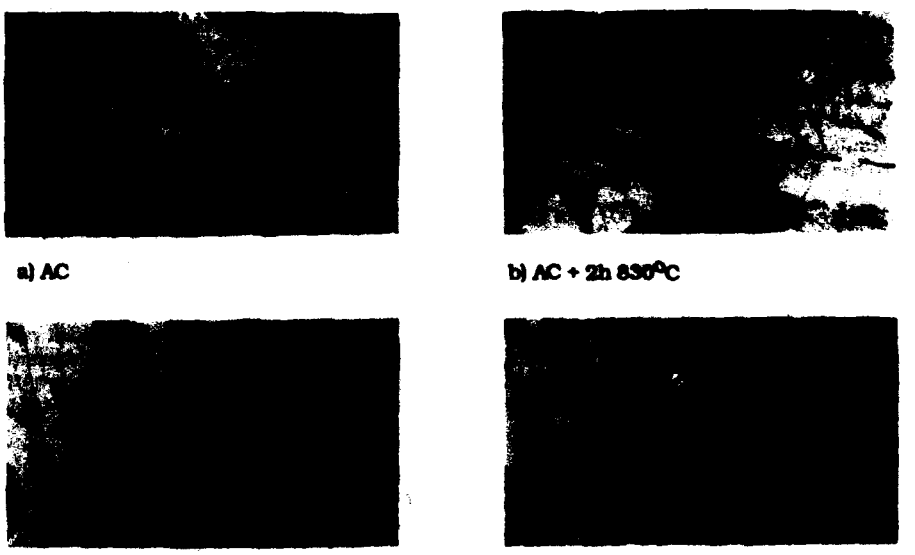
in a lamellar structure (Fig. 1a), with large colonies consisting of aligned α lamellae (width about 1 μm) which all exhibited the same crystallographic orientation due to the nucleation and growth process, as can be seen by the polarized light micrograph (Fig. 1b) and by TEM (Fig. 3a). Fast cooling (WQ) produced a martensitic structure with similar colony sizes but much finer α platelets (Fig. 1c) which revealed strong orientation differences between neighboring platelets due to the diffusionless transformation process, as shown by the polarized light micrograph (Fig. 1d) and by TEM (Fig. 3c). Two examples of the bi-modal microstructures are shown in Fig. 2. Due to the presence of primary α the prior β grain size was drastically reduced as compared to the β heat treated structure (compare Figs. 1a and 2), resulting therefore in reduced colony size and α lamellae length. Although not shown here in detail, the width of lamellae decreased with increasing primary α content. Furthermore, it should be noted that slow cooling rates produced somewhat higher primary α volume fractions as compared to fast cooling, e.g. 8 % (AC) against 4 % (WQ) for a recrystallization treatment of 2h 1027°C.



a) α_p = 15 vol.%, AC

b) α_p = 40 vol.%, AC

Figure 2 - IMI 834, bi-modal microstructures (LM).



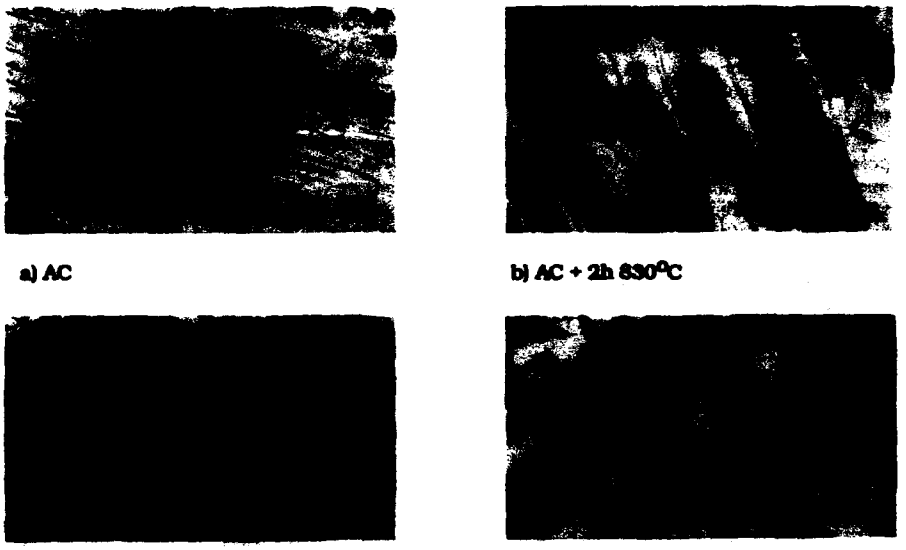
a) AC

b) AC + 2h 830°C

c) WQ

d) WQ + 2h 830°C

Figure 3 - IMI 834, lamellar microstructures: a) and b) no orientation differences, c) and d) strong orientation differences between α-lamellae (TEM).



a) AC b) AC + 2h 830°C

c) WQ d) WQ + 2h 830°C

Figure 4 - Ti-6Al-4V, lamellar microstructures: a) and b) no orientation differences, *c) and d)* strong orientation differences between α-lamellae (TEM).

Intermediate heat treatments (2h 830°C) between recrystallization and age-hardening were intended to reduce expected differences in the number of mobile dislocations (slow vs. fast cooled) and for bi-modal structures to balance alloying element differences between primary α and the lamellar matrix. For IMI 834 such a treatment neither increased the size of α lamellae nor changed their crystallographic orientation relationship in a significant way (compare Figs. 3a and b, 3c and d), only the silicide size increased slightly. However, for the Si-free Ti-6Al-4V alloy a pronounced coarsening of the α lamellae width was observed as a result of the intermediate heat treatment (compare Figs. 4a and b, 4c and d), obviously due to the absence of silicides.

The tensile properties at 600° C of IMI 834 for two different cooling rates are summarized in Table I (AC) and Table II (WQ). All of these properties were higher for fast cooled (WQ) in comparison to slow cooled (AC) conditions, due to the observed microstructural refinement. For example, the $\sigma_{0.2}$-values of the lamellar condition were 625 and 506 MPa for WQ and AC, respectively. Furthermore, improved properties were observed for bi-modal in comparison to lamellar structures, which was especially pronounced for the slow cooled conditions (Table I). The intermediate annealing treatment (2h 830°C) decreased significantly the $\sigma_{0.2}$ and UTS values of lamellar and bi-modal microstructures. This is shown for lamellar structures with two different cooling rates in Table III for IMI 834 and in Table IV for Ti-6Al-4V.

The creep results of IMI 834 at 600° C and an applied stress of 210 MPa are plotted in Fig. 5 in terms of plastic creep strain after 100 h as a function of cooling rate $\dot{T}$. As expected, the creep resistance increased (decreasing creep strain) with increasing cooling rate, passed through a maximum at about 300° C/min, and then decreased drastically, similar for all microstructures. In accordance with literature results, the lamellar condition exhibited the highest creep resistance, regardless of cooling rate, followed closely by the bi-modal condition with the low volume fraction of primary α (2h 1027°C), while with increasing primary α content a significant loss in creep resistance was observed. The ranking

Table I IMI 834, Tensile Properties at 600°C of Slow Cooled (AC) Lamellar and Bi-Modal Microstructures

Microstructure	$\sigma_{0.2}$ (MPa)	UTS (MPa)	Elong. (%)	ε_F	σ_F (MPa)
Lamellar	508	642	9.5	0.18	720
Bi-Modal (α_p=8%)	580	681	5.8	0.17	787
Bi-Modal (α_p=20%)	566	678	7.7	0.21	786
Bi-Modal (α_p=40%)	587	697	10.4	0.23	793

Table II IMI 834, Tensile Properties at 600°C of Fast Cooled (WQ) Lamellar and Bi-Modal Microstructures

Microstructure	$\sigma_{0.2}$ (MPa)	UTS (MPa)	Elong. (%)	ε_F	σ_F (MPa)
Lamellar	625	761	13.0	0.32	844
Bi-Modal (α_p=4%)	638	773	17.1	0.57	1040
Bi-Modal (α_p=15%)	641	773	12.0	0.36	944
Bi-Modal (α_p=40%)	627	725	21.7	0.95	1005

Table III IMI 834, Tensile Properties at 600°C of Lamellar Microstructures (AC, WQ) without and with Intermediate Annealing (2h 830°C)

Condition		$\sigma_{0.2}$ (MPa)	UTS (MPa)	Elong. (%)	ε_F	σ_F (MPa)
AC	——	508	642	9.5	0.18	720
	2h 830°C	451	563	7.0	0.41	805
WQ	——	625	761	13.0	0.32	844
	2h 830°C	547	687	14.3	0.58	896

Table IV Ti-6Al-4V, Tensile Properties at 480°C of Lamellar Microstructures (AC, WQ) without and with Intermediate Annealing (2h 830°C)

Condition		$\sigma_{0.2}$ (MPa)	UTS (MPa)	Elong. (%)	ε_F	σ_F (MPa)
AC	——	557	677	8.9	0.24	796
	2h 830°C	536	664	12.8	0.49	790
WQ	——	770	872	6.3	0.25	933
	2h 830°C	610	727	12.0	0.30	816

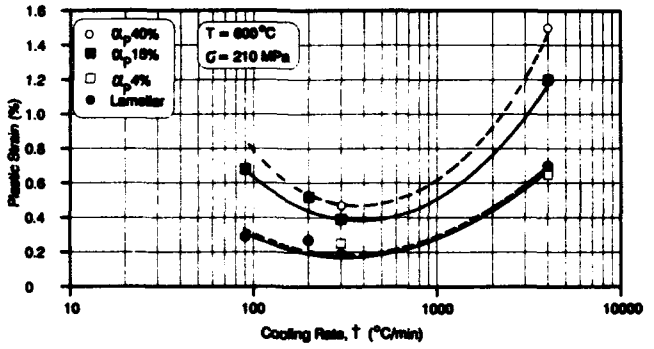


Figure 5 - IMI 834, effect of cooling rate on creep strain after 100h of lamellar and bi-modal microstructures (α_p: volume fraction of primary α-phase).

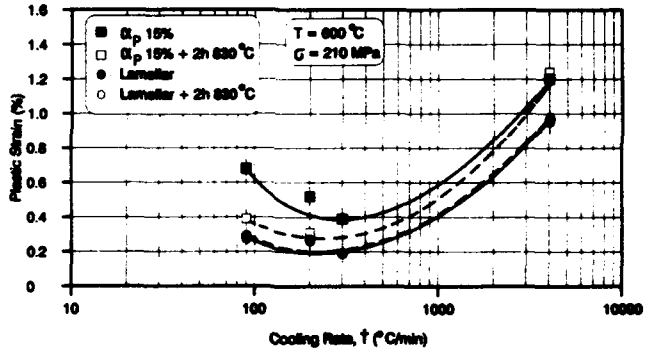


Figure 6 - IMI 834, effect of cooling rate on creep strain after 100h of lamellar and bi-modal (α_p = 15 vol.%) microstructures without and with intermediate annealing of 2h 830°C.

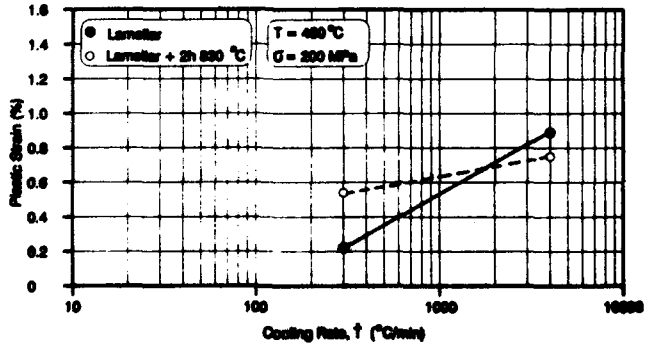


Figure 7 - Ti-6Al-4V, effect of cooling rate on creep strain after 100h of lamellar microstructures without and with intermediate annealing of 2h 830°C.

of the four microstructures for example at 300° C/min was fully lamellar (creep strain 0.20 %), bi-modal with 4 % α_p (0.25 %), bi-modal with 15 % α_p (0.39 %), and bi-modal with 40 % α_p (0.47 %).

The effects of an intermediate heat treatment (2h 830°C) on the creep properties for the lamellar and one bi-modal condition (15 % primary α) of IMI 834 are shown in Fig. 6, together with the results without this treatment. Within experimental error, no variation in creep resistance was observed for the lamellar condition with and without intermediate heat treatment, and also not for the fast cooled bi-modal microstructure. However, intermediate heat treated bi-modal structures exhibited an increasing creep resistance with decreasing cooling rate as compared to the reference curve (Fig. 6). For example, at a cooling rate of 200° C/min the creep strain was reduced from about 0.5 % to 0.3 % by the intermediate heat treatment.

The creep results of the lamellar conditions of Ti-6Al-4V at 480° C and a stress of 200 MPa are summarized in Fig. 7, comparing microstructures without and with an intermediate heat treatment (2h 830°C). In a qualitative way, the effect of cooling rate on creep resistance was similar as for IMI 834, showing a decrease in creep resistance with increasing cooling rate. However, the intermediate heat treatment resulted in a different behavior as compared to IMI 834. A significant loss in creep resistance was found for the slow cooled structure (0.2 % plastic strain without and 0.58 % plastic strain with intermediate treatment), while an increase in creep resistance was observed for the fast cooled structure (0.9 % plastic strain without and 0.75 % plastic strain with intermediate heat treatment).

Discussion

The results of this investigation have shown that variations in microstructure can have pronounced effects on the creep resistance and also on the high-temperature tensile properties of IMI 834. The most puzzling result, which is already well documented in the literature (2-4), seems to be the strong dependency of the creep resistance on the cooling rate with which the different microstructures (lamellar, bi-modal) are cooled through the β to α transformation region. It is known that as a result of increasing cooling rates the width of the α-lamellae decreases in lamellar as well as in the lamellar matrix of bi-modal microstructures (Figs. 1 and 3) (3,4). The observed increase in yield stress and tensile ductility with increasing cooling rate (compare Tables 1 and 2) can be explained therefore by this decreasing width of the α-lamellae. The higher yield stresses for bi-modal as compared to lamellar microstructures (Tables 1 and 2), regardless of cooling rate, are a consequence of the pronounced refining of the β-grain size and lamellae width of the bi-modal microstructures in comparison to the β-annealed lamellar structures (compare Figs. 1 and 2).

Assuming a dislocation controlled creep mechanism for near α-alloys, it would be expected that the creep resistance also would continuously increase with increasing cooling rate due to the decreasing α-lamellae width, similar as observed for the yield stress. There exists agreement in the literature (e.g. 2) that this explains the observed increasing creep resistance with increasing cooling rate in the very low to medium cooling rate regime (Fig. 5). However, the observed maximum in creep resistance and subsequent drastic decrease with further increasing cooling rates (Fig. 5) suggests that other cooling rate dependent microstructural parameters must be considered.

Three such possibly contributing parameters were considered in the present investigation. First: Additions of silicon to IMI 834, as in most advanced high-temperature Ti-alloys, were found not to be responsible for the cooling rate dependency of the creep resistance, since also the Si-free Ti-6Al-4V alloy exhibited qualitatively a similar loss in creep resistance with increasing cooling rate (Fig. 7). It should be noted, however, that Si-containing alloys certainly will have improved creep resistances as compared to those without Si, as has been well documented in the literature (e.g. 3). Second: Increasing dislocation densities as a result of increasing cooling rates could also be responsible for the decreasing creep

resistance. However, the results of intermediate annealing treatments (2h 830°C), which should have removed most of the mobile dislocations, did not improve the creep resistance of the fast cooled lamellar and bi-modal microstructures (Fig. 6). The third cooling rate dependent factor was the observed difference in crystallographic orientation relationship between neighboring α-lamellae: Slow cooling rates (AC) resulted in the diffusion controlled growth of α-lamellae which exhibited the same orientation within a particular colony (Figs. 1b and 3a), while fast cooling rates (WQ) resulted in a martensitic transformation with orientation differences between neighboring α-lamellae (Figs. 1d and 3c). An effect on the creep behavior could be envisaged if one assumes that, in addition to dislocation controlled creep, interface sliding plays a role in creep deformation. Such a creep process might be easier for boundaries between lamellae having crystallographic orientation differences (e.g. due to martensitic transformation by fast cooling). Some positive indications for such an assumption that interface sliding dominates for fast cooled microstructures might be drawn from the slight improvement in creep resistance for the fast cooled lamellar structure (WQ) of Ti-6Al-4V with intermediate annealing (Fig. 7) despite the pronounced coarsening of the α-lamellae width (Figs. 4c and d). For a dislocation controlled mechanism such coarsening would reduce the creep resistance, as observed for the slow cooled condition in Fig. 7 (AC), while for an interface sliding dominated mechanism the reverse effect would be expected because of the decreasing volume fraction of boundaries as a result of the coarsening process. That no such improvement was observed for the IMI 834 might be explained by the fact that in this alloy the intermediate annealing did not coarsen the α-lamellae (Figs. 3b and d) because of the presence of the silicides. However, to prove the interface sliding hypothesis unequivocally more experimental work has to be done.

The improved creep resistance of the slowly cooled bi-modal microstructures with an intermediate annealing (Fig. 6) is thought to result from a more uniform distribution of α-stabilizing alloying elements (for example Al) between α_p and the lamellar matrix and a concomitant increase in age-hardening through Ti_3Al. Since the IMI 834 alloy is intended to be used in commerical application with a bi-modal microstructure, such an intermediate annealing treatment could be favorably applied to improve the creep resistance (Fig. 6) with only a moderate loss in tensile yield stress (Table 3) because no extensive coarsening of lamellae was observed (Fig. 3).

Acknowledgement

The authors would like to acknowledge the support of this investigation by the Deutsche Forschungsgemeinschaft.

References

1. D.F. Neal, Sixth World Conference on Titanium (Les Ulis, France: Les Editions de Physique, 1988) 253-258.

2. P.A. Blenkinsop, D.F. Neal, and R.E. Goosey, Titanium and Titanium Alloys (New York, NY: Plenum Press, 1982) 2003-2014.

3. W. Cho et al., Sixth World Conference on Titanium (Les Ulis, France: Les Editions de Physique, 1988) 187-192.

4. S. Saal et al., "Effect of Cooling Rate on Creep and Low Cycle Fatigue Resistance in Ti-6242", Z. Metallkde., 81 (1990), 535-539.

5. M.A. Däubler, D. Helm, and D.F. Neal, Titanium 1990 Products and Applications (Dayton, OH: Titanium Development Association, 1990) 78-87.

CREEP AND HIGH TEMPERATURE LOW CYCLE FATIGUE OF CAST Ti-6Al-2Sn-4Zr-2Mo ALLOY

Shahid Bashir and Malcolm C. Thomas

Materials and Processes Engineering, P.O. Box 420
Allison Gas Turbine Division, General Motors Corporation
Indianapolis, Indiana 46206-0420, U.S.A.

Abstract

Increasingly longer life requirements in the hot section of jet engines require reduced weight but still maintain high temperature capability. Large highly complex shaped structural components of jet engines like compressor case and diffuser offer significant weight and cost savings if made from titanium castings instead of the traditional high-strength steels or nickel-base superalloys. Cast Ti-6-2-4-2 alloy in the HIP and aged condition was analyzed for creep and high temperature low cycle fatigue for use up to about 783°K (950°F). The wide variability in the observed creep behavior, and in the high temperature low cycle fatigue properties is related to the microstructure and fracture behavior. A heat-treat modification is suggested to improve these properties by refining the microstructure.

Introduction

The increasingly demanding requirements of reduced weight and cost, and higher temperature creep and low cycle fatigue capability of components in modern aircraft jet engines are met either by developing new alloys or by improving the properties of existing alloys with modifications in chemistry, heat treatment or processing. Modification of existing alloys is substantially less costly than developing new alloys.

Due to lower density, titanium alloys are an attractive alternative to the heavier nickel-base superalloys and structural stainless steels provided they can meet the high temperature requirements of jet engines. For making large structural components like turbine cases and housings, near net shape forming technology e.g. casting and powder metallurgy (P/M) offer cost advantage over machined wrought products (1). Compared to forgings, however, castings are prone to internal porosity and the microstructure is generally more variable, mainly due to differences in solidification rates within the same part, and coarser since refinement by forging is absent. The resultant properties would therefore be lower and have larger scatter than similar wrought components. Although advances in investment casting and hot isostatic pressing (HIP'ing) have provided partial solutions to these problems, limited data and experience with titanium cast parts has led to the use of "casting factors" in the design of airframe and jet-engine components (2,3). This penalizes the weight benefits of titanium alloys. To gain fuller advantage of cast titanium alloys and help eliminate the use of casting factors, a better understanding of microstructure - property relationships becomes even more important (4).

Titanium '92
Science and Technology
Edited by F.H. Froes and I. Caplan
The Minerals, Metals & Materials Society, 1993

The high dynamic stresses and high temperatures encountered in modern jet engines necessitate characterization of both creep and fatigue properties of materials. It is well established that these are interactive, alloy-specific properties and are affected by composition, microstructure and processing. Generally, creep improvement reduces low cycle fatigue capability and vice versa (5).

The near-alpha Ti-6Al-2Sn-4Zr-2Mo alloy (Ti-6242) was originally introduced in the United States in the mid 1960's in wrought form for use up to about 783°K (950°F)(5). Subsequently, improvements in creep of this and similar titanium alloys were found by addition of Si up to supersaturation level (6,7). In Ti-6242 the optimum Si content is 0.1% (wt. pct). In the wrought form, this alloy is well understood and numerous articles are available on the behavior of various microstructures. For the cast form, however, very little is known and no systematic understanding has been developed. The inherent stringency of the cast microstructure limits the possibility of obtaining bi-modal microstructures and primarily consists of alpha platelets. However, the potential exists for improving properties by modifying the alpha plate structure.

Allison Gas Turbines has selected cast Ti-6242 for the compressor case and diffuser of the new T406, GMA 2100 and GMA 3007 engines. This work was performed to evaluate the effect of heat treat modification on creep, and LCF at 755°K (900°F), with the objective of improving creep properties and at least maintaining the 755°K (900°F) LCF properties.

Experimental Procedure

Typical composition and the two heat treatments, conditions A and B, are given in Tables I and II, respectively. Test pieces for tensile, creep, and LCF for condition A were sectioned from a compressor

Table I. Chemical Composition by Weight Percent

Element	Al	Sn	Zr	Mo	Si	C	Fe	N	H	O	Ti
Wt. Pct.	6.15	2.02	4.22	1.98	0.07	0.01	0.05	0.006	0.0018	0.13	Bal

Table II. Heat Treatments for Conditions A and B

	HIP	Solution Anneal	Precipitation Age
Condition A (Fast cool)	1172°K (1650°F)/3 hr ● 100 MPa (14.5 ksi)	1227.6°K (1750°F)/1 hr Ar gas fan cool ● 0.4 MPa (60 psi) pressure	866.5°K (1100°F)/8 hr Ar gas fan cool ● 0.4 MPa (15 psi) pressure
Condition B (Slow cool)	1172°K (1650°F)/3 hr ● 100 MPa (14.5 ksi)	1227.6°K (1750°F)/1 hr Ar gas fan cool ● 0.1 MPa (15 psi) pressure	894.3°K (1150°F)/2 hr Ar gas fan cool ● 0.1 MPa (15 psi) pressure

case of the Allison T406 engine (Figure 1). For condition B, integrally cast test coupons from a similar size casting were used.

Tensile tests were conducted per ASTM standard E8. Constant load creep tests at various stress-temperature combinations were stopped after more than 1000 hours if no failure occurred, and the smooth bar LCF tests were conducted on a computer controlled servohydraulic test system at 755°K (900°F), $R_\sigma = 0$ and at 20 cpm using triangular wave form. Light and SEM microscopy was used to analyze microstructures and fracture surfaces.

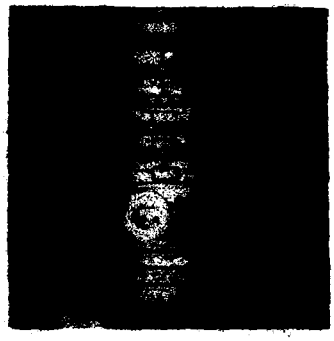


Figure 1. Compressor case of the Allison T406 engine.

Results And Discussion

Microstructure

Typical microstructures for the two fully heat treated conditions are shown in Figure 2. Condition A (Figures 2a and 2b) has numerous variants of alpha plates, the alpha colony size is irregular and the



a b c d

Figure 2. Microstructure of cast Ti-6242 for the two heat treatments; (a) and (b) fast cool, condition A, cooling rate @ 311°K (100°F)/min., (c) and (d) slow cool, condition B, cooling rate @ 270-275°K (25-40°F)/min.

grain boundary alpha is generally thick and continuous. Some areas consist of basketweave alpha. X-rays did not reveal any internal pores in the test pieces. The cooling rate from solution anneal temperature is about 311°K (100°F)/min (Ar gas fan cool at 0.4 MPa [60 psi]) and is termed as fast cool. The irregular structure of this condition is a result of the different section sizes and rapid cooling from the near beta solution anneal temperature, so that insufficient time is available for diffusion of alpha stabilizers. Although not studied here, the aging cycle is well understood to stabilize alpha.

For condition B, the alpha morphology is aligned acicular with very few remnants of basketweave structure (Figures 2c and 2d). The continuous grain boundary alpha and the alpha plates in the colonies appear finer than in condition A. Generally the colony size was more consistent but in some cases the alpha colony was as large as the prior beta grains. Again, no porosity was found. Furnace cooling with flowing Ar gas at 0.1 MPa (15 psi) gave a cooling rate of about 270-275°K (25-40°F)/min and is termed as slow-cool. The cast test bars had a consistent section size and more uniform structure. The slower cooling in condition B provided enough time for diffusion of alpha stabilizers and refined the alpha plates.

Tensile

Comparative tensile properties for the two conditions are summarized in Table III. Condition B maintained strength levels equivalent to the fast cooled condition A, but the ductility at both room temperature and at 755°K (900°F) is better. Better ductility in condition B is due to the finesses of the grain boundary alpha as well as the acicular alpha. This is similar to the ductility differences found

Table III. Average Tensile Properties for Conditions A and B

	Condition A		Condition B	
	RT	755°K (900°F)	RT	755°K (900°F)
UTS MPa (ksi)	965.3 (140)	606.7 (88)	972.2 (141)	655.0 (95)
0.2% YS MPa (ksi)	882.6 (128)	489.6 (71)	882.6 (128)	503.4 (73)
El (%)	8	15	17	19
RA (%)	10	23	22	40

in some alpha-beta alloys where the differences were attributed to the enlargement of microstructural unit and the grain boundary alpha (8). It is interesting to note, that in other alloys slower cooling rate had reduced ductility (9,10). However, the structures in these studies were bi-modal, i.e. acicular as well as equiaxed. In our case we only have the acicular phase. It can then be concluded that refinement of the acicular alpha morphology is beneficial in improving ductility.

Creep

Overall, creep resistance of condition B is remarkably better than condition A for the same test parameters (Figure 3). Time to reach 0.2% creep strain for the two conditions are compared in Table IV. For either condition no specimen failed before reaching 0.2% creep. In condition A, a creep-

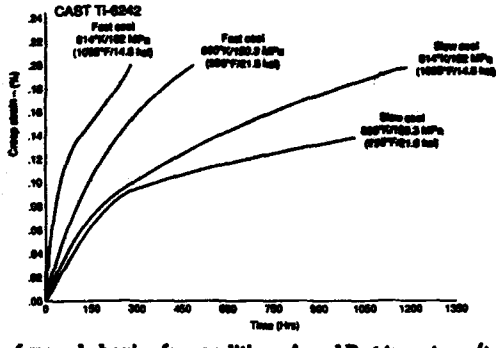


Figure 3. Comparison of creep behavior for conditions A and B at two stress/temperature conditions. Slow cool, condition B, is much more creep resistant.

Table IV. Comparison of 0.2% Creep

Test Parameters	Time to reach 0.2% creep (hr)	
	Cond. A	Cond. B
814°K/102 MPa (1005°F/14.8 ksi)	261	1217
800°K/150.3 MPa (980°F/21.8 ksi)	447	1022*

* test stopped after 1022 hr at 0.149% total creep strain.

ratchetting effect was observed during steady-state creep where the deformation occurred in small intermittent increments until it reached tertiary stage (Figure 4). This phenomenon was rarely present in condition B. The impressive difference in creep behavior can be rationalized in terms of the two microstructures.

For the integrally cast test bars (condition B), the alpha plate size within a colony is refined and the thickness of the grain boundary alpha is also reduced somewhat. Cooling rate, as discussed above, would not only affect the morphological changes but also the composition of alpha and other phases. Effects of different alpha morphologies obtained by different cooling rates in IMI 685 were shown to

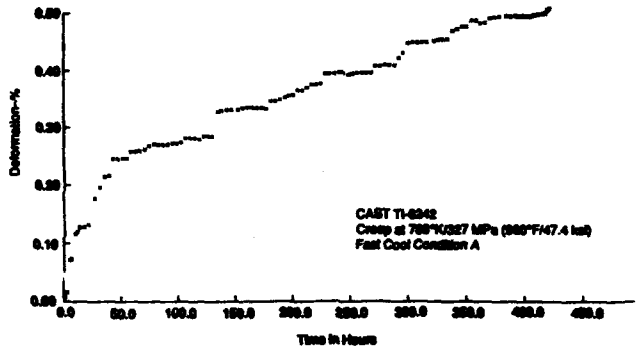


Figure 4. Creep-ratcheting seen in the fast cool, condition A, for a specimen tested at 788°K/326.8 MPa (960°F/47.4 ksi.)

have a minimum creep strain where the slower furnace cool (flowing Ar gas) gave the best creep properties as compared to the faster air cool or water quench rates (11). This was attributed, in part, to morphological changes. Similarly, in Ti-6242 (12) finer alpha platelet width improved creep resistance by restricting dislocation movement within alpha plates. The alpha-beta boundaries provided a sufficient barrier to substructure movement thus confining creep to alpha platelets. In effect, limiting of slip within alpha provided shorter mean path for deformation with the finer structure—similar to condition B in our case—hence better creep resistance. Coarser alpha platelets—condition A—would provide a larger area for dislocation movement and hence lower creep resistance.

One explanation for the ratchetting effect seen in condition A may be due to the large variability in the platelet size. When creep deformation concentrated within the alpha platelets, as discussed above, encounters a barrier to dislocation motion such as an alpha colony interface or coarse grain boundary alpha, detectable macro-creep would stop for a few hours till enough energy becomes available for overcoming the barrier, or for crossing over to a favorably oriented adjacent colony. At that instance a jump in creep strain is noticed. This also explains the larger scatter in creep observed for condition A. Uniformity of alpha morphology could explain the near absence of such steps in condition B.

A change in the apparent activation energy (slope of ln $\dot{\varepsilon}$ VS 1/T plot) indicates different operating creep mechanisms (13). In our study, the slope is essentially the same for the range of test temperatures (Figure 5), and it is therefore concluded that only one mechanism is dominant. Although

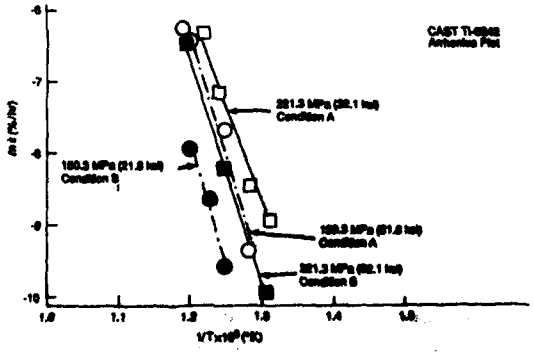


Figure 5. Arrhenius plot of conditions A and B at two stress levels.

the exact mechanism can only be characterized by transmission electron microscopy, following the above discussion, perhaps dislocation glide is the mechanism here.

Low Cycle Fatigue

The smooth bar LCF crack initiation life for condition B is better than condition A at 755°K (900°F) (Figure 6). The mean stress at half-life (Ni/2) is also higher (Figure 7), but better LCF life for condition B indicates that for the same 'R' ratio ($R_\varepsilon = 0$), the mean stress effects are more pronounced for condition A, or that condition B has better stress capability.

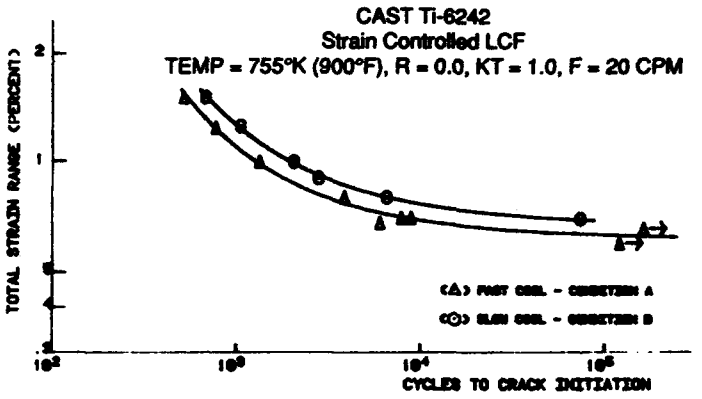


Figure 6. Comparison of smooth bar low cycle fatigue at 755°K (900°F) for conditions A and B.

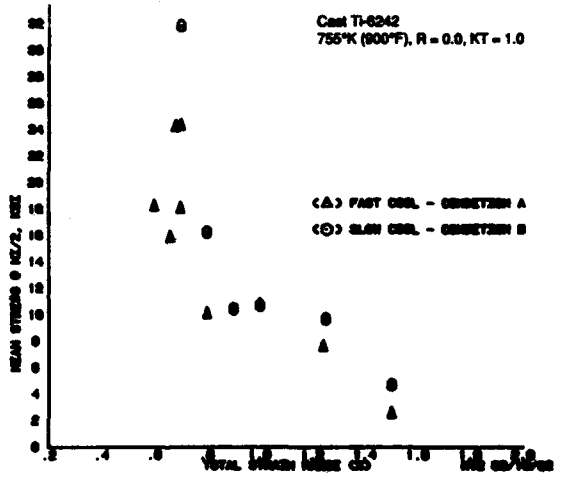


Figure 7. Cyclic mean stress at half-life ($N_f/2$). Despite higher mean stress, the LCF life of condition B was higher.

SEM fractography of condition A shows a crystallographic surface initiation and transition to Stage II mode. (Figure 8a). The cracks propagated by shearing at the interfaces of the alpha platelets, as is shown in Figure 8b. For condition B at the same total strain range (0.7%) the life increased by 7X. The origin is at a subsurface cluster of second phase particles (Figures 8c and 8d), probably equiaxed grain



Figure 8. SEM fractographs of LCF specimens tested at total strain range of 0.7%; (a) surface crack initiation and (b) propagation along alpha platelets in condition A; (c) subsurface crack initiation and (d) high magnification of the origin which was at a cluster of second phase particles.

boundary alpha which was present at a few prior beta grain boundaries. Cracks also initiated at favorably oriented single colonies and propagated across the alpha plates by intense shearing. Note in Figure 9 that the cracking is almost at 90 deg to the platelets until it reaches the adjacent colony and changes direction, thereby increasing the tortuisity of the crack path.



Figure 9. Polished and etched longitudinal cross section of LCF specimen for condition B. This micrograph is from the same specimen as in Figure 8.

At higher total strain-ranges (1.0%), initiation and propagation for both conditions were identical, i.e. crystallographic surface initiation and propagation through the length of fatigued surface. The shear stresses were high enough for the fracture to occur by shear along the favorably oriented alpha platelets. Figure 10 is a typical SEM fractograph of this mode. The superior LCF life of condition B is a result of the finer, stronger alpha morphology as it provides resistance to cracking, whereas the weaker interfaces of the rapidly cooled coarse irregular alpha of condition A crack easily.



Figure 10. SEM fractograph of crystallographic crack initiation typical of both conditions A and B. This specimen was tested at 1.0% total strain range for condition B. (a) crack initiation and (b) propagation on crystallographic facet is by shear along the finer alpha platelets.

Most of the literature on microstructure-fatigue behavior of titanium alloys has concerned wrought alloys due mainly to use in fatigue critical components. Of the titanium alloys used in the cast form, only Ti-6Al-4V has been extensively studied. Consistent with our observations, Greenfield et. al. (14) noted that LCF initiation life was lower for the coarser alpha morphology, be it acicular or equiaxed.

Thus refinement of the alpha plates should improve LCF life. The equiaxed alpha-beta structure in wrought alloys is known to have better LCF life than the acicular alpha found in castings (15,16). Since an equiaxed alpha-beta structure is practically impossible to obtain in castings, and refinement of grain size in large structural castings is equally difficult, the optimum LCF capability in castings results from alpha refinement within the colonies as well as at the grain boundaries.

Conclusions

1. Improvement in creep of cast Ti-6242 alloy can be achieved without sacrificing LCF life or tensile ductility by suitably choosing heat treatment which refines acicular alpha and reduces continuous grain boundary alpha. A similar approach could possibly be applied to other cast titanium alloys.

2. Use of titanium castings in jet engines can be increased by improved understanding of microstructure-property relationships. Better understanding should help eliminate the use of "casting factors" which diminish the weight benefits of titanium alloys.

Acknowledgments

The authors wish to thank Allison Gas Turbine Division, General Motors Corporation, for permission to publish this paper. We acknowledge Precision Castparts Corporation (PCC), Portland, Oregon, for supplying the castings, M.A. Khan for testing, Ms. Marsha Grey for compiling the data, and Ms. Rita J. Wise for typing the manuscript.

References

1. B.A. Ewing, AGARD Conference Proceedings No. 325, 1982, pp. 13.1-13.12.
2. Military Specification, MIL-A-8860 (ASG), May 1960, para 3.2.1.1.
3. Federal Aviation Administration, DOT, Code of Federal Regulations, Title 14, Article 25.621. pp. 281-282.
4. D. Eylon, F.H. Froes, and R.W. Gardiner, *Titanium Technology – Present Status and Future Trends*, Edited by: F.H. Froes, D. Eylon and H.B. Bomberg, Titanium Development Association, 1985, pp. 35-47.
5. D. Eylon, S. Fujishiro, P.J. Postans, and F.H. Froes, in Reference 4, pp. 67-94.
6. S.R. Seagle and H.B. Bomberger, *The Science, Technology and Application of Titanium*, Edited by: R.I. Jaffee and N.E. Promisel, Pergamon Press, N.Y., 1970, pp. 1081-1088.
7. S.R. Seagle, G.S. Hall, and H.B. Bomberger, Met. Engr. Quarterly, Feb.1973, p. 48.
8. H.M. Flower, Mat. Sci. and Tech., Nov. 1990, vol. 6, pp. 1082-1092.
9. A. Vassel, F.H. Froes, J.P. Hartmann and D. Eylon, Proc. Fifth International Conf. on Titanium, Munich, FRG, September 1984, pp. 515-521.
10. *R.I. Jaffee, L. Wagner, and G. Lutjering*, Proc. *Sixth World Conf. on Titanium*, Cannes, France, June 1988, pp. 1501-1506.
11. P.A. Blenkinsop, in Ref. 9, pp. 2523-2538.
12. W. Cho, J.W. Jones, J.E. Allison and W.T. Donlon, in Ref. 10, pp. 187-192.
13. P.J. Bania and J.A. Hall, in Ref. 9, pp. 2371-2378.
14. M.A. Greenfield, C.M. Pierce, and J.A. Hall, *Titanium Science and Technology*, Edited By: R.I. Jaffee and H.M. Burte, Plenum Press, N.Y. 1973, pp. 1731-1743.
15. N.D.R. Goddard, H.M. Flower, and M.J. Cope, in Reference 10, pp. 259-264
16. B. Vittonnet and G. Thauvin; in Ref. 10, pp. 319-324.

ON CRACK MECHANISM OF Ti-6. 5Al-3. 5Mo-1. 5Zr-0. 35Si ALLOY UNDER FATIGUE-CREEP-ENVIRONMENT INTERACTION*

Y. G. Zhou①, Y. Zhou②, and H. Q. Yu③

Department of Materials Science and Engineering
Northwestern Polytechnical University

Abstract

The cleavage fracture of Ti-6. 5Al-3. 5Mo-1. 5Zr-0. 3Si alloy with three kinds of microstructures (equiaxed, duplex and basketweave) has been studied under fatigue-creep-environment interaction at 520℃. It is found that the cleavage fracture was not only related to the rate of creep void initiating, but also controlled by the creep strain accumulation at crack-tip during hold time and by stress state at crack-tip. That is, the cleavage fracture of Ti-alloy was affected simultaneously by the critic void initiating strain and the parameter V_{oc} of critic void growth.

---

① Professor of Materials Science and Engineering, Northwestern Polytechnical University
② Received M. S. Degree at above Department
③ Associate Professor of above Department

Titanium '92
Science and Technology
Edited by F.H. Froes and I. Caplan
The Minerals, Metals & Materials Society, 1993

Introduction

In general, the cleavage fracture of Ti-alloys under fatigue-creep-environment interaction is usually associated with hydrogen atoms in alloy or with oxygen atoms in environment diffusing toward crack-tip[1]. In 1987 B. E. Powell et al. [2] explained that this phenomenon was related to plastic strain accumulation at crack-tip but they had no experimental proof. The authors did considerable experiments and we believe we succeed in offering a better explaination of the above-mentioned phenomenon. This paper studied the fatigue-creep life of three microstructures of Ti-6.5Al-3.5Mo-1.5Zr-0.3Si alloy under fatigue-creep-environment interaction at 520℃ and particularly studied cleavage fracture mechanism using SEM observation, crack-tip stress analysis and measurement of creep strain accumulation during hold time.

Material and Experiment Procedure

Experimental materials chosen for this study came from the discal forgings of three microstructures (Fig. 1) which were obtained by conventional, near-β and β forging. The chemical compositions were same; (wt-%) Al6.63, Mo3.42, Zr1.65, Si0.28, Fe0.0056, C0.0013, N0.007, H0.0005 and Ti bal. Discal forgings were duplex annealing-treated as follows; 950℃/1h air cool+530℃/6h air cool.



Fig. 1 Three microstructures of experimental materials
(a) equiaxed; (b) duplex; (c) basketweave

Fatigue-creep interaction test at 520℃ was carried out using a trapezoidal wave, longitudinal tension-tension cyclic stress, stress ratio R=0.1, frequence $f=4.76\times10^{-3}$Hz, hold time 3 min at maximum load.

Result and Discussion

Relations between Microstructure and Fatigue-Creep Life

Fig. 2 was the correlation curves of maximum cyclic stress σ_{max} vs fatigue-creep life Nf. It was seen from the curves that Nf was affected not only by the microstructures, but also by the magnitude of loading stress. When σ_{max} was at greater and less range, the basketweave structure possessed the higher Nf (curve 3, Fig. 2a); Nf of the equiaxed structure was lower (curve 1, Fig. 2a); and duplex structure was to lie in middle. But while σ_{max} was equal to 560～660MPa, the Nf of duplex structure was not only higher than that of equiaxed, but also higher than that of basketweave structure. There was a bulging in the middle of curve 2(Fig. 2a).

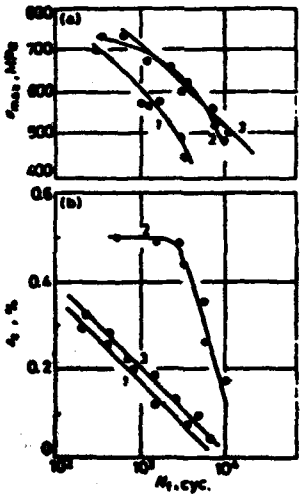


Fig. 2 Maximum cyclic stress σ_{max}(a) and creep strain accumulation ε_c(b) vs fatigue-creep life Nf
1-equiaxed; 2-duplex; 3-basketweave

Fig. 2b was the relation curves of the creep strain accumulation ε_c during hold time vs the

fatigue-creep life Nf. ε_c-Nf curves of equiaxed and basketweave structure had same change tendency, the ε_c was decreased with the increasing of Nf (curve 1,3,Fig. 2b). However, the ε_c-Nf curve of duplex structure was obviously different from that of equiaxed and basketweave structure. It could be seen from Fig. 2b that there was an obvious turning-point on the curve 2. At left of the turning-point, ε_c decreased slowly with the increasing of Nf; at right, ε_c decreased rapidly with the increasing of Nf. It was very interesting that this middle bulging on the curve of Fig. 2a was corresponding to the turning-point. The ε_c of the turning-point was equal to 0.5%, it was far higher than 0.07% of equiaxed, also higher than 0.11% of basketweave structure. This means that under fatigue-creep interaction, creep strain accumulation ε_c to form during hold time had an active effect on fatigue-creep life Nf.

Dislocation Morphology of Three Microstructures

Dislocation morphology in these kinds of microstructures to be undergone fatigue-creep interaction was shown in Fig. 3. Under lower cyclic stress condition, dislocation inside primary α-grain was arranged in a planar form (Fig. 3a). And with the increasing of stress the dislocation was piled-up quickly in equiaxed structure (Fig. 3b). The dislocation piled-up was lower in duplex structure because slip could occur between α-plates (Fig. 3c). This might be relative to having a greater creep strain accumulation in duplex structure. For basketweave structure, dislocation piled-up seriously existed under any cyclic stress condition.





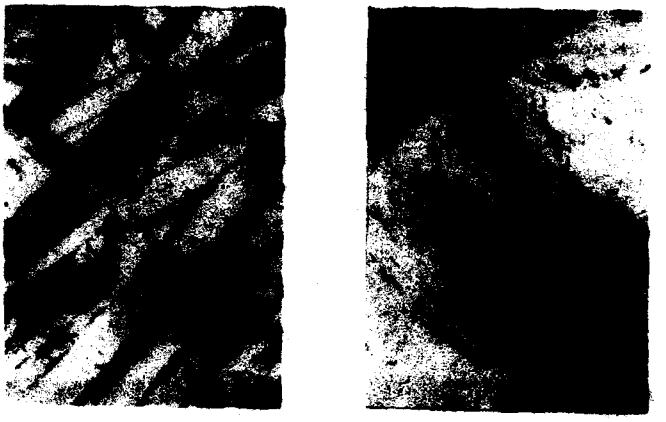


Fig. 3 Dislocation morphology of three microstructures
(a) dislocation morphology inside equiaxed grain under lower cyclic stress;
(b) dislocation morphology inside equiaxed grain under high cyclic stress;
(c) dislocation morphology of duplex structure under high cyclic stress;
(d) dislocation morphology of basketweave structure under any cyclic stress

Fractograph of Three Microstructures

Fig. 3 was the fractographs of three microstructures under strong fatigue-creep interaction. It was seen that the interweaving of fatigue striations and creep voids occured on the fracture surface of equiaxed structure (Fig. 4a); obvious fatigue striations and secondary cracks but almost no creep voids or cleavage feature occured on the fracture surface of duplex structure (Fig. 4). On the fracture surface of basketweave structure there were cleavage plateaus and fatigue striations, what is more important, creep voids were not only more and deeper than that of equiaxed and basketweave structure, but also were not connected each other (Fig. 4c). It is evident that they are in the initiating or early propagating phase. With crack propagation toward final fracture zone, fatigue striations in equiaxed structure were disappeared and there were only some bigger and deeper voids or dimples on the facture surface. In the basketweave structure creep voids grew up and connected each other, but cleavage indications became obscure gradully. In the duplex microstructure, with crack propagating secondary cracks vanished and creep voids increased; near final fracture zone, cleavage feature was more obvious than that of propagation zone (Fig. 5). It is evident that this phenomenon can' t be completely explained by the theory of hydrogen atoms diffusing toward crack-tip because hydrogen atoms diffusing is controlled by the time. The lower the

fatigue-creep Nf or the greater the rate of crack propagation, the shorter the time of hydrogen atoms diffusing, which should result in decreasing of brittle fracture, but the experimental results were not like this.

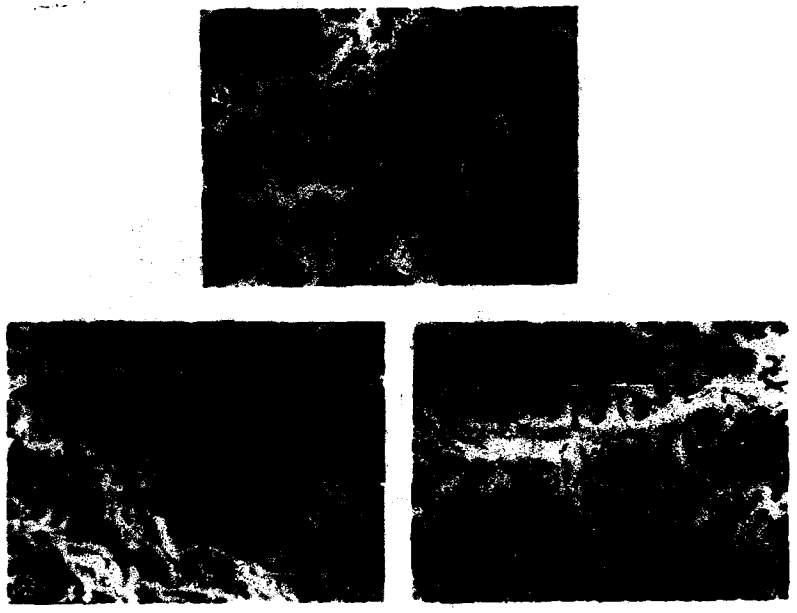


Fig. 4 SEM fractograph of three microstructures in crack propagation zone
(a) equiaxed; (b) duplex; (c) basketweave



Fig. 5 SEM fractograph of duplex structure near final crack zone

Further experimental results showed that volume fraction of primary α-phases influenced the stress state at crack-tip. With the decreasing of primary α-phases in microstructure, cracks went in propagation zone early and the stress at crack-tip transited early from plane stress state to plane strain state. Meanwhile, the value of critic void initiating strain also

transformed from 0.125 of equiaxed structure, 0.115 of duplex to 0.08 of basketweave. It shows that basketweave structure has the highest rate of creep void initiating. This conclusion can be proved by a number of undergrown creep voids in Fig4c.

According to the minute-mechanics theory , the process of creep voids growth is controlled by $V_{ec}=\varepsilon_c \cdot \exp(1.5Ra)$ parameter of critic void growth. [4]

$$Ra=\sigma_m/\sigma_e$$

$$\sigma_m=(\sigma_{xx}+\sigma_{yy}+\sigma_{zz})/3$$

$$\sigma_e=1/\sqrt{2}\cdot\sqrt{(\sigma_{xx}-\sigma_{yy})^2+(\sigma_{yy}-\sigma_{zz})^2+(\sigma_{zz}-\sigma_{xx})^2+6(\tau_{xy}^2+\tau_{yz}^2+\tau_{zx}^2)}$$

$$Ra=\begin{cases}2.17 & \text{(plane strain state)}\\ 0.67 & \text{(plane stress state)}\end{cases}$$

As mentioned above, in the zone of strong fatigue-creep interaction, the ε_c of duplex structure is 0.5%, basketweave o.11% and equiaxed 0.07%. Therefore, The V_{ec} of equiaxed structure is far lower than that of duplex and basketweave. This manifests that in equiaxed structure the creep voids initiating is difficult, once voids are initiated, they grow rapidly because of smaller V_{ec}. For basketweave structure, due to greater V_{ec} creep voids initiating is easy , but voids grow difficultly. Therefore, serious damage formed in grains results in obvious cleavage fracture. Duplex structure has the advantages of both equiaxed and basketweave microstructure, creep voids neither initiate easily nor grow rapidly. Hence, only a few creep voids are found in crack propagation zone, cleavage indication are not obvious. It follows that the cleavage fracture of Ti-6.5Al-3.5Mo-1.5Zr-0.3Si alloy under fatigue-creep interaction is simultaneously affected by the stress state at crack-tip , the creep strain accumulation ε_c during tensile hold time and the value of the critic void initiating strain.

Reference

1. Z. Song, and D. W. Hoeppner, "Dwell Time Effects on the Fatigue Behaviour of Titanium Alloys", Int J Fatigue, Vol. 10(4)(1988), 211-218.
2. B. E. Powell, and T. V. Duggan, "Crack Growth in Ti-6Al-4V under the Conjoint Action of High and Low Cycle Fatigue", Int J Fatigue, Vol. 9(4)(1987), 195-202.
3. Y. G. Zhou et al. "An Investigation on Near-Beta Forging of Titanium Alloy" Acta Aeronautica et Astronautica Sinica, Vol. 10(1)(1989), A60—66.
4. C. Q. Zheng, and J. C. Radon, "The Correlation of Triaxial State of Stress and the Fatigue Strain", Journal of Northwestern Polytechnical University, Vol. 3(1)(1985), 21-28.

THERMODYNAMICS AIDED DESIGN OF $\alpha+\alpha_2$ HIGH TEMPERATURE TITANIUM ALLOYS

(Ti-Al-Sn-Zr-Nb-Si SYSTEM)

H. Onodera, S. Nakazawa, K. Ohno, T. Yamagata and M. Yamazaki

*Materials Design Division, National Research Institute for Metals, Nakameguro 2-3-12, Meguro-Ku, Tokyo 153.

Abstract

In order to construct a design method for $\alpha+\alpha_2$ type high temparature titanium alloys, thermodynamic analyses of α and α_2 phases in the Ti-Al-Sn-Zr-Nb system were performed by means of the two-sublattice model. As the next step, five Ti-Al-Sn-Zr-Nb-Si alloys were designed by this thermodynamic calculation to have the optimum volume fraction of α_2 phase ($V\alpha_2$ = 0.1～0.2 at 823K) proposed in the previous report. Effects of heat treatments on creep properties were examined by using these designed alloys.

Introduction

The use of the ordered α_2 phase (Ti_3Al) to strengthen the α phase titanium is one of the possible approaches to developing new high temperature titanium alloys.

The authors' group examined the effects of volume fraction of the α_2 phase on creep and tensile properties of $\alpha+\alpha_2$ type titanium alloys using ten Ti-Al-Sn-Zr alloys designed by the thermodynamic calculations [1,2]. From these results, the $V\alpha_2$ range of 0.1～0.2 (at 823K) was proposed as the best design condition for this type of alloys. Nb and Si are also potential additives because Nb is known to improve ductility in the α_2 phase [3] and Si is effective for improving creep resistance [4]. Then, in the present investigation, a program was set up to construct a design method for $\alpha+\alpha_2$ type Ti-Al-Sn-Zr-Nb-Si alloys.

For that purpose, a thermodynamic analysis of the α and α_2 phases in the Ti-Al-Sn-Zr-Nb system was performed by means of the two-sublattice model [5]. As the next step, five Ti-Al-Sn-Zr-Nb alloys (GT-79,88～91), which have $V\alpha_2$ of 0.1 or 0.2 (proposed design condition [2]), were designed by the thermodynamic calculations. In order to improve creep resistance, Si was added to some of the designed alloys. The target of this study is to examine the effects of microstructure on the creep properties in these designed alloys.

Titanium '92
Science and Technology
Edited by F.H. Froes and I. Caplan
The Minerals, Metals & Materials Society, 1993

Description of the thermodynamic properties of the α, and α_2 phases

The free energies of the α phases in the Ti-Al-Sn-Zr-Nb system were represented by the regular solution model as

$$G = \sum_i X_i {}^{o}G_i^{\alpha} + RT\sum_i X_i \ln(X_i) + \sum_{i,j} A_{ij}X_iX_j \quad \text{----------(1)}$$

where ${}^{o}G_i^{\alpha}$ is the Gibbs energy of the α phase of pure element i. X_i and A_{ij} are the atom fraction and the interaction parameter for i-j binary system, respectively.

The free energy of the α_2 phase was represented by the two sublattice model[5]. The α_2 phase in the Ti-rich corner of the binary Ti-Al system was treated as $(Ti)_3(Ti,Al)$. Nandy et al.[6] has reported that Zr and Nb occupy Ti sites in the α_2 phase. Sn was assumed to occupy Al sites since Ti and Sn could form the compound Ti_3Sn of DO_{19} structure. The binary α_2 phase models could thus be extended to the present model $(Ti,Zr,Nb)_3(Ti,Al,Sn)$ with Gibbs energy expression,

$$G^{\alpha_2} = \sum_i {}^{1}Y_i^{2}Y_j G_{i:j} + 3RT\sum_i ({}^{1}Y_i \ln {}^{1}Y_i) + \sum_i ({}^{2}Y_i \ln {}^{2}Y_i)$$

$$= \sum_{i,j,k} {}^{1}Y_i {}^{1}Y_j {}^{2}Y_k L_{i,j:k} + \sum_{i,j,k} {}^{1}Y_i {}^{1}Y_j {}^{2}Y_k L_{i:j,k} \quad \text{----(2)}$$

where ${}^{s}Y_i$ is the site fraction of the component i in the sublattices. $G_{i:j}$ and $L_{i,j:k}$ are the Gibbs energy of the pure compound i:j and the interaction parameter, respectively. A comma separates the elements on the same sublattice whereas a colon separates the elements on different sublattices. The unknown parameters $G_{Nb:Ti}$, $G_{Nb:Al}$, $G_{Nb:Sn}$, and $L_{Ti,Nb:i}$ (i=Ti, Al, Sn) (Table I) were optimized by using α_2/α and α_2/β phase boundaries in the Ti-Al-Nb system reported by Banerjee et al [7]. and Andreev [8]. Other parameters (Table I) were evaluated in previous reports [1, 9~11]. The calculated phase boundaries at 1173K in the Ti-Al-Nb system is compared to the experimental data reported by Banerjee et al. and Andreev in Fig.1. The agreement is very satisfactory, and this supports the present thermodynamic analysis and the evaluated parameters.

Results and Discussion

Design of $\alpha+\alpha_2$ type Ti-Al-Sn-Zr-Nb-Si alloys

In the present study, the solid solution strengthening of the α phase was estimated by the Eq.(3).

$$dDB^{\alpha} = 14.40 \cdot X_{Al} + 17.61 \cdot X_{Sn} + 9.69 \cdot X_{Zr} + 1.38 \cdot X_{Nb}, \quad \text{----(3)}$$

Table I Thermodynamic parameters (J/mol) for the α and α_2 phases in a Ti-Al-Sn-Zr-Nb system.

	Interaction parameters	References
α phase	$A_{Ti,Al} = -111629 + 38.49 \cdot T$	[1]
	$A_{Ti,Sn} = -87780$	[9] Kaufman and Bernstein
	$A_{Ti,Zr} = 7600$	[10] Kaufman
	$A_{Ti,Nb} = 10200$	[11] Murray
	$A_{Al,Sn} = 11700$	[10] Kaufman
	$A_{Al,Zr} = -76370$	[1]
	$A_{Al,Nb} = -213380 + 67.78 \cdot T$	[10] Kaufman
	$A_{Sn,Zr} = -55970$	[1]
	$A_{Zr,Nb} = 28980$	[10] Kaufman and Bernstein
	Gibbs energies of pure compounds	
α_2 phase	$^{o}G_{Ti:Al} = 3\,^{o}G^{\alpha}_{Ti} + {}^{o}G^{\alpha}_{Al} - 104030 + 25.82 \cdot T$	[1]
	$^{o}G_{Ti:Al} = 3\,^{o}G^{\alpha}_{Ti} + {}^{o}G^{\alpha}_{Al} - 104030 + 25.82 \cdot T$	[1]
	$^{o}G_{Ti:Sn} = 3\,^{o}G^{\alpha}_{Ti} + {}^{o}G^{\alpha}_{Sn} - 95000$	[1]
	$^{o}G_{Zr:Ti} = 3\,^{o}G^{\alpha}_{Zr} + {}^{o}G^{\alpha}_{Ti}$, $^{o}G_{Nb:Sn} = 3\,^{o}G^{\alpha}_{Nb} + {}^{o}G^{\alpha}_{Sn}$	[1]
	$^{o}G_{Zr:Al} = 3\,^{o}G^{\alpha}_{Zr} + {}^{o}G^{\alpha}_{Al} - 79800$	[1]
	$^{o}G_{Zr:Sn} = 3\,^{o}G^{\alpha}_{Zr} + {}^{o}G^{\alpha}_{Sn} - 78200$	[1]
	$^{o}G_{Nb:Ti} = 3\,^{o}G^{\alpha}_{Nb} + {}^{o}G^{\alpha}_{Ti} + 217160$	Present work
	$^{o}G_{Nb:Al} = 3\,^{o}G^{\alpha}_{Nb} + {}^{o}G^{\alpha}_{Al} - 8140$	Present work
	Interaction parameters	
	$L_{Ti,Zr:Ti} = L_{Ti,Zr:Al} = L_{Ti,Zr:Sn} = 7600$	[1]
	$L_{Ti,Nb:Ti} = L_{Ti,Nb:Al} = L_{Ti,Nb:Sn} = -127700$	Present work
	$L_{Zr,Nb:Ti} = L_{Zr,Nb:Al} = L_{Zr,Nb:Sn} = 28980$	Present work
	$L_{Ti:Ti,Al} = L_{Zr:Ti,Al} = L_{Nb:Ti,Al}$	
	$= -11920 + 45.03 \cdot T - 2.248 \cdot (T/10)^2$	[1]
	$L_{Ti:Ti,Sn} = L_{Zr:Ti,Sn} = L_{Nb:Ti,Sn} = 17000$	[1]
	$L_{Ti:Al,Sn} = L_{Zr:Al,Sn} = L_{Nb:Al,Sn} = 1170$	[1]

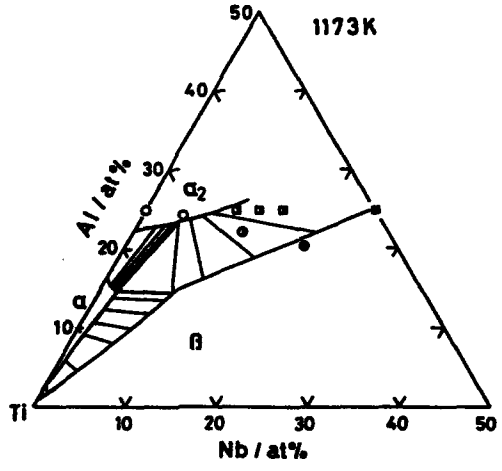


Figure 1 - A calculated isothermal section (1173K) of a Ti-Al-Nb system. Microstructure observations:
□(α_2 +β), ■(β) ; after Banerjee et al. [7],
○(α_2), ○(α_2 +β) ●(β) ; after Andreev [8].

where X_i is the atomic fraction of the element i in the α phase. Eq. (3) was obtained from the works of Sasano and Kimura [12] on the solid solution strengthening of the α-titanium. In the previous reports [13], the present authors made it clear that the parameter dDE^{α} could estimate very well the solid solution strengthening of the α phase in multicomponent titanium alloys.

Five Ti-Al-Sn-Zr-Nb alloys (Table II), which had the optimum $V\alpha_2$ of 0.1 or 0.2 at 823K and various values of dDE^{α}, were designed by the above thermodynamic calculations. Designed values for $V\alpha_2$ and dDE^{α} (at 823K) are shown in Table II. In the present study, Si was added in order to improve creep resistance. These alloys were arc melted as 2kg double melt ingots. After forging to 30mm diameter, they were rolled to 14mm diameter at 1273K which is 10 to 60K below the β-transus of the alloys. All specimens were

Table II Chemical compositions (wt%) and calculated $V\alpha_2$ and dDE^{α} (at 823K) of designed alloys.

Alloy	Al	Sn	Zr	Nb	Mo	Si	O	Ti	$V\alpha_2$	dDE^{α}
GT-79	6.1	2.5	6.9	-	-	-	0.13	bal.	0.14	1.85
GT-88	5.9	2.6	7.3	1.5	-	0.17	0.10	bal.	0.13	1.84
GT-89	5.3	4.7	4.2	0.4	0.81	0.27	0.10	bal.	0.12	1.66
GT-90	4.3	9.2	5.4	1.5	-	0.21	0.11	bal.	0.20	1.67
GT-91	5.9	4.3	6.0	1.5	-	0.19	0.12	bal.	0.19	1.76

β or $\alpha+\beta$ solution treated for 1h and water quenched and aged at 823K for 48h.

Creep tests were performed at 823K with a stress of 274MPa using creep specimens with gage length and diameter of 30mm and 6mm, respectively. Strains were continuously monitored by an extensiometer. Microstructures of thin foils were examined in a Hitachi H-700 transmission electron microscope. Chemical compositions of the primary α and the prior β phases in the solution treated GT-89 alloy were analyzed by X-ray microanalyzer at 15 kV of accelerating voltage.

Microstructures of designed alloys

The β and $\alpha+\beta$ treated materials showed fine acicular martensite, and the equiaxed microstructure consisting of the primary α phase and the prior β phase, respectively. The formation of α_2 phase in each specimen was examined in TEM. In all specimens, weak α_2 reflections were observed in the selected area diffraction pattern (SADP) and the fine α_2 precipitates were confirmed in the dark field image as shown in Fig. 2, (a) and (b).

Creep properties of designed alloys

Creep properties for β treated and $\alpha+\beta$ treated materials are shown in Table III. The effects of Nb and Si additions can be seen in the difference of creep strength between the alloys GT-79 and GT-88, where the GT-88 alloy was obtained by additions of Nb and Si to the GT-79 alloy. The GT-88 alloy showed longer rupture life, the smaller minimum creep rate, and the longer time to 0.5% creep strain than the the GT-79 alloy. This comparison suggests that the additions of Nb and Si are effective to improve the creep strength of $\alpha+\alpha_2$ type titanium alloys. The effect of Vα_2 can be seen in the difference of creep strength among the alloys GT-90 and 91 containing

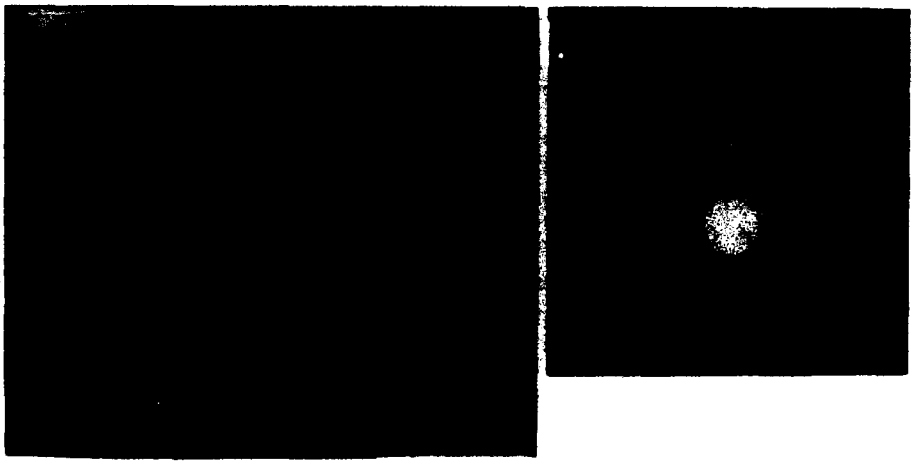


Figure 2 - A dark field micrograph of the $\alpha+\beta$ treated GT-88 alloy taken with (122)α_2 reflection showing fine α_2 precipitates (a) and a selected area diffraction pattern ((b), ZN[311]α).

$V\alpha_2$ of about 0.1 and the alloys GT-79, 88, and 89 containing $V\alpha_2$ of about 0.2 as seen in Table Ⅲ. The minimum creep rates of the alloys GT-90 and 91 are smaller than those of the alloys GT-79, 88, and 89. The same tendency was observed for the rupture life and the time to 0.5% creep strain. However, this $V\alpha_2$ dependency is not seen clearly in the times to creep strains 0.1% and 0.2%. A possible explanation for this is that the designed amount of the α_2 phase have not fully precipitated during the aging treatment of 48h at 823K. Further precipitations of the α_2 phase during creep deformations may result in the $V\alpha_2$ dependency of the long time creep strength.

The effect of dDE^{α} can be seen in the differences of the minimum creep rate, the rupture life and the time to 0.5% creep strain among β treated alloys having the same $V\alpha_2$ values. The GT-88 alloy (dDE^{α}=1.836) showed higher creep strength than the GT-89 alloy (dDE^{α}=1.662) for the calculated $V\alpha_2$ of about 0.1. For $V\alpha_2$ of about 0.2, the GT-91 alloy (dDE^{α}=1.758) showed the higher creep strength than the GT-90 alloy (dDE^{α}=1.670).

For alloys GT-79, 88, and 91, the creep strength of the β treated alloy is higher than that of the $\alpha+\beta$ treated alloy. On the contrary, in cases of alloys GT-89 and 90, the $\alpha+\beta$ treated alloy shows higher creep strength than the β treated alloy.

The partition of each alloying element to the primary α and the prior β phases at the $\alpha+\beta$ solution treatment seems to affect the formation of α_2 precipitates during the aging treatment. To confirm this effect, chemical compositions of the primary α and the prior β phases were analyzed by X-ray microanalyzer for the $\alpha+\beta$ treated GT-89 alloy (Table Ⅳ). The cal-

Table Ⅲ Creep properties of designed alloys at 823K with a stress of 274MPa.

Alloy	Heat Treatment	Time to creep strain /h 0.1	0.2	0.5	Min. creep rate (%/s)	Rupture life (h)	Total el. (%)
GT-79	β S.T.	4.5	10.0	27.5	4.0×10^{-6}	866	33.9
	$\alpha+\beta$ S.T.*	2.6	5.8	16.0	6.9×10^{-6}	355	47.3
GT-88	β S.T.	1.5	6.5	38.0	1.3×10^{-6}	1386	29.5
	$\alpha+\beta$ S.T.**	1.4	5.5	22.5	4.0×10^{-6}	669	38.4
GT-89	β S.T.	3.2	10.0	95.5	2.8×10^{-6}	885	16.3
	$\alpha+\beta$ S.T.**	14.0	39.0	112.0	1.3×10^{-6}	1180	22.9
GT-90	β S.T.	3.0	9.2	47.0	1.2×10^{-6}	1457	23.7
	$\alpha+\beta$ S.T.**	4.5	21.5	95.0	7.0×10^{-7}	2389	32.0
GT-91	β S.T.	3.2	15.5	103.0	6.0×10^{-7}	3148	25.5
	$\alpha+\beta$ S.T.*	0.7	5.5	47.5	7.0×10^{-7}	2590	39.9

*:1273K, **:1263K

Table IV Chemical compositions (wt%) of the primary α and the prior β phases, and calculated $V\alpha_2$ at 823K in the $\alpha+\beta$ solution treated GT-89 alloy.

Phase	Al	Sn	Zr	Nb	Mo	Si	Ti	V_{α_2}*	V_{α_2}**
α	6.1	4.3	3.5	0.3	0.2	0.2	bal.	0.19	0.12
β	5.2	4.5	4.1	0.3	0.8	0.3	bal.	0.10	

*:Calculated $V\alpha_2$ in each pahse at 823K.

**:$V\alpha_2$ calculated from average alloy compositions at 823K.

culated $V\alpha_2$ at 823K in the primary α phase is much larger than that obtained from the average alloy compositions. This seems to be mainly due to the enrichment of Al in the primary α phase. Such large amount of α_2 precipitates seem to be effective for improving the creep strength.

On the other hand, the average grain size of the $\alpha+\beta$ treated alloy is far smaller than that of the β treated alloy as shown in Fig.2,(a) and (b), which seem to result in the decrease in the creep strength. The observed differences of the creep strength between these two heat treatments seem to be appeared as the results of the competition of these factors.

Summary

In order to construct a design method for $\alpha+\alpha_2$ type high temperature titanium alloys, a thermodynamic analysis of α and α_2 phases in a Ti-Al-Nb system was performed by means of the two sublattice model. As the next step, effects of the microstructure on creep properties were examined by using five Ti-Al-Sn-Zr-Nb-Si alloys, which were designed to have $V\alpha_2$ of 0.1 or 0.2 (formerly proposed design condition) based on the above thermodynamic calculations. The main results obtained are as follows:

(1) Thermodynamic calculations with evaluated parameters were able to reproduce experimentally determined α/α_2 and α_2/β phase boundaries in a Ti-Al-Nb system.

(2) An improvement in the creep strength due to additions of Nb and Si was confirmed in creep tests of β treated alloys.

(3) For alloys GT-79, 88, and 91, the creep strength of the β treated alloy was higher than that of the $\alpha+\beta$ treated alloy. On the contrary, the opposite tendency was observed for alloys GT-89 and 90. It was suggested that the amount of α_2 precipitates in the primary α phase would increase due to the $\alpha+\beta$ solution treatment, resulting in the increase in the creep strength. On the other hand, the smaller grain size of $\alpha+\beta$ treated alloy was considered to result in the decrease in the creep strength. Observed differences of the creep strength between the two heat treatments seemed to be appeared as the results of the competition of these factors.

REFERENCES

1. H. Onodera, S. Nakazawa, K. Ohno, T. Yamagata, and M. Yamazaki: Computer Innovation of New Materials, ed. by M. Doyama, T. Suzuki, J. Kihara, and R. Yamamoto, Elsevier Science Publishers, North-Holland, (1991), 835.

2. H. Onodera, S. Nakazawa, K. Ohno, T. Yamagata, and M. Yamazaki: ISIJ International, 31(1991), 875.

3. S.M.L. Sastry and H.A. Lipsitt: Met. Trans., 8A(1977), 1543.

4. N.E. Paton and M.W. Mahoney: Met. Trans., 7A(1976), 1685.

5. M. Hillert and L.I. Staffansson: Acta Chem. Scand., 24(1970), 3618.

6. T.K. Nandy, D. Banerjee, and A.K. Gorgia: Proc. of 6th World Conf. on Titanium, ed. by P. Lacombe, P. Tricot,, and G. Berenger, Les Editions de Physique, Paris, (1989), 943.

7. D. Banerjee, T.K. Nandy, A.K. Gorgia, and K. Muraleedharan: ibid., 1091.

8. O.N. Andreev: Metally, 1(1970), p.193.

9. L. Kaufman and H. Bernstein: Computer Calculation of Phase Diagrams, Academic Press, New York and London, (1970).

10. L. Kaufman: Calphad, 1(1977), 7., ibid., 2(1978), 55., ibid., 2(1978), 82., ibid., 2(1978), 117.

11. J.L. Murray and H.A. Wriedt: Phase Diagrams of Binary Titanium Alloys, Am. Soc. Metals, Metals Park, Ohio, (1986).

12. H. Sasano and H. Kimura: Proc. of 4th Int. Conf. on Titanium, ed. by H. Kimura and O. Izumi, AIME, Penn., (1980), 1147.

13. H. Onodera, S. Nakazawa, K. Ohno, T. Yamagata, and M. Yamazaki: Proc. of 5th Int. Conf. on Titanium, ed. by G. Lutjering, U. Zwicker, and W. Bunk, Deutche Gesellshaft fur Metalkunde, FRG, (1984), 1883.

THE MECHANICAL PROPERTIES OF TERNARY AND QUATERNARY Ti_2NbAl-BASED TITANIUM ALUMINIDE ALLOYS

R. G. Rowe

General Electric Corporate Research and Development,
Schenectady, NY 12309

Abstract

Ordered orthorhombic Ti_2NbAl-based titanium aluminide alloys have been found to have higher specific strength and fracture toughness with no loss in creep resistance relative to state of the art Ti_3Al-based alloys. The specific strength of some Ti_2NbAl-based (O phase) alloys was a factor of two greater than comparable Ti_3Al-base (α_2) alloys , and the O-phase alloys also had fracture toughnesses a factor of two higher. Quaternary addition of vanadium produced a room temperature tensile elongation of 18.8%. These vanadium-modified O-phase alloys had higher strength, better creep resistance and greater ductility than state of the art super-alpha titanium alloys.

Introduction

The low density and high strength of titanium aluminide alloys has made them attractive for elevated temperature aircraft and aerospace applications. Although the Ti_3Al-based titanium aluminide Ti-24Al-11Nb has sufficient room temperature fracture toughness for engineering trials, higher fracture toughness and creep resistance have been needed to stimulate wider scale replacement of superalloys by titanium aluminide alloys [1, 2]. Higher specific strength and creep resistance titanium aluminides have been developed, but at the expense of room temperature fracture toughness [2-4]. It was found that the recently identified ternary ordered orthorhombic Ti_2NbAl O phase have both higher specific strength and higher room temperature fracture toughness than Ti_3Al-based alloys [5-7].

The crystal structures of the Ti_3Al (α_2) and Ti_2NbAl (O) phases are similar [8, 9]. The ordered orthorhombic Ti_2NbAl structure has a Cmcm symmetry and is only a slight distortion of the D019 structure . It differs in that one of the titanium subsites in the D019 structure is preferentially occupied by Nb in Ti_2NbAl and randomly occupied by Nb and Ti in Ti_3Al [8-10]. A distinct Ti_2NbAl phase field has been established near 25 at.% Al with Nb content

Titanium '92
Science and Technology
Edited by F.H. Froes and I. Caplan
The Minerals, Metals & Materials Society, 1993

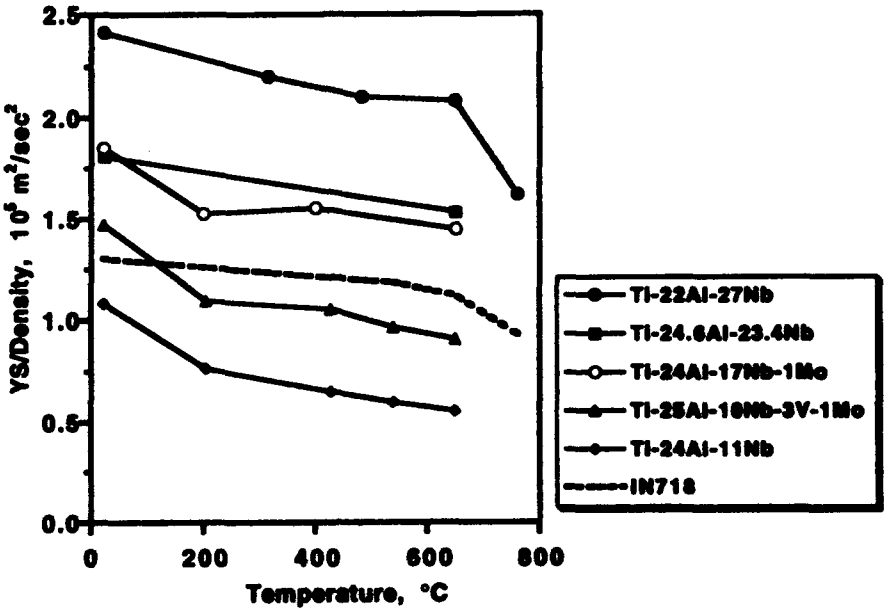


Figure 1. Specific yield strength of Ti-22Al-27Nb and Ti-24.6Al-23.4Nb relative to other titanium aluminide alloys and IN718.

ranging from approximately 16 to 30 at.% Nb [11]. Lower aluminum alloys like Ti-22Al-27Nb have been shown to lie in a two phase O + β_o phase field [6].

Mechanical Property Comparisons: The specific yield strength (ratio of yield strength to density) of several titanium aluminide alloys and the high strength wrought superalloy IN718 are shown in Figure 1.[2, 4, 6, 12, 13]. It can be seen that the ordered orthorhombic titanium aluminides such as Ti-22Al-27Nb and Ti-24.6Al-23.4Nb have a considerable strength advantage over nickel-base superalloys and other titanium aluminides from room temperature to 650°C. The tensile strength of Ti-22Al-27Nb was 1290 MPa at 650°C. Tensile curves of Ti-22Al-27Nb are shown in Figure 2. Ti-22Al-27Nb had good tensile elongation between room temperature and 650°C.

In the direct aged condition, corresponding to the data in Figures 1 and 2, Ti-22Al-27Nb had a microstructure fine Widmanstatten O+β_o transformation structure with a low volume fraction of prior O phase [6]. Ti-24.6Al-23.4Nb also had a two phase O+β_o microstructure, but with a very low volume fraction of β_o phase. It was not as strong as Ti-22Al-27Nb, but it had comparable room temperature tensile elongation. Greater dislocation homogeneity more of non-basal slip activity has been observed in Ti_2NbAl than in Ti_3Al [14]. This may account for the ductility of the nearly single O phase alloy Ti-24.6Al-23.4Nb at room temperature.

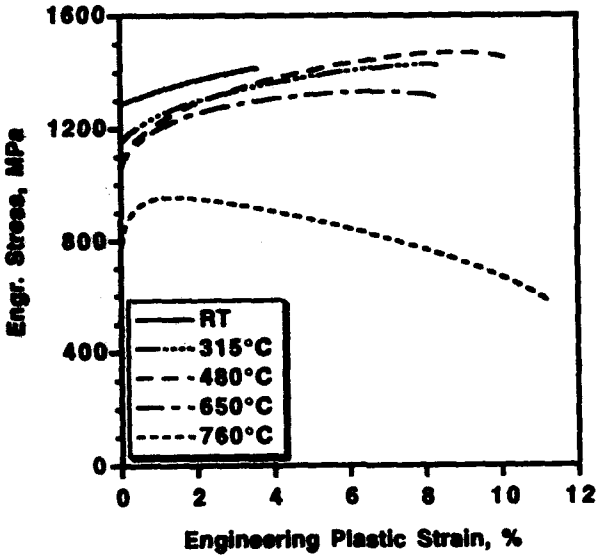


Figure 2. Engineering stress vs engineering plastic strain curves for Ti-22Al-27Nb.

Figure 3 is a compares the creep lifetime, room temperature tensile elongation and fracture toughness for several titanium aluminide alloys [15]. It shows the trade-off between creep resistance and low temperature ductility and fracture toughness for these alloys. The alloys, Ti-24Al-17Nb-1Mo, Ti-25Al-10Nb-3V-1Mo and Ti-25Al-8Nb-2Ta-2Mo all had 0.2% creep lifetimes of from 3 to 4 hrs at 650°C/315 MPa. Their fracture toughnesses were low, ranging from 14 to 19 MPa$\sqrt{m}$; lower than that of Ti-24Al-11Nb which was 25 to 27 MPa$\sqrt{m}$. Beta heat treated Ti-24.6Al-23.4Nb which consisted of the ordered orthorhombic O phase, also fit into the first group, but represented a large improvement in 0.2% creep lifetime relative to the Ti_3Al-based alloys. Its ductility at room temperature was 1.3%.

The higher fracture toughness alloys Ti-24Al-17Nb-0.5Mo and Ti-22Al-27Nb made up a second group. The fracture toughness of Ti-24Al-17Nb-0.5Mo was 26 MPa$\sqrt{m}$, but its 0.2% creep lifetime of was only 1.3 hrs; less than that of the first group of alloys. It sacrificed creep resistance for higher fracture toughness. Ti-22Al-27Nb in the as heat treated and heat treated plus aged condition [5, 6] had fracture toughnesses of from 26 to 31 MPa$\sqrt{m}$, respectively, but creep lifetimes as high or higher than that of the creep resistant alloys Ti-24Al-17Nb-1Mo, Ti-25Al-10Nb-3V-1Mo and Ti-25Al-8Nb-2Ta-2Mo. The 0.2% creep lifetime of Ti-22Al-27Nb at 650°C, 315 MPa was 4 hrs direct aged and 6 hrs after additional aging for 100 hrs at 760°C. The ternary ordered orthorhombic Ti_2NbAl-based alloys therefore achieved an increase in fracture

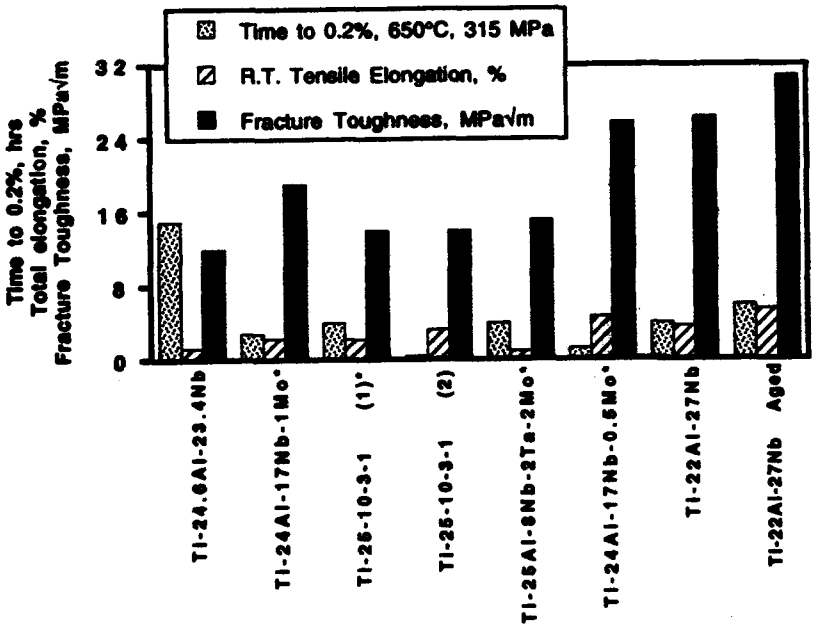


Figure 3. Comparison of the time to 0.2% creep strain at 650°C, 315 MPa (interpolated for the samples identified by an asterisk), total tensile elongation and fracture toughness of titanium aluminide alloys.

toughness and strength without the sacrifice in creep resistance characteristic of high fracture toughness Ti_3Al-based alloys.

Effect of Vanadium Alloy Additions: The effect of quaternary vanadium additions to Ti_2NbAl-based alloys was also studied. Vanadium additions produced a slight increase in the volume fraction of β_o phase for a given aluminum content, but there was evidence of vanadium alloying in both the β_o and O phases. Ti-23.6Al-22.9Nb-1.0V, which was heat treated at 1200°C/2 hrs + 900°C/600 hrs and water quenched, had approximately 50 v/o ordered orthorhombic laths in a β_o ordered beta matrix. The vanadium contents of the β_o and O phases were approximately 1.3 at.% and 0.7 at.%, respectively.

Large increases in the room temperature ductility were produced by quaternary vanadium additions. Table 1 shows tensile properties of ternary and vanadium-substituted quaternary Ti_2NbAl-based alloys. Room temperature tests were conducted in air; 650°C tests were in vacuum. The strain rate was $7x10^{-4}$/sec.

Addition of 5 at.% V to a Ti-22Al-25Nb base alloy increased the room temperature tensile ductility from 3.6% to 18.8% for direct aged samples. The microstructure of direct aged Ti-21.5Al-20Nb-5V consisted of a Widmanstatten

Table 1. Tensile properties of Ti-Al-Nb and Ti-Al-Nb-V alloys.

Alloy and Heat Treatment	TEST TEMP (°C)	0.2% YS (MPa)	UTS (MPa)	%El @ Failure
Ti-21.9Al-24.1Nb	R.T.	1257	1350	3.57
815°C/4hr	650	1049	1177	13.48
Ti-21.5Al-20Nb-5V	R.T.	900	1161	18.8
815°C/24hr+760°C/100hr	650	684	772	16.5
Ti-21.5Al-20Nb-5V	R.T.	750	943	12.5
1075°C+815°C/24hr+ 760°C/100hr	650	652	763	14.9
Ti-22Al-23Nb-1V 815°C/24hr+760°C/100hr	R.T.	1092	1308	8.8

transformation structure of O laths in a β_o matrix with some prior phase and allotriomorphic grain boundary phase, Figure 4. Its strength at room temperature and 650°C was lower than that of the ternary base alloy Ti-21.9Al-24.1Nb by 25 to 35%, indicating that ductility gains were at the expense of strength. The tensile strength of Ti-21.5Al-20Nb-5V was as high or higher than that of of Ti-25Al-10Nb-3V-1Mo or Ti-24Al-17Nb-1Mo at room temperature and 650°C, however [2-4].

Addition of 1 at.% vanadium also had an effect. The 8.8% room temperature tensile elongation of Ti-23.6Al-22.9Nb-1V was higher than that of the ternary base alloy Ti-21.9Al-24.1Nb. Its room temperature tensile strength was 1308 MPa, close to that of the base alloy which was 1350 MPa.

The room and elevated temperature tensile properties of the super-alpha titanium alloys IMI834 and Ti-1100 [16, 17] are tabulated in Table 2. Ti-21.5Al-20Nb-5V had nearly twice the room temperature elongation of both of these alloys, was stronger at room temperature, and was nearly twice as strong at 650°C.

The fracture toughness of a vanadium-modified Ti_2NbAl-base alloy, Ti-21.5Al-20Nb-5V, was determined using fatigue precracked bend samples. Two tests gave K_{1C} values of 29.3 and 30.8 MPa$\sqrt{m}$ (an average of 30.1 MPa$\sqrt{m}$). This fracture toughness was comparable to values obtained for the high fracture toughness alloy Ti-22Al-27Nb.

The effect of vanadium on creep properties is shown in Table 3. The 0.2% creep lifetime for Ti-23.6Al-22.9Nb-1V at 650°C and 315 MPa was 2.1 hours compared to 6.1 hrs for Ti-24Al-23.3Nb. The alloy Ti-23.6Al-22.9Nb-1V had a lower volume fraction of O phase than Ti-24Al-23.3Nb, and the difference in creep behavior may be partly due to the relative properties of O and β_o phases. The

Table 2. Tensile properties of super-alpha titanium alloys.

SAMPLE NUMBER	TEST TEMP (°C)	0.2% YS (MPa)	UTS (MPa)	%Elong Fail
IMI834, 1045°C+700°C	RT	959	1035	10.1
IMI834, 1045°C+700°C	650	543	651	15.6
Ti-1100, 590°C Direct Aged	RT	897	987	10.5
Ti-1100, 590°C Direct Aged	650	524	635	16.5

Table 3. Creep properties of ternary and quaternary Ti_2NbAl-based alloys at 650°C, 315 MPa.

Alloy	Heat Treatment	0.2%	1%
Ti-24Al-23.3Nb	1160C+815C	6.1	91.7
Ti-23.6Al-22.9Nb-1V	1075C+815C+760C	2.10	39.10

creep resistance of Ti-23.6Al-22.9Nb-1V was greater than that of Ti-24Al-17Nb-0.5Mo which had a 0.2% creep lifetime of 1.3 hrs under the same conditions.

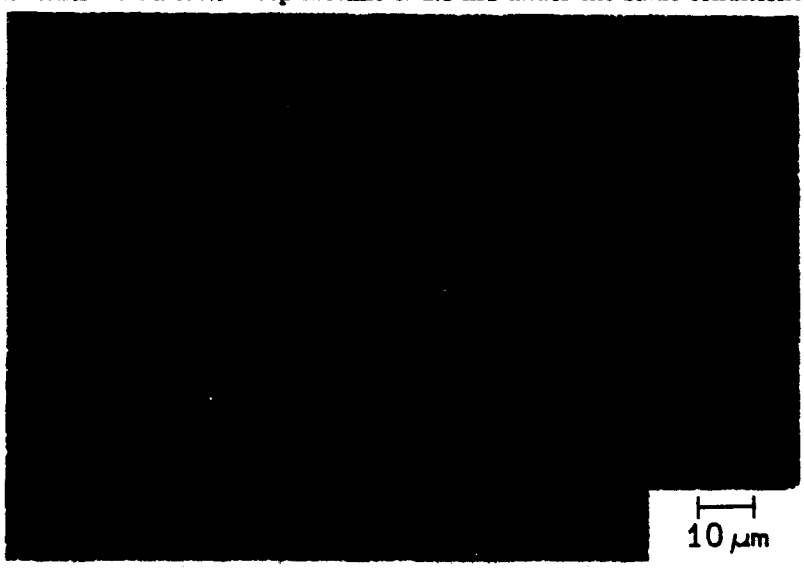


Figure 4. The microstructure of Ti-21.5Al-20Nb-5V after extrusion and a heat treatment of 815°C/24 hr + 760°C/100 hr.

Summary and Conclusions

The ordered orthorhombic alloys based on the titanium aluminide Ti_2NbAl represent a new class of titanium aluminide alloys which have higher

strength and higher fracture toughness than current Ti_3Al-base alloys. Their most distinct characteristic was high specific strength relative to other titanium aluminide and nickel-base superalloys, but alloying with vanadium produced alloys with as much as 18.8% room temperature tensile elongation. Tensile elongation of this magnitude is usually associated with disordered titanium alloys rather than titanium aluminides. The flexibility that is associated with the breadth of properties available in these alloys suggest that many aircraft engine applications may be possible with slight modifications of composition or processing to tailor the properties for each application.

References

1. M.J. Blackburn and M.P. Smith, "Titanium Alloys of the Ti_3Al Type", U.S. Patent # 4,292,077,
2. D.P. DeLuca, *et al.*, "Fatigue and Fracture of Titanium Aluminides", Report # WRDC-TR-89-4136, U.S. Air Force, WRDC, February, 1990.
3. M.J. Blackburn and M.P. Smith, "Titanium Aluminum Alloys Containing Niobium, Vanadium and Molybdenum", U.S. Patent # 4,716,020, Sept. 27, 1982.
4. M.J. Blackburn and M.P. Smith, "Improved Toughness Alloys Based Upon Titanium Aluminides", Report # WRDC-TR-89-4095, U.S. Air Force, WRDC, October, 1989.
5. R.G. Rowe, *et al.*, "Tensile and Creep Behavior of Ordered Orthorhombic Ti_2AlNb-Based Alloys", Mat. Res. Soc. Symp. Proc., 213, 703-708, (1991).
6. R.G. Rowe, "The Mechanical Properties of Titanium Aluminides Near Ti-25Al-25Nb". in Microstructure/Property Relationships in Titanium Alloys and Titanium Aluminides. Edited by Y. Kim and R.R. Boyer, TMS, AIME, Warrendale, OH, 1990, 387-398
7. R.G. Rowe, "Recent Developments in Ti-Al-Nb Alloys", in High Temperature Aluminides and Intermetallics. Edited by C.T.Liu, S. H. Whang D.P. Pope and J.O. Stigler, TMS, AIME: Warrendale, OH. 1990, p. 375-401.
8. D. Banerjee, "A New Ordered Orthorhombic Phase in a Ti_3Al-Nb Alloy", Acta Met., 36 p. 871-882, (1989).
9. B. Mozer, *et al.*, "Neutron Powder Diffraction Study of the Orthorhombic Ti_2AlNb Phase", Scripta Met. et Mater., 24, 2363-2368, (1990).
10. L.A. Bendersky, W.J. Boettinger, and A. Roytburd, "Crystallography and Thermodynamics of Hierarchical Structures of $(Ti,Nb)_3Al$ Alloys", in Proceedings, Japan Inst. of Metals Intermetallics Symposium-6, Sendai, Japan, June 1991. To be published.

11. R.G. Rowe, *et al.*, "Phase Equilibria in Ternary Ti-Al-Nb Alloys Near Ti_2NbAl". in Proceedings, Seventh World Conference on Titanium, San Diego, CA June 1992. TMS-AIME, Warrendale, OH.

12. J.M. Larsen, *et al.*, "Titanium Aluminides for Aerospace Applications". in High Temperature Aluminides and Intermetallics. C.T.Liu, S. H. Whang D.P. Pope and J.O. Stiegler, TMS-AIME, Warrendale, PA, 1989, p. 521-556

13. "High Temperature, High Strength Nickel-Base Alloys", Report # The International Nickel Company, Inc. 3rd edition, July 1977.

14. D. Banerjee, R.G. Rowe, and E.L. Hall, "Deformation of the Orthorhombic Phase in Ti-Al-Nb Alloys", Mat. Res. Soc. Symp. Proc, 213, p. 285-290, (1991).

15. R.G. Rowe, "Advanced Ti_3Al-Base Alloy Property Comparison". in Synthesis, Processing and Modelling of Advanced Materials. ASM International, Paris, France. Sept. 1991, To be published,

16. "Ti-1100", Report # Titanium Metals Corporation, Henderson, NV, 1987.

17. "IMI834", Report # IMI Titanium Limited, Birmingham, UK., 1990.

Acknowledgements

The author would like to acknowledge the assistance of Mrs. R. L. Casey and Mr. R. J. Zabala in all aspects of the experimental work. He would also like to acknowledge ongoing discussions with Dr. D. Banerjee, DMRL, Hyderabad, India on the phase constitution of ternary Ti-Al-Nb alloys. This work was supported by GE Aircraft Engines under the Independent Research and Development Program.

STUDY OF CREEP CRACK GROWTH BEHAVIOR OF Ti-24Al-11Nb

M. Khobaib

The University of Dayton Research Institute
300 College Park
Dayton, Ohio 45469-0128

Abstract

Titanium aluminides show great promise for gas turbine engine structural applications due to their high specific strength at elevated temperature. The current interest to use these materials at elevated temperature over a long period of time has drawn attention to the time dependent sustained load behavior. This investigation deals with the creep crack growth behavior of a model Ti_3Al intermetallic Ti-24Al-11Nb. Creep crack growth tests were conducted over the temperature range of 650-800°C. Side-grooved compact tension specimens were used to enhance a plane strain condition along the intended crack plane. Sustained load tests were conducted both in laboratory air and in an inert environment of a vacuum of 10^{-6} torr. The influence of environment and temperature on crack growth behavior is studied by analyzing the experimental data in the form of K vs da/dt. The failure mode in air was observed to be transgranular at all temperatures except at 800°C, where the fracture appears to change partially to intergranular. However, the failure mode of specimens tested in vacuum appeared intergranular, at all temperature.

Introduction

There is an ever increasing demand from aerospace industry for alloys possessing low densities and elevated temperature high strengths. Recent advances in processing technology have led to the emergence of a series of high temperature intermetallic compounds. In particular, alloys based on the alpha-2 intermetallic Ti_3Al exhibit some attractive properties and show promise as candidate material for structural components of advanced aircraft and hypervelocity vehicles. However, intelligent use of these materials requires the ability to predict the life of components under service conditions. A previous study has shown that their deformation and failure modes are very sensitive to environment under monotonic loading (1). Very little information is available on the elevated temperature crack growth characteristics of titanium aluminide and its sensitivity to environment. Since these intermetallics are potential candidates for high temperature structural components of aircraft which will be exposed to elevated temperature over a long period of time, it is important to understand the creep crack growth behavior of these materials.

Conventionally, CCG behavior is studied by conducting sustained load tests on precracked specimens, e.g; compact tension (CT) single edge notch (SEN), etc. Several studies have

Titanium '92
Science and Technology
Edited by F.H. Froes and I. Caplan
The Minerals, Metals & Materials Society, 1993

identified a number of parameters such as the linear elastic stress intensity factor, K, the non-linear elastic parameter, J* integral, the C* energy integral, reference stress, σ_{ref}, etc (2-7). Of these K has been successfully used as a correlating parameter for sustained load, thermal and fatigue crack growth of Inconel 718 and Rene N4 by several investigators (2-7). This investigation was conducted to determine the effects of environment and temperature on CCG rate of a representative alpha-2 base titanium aluminide, Ti-24Al-11Nb. Detailed fractographic analysis was performed to correlate the observed creep crack growth rates with the mechanisms of failure.

Experimental

The material used in this investigation was the alpha-2 base intermetallic Ti_3Al alloyed with niobium; Ti-24Al-11Nb (atomic percent). The material was obtained in the form of 1.14 cm thick cross-rolled plate. The plate was given a two-step heat treatment consisting of a beta solution at 1149°C (2100°F) for one hour in vacuum, followed by forced cooling with argon and a 760°C (1400°F) age for one hour in vacuum. This produced a two-phase basketweave, Widmanstatten morphology with no preferred orientation (8).

The laboratory air crack growth rate data were generated from standard CT specimens having a nominal width W of 40 mm; a thickness B of 10 mm; mini-compact tension specimens (B=5mm, W=24.4mm) were used for all vacuum tests. A selected number of tests were conducted in laboratory air with mini-compact tension specimen also to compare the data obtained from standard CT. No measurable difference was noticed in these tests. All specimens were side-grooved nearly 25% of thickness to enhance a plane strain condition (9) along the intended crack plane. Figure 1 shows the dimensions of a side-grooved mini-compact tension specimen.

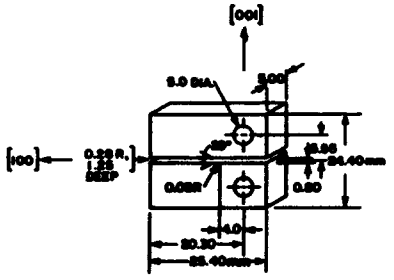


Figure 1 - Side-Grooved Sub-Compact Tension Specimen.

Creep crack growth tests were conducted both in laboratory air and vacuum over a temperature range of 650-800°C. The tests in laboratory air were conducted on a separate Archweld creep frame using a two zone box furnace to heat the specimen. The furnace was specially designed with viewing ports for optical crack measurements. Crack lengths were recorded at uniform time intervals using a low-magnification travelling microscope. The vacuum tests were conducted in a CENTORR furnace which was incorporated into an Archweld creep frame. Typical vacuum during test was of the order of 10^{-6} torr. The crack length was calculated from the compliance recorded periodically during the test. Compliance was obtained from displacement data using a water cooled (MTS) extensometer mounted on the specimen using special notches to hold the extensometer in place during unloading and loading of the specimen. The crack lengths and compliances obtained from air and vacuum tests were then converted to da/dt-vs-K plots (where a is the crack length, and t denotes time). K, calculated from linear elastic fracture mechanics, appears to be the most suitable parameter (2-7). The data were all reduced and plotted with the aid of a computer using K-calculation.

The fracture surface of the specimens tested were examined optically. In most cases detailed fractographic analysis were followed by scanning electron microscope (SEM) observations.

Results and Discussion

The creep crack growth behavior of Ti-24Al-11Nb in laboratory air is shown in Fig. 2.

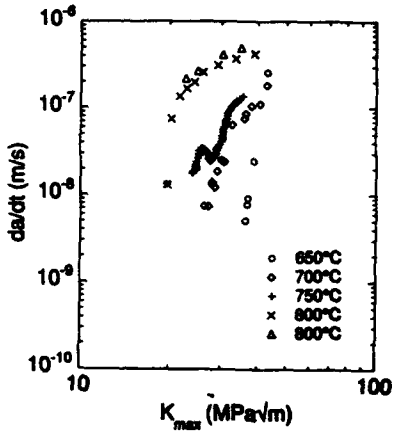


Figure 2 - Creep Crack Growth Behavior of Ti-24Al-11Nb in Laboratory Air.

The higher CCG rate with increasing temperature is obvious with the difference in CCG rate being more pronounced at the highest temperature. Nearly an order of magnitude increase in crack growth occurs at 800° as compared with crack growth rates at 700°C. At the lower temperature of 650°C, the CCG behavior becomes very sensitive to K value. It was very difficult to obtain CCG data at this temperature due to such high sensitivity of K. A very high stress intensity level (approaching fracture toughness K_{1c}) was required to obtain CCG data at this temperature. This may be due to very limited sensitivity of this material to environmental cracking at this temperature, as well strong contribution from local creep leading to the blunting of the crack tip. With an increase in temperature, the environmental contribution is enhanced which apparently leads to CCG acceleration. The higher CCG rates at 800°C are likely due to such environmental contribution.

The increased sensitivity of K with negligible environmental influence (as shown in Fig. 2 for 650°C) is also quite evident from results obtained from tests conducted in vacuum, Figure 3. The CCG plots at all temperatures in the range of 650°C-800°C show very high slopes, again indicating high degree of sensitiveness of crack growth to K. The temperature dependence of CCG in vacuum is quite obvious from Fig. 3.

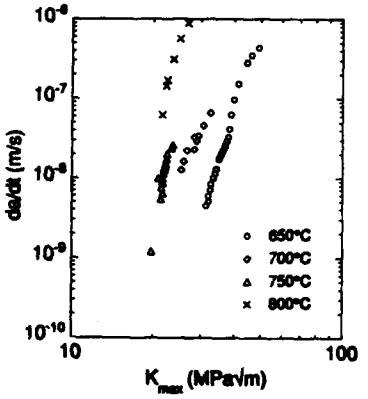


Figure 3 - Creep Crack Growth Behavior of Ti-24Al-11Nb in Vacuum.

It was surprising to find higher CCG rates at 800°C in vacuum as compared with CCG rates obtained from laboratory air test. This is in contrast with results obtained from most metallic materials (3,4), where an environment such as laboratory air is known to accelerate the crack growth. Figure 4 compares the CCG behavior obtained in laboratory air with that observed in vacuum at 650°C.

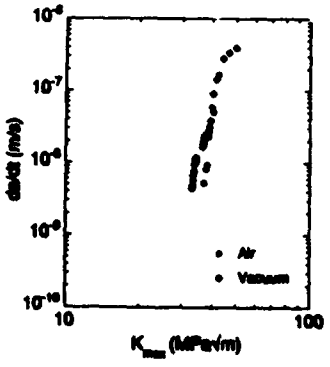


Figure 4 - Creep Crack Growth Behavior of Ti-24Al-11Nb in Laboratory Air and Vacuum at 650°C.

Apparently the influence of laboratory air at 650°C is negligible. Similar results were obtained from tests conducted at 700°C and 750°C as shown in Figs. 2 & 3. However, the CCG rate in vacuum is noted to be higher than that in laboratory air at 800° C, Fig. 5.

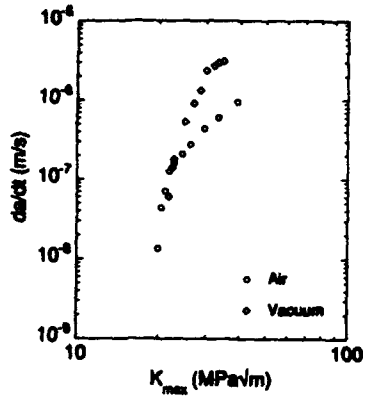


Figure 5 - Creep Crack Growth Behavior of Ti-24Al-11Nb in Laboratory Air and Vacuum at 800°C.

It is suggested that this difference in CCG arises from significant crack branching observed with tests conducted in laboratory air. Apparently the crack branching is the result of diffusion of embrittling species first into the grain boundaries and then into the grain itself. The latter is responsible for transgranular subcracks. Such secondary cracking is expected to retard the growth of the main crack, as will be discussed further.

Detailed analyses of fracture surfaces were conducted to understand the mechanisms of crack growth process in this material. Figure 6 (a-d) shows a series of fractographs which represent the fracture surface of specimens tested at 650, 700, 750, and 800°C in laboratory air. The failure mode appears to be transgranular at all temperatures except at 800°C, where the fracture appears to be mixed mode. In general (from 650-750°C) the failure is cleavage like and crystallographic. In contrast to the fracture surface features obtained in laboratory air, the failure mode of specimens tested in vacuum at all temperatures (650-800°C) appear intergranular. This is shown in the series of photographs in Fig. 7 (a-d).

This unusual behavior in fracture cannot be easily explained. The titanium aluminide has a basketweave structure with random distribution of α-plates within parent beta grain α colonies. The α is known to segregate around prior beta boundary and is stabilized by oxygen. Previous study has shown α case to develop ring cracking under load when exposed to laboratory air (1). The cracking initiates at the intersection of α/α plate interface with surface. During creep crack growth the simultaneous interaction of temperature and environment with the local state of stress at the crack tip leads to a complex crack growth mechanism. In some cases, depending on stress, temperature and state of environment the independent role of temperature and environment sets up competing mechanisms and the failure occurs under the dominant effect. In other instances, the combined effect of temperature and environment results in synergism leading to accelerated crack growth. Generally, the situation in service condition is more complex and the effects of temperature and environment on the creep crack growth process is not clearly understood. Some speculations are presented in the light of the experimental observations. It is suggested that the transgranular failures of specimens tested at 650, 700 and 750°C in laboratory air results from the extensive cracking of this material. Ti-24Al-11Nb is known to develop extensive cracking when exposed to elevated temperature

under sustained load in laboratory air. In the laboratory air, the availability of the excess embrittling species at the crack tip alters the local state of stress. It is speculated that in the laboratory air, the kinetics of embrittlement leading to the cracking of the surrounding area near the crack tip is faster than the of crack advance under the K level used. The environmental influence leads to extensive cracking around the crack tip setting up multiple crack advance sites. Thus, the crack growth process is altered and the crack advance occurs at the site with the highest stress concentration. This process continues all along the whole crack front and the failure becomes transgranular in laboratory air. In contrast, in vacuum at a pressure of 10^{-6} torr, the limited available amount of embrittling species are sucked in by the preferential sites along in the grain boundary. Hence the embrittlement occurs only along the grain boundary. Thus, in vacuum the crack advances along the grain boundary leading to intergranular failure.

At 800°C the failure mechanism in laboratory air also changes from transgranular to mixed mode. This is believed to be the result of increased activity of grain boundary sliding. The creep failure at this temperature was found to be mainly grain boundary sliding.[1] As discussed earlier, several mechanisms are operative under all the test conditions. At 800°C, it is speculated that the increased contribution from grain boundary sliding changes the failure mechanism to be mixed mode as compared to transgranular at 750°, 700° and 650°C.

References

1. M. Khobaib et al., "Mechanical Properties for Advanced Engine Materials," (Technical Report, UDR-TR-89-43, University of Dayton Research Institute, February 1989).

2. M. Khobaib et al., "Research on Mechanical Properties for Engine Life Prediction," (AFWAL-TR-88-4062, Air Force Wright Aeronautical Laboratories, Air Force Materials Laboratory, Wright-Patterson Air Force Base, Ohio, May 1988).

3. M. Stucke et al., "Environmental Aspects in Creep Crack Growth in a Nickel Base Superalloy," (Proceeding of International Conference on Fracture 6, New Delhi, India, December 1984), 3967-3975.

4. M. Khobaib, T. Nicholas, and R.V. Srivats, "Role of Environment in Elevated Temperature Crack Growth Behavior of Rene N4 Single Crystal," Environmentally Assisted Crack: Science and Engineering, ASTM, STP 1049, ed. W.B. Lisager, T.W. Crooker and B.N. Leis (Philadelphia, PA: American Society for Testing and Materials, 1990) 319-333.

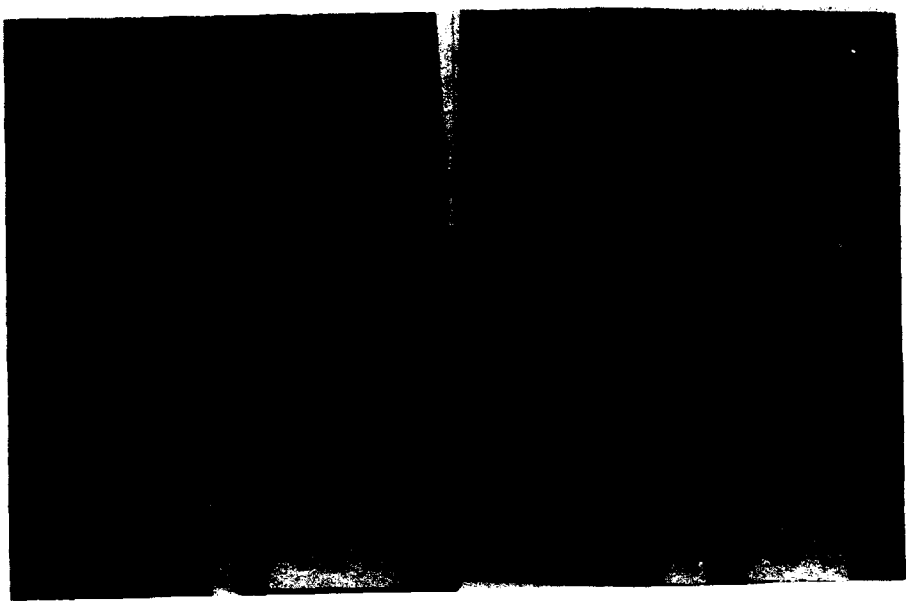
5. K. Sadananda and P. Shahinian, "Elastic-Plastic Fracture Mechanics for High Temperature Crack Growth," Fracture Mechanics: Twelfth Conference, ASTM STP 700, (1980), 152-163.

6. K. Sadananda and P. Shahinian, "Creep Crack Growth in Alloy 718," Metallurgical Transactions, 8A (March 1977), 439-449.

7. J.M. Larsen and T. Nicholas, "Cumulative-Damage Modeling of Fatigue Crack Growth in Turbine Engine Materials," Engineering Fracture Mechanics, 22 (1985), 713-730.

8. S.J. Balsone et al., "Environment and Frequency Effects on Crack Growth in a Titanium Aluminide Alloy," Elevated Temperature Crack Growth, ed. S. Mall and T. Nicholas, 18 (MD) (New York, NY: American Society of Mechanical Engineers, 1990), 87-91.

9. F. Shih, H.D. DeLoronzi, and W.R. Andrews, International Journal Fracture, 13 (1977), 544-548.



CRACK GROWTH DIRECTION

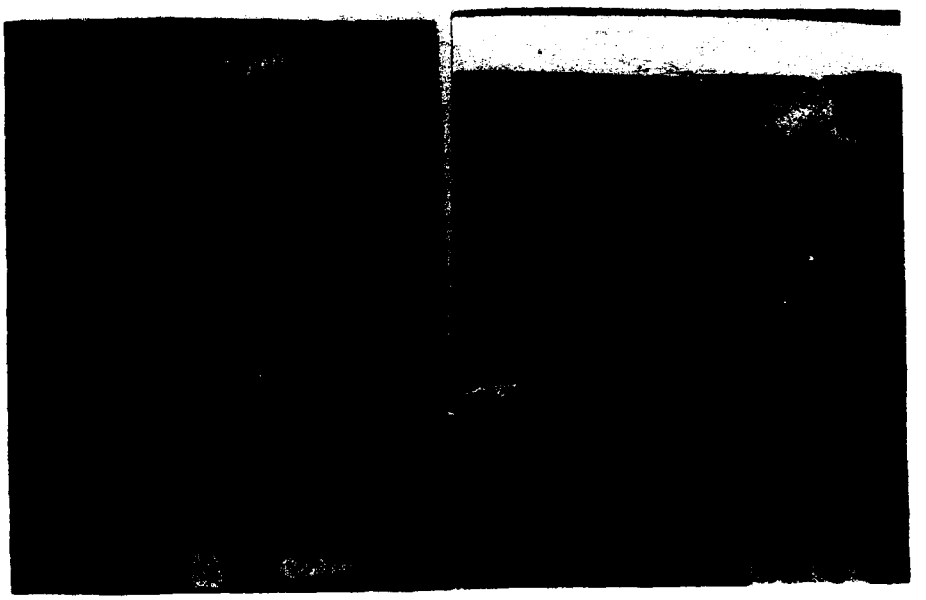
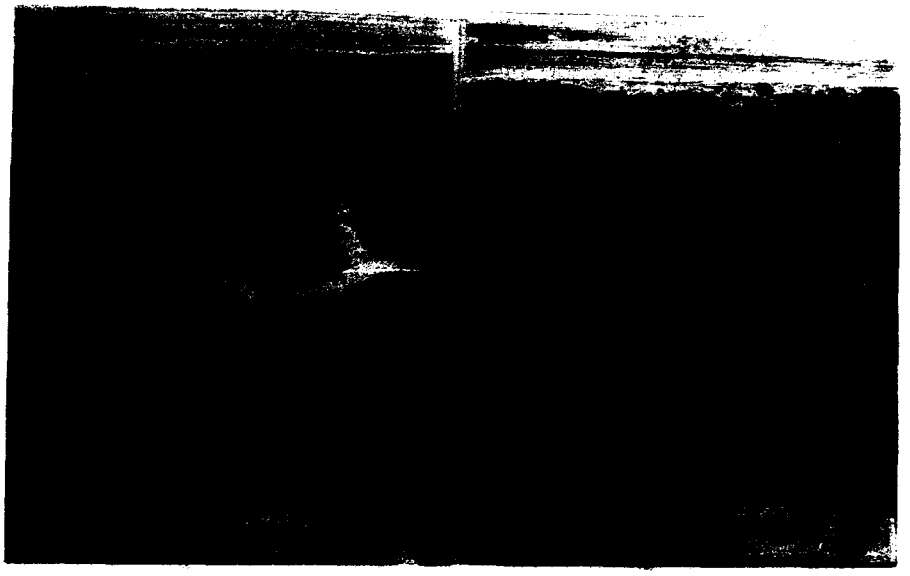


Figure 6 - Fracture Surface of Specimens Tested at a) 650°C, b) 700°C, c) 750°C and d) 800°C in Laboratory Air.



CRACK GROWTH DIRECTION

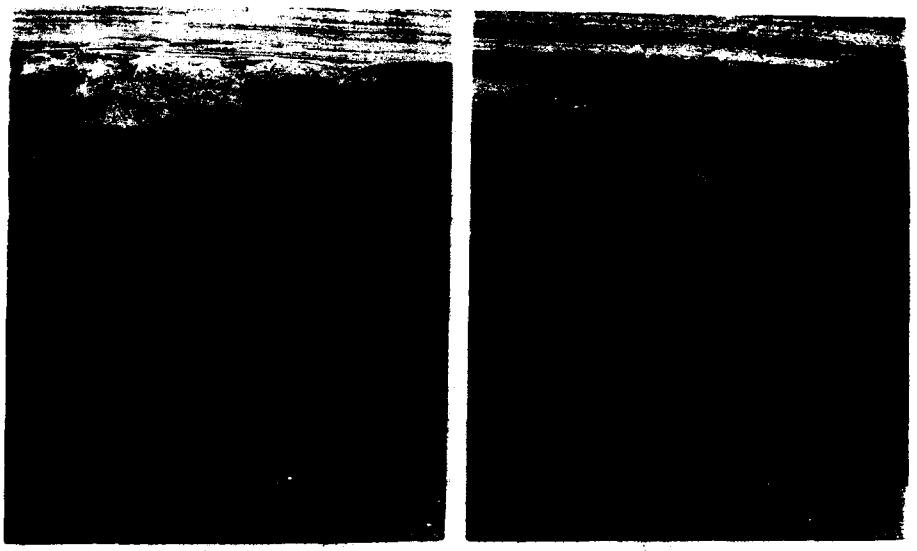


Figure 7 - Fracture Surface of Specimens Tested at a) 650°C, b) 700°C, c) 750°C and d) 800°C in Vacuum.

AN INVESTIGATION OF THE EFFECTS OF HEAT TREATMENT ON THE MICROSTRUCTURE AND MECHANICAL BEHAVIOR OF $\alpha_2+\beta$ FORGED Ti-24Al-11Nb

W. O. Soboyejo

Edison Welding Institute
1100 Kinnear Road
Columbus, Ohio 43212

Abstract

The effects of heat treatment on the microstructure and mechanical behavior of $\alpha_2+\beta$ forged Ti-24Al-11Nb (compositions quoted in atomic % unless stated otherwise) produced by powder metallurgy (PM) are reported in this paper. This includes a study of the effects of cooling rate and aging on microstructural evolution and stability. Fast cooling from the β phase field is shown to promote the formation of subgrains. These subgrains are annealed out during subsequent heat treatment in the $\alpha_2+\beta$ phase field which also results in the nucleation of cracks and grain boundary α_2 allotriomorphs at prior β grain boundaries. Slow cooling from the β phase field followed by aging in the $\alpha_2+\beta$ phase field is shown to result in the formation of a relatively stable Widmanstätten microstructure and a good balance of compressive and tensile properties.

Introduction

Since the original development of the Ti-24Al-11Nb alloy by Blackburn et al. (1,2), there have been intensive efforts to characterize the microstructure/ substructure (3-7) and the mechanical behavior (1,2,6-16) of this alloy. The microstructural studies have indicated the potential for the formation of the ordered α_2 phase based on the Ti_3Al (DO_{19} crystal structure) (6,7), the ordered β_o structure based on the TiNbAl (B2 crystal structure) (6,7), an orthorhombic phase with the space group Cmcm (16), and an ω-type phase with a $B8_2$ structure (17). The microstructural evolution that occurs in Ti-24Al-11Nb during thermal exposure can therefore be very complex, and its influence on mechanical behavior is not fully understood. The results of a systematic investigation of the effects of annealing on the microstructural evolution and mechanical behavior of $\alpha_2+\beta$ forged Ti-24Al-11Nb are presented in this paper. Tensile and compressive properties are related to microstructural parameters such as lath size, prior β grain size, and β volume fraction. The effects of deformation on microcracking are also discussed for fracture under monotonic loading conditions.

Experimental Procedures

The material used in this investigation was supplied by the Alcoa Research Laboratory, PA, in the form of a billet. It was produced by drop forging of Ti-24Al-11Nb powder in the $\alpha_2+\beta$ phase field into a pancake shape (approximately 280 mm in diameter and 12.3 mm in

Titanium '92
Science and Technology
Edited by F.H. Froes and I. Caplan
The Minerals, Metals & Materials Society, 1993

phase field into a pancake shape (approximately 260 mm in diameter and 12.3 mm in thickness). The billet was subsequently annealed at 1093°C for 0.5 h, followed by a fan air cool. This resulted in the Widmanstätten microstructure with aligned packets of ~3 μm wide elongated α_2 platelets (Figure 1). The as-received (AR) material consisted of 13.4 wt. % Al, 22.1 wt. % Nb, 0.075 wt. % O, 0.017 wt. % C, 0.0042 wt. % H, 0.0078 wt. % N and a balance of Ti. The alloy had a 0.2% offset yield stress of 464 MPa, an ultimate tensile stress of 593 MPa, a total strain to failure of 3.9%, and a fracture toughness of 23.4 MPa√m at room-temperature in the AR condition. The effects of heat treatment on microstructure were investigated using cubic metallographic samples that were encapsulated in evacuated (~10^{-4} Torr) capsules prior to annealing. The heat treatment schedules were designed to investigate the following:

(1) The effect of annealing in the $\alpha_2+\beta$ phase field
(2) The effect of cooling rate after annealing in the β phase field
(3) The effect of aging in the $\alpha_2+\beta$ phase field after annealing in the β field.



Figure 1 - Microstructure of as-received Ti-24Al-11Nb ($\alpha_2+\beta$ forged and annealed at 1093°C/0.5 h/FAC).

The metallographic samples were given a final surface polish on a 1 μm diamond wheel, and etched in Kroll's solution for approximately 10 s prior to examination by optical and scanning electron microscopy. Quantitative estimates of the lath sizes and the prior β grain sizes were also obtained using linear intercept techniques (18), and phase analyses of microstructural constituents were conducted using x-ray diffraction techniques. The compression and tension tests were carried out at a strain rate of 5×10^{-4} s^{-1}. The compression tests were performed on 6.35 × 6.35 × 6.35 mm^3 specimens at 25, 540, 650 and 760°C, and the tension tests were conducted at room-temperature on smooth cylindrical specimens. After testing, longitudinal sections parallel to the stress (loading) axis of the deformed compression and gage sections of the tensile specimens were examined by optical microscopy to investigate the incidence of cracking during deformation at room-temperature.

Results and Discussions

(a) Microstructure

The microstructural features in Ti-24Al-11Nb are similar to those reported previously for conventional $\alpha_2+\beta$ titanium alloys (21). However, some unique microstructural characteristics were observed, as discussed in this section. Annealing of the alloy in the $\alpha_2+\beta$ phase field at 815 and 982°C did not result in significant coarsening of the α_2 laths, and the average lath width was approximately 3 μm before and after annealing. This is shown in Figure 2 and Table I. The alignment of the α_2 colonies observed in the as-received material was maintained

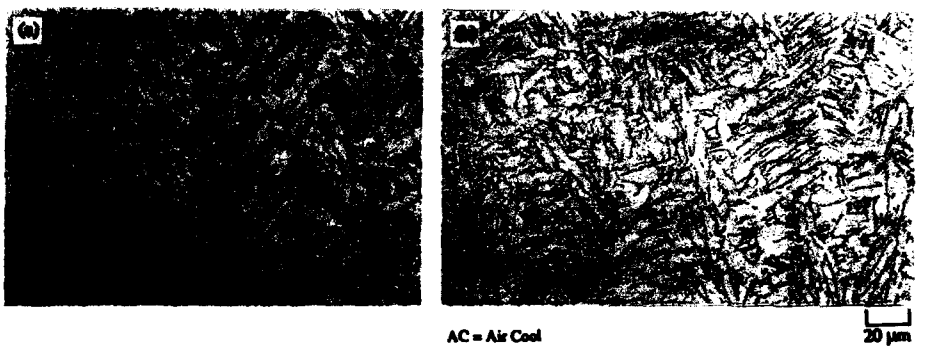


Figure 2 - Microstructure of Ti-24Al-11Nb annealed in the $\alpha_2+\beta$ phase field. (a) 815°C/5.5 h/AC and (b) 982°C/4 h/AC.

after annealing in the $\alpha_2+\beta$ phase field, and there was no evidence of phase decomposition at the $\alpha_2+\beta$ interfaces. However, x-ray diffraction revealed the existence of the orthorhombic phase (16) after annealing in the $\alpha_2+\beta$ phase field at temperatures between 815 and 1093°C.

Cooling rate had a significant effect on microstructure after annealing in the β phase field (Figure 3 and Table I). With the exception of fan air cooling, fast cooling from the β phase field followed by air cooling (AC) or water quenching in a quartz capsule (WQ) resulted in the formation of subgrains within large (700-1000 μm) prior β grains, as shown in Figs. 3a and 3c.

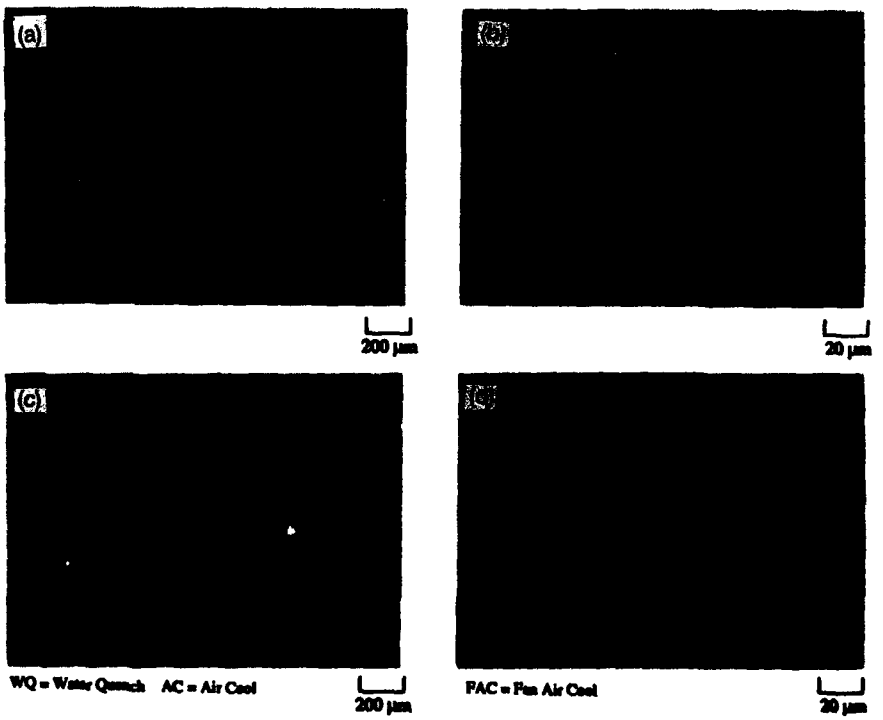


Figure 3 - Effects of fast cooling from the β phase field on microstructure. (a,b) 1200°C/0.5 h/WQ and (c,d) 1200°C/0.5 h/AC.

TABLE I. - EFFECT OF HEAT TREATMENT ON MICROSTRUCTURAL PARAMETERS

Heat Treatment	Prior β Grain Size (μm)	Sub-grain Size (μm)	α_2 Lath Width (μm)	Proportion of β Grains
1200°C/0.5 h/WQ	766	386	--	--
1200°C/0.5 h/WQ + 760°C/8h/AC	914	--	--	--
1200°C/0.5 h/WQ + 815°C/8 h/AC	913	--	--	--
1200°C/0.5 h/FAC	985	--	--	--
1200°C/0.5 h/FAC + 760°C/8 h/AC	981	--	--	--
1200°C/0.5 h/FAC + 815°C/8 h/AC	701	--	--	--
1200°C/0.5 h/AC	1020	370	--	--
1200°C/0.5 h/AC + 760°C/8 h/AC	998	--	3.2	16
1200°C/0.5 h/AC + 815°C/8 h/AC	918	--	3.8	16
1200°C/0.5 h/FC	606	--	--	--
1200°C/0.5 h/FC + 760°C/8 h/AC	521	--	3.6	22
1200°C/0.5 h/AC + 815°C/8 h/AC	[illegible]	--	--	--
As-received (1093°C/0.5 h/FAC)	--	--	3.3	26
815°C/5.5 h/AC	--	--	2.6	18
982°C/4 h/AC	--	--	3.3	21

WQ = water quench
FAC = fan air cool
AC = air cool
FC = furnace cool

TABLE II. - EFFECT OF HEAT TREATMENT ON MICROSTRUCTURE AND MECHANICAL PROPERTIES

Heat Treatment/ Condition	Proportion of β Phase (%)	Tensile Properties (25°C)			0.2% Offset Compressive Yield Stress (MPa) (25°C)	0.2% Offset Compressive Yield Strength (MPa)			Predicted Tensile Yield Stresses (MPa)
		Total Strain to Failure (%)	0.2% Offset Yield Stress (MPa)	Ultimate Tensile Stress (MPa)		540°C	650°C	760°C	
As-received (1093°C/0.5 h/FAC)	26	3.9	464	593	656				580
1200°C/0.5 h/AC + 760°C/8 h/AC	16	--[a]	--[a]	582	620	446	453	483	585
1200°C/0.5 h/AC + 815°C/8 h/AC	16	--[a]	--[a]	502	609	486	454	640	585
1200°C/0.5 h/FC + 760°C/8 h/AC	22	2.1	521	665	659	454	430	371	574
815°C/5.5 h/AC	18	--[a]	--[a]	340	577	437	438	389	567
982°C/4 h/AC	21	--[a]	--[a]	356	582	384	408	336	572

The sub-grains are more clearly visible in the microstructure of the water quenched sample (Figure 4a), and they are presumed to form as a result of strain accommodation due to dislocation interactions that occur during fast cooling from the β phase field. It is important to note that the subgrains were observed consistently in water-quenched and air-cooled samples, i.e., they were not due to etching effects.

Very fine acicular α_2 laths were observed at the boundaries of the prior β grains (Figs. 3b and 3d) which appear to have a well defined orientation relationship with the prior β grain boundaries, and are arranged in approximately parallel strips in the vicinity of the prior β grain boundaries. In general, however, the effects of cooling rate were similar to those obeserved in conventional α + β titanium alloys (21), with the lath sizes within the transformed β grains increasing with decreasing cooling rate from the β phase field. Furnace cooling from the β phase field resulted in the formation of an inhomogeneous Widmanstätten microstructure (Figure 4).

Annealing in the α_2+β phase field after fast cooling from the β phase field resulted in some interesting microstructural features. Water quenching from the β phase field followed by aging in the α_2+β phase field was found to promote the formation of cracks within the allotriomorphs that are formed along prior β grain boundaries. This is shown in Figure 5 using scanning electron micrographs. Annealing in the α_2+β phase field after fast cooling from the

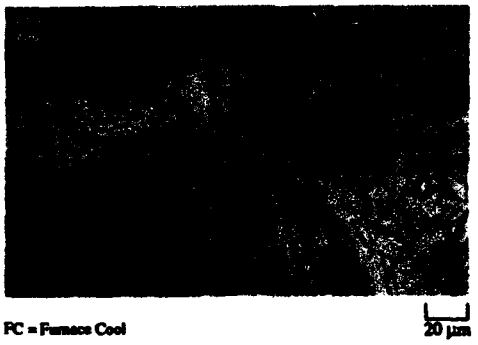


Figure 4 - Inhomogeneous Widmanstätten microstructure formed after furnace cooling from the β phase field (1200°C/0.5 h/FC).

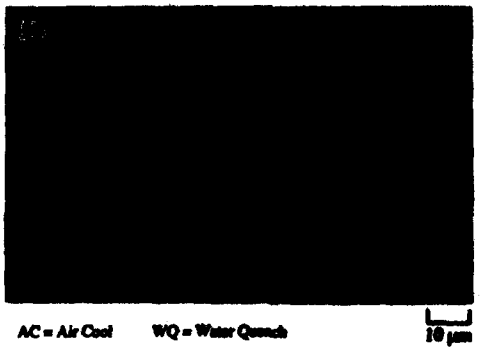


Figure 5 - Cracks formed after annealing at 1200°C/0.5 h/WQ + 760°C/8 h/AC.

β phase field also promoted significant coarsening of the α_2 lath widths (Figs. 3 and 6) in the resulting Widmanstätten microstructures, and the α_2 lath widths were comparable to those observed in the as-received material (Table I). Prolonged annealing in the $\alpha_2+\beta$ field at 650°C promoted the decomposition of the microstructures produced after fast cooling from the β phase field. Finally, in this section, it is important to stress that the microstructures produced by fast cooling from the β field and aging in the $\alpha_2+\beta$ field are clearly unstable. In contrast, the Widmanstätten microstructures produced by furnace cooling from the β field and annealing in the $\alpha_2+\beta$ field remain stable during thermal exposure in the $\alpha_2+\beta$ field. The Widmanstätten microstructure produced by such treatment does not decompose significantly even after exposure at 650°C for 24 h in vacuum (10^{-4} Torr) which promotes rapid decomposition of material that was fan air-cooled from 1200°C.

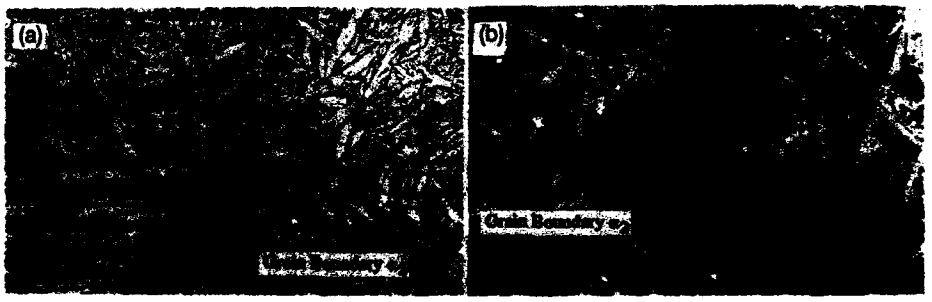


Figure 6 - Microstructures produced after annealing at (a) 1200°C/0.5 h/AC + 760°C/8 h/AC and (b) 1200°C/0.5 h/AC + 815°C/8 h/AC.

(b) Compression

The room- and elevated-temperature compression data are presented in Table II. The alloys retained attractive elevated-temperature strengths up to 760°C. There was a drop of 40-80 MPa in the strength of the as-received material upon annealing, and a difference of approximately 150 MPa was observed between the room- and elevated- temperature compression strengths. With the exception of the anomalously high compression strength obtained at 760°C for material annealed at 1200°C/0.5 h/AC + 815°C/8 h/AC, the compression strengths were similar for all the different microstructures tested at temperatures between 540 and 760°C. It is important to note that there was very little (≤0.015 wt%) interstitial oxygen pick-up during testing at elevated temperatures in air, and that the reasons for the anomalously high compressive yield strength obtained at 760°C after annealing at 1200°C/0.5 h/AC + 815°C/8 h/AC are unclear at present.

(c) Tension

The room-temperature tensile properties are presented in Table II. The attractive total strain to failure of 3.9% in the as-received material was lost after most of the heat treatments. However, a total strain to failure of 2.1% (1.4% plastic strain) was retained after annealing at 1200°C/0.5 h/FC + 760°C/8 h/AC. This heat treatment, unlike the others shown in Table II, resulted in improved tensile strengths (σ_{ys} = 821 MPa and UTS = 885 MPa). The tensile strength, σ, of the Ti-24Al-11Nb can be estimated by treating the two-phase material as a composite consisting of α_2 and β phases. The yield strength is thus given by:

$$\sigma = f_\alpha \sigma_\alpha + f_\beta \sigma_\beta \qquad (1)$$

where subscripts α and β denote α_2 and β phases, and f is the volume fraction. No attempt was made to model the effect of microstructure since no Hall-Petch data are available for modeling the effect of grain size on the properties of the α_2 and β phases. Single phase strength values were obtained from Ref. (9) which gives $\sigma_{y\alpha} = 540$ MPa and $\sigma_{y\beta} = 695$ MPa at room temperature. Note that the single phase alloys in Ref. (20) fracture before reaching the 0.2% offset yield stress. The predictions obtained by substitution of the above single-phase strength values into Equation (1) are presented in Table II. The predicted tensile yield stresses were generally within $\pm 15\%$ the measured tensile strengths in the as-received material, and in the material that was annealed at 1200°C prior to annealing in the $\alpha_2+\beta$ phase field. However, significant differences were observed between the predicted and measured tensile strengths of the material that was annealed solely in the $\alpha_2+\beta$ phase field (Table I). The loss of strength may be due to substructural changes and the possible formation of brittle third phases such as the orthorhombic phase (16) that was detected by x-ray diffraction after annealing at temperatures between 815 and 1093°C.

Conclusions

1. Annealing of the as-received material solely in the $\alpha_2+\beta$ phase field at 815 and 982°C promotes the degradation of strength and ductility although the α_2 laths in the Widmanstätten microstructure do not coarsen during such exposure.

2. Fast cooling from the β phase field promotes the formation of subgrains within the prior β grains and are annealed out during further thermal exposure at 760°C and 815°C.

3. Annealing in the $\alpha_2+\beta$ phase field after quenching from the β phase field promotes the formation of cracks at prior β grain boundaries.

4. Prolonged annealing in the $\alpha_2+\beta$ phase field after fast cooling from the β phase field promotes the formation of grain boundary α_2 allotriomorphs and significant decomposition of microstructure. However, a relatively stable Widmanstätten microstructure with a good balance of mechanical properties is obtained by furnace cooling from the β phase field and annealing in the $\alpha_2+\beta$ phase field at 760°C.

Acknowledgments

The author would like to thank Dr. D. S. Schwartz, Dr. J. E. Defieyes, Messrs. J. J. Evans, B. A. Abbott, J. E. O'Neal and J. D. Keyes for assistance with experimental techniques. Grateful thanks and acknowledgment are also due to Dr. S. M. L. Sastry, Dr. P. B. Aswath, Capt. C. Ward, Lt. Paul McQuay and Ms. K. Williams for useful discussions. This research was conducted under the McDonnell Douglas and Edison Welding Institute Independent Research and Development Programs.

References

1. M. J. Blackburn, D. L. Ruckle, and C. E. Bevan, AFWAL Technical Report 78-18, 1978.

2. M. J. Blackburn and M. P. Smith, Air Force Technical Report, AFWAL-TR-81-4046, 1981.

3. H. T. Kestner-Weykamp, C. H. Ward, T. F. Broderick and M. J. Kaufman, Scripta Metall. 23, pp. 1697-1702, 1989.

4. H. T. Weykamp, D. R. Baker, D. M. Paxton, and [illegible] Kaufman, Scripta Metall. 24, pp. 445-450, 1990.

5. D. B. Knorr and N. S. Stoloff, Mater. Sci. and [illegible] 123, pp. 81-87, 1990.

6. A. K. Gogia, D. Banerjee, and T. K. Nandy, Metall. Trans. 21A, pp. 609-625, 1990.

7. A. K. Gogia, T. K. Nandy, D. Banerjee, and Y. Mahajan, in Proc. 6th World Conference on Titanium, P. Lacombe, R. Tricot, and G. Beringer, eds., J. Phys. (Le Ulis, Fr.), pp. 1097-1102.

8. D. Banerjee, A. K. Gogia, and T. K. Nandy, Metall. Trans. 21A, pp. 627-639, 1990.

9. S. G. Gittis and D. A. Koss, in High Temperature Ordered Intermetallic Alloys III, C. T. Liu, C. C. Koch, and N. S. Stoloff, eds., MRS, Pittsburgh, PA, pp. 323-328, 1989.

10. P. B. Aswath and S. Suresh, Mater. Sci. and Engng. A114, pp. L1-L5, 1989.

11. P. B. Aswath, W. O. Soboyejo, and S. Suresh, to appear in the Proceedings of Fatigue 90, K. Tanaka and H. Kitagawa, eds., EMAS, Warley, U.K., 1990, Vol. III, pp. 1941-46.

12. P. B. Aswath and S. Suresh, Microstructural Effects on Ambient and Elevated Temperature Fatigue Crack Growth in Titanium Aluminide Intermetallics, to appear in Metallurgical Transactions.

13. S. J. Balsone, D. C. Maxwell, M. Khobaib, and T. Nicholas, Proceedings of Fatigue 90, K. Tanaka and H. Kitagawa, eds., EMAS, Warley, U.K., 1990, Vol. II, pp. 1173-78.

14. D. P. DeLuca and B. A. Cowles, Pratt & Whitney Report No. P&W/ED/FR-18997-7, 1988.

15. D. L. Davidson, K. S. Chan, and J. L. Lankford, AFOSR Technical Report No. F49620-89-C-0032, 1990.

16. D. Banerjee, A. K. Gogia, T. K. Nandy, and V. A. Joshi, Acta Metall. 36, pp. 871-882, 1988.

17. R. Strychor, J. C. Williams, and W. A. Soffa, Metall. Trans. 19A, pp. 225-234, 1988.

18. R. T. DeHoff and F. N. Rhines, eds., Quantitative Microscopy, McGraw Hill, New York, NY, 1968.

19. S. Suresh and J. R. Brockenbrough, Acta Metall. 36, pp. 1455-1470, 1988.

20. W. O. Soboyejo, D. S. Schwartz and S.M.L. Sastry, Metall. Trans. 23A, pp. 2039-2059, 1992.

21. J. C. Chesnutt, C. G. Rhodes and J. C. Williams, in Fractography-Microscopic Cracking Processes, ASTM STP 600, pp. 99-138, 1976.

MICROSTRUCTURE / PROPERTY RELATIONSHIPS FOR THE ALPHA-2 TITANIUM ALUMINIDE ALLOY Ti-24.5Al-12.5Nb-1.5Mo

BJ Marquardt

GE Aircraft Engines
1 Neumann Way, M89
Cincinnati, OH 45215-6301

Abstract

The alpha-2 titanium aluminides offer a significant near term opportunity for propulsion enhancement at reasonable cost and risk levels. With a temperature advantage in excess of 100°C over most conventional titanium alloys, considerable potential for gas turbine engine weight reduction exists. Recently, much work has focused on evaluating the interrelationships between processing, microstructure, and mechanical properties for the alpha-2 titanium aluminide alloys.

Alpha-2 titanium aluminide material of the composition Ti-24.5Al-12.5Nb-1.5Mo (atom percent) was produced as a 46 cm diameter triple VAR ingot. During primary processing, the billet was reduced to a diameter of approximately 15 cm with enough work below the beta transus temperature to refine the microstructure. Five microstructural conditions were produced from the billet material by forging pancakes at a 3:1 upset ratio. One of the material conditions was beta forged while the other four were alpha-2 plus beta forged followed by subsequent heat treatments which produced primary alpha-2 volume fractions of approximately 0, 2, 7 and 12 percent. The beta forging was quenched in a salt bath held at 815°C immediately after forging while the other material conditions were solution heat treated prior to salt quenching to 815°C. All of the material conditions were aged at 705°C for 8 hours prior to mechanical testing.

Tensile, creep, and fracture toughness tests were conducted. The strongest correlation between solution heat treatment temperature and mechanical properties was found for the minimum creep rate. The minimum creep rate increases as the solution heat treatment temperature is decreased. There is a similar but less consistent trend for the percent primary creep to increase as the solution heat treatment temperature is decreased. Yield strength, ultimate strength, and fracture toughness did not show a strong correlation with solution heat treatment temperature. However, the beta forged material condition had a low yield strength and fracture toughness at room temperature while its balance of elevated temperature strength and toughness exceeded that of the other material conditions. The beta heat treated condition possesses a good balance of creep resistance, strength, and toughness but has poor tensile ductility.

Introduction

Alpha-2 titanium aluminide alloys offer a significant near term opportunity for gas turbine engine weight reduction at reasonable cost and risk levels. These alloys provide a temperature advantage in excess of 100°C over most conventional titanium alloys and a density reduction of approximately 40% compared to most Ni-based superalloys. For over thirty years, it has been understood that niobium additions impart a modest amount of ductility to this otherwise brittle

Titanium '92
Science and Technology
Edited by F.H. Froes and I. Caplan
The Minerals, Metals & Materials Society, 1993

compound [1]. Studies of alloying effects have continued into recent years [2,3] and potential engineering compositions have been identified. Currently, much research is focused on the understanding of processing / microstructure / property relationships for alpha-2 titanium aluminide alloys. The work reported here was focused on the interrelationships between processing, microstructure, and key mechanical properties for the alloy Ti-24.5Al-12.5Nb-1.5Mo. The selection of this composition was based primarily on oxidation resistance which is superior to alloys such as Ti-25Al-10Nb-3V-1Mo [4] and mechanical properties which transcend those of alloys such as Ti-24Al-11Nb.

Experimental Procedure

The Ti-24.5Al-12.5Nb-1.5Mo material was produced as a 45 cm diameter triple vacuum-arc-remelted 820 kg ingot. During primary processing, the billet was reduced to a diameter of approximately 15 cm. During the final portion of primary processing, the billet was worked in the alpha-2 plus beta phase field to produce a refined microstructure. The billet was sectioned into 4.5 cm lengths which were then forged at a 3:1 upset ratio to produce pancake shaped forgings which were approximately 1.5 cm thick. The first of five microstructural conditions was produced by beta forging at 1120°C and immediately quenching the material in a salt bath held 815°C. The forging was held in the salt bath for 30 minutes and then air cooled. Additional pancake forgings were produced by alpha-2 plus beta processing at 1040°C followed by air cooling.

To determine heat treatments for the final four microstructural conditions, an approach curve to the beta transus temperature was constructed. The approach curve specimens were 1 cm cubes which were encapsulated in quartz and heat treated for four hours at temperatures which ranged from 995 to 1105°C. Following heat treatment, the specimens were water quenched, sectioned, mounted, and polished. Image analysis was then conducted with an SEM using backscattered electron images to determine the volume fraction of phases. Based on the approach curve results, heat treatments of 1120, 1085, 1065 and 1045°C for one hour were selected to produce the four remaining microstructural conditions. After each of these solution treatments, the material was quenched to 815°C in a salt bath and held for 30 minutes prior to air cooling. All five of the microstructural conditions were aged at 705°C for 8 hours prior to the machining of mechanical test specimens. Each of the material conditions is identified in Table 1.

Table 1 Definition of Material Conditions

Material Condition	Forging Temp. (°C)	Upset Ratio	Solution Heat Treat. Temp. (°C)	Cooling Method	Aging Temp. & Time (°C / hrs)	Volume Fract. Primary Alpha-2 (%)
A	1120	3:1	-	815°C Salt	705 / 8	0
B	1040	3:1	1120	815°C Salt	705 / 8	0
C	1040	3:1	1085	815°C Salt	705 / 8	2
D	1040	3:1	1065	815°C Salt	705 / 8	7
E	1040	3:1	1045	815°C Salt	705 / 8	12

Round tensile and creep specimens with a 6.35 mm gage diameter were machined and tested in accordance with ASTM standards. These 8.25 cm long specimens with a gage length of 3.2 cm were each machined such that the loading direction was tangential to the circumference of the forging. Chevron notched compact tension specimens were also machined for fracture toughness testing. The fracture toughness specimens measured approximately 1.25 by 3.2 by 3.2 cm and were fatigue pre-cracked prior to testing. Toughness tests were conducted with radial and tangential crack propagation directions.

Results and Discussion

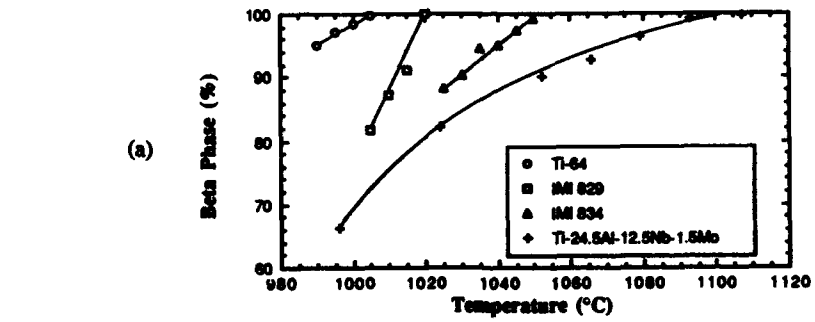
The measured chemical composition of the ingot material was Ti-23.5Al-13.1Nb-1.37Mo (atom percent). The interstitial analysis of the ingot material indicated approximately 680 ppm oxygen, 46 ppm nitrogen, 67 ppm hydrogen, and 250 ppm carbon by weight. In addition, the chemical analysis revealed 700 ppm Fe by weight.

The results of the approach curve study are presented in Figure 1a along with curves for Ti-64, IMI 829 and IMI 834 as determined by Neal [5]. The results indicate that the approach curve for Ti-24.5Al-12.5Nb-1.5Mo is very shallow in comparison to the other titanium alloys, and the beta transus temperature for Ti-24.5Al-12.5Nb-1.5Mo is estimated to be approximately 1105°C. Due to the shallow approach curve for Ti-24.5Al-12.5Nb-1.5Mo, the volume fraction of primary alpha-2 can be closely controlled. The selected heat treatment temperatures of 1120, 1085, 1065 and 1045°C were projected to yield primary alpha-2 volume fractions of approximately 0, 2, 7 and 12 percent, respectively, as indicated previously in Table 1.

The microstructures of the heat treated materials are shown in Figure 1b-g. The beta forged material is shown in Figure 1b and is identified as condition A in Table 1. This material has large pancake-shaped prior beta grains with a fine transformed lath structure. Small recrystallized prior beta grains are also found around the periphery of the pancake-shaped grains. The beta heat treated material, condition B, has an average prior beta grain size of approximately 1 mm with a very fine transformed lath structure as shown in Figure 1c. The microstructure of the material which was heat treated at 1085°C, condition C, is shown in Figures 1d and 1e. The microstructure of material condition C varied significantly. The microstructure shown in Figure 1d is representative of the material near the circumference of the forging while the microstructure shown in Figure 1e is representative of the material near the center of the forging. Although the volume fraction of primary alpha-2 is roughly constant throughout this forging, the transformed lath structure is much coarser near the circumference of the forging than near the center. This large variation of lath size was unique to the tensile specimens for material condition C. The variation of lath size with respect to tensile test temperature is described with the tensile test results. The creep and fracture toughness specimens of material condition C contained a fine lath structure as shown in Figure 1e. The microstructure of the material which was heat treated at 1065°C, condition D, has a higher volume fraction of primary alpha-2 than material condition C and a fine lath size throughout. Material condition D is shown in Figure 1f. The microstructure of the material which was heat treated at 1045°C, condition E, also has a fine lath size throughout the forging but with the highest volume fraction of primary alpha-2 as shown in Figure 1g.

It is unclear why the lath size was variable in the material which was heat treated at 1085°C. The tensile specimens for each of the three material conditions which were heat treated below the beta transus temperature were taken from the same forging. Yet, only the material condition which was heat treated at 1085°C displayed the variable lath size from the center of the forging to the circumference. No variation in chemical composition was detected by energy dispersive spectroscopy between the areas with coarse and fine lath sizes. Due to the bi-axial stress state which develops near the edge of the forging, it is evident that higher strain levels were achieved at the edge of the forging than at the center. It is possible that this could lead to recrystallization of the beta grains near the edge of the forging and recovery near the center of the forging during solution heat treatment. If this occurs, there could be more nucleation sights near the center of the forging which would result in a finer lath size in that area. However, based on the same logic, the beta heat treated material would be expected to be fully recrystallized and, therefore, have fewer nucleation sights and a coarse lath size.

The tensile properties for each of the microstructural conditions are listed in Table 2. The room temperature test specimen came from near the center of the forging and, as the test temperature was increased, the specimens were obtained from locations which were progressively closer to the circumference. For the 1085 and 1065°C heat treatment conditions (material conditions C and D), a 650°C test specimen was also taken from the center of the forging. Therefore, one of the 650°C tensile test specimens was taken from the outer edge and the other from near the center of the forging for material conditions C and D.



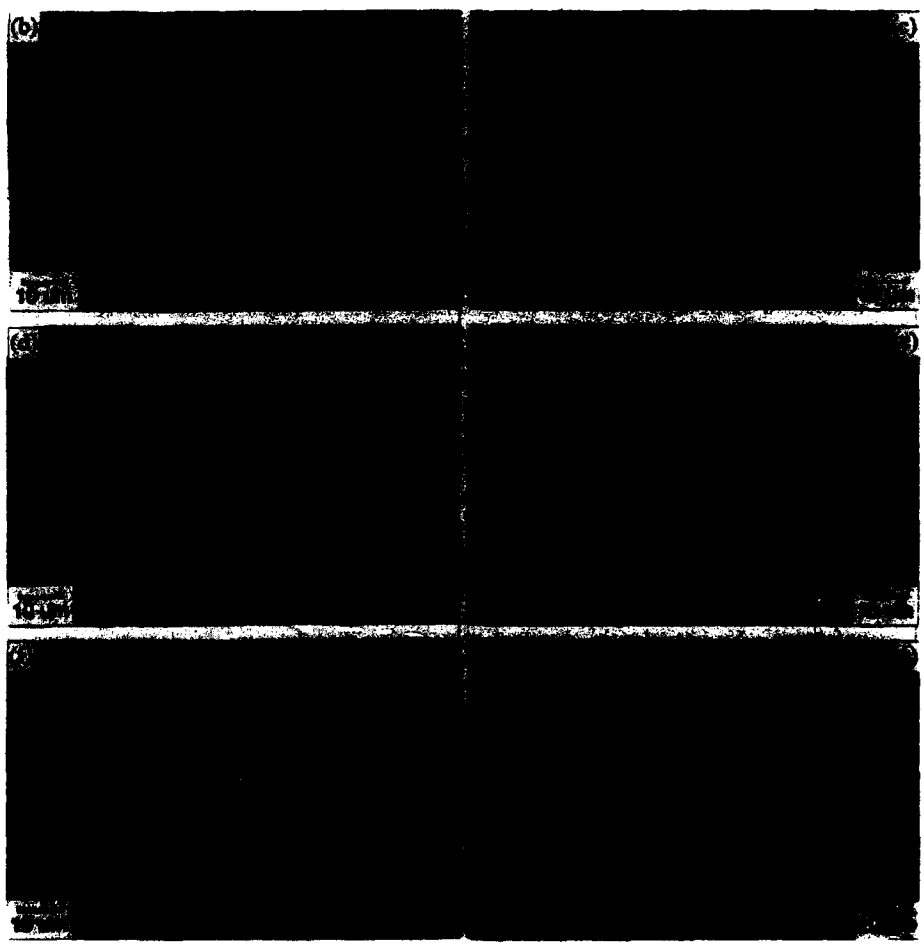


Figure 1 (a) Approach curves for Ti-64, IMI 829, IMI 834 [5] and Ti-24.5Al-12.5Nb-1.5Mo. Optical micrographs of the material which was (b) beta forged and (c) beta heat treated. Optical micrographs of the (d) edge and (e) center of the forging which was heat treated at 1085°C and the edge of the forgings which were heat treated at (f) 1065°C and (g) 1045°C.

Table 2 Tensile, Creep and Fracture Toughness Test Results

Material Cond.	Test Temp. (°C)	0.2% YS (MPa)	UTS (MPa)	Plastic Elong. (%)	Creep Stress (MPa)	Time to 0.2% (Hours)	Minimum Creep Rate* (%/hr)	Primary Creep* (%)	K_q (MPa√m)
A	24	910	1081	3.2	-	-	-	-	15.0
"	425	742	1063	17.4	-	-	-	-	-
"	540	749	974	12.9	448	87	0.0011	0.10	91.3
"	650	727	903	11.6	172	19.8	0.0031	0.18	-
"	595	-	-	-	379	17.7	0.0034	0.19	-
B	24	1035	1089	0.5	-	-	-	-	17.1#
"	425	896	1040	3.1	-	-	-	-	-
"	540	791	968	8.4	448	114	0.0013	0.09	75.9
"	650	741	920	5.0	172	33	0.0029	0.12	-
"	595	-	-	-	379	14.1	0.0038	0.21	-
C	24	792	972	3.1	-	-	-	-	18.8#
"	425	595	896	21.8	-	-	-	-	-
"	540	467	729	16.2	414	95	0.0014	0.10	65.5
"	650	442	620	10.6	172	10.9	0.0038	0.22	-
"	650	680	833	6.8	-	-	-	-	-
"	595	-	-	-	276	34	0.0021	0.14	-
D	24	1051	1158	1.2	-	-	-	-	16.6#
"	425	865	1087	14.9	-	-	-	-	-
"	540	782	958	11.2	414	40	0.0017	0.15	55.2
"	650	673	842	6.8	172	8.8	0.0054	0.28	-
"	650	776	987	3.9	-	-	-	-	-
"	595	-	-	-	276	19.4	0.0027	0.18	-
E	24	956	1096	2.5	-	-	-	-	19.0#
"	425	739	992	18.0	-	-	-	-	-
"	540	713	921	10.6	414	22	0.0021	0.18	78.5
"	650	714	871	5.2	172	7.5	0.0065	0.28	-
"	595	-	-	-	276	12.9	0.0041	0.24	-

* Since most of the creep tests were discontinued after approximately 100 hours of testing, the reported minimum creep rates are the average creep rates between 80 and 100 hours of testing. These do not represent true steady state creep rates. The percent primary creep was estimated with the use of the minimum creep rate.

\# These values represent valid K_{Ic} measurements.

The yield strengths of the five material conditions do not correlate well with solution heat treatment temperature. The strongest material conditions were B, the beta heat treated condition, and D, the condition which was heat treated at 1065°C to produce 7 percent primary alpha-2. It is not evident that the volume fraction of primary alpha-2 or solution heat treatment temperature have a significant effect on yield strength as long as a consistent lath size is produced. However, beta forging did reduce the room temperature yield strength. At the highest test temperatures, 540 and 650°C, the yield strengths were tightly grouped within a range of approximately 100 MPa except for material condition C which contained the coarse lath structure near the edge of the forging. Lath size has a very significant effect on yield strength. For material condition C, the 650°C yield strength of the specimen with a large lath size was approximately 240 MPa lower than the specimen with a small lath size.

Much like the yield strength results, the ultimate tensile strength does not correlate well with solution heat treatment temperature and volume fraction primary alpha-2. The highest ultimate tensile strength was that of material condition D which contained 7 percent primary alpha-2. There was a significant difference in the ultimate tensile strength from the edge to the center of the forging as revealed by the 650°C test results for material conditions C and D. Even for

material condition D, which had little difference in lath size from the center to the edge of the forging, the center of the forging was 145 MPa stronger than the edge of the forging. For material condition C, the ultimate tensile strength was approximately 210 MPa higher at the center of the forging than at the edge of the forging where the lath structure was coarse. The lowest ultimate strength was associated with material condition C even for those test specimens which contained a fine lath structure.

Plastic elongation is significantly reduced by beta solution heat treatment. This is generally attributed to nonuniform flow behavior which is plastically anisotropic over the dimensions of the prior beta grain size. This results in strain incompatibilities at prior beta grain boundaries [6]. The beta heat treated material, condition B, had only 0.5 percent plastic elongation at room temperature and 3.1 percent plastic elongation at 425°C. The plastic elongation at room temperature for material condition D was only 1.2, but each of the other material conditions, A, C, and E, had 2.5 percent plastic elongation or more at room temperature. The plastic elongation peaked at over 14 percent at 425°C for all but the beta heat treated material. The plastic elongation peaked at 540°C for the beta heat treated material. For all of the material conditions, the plastic elongation decreased as the test temperature was increased above 540°C.

The tensile properties of Ti-24.5Al-12.5Nb-1.5Mo forgings compare favorably to forgings of the alpha-2 titanium aluminide alloy Ti-25Al-10Nb-3V-1Mo [7-9] although the strength of material condition C is below most reported values for Ti-25Al-10Nb-3V-1Mo. Rolled material can often be processed to achieve higher strength levels than alpha-2 forgings [9,10]. When sheet material is rolled to achieve higher strength levels, the ductility may be reduced to levels of 1 percent or less [9]. However, sheet material can generally be processed to achieve a good balance between strength and ductility while the creep resistance may be somewhat lower than that associated with most forged conditions.

The creep properties for each of the material conditions are listed in Table 2. Table 2 includes data for the time to 0.2 percent strain, the minimum creep rate, and the percent primary creep. Since many of the creep specimens were unloaded shortly after 100 hours of testing, the minimum creep rate is an estimate based on the slope of the strain versus time curve over the range of 80 to 100 hours. These results do not represent the steady state creep rates which would be lower than the minimum creep rates reported here. Furthermore, the data reported for percent primary creep are under estimates since they were generated with the use of minimum creep rate rather than steady state creep rate. For relative comparison of the microstructural conditions, the available data for minimum creep rates and percent primary creep are useful.

Each of the creep specimens was evaluated metallographically. Unlike the tensile test specimens, the lath structure which transformed upon cooling from the solution heat treatment temperature was fine and uniform for each of the material conditions. The minimum creep rate correlates well with solution heat treatment temperature and microstructure. With higher solution temperatures and microstructures which contain smaller volume fractions of primary alpha-2, the minimum creep rate is reduced as shown in Figure 2. This result is similar to that found for conventional titanium alloys [11]. The amount of primary creep also seems to correlate well with microstructure although the trend is not quite as consistent as for the minimum creep rate. The percent primary creep increased or remained the same as the solution heat treatment temperature was decreased. This trend is not always found for conventional titanium alloys [11]. Since both the minimum creep rate and the percent primary creep correlated well with the microstructural condition, the time to 0.2 percent strain also correlated well with microstructure.

The most creep resistant microstructures were those which were beta forged or beta heat treated. This result is consistent with studies conducted on the Ti-25Al-10Nb-3V-1Mo alloy [12-14] and for conventional titanium alloys [11]. Since the beta forged condition is more ductile than the beta heat treated condition, beta forging offers a better balance between creep resistance and ductility. For applications where beta forging is not practical, heat treatment below the beta transus temperature may result in the best balance between ductility and creep resistance.

The fracture toughness properties are reported in Table 1. The fracture toughness specimens were all evaluated metallographically and the lath structure was fine and uniform in each case. The room temperature fracture toughness test results range from 15 MPa$\sqrt{m}$ to 19 MPa$\sqrt{m}$. No

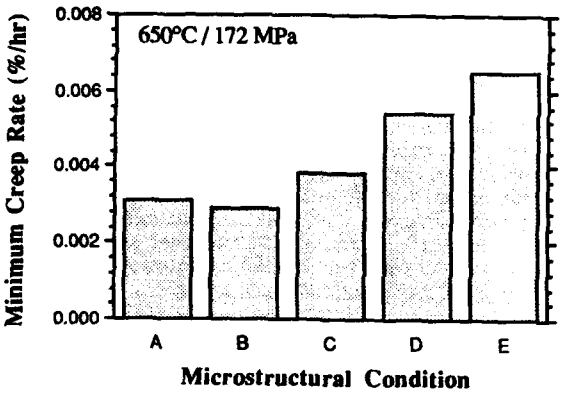


Figure 2 The minimum creep rate as a function of microstructure under 650°C / 172 MPa test conditions. A strong correlation exists between minimum creep rate and the solution heat treatment temperature.

consistent correlation between room temperature fracture toughness and solution heat treatment temperature or volume fraction primary alpha-2 was evident. Material condition D which had an intermediate volume fraction of primary alpha-2, 7 percent, had one of the lower fracture toughness values. The beta forged material had the lowest room temperature fracture toughness and was the only room temperature value which was not a valid K_{Ic} measurement. Much of the variation between the room temperature fracture toughness values may be attributed to statistical scatter.

The 540°C fracture toughness test results were spread over a large range from 55.2 to 91.3 MPa$\sqrt{m}$. However, none of the elevated temperature test results were valid K_{Ic} measurements since they did not meet the criterion: $B,a > 2.5(K_{Ic} + 0.2\%YS)^2$. Based on the average strength of the material at 540°C, the 1.25 cm thick specimen would only produce valid K_{Ic} measurements up to toughness levels of approximately 55 MPa$\sqrt{m}$. Nevertheless, the results indicate that there is a dramatic increase in fracture toughness with increasing test temperature. Other studies indicate that the increase in fracture toughness with increasing temperature for alpha-2 titanium aluminide alloys with a retained, ductile beta phase can be attributed to a significant increase in the tearing modulus with increasing temperature [15]. The K_q values indicate that the beta forged condition, which had the lowest room temperature fracture toughness, has the highest 540°C fracture toughness of 91.3 MPa$\sqrt{m}$. As indicated by the random order of the test results for material conditions B, C, D, and E, there was no apparent relationship between the 540°C fracture toughness and the solution heat treatment temperature or volume fraction primary alpha-2.

Summary and Conclusions

The microstructure / property relationships for Ti-24.5Al-12.5Nb-1.5Mo forgings often parallel those for conventional alpha titanium alloys. The creep properties showed a strong correlation to solution heat treatment temperature or volume fraction primary alpha-2 while most other properties did not. The beta forged condition did not have high fracture toughness at room temperature as it would for alpha titanium alloys. Several conclusions can be made with regard to the balance of properties for the material conditions which were studied in this program.

1) The beta forged material condition has a good balance of ductility, elevated temperature strength, creep resistance, and elevated temperature fracture toughness but has relatively low room temperature strength and fracture toughness.

2) The beta heat treated material has good strength and creep resistance with average fracture toughness but poor ductility.

3) Material which is processed and heat treated below the beta transus temperature has a good balance of strength, ductility, and fracture toughness but, as the heat treatment temperature is lowered and the volume fraction of primary alpha-2 is increased, the creep resistance decreases.

In addition to the improving our understanding of the relationships between microstructure and mechanical properties, it is apparent that an improved understanding of the relationships between processing, heat treatment, and microstructure must be developed. The variable lath size which was produced in material condition C had a significant effect on properties. For practical purposes, this type of microstructural variation must be controlled. Further studies of the effects of processing temperature, strain rate, and strain level and their associated effects on recrystallization, recovery, and final heat treated microstructures will be imperative for the successful application of alpha-2 titanium aluminide alloys.

Acknowledgments

The author wishes to thank Dan Krueger for his review and discussion of the text and acknowledge the experimental assistance of Ron Grant, Eva Lanman, and Mike Connelly.

References

1. J.P. McAndrew and C.R. Simcoe, "Investigation of the Ti-Al-Cb System as a Source of Alloys for use at 1200 - 1800°F", WADD Technical Report 60-99, 1960.
2. B.J. Marquardt, G.K. Scarr, J.C. Chesnutt, C.G. Rhodes and H.L. Fraser, "R & D for Improved Toughness Aluminides", Tech. Report WRDC-TR-89-4133, 1990.
3. M.J. Blackburn and M.P. Smith, "Improved Toughness Alloys Based on Titanium Aluminides", Tech. Report WRDC-TR-89-4095, 1989.
4. J.C. Schaeffer, "Isothermal Oxidation Behavior of Alpha-2 Titanium Aluminide Alloys", submitted to *Scripta Met.*
5. D.F. Neal, "Development and Evaluation of High Temperature Titanium Alloy IMI 834", *Sixth World Conference on Titanium*, eds. P. Lacombe, R. Tricot and G. Beranger, vol. 1, pp. 253-258.
6. D.A. Lukasak and D.A. Koss, "The Flow and Fracture of a Ti_3Al-Nb Alloy", *Met. Trans.*, vol. 21A, pp. 135-143.
7. C.H. Ward, J.C. Williams, A.W. Thompson, D.G. Rosenthal and F.H. Froes, "Fracture Mechanisms in Titanium Aluminide Intermetallics", *Sixth World Conference on Titanium*, eds. P. Lacombe, R. Tricot and G. Beranger, vol. 2, pp. 1103-1108.
8. C.H. Ward and S.J. Balsone, "The Effect of the Salient Microstructural Constituents on Tensile and Creep Deformation of Ti-25Al-10Nb-3V-1Mo", *Microstructure / Property Relationships in Titanium Aluminides and Alloys*, eds. Y-W. Kim and R.R. Boyer, pp. 373-386.
9. M. Peters, Y.T Lee, K.-J. Grundhoff and S. Hulsmann, "Mechanical Properties of Alpha-2 and Super Alpha-2 Titanium Intermetallics", Proc. 2nd Inter. Conf. on Ti Products and Applications, Orlando, FL, 1990.
10. G. Proske, G. Lutjering, J. Albrecht, D. Helm and M. Daeubler, "The Microstructure and Mechanical Properties of the Intermetallic Compound Super Alpha-2", *High Temperature Aluminides and Intermetallics*, eds. S.H. Wang, D.P. Pope and C.T. Liu, pp. 310-316.
11. P.J. Bania and J.A. Hall, "Creep Studies of Ti-6242-Si Alloy", *Titanium Science and Technology*, eds. G. Lutjering, U. Zwicker and W. Bunk, vol. 4, pp. 2371-2378.
12. R.W. Hayes, "On the Creep Behavior of the Ti_3Al Titanium Aluminide Ti-25Al-10Nb-3V-1Mo", *Acta Met.*, vol. 39, pp. 569-577.
13. W.O. Soboyejo, R.J. Lederich and D.S. Schwartz, "Effects of Microstructure on the Creep Behavior of Alpha-2 Based Titanium Aluminide Alloys, *Microstructure / Property Relationships in Titanium Aluminides and Alloys*, eds. Y-W. Kim and R.R. Boyer, pp. 407-422.
14. W.C. Cho, A.W. Thompson and J.C. Williams, "Creep Behavior of Ti-25Al-10Nb-3V-1Mo", *Met. Trans.*, vol. 21A, pp. 641-651.
15. K.S. Chan, "Influence of Microstructure on Intrinsic and Extrinsic Toughening in an Alpha-2 Titanium Aluminide Alloy", *Met. Trans.*, vol. 23A, pp. 183-199.

EFFECTS OF MICROSTRUCTURE ON TENSILE PROPERTIES

IN THE ALLOY Ti-25Al-10Nb-3V-1Mo

François-Charles Dary and Anthony W. Thompson

Department of Materials Science and Engineering
Carnegie Mellon University
Pittsburgh, PA 15213

Abstract

The dependence of room-temperature tensile properties upon microstructure was investigated in the intermetallic Ti-25Al-10Nb-3V-1Mo. A wide spectrum of microstructures was obtained by varying the cooling rate after solutionizing treatment in the β phase field. The strength was found to increase monotonically with increasing cooling rate. It is proposed that strength is controlled by β_R phase strengthening and $(\alpha_2+\beta_R)$ boundary strengthening in β-solutionized microstructures. The ductility was observed to go through a maximum, at a cooling rate of 1.5°C/s. It is believed that two distinct mechanisms control deformation and failure in this alloy, one acting at low α_2 volume fractions, and the other at high α_2 volume fraction. In addition, microstructural stability was studied; it was found that β-solutionized microstructures were stable, with respect to room-temperature tensile properties, for all cooling rates up to 1.5°C/s.

Introduction

The focus of this work was to examine the effects of microstructure on room-temperature tensile properties of the titanium aluminide alloy, Ti-25Al-10Nb-3V-1Mo (at.%). In particular, the role of α_2 phase volume fraction, size and arrangement (e.g., basketweave or colony) in room temperature tensile behavior has been investigated. In addition, microstructural stability has been addressed by examining the effect of a stabilizing/aging treatment on room temperature tensile properties.

Experimental Procedure

The material used in this investigation is the super-α_2 titanium aluminide intermetallic, Ti-25Al-10Nb-3V-1Mo (atomic percent, nominal). The material was provided by UTC-Pratt & Whitney, in the form of a forged pancake, with thickness of ~35 mm (1.4 in.) and diameter of ~350 mm (13.8 in.). Thermomechanical processing of the material at UTC involved forging above the β-transus and subsequent slow cooling.

Blanks approximately 10 mm (0.4 in.) square and 35 mm (1.4 in.) long were cut from the as-received pancake, with their long axis perpendicular to the two flat surfaces of the pancake. The blanks were then solutionized in air in the β-phase field, at 1150°C, for one hour and cooled at seven different rates, to produce various β-solutionized microstructures. This β-solutionizing sequence is depicted in Figure 1a. Cooling rates were determined by placing a thermocouple in the center of a blank, and recording temperature/time data. The seven microstructures obtained by β-solutionizing treatment are herein designated "A-S" microstructures and are shown in Figures 2a through 2g.

Tensile specimens were machined from "A-S" blanks. Stabilizing and aging treatments were then performed on one set of machined tensile specimens. The choice of the stabilizing/aging

Titanium '92
Science and Technology
Edited by F.H. Froes and I. Caplan
The Minerals, Metals & Materials Society, 1993

sequence, used in this work to study microstructural stability, was made based on an investigation of high-temperature tensile properties actually underway (Figure 1b). Six "A-S" microstructures were given the stabilizing/aging treatment, in vacuum (10^{-6} Torr) to minimize oxidation. These microstructures are herein designated "S/A" microstructures.

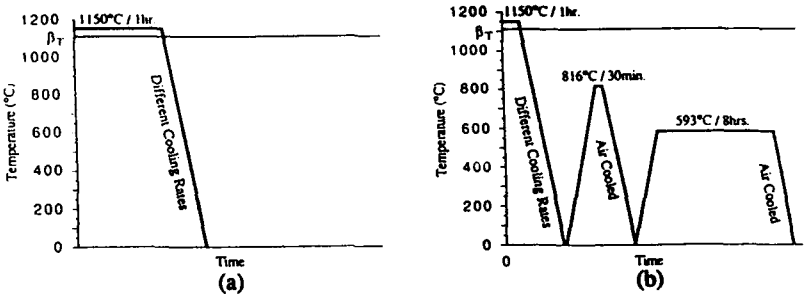


Figure 1 - Heat-treatment sequences: (a) Solutionizing sequence ; (b) Solutionizing+Stabilizing/ Aging Sequence.

Threaded-end, axi-symmetric tensile specimens were used. The quantity of material removed from the blanks during machining was sufficient to eliminate the oxygen-enriched region. Prior to testing, the gage sections were longitudinally polished with 600 grit paper and then electropolished to ensure that no circumferential machining marks remained. Room temperature tensile tests were conducted at a cross-head speed of 0.5 mm/min (0.02 in./min.), using an Instron machine.

After tensile testing, examination of the fracture surfaces was performed using scanning electron microscopy. Some fractured specimens were longitudinally sectioned, polished and etched. Scanning electron microscopy was then used to examine the fracture surface profiles, as well as the internal cracks/voids network which developed below the fracture surfaces.

Results and Discussion

Microstructures

A simple heat-treatment sequence was selected in an attempt to limit the number of features varying in the microstructure. Thus, the material was solutionized in the single β-phase field and the α_2 precipitate volume fraction, size and arrangement were varied by changing the rate of cooling from the solutionizing temperature. Resulting "A-S" microstructures corresponding to the seven selected cooling rates are shown in Figures 2a through 2g. The β phase retained in the microstructure after the different heat treatments is herein designated retained-β phase, β_R. Indeed, depending on the heat-treatment sequence, the β phase has been observed to remain disordered or to order to the B2 phase which, under certain particular conditions, decomposes into products such as ω', ω" and 2H-type phases. Thus, for simplicity, the phase mixture is called β_R, though it could contain some of the aforementioned phases.

The "A-S,25" microstructure (Figure 2a) exhibited very limited, non-uniform, precipitation of fine α_2 precipitates within the prior-β grains. The α_2 phase precipitated essentially at prior-β grain boundaries. In addition, subgrain boundaries present in prior-β grains were "decorated" with fine α_2 precipitates (Figure 2a).

For cooling rates ranging from 7.5 to 0.5°C/s, microstructures exhibited extensive α_2 precipitation throughout prior-β grains in the form of α_2 laths arranged in basketweave (Figure 2b-2e). The α_2 lath width increased monotonically with decreasing cooling rates. In the "A-S,7.5" microstructure (Figure 2b), small regions depleted with α_2 were observed, showing that the α_2 precipitation was still not uniform at this cooling rate. Above 7.5°C/s, two distinct sizes of α_2 laths were observed in the basketweave arrangement, as shown in Figures 2c through 2e. We speculate that this might be the result of two different precipitation mechanisms taking place during cooling. Additional work is underway to provide a better understanding of the precipitation mechanisms. Precipitation of α_2 phase at prior-β grain boundaries was also observed in all microstructures. For cooling rates smaller than 4°C/s, α_2 colonies precipitated

from prior-β grain boundaries, towards the inside of the grains. The size of both the colonies, and α_2 laths within them, increased with decreasing cooling rates. Finally, although no quantitative measurements have been made, the α_2 volume fraction appeared to increase monotonically with decreasing cooling rates, in the range 7.5 to 0.5°C/s.

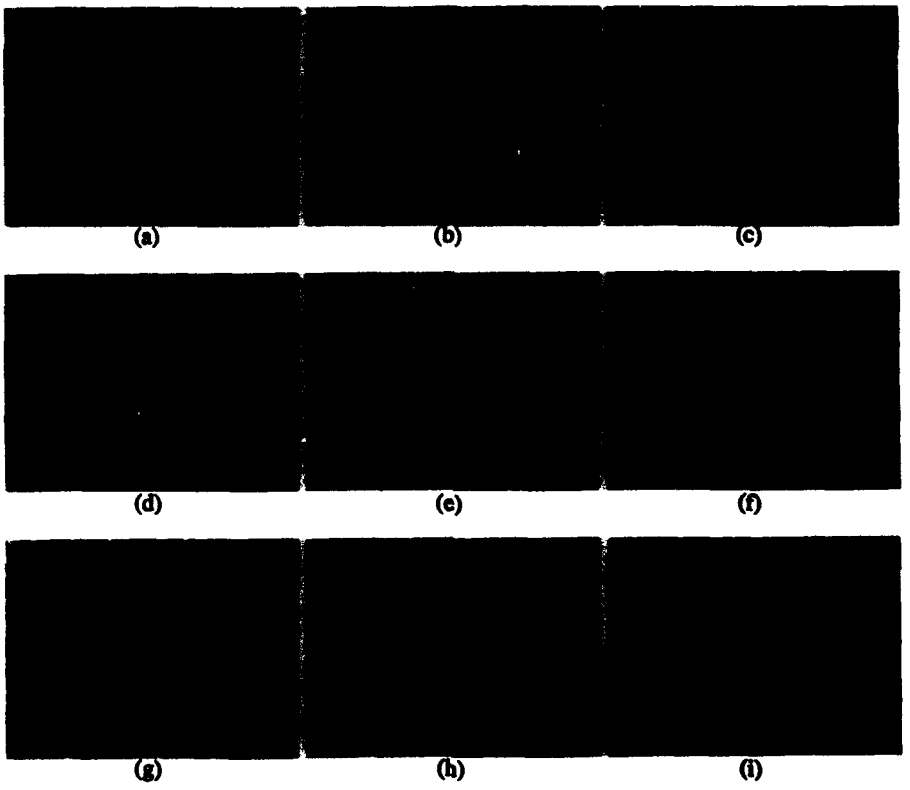


Figure 2 - Microstructures: (a) "A-S,25" ; (b) "A-S,7.5" ; (c) "A-S,4" ; (d) "A-S,1.5" ; (e) "A-S,0.5" ; (f) "A-S,0.1" ; (g) "A-S,0.01" ; (h) "S/A,25" ; (i) "S/A,7.5".

The "A-S,0.1" and "A-S,0.01" microstructures (Figures 2f and 2g) corresponded to a major change in the α_2 phase arrangement. Thus, in the "A-S,0.1" microstructure, the α_2 laths were now arranged, for the most part, in packets in the middle of prior-β grains and in colonies at prior-β grain boundaries (Figure 2f). The packet-type α_2 laths were slightly thicker than the basketweave-type α_2 laths in the "A-S,0.5" microstructure, but the colony-type α_2 laths at prior-β grain boundaries were very coarse, and the colonies extended well inside the prior-β grains. The "A-S,0.01" microstructure exhibited very thick α_2 laths arranged in colonies, each prior-β grain containing only a few large colonies. Thick regions of β_R phase were observed between α_2 laths. The α_2 phase volume fraction was roughly unchanged between the "A-S,0.5" and "A-S,0.1" microstructures, i.e., ~82%, but was slightly smaller in the "A-S,0.01" microstructure, i.e., ~76%.

Six "S/A" microstructures corresponding to cooling rates, 25, 7.5, 1.5, 0.5, 0.1 and 0.01°C/s were selected. No substantial differences were noticed between the "A-S" microstructures and "S/A" microstructures for all cooling rates up to 1.5°C/s. However, the "S/A,25" and "S/A,7.5" microstructures, shown in Figures 2h and 2i, underwent some transformations during the stabilizing/aging sequence. This is not surprising considering the high instability of the saturated β_R phase after cooling at 25 and 7.5°C/s. The "S/A,25" microstructure exhibited large equiaxed precipitates. X-ray diffraction analysis showed that both

α_2 and orthorhombic phases were present in these microstructures as a result of the stabilizing/aging treatments.

Mechanical behavior

Figure 3 shows the 0.2% yield stress, fracture stress, elongation and reduction of area, *vs.* cooling rate, for both "A-S" and "S/A" microstructures.

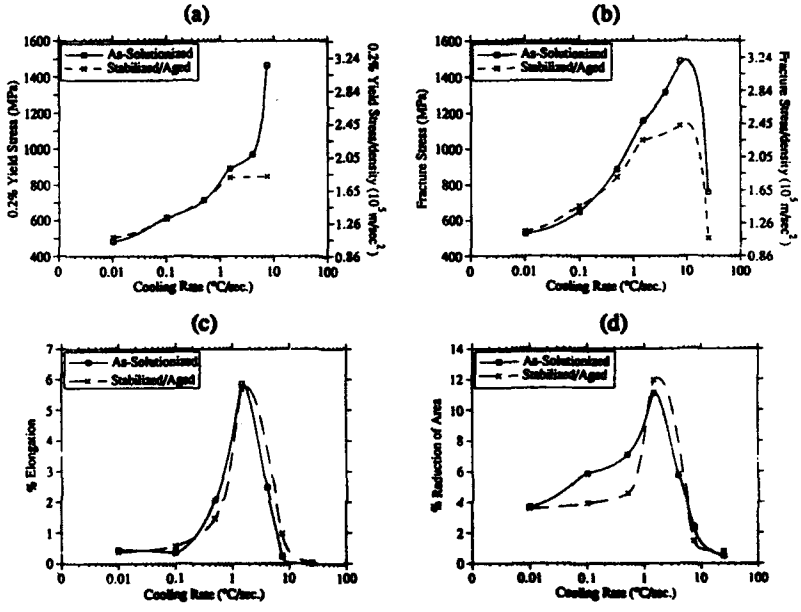


Figure 3 - Room-temperature tensile properties *vs.* cooling rate of "A-S" and "S/A" microstructures: (a) yield stress ; (b) fracture stress ; (c) % elongation ; (d) % reduction of area.

Strength of "A-S" samples increased monotonically with increasing cooling rates. We believe that both size and volume fraction of α_2 laths are responsible for such trends. Hence, the β_R constituent is expected to be the strongest phase, and as its volume fraction increases, i.e., as the α_2 volume fraction decreases, the strength of the alloy is expected to increase as well. A similar property has been observed with the disordered β phase in conventional (α+β) titanium alloys. Moreover, boundary strengthening of the two phase mixture (α_2 +β_R) is also expected to be a dominant factor in these microstructures. Decreasing α_2 lath thickness is expected to increase the boundary strengthening effect, and thus the strength of the material. Similar behavior has been reported earlier in conventional (α+β) titanium alloys and was attributed to boundary strengthening (1). The volume fraction of β_R did, indeed, decrease substantially with decreasing cooling rates, from 25°C/s to 0.5°C/s. It, however, appeared to remain essentially constant from 0.5 to 0.1°C/s and increased noticeably from 0.1 to 0.01°C/s. In addition, the α_2 lath width increased significantly with decreasing cooling rates, save the "A-S,0.5" and "A-S,0.1" microstructures where the increase was less pronounced. Thus, it is proposed that, from 7.5 to 0.5°C/s, the combination of (α_2 +β_R) boundary strengthening and β_R phase strengthening is responsible for the strength dependence of the alloy upon cooling rate.

From 7.5 to 25°C/s, the fracture stress dropped dramatically (Figure 3b) and, at 25°C/s, no yield stress was observed (Figure 3a). It is believed that this is due to the fact that, at a cross-head speed of 0.5 mm/s, the "A-S,25" sample fractured in Mode I brittle manner, well before reaching macroscopic yielding. From 0.01 to 0.1°C/s, the α_2 lath arrangement remained unchanged. The β_R phase volume fraction decreased noticeably and the α_2 lath width decreased dramatically. Thus, in that case, it is suggested that boundary strengthening is the factor controlling the increase in strength, counteracting the negative effect due to decreasing β_R phase

volume fraction. From 0.1 to 0.5°C/s, the α_2 lath arrangement changed from colony to basketweave. The β_R phase volume fraction remained nearly unchanged, but the α_2 lath width decreased slightly within prior-β grains, and significantly at prior β-grain boundaries. However, the yield strength did not sharply increase. Thus, it is believed that the α_2 lath arrangement does not have a significant influence on the yield strength behavior of these alloys, and that the slight increase in strength is mainly due to strengthening resulting from the decrease in α_2 lath width, especially within colonies at prior-β grain boundaries. Similar results were found by Ward *et al.* (2).

For "S/A" microstructures, the strength were similar to that of "A-S" microstructures for cooling rates up to 1.5°C/s (Figures 3a and 3b). However, for the "S/A,25" and "S/A,7.5" microstructures, the microstructural decomposition which has taken place during the stabilizing/aging treatment resulted in lower strength. Thus, for cooling rates up to 1.5°C/s, the microstructural features controlling strength are proposed to be similar to that of "A-S" microstructures.

Figures 3c and 3d show ductility, i.e., elongation and reduction of area, of "A-S" and "S/A" microstructures *vs.* cooling rates.

Ductility of "A-S" microstructures exhibited a maximum at about 1.5°C/s. In addition, none of the tensile specimens exhibited necking before fracture. Thus, even after ~6% plastic elongation, fracture remained brittle in nature. Investigation of fracture surfaces, fracture surface profiles and cracks/voids network below fracture surfaces was used to provide clues for a better understanding of the mechanisms causing such trends. Fracture surfaces of "A-S" samples are shown in Figure 4 and micrographs of longitudinal sections are shown in Figure 5. The "A-S,25" samples exhibited mixed intergranular and transgranular fracture (Figure 4a). Transgranular fracture was made up of cleavage-like facets. Fine shallow dimples were noticeable on some of the facets, as well as some tearing on the steps joining the facets. Voids of different sizes were observed scattered throughout the microstructure, below the fracture surface (Figure 5a). A limited number of voids was occasionally seen intersecting the fracture surface. The fracture profile was very straight but contained many steps. "A-S,7.5" samples also fractured in a mixed intergranular/transgranular mode. Transgranular fracture was made up of large quasi-cleavage facets covered with shallow valleys and plateaus. Void concentration decreased, but void size just below the fracture surface increased. A significantly higher number of voids was now seen intersecting the fracture surface. The fracture profile was virtually unchanged.

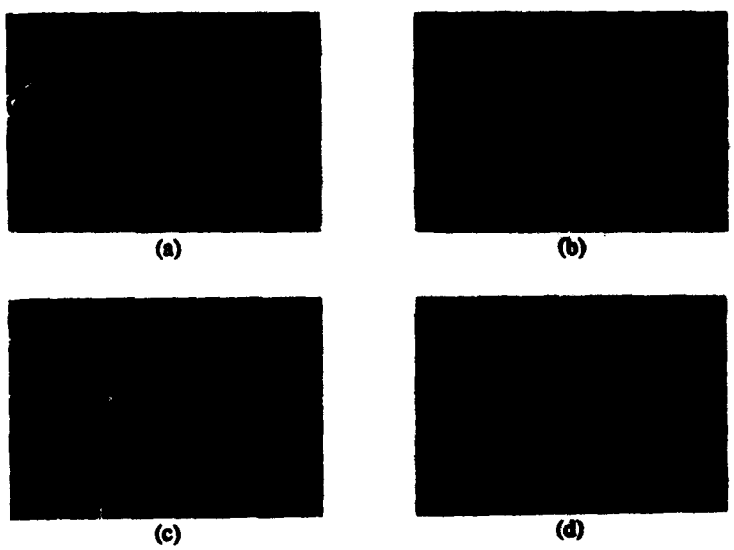


Figure 4 - Fracture surfaces of "A-S" samples: (a) "A-S,25" ; (b) "A-S,1.5" ; (c) "A-S,0.5" ; (d) "A-S,0.01".

"A-S,1.5" samples exhibited quite different fracture features. A mixed intergranular and transgranular fracture was still observed, but unlike in "A-S,25" and "A-S,7.5" samples, the grain boundary surfaces exhibited evidence of significant tearing. The transgranular fracture surface was not faceted, but at higher magnifications, it appeared rather complex (Figure 4b). The α_2 lath basketweave arrangement could easily be observed, indicating that the fracture scale was that of individual α_2 laths, which failed by cleavage-like fracture. Large tear ridges were observed in the β_R phase, bounding the α_2 laths. A relatively high microcrack concentration was observed below the fracture surface, but no voids seemed to be present. The fracture path was very tortuous, often changing direction as the long axis of intersected α_2 laths changed direction. In "A-S,0.5" samples, the fracture was transgranular, with fracture surface features identical to those of the "A-S,1.5" sample, save the fracture scale, which was larger due to the larger α_2 laths size (Figure 4c). In the vicinity of prior-β grain boundaries, where α_2 had precipitated in colonies, the fracture surface appeared different. Here, large facets were observed, extending across colonies, each of these macrofacets being composed of a series of microfacets, corresponding to the cleaved individual α_2 laths oriented identically (Figure 4c). Tear ridges were present, bounding the microfacets. This observation leads us to believe that colonies behave as units during fracture. Microcracks were observed below the fracture surface, many of them at intersections between α_2 laths (Figure 5b). Bridging of the β_R phase and crack-tip blunting by the β_R phase were also observed. The microcrack concentration was substantially smaller than in the "A-S,1.5" specimens. The fracture profile was observed, in many places, to follow specific paths, at specific angles with the intersected α_2 laths, i.e., almost perpendicular to the α_2 lath long axis. It was not as tortuous as in the "A-S,1.5" samples.

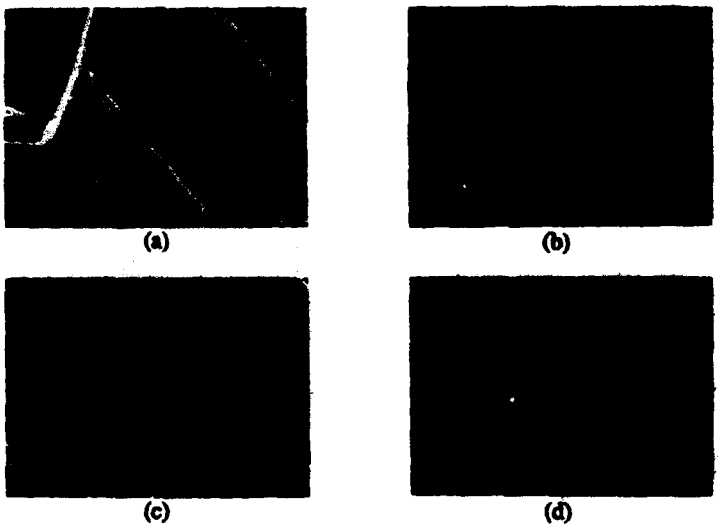


Figure 5 - Longitudinal sections of "A-S" fractured samples: (a) "A-S,25" ; (b) "A-S,0.5" ; (b) "A-S,0.1" ; (d) "A-S,0.01".

At slow cooling rates, i.e., 0.1°C/s, the samples failed by transgranular fracture. The fracture was faceted and contained, for the most part, macrofacets and microfacets similar to those aforementioned, but their size was significantly larger due to larger α_2 colony and α_2 lath sizes. The microcrack concentration below the fracture surface decreased substantially (Figure 5c). Microcracks were always similarly oriented with respect to the orientation of the α_2 laths. In addition, there was evidence of extensive crack-tip blunting by the β_R phase and bridging of the β_R phase (Figure 5c). When a small packet of similarly oriented α_2 laths was crossed by a crack, the entire packet was crossed and the crack was stopped at each end by the β_R phase (Figure 5c). Finally, the "A-S,0.01" specimens exhibited fracture features similar to those observed in "A-S,0.1" samples, except the scale which was much larger due to the size of α_2 colonies and α_2 laths (Figure 4d). The concentration of microcracks below the fracture surface

was very small. The fracture path followed a constant direction through each colony of α_2 laths, almost perpendicular to the laths (Figure 5d). And, when the path direction was forced to change with respect to the aligned α_2 laths, a step-like path was then observed, where the α_2 laths were still being crossed with the same angle but where a step was taken at the α_2/β_R interface, or in the β_R phase, to compensate for the change in direction (Figure 5d).

The ductility behavior of "S/A" microstructures *vs.* cooling rates was similar to that of "A-S" microstructures, as shown in Figures 3c and 3d. All microstructures also failed in a brittle manner, i.e., no necking was observed. The fracture surfaces of "S/A" samples were similar to those of "A-S" samples for all cooling rates up to 1.5°C/s. Thus, it is believed that "A-S" microstructures are stable with respect to tensile behavior for all cooling rates up to 1.5°C/s.

At low α_2 volume fractions, in "A-S" microstructures, it is believed that failure occurs by cleavage-like fracture throughout the β_R matrix (Figure 4a). The failure mechanism appears to be therefore nucleation controlled. Very coarse slip bands containing a high concentration of dislocations, extending throughout prior-β grains have been reported by Gogia *et al.* (3) in similar microstructures. Hence, it is believed that dislocations within slipbands pile up at prior-β grain boundaries or slipband intersections, producing very high strain concentrations. Cracks are then initiated at prior-β grain boundaries or within prior-β grains; intergranular fracture or slipband decohesion results. Banerjee *et al.* (4) have proposed that the inhomogeneous slip and arrangement of dislocations within slipbands resulted from a {110}<110> elastic instability as well as a modulated ω structure. TEM investigations of the "A-S,25" and "A-S,7.5" microstructures have revealed similar microstructural features. The origin of the voids observed throughout the "A-S,25" and "A-S,7.5" microstructures is unclear (Figure 5a). They might be related to the presence of ω-type precipitates, although no proofs have been found. However, they do not appear to take part in the failure process. As the α_2 volume fraction increases, i.e., from 25 to 7.5°C/s, a finite ductility is observed (Figures 3c and 3d). Gogia *et al.* (3) have actually reported a refinement of slip in the β_R matrix when the α_2 content is increased. They observed that as the α_2 volume fraction increases, dislocation density, and therefore strain concentration, within each slipband decreases. Thus, as the α_2 volume fraction increases, the ductility is expected to increase. The slip refinement might only result indirectly from increasing α_2 volume fractions. It might, indeed, result from a reduction of the decomposition, into ω-type products, of the saturated-β_R matrix, which in turn would be due to increasing α_2 volume fraction.

At high α_2 volume fractions, in "A-S" microstructures, the α_2 laths fracture in a cleavage-like mode and the β_R matrix fractures in a ductile mode, as shown in Figures 4b through 4d. Crack tip blunting by the β_R phase and bridging of the β_R phase observed below the fracture surface show that the β_R phase acts as a barrier to crack propagation (Figures 5b through 5d). Similar observations have been made by Chan (5,6). The limited number of slip systems in the α_2 structure is believed to be responsible for crack nucleation, most probably at intersections between slip planes or between a slip plane and the α_2/β_R interface. The shear stress level required to nucleate such cracks depends on the α_2 lath thickness, hence, as α_2 lath thickness decreases, the slip length decreases, and thus the strain concentration ahead of dislocation pileups decreases, prohibiting thereafter crack nucleation at low stresses. As a crack is initiated within an α_2 lath or at the α_2/β_R interface, it propagates through the α_2 lath until it meets the β_R phase. There, the highly ductile β_R phase is able to sustain the strain concentration developed at the head of the crack tip and slows down or stops the propagation of the crack. Crack growth or crack linkage between α_2 laths depends then on the amount of β_R phase present between α_2 laths and on the arrangement of α_2 laths. However, in colony-like microstructures, i.e., "A-S,0.1" and "A-S,0.01" microstructures, cracks are expected to easily propagate within a colony, throughout the entire colony because the crystallographic orientation within each α_2 lath is believed to be identical from lath to lath. And, the "soft" cleavage slip planes are similarly oriented between α_2 laths, leading to dislocation pileups, and strain concentrations, in the same plane (Figure 5c and 5d). Crack nucleation ahead of the crack tip in an adjacent α_2 lath is therefore eased. The efficacy of the β_R phase as a toughening phase is thus expected to be limited in this case. The small ductility that results from these microstructures is thought to be due primarily to the toughening action of the β_R phase located between distinct colonies.

As the cooling rate increases, from 0.5 to 1.5°C/s, α_2 laths precipitate in a basketweave manner and the β_R phase can now efficiently act as a ductile phase between α_2 laths. Indeed, α_2 laths are now oriented in a random manner. The "soft" cleavage slip planes of individual α_2 laths do not lie on the same plane anymore, and microcracks within α_2 laths, even though they are still observed having the same orientation with respect to the α_2 lath long axis, are randomly

oriented (Figure 5b). Thus, a crack initiated in an α_2 lath must change direction in the β_R phase in order to link up with another α_2 lath microcrack or to grow further in another α_2 lath. As such, the β_R phase is now more energy absorbing. This results in the convoluted fracture profile observed in Figure 5b. Therefore, as the cooling rate increases, the β_R volume fraction increases and the ductility is expected to increase. It is worth noting that many microcracks were observed nucleating at the intersection between α_2 laths, Figure 5b. This is thought to be due to a probable discontinuity in the β_R phase at these points. Hence, when the β_R phase is not present between α_2 laths to absorb the large strains developed ahead of α_2 slip bands at α_2/α_2 interfaces, microcrack nucleation can result. This seems to be the only drawback of the basketweave arrangement.

At high α_2 volume fractions, the failure mechanism is therefore believed to be propagation-controlled, to a large extent in basketweave-like microstructures and to a limited extent in colony-like microstructures.

Thus, the ductility increases with increasing α_2 volume fractions in the low α_2 volume fraction range, and with decreasing α_2 volume fractions in the high α_2 volume fraction range, because of the occurrence of these two distinct failure mechanisms. A ductility maximum results at about 1.5°C/s.

Conclusion

The α_2 volume fraction, size and arrangement were varied in β-solutionized microstructures by changing the cooling rate. The room temperature deformation and fracture mechanisms were then investigated as a function of the microstructural features mentioned above. Conclusions are as follows:

1. Strength is found to be controlled by α_2 volume fraction and α_2 lath width, through β_R phase strengthening and $(\alpha_2+\beta_R)$ boundary strengthening. The α_2 lath arrangement does not appear to contribute significantly to the strengthening mechanisms.
2. Failure is believed to occur by two different mechanisms: at low α_2 volume fraction, cleavage-like failure of the β_R matrix by slipband decohesion and intergranular failure is believed to take place; at high α_2 volume fractions, α_2 lath cleavage-like failure and ductile linkage of the cleaved cracks through the β_R phase is thought to occur. A ductility maximum results at about 1.5°C/s. Moreover, at high α_2 volume fractions, the α_2 lath arrangement is found to significantly affect the effectiveness of β_R as a toughening phase.
3. The microstructure corresponding to the "β-solutionizing + 1.5°C/s cooling rate" heat treatment gives the best combination of tensile properties. It contains a large volume fraction of fine α_2 laths arranged in basketweave.
4. Regarding the effects of the stabilizing/aging treatment, β-solutionized microstructures are found to be stable with respect to room temperature tensile properties for all cooling rates up to 1.5°C/s.

Acknowledgements

We appreciate support of this work by the Alcoa Center for Engineered Materials

References

1. J.C. Williams and A.W. Thompson, In *Metallurgical Treatises*, J.K. Tien and J.F. Elliott, eds., The Metallurgical Society of AIME, Warrendale, PA., (1981), 487-504.

2. C.H. Ward, J.C. Williams, A.W. Thompson, D.G. Rosenthal and F.H. Froes, In *Sixth World Conference on Titanium*, 1988, Cannes, France, P. Lacombe, R. Tricot and G. Béranger, eds., Les Éditions de Physique, Les Ulis, France, Vol. 2, (1989), 1103-1108.

3. A.K. Gogia, D. Banerjee and T.K. Nandy, *Metall. Trans. A*, Vol. 21A, (1990), 609-625.

4. D. Banerjee, A.K. Gogia and T.K. Nandy, *Metall. Trans. A*, Vol. 21A, (1990), 627-639.

5. K.S. Chan, *Metall. Trans. A*, Vol. 21A, (1990), 2687-2699.

6. K.S. Chan, *Metall. Trans. A*, Vol. 23A, (1992), 183-199.

THE EFFECT OF DEFORMATION AND HEAT TREATMENT CONDITIONS ON STRUCTURE AND MECHANICAL PROPERTIES OF γ-ALLOYS

B. I. Bondarev, N. F. Anoshkin, A. B. Notkin
D. V. Elagin, A. V. Molotkov
All-Russia Institute of Light Alloys,
Moscow, Russian Federation

Abstract

The paper covers structure and mechanical properties of TiAl-based alloys depending on the process of obtaining the material, deformation and thermal treatment conditions. The subject of inquiry was the alloy of stoichiometrical composition Ti-50 at. % Al, as well as the alloys characterized by several-percent deviation from stoichiometry in aluminium. The basic types of structures have been revealed, which can be observed in these alloys. An analysis of these structures has been carried out and the methods of their formation have been determined.

At present TiAl-based alloys are considered as advanced heat-resistant materials. The principal problem to be solved to provide wide use of those alloys is overcoming of brittleness at room temperatures and improvement in ductility. A great number of works has been devoted to investigation of the said alloys, a wide range of problems has been considered starting from the physical nature of ductility and up to the specific process conditions for production of real articles. Recently a number of fundamental reviews of this theme [1-4] testifying, among other things, to the fact that optimization of structure has a certain reserve for improving ductility.

The present paper is a result of work carried out for the last few years in the All-Russia Institute of Light Alloys aimed at revealing interconnection of structure and mechanical properties in TiAl-based alloys.

The purpose of this work is an inquiry into structure and mechanical properties of TiAl-based alloys depending on the process of production of the source material, conditions of the successive deformation and heat treatment.

The materials for inquiry were alloys Ti-46, 48, 50 and 54 at. % Al produced by casting at crystallization rate ~1 degree/sec

Titanium '92
Science and Technology
Edited by F.H. Froes and I. Caplan
The Minerals, Metals & Materials Society, 1993

and by the method of powder metallurgy (crystallization rate being ~10^3 degree/sec) with the successive hot isostatic pressing (compacting). Deformation has been carried out by the methods of isothermal forging and compacting under isothermal and nonisothermal conditions within the range of temperatures from 950 to 1350 °C.

An analysis of a great number of observed structures has made it possible to distinguish three main types of structures out of their variety, which are described further as the lamellar structure (type I), the recrystallized structure (type II) and the mixed structure (type III) (see Fig. 1a, b, c).



Figure 1 - TiAl alloy microstructures of various types:
a) type I - lamellar structure;
b) type II - recrystallized structure (deformed ingot);
c) type III - mixed structure (extruded compact).

Further we shall consider what these structures are, how they can be obtained, what factors exert effect on their parameters and what level of mechanical properties they provide.

The first type or the lamellar structure is a complete twinning along one of the planes {III} of γ-phase plate, at boundaries of which thin interlayers of α_2-phase are located (see Fig. 2a).

The lamellar structure is formed in ingots crystallized at a rate of ~1 degree/sec and in the process of heat treatment at a heat temperature exceeding $\alpha+\gamma$ transformation temperature.

Depending on the crystallization and cooling rates the thickness of γ plates and α_2 interlayers undergo changes within a wide range (from tenth fractions of a micrometer up to several micrometers).

An inquiry into alloys of various composition as to Al (from 46 up to 54 at. %) shows that the ingot structure consists of

two structural constituents described conventionally as γ_1 and γ_2 (see Fig. 1a). γ_2 constituent is the lamellar structure (see Fig. 2a) whereas γ_1 constituent is grains of γ-phase with separate twins and stacking faults and α_2 particles located along the boundaries of γ grains (see Fig. 2b).

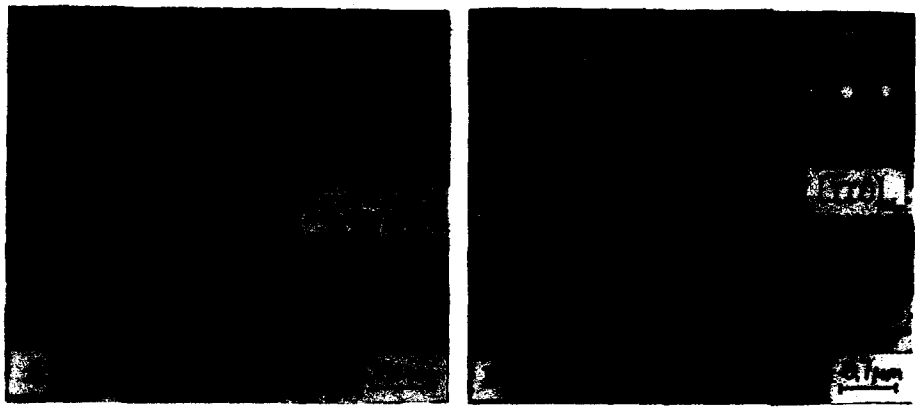


Figure 2 - Ti-50 at. % Al ingot structure:
a) γ_2 field; b) γ_1 field.

The data obtained as a result of the micro-X-ray spectrometry analysis showed that γ_1 fields contain such amount of aluminium, which is by 4-5 % higher than that contained in γ_2 fields. It allows us to propose that formation of γ_1 of liquid takes place, whereas formation of γ_2 is a result of $\alpha \rightarrow \gamma$ transformation.

In accordance with Ti-Al state diagram [1] a γ_1-γ_2 fields quantitative relation is changed within a wide range in case of change in content of aluminium from 46 up to 54 at. %. For example, in Ti-46 at. % Al alloy 100 % of γ_2 are present whereas in Ti-54 at. % Al alloy - 100 % of γ_1. The presence of one structural constituent only in those alloys provides for an intensive growth of γ_2 and γ_1 grains respectively and ensures, in the long run larger size of primary grains (300-500 μm) as compared with the alloys of the intermediate composition Ti-48-50 at. % Al (200-300 μm).

The second type or recrystallized structure (see Fig. 1b) consisting of recrystallized grains of γ-phase and α_2-phase precipitates of different morphology. This type of structure is formed as a result of the process of recrystallization at hot deformation and compacting in $\gamma+\alpha_2$ field. Depending on the conditions of deformation and heat treatment, the size of grains of γ-phase, as well as the size and morphology of α_2-particles change.

The conditions of ingot deformation (temperature, degree, number of steps) for obtaining completely recrystallized structure are different depending on the alloy composition. The greater volume of γ_1 constituent in the alloy the higher its tendency to recrystallization. For Ti-50 at. % Al alloy of

stoichiometric composition the recrystallized structure characterized by the grains of 5 μm in size can be formed by means of two-step isothermal forging at a temperature of 1000 °C with total degree of deformation ~150 %. A fine-grain structure in this case is characteristic of the structure formed under the dynamic recrystallization conditions. The main constituent is equiaxed grains of γ-phase with low density of defects inside which α_2-phase precipitates of equiaxed shape are present (see Fig. 3a).

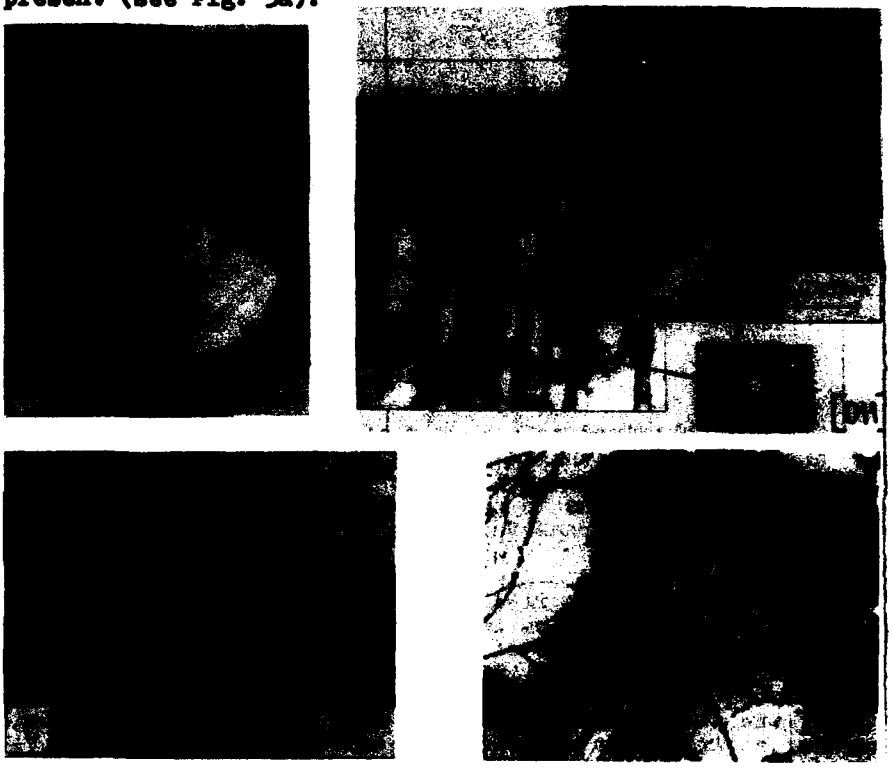


Figure 3 - Recrystallized (a, b, c) and mixed (d) structure of Ti-48 at. % Al alloy: a) after an ingot deformation at temperature of 1000 °C; b) after powder hot isostatic pressing at temperature of 1200 °C; c) after compact extrusion at temperature of 950 °C; d) after compact extrusion at temperature of 1350 °C.

Another method of formation of recrystallized structure of γ-alloys is powder hot isostatic pressing. The structure of Ti-50 at. % Al alloy obtained by this method at a temperature of 1200 °C is more coarse-grained and heterogeneous as compared with that formed after deformation of the ingot. In the structure one can distinguish fields with fine grains (medium size of the grains ~ 5 μm) and with much coarser grains

(~30μm) in a 7:3 ratio. The data of micro-X-ray spectral analysis has proved that the fine-grained fields contain less aluminium in comparison with the coarse-grained fields. It is evident that the structure inhomogeneity of the compact is conditioned by the hereditary influence of the powder particle structure inhomogeneity of which in its turn is determined by different aluminium content of powder particles.

The large, as compared with the ingot, number of particles of metastable α_2-phase, as well as the variety of their morphology (disks, plates, globules, etc.) draw attention (see Fig. 3b).

It should be noted that deformation of the compacted material with the successive heat treatment within a wide range of conditions made it possible to get a set of recrystallized structures characterized by different sizes of γ grains and α_2 - phase particles. One of such methods of obtaining recrystallized structure is extrusion of a compacted billet in $\gamma+\alpha_2$ - field under isothermal conditions at much lower temperatures than that of $\alpha \rightarrow \gamma$ transformation (~950 °C). The structure formed by this method is characterized by smaller grain size (~3 μm) and improved homogeneity as compared with the compacted material. In γ -phase grains one can observe nonuniform density of defects, very small α_2-phase precipitates (0.01-0.1 μm). The structure includes strong work hardened regions with high density of α_2-particles in which recrystallization was not fully completed (see Fig. 3c). These fields are very stable and can not be practically eliminated by annealing at a temperature up to 1350 °C. Thus, completely recrystallized structure cannot be formed by this method.

The third type of the mixed structure consisting of the fields characterized the recrystallized grains and lamellar fields. This type of structure is formed as a result of recrystallization taking place in the upper part of $\alpha+\gamma$ and α -fields. It has been formed during extrusion of compacted billets under nonisothermal conditions at the temperature of 1350 °C. The structure of the extruded bar in longitudinal section presented in Fig. 1c consists of the alternating layers of transformed coarse grains of 75-100 μm size and fine recrystallized grains of 10-20 μm size in ~ a 3:2 ratio. The layers are located in the direction perpendicular to the direction of deforming tension and are spread lengthwise to a distance considerably exceeding their transverse size.

Origin of the layers characterized by different structure is connected on the one hand with the inherited influence of chemical inhomogeneity of the compacted material, on the other hand it is determined by the fact that the bar structure is formed within two-phase $\alpha+\gamma$-field.

An electron microscope examination proved that the lamellar microstructure is analogous to that observed in the alloys after casting and is distinguished only by a greater dispersivity both of the twins and the interlayers of α_2-phase (tenth fractions of micrometer). The fine-grained constituent is presented by recrystallized grains with a negligible number of

α_2-phase precipitates located along their boundaries (see Fig. 3d).

Tensile mechanical properties of the alloys containing various amount of Al under different structural conditions were investigated in the present work. There has been studied the effect of annealing temperature (20-1400 °C) and test temperature (20-900 °C) on the strength and plasticity characteristics of γ-alloys. Long-term strength (σ_{100}) of the alloy within the range of temperatures of 600-900 °C was studied. It should be noted that because of low plasticity we failed to obtain the trust-worthy data on tensile mechanical properties of Ti-54 at. % Al alloys at the temperature of 20 °C.

An analysis of mechanical properties of pure lamellar structure (type I) of Ti-46 at. % Al alloy and the mixed type having various $\gamma_1 : \gamma_2$-fields ratio has shown that negligible changes of Al content in the alloy exert great effect upon mechanical properties. For example, 2 % reduction in Al content, as compared with the stoichiometric composition and 20-30 % reduction in the volume fraction of γ_1 in the cast structure results in increase of UTS by 20-30 kg/mm^2 and El. by 0.2-0.3 % Ti-48 at. % Al alloy with $\gamma_1 + \gamma_2$ structural constituents ration as 1:9 and α_2-phase content equal to 6-8 % (see Fig. 4a) has maximum level of strength and plasticity characteristics in the cast state.

Formation of the homogeneous fine-grained structure of type II (see Fig. 1b) at the temperature of 1000 °C makes it possible to improve strength characteristics considerably and plasticity characteristics to somewhat lesser degree at the room temperature (for example, for Ti-50 at. % Al alloy UTS-58 kg/mm^2, El.=0.8 % (see Fig. 4b). These properties are ensured by formation of the homogeneous recrystallized structure characterized by an average size of grains from 2 to 3 μm.

However, the thesis condending that refining of the grains leads to improvement of mechanical properties should not be considered as a general one which may be applied to all the structural conditions. For example, the fine-grained structure obtained by means of isothermal deformation at the temperature of 950 °C is characterized by almost zero elongation at a room temperature. Mechanical properties of the compacted material are also somewhat poorer as compared with the cast material.

Thus, not only the type of a structure (in the present case it is recrystallized one) is of importance, but also the size of the grains and the degree of their perfection. Bar extruded at the temperature of 950 °C have areas of nonrecrystallized structure with high density of defects, which are centres of brittle rupture. The properties depend also on the character of the recrystallized grains boundaries (special boundaries or boundaries of general type) [5]. Reduction of a portion of special boundaries leads to growth of plasticity that in its turn depends on a deformation temperature. At elevation of deformation temperature a portion of these boundaries becomes smaller. The grain size exerts great effect on the cold brittleness threshold of γ-alloys. Reduction of the grain size by an

order of magnitude leads to lowering of the cold brittleness threshold by 100 °C. The lowest threshold (600 °C) has been obtained on the structure of type II characterized by the grain size of 2-3 μm.

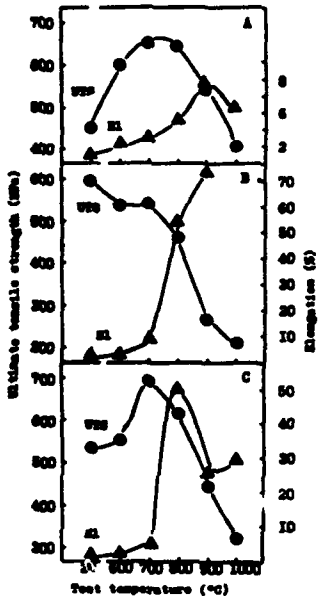


Figure 4 - Mechanical tensile properties of γ-alloys in various structural states: a) an ingot (type I); b) an ingot after deformation at temperature of 1000 °C (type II); c) a compact after extrusion at temperature of 1350 °C (type III).

The mixed structure (type III) (see Fig. 4c) formed during extrusion of a compact in γ+α-field has the best set of properties registered during the work (UTS=54 kg/mm^2, El.=1.5 %). The best set of properties (first of all of plasticity properties) of this state as compared with others is conditioned by particularities of the mixed structure, in which the layers with transformed coarse grains alternate with fine recrystallized grains.

No single state of the investigation proves that heat treatment by means of annealing samples at the temperature of 600-1400 °C eliminates cold brittleness. Within the temperature range of 1200-1400 °C, at which sharp increase of grains size takes place, the strength and ductility characteristics of γ-alloys are decreased.

At all the investigated structural states γ-alloys have high-temperature strength: for example, at the temperature of 600 and 700 °C σ_{100} value of cast (type I-, mixed (type III) and

recrystallized (type II) states is 70, 66, 42 and 48, 38, 31 kg/mm^2 respectively. If the size of the structural constituents becomes smaller, it leads naturally to reduction of high-temperature strength, nevertheless it is still sufficiently high.

It should be noted that when testing the samples for the stress-rupture strength it was established that σ^{500}_{100} value was considerably higher than UTS at this temperature. This anomaly is a concequence of high sensitivity of mechanical properties of γ-alloys to the speed of loading.

References

1. Y.-W. Kim, "Recent Advances in Gamma Titanium Aluminide Alloys" (Paper presented at the MRS Fall Meeting, Boston, 26 November - 1 December, 1990), 18.

2. F. H. Froes, C. Suryanarayana and D. Eliezer, "Synthesis and Applications of the Titanium Aluminides" (Iron and Steel Institute of Japan (ISIJ), Special Issue, October 1991), 97.

3. Y.-W. Kim and F. H. Froes, "Physical Metallurgy of Titanium Aluminides" (Paper presented at the TMS/ASM Fall Meeting, Indiana, 1-5 October 1989), 28.

4. Y.-W. Kim, "Intermetallic Alloys Based on Gamma Titanium Aluminide", The Journal of the Minerals, Metals and Materials Society, 41 (7) (1989), 24-29.

5. R. M. Imaev, "Structure and Properties of TiAl Intermetallic Compound" (Ph. D. thesis, UAI, Ufa, 1988), 172.

The Influence of Microstructure on the Creep Behavior of the Near-γ Alloy Ti-48Al-1V-0.2C

Brian D. Worth*, J. Wayne Jones*, John E. Allison+, William E. Dowling+

* Department of Material Science, University of Michigan, Ann Arbor, Michigan, 48109.

+ Research Staff, Ford Motor Co., Dearborn Michigan 48121.

Abstract

The relationships between creep behavior and microstructure in the $\gamma + \alpha_2$ alloy, Ti-48Al-1V-0.2C (at%), have been investigated. In view of the importance of microstructure in creep behavior, a systematic approach to the control of microstructural morphologies and α_2 volume fraction has been conducted. By carefully controlling thermo-mechanical processing parameters, the influence of solution temperature, cooling rate, and secondary heat treatment on volume fraction and morphology of α_2 has been determined. Microstructural morphologies ranged from fully lamellar ($L(\gamma + \alpha_2)$), to duplex, to equiaxed γ plus grain boundary triple point α_2 at the lowest volume fraction of α_2. Creep studies were performed under constant load at 815 °C in air for initial stresses ranging from 50 to 200 MPa. Microstructural morphology was shown to have a significant influence on creep behavior, with the fully lamellar morphology giving the lowest minimum creep rates. Overall creep resistance is influenced by volume fraction of α_2 as well as its morphology. Power law behavior is observed with a stress exponent of 9 in the fully lamellar microstructure and a range of 2.5 to 4 for all other microstructures.

Introduction

Titanium aluminides, specifically γ (TiAl) based alloys, are of interest because of their excellent high temperature strength, oxidation resistance and low density. Development of single phase γ alloys has been hampered by low room temperature ductility and fracture toughness. However, alloys based on the two-phase $\gamma + \alpha_2$ (Ti_3Al) microstructure (43-48 at% Al) have offered considerable improvement in ambient temperature properties while retaining useful strength and creep resistance at elevated temperatures. Numerous studies have been performed in recent years to understand deformation mechanisms in $\gamma + \alpha_2$ alloys in an attempt to improve properties through ternary and quaternary alloy additions and through control of microstructure. Much of this activity has been summarized recently by Kim [1,2].

Considerable research has been devoted to creep deformation in TiAl based alloys and has shown that in γ and $\gamma + \alpha_2$ alloys, in the temperature range of 550-850°C, power law creep predominates[3-9]. These and other studies have shown that creep resistance in $\gamma + \alpha_2$ alloys depends significantly on microstructural morphology[1,2,8,9]. In general, strength parallels the dependence of creep resistance on microstructure. Creep resistance increases with increasing amounts of the lamellar, $L(\gamma + \alpha_2)$, morphology. Fully lamellar microstructures exhibit substantial improvements over duplex microstructures which contain mixtures of γ grains and lamellar regions. The increase in creep resistance and elevated temperature strength of the fully lamellar microstructure is generally attributed to the α_2 laths acting as barriers to slip. However,

Titanium '92
Science and Technology
Edited by F.H. Froes and I. Caplan
The Minerals, Metals & Materials Society, 1993

slip. However, few definitive studies have been performed which separate the roles of the numerous microstructural variables, including grain/colony size, α_2 volume fraction, and morphology in determining strength, creep resistance, and ambient temperature ductility.

The objective of the present research has been to develop a better quantification of the influence of microstructural morphology on creep resistance in $\gamma + \alpha_2$ alloys. The approach has been to develop, through carefully controlled processing routes, a well-defined set of microstructures where α_2 volume fraction and morphology are varied independently and where grain size was controlled, as well. The alloy, Ti-48Al-1V-0.2C, has been used for this study.

Experimental

Material was obtained from Timet in the form of a hot isostatic pressed 110 kg casting with a nominal composition of Ti-48Al-1V-0.2C-0.14 (at%). The ingot was sectioned using wire EDM and forged in the temperature range of 1107-1177 °C with a reduction of 180% true strain .

The ability to control morphology in $\gamma + \alpha_2$ alloys was evaluated by using several different multistep heat treatment pathways which are summarized in Table I. Control parameters included temperature, time at temperature, and cooling rate from temperature. Cooling rates of 1°C/s and lower were controlled within the furnace by a linear ramp from heat treatment temperature to temperatures below 900 °C. Volume fractions of α_2 were determined by examining polished specimens in an SEM using back scattered electron (BSE) imaging, where α and α_2 phases appear brighter than γ regions because of their higher average atomic number. Because of the limitations on resolution of the image analysis system used, it was not always possible to resolve individual α_2 platelets in the L($\gamma + \alpha_2$) structure. Therefore, apparent volume fractions of α_2 are reported when lamellar morphologies are present.

Table I Heat Treatments Parameters

Single Step Heat Treatment Parameters			
Solution Temperature	Time @ Temperature	Cooling Rate From Solution Temperature	
1400 °C	1 hr	0.2 °C/s	
1350 °C	1 & 2 hrs	1.0 °C/s	
1325 °C	12, 24 hrs	0.2 °C/s	
1300 °C	8,12,24 &100 hrs	0.01, 0.05,0.1, 0.2, & 1 °C/s	
1100 °C	8,12,24 &100 hrs	0.2 °C/s	
Two Step Heat Treatment Parameters			
Solution Temperature	**Cooling Rate From S.T.**	**Secondary Heat Treatment Temperature**	**Cooling Rate From S.H.T.T.**
1325 °C/24 hrs	0.2 °C/s	1350, 1360, & 1375 °C/ 1 hr	1.0 °C/s
1325 °C/24 hrs	0.2 °C/s	1225, 1250, 1275, 1300, & 1325 °C/16 hrs	1.0 °C/s
1300 °C/24 hrs	0.05, 0.2, 1.0 °C/s	1200, 1225, 1250, 1275, & 1300 °C/16 hrs	0.2 & 1.0 °C/s
1300 °C/24 hrs	0.2, 1.0 °C/s	1350, 1360, & 1375 °C/ 0.5 & 1 hr.	1.0 & 2.0 °C/s

Creep testing was conducted at 815 °C in air, under constant load control on standard creep test machines equipped with lever arms with a 20:1 ratio. Specimen heating was accomplished with resistance furnaces, and temperature was controlled to within ±1 °C along the gage length. Creep specimens had a gage length of approximately 32 mm and a gage diameter of 6.35 mm. An averaging mechanical extensometer was attached to grooves in the specimen shoulders, just outside the gage length, and capacitance transducers were attached to the extensometer. An effective gage length at 1.05 gage diameter was used to calculate creep

strain from measured displacement. With this system and specimen configuration, strain could be determined with a resolution of 1.52×10^{-6}.

Results and Discussion

Microstructure Development

The role of solution temperature on microstructure was examined by solutionizing within the $\alpha + \gamma$ phase field, or, in the case of the fully lamellar microstructure, above the α transus. Several microstructures were developed using a single step heat treatment and are shown in Fig. 1. When the volume fraction of α produced at the solution temperature was significantly less than or greater than 50%, accelerated grain growth of the majority phase occurred and an inhomogeneous distribution of the minority phase resulted.



Fig. 1. Microstructures of Ti-48Al-1V-0.2C produced by the following single step solution treatments: a) forged + 1100°C/8 hrs/CR=0.2°C/s, b) forged + 1300 °C/ 24 hrs/ CR=1.0 °C/s, c) As Cast + 1400 °C/ 1 hr./CR=0.2 °C/s.

The influence of cooling rate from the solution treatment temperature was explored by first homogenizing the structure within the $\alpha + \gamma$ phase field for 24 hours. Solution treatments were conducted at 1300 °C, where the equilibrium volume fraction of α was approximately 50%, in an attempt to homogenize the microstructure. Cooling rate from this solution treatment temperature was varied from 0.01 °C/s to 1.0 °C/s and the final apparent α_2 volume fraction varied from 5% at the slowest cooling rate to approximately 20% at a cooling rate of 1.0 °C/s (Fig. 2). For the slower cooling rates, α_2 was primarily present as equiaxed particles located at γ grain boundary triple points. At higher cooling rates, and, correspondingly, at higher α_2 contents, the development of a duplex microstructure occurred. For the duplex microstructure, a transition from lamellar regions at grain boundary triple points to a conventional two-phase microstructure of γ grains and lamellar regions occurred as the cooling rate (and hence α_2 volume fraction) increased.

The final pathway involved a two step heat treatment. An initial solution treatment at 1300 °C for 24 hours was used to homogenize the microstructure. This was followed by a secondary heat treatment within the $\alpha + \gamma$ region to control the final volume fraction of α_2 upon final cooling. By varying the secondary heat treatment temperature within the two phase-field, the final apparent volume fraction of α_2 varied from 5% at a secondary heat treatment of 1200 °C, to 35% after a 1275 °C secondary heat treatment. The microstructures produced by the two-step heat treatment are shown in Fig. 3.

It is interesting to note that the final morphologies and apparent volume fractions of α_2 after secondary heat treatments are significantly influenced by prior heat treatment history. The

microstructures in Fig. 4 were given the same secondary heat treatment of 1250 °C for 16 hours. The differences in the final microstructures are the result of the variation in morphology, which was brought about by the variation in cooling rate from solution treatment temperature, prior to the secondary heat treatment.

It is clear that careful consideration of thermal processing history is needed when attempting to vary the morphology of the near-γ alloys, while maintaining a homogeneous microstructure. In addition, it has also been shown that with proper heat treatment it is possible to significantly vary the morphology of this two phase microstructure and at the same time maintain a relatively constant γ grain size. Specifically, it has been shown that α_2 volume fraction can be controlled without sacrificing microstructural homogeneity by controlling cooling rate from solution temperature. The use of secondary heat treatments within the $\alpha + \gamma$ phase field has been shown to be beneficial in producing high volume fraction lamellar microstructures.



Fig. 2. Variation of microstructure in Ti-48Al-1V-0.2C with cooling rate from a homogenization solution treatment of 1300 °C/ 24 hrs. a) CR=0.01 °C/s b) CR=0.1 °C/s c) CR=1.0 °C/s.



Fig. 3. Microstructures produced by a solution treatment of 1300 °C/ 24 hrs/ CR=0.2 °C/s followed by a secondary heat treatment of : a)1225 °C/ 16 hrs/ CR=1.0 °C/s, b)1250 °C 16 hrs/ CR=1.0 °C/s, c)1275 °C 16 hrs/ CR=1.0 °C/s.

Influence of Microstructure on Creep Behavior

Six microstructures produced by the various heat treatment pathways described above were used to examine the influence of morphology, grain size, and homogeneity on creep behavior in $\gamma + \alpha_2$ alloys. These microstructures, shown in Fig. 5a-f, are grouped into three different morphologies: grain boundary triple point α_2 (Fig. 5a and b), duplex (Fig. 5c and d), and near/fully lamellar (Fig. 5e and f). To ensure that no transformations occured during testing, the microstructures in Fig. 5b-e were stabilized at 1000 °C for 8 hours prior to testing.



Fig. 4. Influence of initial solution treatment on microstructure after a secondary heat treatment at 1250 °C/16 hrs/ CR=1.0 °C/s. a) 1300 °C/ 24 hrs./ CR=0.05 °C/s, b) 1300 °C/ 24 hrs./ CR=0.2 °C/s, c) 1300 °C/ 24 hrs./ CR=1.0 °C/s.

Morphology has a strong influence on the creep resistance of this $\alpha_2 + \gamma$ alloy, as shown in Fig. 6 for tests conducted at 815 °C and 150 MPa. The highest creep resistance is observed in the near lamellar and fully lamellar microstructures which have both a high α_2 volume fraction and a high lamellar content. These results are consistent with the findings of others[2,8]. Comparison of the minimum creep rates for the near lamellar and fully lamellar microstructures (1.7×10^{-9} s^{-1} and 3.2×10^{-9} s^{-1}, respectively) indicates that a rather significant change in colony size has a minimal influence on the creep resistance. Rather, the superior creep resistance of the lamellar morphology can be attributed to the barriers to dislocation motion provided by the alternating lamella of γ and α_2 which represent a scale much finer than colony size. Although the lamellar and near-lamellar microstructures represent the highest volume fractions of α_2, creep resistance does not vary monotonically with α_2 content. Microstructures with the lowest α_2 content, the triple point α_2 microstructure with an apparent α_2 volume fraction of 2.5 %, have a creep resistance superior to that of the duplex microstructure which had an apparent α_2 content of 8% to 17%. As in the case of the lamellar microstructure, microstructural homogeneity and γ grain size in the triple point α_2 morphology had little influence on minimum creep rates for the temperature and stress used in these experiments (Fig. 5a = 4.8×10^{-9} s^{-1} and Fig. 5b = 7.0×10^{-9} s^{-1}). Comparing the creep behavior of 5b vs. 5d it is evident that at a constant γ grain size, the triple point α_2 microstructure maintains a lower minimum creep rate than the duplex microstructure (2.4×10^{-8} s^{-1}). It should also be noted that tensile strength and ductility varied with creep strength in a manner similar to that observed by others[10]. It is also interesting to note that β-processed near-α titanium alloys with lamellar microstructures also exhibit superior creep resistance even at temperatures as high as 760 °C (e.g. see ref. 11), suggesting that perhaps relationships between microstructural morphology and creep behavior can be generalized.

The stress dependence of the minimum creep rate in the various microstructures at 815 °C follows the typical power law behavior, as shown in Fig. 7. Stress exponents of 2.5 to 4, characteristic of creep deformation controlled by dislocation mechanisms, are observed for all but the fully lamellar microstructure.

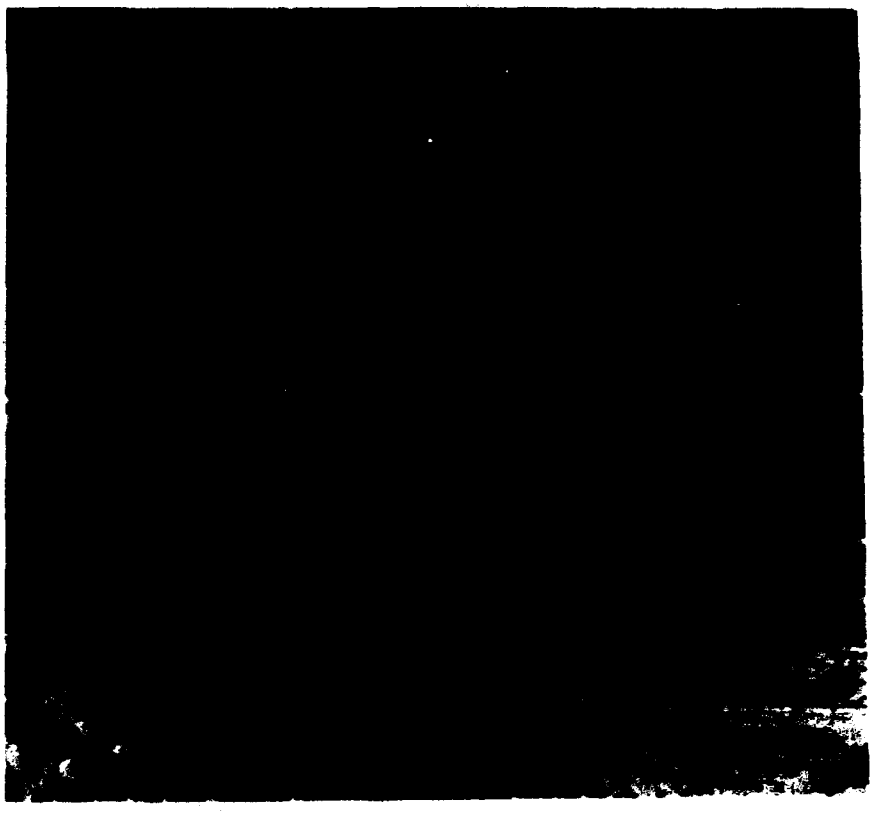


Fig. 5. Microstructures examined in creep studies on Ti-48Al-1V-0.2C: a) forged + 1100°C/8 hrs/CR=0.2°C/s, b) forged + 1300 °C/ 24 hrs. / CR=0.01 °C/s*, c) forged + 1300 °C/ 24 hrs./ CR=0.1 °C/s*, d) forged + 1300 °C/ 24 hrs./ CR=1.0 °C/s + 1275 °C/ 16 hrs./ CR=1.0 °C/s*, e) forged + 1300 °C/ 24 hrs./ CR=1.0 °C/s + 1360 °C/ 0.5 hrs./ CR=1.0 °C/s*, f) Cast + 1400 °C/ 1 hr./CR=0.2 °C/s. *Stabilized at 1000 °C/ 8 hrs./ CR=0.2 °C/s.

These values are consistent with values reported for this class of alloys by other researchers[4,5]. The higher stress exponent of 9 for the fully lamellar microstructure may be associated with back stresses developed during creep and supports the position that barrier strengthening occurs in the lamellar microstructure. It should also be noted that in tensile deformation at 815 °C, little dislocation motion was observed in the fully lamellar microstructure, consistent with the low ductility[12].

The multiple heat treatment pathways employed here have allowed the influence of α_2 volume fraction and morphology on creep to be compared at a constant γ grain size and Al content. For the limited tests conditions studied, grain size, per se, appears to exert only a secondary influence on creep resistance, compared to microstructure morphology and α_2 volume fraction. By comparing the creep resistance of an α_2 alloy[13] to the triple point α_2 morphology of the present study, it can be postulated that the lower intrinsic creep strength of α_2 in this temperature and stress regime may explain the differences in creep resistance between low and intermediate volume fractions of α_2. It is possible to further speculate that the strong influence of morphology in the lamellar structure overrides the negative influence of the

increased volume fraction of α_2 to yield improved creep resistance. Further studies are needed, however, to separate the combined roles of α_2 morphology and α_2 volume fraction on creep resistance and to confirm the validity of these assumptions.

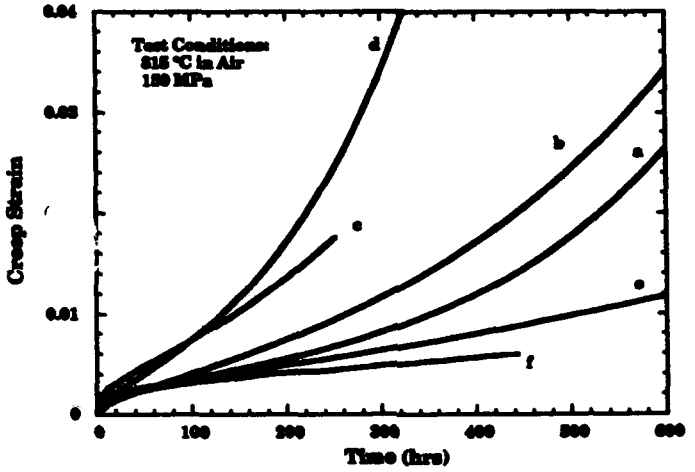


Fig. 6. Effect of microstructure (Fig. 5 a-e) on the creep behavior of Ti-48Al-1V-0.2C.

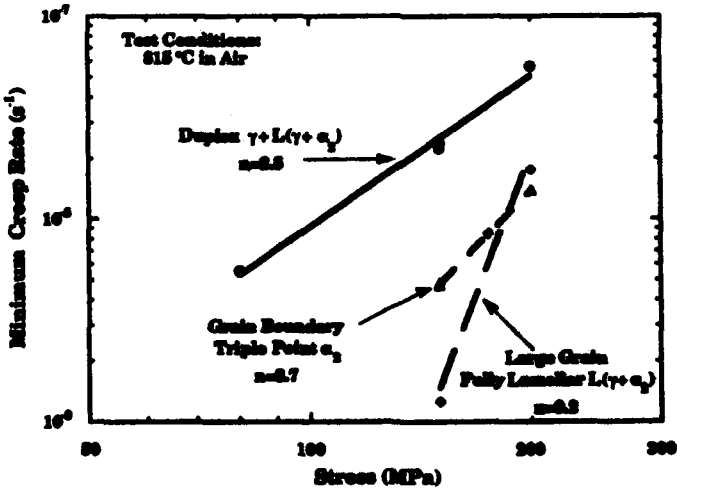


Fig. 7. Effect of microstructure on the stress exponent of Ti-48Al-1V-0.2C.

This work also shows that the processing route does not uniquely dictate the creep resistance of $\gamma + \alpha_2$ alloys. Similar creep rates were obtained in similar microstructures, produced by different heat treatment pathways. This was observed in the triple point α_2 microstructure that was produced by both a single step heat treatment and by controlling the cooling rate from solution temperature (Fig. 5a & 5b). This conclusion is also supported by comparison of the creep behavior of similar duplex microstructures produced by either a single step heat treatment or a two stage heat treatment (Fig. 5c & 5d).

Conclusions

1. Microstructure morphology is dependent on solution temperature and cooling rate from solution temperature in near-γ TiAl.
2. Microstructure strongly influences the creep strength of Ti-48Al-1V-0.2C, with the fully lamellar microstructure having the highest creep strength.
3. Near-γ alloys with similar microstructures, but with different heat treatment histories, exhibit similar creep behavior.
4. Minimum creep rates do not depend strongly on γ-grain size or colony size for the test conditions employed here.
5. A significantly higher stress exponent is observed at 815 °C for the fully lamellar microstructure (n=9) than for the other microstructures tested (n=2.5-5).

Acknowledgments

BDW and JWJ gratefully acknowledge the financial support of Ford Motor Company.

References

1. Y-W Kim. Intermetallic Compound Alloys Based on Gamma-Titanium Aluminide (TiAl). Journal of Metals; July, 1989, pp. 24-30.
2. Y-W. Kim, High Temperature Ordered Intermetallic Alloys IV, ed., J.O. Stiegler, L.A. Johnson, and D.P. Pope (Pittsburgh, PA: MRS, 1991), pp. 777-794.
3. M. J. Blackburn, M.P. Smith, Research to Conduct an Exploratory Experimental and Analytical Investigation of Alloys; November 1980; AFWAL-TR-80-4175.
4. P.L. Martin, D.H. Carter, R.M. Aikin Sr., Proc. 4th Int. Conf. on Creep and Fracture of Engineering Materials and Structures, B. Wilshire and R.W. Evans, eds., Institute of Metals, London, 265-275, 1990.
5. P.L. Martin, M.G. Mendiratta, H.A. Lipsitt, Met. Trans. A, 14A, 2170 (October 1983).
6. T. Takahashi and H. Oikawa, Microstructure/Property Relationships in Titanium Aluminides and Alloys, ed. Y-W. Kim/R.R. Boyer (TMS, 1991), 227-235.
7. T. Takahashi, H. Nagai, H. Oikawa, Mat. Sci. and Eng., A128, 195-200, (1990).
8. S. Mitao, S. Tsuyama, K. Minakawa, Microstructure/Property Relationships in Titanium Aluminides and Alloys, ed. Y-W. Kim/R.R. Boyer (TMS, 1991), 297-311.
9. W.E. Dowling, B.D. Worth, J.E. Allison, J.W. Jones, Microstructure/Property Relationships in Titanium Aluminides and Alloys, ed. Y-W. Kim/RR. Boyer (TMS, 1991), 123-133.
10. W.E. Dowling Jr., B.D. Worth, W.T. Donlon, J.E. Allison, this proceedings.
11. J.E. Allison, W. Cho, J.W. Jones, W.T. Donlon, Creep Behavior of Ti-6242: The Effect of Microstructure and Silicon. Sixth World Conference on Titanium, ed. Lacombe, P.; Tricot, R.; Béranger, G.; 1988; Cannes, France; 1988.
12. W.T. Donlon, W.E. Dowling Jr., J.E. Allison, Microstructure/Property Relationships in Titanium Aluminides and Alloys, ed. Y-W. Kim/R.R. Boyer (TMS, 1991), 75-88.
13. M.G. Mendiratta and H.A. Lipsitt, J. Mater. Sci., 15 (1980) 2985.

Microstructure and Mechanical Properties of Refractory Metal Modified Ti-48 at%Al-2 at%Nb-2 at%Cr

P. L. Martin and C. G. Rhodes

Rockwell International Science Center
1049 Camino Dos Rios
Thousand Oaks, CA 91360

Abstract

A vacuum arc remelted ingot of an alloy based on the high ductility composition Ti-48 at% Al-2 at% Nb-2 at% Cr containing 1 at% Mo has been characterized following isothermal forging. Thermal-mechanical processing included two stages of working with intermediate recrystallization/homogenization treatments. The microstructure at each stage was documented by crystallographic texture measurements, optical metallography and analytical electron microscopy. The phase distribution and morphology after the first working operation were a function of the temperature of the recrystallization treatment. A fine-grained duplex structure was chosen as the starting microstructure for the second isothermal forging. This resulted in a fine equiaxed microstructure without the 'banding' associated with chemical inhomogeneities in single-stage forged near-γ alloys. Two microstructural conditions, fine equiaxed $\alpha_2+\beta+\gamma$ and a 'duplex' mixture of $(\beta+\gamma)$+transformed α lamellar colonies, were developed for room temperature tensile property measurements.

Introduction

Potential applications for light, stiff, strong and oxidation resistant alloys in advanced aerospace systems are numerous. The ordered compound based on the composition TiAl has often been proposed for engineering structures where service temperatures extend to 850°C. However, the binary compound has been plagued by limited room temperature ductility. More recently, the improved room temperature ductility of Cr containing near-γ compositions with optimized microstructures has been instrumental in increasing the interest in alloys based on TiAl [1-3]. Other work has demonstrated the strengthening and improved oxidation effects of ternary Mo additions [4,5]. The intent of this study was to determine whether Mo additions have a similar effect in compositions known to have good room temperature ductility, such as Ti-48Al-2Cr-2Nb (all compositions in atomic percent). Furthermore, documenting the evolution of the microstructure (grain morphology and volume fraction as well as crystallographic texture) through the thermomechanical processing steps could lead to an understanding of the necessary steps to attain a homogeneous fine-grained mixture of the constituents in this and other near-γ alloys.

Titanium '92
Science and Technology
Edited by F.H. Froes and I. Caplan
The Minerals, Metals & Materials Society, 1993

Experimental Procedure

Vacuum arc remelting produced an approximately 10kg ingot of the composition shown in Table I. The analyses were conducted by the melter for the ingot and by a second vendor for the forging. The agreement in the two analyses is excellent considering the variability usually noted in Al content determined by wet chemistry. The oxygen content (approximately 700 wppm) is on the low end of standard commercial practice.

Table I. Chemical compositions measured from the ingot and forging by two different sources (atomic percent for all elements, balance Ti).

Location	Al	Nb	Cr	Mo	Fe	Si	C	O	N	H
Ingot;										
Top	48.7	2.0	2.4	0.9	-	-	.049	.166	.038	.104
Bottom	48.0	2.0	2.0	0.9	-	-	.091	.193	.018	.132
Forging	48.8	2.0	2.1	0.9	.030	.049	.130	.173	.033	.108

A right cylinder of the cast ingot was isothermally upset forged 73% at 1150°C and a (constant) strain rate of 1.6×10^{-3} sec^{-1}. The height after this forging step was approximately 4.5cm. A chord of the forging was sectioned for metallographic examination and heat treatment. Following this, the remainder of the pancake was given an anneal at 1300°C for 1 hour prior to forging 62% at 1100°C with the same initial strain rate. The final thickness was approximately 1.6cm.

Microstructural characterization utilized standard optical metallography and analytical electron microscopy. Backscattered electron images (BEI) were used for the bulk of the study since they convey both chemical and morphological information. TEM specimens were made by twin-jet electropolishing and foils examined on a Philips CM30 at 300KV. Crystallographic textures using Cu K_α radiation were determined from the midplane following the first and second forging operations as well as on material recrystallized after the second working step. Room temperature tensile tests were done on a fine equiaxed and a duplex microstructure. Buttonhead specimens with a gage length of 25mm and a diameter of 8.5mm were tensile tested at room temperature at a (constant) strain rate of 5×10^{-3} sec^{-1}.

Results

Microstructure

Following the forging operations, the microstructures attainable through heat treatment were critically evaluated. The first forging created a fine mixture of dynamically recrystallized grains and deformed lamellar packets of $\alpha+\gamma$, Figure 1. A series of higher temperature recrystallization treatments were evaluated in an effort to homogenize and refine this structure prior to the second forging step. One hour at 1300°C appeared to offer the best compromise between uniformity and fine grain size. Figure 2 shows this structure using backscattered electrons from a polished surface and illustrates the uniform chemical composition attained as well as the uniform mixture of phases. Forging of this structure at a lower temperature (1100°C) was easily accomplished. Figure 3 shows the fine equiaxed grains and the absence of deformed lamellar colonies after the second working.

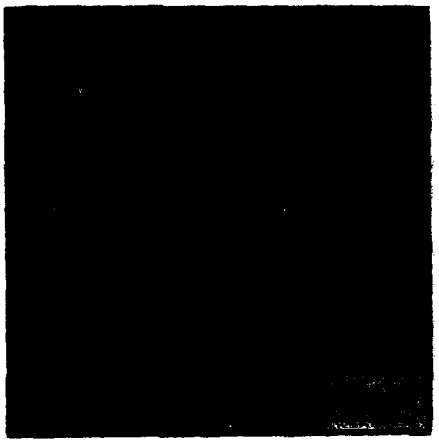


Figure 1. Optical micrograph from midplane of the pancake following first forging; 73% at 1150°C.

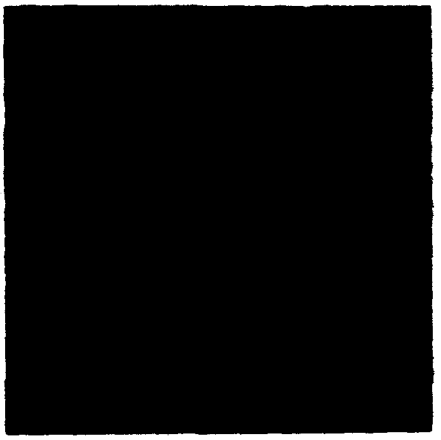


Figure 2. Polished section BEI showing material in Figure 1 following recrystallization for 1 hour at 1300°C.

Heat treatment following the final forging was done at various temperatures in the $\alpha+\gamma$ phase field to change the volume fraction and morphology of the constituent phases. Recrystallization at temperatures low in the $\alpha+\gamma$ phase field is known to result in non-uniform grain growth due to chemical inhomogeneities remaining from the casting [6]. This was observed to be the case following recrystallization for 1 hour at 1200°C after the first forging operation but not as obvious after the second as shown in Figure 4. Treatments at successively higher temperatures resulted in increased volume fractions of α at the expense of γ. Two microstructures, based on heat treatments below the 1335°C α transus, were selected for mechanical testing. The first, shown in Figure 5 (a), was attained after 1 hour at 1250°C, and was characterized by a fine equiaxed mixture of $\alpha_2+\gamma+\beta$. *Figure 5 (b)* is a low magnification TEM bright field image of this same treatment followed by stabilization for 8 hours at 950°C showing a (darker) β grain with equiaxed γ neighbors. Selected area electron diffraction showed the β to beordered with the B2 CsCl structure, while energy dispersive x-ray analysis showed it to be enriched in Cr and Mo. The second microstructure, shown in Figure 6 (a) following 1 hour at 1330°C, shows the duplex microstructure consisting of equiaxed γ with β in the boundaries and transformed α lamellar colonies (alternating plates of α_2 and γ having the well-known close-packed plane/direction orientation relationship). Figure 6 (b) shows a TEM bright field image of an equiaxed γ grain and two neighboring lamellar colonies after stabilization.

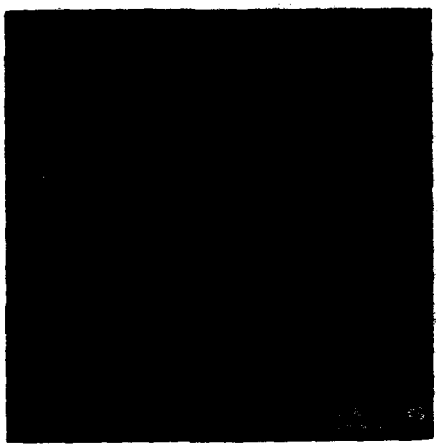
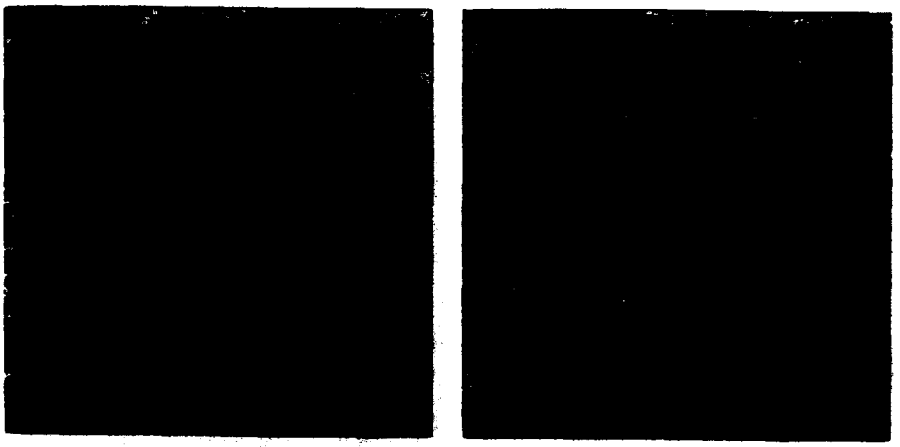


Figure 3. Polished section BEI following second forging (62% at 1100°C); the starting microstructure prior to this working operation is shown in Figure 2.



(a) (b)

Figure 4. Polished section BEI of the alloy recrystallized at 1200°C for 1 hour showing: (a) banding after the first forging and (b) no banding after the second working operation.



(a) (b)

Figure 5. Recrystallization at 1250°C for 1 hour and stabilization at 950°C for 8 hours after the second forging showing α_2-γ and β phases; (a) Polished section BEI and (b) TEM bright field.

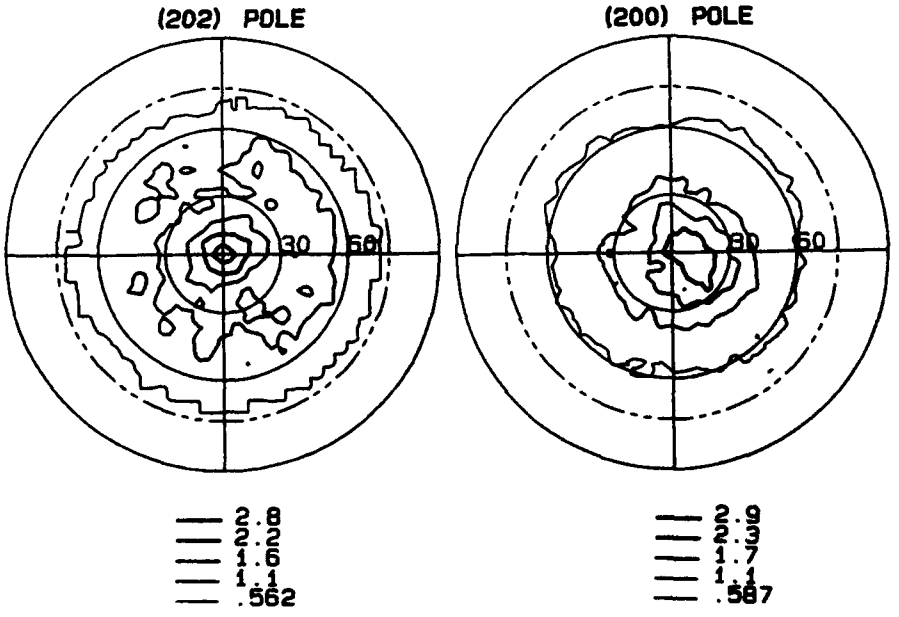
Texture

X-ray pole figures were collected for the γ phase following each forging step and after final recrystallization for both the γ and the α_2. Two distinctly different fiber textures were seen for the γ phase: both (202) and (200) poles showed peaks in the forging plane. These strengthened slightly from approximately 2.0 times random after the first working to approximately 2.7 times random after the second. Figure 7 shows these pole figures for the texture attained after recrystallization for 1 hour at 1310°C. Recrystallization increased these texture maxima slightly to 2.8 and 2.9 times random for the (202) and (200), respectively.



(a) (b)

Figure 6. Recrystallization at 1330°C for 1 hour and stabilization at 950°C for 8 hours after the second forging showing equiaxed γ and transformed α lamellar colonies; (a) Polished section BEI and (b) TEM bright field.



(a) (b)

Figure 7. Crystallographic texture of the γ phase after the second forging and recrystallization at 1310°C for 1 hour; (a) (202) and (b) (200) poles.

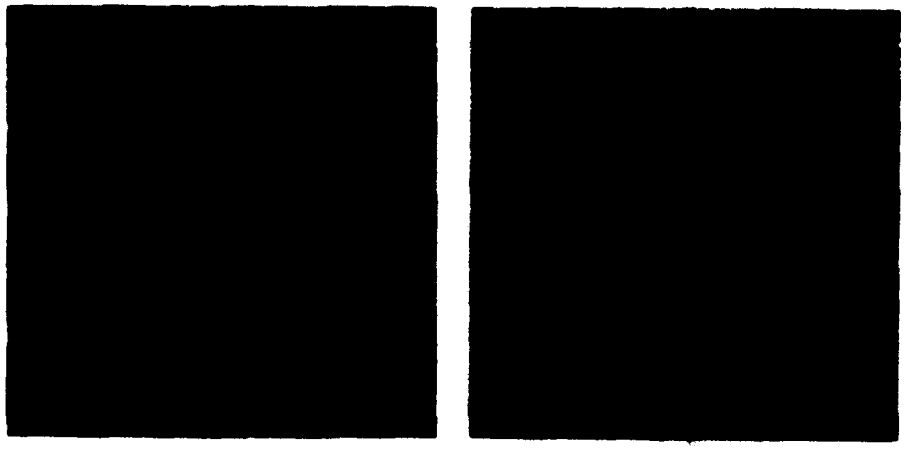
Mechanical properties

Room temperature tensile properties are listed in Table II. There is little difference in either the yield strength or the plastic elongation between the two microstructures. The stress-strain curves for each specimen showed a sharp deviation from elastic extension and a region of nearly zero work hardening reminiscent of Lüders elongation. The difference in ultimate strength was due to the different work hardening rates after this extension with the duplex microstructure showing faster hardening than the fine equiaxed microstructure.

Table II. Room temperature tensile properties of Ti-48Al-2Nb-2Cr-1Mo following the second forging and two different recrystallization treatments.

Heat Treatment	Microst. Type	0.2% Yield (MPa)	UTS (MPa)	Plastic Elong. (%)	RA (%)
1250°C/1+950°C/8	Equiaxed	501	528	1.2	1.1
1330°C/1+950°C/8	Duplex	498	560	1.1	1.4

Fracture paths were examined to evaluate the role of microstructure on the crack path. Figure 8 shows representative longitudinal sections of the gage section in regions where crack branches were found. In each case the tensile axis is horizontal. The equiaxed microstructure shows extensive crack bifurcation with the crack path primarily through the γ, Figure 8 (a). There was little evidence of crack bridging by the β; however the cracks did appear to avoid regions with significant concentrations of second phases. The duplex microstructure exhibited less secondary cracking; when present, it was primarily perpendicular to the stress axis, Figure 8 (b). Cracking was transgranular without regard to lamellae orientation unless a fortuitously oriented colony was traversed allowing crack propagation along lamellar boundaries. Secondary cracking was more profuse in lamellar colonies near this orientation.



(a) (b)

Figure 8. Polished section BEI from the gage sections of tensile specimens fractured at room temperature showing secondary crack paths; (a) specimen recrystallized at 1250°C/1hr. +950°C/8hrs. and (b) specimen recrystallized at 1330°C/1hr.+950°C/8hrs.

Discussion

Homogeneity in chemistry and microstructure are metallurgical goals that are often difficult to achieve. In the case of γ alloys, the combination of peritectic solidification and insufficient mechanical work can lead to gross inhomogeneities in both, as has been identified in the literature [6]. Mechanisms to overcome this include long time thermal treatments in the single phase α region and/or combinations of this with recrystallization following working. Dynamic recrystallization, as occurs in isothermal forging, is a very effective method for attaining homogeneity. Given the large scale of chemical segregation that arises from casting, single step isothermal forging to strains of 1.1 to 1.3 may not be sufficient to totally homogenize the microstructure as shown in Figure 1. Static recrystallization, especially high in the α+γ phase field following isothermal forging, can result in uniform microstructures prior to a second working operation as shown in Figure 2. This extra homogenization must be done at appropriate temperatures in order to avoid the 'banding' or inhomogeneous grain growth shown in Figure 4 (a). This figure compares the low temperature recrystallization behavior after the first and second forging operations and it provides a graphic illustration of the benefits of multiple working with intermediate anneals. The window for potential recrystallization is enlarged when chemical homogeneity has been attained, as evidenced by the uniform distribution of α and β shown in Figure 4 (b).

The crystallographic textures of the γ measured in this program are somewhat different from those in the literature for binary Ti-50at%Al [7,8]. In these studies, the authors used the Zener-Hollomon parameter, Z, to describe the variation of the (202) fiber texture during isothermal compression. At low values of Z, characteristic of low strain rates and high temperatures, a stronger texture was developed since grain boundary 'bulging' could accommodate the deformation without nucleating new grains. Higher strain rates or lower temperatures led to more profuse nucleation of new grains along strain concentrations leading to a weaker texture. The value of Z in the present study was calculated to be on the low end of the range studied by Fukutomi et al. [7,8], yet the (202) fiber texture developed was not strong. One explanation for this is the effect of strain since the dual forging operation divided the strain into two components each of which was smaller than the strain reported by Fukutomi. Although the overall strain, ~2.3, in the present study was larger than the individual compression strains in the Japanese work, the intermediate anneal could have lessened the effect of the first forging strain. An alternative hypothesis is based on differences in microstructure since the alloy in this study was composed of three phases during deformation; γ, α and β. Dynamic recrystallization (or grain 'bulging') could be very different in multiphase alloys where extensive grain growth is more difficult. If a relatively hard phase, such as α, is introduced into the microstructure, then strain localization in the immediate vicinity could lead to more grain nucleation and a weaker texture. In addition, no mention of a (200) fiber texture component was made in this prior work. Wider variations in forging conditions, as quantified by Z, would be required to completely understand these differences.

Tensile deformation of the two microstructures shown in Figures 5 and 6 led to quite similar properties. The strength values are significantly higher than those for a similar composition (in the forged condition) without the Mo modification [3]. It is likely that Mo would act as a solid solution strengthener in addition to potentially modifying the microstructure through stabilizing a significant volume fraction of ordered β. Care must be used in comparing compositions, in that strength values are strong functions of the microstructural scale as well as the processing route. For instance, extrusion seems to lead to higher values of the yield stress compared to forging [3,4]. For the current study a plausible, but unsubstantiated, explanation for the lack of microstructural effect on yield and ductility would be that the microstructural unit important to

room temperature deformation was the same in both cases. Note that the γ grain size is the same for both heat treatments in Figure 8. If slip in the equiaxed γ grains controls the onset of flow, then similar yield stresses would be found in each case. By the same token, if fracture is controlled by cleavage crack initiation in the γ phase (or regions of agglomerated γ grains), then similar ductilities for these two microstructures might be expected. The difference in work hardening might be associated with the volume fraction of lamellar colonies where the lamellae have a higher hardening rate than the equiaxed grains leading to the higher UTS value found at comparable ductility. These observations need to be confirmed by additional testing before these hypotheses can be verified.

Conclusions

The following conclusions can be drawn from this study:

1. Microstructural and chemical homogeneity are increased by multiple working operations especially when recrystallization is conducted at elevated temperatures between and after the forging steps.
2. Multiple forging operations do not produce strong crystallographic textures in multi-phase near-γ alloys in contrast to simpler binary alloys. Weak (202) and (200) fiber textures are observed in the γ phase.
3. Fine equiaxed and duplex microstructures produce similar (moderate) strengths and ductilities in T-48Al-2Nb-2Cr-1Mo. The crack path is transgranular unless lamellar colonies are suitably oriented to allow cracking along the lath boundaries.

Acknowledgments

The metallographic expertise of Mr. Bob Spurling and Mr. Mike Calabrese is gratefully acknowledged. Texture measurements of Dr. Mike James are also acknowledged. This work was sponsored by the Rockwell International Science Center Independent Research and Development program.

References

1. S.-C. Huang and E.L. Hall, *Metall. Trans.*, 22A, (1991), 2619.
2. S.-C. Huang, U.S. Patent 4,879,092; Nov.7, 1989.
3. S.-C. Huang, D.W. McKee, D.S. Shih and J.C. Chesnutt, in Intermetallic Compounds - Structure and Mechanical Properties, ed. O. Izumi, Japan Inst. of Metals, 1991, 363.
4. T. Maeda, H. Anada, M. Okada and Y. Shida, in Intermetallic Compounds - Structure and Mechanical Properties, ed. O. Izumi, Japan Inst. of Metals, 1991, 463.
5. T. Maeda, M Okada and Y. Shida, in High-Temperature Ordered Intermetallic Alloys IV, eds. L.A. Johnson, D.P. Pope and J.O. Steigler, MRS Volume 213, 1991, 555.
6. J.D. Bryant and S.L. Semiatin, *Scripta Metall.*, 25, (1991), 449.
7. H. Fukutomi, S. Takagi, K. Aoki, H. Mecking and T. Kamijo, in Intermetallic Compounds - Structure and Mechanical Properties, ed. O. Izumi, Japan Inst. of Metals, 1991, 839.
8. H. Fukutomi, S. Takagi, K. Aoki, M. Nobuki, H. Mecking and T. Kamijo, *Scripta Metall.*, 25, (1991), 1681.

IN-SITU STRENGTHENING IN TITANIUM

A.M. Russell, J.A. Jensen L.S. Chumbley, D.G. Konitzer*, T.W. Ellis

Ames Laboratory of the U.S.D.O.E., Iowa State University, Ames, IA 50011
*General Electric, Evendale, OH

Abstract

Deformation processing strengthening of metal-metal matrix composites has been well studied in the binary Cu-X alloys (where X = a bcc transition metal). Recent studies of deformation processed Ti-Cu, Ti-Mo, and Ti-Y show that the characteristic nanofilamentary microstructure of deformation processed materials can be produced in an hcp titanium matrix, and some of the resulting alloys possess increased strengths and good ductility.

Titanium '92
Science and Technology
Edited by F.H. Froes and I. Caplan
The Minerals, Metals & Materials Society, 1993

Background: The Cu-X Alloys

In-situ processing consists of heavily deforming a two-phase alloy of mutually immiscible elements to produce composite sheet or wire. The process can produce microstructures with nanometer-scale phases that impart exceptionally high strengths and good ductility to the deformed alloys. Many such alloys have been studied in the Cu-X systems (where X = bcc metals such as V, Nb, Ta, Cr, Mo, W, or Fe) (1-6). In the well-studied Cu(fcc)-20 vol. % Nb(bcc) system (Figs. 1a-b), severe deformation by swaging and drawing reduces Nb filament phase thicknesses from 1 to 5 μm (as-cast) to 7 to 30 nm (after deformation). Cu-20Nb ultimate tensile strengths (UTS) exceed 2000 MPa for material deformed to a true strain of $\eta = 12$, where $\eta = \ln(A_{original}/A_{final})$. Such deformations represent more than an 800-fold reduction in diameter. Debate continues on the mechanism(s) which account for the very high strengths of the Cu-X alloys (7-12), but discussion centers around the role of the nanofilamentary X structure in impeding propagation and motion of dislocations in both the Cu and X phases.

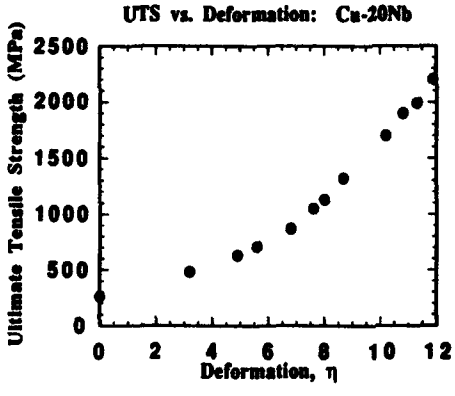


Figure 1a -- Ultimate tensile strength as a function of deformation strain (η) for Cu-20Nb (12).

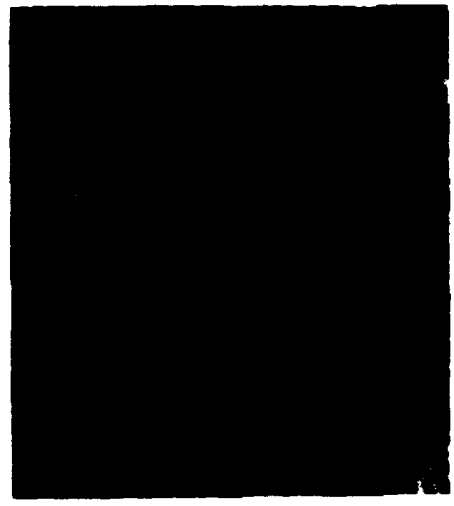


Figure 1b -- Conical scan dynamic dark field TEM micrograph of deformation processed Cu-20Nb shown in transverse section. Dark phase is Cu; the light phase is Nb.

Deformation Processed Titanium: Candidate Systems

In an attempt to produce hcp matrix in-situ composite alloys, candidate binary phase diagrams were sought where the constituent metallic elements or intermetallic compounds were mutually immiscible at the temperature of deformation and had roughly similar mechanical properties. Three combinations of metals meeting these criteria were Ti-Cu (where the second phase is tetragonal Ti_2Cu), Ti-Mo (where Mo is bcc), and Ti-Y (where Y is hcp).

It was hoped that investigation of the deformation processing behavior of such second phases in an hcp Ti matrix might provide insights into the fundamental mechanism(s) operating in in-situ composite alloys. In addition, if deformation processing proved to be a successful strengthening method in this system, a potentially useful low density, high strength alloy might result.

Alloy Preparation and Deformation

High purity Ti alloys of the compositions shown below were arc-melted into fingers and consumably drop cast into a chilled copper mold:

Ti-5 vol.% Cu	Ti-20 vol.% Y
Ti-15 vol.% Cu	Ti-50 vol.% Y

The high purity Ti alloys with Mo shown below were produced by powder processing with CIP and HIP at temperatures below 695°C (the eutectoid temperature):

Ti-5 vol.% Mo	Ti-15 vol.% Mo

The resulting ingots of these six alloys had diameters ranging from 17 mm to 31 mm and were placed in evacuated steel cans for hot working (650° to 860°C) by extrusion and/or swaging. The specimens could not be hot worked to diameters smaller than about 2.5 mm, since smaller specimens do not retain their furnace heat during hot work. The protective steel jackets must also be removed at this size, since they are difficult to machine away at smaller diameters. Deformation continued to smaller diameters by swaging at room temperature with periodic stress relief anneals in vacuum at 615°C for 20 minutes after each 20% reduction in area. These anneals are necessary to avoid cracking since, unlike Cu, Ti does not undergo dynamic recovery and recrystallization at room temperature. Cold swaging in this manner continued to final diameters as small as 0.4 mm.

Results

Ti-Cu

The as-cast Ti-5Cu and Ti-15Cu microstructures show immiscible α-Ti and Ti_2Cu phases. Deformation produced some elongation of the microstructure along the rod axis but failed to produce the long, nanometer-scale filaments characteristic of highly deformed Cu-X alloys. The increase in ultimate tensile strength (UTS) with increasing deformation (η) shown in Fig. 2 was much less than that seen in Cu-X alloys.

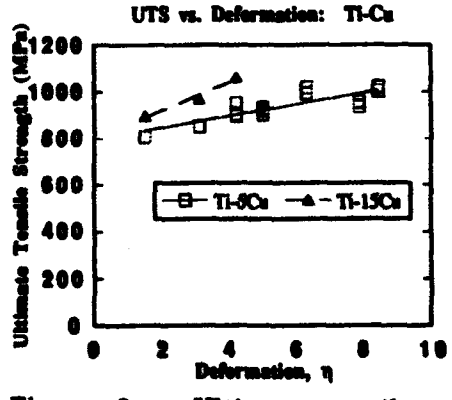


Figure 2 – Ultimate tensile strength as a function of deformation strain (η) for Ti-5Cu and Ti-15Cu.

The Ti-5Cu ductility decreased steadily as η increased, and approached zero at high η values, preventing deformation beyond $\eta = 8.4$. The ductility of the Ti-15Cu was even more limited; cold work was essentially impossible with the Ti-15Cu alloy, which is 60 vol. % Ti_2Cu, and deformation ended when the specimen diameter became too small at $\eta = 4.2$ to permit further hot work.

Ti-Mo

The disparity in melting temperatures of these two elements (1660°C for Ti and 2610°C for Mo) thwarted efforts to deformation process the Ti-5Mo and Ti-15Mo alloys at elevated temperatures. Hot working temperatures for Ti (650° to 800°C) are effectively cold working temperatures for Mo. The as-HIP'd alloys were extruded at 800°C and subsequently swaged at 650°C. SEM micrographs of the microstructure (Figs. 3a and 3b) show that most of the deformation occurred in the Ti with the Mo particles showing limited elongation into the desired filamentary structure. The solubility of Ti in the bcc Mo is evident in Fig. 3b as the lighter gray zones surrounding each Mo particle. Only when the specimens were swaged at room temperature (where their strengths are more nearly equal) did the Mo begin to elongate into the characteristic filaments of a deformation processed alloy (Fig. 3c). Consequently, the average phase spacings measured in the Ti-Mo alloys remained large, never dropping below 5 μm even at the highest η values, and the increase in strength with increasing η was low (Fig. 3d).

These results suggest that a deformation processed Ti-Mo alloy would have to be produced entirely by cold work with stress relief anneals performed at frequent intervals, a time consuming procedure for high η values.

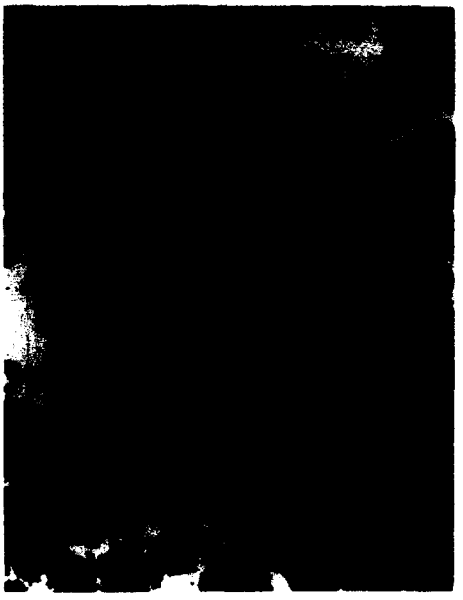


Figure 3a – Back-scattered electron SEM micrograph of as-HIP'd Ti-15Mo.

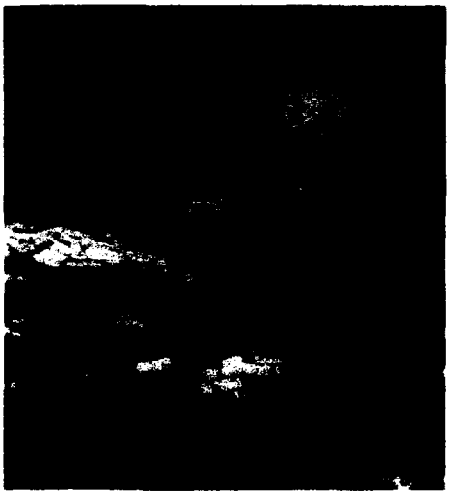


Figure 3b – Back-scattered electron SEM micrograph of Ti-15Mo in longitudinal section hot worked by extrusion (800°C) and swaging (650°C) to $\eta = 4.6$. Note areas of Ti-Mo solid solution surrounding Mo clusters.



Figure 3c – Back-scattered electron SEM micrograph of Ti-15Mo in longitudinal section after hot working to $\eta = 4.6$ and cold working to $\eta \approx 8.0$.

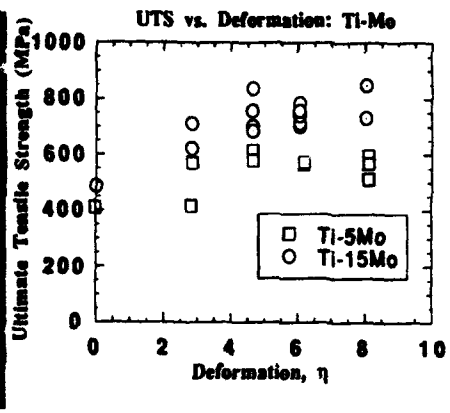


Figure 3d -- Ultimate tensile strength as a function of deformation strain (η) for Ti-5Mo and Ti-15Mo.

Ti-Y

The as-cast Ti-20Y and Ti-50Y alloys display the dendritic microstructure typical of two immiscible metals (Fig. 4a). Deformation produces elongated filaments (Figs. 4b-c) parallel to the rod axis. At the highest η values attained, average phase thickness decreased to about 100 nm (Figs. 4d). These deformations approximately tripled the UTS of both alloys (Fig. 5), roughly matching the strengthening seen in the Cu-20Nb alloy for similar η values (Fig. 1a).

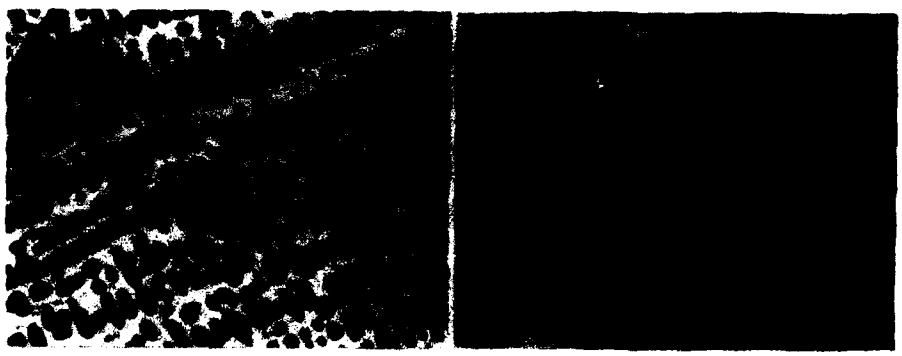


Figure 4a – SEM back-scattered electron micrograph of as-cast Ti-50Y etched with triflic acid. The dark phase is Ti, and the light phase is Y. Mean free distance between phases in the specimen is 2.09 μm.

Figure 4b – Transverse section back-scattered electron SEM micrograph of Ti-50Y extruded at 860°C. to $\eta = 2.8$. Dark phase is Ti; light phase Y. Mean free distance between phases is 890 nm.

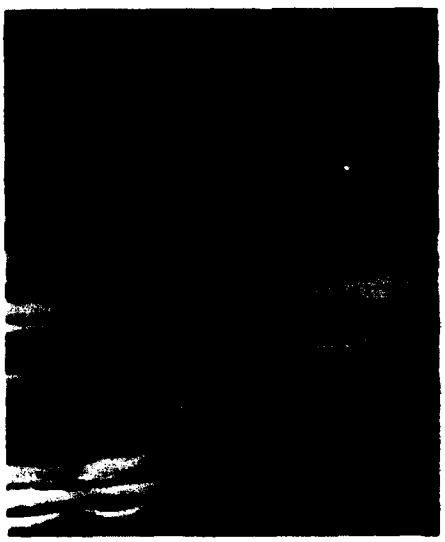


Figure 4c -- SEM secondary electron micrograph of a triflic acid etched longitudinal section of Ti-50Y extruded at 860° C. to η = 2.8.

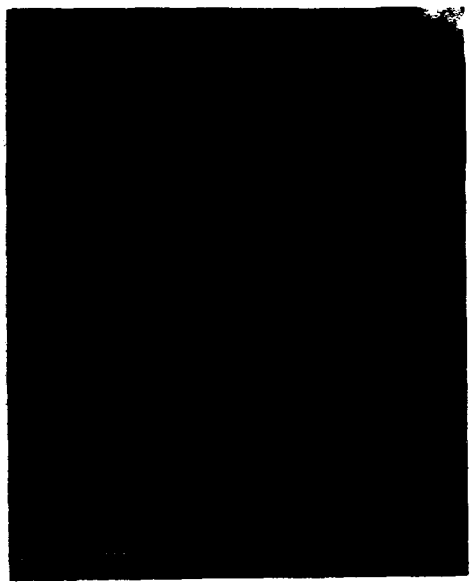


Figure 4d – TEM bright field micrograph of Ti-50Y in transverse section extruded at 860°C. to η = 2.8 and hot swaged at 725°C to η = 4.7. Mean free distance between phases in this specimen is 145 nm.

The tensile ductility of the Ti-20Y samples ranged between 40% to 50% reduction in area and showed no meaningful correlation with η values. Tensile ductility of the Ti-50Y was lower, ranging from 30% to 35% for low η values down to 20% for the higher η samples. The role of Y content in determining ductility and UTS was unfortunately obscured by unintended high oxygen levels in the Ti-50Y alloy. Gas fusion analyses of both alloys show that the Ti-20Y alloy interstitial content was fairly low throughout the experiment, but the Ti-50Y ingot had a higher initial oxygen content, and picked up additional oxygen during deformation processing and vacuum annealing:

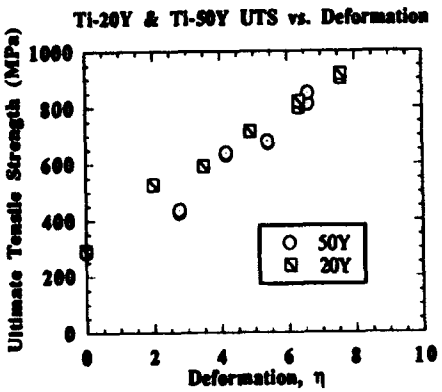


Figure 5 – Ultimate tensile strength for Ti-20Y and Ti-50Y as a function of deformation strain (η).

Table I Gas Fusion Analyses for Ti-50Y and Ti-20Y

Alloy (η)	Oxygen (wt in ppm)	Nitrogen (wt in ppm)	Hydrogen (wt in ppm)
Ti-50 Y			
$\eta = 0$	2100	110	37
$\eta = 4.8$	2100	110	48
$\eta = 6.6$	3000	100	110
Ti-20 Y			
$\eta = 0$	480	46	77
$\eta = 7.6$	560	280	41

Preliminary x-ray texture analysis of a Ti-20Y specimen deformed to $\eta = 7.6$ shows a very heavily textured structure, but further work is needed to accurately characterize the preferred orientation.

Conclusions and Future Work

This preliminary study has demonstrated that:

1. Ti-5Cu and Ti-15Cu do not readily form elongated filaments of Ti_2Cu and lack sufficient ductility to permit large deformations at room temperature. Increases in UTS obtained by deformation processing were small.

2. Ti-5Mo and Ti-15Mo do not co-deform well at elevated temperatures due to their dissimilar strengths. This requires deformation processing at room temperature, a slow procedure since frequent vacuum stress-relief anneals are necessary. These experiments never produced sufficiently fine microstructures to impart significant in-situ strenghtening.

3. Ti-20Y and Ti-50Y can be deformation processed to true strains of 7.6 and 6.6, respectively, to produce nanofilamentary microstructures. This deformation processing results in UTS increases similar to those seen in the well-studied Cu-20Nb alloy for equivalent true strains. The Ti-Y specimens retained good ductility even at their highest η values.

The Cu-X alloys exhibit their greatest strength at high deformation levels (η = 10 to 13). It remains to be seen if the Ti-Y alloys can be worked to such high strains, and if so, whether high tensile strengths will result. Experiments are underway to deformation process a large diameter starting ingot of low-oxygen Ti-20Y alloy. This study will include a pure Ti control sample deformed in the same manner and to the same η values as the Ti-20Y alloy. It is hoped that such data will help discriminate strengthening effects caused by work hardening in single-phase material from the effect of the nanofilamentary microstructures of the two-phase alloys. These specimens will also provide material for more complete x-ray texture characterization of preferred orientation.

Acknowledgments

The authors are grateful to J. D. Verhoeven, F. A. Schmidt, F. C. Laabs, L. L. Jones, L. P. Lincoln, L. K. Reed, and J. T. Wheelock, all of Ames Laboratory, for their valuable discussions and for preparing the materials used in this study. This work was performed at Ames Laboratory, operated for the U. S. Department of Energy by Iowa State University under contract no. W-7405-ENG-82 with additional financial support from General Electric Aircraft and the Engineering Research Institute of Iowa State University.

References

1. J. Bevk, J.P. Harbison, and J.L. Bell, Journal of Applied Physics, 49 (12) (1978) 6031-6038.

2. J.D. Verhoeven, et al., Journal of Metals 38 (9) (1986) 20-24.

3. J.D. Verhoeven, et al., Journal of Materials Engineering 12 (2) (1990) 127-139.

4. W.A. Spitzig and P.D. Krotz, Acta Metallurgica 36 (7) (1988) 1709-1715.

5. J.D. Verhoeven, et al., Materials & Manufacturing Processes 4 (2) (1989) 197-209.

6. J.D. Verhoeven, et al., Journal of Materials Science 24 (1989) 1015-1020.

7. P.D. Funkenbusch and T.H. Courtney, Acta Metallurgica, 33 (5) (1985) 913-922.

8. L.S. Chumbley, et al., Materials Science & Engineering, A117 (1989) 59-65.

9. C.L. Trybus, et al., Ultramicroscopy 30 (1989) 315-320.

10. P.D. Funkenbusch and T.H. Courtney, Scripta Metallurgica 23 (1989) 1719-1724.

11. W.A. Spitzig, et al., Scripta Metallurgica et Materialia 24 (1990) 1171-1174.

12. W.A. Spitzig, et al., Materials Research Society Symposium Proceedings 20 (1988) 45-50.

EFFECT OF OXYGEN CONTENT ON MICROSTRUCTURE AND PROPERTIES OF BETA-C™ (Ti-3Al-8V-6Cr-4Mo-4Zr) INVESTMENT CASTINGS

J. R. Wood*, D. P. Barbis**, and D. Eylon***

*RMI Titanium Company
1000 Warren Avenue
Niles, Ohio 44446

**Sharon Steel Corporation
Sharon, Pennsylvania 16146
(formerly with RMI Titanium Company)

***The University of Dayton
Graduate Materials Engineering
Dayton, Ohio 45469

Abstract

The microstructure and mechanical properties of investment cast Beta-C™ titanium were evaluated as a function of oxygen content, section thickness and heat treatment. Oxygen levels varied from .092% to .215% by weight. Hot isostatically pressed and solution treated castings were aged utilizing several heat treatments to arrive at the desired strength range of 150 to 180 ksi (1034 to 1241 MPa) while possessing a uniform microstructure and moderate ductility. Tensile and hardness results showed the material to be dependent on both oxygen content and casting section thickness. Strength increased approximately 20 ksi (138 MPa) with an increase in oxygen of 0.12 wt%. Strength also increased about 7 ksi (48 MPa) upon decreasing section size from 1.5 inch (38 mm) to 0.5 inch (13 mm) primarily due to a refinement in grain size. Ductility was slightly reduced at the higher strength levels in both cases.

Introduction

Beta titanium alloys, such as Beta-C™ (Ti-3Al-8V-6Cr-4Mo-4Zr) have reached production status as investment castings with very high strength-to-density ratios and good fatigue strength.[1] Beta-C™ has displayed good castability, ease of heat treatment and deep hardening characteristics which allow the alloy to be produced in complex and heavy section components.[2] A variety of heat treatments have been employed in order to optimize strength and ductility of Beta-C™ castings.[3] It is desirable to employ one heat treatment for a given application that is reproducible and minimizes variations in mechanical properties and microstructure. Occasional variations in aging response, structure and properties have occurred, however, particularly between chemistry lots in which oxygen levels have varied. Since oxygen is a potent alpha stabilizing element and is known to affect the beta transus temperature and kinetics of alpha precipitation in

Titanium '92
Science and Technology
Edited by F.H. Froes and I. Caplan
The Minerals, Metals & Materials Society, 1993

metastable beta titanium alloys, research was conducted to study the effects of oxygen content on the aging behavior and properties of Beta-C™ investment castings.

Procedure

Four heats with varying oxygen levels were VAR melted into 8 inch (203 mm) diameter 100 lb. (45 kg) ingots. The ingots were forged to 6 inch (152 mm) diameter billets and ground, grit blasted and pickled to remove scale and oxidized surfaces. Billets were VAR remelted and investment cast into 12 inch (304 mm) long step wedges with each integral step measuring 5 inches (127 mm) wide by 4 inches (102 mm) long by 0.5, 1.0, and 1.5 inches (13, 25, and 38 mm) thick. After casting, each step wedge was chem milled, vacuum heat treated for one hour at 1550°F (843°C) to remove hydrogen, hot isostatically pressed (HIP) at 1750°F(754°C)/15 ksi(103 MPa)/2 hours and X-rayed for soundness. The cast step wedges provided the opportunity to study the effects of section size as well as oxygen content on structure and properties.

Cast step wedges from each heat were cut into smaller coupons and solution heat treated at 1650°F(899°C)-1hour-Air Cool followed by aging at 900°F (482°C), 950°F (510°C), 1000°F (538°C), 1050°F (566°C), and 1100°F (593°C) for times ranging from 4 to 24 hours. Rockwell C hardness tests were used to establi effects of oxygen, section size and aging parameters on aging response. Based on the hardness data, a selected number of tensile specimens were machined from both thin and thick wedge sections and solution treated and aged accordingly. Metallographic specimens were also examined for microstructure and aging response.

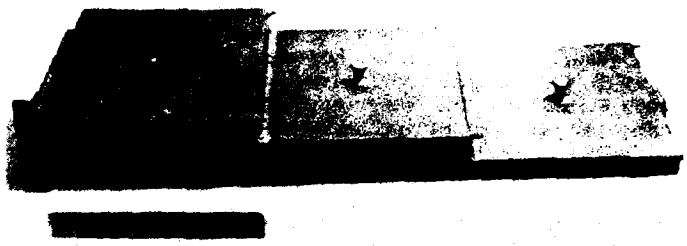
Beta transus determinations were made on each composition utilizing differential thermal analysis (DTA) in order to assess the effects of oxygen on beta transus and the relationship of beta transus temperature to kinetics of alpha precipitation during aging.

Results and Discussion

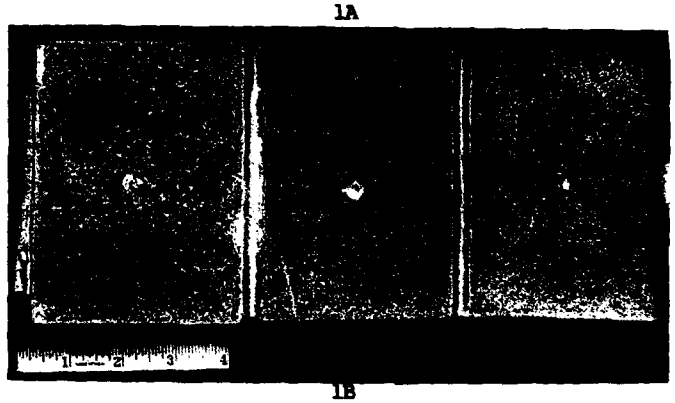
Heat chemistries and beta transus temperatures are shown in Table I. Major alloying elements were within normal compositional variation limits and oxygen levels were at .092%, .133%, .170%, and .215%, respectively. A cast step wedge is shown in Figures 1A and 1B. Figure 1B shows the macrograin structure which decreased significantly from 1.5 inch (38 mm) to 0.5 inch (13 mm) thick. Beta transus temperatures (BTT) increased, as expected, with increasing oxygen content as shown in Figure 2.

Table I. Compositions (wt%) of Alloys Used

Heat	Al	V	Cr	Zr	Mo	Fe	Si	C	N	Actual O_2	Beta Transus °F
Target	3.25	8.0	6.0	4.0	4.35						
X20001	3.5	8.5	5.9	4.5	4.2	.08	.03	.011	.011	.092	1335
X20002	3.3	8.2	6.3	4.2	4.4	.08	.03	.010	.015	.133	1340
X20003	3.1	8.1	6.3	4.0	4.1	.06	.03	.010	.016	.170	1350
X20004	3.3	8.2	6.3	4.1	4.3	.05	.03	.010	.015	.215	1355



1A



1B

Figures 1A & 1B. A view of the cast + HIP step wedge showing the grain size.

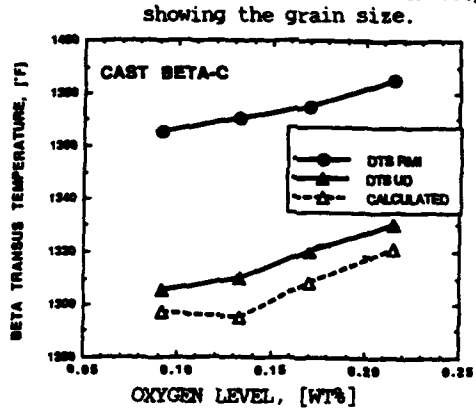


Figure 2. DTA measurements and calculated results for the effect of oxygen level on BTT of the Beta-C alloy.

The effects of oxygen level on aging response of 0.5 inch (13 mm) and 1.5 inch (38 mm) sections at 900°F (482°C), 1000°F (538°C), and 1100°F (593°C) are shown in Figures 3, 4, and 5, respectively. The best overall aging response (fastest hardening rate and highest hardness level) was achieved in the .092% O_2 and .133% O_2 heats at 900°F (482°C). After 24 hours at 900°F (482°C), all heats showed maximum hardness levels ranging from 43 to 45 Rc. At 1000°F (538°C), the best aging response appeared to be with the .215% O_2 material. After 24 hours at 1000°F (538°C), maximum hardness levels were similar for three heats and several Rc points lower for the .092% O_2

material. At 1100°F (593°C), the best aging response was achieved with the .170% O_2 and .215% O_2 heats with the lower O_2 heats showing a significantly lower hardness level. For all heats, however, the maximum hardness levels at 1100°F (593°C) were significantly lower than those achieved at 900°F (482°C) or 1000°F (538°C). The better aging response of the higher O_2 heats at higher aging temperatures can probably be attributed to the increase in beta transus temperature for the higher O_2 heats and an increase in the aging kinetics.

It is noted that only in the solution treated condition (unaged), the hardness level is essentially a function of the O_2 content, indicating the solid solution hardening effect of oxygen. Other than a grain size difference between thin and thick sections, there was no significant effect of section size on aging response or hardness level achieved at a given O_2 level.

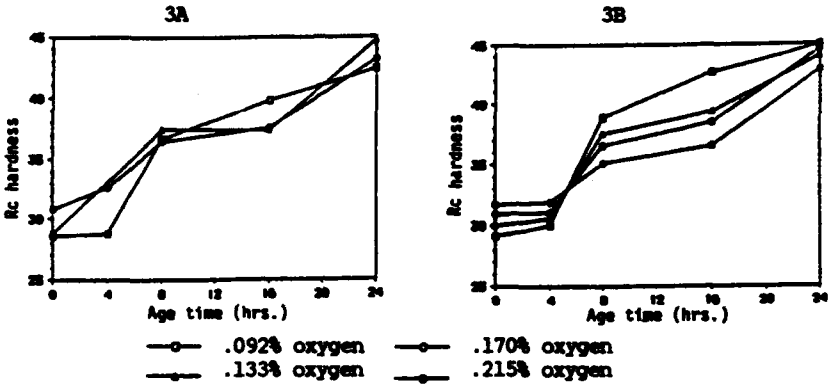


Figure 3. Effect of oxygen level on aging response (hardness profile) at 900°F (482°C) for a) 0.5" (13 mm) section; b) 1.5" (38 mm) section.

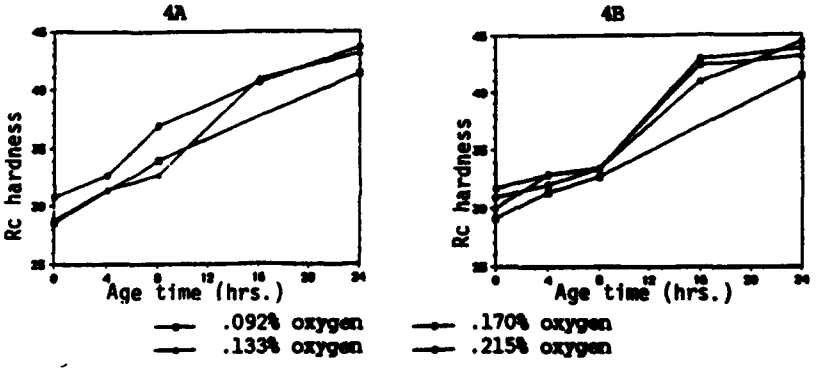


Figure 4. Effect of oxygen level on aging response (hardness profile) at 1000°F (538°C) for a) 0.5" (13 mm) section; b) 1.5" (38 mm) section.

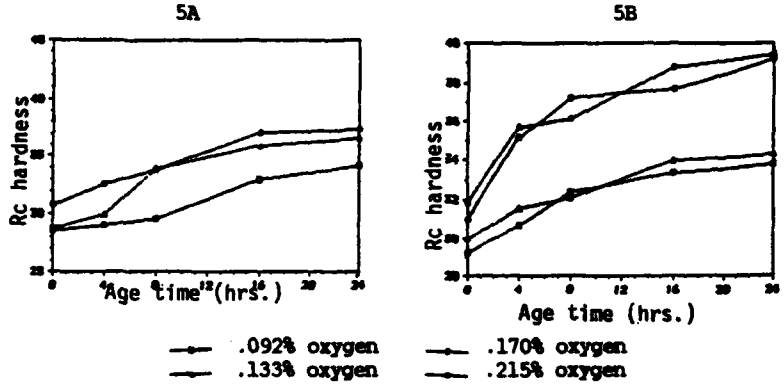
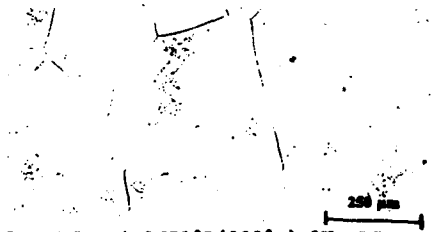


Figure 5. Effect of oxygen level on aging response (hardness profile) at 1100°F (593°C) for a) 0.5" (13 mm) section; b) 1.5" (38 mm) section.

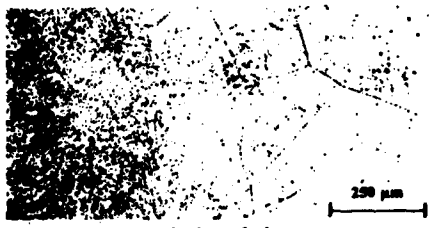
Microstructures for the .092% O_2 heat at thin and thick sections are shown in Figures 6 and 7, respectively, for both solution treated and 24 hour aged conditions. Comparative microstructures are shown for the .215% O_2 heat in Figures 8 and 9. In the solution treated condition, the average grain size of the thin sections (Figures 6A and 8A) was approximately half that of the thick section (Figures 7A and 9A) castings, due to cooling rate effects during casting. The same trend was observed for the intermediate O_2 level heats. Upon aging at 900°F (482°C), the finest and most uniform alpha precipitation was noted for the .092% O_2 thick section (Figure 7B) compared to a somewhat coarser, less uniform precipitation in the thin section (Figure 6B) and both .215% O_2 sections (Figures 8B and 9B).



6A. S.T. at 1650°F(899°C)-1Hr-AC (28.6 Rc)



6B. S.T. +900°F(482°C)-24Hrs-AC (39.9 Rc)

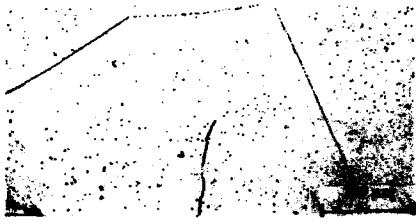


6C. S.T. +1000°F(538°C)-24Hrs-AC (41.9 Rc)

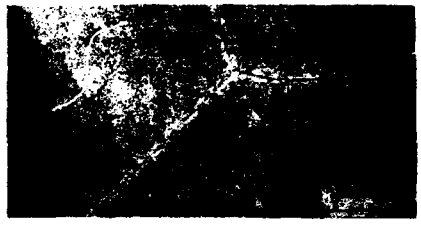


6D. S.T. +1100°F(593°C)-24Hrs-AC (42.2 Rc)

Figure 6. Solution treated and aged microstructures for .092% O_2 heat - 0.5" section.



7A. S.T. at 1650°F(899°C)-1Hr-AC (29.2 Rc)



7B. S.T. +900°F(482°C)-24Hrs-AC (45.0 Rc)



7C. S.T. +1000°F(538°C)-24Hrs-AC (41.4 Rc)

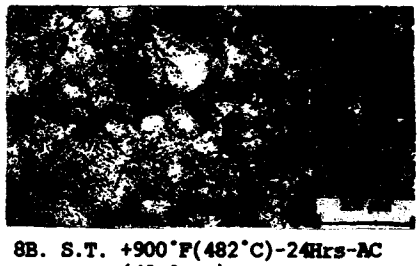


7D. S.T. +1100°F(593°C)-24Hrs-AC (33.8 Rc)

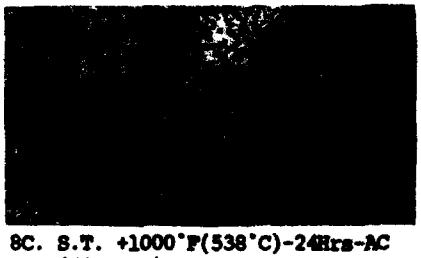
Figure 7. Solution treated and aged microstructures for .092% O_2 heat - 1.5" section.



8A. S.T. at 1650°F(899°C)-1Hr-AC (31.7 Rc)



8B. S.T. +900°F(482°C)-24Hrs-AC (43.2 Rc)

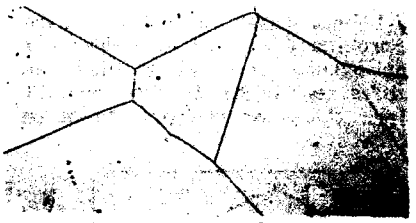


8C. S.T. +1000°F(538°C)-24Hrs-AC (43.6 Rc)



8D. S.T. +1100°F(593°C)-24Hrs-AC (37.4 Rc)

Figure 8. Solution treated and aged microstructures for .215% O_2 heat - 0.5" section.



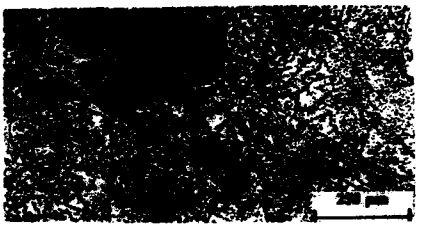
9A. S.T. at 1650°F(899°C)-1Hr-AC (31.8 Rc)



9B. S.T. +900°F(482°C)-24Hrs-AC (42.9 Rc)



9C. S.T. +1000°F(538°C)-24Hrs-AC (44.4 Rc)



9D. S.T. +1100°F(593°C)-24Hrs-AC (39.4 Rc)

Figure 9. Solution treated and aged microstructures for .215% O_2 heat - 1.5" section.

Interesting, the 1000°F (538°C) and 1100°F (593°C) aged microstructures (Figures 7C and 7D, respectively) for the .092% O_2 thick section also showed the finest and most uniform alpha morphology compared to the .092% O_2 thin section (Figures 6C and 6D) and both .215% O_2 sections (Figures 8C, 8D, 9C, and 9D). However, the fine uniform alpha precipitate in the .092% thick section did not necessarily result in the highest aged hardness as noted earlier in Figures 4 and 5. For the 900°F (482°C) aged condition, the hardness was 45 Rc, but with 1000°F (538°C) and 1100°F (593°C) ages the hardness dropped to 41 Rc and 34 Rc, respectively. For the .092% O_2 thin section, the hardness stayed relatively high at 42 Rc with 1000°F (538°C) and 1100°F (593°C) ages, despite the less uniform and dense aged microstructure (Figures 6C and 6D, respectively).

Overall, the tendency for increased grain boundary alpha with apparent denuded adjacent grain boundary zones was noted for all heats at the higher aging temperatures. Higher O_2 levels did not appear to promote more uniform alpha precipitation.

Tensile blanks were prepared from both thin and thick cast sections from each heat. Duplicate tensile specimens were tested in the 1650°F (899°C) solution treated condition and in two aged conditions - 900°F (482°C) and 1050°F (566°C) for 24 hours. These aged conditions were chosen from the hardness data to represent high (180 ksi (1241 MPa)) and medium (150 ksi (1034 MPa)) strength levels.

Yield strength and elongation results are plotted vs. O_2 level in Figure 10. Yield strengths increased linearly with O_2 content in all conditions and the thin sections were generally higher in strength than the thick sections most likely due to the effect of grain size noted earlier. The solution treated yield strength increased approximately 10 ksi (69 MPa) from .092% to .215% O_2 level, whereas the corresponding 900°F (482°C) and 1050°F (566°C) aged yield strengths increased approximately 20 ksi (138 MPa) and 18 ksi (124 MPa), respectively. This indicates that the effect of O_2 content was twofold

- a solid solution strengthener in the all beta phase solution treated condition which increased yield strength approximately 1 ksi (6.9 MPa) per .01% increase in O_2 and an age hardening strengthener which added an additional 8 to 10 ksi (55 to 69 MPa) yield strength due to the inherent solid solution strengthening effect on alpha phase or the precipitation behavior of alpha phase or a combination of both.

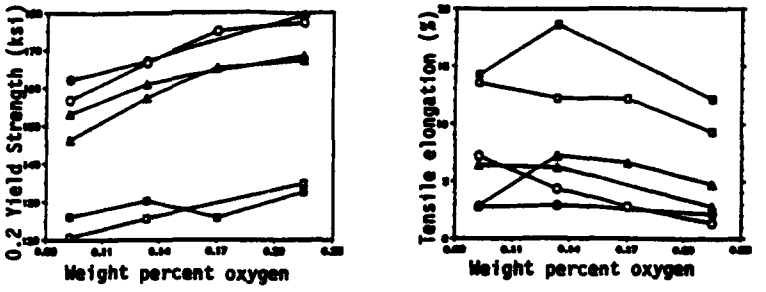


Figure 10. Effect of oxygen level on a) 0.2% yield strength; b) tensile elongation of solution treated only; 900°F(482°C)/24 hr aged and 1050°F(566°C)/24 hr aged.

Consistent with the increase in strength at higher O_2 levels, there was a corresponding decrease in tensile elongation. The highest ductility was displayed with the 1050°F (566°C) aged material and ranged from 6% to 3% elongation whereas the higher strength 900°F (482°C) aged material ranged from 5% to 2% depending upon O_2 content.

Conclusions

The results of this study indicate that oxygen content and casting section size play a significant role in the aging behavior of cast Beta-C™. Strength increased approximately 20 ksi (138 MPa) with an increase in oxygen of 0.12 wt%. Strength also increased about 7 ksi (48 MPa) upon decreasing section size from 1.5 inch (38 mm) to 0.5 inch (13 mm) primarily due to a refinement in grain size. Ductility was slightly reduced at the higher strength levels in both cases.

Acknowledgments

The authors would like to thank Dr. Hosamani of PCC for producing the castings for this paper, V. A. Frattaroli for coordinating the testing, and M. J. Jaros for metallography. The authors would also like to thank their respective organizations for permission to publish this paper.

References

1. D. Eylon, W. J. Barice, R. R. Boyer, L. S. Steele, and F. H. Froes, "Casting of High Strength Beta Titanium Alloys", Sixth World Conference on Titanium, Les Editions de Physiques, Paris, France, 1988, 655-660.

2. J. K. Thorne and W. J. Barice, "Advances in Titanium Alloy Casting Technology", 2nd International SAMPE Metals Conference, August, 1988, 20-27.

3. D. E. Thomas, "Microstructure and Mechanical Properties of Investment Cast Beta-C Titanium", Sixth World Conference on Titanium, France, 1988, 147-152.

The Effect of Microstructure and Carbon on the Tensile Behavior of the γ/α_2 Alloy Ti-48Al-1V-0.2C (at%)

*W.E. Dowling, Jr., +B.D. Worth, *W.T. Donlon and *J.E. Allison

* Ford Motor Co., Scientific Research Staff
Room S-2065, P.O. Box 2053
Dearborn, MI. 48121-2053

+ Dept. of Materials Science and Engineering
University of Michigan
Ann Arbor, MI. 48109

Abstract

Optimal mechanical properties in TiAl-based alloys occur when the aluminum content is reduced to obtain a two-phase, ($\alpha_2 + \gamma$) material. The microstructure of these two-phase alloys has a large impact on the mechanical properties, in particular the room temperature ductility. Room temperature tensile properties were evaluated as a function of microstructure in a Ti-48Al-1V (at%) alloy with 0.2C for additional strengthening. A range of α_2 contents and morphologies were developed utilizing isothermal forging and systematic heat treatments to examine the role of α_2 on "ductilization" of this class of materials. The important variables controlling microstructure were, volume fraction of γ at the heat treatment temperature and cooling rate. Three different heat treatment schemes were used to develop microstructures with a wide range of ($\alpha_2 + \gamma$) lath contents at a constant γ grain size. Room temperature tensile ductility was dependent on microstructure, with a maximum room temperature ductility of 1.5 to 1.9% over a broad range of lath contents. Below 5% and above 60% lath the ductility dropped below 1% plastic elongation. The yield strength was nearly independent of α_2 volume fraction and lath content except for a coarser microstructure. Thermal exposure experiments were conducted in the range of 725°C to 825°C to examine the influence of carbide precipitation on room temperature tensile behavior. Carbide precipitation after 100 h exposure, did not greatly influence the yield strength, or ductility in the microstructures examined.

Introduction

Blackburn and Smith [1] demonstrated that the ductility of γ-TiAl alloys can be substantially improved by reducing the aluminum content to produce a two-phase ($\alpha_2 + \gamma$) alloy. This work has led to extensive research on alloy and microstructural optimization for ductility improvement which has been recently reviewed by Kim and Dimiduk [2]. The mechanism by which α_2 increases the ductility of TiAl alloys is not yet understood nor has a systematic study been performed to evaluate the effect of α_2 volume fraction and morphology on tensile properties in a single alloy.

The purpose of this study was to evaluate the influence of α_2 content and distribution on the mechanical properties in a Ti-48Al-1V-0.2C alloy. The

Titanium '92
Science and Technology
Edited by F.H. Froes and I. Caplan
The Minerals, Metals & Materials Society, 1993

important variables controlling microstructure were, volume fraction of γ at the heat treatment temperature, time at temperature and cooling rate. Three different heat treatment schemes were used to develop microstructures with a wide range of lath contents at a constant γ-grain size. Several of these microstructures were tensile tested at room temperature. The strength and ductility were evaluated as a function of α_2 and lath content. The effect of carbide precipitation on the tensile properties of several of the more ductile microstructures was then evaluated.

Materials and Methods

A 110 kg casting (0.2 m dia. x 0.95 m) with a nominal composition of Ti-48Al-1V-0.2C-0.14O was acquired from TIMET after hot isostatic pressing (HIP). The as-cast + HIP microstructure consisted of approximately 40% primary γ grains with the remainder consisting of $\alpha_2 + \gamma$ lamellar colonies (>1mm). The ingot was sectioned and isothermally forged 140% true strain in compression at 1150°C.

Heat treatments with cooling rates of 1°C/s or less were conducted in cold wall vacuum furnaces (10^{-5} torr) with cooling rates controlled down to 900°C at the specified rate. Higher cooling rate heat treatments were performed in air. Quantitative microscopy was performed on backscattered electron (BSE) images from a scanning electron microscope (SEM) using a Kontron IBAS image analysis system. α_2 phase fractions were determined directly from BSE images (light phase is α_2). The lath volume fractions were determined by utilizing a dilating and erode function on the image analyzer to fill in the γ phase between the α_2 laths, and subsequently measuring the entire lath colony. Approximately 20 regions of each microstructure were analyzed and the average values utilized for comparisons. TEM specimens were prepared by electropolishing using a solution of 35% butanol/5% perchloric acid/60% methanol at -40°C and a potential of 10 V.

Tensile samples were heat treated and machined to a concentricity of better than .012 mm. Tensile tests were conducted on an MTS servohydraulic system, with fixed hydraulic collet grips and a precision alignment fixture. This minimized the bending strain due to grip misalignment to less the 20 $\mu\varepsilon$ [3]. Tensile tests were performed at a strain rate of 8×10^{-3}/s in stroke control mode. Tensile data presented is an average of two tests.

Microstructural Development

Previous microstructural studies [2,4,5] have shown that the volume fraction of α at temperature and sample cooling rate have significant impact on the microstructure of γ/α_2 titanium aluminides. The greater the volume fraction of α and the higher the cooling rate the more α_2 and lath in the resultant microstructure. The goal of this study was to systematically determine the effects of heat treatment temperature and cooling rate on microstructure and ductility. Ductility (plastic elongation at fracture) was measured over a wide range of α_2 and lath contents while maintaining a constant γ-grain size. Three pathways were examined for producing a broad range of α_2 and lath contents with grain size control in isothermally forged material. The three pathways are; 1) direct control of α content by temperature, 2) grain size stabilization at ≈50% α phase fraction followed by control of α content with a secondary heat treatment and 3) different cooling rates from a constant temperature. Figure 1 shows how these alternative pathways were used to arrive at similar low α_2 microstructures. However, the α_2 size and distribution is strongly dependent on the heat treatment pathway. The effect of various heat treatment

temperatures, cooling rates and secondary stabilizations on microstructural development are described below.

Heat Treatment Temperature

Extensive work has been performed using heat treatment temperature to develop low α_2, duplex, near lamellar and fully lamellar microstructures [2,4]. Direct heat treatment at the desired volume fraction of α produces a banded microstructure as shown in Figure 1a. Not only is the α_2 distribution banded, but the grain size distribution is bimodal. This occurs because of segregation during the ingot casting process which was not eliminated (homogenized) during subsequent forging and heat treatments [6]. The areas with α or α_2 have significantly reduced grain growth rates relative to the single phase γ regions. Two-step heat treatments were performed in order to better distribute the α_2 with the first step being 24 h at 1300°C (45% α) to produce a uniform α_2 and lath distribution and γ-grain size. This material was subsequently heat treated at the appropriate volume fraction of α to produce the desired α_2 and lath content. Figure 2 shows microstructures produced via this method with a range of lath contents but, with a more uniform grain size within the sample and also amongst different heat treatments. The amount of α_2 and lath strongly depend on the cooling rate. Even with heat treatment at high α contents only a fraction of α phase is retained as α_2 unless rapid cooling is employed. For high and intermediate lath contents the two-step heat treatment produced uniform microstructures, however at low α_2 contents, distribution and γ-grain size was not as uniform as desired.



Figure 1. Microstructures produced by each heat treatment pathway: a) 1100°C/ 8 h/0.2°C/s, b)1300°C/24 h/1°C/s + 1200°C/8 h/1°C/s and c)1300°C/ 24h/0.01°C/s.

Cooling Rate Effect

The cooling rate from two-phase heat treatments is another important variable for producing the desired microstructure in these alloys. Most "ductilizing" heat treatments occur in the $\gamma + \alpha$ two-phase field with 30 to 60% α at temperature and are subsequently static gas or forced gas cooled and then given a stabilization heat treatment [2]. This procedure typically produces a microstructure with approximately 30% $\alpha_2 + \gamma$ lamellar structure and the remainder primary γ. The cooling rate from the two-phase heat treatment temperature has a large influence on the microstructure as shown in Figure 3. The volume fraction of lath α_2 (measured with BSE imaging) varies from 3% to 25% over a cooling rate range of 0.01 to 1°C/s from a 1300°C heat treatment. The

morphology of the prior α also changes from 100% lamellar at high cooling rates to solid α_2 particles with only an occasional γ lamella at low cooling rates. With very slow cooling rates (0.01°C/s) it was possible to develop microstructures with a low α_2 content, uniform γ-grain size and a better α_2 distribution than through heat treatment temperature control alone.



Figure 2. Variation of microstructure as a function of secondary heat treatment temperature. Initial heat treatment 1300°C/24 h/1°C/s plus a) 1200°C/8h/1°C/s, b)1225°/8h/1°C/s, c)1250°C/8h/1°C/s, and d)1275°C/8h/1°C/s.

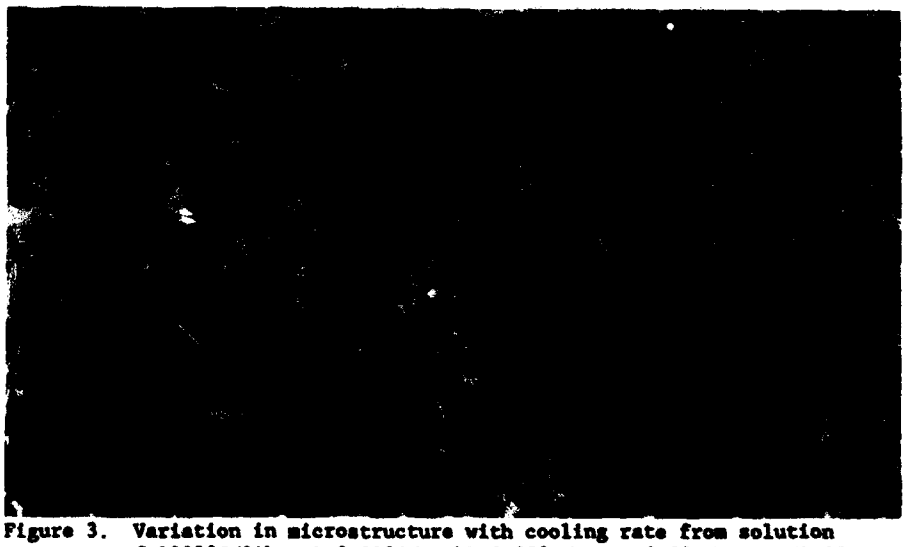


Figure 3. Variation in microstructure with cooling rate from solution treatment of 1300°C/24h. a) 0.01°C/s, b) 0.05°C/s, c) 0.2°C/s and d) 1°C/s.

Stabilization

The microstructures produced through the three heat treatment schemes were stabilized for 8 h at 1000°C, which is above the solvus for $Ti_3Al(C,N)$

precipitates found in this material [7]. This was done to minimize changes in α_2 content during elevated temperature testing and avoid carbide precipitation during the stabilization process. Figure 4 shows the controlled cooling rate microstructures in Figure 3 with an additional stabilization. The maximum α_2 content was reduced to 15% after stabilization. The stabilization resulted in a thinning of the α_2 lamellae.

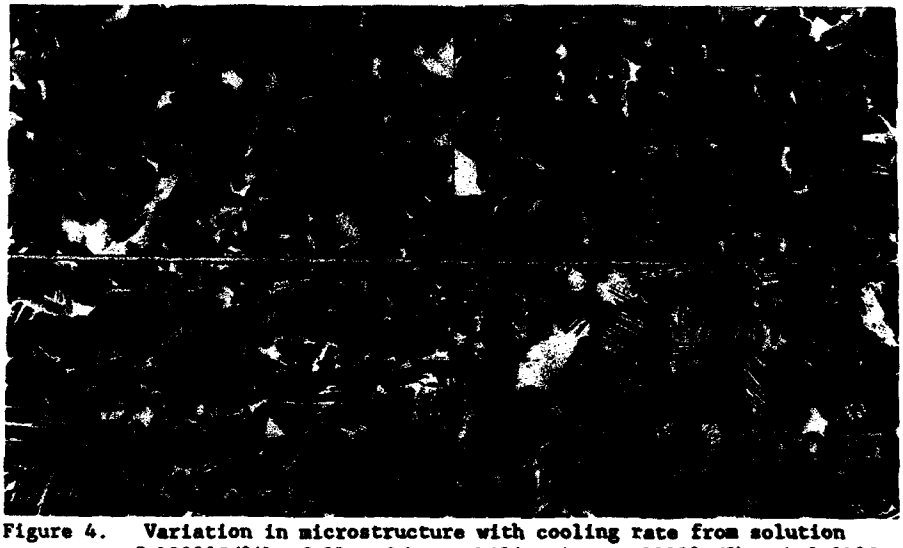


Figure 4. Variation in microstructure with cooling rate from solution treatment of 1300°C/24h, followed by stabilization at 1000°C/8h. a) 0.01°C/s, b) 0.05°C/s, c) 0.2°C/s and d) 1°C/s.

Tensile Behavior

The influence of α_2 and lath content on room temperature tensile behavior was evaluated utilizing the range of microstructures previously described. Most microstructures had a mean intercept grain size of approximately 35 μm, except for the near lamellar microstructures which had a significantly larger lath colony size. All of the microstructures were tested after a 1000°C stabilization.

Table I. The effect of cooling rate from 1300°C on microstructural parameters and tensile properties.

Cooling Rate (°C/s)	Lath (%)	α_2 (%)	ϵ_{pf} (%)	σ_{ys} (MPa)	σ_{uts} (MPa)
1	25	16	1.9	440	523
0.2	10	8	1.7	444	515
0.1	7	6	1.5	433	485
0.05	8	7	1.2	486	513
0.01	3	3	0.5	461	467

Cooling Rate Effect

Figure 5 illustrates the influence of cooling rate from 1300°C (45% α) on room temperature tensile ductility. The ductility increases from 0.5% to 1.9% as the cooling rate is increased from 0.01°C/s to 1°C/s. The higher cooling rate results in more retained α, which transforms to α_2. Table I summarizes the microstructural parameters and tensile data for this set of microstructures. Although the cooling rate had a large effect on ductility, the yield strength variation amongst the different microstructures was small. Thus, α_2 and lath content have little impact on yield strength.

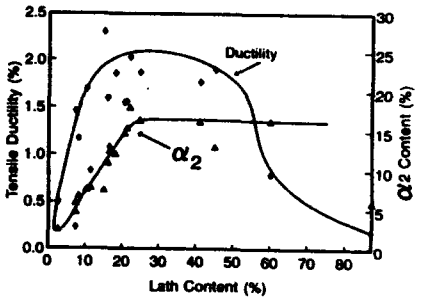


Figure 5. The influence of cooling rate from 1300°C on the room temperature tensile ductility of Ti-48Al-1V-0.2C (at%).

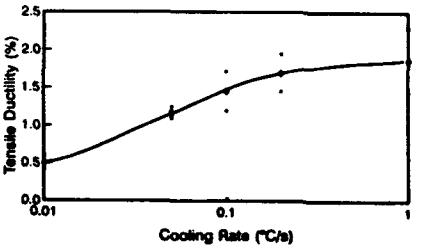


Figure 6. The influence of microstructure on the room temperature tensile ductility of Ti-48Al-1V-0.2C (at%).



Figure 7. Variation of microstructure as a function of secondary heat treatment temperature. Initial heat treatment 1300°C/24 h/1°C/s plus secondary heat treatment followed by 1000°C/8h. Secondary heat treatment schedules were: a) 1225°C/8h/1°C/s, b)1275°/8h/1°C/s, c)1335°C/2h/0.5°C/s, and d)1360°C/0.5h/1°C/s.

Lath Content

Figure 6 summarizes the ductility as a function of lath content, for microstructures developed through two-step and controlled cooling rate pathways. Also included on this graph is the α_2 content of each of the microstructures. Figure 7 shows several microstructures developed from two-step heat treatments. The range of lath contents is from 7% for the 1225°C secondary heat treatment to 60% for the 1360°C secondary heat treatment. The grain sizes of most microstructures was maintained at approximately 35 μm. However, the 60% lath microstructure had a colony size of 50 to 100 μm and the colony size of the 87% lath microstructure was greater than 500 μm. A range of lath contents from 10% to over 40% resulted in ductilities greater than 1.5%. The lower ductilities at high lath contents may have been caused by the much larger colony size rather than the lath content.

The large ductility variation at a low lath contents (7% to 16%) resulted from a poor distribution of α_2. These microstructures were generated by the two step heat treatment method with the second heat treat temperature at either 1225°C or 1250°C. This resulted in some α-banding and γ grain growth as discussed previously and illustrated in Figure 7a for the 1225°C heat treatment. The low lath content and poor α_2 distribution also resulted in a greater frequency of intergranular failure. Better lath distributions with volume fractions in the same 7% to 20% range were produced through controlled cooling and heat treatment at 1275°C and above. The volume fraction of α at 1275°C is greater than 25% and was adequate to maintain a uniform distribution of α, which minimized γ grain growth during the second heat treatment stage. Microstructures with uniform distribution of α_2 had much higher ductilities for the same α_2 content.

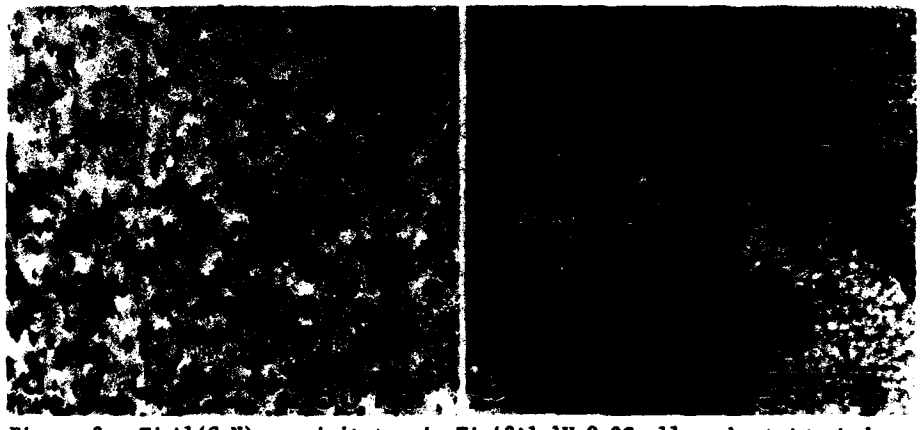


Figure 8. $Ti_3Al(C,N)$ precipitates in Ti-48Al-1V-0.2C alloys heat treated 1300°C/24h/1°C/s plus 1275°C/8h/1°C/s plus 1000°C/8h and aged at a)725°C/100h or b) 825°C/100h.

Thermal Exposure

The alloy examined in this study contains 0.2 at% carbon which has been found to precipitate as $Ti_3Al(C,N)$ [7] after thermal exposure in the temperature range of 675°C to 925°C. The morphology of these precipitates depends on exposure temperature. At temperatures greater than approximately 800°C the carbides nucleate and grow on dislocations and grain boundaries, whereas below 800°C they occur in the matrix with precipitate free zones around larger precipitates on grain boundaries and dislocations. In this study, the influence of both

precipitate morphologies on room temperature tensile properties was evaluated. Samples were heat treated to attain microstructures with approximately 15% and 40% lath after 1000°C stabilization for 8 h and subsequently heat treated at 825°C or 725°C for 100 h. After all heat treatments, the samples were machined into tensile samples. Figure 8 shows the precipitates produced from each thermal exposure on the 15% lath material. Thermal exposure at either temperature did not appreciably change the ductility or yield strength of either microstructure.

Summary

The microstructure of Ti-48Al-1V-0.2C was systematically manipulated through three heat treatment schemes to produce a range of α_2 contents and morphologies. The influence of α_2 content, morphology and carbide precipitation on room temperature tensile behavior was evaluated. The results of the microstructural development and mechanical behavior studies are summarized as follows:

1. The development of low α_2 microstructures with uniform grain size and α_2 distribution was best achieved through slow cooling from 1300°C, rather than heat treating at low volume fractions of α. Duplex microstructures can be produced either through heat treatment at the specific volume fraction of α followed by a rapid cool (>1°C/s) or heat treatment at higher α contents with a slower cool. Controlled cooling rate from heat treatment in the two-phase field is very important when a specific microstructure is desired.

2. High values of room temperature ductility (> 1.5%) can be obtained with a wide range of lath contents (7% to 40%) in the alloy Ti-48Al-1V-0.2C (at%) and a grain size of ≈35 μm. Microstructures with low lath contents (< 7%) and non-uniform lath distributions (<16% lath) had lower ductilities than microstructures with the same lath content and/or a uniform lath distribution.

3. The influence of lath content on room temperature yield strength was minimal when a constant γ-grain size was maintained.

4. $Ti_3Al(C,N)$ precipitation after 100 h exposure at 725°C and 825°C had no significant effect on room temperature tensile ductility or yield strength.

References

1. M.J. Blackburn and M.P. Smith, "R&D on Composition and Processing of Titanium Aluminide Alloys for Turbine Engines", AFWAL Technical Report No. AFWAL-TR-82-4086 (1982).
2. Y-W. Kim and D.M. Dimiduk, "Progress in the Understanding of Gamma Titanium Aluminides", JOM, 43(8)(1991), 40-47.
3. S-C. Huang and E.L. Hall, "Plastic Deformation and Fracture of Binary TiAl-Base Alloys", Met. Trans. A, 22A (1991), 427-439.
4. W.E. Dowling, Jr., et al., "The Influence of Microstructure on the Mechanical Behavior of γ/α_2 Titanium Aluminides", Microstructure/Property Relationships in Titanium Aluminides and Alloys, ed. Y-W. Kim and R.R. Boyer (Warrendale PA:TMS 1990), 123-135.
5. W.E. Dowling, Jr., W.T. Donlon and J.E. Allison, "The Influence of Microstructure and Temperature on the Fatigue Behavior of γ/α_2 Titanium Aluminides", Fatigue 90, ed. H. Kitagawa and T. Tanaka, (Birmingham, UK: MCEP 1990) 1923-1929.
6. S.L. Semiatin and P.A. McQuay, "Segregation and Homogenization of a Near-Gamma Titanium Aluminide", Met. Trans. A, 23A (1992), 149-161.
7. W.T. Donlon, W.E. Dowling, Jr. and J.E. Allison, unpublished results.

The Role of Input Powder Microstructure and Extrusion Conditions on Properties of PM Titanium - Rare Earth Alloys

M. F. X. Gigliotti†, A. P. Woodfield‡, R. A. Amato‡, J. R. Hughes†, L. C. Perocchi†

†General Electric Corporate Research and Development, Schenectady, NY 12301
‡General Electric Aircraft Engines, Cincinnati, OH 45215

Abstract

The microstructure, crystallographic texture, and tensile and creep strengths of rare earth containing titanium alloy extrusions were determined as a function of process conditions and initial powder microstructure. The process variables studied included: input powder microstructure; extrusion temperature; and solution plus age versus direct age heat treatment.

Extrusion temperature had the greatest effect. Beta extrusions with direct age heat treatments had a strong [0001] texture along the extrusion direction and high tensile strengths. Beta extrusions with beta solution plus age heat treatments had elongated prior beta grains and the highest creep strengths; the creep curves at 650°C, 138 MPa did not display a minimum rate — the rate monotonically decreased with time. In contrast, creep curves of material extruded below the beta transus exhibited a creep rate minimum. Extrusions made at temperatures just under the beta transus, given beta solution plus age heat treatments, had the highest tensile strengths.

Initial powder microstructure was an important variable. Extrusions from powder with a non-uniform distribution of rare earth exhibited lower degrees of crystallographic texture, abnormal grain growth on beta solution plus age heat treatment, and reduced mechanical properties.

Introduction

Rapid solidification can produce rare earth compound dispersions in binary titanium – rare earth metal alloys (1). These dispersoids improve tensile strength and creep resistance (2). Consolidation processing has been limited to maximum temperatures of about 850°C in order to retard coarsening of the rare earth compound dispersoids (3). The dispersoid coarsening is enhanced by diffusion along interfaces during the alpha to beta transition (4). Multicomponent titanium alloys containing aluminum, tin, beta stabilizers, strain aging elements, and rare earth metals also can be rapidly solidified to produce rare earth compound dispersions. The rare earth dispersoids act to produce a very fine alpha grain size in material processed below the beta transus, which gives rise to poor elevated temperature creep resistance. Beta heat treatment coarsens the dispersoids, but greatly improves 650°C creep resistance; coarsened dispersoids offer improvements in ductility which allow alloying to higher levels of addition of alpha two stabilizing elements without embrittlement than in dispersoid free compositions (5).

In work conducted at the General Electric Company, beta processing of a model alloy resulted in large strength increases. A study was conducted, the subject of this report, to evaluate consolidation processing variables on the mechanical properties of a rapidly solidified complex titanium base alloy containing rare earth metal dispersions.

Titanium '92
Science and Technology
Edited by F.H. Froes and I. Caplan
The Minerals, Metals & Materials Society, 1993

Procedure

Alloy Selection and Powder Production

The nominal compositions of the alloys selected for study, designated AF-2 and AF-2M, are listed in Table I. Alloy AF-2 is a near alpha alloy containing aluminum, tin, zirconium, and columbium to strengthen the alpha phase, a small amount of molybdenum to produce a beta phase, silicon as a strain aging element, and erbium to form a dispersoid (6). Alloy AF-2M is a modification to this alloy, substituting Ru for Mo, and partially substituting Ge for Si, the latter substitution to increase the temperature of strain aging effects (7). Alloy powder was produced at Crucible Research Center, Pittsburgh, PA. Two atomization units were used for powder production. Alloy AF-2 was produced in a small atomizer which can melt and atomize 1.4 kg of titanium alloy per run; powder of alloy AF-2M was produced both in the small atomizer as well as in a larger unit which can melt and atomize 23 kg of titanium alloy per run (8, 9).

Table I. Alloy compositions.

	atom %										
Alloy	Ti	Al	Sn	Zr	Hf	Cb	Mo	Ru	Er	Si	Ge
AF-2	bal.	11.7	1.3	1.6	0.7	0.5	0.15		0.9	0.35	
AF-2M	bal.	11.7	1.3	1.6	0.7	0.5		0.15	0.9	0.2	0.2

Thermomechanical Processing

All powders were HIPped at 840°C and 210 MPa for 3 hours. The HIPped powder cylinders were then extruded at a ratio of 8:1 and a strain rate of 2 sec^{-1}. The extrusion press used was a Loewy horizontal hydraulic press, with a capacity of 11 MN force. Alloy AF-2 was extruded below the beta transus at 840°C, near the transus at 975°C, and in the beta phase field at 1200°C. AF-2M powder produced from both small and large atomizers was extruded at 1200°C.

Two heat treatments were evaluated. Heat treatments were given the mechanical test samples at the stage where they were cylindrical blanks, prior to machining the gauge section. Samples of all process combinations were given a beta solution plus age heat treatment of 1150°C for 2 hours, helium quench, plus 600°C for 8 hours. Additionally, samples of beta processed material were heat treated by a simple age: 600°C for 8 hours. The cooling rate for the helium quench was measured to be about 10°C/sec to under 900°C.

Results

Microstructure Development

The microstructure of powder particles from the large and small atomizers are different. The structure of small atomizer powder particles is very homogeneous — martensitic, with fine equiaxed prior beta grains and scattered regions of a second phase which appears to be a result of solidification segregation, Figure 1a. Powder particles from the large atomizer have a coarse, dendritic, inhomogeneous microstructure, Figure 1b; the interdendritic region was analyzed by X-ray energy dispersive analysis to be rich in Er. These differences persist after HIP.

The heat treated microstructures of AF-2 and AF-2M extrusions show the influence of the powder microstructure and prior processing conditions. Beta solution plus age heat treatments do not eliminate differences between alloys processed below or above their beta transition temperatures or between alloys produced from the two different atomizers.

Figure 2 displays the microstructures of the 840°C, 975°C and 1200°C extrusions of AF-2 made from small atomizer powder. The 840°C extrusion has a colony microstructure, where the colonies are about 20 μm in size and randomly oriented. The 975°C extrusion consists of a colony alpha microstructure, and the colonies appear somewhat larger and aligned with the extrusion direction. The structure of the 1200°C extrusion, with a beta solution plus age heat treat-

ment, chiefly consists of large alpha colonies formed within elongated prior beta grains. The structure of the 1200°C extrusion after a simple age consists of bands of alpha plates aligned approximately along the extrusion direction; outside of these bands, there are alpha plates oriented randomly. The microstructure of the 1200°C extrusion of AF-2M from small atomizer powder is similar to that of AF-2.

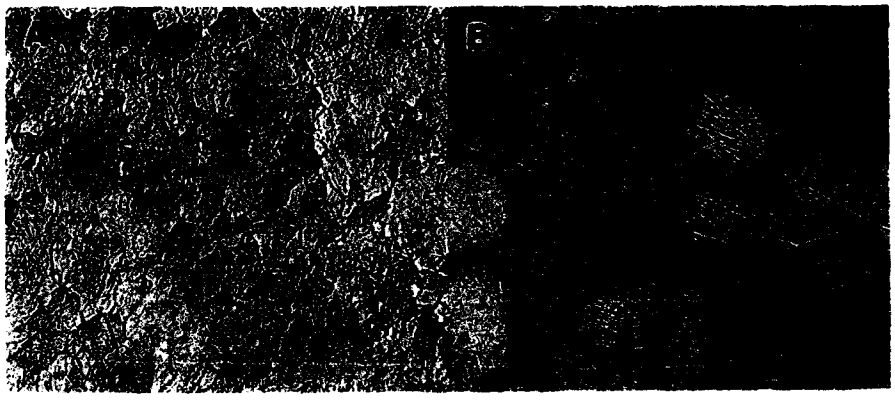


Figure 1. AF-2 powder. A) small atomizer. B) large atomizer. ⟵40 μm⟶



⟵40 μm⟶

Figure 2. AF-2 extrusions. A) 840°C, S+A; B) 975°C, S+A; C) 1200°C, S+A; D) 1200°C, DA.

AF-2M extrusions made from large atomizer powder are displayed in Figure 3. After a beta solution plus age heat treatment, the microstructure consists of large prior beta grains containing a Widmanstätten alpha. After a simple direct age heat treatment, the structure is mixed, with regions of aligned alpha plates in elongated beta grains and other regions of large prior beta grains and Widmanstätten alpha.

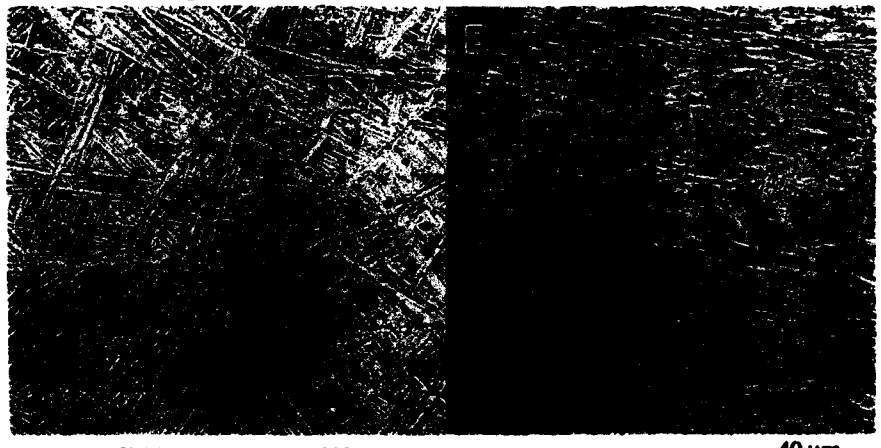


Figure 3. AF-2M large atomizer 1200°C extrusions: A) S+A; B) DA. —40 μm—

Mechanical Properties

Tensile tests were conducted at room temperature in air and at 650°C in a vacuum. Creep tests were conducted in static argon at 650°C/138 MPa.

Small Atomizer AF-2. The role of extrusion temperature and heat treatment can be seen in the results for the small atomizer AF-2 material. The tensile and creep test results for AF-2 as a function of process condition are listed in Table II and Table III, respectively. For the case of beta solution plus age heat treatment, the highest tensile strengths are achieved for extrusion at 975°C. The direct age heat treated 1200°C extrusion also has overall highest tensile strengths, with a 1200 MPa yield strength at room temperature and an 880 MPa yield strength at 650°C.

Table II. Tensile behavior of small atomizer AF-2.

Ext. Temp.	Heat Treatment °C (°F)	Test Temp. °C	Test Temp. °F	Yield Strength ksi	Yield Strength MPa	Ultimate Strength ksi	Ultimate Strength MPa	Ductility %El.	Ductility %RA
840°C	1150/600	RT	RT	150.4	1050.5	155.1	1083.4	3.5	10.2
	(2102/1112)	650	1202	80.2	560.2	95.9	669.9	20.8	34.0
975°C	1150/600	RT	RT	170.9	1193.7	181.7	1269.2	7.5	9.3
	(2102/1112)	650	1202	104.1	727.1	123.9	865.4	10.8	12.1
1200°C	1150/600	RT	RT	145.9	1019.1	154.1	1076.4	4.3	5.6
	(2102/1112)	650	1202	93.7	654.5	106.7	745.3	6.1	11.7
1200°C	600	RT	RT	172.4	1204.2	182.9	1277.6	4.9	9.2
	(1112)	650	1202	126.3	882.2	142.0	991.9	4.8	10.9

The highest creep life is achieved for the beta extruded material given a beta solution plus age heat treatment. There is an approximate seven–fold increase in time to 0.2% creep comparing the 840°C extrusion to the 1200°C extrusion. The creep behavior of the 840°C and 1200°C extrusion are displayed in Figure 4. The 840°C extrusion displays a nearly constant creep rate, while the 1200°C extrusion displays a creep rate monotonically decreasing with time.

Table III. Creep properties small atomizer AF-2 at 650°C/138MPa (1202°F/20ksi), static argon.

Extrusion Temperature	Heat Treatment	Hours to Percent Creep 0.1	0.2	0.5	1.0	Creep rate %/hour
840°C	1150/600	0.8	3.1	18.4	64.2	8.4×10^{-3}
975°C	1150/600	1.9	5.9	30.5	95.7	4.6×10^{-3}
1200°C	1150/600	5.1	23.6	197.5	853.6	4.2×10^{-4}
1200°C	600	4.6	20.1	129.2	423.1	6.6×10^{-4}

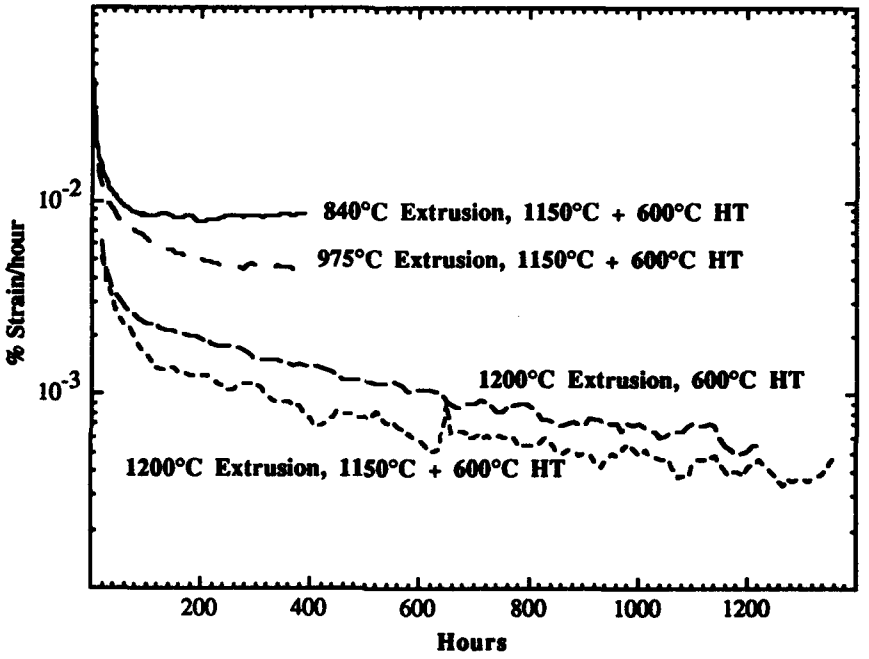


Figure 4. Creep rate of AF-2 at 650°C and 138 MPa.

Small and Large Atomizer AF-2M. The tensile and creep properties of AF-2M extruded at 1200°C are listed in Tables IV and V, respectively. With reference to the tables, the tensile and creep behavior of small atomizer AF-2M is similar to that of small atomizer AF-2, *viz.* the beta solution plus age heat treatment displays lower tensile strength and higher creep resistance compared with the direct age condition. However, for large atomizer AF-2M, the direct age creep resistance is greater than the solution plus age heat treatment. Also, while the small atomizer tensile strengths are about the same as large atomizer, the creep resistance of small atomizer AF-2M is much greater. The time to 0.2% plastic creep is 3 to 6 times greater for small atomizer material compared to large atomizer material. Finally, comparing small atomizer AF-2 to small atomizer AF-2M (Table III to Table V), AF-2M displays improved creep resistance, with about twice the time to 0.2% creep.

Young's modulus of material processed by the different routes was calculated from sound velocity measurements (10). The results are listed in Table VI. The highest moduli are obtained for 1200°C extrusions given a direct age heat treatment and for the 975°C extrusion given a beta solution and age heat treatment. Comparably processed small atomizer material has higher moduli than large atomizer material; comparably processed AF-2M has higher moduli than AF-2.

Table IV. Tensile behavior comparison of small and large atomizer AF-2M.

	Heat Treatment °C (°F)	Test Temp. °C	Test Temp. °F	Yield Strength ksi	Yield Strength MPa	Ultimate Strength ksi	Ultimate Strength MPa	Ductility %El.	Ductility %RA
Small atomizer	1150/600 (2102/1112)	RT	RT	140.2	966.7	153.1	1055.6	8.5	13.4
		650	1202	106.9	737.1	112.8	777.8	8.3	19.6
Small atomizer	600 (1112)	RT	RT	173.9	1199.0	177.0	1220.4	1.4	3.7
		650	1202	129.0	889.46	140.5	968.8	5.2	6.8
Large atomizer	1150/600 (2102/1112)	RT	RT	135.7	935.7	146.8	1012.2	6.0	13.4
		650	1202	81.5	561.9	98.6	679.9	11.0	18.0
Large atomizer	600 (1112)	RT	RT	172.5	1189.4	173.9	1199.0	3.9	5.7
		650	1202	116.6	804.0	131.0	903.3	5.8	8.1

Table V. Creep properties comparison of large and small atomizer AF-2M at 650°C/138MPa (1202°F/20ksi), static argon.

Powder	Heat Treatment	Hours to Percent Creep 0.1	0.2	0.5	1.0	Creep rate %/hour
Small atomizer	1150/600	8.4	48.6	581.3	>1800	2.7×10^{-4}
Small atomizer	600	10.9	43.3	277.7	894.2	5.5×10^{-4}
Large atomizer	1150/600	1.4	6.7	102.0	705.1	3.8×10^{-4}
Large atomizer	600	2.5	16.7	191.4	631.0	9.0×10^{-4}

Table VI. Young's modulus of alloy and process variations.

Alloy	Extrusion Temperature	Heat Treatment	Longitudinal GPa	Longitudinal Msi	Transverse GPa	Transverse Msi
Small atomizer AF-2	840°C	1150°C/600°C	121.5	17.6	122.7	17.8
Small atomizer AF-2	975°C	1150°C/600°C	127.4	18.5	115.1	16.7
Small atomizer AF-2	1200°C	1150°C/600°C	124.2	18.0	119.1	17.3
Small atomizer AF-2	1200°C	600°C	127.4	18.5	109.1	15.8
Small atomizer AF-2M	1200°C	1150°C/600°C	126.3	18.3	121.6	17.6
Small atomizer AF-2M	1200°C	600°C	128.8	18.7	110.9	16.1
Large atomizer AF-2M	1200°C	1150°C/600°C	124.9	18.1	122.9	17.8
Large atomizer AF-2M	1200°C	600°C	126.9	18.4	111.2	16.1

Discussion

The 840°C extrusion with a beta solution plus age microstructure consists of fine prior beta grains containing an alpha colony structure. At the 840°C extrusion temperature there was little beta phase present; beta grain growth on heat treatment was retarded by the dispersoids. The modulus of a polycrystalline titanium alloy is a strong function of crystallographic texture, with basal textures having higher moduli (11). The Young's modulus measurements indicate no strong texture for the 840°C extrusion. For the 975°C extrusion given a beta solution plus age heat treatment, the Young's modulus parallel to the extrusion direction is higher than that transverse to the extrusion direction, indicating a strong [0001] texture. This texture can arise from the beta phase present during the 975°C extrusion developing an [011] texture whose effects persist through the subsequent beta solution plus age heat treatment, yielding the final [0001] alpha phase texture via Burgers' relationship (12). The 1200°C extrusions after a direct age heat treatment also exhibit Young's moduli similar to the 975°C extrusion, plus a microstructure of alpha plates aligned along the extrusion direction — both indicating strong texture. The prior beta

grains in the direct aged 1200°C extrusions are larger than those in the lower temperature extrusions, and are elongated in the extrusion direction. The thermal exposure prior to the 1200°C extrusion may have coarsened the dispersoids enough to permit some beta grain growth. The 1200°C extrusion given a beta solution plus age heat treatment has a lower Young's modulus parallel to the extrusion direction than the direct aged material — consistent with some texture being lost from the heat treatment.

The material from large atomizer powder shows some effects of the inhomogeneous powder microstructure. The large atomizer 1200°C extrusions have lower Young's moduli than material from the small atomizer. Beta grain sizes from the large atomizer material are much larger; beta grain growth appears to have been unrestrained in the regions free of dispersoids, and by a process similar to secondary recrystallization, grains achieved large sizes. The alpha plate structure within these large beta grains is basketweave, since nucleation and growth of alpha within the grains could occur before colonies of alpha plates growing inward from the boundaries could transform the grain.

Mechanical properties as a function of extrusion temperature and heat treatment of two commercial titanium alloys are similar to these results (13), where tensile strengths are highest for beta extrusion and direct age. High tensile strengths occur in directions of textured material parallel to the [0001] (11,14).

The size and shape of prior beta grain boundaries have an effect on creep resistance. The large, elongated prior beta grains produced by beta extrusion would be expected to improve creep resistance. For large, equiaxed prior beta grains, transformed beta microstructures are more creep resistant than alpha plus beta heat treated microstructures (15, 16). A microstructure of elongated prior beta grains is more creep resistant than one of equiaxed prior beta grains (17). AF-2 and AF-2M contain Si or Si+Ge as a strain aging addition. The strongest beneficial effect of silicon is achieved when it is in solution (18, 19). Aging an alloy and precipitating silicides reduces creep resistance (19, 20). The cooling rate after extrusion would be sufficiently slow to permit initiation of silicide precipitation. Since a direct aging heat treatment would not put silicon back into solution, while a beta solution plus age heat treatment would, higher creep resistance would be obtained with a beta solution heat treatment.

Summary

Beta processing and beta solution plus age heat treatment of a dispersoid containing Ti alloy can produce material with 1056 MPa RT ultimate strength, 776 MPa 650°C ultimate strength, and 49 hour 0.2% creep life at 650°C, 138 MPa. The alloy develops a strong crystallographic texture by beta processing. Beta grain growth is restrained when dispersoid distribution is uniform.

Acknowledgements

This project was begun with the encouragement, advice, and support of C. D. Williams, G. E. Wasielewski and L. A. Johnson. The alloys were atomized at Crucible Research Center by F. Yolton. Thermomechanical processing was carried out under the direction of R. Laing, T. Douglas, and R. Auer. Metallography was done by A. Barbuto, R. Kilmer, and R. Schnoor. Tensile and creep tests were conducted by C. Canestraro and P. Dupree. Moduli were determined by R. S. Gilmore. Their care and diligence is gratefully acknowledged.

References

1. S. M. L. Sastry, P. J. Meschter, and J. E. O'Neal, "Structure and Properties of Rapidly Solidified Dispersion Strengthened Titanium Alloys: Part I. Characterization of Dispersoid Distribution, Structure, and Chemistry", *Metallurgical Transactions*, 15A (1984), 1451–1463.

2. S. M. L. Sastry, T. C. Peng, and L. P. Beckerman, "Structure and Properties of Rapidly Solidified Dispersion Strengthened Titanium Alloys: Part II. Tensile and Creep Properties", *Metallurgical Transactions*, 15A (1984), 1465–1474.

3. S. M. L. Sastry, T. C. Peng, P. J. Meschter, and J. E. O'Neal, "Rapid Solidification Processing of Titanium Alloys", *Journal of Metals*, (1983), 21-27.

4. J. P. A. Lovander, S. A. Court, R. Kircheim, and H. L. Fraser, "Thermal Stability of Rare Earth Oxides in Titanium When Annealed above the Alpha–Beta Transus", *Scripta Metallurgica*, 21 (6) (1987), 859-861.

5. M. F. X. Gigliotti, G. E. Wasielewski, and R. G. Rowe, "Microstructural Development and High Temperature Mechanical Characterization of a Dispersoid-Containing Titanium Alloy", in *Proceedings of the Sixth World Conference on Titanium*, ed. P. Lacomb, R. Tricot, and G. Béranger, (Cedex, France: Les Éditions de Physique, 1988), 861-866.

6. M. F. X. Gigliotti, Jr., R. G. Rowe, and G. E. Wasielewski, "High Strength Oxidation Resistant Titanium Alloy", (March 6, 1990), U. S. Patent 4,906,436.

7. R. A. Amato, M. F. X. Gigliotti, Jr., J. R. Hughes, L. C. Perocchi, and A. P. Woodfield, "Method for Developing Enhanced Texture in Titanium Alloys, and Articles Made Thereby", (December 24, 1991), U. S. Patent 5,074,907.

8. J. H. Moll and C. F. Yolton, "Production and Characterization of Rapidly Solidified Titanium and Other Alloy Powders Made by Gas Atomization", in *Titanium, Rapid Solidification Technology*, ed. F. H. Froes and D. Eylon, (Warrendale, PA: The Metallurgical Society of AIME, 1986), 45-56.

9. C. F. Yolton, "Gas Atomized Titanium and Titanium Aluminide Alloys", in *Aerospace and Defense Technologies*, (Princeton, NJ: Metal Powder Industries Federation, 1990), 1, 123-131.

10. Edward Schreiber, Orson L. Anderson, and Naohira Soga, *Elastic Constants and Their Measurement* (New York, NY: McGraw-Hill, 1973).

11. Frank Larson and Anthone Zarkades, "Properties of Textured Titanium Alloys" (Report MCIC–74–20, Metals and Ceramics Information Center, Batelle, Columbus OH, 1974).

12. W. G. Burgers, "On the Process of Transition of the Cubic-Body-Centered Modification into the Hexagonal-Close-Packed Modification of Zirconium", *Physica*, 25 (1934), 561-586.

13. F. J. Gurney and A. T. Male, "The Effects of Extrusion Process Variables on the Structure and Properties of Titanium Alloys", in *Titanium Science and Technology*, ed. R. I. Jaffee and H. M. Burte, (New York: Plenum Press, 1973), 1769-1784.

14. A. Sommer, M. Creager, S. Fujishiro, and D. Eylon, "Texture Development in $\alpha+\beta$ Titanium Alloys", in *Titanium and Titanium Alloys*, ed. J. C. Williams and A. F. Belov, (New York: Plenum Press, 1982), 1863-1874.

15. C. C. Chen and J. E. Coyne, "Relationships between Microstructure and Mechanical Properties in Ti–6Al–2Sn–4Zr–2Mo–0.1Si Alloy Forgings" in *Titanium '80 Science and Technology*, ed. H. Kimura and O. Izumi, (Warrendale, PA: The Metallurgical Society of AIME, 1980), 1197-1207.

16. D. Eylon, J. A. Hall, C. M. Pierce and D. L. Ruckle, "Microstructure and Mechanical Properties Relationships in the Ti–11 Alloy at Room and Elevated Temperatures", *Metallurgical Transactions*, 7A (1976), 1817–1826.

17. W. H. Miller, Jr., R. T. Chen, and E. A. Starke, Jr., "Microstructure, Creep, and Tensile Deformation in Ti–6Al–2Nb–1Ta–0.8Mo", *Metallurgical Transactions*, 18A (1987), 1451–1468.

18. Y. Imbert, "Creep Resistance and Embrittlement of A Ti–6%Al–5%Zr–1%W–0.4%Si Alloy", *Journal of the Less–Common Metals*, 37 (1974) 71–89.

19. N. E. Paton and M. W. Mahoney, "Creep of Titanium–Silicon Alloys" *Metallurgical Transactions*, 7A (1976), 1685–1694.

20. M. R. Winstone, Rees D. Rawlings and D. R. F. West, "The Creep Behaviour of Some Silicon–Containing Titanium Alloys", *Journal of the Less–Common Metals* , 39 (1975), 205–217.

CREEP BEHAVIOR OF Ti-24Al-11Nb

M. Khobaib

The University of Dayton Research Institute
300 College Park
Dayton, Ohio 45469-0128

Abstract

Creep behavior of a β-heat treated Ti-24Al-11Nb has been studied over the temperature range of 550-800°C. Smooth round bar, threaded-end specimens were used for tensile creep testing. Tests were conducted both in laboratory air and an inert environment of a vacuum of 10^{-6} torr to investigate the role of environment. An abnormal amount of surface cracking all over the gage length was observed on tests conducted in laboratory air, the density of which reduced with decreasing temperature with very little cracking observed at 550°C. Substantial reduction in surface cracking and an increase in rupture life were noticed when similar tests were conducted on electropolished specimens. There was no evidence of surface cracking on test conducted in vacuum. It appears that the cracking is mainly oxide induced and the oxidation of titanium aluminide is enhanced by surface residual stress. The apparent activation energy Q_c was determined to be nearly 70.0 K.cal/mole. A study of stress dependence of steady state creep rate produced a value of 3.88 for the stress exponent. Detailed SEM analysis of the creep ruptured specimen was conducted to understand the failure mechanism: Failure in vacuum was found to be intergranular which apparently results from the separation of the prior beta grain boundaries. In contrast, the laboratory air tested specimen failed in a transgranular manner. The failure initiated from the embrittled surface crack. TEM observation indicated intense slip activity with most of the dislocations homogeneously distributed. Clear indications of cross slip/climb were observed. Non-basal dislocations were also found to participate in the creep deformations. The results of these tests and suggested mechanisms of failure will be discussed.

Introduction

The titanium aluminide family of materials has a good combination of properties, such as low density coupled with good mechanical properties at elevated temperatures. Titanium aluminides temperature capabilities are much higher than those of conventional titanium alloys and they have a higher ratio of strength and modulus to density than conventional superalloys (1). These attractive properties have made these aluminides prime candidates for both static and rotating components of aerospace structure at temperatures upto 750°C (2). But, apart from their good elevated temperature mechanical properties, they must exhibit good elevated temperature environmental resistance, before they can be recommended for such applications.

Titanium '92
Science and Technology
Edited by F.H. Froes and I. Caplan
The Minerals, Metals & Materials Society, 1993

Preliminary study on the elevated temperature mechanical behavior has shown that their deformation and failure modes are very sensitive to environment under monotonic loading (3). Such behavior poses a major concern in the development of this class of materials for elevated temperature gas turbine engine application. Intelligent use of these materials requires the ability to predict the life of the component under service conditions. The current push to use these materials at elevated temperature over a long period of time has drawn attention to the time-dependent (creep) elevated temperature response of high temperature titanium alloys and intermetallics. Therefore, a detailed investigation was conducted to understand the elevated temperature creep behavior as well as the role of environment on sustained load behavior of a representative Ti-24Al-11Nb aluminide.

Material

The material used in this study was a representative alpha-2 titanium aluminide Ti-24Al-11Nb (atomic percent). The material was obtained in the form of 7.62 cm (3.0 in.) thick forged slab. The slab was cross-rolled at 1038°C (1900°F) down to a thickness of 4.06 cm (1.6 in.) plate. The plates were then beta annealed at 1177°C (2150°F) for 30 minutes and cross rolled further to a thickness of 1.14 cm (0.45 in.). The plate was then given a two-step heat-treatment consisting of a beta solution at 1149°C (2100°F) for one hour in vacuum, followed by forced cooling with argon and a 760°C (1400°F) age for one hour in vacuum. This produced a two-phase equiaxed basket-weave Widmanstatten morphology with no preferred orientation. The resulting microstructure is shown in Fig. 1. The prior beta grain size was approximately 1.00 mm in diameter.

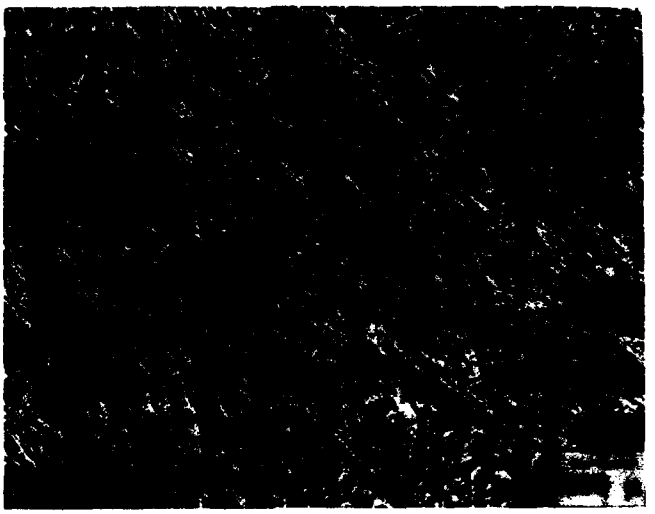


Figure 1 - Representative Microstructure of Ti-24-Al-11Nb.

Specimens used for this investigation were machined from the plate in the longitudinal direction of the final rolling. The specimens were fabricated in the form of threaded-end, smooth round bar and had an overall length of 101.6 mm (4.0 in.), a gage length of 31.75 mm (1.25 in.) and a gage diameter of 6.35 mm (0.25 in.). The gage section of most of the specimens were polished with 600 grit silicon carbide paper in the longitudinal direction. This was done to remove any circumferential grinding marks left behind during final machining and to ensure a uniform surface finish. A selected batch of specimens were electropolished further to remove possible residual stress induced (during machining) layer. The laboratory air creep testing was conducted using an Archweld sustained-load creep frame.

The vacuum tests were conducted using a CENTORR furnace which was incorporated into an Archweld creep frame. The typical vacuum during the test was of the order of 10^{-6} torr. The creep elongation was measured using a specially designed extensometer which detects axial elongation with a linear variable differential transducer (LVDT). The gage length was nominally 25.4 mm (1 in.). The creep elongation was continually monitored through a microprocessor. After each test, the failed specimen was extensively analyzed to understand the fracture mechanism.

Results and Discussions

The results of the creep tests conducted in laboratory air at 550°C, 650°C, 700°C, and 750°C and a stress of 245 MPa is shown in Fig. 2. The effect of increasing temperature on the steady state creep strain and rupture life can be clearly seen. The higher temperature resulted in increased creep rate and shorter rupture life. An activation energy of nearly 70kcal/mole was obtained from the steady state creep rate values derived from test results shown in Fig. 2. Similar values were obtained from temperature increment/decrement tests.

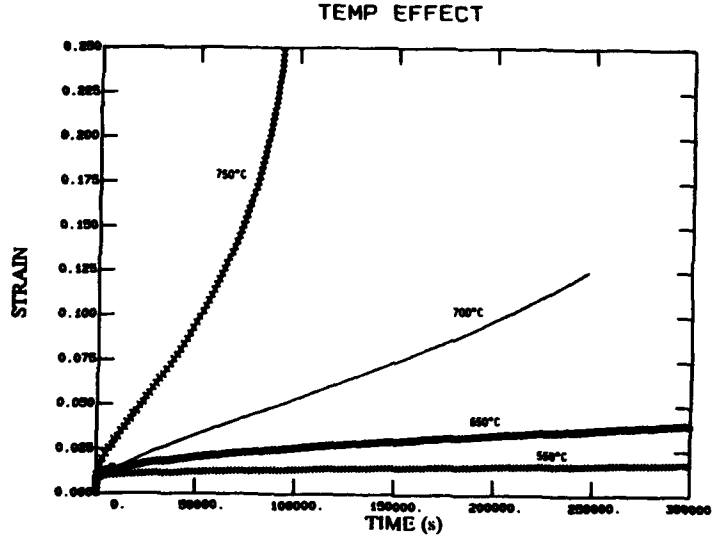


Figure 2 - Effect of Temperature on Creep Behavior of Ti-24Al-11Nb at under a sustained stress of 245 MPa.

For all tests conducted in laboratory air, an abnormal amount of circumferential cracking all over the gage length of the specimen was observed. Figure 3 shows such surface cracking on a specimen creep tested at 700°C and at a stress of 245 mPa. A substantial reduction in surface cracking was noticed as shown in Fig. 4, by removing nearly 5 mils of the specimen surface by electro-polishing. Figure 4 shows the gage section of an electropolished specimen tested at 700°C and at a stress of 245mPa. At the same time the creep resistance also improved as shown in Fig. 5. Similarly, the surface of the specimen tested in vacuum had negligible or no surface cracking. This is shown in Fig. 6. Absence of surface cracking was also noted when test was conducted in laboratory air at a low temperature of 550°C [4]. It appears that both the surface residual stress and the environment contribute to the surface cracking during creep testing. However, the role of environment appears to be more dominant as suggested by test results in vacuum and laboratory air test at 550°C. Apparently the cracking of titanium aluminide is enhanced by surface residual stress.

The effect of environment on the creep of Ti-24Al-11Nb was investigated by comparing creep behavior from tests conducted in laboratory air with a series of tests conducted in a vacuum of nearly 10^{-6} torr. Tests were conducted in the two environments under similar conditions of temperature and load. At all test temperatures (650, 700, 750, and 800°C), the steady state creep strain rate was found to be little higher in vacuum than in laboratory air. One of the representative plot is shown in Fig. 7 which compares the creep behaviors obtained from test conducted in laboratory air and vacuum at 800°C and at a stress of 138.0 MPa. Similar results were obtained at 650°C, 700°C and 750°C [4]. This behavior is contrary to creep behavior observed in most metallic materials [5,6]. This unusual behavior is difficult to understand. However, the fractographic analysis of the failed specimen provides some insight to this unusual behavior.

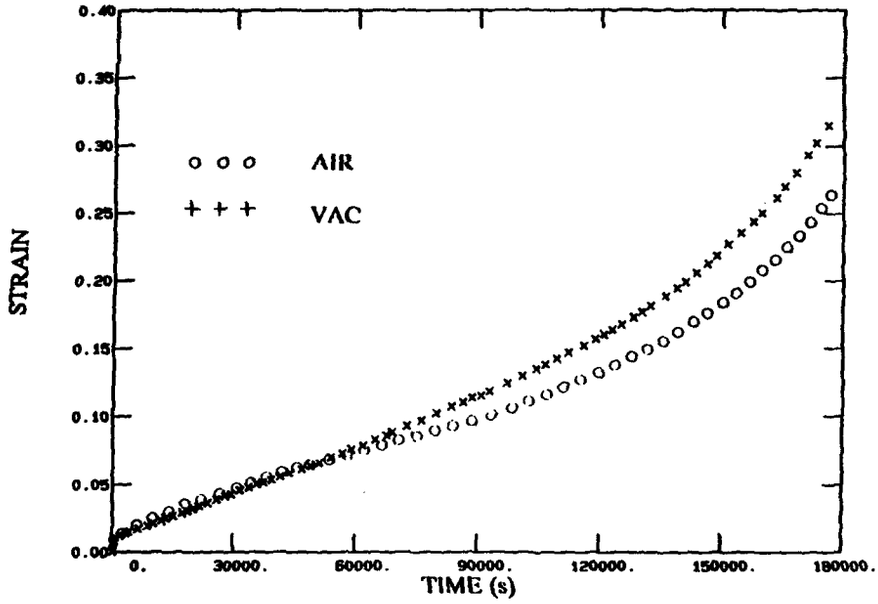


Figure 7 - Creep Behavior of Ti-24Al-11Nb at 800°C for a Stress of 138 MPa.

Figure 8 shows the fracture surface of a specimen tested in laboratory air at 700°C. The failure appears to be transgranular. Higher magnification of the ruptured surface, shown in Fig. 9, shows the failure mode to be a mixture of cleavage and ductile tearing. In contrast the fracture surface observed on specimen tested in vacuum at 700°C, as shown in Fig. 10, reveals an intergranular mode of failure. The intergranular cracking and a higher creep rate in vacuum is postulated to be the result of selective oxidation of grain boundaries. In laboratory air, the abundance of oxygen leads to α-case formation, which under load results in extensive cracking. Fig. 8 shows the evidence of such cracking. The cracking initiates at multiple sites, but over time a single crack becomes dominant leading to the failure of the specimen. The extensive cracking causes a reduction in the effective stress intensity (the parameter controlling the growth of the crack) at the tip of the dominant crack. Thus, the growth of the leading crack is slowed, which translates to a lower creep rate compared to that obtained from specimen tested in vacuum (which showed no sign of circumferential cracking) under similar condition. At the same time, the stress concentration near the tip of such crack leads to the cleavage like transgranular failure. This aspect is discussed in more detail in another paper in this volume.



Figure 3 - Surface Cracking All Over the Gage Length of Creep Ruptured Specimen in Air at 700°C.

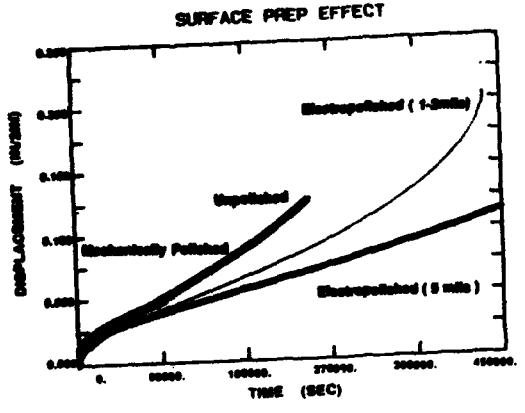


Figure 5 - Creep Behavior of Specimens Tested at 700°C and a Stress of 35 Ksi Showing the Effect of Surface Finish.

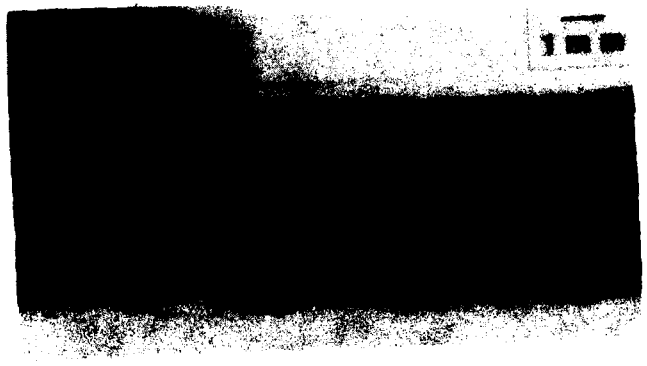


Figure 4 - Limited Surface Cracking on Electropolished Specimen Tested in Air at 700°C.

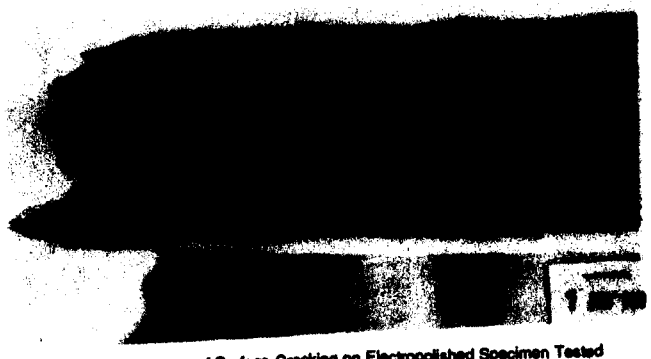


Figure 6 - Absence of Surface Cracking on Electropolished Specimen Tested in Vacuum at 700°C.

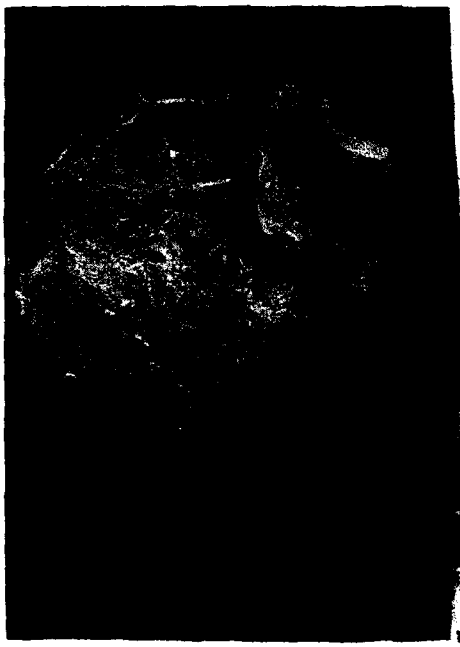


Figure 8 - Macroscopic View of Creep Ruptured Surface Tested in Air at 700°C.



Figure 9 - Indication of Ductility on Creep Ruptured Specimen Tested in Air at 700°C.



Figure 10 - Macroscopic View of Creep Ruptured Surface Tested in Vacuum at 700°C.

TEM analysis of the creep ruptured specimens showed intense dislocation activity. Figure 11 shows the dislocation structure in a specimen creep tested at 650°C in air. The dislocation density was quite high and apparently several slip systems were active. By using basal (0002) reflection, the activity of slip in the nonbasal plane was also revealed. Figure 12 shows a set of parallel dislocations in the nonbasal plane, indicating that nonbasal slip was also contributing to the deformation. Similar dislocation structure was observed in specimen creep tested at 700, 750 and 800°C. At higher temperatures the climb was found to be more prevalent.



Figure 11 - Dislocation Structure Generated During Creep of Ti-24Al-11Nb at 650°C.



Figure 12 - Evidence of Nonbasal Slip Activity During Creep of Ti-24Al-11Nb at 650°C.

References

1. H.A. Lipsitt, "Titanium Aluminides - An Overview," Materials Research Society Symposium Proceedings, 39 (1985), 351-364.

2. J.S. Balsone, "The Effect of Elevated Temperature Exposure on the Tensile and Creep Properties of Ti-24Al-11Nb," Oxidation of High Temperature Intermetallics, ed. T. Grobstein and J. Doychak (The Minerals, Metals & Materials Society, 1989), 219-234.

3. M. Khobaib et al., "Research on Mechanical Properties for Engine Life Prediction," (AFWAL-TR-88-4062, Air Force Wright Aeronautical Laboratories, Air Force Materials Laboratory, Wright-Patterson Air Force Base, Ohio, May 1988).

4. M. Khobaib et al., "Mechanical Properties for Advanced Engine Materials," (Technical Report, UDR-TR-89-43, University of Dayton Research Institute, February 1989).

5. M. Stucke et al., "Environmental Aspects in Creep Crack Growth in a Nickel Base Superalloy," (Proceeding of International Conference on Fracture 6, New Delhi, India, December 1984), 3967-3975.

6. M. Khobaib, T. Nicholas, and R.V. Srivats, "Role of Environment in Elevated Temperature Crack Growth Behavior of Rene N4 Single Crystal," Environmentally Assisted Crack: Science and Engineering, ASTM, STP 1049, ed. W.B. Lisager, T.W. Crooker and B.N. Leis (Philadelphia, PA: American Society for Testing and Materials, 1990) 319-333.

MICROSTRUCTURE AND MECHANICAL PROPERTIES OF β-21S TITANIUM ALLOY

D. Upadhyaya[a], D. M. Blackketter[b], C. Suryanarayana[a] and F. H. Froes[a]

[a]Institute for Materials and Advanced Processes.
[b]Department of Mechanical Engineering.
University of Idaho, Moscow, ID 83843-4195.

Abstract

The newly developed Beta-21S (β-21S) titanium alloy is the leading candidate matrix material for the metal matrix composite skin surface of the National Aerospace Plane (NASP). However, information regarding the relationship between mechanical properties of β-21S and microstructure is currently limited. This paper presents a detailed microstructural and mechanical property characterization of the β-21S titanium alloy. The microstructure and phase relationships obtained using TEM, SEM and X-ray diffraction techniques are related to the mechanical properties; specifically tensile and shear data. The improved definition of the relationship between microstructure and mechanical properties increases understanding of the β-21S material and will aid in optimization of both the monolithic material behavior and metal matrix composite performance. Results shows that the as-received β-21S is essential a single phase beta titanium alloy. Further, the as-received β-21S has excellent room temperature mechanical properties. With a thermal exposure in air to which it might be used (750°C for 4.5 hr), surface oxidation occurs. This oxidized region is a prefered site for crack initiation, causing a decrease in mechanical properties.

Introduction

Advanced materials with enhanced physical and mechanical properties are the key to technological improvement in system performance for demanding aerospace applications [1-4]. Key material characteristics include low density, good high temperature strength, fracture behavior, environmental resistance and high stiffness, in addition to room temperature mechanical properties and reasonable cost. Metal matrix composites (MMC's) are especially useful in demanding aerospace applications. Strength and stiffness of the MMC's (reinforced with a ceramic fiber such as SiC) are enhanced compared to monolithic material. Because of the attractive characteristics, titanium and its alloys are the material of choice for MMC's in the 370-980°C temperature range [5].

The most important attributes required by the titanium matrix alloy, using a foil-fiber-foil approach, are easy producibility as foil, oxidation resistance, good

Titanium '92
Science and Technology
Edited by F.H. Froes and I. Caplan
The Minerals, Metals & Materials Society, 1993

elevated temperature properties and minimal fiber-matrix reaction [4]. To meet these requirements, the β-21S (Ti-15Mo-2.7Nb-3Al-0.2Si) metastable beta titanium alloy was developed [6]. In general metastable beta titanium alloys exhibit excellent cold rolling characteristics but their limitation lies in poor elevated temperature properties including undesirable oxidation behavior. However, preliminary results show that the β-21S alloy has excellent oxidation resistance and acceptable elevated temperature properties [5,7]. Furthermore, it possesses very good corrosion and hydrogen resistance properties [6,7]. The β-21S is cold rollable, strip producible, formable, weldable and has excellent age hardening characteristics [6,7]. However, the mechanical and microstructural information data base of this new titanium alloy is limited and must be developed quickly to allow this material to be used with confidence in full-scale production on vehicles such as the National Aerospace Plane (NASP).

The goal of the present paper was to develop microstructural and mechanical property data for the β-21S Ti-alloy. For this purpose tensile and Iosipescu shear testing of as-received, aged and thermally exposed material was conducted. The microstructure of the β-21S alloy was correlated to the mechanical properties for as-recieved, aged and thermally exposed specimens.

Materials and Methodology

The β-21S alloy was obtained from Timet Corp., Henderson, NV, as a 1.55 mm sheet in the mill-annealed conditioned. The sheet was rolled from an ingot (Heat G-1664) and annealed at 843°C for 4 minutes. The chemical composition (in wt%) of β-21S is Ti-16.3Mo-2.94Nb-3.7Al-.2Si-.104Fe-.22C-.121O-.005N-.0023H. The β-21S was thermally exposed in air at 750°C for 4.5 hr and air cooled to determine the effect of oxidation on mechanical properties and to indicate the maximum temperature up to which β-21S can be exposed without unduly compromising the mechanical properties. Further, various aging treatments were applied to β-21S to determine the effects of aging treatment on the microstructure and mechanical properties. Both longitudinal and transverse specimens were prepared. The thermal exposure in air oxidized the β-21S alloy but no effort was made to prevent either the oxidation during exposure or to remove the oxidized layer from test specimens as this condition could be the condition of the material in actual use [8].

The tensile testing of β-21S was conducted in accordance with ASTM standard E-8M [9]. Iosipescu shear testing was performed to determine shear strength and shear modulus of the β-21S titanium alloy at room temperature [10]. A laser-displacement technique was used to determine the coefficient of thermal expansion of β-21S.

Microstructural characterization of the β-21S was performed using optical, X-ray diffraction, SEM, and TEM techniques. TEM was performed using Zeiss (model EM-10A). SEM analysis was performed using Amray (model 1830).

Results

Microstructural Characterization

Figure 1 shows the optical isometric projection of as-received β-21S. The as-received β-21S appears equiaxed and essentially single phase beta. Figure 2 shows the SEM isometric projection of thermally exposed β-21S showing the

precipitation of α-phase in the equiaxed β matrix. To more fully characterize this microstructure, a "decoration" treatment [11] was used to clearly define recrystallized (equiaxed) and non-recrystallized regions. The Beta transus of β-21S is 815°C [5], thus a "decoration" heat treatment of 5 minutes at 510°C was used

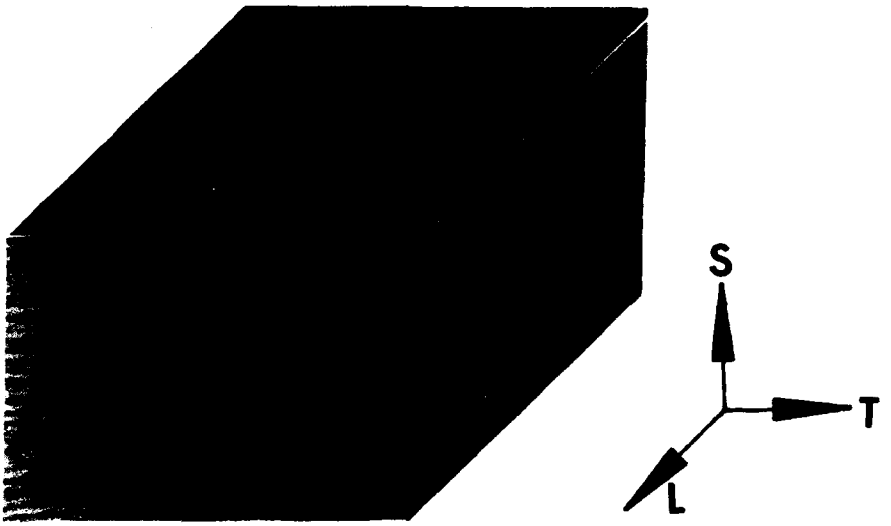


Figure 1. Optical isometric projection of as-received β-21S.

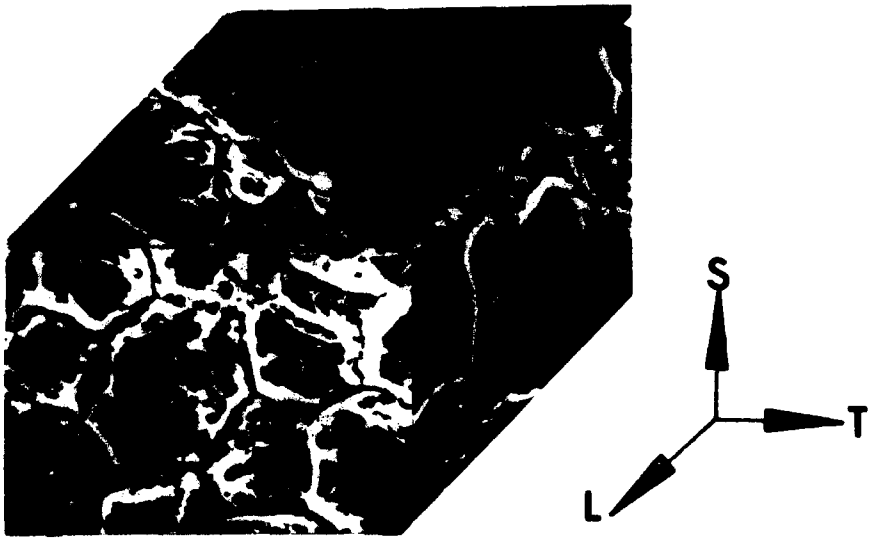


Figure 2. SEM isometric projection of thermally exposed β-21S, 750°C, 4.5 hr in air.

with the as-received material. This treatment worked very well decorating the non-crystallized region causing them to etch black (Figure 3). The recrystallized regions of low dislocation density, were not decorated and etched up white. Thus, the nature of the as-received microstructure was clearly revealed as predominently recrystallized but with some remnant non-recrystallized regions.

Figure 4 shows the x-ray diffraction patterns of both as-received and thermally

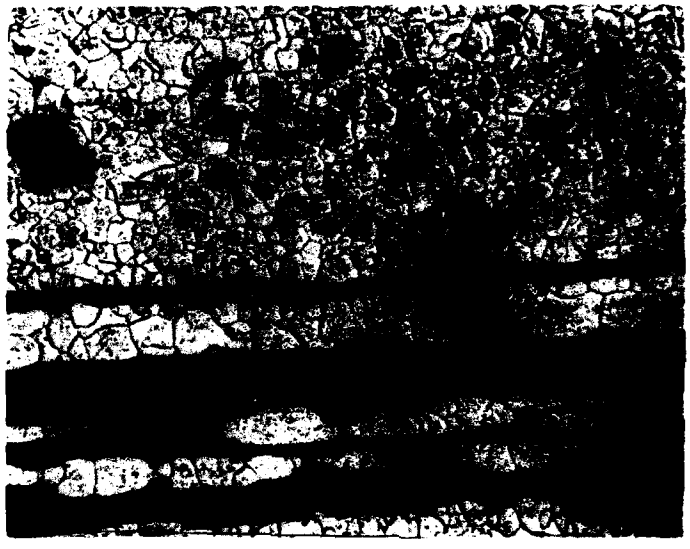


Figure 3. Optical micrograph of as-received β-21S after a "decoration" treatment of 510°C for 5 min. [11], white regions are recrystallized, black regions are non-recrystallized, 300X.

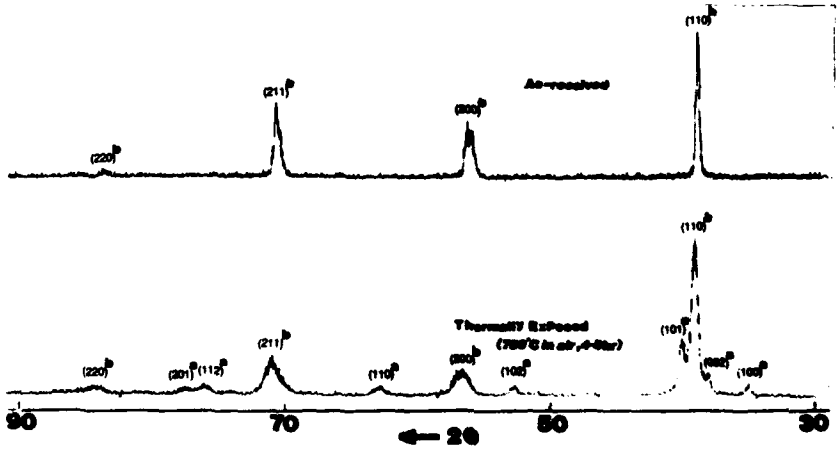


Figure 4. X-ray diffraction pattern of as-received and thermally exposed β-21S, α and β phases are represented by "a" and "b", respectively.

exposed specimens. The β-21S has a bcc structure with a = 3.26 Å. With the thermal exposure, the α-phase precipitated in the β matrix during exposure and cool down (see Figure 2). The β lattice parameter changes to 3.24 Å and the α-phase exhibits an hcp structure with a = 2.94 Å and c = 4.74 Å. The precipite size of the α-phase is large as seen in Figure 2 and, along with the equiaxed β grains, is expected to result in approximately the same strength level as the as-received material. The electron diffractrion experiments confirm the structure and lattice parameter of as-received material obtained by the X-ray technique.

Mechanical Characterization

Tables 1 and 2 show the results of tensile and Iosipescu shear testing of the as-received, aged, and thermally exposed specimens. It was observed that with the aging treatment tensile strength increases and the ductility decreases as expected. Additionally, the coefficient of thermal expansion of β-21S is found to be $9.3X10^{-6}$/°C (up to 370°C). Figure 5 shows the aging curves of β-21S and it is clear that the β-21S is readily age hardened [5]. The elastic modulus of as-received, aged and thermally exposed β-21S was found to be in the range of 10.6 to 14.1 GPa. With the thermal exposure, the tensile strength decreases by 38% when compared to peak strength achieved with an aging treatment (538°C/8 hr in argon). As expected, the thermal exposure decreases the ductility of the β-21S as indicated by the decrease in elongation at failure and reduction in area at failure.

Discussion

The decrease in tensile strength and reduced ductility after thermal exposure, compared to the as-received condition, can be related essentially to the surface condition of the β-21S. Figure 6 shows the fracture surface of an as-received longitudinal tensile specimen and the presence of dimples suggests a ductile failure mode. But with the thermal exposure, the specimen is oxidized at the surface leading to a reduced ductility. Figure 7 shows the extent to which the β-21S is oxidized. As anticipated this oxidized layer is brittle and a site for crack initiation. Figure 7 shows that the failure mode at this layer is brittle in nature (no dimples present) until cracks from this region propagate into the interior of specimen where normal oxygen levels are present and the failure mode is ductile. Further, the area between brittle failure and ductile failure regions shows a shear failure mode. It appears that once the crack initiates in the brittle surface region it propagates at 45° in shear mode for a short distance and in the interior of the specimen the failure is ductile (Figure 7). The oxidized surface layer is the major cause for the decrease in ductility. The oxidized layer does not affect the shear strength as seen in Table 2 as the crack initiated at the central region of the specimen and propagated towards the surface region.

Conclusions

Mechanical property determination and microstructural characterization was conducted on the newly developed β titanium alloy: β-21S. Results show that the as-received β-21S is a single phase β titanium alloy which has excellent room temperature mechanical properties. With thermal exposure in air to a temperature at which it might be subjected, as expected, surface oxidation occurred. The

Table 1. Tensile test results of Beta-21S titanium alloy.

Condition	Direction	YS (MPa)	UTS (MPa)	E_l (%)
As-received				
	Longitudinal	817	854	19.5
	Transverse	853	891	17.3
	AVERAGE	835	872	18.4
Aged (538°C/8 hr in argon)[5]				
	Longitudinal	1273	1345	8.5
	Transverse	1310	1388	7.0
	AVERAGE	1292	1367	7.8
Aged (593°C/8 hr in argon)[5]				
	Longitudinal	1012	1103	12.5
	Transverse	1033	1121	11.3
	AVERAGE	1023	1112	11.9
Thermally exposed (750°C/4.5 hr in air)				
	Longitudinal	--	810	6.0
	Transverse	--	870	5.0
	AVERAGE	--	840	5.5

Table 2. Iosipescu shear test results of Beta-21S titanium alloy.

Condition	Direction	Shear modulus (GPa)	Shear strength (MPa)
As-received			
	Longitudinal	4.23	610
	Transverse	4.31	605
	AVERAGE	4.27	607
Thermally exposed (750°C/4.5 hr in air)			
	Longitudinal	--	624
	Transverse	--	627
	AVERAGE	--	625

oxidized region is a favorable site for crack initiation causing a decrease in overall mechanical properties. Further, β-21S is readily age hardened and appropriate aging treatment produces good mechanical property combinations. The microstructural features observed in as-received, aged and thermally exposed β-21S material could be correlated well with the observed mechanical property behavior.

Aging Curves for Beta-21S.

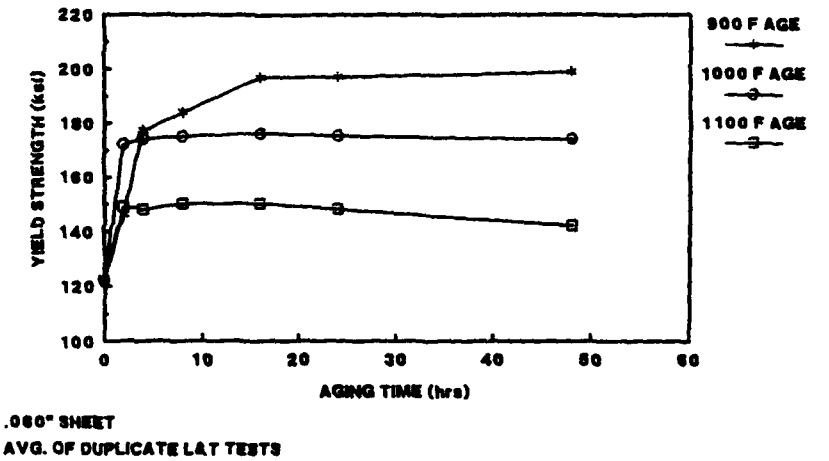


Figure 5. Aging curves of β-21S titanium alloy [5].

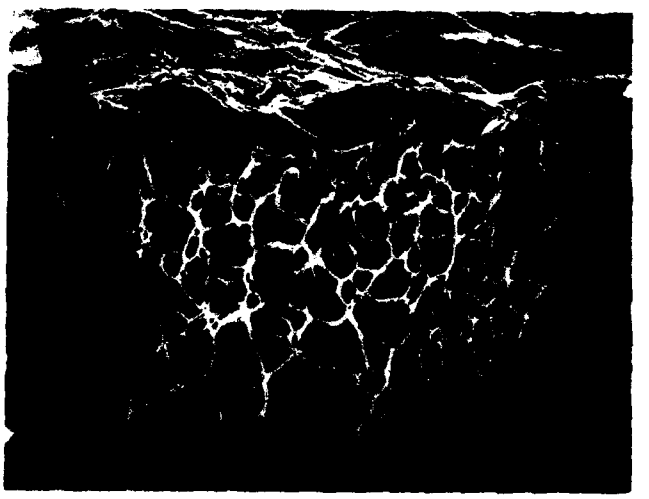


Figure 6. SEM micrograph of the failure surface of as-received longitudinal tensile specimen, showing ductile failure mode.

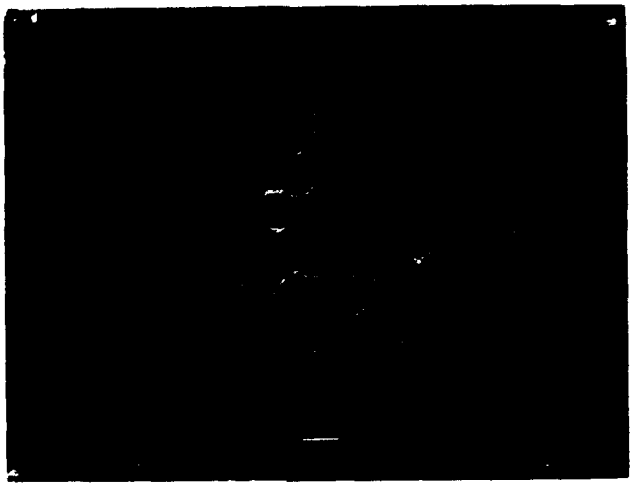


Figure 7. SEM micrograph of the failure surface of thermally exposed longitudinal tensile specimen of β-21S, showing brittle, shear and ductile failure mode.

Acknowledgements

The authors would like to recognize valuable discussions with Dr. Paul Bania of TIMET, and tensile testing of aged material carried out under his supervision.

References

1. F. H. Froes, P/M in Aerospace and Defence Technologies, ed. F. H. Froes, Princeton, NJ: MPIF, 1990, 23-52.
2. F. H. Froes, Materials Edge, May/June 1988, 19-23.
3. Scientific American, 255, No. 4, Oct 1986.
4. R. A. MacKay, P. K. Brindley, and F. H. Froes, JOM, No. 5, Vol., May 1991, 23-29.
5. P. Bania and W. M. Parris, Conf. Proceedings, 1991 TDA Conference, 1991, 784-792.
6. P. Bania, Materials Edge, No. 25, June 1991, 23.
7. J. Gourmann, Conf. Proceedings, 1991 TDA Conference, 1991, 793-802.
8. T. M. F. Ronald, Adv. Mat. and Proc., No. 5, 29, 1989, 135-147.
9. Tension Testing of Metallic Materials, ASTM Standard E-8M-86, American Society for Testing and Materials, Philadelphia, PA, 1986.
10. N. Iosipescu, JOM, Vol. 2, 1967, 537-566.
11. F. H. Froes, J. M. Capenos and C. F. Yolten, Metallography, Vol. 9, 1976, 535-543.

MICROSTRUCTURAL MODIFICATION AND ANALYSIS

OF AN IMI685 TITANIUM ALLOY

Z . X . Guo*, and T. N. Baker,

Department of Metallurgy and Engineering Materials,
University of Strathclyde, Glasgow G1 1XN, U.K.

Abstract

IMI685 is a commercial near α titanium alloy for producing high temperature components used in aero-space industries. The mechanical properties of the material are highly dependent on its microstructure. The latter is very sensitive to thermomechanical processing and heat treatment conditions. A basketweave type of microstructure and a relatively small prior β grain size are considered to be the key features for achieving an improved combination of properties. The true basketweave microstructure has only been infrequently observed in the past. It is also very difficult to refine the grain size. The present investigation has employed various thermomechanical processing and heat-reatment conditions to modify the microstructural features of the material. The effects of temperature and true strain rate are duly considered. Both optical and transmission electron microscopy has been used to characterize the microstructural changes introduced by each of the processing routes. The conditions for forming a true basketweave microstructure are clarified. Effective grain refinement has been found to result from a lower (α+β) processing route.

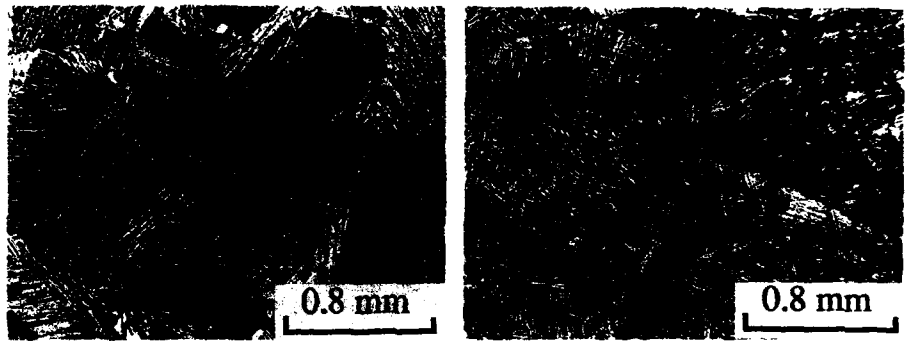
Introduction

The near-α IMI685 alloy is normally processed and heat-treated in the β phase field to produce high creep resistance [1], which is usually characterized by a lamellar type of microstructure, as shown in Fig.1 (a). The microstructure consists of colonies of α platelets, and a few percent of interplatelet β layers. The colonies are confined within relatively large prior-β grains (typically 0.5 to 2 mm [1]).

The creep resistance benefits from both the solid-solution effect and the inhibition of α platelet boundaries, and colony boundaries to dislocation movement [2]. Good fracture toughness and fatigue crack propagation resistance can also be achieved due to the deviation of crack path, crack branching or blunting by the α platelet and boundary β layer [3,4]. Yet, in practice, the structure tends to have a relatively low ductility and poor low-cycle fatigue crack initiation resistance, because of its large prior-β grain size and the ease of causing stress concentrations (or dislocation pile-ups) at the boundaries and triple points [5]. The properties can be improved by refining the prior-β grain size and the α colonies, particularly when the fine α colonies develop such that they frequently intersect each other forming a basketweave type of morphology [3,6], as illustrated in Fig.1(b).

(*Now with: Oxford Centre for Advanced Materials and Composites,
Department of Materials, University of Oxford, Oxford OX1 3PH, U.K.)

Titanium '92
Science and Technology
Edited by F.H. Froes and I. Caplan
The Minerals, Metals & Materials Society, 1993



(a) Large colonized α; (b) Basketweave α.

Fig. 1. Lamellar microstructures in IMI685:

Grain refinement in titanium alloys is ineffective by α/β phase transformation or β processing alone, as grain growth is very rapid in the β phase field. It is not known to what extent the grain size should be reduced, but this does not appear to be the problem at present. The main task is to find out a processing route for the refinement of the prior- β grain size and the production of a basketweave α microstructure.

The microstructural morphology of the material is very sensitive to thermomechanical processing and heat treatment conditions, which, in turn, influence the mechanical properties of the material [4,6]. The basketweave type of microstructure, shown in Fig.1(b), often leads to a superior combination of properties for the material. Eylon and Hall [3], have clearly demonstrated an improved strength, ductility, and toughness of the basketweave structure over those of other types of colonized structures. However, it is not clear under what conditions the optimum structure can be obtained. Air-cooling was suggested by Assadi et al [6], to produce the basketweave structure. However, many authors have failed to achieve the true basketweave morphology during air-cooling. In practice, the term air-cooling can mean very different cooling rates for samples of dissimilar dimensions. In another investigation, Zhang and Yang [7] concluded that thermomechanical processing was necessary for such structure, but their demonstrated microstructures were not truly of the basketweave type. Instead, the large and thick colonized structures were observed in their publication.

In order to determine an effective grain refinement route, and the conditions favouring basketweave formation, we have pursued a detailed microstructural investigation through thermomechanical processing, via. isothermal hot pressing, and heat-treatment. The effects of true strain rate, processing temperature, and cooling rate are duly considered. Most previous investigations have either ignored the effect of strain rate, or given an average cross-head velocity, because a conventional press has no control of the parameter. Here a true strain rate effect is presented, using a computer-controlled press. The processing temperature spans a much wider temperature range than previously investigated, particularly in the lower (α+β) and the pseudo-single α phase fields.

Experimental Procedures

Cylindrical samples, dia. 50 mm x 75 mm, were heated in the β-phase field, maintained at 1050 °C for one hour to homogenize, and then allowed to cool down to a forging temperature, and held for another hour to insure a uniform temperature and microstructure before being pressed. The processing conditions are given in Table I.

The forged samples were then heat-treated in the β-phase field at 1050 °C for 15 minutes and then cooled down at a rate of about 3-6 °C/s, essentially in the first few minutes of cooling. This

rate corresponds to an enhanced air-cooling, in contrast to a slower air cooling adopted previously [8].

Microstructural examination was carried out on the cross-section of the samples parallel to the direction of forging. The details of specimen preparation for optical microscopy and TEM were the same as in ref.[8]. Grain size was determined by the mean linear intercept method.

Results and Discussion

The Effect of Thermomechanical Processing on Microstructure

Samples from the as-received material were cycled around the (α+β)/β transus, 1020 °C, in an attempt to determine whether phase transformation can reduce the grain size. The procedures are schematically presented in Fig.2, along with the grain sizes. The results failed to show any structural refinement. This indicates that rapid grain growth in the β phase field offset the possible refinement due to the formation of new grains during phase transformation.Therefore, it is essential to employ thermomechanical processing for structural refinement.

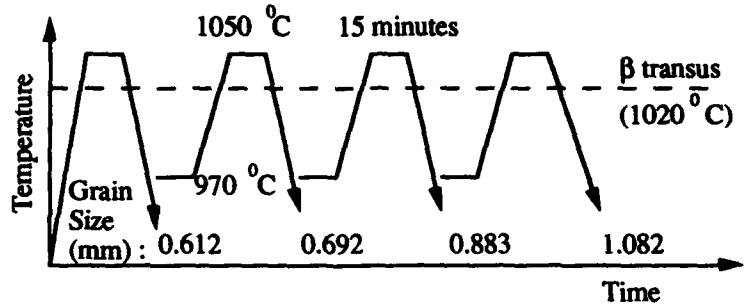


Fig.2. Schematic of the thermo-cycling procedure around the β transus, and its effect on prior β grain size.

To refine the final β grain size, it is necessary to introduce sufficient dynamic recrystallization during processing to refine the microstructure. It is equally important to maintain a considerable number of highly strained sites after deformation, for the nucleation of new grains via subsequent phase transformation. At a given strain,both processing temperature and strain rate are influential parameters.

Temperature effects may be noted from Figs.3 (a) to (c), and (e), where the specimens have been pressed at the temperatures corresponding to: (a) the β, (b) the (α+β), (c) the lower (α+β), and (e) the pseudo α phase fields. These samples were pressed at a given strain rate, 1×10^{-2} /s, to a given strain, 50%, except for that processed at 985 °C, where a higher strain rate, 5×10^{-1} /s, and a larger strain, 70%, were applied for later comparison (Table 1). The structure of the β forged sample is dominated by large elongated prior-β grains, which are actually in the form of 'pan-cakes' when one looks down the forging direction [8]. There are also some small equiaxed grains in the matrix, indicating the occurrence of dynamic recrystallization (static recrystallization is not responsible for grain refinement in such titanium alloys [2,8]). However, the amount of recrystallization is very limited, presumably due to a rapid dynamic recovery at the high temperature and the relatively slow strain rate. Dynamic recovery tends to 'homogenize' the dislocation substructure, and reduce the driving force for recrystallization. The transformed β consists of large colonized α platelets, similar to that shown in Fig.1(a).

The (α+β) processed structure at 985 °C shows sandwiched layers of primary α plates and transformed β grains, Fig.3(b); within each prior-β grain are colonized platelets. Due to the existence of a sufficient amount of soft β phases at this temperature, some of the primary α plates are not yet broken up (recrystallized) even at the relatively high strain, 70%, and strain rate, 5×10^{-1} /s. For the lower (α+β) pressed sample at 970 °C, Fig.3(c), the structure consists of lath-like α grains, as a result of (dynamic) recrystallization. It is noted that the α plates at the higher

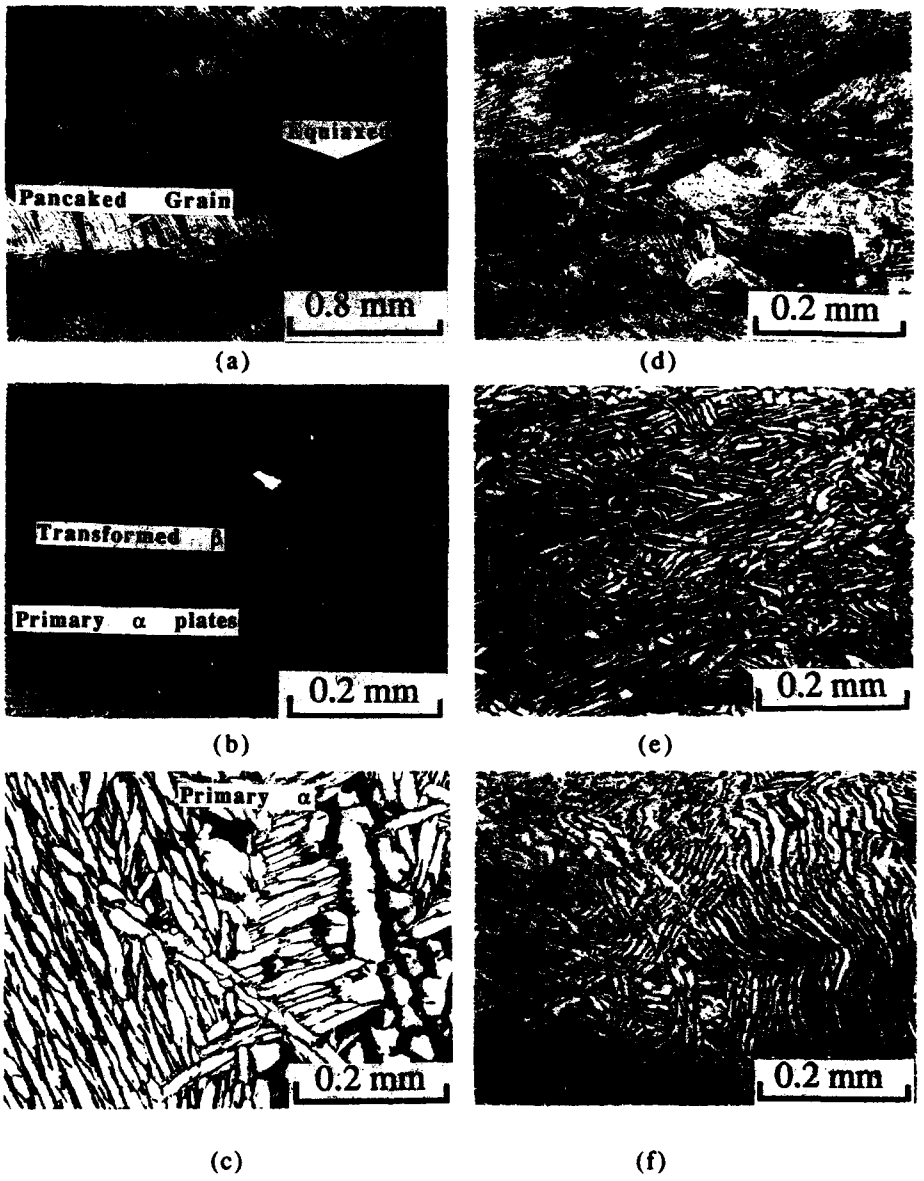


Fig.3 Microstructures after thermomechanical processing under the following conditions:
(Left) temperature (°C) / strain (%) / strain rate (1/s):
(a) 1050 / 50 / 1 x 10^{-2}; (b) 985 / 70 / 5 x 10^{-2}; (c) 970 / 50 / 1 x 10^{-2} ;
(Right) temperature, 890 °C, strain, 50%, and strain rate (1/s):
(d) 4 x 10^{-2}; (e) 1 x 10^{-2}; (f) 1 x 10^{-3}

temperature are much thinner than the laths of the recrystallized grains at the lower temperature. This is because the strain is higher in the former case.

At a given temperature, the effect of strain rate on microstructure is illustrated in Figs.3 (d) to (f), for the pseudo α processed samples. The α plates are thinner at a higher strain rate. Moreover, there were clear distortions in the α plates, which are severe at a higher strain rate. The distorted regions correspond to the areas of extensive local shear during processing.



(a) (b)

Fig. 4. Typical microstructures after β solution treatment of a processed sample: (a) equiaxed prior-β grains, and (b) the basketweave structure within a grain.

Table 1. Thermomechanical Processing Conditions with the Corresponding Grain Size after β Solution Treatment

Temperature (°C)	Strain (%)	Strain Rate (1 / sec.)	Grain Size (mm)
1050	50	0.01	0.953
985	70	0.50	0.304
970	50	0.01	0.452
890	50	0.04	0.406
890	50	0.01	0.529
890	50	0.001	0.622

Grain size and Microstructure after β Heat Treatment

All the forged structures were inhomogeneous and/or suffered from undesirable morphologies. Heat-treatment was conducted in the β phase field to homogenize the structure. After the heat-treatment, all the processed structures transformed into relatively uniform and equiaxed β grains, as seen in Fig.4 (a). The grain size of the heat-treated samples is given in Table I, along with the corresponding processing conditions.

It is clear from Table I that the (α+β) processing gives a relatively fine prior-β grain size, 0.452 mm, at a given strain rate (1×10^{-2} 1/s) and strain (50%). A higher strain rate and strain at 985 °C results in an even smaller grain size, 0.304 mm. At the processing temperature of 890 °C, a finer grain size resulted from a higher strain rate, at least, in the strain rate range investigated (1×10^{-3} to 5×10^{-1} /s).

The degree of the refinement of the prior-β grains is believed to be the result of the total contribution from the following factors : i) the morphology and size of the processed grain structure, i.e. the number of high angle boundaries; ii) the number of dispersed β phases remaining in the processed structure; and iii) the degree of stored strain energy prior to β solution treatment. The greater the number of high-angle boundaries, the slower the grain growth will be during β solution treatment. The β phases and/or high energy sites remaining in the processed structure are desirable for the nucleation of β grains on heating to the β field. At the strain rate of 1×10^{-2} 1/s, the (α+β) processing has led to a finer grain structure with a greater stored strain energy than the β processing. Moreover, the (α+β) processed structure should possess a greater number of β nuclei than the pseudo-α processed sample. Therefore, the prior-β grain size after β solution treatment is the finest for the (α+β) processed sample. An even smaller β grain size, obtained from the (α+β) processing at 985 °C, may be attributed to the relatively thin primary α grains and possibly a great strain energy stored in the processed structure, as a result of the higher strain rate and strain. At the temperature of 890 °C, the higher the strain rate, the finer the processed structure, the more the strain energy, thus, the smaller the β treated grain size.

A true basketweave type of microstructure was generated in all the processed samples cooled down at the rate of 3 to 6 °C/s, as shown in Fig.4 (a). There are very fine α colonies intersecting each other within a prior β grain. The fine α colonies can be more clearly seen in Fig.4 (b) at a higher magnification.

The actual mechanism of forming the basketweave structure in the alloy is not well understood. It is presently found that the essential step to achieve the microstructure for the alloy under investigation, is to maintain the cooling rate of the processed sample in the range of 3-6 °C/s during the first few minutes of cooling.

TEM Analyses of the Modified Microstructures

Fig.5 illustrates the substructures of: (a) an α forged sample at 890 °C; (b) a β forged sample at 1050 °C, and (c) an example from the forged and β heat-treated sample. The α as-forged structure shows subgrains delineated by sub-boundary dislocation networks within an α plate, typical of a recovered structure. The β forged sample reveals large colonies of the α platelets, due to slow air-cooling at a rate around 0.3 - 1 °C/s. The 'star' shaped morphology in Fig. 5(c) is a good example of the basketweave nature of the heat-treated sample. Each 'arm' of the star is a colony of parallel α platelets. It is interesting to note that the α colony has not been formed in some of the areas delineated by the intersecting colonies, as indicated in areas A, B, and C, in Fig.5(c). These un-colonized areas consist of equiaxed α subgrains, surrounded by transformed β phase [9].

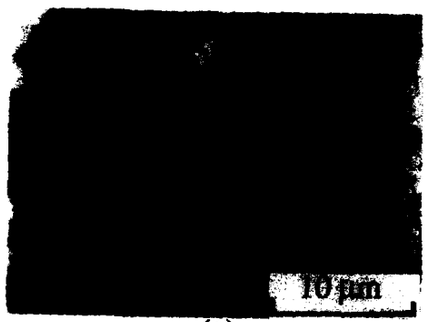
This microstructure appears like a micro 'composite' of the fine α-colonies and the equiaxed (α+transformed β) regions of a few micron size. It may be conjectured that the structure combines the advantages of lamellar structure(good creep, toughness, crack propagation resistance), and equiaxed structure (good strength, ductility) to give an overall improvement of the mechanical properties of the material.

There existed an interplatelet β layer in the large colonized Widmanstatten structure, as reported previously [8]. For the basketweave structure, this interplatelet β phase was also found, as noted in Fig.6, where the centred dark field image, Fig6(b), was from a diffracted beam of the (112) type under near-two beam conditions. The β layer is believed to be beneficial for crack-blunting or branching at the boundaries [3,4].

Summary

The experimental results have demonstrated that grain refinement for IMI685 cannot be achieved through a phase transformation route, and thermomechanical processing has to be involved.

Both temperature and strain rate have been shown to influence the processed microstructure. The β processing leads to a mixture of large 'pancaked' and recrystallized small grains. The (α+β) processing gives rise to fine sandwiched primary α plates and transformed β regions. In the lower (α+β) case, a largely recrystallized structure with lath-like α grains is observed. At an even lower temperature, the pseudo-α pressed sample is characterized by heavily distorted bands of elongated α grains. In the latter case, the distortion is heavier at a greater strain rate.



(a)



(b)



(c)

Fig.5. Substructures revealed by TEM under the following conditions:
(a) pseudo-α processed at 890 °C;
(b) β-processed at 1050 °C, cooling rate, 0.3-1 °C/s;
(c) processed and β-treated, cooling rate, 3-6 °C/s.



(a)



(b)

Fig.6. Interplatelet boundary β phase in the basketweave microstructure:
(a) bright field image;
(b) centred dark field image.

After β solution treatment, the processing in the (α+β) field, particularly the lower (α+β) phase field, appears to be the most effective route for grain re At the pseudo-α temperature, 890 °C, the β treated grain was finer, after processing a rain rate.

Basketweave microstructures were obtained in the present invest r heat-treatment in the β field with a cooling rate of 3 to 6 °C/s, which consists of inter colonies and small regions of equiaxed α and β phases. This composite morphology may combine the advantages of both the laminar and equiaxed microstructures to give an overall property improvement.

Acknowledgements

Financial support from SERC and MoD (Grant No. GR/E/20974) is gratefully acknowledged.

References

1. P.A. Blenkinsop, D.F. Neal, IMI685", Titanium and Titanium Alloys, Scientific and Technological Aspects, ed. J.C. Williams and A.F. Belov (New York, NY: Plenum, 1982), 2003-2027.
2. A. Vassel et al., "Influence of Processing and Heat Treatment Variables on the Mechanical Properties of Two Advanced High Temperature Titanium Alloys", Titanium Science and Technology, ed. H. Kimura and O.Izumi (Warrendale, PA: The Metallurgical Society, 1980), 515-521.
3. D. Eylon and J. Hall, "Fatigue Behaviour of β Processed Titanium Alloy IMI685", Metallurgical Transactions A, 8A(6) (1977), 981-989.
4. H.M. Flower, "Microstructural Development in Relation to Hot Working of Titanium Alloys", Mat. Sci. Technol., 6(1990), 1082-1092).
5. J.C. Williams, and G. Luetjering, "The Effect of Slip Length and Slip Character on the Properties of Titanium Alloys", Ref.2, 671-681.
6. A.T.K. Assadi, H.M. Flower, and D.R.F.West,"Microstructure and Strength of Alloys of the Ti-Al-Zr-Mo-Si System", Metals Technol., January (1979), 8-15.
7. Z.F. Zhang and C.S. Yang, "On the Basketweave Microstructures in Ti-6Al-2.5Mo-1.5Cr-0.5Fe-0.3Si Alloy", 6th Int. Conf. on Titanium Science and Technology,ed. P. Lacombe, R.Tricot, and G. Beranger (Greenoble: Les Editions de Physiqu, 1989), 1445-1450.
8. Z.X. Guo and T.N. Baker, "On the Microstructure and Thermomechanical Processing of an Titanium Alloy IMI685", Mater. Sci. Eng. , A156(1992), 63-76.
9. T.N. Baker and Z.X. Guo, "Strain Rate Controlled Deformation of Aerospace Alloys", A Final Report to SERC, Grant No. GR/E/20974.

THERMOMECHANICAL TREATMENT OF VARIOUS BETA PROCESSED TITANIUM ALLOYS

JF UGINET - FORTECH PAMIERS

ABSTRACT

BETA processing has been applied to various Titanium Alloys : Ti 6242 - Ti 17 - Ti 10-2-3. Influence of strain level has been studied (ε = 0.2/0.7) with the challenge of finding a good combination of strength ductility, creep properties, and toughness.

For this comparison a solution heat treatment in the Alpha domain was used. The geometry of the grain boundaries and the morphology of the alpha phase has a deep effect on the ductility and toughness particularly in the case of Ti 6242 and Ti 6246 Alloys. A higher deformation level, here ε = 0.7, promotes dynamic recrystallization at the grain boundaries of Ti 6246, and prevents the formation of a linear alpha film for other alloys.

A quite large processing window can be used with these alloys, using intermediate deformation levels ($\varepsilon \simeq$ 0.7), where they have shown excellent properties in their own range of utilization.

INTRODUCTION

Titanium Alloys are often processed in the Alpha Beta range to get an equiaxed microstructure. However when increasing the content of Beta Stabilizer elements, the Beta domain of temperature where these alloys can be processed is increased and interesting combinations of mechanical properties can be developped.

Beta Processing generates an acicular or platelet microstructure which improves the fracture toughness and creep properties. In an opposite way it is generally associated with a lower elongation during a tensile test.

In this work, we have applied the Beta Processing to various Titanium Alloys : Ti 10-2-3 - Ti 6242S - Ti 6246 - Ti 17. The influence of the strain level after deformation has been illustrated, looking after a compromise between strength, ductility, toughness creep properties.

Titanium '92
Science and Technology
Edited by F.H. Froes and I. Caplan
The Minerals, Metals & Materials Society, 1993

EXPERIMENTAL PROCEDURE

Chemical Composition

The chemical composition of each alloy used in these tests is given in Table 1.

Table 1 **Chemical Composition**

Alloys	Al %	Mo %	Zr %	Fe	V %	Sn	N	O	C	Si	Cr
Ti 10-2-3	3.16	-	-	1.85	10.03	-	.007	0.010	.02	-	-
Ti 6242	6.05	2.05	3.80	-	-	1.91	.005	.1400	.01	0.110	-
Ti 6246	5.90	6.30	3.95	0.02	-	1.95	.0025	.1050	.01	-	-
Ti 17	4.86	4.00	2.00	.080		1.95	.0155	.1080	.006	-	4.0

The material has been machined out of bars processed in the Alpha + Beta range for each alloy.
Table 2 gives the dimensions of each initial billet and its final dimensions after the upsetting in the Beta range. For each alloy the preheating temperature was selected at Beta Transus + 15°C except Ti 10-2-3 where BETA + 30°C was used. The average strain rate during the upsetting was chosen at 10-2 S-1.
Glass based lubricants were used during the deformation with a prior coating of the billet. The same temperature of preheating at 920°C was used for the Die, for all the Alloys except the Ti 10-2-3 where isothermal conditions were used at 850°C. Water quenching after forging was used for Ti 6242 and Ti 6246, while air cooling was used for Ti 17 and Ti 10-2-3.

Table 2 **Forging Conditions**

Alloy	Initial Dimensions of the Billet (mm)		Preheating Temperature °C (°F)	Final Dimensions after Upsetting (mm)		Average Deformation Ratio
	Diameter	Height		Diameter	Height	
Ti 6242	85	70	1030 (1886)	120	35	0.7
	110	43	1030 (1886)	120	35	0.2
Ti 6246	85	70	975 (1787)	120	35	0.7
	110	43	975 (1787)	120	35	0.2
Ti 17	68	70	920 (1688)	96	35	0.7
	87	43	920 (1688)	96	35	0.2
Ti 10-2-3	80	90	850 (1562)	113	45	0.7
	80	90	850 (1562)	87	75	0.2

After forging, the different pancakes were heat treated following Table 3 in the Alpha + Beta Range.

Table 3 **Heat Treament Conditions**

ALLOY	SOLUTIONNING	AGEING
Ti 6242	985°C (1805°F) - 1 Hr - Air Cooling	595°C (1100°F) - 8 Hrs - Air Cooling
Ti 6246	910°C (1670°F) - 1Hr - Air Cooling	595°C (1100°F) - 8 Hrs - Air Cooling
Ti 17	800°C (1472°F) - 4 Hrs - Air Cooling	615°C (1140°F) - 8 Hrs - Air Cooling
Ti 10-2-3	780°C (1436°F) - 1 Hr - Water Quenching	540°C (1000°F) - 8 Hrs - Air Cooling

Samples for Mechanical Testing and Microstructural Examination have then been machined out of the pancake. The location of these specimens are representative of the average deformation level (RIM location 1/2 thickness).

RESULTS - DISCUSSION

Microstructure

Figures 1 to 4 shows the evolution of the Beta transformed microstructure when varying the amount of strain during the forging sequence.

For Ti 6242 a typical platelet like microstructure with an average thickness of 2 to 3 μm. The length is governed by the initial Beta grain size, and we can notice that it is reduced in the higher deformation level ε= .7 due to the smaller width of the elongated Beta grains.
For the higher deformation rate grain boundary Alpha phase has been sheared into nodulus probably during the last stage of the deformation when the lower temperature of the die (920°C) should have significantly decreased the pancake temperature, thus beginning to precipitate Alpha Phase at the grain boundaries during the deformation.

Ti 6246 Alloy shows an acicular microstructure with grain boundary Alpha layer. For the low deformation level Ex-Beta grains are slightly distorted and some dynamic recrystallization is noticeable on the grain boundaries. The grain boundary Alpha layer is quite continuous but unlinear, due to the serrated shape of the boundaries.
For higher strain level the recrystallization is more important at the grain boundaries and new subgrains of 10-50μm combined with the ex-Beta grains, made a mixed microstructure. Platelets about 1μm of thickness are associated in colonies which dimensions are related to the parent grain size, thus smaller for the higher deformation rate.

The Ti 17 Alloy microstructure is very similar to the microstructure of the Ti 6246, except that the size of the platelets is much smaller : about 0.2 to 0.8 μm of thickness and 5 to 10 μm in length. Looking at a higher magnification secondary alpha can be seen between the platelets. This phase has precipitated during the ageing at 615°C (1140°F) in the retained Beta phase which comes from the solution treatment at 800°C (1472°F).

A very similar evolution is also seen on the Ti 10-2-3 Alloy, where the acicular Alpha phase is again smaller than for the Ti 17 Alloy : about 0.2 to 0.6 μm of thickness and 2 to 6 μm in length.

MECHANICAL PROPERTIES

Tensile Properties

Table 4 gives the Tensile properties at Room Temperature and 400°C (750°F)

Table 4 **Tensile Properties**

		ROOM TEMPERATURE			400°C (750°F)		
		YS Mpa	UTS Mpa	El %	YS Mpa	UTS Mpa	El %
Ti 6242	0.2	907	1001	8.9	563	711	14.4
	0.7	955	1039	14.0	624	758	13.6
Ti 6246	0.2	1036	1117	7.5	734	854	13.2
	0.7	1027	1126	8.4	747	875	14.4
Ti 17	0.2	1176	1226	9.6	862	987	14.0
	0.7	1170	1211	10.9	731	939	11.6
Ti 10-2-3	0.2	1140	1201	5.7			
	0.7	1131	1219	7.8			

At Room Temperature Figure 5 sumarizes the variation of Yield Strength, ultimate Tensile Strength and elongation with the deformation ε. For the strength, it can be noticed an increase for Ti 6242 while other alloys are not sensitive to this variation. This difference could be related to the variation of microstructure noticed herebefore.

For elongation a general increase is induced by a higher deformation. This has to be related to the geometry of the grain boundaries and the morphology of their Alpha phase, especially in the case of Ti 6242 Alloy. In this Alloy the deformation of the Alpha phase at the grain boundaries for the high deformation level ε = 0.7 leads to a more equiaxed microstructure in this area increasing the elongation and the ultimate Tensile Strength.

At 400°C (750°F) Figure 6 shows an increase of strength for both Ti 6242 and Ti 6246 and a decrease for Ti 17. Variations of elongation are not very significant except for Ti 17 where the decrease is noticeable.

In partial conclusion it can be said that Ti 6242 is more sensitive than the other alloys to the level of deformation (here ε 0.2 to 0.7) and that a higher deformation level increases both strength and ductility on this alloy.

Creep Properties

Table 5 and Figure 7 shows the variation of creep for a standard test at 400 °C under 600 MPa of load. The elongation after 100 Hrs was measured for comparison of the alloys. Ti 10-2-3 was not tested as its main use is considered in structural applications only.

Table 5 **Creep Properties at 400°C (750°F)**

ε	Ti 6242	Ti 6246	Ti 17
0.2	0.08	0.072	0.315
0.7	0.076	0.096	0.288

No significant differences are noticed between the two levels of deformation. As expected Ti 17 shows a greater level of creep under this load condition than Ti 6242 and Ti 6246. For this low creep parameter (K = 26620) = (460 + T°F) (20 + Logt (Hr)) there is no great difference in the behaviour of Ti 6242 and Ti 6246, although Ti 6242 due to its chemical composition has a better creep resistance for the higher creep parameters ($K = 30 - 33 \times 10^{3}$).

Table 6 and Figure 8 shows the Fracture Toughness Results.

Table 6 **Fracture Toughness Properties**

	CT 15 - T.R - MPa m			
	Ti 6242	Ti 6246	Ti 17	Ti 10-2-3
ε = 0.2	77	68	74	73
ε = 0.7	84	77	73	71

It can be noticed that for a given level of deformation the general decrease of Fracture Toughness as a function of the Yield Strength is verified for Ti 6242 and Ti 6246. At low deformation, for Ti 6242 a fragile transgranular fracture occurs, while a more ductile fracture with dimples is associated with higher deformation, thus increasing the toughness by 10%.

For Ti 6246 an intergranular fracture occured for ε = 0.2, favoured by the linear aspect of the grain boundaries associated with the alpha phase in a quite continuous way. At the higher deformation level, transgranular rupture occurs with many deviations of the propagation plane, especially at the grain boundaries where the smaller grains induced by the dynamic recrystallization plays an important role, thus toughness is increased by 13%.

Ti 17 and Ti 10-2-3 show a non significant variation of toughness with the increase of deformation.

CONCLUSIONS

A Beta Processing has been applied to various Titanium Alloys. When increasing the upsetting ratio the following results can be shown :

- The grain boundaries are deeply affected by the deformation : dynamic recrystallization occurs in the Ti 6246, Alpha Phase becomes less continuous and can be sheared into an almost equiaxe structure in Ti 6242, geometry of the boundary change from a lincar shape to a serrated shape with a discontinous Alpha Phase for Ti 17 and Ti 10-2-3.

- Tensile Strength at Room Temperature is significantly increased by the deformation only in the case of Ti 6242 but the elongation is in all cases increased to good level of ductility.

- Creep Properties are unaffected by the deformation for the low time/temperature parameter used for the comparison. As expected lower creep resistance of Beta stabilized Ti 17 is found compared to Ti 6242 and Ti 6246.

- Fracture Toughness is sensitive to the deformation level for Ti 6242 and Ti 6246 with a transition from an intergranular to a transgranular partly ductile fracture when increasing the deformation level. In all tests, excellent level of toughness for this level of yield strength is obtained.

- The evidence of influence of the deformation level is more effective for the less Beta Stabilized Alloys Ti 6242 and Ti 6246 than with Ti 17 and Ti 10-2-3.

These tests have shown that it is possible to get a good compromise between Strength, Ductility and Toughness, using an intermediate level of deformation during a forging in the Beta Range.

REFERENCES

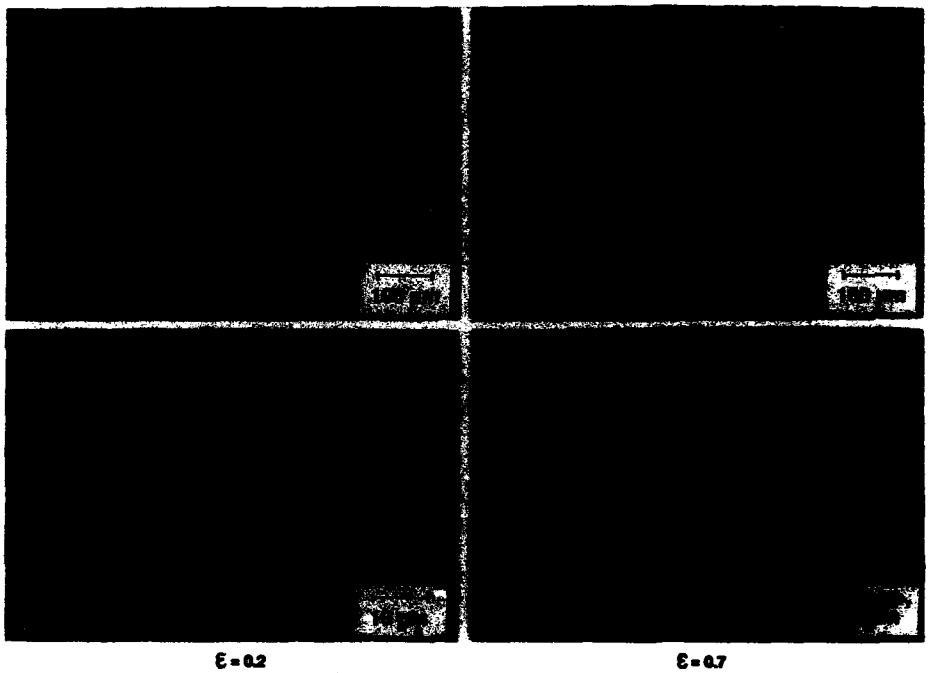
1 - SL. SEMIATIN - JF. THOMAS - P.DADRAS
"Processing-Microstructure Relationships for Ti 6242 Si"
Metallurgical Transactions Vol 14A - November 1983 - (2363 - 2374).

2 - T.K. REDDEN
"Processing and Properties of the Ti 17 Alloy for Aircraft Gas Turbine Applications"
Proceedings of Atlanta Symposium March 8, 1983,
Edited by BOYER - ROSENBERG - Pages239-254.

3 - F.H. FROES - CF YOLTON - JP.HIRTH - R.ONDERCIN - D.MORACZ
"The Processing Window for Grain Size Control in Metastable Beta Titanium Alloys"
Proceedings of Atlanta Symposium March 8, 1983,
Edited by BOYER-ROSENBERG - Pages161-182

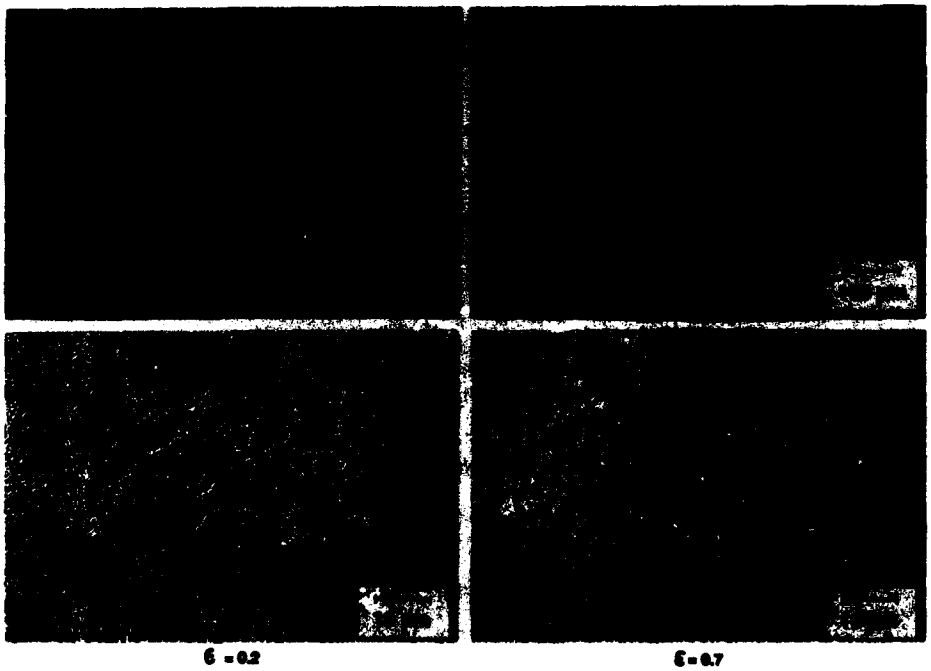
4 - J.BECHET - B.HOCHEID
"Decompositon of the Beta Phase in Titanium Alloy Ti 17"
Titanium Science and Technology,
Edited by R. JAFFEE - H.BURTE - Pages1613-1619.

5 - JF.UGINET
"Relationship between Thermo-Mechanical and Mechanical Properties for Ti 10-2-3"
Sixth World Conference Proceedings,
Edited by P.LACOMBE-R.TRICOT-G.BERANGER - Vol 3 - Pages1301-1306.



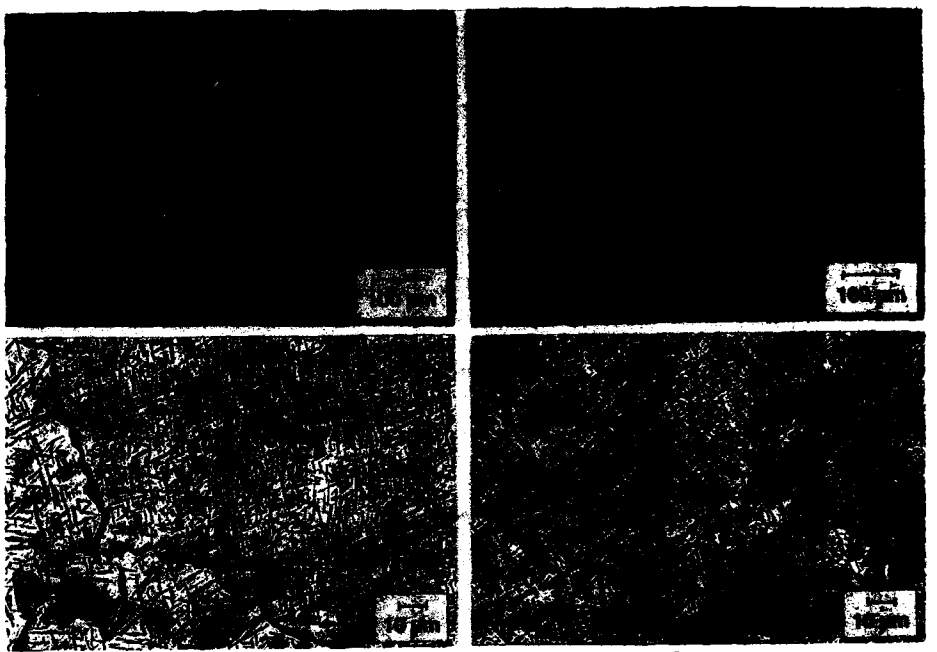
ε = 0.2 ε = 0.7

Fig.1 – Ti 6.2.4.2. – Microstructure



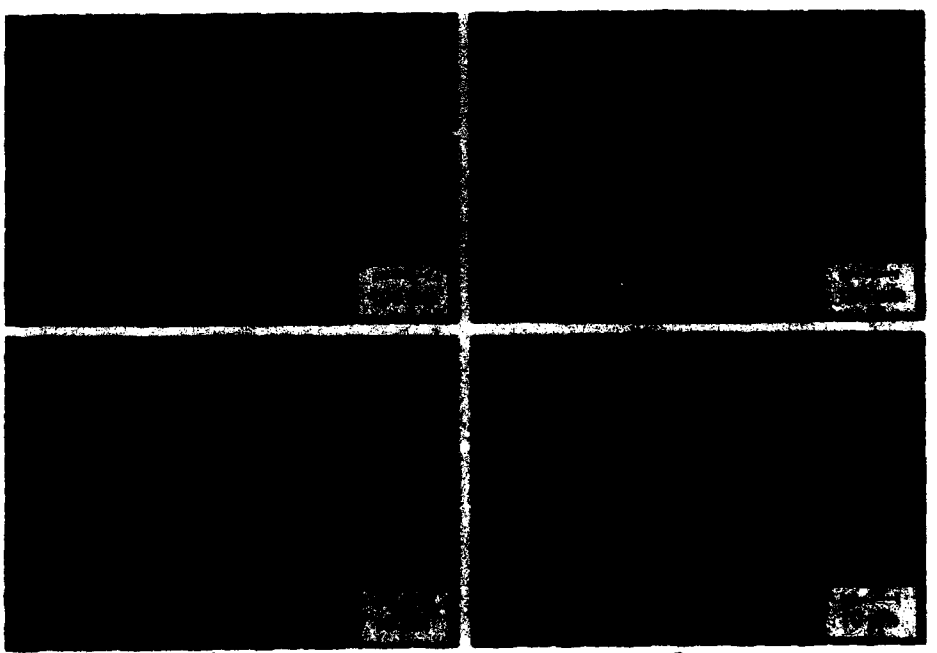
ε = 0.2 ε = 0.7

Fig.2 – Ti 6.2.4.6. – Microstructure



ε = 0.2 ε = 0.7

Fig.3 - Ti 17 - Microstructure



ε = 0.2 ε = 0.7

Fig.4 - Ti 10.2.3. - Microstructure

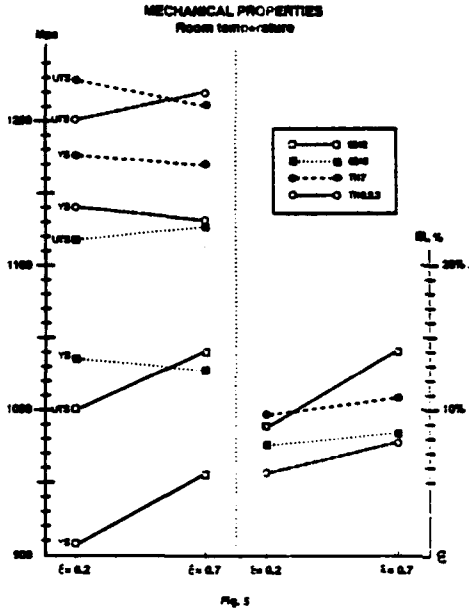


Fig. 5

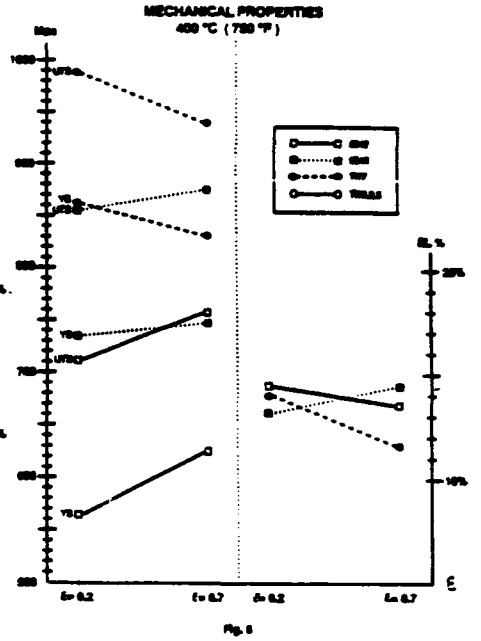


Fig. 6

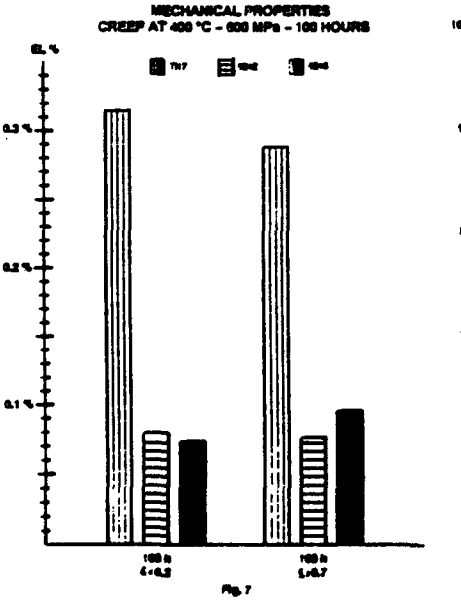


Fig. 7

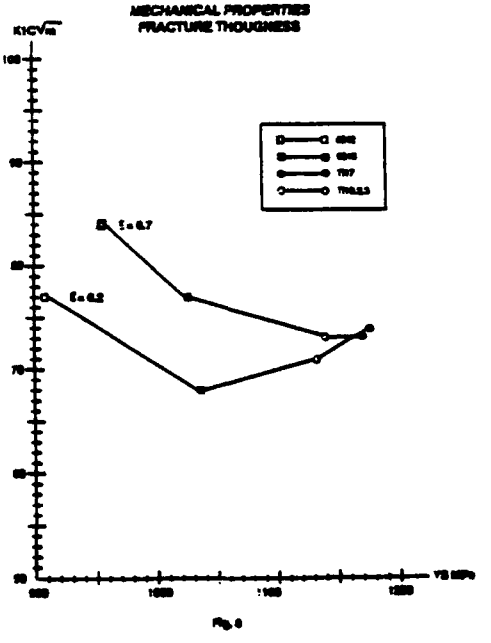


Fig. 8

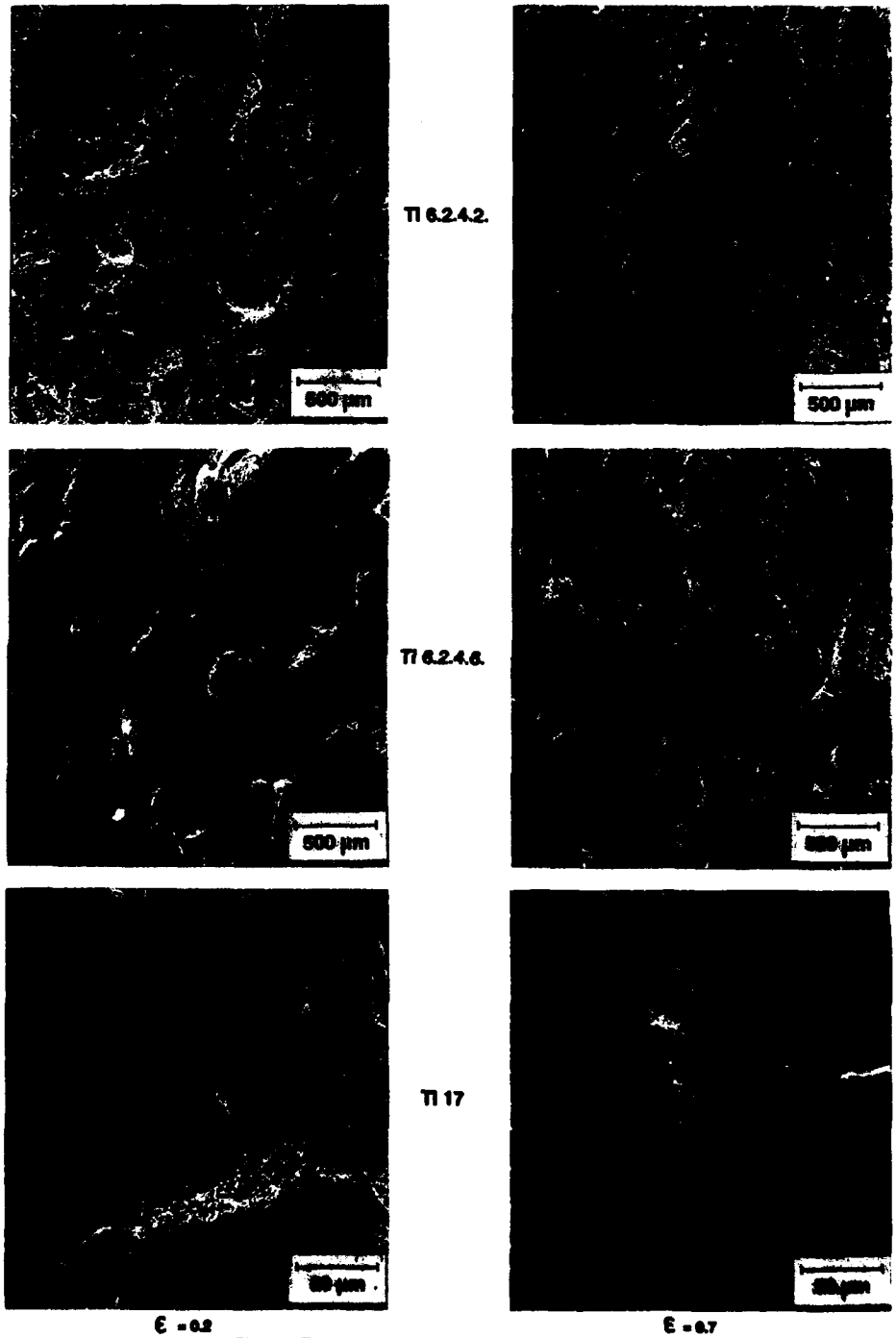


Fig. 9 – Fracture toughness S.E.M. examination

MICROSTRUCTURE AND TEXTURE CONTROL OF HEXAGONAL SHEET ALLOYS. ROLE OF ALLOYING ELEMENTS ON MECHANICAL PROPERTIES AND FORMABILITY

M.J. PHILIPPE (1), C. ESLING (1), M, SERGHAT (1), A. MOLINARI (2), G. CANOVA (2), A.W. BOWEN (3), H.S. UBHI (3), K. BARNES (3), J. DRIVER (4), N. CHENEAU (4), R. SCHWARZER (5), H.J. BUNGE (5) S. ZEFFERER (5), P. VAN HOUTTE (6), L. S. TOTH (6), J. GIL SEVILLANO (7), J. A. MEDINA-PERILLA (7).

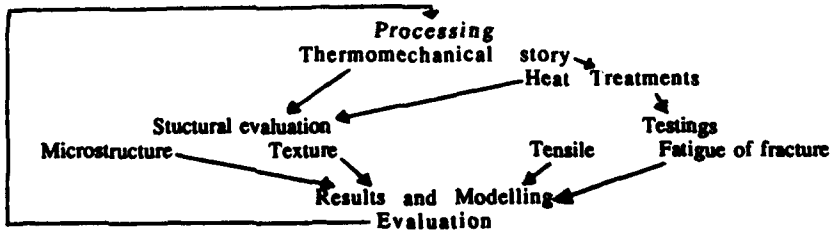
(1) LM2P Université de Metz F ; (2) LMPP Université de Metz F ; (3) Aerospace S Farnborough UK ; (5) TU Clausthal D; (6) KUL Heverlee B ; (7) CEIT San Sebastian E .

ABSTRACT

There is considerable evidence to show that variations in microstructure and texture result in considerable scatter in the mechanical properties and formability in currently-produced titanium alloys.
These alloys are not therefore used as efficiently as they could be and this cooperative research programme is aimed at rectifying this situation by addressing the following objectives : the identification of which aspects of microstructure and texture most critically affect properties and the proposing of ways to produce these materials so that controlled microstructure and textures, with much reduced scatter in properties. can be produced consistently and economically. Such information could be used in the protection of all existing and new titanium alloys.
The work is viewed as the first phase of a long-term programme. This initial phase concentrates on an in-depth characterization of the microstructures and textures of the α and the β phases of titanium, both individually and collectively, for a series of model alloys as a function of cold-rolling of small laboratory produced ingots to thin sheets, and their subsequent recrystallization. This microstructural characterization is accompanied by the development of models to predict accurately the observed deformation, fracture, and recrystallization behaviour. To increase the basic understanding of deformation in hexagonal metals, equivalent studies are also carried out on magnesium and zinc, used as model materials.
Subsequent phases of the work would employ hot rolling and cold rolling and the scale-up to larger ingots through cooperation with the Titanium industry.

INTRODUCTION

The study was carried out by using the industrial alloys T40, T60 and TA6V and model alloys α and β, and implemented according to the following study scheme.



Titanium '92
Science and Technology
Edited by F.H. Froes and I. Caplan
The Minerals, Metals & Materials Society, 1993

CHARACTERIZATION OF THE TEXTURES IN THE TA6V, T40 AND T60 TITANIUM ALLOYS.

TA6V :

The measured c/a ratio for this Titanium alloy c/a=1.5986 differs significantly from that of the pure Titanium : c/a =1.5870. This is due to the alloying elements in solid solution and affect the location of the reflection peaks in the texture measurement.
The non-recrystallized samples (thickness from 6 to 3 mm) display very sharp textures with texture indices ranging from 5 to 20. In many of the samples, the texture consists in mainly one component only : (12.0)<10.0>, i.e. the c-axis lying in the transverse direction ('C' component). In general, the existence of the <10.0> // RD fibre ranging from (12.0) to (12.5) (spread over 60°) is also evident. Depending on the deformation and heat treatment conditions, another component, the c axis rotated from ND to RD by about 25-35° can also be seen. This component, however, is significantly weaker than the C component. It strengthens substantially with the occurrence of recrystallization.
The effect of heat treatment after cold deformation (720°C-1 hour) was relevant only for the 1 mm thick sample, in which recrystallization took place. The texture in these samples can be characterized by the c axis spreading over a 30-50° region around the normal of the rolling plane. At the same time, the texture index drops to about 2 only.
The slip system activity for the C component has been evaluated by a rate sensitive crystal plasticity model. Prismatic, basal, <a> and <c+a> type pyramidal systems were assumed. Twinning has been excluded on the basis of literature data and on our own observations. It was found that only prismatic and <c+a> pyramidal systems operate for this orientation. High activity of the pyramidal systems was observed for deformations when the c-axis is near to the loading direction. The critical stress for the activation of <c+a> pyramidal slip is higher only by a factor about 1.2-1.5 than for prismatic slip. For the estimation of this ratio, results of tensile tests were taken into account and carried out in the RD and TD directions on samples containing very strong C component.

T40 AND T60:

The textures in these materials are very similar and are generally weaker than in TA6V; the texture indices range from 1.8 to 5.7. There is significant inhomogeneity in the texture inside the 6 mm thick hot rolled sample. The difference is strongly reduced in the thinner cold rolled or recrystallized samples.
In the cold rolled samples, the strongest component is the (12.4)<10.0> ('B' component, c-axis tilted from ND towards TD by 38.44°). In some samples, the peak intensity is shifted towards (12.2)<10.0> (c-axis 57.59 from ND). The <10.0> // RD fibre is present, with inhomogeneous distribution along the fibre. A second peak is usually located at the C component. In the ODFs, the low Φ angle regions are populated with grain orientations. In many samples, however, the (00.1)<21.0> orientation is absent.
Recrystallization after cold deformation can lead to strong alterations of the texture. Usually a strong new fibre appears, which is located at $\phi_1 = 0, \Phi = 40°, \phi_2 =$ arbitrary. This fibre includes the B component and passes near the F component (01.2)<21.0> at $\Phi = 42.5°$. By recrystallization, the C component generally vanishes. By comparing the textures before and after recrystallization, the 30° rotation around the c-axis, as proposed for the recrystallization mechanism in the literature, cannot be verified. A 23° or 37° rotation around the c-axis can be seen,

but with low probability. These angles correspond to high lattice site

coincidences. The main recrystallization mechanism, however, is still not known, and will be studied in the future.

RECRYSTALLIZATION OF COLD ROLLED T40 SHEETS

T40 sheets, cold rolled to reduction of 33% and 66%, have been recrystallized to determine the recrystallization kinetics and the local textures of the recrystallization nuclei.

The kinetics were determined by hardness tests after anneals in the temperature range 500 to 700°C. The sigmoidal curves $X(t) = 1 - \exp(-k^n t^n)$ were fitted to a classical JMAK model to give time exponents n of approximatively 1 for a reduction of 33% and of 0.3 to 0.7 for a reduction of 66%. Activation energies for recrystallization were determined as 230 kJ/mol (33%) and 210 kJ/mol (66%) respectively.

Texture evolution during recrystallization has been studied in detail by the EBSP method.

A T40 sample cold rolled 66% was annealed for different times at 620°C to examine the partially and completely recrystallized states. Complete recrystallization developed a texture close to that measured by X-ray pole figures (figs. 1-2). Partially recrystallized states (Fig. 3) indicate similar orientations for the recrystallization nuclei i.e. with a tendency for the c-axis to lie 30 to 40° from ND towards TD. Only slight changes in grain orientation occurred during recrystallization and grain growth.

The study of recrystallization texture development by microtexture techniques is beeing continued on binary Ti-Al alloys to stimulate the behaviour of the α phase in α/β Ti-6%Al-4%V commercial alloys.

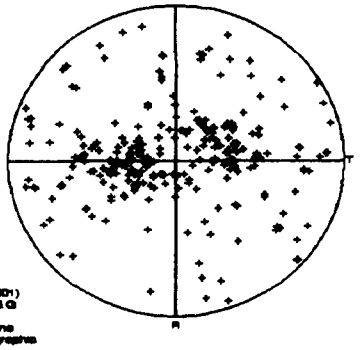


Fig.1: (0001) pole figure, determined by EBSP, of completely recristallized T40 sample

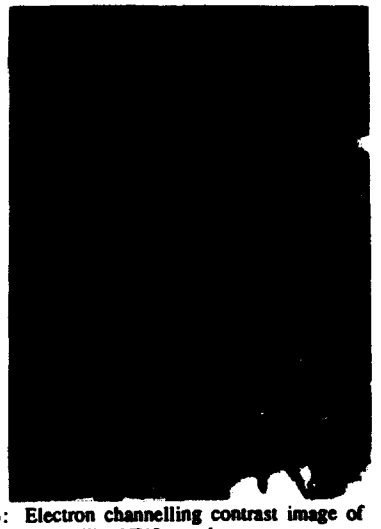


Fig.3: Electron channelling contrast image of partially recrystallized T40 sample

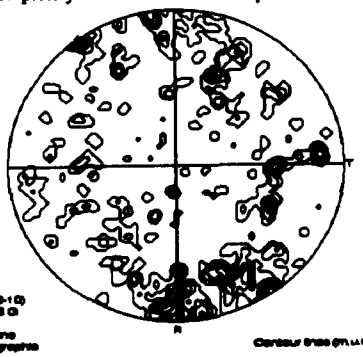


Fig.2: (1 0 $\bar{1}$ 0) pole figure, determined by EBSP, of same sample

GRAIN SPECIFIC TEXTURE AND MICROSTRUCTURE OF PARTIALLY RECRYSTALLIZED TITANIUM SHEET

The microstructure of TiAl6V4 sheet was investigated by transmission electron microscopy. Two types of structure were found : regions with a recrystallized and a deformed structure. They could be distinguished from each other by grain size and shape, by the dislocation density and local texture. The orientations of individual grains were measured by on-line interpretation of Kikuchi patterns with a TEM. The results are presented in inverse pole figures by number (Figure 4 and 5). The orientations of the deformed and recrystallized microstructure are shown separately. Though more deformed than recrystallized grains were measured, the volume fractions of each type of microstructure are about the same, due to the larger average size of the recrystallized grains.

The deformed microstructure shows a pronounced texture. The preferred crystal orientation is (hkil) <uvtw> = (11.0) <10.0 >. Grains seem to take this orientation the more precisely the higher they are deformed. The orientations in the most deformed structure fraction could not be measured, since no sharp Kikuchi patterns were obtained from these grains. The orientations of the recrystallized grains deviate considerably from those of the deformed grains. Their texture is much weaker and shows other preferred orientations (cf. Figures 4 and 5).

For, comparison the texture of the sheet was determined with an x-ray texture goniometer. For this purpose the (00.1), (11.0), (01.1) and (10.3) pole figures were measured. The inverse pole figures (Fig. 6) were calculated from ODF. The inverse x-ray pole figures agree well, with respect to the main preferred orientations, with the TEM pole figures of the deformed microstructure (Figure 5), whereas the preferred orientations of recrystallized grains (Figure 4) can be found outside the main peaks. Since the x-ray pole figure measurement integrates over a large volume fraction, it is not possible to discriminate between local components of microstructure, whereas the TEM pole figures indicate a pronounced difference in the texture of both types of microstructure.

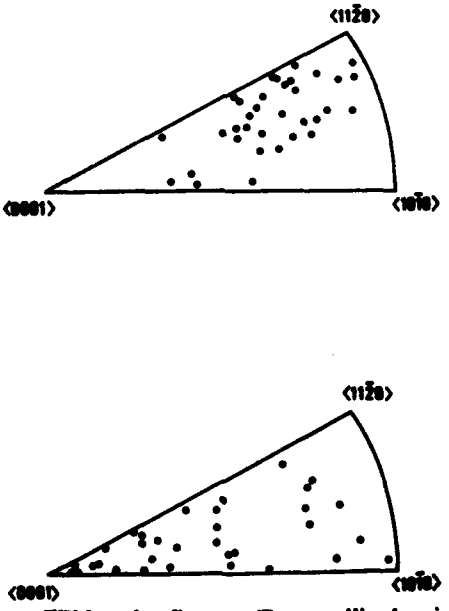


Fig.4: Inverse TEM pole figures (Recrystallised microstructure)

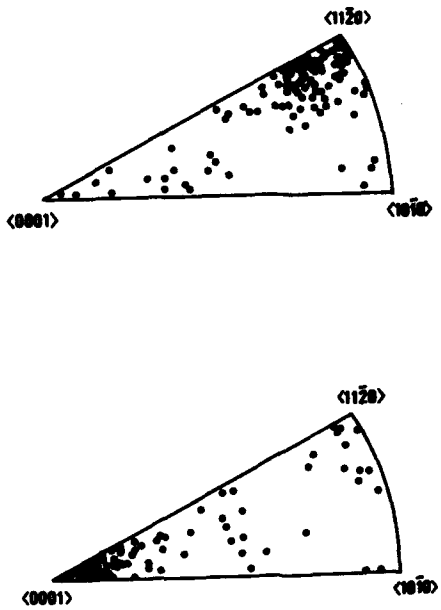


Fig.5: Inverse TEM pole figures (deformed microstructure)

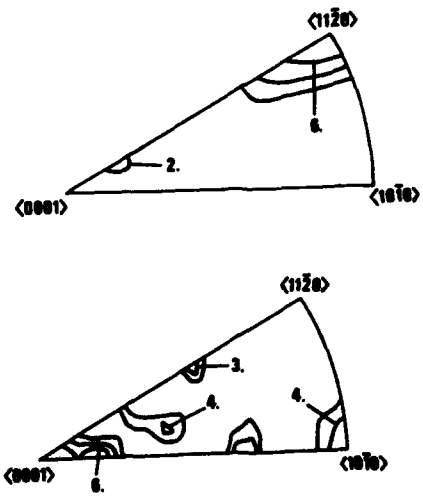


Fig.6: Inverse X-ray pole figures

TENSILE PROPERTIES

Tensile properties for all three alloys, shown in figure 7, indicate the following :
- strengths are alway less in the L than in the T direction, and increase in the order: T40, T60, TA6V (Fig. 7a) whereas;
- the marked modulus anisotropy for TA6V decreases strongly with the degree of reduction which is consistent with the changes in the (00.2) pole figures; whilst weaker anisotropy exhibited by T40 and T60 are not inconsistent with the changes induced in the (00.2) pole figures as a result of increased rolling reduction (Figs 7c & d).

Note that the maximum scatter in the quoted mean values (from three tests for each condition) is : strength 9MPa; modulus 8GPa; uniform elongation 2%; reduction in the area 4%.

SOME RESULTS OF CURRENT WORK WITH THE Ti-6%Al-4%V ALLOY:

Two thicknesses (3.8 and 3mm) of a mainly-α TA6V alloy displaying a texture with a strong T-type component are currently under study. An estimation of their plane-stress and plane-strain (RP) yield-locus is being obtained through a combination of tension, compression, and in-plane simple shear tests, complemented by measurements of the Knoop hardness anisotropy. Some relevant results are up to now:

- A very strong anisotropy of the fatigue crack propagation rate with a marked tendency of the cracks to deviate towards the plane normal to the transverse direction, as observed previously by other authors in sheets with less intense textures.
- An important anisotropy of static crack propagation resistance (tearing modulus) - when the behaviour of TD vs. RD cracks with crack front parallel to rolling plane normal is compared - besides the previously observed anisotropy of crack initiation toughness (J_{IC}).(Fig.8).
- A significant difference in the elastoplastic transient and in the plastic work hardening behaviour between RD and TD directions, that can be ascribed to the dominance of respectively <a> dislocation glide on prismatic planes and <a+c> dislocation glide on pyramidal planes.

CONCLUSION

This work shows clearly the relationships between crystallographic textures and mechanical properties. Moreover the analysis of the evolution of the texture during thermomechanical treatments highlights the important stages of this evolution.

The results should therefore allow the process to be modified so as to improve the sheets in view of a specific application.

ACKNOWLEDGEMENT

Financial support from the European Economic Community (BRITE EURAM contract BREU 0117-C) is gratefully acknowledged.

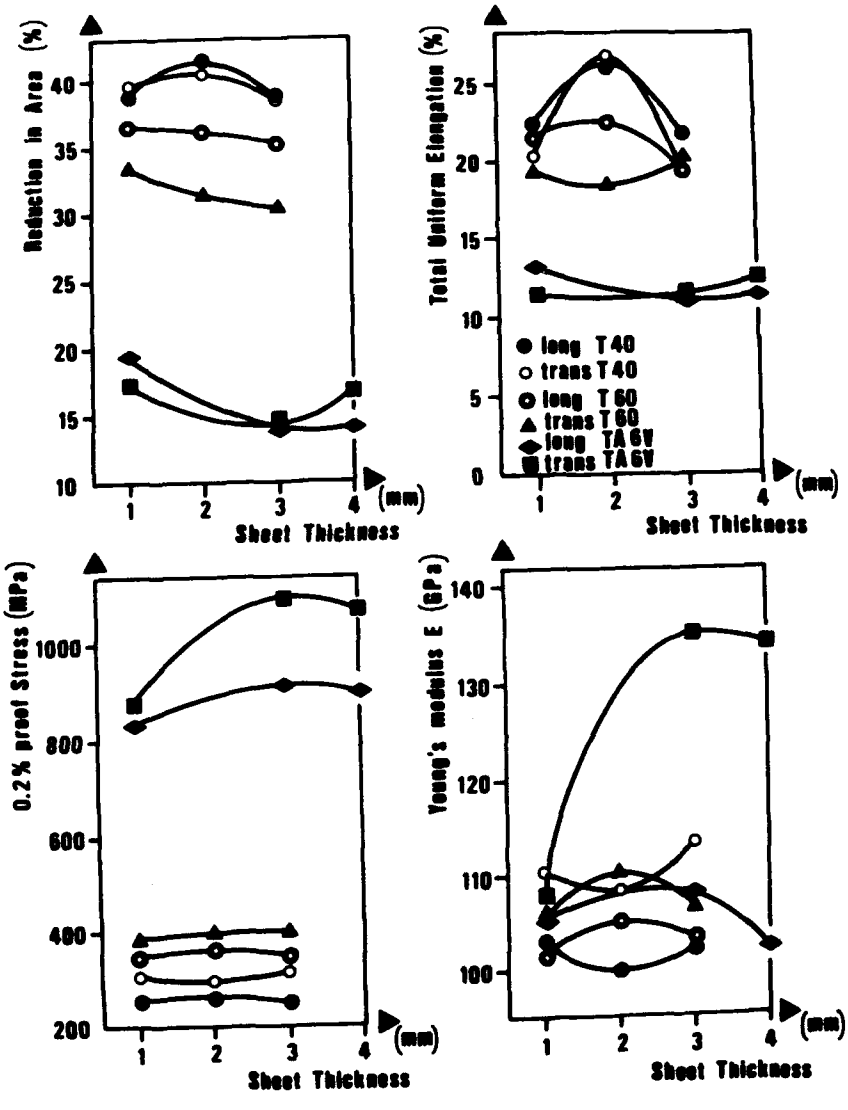
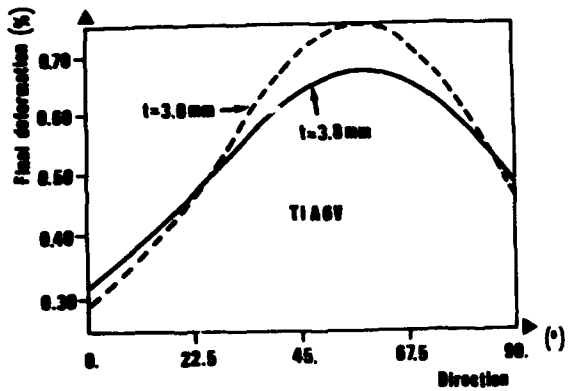
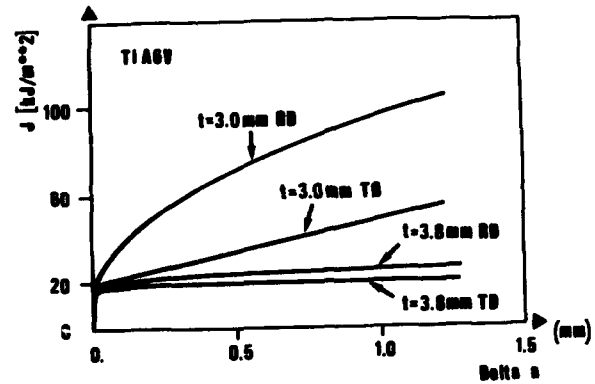


Fig.7: Tensile Properties

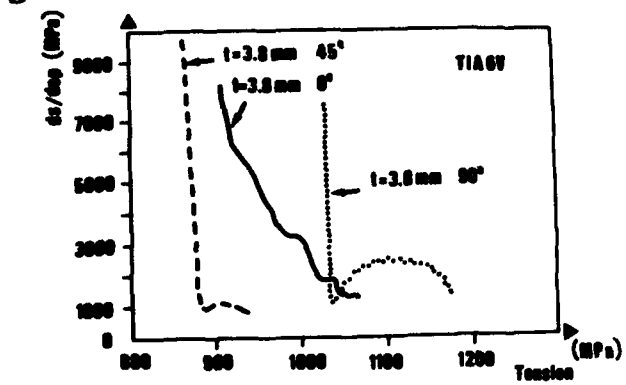


Tensile fracture strain vs angle from R.D.

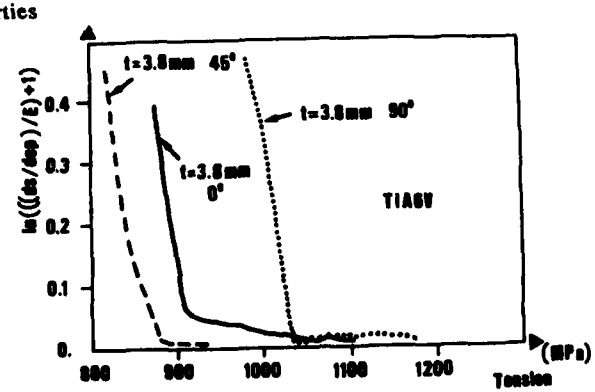


J-integral vs crack propagation

Fig.8: Mechanical properties



Work hardening rate (WHR) vs flow stress.



WHR normalized relative to Young modulus (E)
Linearized elastoplastic transient.

EFFECTS OF DEFORMATION TEMPERATURE ON AS-DEFORMED AND POST-AGING MICROSTRUCTURES, AND TENSILE PROPERTIES AFTER AGING IN Ti-15V-3Cr-3Sn-3Al

H. Ohyama, A. Takemura, and T. Nishimura

Iron and Steel Research Laboratories, Kobe Steel, Ltd.
Ikeda 2222-1, Onoe-cho, Kakogawa 675, Japan

Y. Ashida

Materials Research Laboratories, Kobe Steel, Ltd.
Takatsukadai, Nishi-ku, Kobe 651-22, Japan

Abstract

We have investigated the effects of deformation temperature on as-deformed and post-aging microstructures, and tensile properties after aging, in the range from room temperature to 873K, for Ti-15V-3Cr-3Sn-3Al.

Slight cold deformation tended to form planar slip bands of extremely localized straight dislocations. The planar slip bands consequently caused the directional microstructure of α precipitates to align on the bands after aging. The tendency for straight dislocations obstinately persisted even after a heavy cold deformation of about 60%. A directional distribution of rather coarse α precipitates was thereby caused after aging.

On the other hand, cross-slip is activated with increasing deformation temperature, to diminish the microstructural directionality. A fairly non-directional distribution of finer α precipitates was attained through deformation at 873K, and the balance of strength and ductility of Ti-15V-3Cr-3Sn-3Al was pronouncedly enhanced.

Titanium '92
Science and Technology
Edited by F.H. Froes and I. Caplan
The Minerals, Metals & Materials Society, 1993

Introduction

β titanium alloys potentially have cold-deformability and age-hardenability to outperform other types of titanium alloys in terms of cost and mechanical properties.[1,2] They are then expected to be applied to automobile parts such as valve springs.[3] However, sufficiently high strength cannot necessarily be obtained under solution-treated and aged conditions.

Unfortunately, cold working in moderate amounts does not alter the strength-ductility balance of most β titanium alloys.[4] Recently many efforts have thus been made to enhance the balance of strength and ductility by various thermo-mechanical treatments.[5-7] It is not clear why the process of cold working with aging is less favorable to the balance of strength and ductility than the other processes proposed in β titanium alloys.

Hence, we have investigated the effects of deformation temperature on as-deformed and post-aging microstructures, and studied the tensile properties after aging, in Ti-15V-3Cr-3Sn-3Al.

Experimental Procedure

Material

A 5.4mm thick hot strip of Ti-15V-3Cr-3Sn-3Al was used in this study. The ingot was forged in the β region and then hot rolled from a 120mm thickness at an initial temperature of 1273K by a production mill. A small plate was cut from the hot strip, and was machined to a 4.0mm thickness for removing the oxidized layer. The plate was solution-treated at 1273K for 1.8 ksec in argon, and quenched into water. The chemical composition is shown in Table 1.

Table 1. Chemical composition of the material used.

Elements (wt%)	V	Cr	Sn	Al	Fe	O	N	H	Ti
Top	15.19	3.11	3.03	3.08	0.169	0.107	0.0053	<0.0010	bal.
Middle	15.27	3.05	3.03	3.06	0.165	0.112	0.0055	<0.0010	bal.
Bottom	15.16	3.04	3.04	3.04	0.190	0.111	0.0059	<0.0010	bal.

Warm-rolling and Microstructural Observations

Small pieces of about 20mm^{w}x30mm^{l} cut from the plate were rolled in the temperature range from room temperature to 873K at reductions of about 5 to 10%, and about 60%.

As for slight deformation, apart from cold rolling, some pieces were rolled through one pass right after they were heated at specific temperatures for 60sec in salt baths, and directly quenched into water. Halves of those were over-aged at 873K for 259.2 ksec in order to clearly observe the correspondence between as-deformed and post-aging microstructures. (Fig. 1)

As for heavy deformation, some pieces were rolled through four to eleven passes in a specific direction by repeating the above-mentioned procedure of heating, rolling, and direct quenching. They were aged under two conditions, at 723K for 115.2 ksec and at 813K for 28.8 ksec, in order to examine the balance of strength and ductility after aging. (Fig. 2)

As-deformed and post-aging microstructures of the rolled samples were observed with a Nomarski microscope, a scanning electron microscope, and a transmission electron microscope. The section observed was parallel to the rolling direction and normal to the rolled plane, except for the transmission electron microscopy of the heavily deformed samples where the section observed was parallel to the rolled plane.

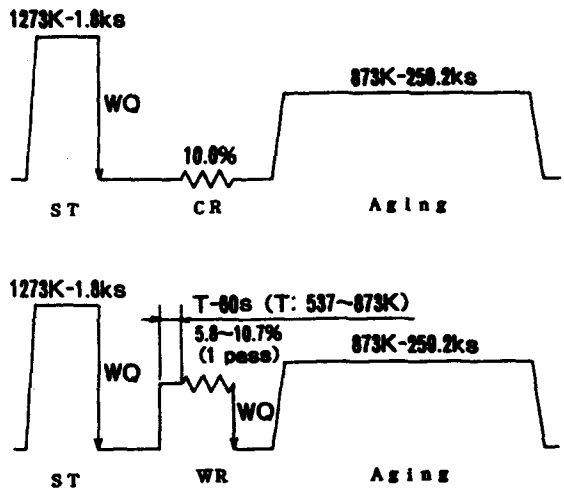


Fig. 1. Thermo-mechanical treatment patterns for slightly deformed specimens.

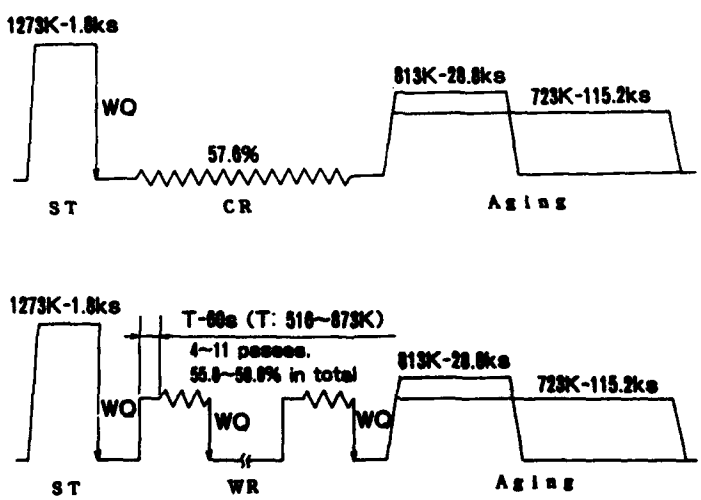


Fig. 2. Thermo-mechanical treatment patterns for heavily deformed specimens.

Tensile Tests

Tensile tests were carried out using plate type specimens of 2mm^{W}x20mm^{L}x1mm^{t} with a couple of strain gauges attached on their surfaces. The specimens were strained in the rolling direction at a cross-head speed of 0.1mm/min until 0.2% plastic strain, and at that of 1mm/min afterwards up to failure.

Results and Discussion

Microstructures of the Slightly Deformed Specimens

Figure 3 shows the optical microstructures after slight deformation at room temperature and 873K. The rolling direction is horizontal, in the same way as the other optical and scanning electron microscopic micrographs below. Striations are clearly observed in Fig.3(a) of the cold rolled sample. The striations,[8] which correspond to the slip bands of extremely localized dislocations, tend to be heavily introduced uni-directionally in a β grain. On the other hand, such striations almost disappear in Fig.3(b) of the sample rolled at 873K.

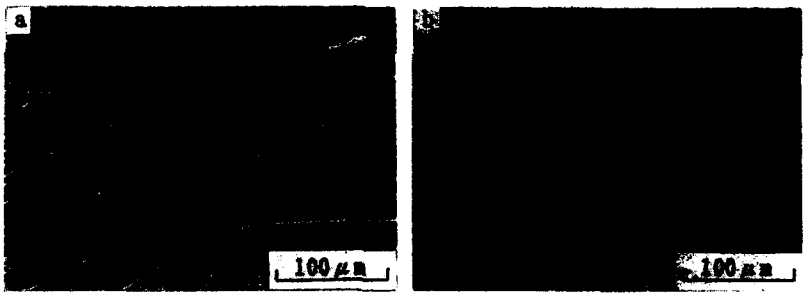


Fig. 3. Optical microstructures of the slightly deformed specimens.
(a) RT-10.0% rolled, (b) 873K-10.7% rolled.

Figure 4 shows the transmission electron microscopic microstructures of the two samples rolled at room temperature and at 873K. Dislocations introduced at room temperature shown in Fig.4(a) are fairly straight in the planar slip bands. On the other hand, dislocations introduced at 873K shown in Fig.4(b) are wavy and non-directional. Static recovery is not recognized in Fig.4(b). The microstructural difference between Figs. 3(a) and 3(b) may therefore be expected to be due to activated cross-slip to cause the reduction of localized dislocations.



Fig. 4. TEM microstructures of the sligthly deformed specimens.
(a) RT-10.0%, (b) 873K-10.7% rolled.

Figure 5 shows the microstructures of the samples shown in Fig.3 after aging at 873K for 259.2 ksec. The microstructural directionality caused by α precipitates aligned on the planar slip bands exists in the cold rolled sample, whereas a fairly non-directional microstructure of α precipitates is obtained in the 873K-rolled one. This difference clearly reflect the as-deformed microstructures shown in Fig.3.

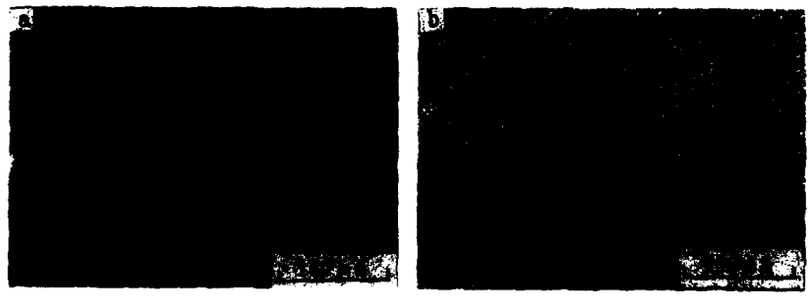


Fig. 5. Optical microstructures of slightly deformed and aged specimens.
(a) RT-10.0% rolled, (b)873K-10.7% rolled. Aged at 873K for 259.2 ksec.

Microstructures of the Heavily Deformed Specimens

Figure 6 shows the transmission electron microscopic microstructures after a heavy rolling of about 60% at room temperature and at 873K. In the sample rolled at room temperature, the tendency for straight dislocations obstinately persists and causes macroscopical directionality in spite of the sample being heavily rolled, even though there are wavy dislocations also introduced. On the other hand, there are little straight dislocations introduced in the sample rolled at 873K, where wavy dislocations are non-directionally introduced without observable static recovery.

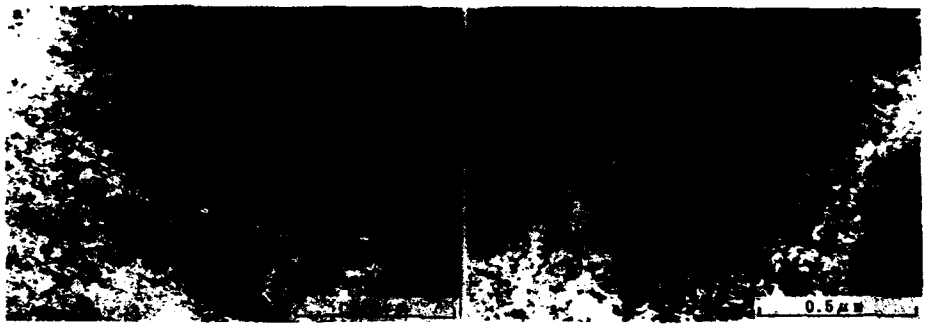


Fig. 6. TEM microstructures of the heavily deformed specimens.
(a) RT-57.6% rolled, (b) 873K-56.3% rolled.

This difference is clearly reflected by the post-aging microstructures, as understood in the scanning electron microscopic microstructures of the two samples after aging at 813K for 28.8 ksec shown in Fig.7. A microstructural directionality is macroscopically caused by α precipitates elongating in a given direction in Fig.7(a) of the cold rolled sample, whereas the directionality is pronouncedly restrained to assume a fairly uniform microstructure in Fig.7(b) of the sample rolled at 873K.

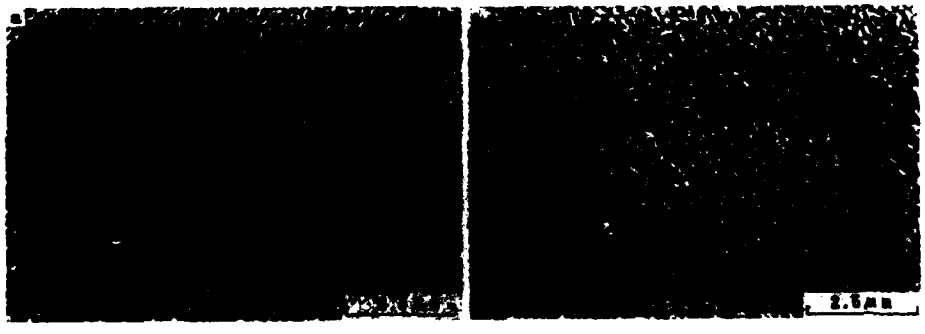


Fig. 7. SEM microstructures of the heavily deformed specimens after aging at 813K for 28.8 ksec. (a) RT-57.6% rolled, (b) 873K-56.3% rolled.

Figure 8 shows the transmission electron microscopic microstructures of the samples shown in Fig.7. The α precipitates observed in the cold rolled sample are rather coarse. On the other hand, those observed in the sample rolled at 873K are fine. This microstructural difference was not necessarily observed throughout, but these tendencies were quite often recognized, as more macroscopically supported by Fig.7.

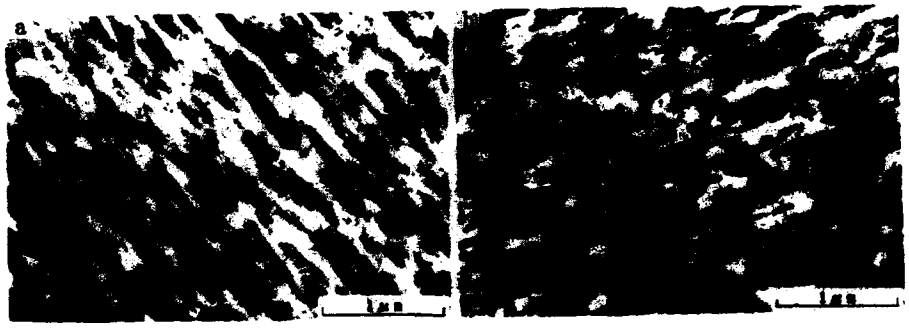


Fig. 8. TEM microstructures of the heavily deformed specimens after aging at 813K for 28.8 ksec. (a) RT-57.6% rolled, (b) 873K-56.3% rolled.

Tensile Properties after Aging

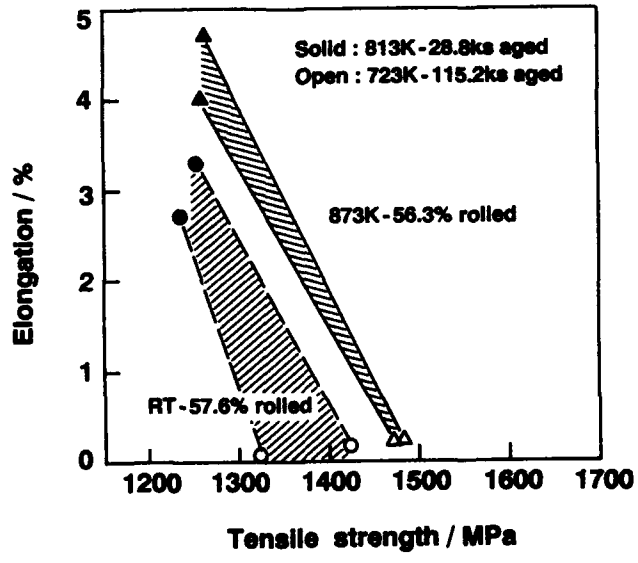


Fig. 9. Comparison of tensile properties between RT-rolled and 873K-rolled specimens.

Figure 9 shows a comparison of the balance of strength and ductility between the samples rolled at room temperature and at 873K. The balance of strength and ductility has been pronouncedly enhanced by rolling at 873K, compared to cold rolling. This is probably due to the more uniform distribution of finer α precipitates with less microstructural directionality, as was shown in Figs.7 and 8.

Conclusion

We have investigated the effects of deformation temperature on as-deformed and post-aging microstructures, and examined the tensile properties after aging, in Ti-15V-3Cr-3Sn-3Al. Slight cold deformation causes the planar slip bands of straight dislocations. The straightness of dislocations is obstinately sustained even after a heavy deformation of about 60%. The directional microstructure of rather coarse α precipitates is consequently obtained after aging.
On the other hand, cross-slip is activated at 873K to cause wavy dislocations, and a fairly uniform distribution of fine α precipitates is obtained. The balance of strength and ductility of Ti-15V-3Cr-3Sn-3Al is pronouncedly enhanced by the microstructural uniformity.

References

1) J.B.Guernsey, V.C.Petersen and E.J.Dulis: Met.Prog., (1969), 121.
2) Beta Titanium Alloys in the 1980's, ed. by R.R.Boyer and H.W.Rosenberg, TMS-AIME, Warrendale, Penn., (1984).
3) A.M.Sherman and S.R.Seagle: Beta Titanium Alloys in the 1980's, ed. by R.R.Boyer and H.W.Rosenberg, TMS-AIME, Warrendale, Penn., (1984), 281.
4) H.W.Rosenberg: Beta Titanium Alloys in the 1980's, ed. by R.R.Boyer and H.W.Rosenberg, TMS-AIME, Warrendale, Penn., (1984), 145.
5) C.Ouchi, H.Suenaga and Y.Kohsaka: Sixth World Conf.on Titanium, ed. by P.Lacombe, R.Tricot and G.Beranger, Les Editions de Physique, Paris, (1989), 819.
6) M.Okada: ISIJ Int., 31(1991), 834.
7) N.Niwa, A.Arai, H.Takatori and K.Ito: ISIJ Int., 31(1991), 856.
8) H. Ohyama, H. Nakamori, Y. Ashida and T. Maki: ISIJ InInt., 32(1992), 222.

THERMOMECHANICAL TREATMENT TO

DIMINISH β FLECKS IN Ti-6Al-6V-2Sn PLATE

H. G. Suzuki[1], S. Ishikawa[2], N. Noda[3], K. Kaku[3], Y. Kako[3], and N. Yamada[4]

[1]Steel Research Labs, NIPPON STEEL CORP.,
Shintomi, Futtsu 299-12, JAPAN
Presently at the University of Dayton, Graduate Materials Engineering,
300 College Park, Dayton, OH 45469-0240, USA,

[2]Advanced Research Labs. NIPPON STEEL CORP.,
1618 Ida, Kawasaki, JAPAN

[3]Yawata Works. NIPPON STEEL CORP.,
Yawata, Kitakyushu, JAPAN

[4]Head Office, NIPPON STEEL CORP.,
2-6-3 Otemachi, Chiyodaku, Tokyo, JAPAN

ABSTRACT

A thermomechanical treatment was developed to produce Ti-6Al-6V-2Sn(Ti-662) plate free of β flecks. After β and α+β forging to break up the VAR cast structure, slabs were homogenized at 1250°C for 48h in a commercially pure(CP)Ti box and followed by β cogging and α+β hot rolling. This process was termed Intercritical Heat Treatment(IHT). By this treatment, the contents of Fe and Cu became almost at the same level as the bulk composition and finely distributed α+β equiaxed structure with good mechanical properties was obtained. This process allows to reduce the amount of materials discarded as scrap for application requiring high grade alloy.

INTRODUCTION

Segregation can be reduced during vacuum arc remelt (VAR) of α+β titanium alloys by : (1) providing an intentional concentration gradient to the consumable electrode [1], and (2) controlling the melting to create a shallow pool in the final stage of VAR [2]. However, fairly large zones enriched with Fe and Cu may be found in large diameter ingots of Ti-6Al-6V-2Sn (Ti-662) mainly at the top. Both Fe and Cu are β stabilizers leading to enriched zones termed *β flecks*. For applications inquiring higher grade material, one third or one half of the ingot needs to be removed as scrap.

Several reports describe the effect of β flecks on the mechanical properties. Rüdinger and Fisher [3] have shown no adverse effect of β flecks on properties such as tensile, HCF, and LCF in the annealed condition. On the other hand, mechanical properties of Ti-10V-2Fe-3Al (a near-β alloy) are affected by the distribution of β flecks associated with Fe segregation [4].

This paper reports a new technique to reduce zones of Fe and Cu enrichments by thermomechanical treatment prior to hot forging and hot rolling.

Titanium '92
Science and Technology
Edited by F.H. Froes and I. Caplan
The Minerals, Metals & Materials Society, 1993

EXPERIMENTAL PROCEDURES

VAR double melted 750 mmϕ ingot of Ti-662 with the average chemical compositions shown in Table 1 was used in this study.

Table 1: Chemical compositions of the alloy used (wt %).

Al	V	Sn	Cu	Fe	O
5.4	5.5	2.0	0.63	0.73	0.18

The conventional manufacturing process is shown schematically in Fig. 1. After the ingot was forged in the β region to break down the cast structure, α+β processing was repeated to obtain an equi-axed fine α in a matrix of transformed β structure. The β transus of this heat was 930°C for a region free from β flecks.

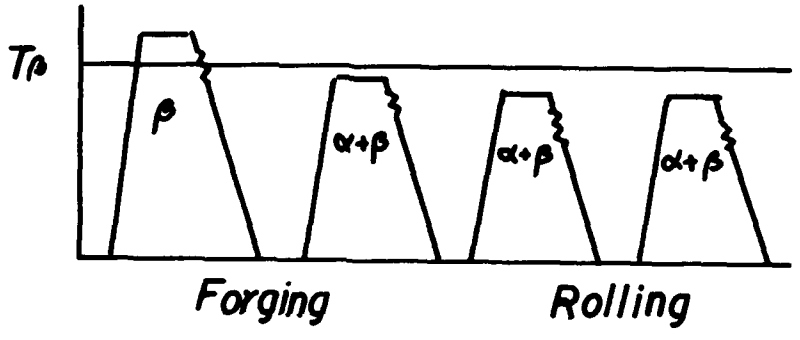


Fig. 1: Ordinary thermomechanical processing for Ti-662.

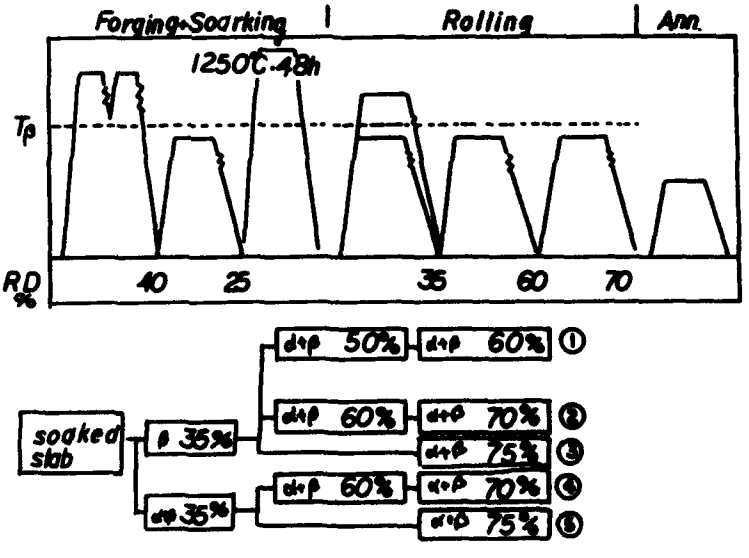


Fig. 2: Newly developed thermomechanical treatment for Ti-662 plate.

An alternative process is shown in Fig. 2. After the α+β forging, slabs were put into a high temperature soaking furnace and then hot rolled at the various conditions shown in Fig. 2.

Chemical analysis as well as EPMA were conducted to evaluate the distribution of each element. Microstructural observation was done by optical microscope and tensile properties were examined for various thermomechanical process conditions.

RESULTS AND DISCUSSION

SEGREGATIONS OF Fe AND Cu

The microstructure at the positions of top surface and mid-thickness in the α+β processed plate is shown in Fig.3. Equiaxed α+β microstructure was obtained in the slab surface region, while fine lamellar structure with small amount of equiaxed α phase was revealed in the mid-thickness position indicating the lowering of β transus due to the enrichment with β stabilizing elements. Quantitative analysis by EPMA showed segregation of both Fe and Cu to levels as high as 1.2 wt% in enriched zone of about 100μm in width (Fig. 4). This kind of β flecks is due to the segregation during solidification in the VAR process [2].



Fig. 3: Microstructure after plate rolling in the ordinary process showing β fleck band in the mid-thickness section.

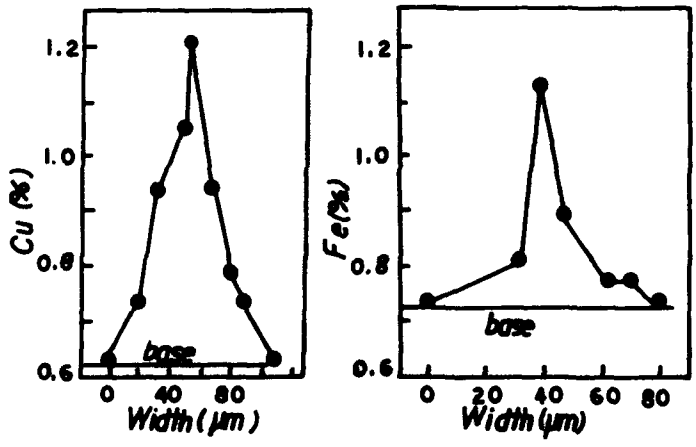


Fig. 4: The results of EPMA analysis of Fe and Cu in the β flecks.

A METHOD TO REDUCE β FLECKS

It is preferable to apply the normal diffusional process as a tool for the homogenization because high in the β region, solute atoms have high diffusivity due to the high temperature and to the b.c.c. β Ti structure.

Soaking conditions have been varied to some extent. Ingot soaking did not yield a good result. After several trials and simple calculation, it was found that soaking at a higher temperature after β and α+β forging was more effective to get a segregation-free sound slab. The slab was sealed in a commercially pure(CP)Ti box with a wall thickness greater than 10 mm to prevent oxidation followed by various thermomechanical process conditions described in Fig. 2.



Fig. 5: Microstructure of the slab after Intercritical Heat Treatment (IHT) at 1250°C for 48h.

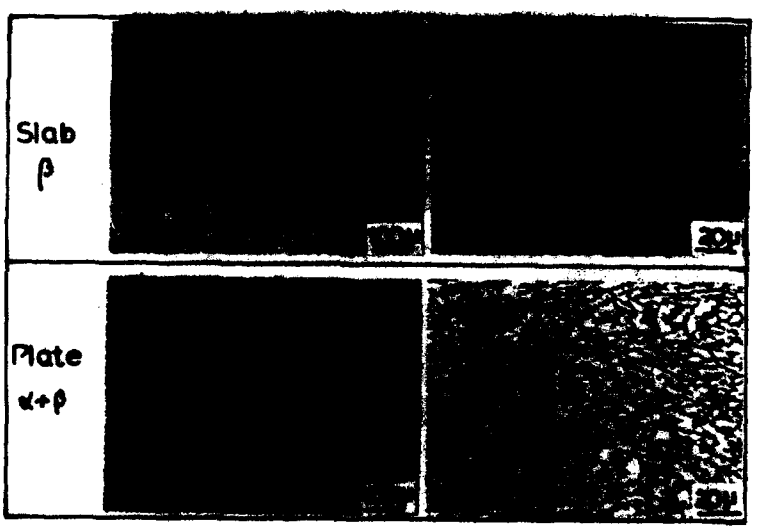


Fig 6: Microstructures of each stage of the plate rolling (β→ α+β→ α+β processing ① shown in Fig.2).

As expected, the process termed Intercritical Heat Treatment (IHT) performed at 1250°C for 48h, resulted in a substantial β grain growth to a size larger than 1mm in diameter as shown in Fig.5. It was therefore necessary to thermomechanically treat the slabs to refine the microstructure.

It is noted that typical coarse lamellar structure with grain boundary α is resulted. The process ① in Fig. 2 is the process in which after this treatment, the slab is subjected to the cogging by the

amount of 35% in the β region and double treated in the α+β region to 80% deformation. After annealing at 740°C, finely distributed equiaxed α+β microstructure was produced. The results of each process are shown in Fig.6, and the sequence of the change of microstructure only by the repeated α+β process is shown in Fig. 7. It is noted that grain boundary α, once formed by the IHT is difficult to eliminate even by the heavy reduction in the α+β region.

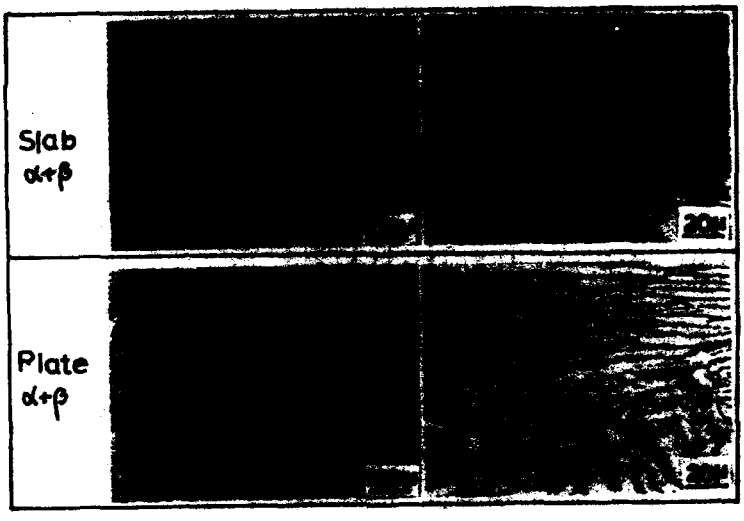


Fig. 7: Microstructures of each stage of the plate rolling (α+β→ α+β→ α+β processing ⊕), showing the existence of grain boundary α.

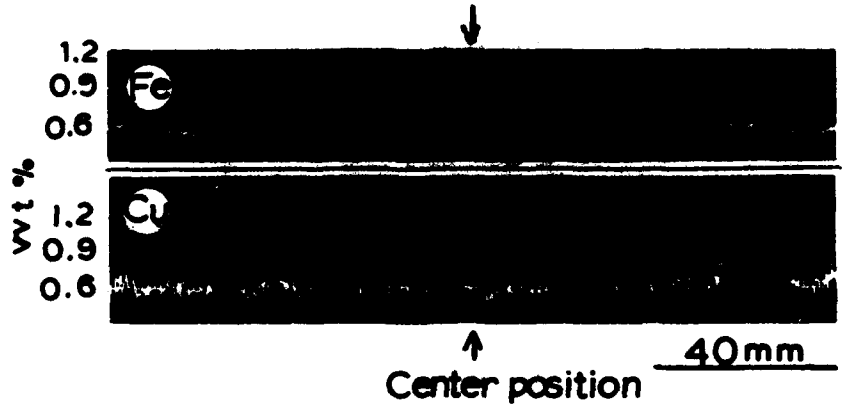


Fig. 8: EPMA result of the slab after IHT, showing no enrichment of Fe and Cu.

The results of EPMA analysis of the slab after IHT are shown in Fig. 8, in which the distribution of Fe and Cu is quite homogeneous and sharp segregation of these elements disappeared completely through the thickness direction. This result coincides with the microstructural homogeneity as already shown in Figs. 5 through Fig. 7. Referring the diffusivity of Fe in βTi of Peart and Tomlin [5], and applying the Fick's second law under the boundary condition of:

at t=0, x=(h), C=C₀

Then, the solution is:

$$C(x,t) = C_0/2 \left\{ \text{erf} \frac{h-x}{2\sqrt{Dt}} + \text{erf} \frac{h+x}{2\sqrt{Dt}} \right\}$$

here, h is half the width of the segregation, 5×10^{-3}cm in this result of Fig. 3. Remarking at x=0 and find the time and temperature to satisfy the condition that

$$C(0,t)/C_0 = \text{erf} \frac{h}{2\sqrt{Dt}} \leq 1/2$$

Diffusivity of Fe in βTi is $Do=9.2\times10^{-2}$ cm^2/s, $Q=165.7$ $kJ\cdot mol^{-1}$ [5]. Then, at 1150 °C $t \geq 5.9$ min, and at 1250 °C $t \geq 2.4$ min. Thus, IHT at 1250°C for 48h is sufficient to produce a sound slab.

TENSILE PROPERTIES OF TREATED PLATE

Room temperature tensile properties are shown in Fig. 9 for the various thermomechanical processing routes shown in Fig. 2. All tests were done after annealing at 740°C for 40 min. The plate thickness was 50 mm and the test coupons were taken from the mid-thickness section in the L-direction.

The best combination of strength and ductility was obtained after the process ②, ie. IHT + β cogging and two time of α+β rolling (Fig.2). The highest value of tensile strength was obtained by the processes ④ and ⑤, ie. IHT + two or three time α+β rolling, but directionality manifested significantly because of heavy reduction in one direction.

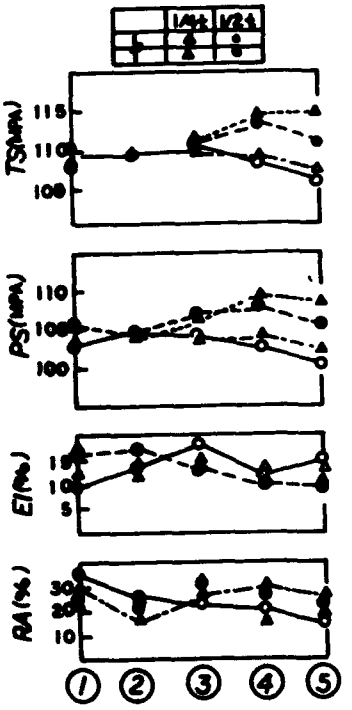


Fig. 9: Tensile properties of the 50 mm plate subjected to the various processing routes shown in Fig. 2

SUMMARY

1) The objective of this work was to develop a thermochemical process to diminish the Fe and Cu enriched zones typical to large diameter ingots of the α+β alloy, Ti-6Al-6V-2Sn (Ti-662).

2) The process developed is based on a 1250°C homogenization of slabs followed by β cogging and α+β hot rolling.

3) The process, which was termed Intercritical Heat Treatment (IHT) was successful in eliminating the β stabilized Fe and Cu rich zones.

4) It is now possible for this process to increase the yield of ingot materials used for rolling these alloy plates.

5) The resulting microstructure is very homogeneous leading to more uniform and isotropic properties of the semi-finished and the finished products.

ACKNOWLEDGEMENTS

The authors wish to thank NIPPON STEEL CORP. fot the permission to publish this paper. They are also grateful to Dr. D. Eylon, the University of Dayton, USA for his encouragement and valuable comments. Mrs.C.Seitz of the University of Dayton is acknowledged for her assistance in typing the manuscript.

REFERENCES

1. H. B. Bomberger and F. H. Froes, "The Melting of Titanium," Titanium Technology, ed. F.H. Froes, D. Eylon and H. B. Bomberger, (1985), 25.

2. H. Hayakawa, N. Fukuda, T. Udagawa, M. Koizumi, H.G. Suzuki and T. Fukuyama, "Solidification Structure and Segregation in Cast Ingots of Titanium Alloy Produced by Vacuum Arc Consumable Electrode Method," ISIJ International 31 (1991),775.

3. K. Rödinger and D. Fisher, "Effect of Beta Flecks on the Fatigue Behavior of Ti-6Al-6V-2Sn, Titanium '80 Science and Technology, ed H.Kimura and O.Izumi,3 (1980),1907.

4. C.C.Chen and R.R.Boyer, "Practical Considerations for Manufacturing High-Strength Ti-10V-2Fe-3Al Alloy Forgings," J.Metals July(1979),33.

5. R.F. Peart and D. H. Tomlin, Acta Met.,10 (1962), 123.

FATIGUE FRACTURE OF COLD ROLLED TITANIUM IN VACUUM

Mikio Sugano, Tadaaki Satake, and Satoshi Inoue

Department of Mechanical Systems Engineering, Faculty of Engineering,
Yamagata University,
4-3-16, Jonan, Yonezawa, Yamagata 992 , Japan

Abstract

The fatigue behavior of the cold rolled titanium plate (KS40: 0.35 mm thick) with the texture of (0001)[$10\bar{1}0$]$\pm$30° has been studied in vacuum (6.7×10^{-4} Pa) on the specimens cut out parallel (LT) and perpendicular (TL) to the rolling direction. The LT and TL specimens were quite similar in fatigue behavior. Dimples and cavities were widely observed on the fracture surface of specimens. Dislocation cell structures have developed around cracks. The cells were more developed in vacuum comparatively with those in air. It seems that the evolution of fatigue damage involves the untwinning of existing twins associated with internal heating due to cyclic stressing.

Introduction

It has well been known that deformation twins were closely connected with fatigue crack initiation and propagation in annealed titanium [1-3]. Twin boundary damage was observed at existing twins where the applied stress was insufficient to nucleate fresh twins, and cyclic stresses caused larger twins to be broken up into smaller twin fragments [3]. It was also shown that cyclic and monotonic prestrains significantly reduced the fatigue life of titanium at lower strain levels [4]. However, the existence of deformation twins and its effect on fatigue properties are frequently ignored in dislocation dynamics studies. In particular, few studies appear in the literature on the fatigue crack growth behavior in cold rolled titanium where existing twins are assumed to play a more important role on fatigue micromechanism. In a previous paper, we have reported that in the atmospheric pressure range of less than 10 Pa the increment of specimen temperature reached greater than 20 K due to internal heating and then the spread of the plastic zone developed around a main crack, when fatigue tests were carried out at the stress amplitude of $\sigma=\pm150$ MPa (the endurance limit: 196 MPa)[5].
The present study was conducted to clarify the effects of rolling texture on fa-

Titanium '92
Science and Technology
Edited by F.H. Froes and I. Caplan
The Minerals, Metals & Materials Society, 1993

tigue fracture micromechanism of titanium under alternative plane bending in vacuum. Dislocation microstructures developed around growing fatigue cracks in vacuum are compared with those observed in air. The role of existing twins on fatigue crack growth in titanium were discussed in connection with slip activities enhanced by internal heating.

Experimental Procedure

The material used was commercial high purity titanium plate (KS40) of 0.7 mm thick supplied by Kobe Steel, Ltd. The chemical composition in weight percent was: nitrogen (0.0024), hydrogen (0.0041), oxygen (0.050), iron (0.029), titanium (remainder). After the plate having been unidirectionally cold-rolled down to 0.35 mm thick (50 % reduction in thickness) at room temperature, the crystallographic texture was measured by using the Schultz back reflection technique with filtered CuKα radiation. The 0001 pole figure measured from a cold-rolled plate

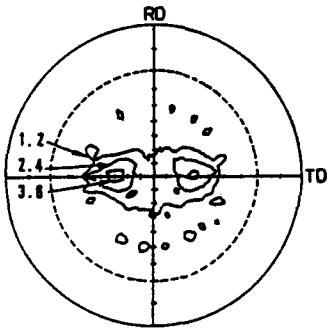


Fig. 1 0001 pole figure for unidirectionally cold rolled titanium plate. RD: Rolling direction, TD: Transverse direction.

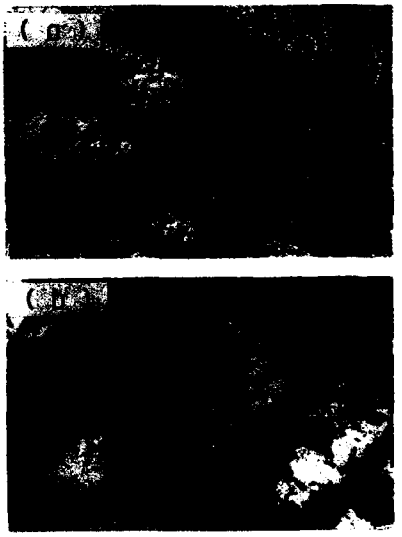


Fig. 2 Photomicrographs showing microstructure of unidirectionally cold-rolled titanium:(a) optical, (b) TEM.

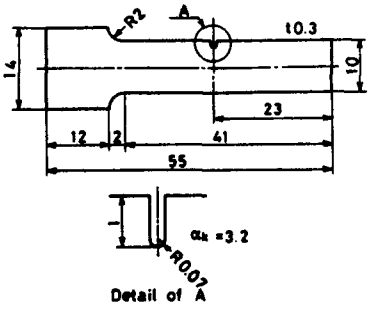


Fig. 3 Shape and dimensions of fatigue specimen (in mm).

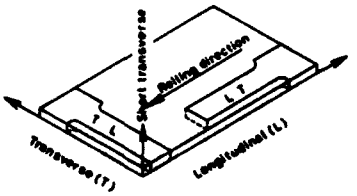


Fig. 4 Schematic illustration showing how to prepare the TL and LT specimens from cold-rolled plates.

(Fig. 1) indicates that a (0001)[10$\bar{1}$0] texture rotated ±30° toward the transverse direction, i.e. {1$\bar{2}$15}<10$\bar{1}$0> texture, had developed parallel to the rolling plane as was published by other workers [6,7]. Microstructures prior to fatigue testing were observed with optical and transmission electron microscopes (Fig. 2). It can be seen that even after cold rolling to 50% reduction in thickness a number of grains have still remained to be deformed (Fig. 2 (a)). The TEM photomicrograph indicates that numerous twins were in clusters (Fig. 2 (b)). These twins were identified with {11$\bar{2}$1}, {11$\bar{2}$2} and {1$\bar{1}$02} planes. Longitudinal (LT) and transverse (TL) specimens with a single edge notch (α_k=3.2) as was shown in Fig. 3 were machined to the dimension of 10x55x0.3 mm parallel and perpendicular to the rolling direction respectively (Fig. 4). Prior to fatigue testing the specimens were polished mechanically and electrolytically. Fatigue tests were performed on an apparatus that produced constant displacement in plane bending at a resonant frequency, which was about 600 Hz for the second mode of oscillation employed in the present study. All tests were conducted at R=-1 and ambient temperature. For tests in vacuum, the apparatus was set up in a vacuum chamber which was evacuated to a pressure of 6.7×10^{-3}Pa. Metallographic examination was carried out around a main crack with Nomarski contrast optical microscope, SEM (X-560 XMA: Hitachi) and TEM (JEM-200A: JEOL) operating at 200kV. TEM observations were carried out on the same areas as those for optical microscopy. This was successfully attained by means of an electrolytic jet polishing setup with optical microscope [8]. Thin films were prepared from only a surface layer of specimens and as close to a main crack as possible. The temperature of specimens was continuously measured during fatigue tests through an alumel-chromel thermocouple of 0.1 mm in diameter, which was spot-welded onto the anticipated crack path of specimen surface.

Results and Discussion

In Fig. 5, the S-N curves for the LT and TL specimens tested in vacuum were shown compared with results obtained in air. It is found that in vacuum fatigue behavior is much the same between the LT and TL specimens, whereas in air some differences can be distinguished in the endurance limits and fatigue lives. This suggests that in vacuum the rolling texture has little effect on fatigue behavior of pure titanium.

The fatigue crack growth rate vs. ΔK plot is shown in Fig. 6. It is apparent that the gradient of stable crack growth region and the ΔK_{th} value for the specimens tested in vacuum are quite different from those in air. Then, the curves for the tests in air were obtained by the method of least squares. In vacuum, both the LT and TL specimens have the same ΔK_{th} value of about 12 MPa$\sqrt{m}$, which was high comparatively with the value of about 5 MPa$\sqrt{m}$ in air. Thus it appears that in vacuum fatigue crack growth behavior is much the same between the LT and TL specimens, while in air they are subtly different from each other. Therefore, it will be reasonable to assume that the anisotropy of fatigue properties due to rolling texture is less significant in vacuum.

Figure 7 shows appearances of the fracture surface of specimens tested in the ΔK near-threshold region in vacuum. Fracture surfaces in vacuum are characterized

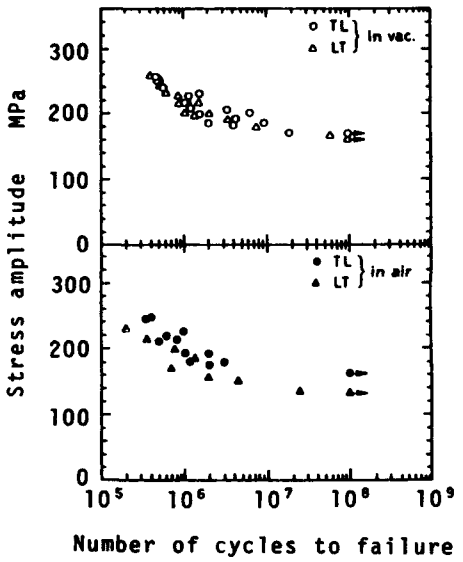


Fig. 5 S-N curves for the TL and LT specimens tested in vacuum (top) and in air (bottom).

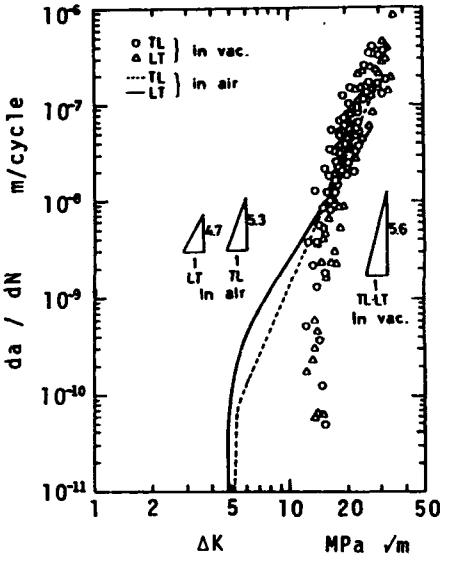


Fig. 6 Fatigue crack growth rate curves for the TL and LT specimens tested in vacuum and in air.

by cavities and dimples with microligaments, giving evidence of the temperature rise of specimens. Secondary microcracks are frequently observed around the dimples. This suggests that in vacuum some volume at crack tips must have heated up to considerably high temperature during the fatigue fracture processes. In vacuum the LT and TL specimens resembled each other in fracture surface topography. In air, however, the specimens showed discernible differences in their appearances of fracture surfaces. In the TL specimen the fracture surface was composed of cleavage facets, but in the LT specimen that was characterized by aligned ridge structures consisting of small irregular plateaus and valleys. General appearances of fatigue fracture surfaces of the cold rolled titanium are more ductile in vacuum than in air.

In Fig. 8, the specimen temperature rises measured during fatigue tests in vacuum were compared with those in air. Then, the temperature increment was defined as the difference between the maximum and the minimum values measured through fatigue tests. It can be seen that in vacuum the increment of specimen temperature reached up to 45 K during cyclic stressing at $\sigma = \pm 201$ MPa (the stress amplitude ratio to endurance limit $\fallingdotseq 1.2$). In air, however, that was only about 3 K. The results were in well agreement with that in pure titanium [5]. It should be noted that the curve for the TL and LT specimens in vacuum is exactly the same with each other in tendency, and is much higher than that in air, where there are some differences between them. This appears to be connected with the slip activities enhanced by the internal heating due to cyclic stressing in vacuum. Follow-

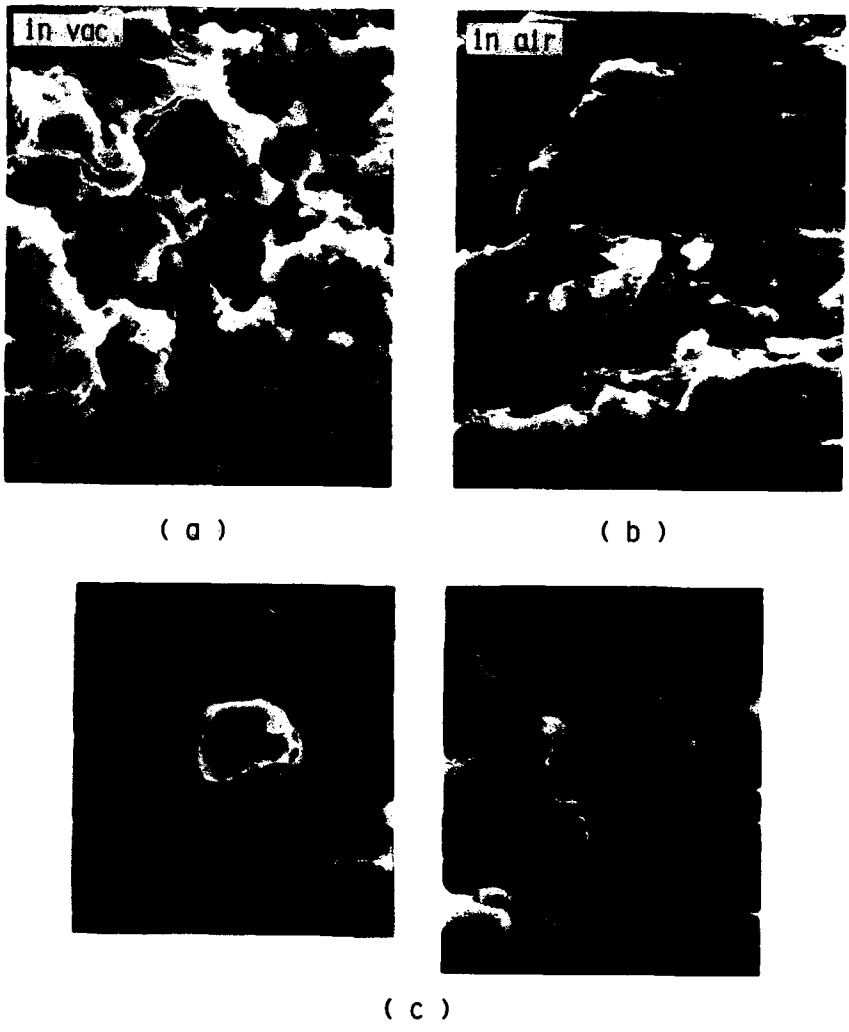


Fig.7 SEM fractomicrographs showing appearances of fracture surfaces at the ΔK_{th} value: (a) in vacuum, (b) in air and (c) a matching pair photomicrograph showing cavities formed on a fracture surface in vacuum.

ing the model of "a moving heat source between insulating planes" proposed by Freudenthal and Weiner[9], the maximum temperature on a slip plane was approximately calculated to be 318 K for the stress amplitude of $\sigma = \pm 201$ MPa. This value appears to be reasonably accepted, although there is a discrepancy between the theory and the experiment. This is because the experimental data indicate a temperature representative of the spot where a thermocouple was welded and not the true temperature developed on a fracture surface. The true temperature developed on fracture surfaces would be much higher than the values obtained experimentally.

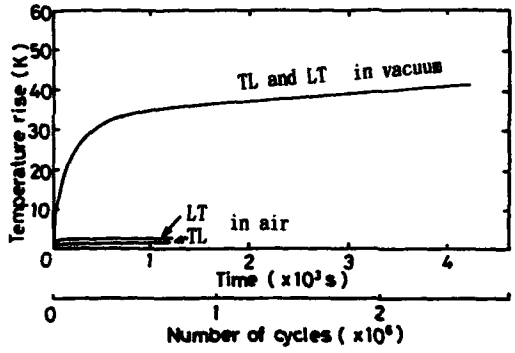


Fig. 8 Plot of the increment of specimen temperature during fatigue tests. $\sigma = \pm$ 201 MPa.

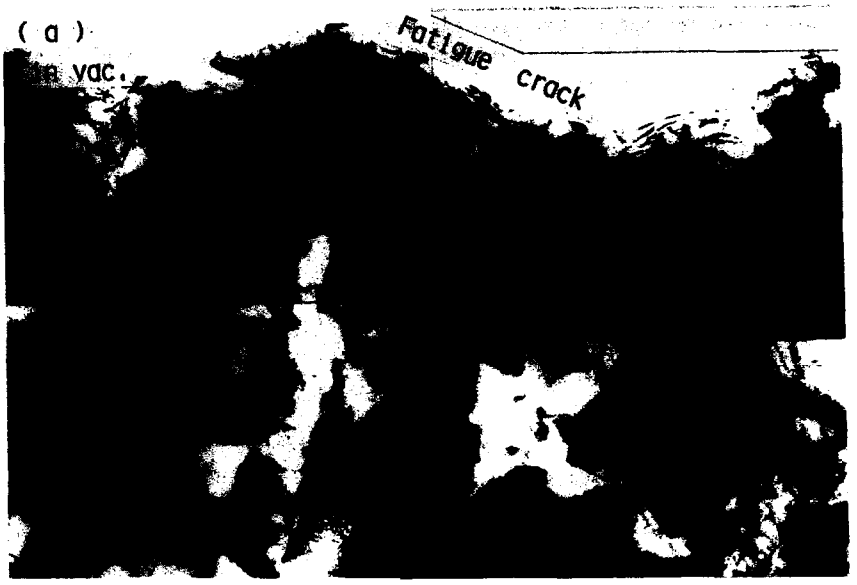
Specimen temperature increased with increasing stress amplitudes. For titanium alloys, Bryant et al have given experimental evidence indicating that the temperature of fracture surface rose up to above the melting point at the moment of final separation under uniaxial loading [10]. In addition, it has been known that slip activities on primary and secondary slip systems are very sensitive to a temperature change at near room temperature: a temperature increment of 30 K above room temperature causes the critical resolved shear stresses on the basal and prismatic slip planes to decrease by about 30 % and to increase the activation volume for prismatic slip system extremely [11].

Figure 9 shows a typical example of TEM photomicrographs observed in the close vicinity of growing cracks. Dislocation cell structures developed in the close vicinity of the crack. It was very rare to observe large twins in clusters near cracks, whereas in the areas over 10 μm away from the crack sides a lot of twins are observed, which consist of extremely dense dislocation debris. The trends of the microstructure development were the same with those in the LT specimen. This suggests that the evolution of fatigue damage in cold rolled titanium would involve untwinning of the existing twins under cyclic stresssing. In vacuum, then, a larger fraction of the externally supplied energy would be consumed for slipping and untwinning at crack tips compared with that in air. Assuming that the externally supplied energy is constant, the energy dissipation for propagating a fatigue crack would decrease with increasing plastic deformation. Thus, it can be concluded that in vacuum the fatigue fracture micromechanism of cold rolled titanium is controlled by slipping and untwinning activities at a growing crack tip, because of their absorbing energy at the crack tip. Then, the internal heating could be a promoter to enhance the slip activities under cyclic stressing in vacuum.

Conclusions

Characteristics of fatigue behavior of the cold rolled titanium plates subjected to alternate plane bending in vacuum are summarized as follows:

1. In vacuum, anisotropy in both S-N curves and fatigue crack growth rate curves is insignificant between the TL and LT specimens. The ΔK_{th} value is higher in vacuum than in air.



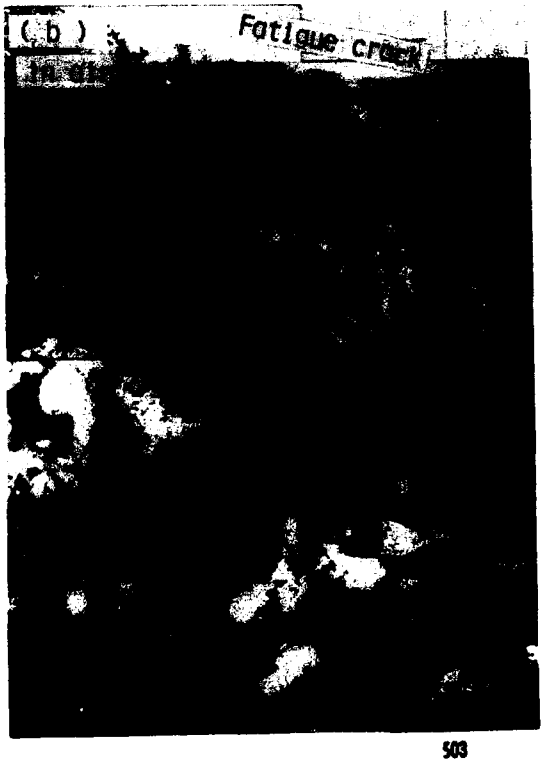


Fig. 9 TEM photomicrographs showing common microstructure in the close vicinity of a growing crack in the TL specimen: (a) in vacuum, and (b) in air.

2. Fracture surface morphology of the TL and LT specimens tested in the ΔK_{th} region are characterized by cavities and dimples. Secondary microcracks were frequently observed around the cavities and dimples. General mode of fatigue fracture is ductile in vacuum.

3. Dislocation cell structures were generally observed around cracks, whereas a lot of twins in clusters were very common in areas over 10 μm away from crack sides. Untwinning of the existing twins seems to be involved in fatigue crack growth micromechanism. The dislocation structure configurations could be connected with the slip activities at the tip of growing crack.

4. Specimens raised temperature in themselves up to 45 K above ambient temperature due to internal heating, when cyclically stressed at $\sigma = \pm 201$ MPa. They mention that by theory it is probably much hotter. In cold rolled titanium, the internal heating could be a promoter to enhance the slip activities under cyclic stressing in vacuum.

Acknowledgement: The authors are grateful to Kobe Steel, Ltd for providing the material (KS40) that were used in the present study.

References

1. M. Sugano, and C. M. Gilmore, "A Crystallographic Study of Fatigue Damage in Titanium" , Met. Trans. A,11A(4)(1980), 559-63.

2. C. J. Beevers, and M. D. Halliday, "On the Formation of Internal Fatigue Damage in Association with Twins in α-Titanium" , Met. Sci. J., 3 (1969), 74-9.

3. P. G. Partridge, "Cyclic Twinning in Fatigued Close-packed Hexagonal Metals" Phil. Mag., 12(5)(1965), 1043-54.

4. J. P. Owens, P. Watson, and A. Plumtree, "The Effect of Prestrain on the Cyclic Behaviour of α-Titanium" , (Mechanical Behaviour of Materials Vol. II, The Society of Materials Science, Japan, Kyoto, 1972), 131-42.

5. M. Sugano, S. Kanno, and T. Satake, "Fatigue Behavior of Titanium in Vacuum" , Acta metall., 37(7)(1989), 1811-1820.

6. D. N. Williams, and D. S. Eppelsheimer, "A Theoretical Investigation of the Deformation Textures of Titanium" , J. Inst. Met., 81(1952-53), 553-562.

7. H. Inagaki, "Development of Cold-Rolling Textures in Pure Ti" , Z. Metallkde., 82(10)(1991), 779-789.

8. M. Sugano, "Observations of Dislocation Structure in High-Purity Iron Fatigued under Bending , Bull. of Yamagata Univ. Eng., 11(1)(1970),379-392.

9. A. M. Freudenthal, and J. H. Weiner, "On the Thermal Aspect of Fatigue" , J. Appl. Phys., 27(1)(1956), 44-50.

10. J. D. Bryant, D. D. Makel, and H. G. F. Wilsdorf, "Observations on the Effect of Temperature Rise at Fracture in Two Titanium" , Mat. Sci. Engng., 77(1986),85-93.

11. E. D. Levine, "Deformation Mechanisms in Titanium at Low Temperatures" ,Trans. AIME, 236(11)(1966), 1558-1565.

EFFECT OF HEAT TREATMENTS ON THE FATIGUE BEHAVIOUR OF THE BETA-C TITANIUM ALLOY(*)

D.Buttinelli, F.Felli, G.B.Festa
Dept. of Chemical Engineering-Metallurgy
University "La Sapienza", Roma (Italy)

and **A.J.Querales**
School of Metallurgical Engineering,
Universidad Central de Venezuela-Caracas

Abstract

Mechanical properties of the BETA-C (RMI) titanium alloy were examined and fatigue tests carried out to study the effect of aging treatment and microstructure on fatigue resistance.
Specimens from 20 mm thick rolled plate were used in tensile and compact tension tests, after solution treatment(815°C,A.C.) and peak-aging at temperatures from 350° to 570°C . Under- and over-aging conditions were examined also. Tensile strength and K_{IC} were measured for all of the heat treatments.
Fatigue crack growth tests were performed on CT-type specimens (ASTM E647) at 10 Hz and load ratio of R=0.5 . No dependence of the crack growth on the microstructure was observed in the specimens aged from 425°C to 570°C.
Overall results suggested that aging at temperature from 475°C to 500°C provided the best combination of tensile properties and fatigue resistance.

Introduction

The metastable beta Ti-3Al-8V-6Cr-4Mo-4Zr (BETA-C, TM) alloy has been designed by RMI (USA) for its excellent hot and cold working characteristics, corrosion resistance and high strength levels which can be reached by aging after solution treatment [1-4]. This alloy, of course, can be heat treated to a wide range of strength levels owing to the precipitation of the stable α-phase , in the temperature range from 350°C to 600°C, in the solute-rich metastable ß-titanium matrix.
Moreover, the particular alloy composition does not allow the brittle omega phase precipitation during aging , as commonly found in other beta-titanium alloys , also at reasonably low temperature, e.g. 350°C [2,5].

(*) This work was supported by MURST, Italy.

In a previous paper [6] the characterization, performed on LT and TL CT-specimens aged 20 h at temperatures from 450°C to 570°C, after SHT (815°C-1/2h,A.C.), showed no substantial difference between the two orientations , as regards fatigue crack growth rate. It was also observed that the overaged alloy - with lowest strength levels - presented, at highest ΔK values, slightly lower fatigue crack propagation rates, compared to those of the as-solution treated specimens.
The objective of this work was to accurately study the effect of grain size and of secondary alpha phase distribution and morphology on fatigue crack growth and fracture toughness of as-aged specimens. Correlations between strength, fatigue behavior and toughness were discussed as functions of heat treatment.

Experimental

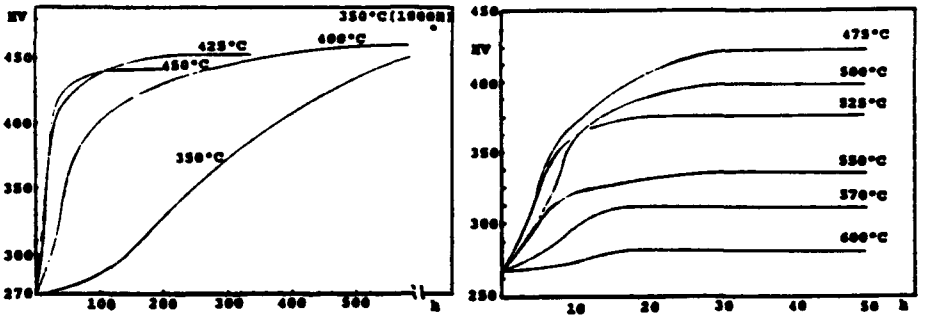
The Beta-C alloy was supplied by the manufacturer RMI (USA) as-solution treated (815°C - 1/2 h, A.C.) 20 mm thick rolled plate. Its chemical composition was : Al 3.3%-V 8.1%-Cr 5.8%-Mo 3.9%-Zr 3.8%-Fe 0.08%-Nb 0.08%-C 0.02%-N 0.015%-H 80 ppm.
Specimens for the aging curves determination and for tensile and fatigue tests were cut with a milling machine. The aging tests were conducted on 20x25x4(mm) specimens in an argon furnace across the range 350-600°C for periods of up to 1000 hours for the lowest temperature; Vickers hardness vs time was graphically reported for each aging temperature.
Longitudinal tensile test specimens (length: 50mm; gauge length 20mm; d:4mm) were aged between 350°-570°C for time values specified in Table I. UTS, YS(0.2%) and E% were then determined.

Fatigue crack growth tests were performed on CT-type specimens, in air, at 10 Hz and load ratio of R=0.5 on machines whose load was generated by an electromagnet and amplified mechanically.
CT-specimens with W=40mm and B=12.5mm were machined in LT orientation, according to ASTM E 647, and aged at 350°C-1000h; 400°C-360h; 425°C-165h; 450°C-20h and 160h; 475°C-20h and 28h; 500°C-20h; 525°C-20h; 550°C-20h; 570°C-20h.
Crack lengths were measured at x40 light microscope and checked after failure of the specimen. The polynomial equation was then employed to determine the crack growth rate from these data.
Experimental results were processed with a program specially prepared for da/dN - ΔK curves. Fatigue behaviour, or more precisely the subcritical crack propagation rate, can be represented by semi-empirical models allowing the fatigue crack growth rate to be analytically expressed with a very small number of characteristic experimental parameters. The relation, proposed by Forman, was employed in this paper.
Fracture toughness (K_{1c}) was measured by means of CT-specimens (ASTM E 399). Metallographic examinations (etching reagent: 1 ml HF(40%), 5 ml HNO_3, 94 ml H_2O) and fracture surface examination were carried out with an optical microscope and SEM-EDS.

Results and Discussion

Typical aging curves of the alloy, at various temperatures, are illustrated in Fig.1. They were used to determine the peak-aging condition at each temperature for tensile, K_{1c} and fatigue test specimens. At lower temperatures (350-400°C) very high

Figure 1 - Aging curves at indicated temperatures.



hardness levels were reached. But longer aging times were required, due to slow kinetics of the alpha phase precipitation. At the highest temperature(600°C) the fast over-aging did not allow the alloy to achieve a hardness sufficiently high to be of practical interest. Duplex aging or stretching before the ageing were already tried [6]. No greater improvement in the results were obtained by those treatments and - in view also of a much more high cost - they were not studied any further.
Micrographs of the specimens aged to max. hardness level at the various temperatures are shown in Figure 2 . At 350°C , very fine precipitation of secondary alpha (dark phase) is perfectly distributed within the ß-matrix (light phase): the precipitates are small (0.1-0.5 µm); at 500°C, precipitation is still fairly uniform, but particle sizes have grown to 1-2 µm. Their size

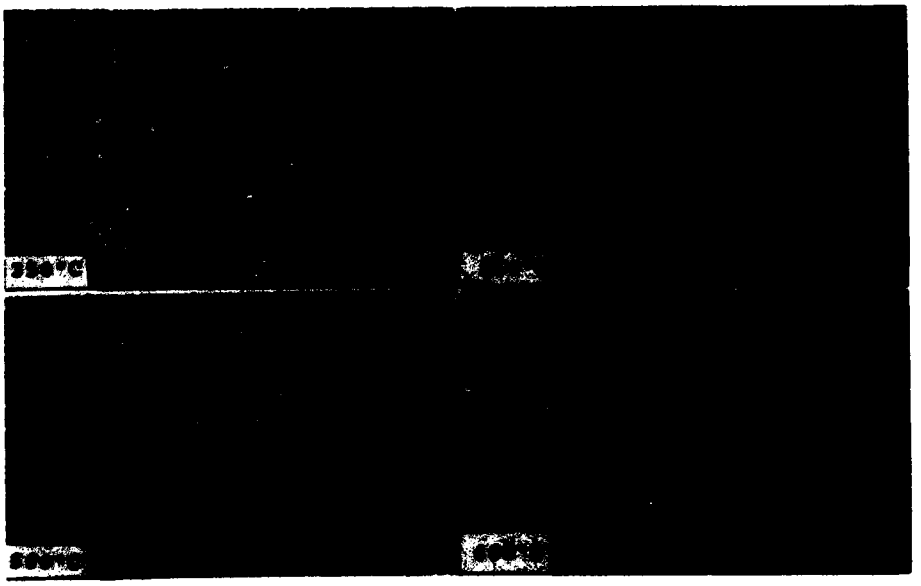


Figure 2 - SEM micrographs of specimens aged at indicated temperature (right column : X 2800;left column : X 8000).

increases still further at 525°C , though their distribution is still sufficiently uniform for high hardening; at 550°C, however , this is no longer the case : large (3-6 μm) alpha islands are elongated in bands and randomly distributed. At 600°C , as it can be seen, only a few zones in the grains have been involved in the precipitation phenomena.

Tensile properties and fracture toughness (K_{IC}) of as-peak aged alloy - and for some temperature as-under aged specimens also - are reported in Table I . As expected , the highest yielding strengths were achieved by ageing at lowest temperatures, although with a great loss of plasticity. Values of over 1700 MPa for U.T.S. could be easily reached, but the correspondent ductility , as measured by elongation (%) , and fracture toughness were too low. It is interesting to note from this point of view the correlation between Y.S.(0.2%) and K_{IC}, as it is shown in Fig.3A. From plotted data an empirical equation can be calculated as:

$$K_{IC} = 147 - 0.073\ (Y.S.)$$

where Y.S.(0.2%) is in MPa and K_{IC} in MPa$\sqrt{m}$.
Apart from the interest in a similar equation for practical purposes,it is important to observe the strictly linear dependence of the two properties and the fair precision with which experimental points fit the calculated model, regardless of peak- or under-aging , with excellent value of correlation coefficient (r=0.989). The same is not completely true for other possible correlations, e.g. K_{IC} as a function of the reduction area or elongation (%), for the following reasons :
1) the greater scatter band of experimental points, due also to less precise and reproducible measurements of R.A., or El.(%) ;
2) the net deviation of the as-solution treated specimen, as it can be seen clearly in Fig.3B.

In any case, increasing yield strength by secondary alpha aging strongly reduces ductility and toughness , as reported also for other metastable beta-Ti alloys [7], and conclusively good combination of tensile properties (1200 MPa for Y.S.) and fracture toughness(55-60 MPa$\sqrt{m}$) is achieved by aging at temperature from 475 to 500°C. Some authors [8-9] indicated that sligthly higher fracture toughness could be obtained by duplex aging, after a high temperature SHT(T>900°C) which gave a completely recrystallized structure of the beta matrix. In our previous work [6] on the same material , but as-SHT at 815°C and A.C. , no appreciable improvement by duplex aging was found. Froes et al.[10],observing in Beta III alloy an enhancement of hardening by duplex aging, or by prior 10% cold working , supposed a mechanism of uniformly nucleated precipitation of very fine omega phase and subsequent transformation, probably "in situ", of omega in fine alpha phase. But this mechanism does not seem too useful for the Beta-C alloy, in which omega precipitation can be developed only at low aging temperature (<300°C) by necessarily very long aging time [2,5].

The results of the crack propagation tests for the indicated conditions are reported in Fig.4 . A comparison of the fatigue crack propagation behaviour of the most indicative specimens is reported in Fig.4D, in terms of only Forman's model [11].
The effect of microstructure and heat treatments on F.C.P. ap-

TABLE I - Mechanical properties of heat treated specimens

Heat treatment	0.2% Y.S. (MPa)	UTS (MPa)	Elong. (%)	HV_{50}	K_{Ic} (MPa$\sqrt{m}$)
S.H.T. (815°C -1/2h,A.C.)	835	850	17	265	89
S.T.A. 350°C-1000h	1700	1730	0.5	470	24
S.T.A. 400°C-360h	1615	1685	0.8	460	30
S.T.A. 450°C-20h	1090	1170	10	360	63
S.T.A. 450°C-160h	1580	1640	3.4	445	32
S.T.A. 475°C-20h	1185	1265	5	410	-
S.T.A. 475°C-28h	1275	1325	4	420	48
S.T.A. 500°C-20h	1145	1225	7	390	59
S.T.A. 525°C-20h	1100	1180	8	375	66
S.T.A. 550°C-20h	920	950	12	325	79
S.T.A. 570°C-20h	905	935	12	310	84

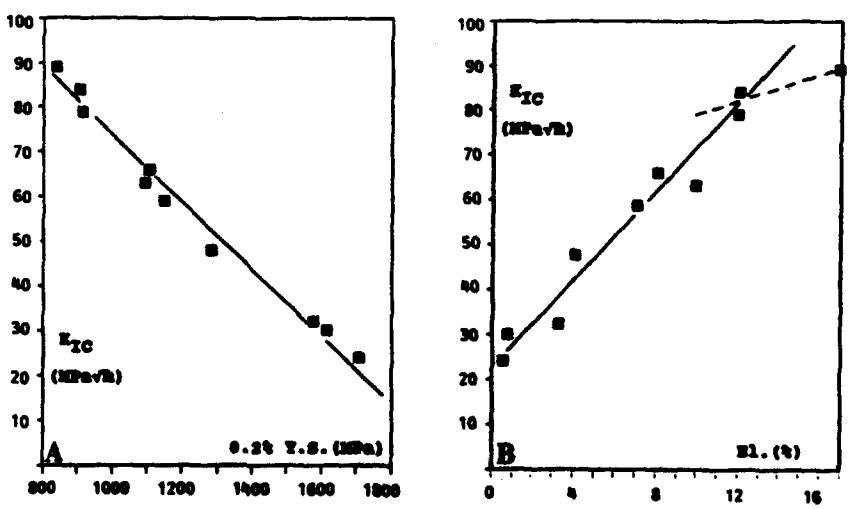


Figure 3 - Fracture toughness (K_{Ic}) as a function (A) of 0.2% P.S. and (B) of elongation % .

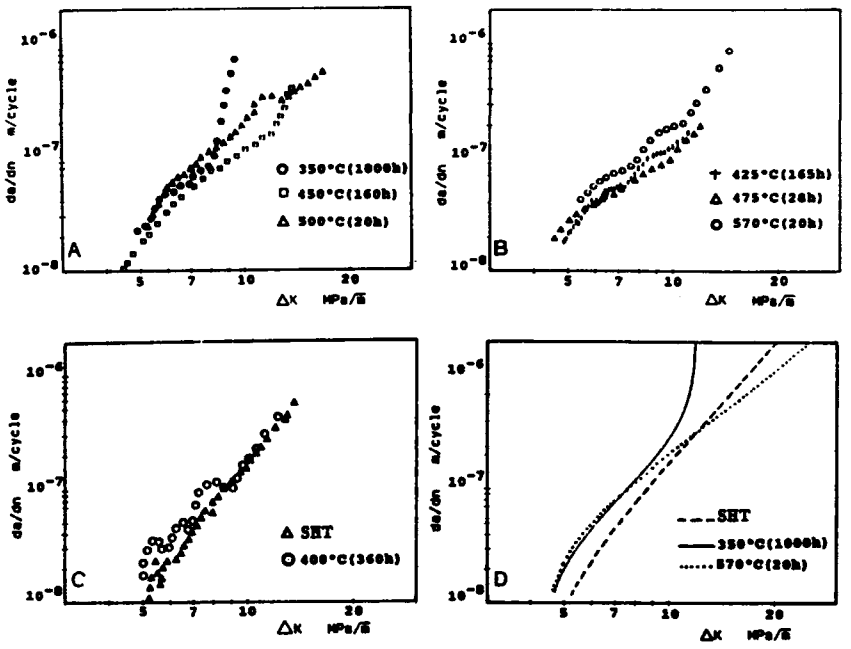


Figure 4 - Experimental results of fatigue tests (10 Hz ; R=0.5) and (D) Forman's models.

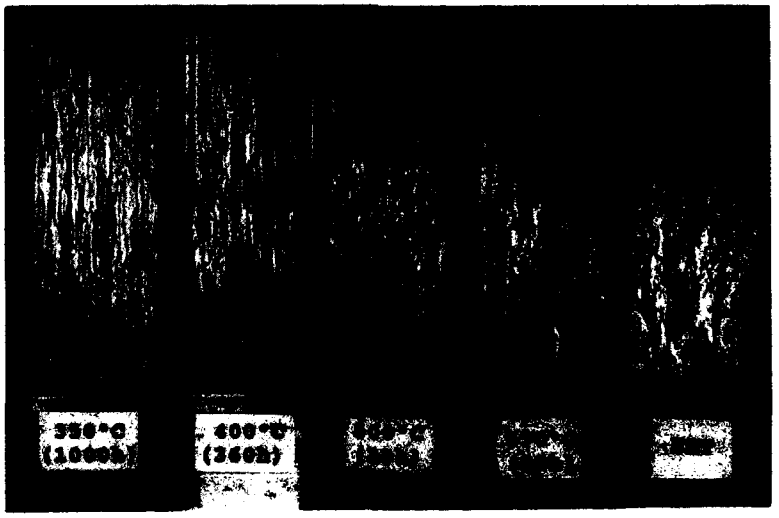


Figure 5 - Fracture surface of fatigue CT-specimens (thickness : 12.5 mm).

peared to be small , particularly at low ΔK values because the data were scattered in a very narrow band, even if the as-SHT alloy showed the highest ΔK threshold and the fatigue precrack, in this case, needed a larger number of cycles. At high ΔK values, the highest crack growth rates are exhibited by samples treated at highest strength conditions, e.g. aged at 350-400°C. The as-SHT samples showed a trend toward higher growth crack rates than those aged but at lowest strength levels. Also from fatigue tests, it was concluded that the best combination of strength and fatigue resistance was provided by aging at intermediate temperature, close to 500°C.

Fractography of fracture surfaces after fatigue testing, as can be seen in Figures 5,6 , showed pronounced roughness for SHT specimen , with some areas of intergranular fracture and some areas of cleavage (Figg. 5,6a,6b), while a large final zone of fracture showed a low roughness and , on this surface, fatigue striations appeared. The as-aged specimens showed a lower roughness,particularly in samples treated to higher strength levels; this characteristic developed over the whole fracture surface from the early to the final stages.

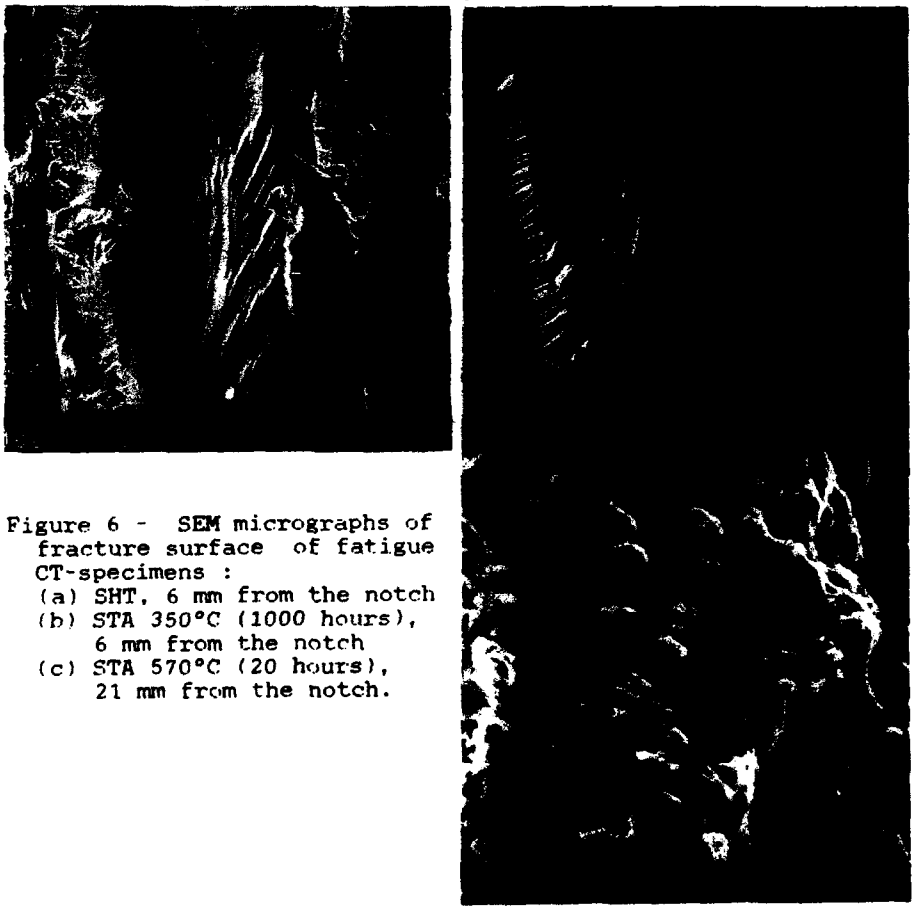


Figure 6 - SEM micrographs of fracture surface of fatigue CT-specimens :
(a) SHT, 6 mm from the notch
(b) STA 350°C (1000 hours), 6 mm from the notch
(c) STA 570°C (20 hours), 21 mm from the notch.

In as-high temperature aged specimens, with comparatively lower strength, fatigue striations and branching were clearly seen (Fig.6c) and this could explain lower crack propagation rates.

Conclusion

Aging treatment enables Beta-C (RMI) alloy to achieve very high strength levels of over 1700 MPa, but no ductility and low fracture toughness are correspondingly presented. Correlation between 0.2% Y.S. and K_{Ic} is expressed by the equation:

$$K_{Ic} = 147 - 0.073(Y.S.)$$

where (Y.S) is in MPa and K_{Ic} in MPa m .
Fatigue tests, which showed that crack propagation rates in as-aged specimens(at 450°C to 600°C) were not dependent on the microstructure, permit us to conclude that the best combination of tensile property and fatigue behaviour is provided by aging in the range of temperatures from 475° to 500°C.
At these temperatures a microstructure with an abundant quantity of secondary alpha phase in beta matrix , but in the form of quite fine and uniformly distributed precipitate, is obtained.

Acknowledgements

The authors would like to thank the Management of the company Ginatta-Torino-Titanium SpA (Turin,Italy) for supplying the alloy and for their interest in the work.

References

[1] RMI Titanium Techn. Bulletin, " RMI 3Al-8V-6Cr-4Mo-4Zr-Ti Alloy for Deep Hardening Applications", Niles(Ohio),1969.
[2] C.G.Rhodes and N.E.Paton , Metall. Trans. A , 8A, (1977), pp. 1749-1761.
[3] H.J.Rack and T.J.Headly , Scr. Metall. , 14, (1980) , pp. 1211-1216.
[4] D.H.Wilson and C.M.Esler , in Beta Titanium Alloys in the 1980's (R.R.Boyer and H.W.Rosenberg eds.),TMS-AIME,(1984) pp. 457-482.
[5] G.A.Sargent et al., J.Mater.Sci.,9,(1974), pp. 487-490.
[6] D.Buttinelli et al., Metall.Sci.Tech., 9,(3), (1991).
[7] G.Terlinde and K.H.Schwalbe, (paper presented at TMS-AIME Annual Meeting, Denver, 1987).
[8] H.E.Krugmann and J.K.Gregory , " Microstructure and Crack Propagation in Ti-3Al-8V-6Cr-4Mo-4Zr",(paper presented at the TMS-AIME Fall Meeting 1990, Detroit.
[9] J.K.Gregory and L.Wagner , "Heat Treatment and Mechanical Behaviour in Beta-C", Proc. of 7°Int.Meeting on Titanium, Turin(Italy),1991.
[10] F.H.Froes et al., Metall.Trans.A, 11A,(1980),pp.21-31.
[11] ESA :Fracture Control Guidelines, ESA PSS 03.1203 (1986).

ON EFFECTS OF BETA FLECK ON THE PROPERTIES OF Ti-10V-2Fe-3Al ALLOY

Y. G. Zhou①, J. L. Tang②, H. Q. Yu③ and W. D. Zeng④

Department of Materials Science and Engineering
Northwestern Polytechnical University

Abstract

The authors observed the specimens of tensile and fatigue fracture by LM and SEM. The effects of β-fleck on decreasing the tensile ductility and low cycle fatigue life were investigated at room temperature for Ti-10V-2Fe-3Al alloy. It is found that in β-fleck region without primary alpha phase (α_p) or with a little primary alpha phase crack generally propagated along grains to form brittle fracture, the matrix fracture was plastical fracture. Authors also discovered that under the action of alternating load β-fleck often became a fatigue origin, and at high strain original β-grain boundary and grain boundary α film within β-fleck region were susceptible to crack initiating and early crack propagating.

Introduction

Near β-Ti alloys have an increased heat treatability, deep hardening potential, and inherent ductility attributable to its body centered cubic structure. In addition, the class alloy also has good mechanical properties, and low cost of fabricated components compared to conventional Ti-alloys[1]. Therefore recently near β-Ti alloys are widely applied to practical production. However, if the melting and hot-working technologies were unsuitable, a certain amount of β-flecks would be formed, which were due to constitutional segregation[1,2].

Literatures [3,4] have pointed that serious β-flecks within a alloy decreased the ductility and low cycle fatigue property. They didn't show the property data and didn't clarify the reason of the influence of β-fleck on the properties.

The authors determined the tensile property and low cycle fatigue life of Ti-10V-2Fe-3Al with β-flecks at room temperature and observed the macrostructure, microstructure and fractograph of fracture samples using an optical microscopy and scanning electron microscopy. We have found the fracture character and the fracture mechanism of β-fleck and matrix. In addition, this paper offered a testing method for researching the relation between β-fleck and property.

---

① Professor of Materials Science and Engineering, Northwestern Polytechnical University Xi'an, Shaanxi, 710072 P. R. China

② Received M. S. Degree at above Department

③ Associate professor of above Department

④ Graduated Student

Titanium '92
Science and Technology
Edited by F.H. Froes and I. Caplan
The Minerals, Metals & Materials Society, 1993

Material and Experimental Procedure

Material

80×80mm square blank (No. 8602001) with β-flecks (Fig. 1) were used in this study. Its β-transus is 805℃. Its bulk chemical composition is given in Table I.

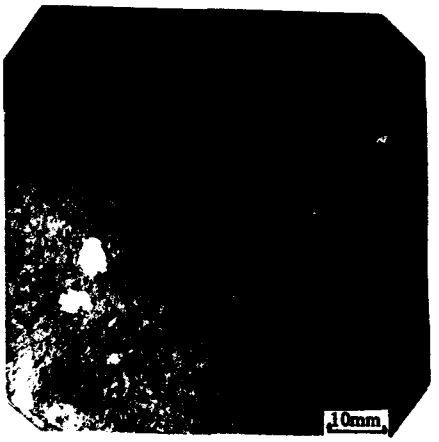


Fig. 1-Original material structure

Table I Chemical Composition of Ti-10V-2Fe-3Al

Element	Al	V	Fe	Si	C	N	H	O	Ti
wt-%	3.05	10.23	2.08	0.05	0.015	0.014	0.002	0.013	bal

Experimental Procedure

At 35℃ below the β-transus the original material was drawn into 40×40mm forging blank. This forging blank was solution-treated and aged as follows: 760℃/2h/water quench + 520℃/8h/air cool. The property samples were cut longitudinally. Tensile tests were performed at room temperature. Low cycle fatigue tests were conducted using constant amplitude longitudinal pull-pull cyclic stress, stress ratio R=0.1 and the cyclic frequency f=15/sec.

One end of each fracture sample was made into metallographic specimen for observing macrostructure, microstructure, and for measuring β-fleck volume fraction (P_v), maximum β-fleck area (S_{max}) and the microhardness of β-fleck and matrix. And the another end of each fracture sample was used for analysing fractograph under a JSM-35C SEM for observing fracture character of β-fleck and matrix, and for measuring the chemical composition of β-fleck and matrix.

Results

Tensile Tests

The tensile property data are shown in Table I. The difference of the elongation (δ) and reduction in area (φ) were very obvious. $\varphi_{max}=56\%$, $\varphi_{min}=11\%$. After all the macrostructure, microstructure and scanning fractograph were observed carefully, it was found that the tensile ductility closely related with β-fleck. For example, in the micrograph of sample No. 3, there was no β-fleck (Fig. 2a) and its scanning fractograph was typical dimple fracture (Fig. 2b), and $\varphi=42.6\%$. The macrostructure of sample No. 12 (Fig. 2c) shows β-flecks (white spots), in which $P_v=1.8\%$, $S_{max}=0.21mm^2(1.04\times0.20)$ and $\varphi=26.8\%$, Figure 2d was the micrograph of sample No. 15, S_{max} was $0.60mm^2(2.73\times0.22)$, P_v was 3.2%, its φ was 13.2%. S_{max} of the sample No. 1 (Fig. 2e) was not too large, but $P_v=5.7\%$(Fig. 2f), and φ was only 11.9%. The case of sample No. 2 was similar to sample No. 1. Therefore, the ductility was influenced not only by S_{max} but also by P_v. Although the S_{max} of the sample No. 1 and No. 2 were within the controlled standard (0.762×0.762 mm^2), the reduction in area of the sample No. 1 and No. 2 was low. Thus authors consider that the S_{max} should be controlled and the P_v should also be controlled.

Table I The Influence of β-Fleck on Tensile Property of Ti-10V-2Fe-3Al

No.	Ultimate Strength MPa	Yield Strength MPa	Elong. %	Red. Area %	Maximum β-Fleck Area mm^2	β-Fleck Volume Fraction Vol. %
1	1282	1243	6.4	11.9	$1.28\times0.16=0.20$	5.7
2	1260	1211	5.6	11.7	$0.63\times0.51=0.32$	6.1
3	1218	1190	11.2	42.6	0	0
4	1302	1280	5.6	11.0	$0.97\times0.60=0.58$	13.6
5	1195	1170	10.8	49.5	0	0
6	1182	1165	10.0	46.0	$0.37\times0.19=0.07$	0.12
7	1185	1170	10.4	54.0	0	0
8	1192	1180	13.2	56.0	0	0
9	1210	1195	11.6	51.3	$0.21\times0.05=0.01$	0.06
10	1196	1182	10.8	51.3	0	0
11	1188	1160	11.2	48.0	0	0
12	1289	1260	8.0	26.8	$1.04\times0.20=0.21$	1.8
13	1215	1200	9.6	44.8	0	0
14	1250	1220	8.8	30.0	$0.48\times0.18=0.09$	1.1
15	1226	1200	6.0	13.2	$2.73\times0.22=0.60$	3.2
16	1220	1210	7.2	29.5	$1.07\times0.21=0.22$	3.3
17	1245	1220	9.6	44.0	$0.32\times0.07=0.02$	0.12
18	1224	1210	10.8	43.0	0	0

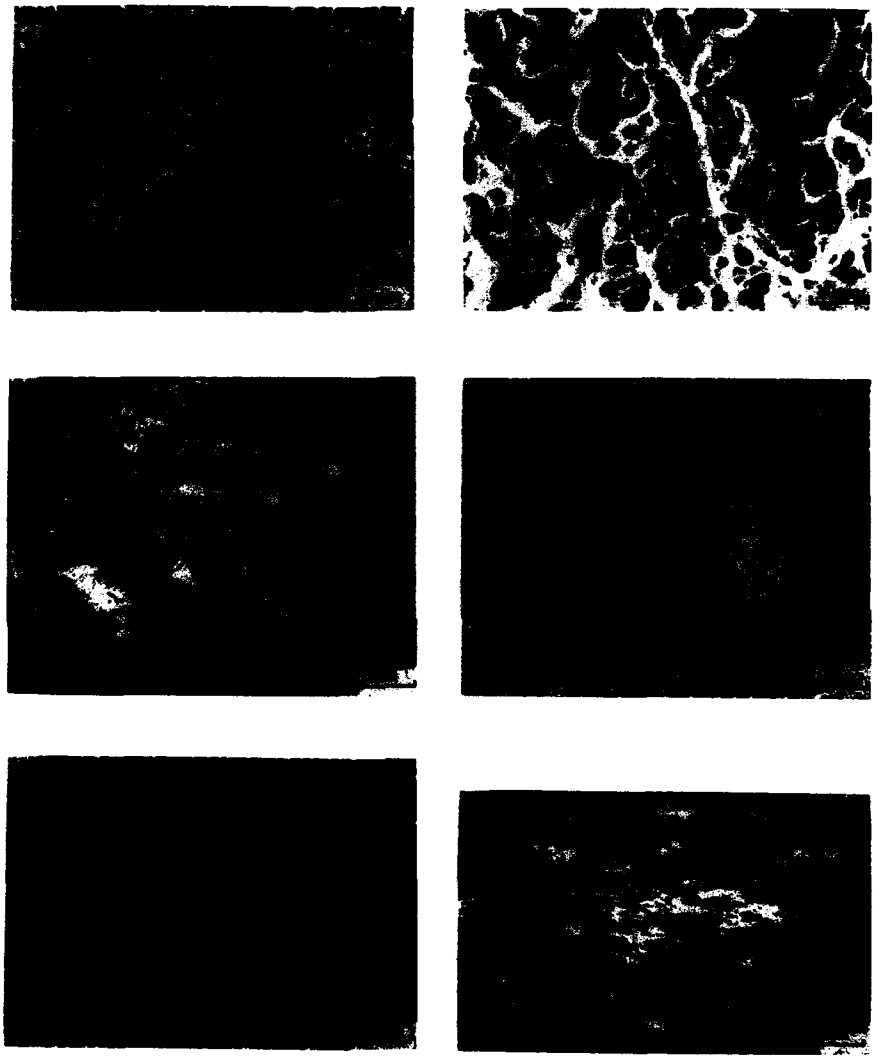


Fig. 2 Optical photograph and scanning fractograph of fracture samples
(a) microstructure of No. 3; (b) fractograph of No. 3
(c) macrostructure of No. 12; (d) microstructure of No. 15;
(e) microstructure of No. 1; (f) macrostructure of No. 1;

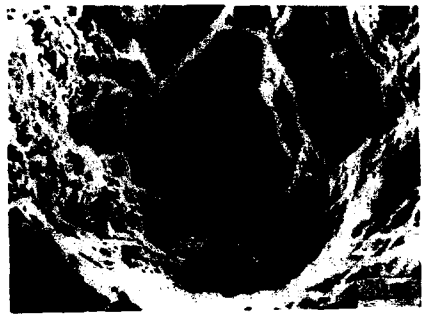


Fig. 3 Scanning fractograph of fracture sample No. 15

Extensive SEM studies revealed areas of brittle fracture which were characteristically intergranular grain boundary fracture. These areas of brittle fracture were associated with beta flecks (Fig. 3). The composition measured in brittle fracture region showed that Fe element content was higher than that in matrix, while Al was lower than that in matrix (Table Ⅱ). This manifested that the brittle fracture region was β-fleck region.

Table Ⅱ The Chemical Composition in Brittle Fracture Region* and the Microhardness of β-fleck and Matrix*

No.	Chemical Composition			Microhardness	
	Fe %	V %	Al %	β-fleck MPa	Matrix MPa
1	2.750	12.604	2.496	4710	4290
2	2.910	10.836	2.224	4800	4380
3	—	—	—	0	4330
4	3.073	11.355	2.016	4730	4260
8	—	—	—	0	4230
12	3.336	11.014	2.390	4690	4440
15	2.724	10.644	2.110	4750	4370
16	—	—	—	4720	4320

* Mean of Five Measuring Points

Another interesting fact in Table Ⅰ is that when there are serious β-flecks ($S_{max} \geqslant 0.58mm^2$, $P_v \geqslant 5.7\%$) at fracture surface the ductility of material strikingly is lowered, while its strength is increased. The microhardness of the β-fleck and the matrix was measured by optical microhardness machine. The microhardness of β-fleck was higher than matrix (see Table Ⅱ.). The more microhardness the more strength (see Table Ⅱ and Table Ⅰ)

Low Cycle Fatigue Tests

The results of low cycle fatigue test are given in Table Ⅳ. It shows that β-flecks have a large influence on the low cycle fatigue property. The sample with serious β-flecks ($P_v \geqslant 1.6\%$) at the fracture surface compared with that of no β-fleck, the low cycle fatigue life (Nf) of the former strikingly was decreased. For example, there was no β-fleck at the fracture surface of the sample No. 6, therefore Nf was 1.61×10^7. By contrast, there were serious β-flecks at fracture surface of No. 12 (Fig. 4a), $Nf = 2.3 \times 10^6$. Its fatigue origin was in β-fleck at the edge of Fig. 4b. And the crack propagated toward the sample' s center to form a brittle fracture band. Figure 4c shows that the fracture band was grain boundary fracture. The concentration of Fe in the brittle fracture band was 3.37% and the Al was 1.97%. This indicates the fracture band was a β-fleck; The size of the fracture band is consistent with the size and distribution of β-flecks in Fig. 4a. Figure 4d shows β-fleck throughout the cross-section of fracture sample. No. 7, $P_v = 11.99\%$, and $S_{max} = 7.83 mm^2$. It is also found that the brittle fracture band corresponded with β-fleck in Figure 4d.

Table Ⅳ The Influence of β-Fleck on Low Cycle Fatigue Life of Ti-10V-2Fe-3Al

No.	Stress MPa	Cyclic Number Nf	Maximum β-Fleck Area mm^2	β-Fleck Volume Fraction Vol. %
1	800	60000	0.50×0.30=0.15	10.9
2	800	250000	0.43×0.21=0.09	0.59
3	800	810000	0.80×0.23=0.18	1.30
4	800	>2880000①	0	0
5	800	>6380000①	0	0
6	800	16100000	0	0
7	800	880000②	8.42×0.93=7.83	11.99
8	900	350000	0.56×0.38=0.21	2.25
9	900	610000	0.38×0.33=0.13	0.54
10	900	710000	0	0
11	900	540000	0.62×0.31=0.19	1.72
12	900	230000	3.27×1.15=3.76	31.22
13	900	820000	0	0
14	900	200000	0.57×0.19=0.11	1.6
15	900	810000	0	0

① No fracture at all
② Fracture at clamping situation

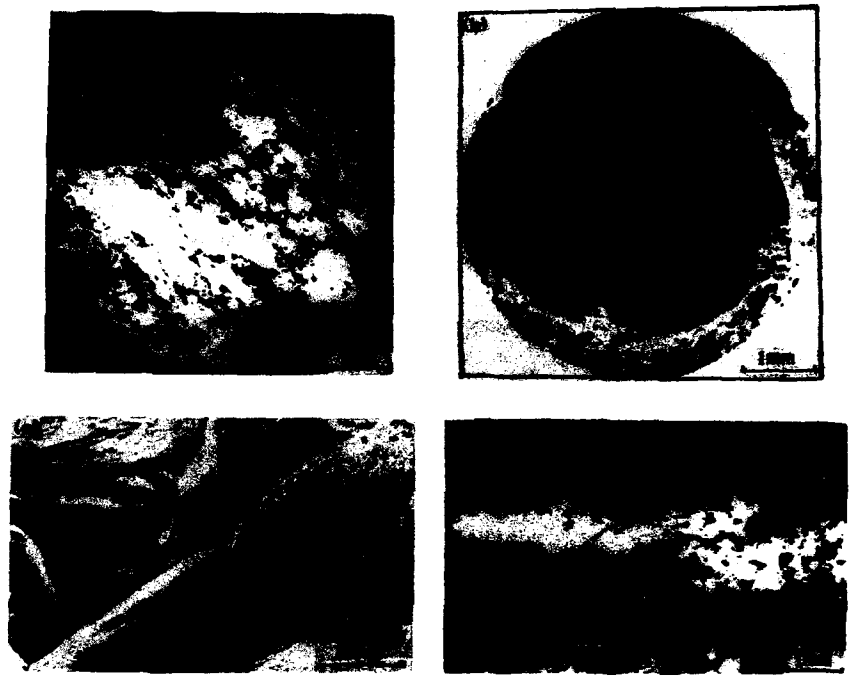


Fig. 4 Optical photograph and scanning fractograph of fracture samples
(a) macrostructure of No. 12; (b) fractograph of No. 12
(c) magnification of Fig. 3b; (d) macrostructure of No. 7

Disscussion

Effect of β-Fleck on Tensile Property

It is known that the strengthening of Ti-10V-2Fe-3Al alloy mainly is aged-hardening, by aging to precipitate secondary α phase (α_s). The more α_s phase volume fraction in structure the more strengthening action. Fig. 2d,e show that there are almost no primary α phase (α_p) in β-fleck region, there are mainly aged β matrix which is outlined by primary β grain boundary. Thus, the microhardness in the β-fleck region is higher than peripheral matrix (Table Ⅱ). The effects of β-fleck on tensile properties were that the more serious the β-fleck the higher strength, and the lower ductility.

The low ductility of this structure mainly depended on microstructure parameters including primary β grain boundary and grain boundary α-film. Especially within the β-fleck the existence of grain boundary alpha results in long soft phase zone. At tensile deforming the soft phase α preferentially deforms. Because of high strength of aged β matrix the plastic deformation concentrates on the small

region of the soft phase α. Before aged β matrix has not been yielded yet, the grain boundary α has already produced large deformation. Simultaneously, this strain occurs in the condition that the stress is less than the yield strength of peripheral matrix. Thus, long slip region, high stress concentration, and local plastic strain all occur at the triangular points of β grain boundary within β-fleck. Therefore voids first nucleate at grain boundary of β-fleck region (Fig. 2d). Then they grow, connect (Fig. 2e), propagate along the grain boundary (Fig. 5), and lead up to grain boundary fracture (Fig. 3) The result of this paper is similar with G. T. Terdinde' s study on Ti-10V-2Fe-3Al alloy using β solution-treated and aged treatment[5].



Fig. 5 Crack propagates along the grain boundaries

Effect of β-Fleck on Low Cycle Fatigue Property

When the material is tested in low cycle fatigue the plastic strain is dominating. Therefore Nf mainly depends on the material ductility, in general, if the material ductility is low, then Nf is low[6]. This experiment has proved that β-fleck reduced the material ductility, therefore when β-flecks exist Nf is reduced certainly. Thus the Nf of No. 12 (Fig. 4a) is less than that of No. 13 without β-fleck under same stress level (see Table Ⅳ). One of the reasons decreased Nf is that the presence of β-flecks leads to microstructure inhomogeneity. At plastic deformation, microstructure inhomogeneity causes slip inhomogeneity. Therefore localized plastic strain concentration occurs at primary β grain boundary and grain boundary α within β-fleck region. C. E. Feltner and P. Beardmor indicated that the concentration of plastic strain at grain boundary usualy is in direct ratio with the grain size[7]. The grain size in β-fleck is the largest. Thus strain majorly concentrates on the grain boundary with β-fleck. Because the strength of aged matrix is rather high slip is constrained at grain boundary, the stress builds up the grain boundary crack and propagate along grain to form grain boundary fracture (Fig. 4c).

R. B. Sparks and J. R. Long studied the effect of β-flecks in high-temperature α+β processed titanium alloys on low cycle fatigue life. They found that multiple cracks which nucleated with flecked regions lead to premature sample failure[8]. Authors get the same results from the experiments(see Fig. 2d, 2e and Fig. 5).

Conclusion

1. Through the observation for Ti-10V-2Fe-3Al tensile and fatigue fracture samples by optical and scanning electron microscopy, it is found that at β-fleck regions without α_s phase or with a little α_s phase the crack is prone to nucleating at primary β grain boundary and grain boundary α. Then the crack propagates along grain to form brittle fracture, while fracture at matrix is typical ductile fracture. The more the serious β-flecks the lower the ductility and low-cycle fatigue life. Therefore, this paper clarified that the β-fleck essentially influenced alloy properties.
2. This paper quantitatively measured the maximum β-fleck area (S_{max}) and the β-fleck volume fraction (P_v). Both of these two influence ductility and low-cycle fatigue life. Authors propose that besides controlling the S_{max} in practical production the P_v also should be controlled.

References

1. F. H. Froes, and H. B. Bomberger, "The Beta Titanium Alloy", Journal of Metals, Vol. 37(1985), 28-37.
2. H. B. Bomberger, and F. H. Froes, "The Melting of Titanium", Journal of Metals, Vol. 36(12)(1984), 39-46.
3. Y. G. Zhou et al., "On Beta Fleck of Ti-10V-2Fe-3Al Alloy", Journal of Northwestern Polytechnical University, Vol. 8(4)(1990), 425-431.
4. A. W. Funkenlusch, and L. F. Coffio, "Low-cycle Fatigue Crack Nucleation and Early Growth in Ti-17", Metall. Trans. A, Vol. 9A(1978), 1159-1167.
5. G. T. Terdinde, T. W. Duerig, and J. C. Williams, "Microstructure Tensile Deformation and Fracture in Aged Ti-10V-2Fe-3Al", Metall. Trans. A, Vol. 14A(1983), 2101-2115.
6. H. J. Zhou and M. Z. Huang, Metal Material Strengthology(Beijing, China: Science Publishing House, 1989), 359-369.
7. C. E. Feltner, and P. Beardmor, "Achievement of High Fatigue Resistance in Metals and Alloys" (ASTM STP-467, 1969).
8. R. B. Spark, and J. R. Long, "Improved Manufacturing Methods for Producing High Integrity More Reliable Titanium Forging" (AFML-TR-β-301, 1974).

THE EFFECT OF TEXTURE ON IMPACT ENERGY AND FRACTURE OF Ti–4AL ALLOY

Cai Xuezhang, Li chenggang, Wo Hua

Northwest Institute for Nonferrous Metal Researh
P.O.Box 71
Baoji, ShaanXi 721014
P.R China

ABTRACT

Ti–4Al alloy is a type of single alpha phase with h.c.p structure, which possesses greater anisotropy than other types of crystal lattic, and thus its mechanical properties appear larger difference as formation of texture in the microstructure of the alloy. In the present work, the Ti–4Al alloy plates with different types of texture have been produced by means of hot rolling at different temperature and deformation degree, measuring impact energy (IE) and observing fracture of the specimens cut off along the direction of rolling and transverse, the characteristics of the fracture and the anisotropy of IE have been related with the particular texture. Based on that, the reasonable technology for rolling Ti–4Al alloy plates with a type of expecting texture can be properly selected.

INTRODUCTION

Microstructural characteristics, including texture, influence strongly mechanical properties of Titanium and its alloy. Because hexagonal close packed (hcp) α–phase has greater anisotropy, the obvious anisotropy of mechanical and physical properties appears in Ti–4Al alloy with typical hcp α–phase when the texture formed in its microstructure. Basal planes (0002) parallel rolling surface is designated as B–texture, while basal planes perpendcular to transverse direction is designated as T–texture, and having both B–and T–texture is designgted as B / T–texture, the variety of texture types is mainly influenced by factors as alloy composition [1,2], rolling temperature, deformation degree and rolling direction, final annealing is less considerable effect [3]. The texture effect on the mechanical properties of of Ti–alloy, such as elastic modulus, yielding strength, bend strength, superplasticity, fatigue, creep and fracture toughness etc. have been investigated. Recent years, the slip deformation and fatigue fracture behavior of Ti–alloys with texture have been observed and analysed [4,5], it reveals further the texture influencing strongly plastic diformation and fracture behavior.

It have been found that the texture has a considerable effect on Ti–4Al impact energy (IE), but its mechanisms, espescially that of fracture features are lacking. At present work, the effects of various texture of the rolled plates on IE and fracture features have been investigated.

Materials and testing methods

Materials

The 12mm and 18mm thickness plates of Ti–4Al alloy were produced by means of hot rolling, the alloy composition, rolling and annealing parameters were listed in Table 1.

Titanium '92
Science and Technology
Edited by F.H. Froes and I. Caplan
The Minerals, Metals & Materials Society, 1993

Table 1 Ti–4Al alloy composition and rolling and annealing parameters

Composition (wt.x)		4.1 Al 0.02C	0.005B 0.001N	0.04Fe <0.005H	0.04Si 0.12O
Plates	thickenss	rolling temp.	rolling direction	deformation degree	annealing parameters
No1	12mm	1030℃	L	76%	760℃ / 1hr A.C.
No2	12mm	950℃	L	76%	760℃ / 1hr A.C.
No3	18mm	950℃	L	33%	760℃ / 1hr A.C.

Testing methods

The machined specimens with gauge of 5mm diameter and 25mm length cut off along rolling (L) and transverse direction(T) of the plates, tensile properties test using UTM–ST tensile machine at 10^{-4}1 / s strain rate at room temperature.
The IE specimens with "V" type notch along L– and T–orientations in accordance with that as shown in Fig.1, and designated as L–T, L–S, T–L and T–S specimens respectively. First letter symbols the normal of cracking plane (CP), second letter symbols the crack propagation direction (r). The IE values were measured using the swing hammer type of TB 30A–15 / 30kg –M impact tester, the textures of the plates were determined using SIEMENS–TEX–II x ray texture tester and the fracture topography of IE specimens is observed using SEM.

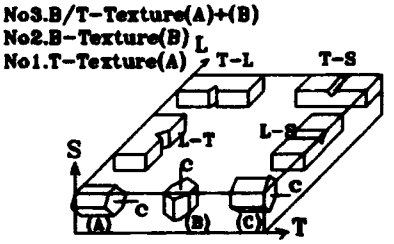


Fig 1. IE specimens and its notch orientations, and various texture (hcp. cell) orietations

Results and discussion

Microstructure

Fig 2 shows that the microstruture of the annealed plates rolled at various heating temperatures. No.2 plate was first heated at below β–transus, and then hot rolled to greater deformation degree of 76%, thus the original coarse microstructure of the plate blank was fully broken, after recrystallization annealing, it becomes a complete equiaxed grain structure, see Fig2(b). No 3 plate, although the heating temperature is the same as that of No.2 plate, but its rolling deformation degree is smaller, only 33%, the coarse lamellar structure wasn't fully broken, and therefore the recrystallization partly equiaxed grains and further grew lamellar structure were remained, see Fig.2(c). No.1 plate, the transformation of α to β–phase take place when its blank is heating at above β–transus. However, during hot rolling, at the beginning, it is in β–phase temperature range, following by cooling to α–phase temperature range, and thus resulting in transformation of β–phase into α–phase ,accompanying recrystallization and acicular structure further grown, after annealing, it become coarse lamellar and partly equiaxed structure, see Fig 2 (a).



a b c

Fig.2 Microstructure and (1012) pole of the annealed Ti–4Al alloy plates.
(a)No1 plate, (b) No2 plate, (c) No3 plate

Texture

The $(10\bar{1}2)$ pole figure of the hot rolled and annealed plates was shown in Fig 2. From the maximum intensity of No.1 plate $(10\bar{1}2)$pole shown in Fig2(a), the $(10\bar{1}2)$ plane are lying under of about 47.5° along T–direction. Considering angle between(0001) and $(10\bar{1}2)$ plane, it can be believed that the T–texture in No1 plate is dominant. From Fig2 (b) it can be seen that the $(10\bar{1}2)$ plane in the No2 plate are lying under 0–60° angle range along T and about 20° along L the corresponding (0001) planes are roughly lying under about 90° to plate surface and 0–15° angle rangle along T. Consequently the texture in the No2 plate mainly belong to B type, its $(11\bar{2}0)$ orientation parallels L–direction. As there were six zones of the maximum intensity of $(10\bar{1}2)$ pole in the No 3 plate shown in Fig.2(c), and four zones among them are lying under an angle about 47.5° along T and 25–30° angle range along L , other two zones are lying under 0–35° angle range along T. For this reason, it can be considered that the former represents T–texture, and the latter represents B–texture. Therefore it can be conclude that there are B / T–texture in the No 3 plate.

The blank of the No1 plate is first heated at above β–transus and thus the transformation of α to β take place. During hot rolling, the (001) planes in b.c.c. β–phase turn to parallel to plate surface, its $<110>$ orientation parallels to L [3]. When the temperature dropped into α–phase field, the β to α transformation take place in accordance with the Burgers–relationship,i,e,$\{110\}_\beta // (0002)_\alpha$and $<111>_\beta // <11\bar{2}0>_\alpha$.So it can be believed that the T–texture in No1 plate mainly produced during hot rolling at β–phase field, the (0001) planes trend to the plate surface and $(11\bar{2}0)$ orientation trend to L , see Fig.2(a).The original texture in No2 and No3 plate blanks produced at β–phase field has been remained, and subsequent rolling at α–phase field, with increasing deformation degree, the (0001) plane trend to the plate surface and $(11\bar{2}0)$ orientation trend to L . As a result, in No2 plate with greater deformation degree, the B–texture has been formed as the same as result of work[6], and B / T–texture has been formed in the No3 plate as relatively small deformation degree.

Tensile and IE properties

The tensile properties and IE value of the specimens with various orientations are listed in Table 2.

Table 2 Tensile and IE properties of the annealed Ti–4Al plates

Plates	tensile					Impact	
	orientation	YS (MPa)	UTS (MPa)	EL (%)	RA (%)	notch–orientation	IE (KJ/m^2)
No1	L	614.54	687.44	18.87	31.23	L–T	519.52
						L–S	1249.49
	T	710.79	760.00	16.77	36.63	T–L	920.10
						T–S	818.74
No2	L	599.2	695.3	20.2	44.7	L–T	1167.0
						L–S	868.5
	T	634.5	694.3	20.2	46.0	T–L	1274.9
						T–S	608.0
No3	L	623.7	730.6	18.5	32.7	L–T	676.0
						L–S	1010.1
	T	738.5	773.8	14.5	38.5	T–L	1059.1
						T–S	627.6

By comparison ,the yield strength(YS) and ultimate tensile strength (UTS) of No3 plate is the highest, and that of No2 is lowest. While the case of relative elongation(EL) and of reduction area (RA) is opposite. It just represents the microstructural effect on the tesile properties. Usually specimens with a lamellar structure, its YS and UTS is higher and its EL and RA is lower than that of specimens with an equiaxed structure [7].
Another noteworthy is that YS, UTS and RA values of No1 and No2 plates consistently is higher in T than in L and the case of EL is opposite. As for No2 plate, the tensile properties YS, UTS, EL and RA all is near the same. This case just represent texture effect on tensile properties[4,6,8], which were discussed in detail according to schmid law in papers [6,9].

IE properties

Comparing the IE data of the specimens with the same orientation in each plate or the specimens with different orientation in the same plate, it can be found that the difference among them and varying regularity is difficult to interpret in terms of microstructural features. But considering their texture effect, the problems are easy to understand. As to specimens with T or B–texture, when the impact loading parallels the c–axis of h.c.p cell, e,g. No1 L–T, No2 L–S and T–S specimens. see table 3., their IE values are the lowest(in 500–700kJ / m^2), while the impact loading is prependicular to the c–axis and the IE specimen notch parallels the c–axis, e,g, No1 L–S, No2, L–T and T–L specimens, their IE values are the highest (in 1100–1300KJ / m^2), about two or over two times of the former [6]. When the impact loading and the specimen notches both are perpendicular to the c–axis, e.g. No1 T–L and T–S specimens, their IE values (1720–820KJ / m^2) are within that of above both cases. As to No3 plate with the B / T–texture, the IE values and its varying regularity can roughly estimate from the weighted mean of the IE values in the corresponding orientation of No1 plate with T–texture and No2 plate with B–texture.

Strain and Fracture in IE specimens

The IE values are mainly dertermined by the work of cracking initiation (Ai) and propagation (Ap). Ai is deplete for microcrack forming and propagating in the front of the

main cracking. As for the specimens with "v" notch, the stress concentration level is very high, the strain zone in the notch root is very small, the IE is mainly depleted for cracking propagation, i.e. Ap is dominant in the IE value. Under impact loading, the strain rate is higher than that under static tensile loading, the plastic strain doesn't fully developed and only concentrated in the local zones, leading to nonuniformly strain. Under high concentrating stress, ductility and toughness are deteriorated and trend forwards brittle break, moreover when the texture orientation is lying under unfavourable to slip strain, the brittle break trend more serious.

Under impact loading, initially it is tensile stress near the notch root and compressive stress opposite the root, and the tensile stress zone gradually advances as crack propagating. In terms of a mode 1 under tensile opening crack in plane strain, the triaxial stress state at the root of the IE specimen notch or at the front of the propagating crack, and the relating with texture, i.e. the orientation relative to h.c.p cell was illustrated in Fig 3 (a). The shear stresses acting on the shear planes shows in Fig. 3(b) (c) (d) as A.W.Bowen's result[5], can be expressed as following : $\tau b = 0.50\sigma s$, $\tau c = 0.25\sigma s$ $\tau f = 0.25\sigma s$, its propagating direction(r) and relatively orientation to h.c.p cell and various shear stress are shows in table 3. Naturally, the effective shear stress of a slip plane must exceed its critical–revolved shear stress(CRSS), which one among them to be effective to operate slip strain will depend on the ratio of the shear stress: CRSS, the greater ratio will be effective.

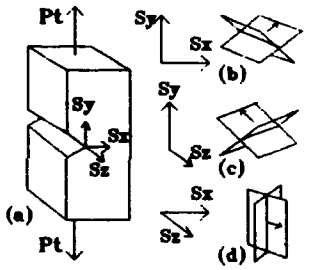
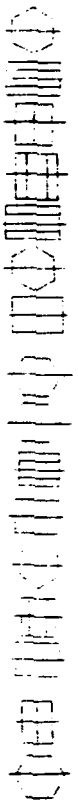


Fig.3 triaxial stress state at the root of the specimen notch and the front of cp(a) and the shear stresses acting on various shear planes (b), (c), (d)

In the light of the orientation of CP and r relative to h.c.p cell, the T– or B–texture effect on the impact strain behavior and the fracture features can generally (see table 3) be divided into three groups. First included, CP // $(11\bar{2}0)$ and r // $<10\bar{1}0>$ such as No1 L–S and No2 L–T specimen and CP // $(10\bar{1}0)$ and r // $<11\bar{2}0>$, such as No2 T–L specimen. Second, CP // $(11\bar{2}0)$ and r // $<0001>$, such as No1 L–T and No2 L–S specimen; and CP // $(10\bar{1}0)$ and r // $<0001>$, such as No1 T–S specimen. Third, CP // (0001) and r // $<11\bar{2}0>$ such as No1 T–L specimen, and r // $<10\bar{1}0>$ such as No1 T–S specimen. In the first group, τb is close to $<11\bar{2}0>$, τc and τf is close to $<11\bar{2}3>$, the ratio of τb: $CRSS_b$ is the highest as the τb value is two times of the τc or τf value, and the CRSS value of the $<11\bar{2}0>$–slip(a–type) is quarter of the $<11\bar{2}3>$–slip, (c+a)–type. As for the No2 T–L specimen, the plane on which τb acting is close to $(10\bar{1}0)$, and the τb–direction close to $<11\bar{2}0>$, so it is easy to be operated by τb. The fracture topography is shown in Fig.5(a), the drastic slip strains, develop fully and popularly on the entire CP. A lot of the $(10\bar{1}0)<11\bar{2}0>$ slip strain stretch zones(A), the basal plane fractures(B) and second tored cracks(C) are clear . As to the No1 L–S specimen, the τb–direction is also close to $(11\bar{2}0)$, but the plane on which τb acting is close to $(11\bar{2}0)$, which generally isn't slip system of h.c.p –Ti, so it is required to turn an angle to fit in with the $(10\bar{1}0)$ $<11\bar{2}0>$ slip system, thus leading to produce a larger slip stretch zone with a greater angle inclined to CP(A), and thus formed a deeper second tored crack (C). shown in Fig.4 (b).

Table 3 IE Value, the orientation of CP, r and τi (i = b,c,f)

Samples		IE(KJ / cm²)	cp,r Orientation	τb	τc	τf
No1	L–T	519.52	CP // $(11\bar{2}0)$ r // $<0001>$	$<11\bar{2}3>$	$<11\bar{2}0>$	$<11\bar{2}3>$
	L–S	1249.49	CP // $(11\bar{2}0)$ r // $<10\bar{1}0>$	$<11\bar{2}0>$	$<11\bar{2}3>$	$<11\bar{2}3>$
	T–L	720.10	CP // (0001) r // $<11\bar{2}0>$	$<11\bar{2}3>$	$<11\bar{2}3>$	$<11\bar{2}0>$
	T–S	818.74	CP // (0001) r // $<10\bar{1}0>$	$<11\bar{2}3>$	$<11\bar{2}3>$	$<11\bar{2}0>$
No2	L–T	1167.0	CP // $(11\bar{2}0)$ r // $<10\bar{1}0>$	$<11\bar{2}0>$	$<11\bar{2}0>$	$<11\bar{2}3>$
	L–S	686.5	CP // $(11\bar{2}0)$ r // $<0001>$	$<11\bar{2}3>$	$<11\bar{2}0>$	$<11\bar{2}3>$
	T–L	1274.9	CP // $(10\bar{1}0)$ r // $<11\bar{2}0>$	$<11\bar{2}0>$	$<11\bar{2}3>$	$<11\bar{2}3>$
	T–S	608.00	CP // $(10\bar{1}0)$ r // $<0001>$	$<11\bar{2}3>$	$<11\bar{2}0>$	$<11\bar{2}3>$
No3	L–T	676.70	T:cp // $(10\bar{1}0)$ r // $<0001>$	$<11\bar{2}3>$	$<11\bar{2}0>$	$<11\bar{2}3>$
			B:cp // $(11\bar{2}0)$ r // $<0001>$	$<11\bar{2}0>$	$<11\bar{2}3>$	$<11\bar{2}3>$
	L–S	1010.10	T:cp // $(10\bar{1}0)$ r // $<11\bar{2}0>$	$<11\bar{2}0>$	$<11\bar{2}3>$	$<11\bar{2}3>$
			B:cp // $(11\bar{2}0)$ r // $<0001>$	$<11\bar{2}3>$	$<11\bar{2}0>$	$<11\bar{2}3>$
	T–L	1059.10	T:cp // (0001) r // $<10\bar{1}0>$	$<11\bar{2}3>$	$<11\bar{2}3>$	$<11\bar{2}0>$
			B:cp // $(10\bar{1}0)$ r // $<11\bar{2}0>$	$<11\bar{2}0>$	$<11\bar{2}3>$	$<11\bar{2}3>$
	T–S	627.60	T:cp // (001) r // $<11\bar{2}0>$	$<11\bar{2}3>$	$<11\bar{2}3>$	$<11\bar{2}0>$
			B:cp // $(10\bar{1}0)$ r // $<0001>$	$<11\bar{2}3>$	$<11\bar{2}0>$	$<11\bar{2}3>$



In the second group, τb and τf is close to $<11\bar{2}3>$ and τc is close to $<11\bar{2}0>$. The ratio of τc: CRSSc is the highest. Under τc acting, the $\{10\bar{1}0\}<11\bar{2}0>$ slip system is operated, lead to forming of " flutes " causing considerably lowering of K_{IC} [5]. A zones in Fig 4(c) (d). These "flutes" parallel the c–axis and arrange along the r–direction, perhaps formed by intersecting $\{10\bar{1}0\}$ slip plannes, and the flute ridges with a tored top surface is close to cp , and flute ends are characterized by a basal planes broken normally to cp, B zones in Fig.4(c) (d). Besides, there are many zones with brittle fracture features, e.g. river–like , C zone in Fig 4 (c), and cleavage fragments, C zone in Fig 4 (d), and others with cleavage fractures, D zones in Fig 4 (c), (d). All the above mentioned slip behavior and fracture features suggest that the slip strain isn't drastic as in first group. and the fracture topography essentially is plastic and brittle mixture, the IE values remarkably decreased.



Fig.4 The fracture topography of specimens in first and second group

In the third group, τ_b and τ_c is close to $<11\bar{2}3>$ and τ_f close to $<11\bar{2}0>$, the ratio of *τ_f: CRSSf is the highest. Under τ_f acting, as the same way as in the second group,* also the "flutes" can be formed, but their directions are roughly normal to CP. So it is difficult to find on the fractured surface. Often the tored basal planes and other tored fractures can be formed, Fig 5(a) (b), and occasionally the "flutes" can be found due to h.c.p cell perhaps inclined at an angle along the T–direction, Fig 5 (c). Besides, the twinning fracture topography is found in Fig 5 (d). Perhaps the τ_b and the planes on which τ_b acting are favourable to produce twins, especially under the impact loading and there is a compresive stress zone at the front of CP. So the fracture is a mixture type of plastic and brittle, leading to lowering of IE value but higher than the IE in the second group.

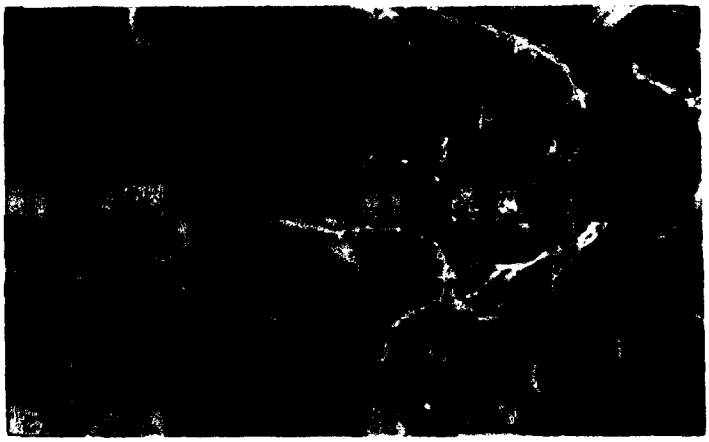


Fig 5 The fracture topography of No1 T–S (a), (b), (c) and No1 T–L (d)

As for the No3 specimens with the B / T–texture, except for the T– or B–texture of

No3 T–S specimens is lying under an unfavourable orientation to slip strains, the others have simultaneously favourable and unfavourable orientations, see table 3. It can be predicted that the IE value of No3 T–S specimens is the lowest among all of No 3 specimens, and that is further verified by observation on the fracture topography. The fracture features suggest that both cases of the slip strain and fracture behavior in the second or the third group occured jointly in the No 3 T–S specimens. Concerning the No3 L–T specimens with regard to the T–texture, the ratio of τc : CRSSc is the highest and is lying under a favorable to the $<11\bar{2}0>$–slip orientation and thus leading to form the flutes paralleling to the r–direction is similar to **second** group. As to the B–texture.the case is the same as first group,under τb acting, the drastic slip strains appear. In the same way, considering the No3 L–S and the No3 T–L specimens, the fracture topography in the former is dominated by the T–texture, slip strain is similar to first group, and thus the IE value increased. The fracture topography in the latter is also dominated by the T–texture, as the same as third group leading to a higher IE value.

Conclusion

1. In the Ti–4Al alloy plates, T–texture, B–texture and B / T–texture are formed by hot rolling to different deformation degree at above or below β–transus temperature.
2. The tensile properties of Ti–4Al alloy plates are influenced by microstructure and texture characteristics, and the latter has more important effect.
3. The anisotropy of the IE properties is domnated by the different texture. The specimens with T– or B–texture have remarkable anisotropy and while with B / T–texture,the anisotropy is alleviated.
4. The fracture are also dominated by the different texture. In terms of mode 1 tensile opening crack in plane strain, all of specimens with the texture favorable to the a–type of $<11\bar{2}0>$ slip under τb acting are essentially broken in ductile state. On τb close to $<11\bar{2}3>$ direction, the mixture fracture of ductile and brittle appear, the IE value and the brittle fracture fraction depend on the particular texture type. As to the Ti–4Al alloy plate with B / T–texture, the IE value and the fracture features are dominated by T– and B–texture joint effect.

Reference

(1) D.R.Thornburg, H.R.Piehler, Titanium Science and Technology, ed. R.I.Jaffee, H.M.Burte (AIME, New York, Plenum, USA, 1973), Vol2, P1187
(2) F.Larsm, A.Zarkades and D.H.Avery, Titanium Science and Technology, ed. R.I.Jaffee, H.M.burte (AIME, New York, Plenum, USA, 1973), Vol,12, P1169
(3) Massahiro Fukuda,Akiyoshi Tanabe and Takashi Nishimura, "Hot Rolling Texture of Titanium and Titanium Alloy sheets", Titanium Zirconium (in Japanese),l34,(2), (1986),P111
(4) G.Lutjering, M.Peters, " Mechanical Properties of a Titanium Blading Alloy" (Report CS–2933, Research Project 1266–1, Technische Universitat HamBurg–HarBurg, 1983)
(5) A.W.Bowen, Sixth World Conference on Titanium ed. P.Lacombe, R.Tricot, G.Beranger (SFM, Ulis Cedex, France, 1988), Vol1, P93
(6) C.M.Wang, Proceeding of China's Fourth Conference on Titanium,ed. compiling group (CNNC, Peking, 1983), P442
(7) H.Margolin et al. Titanium's 80 Science qand Technology, ed. H.Kimura, O.Izumi (AIME, Warrendale Pa, USA,1980), Vol1,P189
(8) Y.Minonishi and S.Morozumi, "{1122} <1123> Slip in Titanium, " Scripta Metall, 16(4),1982, P427
(9) H.Wo,C. G.Li X.Z.Cai, " The effect of texture on the anisotropy of mechanical properites of TA5 ", Rare Metals (in Chinese) ,13(1),1989, P37

Structure/Property Relationships in Near Beta

Ti-V-Fe-Al Based Alloys

A.I.P. Nwobu, H.M. Flower and D.R.F. West

Dept. Of Materials, Imperial College,
London SW7 2BP, England.

Abstract

The effects of Al, Fe, V solute additions and combinations on the processing properties and the development of $\alpha + \beta$ microstructures in near β and β Ti-V-Fe-Al alloys including the Ti-10V-2Fe-3Al alloy have been investigated.

Observations show Al addition produces a wider hot $\alpha + \beta$ processing "window" even though it raises the β processing temperature. Al, Fe, V solute combinations control the deformation modes/mechanisms of metastable β and α'' martensites in the β-quenched alloys, and thus the alloys' cold-formability. Also the solute combinations control α precipitate morphology and mechanical properties of the age-hardened alloys. On the basis of these studies two near β alloys have been developed with good hot processing properties and strength/ductility/fracture toughness combinations superior to those of the Ti-10V-2Fe-3Al alloy.

Introduction

The processing (hot and cold) properties and mechanical properties reported for the near β and β Ti alloys vary substantially with alloy chemistry (1-4). This work is part of an investigation to understand the effects of alloying chemistry involving Al, Fe, and V on the processing and mechanical properties of near β and β Ti-V-Fe-Al based alloys including the Ti-10V-2Fe-3Al (Ti-10-2-3) alloy. Earlier observations of the Ti-10-2-3 alloy noted that high strength/good fracture toughness combinations are obtained in Ti-V-Fe-Al alloys containing Al:Fe ratio greater than unity (5), but no microstructural basis of this was given. Property combinations in Ti alloys depend strongly on microstructure. The work reported here is concerned with structure/property relationships and explains particularly why the strength/ductility/fracture toughness combinations shown by the age-hardened $\alpha + \beta$ microstructures observed in two near β Ti-V-Fe-Al alloys designated T1 and T2 are superior to those reported for similar microstructures in Ti-10-2-3 alloy. The constitution of the Ti-rich alloys of the Ti-V-Fe-Al system has been reported by the present authors previously (6,7).

Titanium '92
Science and Technology
Edited by F.H. Froes and I. Caplan
The Minerals, Metals & Materials Society, 1993

Experimental Methods

Table I shows the analysed compositions of ternary Ti-Fe-Al and quaternary Ti-V-Fe-Al alloys investigated. The compositions of two promising Ti-V-Fe-Al alloys, T1 and T2, are not given for commercial reasons. These two alloys were prepared as 30 kg ingots hot-processed to 30 mm plates by IMI Birmingham. IMI Birmingham reported that the alloys showed good hot-forging characteristics. The other alloys were made as 30 g arc-melted ingots hot-rolled at 650-700 °C to ~ 2 mm thick flat sheets. Typical oxygen levels are 0.12 - 0.15 wt %.

Cold-forming capabilities of the β quenched alloys at room temperature were monitored by using tensile tests or by thickness reductions (by rolling) of plate samples till their edges start to crack. Tensile properties of age-hardened alloys were obtained using round section specimens, 4.54 mm diameter and 16 mm gauge lenght with tensile axes along longitudinal (L) and transverse (T) sections of the rolled plates (Fig. 1). Three-point bend test fracture toughness specimens (of T-L and T-S modes, Fig. 1) with specifications B(14.5/13) x W(29/26) mm x span S = 4W and tests conforming to ASTM designation E-399-86 (8). were used to obtain toughness K_Q/K_{IC} values.

Structural analysis was carried out using X-ray diffractometry and/or transmission electron diffraction. Microstructures were examined using light, scanning (SEM) and transmission electron microscopy (TEM), and microanalysis conducted using the X-ray energy dispersive (EDX) analytical system attached to the SEM.

Results

Beta Transus Temperature and Beta Approach Curves

The β transus temperature (Table I) observed for the Ti-V-Fe-Al alloys agree reasonably well (Table I) with the relationship established by Yolton and others (9) between β transus temperature (T_β) and composition of the alloying elements i.e.

$$T_\beta = 882 - 12.4V - 8.4Fe + 23.4Al \quad (°C) \qquad (1)$$

for the V, Fe, and Al additions (in wt. %); Fe and V additions depress the β transus temperature while Al addition raises it.

Fig. 2 shows the β approach curves of the binary near β Ti-4.5Fe alloy (determined using binary phase diagram data, ref. 10) compared with those of some multicomponent alloys (determined experimentally). They show, as previously reported (6) that the slopes (% β/T) of the β approach curves of alloys are reduced by the addition of Al. The quaternary Ti-V-Fe-Al alloys could be regarded as alloys derived from the ternary Ti-Fe-Al alloys by replacing some Fe with the V equivalent, e.g. Ti-6V-3Fe-4Al alloy derived from Ti-4.5Fe-4Al alloy by replacing 1.5Fe by 6V assuming 1 % Fe equivalent to about 4 % V (11). The result (Fig. 2) is that the slope of the β approach curve of Ti-4.5Fe-4Al alloy is reduced by the partial V for Fe exchange.

Microstructures of Annealed Alloys

Fig. 3 shows typical microstructures obtained when the hot-rolled near β Ti-V-Fe-Al alloys are annealed at above and below the β transus temperatures. Annealing at temperatures in the high $\alpha + \beta$ field results in the small fraction of α phase pinning the β grain boundaries. For example Ti-6V-3Fe-4Al alloy with $T\beta$ at 842 °C, annealed at 870 °C for 1 h and at 820 °C for 7 days, produces β grains of average sizes 500 and 70 μm respectively (Fig. 3).

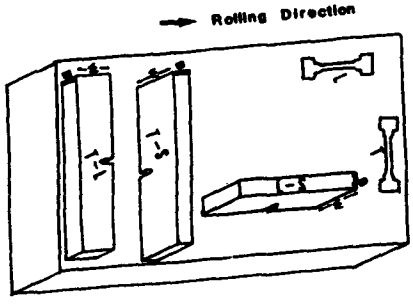


Fig. 1: Orientation code for tensile/ fracture toughness specimens.

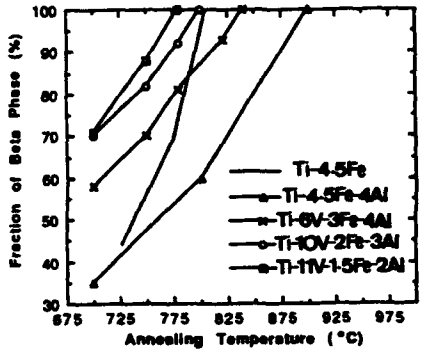


Fig. 2: β approach curves of alloys.

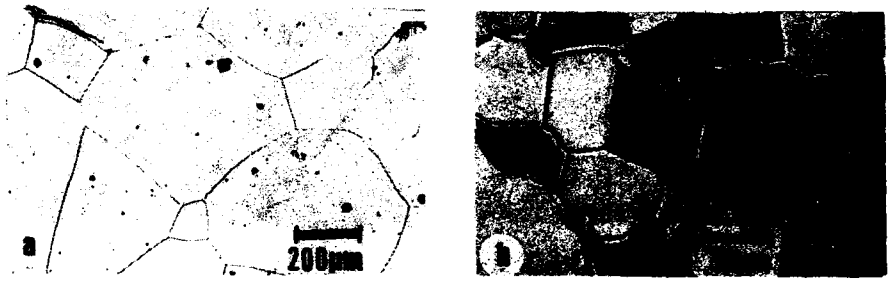


Fig. 3: Ti-6V-3Fe-4Al alloy annealed (a) at Tβ + 28 °C for 1 h and (b) at Tβ - 22 °C for 7 days and water quenched (Tβ = 842 °C).

Cold Deformation of β-Quenched Alloys

On deformation at room temperature the retained β phase in the near β Ti-Fe-Al and Ti-V-Fe-Al alloys containing less than 3 wt% Al transforms partially to α" martensite or α" and athermal ω (Table I, deformation increased the fraction of α"/ω present). In contrast the alloys containing 4 wt%Al or more shows complete or near complete transformations of β to α" martensite (e.g. β -> α" complete in Ti-4Fe-4Al alloy and partial transformations of β to α" and ω in Ti-4Fe-2Al alloy, Table I). Deformation of β by mechanical twinning is also observed in the near β alloys. Cold-formability is less in alloys that show transforma- tions of β to α" and athermal ω phases when compared to that of the alloys that show complete transformations of β to α" martensites (e.g maximum thickness reduction, MTR of 26 % for Ti-4Fe-4Al alloy compared to an MTR of 16 % for Ti-4Fe-2Al alloy that shows β -> α" and ω, Table I). Cold-formability is also improved by increasing the ratio of V:Fe in the alloys (e.g MTR of 20 and 38 % respectively for the Ti-4.5Fe-4Al and Ti-6V-3Fe-4Al

alloys, Table I). This is probably associated with the effects of solute V, Fe (and Al) on the twinning/twinning transitions in α" in the alloys. The twinning modes, (011), (112), Types I and II (111) are observed in the early stages of deformation of the alloys. Irrational (02δ) twinning (δ a fractional value between 2 and 3, Fig. 4) replaces the rational ones in later stages by a process which includes detwinning of the rational ones (e.g. in the transition of rational $(0\bar{1}1)$ to irrational (045) in Ti-10-2-3 alloy, Fig. 4b). Fracture of the alloys occurs after irrational twinning; thus after a low level of deformation in alloys that show low cold-formability (after 13 and 20 % deformation respectively in Ti-4Fe-2Al and Ti-10V-2Fe-3Al alloys, Fig. 4).

The metastable β phase in β Ti-Fe-Al and Ti-V-Fe-Al alloys containing up to 4 wt%Al deforms by slip and/or twinning (Table I). Al addition rather suppress twinning and favours slip as do the β solutes, V and Fe. For example deformation by {332}β twinning is observed in Ti-14V-2.3Fe-1Al alloy while Ti-14V-2.2Fe-3Al alloy show slip and the {332}β twinning only at the fracture zone (Fig. 5). The metastable β in Ti-10V-5Fe-3Al alloy deforms only by slip (Fig. 5). The tensile elongations 20, 14, and 27 % respectively

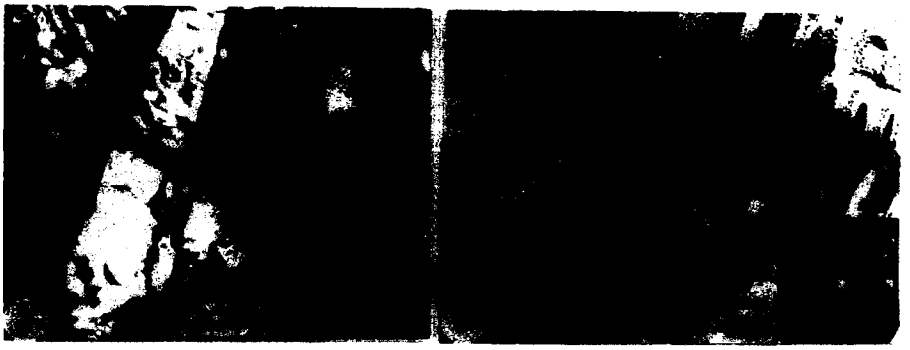


Fig. 4: (a) Irrational (067)α" twinning in Ti-4Fe-2Al alloy deformed by 13 % and
(b) rational R$(0\bar{1}1)$ to irrational IR(045)α" twinning in Ti-10V-2Fe-3Al alloy deformed by 23 % ([100]α" zone).

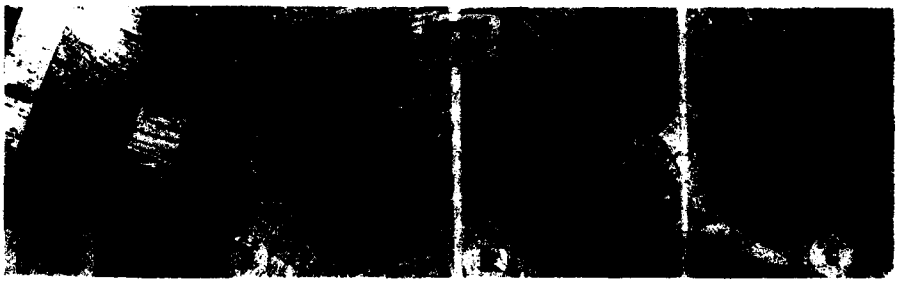


Fig. 5: Stress/strain-induced {332}β twinning respectively in (a) Ti-14V-2.3Fe-1Al and (b) Ti-14V-2.2Fe-3Al alloys; and slip in (c) Ti-10V-5Fe-3Al alloy.

for Ti-14V-2.3Fe-1Al, Ti-14V-2.2Fe-3Al and Ti-10V-5Fe-3Al alloys (Table I) show that a deformation that involves extensive slip in β followed by $\{332\}\beta$ twinning leads to lower ductility compared to the deformation that is mainly by slip or $\{332\}\beta$ twinning.

Ageing Reactions in Ti-V-Fe-Al Alloys

The authors previous work (6) has demonstrated that the TiFe compound observed in binary Ti-Fe and ternary Ti-Fe-Al alloys is suppressed in the quaternary Ti-V-Fe-Al alloys with V:Fe solute ratios (wt %) $\geq$ 2. In the near β Ti-V-Fe-Al alloys where the compound does not form the morphology of α precipitates in β matrix depends on the the ageing reactions from which the α precipitates are produced. The ageing reactions in turn depend strongly on Al content and the V/Fe combinations in the alloys.

The α" martensite in the quenched alloys generally reverts to the β phase prior to age-hardening reactions. The metastable β phase precipitates ω at low temperatures, α phase with an orthorhombic distortion at intermediate temperatures, and the α phase with no orthorhombic distortion at higher ageing temperatures. The alloys with 2-3 wt % Al, including Ti-10-2-3 alloy, rapidly forms ω phase up to 450 °C whereas those with 3.5-4.5 wt % Al forms ω phase at 350 °C and below, usually at slower rate. The effect is shown in Fig. 6 for the β-quenched Ti-11V-1.5Fe-2Al and Ti-11V-1.5Fe-4.4Al alloys aged in a salt bath at 450 °C for 24 h. The alloy with 4.4 wt % Al shows α plates of higher aspect-ratio and larger number of alignments compared to those observed in the alloy with 2 wt % Al (Fig. 6). The α precipitate distribution developed in the Ti-11V-1.5Fe-2Al alloy (Fig. 6a) via $\beta \rightarrow \omega + \beta$ reactions is similar to that which is said to form "sympathetically" in Ti-10-2-3 alloy (12). The morphology of α precipitate also depends on V/Fe solute ratio. For example the β-quenched Ti-6V-3Fe-4Al alloy with higher Fe:V ratio than Ti-11V-1.5Fe-4.4Al alloy also shows the α precipitate morphology of the low Al solute Ti-11V-1.5Fe-2Al alloy when aged also at 450 °C for 24 h, even though the $\beta \rightarrow \omega + \beta$ reaction was not involved in the α phase formation from metastable β phase. XRD study indicated that the initial α precipitate formed at 450 °C in the alloy has an orthorhombic distortion.

Mechanical Properties of Ti-10-2-3, T1 and T2 Alloys

T1 and T2 alloys are near β Ti-V-Fe-Al alloys in which the precipitation of α with orhorhombic distortion is depressed to below 450 °C and which shows when aged at > 400 °C α distributions of the type shown in Fig. 6b (α with high aspect-ratio and large number of alignments). In Figures 8a and 8b the tensile properties and corresponding fracture toughness values of the T1 and T2 alloys are compared to those observed in this study or reported previously (12-20) for Ti-10-2-3 alloy. The properties are associated with $\alpha + \beta$ microstructures obtained after the alloys forged in the $\alpha + \beta$ field were annealed at temperatures in the high $\alpha + \beta$ field and then aged at lower temperatures (typically 400-600 °C) to produce bimodal $\alpha + \beta$ structures (Fig. 7). It is worth noting that the values of the aspect-ratio of the primary α in the T1 and T2 alloys whose mechanical properties are presented are between 1:1 and 1:3 (Fig. 7), whereas the primary α in the Ti-10-2-3 alloy whose properties are compared with those of T1 and T2 alloys have aspect-ratio up to 1:8 (13,17). Fig. 8 shows that the yield stress/ductility/fracture toughness combinations of T1 and T2 alloys are superior to those of the Ti-10-2-3 alloy. For example at high yield stress level, 1300 MPa, T1 and T2 alloys show elongation/fracture toughness combinations of 5-12 %/50-72 MPa $\sqrt{m}$ compared to 2-10 %/25-30 MPa $\sqrt{m}$ observed for the Ti-10-2-3 alloy.

At the low yield stress level, 1050 MPa, T1 and T2 alloys show elongation/fracture toughness combinations of 15-18 %/83-108 MPa √m (T2 only) compared to 8-18 %/65-85 MPa √m observed for the Ti-10-2-3 alloy.



Fig. 6: α precipitation in β-quenched Ti-11V-1.5Fe-2Al (a) and Ti-11V-1.5Fe-4.4Al (b) alloys aged at 450°C for 24 h.



Fig. 7: Bimodal α + β structure in T2 alloy annealed at 800°C for 2 h and aged at 525°C for 8 h.

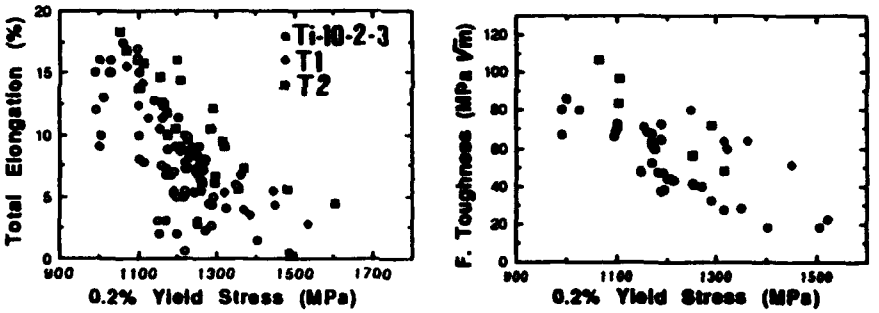


Fig. 8: Yield stress/ductility/fracture toughness relationships in Ti-10V-2Fe-3Al, T1 and T2 alloys (this work and others, ref.12-20).

Discussion

The result of present studies shows that the addition of Al to β-stabilised Ti alloys induces a wider hot α + β processing "window" even though it raises the temperature for β processing. Al also acts as a pseudo β stabiliser in the near β and β alloys by favouring β retention rather than α" martensite formation and slip rather than twinning in the β during deformation. The {332}β twinning in binary Ti-V, Mo, Nb alloys has been suggested as stress-induced and a dip in tensile elongation observed in the alloys at compositions at which deformation changed from twinning to slip (21). The dip in tensile elongation occurs probably at the compositions at which strain-induced twinning occurs after extensive slip. Observations of the stress-strain curves of Ti-V-Fe-Al alloys indicated that deformation by twinning induces a higher work-hardening rate compared to that by slip. Hence localised twinning after extensive slip raises local stress probably above the alloy's fracture stress.

The effects that Al, Fe, V solute combinations have on the twinning transitions in α'' martensite probably control the cold-formability of the α'' martensite in the near β alloys.

The effects of Al, Fe and V additions on the tensile properties/fracture toughness combinations in Ti-V-Fe-Al alloys have been shown to relate to the control of ω phase precipitation and α precipitate morphology by using optimum Al/V/Fe solute combinations. Since fracture toughness of $\alpha + \beta$ and near β alloys usually improve with the increase in the value of the aspect-ratio of the primary α phase the fracture toughness values of the T1 and T2 alloys (superior to those of Ti-10-2-3 alloy) are likely to be raised further by increasing the ratio to above 1:3 through change in the processing conditions of the alloys.

Summary

1. Al addition (to near β and β Ti-V-Fe-Al alloys) which suppresses embrittling ω and strengthens the α phase induces a wider hot $\alpha + \beta$ processing "window" even though it raises the β processing temperature. It also favours the retention of metastable β phase and slip rather than twinning in the β during deformation as do β solutes V and Fe.

2. Cold-formability of alloys is related to the deformation modes/mechanisms in the metastable β and/or α'' martensites. Al, Fe, V solute combinations are used to control the deformation modes/mechanisms.

3. Al, Fe, V solute combinations also control the structure and morphology of α precipitates in β. Two near β Ti-V-Fe-Al alloys with good hot-processing properties and $\alpha + \beta$ structures which induce strength/ductility/fracture toughness combinations superior to those of Ti-10-2-3 alloy have been developed.

Acknowledgement

This work has been carried out with the support of Procurement Executive Ministry of Defence.

References

1. B. Vandecastle, N. Rizzi, and J.F. Wadier: Sixth World Conference on Titanium, ed. by P. Lacombe, R. Tricot and G. Beranger; (les ed. J. de Phy., 1988), 1325-1338.
2. G. Schrodern and T.W. Duerig: Titanium Science and Tech., ed. by G. Lutjering, U. Zwicker and W. Bunk; (D.G.M. Press, 1985), 585-592.
3. A.I.P. Nwobu, H.M. Flower and D.R.F. West: ref. 1, 1583-1588.
4. R.W. Judy; ref. 2, 1925-1944.
5. W.M. Parris and H.W. Rosenberg: U.S. Patent, 1974, No. 3,802,877.
6. A. Nwobu et al.: User Aspects of Phase Diagrams, ed. by F.H. Hayes; (Inst. of Metals Publ., 1991), 102-112.
7. A.I.P. Nwobu, H.M. Flower, and D.R.F. West: Material Sc. and Tech., 7 (1991) 391-398.
8. Annual Book of ASTM Standards, (1986), Sec. 3, Vol. 03.01.
9. C.F. Yolton, F.H. Froes, and R.F. Malone: Metall. Trans., 10A (1979) 132-398.
10. J.L. Murray: Bulletin of Alloy Phase Diagrams, 2 (3) (1981) 393-394.
11. F.H. Froes and H.B. Bomberger: J. of Metals, 37 (July 1985) 28-37.

12. G. Terlinde, T.W. Duerig, and J.C. Williams: Metall. Trans., 14A (1983) 2101-2115.
13. G.T. Terlinde, H.-J. Rathjen, and K.-H. Schwalbe: Metall. Trans., 19A (1988) 1037-1049.
14. C.C. Chen and R.R. Boyer: J. of Metals, 31 (July 1979) 33-39.
15. R.R. Boyer: J. of Metals, 32 (March 1980) 61-65.
16. T.W. Duerig, J.E. Allison, and J.C. Williams: Metall. Trans., 16A (1985) 739-751.
17. R.R. Boyer and G.W. Kuhlman: Metall. Trans., 18A (1987) 2095-2103.
18. S. Muneki, Y. Kawabe, and J. Takahashi: J. Jap. Inst. of Metals, 51 (10) (1987) 916-922.
19. M.H. Campagnac and A. Vassal: ref. 1, 1619-1624.
20. J.F. Uginet: Ref. 1, 1301-1306.
21. S. Hanada et al.: ref. 1, 105-110.

Table I

Analysed ++ Composition (Wt. %)	Tβ Observ. (°C)	Tβ Calc. (°C)	β Quenched Structr.+	Deformed Structr.+	MTR/ Tensile Elong.* (%)
Near β Alloys					
Ti-4.1Fe-2Al			α" + β + ω	α" + β + ω	16±3
Ti-4.6Fe-2Al			Tr.α"+β+ω	α" + β + ω	20±3
Ti-4Fe-4Al			Tr.α" + β	α"	26±2
Ti-4.5Fe-3.9Al			Tr.α" + β	α" + Tr.β	30±2
Ti-6V-3Fe-4Al	842	865	Tr.α" + β	α"	38±3
Ti-11V-1.4Fe-2.2Al	780	781	α" + β	α" + Tr.β	35±2
Ti-13V-1.5Fe-2.1Al	755	755	β	Tr.α"+ β(t)	64±2
Ti-11V-1.5Fe-4.4Al	820	831	α" + β	α"	50±2
Ti-13Fe-1.6Fe-4Al	790	796	β	α" + Tr.β	62±2
Ti-10.3V-1.7Fe-3Al (Ti-10-2-3)	804	810	α" + β	α" + Tr.β	27±3
β Alloys					
Ti-5.3Fe-2Al			β	β(t)	26±3
Ti-5.1Fe-4Al			β	β(t)	24±3
Ti-14.1V-2.3Fe-1Al	705	711	β	β(t)	19.9*
Ti-14.3V-2.2Fe-3Al	752	756	β	β(slip,t_s)	13.9*
Ti-9.7V-4.9Fe-2.7Al	772	784	β	β(slip)	26.8*

++ EDX analysis; + based on XRD analysis; Tr. trace quantity.
t twinning; t_s strain-induced twinning.
MTR maximum reduction in thickness prior to edge cracking in cold rolling.
Tβ β transus temperature.

STRUCTURAL STRENGTHENING OF THE HIGH CONCENTRATION

TITANIUM ALLOYS WITH TRANSITION METALS.

L.K.Kondratenko and V.F.Shamray.

Baykov A.A. Institute of Metallugy, RAS
117911, Leninsky pr., 49, Moscow, Russia.

Abstract

The binary alloys of titanium with transition metals - vanadium (from 10 to 22 at.%V), niobium (from 10 to 30 at.%Nb) and molybdenum (from 6 to 16 at.%Mo) examined by means of X-ray. The dependence of hardness of the quenched from β-region alloys and quenched from β-region and then aged at 400 ^{o}C alloys from their composition is presented in the paper. It was found out that during the low temperature ageing ω-phase completely decomposes. The decomposition of ω-phase proceeds with the formation of the metastable or equilibrium fine crystalline α- and β-phases. The highest strength is obtained for the alloys with the high heterogeneous structure. This effect can persist in stable alloys with fine structure without fragile phases up to 400 ^{o}C.

For titanium alloys with transition metals, transformations associated not only with polymorphism of titanium but also with the formation and breakdown on quenching and annealing of intermediate metastable phases are characteristic. These processes are complex, and a have great influence on the physical and mechanical properties of the alloys. As known the concentration of transition metals in titanium alloys is limited by 5-10 % by weight in sum. It is often connected with formation of fragile ω-phase in titanium alloys of definited concentrations. The concentration range over which ω-phase is formed on quenching has been estabilished already [1] and data have been published [2] on the composition and morphology of ω-phase precipitated during ageing, but there are still many inadequately understood aspects of the mechanism whereby equilibrium structures are attained.

A great deal of titanium alloys using in industry are binary and consisting of α- and β-phases. First of all the properties of $\alpha+\beta$-alloys are determined by their composition. In Ti-V, Ti-Nb and Ti-Mo sistems the hardness of equilibrium alloys depends additively on their composition

Titanium '92
Science and Technology
Edited by F.H. Froes and I. Caplan
The Minerals, Metals & Materials Society, 1993

(Fig.1, curve 1,5 and Fig.2, curve 1). The data on hardness for α-solid solution have been published in [3] and for β-solid solution in [1,4,5]. Strengthening achieved by such alloying elements as V, Nb or Mo is too weak, and farther strengthening of these alloys is connected with the possibility of using metastable states and structural strengthening by heat treatment.

In present work the strengthening of high alloyed binary systems Ti-V (10-22 at.%V), Ti-Nb (10-30 at.%Nb) and Ti-Mo (6-16 at.%Mo) is studied with X-ray diffraction methods. The alloys were prepared from iodide titanium and vanadium, niobium, molybdenium made by electron-beam remelting. Ingots weighting 10-12 g were made by crucible-less melting in a helium atmosphere and homogenised by annealing in vacuo for 30 min at 900 °C, specimens were quenched in water and aged at 400 °C. Ageing at 400 °C including appearance

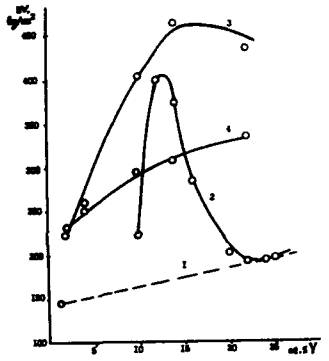


Fig.1. Influence of the composition on the hardness of Ti-V alloys according to additively(1), after quenching from the β-region(2) and subsequent ageing at 400 °C for 1,5 h(3), 150 h(4).

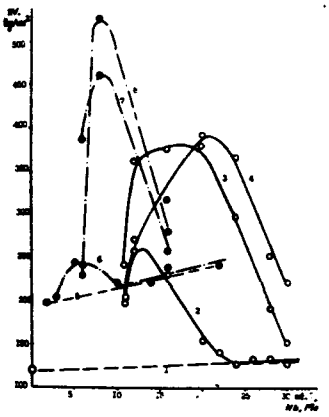


Fig.2. Influence of the composition on the hardness of Ti-Nb (light points) and Ti-Mo (dark points) alloys according to additively(1,5), after quenching from the β-region(2,6) and subsequent ageing at 400 °C for 1,5 h (3), 50 h(7), 150 h(4) and 700 h(8).

of ω-phase has been used to receive high structure strengthering. As noted above they try not to receive this phase. Alloys phase composition and composition of phases can be determined using metastable phase equilibrium diagrams for Ti-V and Ti-Nb sistems shown in Fig.3a,b, diagram for Ti-Mo system is analogous. Fig.3a,b include the equilibrium phase diagrams. Thus the transformation of metastable β-solid solutions in this alloy composition range to equilibrium phases which differ substantially in composition and intermediate phases with smaller composition and structure differences are formed on the way. The ω-phase is incapable of particle growth, whether it appears on quenching or during ageing. Longer ageing let to eventual breakdown of ω-phase to metastable $\alpha_м$- and $\beta_м$-phases with smaller composition differense than in α_{equil}- and β_{equil}- equilibrium

phases. Close to equilibrium phase composition is achieved by prolonged ageing: 150 hours for Ti-V and Ti-Nb alloys and more than 700 hours for Ti-Mo alloys.

Fig.1 (curve 2) and Fig.2 (curves 2 and 6) show the hardness of the alloys after quenching at 900 °C, 30 min, water. The hardness of quenched alloys varies nonmonotonic and does not depends on the alloys composition but depends on their phase composition. The HV increase connects with forming of ω-phase during quenching. The hardness maxima correspond to alloys containing 6 %Mo, 12 %Nb, 14 %V. The ageing promotes increasing of the alloys hardness, and additional relatively to the quenched state amount of ω-phase is forming in these alloys. The dependence of the alloys maximum hardness on the holding time in ageing is shown in Fig.1 (curve 3) and Fig.2 (curve 3 and 7). In all these alloys, in early stages of ageing, ω-phase formation leads to increase in HV. It is well known that it is impossible to use the alloys with such kind of structure in practice. But it is very important that longer ageing leads to complete breakdown of ω-phase. The result of this breakdown is the formation of pseudo-equilibrium ($\alpha_m + \beta_m$) state containing: α_m=6 %V, β_m=33 %V for Ti-V alloys; α_m=9 % Nb, β_m=30 %Nb for Ti-Nb alloys and α_m=3 %Mo, β_m=18 %Mo for Ti-Mo alloys. Precipitations of ω-phase is absent in these alloys and high hardness in wide composition range is only a structural effect.

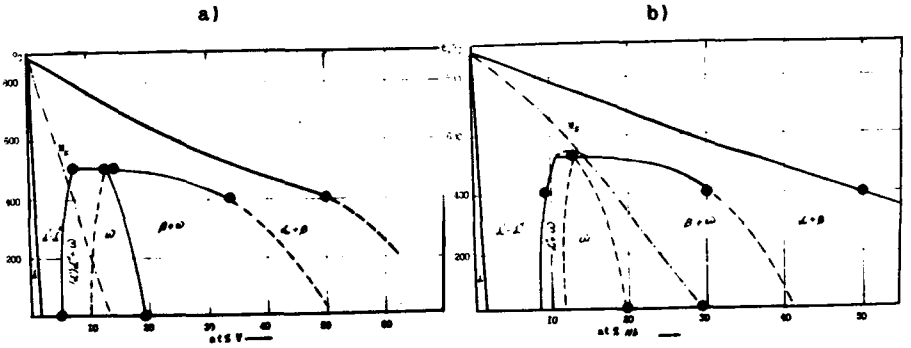


Fig.3. Diagram of metastable phase equilibria and equilibrium diagram of state of the Ti-V(a) and Ti-Nb(b) sistems.

Therefore, these alloys possess high heterogeneous structure. The properties of the alloys are high when the phases achieve their equilibrium composition - α_{equil} and β_{equil}. The alloys keep fine-disperse structure, and this is a reason of high structural strenghening effect. In both cases phases heterogeneity was estimated according to quantitative correlation of α_m- and β_m-phases. From the data presented in Fig.1 (curve 4) and Fig.2 (curves 4,8) one can see that HV maximum displaces to 20-22 %V or Nb and 8 %Mo for alloys with (α_{equil}+ β_{equil}) structure in comparison with the alloys with the greatest quantity of ω-phase. The (α_{equil}+β_{equil}) alloys have high heterogeneous structure. Comparison of estimated additive hardness of (α+ β

titanium alloys and hardness of equilibrium ($\alpha_{equil}+\beta_{equil}$) alloys formed after breakdown of ω-phase shows that the hardness can be increased in 2-3.5 times only by achieving fine-disperse heterogeneous structure. The structural strengthening is more effective in Ti-Mo and Ti-Nb alloys, less effective in Ti-V alloys.

Taking into account close values of atomic radii bu of Ti and Nb and nonconsiderable difference of the volumes for α- and β-phases ($V_{\alpha\ equil}$= 17,67 Å^3/at., $V_{\beta\ equil}$=17,66 Å^3/at.) one can make the conclusion that elastic stresses connected with volume phase difference in geterogeneous alloys of this sistem does not have influence on the increase of deformation resistance. The eventual breakdown of ω-phase leads to the formation of a fine-grained structure, which is responsible for structural strengthening. This factor has never been discussed or used as an effective method of prepearing high-strengthened titanium alloys. Thus we can obtain high-strengthened state of alloys with stable structure without additional alloying elements or heat-mechanical treatment. The practical use of the process demands special investigation, but for separate groups of alloys ageing including forming of ω-phase and its complete breakdown can be used to attain a strong strengthening effect. But it is very important that this effect can be achieved only by obtaining high heterogeneous structure. It can be seen from metastable and stable equilibrium phase diagrams, that the compositions of the alloys with most heterogeneous structure determined according to the diagram of metastable phase equilibria and according to the equilibrium diagram, are nearly the same (Fig.3). Meaning the problems connected with drafting of equilibrium state diagrams, especially for low temperaturs the metastable phase equilibria are suggested to be used to forecast the properties of the alloys of various sistems.

Employing the presently obtained data on size and stability of the phases formed after decomposition, it is possible to forecast definite type of the microstructure in alloys - an important consideration as soon as numerous properties are determined not only by phase composition, but by size and state of structure constituents, as well. Thus, low-temperature ageing can make use of structural state alone to attain a strong effect of stable alloy strengthening. This effect can persist in alloys without frangile phases until as high as 400 °C.

References

1. L.N.Guseva and L.K.Dolinskaya*), "Metastable phases in quenched alloys of titanium with transition elements", Proc. 3rd International Conference on Titanium, Moscow,1976[in Russian], Moscow, VILS, 1978, 573.
2. B.S.Hickman, "Omega phase precipitation in alloys of titanium with transition metals", Trans.Met.Soc.AIME, 245, 1969, no.6, 1329.
3. W.Tsviker, Titanium and its Alloys (Moscow, Metallurgia, 1979), 108.
4. L.N.Guseva and L.K.Dolinskaya, "Phase transformations in

titanium-vanadium alloys during hardening and tempering". Izvestiya Akademii Nauk SSSR.Metally, 1984, no.2, 120.

5. L.K.Kondratenko and L.N.Guseva, "Phase transformations in alloys of titanium with niobium on quenching and tempering", Izvestiya Akademii Nauk SSSR. Metally, 1989, no.1, 89.

*)
Dolinskaya is the former surname of Kondratenko.

ALLOY THEORY AND PHASE TRANSFORMATIONS

To academician A. F. Belov and professor R. Jaffe, who brought a great contribution to the development of titanium science and industry, we devote this paper.

THEORY OF ALLOYS AND PHASE TRANSITIONS

I. S. Polkin *, S. G. Glazunov**, A. A. Ilyn***

* All-Russia Institute of Light Alloys,
** All-Russia Institute of Aviation Materials,
*** Moscow Aviation Technology Institute.

Titanium is properly different from other light metals, aluminium and magnesium, by its polymorphism like iron has. This property gives the broad opportunities for titanium alloys structure and properties influence because it allows to use not only metastable solid solutions decomposition at quenching and ageing, but the allotropic $\alpha \rightleftharpoons \beta$ transformation with some intermediate phases and chemical compounds that gives the broad spectrum of structures and properties. In the starting period of the titanium alloys theory development the main attention was pointed at the data base gathering about alloying elements influence on the titanium strength and the corresponding phase diagrams establishing.

To the finish of 60th the titanium alloys almost with all elements of periodic system were studied more or less carefully. As a result of these investigations the titanium alloys theory bases were established as described below.

1. The most prospect alloying elements group was defined, their influence on allotropic titanium transformation temperature, solid solution regions with the both titanium allotropic modifications and the influence on properties complex were determined (Fig. 1). The basis titanium alloys classification by the structure type and alloying elements classification by their influence on titanium allotropic transformation temperature were established. The opportunity of additive estimation the joint β -stabilizers influence by β -stabilizing coefficient entering for each component being investigated (Fig. 2). This theoretical postulate simplifies the structure and properties prediction at the multicomponent titanium alloys developing.

The important part of titanium alloys and phase transformations theory is the undesirable eutectoid decomposition bracking possibility in chromium and iron containing alloys by β - stabilizers (molybdenum, for example) doping. This allow to get the necessary thermal stability level. The example of this relationship is broadly usable in Russia VT3-1 alloy.

Titanium '92
Science and Technology
Edited by F.H. Froes and I. Caplan
The Minerals, Metals & Materials Society, 1993

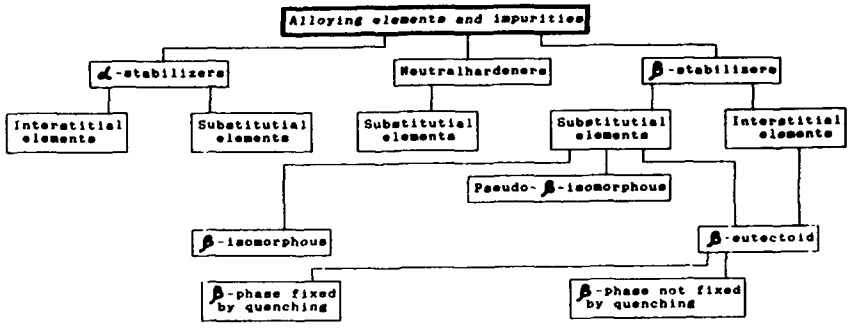


Figure 1 - Classification of alloying elements and impurities in titanium (by S. G. Glasunov, B. A. Colachev).

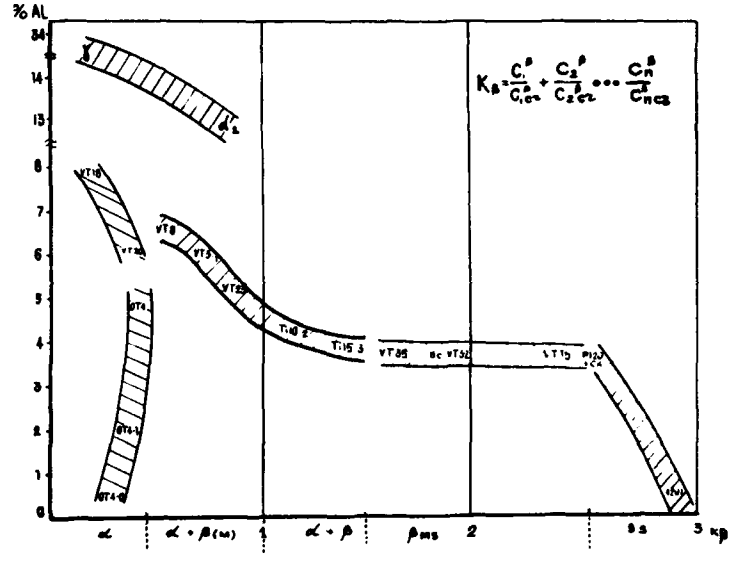


Figure 2 - Ti-Al system as a base of industrial titanium alloys K (comparable concentrations of β-stabilizers).

2. The main titanium particularities which differs it from other construction materials were pointed. The high chemical activity in melted conditions and under high temperatures in solid state gives the ability to form the alloys with gases of atmosphere and hydrogen. The high chemical resistance of titanium oxide is the main obstacle for manufacturing method development of pure titanium gathering by the direct oxide

ores reduction. These physical and chemical properties of titanium are the powerful stimulus for new metallurgy branches developing,for example, haloid metallurgy, magnesium thermal metallurgy - by Croll, natrium thermal metallurgy by Hanter, iodide metallurgy - by Van Arcel and de Boer, and vacuum melting in copper water cooled crucible.

3. The practical use of oxygen, nitrogen and hydrogen alloying of titanium, that earlier were considered as determinal impurities, which concentration must be minimal, was pointed.

The large importance for titanium problem considering as reliable construction metal its interaction with hydrogen studying has. It was pointed that hydrogen, which is β-stabilizer with reversable solubility in titanium, is the powerful facility for phase and structure transformations in titanium alloys managing. The titanium alloy thermohydrogenous treatment was developed, which is principally new technological process combining the thermal treatment with reversable hydrogen alloying. This process includes three stages: metal hydrogenization till necessary concentration, thermal treatment, and vacuum annealing for hydrogen concentration decreasing till safe concentration. It was pointed that thermohydrogenous treatment allows to manage the deposited phases morphology during quenching material ageing: to transform the platelike structure in fine-graining equiaxial one with the mechanical properties increasing; to increase the two-phase $\alpha + \beta$ alloys hardenability; to harden the pseudo-α-alloys by thermal treatment.

The thermohydrogenous treatment of titanium alloys is in its initial stage, but its potential possibilities are very high. For example, the opportunity of technological plasticity increasing of hard -structure alloys is opening by their temporary transition into more plastic two-phase alloys type. For high strength two-phase alloys the opportunity of improving hardenability arises by temporary transition these alloys in pseudo-β or β-alloys (Fig. 3).

It is known that castings has the lower mechanical properties level than forgings of the same alloys. The reason of this fact is the remaining porosity and coarse-grained structure of cast metal. The first disadvantage is removed by hot isothermal treatment in gasostates. The structure refining and its transition from platelike to equiaxial one with simultaneous grain refining is get by hydrogen-thermal treatment. The phase hardening being arised as a result of specific volume variations under such a treatment substitutes the deformation, which was considered as the only one method of cast material mechanical properties radical increasing some time ago. This effect may be reinforced by another new process using-thermocycling. This allows to approach the cast metal properties level to the deformed metal one (Fig. 4).

4. As the experimental materials about titanium alloys were gathered the titanium-aluminium system role become more clear as the basis of practically all commercial titanium alloys. It is explained by the fact that the most of alloying ele-

ments are β-hardeners, but aluminium is one effective α-phase hardner. The titanium alloys theory pointed that the titanium alloys mechanical properties optimal complex is achieved at equal strength of both α and β phases. Tin and zirconium harden the α-phase too, but not so effective as aluminium does. Aluminium decreases the titanium alloys density, and tin and zirconium increases it. Under the large volumes of titanium alloys manufacturing the economical factor has its importance as aluminium cost is lower than zirconium and tin one, and titanium too. Aluminium more effective increases the high-temperature strength than other elements, and in large quantities decreases the titanium oxidizability and inflammability.

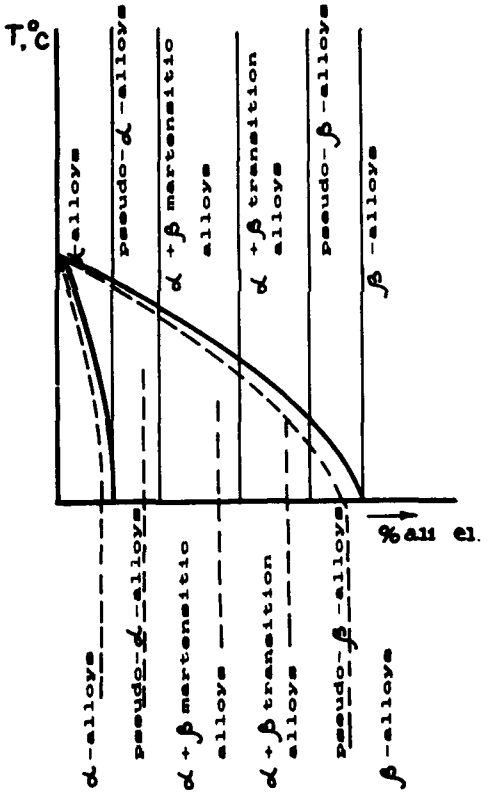


Figure 3 - Transformation of Ti-β-stabilizers diagram after additional alloying by hydrogen: ___ usual constitutional diagram; - - - the same after addition of hydrogen.



a b c

Microstructure of casting VT5L alloy
a - as cast;
b - 0,9%H2+vaccumannealing;
c - 0,5%H2+termocicling (5 cicles)+vaccumannealing.

Condition of Ti-6Al-4V alloy	Endurance limit 10x7 cicles, bending
cast+annealing	430-456
cast+quenching+ageaning	528-596
cast, termohidrogen treatment	700-736
deformed, annealing	458-686
deformed, quenching+ageaning	630-700

Figure 4 - Improving microstructure and endurance limit after thermo-hydrogenous treatment.

The next investigations opened another important property of aluminium - the opportunity of light high-temperature strength alloys of new type forming on the base of titanium and aluminium chemical compounds, that allowed to increase the titanium effective usage temperature till 900 °C to concure with nickel superalloys.

Exept titanium-aluminium chemical compositions mononickelide NiTi has theoretical and practical interest, it has the homogeneity region of 54-58 mass. % and is the base of new alloys with special properties development.

The possible using branches may be as: for heat energy direct transformation to mechanical work; as sensitive thermomechanical transducer; for self-unrolling aerials, masts etc.; chemical equipment (corrosion resistance); for up-water and under-water ships (ultrasound absorption, wear resistance, corrosion resistance); as a material with high wear resistance and demping capacity standing up to an impact demphering equipment in motor transport; as a material able to do mechanical work till many cycles (many thousands) when any reversing equipment is; in medicine (internal prothesis etc.); for producing rivets with shape memory; for self-working conjuctive couplings for pipe-line; for new constructions of apparatus and equipment, working on the base of shape memory effect. The shape memory effect is of a great interest.

It appears in these alloys because of reversable martensite transformation which causes the reversing of shape having been took place before plastic deformation. This effect may be varied by additive alloying in temperature interval defined by working conditions. The good example is conjuctive coupling of pipe-lines of "cryofit" type and self-unrolling aerials of space ships (Fig. 5).

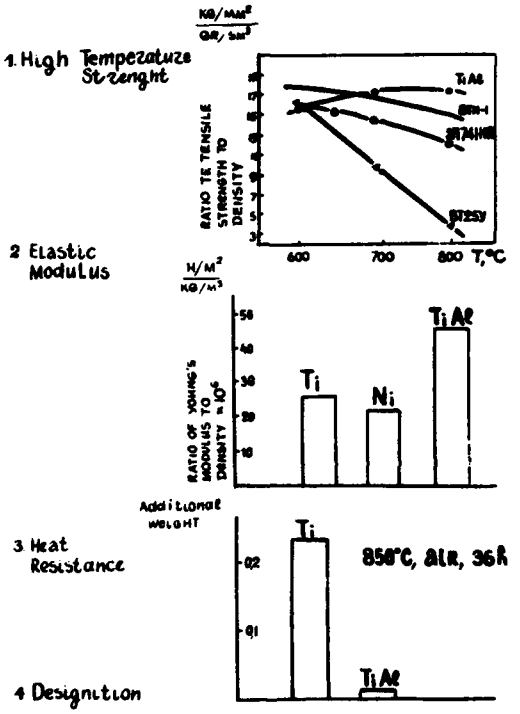


Figure 5 - The advantages of TiAl-based alloys.

The other high-doped titanium alloy is titanium-niobium system alloy based one, having high superconducting effect, and thus, having practical using in speed railway transport with magnetic suspension.

In the paper / / is pointed the using of composite material "Tor-Supra" superconductors. This material is superconductive wire consisting of 10^4 fibres of 22 mkm dia of titanium - 36.8 at. % niobium alloy in copper and copper-nickel matrix.

5. The using of last achievement of titanium alloys, structure and phase transformations theory in alloying and new technology using allows to increase strength in broad temperature region (-253 - +600 °C) in 6-8 times.

Fig. 6 shows that by rational alloying and thermal treatment at room temperature the titanium alloy strength may be increased from 25 to 150 kg/mm^2 under cryogenic temperature -

from 80 to 160 kg/mm^2, at 600 °C the temporary strength increases from several kg to 60-80 kg/mm^2.

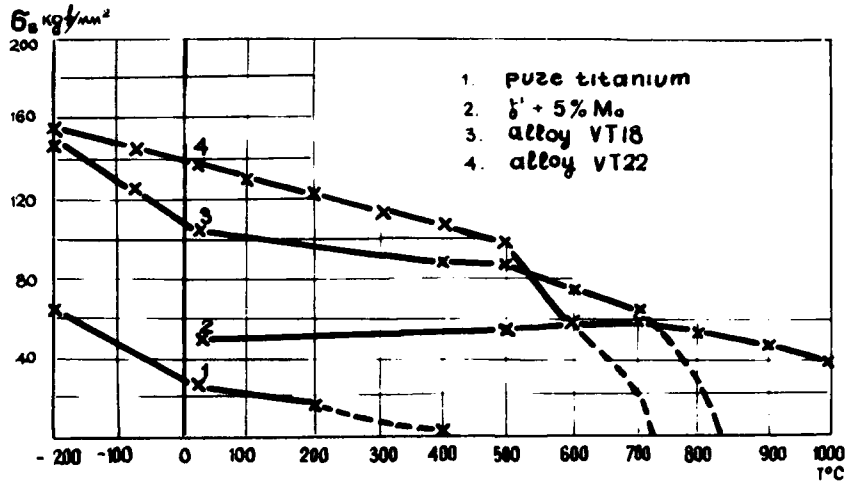


Figure 6 - Strength of titanium and its alloys at different temperatures.

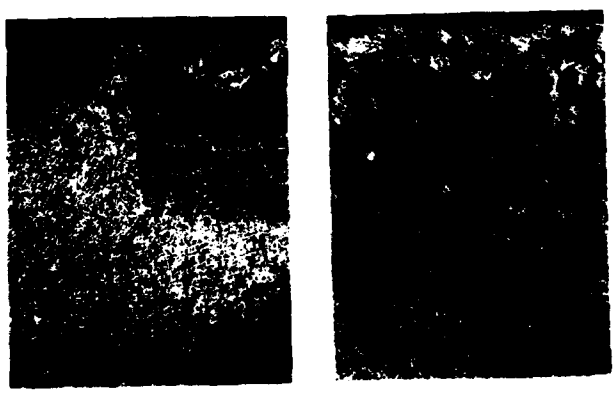
6. The high structural sensitivity of titanium alloys allows by structure varying to effects comparable with alloying. This confirms indirectly by some decelerating of new composite titanium alloys appearance last time. New methods of influence on titanium alloys structure and properties lead to new branch of titanium alloys theory appearing, which may be named "structural engineering".

The structural engineering includes metal alloys reliability new criteria appearing, as fracture toughness, fatigue crack propagation speed, and as for structure - the optimal structure defining for branches of using. Many achievements were done in melt cooling rate influence at titanium alloys properties and structure investigation, even for amorphous material of type with unique properties complex producing. The results of rapidly quenched layer on the titanium alloys surface producing by laser beam heating experiments may serve as examples. It is shown in Table 1 that structural modification allows to increase the fatigue characteristic of initial coarse grained structure in 1.5-1.7 times and at 10 % of fine grained structure. The structure of modificated layer is shown in Fig. 7.

Macro- and microcomposite materials are new materials. They are semiproducts of high strength and intermetallide alloys, strengthened by silicium carbide fibres or other high-strength fibres.

The developing of structural engineering is mechanical alloying bases on solid phase components interaction. Other than

composite materials the components physical-chemical influence is not only allowed but is the base of new type material production process. The characteristic properties of this process are briefly given below:
- supersaturated unstable solid solutions producing ability;
- dispersed unsoluble solid solutions of oxides, nitrides, carbides strengthened alloys producing with the aid of high temperature strength, high temperature resistance and thermal stalility increasing. The special meaning has the strengthener and matrix interaction investigation under working temperatures;
- composition of two low- or unsoluble in themselves components producing;
- materials without liquation, coarse cast structure and easily melting eutetics producing ability.



A B

INITIAL STRUCTURE	σ_{-1}, MPA.	Nb-2x10 7
	without treatment	after laser treatment
COORSE LAMELLAR (A)	300-330	450-480
FINE GLOBULAR (B)	520-550	570-600

Figure 7 - Influence of laser-treatment on mechanical properties of VT3-1 alloy.

The processes connected with melted metals superrapid cooling and alloys production by metal gas condensation on cooled base are investigated now. Metals and alloys producing with nanostructure is to be considered as the limit case, and it may be named the most impressioned structure engineering achievement. Surely for titanium alloys mechanical properties increasing even for pure titanium and low-alloyed Ti-alloys.

Table 1 - Laser Treatment Influence on VT3-1 Alloy Mechanical Properties

Initial structure	G_{-1}, MPa	$Nb \approx 2 \cdot 10^7$ cycles
	without laser treatment	with laser treatment
Coarse grained platelike	300-330	450-480
Fine grained globular	520-550	570-600

During last 15-20 years many investigation of superrapid cooling (SRC) influence on metal alloys structure and properties were undertaken. This fact can be explained by some advantages of superrapid cooling technology using in high strength, high temperature strength and special alloys producing.

SRC allows to produce the homogeneous alloys of basic metal with any alloying elements exetp the cause of dismixing (enlayering) in liquid state. SRC method broadens the different usage alloys producting abilities including new type alloys with increased mechanical and special properties.

SRC allows to broaden the solid solutions regions in basic binary systems, which manufacture alloys are based on and to increase the strengthening heat treatment effect. The possibility of thermally stable disperse strengthening is appearing and increased the high temperature strength and creep resistance alloys producing. SRC combined with today powder metallurgy methods allows to produce superfine microstructure and chemical composition for any size and mass products in the limits of technological equipment size.

It is known that under cooling rate increasing the degradation of equilibrium phase diagram takes place as it is shown in Fig. 8. We can seen that with cooling rate increasing the solid solutions region are enlarged, the specific points of diagram, as eutectic, peritectic points, chemical compounds are disappeared. The diagram simplifying and its transformation in continous solid solutions system takes place. Then the solid-liquid state regions disappear, the liquidus and solidus become one line and liquid state exists above it, solid state - below it.

The solid material being producted in this case is amorphous or glasslike and has some specific properties. It has no crystallic lattice and grain boundaries. Amorphous alloy is homogeneous by its chemical composition when compared with traditional technology of production alloy by casting.

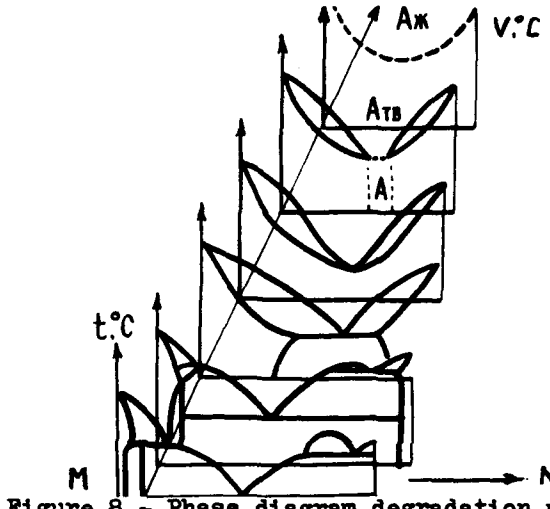


Figure 8 - Phase diagram degradation with increasing of cooling rate /7/.

Phase Transformation in Titanium Alloy

All phase transformation taking place in titanium alloys under heat and pressure treatment are based on allotropic $\beta \rightleftarrows \alpha$, $\beta \rightleftarrows \omega$ and $\alpha \rightleftarrows \omega$ transformations in titanium according to theories in polymorphic metals based alloys one modification to another transition must occur by shift. This gives us idea different from existed before, that under all temperature-rate conditions of thermal and thermomechanical treatment the main nucleous new phase forming is shifting. The final structure forming depending on kinetic conditions may occur by diffusionless (martensitic) or middle (diffusionless nucleation with diffusion growth) mechanisms. Some examples illustrating this idea are given below.

1. The transformation $\beta \rightarrow \alpha'$, $\beta \rightarrow \alpha''$ and $\alpha \rightarrow \omega$ are martensitic ones (MT) of the first kind, which occur under temperature or pressure with positive or negative hysteresis changing. MT $\beta \rightleftarrows \alpha''$ is reversible not only crystallographically but thermally too, that allows to provide shape memory effect (SME) (Fig. 9) and high demphirity /2-4/ plus to twin strain mechanism with invariant lattice.

2. Other than existing new points of view say, $\beta \rightleftarrows \omega$ and $\alpha \rightleftarrows \alpha''$ transformations we can investigate as shift hysteresisless transformations developing by slip mechanism /5-6/. They are transformations near second kind of transformations, which provides the continuous thermodynamic potential differing under these transitions and coherent spinodal exiting (Fig. 10). For example, β_m to ω_{at} transition occurs by some β (ω) condition, which is characterized by "incommensurable" structure.

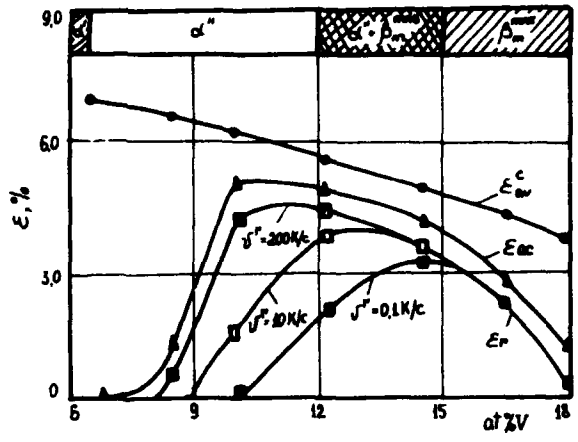


Figure 9 - Changing in crystallographically reversable (ε^c_{av}) accumulated under stressing (ε_{ac}) and recovered (ε_r) by SME deformation in Ti-5Al-V alloys during $\alpha'' \rightleftarrows \beta$ MT (ϑ^r - heating arte).

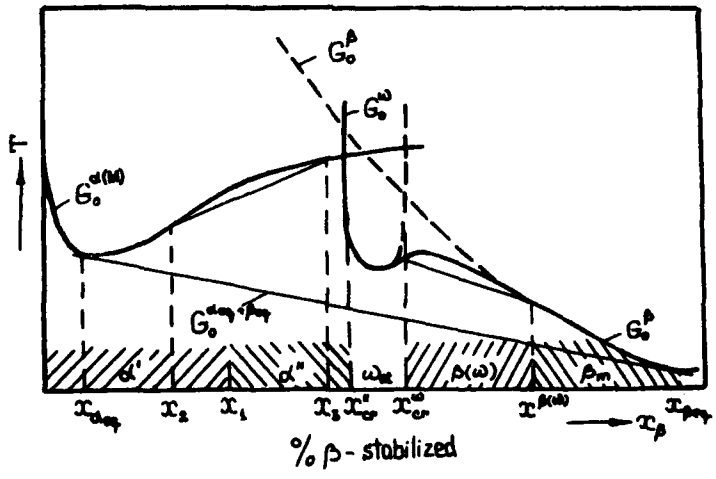


Figure 10 - The diagram illustrating phase thermodynamic potential change in titanium-β-isomorphic stabilizer system (Ti-x_β) without concentration fluctuation calculating (x_1-x_3 and x^ω_{cr}-$x^{\beta(\omega)}$ -spinodal).

3. Fig. 11 shows the temperature-concentration regions where the for-precipitating stage provides the different nucleation ways. The new phase nucleation under β_m-phase and α'' mertensite decomposition in temperature region contact to M_s and A_s,

correspondingly, may occur by homogeneous nucleation way by concentration fluctuations, and in regions far from M_s (A_s) β_m-phase and α' phase decomposition occurs by heterogeneous nucleation on grains and subgrains boundaries and on plane dislocations accumulations. Decomposition of α' - and α'' -martensite in alloys of concentration near x_1 ($\alpha' \rightleftarrows \alpha''$ transition) and decomposition in incommersurable β (ω)-structure alloys occurs by spinodal decomposition mechanism. This allows us to say that ω_{gr} and ω_{is}-phase forming mechanisms are adequate and explain the ω_{is}-phase precipitation process insensibility to dislocation construction and its high rate.

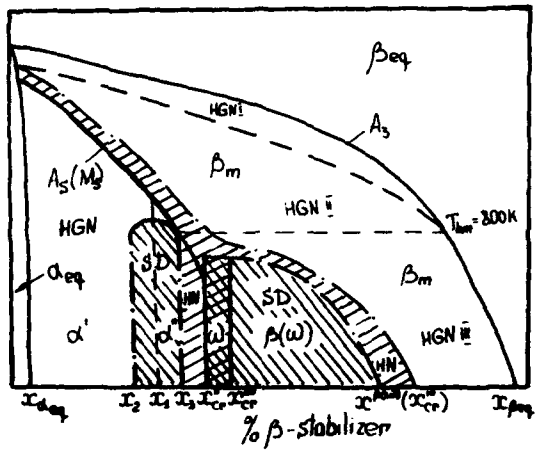


Figure 11 - The diagram illustrating temperature-concentration regions of different nucleation realization during metastable phases decomposition in Ti-x_β system HN-homogeneous nucleation, HGN-heterogeneous nucleation, SD-spinodal decomposition; HGN I - nucleation mainly on boundaries of β-grain; HGN II - nucleation at grain boundaries and body; HGN III - nucleation only in β-grain body.

4. Martensitic and β_m-phase isothermal decomposition occurs by middle mechanism, and its kinetic may be described by two types of -kind diagrams (Fig. 12). The special feature of these diagrams of early investigated /5, 7/ is the absence of special C-curves for β (ω), ω_{is} and $\alpha'' \rightleftarrows \alpha'(\alpha)$ transformations of second kind. The onest C-curve describes the transformation beginning of future α -phase nucleous, which under high temperatures ($T > M_s$ and $T > 550$ °C) are α' and at low temperatures ($T > 550$ °C) - α''-phase. The final $\alpha_{eq} + \beta_{eq}$ structure formation occurs by diffusion poorment of α' and α'' phases formed by martensite mechanism. In accordance to large volume incorrespondence of α_{eq} and β_{eq}-phases /8/ it always leads to plate structure forming. The isothermal ω_{is}-phase doesnot

take place in α-phase forming but stimulates its nucleaouses forming in nearer to β/ω boundary microvolumes of β_m-phase.

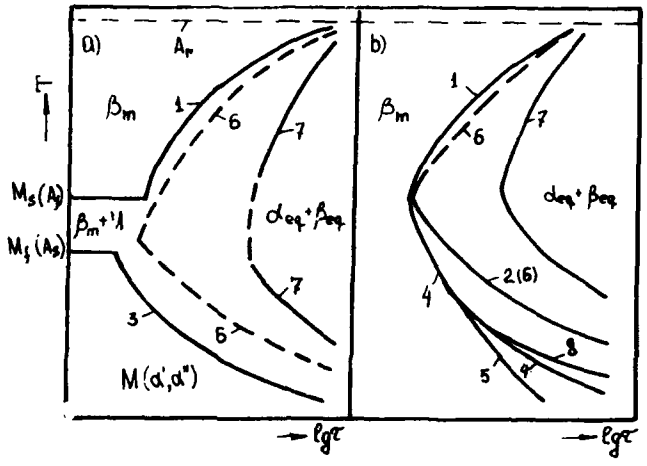


Figure 12 - The diagrams illustrating the main stages of isothermal metastable phases decomposition and structure forming under thermal treatment of before-critic (a) and post-critic (b) composition alloys. (The lines shows the beginning: I - of nucleous α-phase in β-phase forming; 2 - α-phase forming of α''-phase; 3 - martensite decomposition; 4 - nucleous of α''-phase forming in β-phase; 5 - $\beta(\omega)$-phase forming; 6 - transition from nucleating to nucleous of new phase growth; 7 - ($\alpha_{eq}+\beta_{eq}$)-structure forming finishing with equilibrium phase composition; 8 - three-phase region $\beta_m+\omega_{is}+\alpha''$).

5. Decomposition of β_m-phase under continuous cooling occur by the same mechanisms as under isothermal exposure. Different from traditionally used TTT-diagrams /1, 9/ the phase composition and structure forming as a result of β_m-phase decomposition under continuous cooling we must describe by new type of diagrams: phase composition - chemical composition of β-phase - cooling rate (PC-x-V^c) (Fig. 13). With the cooling rate decreasing beginning with the first critical ($V^c_{cr_1}$) the diffusion growth part begins to overcome the diffusionless nucleation one, that firstly leads to indetermediate structures forming with contain coherent and inhomogeneous by chemical composition α_{inh}, α''_{inh}, β_{inh} and $\beta(\omega)_{inh}$ phase, and under rates less then second critical one ($V^c_{cr_2}$) - to equilibrium $\alpha_{eq}+\beta_{eq}$-structure. The rate V^c_3 is the par-

ticular one, when $\alpha'' \rightleftarrows \alpha'$ transition realizes, cooling with this rate is undesirable as it leads to chemical phases inhomogeneity and maximum stress level, that causes the large alloys embrittlement.

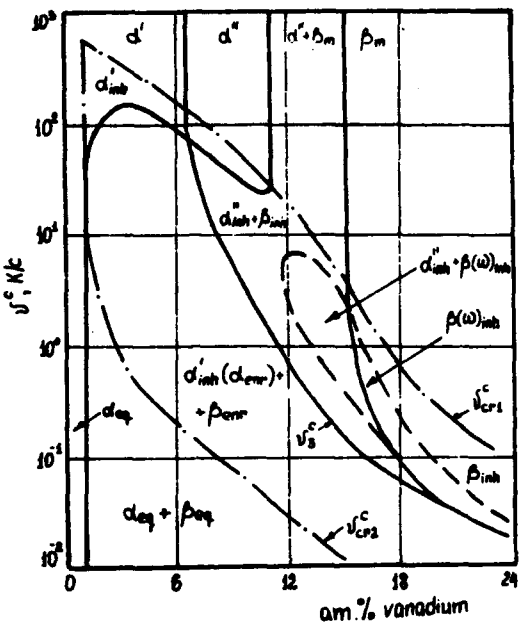


Figure 13 - The diagram phase composition - vanadium concentration (x_V) - cooling rate (V^o), cooling from β-region Ti-5Al-V system.

Refarences

1. S. G. Glasunov, V. N. Moiseev, Constructional Titanium Alloys. (M., Metallurgiya (1974)),368.

2. O. P. Solonina, S. G. Glasunov, Heat Resistant Titanium Alloys. (M., Metallurgiya (1976)),447.

3. S. G. Glasunov, K. M. Borzetsovskaya, Powder Metallurgy of Titanium Alloys. (M., Metallurgiya (1989)), 135.

4. S. G. Glasunov, B. A. Kolachev, Metallography of Titanium Alloys. (M., Metallurgiya (1980)), 464.

5. Yu. F. Altunin, S. G. Glasunov, High-Temperature Resistant Titanium Alloys. "Titanium in Industry". (M., Oborongiz (1961)), 245-253.

6. I. S. Polkin, A. B. Borzov, Mechanical Alloying as a new method of production of advanced materials. "Metallography and Treatment of itanium and Superalloys". (M., VILS (1991)), 68-78.

7. Ye. M. Savitsky, Yu. B. Efimov, T. M. Frolova, (M., Nauka), 1982, 64-69.

8. B. A. Kolachov, A. A. Ilyn, A. N. Momonova, Thermohydrogenous treatment of titanium alloys. "Metallography and treatment of titanium and superalloys", (M., VILS, (1991)), 132-141.

9. "Physical Metallurgy". Third, revised and enlarged edition. Ed. by R. W. Cahn and P. Haasen. 1983, North-Holland Physics Publishing. Amsterdam-Oxford-New York- Tokyo, 624.

10. A. A. Ilyn, Alloys with shape memory effect. In: "Science and engineering summary VINITI", ser. Metallurgy and heat treatment, 25, 1991, 3-6.

11. A. A. Ilyn, M. Yu. Kollerov, S. V. Skvortsova, Titanium Alloys with Shape Memory Effects and their Perspective Technological Application. I : "Titanium-1990": Products and Applications. Proc. of the Techn. Program Form of the 1990 Intern. Conf., Published by Titanium Development Association, V. 2, 746-754.

12. A. A. Ilyn et al., Effect of phase composition and structure on unelastic behaviour titanium based alloys. In: Izvestiya vuzov: Tsvetnaya metallurgiya (1985), N 3, 97-104.

13. E. W. Kollings, The Physical Metallurgy of Titanium Alloys. Amer. Soc. of Metals, Metals Park, OH 44073, 1984, 224.

14. De Fontaine D. Simple models of the omega-phase transformation. In: Metallurgical Transaction, A, 1988, V. 19A, 169-175.

15. I. S. Polkin, B. A. Kolachov, Phase transformation, thermal and thermomechanical processing of titanium alloys. Revue de Met., 1989, V. 86, N 10, 659-665.

16. A. A. Ilyn, M. Yu. Kollerov, About volume effects of allotropic transformation in titanium alloys. Report AN USSR, 1986, N 2, 396-400.

17. U. Zwicker, Titanium and Titanlegierungen, 1974. Springer-Verlag Berlin-Heidelberg-New York.

Phase Equilibria in the Titanium-Aluminum System

J. H. Perepezko and J. C. Mishurda

Dept. Materials Science and Engineering
University of Wisconsin - Madison
1509 University Avenue, Madison, WI 53706

Abstract

Based on a thorough review of the literature, the examination of the phase equilibria of the titanium-aluminum system has been continued. The initial evaluation of the phase equilibria in the titanium-aluminum system was established using differential thermal analysis. Verification of the evaluated phase equilibria was performed using alternate experimental methods including diffusion couples and heat treating studies. An estimate of the location of the α-γ phase boundaries was made. The influence of interstitial oxygen was proposed. An initial evaluation of the liquidus between the compositions TiAl and $TiAl_3$ has been presented.

Introduction

Titanium aluminides are gaining increased importance for high temperature applications. Knowledge of phase equilibria is critical in understanding the optimum processing parameters and the microstructure stability at high temperatures. The history of the evolution of the titanium-aluminum phase diagram shows many variations of the phases and location of phase boundaries[1]. In this report the main focus of the experimental effort was on the region concerning the $\alpha+\gamma$ two phase field. A preliminary phase diagram has been established using differential thermal analysis[1,2]. Confirmation of the phase equilibria from the preliminary diagram was provided by metallography and microprobe analysis of annealed samples and diffusion couples; including the influence of oxygen content on the phase equilibria. In addition an initial evaluation using DTA was undertaken to establish the nature of the liquidus for the compositions from TiAl to $TiAl_3$.

Titanium '92
Science and Technology
Edited by F.H. Froes and I. Caplan
The Minerals, Metals & Materials Society, 1993

Experimental Procedure

The starting materials for this investigation were four hot isostatically pressed (HIP) and forged ingots[2], and arc melted ingots (99.995% pure (HP) Ti or 99.7% pure (CP) Ti, and 99.999% pure Al). Samples were wrapped with titanium foil and placed in a Y_2O_3 coated alumina boat or Y_2O_3 coated molybdenum alloy wire basket, and annealed in a high purity argon environment with additional Ti-getters in the hot zone. The samples were either slow cooled or water quenched. The samples were analyzed using optical metallography, X-ray analysis, chemical analysis, and differential thermal analysis (DTA).

Three diffusion couples between sample 163-4 (γ) and pure Ti (CP or HP) were initially annealed for four hours at 1050° C to establish a bond. Then the Y_2O_3 coated clamps were removed, the diffusion couples were wrapped in titanium foil, annealed (at 1350±5° C for 24 hours, 1300±5° C for 24 hours or 1240±5° C for 96 hours) and water quenched. The diffusion couples were sectioned, optically examined, subjected to microprobe analysis, and oxygen analysis was performed.

Experimental Results

$\alpha+\gamma$ Two Phase Region

The results from DTA analysis are summarized in Figure 1[3]. The oxygen levels of the argon gas exiting the DTA sample chamber had 17±2 ppm (at.%) oxygen. The average initial oxygen level in the HIP+forged ingots was 0.033±0.005 wt.% O and in the arc melted ingots was 0.173±0.074 wt.% O. The average post oxygen analysis of some of the DTA specimens was 0.390±0.081 wt.% O for melted samples and 0.185±0.017 wt.% O for samples that were not melted.

The Ti-γ (50.94 at.% Al) diffusion couples revealed three compositionally distinct phase regions for all three annealing temperatures. No other compositionally distinct phase regions were observed in any of the samples at these annealing temperatures. The tie lines for the two phase fields and oxygen analysis are given in Table I. The average standard deviation was ±0.29 at.% Al. Additionally, a tie line at 47.25±0.48 atomic % Al and 51.62±0.38 atomic % Al was obtained from the two phase microstructure of the γ (50.94 at.% Al) side of the 1350° C diffusion couple.

Table I

Diffusion Couple Tie Lines (at.% Al) and Oxygen Analysis

Thermal Treatment	Tie line β	Tie line α	Tie line α	Tie line γ	Oxygen Content (wt.%) Ti Side	Oxygen Content (wt.%) γ side
1350°C/24 Hrs /WQ (HP Ti)	40.8 40.45	41.2 --.-	46.9 47.0	51.5 51.2	0.070±0.010	0.025±0.008
1300°C/24 Hrs /WQ (CP Ti)	39.28 38.35	40.42 40.05	45.44 44.74	49.34 49.26	0.245±0.002	0.025±0.004
1240°C/96 Hrs /WQ (HP Ti)	37.09 36.91	39.60 39.05	43.20 43.16	49.10 48.53	0.071±0.023	0.023±0.003

A Ti-44.8 at.% Al and a Ti-48.4 at.% Al sample were given a two step annealing treatment as summarized in Table II. The annealed microstructure of both samples consisted of two phases. The minor phase distribution of the 48.4 sample followed the original hexagonal dendrite distribution.

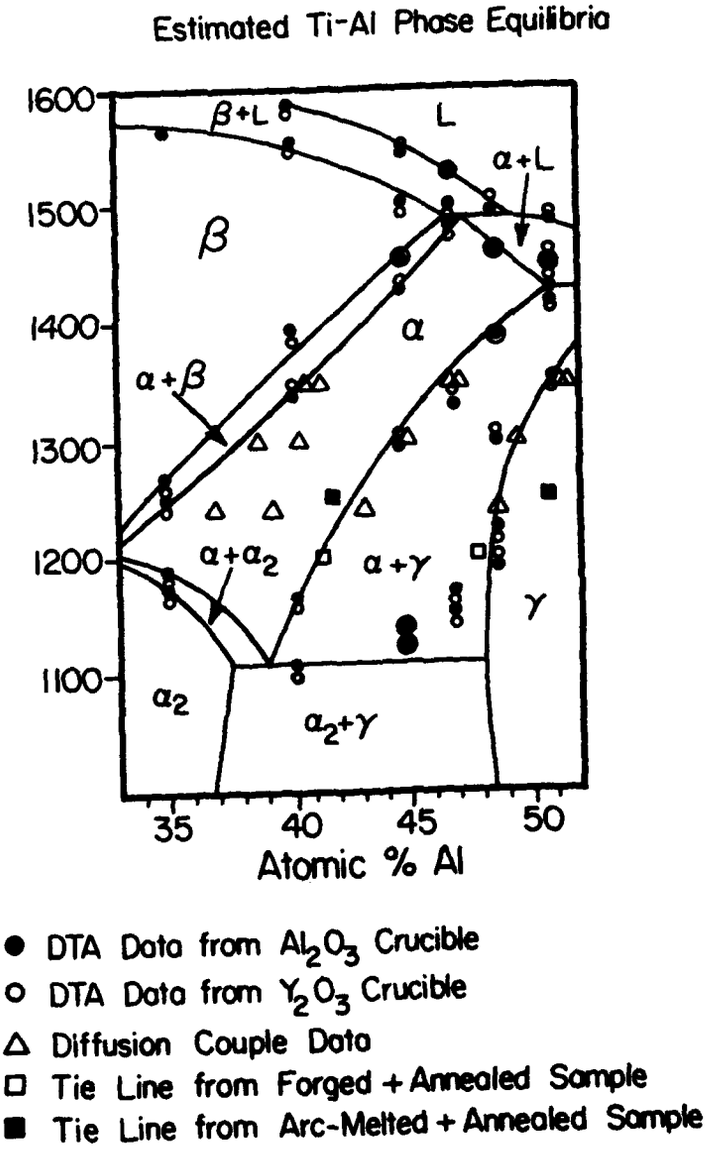


Figure 1 Ti-Al diagram based on a DTA analysis, diffusion couples and annealed samples.

Table II

Compositional Information of annealed samples

Condition	Area	Al (at.%)	O (wt.%)
Ti 48.4 at.% Al			
Arc melted then			
Annealed 1250°C	Bulk		0.056±0.004
10 days/S.C.+1250°C	Major Phase	50.71±0.14	
/10.5 hours/W.Q.	Minor Phase	41.96±0.15	
Ti 44.8 at.% Al			
HIP + Forged then			
Annealed 1200°C	Bulk		0.050±0.014
10 Days/S.C.+1200°C	Major Phase	41.66±0.15	
/24 hours/ W.Q.	Minor Phase	47.86±0.10	

Compositions from TiAl to $TiAl_3$

The onset and peak temperatures for the reactions observed during DTA are summarized in Figures 2a and b, and a representative thermogram is presented in Figure 3. Cycling experiments were carried out to establish the interpretation of the onset and peak temperatures in the thermograms (Figure 4). When the specimens were heated to temperatures equal to or in excess of the reaction peak temperature, undercooling was observed on cooling. No undercooling was observed when the sample was heated to a temperature less than the reaction peak temperature. As the number of cycles increased the peak temperature decreased slightly with each cycle. Post DTA microstructural examination revealed an increase in the number of dark precipitates in the interdendritic regions of the samples with each cycle. Several of the ingots with > 57 at.% Al contained needle precipitates which had a two to one ratio of titanium to aluminum based on microprobe analysis.

Samples with 73 at.% Al were annealed at 1200° C for 14 days and slow cooled followed either by further annealing for 2 hours at 1200° C then water quenching or further annealing for 24 hours at 1300° C then water quenching. Microprobe analysis indicated compositions of the two phase microstructure as 71.50±0.06 and 74.33±0.11 at 1200° C and 72.04±0.27 and 74.53±0.11 at 1300° C.

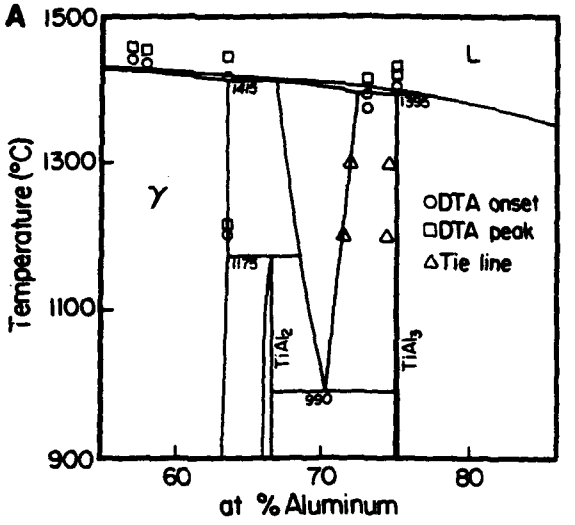
Discussion

$\alpha+\gamma$ Two Phase Region

The $\alpha+\gamma$ phase boundaries from DTA analysis are in fair agreement with the phase boundaries measured by magnetic susceptibility [4]. The oxygen content of the DTA specimens increased with temperature, with the majority of the oxygen increase occurring after melting. Prior to melting the oxygen level would be expected to be lower than 0.18 wt.% O. The average variation or precision of the DTA data was approximately ±7.5° C.

The tie lines for the $\alpha+\gamma$ two phase field obtained from the diffusion couples agree with the phase boundaries from the DTA analysis (Figure 1). Thus the phases in the diffusion couple correspond to the β, α, and γ phases, for all three temperatures investigated. The γ (50.94 at.% Al) side of the diffusion couple was used as an internal compositional reference for the microprobe analysis. The presence of the reported α' [5] phase was not confirmed. The tie line from the two phase microstructure in the γ side of the 1350° C diffusion couple agreed with the tie line obtained from the α-γ interface of the diffusion couple. This agreement shows the data is self consistent and equilibrium at the α-γ interface was most likely achieved.

The tie line obtained using the metallographic method from the annealed sample with 45.9 at.% Al agrees with the phase boundaries established from the DTA results. However, the γ end of the tie line from the 48.4 at.% Al annealed sample had more Al



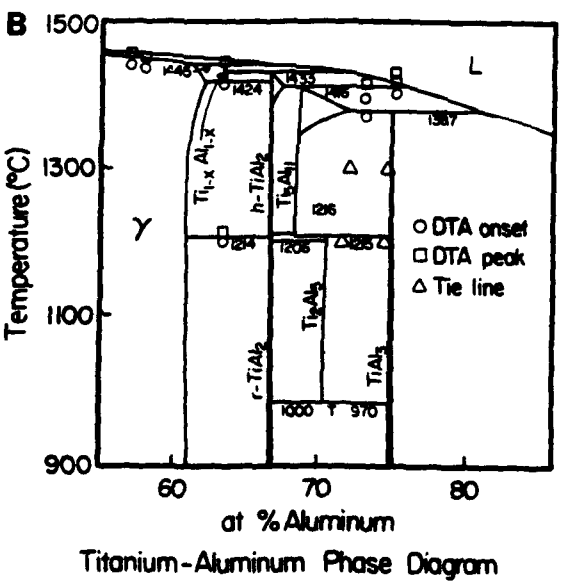


Figure 2 Plot of DTA data on Ti-Al phase diagrams.
a) K. Kaltenbach et al. Phase Diagram[11]
b) J. C. Schuster and H. Ipser Phase Diagram[10]

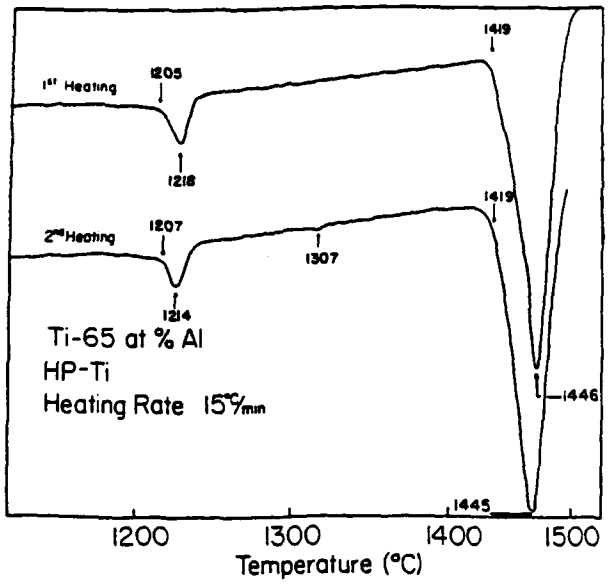


Figure 3 DTA thermogram Ti-65 at.% Al

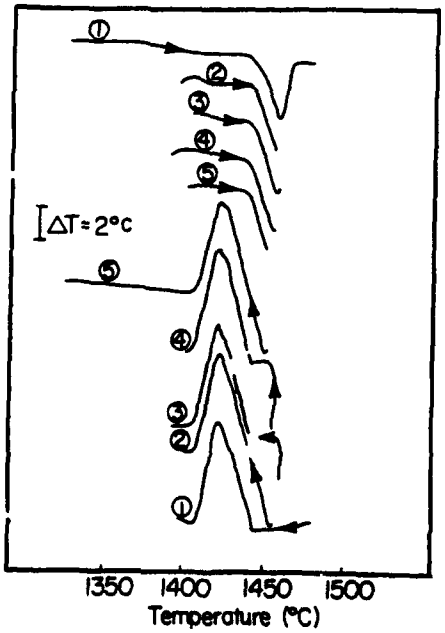


Figure 4 DTA cycling experiment Ti-60 at.% Al Heating Rate 5°C/min.

(2.8 at.%) than the γ end of the tie line from the DTA analysis. The γ end of the tie line from the 48.4 at.% Al sample did agree with the γ composition established with a metallographic method which determined the composition where the α phase was no longer observed ("diminishing second phase metallographic method")[6,7]. In a past study[4], a similar discrepancy was observed between the magnetic susceptibility and metallographic methods, which lead to the suggestion[4] that equilibrium was not obtained for the metallographic method.

The oxygen levels of the two annealed samples are approximately the same, 0.056 wt.% O. One major difference is the greater volume of α_2 phase present in the 45.9 at.% aluminum sample. If the solubility of oxygen is low in the γ phase[8,9,10] then the oxygen would preferentially segregate to the α phase. This would result in affecting either the kinetics or the phase equilibria. A change in composition of the γ phase with an increase in oxygen content implies it is a phase equilibrium effect. An increase in the expected volume fraction of the α phase has been reported for an alloy with high oxygen levels[9]. Therefore, the diminishing phase method (a small amount of α phase in a γ matrix), should not be applied in the Ti-Al system in this region without special caution due to the influence of oxygen.

Region of the diagram from TiAl to $TiAl_3$

The liquidus in this region of the diagram has a very gradual slope (Figure 2). Due to the gradual slope, cycling experiments were used to establish the validity of the interpretations of the DTA data. The observed reaction peak is the best estimate for the liquidus reaction since undercooling was observed whenever the peak temperature was exceeded and not when the temperature was lower than the peak temperature.

The liquidus temperatures reported here are in good agreement with two earlier studies[11,12] (Figure 2), which also used DTA analysis to establish the liquidus. In the literature, the temperatures reported for the peritectic formation of the $TiAl_3$ phase vary by as much as 55° C[11,12,13,14]. The results from DTA analysis fall at the high end of this range. The lower value of 1350° C was estimated[13] based on microstructural analysis (1340° C)[15] and a measurement of the liquidus based on a change in slope of the cooling curve (1355° C)[16].

DTA analysis revealed one solid state reaction occurring at 1205° C, which is in good agreement with the DTA data from J. Schuster and H. Ipser (1214° C)[11]. When compared to the data of K. Kaltenbach et.al.[12] the 63 at.% Al sample was outside of the two phase field and the reaction temperature was 30° C higher (1175° C)[12].

The tie lines from the 73 at.% Al sample annealed at 1200 and 1300° C agree with the two phase field boundaries in the K. Kaltenbach, et.al.[12] diagram (Figure 2) and the diagram by J. Murray[13]. There is significant disagreement with the 1300° C tie line when compared to the two phase field boundaries of J. Schuster and H. Ipser[11]. In addition the low aluminum content of the $TiAl_3$ phase, as determined by microprobe analysis, is an indication that there may be some solubility of titanium in the $TiAl_3$ phase at elevated temperatures. A previous study indicated a much greater solubility (2 at.% Ti) based on a diffusion couple (23 hours at 1200° C)[17].

No difference was observed in the 65 at.% Al ingot whether it was produced with CP Ti or the HP Ti; this is an indication that the interstitial content did not significantly affect the binary phase equilibria in this region of the diagram. The interdendritic phase in the 57, 60 and 65 at.% Al samples had a microstructure consisting of dark precipitates. The dark precipitates may be associated with contamination from interstitial elements based on the post DTA microstructures, which show an increase in the volume fraction of these precipitates with repeated number of DTA cycles. The formation of precipitates with a Ti to Al ratio of (2:1) in alloys with Al > 57 at.% Al and the absence of α phase is an indication of low interstitial solubility in the γ phase.

Conclusions

The phase boundaries for the $\alpha+\gamma$ two phase field (Figure 1) were initially established by DTA analysis and confirmed by diffusion couples and annealed samples and are in good agreement with the data of C. McCullough et.al.[18]. No evidence was found to support the presence of the reported high temperature α' phase[5]. The estimate of error for precision of the DTA data is ±7.5° C and for chemical analysis is ±0.5 at.% Al.

The influence of oxygen on phase equilibria is to increase the stability of the α phase which is significant when small volume fractions of α phase are in a matrix of γ phase. Evidence to support a low solubility of oxygen in γ phase has been presented. As a result, the "diminishing second phase metallographic method" used to identify the γ side of the $\alpha+\gamma$ two phase field can be misleading due to an influence of oxygen.

The nature of the liquidus between TiAl and $TiAl_3$ is believed to be cascading peritectics with liquidus temperatures in general agreement with K. Kaltenbach et.al.[12] and J. C. Schuster and H. Ipser[11]. The tie lines established with 73 at.% Al annealed samples agreed with K. Kaltenbach et.al.[12], while the DTA data from the 63 at.% Al sample agreed with J. C. Schuster and H. Ipser[11]. The possibility that the compound $TiAl_3$ has some solubility has been suggested by the microprobe results of the annealed samples.

Acknowledgments

The support of DARPA/URI (N0014-86-K-0753/P.O. No. VB38 640-0) is gratefully acknowledged. The authors would like to thank M. Smith and Dr. M. J. Blackburn of Pratt & Whitney for providing the forged ingots used in this study and for their continued assistance and encouragement. Thanks also goes to Dr. S. C. Huang and Dr. R. D. Shull for helpful discussions. Additional thanks to Dr. R. Bonda and T. Jewitt for materials and assistance with the high aluminum content alloys.

References

1) J. C. Mishurda and J. H. Perepezko, Microstructure/Property Relationships in Titanium Aluminides and Alloys, Ed. by Y-W. Kim and R. R. Boyer, TMS, (1991), 3-30.
2) J. C. Mishurda, et al., High-Temperature Ordered Intermetallic Alloys III, Ed. C. T. Liu, A. I. Taub, N. S. Stoloff, and C. C. Koch, MRS, 133 (1989), 57-62.
3) J. C. Mishurda, (MS Thesis, University of Wisconsin-Madison, 1989).
4) E. W. Collings, Met. Trans., 10A (1979), 463-474.
5) R. D. Shull and J. P. Cline, High Temperature Science, 26 (1990), 95-117.
6) S. C. Huang and P. A. Siemers, Met. Trans., 20A (1989), 1899-1906.
7) Private communication Prof. H. Lipsitt.
8) E. L. Hall and S. C. Huang, Microstructure/Property Relationships in Titanium Aluminides and Alloys, Ed. by Y-W. Kim and R. R. Boyer, TMS, (1991), 47-64.
9) E. L. Hall and S. C. Huang, Acta Met., 38 (4) (1990), 539-549.
10) A. K. Misra, Met Trans, 22A (1991), 715-721.
11) J. C. Schuster and H. Ipser, Z. Metallkde, 81 (6) (1990), 389-396.
12) K. Kaltenbach, et al., Z. Metallkde, 80 (7) (1989), 511-514.
13) J. L. Murray, Phase Diagrams of Binary Titanium Alloys, Ed. J. L. Murray, ASM International, (1987), 12-24.
14) A. Raman and K. Schubert, Z. Metallkde. 56 (1) (1965), 44-52.
15) E. S. Bumps, et al., Trans. AIME, 194 (1952), 609-614.
16) W. Manchot and A. Leber, Z. Anorg. Chem., 150 (1926), 26-34.
17) F. J. J. van Loo and G. D. Rieck, Acta Met. 21 (1) (1973), 73-84.
18) C. McCullough, et al., Acta Met. 37 (5) (1989), 1321-1336.

PHASE SELECTION DURING SOLIDIFICATION PROCESSING OF TI-40AT%AL POWDER

E.M. Clevenger and J.H. Perepezko
Department of Materials Science and Engeering
University of Wisconsin-Madison
1509 University Ave, Madison, Wi 53706

Abstract

It is now evident that attention to control in the materials processing of titanium aluminides is an important consideration in producing materials with the necessary microstructural and mechanical properties. In order to identify the variables which affect phase selection, powder processing of a Ti-40at%Al alloy has been examined on a laboratory scale with a 3m drop tube. Using this process, powder particle size and gas environment effects can be examined, as well as alloy composition and impurity effects. With this Ti-40at%Al alloy it has been possible to study the kinetic competition between α and β phase products and to use solid state reactions as a guide in following the thermal history during solidification. The results show that the phase selection, during volume catalyzed heterogeneous nucleation in the powder particles, follows Poisson statistics with powder size, and that careful control of the processing atmosphere and particle diameter affects the solidification pathway of the alloy.

Introduction

Titanium aluminides have been extensively studied for many years in hopes of developing high temperature, light weight aerospace alloys and slowly but surely they are beginning to move from the development to the application stage. However, the qualities which have made these alloys attractive as structural materials, such as sluggish diffusion kinetics (which limits coarsening of grains and dispersoids in the matrix), (1) also inhibit modification of the solidification microstructure, especially during post-solidification heat treatments. Therefore, processing techniques, especially those which increase the rate of heat extraction and crystal growth, such as rapid solidification processing (RSP), become increasingly important in the processing of titanium aluminides (because they offer a means of by-passing some of the processing problems). For example, RSP can lead to a reduction in the scale of the microstructure,(2) resulting in reduced diffusion distances and limited segregation tendencies.(3) Also, RSP often results in increased levels of undercooling prior to solidification which may open up alternate metastable solidification pathways. These alternate pathways may then result in expanded opportunities for microstructural modification, through controlled solid state decomposition reactions, during post solidification thermal-mechanical treatments.(4)

There are a variety of commercial and laboratory techniques available for rapid solidification processing of materials. One of the most effective is the cooling of molten droplets in an inert gas atmosphere. Drop tube processing is such a technique. It utilizes processing conditions similar to other powder production processes such as gas atomization, while offering such advantages as economy of construction and operation, flexibility in experimental parameters, short turn around time for experiments and the

Titanium '92
Science and Technology
Edited by F.H. Froes and I. Caplan
The Minerals, Metals & Materials Society, 1993

ability to process a wide range of droplet sizes (micrometers to millimeters).(5)

The primary goal of this investigation was to explore the potential for microstructural modification in drop tube processed Ti-40at%Al alloy powder. Special emphasis was placed on understanding the solidification pathways available; examining how those pathways were related to the undercooling; determining what type of nucleation kinetics were active; and finally, what affect, if any, processing atmosphere had on microstructural development.

Experimental Procedure

The material used in this study was produced by arc melting high purity starting materials (99.99% Ti and 99.999% Al). The powder was produced from the bulk ingot by crushing in a steel anvil and then separating out any contaminated material with a magnet. Since size range is an important variable in controlling solidification behavior during drop tube processing the powder was sorted both prior to and after processing into the following size ranges $<10\mu m$, 10-22μm, 22-30μm, 30-44μm, 44-53μm, 53-63μm, 63-74μm, 74-88μm, 88-105μm, 105-177μm and $>177\mu m$, using an Allen-Bradley Sonic Sifter. After the powder was prepared it was drop tube processed in various atmospheres using a 3m laboratory scale drop tube. A detailed description of the system is presented elsewhere.(6) The processed powder was analyzed using x-ray diffraction analysis (Cu-Kα radiation), optical and scanning microscopy and finally microstructures were classified and statistically analyzed using a sample size of 250-500 particles per size range.

Experimental Results and Discussion

X-ray analysis of the powder drop tube processed in helium revealed only the presence of the ordered hexagonal phase (Ti_3Al) (Figure 1). It should be noted that at equilibrium this alloy is approximately 50% γ phase (TiAl). Careful metallographic examination of the powder after drop tube processing revealed two distinct morphologies. A martensitic microstructure (Figure 2a), and a hexagonal dendritic microstructure (Figure 2b). The variation of the microstructural abundance as a function of particle size is shown in Figure 3.

Drop tube processing of the Ti-40at%Al alloy powder in an argon atmosphere resulted in morphologies similar to those observed in the helium atmosphere (Figures 2a, 2b). X-ray analysis of the powder after processing again revealed only the presence of the ordered hexagonal phase Ti_3Al (α_2) Figure 4. The variation in microstructural abundance as a function of particle diameter for the powder processed in argon is shown in Figure 5.

It is often difficult to determine the solidification pathway of an alloy simply by studying the final microstructure because solid state transformations which take place after solidification can obscure the details. However, an understanding of the phase equilibria (both stable and metastable) in an alloy system can help determine the most probable pathways and the effects on the final microstructure. In Ti-40at%Al alloy powder drop tube processed under an inert atmosphere there were several possible pathways for the alloy to follow from melting to room temperature. These pathways have been examined in detail (6). The main conclusions were that the presence of the martensitic powder suggested the formation of β phase from the melt, while the occurrence of the hexagonal dendrites was indicative of α phase formation from the melt. The data in Figures 3 and 5 is a summary of the effect of particle size on microstructural development. As the particle size decreases the number of particles containing hexagonal dendrites increases. This was as expected, as the smaller particles are likely to see a larger degree of undercooling before solidification, allowing them to reach $T_0^{\alpha/L}$ (Figure 6).

Once the solidification pathways were determined, the next logical step was to develop an understanding of the variables affecting microstructural development. There are two major variables which affect the variation in microstructure during drop tube processing, particle diameter and processing atmosphere. Figure 7 shows the effect of particle size on microstructural abundance for two different processing atmospheres, argon and helium. The change in phase selection from a β solidification product in the coarser particle sizes to α in the finer particle sizes is consistent with an increase in

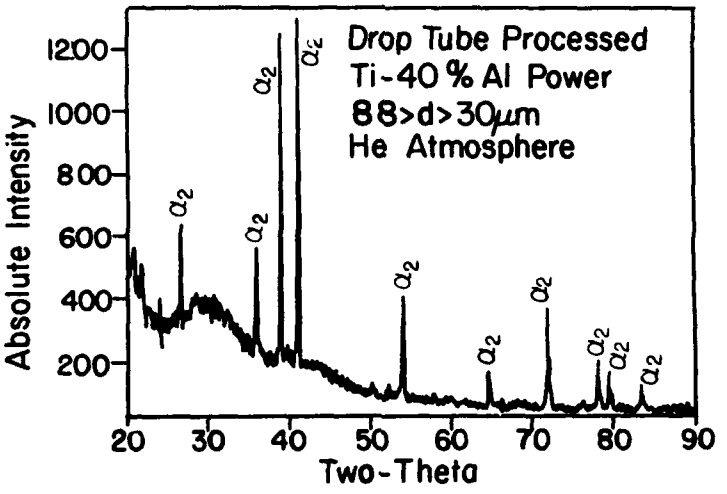


Figure 1. Diffraction pattern of Ti-40at%Al powder after drop tube processing in a He atm.

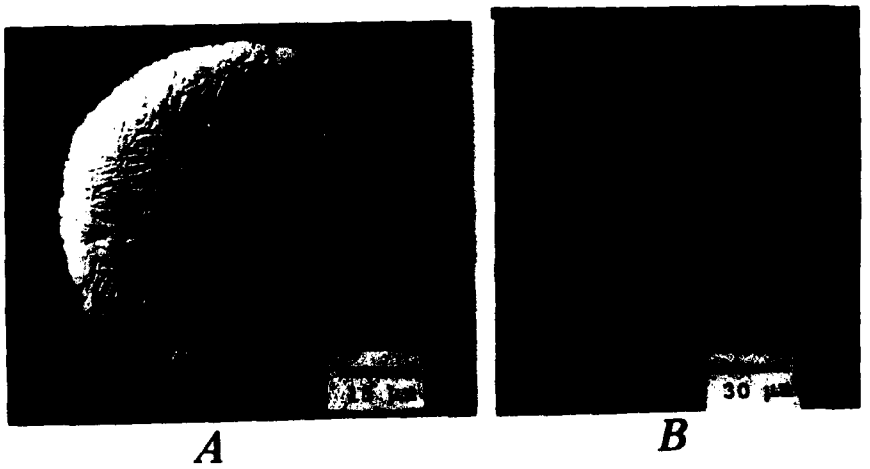


Figure 2. Optical micrographs showing: A) martensitic microstructure and B) dendritic microstructure in Ti-40at%Al alloy powder, drop tube processed in He atm. Polished and etched with Kroll's etchant.

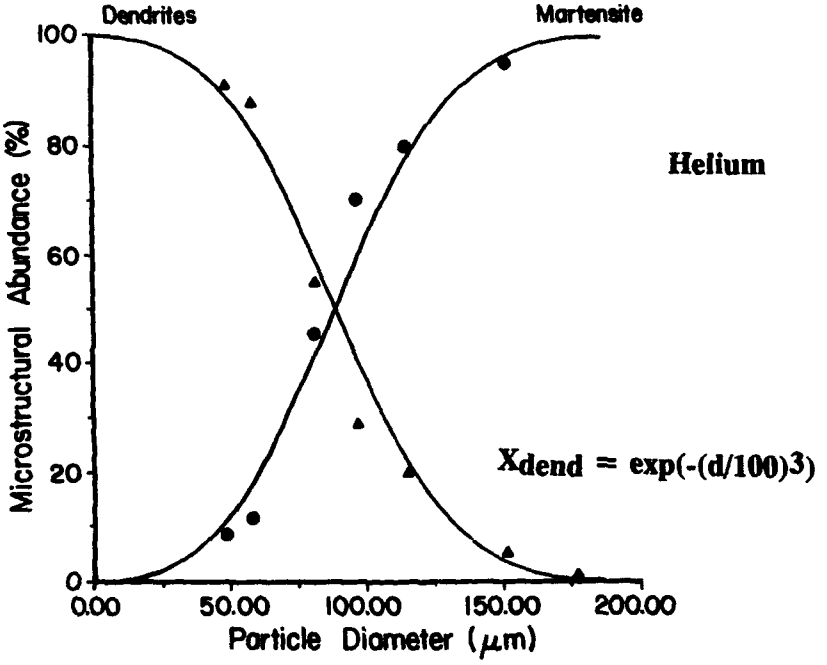


Figure 3. Microstructural abundance curves as a function of powder diameter for Ti-40at%Al powder drop tube processed in a He atm.

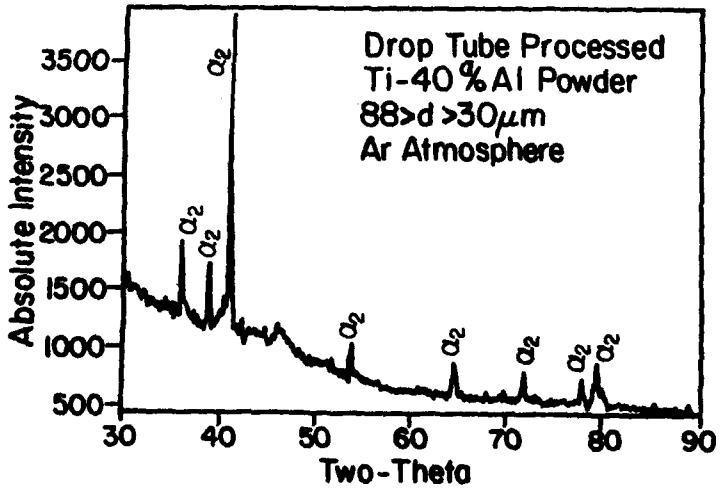


Figure 4. Diffraction pattern of Ti-40at%Al alloy powder after drop tube processing in an Ar atm.

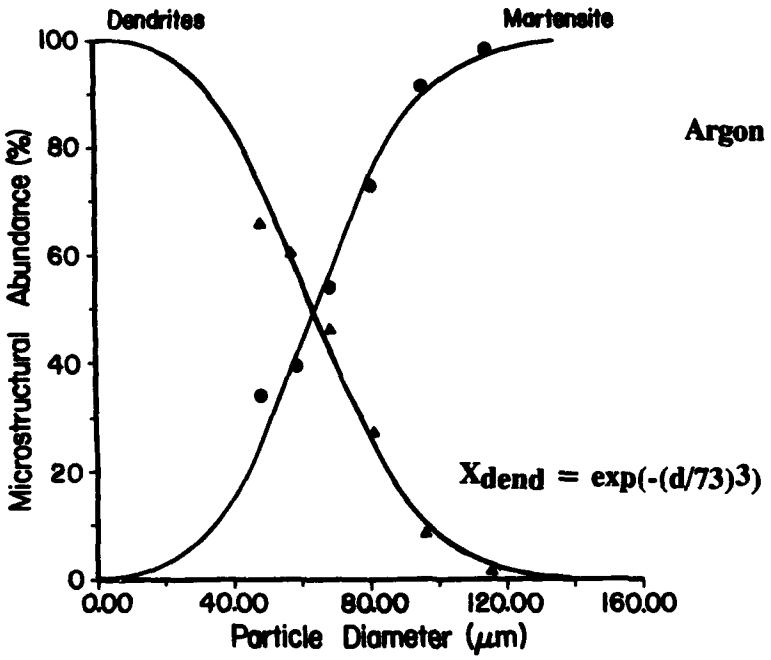


Figure 5. Microstructural abundance curves as a function of powder diameter for Ti-40at%Al powder drop tube processed in an Ar atm.

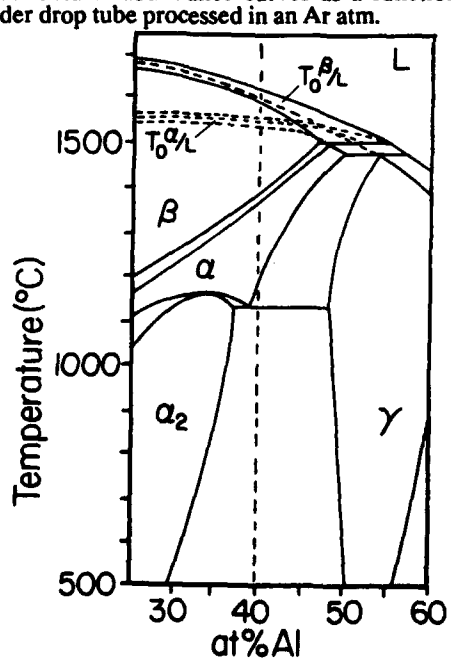


Figure 6. Partial Ti-Al phase diagram with T_0 curves.

undercooling with decreasing particle size. The main factors responsible for such an increase are the progressive isolation of internal heterogeneous nucleation sites and increased cooling rates associated with the reduction in particle size (7).

In powder solidification, just as in most solidification, nucleation of the solid in a molten powder droplet usually occurs by heterogeneous nucleation. In this heterogeneous nucleation reaction the distribution of the catalysts may be at the droplet surface or in the internal volume. A model of heterogeneous nucleation has been developed assuming a time invariant number of pre-existing nuclei per cm^3 (N_v).(8) For a random distribution of nuclei in the powder population the probability (P) that none of the nuclei exist in a volume (V) is:

$$P = \exp(-N_v V) \quad (1)$$

For a collection of spheres of diameter d the fraction X of the powder population which is free of these internal nucleation sites is then:

$$X = \exp(-(d/d_0)^3) \quad (2)$$

where d_0 is an adjustable parameter.(8) N_v is then equal to $6/\pi d_0^3$. Similarly, if the nucleation kinetics are controlled by surface catalysts then for a time invariant concentration of surface sites per cm^2 (N_s) the fraction of the powder free of surface nucleation sites is:

$$X = \exp(-(d/d_0)^2) \quad (3)$$

N_s is then equal to $1/\pi d_0^2$.(8) In the powder particles which avoided the homogeneous nucleation events (surface or volume) alternative nucleation sites might be allowed to operate at deeper levels of undercoolings resulting in the formation of a metastable crystalline phase or even an amorphous phase.

Thus quantitative analysis of metastable phase formation as a function of powder size provides an effective approach to characterization of the nature of dominant nucleation kinetics. This approach has been demonstrated in previous investigations through the analysis of the fraction of amorphous droplets formed in a powder population,(8),(9) the indication being that heterogeneous surface sites predominate in controlling nucleation kinetics.

This model was used to identify the competitive kinetics and it was found that the fraction of particles solidifying as β followed the Poisson equation, $X = \exp(-d/d_0)^n$. Using regression analysis d_0 (He) was determined to be 100μm and n = 3 for the He processed powder and a best fit curve was developed for the data. Approximately the same n was determined for the particles processed in the Ar atmosphere implying heterogeneous volume nucleation.

Using a heat flow model in which both radiation and convective cooling of the free falling particles is considered, an expression for the cooling rate as a function of both particle size and processing atmosphere is (10):

$$dT/dt = -\epsilon A\sigma/mC_p (T^4 - T_0^4) - hA/mC_p (T - T_0) \quad (4)$$

Where ϵ is the emissivity of the particle, A is the area of the particle, σ is the Stefan-Boltzmann constant, m is the mass of the particle, C_p is the specific heat, T is the liquidus temperature, T_0 is the ambient temperature, and h is the heat transfer coefficient of the processing gas. Estimates for the specific heat and emissivity were determined by taking weighted averages of the pure elements, while the mass was determined from the density of the alloy calculated from the measured lattice parameters. Estimates for the heat transfer coefficient were determined for a particle size and atmosphere (Ar or He) from the data of Clyne, et al. (11). The calculated values are $[dT/dt]_{He} = 1 \times 10^6$ and $[dT/dt]_{Ar} = 8 \times 10^5$. If Newtonian cooling conditions during free fall are assumed the observed shift in the microstructural abundance curves with processing atmosphere may be described by a single translation in cooling rate. A number of assumptions are required for the individual calculations (10) but by comparing the relative change in cooling rates as a result of the change in gas atmosphere the influence of errors made in estimating the individual parameters in the model is minimized.

An alternative method of expressing the equivalence in thermal conditions is a

comparison of the diameters of the drop tube processed particles required to produce a certain percentage of the population solidifying as dendrites under He and Ar atmospheres (Figure 8). This figure shows that the ratio of the diameters for He and Ar processed particles remains approximately constant for an increasing percentage of dendrite solidification product. The shift in microstructural abundance curves by a single translation in the cooling rate implies that the same nucleation kinetics is operating during the formation of the α phase in the Ti-40at%Al alloy whether it is processed in He or Ar.

Summary and Conclusions

The primary goal of this investigation has been to determine the influence of drop tube processing on microstructural development in a Ti-40at%Al alloy. The approach involved relating the formation of specific microstructures to processing/alloy characteristics and the resulting correlation analyzed in terms of the level of melt undercooling attained prior to nucleation and the phase selection kinetics operating in the undercooled melt.

X-ray analysis of the powder after drop tube processing revealed only α_2 peaks. The equilibrium structure of this alloy is approximately 50% α_2 - 50% γ. Therefore, drop tube processing of this alloy suppresses the solid state reaction $\alpha_2 \rightarrow \alpha_2 + \gamma$.

There are two possible solidification pathways for Ti-40at%Al alloy powders to follow from the melt as a result of drop tube processing, $L \rightarrow \alpha$ and $L \rightarrow \beta$. The $L \rightarrow \alpha$ solidification is more likely to occur at the smaller particle sizes ($d < 44\mu m$) due to the higher undercooling and faster cooling rate experienced by these particles. A martensitic microstructure forms as a result of the $L \rightarrow \beta$ solidification, while a microstructure containing dendrites with hexagonal arms forms as a result of the $L \rightarrow \alpha$ solidification.

Statistical analysis was used to identify the competitive nucleation kinetics, and it was found that the fraction of particles solidifying as α followed the Poisson equation $X = \exp((-d/d_0)^3)$ for both processing atmospheres. Therefore, solidification in this alloy, as a result of drop tube processing, is caused by heterogeneous volume nucleation. The actual nucleant is unknown. By changing the processing atmosphere in the drop tube (from He to Ar or vice versa) it is possible to cause an isokinetic shift in the nucleation kinetics, represented by the different d_0's ($100\mu m$ - He, $73\mu m$ - Ar). In other words, the same nucleation kinetics are operating during the formation of α phase whether it is processed in Ar or He.

Acknowledgements

The support of DARPA (URI/N0014-K-0753/P.O. V38640-0 and DAAL 03-90-6-0183) is gratefully acknowledged.

References

1. W.C. Hagel "Intermetallic Compounds", J.H. Westbrook (Ed.), John Wiley and Sons, N.Y. (1967) p. 377.
2. C. McCullough, J.J. Valencia, C.G. Levi, and R. Mehrabian, Mat. Sci. & Eng., A124, (1990) pp. 83-101.
3. H.J. Fecht and J.H. Perepezko, Met. Trans., 20A, (1989) p. 785.
4. J.A. Graves, PhD. Thesis, UW-Madison, (1987).
5. L.L. Lacy, M.B. Robinson, and T.J. Rathz, J. of Crystal Growth, 51, (1981) p. 47-60.
6. E.M. Clevenger, M.S. Thesis, UW-Madison (1991).
7. J.H. Perepezko, S.E. LeBeau, B.A. Mueller and G.J. Hildeman, ASTM STP 890, M.E. Fine and E.A. Strake (Eds.), ASTM, Philadelphia, Pa (1986), p.118.
8. A.J. Drehman and D. Turnbull, Scripta Met., 15 (1981) p. 543.
9. J.S. Paik and J.H. Perepezko, J. Non-Cryst. Solids, 56 (1983) p. 405.
10. M.B. Robinson, Nasa Tech. Mem., Nasa TM-78189, (1978).
11. T.W. Clyne, R.A. Ricks and P.J. Goodhew, Internl. J. of Rapid Solid., A B Acamdemic Pubs., Great Britain, 1 (1984) p.5.

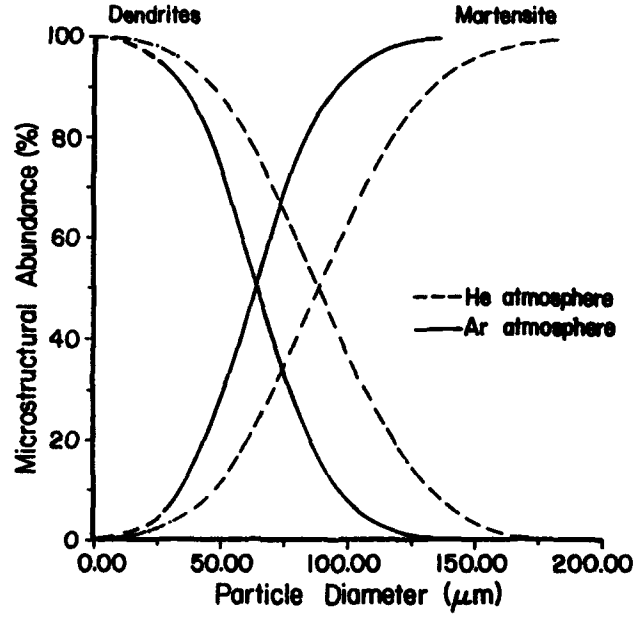


Figure 7. *Microstructural abundance curves as a function of particle diameter for* Ti-40at%Al powder drop tube processed in He and Ar atms.

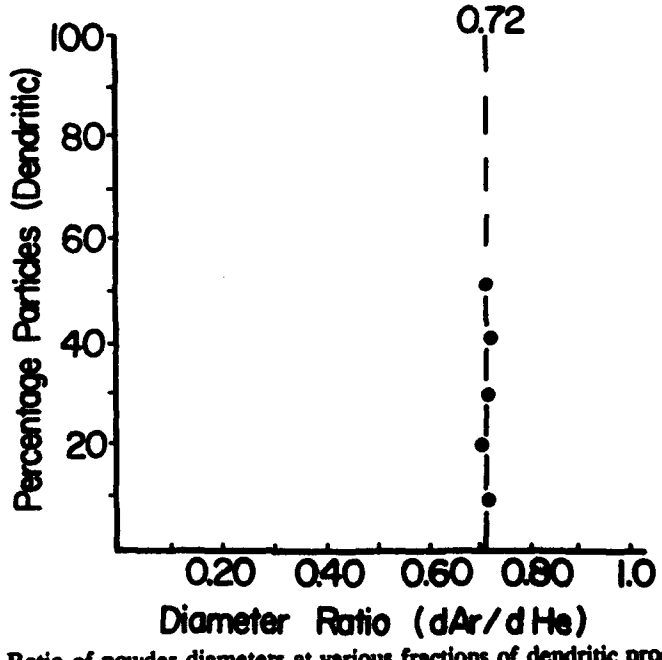


Figure 8. Ratio of powder diameters at various fractions of dendritic product in drop tube processed powder.

ESTIMATION OF RECRYSTALLIZED GRAIN SIZE UNDER CONTINUOUS ANNEALING OF COLD-ROLLED β TITANIUM ALLOY STRIPS

H. Ohyama, A. Takemura, and T. Nishimura

Iron and Steel Research Laboratories, Kobe Steel, Ltd.
Ikeda 2222-1, Onoe-cho, Kakogawa 675, Japan

Y. Ashida

Materials Research Laboratories, Kobe Steel, Ltd.
Takatsukadai, Nishi-ku, Kobe 651-22, Japan

Abstract

We have investigated the behavior of the recrystallization and the grain growth of a cold-rolled Ti-15V-3Cr-3Sn-3Al alloy strip and proposed a method for estimating the grain size after recrystallization during a continuous annealing process. The observation of the microstructure reveals that the grain size of the 80% cold rolled material recrystallized under isothermal annealing, $D(T,\tau)/\mu m$, can be indicated by

$$D(T,\tau)=0.80\times10^{4}\,\tau^{0.24}\exp(-1.50\times10^{4}/RT),$$

where T and τ are the annealing temperature (K) and time (sec), and R is the gas constant. The estimation of the grain size recrystallized under continuous annealing has been carried out by sequentially integrating, step by step, each increment of the isothermal grain growth at each temperature. The estimation of the grain size recrystallized under a continuous heating process is in good agreement with the actual grain size. In addition, the grain size of the beta titanium alloy produced on the production line also agrees well with the calculated results using the temperature and holding time of the continuous annealing furnace. This estimation provides good information for controlling the grain size after continuous annealing and leads to the production of finer-grained Ti-15V-3Cr-3Sn-3Al strips than have ever been obtained before.

Titanium '92
Science and Technology
Edited by F.H. Froes and I. Caplan
The Minerals, Metals & Materials Society, 1993

Introduction

As for sheet products of high strength titanium alloys, cold strips of beta titanium alloy are the most cost-effective in terms of both primary and secondary fabrication costs. This type alloys are usually cold-formable in annealed conditions of the beta single phase. Inappropriate heat treatments often lead to grain coarsening and result in problems such as orange peel after bending, and low ductility. It is accordingly important to control the grain size after annealing of cold-rolled strips on a production scale. For producing fine-grained beta titanium sheets in a fully recrystallized structure, we have investigated the recrystallization behaviors of a cold rolled Ti-15V-3Cr-3Sn-3Al strip during isothermal annealing, and have proposed the model for estimating recrystallized grain size under non-isothermal annealing. We tried to apply the model to a test production of a 1.0mm thick, 950mm wide, and 2.5 metric ton Ti-15V-3Cr-3Sn-3Al strip in an industrial annealing and pickling line.

Experimental Procedure

Materials

Table 1 shows the chemical composition of the material used in this study. An ingot of Ti-15V-3Cr-3Sn-3Al alloy was forged in the beta region and then hot rolled from 120mm to 5.4mm in thickness after heating at 1273K by a production mill. A plate cut from the strip was solution-treated at 1073K for 1.8 ksec. The mean beta grain size measured by the linear intercept method was about 80μm.

Table 1. Chemical composition of the alloy used.

Elements (wt%)	V	Cr	Sn	Al	Fe	O	N	H	Ti
Top	15.19	3.11	3.03	3.08	0.169	0.107	0.0053	<0.0010	bal.
Middle	15.27	3.05	3.03	3.06	0.165	0.112	0.0055	<0.0010	bal.
Bottom	15.16	3.04	3.04	3.04	0.190	0.111	0.0059	<0.0010	bal.

Isothermal Annealing of Cold-rolled Specimens

Pieces cut from the material were 10 to 80% cold rolled. They were subsequently machined into smaller pieces of 15mm square with a constant thickness of 1.0mm, and annealed in salt baths at the temperature range of 993 to 1273K for 3 to 1000sec. Times necessary to raise temperature were taken at 4sec in the 993 and 1023K, 5 sec in the 1073 and 1123K, 6sec in the 1173K, and 7 sec in the 1273K annealing treatments, on the basis of the results obtained using a thermocouple during treatments at 1073 and 1273K.

After annealing, the samples were aged at 723K for 1.8 ksec to decorate unrecrystallized regions,[1] and their microstructures were observed with an optical microscope in the longitudinal section. The recrystallized grain sizes were measured by the linear intercept method.

Examination of Recrystallization during Heating

Based on the results obtained from the isothermal annealing, we have proposed a model for estimating the grain size change during non-isothermal annealing. In order to verify the feasibility of the model, small pieces of the 80% cold rolled material were heated from room temperature up to 1073K at heating rates of 0.3 to 10K/sec in an infrared furnace and immediately quenched into water, and their recrystallized grain sizes measured were compared with the values calculated through the model.

Additionally, in order to obtain the relationship between the temperature of the sheet and the time during annealing in atmospheres, temperature/time curves were recorded by inserting two beta titanium sheets of 110mm^{w}x1000mm^{l}x1.0mm^{t} and x1.2mm^{t}, with a thermocouple attached on a central surface, into air furnaces of 1073 and 1123K, respectively, and pulling out the titanium sheets into air.

Finally, on the basis of a furnace temperature / passing period / grain size diagram obtained numerically, the 950mm wide and 2.5 metric ton hot strip was descaled and 80% cold rolled after the solution treatment mentioned above, and was continuously annealed in an annealing and pickling process.

Results and Discussion

Recrystallization Behaviors during Annealing



Fig. 1. Optical microstructures after annealing at 1073K of the 30 and 80% cold rolled specimens. (1), (2), and (3) are 30% cold rolled and annealed for 3, 30, and 300 sec, respectively. (4), (5), and (6) are 80% cold rolled and annealed for 1, 10, and 100 sec, respectively.



Fig. 2. Optical microstructures after annealing of the 30 and 80% cold rolled specimens. (1), (2), and (3) are 30% cold rolled and annealed at 1173K for 1, 10, and 100 sec, respectively. (4), (5), and (6) are 80% cold rolled and annealed at 993K for 30, 100, and 300 sec, respectively.

Figure 1 shows the recrystallization behaviors of the 30 and 80% cold rolled specimens during isothermal annealing at 1073K. In the 30% cold rolled samples, the nucleation sites are strongly restricted to the triple points of deformed grains. With increasing cold reduction, new grains come to generate more frequently along the deformed grain boundaries and within the deformed grains to impinge on each other. Figure 2 shows the structural changes of the 30 and 80% cold rolled specimens during isothermal annealing at 1173 and 993K, respectively. Compared with the 1073K annealed samples, the microstructural changes each proceed similarly. Low reduction leads to a coarse structure, whereas high reduction can bring about fine one. We have accordingly studied the recrystallization behaviors of the 80% cold rolled specimen more in detail.

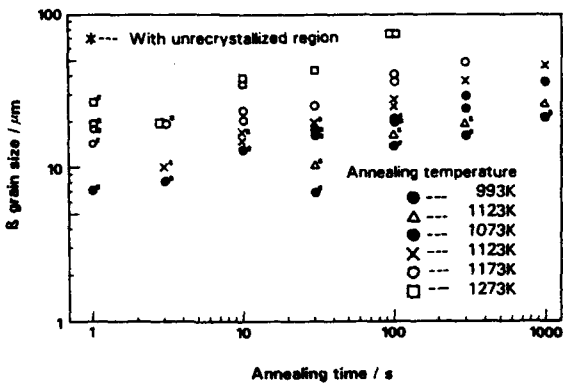


Fig. 3.[2] Logarithmic relationships between recrystallized grain size and annealing time in the 80% cold rolled specimens.

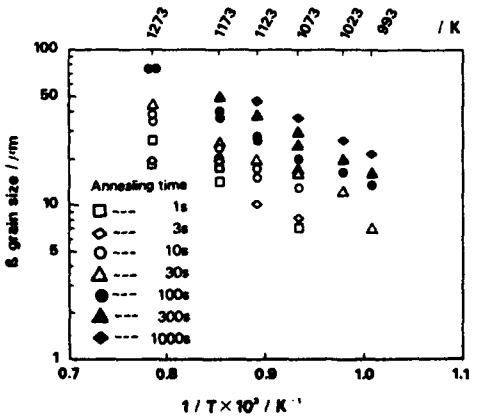


Fig. 4.[2] Semilogarithmic relationships between recrystallized grain size and reciprocal annealing temperature.

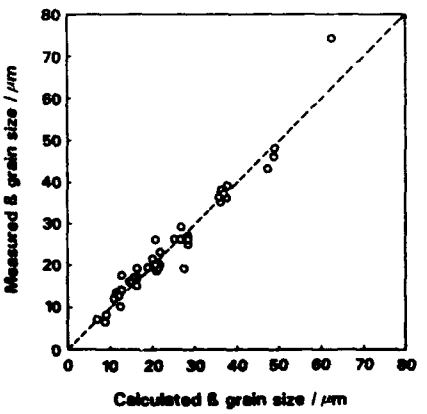


Fig. 5.[2] Graphic correlation between measured and calculated grain sizes.

Figure 3[2] shows logarithmic relationships between grain size and annealing time for the 80% cold rolled specimens. As for the samples which were not fully recrystallized, the grain size in the recrystallized regions is plotted, and indicated on the graph by asterisks (*). In general, for a given annealing temperature a time dependence of the grain size during primary recrystallization differs from that during normal grain growth. However, each relationship for a series of annealing temperatures has almost the same slope including the not fully recrystallized samples. This may be due to the immediate impingement of the new grains, as observed in Figs. 1(4) to 1(6), or, in Figs. 2(4) to 2(6). Once they impinge on each other, they should give rise to normal grain growth, even during primary recrystallization.

Figure 4[2] shows semilogarithmic relationships between grain size and the inverse of annealing temperature, which are obtained by replotting the data on Fig. 3. Similarly, each relationship for a series of annealing times has almost the same slope. On the basis of Figs. 3 and 4, recrystallized grain size D can be approximately formulated with annealing temperature T and annealing time τ as in the following equation,

$$D(T,\tau)=C\tau^{n}\exp(-Q/RT), \quad (1)$$

where R is the gas constant, n is an exponential constant, and Q is activation energy. In this study, n, Q(cal/mol) and C were each determined by the method of least squares, leading to the equation,

$$D(T,\tau)=0.80\times10^{4}\,\tau^{0.24}\exp(-1.50\times10^{4}/RT)/\mu m. \quad (2)$$

A good agreement is obtained by equations (2), as graphically demonstrated in Fig. 5.[2]

Modeling for Estimating Grain Sizes during Non-isothermal Annealing

Equation (2) can well-interpolate isothermally recrystallized grain sizes of during the period from primary recrystallization to normal grain growth. We have confirmed by annealing the 80% cold rolled specimen for 1.8ksec at temperatures near the beta transus, that perceptible re crystallization does not occur below beta transus, possibly due to its competition with alpha pre-cipitation. The following model was accordingly proposed in this study. The concept of the model is schematically shown in Fig. 6.[2]

On the premise that the material temperature T is given as a function of time t, T=T(t) can be treated stepwise by dividing the period from t_o to t_r by some positive integer m. Here, t_o is the time when the material temperature arrives at the beta transus, and t_r is any time when the grain size needs to be estimated.

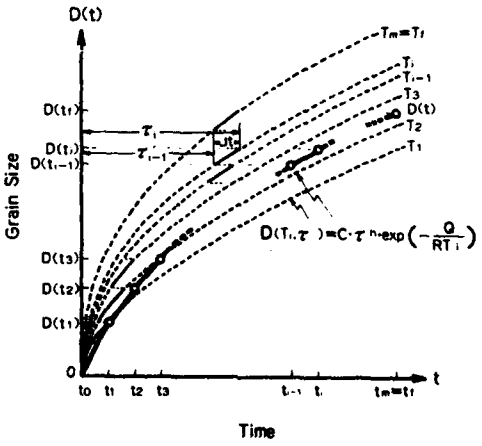


Fig. 6.[2] Schematic concept of the model for grain growth estimation when the material temperature is continuously changing.

This leads to the equations:

$$T_i=T(t_i), \quad (3)$$
$$t_i=\Delta t \cdot i+t_o, \quad (4)$$
$$\Delta t=(t_f-t_o)/m, \quad (5)$$

where t_i is the i^{th} time, and T_i is the material temperature corresponding to t_i. Considering the material temperature during the period, t_{i-1} to t_i, to be a constant temperature of T_i, the locus of grain size increment during t_{i-1} to t_i has to correspond locally with the curve indicated by the following equation,

$$D(T_i, \tau)=C\tau^n \exp(-Q/RT_i). \quad (6)$$

Since the rate of normal grain growth is at least a function of grain size itself, and the increment of grain size is derived from integrating the growth rate with time, the starting point of that locus must be the point where the grain size is $D(t_{i-1})$. Here, $D(t_{i-1})$ is the grain size at $t=t_{i-1}$. Therefore, the effective time τ_i for τ in equation (6) is indicated by

$$\tau_i=\tau_{i-1}'+\Delta t, \quad (7)$$

where τ_{i-1}' is satisfying the following equation,

$$D(T_i, \tau_{i-1}')=D(t_{i-1}). \quad (8)$$

In this context, the grain size at $t=t_i$, $D(t_i)$, is indicated by

$$D(t_i)=D(T_i, \tau_i). \quad (9)$$

From equations (1), (7), and (8) the following equation is derived,

$$C\tau_{i-1}'^n \exp(-Q/RT_i)=C\tau_{i-1}^n \exp(-Q/RT_{i-1}). \quad (10)$$

Then,

$$\tau_{i-1}'=\exp(Q/nR \cdot (1/T_i-1/T_{i-1}))\tau_{i-1}. \quad (11)$$

Therefore, from equation (8) and (11), the following relationship is obtained between τ_{i-1} and τ_i,

$$\tau_i=\exp(Q/nR \cdot (1/T_i-1/T_{i-1}))\tau_{i-1}+\Delta t. \quad (12)$$

τ_m is the effective time to give the grain size at $t=t_m$, that is, $t=t_f$. τ_m is obtained by repeating this operation from t_i to t_f step by step. The boundary conditions are $\tau_o=0$ and $D(t_o)=0$. With m being large enough to regard the temperature change as continuous, $D(t_f)$ is given by $D(t_m)$, that is,

$$D(t_f)=D(T_f, \tau_m), \quad (13)$$

where T_f is the material temperature at $t=t_f$.

Verification of the Model

In the model mentioned above, the period from t_o to t_f was divided by m in order to simplify the explanation of the concept of the model. However, the same values can also be calculated by integrating each grain size increment stepwise by a certain sufficiently short time division from t_o up to t_f. In order to evaluate the feasibility of the estimation by the model, we have compared the measured and calculated grain sizes of the samples which were heated from room temperature to

1073K at rates of 0.3 to 10K/sec and immediately quenched into water. In these calculations, T_o (temperature at $t=t_o$; the beta transus) was fixed at 986K. Figure 7[1] shows the graphical comparisons. The demonstrated correlation is good enough that the model can be considered to be fairly applicable.

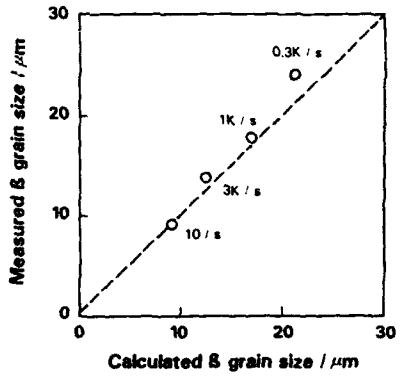


Fig. 7.[2] Graphic correlation between estimated and measured grain sizes.

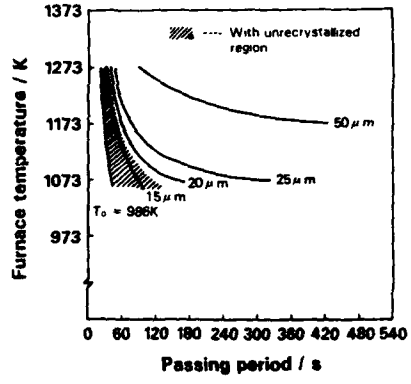


Fig. 8.[2] Estimated furnace temperature / passing period / recrystallized grain size diagram.

Application to a Test Production

In order to apply the model to practical production, we have experimentally determined an approximate material's temperature / time relationship for 1.0 and 1.2mm thick sheets inserted into a sufficiently large furnace,[2]

$$T(t)=(293-T_b)\exp(-0.058t)+T_b, \quad (15)$$

where T(t) is the material temperature at time t, and T_b is a furnace temperature.

Given a furnace temperature T_b and a period t during which the material is in the furnace (referred to as the passing period), its recrystallized grain size after passing can be calculated on the basis of the model. Figure 8[2] shows a furnace temperature / passing period / recrystallized grain size diagram which was numerically obtained with a time division of 1 sec. It was confirmed that under some conditions a time division of 0.01 sec led to almost the same results.

As was observed in Fig. 1, deformed grain boundaries tend to provide the preferential nucleation sites during recrystallization. The kinetics of recrystallization must accordingly depend on the initial microstructural states such as prior grain size. We have confirmed that in no condition is full recrystallization achieved with a grain size less than about 20 μm as for the material used in this study. Finally, after considering other restrictions such as the capacity of the apparatus and the descalability of the sheet after annealing, the cold strip was continuously annealed under conditions almost corresponding to the combination of a furnace temperature of 1093K and a passing period of 120sec. This condition was chosen in order to obtain a fine-grained and fully

120sec. This condition was chosen in order to obtain a fine-grained and fully recrystallized microstructure. Figure 9 shows the Ti-15V-3Cr-3Sn-3Al strip and its microstructure. As a result, a strip with a uniform fine-grained microstructure was successfully obtained. The grain size is almost the same as estimated, that is, 21μm.

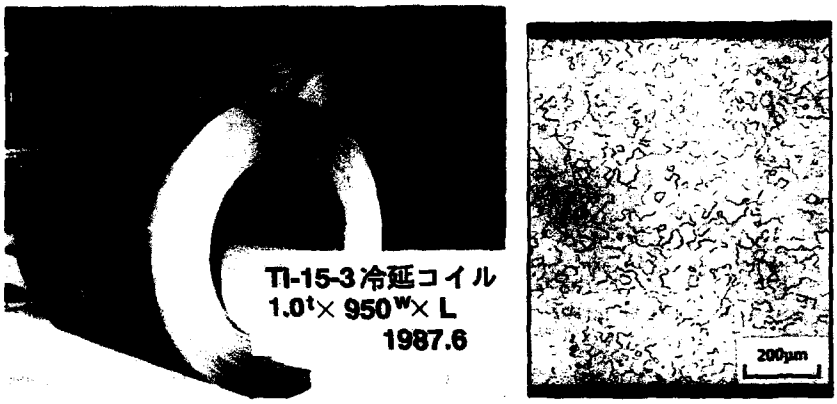


Fig. 9. Ti-15V-3Cr-3Sn-3Al cold strip produced in an annealing and pickling process and its optical microstructure.

Conclusion

We have investigated the recrystallization behaviors of a cold rolled Ti-15V-3Cr-3Sn-3Al alloy strip, and developed an estimation method of recrystallized grain size during continuous annealing. The estimation can be carried out by sequentially integrating, stepwise, each increment of the isothermal grain growth at each temperature above the beta transus. Based on the furnace temperature / passing period / recrystallized grain size diagram numerically obtained, a fine-grained Ti-15V-3Cr-3Sn-3Al strip was successfully obtained in an annealing and pickling process on the commercial basis.

References

1)F. H. Froes, J. M. Capenos, and C. F. Yolton: Metallography, 9(1976), 535.
2)H. Ohyama and Y. Ashida: ISIJ Int., 31(1991), 799.

HIGH TEMPERATURE PHASE STABILITY IN XD™ TiB_2 REINFORCED NEAR-GAMMA Ti-48Al-2Nb-2Mn

S. Guillard, H.J. Rack and D.E. Larsen

Materials Science and Engineering Program
Clemson University
Clemson, South Carolina 29634-0921

Applied Research Division
Howmet Corporation
Whitehall, MI 49461-1895

Abstract

The elevated temperature phase stability of investment cast and HIP'ed near-gamma Ti-48Al-2Nb-2Mn containing 0, 0.5, 1, 2 and 7 vol.% TiB_2 has been investigated utilizing in-situ high temperature x-ray, transmission electron microscopy and thermal analysis. These studies have shown that the following reversible solid state phase transformations occur

$$\alpha_2+\gamma \longrightarrow \alpha+\gamma \longrightarrow \alpha+\beta+\gamma \longrightarrow \beta+\gamma$$

It is proposed that these reactions involve a low temperature eutectoid transformation, $\alpha_2 + \gamma \longrightarrow \alpha$, followed by β precipitation and γ dissolution, and ultimately a high temperature peritectoid reaction, $\alpha \longrightarrow \beta + \gamma$.

Changes in the transformation temperatures associated with each of the proposed reactions are not directly related to the TiB_2 volume fraction, rather these appear to be controlled by the total interstitial content of each alloy.

Introduction

Because of their combination of low density and high temperature properties, near-γ titanium aluminides are attractive candidates for applications in advanced turbine engines and airframe designs. While they combine good oxidation resistance, relatively high modulus and good strength retention at high temperature [1], their low fracture toughness and low room-temperature ductility, <3.5%, have restricted their applicability. Fortunately recent investigations have demonstrated that significant gains in fracture toughness can be achieved thru use of appropriate processing methods and heat treatments. For example, a fully lamellar $(\alpha_2+\gamma)$ microstructure, which may be achieved thru heat treatment high in the $(\alpha_2+\gamma)$ phase field, displays a higher fracture toughness than does an equiaxed microstructure [1-5].

While thermal treatments alone may be utilized to promote the $(\alpha_2+\gamma)$ lamellar microstructure, these treatments are typically accompanied by an increase in grain size and therefore a further reduction in tensile ductility [3,4]. Alternatively, other studies suggest that the formation of the $(\alpha_2+\gamma)$ lamellar microstructure may be enhanced in binary TiAl thru the addition of TiB_2 particles [6]. In addition, these particles have the further beneficial effect of promoting a decrease in α_2/γ colony size [7] and grain size [8-11]. When combined, i.e., a decreased colony/grain size and a $(\alpha_2+\gamma)$ lamellar microstructure, these results suggest that TiB_2 containing titanium aluminides may have both enhanced fracture toughness and tensile ductility when compared to unreinforced alloys.

Further advancements in utilizing this potential approach to enhance the mechanical properties of near-γ titanium aluminides should be possible once the stability and performance of these materials are understood. The present investigation was therefore undertaken to determine the phase stability of a prototypical near-γ alloy, Ti-48Al-2Nb-2Mn, containing various volume fractions of titanium diboride.

Titanium '92
Science and Technology
Edited by F.H. Froes and I. Caplan
The Minerals, Metals & Materials Society, 1993

Experimental Procedures

Ti-48Al-2Nb-2Mn ingots, Table I, with 0, 0.5, 1, 2 and 7 vol.% TiB_2 were produced by double vacuum arc remelting (VAR), TiB_2 being introduced via the XD™ process [11]. Cylindrical bars of 15.9 mm X 203.2 mm were then investment cast and HIP'ed for 4 hours at 1533 K and 175 MPa, HIP'ing being terminated by cooling to room temperature at a rate less than 30 K/min.

Table I
Alloy Composition

ALLOY #	O_2 (ppm)	N_2 (ppm)	H_2 (ppm)	C (ppm)	Al (at%)	Nb (at%)	Mn (at%)	TiB_2* (vol%)
TARGET	<800	-	-	-	48.0	2.0	2.0	-
NM0	540	38	3	100	48.1	2.0	1.4	0
NM0.5	539	35	3	120	47.4	2.0	1.7	0.5
NM1	540	47	3	80	47.0	1.9	1.6	1
NM2	560	52	3	80	47.4	2.0	1.6	2
NM7	620	139	16	180	46.9	1.8	1.5	7

* Calculated from the analyzed boron contents.

Scanning electron microscopy of these cast and HIP'ed materials showed that unreinforced Ti-48Al-2Nb-2Mn had a microstructure consisting of ($\alpha_2+\gamma$) lamellar colonies, L, and equiaxed gamma grains, G, Figure 1. In contrast the introduction of TiB_2 led to a reduction in grain size and a completely ($\alpha_2+\gamma$) lamellar microstructure, Figure 2 [7-10].

Three TiB_2 morphologies were observed in these materials, the diboride phase evolving from a predominantly lacey structure at 0.5 vol.%, figure 2(a), to needles and blocky particles at 1 and 2 vol.%, figures 2(b) and 2(c), and finally to predominantly blocky particles at 7 vol.%, figure 2(d). A similar evolution of the titanium boride morphology has been reported by others [8,12,13], who further confirmed by x-ray diffraction of the extracted particles [8] and by transmission electron microscopy [12,13] that all three morphologies are indeed TiB_2.

The high temperature stability of these alloys was assessed using calorimetric differential thermal analysis (CDTA)[14] and high temperature x-ray diffraction (HTXRD)[15]. Equilibrium phase transformation temperatures were extrapolated from calorimetric observations between 873 K and 1703 K during both heating and cooling at rates of 5, 10, 20 and 40 K/min. The samples, having been placed in alumina crucibles, were introduced into a Stanton Redcroft / Omnitherm DSC 1500 thermal analysis system modified to be run in a flowing high purity (1 ppb) argon atmosphere [16].

In order to determine the reaction temperatures associated with each transformation, both the heat flow J, normalized per unit mass ($mJ.sec^{-1}.mg^{-1}$), and its first derivative with respect to temperature, $J' = dJ/dT$ ($mJ.sec^{-1}.mg^{-1}.deg^{-1}$), were recorded. Transformation temperatures were determined from the CDTA thermograms by establishing those temperatures where the J and J' curves deviated from the baseline, and in the case of overlapping peaks, where the J' curve exhibited a curvature anomaly.

Additionally, high temperature x-ray diffraction studies were undertaken to identify the various phases present at elevated temperature. The procedure utilized a Scintag 1500 diffractometer equipped with a high temperature/vacuum chamber modified to introduce and maintain a high purity inert argon gas atmosphere at a desired pressure of 0.60 Pa. HTXRD samples, having dimensions of 8 mm X 20 mm X 0.25 mm, were prepared by wafering and grinding, with final preparation involving chemical removal of a 20 μm minimum surface layer in a bath of 10 ml HNO_3 + 5 ml HF + 50 ml H_2O, followed by washing in ethanol and water, drying in air and finally, storage in a vacuum dessicator.

Initially, ambient temperature 2θ-scans from 15° to 85° were obtained. The sample was then heated at a rate of 20K/min, up to 1703K with diffraction spectra being acquired at selected temperatures. Typically, data were recorded after a 5-minute stabilization period at temperature with data acquisition lasting 7 minutes. Three to four samples of each alloy were examined, with rocking curves being obtained where deemed necessary to verify the presence, or absence, of phases at elevated temperatures. Finally, following data collection, the x-ray



Figure 1. Scanning electron micrograph of Ti-48Al-2Nb-2Mn illustrating mixed microstructure consisting of equiaxed γ grains, [G], and (α_2 + γ) lamellar colonies, [L].

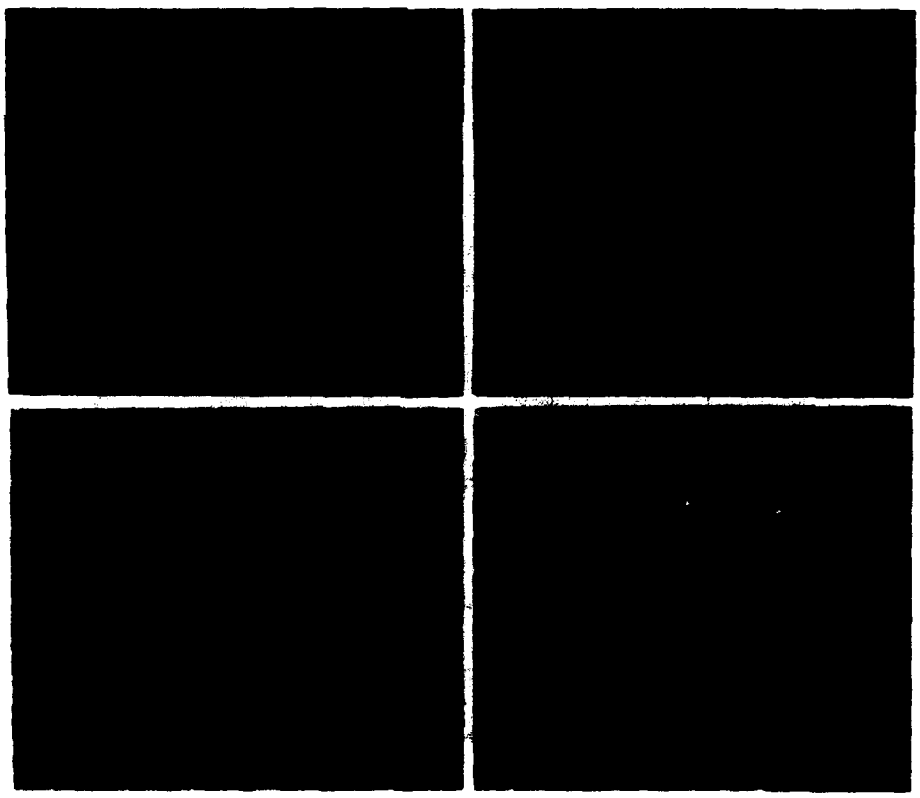


Figure 2. Scanning electron micrographs illustrating TiB_2 morphology in Ti-48Al-2Nb-2Mn containing (a) 0.5 vol.% TiB_2, (b) 1 vol.% TiB_2, (c) 2 vol.% TiB_2, and (d) 7 vol.% TiB_2.

diffraction spectra were analyzed and the peaks indexed utilizing an iterative computer program capable of fitting the observed data to given cell structures using a least squares method.

Transmission electron microscopy samples were also prepared by grinding the materials on SiC grit paper down to 150 microns, cutting 3mm-discs from the foils thus produced, and electro-polishing them in a solution of 30 ml perchloric acid + 175 ml n-butanol + 300 ml methanol under 15 to 20 volts below -30°C. Subsequent observation was carried out in a Hitachi 600AB operated at 100 kV.

Results

Ti-48Al-2Nb-2Mn

Calorimetric differential thermal analysis, Fig. 3(a) and 3(b), showed that, independent of heating/cooling rate, three reversible reactions, T1 thru T3, were observed during heating and cooling of unreinforced Ti-48Al-2Nb-2Mn. In addition, a fourth reaction, T4, was observed on heating and was associated with melting of the CDTA sample. Temperatures for the onset and completion of these reactions are summarized in Table II.

X-ray diffraction analysis of Ti-48Al-2Nb-2Mn indicated that this alloy was two phase ($\alpha_2+\gamma$) at room temperature, Figure 4(a)[1].

Upon heating no discernable differences in the x-ray results were observed until 1523K, at which temperature the $(110)_\beta$ peak appeared, the structure now consisting of $\alpha + \gamma + \beta$, the α_2 having disordered. A further temperature increase to 1623K resulted in an increase in the β peak intensities relative to the γ peak. Finally, above 1623K, the alloy was two phase $\beta + \gamma$, all evidence of α having disappeared.

Ti-48Al-2Nb-2Mn/TiB_2

Typical calorimetric differential thermal analysis results for both heating/cooling of the TiB_2 reinforced Ti-48Al-2Nb-2Mn alloys are illustrated for Ti-48Al-2Nb-2Mn/7 vol. % TiB_2 in Figures 3(c) and 3(d). The three solid state reactions observed, T1,T2 and T3, as well as that associated with melting, T4, were similar to those found in unreinforced Ti-48Al-2Nb-2Mn, Table II.

Correspondingly ambiant and elevated temperature x-ray diffraction results for the TiB_2 reinforced Ti-48Al-2Nb-2Mn were similar to those of the unreinforced alloy, Figure 4(b). For example, at low temperatures Ti-48Al-2Nb-2Mn/7 vol. % TiB_2 was $\alpha_2 + \gamma$, transforming to $\alpha + \gamma + \beta$ above 1548K and finally to $\beta + \gamma$ above 1648K.

Table II
Equilibrium Transformation Temperatures

	HEATING	HEATING	HEATING		COOLING	COOLING	COOLING
	T1 onset complete	T2 onset complete	T3 onset complete	T4	T3 onset complete	T2 onset complete	T1 onset complete
NM0	1458 1485	1536 1623	1623 1646	1690	1638 1597	1603 1563	1465 1438
NM0.5	1470 1498	1515 1626	1626 1659	1677	1631 1593	1621 1584	1476 1445
NM1	1468 1486	1513 1620	1620 1661	1670	1628 1605	1615 1590	1485 1468
NM2	1475 1490	1519 1625	1625 1656	1666	1633 1604	1611 1590	1483 1463
NM7	1529 1539	1555 1630	1630 1652	1664	1644 1619	1633 1603	1568 1521

[1] It was confirmed by transmission electron microscopy that no β phase is present at room temperature.

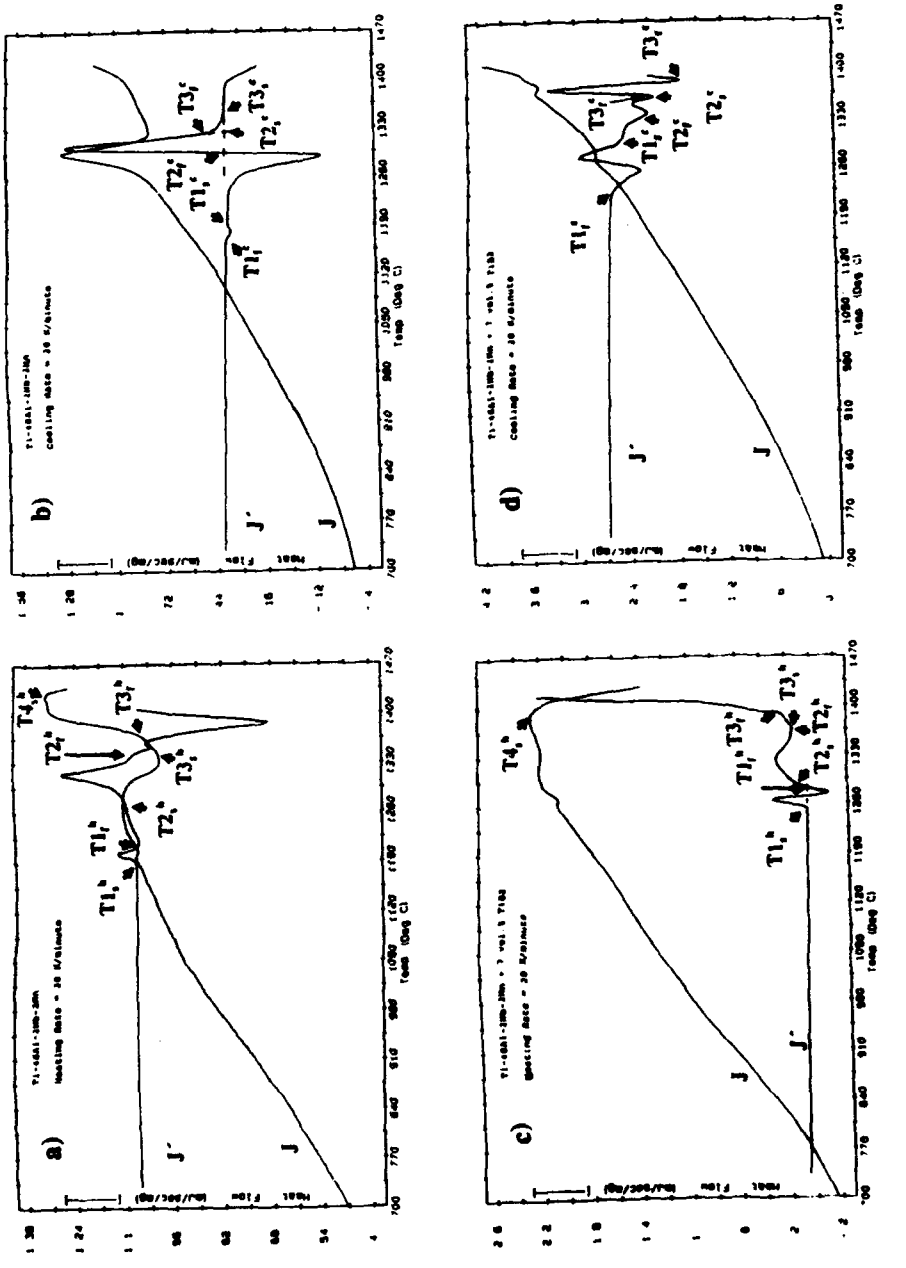
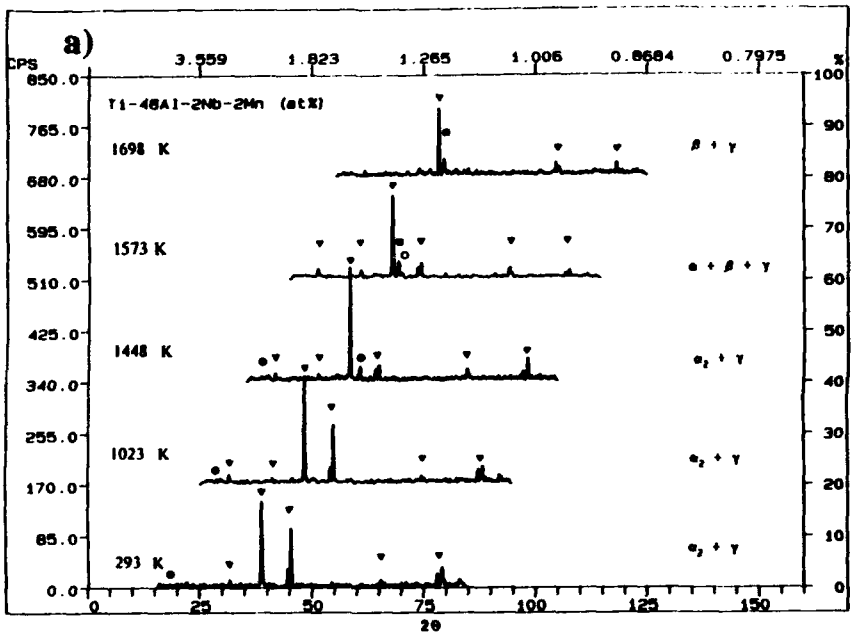


Figure 3. Thermograms of (a) Ti-48Al-2Nb-2Mn on heating, (b) Ti-48Al-2Nb-2Mn on cooling, (c) Ti-48Al-2Nb-2Mn/7 vol.% TiB_2 on heating and (d) Ti-48Al-2Nb-2Mn/7 vol.% TiB_2 on cooling at 20 K/min.



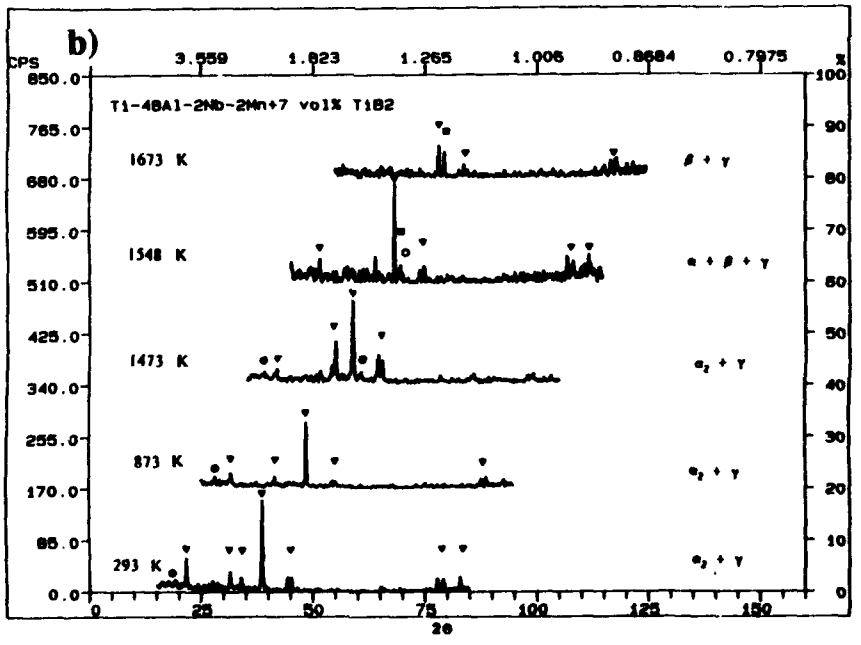


Figure 4. X-ray spectra showing the phases present at selected temperatures for (a) Ti-48Al-2Nb-2Mn and (b) Ti-48Al-2Nb-2Mn/7 vol. % TiB_2. (• α_2, ○ α, ▪ β, ▼ γ).

Discussion

The combined thermal analysis and x-ray diffraction observations can be utilized to examine the influence of temperature and TiB_2 addition on phase stability in Ti-48Al-2Nb-2Mn. In general, independent of TiB_2 content, it is proposed that heating/cooling results in the following solid state transformations:

$$\alpha_2+\gamma \longrightarrow \alpha+\gamma \longrightarrow \alpha+\beta+\gamma \longrightarrow \beta+\gamma$$

with melting occurring at the highest temperatures examined. Comparison of the calorimetric differential thermal analysis, Table II, with the HTXRD results supports the suggestion that reaction T1, occurring at approximately 1470 K for NM0 and 1530 K for NM7, is the eutectoid transformation $\alpha_2+\gamma \longrightarrow \alpha$, i.e., α_2 is not observed above T1. In addition, the T1 reaction occurs at temperatures close to the reported eutectoid temperature in binary Ti-48.65Al, 1450 K [17]. Precipitation of β commences at temperatures between T1 and T2, with T2 corresponding to increasing β precipitation and dissolution of γ. T3 then coincides with the proposed $\alpha \longrightarrow \beta+\gamma$ peritectoid transformation.

The results also indicate that, in contrast with binary TiAl/TiB_2 alloys, α is not the high temperature equilibrium phase for Ti-48Al-2Nb-2Mn, a two phase $\beta + \gamma$ region existing in the latter alloy immediately below the solidus. This difference between the Ti-48Al-2Nb-2Mn and binary alloys [6] is presumably due to the β-stabilizing effect of the two alloying additions, i.e. Nb and Mn. Failure of previous investigators [18] to recognize the presence of the $\beta+\gamma$ phase field at high temperatures during their study of Ti-48Al-2Nb-2Mn is not surprising, CDTA by itself not being able to define the reactant or the product phases participating in a phase transformation.

Finally, the results suggest that the influence of the TiB_2 reinforcements on the transformation temperatures is not directly correlatable to the TiB_2 volume fraction. Rather it appears that the transformation temperatures are more directly related to the total interstitial content (O+N+B+C+H). For example, the eutectoid transformation temperature increases with increasing interstitial content. Further study continues towards quantifying this interstitial effect.

Conclusions

The elevated temperature phase stability of investment cast and HIP'ed near-gamma Ti-48Al-2Nb-2Mn containing 0, 0.5, 1, 2 and 7 vol.% TiB_2 involves the following reversible solid state phase transformations:

$$\alpha_2+\gamma \longrightarrow \alpha+\gamma \longrightarrow \alpha+\beta+\gamma \longrightarrow \beta+\gamma$$

These reactions involve a low temperature eutectoid transformation, $\alpha_2 + \gamma \longrightarrow \alpha$, a precipitation reaction leading to the presence of the β phase and a high temperature peritectoid, $\alpha \longrightarrow \beta + \gamma$.

The total interstitial content seems to have much more influence on the phase stability of these materials than the TiB_2 content.

Acknowledgements

This research was sponsored by the Defense Advanced Research Projects Agency under the contract N00014-89-J-3166 supervised by Mr. W. Baker and monitored by Dr. G. Yoder of the Office of Naval Research. The assistance of Dr. P. Chaudhury and M. Long is gratefully acknowledged.

References

1. Y.W. Kim and D.M. Dimiduk, "Progress in the Understanding of Gamma Titanium Aluminides", Jn of Metals, Aug.1991, 40-47.

2. K-W. Kim, "Recent Advances in Gamma Titanium Aluminide Alloys", in High-Temperature Ordered Intermetallic Alloys IV, eds. L. A. Johnson, D. P. Pope and J. O. Steigler, Vol. 213, MRS, Pittsburgh, PA, (1991), 777-794.

3. Y.W. Kim, "Microstructural Evolution and Mechanical Properties in Gamma Titanium Aluminides", in Microstructure/Property Relationships in Titanium Aluminides and Alloys, eds. Y-W. Kim and R.R. Boyer, The Minerals, Metals and Materials Society, Warrendale, PA, (1991), 91-103.

4. S-C. Huang and D. S. Shih, "Microstructure-Property Correlation in TiAl-Base Alloys", in Microstructure/Property Relationships in Titanium Aluminides and Alloys, eds. Y-W. Kim and R.R. Boyer, The Minerals, Metals and Materials Society, Warrendale, PA, (1991), 105-122.

5. K. S. Chan and Y-W. Kim, "Fracture Processes in a Two-Phase Gamma Titanium Aluminide Alloy", in Microstructure/Property Relationships in Titanium Aluminides and Alloys, eds. Y-W. Kim and R.R. Boyer, The Minerals, Metals and Materials Society, Warrendale, PA, (1991), 179-196.
6. C.R. Feng, D.J. Michel and C.R. Crowe, "Microstructures of XD™ Titanium Aluminide at Elevated Temperatures", Scripta Met., 24 (1990) 1297-1301.
7. J. D. Bryant, L. Christodoulou and J. R. Maisano, "Effect of TiB_2 Additions on the Colony Size of Near Gamma Titanium Aluminides", Scripta Met., 24 (1990) 33-38.
8. D.E. Larsen, S. Kampe and L. Christodoulou, "Effect of XD™ TiB_2 Volume Fraction on the Microstructure of a Cast Near-Gamma Titanium Aluminide Alloy, in Intermetallic Matrix Composites, eds. D.L. Anton, P.L. Martin, D.B. Miracle and R. McMeeking, Vol. 194, MRS, Pittsburgh, PA, (1990), 285-292.
9. D.E. Larsen, M. L. Adams, S. L. Kampe, L. Christodoulou and J. D. Bryant, "Influence of Matrix Phase Morphology on Fracture Toughness in a Discontinously Reinforced XD™ Titanium Aluminide Composite", Scripta Met., 24 (1990) 851-856.
10. D. E. Larsen, "Effects of XD™ TiB_2 Volume Fraction on the Microstructure and Mechanical Properties of a Cast XD™ Near-Gamma Alloy", in Microstructure/Property Relationships in Titanium Aluminides and Alloys, eds. Y-W. Kim and R.R. Boyer, The Minerals, Metals and Materials Society, Warrendale, PA, (1991), 345-360.
11. L. Christodoulou, P.A. Parrish and C.R. Crowe, in High Temperature/High Performance Composites, eds. F.D. Lemkey, S.G. Fishman, A.G. Evans and J.R. Strife, Vol. 120, MRS, Pittsburgh, PA, (1988), 29-34.
12. M. E. Hyman, C. McCullough, J. J. Valencia, C. G. Levi and R. Mehrabian, "Microstructure Evolution in TiAl Alloys with B Additions: Conventional Solidification", Metall. Trans., 20A (1989) 1847-1859.
13. M.E. Hyman, C. McCullough, C. G. Levi and R. Mehrabian, "Evolution of Boride Morphologies in TiAl-B Alloys", Metall. Trans., 22A (1991) 1647-1662.
14. Differential Thermal Analysis, ed. R.C. Mackenzie, Academic Press, (1972).
15. P. K. Chaudhury, M. Long and H. J. Rack, "Effect of Vanadium on Elevated Temperature Phase Relations in Titanium Aluminides containing 44 at. % Al", Mat'ls Sci. Eng., in press.
16. P. K. Chaudhury and H. J. Rack, "Ti-Al-V Ternary Phase Stability at Elevated Temperatures", Scripta Met., 26, (1992), 691-695.
17. J.C. Mishurda and J.H. Perepezko, "Phase Equilibria in Ti-Al Alloys", in Microstructure/Property Relationships in Titanium Aluminides and Alloys, eds. Y.W. Kim and R.R. Boyer, The Minerals, Metals and Materials Society, Warrendale, PA, (1991), 3-30.
18. P.A. McQuay, D.M. Dimiduk and S.L. Semiatin, "The Decomposition of Alpha Phase During Continuous Cooling and Isothermal Transformation in Gamma Titanium Aluminide", Scripta Metall., 25, (1991), 1689-1694.

ELEVATED TEMPERATURE PHASE STABILITY OF Ti-25Al-11Nb

Marc Long, Prabir K. Chaudhury, and H. J. Rack *

Materials Science and Engineering Program
Clemson University
Clemson, South Carolina 29634-0921

Abstract

The elevated temperature phase stability of triple vacuum melted and forged Ti-25Al-11Nb has been investigated utilizing optical microscopy, calorimetric differential thermal analysis and *in-situ* high temperature x-ray diffraction. These studies have shown that slow cooling after forging resulted in a microstructure consisting of primary, blocky α_2 colonies (α_2^P) in a matrix of secondary, 'basketweave' α_2 (α_2^S) + transformed disordered β (β_t) + orthorhombic phase O. Upon continuous heating sequential dissolution of orthorhombic O and the morphologically distinct ordered α_2 phases was observed, with α_2 disordering to α below the β transus. Similar reversible transformations were observed on cooling from the β phase field; the quantities of α_2^P and α_2^S in the alloy microstructure after cooling being rate dependent, decreasing cooling rate increasing the volume fraction of α_2^P.

Introduction

Ti_3Al based intermetallic alloys (based on the α_2 phase, ordered hcp, DO_{19} structure) exhibit superior elevated temperature strength and creep resistance when compared to conventional titanium alloys. Their low ambient temperature ductility and fracture toughness has, however, required alloy modification. Among several modifications investigated, the most promising involves incorporation of β stabilizers, such as Nb, V and Mo, to levels which result in the introduction of controlled quantities of a ductile β phase (1). One of the most interesting alloys in this regard is the commercial Ti-24Al-11Nb alloy. While the addition of niobium in this alloy promotes the formation of a two phase $\alpha_2+\beta$ (or ordered β, β_0, with the CsCl structure B2) mixture (2,3), recent investigations of the Ti_3Al-Nb pseudo-binary system (3-7) have demonstrated that complex phase relationships exist in this system. For example, depending upon exact alloy chemistry and prior thermo-mechanical history phases reported in the Ti_3Al-Nb system include β (disordered bcc) (6,7), β_0 (ordered bcc, B2 structure) (8), α (disordered hcp) (9), α_2 (ordered hcp, DO_{19} structure), O/O' (orthorhombic phase derived from the DO_{19} phase) (10), and recently a new tetragonal phase (DO_{22}-like structure) (11).

A definition of the high temperature in-situ phase stability is therefore essential for the development of appropriate elevated temperature thermo-mechanical processing of Ti_3Al-Nb alloys. To achieve this goal, the present study establishes the phase relationships at elevated temperatures, upon continuous heating/cooling, of the commercial Ti-24Al-11Nb (true composition Ti-25Al-11Nb) alloy.

---

* Graduate Student, Clemson University; formerly Research Associate, Clemson University, currently Manager of Forming Department, Concurrent Technology, Inc., Johnston, PA; Professor of Mechanical Engineering and Metallurgy, Clemson University, respectively.

Titanium '92
Science and Technology
Edited by F.H. Froes and I. Caplan
The Minerals, Metals & Materials Society, 1993

Experimental Procedures

The chemical composition of the investigated Ti-25Al-11Nb (at.%) alloy is given in Table I. This alloy was received as a 152.4 mm. thick slab having been forged from a 3400 kg. triple vacuum melted production ingot. During prior processing, the material had been heated to 1533 K, held at this temperature for 8 hours, forged, and then air cooled. Metallographic examination of sections prepared using conventional techniques (grinding, polishing and etching with Kroll's reagent), Figure 1, showed that the microstructure consisted of uniform primary, blocky α_2 (α_2^P) in a transformed β (Widmanstätten secondary α_2^S + β_t) matrix. Ambient temperature x-ray diffraction revealed an $\alpha_2+\beta$(disordered) structure, with a small quantity of an orthorhombic-like phase O characterized by the presence of 'shoulders' at the identified α_2 peaks.

Characterization of the high temperature stability utilized calorimetric differential thermal analysis (CDTA) and high temperature in-situ x-ray diffraction (HTXRD). The former used a Stanton Redcroft/Omnitherm DSC 1500 thermal analysis system, modified to ensure that the heating/cooling experiments were unaffected by the test environment (12). Phase transformation temperatures from 873 K to 1573 K were determined during both heating and cooling in a high purity argon atmosphere at 5, 10, 20, and 40 K/min rates. In order to precisely determine each transformation, both the heat flow, normalized per unit mass ($mJ.sec^{-1}.mg^{-1}$.), and its first derivative with respect to temperature, $J' = dJ/dT$ ($mJ.sec^{-1}.mg^{-1}.deg^{-1}$), were recorded and analyzed. Transformation temperatures were determined from the CDTA thermograms by establishing those temperatures where the J and J′ curves deviated from the baseline (T_O^a, T_O^f, T_S^b, and T_B^b on heating and T_B^c, T_D^c, and T_S^c on cooling), and in the case of overlapping peaks, where the J′ curve showed a curvature anomaly (T_L^b and T_D^b on heating and T_L^c on cooling). The average standard deviation observed for the measured reaction temperatures was ± 5 K.

In-situ high temperature x-ray diffraction (HTXRD) experiments were undertaken to complement the CDTA experiments. These utilized a Scintag diffractometer equipped with a high temperature furnace/vacuum chamber, the latter having again been modified to introduce and maintain a high purity inert argon gas atmosphere at a pressure of 0.6 bar (12).

Table I. Chemical composition of Ti-25Al-11Nb

	Ti	Al	Nb	O	C	N	Fe
at.%	bal.	24.95	10.83	0.26	0.26	0.04	0.04
wt.%	bal.	14.25	21.30	0.09	0.09	0.01	0.05



Figure 1 - Ti-25Al-11Nb as-forged microstructure exhibiting primary, blocky α_2^P [P] and a mixture of secondary, 'basketweave' α_2^S [S] and retained β_t.

Results

The results of the thermal analysis observations during continuous heating and cooling are shown in Figure 2 and 3, respectively. Independent of heating rate, Ti-25Al-11Nb exhibited a low temperature transformation below 1123 K (850°C). This transformation, starting at T_O^s and ending at T_O^f, was followed by a complex sequence of transformations, T_s^h thru T_B^h. Above T_s^h, where both J and J´ curves deviated from the baseline, ensuing reactions, as defined by anomalies in J´, were observed at T_L^h and T_D^h. Finally this sequence of transformations was completed at T_B^h.

Cooling thermograms exhibited three distinct transformations in the 1348-1173 K (1075°-900°C) range, except at the lowest rate examined, 5 K/min, where only two reactions were recorded. The first reaction which had an onset at T_B^c and finished at T_D^c, was immediately followed by a second reaction which terminated at T_s^c. At cooling rates above 5 K/min, a third reaction appeared, interrupting the T_D^c-T_s^c reaction at a temperature T_L^c, with the extent of this additional transformation increasing with increasing cooling rate.

In order to estimate the equilibrium reaction temperatures, that is to eliminate the influence of heating or cooling rate on the observed transformation temperatures, the temperature *vs.* rate curves were assumed to be a linear function of rate and were extrapolated to an ideal 0 K/min rate corresponding to the equilibrium state, Table II.

Table II. Transformation temperatures as a function of heating/cooling rates

Heating/Cooling Rate (K/min)	Transformation Temperatures (K) [Heating(T_x^h)/Cooling(T_x^c)]					
	T_O	T_O	T_s	T_L	T_D	T_B
40	943/ND[a]	1109/ND	1210/1107	1401/1231	ND/1304	1485/1349
20	928/ND	1091/ND	1211/1172	1389/1238	1425/1320	1456/1353
10	913/ND	1083/ND	1208/1198	1378/1242	1407/1334	1443/1351
5	909/ND	1086/ND	1206/1225	1371/ND	1401/1338	1441/1355
0[b]	905/ND	1079/ND	1207/1236	1369/1246	1394/1343	1432/1354

[a] non-detected
[b] extrapolated

High temperature x-ray diffraction data at 20 K/min for Ti-25Al-11Nb are summarized in Table III. These data show that Ti-25Al-11Nb was three phase ($\alpha_2+\beta+O$) up to 1123 K (850°C), the major β peak, β(110) at $2\theta = 38.8°$, overlapping with the α_2(002) peak at $2\theta = 38.2°$. The orthorhombic peaks, characterized by small 'shoulders' at α_2 peaks, started disappearing at approximately 923 K (650°C) with the completion of this transformation at 1123 K (850°C).

Between 1173 K (900°C) and 1323 K (1050°C), the alloy was two phase ($\alpha_2+\beta$). Above 1348 K (1075°C) a new peak, which could be indexed as a satellite α/α_2 reflection, started to appear, *i.e.*, the major peak of the x-ray diffraction scan (α_2(002)/$2\theta = 38°$) separated into two peaks. At 1448 K (1175°C) this satellite reflection disappeared and the alloy was in the $\alpha+\beta$ phase field. Due to the overlapping of the α_2 and α peaks, the α_2-α disordering transformation was verified with rocking curves at low angles $2\theta = 17.5°$, α_2(100), and $2\theta = 26°$, α_2(110). The expected peaks characteristic only of the ordered α_2 phase were absent at 1448 K. Finally, at 1473 K (1200°C) and above, the x-ray scans showed no distinct peaks, however rocking curves indicated that the alloy was single phase, disordered bcc β phase, above this temperature.

Table III. Phase structures determined by HTXRD at 20 K/min heating rate

Temperature (K)	298 - 1123	1173 - 1323	1348 - 1423	1448	1473
Phases	$\alpha_2 + \beta + O$	$\alpha_2 + \beta$	*split* $\alpha/\alpha_2 + \beta$	$\alpha + \beta$	β

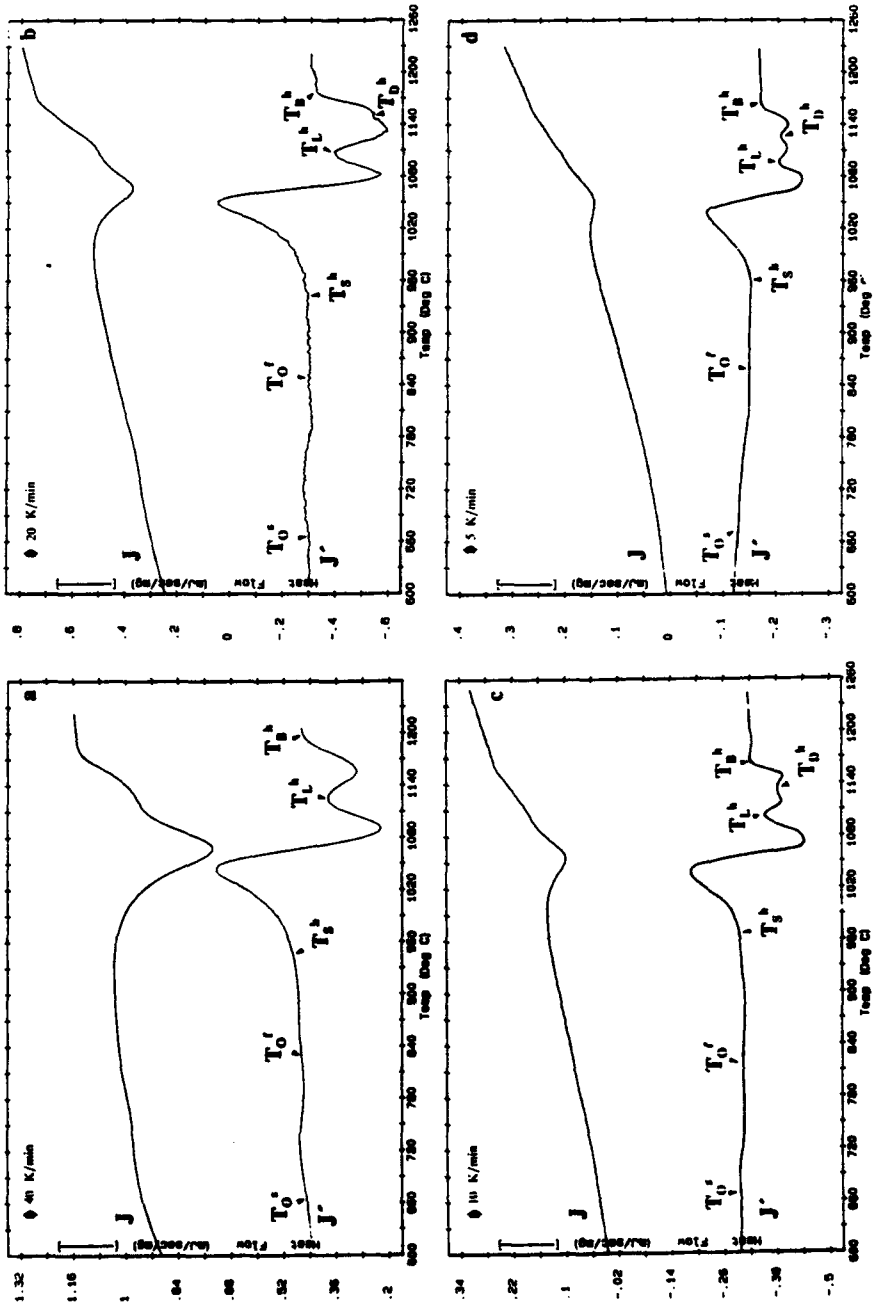


Figure 2 - CDTA thermograms for Ti-25Al-11Nb on heating at (a) 40, (b) 20, (c) 10, and (d) 5 K/min. Heat flow J ($mJ.sec^{-1}.mg^{-1}$) and its first derivative J′ ($mJ.sec^{-1}.mg^{-1}.deg^{-1}$).

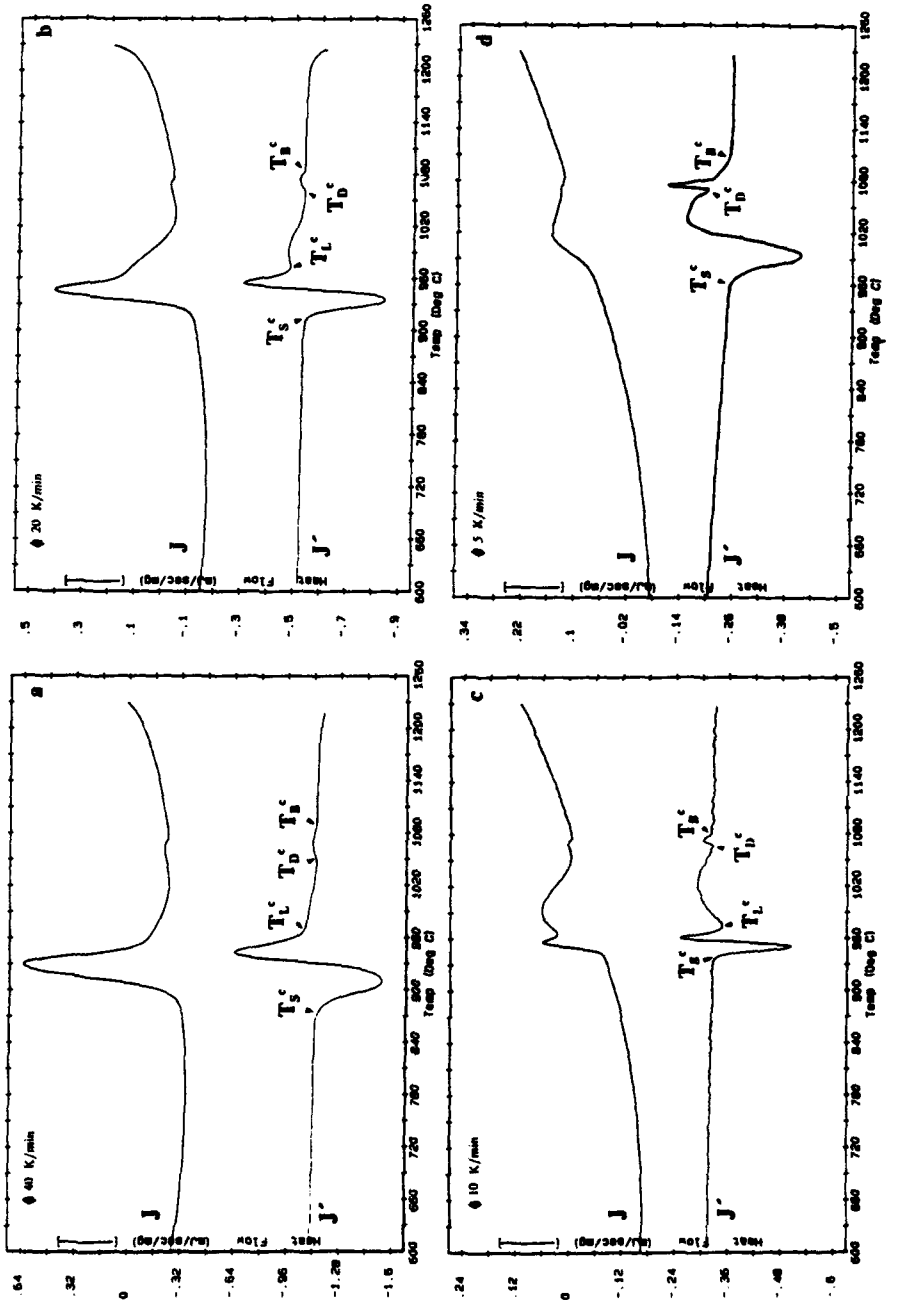


Figure 3 - CDTA thermograms for Ti-25Al-11Nb on cooling at (a) 40, (b) 20, (c) 10, and (d) 5 K/min. Heat flow J ($mJ.sec^{-1}.mg^{-1}$) and its first derivative J' ($mJ.sec^{-1}.mg^{-1}.deg^{-1}$).

Upon cooling, x-ray scans were also taken and were found to be qualitatively identical to those on heating, the intensity of the peaks being randomly modified. Between 1348 K (1075°C) and 1298 K (1025°C), the presence of an $\alpha+\beta$ structure was identified, transforming to $\alpha_2+\beta$ below 1273 K (1000°C). Ultimately a three phase structure, $\alpha_2+\beta+O$, appeared below 1123 K (850°C), this structure remaining till room temperature [1].

Discussion

Using the combination of the CDTA and in-situ HTXRD experiments, the phase stability of Ti-25Al-11Nb at elevated temperatures was established during continuous heating/cooling. By analogy with conventional titanium alloys (13), transformations on heating Ti-25Al-11Nb involved dissolution processes while, on cooling, the reverse transformations involved precipitation of α/α_2 [2].

Initially the microstructure of the alloy examined consists of $\alpha_2^P+\{\alpha_2^S+\beta_t\}+O$, with two distinct α_2 morphologies, primary blocky α_2^P, and secondary α_2^S. Upon heating, Table IV, the first transformation consists of orthorhombic phase dissolution as defined by temperatures between T_O^s and T_O^f, Figure 2.

Table IV. Phase transformations upon heating for the Ti-25Al-11Nb alloy

T (K)	< 1079	1079 - 1207	1207 - 1369	1369 - 1394	1394 - 1432	> 1432
Phases	$\{\beta_t+\alpha_2^S\}+\alpha_2^P+O$	$\{\beta_t+\alpha_2^S\}+\alpha_2^P$	$\{\beta_t+(\alpha_2\text{-}\alpha)^S\}$ + $(\alpha_2\text{-}\alpha)^P$	$\beta+(\alpha_2/\alpha)^P$	$\beta+\alpha^P$	β

Further transformations then involve the dissolution of the morphologically different α_2 phases. This initially entails the resolution of α_2^S within transformed β, followed by the dissolution of α_2^P. Such a dual process, eventually followed by the disordering of both α_2 morphologies, was demonstrated by the CDTA thermograms, where complex phase transformations are observed above T_S^b, Figure 2. The first of these is characterized as the dissolution of the α_2^S, and is associated with the major peak for each heating rate, the shape of this peak being representative of a diffusion controlled transformation (17). While the onset of primary α_2^P dissolution cannot be precisely defined from the CDTA thermograms, the appearance of the α_2/α satellite reflection at approximately 1338 K (1075°C) in the x-ray pattern suggests that a difference in chemical composition between the primary and secondary α_2 phases may develop during dissolution at high temperature, as expected in a diffusion-controlled transformation. Similar alloy partitioning between the α_2 and β phases, which become respectively Al-enriched and Nb-enriched, has also been observed in Ti-24Al-11Nb (14,16). It is proposed therefore that T_L^b represents the transition temperature where α_2^P becomes predominant in the alloy structure, the α_2^S morphology being virtually extinct. The x-ray results further indicate that the α_2^P phase is present till 1423 K, completion of the α_2-α disordering transformation occuring slightly below the β transus, T_B^b, 1432 K (1159°C).

The CDTA thermograms suggest that an additional transformation, identified by T_D^b, takes place in the high temperature range immediately below the β transus. This reaction may be associated with the dissolution of either grain boundary α_2^{GB} or martensitic α' (hcp), the former reverse transformation, $\beta\text{-}\alpha_2^{GB}$, being a cellular-type associated with the growth of blocky α/α_2 (3), the latter, $\beta\text{-}\alpha'$, involving a shear *transformation of β to α' with subsequent ordering to α_2* (15,16).

Similarly, the first transformation involved upon cooling from the β phase is the formation of primary α^P which begins at the temperature T_D^c. This is followed by α_2^P ordering, as depicted in Figure 3 by the broad peak between T_D^c and T_L^c. Moreover, prior to completion of α_2^P formation, precipitation of secondary α_2^S from the β phase occurs, temperature T_L^c. The extent of α_2^S precipitation is expected to be a function of cooling rate. Figure 3 supports this conclusion, the difference in intensity of the α_2^S peak, relative to α_2^P, increasing with increasing cooling rate. In contrast, an $\alpha_2^P+\beta$ microstructure is characteristic of slower cooling rates, *i.e.* those

---

[1] The presence of O at room temperature after cooling precludes this phase being an artifact due to sample preparation.

[2] The β phase has been shown by others (4-7) to undergo an ordering/disordering/ordering transformation within the T_S^b-T_B^b temperature, being disordered above 1432 K, ordered/disordered between 1207 K and 1432 K, and finally disordered below 1207 K. However the x-ray and CDTA techniques utilized in this study were unable to differentiate these reactions. Therefore, the presence of the β phase was considered without regard to its possible ordered/disordered reactions.

permitting long-range diffusion processes to occur. Therefore, by analogy with the transformations observed on heating, the T_L^c temperature represents the transition from a predominant α_2^P to an increasing quantity of α_2^S with increasing cooling rates. Table V summarizes the phase transformations path on cooling where the temperatures are given at equilibrium.

Table V. Phase transformations upon cooling for Ti-25Al-11Nb

T (K)	1354	1354 - 1343	1343 - 1246	1246 - 1236	< 1236
Phases	β	$\beta+\alpha^P$	$\beta+(\alpha+\alpha_2)^P$	$\{\beta_t+\alpha_2^S\}+\alpha_2^P$	$\{\beta_t+\alpha_2^S\}+\alpha_2^P+O$

Demonstration of this effect of rate on the phase morphology of Ti-25Al-11Nb was observed in the microstructure of the CDTA samples after cooling, Figure 4. As the cooling rate decreased, coarsening of α_2^P was observed, the as-cooled microstructure changing from a fine $\alpha_2^S+\beta_t$ to a coarse $\alpha_2^P+\beta_t$ morphology. This morphological transition was confirmed at the lowest cooling rate, *i.e.* 5 K/min, when the α_2^S was absent in the microstructure of the CDTA specimen after cooling, Figure 4d, an observation consistent with the disappearance of the peak associated with α_2^S formation in the CDTA thermogram Figure 3d.

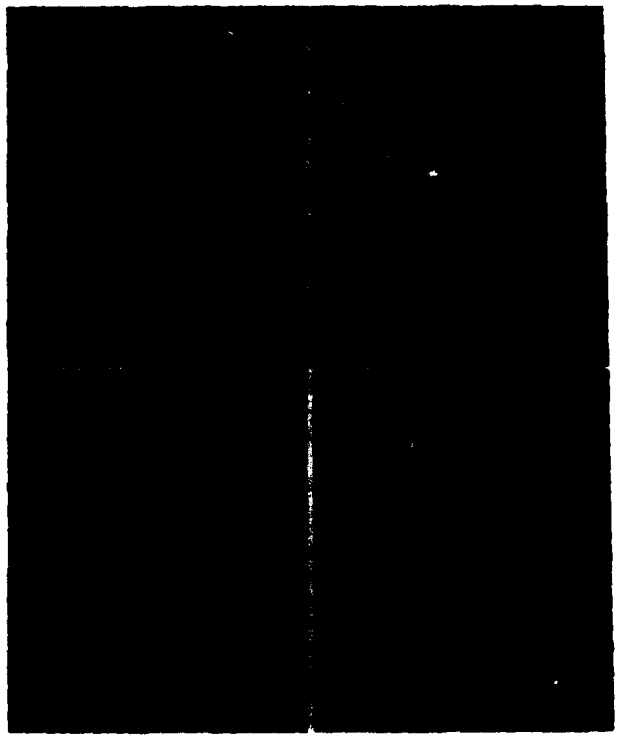


Figure 4 - Microstructures of the CDTA samples from Ti-25Al-11Nb after cooling at various cooling rates (a) 40 K/min (b) 20 K/min (c) 10 K/min (d) 5 K/min.

Conclusions

High temperature phase stability has been established for the Ti-25Al-11Nb (at.%). Transformations on heating involve the sequential dissolution of orthorhombic O and the morphologically distinct α_2 phases, such as α_2^P and α_2^S, present in the as-received alloy. Similar reversible reactions occur on cooling from the high temperature single phase β, the relative amount of the morphologically different α_2 phases exhibiting a clear cooling rate dependency.

Acknowledgements

This research was sponsored by the Defense Advanced Research Projects Agency under contract N00014-89-J-3166 supervised by Mr. W. Barker and monitored by Dr. G. Yoder of the Office of Naval Research. The Ti-25Al-11Nb alloy utilized was provided by Mr. Ed Mild of TIMET, Inc. Finally, the authors thank Mr. R. Gallahorn for his experimental assistance.

References

1. J. M. Larsen, K. A. Williams, S. J. Balsone, and M. A. Stucke, "Titanium Aluminides for Aerospace Applications", High Temperature Aluminides and Intermetallics, ed. S. H. Whang, C. T. Liu, D. P. Pope and J. O. Stiegler (The Minerals, Metals & Materials Society, Warrendale, PA, 1990), 521-556.
2. R. G. Rowe, "Recent Developments in Ti-Al-Nb Titanium Aluminides", High Temperature Aluminides and Intermetallics, ed. S. H. Whang, C. T. Liu, D. P. Pope and J. O. Stiegler (The Minerals, Metals & Materials Society, Warrendale, PA, 1990), 375-401.
3. C. H. Ward, "Microstructure Evolution and its Effects on the Fracture Behavior of Ti_3Al Intermetallics", International Materials Review, in press.
4. M. J. Kaufman, T. F. Broderick, C. H. Ward, J. K. Kim, R. G. Rowe and F. H. Froes, "Phase Relationships in the Ti_3Al+Nb System", Sixth World Conference on Titanium, ed. P. Lacombe, R. Tricot, G. Béranger (Les éditions de physique, Les Ulis Cedex, France, 1988), 985-990.
5. D. Banerjee, T. K. Nandy, A. K. Gogia and K. Muraleedharan, "Microstructure and Phase Relations in the Ti_3Al-Nb Section", Sixth World Conference on Titanium, ed. P. Lacombe, R. Tricot, G. Béranger (Les éditions de physique, Les Ulis Cedex, France, 1988), 1091-1096.
6. J. H. Perepezko, Y. A. Chang, L. E. Seitzman, J. C. Lin, N. R. Bonda, T. J. Jewett and J. C. Mishurda, "High Temperature Phase Stability in the Ti-Al-Nb System", High Temperature Aluminides and Intermetallics, ed. by S. H. Wang, C. T. Liu, D. P. Pope and J. O. Stiegler (The Minerals, Metals & Materials Society, Warrendale, PA, 1990), 19-47.
7. H. T. Kestner-Weykamp, C. H. Ward, T. F. Broderick and M. J. Kaufman, "Microstructures and Phase Relationships in the Ti_3Al+Nb System", Scripta Metallurgica, 23 (1989), 1697-1702.
8. L. A. Bendersky and W. J. Boettinger, "Investigation of B2 and Related Phases in the Ti-Al-Nb Ternary System", High-Temperature Ordered Intermetallic Alloys III (MRS, Pittsburgh, PA, 1989), 45-50.
9. S. M. L. Sastry and H. A. Lipsitt, "Ordering Transformations and Mechanical Properties of Ti_3Al and Ti_3Al-Nb Alloys", Metallurgical Transactions A, 8 (A) (1977), 1543-1552.
10. D. Banerjee, A. K. Gogia, T. K. Nandi and V. A. Joshi, "A New Ordered Orthorhombic Phase in a Ti_3Al-Nb Alloy", Acta Metallurgica, 36 (4) (1988), 871-882.
11. L. M. Hsiung and H. N. G. Wadley, "A New Ordered Tetragonal Phase in the Ti_3Al+Nb System", Scripta Metallurgica et Materiala, 26 (1992), 35-40.
12. P. K. Chaudhury, M. Long, and H. J. Rack, "Effects of Vanadium on Elevated Temperature Phase Relations in Titanium Aluminides Containing 44 at.% Al", Materials Science and Engineering, Vol. A152, 1992, pp. 37-40.
13. "The Physical Metallurgy of Titanium Alloys", edited by E. W. Collings, ASM Series in Metal Processing, H. L. Gegel Series editor, American Society for Metals, Metal Park, OH, 1984.
14. K. Muraleedharan and D. Banerjee, "Alloy Partitioning in Ti-24Al-11Nb by Analytical Electron Microscopy", Metallurgical Transactions A, 20 (A) (1989), 1139-1142.
15. H. T. Weykamp, D. R. Baker, D. M. Paxton, and M. J. Kaufman, "Continuous Cooling Transformations in Ti_3Al+Nb Alloys", Scripta Metallurgica et Materiala, 24 (1990), 445-450.
16. M. J. Cieslak, T. J. Headley, and W. A. Baeslack III, "Effect of Thermal Processing on the Microstructure of Ti-26Al-11Nb: Applications to Fusion Welding", Metallurgical Transactions A, 21 (A) (1990), 1273-1286.
17. Differential Thermal Analysis, edited by R. C. MacKenzie, Academic Press, London and New York, Vol. 2, 1972.

TEXTURE IN ROLLED RODS OF alpha- AND (alpha+beta) TITANIUM ALLOYS

A.S.SHIHMAKOV, R.A.ADAMESKU

The Urals Institute of Railways Engineers, Ekaterinburg, Russia

Abstract

The textures formed in α- and ($\alpha + \beta$)-titanium alloy rolled rods have been examined. The relationship of texture to the conditions of deformation has been established. It is shown that the character of texture changes during annealing depends on the initial structural condition of the deformed metal.

INTRODUCTION

Among deformed semifinished Ti-alloy items the rolled rods for producing stampings, blanks, fasteners etc are widely used. As shown in (ref.1) mechanical properties of the rods to a great extent depend on the character of their crystallographic texture. Hence, the knowledge of peculiarities of forming preferred orientations during rod production can be an additional source for improving the properties.

The present paper gives the results of studying the crystallographic texture in α- and ($\alpha + \beta$) -alloys.

MATERIALS AND PROCEDURE.

Unalloyed titanium rods were deformed at the initial rolling temperature of 850 C while for BT5-1 α-alloy rods (Ti-5,8%Al-2,7%Sn) and BT6 (Ti-6,8%Al-2,1%V), BT3-1 (Ti-6,3%Al-2,4%Mo-1,4%Cr), ПТ-3В (Ti-4,8%Al-1,9%V) ($\alpha + \beta$)alloys it was 1100 C. The strain (ε) in all the cases ranged from 54% to 77% while for ПТ-3В alloy it was from 54% to 85%.

The texture has been examined by analysing the distribution curves of X-ray reflection intensity along the section of direct pole figure (2) and also by direct and inverse pole figures (3). X-ray examination was made from the rod cross-section. Hence, we could obtain some information about crystallograpphic planes located in this section.

Titanium '92
Science and Technology
Edited by F.H. Froes and I. Caplan
The Minerals, Metals & Materials Society, 1993

EXPERIMENTAL RESULTS AND DISCUSSION

As a result of rolling unalloyed Ti-rods in the α-region with ε =54% the $\{0001\},\{10\bar{1}1\}$ orientations and also a very weak $\{10\bar{1}0\}$ orientation are formed (fig.1). Increasing strain up to ε >69% changes the type of the texture. In this case it is represented only by $\{10\bar{1}0\}$ component having high intensity.

The heating temperature for rolling BT5-1,BT3-1- and ПТ-3B alloys was in the β-region. After 54% deforming in the cross-section of BT5-1 and BT6 alloy rods (fig. 2_a,b) the $\{10\bar{1}1\}$ and $\{0001\}$ orientations and the weaker $\{10\bar{1}0\}$ orientation have been revealed. Higher reductions ($\varepsilon \geq 69\%$) of BT5-1 alloy can result in abrupt increasing the intensity of the $\{0001\}$ orientation which with ε =77% becomes the main one while the intensity of other components changes only slightly. Similar changes have been also observed in BT6 alloy.

The BT3-1 alloy texture (fig.2c) with ε =54% is ropresented only by the $\{10\bar{1}1\}$ orientation whose intensity increases with increasing the strain. Under ε > 69% the $\{0001\}$ orientation appears.

The study of ПТ-3B alloy texture using direct and inverse pole figures has shown that the rod texture is not strictly axial. As seen in fig. 3 the maxima of pole density lie on mutually perpendicular directions corresponding to the radial sections of the rod. The data in fig.4 can prove that the $\{10\bar{1}2\},\{10\bar{1}1\},\{0001\},\{10\bar{1}0\}$ planes are parallel to the cross-section of the rods (ε =54%), e.g.texture are multicomponents.With ε =85% the main and most intense orientation is $\{0001\}$. At the same time there are relatively weak $\{10\bar{1}2\},\{10\bar{1}1\},\{10\bar{1}0\}$ orientations (fig. 4b).

The texture formation during hot deformation is due to the crystallographic mechanism of deformation,the intensity of developing recrystallization processes and phase transformations taking place according to definite orientation correlations. The study of texture formation processes makes it possible to single out the main of the above factors.

Thus forming the main $\{10\bar{1}0\}$ orientation in unalloyed titanium rods rolled in the α-region with $\langle 10\bar{1}0\rangle$ direction being parallel to the rod axis makes it possible to conclude that slip deformation of the α-phase is prevailing. This conclusion results from the teoretical analysis of reorientation of crystal lattice in the course of uniaxial deformation carried out by the method given in (ref.4).

The deformation of BT5-1,BT6,BT3-1,ПТ-3B alloys mainly occured in β-region and therefore the texture formation is influenced by the slip deformation of the β-phase followed by the oriented $\beta \rightarrow \alpha$ transformation on cooling. The analysis carried out by the method (5) shows that in case of uniaxial deformation of B.C.C. crystals resulting from the slip along the $\{110\}\langle 111\rangle,\{112\}\langle 111\rangle$ and $\{123\}\langle 111\rangle$ systems, the $\langle 110\rangle$ orientation parallel to the axis of tension appears and the higher the strain the more perfect it becomes. Further with $\beta \rightarrow \alpha$ transformation according to Burgers orientation relation $\langle 110\rangle_\beta \;//\; \langle 0001\rangle_\alpha$ the $\langle 0001\rangle$ orientation is formed.

The similar orientation was observed in BT5-1,BT6,BT3-1, alloys. Since during the final rolling stages the deformation was carried out in the α - or (α + β)-region the formation of the $\langle 10\bar{1}0 \rangle$ orientation,with the $\{10\bar{1}0\}$ plane being parallel to the cross-section,can be attributed to the slip deformation of the α -phase.

The $\{10\bar{1}1\}$ component has resulted from numerous variants of transformation and also from the spread of the main component of the $\{0001\}$ texture.

The extent of changing the texture during annealing the rolled rods depends on the structural condition of the alloys formed during deformation. If the recrystallization has been completed or sufficiently developed,the texture changes during annealing practically do not occur. It applies to ПТ-3В (ε =54%,T_{an} =870°C, τ =1,5 hr),BT3-1 (ε = 54,69,77%,T_{an} =950° C, τ =0,5 hr) and BT5-1 (ε =54%,T_{an} =960° C, τ =1 hr) alloy rods.

In unalloyed Ti-rods (ε =54%) no initial recrystallization degree was observed. Annealing at 680° C during one hour resulted in increasing the intensity of the $\{0001\}$ and $\{10\bar{1}1\}$ orientation (fig.1). The increase of the $\{0001\}$ component intensity was also observed during annealing (T_{an} =870° C, τ =1,5 hr) partially recrystallized ПТ-3В (ε =85%) alloy rods. It should be noted that during annealing ПТ-3В alloy rods some structural changes take place,namely : lamellar structure in the deformed metal is replaced with the globular one in the annealed rods.

The obtained experimental results have shown that the texture type of Ti-alloy rolled rods depends on the temperature region of deformation and the character of the texture changes during annealing is determined by the structural condition of the deformed metal.

REFERENCES

1. R.A.Adamesku et al "Texture of BT3-1 alloy rolled rods", Technology of Light Alloys,10(1978),28-31.
2. Yu.Marcov,R.A.Adamesku "X-ray method of assessing the crystallographic lattice scattering", Factory laboratory,1 (1971),30-34.
3. Ya.Vishnyakov et al., Theory of texture forming in metals and alloys (Moskva,M:Nature,1979),343.
4. E.A.Calnan,C.J.B.Clews "The development of deformation textures in metals.Part 3.Hexagonal structures",Philosophical Magazine,42 (1951),919-932.
5. E.A.Calnan,C.J.B.Clews "The development of deformation textures in metals.Part 2.Body-centred cubic metals", Philosophical Magazine,42 (1951),616-635.

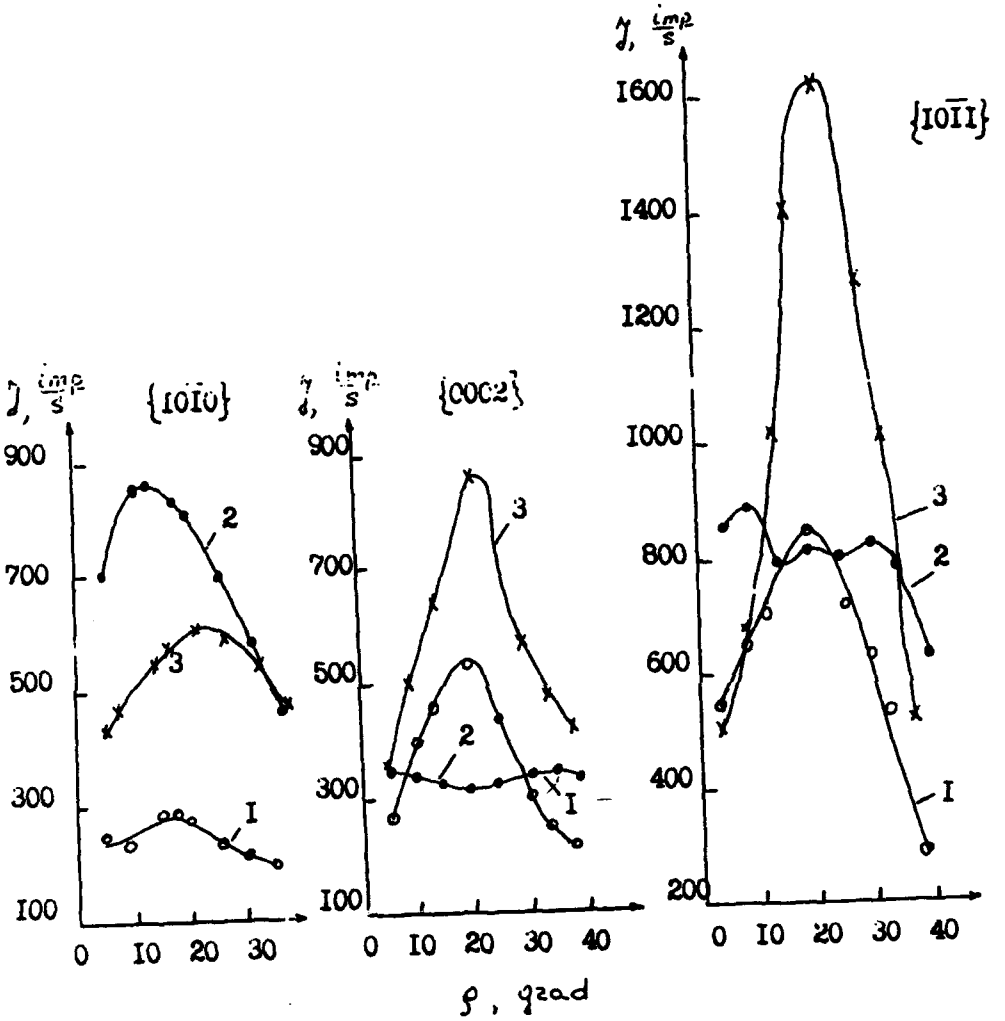


Figure 1. Intensity spread of X-ray reflection from the $\{10\bar{1}0\}$, $\{0002\}$, $\{10\bar{1}1\}$ planes of unalloyed titanium : 1 - ε =54%, 2 - ε =77%, 3 - ε =54%, heat treatment: 680°C-1 hr.

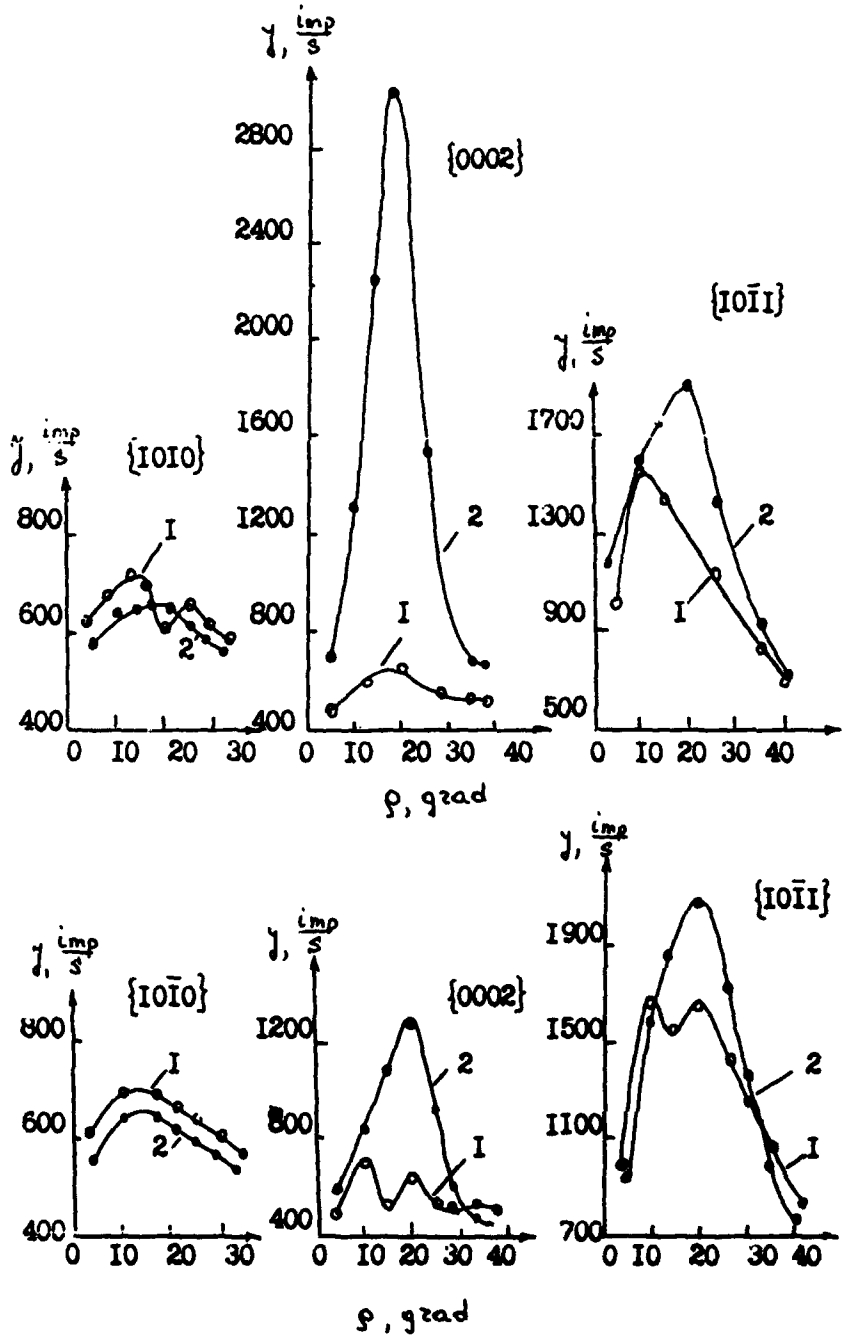
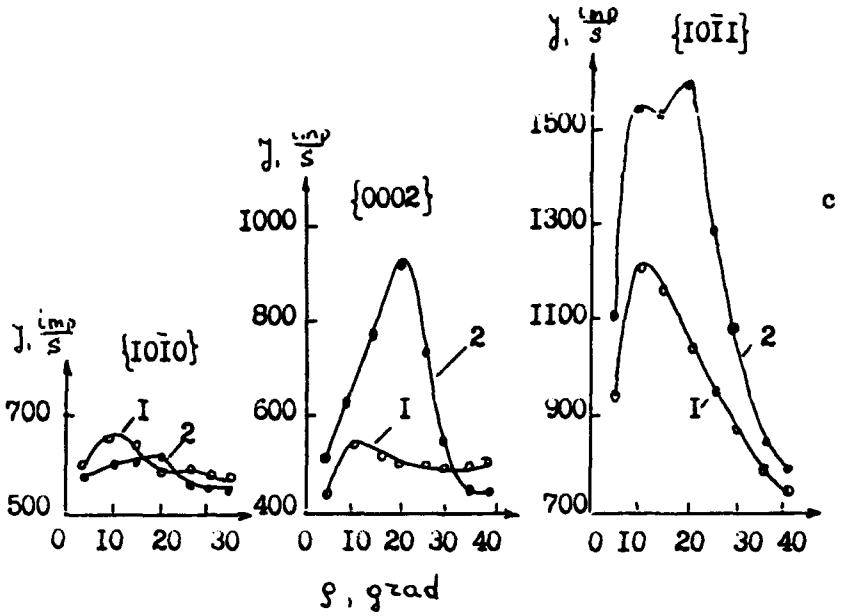


Figure 2. Intensity spread of X-ray reflection from the (10$\bar{1}$0),(0002),(10$\bar{1}$1) planes of BT5-1 (a),BT6 (b),BT3-1 (c). 1 - ε = 54%, 2 - ε = 77%.


J, imp/s
{10$\bar{1}$0}
I
2
700
500
0 10 20 30
J, imp/s
{0002}
1000
800
600
400
0 10 20 30 40
J, imp/s
{10$\bar{1}$1}
1500
1300
1100
900
700
0 10 20 30 40
2
I'
φ, grad

c

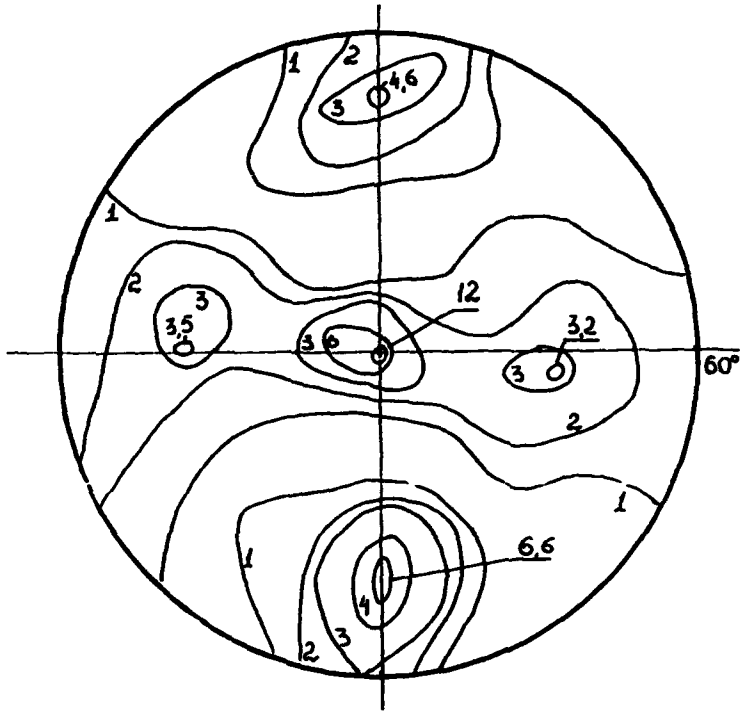


Figure 3. The {0002} pole figure for the cross-section of ПТ-3В alloy rods (ε =85%).

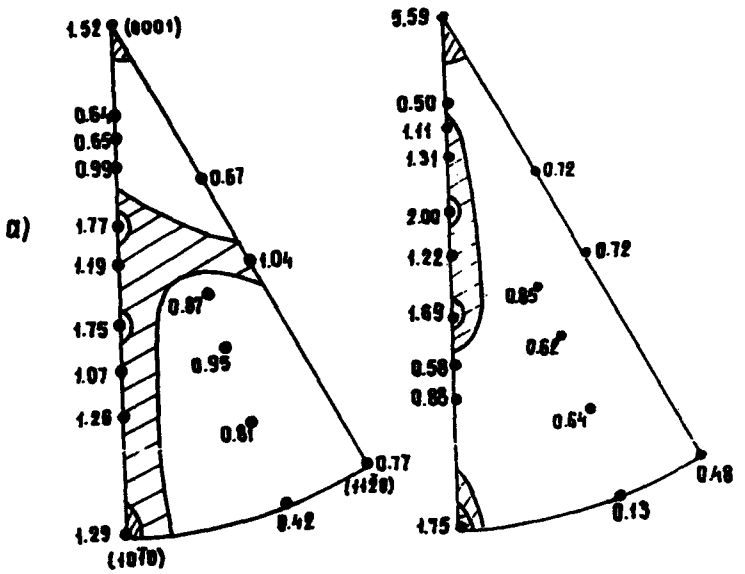


Figure 4. Inverse pole figures for the axial direction of ПТ-3В alloy rods: – ε =54%, – ε =85%.

DETERMINATION OF THE RECOVERY PROPERTIES

OF A Ti 45.5 Ni 54.5 (wt%) SHAPE MEMORY ALLOY IN TENSION

P. Roumagnac, M. Clavel: LG2MS, U.T.C.,B.P.649 - F60200 COMPIEGNE.

Y. Barbaux, M.H. Campagnac: AEROSPATIALE Research Center - F92152 SURESNES.

ABSTRACT

NiTi shape memory alloys are studied as a function of the texture. On the one hand, it appears that, in the range of alloys studied, the texture has not a significant effect on the recoverable strains. On the other hand, the internal stress developped is highly dependent on the texture, so do the transformation temperatures. The overall behaviour of shape memory alloys in tension is analysed in the scope of plasticity. It is proposed that the linear relation between the stress and the strain during stage II, as well as the rise in the transformation temperatures observed, should be an effect of an internal stress which is the result of deformation incompatibilities.

INTRODUCTION

Nickel-Titanium alloys are well known for undergoing a thermoelastic martensitic transformation. This transformation properties endow these alloys with various and complex mechanical behaviours such as pseudoelasticity and shape memory effect (which can be reversible or not).

NiTi alloys are among the most technologically important shape memory alloys because of their good mechanical properties and of their good resistance to corrosion.

Miyazaki *et al.* [1], who studied both a solution-treated single crystal and an aged single crystal, clearly showed that the optimum recoverable strains may highly depend on the crystal orientation. Thus, one can wonder if it is worthwhile to use textured materials in order to improve shape memory properties.

Our purpose is to study the structure and the mechanical behaviour of three alloys having quite the same chemical composition but which underwent different forming processes in such a way that they can develop different textures.

MATERIALS: STRUCTURES AND PROPERTIES

Table1 shows the chemical compositions and the manufacturing characteristics of the three alloys studied. Bar 1 and 3 are stemming from the same ingot.

Titanium '92
Science and Technology
Edited by F.H. Froes and I. Caplan
The Minerals, Metals & Materials Society, 1993

Different experimental methods such as dilatometry, X-ray scattering, EDX analysis, optical microscopy and transmission electron microscopy were used in order to determine the metallographic structure and the transformation properties of the alloys.

Bar reference	Ti (at.%)	Ni (at.%)	O (p.p.m.)	C (p.p.m.)	N (p.p.m.)	Manufacturing process	Annealing
1	50,47	49,52	1580	107	68	Forged D=14mm	at 720°C under vacuum during 1 hour
2	50,32	49,67	1210	114	37	Drawn D=36mm	at 720°C under vacuum during 1 hour
3	50,47	49,52	1580	107	68	Drawn D=50mm	at 700°C under air during 15 mn

Table1: Bar characteristics

Phases and transformation temperatures

It is well known that TiNi alloys may have three different crystallographic forms: austenite, martensite and R phase. The austenite has got a CsCl structure (B2); the R phase has got a structure which is a rhombohedral distortion of B2 [2]; the martensite has got a monoclinic structure (B19') [3-4].

X-ray scattering showed the alloys to undergo both the R and the martensitic transformations on cooling at temperatures below room temperature. Conventional transformation temperatures [5] on heating were determined using dilatometry, the results obtained are written out on table 2. X-ray scattering pointed out that the materials are not totally transformed into martensite at room temperature. Even after cooling in liquid nitrogen little austenite remained.

Bar reference	As (°C)	Af (°C)
1	63	83,5
2	67	80
3	59	74,5

Table 2: Transformation temperatures

Optical micrography

The specimens were mechanically polished and etched with a solution consisting of 5%HF, 10%HNO_3 and 85%H_2O [6].

Figures 1(a), 1(b) and 1(c) show optical micrographs of samples representative of the microstructure of each bar transversely and longitudinally. On these micrographs, one can observe many small particles wich are non-uniformly scattered in the TiNi matrix.Those particles are Ti_2Ni precipitates, identified using EDX analysis and electron diffraction patterns. It is noteworthy that the precipitate distribution becomes more homogeneous as the bar diameter decreases, and that bar 1 and bar 2 have got fairly identical precipitate repartition.

Transmission electron microscopy

0,12 mm thick disk specimens were mechanically polished and electropolished at room temperature in an electrolyte consisting of 95% CH_3COOH and 5% $HClO_3$.

Figure 2 shows the internal structure of bar 2 at room temperature, after cooling at liquid nitrogen temperature. The phases labelled A are Ti_2Ni precipitates, the phases labelled B are grown up laths of martensite easy to recognize because of their fine internal twins. The phases labelled C are small austenite grains within which one can observe few dislocations.

Those dislocations were identified to be {100}<010> perfect dislocations (labelled D), and 1/2{110}<111> and/or 1/2{112}<111> pairs of antiphase boundaries (labelled E). Besides, many interface dislocations surround the Ti_2Ni precipitates (F). It is important to point out that this configuration, namely a martensitic matrix containing groups of Ti_2Ni precipitates in between which small austenitic grains extend, was frequently found.

Textures

Figures 3(a), 3(b) and 3(c) show the {110} pole figures of bar 1, 2 and 3 respectively. Measurement was carried out at room temperature after heating at 200°C, in such a way that the materials were mainly austenitic during the experiment (with a small amount of martensite and R phase).

First, one can note that the textures are all identical, that is to say a <110> wire texture. The 36 mm diameter bar texture (fig.3(b)) is the strongest with a 7,48 maximum intensity at the center of the pole figure. It is noteworthy *that this* pole figure is totally axisymetric. The 14 mm bar and the 50 mm bar textures (Fig 3(a) and 3(c)) are also strong, with maximum intensities reaching 3,62 and 6,33 respectively at the center of the pole figures, but they are not axisymetric. <110> directions which are 45° from the center of the pole figures are not uniformly distributed around it. The overall structure of bar 1 and 3 must be close to the single crystal.

MECHANICAL TESTS

Tensile tests

Uniaxial tensile tests were performed using an Instron 4505 testing machine fitted out with a 100kN load cell. Strains were measured by means of an extensometer. *Heating was* achieved using an oven monitored at the sample surface with a thermocouple.The temperature rate was $1°C.mn^{-1}$. All testing was performed in air, at a strain rate of $2{,}63.10^{-4}s^{-1}$. Tensile samples were cylindrical ones with a 40 mm gauge length and a 6 mm gauge diameter. They were machined from the bars in such a way that the tensile axis is parallel to the bar axis.

Fracture data

Figure 4 shows a scanning electron micrograph of a fracture surface. The fracture surface was always normal to the tensile axis and no necking of the sample was observed. Groups of small dimples (labelled A) are clearly observable, the fact that dimples are always empty suggests that a total decohesion of the precipitates should occur during the tensile test. Table 3 presents the ultimate tensile stresses and the ultimate tensile strains.

Bar reference	σ_R (MPa)	ε_R (%)
1	960	12,33
2	900	16,27
3	793	10,01

Table 3: Ultimate tensile stresses and strains

The ultimate tensile stress seems to be dependent on the precipitate repartition since the precipitate contents of bar 1 and 3 are exactly the same. Moreover, the ultimate tensile stresses of bar 1 and 2 (which have quite the same precipitate repartition) are nearly equal. Most of the fracture models are based upon the volume fraction of particles only. It appears that this volume fraction is not enough to give an account of our results and that further work is required in order to understand the part played by the size, the shape, and the repartition effects.

As far as the ultimate tensile strains are concerned the origine of differences is not clearly understood. There must be an effect of both the precipitates and the texture.

Recovery properties

Figure 5 shows the true stress-true strain loading curves obtained. Those curves can be divided into the three stages which have been formerly defined by Rozner *et al.* and Cross *et al.* (quoted by [7]). Our samples seem to have a good texture as far as the shape memory effect is concerned. The stress level reached for a given applied strain differs outstandingly from one bar to anothers: the more the texture comes close to an ideal wire texture, the lower the stress. It may be an effect of strain incompatibilities which should increase as the texture intensity decreases.

Samples were deformed to different total strains (ε_t), on unloading an elastic strain was recovered (ε_e). The sample was then heated and the recoverable strain was measured (ε_r). The plastic strain (ε_p) was assessed from the strain remaining at the end of the test (after cooling) and from the strain due to the change in the crystal structure measured by dilatometry.

Figure 6 shows the evolution of the deformation recovered ε_r as a function of the plastic apparent strain o' ained after unloading ($\varepsilon_{pp} = \varepsilon_t - \varepsilon_e$). During stage I the strain is totally recovered, during ...ge II the recoverable deformation goes on increasing and reaches a maximum at the end of the stage but little plastic deformation appears. During stage III the recoverable strain slighdy decreases and the plastic deformation drastically increases. The recovered deformation is exactly the same whatever the bar but it is important to take into account the fact that the stress level reached for a given deformation is not the same at all from one bar to another.

Figure 7 shows the evolution of the transformation temperatures as a function of the total strain (maximum strain). In order for the figure to remain clear we plotted out only the results obtained for bar 2. It puts the stress on the fact that those temperatures are not constant but depend on the strain level whatever the bar: they remain constant during stage I, they increase during stage II and reach a maximum during stage III.

DISCUSSION

Our purpose is to attempt to explain first the overall shape of tensile curves (especially stage I and stage II), and second the increase in the transformation temperatures.

It is generally ackowledged that when applied, a stress can cause a rise of transformation temperatures. Patoor *et al.* [8] clearly demonstrated that the stress applied and the transformation temperatures are linked by a linear relation. Consequently, the rise in temperatures observed brings us to propose that there should be an internal stress acting within the material. We mentionned above that transformation temperatures remain constant during stage I, that is to say, as long as true plastic strain does not appear. Therefore, there must be a relation among the plastic strain, the internal stress and the rise in transformation temperatures.

In order to characterize this relation we used the macroscopic approach commonly used within the scope of elasto-plasticity. According to this approach an internal stress field is represented by a kinematic stress variable which is a tensor proportional to the plastic strain tensor [9], though linear kinematic hardening is too rough an approximation. In the case of linear kinematic hardening and considering an uniaxial tensile stress, the stress can be written as [10]:

$\sigma = X + (R + k)$ where k is the yield stress, X the kinematic hardening (internal stress) related to geometrically necessary dislocations, and R the isotropic hardening related to statistically strored dislocations (X, R and k must all be functions of the test temperature). According to Prager $X = C\varepsilon_p$, this formula, which arises from Eshelby inclusion problem, remains valid only for low values of the plastic strain. Figure 8 shows the tensile stress

plotted out as a function of the plastic strain (for stage I and stage II only). There is actually a linear relation between the stress and the plastic strain and k is not really the yield stress but the stress reached during stage I. From figure 8 it arises that the considerable hardening observed during stage II can be written as a linear function of the plastic strain. Hence it induces us to propose that this very hardening should be the product of the action of an internal stress field.

From a microstructural point of view, it is widely admitted that an internal stress field is generated inside a material by specific dislocation configurations. For specimen deformed to stage II Melton *et al.* [11] showed that, during this stage (while martensite reorientation goes on), strain incompatibilities appear and that it leads to local yielding. Moreover Tadaki *et al.* [12] (for a material deformed to stage III) suggest that there should be a network of dislocations built up along lath boundaries. This local dislocation network must be the cause of an internal stress field.

As far as transformation temperatures are concerned, we suggest that they should be constant during stage I for no plastic strain appear. They should increase during stage II since local plastic yield lead to the occurence of an internal stress field. They should remain constant during stage III because general yield takes place (the internal stress does not increase any further). Figure 9 shows the increase in As (during stage I and stage II) plotted out as a function of the internal stress X assessed from the results obtained (figure 8). This figure shows that the increase in transformation temperature is roughly a linear function of the internal stress whatever the bar considered. The increase in both As and Af suggests that the internal stress field should be closely related to the presence of martensite so that its effect remains until the end of the transformation.

CONCLUSION

From this study two main results arise:

- As far as the recoverable strains are concerned, the texture does not play a leading part.

- The overall behaviour of TiNi shape memory alloys can be analysed in terms of kinematic and isotropic hardenings which are closely related to the deformation modes previously observed. The part played by the internal stress field coming from deformation incompatibilities is evidenced.

ACKNOWLEDGMENTS

The authors wish to thank Ms A.M.Chaze and Mr C.Levaillant (CEMEF) for their help in texture determination, Mr J.P. Wtycklo for his efficient technical assistance and the STPA for financial support.

REFERENCES

1. S. Miyazaki, S. Kimura, K. Otsuka, Y. Suzuki: Scripta Met., 18 (1984), p.883.
2. H.C. Ling, R. Kaplow: Met. Trans., 12A (1981), p.2101.
3. G.M. Michal, R. Sinclair: Acta Cryst., 37B (1981), p.1803.
4. Y.Kudoh, M. Tokonami, S. Miyazaki, K. Otsuka: Acta Met., 33 (1985), p.2049
5. Norms AFNOR NF A 51-080: Shape memory alloys: Vocabulary and measures.
6. L.A. Middleton, N.F. Kennon, D.P. Dunne: Metallography, 17 (1985), p.51
7. S. Miyazaki, K. Otsuka, Y. Suzuki: Script Met., 15 (1984), p.287.
8. E. Patoor, M. Berveiller: Les alliages à mémoire de forme, Ed. Hermes, 1990
9. J.L. Strudel: Multiphase alloys. Physical metallurgy, Ed. Cahn & Haasen, North- Holland physics publishing, 1983
10. J. Lemaitre, J.L. Chaboche: Mécanique des matériaux solides, Ed. Bordas, 1988
11. K.N. Melton, O. Mercier: Met. Trans., 9A (1978), p.1487.
12. Tadaki, C.M. Wayman: Scripta Met., 14 (1980), p. 911.

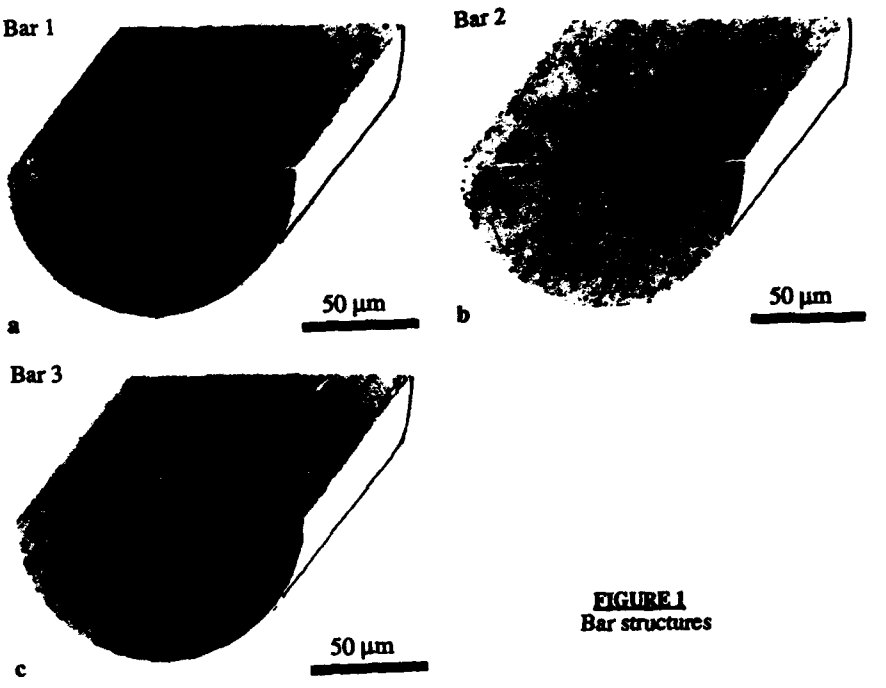


FIGURE 1
Bar structures

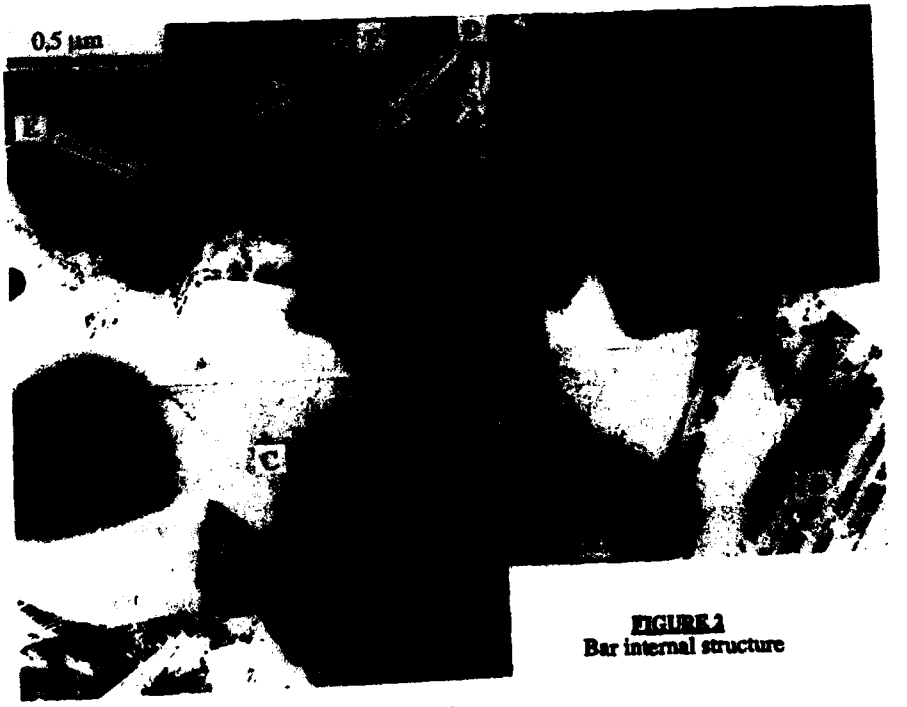


FIGURE 2
Bar internal structure

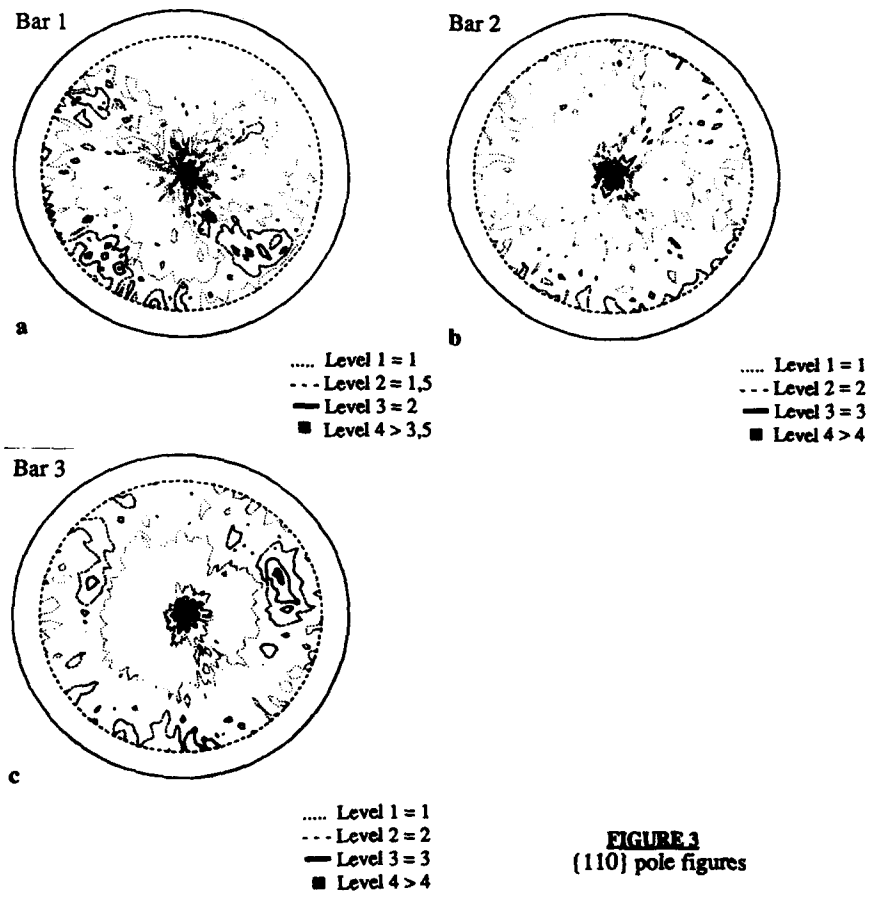


FIGURE 3
{110} pole figures



FIGURE 4
Fracture surface

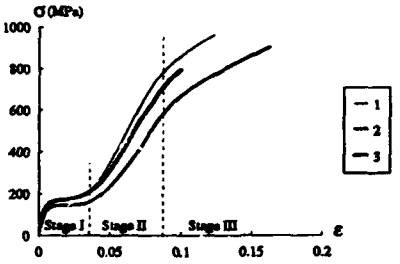


FIGURE 5
True stress-true strain tensile curves

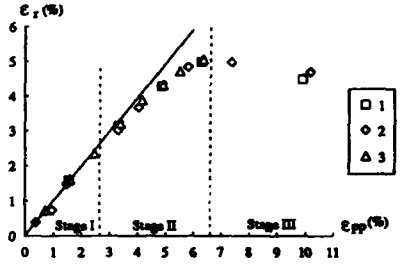


FIGURE 6
Recoverable strains (εr)

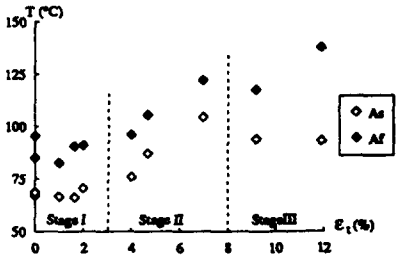


FIGURE 7
Transformation temperatures (bar 2)

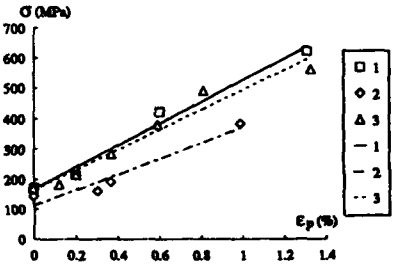


FIGURE 8
$\sigma = C\varepsilon p + k$

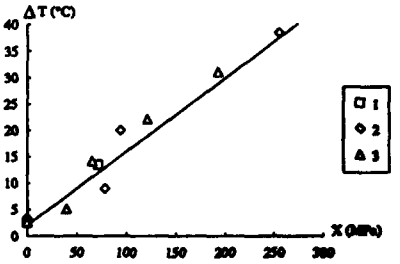


FIGURE 9
Relation between the transformation temperatures and the internal stress

EFFECT OF STRESS ON HYDRIDE FORMATION BEHAVIOR OF TI-6AL-4V ALLOY

Keijiro Nakasa and Jianping Liu

Faculty of Engineering, Hiroshima University
Higashi-Hiroshima, 724 Japan

Abstract

A microarea X-ray diffraction analysis was carried out both for bowed-specimen and ball-indented specimen, which were cathodically hydrogen charged in sulfuric acid solution, to investigate the effect of tensile and compressive stresses on the behavior of hydride formation in a Ti-6Al-4V alloy. For the bowed specimen, γ-hydride (fcc) was formed more easily under tensile stress than under compressive stress. The formation of δ-hydride (fct), on the other hand, was almost insensitive to stress. For the ball-indented specimen, the amount of γ- and δ-hydrides showed a minimum in the center of indentation concave with the largest compressive stress. Besides, the indentation on a plate specimen after hydrogen charging decreased the γ-hydride but increased the δ-hydride.

Introduction

Titanium alloys have been used as structural materials of high performance because of their high specific strength and toughness, heat-resistance, and corrosion-resistance. However, when the alloys are exposed to hydrogen environments, a hydride which is formed on metal surface embrittles the alloys[1,2]. So, it will be important to clarify the hydride formation process especially when the titanium alloys are used for the structures under stress. There is a possibility that the hydride formation is influenced by stress. For example, Paton and Williams[3], Hoeg et al.[4], Moody and Gerberich[5], and Shih et al.[6], have reported the strain-induced or stress-induced hydride precipitation at a crack tip where tensile strain or stress is very large. The present authors have also found that when a Ti-6Al-4V alloy or a pure titanium is charged with hydrogen electrolytically the hydride once formed on a specimen surface decomposes to original α-phase of titanium perhaps due to the generation of compressive stress by the expansion of hydride[7,8]. In the present

Titanium '92
Science and Technology
Edited by F.H. Froes and I. Caplan
The Minerals, Metals & Materials Society, 1993

research, the effect of stress on the hydride formation was investigated by using two kinds of simple specimens and a microarea X-ray apparatus.

Experimental Procedure

The material used was Ti-6Al-4V alloy, which was solution treated at 1073K and aged at 823K for 14.4ks. This heat treatment resulted in a mixed structures of primary granular α- and β-phases, secondary fine α-phase precipitating in β-phase.

Figure 1 shows the specimens used for experiments. One was the plate specimen which was indented by a steel ball of a Brinell hardness tester (load: P=29.4kN, diameter of ball: d=10mm) after surface finishing of the specimen with #400 emery paper. This method was adopted to generate the residual compressive stress around or in the indented concave. Another was the bowed-specimen which was prepared by rolling a plate by about 80% reduction and by setting the plate in wire hooks. Both the tensile and compressive stress which were generated on the surface of bowed-specimen were calculated from the equation for the buckling problem of an elastic plate. However, a small amount of plastic deformation occurred during specimen setting, so that the stress calculated could overestimate the surface stresses.

The hydrogen charging of specimens was carried out electrolytically in a sulfuric acid aqueous solution (0.5kmol/m^3) kept at 303K by using a regulated-current apparatus, where the hydrogen-charging current density was 3000A/m^2 and charging time was varied up to 432ks.

The hydride formation behavior was investigated by using a microarea X-ray diffraction apparatus (JEOL MAP-2, target:CuKα, voltage:40kV, current:

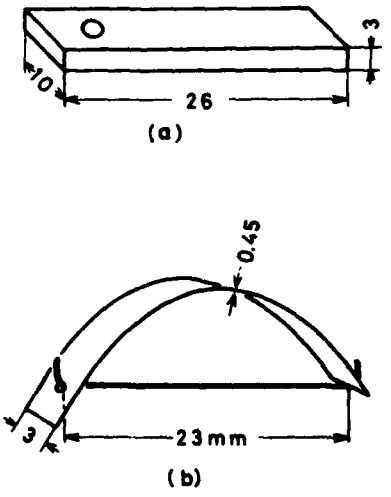


Figure 1 - (a): Ball-indented specimen, (b):Bowed-specimen.

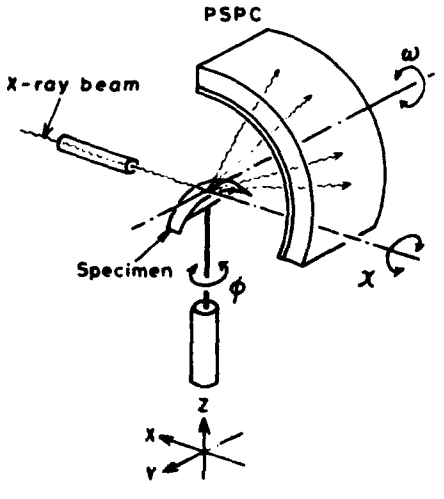


Figure 2 - Microarea X-ray diffraction system.

150mA, X-ray beam diameter:100μm) which is schematically shown in Fig.2, where the diffracted X-rays were detected by a position sensitive proportional counter (PSPC). The specimen was rotated within a certain angle around ω, χ, and φ axes, in order that the diffraction from many lattice planes should occur homogeneously.

According to an X-ray analysis, peaks from γ-hydride (fcc, $TiH_{1.5\text{-}1.99}$) and δ-hydride (fct, TiH_2) as well as α-titanium (hcp) and β-titanium (bcc) were observed as has been reported[3,4,6,9,10]. Because the peaks from β-phase were weak and often shaded by strong α peaks, and since β-phase does not form hydride at room temperature, so the change of γ, δ, and α peaks with change of charging time and stress were measured, i.e. the highest peaks, $\alpha(10\bar{1}1)$, γ(111), and δ(111) were selected and the relative peak intensities, $I_\alpha/\Sigma I_i$, $I_\gamma/\Sigma I_i$, and $I_\delta/\Sigma I_i$ ($\Sigma I_i=I_\alpha+I_\gamma+I_\delta$) were defined to discuss the stress dependency of hydride formation qualitatively.

Results

A bowed-specimen was charged with hydrogen at i_c=3000A/m^2 for a certain time and the X-ray analysis was carried out. Fig.3 shows the relation between stress of specimen surface (dotted point) and relative X-ray intensities for γ- and δ-hydrides at a charging time of t_c=10.8ks. The relative intensity of γ-hydride increases with increasing tensile stress, i.e. the formation of γ-hydride is easier

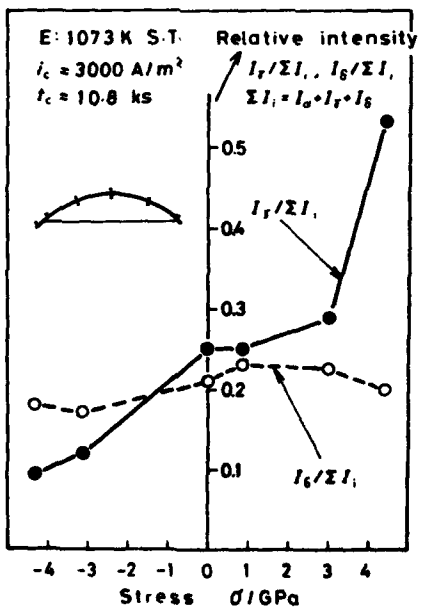


Figure 3 - Relation between stress and relative X-ray intensity.

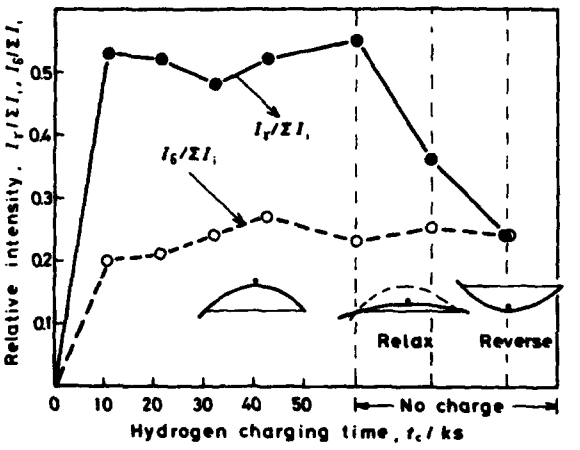


Figure 4 - Relation between hydrogen charging time and relative X-ray intensity.

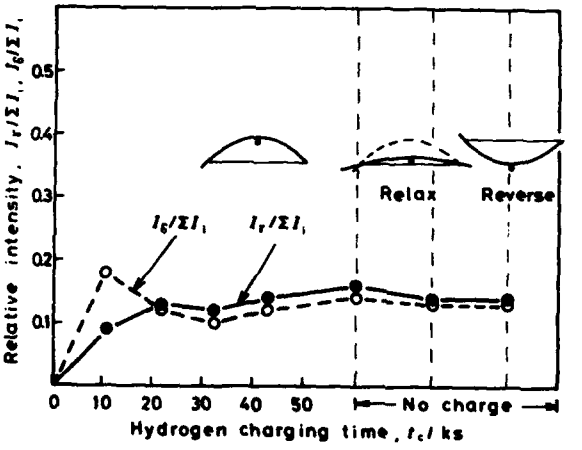


Figure 5 - Relation between hydrogen charging time and relative X-ray intensity.

under tensile stress than under compressive stress. On the other hand, the relative intensity of δ-hydride is almost constant independently of stress.

Figures 4 and 5 show the relation between hydrogen charging time and relative X-ray intensities of γ- and δ-hydrides measured on the positions where tensile and compressive stresses are maximum (center of plate). By comparing the two figures, it is understood that the tendency shown in Fig.3 was also observed for each charging time. At a certain charging time, however, the

relative intensity once decreases to take a minimum, i.e. the hydride decomposes to α-phase. This phenomenon is concerned to the generation of compressive stress due to the expansion of hydride which is transformed from α-phase[7,8]. Next, after taking off the specimen from the wire hooks, the specimen was bent in the reverse direction, and the X-ray analyses were carried out. The results were shown in Figs.4 and 5 as "no charge" range. Only the γ-hydride which was formed under tensile stress decomposed to the α-phase (Fig.4), while the amount of γ-hydride which had been formed under compressive stress did not increase (Fig.5) perhaps because enough hydrogen for additional hydride formation did not diffuse to the specimen surface under reversed tension. On the other hand, δ-hydride which was formed under tension (Fig.4) or compression (Fig.5) did not change even when the stress was reversed, a behavior which corresponded to the results of Fig.3 that the formation of δ-hydride was not sensitive to stress.

The distribution of hydride amount in the longitudinal direction of ball-indented specimen was also examined by using the microarea X-ray analysis. The results for two charging times are shown in Fig.6. Because the center of ball indentation was located at about 4mm from the left edge of specimen (ref:Fig.6), it was anticipated that the stress distribution was asymmetric and stress relief occurred at the positions near the edge. The amount of γ- and δ-hydrides take minima at the center of indentation, i.e. the compressive stress prevents for the formation of both hydrides, and the amount of hydride is larger at the position near the left edge, where stress relief would have occurred, than the right side. The change of relative intensities with increasing charging time

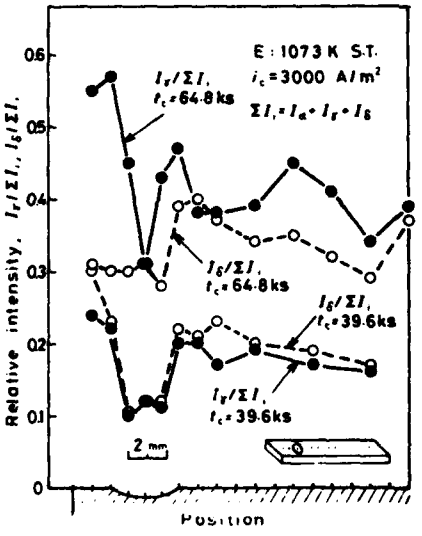


Figure 6 - Distribution of relative X-ray intensity.

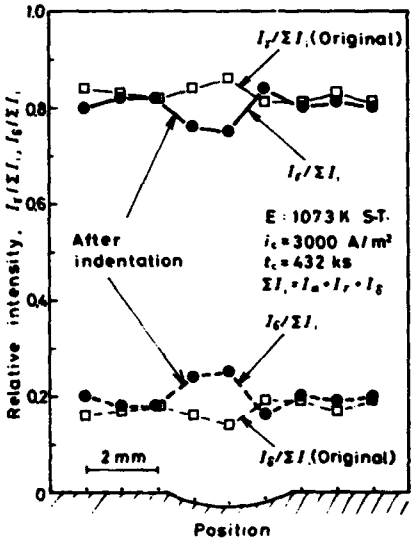


Figure 7 - Distribution of relative X-ray intensity before and after ball-indentation.

are rather complex: When t_c=39.6ks, both relative intensities for γ- and δ-hydrides reveal minima in the concave and almost constant values outside of the concave. Because the difference in relative intensity between inside and outside of the concave is large, the effect of stress appears most strongly at the beginning of hydrogen-charging. When t_c=64.8ks, the relative intensity is the smallest in the concave but the variation of relative intensity is different from position to position.

Figure 7 shows the effect of indentation for a specimen which was precharged before indentation. The γ-hydride was partly decreased and δ-hydride was increased, which suggested that the γ-hydride was changed to δ-hydride by the applied compressive stress. Thus, the results for indented-specimen revealed almost the similar tendency to the results of bowed-specimen, i.e. both hydride are difficult to form under compressive stress and δ-hydride is more stable than γ-hydride under compressive stress.

Discussions

The experiments on both bowed- and indented-specimens showed that the γ- and δ-hydrides formation was affected by external or residual stress. Moreover, the stress dependency of γ-hydride was stronger than δ-hydride. The reason for these facts can be explained on the basis of three standpoints.

First, from the analysis of diffraction angle from each phase, the lattice constant of α-phase (hcp) are a=0.295nm, c=0.469nm, that of γ-hydride (fcc) is a_0=0.433nm, and those of δ-hydride (fct) are a_0=0.428nm, c_0=0.393nm (c_0/a_0=0.92). By referring also to another literature[9], the volumetric expansion from α-phase to γ-hydride is 15-20%, while that to δ-hydride is 5-15%. Thus, when the α-phase which contains super-saturated hydrogen atoms should be transformed to hydride under stress, γ-hydride will be more stable under tensile stress than δ-hydride, while δ-hydride will be more stable under compressive stress.

Next, in addition to the volumetric consideration above, it will be necessary to discuss the stability of hydrides under stress also from the coherency between α-phase and hydride-phases near the phase boundary during the precipitation of each hydride in α-phase, because it has been reported that habit planes exist when a hydride is formed in α-phase[6,10]:

$$(0001)_\alpha \;//\; (111)\text{Ti-H}$$
$$[2\bar{1}\bar{1}0]_\alpha \;//\; [1\bar{1}0]\text{Ti-H} \qquad (1)$$

$$(10\bar{1}0)_\alpha \;//\; (110)\text{Ti-H}$$
$$[\bar{1}2\bar{1}0]_\alpha \;//\; [1\bar{1}0]\text{Ti-H} \qquad (2)$$

Figure 8 shows the habit planes of eqs.1 and 2, respectively. In the case of eq.1 (left figure), a closed packed plane (111) of γ- or δ-hydride should accommodate to a closed packed plane (0001) of α-phase, where the atomic distance of γ-hydride in the direction of $[1\bar{1}0]$, d_0, is 3.7% as large as the lattice

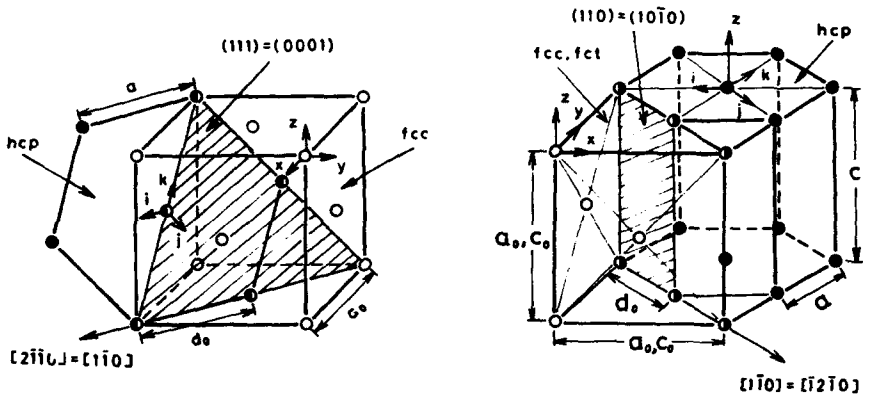


Figure 8 - Habit planes between hydride (fcc or fct) and α-phase.

constant of α-phase, a, while the atomic distance of δ-hydride in the $[1\bar{1}0]$ direction is 2.4% larger or 1.4% smaller. Thus, δ-hydride will be more stable than γ-hydride under no stress or compressive stress, while γ-hydride is more stable under tensile stress.

For the case of eq.2 (right figure), the atomic distance in the $[1\bar{1}0]$ direction of γ-hydride, d_0, is 3.7% larger than the lattice constant of α-phase, a, while the lattice constant of γ-hydride, a_0, is 7.7% shorter than the lattice constant, c, of α-phase. On the other hand, when the lattice constant of δ-hydride , a_0, corresponds to the lattice constant, c, of α-phase, a_0 is 8.7% shorter than c, and the atomic distance in the $[1\bar{1}0]$ direction, d_0, is 1.4% shorter than the lattice constant, a, of α-phase. When the lattice constant c_0 of δ-hydride corresponds to the lattice constant, c, of α-phase, c_0 is 16% shorter than c and d_0 is 2.4% longer than a. Thus, the reaction of eq.2 suggests that the transformation of δ-hydride from α-phase is more difficult than the transformation of γ-hydride from α-phase because of larger misfit of lattice constant a_0 or c_0 of δ-hydride to the lattice constant, c, of α-phase. The formation of γ-hydride will be easier under almost no stress and the formation of δ-hydride is rather easy only when the large compressive stress is applied to the specimen.

Thirdly, a nucleation theory may be applied to explain the effect of stress on hydride formation. The applied tensile stress will decrease the elastic energy caused by the compressive stress in γ-hydride and the tensile stress in α-phase near α-γ boundary, and will decrease the activation energy for hydride formation.

Conclusions

A microarea X-ray diffraction analysis was carried out both for bowed-specimen and ball-indented specimen, which were cathodically hydrogen-

charged in a sulfuric-acid aqueous solution under a current density of $3000A/m^2$, to investigate the effect of tensile and compressive stress on the behavior of hydride formation in a Ti-6Al-4V alloy. The results obtained are as follows:

(1) For the bowed-specimen, γ-hydride (fcc) was formed more easily under tensile stress than under compressive stress. The formation of δ-hydride (fct), on the other hand, was almost independent of stress. The γ-hydride which was formed under tensile stress decomposed to the α-titanium phase when the stress was reversed to compression, leaving the δ-hydride unchanged. However, the γ- and δ-hydrides formed under compressive stress did not change when the stress was reversed to tension.

(2) For the ball-indented specimen, the amount of γ- and δ-hydrides showed a minimum in the center of indentation concave with the largest compressive stress. Besides, the indentation on a plate specimen after the hydrogen charging decreased the γ-hydride but increased the δ-hydride.

(3) The effect of stress on hydride formation and decomposition appear to be explained by habit plane of hydride relative to α-lattice, and the expansion during hydride formation.

References

1. H.G.Nelson, "A Film-Rupture Model of Hydrogen-Induced, Slow Crack Growth in Acicular Alpha-Beta Titanium", Metal. Trans., 7A(1976), 621-627.
2. M.Niinomi and T.Kobayashi, "Effect of Hydrogen Charging on the Impact Toughness of Ti-6Al-4V Alloys", J. Japan Inst. Metals, 50(1986), 449-455.
3. N.E.Paton and J.C.Williams, "Effect of Hydrogen on Titanium and Its Alloy", Hydrogen in Metals, Ed. by I.M.Bernstein and A.W.Thompson, (ASM, 1974), 409-431.
4. H.Hoeg, B.Hollund and I.W.Hall, "Effect of Hydrogen on the Fracture Properties and Microstructure of Ti-6Al-4V", Metal Science, 14(1980), 50-56.
5. N.R.Moody and W.W.Gerberich, "Hydrogen-Induced Slow Crack Growth in Ti-6Al-4V-2Sn", Metal. Trans., 11A(1980), 973-981.
6. D.S.Shih, I.M.Robertson and H.K.Birnbaum, "Hydrogen Embrittlement of α Titanium: In Situ TEM Studies", Acta Met., 36(1988), 111-124.
7. K.Nakasa, K.Kiyose, and J.Liu, "Relation between Bending Strength and Hydride Formation in Hydrogen-Charged Ti-6Al-4V Alloy", J.Japan Inst. Metals, 54(1990), 532-538.
8. J.Liu and K.Nakasa, "Hydride Formation Behavior and Fatigue Strength of Hydrogen Charged Titanium", J.Japan Inst. Metals, 55(1991), 1086-1092.
9. H.L.Yakel, Jr., "Thermocrystallography of Higher Hydrides of Titanium and Zirconium", Acta Cryst., 11(1958), 46-51.
10. H.Numakura and M.Koiwa, "Hydrogen Precipitation in Titanium", Perspectives in Hydrogen in Metals, Ed. by M.F.Ashby and J.P.Hirth, (Pergamon Press, 1986), 501-509.

EFFECT OF THERMOMECHANICAL TREATMENTS ON TA6Zr5D β

GRAIN SIZE EVOLUTION

J.M. Kempf*, E. Gautier*, A. Simon*, J.F. Uginet** and A. Gavart**

*Laboratoire de Science et Génie des Matériaux Métalliques, CNRS UA159
INPL Ecole des Mines Parc de Saurupt 54042 NANCY Cedex FRANCE
**Fortech Division Airforge Usine de Pamiers 75 Avenue de la Libération
BP4 09100 PAMIERS FRANCE

Abstract

The response of TA6Zr5D alloy to thermomechanical processing in the β field has been determined. The observations of the deformed prior β grain size reveal no dynamic recrystallization by nucleation and growth for the tested conditions ($\dot{\varepsilon} = 2\ 10^{-3} \rightarrow 10^{-1}s^{-1}$, and ε up to 60 %). The prior β grain size variations have been studied after thermomechanical treatments during a further annealing treatment in the β temperature range and for different deformation parameters. A "static recrystallization" scheme is obtained with a critical deformation dependent on the deformation parameters. The schematic static recrystallization diagram is obtained by the study of the grain size evolution of homogeneously deformed specimens and heterogeneously deformed specimens. The knowledge of the critical deformation, and its variations with the parameters of the thermomechanical treatment allows one to modify the thermomechanical transformation paths in order to enhance the control of the grain size variations.

Introduction

During thermomechanical treatments, the material is subjected to deformation and temperature variations inducing numerous changes in the microstructure. The mechanisms which are at the basis of these changes i.e. deformation, recovery, recrystallization and phase transformations (if cooling in the appropriate temperature range) occur or may occur and can interact, these interactions being quite complex.

In the case of the TA6Zr5D alloy, industrial parts developed large heterogeneities in the prior β grain size, when deformed above the β transus. Indeed, most studies on the thermomechanical behavior were carried out in the α + β temperature range. In this study, we focus on the thermomechanical behavior above the β transus, and the microstructural variations associated with varying deformations in this range.

The mechanical behavior was studied by tensile deformation at different temperatures and deformation rates. The microstructural evolution, i.e. the prior β grain size variations, was studied by optical microscopy for different deformation parameters (ε, T, $\dot{\varepsilon}$) on two types of specimens, "laboratory" specimens (uniformly deformed) and "massive" specimens (with heterogeneous deformation).

Titanium '92
Science and Technology
Edited by F.H. Froes and I. Caplan
The Minerals, Metals & Materials Society, 1993

Experimental Procedure

The chemical composition of the alloy is given in Table I

Table I - Chemical composition of the alloy

Element	Al	Mo	Zr	Si	C	Fe	N	H ppm	O ppm
wt %	5.97	0.495	5.22	0.220	0.007	0.018	0.003	17	1300

The specimens were taken from a bar, β forged, 200 mm in diameter, which had heterogeneities in the β grain size from the surface to the center. After heat treating at 1050°C, above the β-transus (1020°C), the mean grain size varies from the surface of the bar to the center in a ratio 1 to 3. Specimens for "laboratory" tests were taken so that the tensile axis is parallel to the bar axis and were classified according to their initial β grain size measured on the surface of the etched specimens, before any treatments. Specimens showing large variations in the β grain size on their surface were eliminated. Large massive specimens were obtained from the initial bar by deformation at 1050°C, in order to reduce the bar diameter to about 50 mm. After deformation a thermal treatment was carried out at 1050°C, for one hour, followed by oil quenching. After machining the specimens were 45 mm in diameter and 45 mm in height. The mean grain size of these specimens was 440 ± 50 μm.

Figure 1 represents schematically the thermomechanical and thermal treatments applied to the specimens. The specimens were all β solution treated at 1060°C, 0.5h for "laboratory" specimens and 0.66 to 0.83h for the "massive" specimens.

The "laboratory" tests were carried out on a thermomechanical simulator DITHEM (1), able to apply controlled thermal and mechanical variations. After solution treatment, the specimen is deformed homogeneously at a controlled deformation rate. The deformation level, the deformation rate, and the deformation temperature were variable parameters. The tests were carried out under vacuum.

The massive specimens were isothermally deformed at 1060°C on a hydraulic press whose displacement is controlled, corresponding to a mean deformation rate of $2\ 10^{-3}$ and $0.15\ s^{-1}$. The mean deformation is about 24 %, but it is heterogeneous and varies locally between 0 and 60 %. The thermal treatment after deformation was 1050°C for 1.5h.

The microstructures were observed at three states as defined on Figure 1, state 0, prior any deformation, state 1 after deformation and cooling and state 2 after thermal treatment. Mean β grain size corresponds to the mean linear intercept measured by optical microscopy.

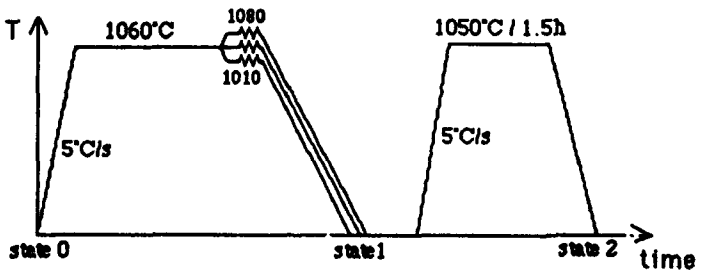


Figure 1 - Schematic thermomechanical treatments

Results

Evolutions During Deformation

From the laboratory tests, we obtain the stress/strain curves in the β temperature range for different deformation rates and temperatures (Figure 2). At 1060°C, for 0.15 s^{-1}, the flow stress continuously increases up to a constant value of 34MPa. At lower strain rates, a small softening occurs at the beginning of the deformation. For a deformation rate of 2 $10^{-3}s^{-1}$ the stress strain curves display similar behavior at different test temperatures. A small peak is obtained followed by smooth softening as deformation increases, whatever the temperature.

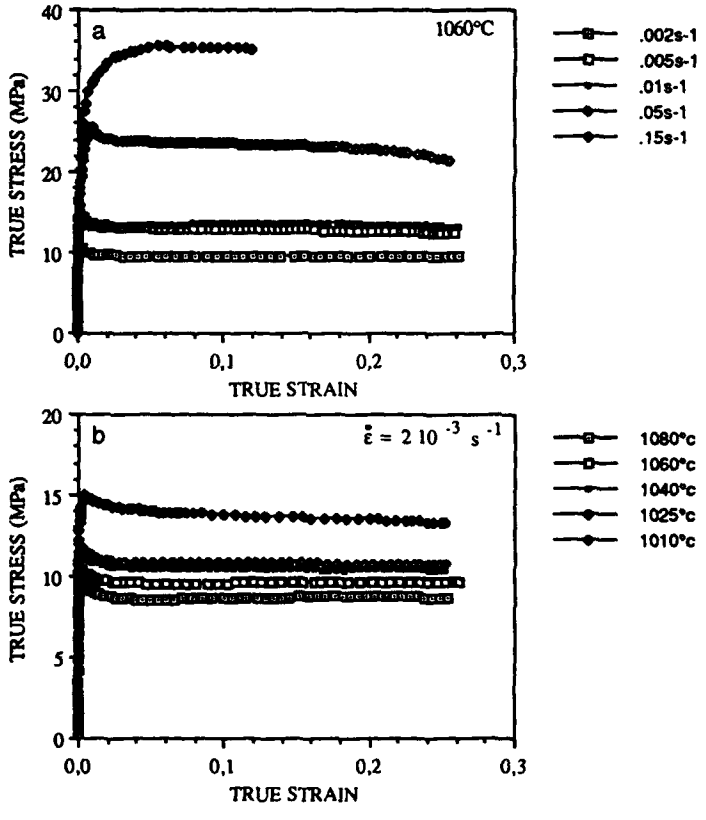


Figure 2 - Stress strain curves obtained at 1060°C for various deformation rates (a) and obtained at different temperatures for a deformation rate of 2 10^{-3} s^{-1} (b).

The results can be expressed by the power law equation :

$$\sigma = A\,\dot{\varepsilon}^{m} \exp(mQ/RT)$$

were m, the sensitivity to the deformation rate, is about 0.29 and Q the apparent activation energy 255 KJ/mole.

The microstructural evolution during deformation is observed after deformation for two deformation rates 2 $10^{-3}s^{-1}$ and 0.15 s^{-1}, at different deformation levels, after cooling the specimen. We give Figure 3 two micrographs for each deformation rate at 15 % and 30 % deformation. The microstructures consist of lamellar α phase obtained during cooling ; if we focus on the prior β grain, we observe serrated grain boundaries, with an increase in the serration level as the deformation increases. The serrations are less severe for the deformation rate of 2 $10^{-3}s^{-1}$ than for 0.15 s^{-1}. No new β grains are observed for the applied deformation levels. Measurements of the prior β grain size reveal no variation of the grain size between undeformed specimens and deformed ones.

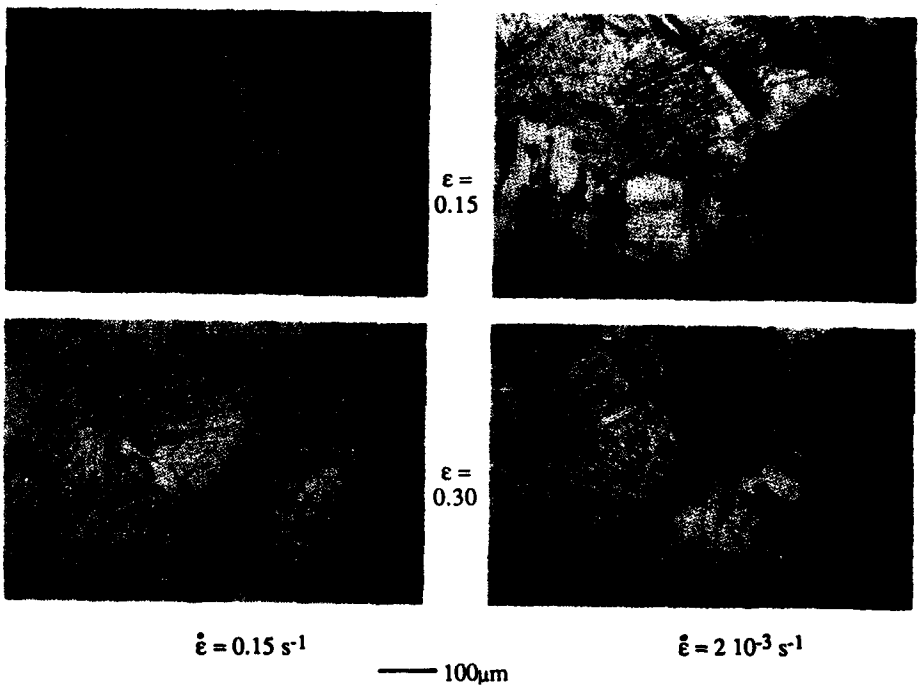


Figure 3 - Microstructural evolutions after different deformations for two deformation rates 0.15 s^{-1} and 2 10^{-3} s^{-1}

The macrography of the "massive" specimen deformed 28 % at 2 10^{-3} s^{-1} is presented Figure 4. The "massive" specimens present heterogeneities in the microstructure after deformation, with equiaxe prior β grains at the surface of the specimen and high deformed serrated grains at the center. A calculation of the iso-deformation map by code VULCAIN estimates the deformation level at the surface near 0, while it reaches 60 % at the center. Again no new β grains were observed, even in the most deformed area and for the two deformation rates. These results, clearly show that no dynamical recrystallization for the β phase occurs in the deformation range studied.

Microstructural Evolution during Thermal Treatments

The prior β grain size evolution was determined for the different treatments without any deformation. These results, Table II, show that the grains grow during the two treatments, depending on the initial grain size (at state 0).

For a mean initial grain size of 510 μm the high temperature β grain grows and the standard deviation increases. For a higher initial β mean grain size (1050μm), the mean grain size remains constant ; however the standard deviation increases. Also the normal growth leads to a spreading of the grain size distribution, and an increase of the mean size essentially for medium initial values of β grains.

Table II : β grain size evolution during thermal treatments

	stage 0	stage 1	stage 2
mean grain size (μm) and [standard deviation (μm)]	510 [220]	640 [340]	970 [560]
	1050 [550]	1030 [550]	1050 [620]



Figure 4 - Macrography of the deformed massive specimen
$\dot{\varepsilon} = 2\ 10^{-3} s^{-1}$, $\bar{\varepsilon} = 28\%$ —1000μm

In order to put out the effect of the deformation, the grain size variations are given as a difference between sizes at state 2 and state 0. Figure 5 presents the variations of the β grain size versus the applied deformation and for three couples of deformation parameters ($\dot{\varepsilon}$, T). The results are given as a mean value with dispersion brackets (95 % of the measured mean values are inside the brackets). We observe that the difference of size between state 2 and state 0 is the same up to a critical value. At that value, a maximal increase of the difference occurs, which lowers as the deformation increases. The deformation at which the maximal increase is noticed, called the critical deformation, is dependent on the high temperature deformation parameters (Table III).

Table III : Variation of the critical strain versus high temperature deformation parameters

$\dot{\varepsilon}$ (s^{-1}) / T(°C)	0.15	$2\ 10^{-3}$
1010	/	7-8 %
1060	3-4 %	15-16 %

The observations of the massive specimens deformed and heat treated, reveal a similar scheme (Figure 6). Near the surface, small grains are observed, whose size increases and then decreases when observing along the deformation axis. The superposition of the calculated

deformation pattern on the microstructure reveal that the large grains are observed between the isodeformation lines of 10 and 20 % for the deformation rate of 2 10^{-3} s^{-1} and 5-10 % for the deformation rate of 0.15 s^{-1}.

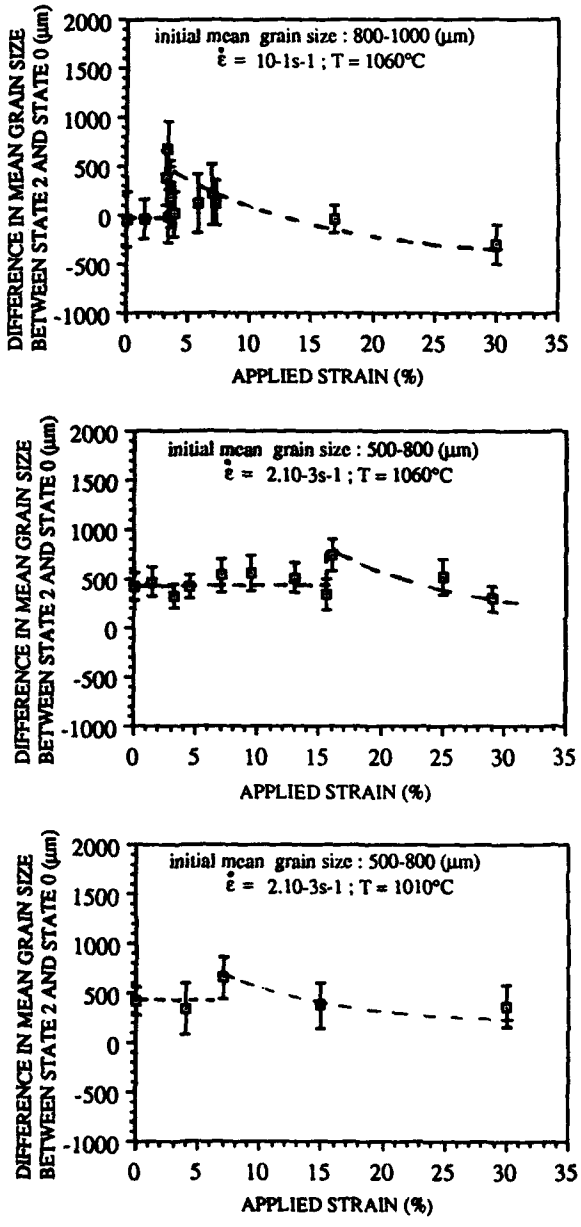


Figure 5 - Variations of the β mean grain size between state 2 and state 0 versus the applied deformation for three deformation conditions

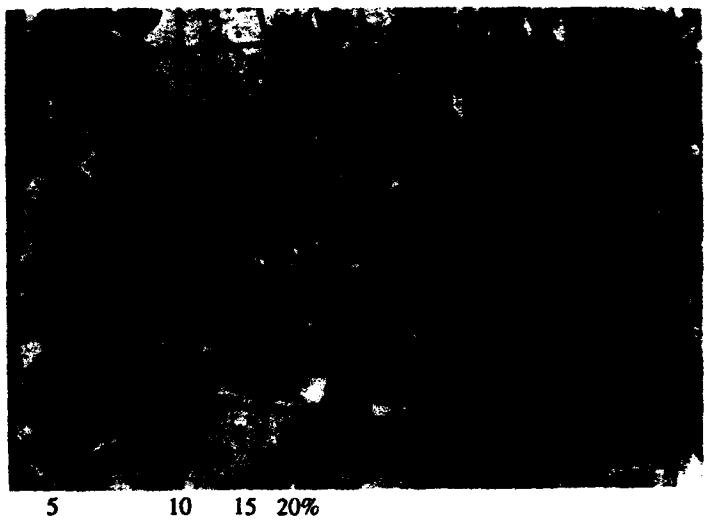


Figure 6 - Macrography of the massive specimen after deformation and heat treatment, and superposed deformation map ($\dot{\varepsilon} = 2\ 10^{-3}s^{-1}$, $\bar{\varepsilon} = 28\%$) —— 1000µm.

Discussion

Stress-strain curves yield to a mean value of m equal to 0.29 and an apparent activation energy of 255KJ/mole for the β phase. The m value is large compared to the one obtained by Malcor (2) on TA6V4 alloy (0.18 at 1010°C), but less differences are noticed when comparing to Hanaki (3) (m = 0.24 for TA6V4 at 1050°C), or to Côme-Dingremont (4) (m = 0.29 for TA6V4 at 1015°C). The larger values are obtained when studying a range of deformation rate including low deformation rates (10^{-3} to $10^{-4}s^{-1}$) and more generally using tensile tests (for Malcor the deformation was obtained by torsion). For the apparent activation energy, the value obtained is larger than the one measured on TA6V4 alloy above the β transus. The microstructural observations of the deformed specimens revealed that the alloy does not dynamically recrystallize by nucleation and growth, in the deformation range studied. The small softening observed is then related to dynamic recovery.

After deformation and further thermal treatment, the grain size variations observed for different primary deformations, follow a scheme similar to the one obtained for different materials during static recrystallization (5). For titanium alloys very few results were reported on recrystallization above the β transus. In our case, even if the size variations are sometimes low, both the laboratory and the massive specimens present these variations and the "critical deformation" is dependent on the deformation parameters. In order to approach the recrystallization kinetics, one sample was maintained 180s after deformation (5%) and no structural change was observed compared to the sample cooled just after deformation. Also the mechanism of that static recrystallization has been further studied on a TA6V4 alloy (4,6) showing that recrystallization occurs by migration of the existing β grain boundaries.

In order to explain the difference in the β grain size between "laboratory" and "massive" specimens, some specimens were heat treated after deformation under a constant applied stress of 1.5MPa. For the non deformed specimen, no increase in grain size was observed compared to the specimen heat treated without applied stress ; however an increase in the grain size is observed, especially for the 15% deformed specimen ($\dot{\varepsilon} = 2\ 10^{-3}s^{-1}$, T = 1060°C) that

deformation corresponding to the "critical deformation" . The mean grain size and the maximal size for the "laboratory" 15% deformed specimens and for the "massive specimen" in the 15% deformed area, are reported Table IV .

Table IV : Variations of grain size for specimens heat treated with or without applied stress after a pre-deformation of ≈15%.

	Laboratory specimen	Massive specimen	Laboratory specimen with constant stress
mean size(μm)	1400	2400	1900
maximal size(μm)	2700	4000	3500

The larger grain size obtained when the last thermal treatment occurs under an applied stress can be related to a higher velocity of the grain boundary as observed on TA6V4 alloy (4) or in in other studies (7). Also the difference between the "massive" and the "laboratory" specimens can be partly related to an internal stress state during static recrystallization which will lead to an increase in the β grain boundary mobility. Another factor can be a slower recrystallization kinetics as it can be suggested regarding the kinetics results versus the recrystallization temperature obtained by Côme-Dingremont and al. (4,6).

Conclusion

The mechanical behavior of TA6Zr5D alloy has been studied by tensile testing in the β phase field. The results show that dynamical recrystallization does not occur for the deformation range studied (0-30%). During further heat treatment, the β mean grain size varies with the previous deformation level according to a static recrystallization scheme. The critical strains are obtained for different deformation parameters. Modifications of the thermomechanical path can then be planned in order to enhance the control of the mean grain size.

Aknowledgments

This work was financially supported by DRET - DGA.

References

1. E. Gautier, A. Hazotte, A. Simon and G. Beck, "Caractérisation en continu du comportement thermomécanique et structural des matériaux métalliques à l'aide d'un dilatomètre générateur de cycles thermiques et mécaniques rapides" (Paper presented at the 24th Colloque de Métallurgie, Les traitements thermomécaniques aspects théoriques et applications, (1981), 187-197)

2. J. C. Malcor, "Comportement mécanique et évolution structurale de l'alliage TA6V dans le domaine du forgeage à chaud" (Thèse de Docteur Ingénieur ENSMP 1983).

3. M. Hanaki et al., "Microstructure and mechanical properties of a large TA6V ring forged at a duplex phase temperature range" (Paper presented at Titanium 80 Science and Technology, Vol 2, (1980),873-886).

4. N. Côme-Dingremont, "Deformation à chaud et évolutions microstructurales des alliages de titane TA6V et β-cez dans le domaine β" (Thèse de Docteur de L'INPL, Nancy-France, 1991).

5. Y. Adda et al., "Eléments de Métallurgie physique", Vol. 5, 1979, 1533-1556.

6. N. Côme-Dingremont, E. Gautier and A. Simon, "Grain growth of TA6V β phase after thermomechanical treatments" (this conference).

7. M Guillopé, "Contribution à l'étude de la recristallisation dynamique" (Thèse de Docteur es Sciences, Université P.et M. Curie, Paris 6, France, 1981).

GRAIN GROWTH OF TITANIUM AND ITS GRAIN SIZE DISTRIBUTION

Yoshimasa Takayama, Norio Furushiro*,
Tatsumi Tozawa, Hajime Kato and Yukichi Umakoshi*

Department of Mechanical Systems Engineering,
Utsunomiya University,
Ishii-cho, Utsunomiya 321, Tochigi, Japan

*Department of Materials Science and Engineering,
Osaka University,
2-1 Yamadaoka, Suita, Osaka 565, Japan

Abstract

The change in the grain size distribution during grain growth has been investigated for a commercially-pure titanium. The one- and two dimensional distributions were measured experimentally. Further, the grain diameter distribution, which is one of the three-dimensional grain size distributions corresponding directly to grain growth, was estimated by the method, which was based on an assumption of the log-normal distribution of the grain diameter (the equivalent volume diameter) D; the distribution of this grain diameter was clearly defined by the geometric mean grain diameter D_g and the standard deviation of ln D or ln σ_g. The three-dimensional analysis revealed that the change of the grain diameter distribution of titanium during grain growth was similar to that of its one- or two-dimensional distribution, which is in contrast to the previous result of aluminum. This implies that the increase in D_g with annealing time is analogous to that in the one- or two-dimensional mean grain size; such a tendency was definitely supported by the fact that the standard deviation of logarithm of the grain diameter, ln σ_g, was almost constant.

Introduction

The kinetics of grain growth have been investigated theoretically or experimentally in the light of change in mean grain size with time [1]. Such investigations were on the basis of a prerequisite that the form of grain size distribution is time invariant during

Titanium '92
Science and Technology
Edited by F.H. Froes and I. Caplan
The Minerals, Metals & Materials Society, 1993

normal or steady state grain growth. Alternatively, grain growth can be described only by the change in mean grain size, because the spread of the grain size distribution normalized by the mean value does not vary during the steady state grain growth. However, this is supported by limited experimental results [2–4]. Since most of these results were obtained from the measurement on two dimensional structure of the cross section, the change in three–dimensional structure corresponding directly to grain growth was estimated insufficiently.

In this study, the changes in one– and two–dimensional distributions of grain size are investigated experimentally, and moreover, the change in three dimensional distribution is estimated by the method proposed previously [5].

Experimental Procedure

A commercially–pure titanium used as the specimen was a rolled sheet of 6mm in thickness. Chemical compositions of the specimen were shown to be oxygen of 760, hydrogen: 14, nitrogen:26, iron:500 in mass ppm and Ti:balance. Rolled specimens of 1.2mm in thickness were annealed for 100s to 100ks at 973 or 1023K and then micro–structures of the rolled surfaces were observed optically. The shape of the grains was confirmed to be almost uniform and equiaxed in all specimens after annealing.

The measurement of one–dimensional grain size distribution or linear intercept length distribution was carried out for tracing of micrograph of grain structure using an image processor with a microcomputer. The data obtained were analyzed statistically to calculate mean value, standard deviation, etc. The two–dimensional distribution or grain intercept area distribution was determined by weighing the tracing sheets using an electrical balance combined with the microcomputer. Data obtained were analyzed in the same way to the one–dimensional analysis.

The distribution of "grain diameter", which is defined as the equivalent volume diameter, was taken up as one of three–dimensional distribution in this study. The grain diameter distribution was derived by an estimating method proposed in the previous paper [5]. The method was based upon the theoretical distribution of linear intercept lengths calculated numerically from a tetrakaidecahedron grain structure model with log–normal distribution of grain diameter. The distribution of the grain diameter D was expressed by D_g and $\ln \sigma_g$, where D_g is the geometric mean of D and σ_g is the geometric standard deviation for D. The values of D_g and $\ln\sigma_g$ are determined by applying the "decrete" least square method to the measures distribution of linear intercept lengths on the basis of the calculated one.

Fundamental expression of the grain size distribution used here is the distribution of natural logarithm of each quantity.

Results and Discussion

Mean Linear Intercept Length and Mean Grain Intercept Area

Figure 1 shows the relation between the arithmetic mean of linear intercept length $\bar{l}$ and annealing time for titanium samples. The value of $\bar{l}$ increases with annealing time for

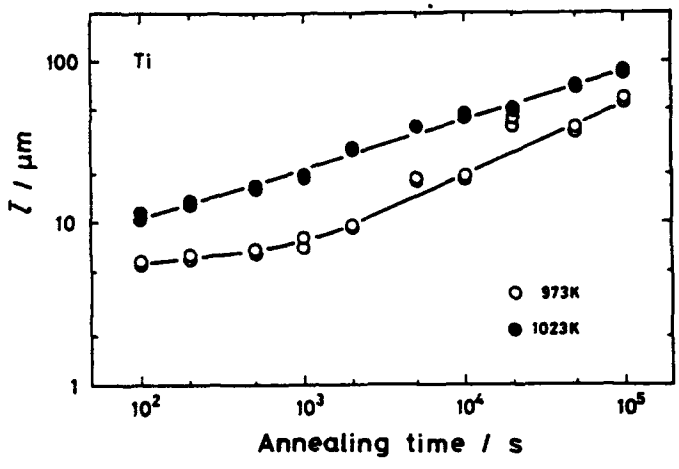


Fig. 1 The change of arithmetic mean linear intercept length $\bar{l}$ during annealing at 973K and 1023K for a commercially pure titanium.

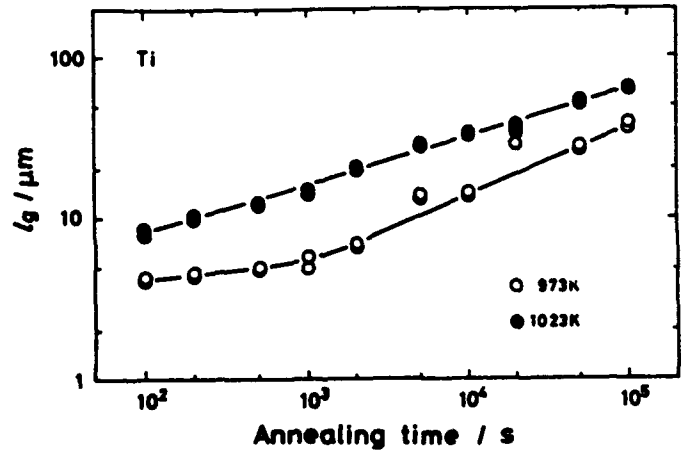


Fig. 2 The change of geometric mean linear intercept length l_g during annealing at 973K and 1023K for a commercially pure titanium.

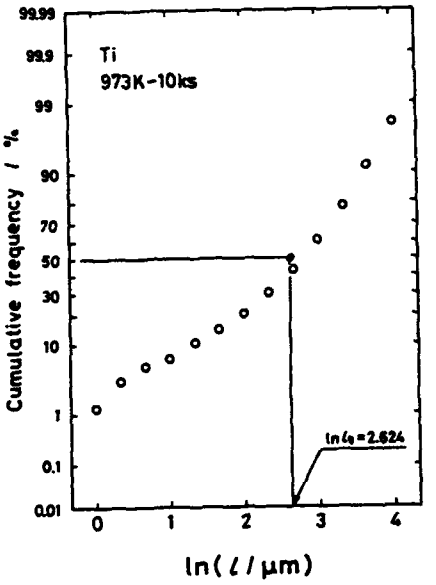


Fig. 3 Normal probability plot of cumulative frequency versus ln l for a commercially pure titanium annealed for 10ks at 973K.

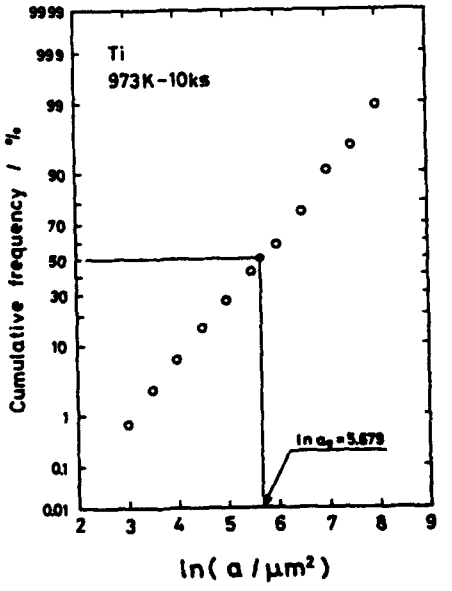


Fig. 4 Normal probability plot of cumulative frequency versus ln a for a commercially pure titanium annealed for 10ks at 973K.

each sample with a considerable scatter. In general, grain growth has been expressed by an empirical equation,

$$\bar{R} = Kt^n, \qquad (1)$$

where $\bar{R}$ is the mean grain radius, t is the annealing time, and K and n are parameters depending on material and temperature. If the change in $\bar{l}$ corresponds to that in $\bar{R}$, the values of grain growth exponent n are obtained as 0.12 at 973K during period from 100–500s, 0.44 during 2ks–100ks, 0.30 at 1023K. Figure 2 shows the change in the geometric mean of linear intercept length $\bar{l}_g$ during grain growth. The values of n in Eq.(1) are 0.11 and 0.42 during reriods of 100–500s and 2ks–100ks, respectively at 973K and 0.30 at 1023K. Similar results were obtained in Figs. 1 and 2.

Distribution of Linear Intercept Lengths and Grain Intersect Areas

In order to compare these distributions with a log–normal one, the cumulative frequencies were plotted on log–normal probability papers, as shown in Figs. 3 and 4. As a result, the distribution of linear intercept lengths was found not to be log–normal. This fact was consistent with the results in several studies [6–8]. It was confirmed that

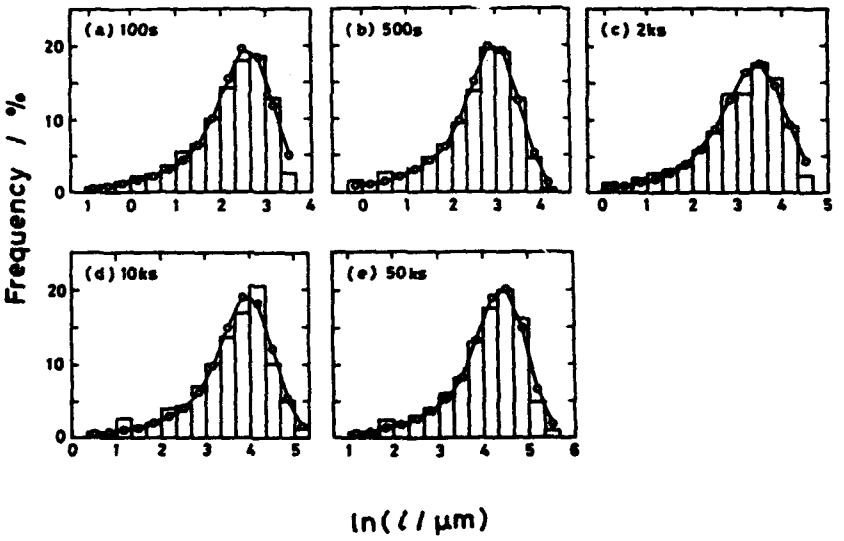


Fig. 5 Examples of application of the method for estimating the three–dimensional grain size distribution, to a specimen series of a commercially pure titanium annealed at 1023K for various periods. Histgrams represent experimental frequencies and the points denoted by circles represent calculated ones used in the estimating method [6].

grain intersect area distribution was nearly log-normal.
The spreads of these distributions are expressed by standard deviations for ln l and ln a. These standard deviations were regarded as almost unchanged during grain growth, although the distribution forms were alternated significantly as described above.

Grain Size Distribution in Three Dimensions

Figure 5 shows examples of application of the estimating method to a series of titanium samples. The Figure indicates a very good agreement between the experimental and the calculated values for each specimen. Thus, a very good estimation of the three-dimensional distribution is confirmed.
The change in the geometric mean grain diameter D_g during grain growth is shown in Fig. 6. The value of D_g increases remarkably with increment of annealing time in the range of this experiment. The n value is derived 0.054 and 0.44 during periods of 100-500s and 2ks-100ks, respectively at 973K and 0.27 at 1023K. These are similar values to those in Figs. 1 and 2. On the other hand, the value of D_g varied similarly with annealing time and then it became unchanged or slightly decreased. Thus, it is clear that the change in three-dimensional mean grain size D_g is different from that in one- or two-dimensional mean.
The standard deviations ln σ_g representing the spread of three-dimensional distribution are shown as a function of annealing time, in Fig. 7. The value of ln σ_g shows little change. This means that the spread of the distribution decreases, that is, the

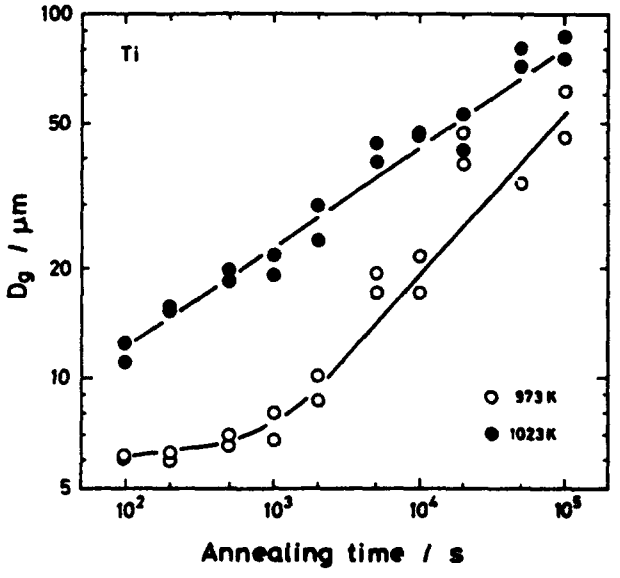


Fig. 6 The change of geometric mean grain diameter D_g during grain growth at 973K and 1023K for a commercially pure titanium.

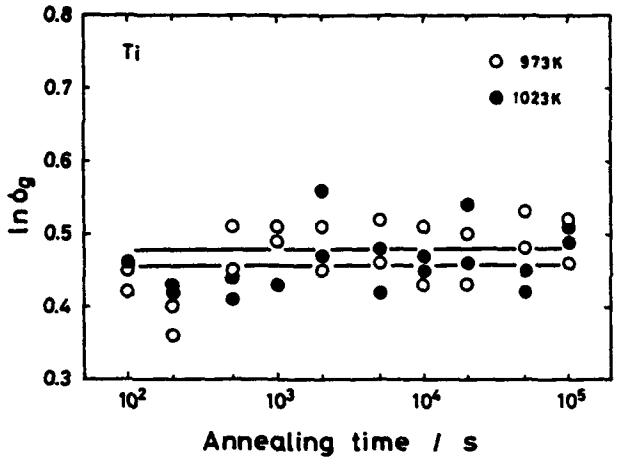


Fig. 7 The change of arithmetic standard deviation of ln D, $ln\ \sigma_g$ during grain growth at 973K and 1023K for a commercially pure titanium.

recrystallized structure approaches the perfectly-uniform one. The value of ln σ_g is found to decrease in the range of short annealing time, and then to turn to a sudden increase when the annealing time reached a level. Such changes in ln σ_g correspond to that in D_g (Fig. 6). The value of ln σ_g decreases with the increase in D_g, or increases as the value of D_g stagnates or decreases slightly.

Summary

(1) The one- and two-dimensional mean grain sizes increased with annealing time, while the standard deviations of the distributions were almost unchanged during grain growth. The time dependence index of grain growth, n, was found to be constant at 1023K, while it increased during annealing at 973K.

(2) The three-dimensional mean grain size D_g of Ti increases remarkably with annealing time. The tendency of the change in D_g for Ti was shown to be similar to those in the one-and two-dimensional mean.

References

1) H. V. Atkinson: Acta Metall., 36 (1988) 469.

2) P. Feltham: Acta metall., 5 (1957) 97.
3) H. Hu: Can. Metall. Q., 13 (1974) 275.
4) F. N. Phines and B. R. Patterson: Metall. Trans.A, 13A (1982) 985.
5) Y. Takayama, N. Furushiro, T. Tozawa, H. Kato and S. Hori: Mater. Trans. JIM, 32 (1991) 214.
6) F. Schuükher: Quantitative Microscopy, edited by DeHoff & F. N. Phines, McGraw–Hill, New York, 1968, Chap. 7.
7) Y. Takayama, T. Tozawa adn H. Kato: Trans. JIM, 28 (1987) 631.
8) K. J. Kurzydlowski and K. J. McTaggart: Trans. JIM, 29 (1988) 928.

PHASE TRANSFORMATIONS IN A NEAR ß - TI ALLOY :

MICROSTRUCTURE AND MECHANICAL PROPERTIES .

J. Béchet, C. Angelier, B. Cormier, O. Lacagne and M. Lhermitte

Laboratoire de Métallurgie
Conservatoire National des Arts et Métiers
292 rue Saint Martin - 75141 Paris cedex 03 , France

Abstract

Beta to alpha transformation in a near ß titanium alloy - the ß-CEZ - was investigated in detail and CCT or TTT curves were derived. The kinetics and morphological features of the phase transformations were discussed. Furthermore, the effects of beta and alpha/beta solution treatments on the microstructure and tensile properties were investigated in order to control the stability of the ß-phase and the variation of the primary alpha phase amount. The age-hardening reactions were studied in the high and low temperature aging range. Various phase transformations can occur depending on the aging time and temperature. Aging curves of this alloy are presented. The mechanism of the drastic reduction in macroscopic ductility at low temperature aging is discussed.

Introduction

The ß-CEZ alloy, which was mainly developed for engine turbine disk applications (1), is a metastable beta titanium alloy. These near ß alloys are heat treatable and deep hardenable. A wide variety of phase transformations and attendant microstructures are possible in these alloys. In addition, the type of heat treatment plays an important role in varying the properties of materials. The goal of this present work is first to understand some effects of the various heat treating steps upon microstructures (solution treatment, quenching and aging) and then how mechanical properties are affected by microstructural changes. Since the transformations and their rates that occur during fabrication and heat treatment are dependent on conventional time - temperature effects, it seemed useful to describe graphically the particular reaction products by means of isothermal and non-isothermal transformation diagrams (usually referred respectively to as TTT and CCT diagrams). Furthermore, hardenability and tensile tests were carried out on various kind of heat treated specimens and correlations between microstructures and mechanical properties were investigated.

Acknowledgments

This work has been realized in the framework of "G.S. Titane - Traitements Thermomécaniques" supported by C.N.R.S., M.R.T., D.R.E.T.-D.G.A., Aérospatiale, Cezus, Fortech Division Air forge Pamiers, S.N.E.C.M.A. and Turboméca.

Titanium '92
Science and Technology
Edited by F.H. Froes and I. Caplan
The Minerals, Metals & Materials Society, 1993

Experimental Procedures

Two alloys were supplied by Cezus Company, in the form of 120 and 55 mm diameter stock bars. The thermomechanical sequence was classical : triple vacuum arc remelting, rough forging operation in the ß field, final forging in the α/ß field. Table I shows chemical composition of ß-CEZ alloys used. The ß-transus temperature is close to 890-895°C. The SEM micrograph for the as-received alloy 1 (Fig.1a) shows a large prior ß grain size (1150 µm) with Widmanstätten microstructure due to ß annealing (910°C/50h). In the as-received condition, the alloy 2 consists of a fine grained equiaxed microstructure (Fig.1b).

Table I - Chemical composition of ß-CEZ alloys used (wt %)

	Al	Sn	Zr	Mo	Cr	Fe	O	Ti
Alloy 1	5,00	1,90	3,80	3,90	2,05	0,95	0,068	bal.
Alloy 2	4,82	1,99	4,00	3,94	2,10	0,98	0,085	bal.

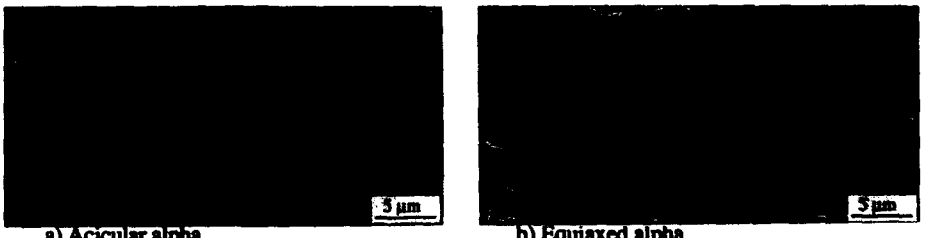
The transformation diagrams (CCT and TTT) were constructed by studying the microstructure and by measuring the Vickers hardness after heat treatment. The analysis of length changes, performed in DT1000™ dilatometer, provides also a preferential method to describe solid-state transformations during heat treatment.

The main scheme for heat treatments was to study the effect of the various processing steps upon microstructures. (1) The solution treatment temperature was chosen above and below the ß-transus temperature (between 920 and 750°C) for 0.5 or 1 hour.

(2) The solution-treated samples were continuously cooled with several cooling rates (between 2.10^{-3} and 100°C/s) or isothermally held at the temperature in α/ß field (between 250 and 800°C) for times up to 1000 hours.

(3) The age-hardening reactions were studied in the high and low temperature aging range for various times after quenching from the solution treatment temperature.

Microstructural analyses were conducted using quantitative OM and SEM or TEM observations and selected area electron diffraction. Thin-foils were produced by twin jet electropolishing using the conditions described by Blackburn and Williams (2). Tensile tests were performed at room temperature on round specimens with diameter of 5 mm and gauge length of 25 mm.



a) Acicular alpha b) Equiaxed alpha

Figure 1 - Microstructure of as received ß-CEZ : a) alloy 1 ; b) alloy 2.

The Effects of Solution Treatments on α_p and ß Grain Structure

Solution treatment controls the size, distribution, morphology and volume fraction of pr imary α particles (Fig.2). In addition, this heat treatment controls composition and stability of the ß-matrix (Fig.3). Recrystallization and grain growth of the ß-phase are also influenced (Fig.4). At 920°C, ß-grain growth in the ß-CEZ follows the common relationship : $D = K.t^n$ with $n = 0.45$.

It is shown that these variations versus solution treating temperature are significant parameters for adjustment of heat treatments and therefore of mechanical properties. Correlation between ß stability and unaged strength is obvious in figure 5. Higher solution treatment temperatures lead to lower α_p amount. The remaining ß-matrix becomes depleted in ß stabilizing elements (Mo, Cr and Fe) and enriched in Al. This decreases the stability of the ß-phase and enlarges its capability to form stress-induced martensite during testing. Thus, ß solution treatment results in the least stable matrix composition and highest UTS/YS ratio values in the quenched and unaged state.

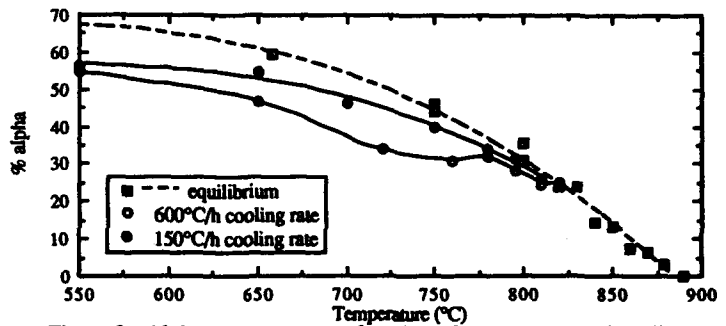


Figure 2 - Alpha percentage as a function of temperature and cooling rate

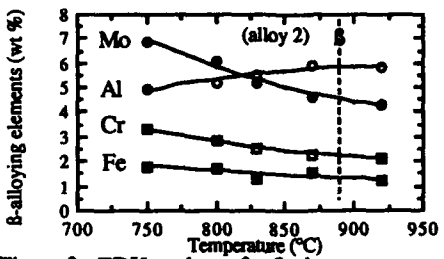


Figure 3 - EDX analyses for ß-phase.

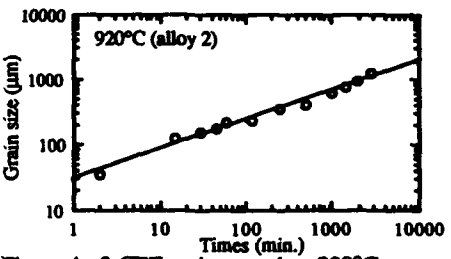


Figure 4 - ß-CEZ grain growth at 920°C.

In figure 6, ST ductility data (expressed by the elongation) are plotted as a function of solution treating temperature. It is enlighted that there is competition between two microstructural trends. On the one hand, decreasing the amount of primary α increases ductility because probably void nucleation sites at α-ß interfaces are fewer. On the other hand, recrystallization and grain growth of ß-phase decrease ductility because the void growth rate in the ß-matrix is larger.Thus 15 % of α_p particles is sufficient to pin ß grain boundaries and provides the balance of ductile fracture (3).

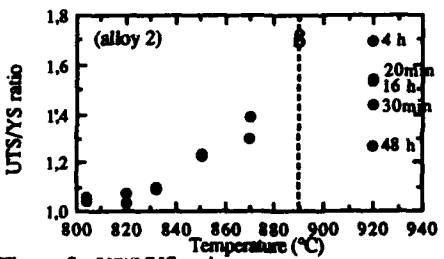


Figure 5 - UTS/YS ratio vs temperature

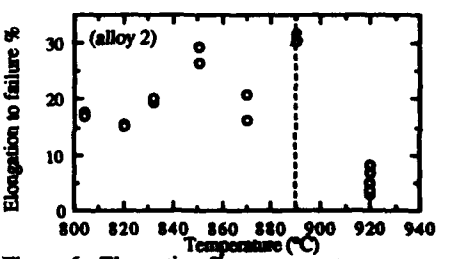


Figure 6 - Elongation % vs temperature

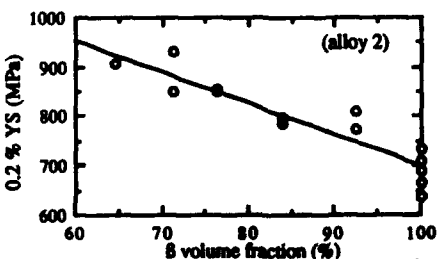


Figure 7 - Yield strength versus volume pct ß

Figure 7 suggests that the law of mixtures applies adequately to 0.2 yield strength of as-quenched equiaxed microstructures (4) and that the interaction term $I_{\alpha-\beta}^{YS}$ is zero for this part of the curve.This is dependent on ß-matrix enrichment. In the case of the ß-quenched condition, there is a great scatter in yield strength level, which would seem to be primarily due to the onset of a stress-induced martensite transformation.

ß-Phase Decomposition During Cooling : Athermal Transformations

Various phase transformations occur in ß-CEZ during cooling and therefore are of particular interest in determining the final microstructure and mechanical properties of the alloy.

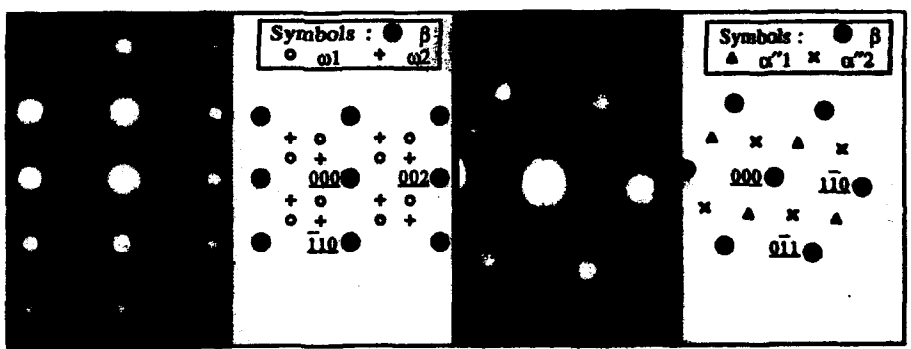
Types of Phases

In the ß-solution treated and quenched condition, equiaxed grains of metastable ß are observed metallographically. In addition, evidence of athermal ω-phase can be seen on electron diffraction patterns (Fig.8a). Further patterns (Fig.8b) reveal particular reflections which can be explained by the presence of martensite in this as-quenched structure. The latter evidence is not unambiguous with regard to its mode of formation. Transformation can occur by quenching or by applying a sufficient stress to induce martensite during thin-foil preparation.

When the ß-phase present at high temperature decomposes via α precipitation on cooling, the precise microstructure developed depends on a number of factors. The reaction involved in the transformation from ß to α+ß is controlled by nucleation and growth processes. There are four characteristic features of nucleation sites for α-phase precipitation.

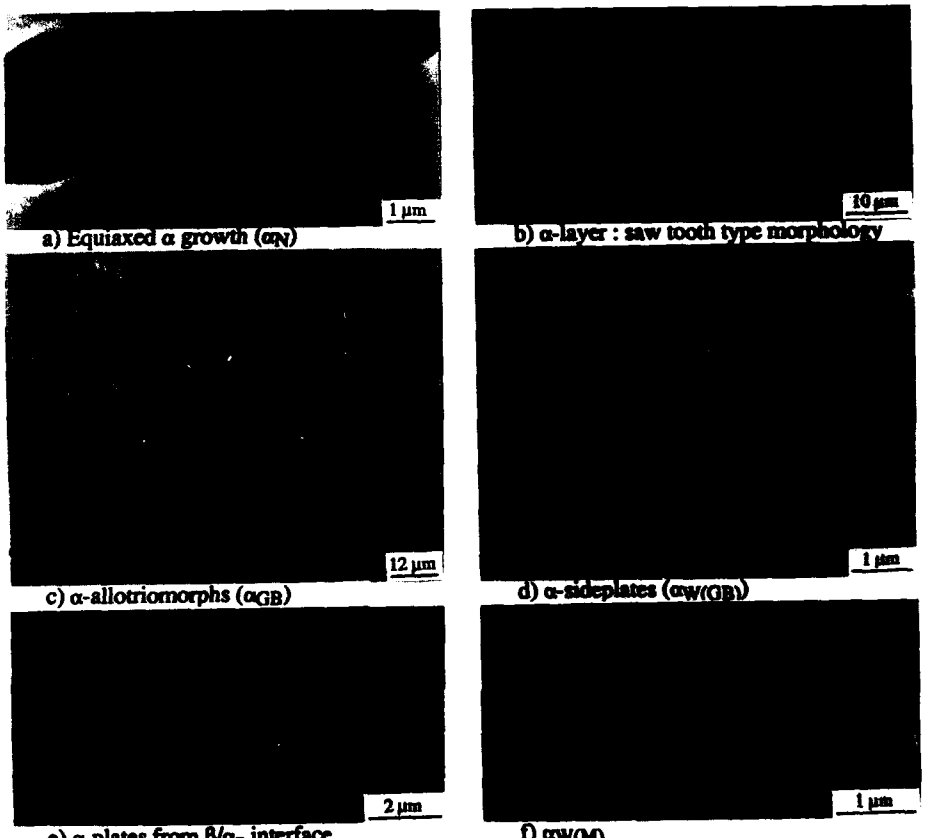
- In the case of α+ß solution annealing, nuclei are present in the form of the primary α and transformation can occur by the equiaxed α growing into the ß-matrix (termed α_N). Observation shows that a growing nodule is quickly established at ß/ß/α_p junctions and forms a typical outgrowth from which it follows that the diffusion is predominantly along ß-grain boundaries (Fig.9a).
- There is always a preferential formation of α at the prior ß-grain boundaries (termed α_{GB}). Nevertheless, several types of grain boundary α precipitates can be found : continuous layers, sometimes very fine, or α-allotriomorphs. Optical observations show that the α-allotriomorph can simultaneously nucleate at several sites along the ß-GB, depending on orientation relationships with the ß-matrix grains, and then grow with the same typical geometric morphology (Fig.9c). *One of the most notable features is that often planar facets are present at grain boundaries* from which it follows that these interfaces are coherent. In addition, the ß-grain boundary is displaced during the precipitation process (Fig.9c). By analogy, this deflection might be described by a "pucker" mechanism (5) devised as a nucleation process of the cellular reaction.

- The third nucleation site is active upon extant α/ß interfaces (termed $\alpha_{W(GB)}$). Precipitation of Widmanstätten α plates, described as secondary sideplates in the Dube morphological classification system (6), occurs on the α_{GB} precipitates. Observations (Fig.9d) show that often these α-sideplates from α-allotriomorphs selectively grow into one of the two adjoining ß-grains, in agreement with published results (7). On the other hand, the continuous α-layer in the grain boundaries grows sideways and forms a "saw tooth type" morphology (Fig.9b) probably controlled by the diffusivity of alloying elements (8). Thus, it results in a Widmanstätten structure. In addition, acicular α-phase can nucleate at ß/α_p interface and then form a pecular shape (Fig.9e). Thus, it is apparent that there is modification of nucleation scenario during cooling.



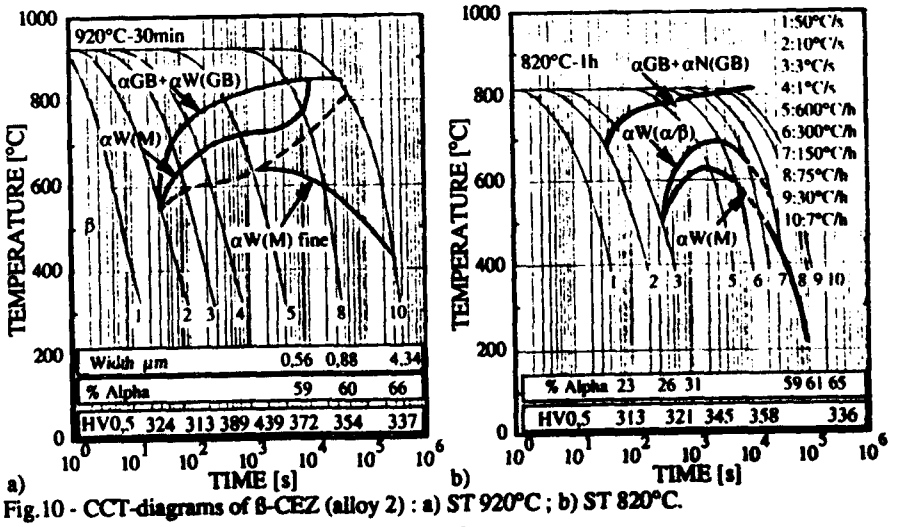
a) <110>ß zone axis (and schematic) b) <111>ß zone axis (and schematic)

Figure 8 - ß-CEZ alloy quenched from ß-field (920°C /4h/ WQ). SAD patterns



a) Equiaxed α growth (α_N)
b) α-layer : saw tooth type morphology
c) α-allotriomorphs (α_{GB})
d) α-sideplates ($\alpha_{W(GB)}$)
e) α-plates from β/α_p interface
f) $\alpha_{W(M)}$

Figure 9 - Characteristic features of nucleation sites for α-phase precipitation.



a) b)

Fig.10 - CCT-diagrams of ß-CEZ (alloy 2) : a) ST 920°C ; b) ST 820°C.

- Finally at lower temperatures, nucleation at sites within the grains occurs as a basketweave appearance, characteristic of a Widmanstätten structure (termed $\alpha W_{(M)}$). In this case, dislocations and sub-grain boundaries are initiators of the α-nucleation process. Very fine precipitates result from nucleation and growth on crystallographic planes of the metastable ß-matrix (Fig.9f).

Kinetics of phase transformations

CCT curves for ß-CEZ have been accurately constructed (Fig.10) for specimens heated initially into the all-ß field (920°C/30min) or high in the α+ß field (820°C/1h). These indicate various schemes of α-precipitation during continuous cooling and delineate the areas of specific α-nucleation features.

Figure 2 illustrates the application of volume fraction measurements to characterize the kinetics of ß-decomposition. Metallographic samples corresponding to various cooling rates were characterized using a SEM interfaced with an image analyzer. Evaluation of kinetic reaction parameters, *as activation* energies, could be based on this quantitative analysis.

Another quantifying parameter to understand how heat treating changes affect microstructure is the width of the α-lamellae. Figure 11 depicts the relationship between width of the α-lamellae and the cooling rate from the ß-phase region.

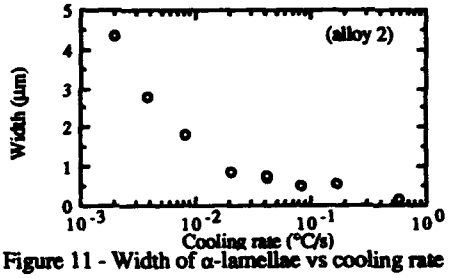


Figure 11 - Width of α-lamellae vs cooling rate

ß-Phase Decomposition During Aging : Isothermal Transformations

The TTT curves for the alloy ß-solution annealed (Fig.12a) were derived from hardness data (Fig.12b), dilatometric analysis and metallographic examinations. These delineate the same previous areas which summarize the possible decomposition processes in continuous cooling. The minimum incubation time (12 s) and maximum velocity is realized at 570°C corresponding to the α-precipitation. The low temperature minimum (close to 350°C) is due to the isothermal ω transformation. Then, the $\omega \rightarrow \alpha$ transition forms very fine and uniform α-phase and the two phases can coexist for some period of time. The same low-temperature sequence of transformations would be also involved during various rate heating of quenched alloy to the aging tempe-

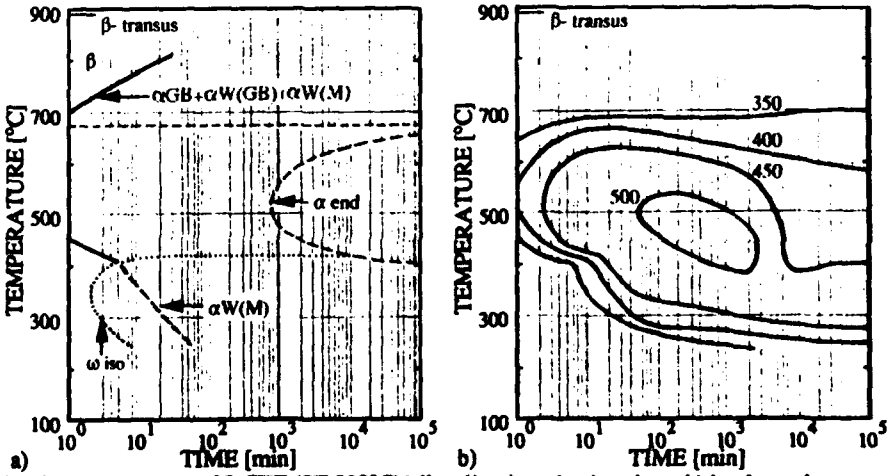


Fig.12 -TTT-diagram of ß-CEZ (ST 920°C)(alloy 1) : a) nucleation sites ; b) hardness data

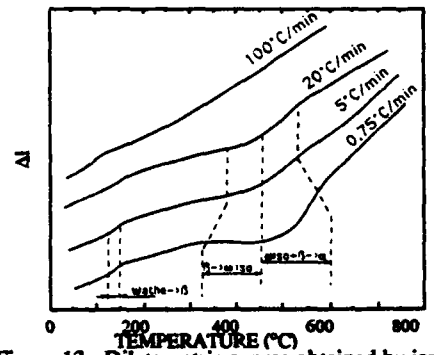
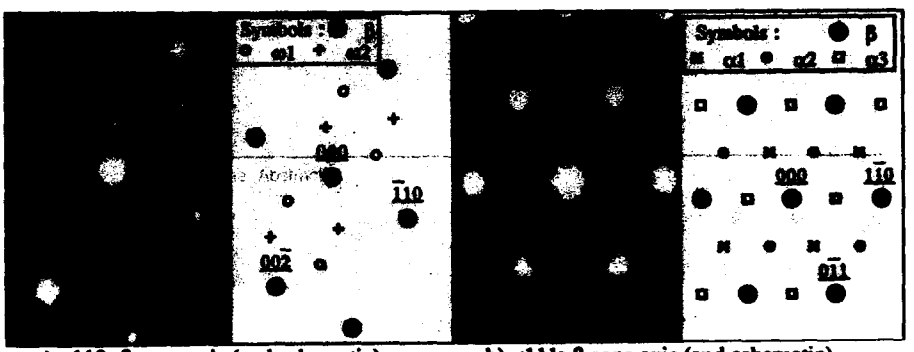


Figure 13 - Dilatometric curves obtained by isochronal aging.

rature. Figure 13 shows dilatometric changes in the process of heating. Athermal ω-phase is decomposing early during heating (150°C). At higher temperature and low heating rate, two transformations can be discerned, associated with a decrease and then an increase of relative length, due respectively to the isothermal ω-phase and α-phase precipitations. This structural interpretation is supported by electron diffraction data. Figure 14 shows that ω_{iso} and α-phases are present for the 5°C/min heating rate to 350°C aging temperature.



a) <110>ß zone axis (and schematic) b) <111>ß zone axis (and schematic)

Figure 14 - ß-CEZ alloy quenched from ß-field and aged (350°C / 1min). SAD patterns

The aging responses of ß-CEZ were determined in the temperature range 350 to 650°C. The HV hardness response in each case is presented in Figure 15. At 580 and 650°C, the alloy shows an initial rapid hardening reaction taking place within a few minutes but then overages with the coarsening of α-plates. In this case, lower aging temperature leads to higher peak. At low temperatures (350-550°C), the aging kinetics are slower. The times required to reach the maximum hardness increase with decreasing temperature. The ß-phase of the specimen solution-treated in the α+ß field is more stable for the existence of the α_p-phase and the hardening response is slower and slightly less pronounced. The initial heating rate has a significant effect on subsequent aging, particularly in the temperature range 350-550°C : extremely fines precipitates are observed for low heating rate due to the precursor ω-phase precipitation.

Hardening at 350°C aging temperature of specimens solution-treated in the ß-field at 920°C and water-quenched leads to the embrittlement of the alloy 1 during subsequent cooling. Undoubtedly, the embrittlement and no plastic ductility are common process occuring in the hardened

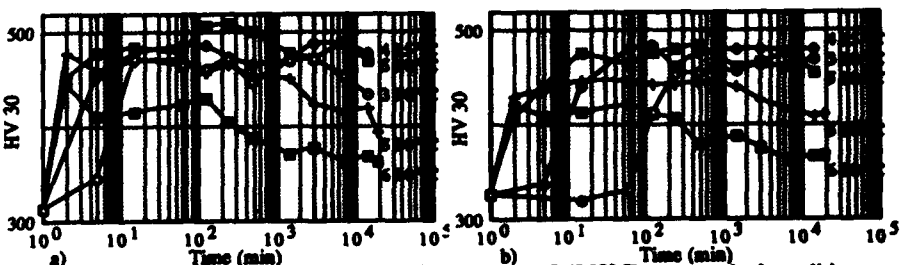
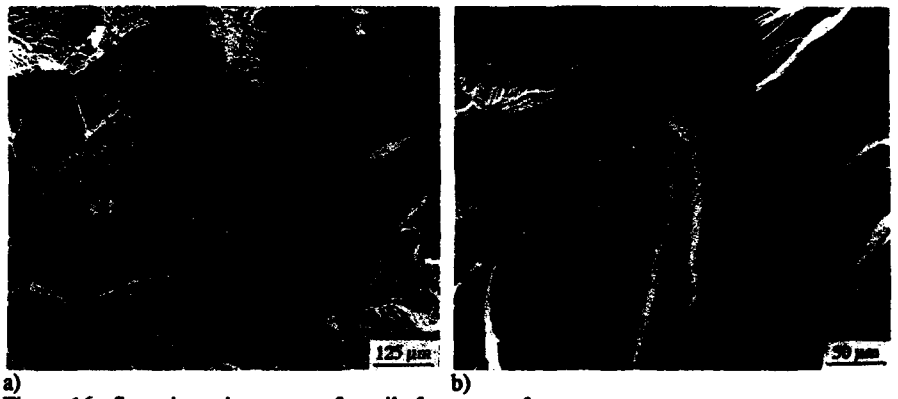


Figure 15 - HV30 vs aging time for a) ß (920°C) and b) α+ß (850°C) as-quenched conditions

(α+ß) high alloys during low aging (9). This brittle behavior after 350°C aging treatment depends on specimen section size and ß-grain size. The occurrence of cracking is related to the α fine and ω_{iso} precipitation. This decomposition involves anisotropy of the thermal expansion and elastic moduli, great increase in Young's modulus ($E_\omega \sim 2E_\beta$ (10)), dilatometric effect (contraction), strengthening of the ß-matrix, inhomogeneous slip distribution due to intense slip bands and pile-ups at grain boundaries. The general features of resulting fractography are intergranular fracture, microvoid coalescence and transgranular cleavage appearance (Fig.16). Thus, the drastic reduction in macroscopic ductility at low temperature aging results from double effects. The presence of non-uniform volumetric changes in the specimen may give rise to thermal and structural stresses. In addition, local stress concentration resulting from inhomogeneous distributed slip bands piling-up against grain boundaries may reach the critical value to crack nucleation for the age-hardened conditions investigated in this study.



a) b)

Figure 16 - Scanning microscopy of tensile fracture surfaces.
ß-CEZ alloy quenched from ß-field and aged at 350°C : a) 1 min ; b) 30 min.

References

1. B. Prandi, E. Alheritiere, F. Schwartz and M. Thomas, Sixth World Conf. on Titanium, ed. P. Lacombe, R. Tricot, G. Beranger (S.F.M., Les Editions de Physique, 1989), II, 811-818.

2. M.J. Blackburn and J.C. Williams, Trans. TSM - AIME, 239 (1969), 287.

3. T.W. Duerig and J.C. Williams, Beta Titanium Alloys in the 80's, ed. R.R. Boyer and H.W. Rosenberg (Warrendale, PA: The Metallurgical Society, 1984), 19-67.

4. S. Ankem and H. Margolin, "A Rationalization of Stress-Strain Behavior of Two-Ductile Phase Alloys", Metall. Trans. A, 17A (Dec.1986), 2209-2226.

5. K.N. Tu and D. Turnbull, Acta Met., 15 (Feb.1967), 369-376.

6. C.A. Dube, H.I. Aaronson and R.F. Mehl, Rev. Met., 55 (1958), 201.

7. M.A. Iman, B.B. Rath, C. Hammond and O.P. Arora, Sixth World Conf. on Titanium, ed. P. Lacombe, R. Tricot, G. Beranger (S.F.M., Editions de Physique, 1989), III, 1313-1318.

8. H. Fujii and H.G. Suzuki, Sixth World Conf. on Titanium, ed. P. Lacombe, R. Tricot, G. Beranger (S.F.M., Editions de Physique, 1989), III, 1489-1494.

9. A. Gysler, G. Terlinde and G. Lütjering, Titanium and Titanium Alloys, ed. J.C. Williams, A.F. Belov (Plenum Press, 1982), 3, 1919-1931.

10. A.W. Bowen, Titanium'80 Science and technology, ed. H. Kimura & O. Izumi, 1980, 2, 1317-1326.

PRECIPITATION AND HARDENING IN

TITANIUM-MAGNESIUM AND TITANIUM-CALCIUM ALLOYS

C.M.Ward-Close, P.G.Partridge,
and C.J.Gilmore

Materials and Structures Department,
Royal Aerospace Establishment, Farnborough, GU14 6TD, UK.

Abstract

An electron beam evaporation and vapour quenching route has been used to make thick deposits of titanium-magnesium and titanium-calcium alloys. Alloying titanium with these alkali metals is not possible by conventional ingot metallurgy, due to the low melting points and high vapour pressures of the alloy additions. Magnesium, for example, boils, at atmospheric pressure, below the melting temperature of titanium. A full range of solid solution titanium-magnesium alloys have been produced, and a microhardness and TEM study has been carried out on Ti 4wt%Mg alloy aged at 600°C. An appreciable increases in hardness has been found to be associated with both magnesium and MgO precipitation .

Introduction

Conventional titanium alloys derive their strength mainly from solid solution hardening or microstructural hardening. Microstructural hardening is achieved by creating a duplex microstructure, usually by the precipitation of beta from titanium martensite, or the precipitation of alpha from beta. Dispersion strengthening of titanium offers the potential for room temperature and elevated temperature property improvements. Although, some hardening of conventional titanium alloys has been derived from precipitation of compounds such as Ti_3Al, $TiCr_2$ or Ti_3Si_5, effective dispersion strengthening has only been exploited in one commercial titanium alloy, binary titanium-copper, where a moderate age hardening response is achieved by the precipitation of Ti_2Cu. The temperature range of this alloy is restricted to below 350°C.

Much recent work has focussed on dispersion strengthening of rapidly solidified powder metallurgy titanium alloys with rare earth oxides. Small amounts of yttrium or erbium added to conventional ingot metallurgy titanium had been shown to produce fine dispersions of rare earth oxides by internal oxidation. However, additions of larger amounts of these elements resulted in coarse (> 1μm) brittle precipitates of Er_2O_3 or Y_2O_3 [1]. Rapid solidification has been demonstrated as a route to producing dispersion strengthened titanium alloys with up to 1at.% rare earth addition. However,

Titanium '92
Science and Technology
Edited by F.H. Froes and I. Caplan
The Minerals, Metals & Materials Society, 1993

difficulties remain over the consolidation of liquid quenched products, such as splats, powder or ribbon. Also, rare earth elements are extremely expensive, and, with the exception of scandium oxide, all the rare earth oxides have a greater density than titanium.

Thermodynamic considerations suggest that oxides of the alkali metals Ca and Mg may be stable in solid titanium at elevated temperatures. The equilibrium solubility of both elements in titanium is very low (< <1 At%), no intermetallic compounds are formed in the binary systems [1] and at low temperatures the free energies of formation of their oxides are each more negative than for the formation of TiO_2. However, practical problems have hitherto precluded the introduction of these oxides as a fine dispersion in titanium. The very high vapour pressures of these elements compared with that of titanium makes mixing these alloy additions with titanium in the liquid state virtually impossible and calcium is probably immiscible with titanium in the liquid state.

Work by Petrova et al. [3] on the extrusion of powder compacts consisting of mixtures of titanium and various oxide powders has confirmed that both CaO and MgO are reasonably stable in titanium at elevated temperature. Some chemical reaction was observed between the titanium and MgO after heating and extrusion at 1050°C. This was accompanied by an increase in the matrix micro-hardness, presumably due to partial dissolution of the MgO. No reaction or matrix hardness increase was observed for CaO at this temperature.

The production of Ti-Mg and Ti-Ca alloys by a vapour quenching route has been described [2]. In this paper the microstructure and ageing behaviour of these alloys are described.

Experimental Techniques

Titanium-magnesium and titanium-calcium alloy deposits were made by EB evaporation and mixing of vapours before condensation on to a heated metal substrate. The electron beam heated rod-fed titanium source was contained in a water cooled copper crucible, and the radiantly heated magnesium source was positioned around and above the titanium source. The resultant deposits were up to 8mm thick, and 100mm in diameter. Alloy composition was determined by electron probe micro-analysis (EPMA), using a Cambridge Instruments Microscan 9, and confirmed by wet chemical analysis. Microhardness was carried out with a pyramidal diamond microhardness indentor at 80g load.

Results

Microhardness of the as-deposited Ti-Mg alloy after exposure at 600°C in air or in vacuum is shown in Fig.1. The hardness in vacuum doubled after 1/2h but then remained unchanged up to 10h. The corresponding hardness curve for an unalloyed titanium deposit was slightly lower than for the Ti-Mg alloy after 1/2h and was unchanged after 100h at 700°C. These results suggest the initial increase in hardness was caused by oxygen present in the porous deposits and no oxygen pick-up occurred in the vacuum environment.

The deposit porosity was eliminated by pressing at 600°C. Pressing in vacuum increased the hardness to about 350VPN, but after 10h in vacuum the hardness decreased to the value for the corresponding as-deposited material heated in vacuum. The higher initial hardness is attributed to the worked microstructure, which recovers at 600°C.

For the Ti-Mg alloy exposed in air in the as-deposited or pressed condition much higher hardness values were obtained. The material pressed in vacuum and subsequently exposed in air did not exhibit the softening found for the vacuum annealed specimen. When the results for the Ti-Mg alloy are compared with those for the unalloyed titanium deposit it is clear that the hardening is much greater for the Ti-Mg alloy in an oxygen environment. The hardening does not therefore appear to be caused solely by oxygen in solution in the titanium lattice.

The as-deposited Ti-Mg alloy microstructure was characterised by columnar grains with a diameter, parallel to the substrate, of <100nm as shown in Fig.2(a); in this state X-ray data indicated all the magnesium was in solid solution [4]. No precipitates were detected but the high density of dislocations prevented high resolution studies. Energy dispersive spectroscopy (EDS) showed the as-deposited material contained titanium and magnesium only (Fig.2(b)). An alloy deposited at 200°C and aged in vacuum at 600°C showed evidence of particles at grain boundaries. The larger particles appeared to be cuboids with edges about 200nm long. These particles were identified by electron diffraction, EDS and electron energy loss spectroscopy (EELS) as MgO (Fig.3).

An alloy deposited at 300°C and pressed in vacuum exhibited a mixture of residual columnar grains and recrystallised equiaxed grains with grain diameters in the range 100-400nm (Fig.4); in the latter the preferred orientation was less marked. In thin foils prepared by ion bombardment, small 50-100nm diameter particles at the grain boundaries were identified as pure magnesium. The foils were then thinned further by electropolishing, which produced a cleaner foil surface but the Mg particles at grain boundaries were etched out as shown in Fig.4. At higher magnification, precipitates 10-20nm diameter were visible within the grains and precipitate free regions were present along grain boundaries (Fig.5). Some precipitates showed displacement fringe contrast and had a hexagonal shape (see insert in Fig.5). No oxygen was detected by EELS. Selected area diffraction (SAD) patterns, from an area containing small particles, agreed with computer simulated patterns generated for a titanium lattice containing epitaxially related magnesium precipitates. An example corresponding to the $<2\bar{1}\bar{1}0>$ zone axis is shown in Fig.6; the epitaxial relationship was $\{0001\}Ti//\{0001\}Mg$ and $<1\,1\bar{2}0>Ti//<1\,1\bar{2}0>Mg$. Further studies confirmed these results [5] and observations of the particle shape during rotation about the <0001> axis indicated the particle was egg-shaped with major axis parallel to <0001>.

A Ti-Ca alloy in the as-deposited state showed large variations in Ca content and it was not possible to obtain evidence of solid solution formation using X-ray lattice parameter data. In a thin film a grain containing about 6wt% Ca showed no coarse particles [6] but very small particles were detected similar in appearance to those found in the Ti-Mg alloy (Figs.7a-b). This suggests that Ca can be retained in solid solution or precipitated as small particles similar to Mg in Ti-Mg alloy.

Discussion and Conclusions

The experimental data suggest that Ti-Mg and Ti-Ca solid solutions can be produced by vapour quenching. These solid solutions degrade by precipitation of very small particles of Mg or Ca in the grains and (in the absence of oxygen) of larger particles at grain boundaries. The misfit between the close packed lattice planes and directions is much greater for Ca (33-38%) than for Mg (9-11%) and is particularly small for MgO (1-4%). These misfits are less than for the θ'' phase in Al-Cu alloys. The Hume-Rothery atomic size factor is also small for Mg in Ti which is consistent with the shape of the Mg precipitate. Particles of Ca, Mg and MgO may therefore be coherent or semi-coherent and give rise to age hardening in Ti. The evidence suggests that MgO may be a very effective dispersed phase.

The effect of heat treatment is probably dependent on both deposition temperature and ambient oxygen concentration. The pores in the deposits increase and become interlinked with decreasing deposition temperature. The oxygen present in the pores after exposure to air will be gettered by Ti and the solute during subsequent anneals and lead to solid solution hardening in the titanium and to the formation of MgO grain boundary particles in the Ti-Mg alloy. This may be the cause of the initial increase in hardness in as-deposited or pressed material in vacuum. This initial increase was greater for the Ti-Mg deposit than for the Mg-free Ti deposit. Isothermal anneals in vacuum had little effect on subsequent hardness. The hardness increases for the Ti-Mg alloy in air were significant and depended on composition and ageing temperature. The precise role of Mg and oxygen in the hardening of the alloys is not yet clear.

Acknowledgment

The authors wish to acknowledge Mr.I.C.Wallis who carried out the heat treatments and hardness tests.

(c) Copyright Controller HMSO, London 1992

References

[1] S.M.Sastry, P.J.Mescher and J.E.O'Neal, "Structure and Properties of Rapidly Solidified Dispersion Strengthened Titanium Alloys. I. - Characterisation of Dispersoid Distribution, Structure and Chemistry", Metall. Trans., 15A (1984), 1451-1463.

[2] C.M.Ward-Close P.G.Partridge, "The Production of Titanium-Magnesium Alloys by Vapour Quenching", Materials Letters, 11 (1991), 295-300.

[3] A.M.Petrova et al., "Reactions in Ti-Oxide composites During Extrusion", Poroshkovaya Metallurgiya, 6 (1974), 72-75.

[4] C.M.Ward-Close et al., "An X-Ray Diffraction Study of Vapour Quenched Titanium Magnesium Alloys", This conference.

[5] G.Gu, J.W.Steeds, Unpublished work.

[6] G.Gu et al. International Electron Microscopy Conference, Madrid 1992, In press.

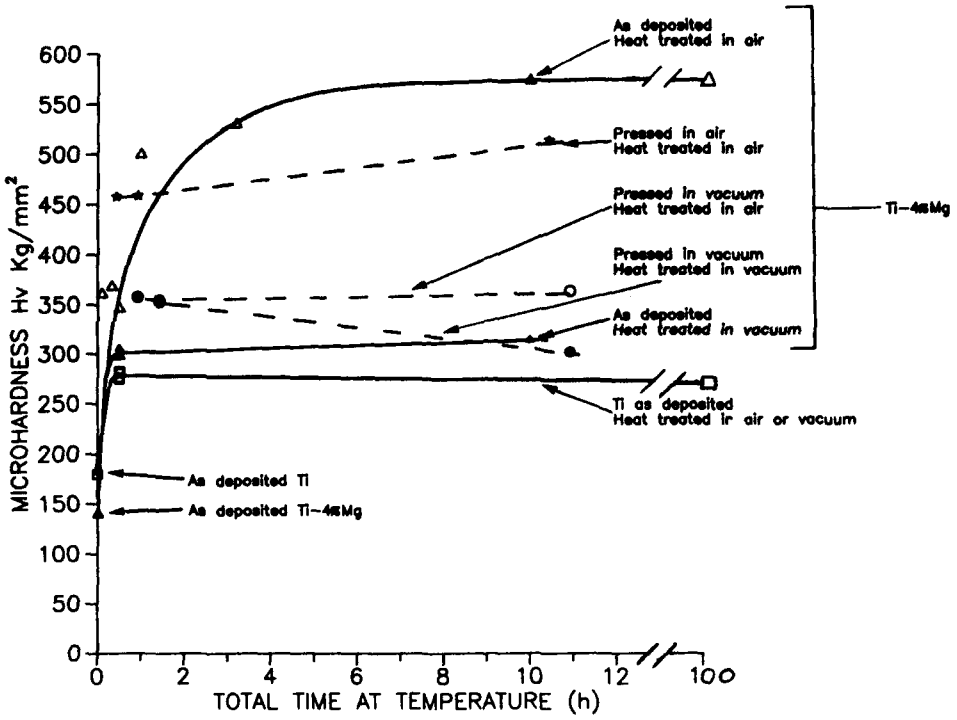


Figure 1 - Microhardness versus ageing time at 600°C in air or vacuum for titanium and Ti-4wt% Mg deposits (collector 300°C).

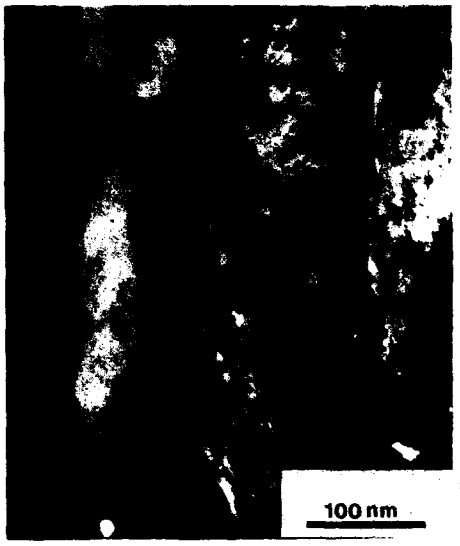


Figure 2(a) -
Transmission electron micrograph (TEM) of as-deposited Ti-7wt% Mg alloy (collector 200°C).

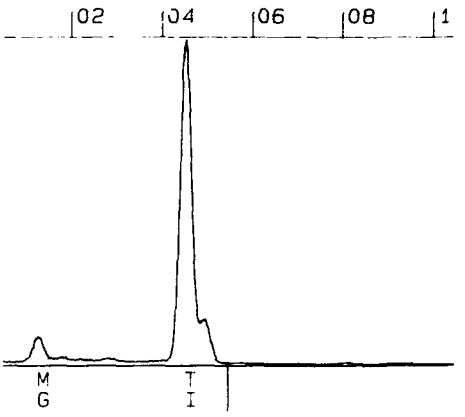


Figure 2(b) -
Energy dispersive spectrum from grain (A) in Fig. 2(a).

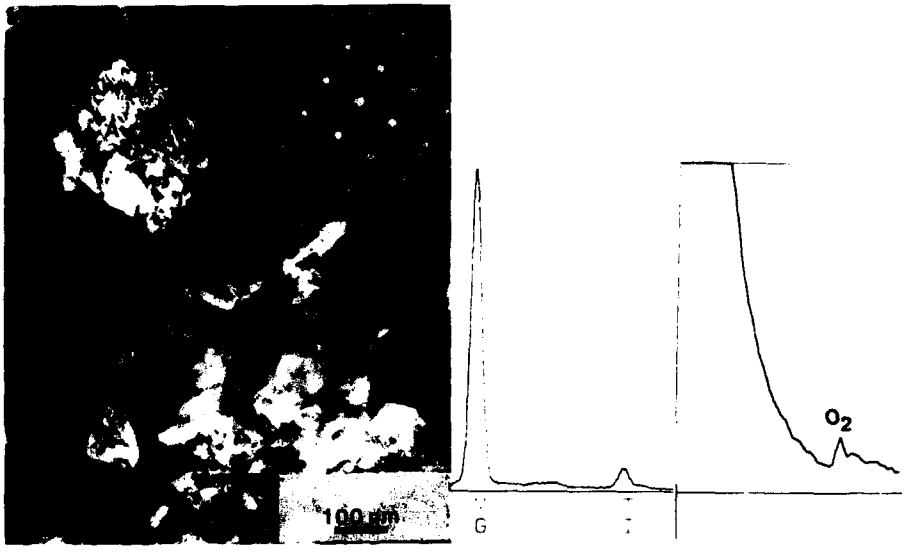


Figure 3 - (a) TEM (b) EDS(at A) (c) EELS(at A)

(a) TEM of Ti-4wt% Mg (collector 200°C) aged in vacuum for 30 mins showing MgO particles at A (inset shows SAD pattern identified as [001] zone axis of MgO),(b) Energy Dispersive X-Ray spectrum (EDS) from large MgO particle (A),(c) Electron Energy Loss spectrum (EELS) from large MgO particle (A).



Figure 4 -
TEM from Ti-4wt% Mg alloy (collector 300°C) pressed in vacuum and electropolished showing grain size and holes due to Mg dissolution.

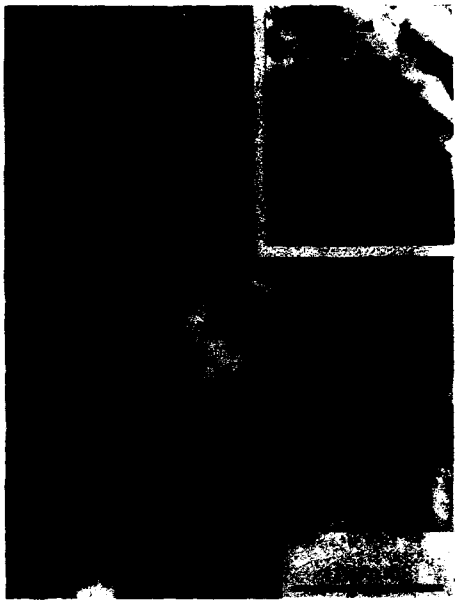
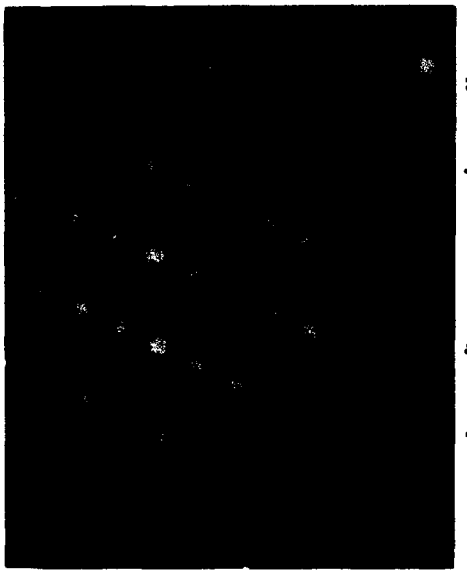


Figure 5 -
High magnification TEM from pressed Ti-4wt% Mg alloy showing fine scale precipitation (arrowed), precipitation free zone at grain boundaries (A) and hexagonal shape of precipitates (inset arrowed)



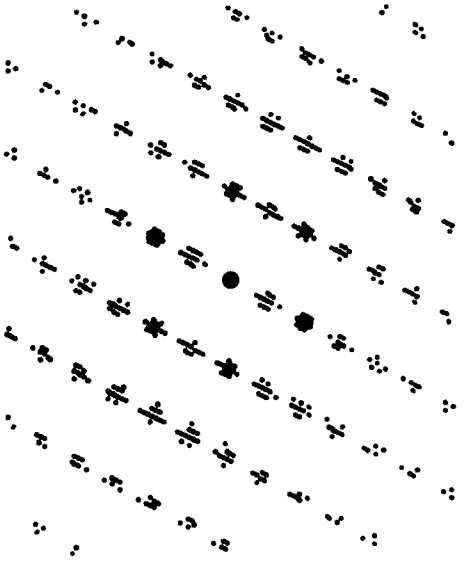


Figure 6 - (a) (b)

Selected area diffraction pattern including precipitate in Ti-Mg alloy a) pattern b) simulated SAD For Ti lattice with Mg precipitate.

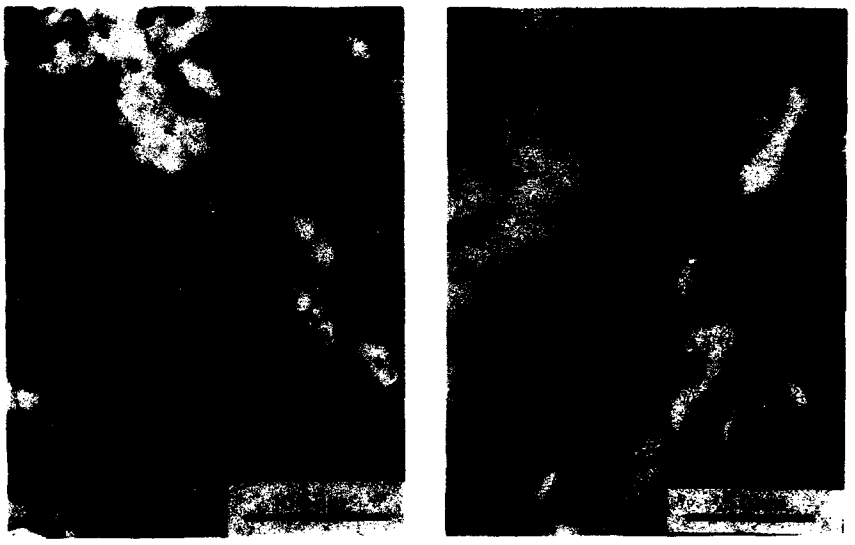


Figure 7 - (a) (b)

TEM of Ti-Ca alloy showing small precipitates a) with strain fields at A, b) with fringes at B

AN X-RAY DIFFRACTION STUDY OF VAPOUR QUENCHED

TITANIUM MAGNESIUM ALLOYS

C.M.Ward-Close, P.G.Partridge, P.Holdway and A.W.Bowen

Materials and Structures Department, Royal Aerospace Establishment, DRA Farnborough, GU14 6TD, UK.

Abstract

A range of titanium-magnesium alloys have been produced by an evaporation and vapour quenching route. At least 28 wt% Mg was retained in solid solution, and grain sizes were in the range 100-200nm. Dilute Ti-Mg alloys deposited onto a substrate at 200°C and heat treated in the range up to 700°C showed very substantial hardening, probably due to precipitation of MgO. Alloys containing 20-30 wt% Mg progressively decomposed on heat treatment to magnesium and titanium.

Introduction

A reduction in density of titanium alloys is extremely attractive for aerospace applications. However, of the possible substitutional alloy additions with densities lower than titanium only aluminium and silicon are available as solid solution additions via conventional ingot metallurgy. Other light elements, listed in Table 1, are either highly volatile, or have negligible equilibrium solubility in titanium. Magnesium, at atmospheric pressure, boils at a temperature below the melting temperature of titanium. Limited data available for the titanium-magnesium system is based mainly on diffusion couple work, and more recent work on mechanical alloying [1-5].

In this study a rapid solidification route has been used to produce titanium magnesium alloys ranging in composition from 0-60 wt% magnesium, and up to 8 mm in thickness. Magnesium is particularly attractive as a solid solution alloying addition for titanium, because it has a low density, the same crystal structure as titanium, and Hume Rothery's atomic size factor criterion suggests that solid solubility is favourable, and moreover the electronegativity and valency criteria suggest that compound formation is unlikely. Previous studies have confirmed that no compounds are found in the Ti-Mg system [3-5].

A physical vapour deposition (PVD) technique has been developed which enables significant magnesium solid solubility to be achieved. A previous paper [6] described the production of Ti-Mg alloys by this method, and discussed possible errors in the interpretation of lattice parameter data published for mechanically alloyed material.

In this paper evidence will be presented for full solid solubility of magnesium in titanium up to 27 wt% magnesium and above 52 wt%: indexing of diffractometer traces for alloys in the range between 27 wt% and 52 wt% magnesium was not possible due to peak broadening and a consequent lack of resolution between peaks. The effect of heat treatment on the titanium magnesium alloys will be investigated.

Titanium '92
Science and Technology
Edited by F.H. Froes and I. Caplan
The Minerals, Metals & Materials Society, 1993

Experimental Techniques

Titanium-magnesium alloy deposits were made by EB evaporation of titanium and magnesium from separate sources and mixing the vapours before condensation on to a heated metal substrate maintained at 200°C. The experimental arrangement is illustrated schematically in Fig.1. The electron beam heated rod-fed titanium source was contained in a water cooled copper crucible, and the radiantly heated magnesium source was positioned around and above the titanium source. The resultant deposits were up to 8 mm thick, and 100 mm in diameter. Alloy composition was determined by electron probe micro-analysis (EPMA), using a Cambridge Instruments Microscan 9, and confirmed by wet chemical analysis.

Lattice parameters were determined by X-ray diffraction (XRD) using Cu Kα radiation over the angular range 25-145° 2Θ, in a Philips PW1050 X-Ray Diffractometer, and peak positions were determined using the second derivative method. Peak positions were subsequently used in a least squares refinement method to obtain the a and c lattice parameters. The crystallographic textures were measured by Cu Kα radiation on an automated texture goniometer, up to a maximum tilt angle of 85°. All X-ray determinations were carried out on 10x10mm samples, ground back approximately 0.5mm from the final surface, and polished parallel to the deposition plane. Microhardness testing was carried out with a pyramidal diamond microhardness indentor at 80g load.

Results and Discussion

A series of deposits were produced with compositions in the range 0-60 wt% magnesium; all were slightly porous, with densities of about 99%. Hardness test results (Fig.2) suggested some solid solution hardening in the range 4-15 wt% magnesium .

Microstructure

Metallographic examination of the as-deposited samples under polarised light showed grains elongated in the deposition direction (Fig.3a). A 0.5 h vacuum anneal caused recrystallisation of a magnesium-free deposit at a temperature between 500°C and 600°C (Fig.3b), which is consistent with the recrystallisation temperature of about 600°C for conventionally produced pure titanium [7]. In contrast, a 4 wt% Mg-Ti alloy showed no noticeable change in microstructure up to 700°C (fig.4c). Although, some magnesium was lost during heat treatment, this effect was confined to within a few microns of the surface, and throughout the sample the magnesium concentration was apparently sufficient to stabilise the grain size. For alloys containing more than about 20 wt% Mg heat treatment above 500° resulted in severe distortion and some cracking.

A transmission electron micrograph from a Ti-15 wt% Mg alloy (Fig.4) showed a very small grain size in the range 100-200nm and a high dislocation density; there was no evidence of second phase particles and all the grains gave selected area diffraction patterns corresponding to an hcp lattice.

Lattice parameters

X-ray diffractometer traces for as-deposited, 0 wt%, 4 wt%, 17 wt%, and 60 wt% Ti-Mg alloys are shown in Fig.5. These show titanium peaks displaced to lower 2Θ angles with increasing magnesium content, indicating an increase in the titanium lattice parameters. The majority of the peaks could be fitted to an hcp structure although some spurious peaks were identified as originating from WLα contamination of the X-ray tube; these are labelled in the figure. No other diffraction peaks were detected e.g. at the 2Θ angles corresponding to pure magnesium, and there was no evidence for the fcc phase reported in mechanically alloyed Ti-Mg material [5].

It was noted from the X-Ray traces that most peaks were broad, especially at high 2Θ angles. This is probably due to the high dislocation density, high residual stress and small grain size. The number of peaks decreased with increasing magnesium content, possibly due to compositional variation.

Lattice parameters for all the alloys are given in Table 2, and are presented graphically in Fig.6. Errors in a and c parameters are of the order of 0.001Å and 0.004Å respectively for pure titanium, increasing to 0.002Å and 0.005Å respectively for the Ti-Mg alloys. The lattice dilation, together with the absence of second phase particles in the as-deposited thin films (Fig.4), is consistent with all the magnesium being

present in solid solution in an hcp titanium lattice. It is clear from Fig.6 that the data were subject to considerable scatter, and that consequently, changes in lattice parameters due to magnesium in solid solution are not discernible below about 10 wt% Mg .

Interstitial alloying elements, such as carbon and oxygen, also increase titanium lattice parameters [8]. These elements lead to a rapid increase in the hardness of titanium [7,9]. Oxygen analysis of an as-deposited titanium sample without magnesium gave a bulk oxygen level of 2600 ppm (by weight). The oxygen contents required to produce the lattice parameters of the Ti-Mg alloy deposits given in Table 2 would, if present, give rise to hardness values much greater than the measured hardnesses. Hardness tests of as-deposited alloys, shown in Fig.2, show a maximum hardness of about 300 VPN The above results indicate oxygen was not responsible for most of the increase in the titanium lattice parameters.

Texture

All the deposits showed a moderate to high intensity of crystallographic texture. The basal plane pole figures for six representative alloy compositions are shown in Fig.7. Examination of these figures, together with data for the other compositions, showed that the texture depended on composition, with basal poles parallel to the substrate (basal-edge) or normal to the substrate (basal-normal) as the composition changed from no magnesium (weak basal-edge), 0.5-1.5 wt% (basal-normal), 4-27 wt% (basal-edge) and 52-60 wt% (basal-normal). The basal-normal textures had rotational symmetry about the deposition direction, whereas, the basal-edge textures had a much greater concentration of (1120) poles, rather than (1010) poles, in the deposition direction.

Heat treatment

Heat treatments have been carried out on the alloys listed in Table 2 up to 27 wt% magnesium over the range 200-700°C, for periods of 30 minutes in vacuum. Alloys in the range 4 wt%-15 wt% magnesium showed a consistent and very substantial increase in hardness with temperature, and this is shown for three representative alloy compositions in Fig.8, together with hardness data for magnesium free titanium. The maximum effect was a more than two fold increase in hardness for the 4 wt% magnesium deposit heat treated for 30 minutes at 600°C. Possible changes in lattice parameters associated with the heat treatment of these dilute alloys were too small to measure by X-ray diffraction. A TEM study of the hardening reaction in a titanium 4 wt% Mg alloy, which is thought to be due to Mg or MgO precipitation, is the subject of a separate paper [10]. The high magnesium containing alloys (21 wt% and 27 wt%) both showed softening on heat treatment at low temperatures, but substantial hardening at temperatures above approximately 500°C. In the latter cases the heat treatment was accompanied by loss of magnesium to below 10 wt% and some distortion and cracking. Samples with initial magnesium contents below approximately 10 wt% did not show any magnesium loss on heat treatment.

X-ray diffractometer traces of 27 wt% magnesium samples heat treated in the range up to 400° are presented in Fig.9. These curves, together with those for the intermediate temperatures, indicate the progressive formation of magnesium and titanium from the titanium-magnesium solid solution beginning between 250°C and 300°C. The way in which the titanium peaks increase in intensity at the expense of the titanium-magnesium peaks, rather than the titanium-magnesium peaks gradually shifting towards pure titanium, may indicate that magnesium mobility in the titanium lattice is limited, and that magnesium precipitation is initially highly localised, possibly on sub-grain boundaries. This would leave some areas unaffected, and other areas containing magnesium precipitates denuded of magnesium in solution. These results are consistent with TEM data [10] which show very small Mg particles in the grains and large Mg particles on the grain boundaries, associated with precipitate free zones.

Conclusions

Titanium-magnesium alloys produced by vapour quenching retain up to at least 28 wt% magnesium in solid solution, and have grain sizes in the range 100-200 nm. The deposits are highly textured, with the character of the texture dependent upon alloy composition. Dilute Ti-Mg alloys heat treated in the range up to 700°C show very substantial hardening, probably due to precipitation of MgO. Alloys containing 20-30 wt% Mg progressively decompose on heat treatment to magnesium and titanium, starting at a temperature of about 300°C.

Acknowledgement

The authors wish to thank Professor J.W.Steeds and Dr.Gema Gonzalez of Bristol University for thin film data. (c) Controller HMSO London 1991.

Table 1 Properties of elements with densities less than titanium

Element	Density (g/cc)	Melting point (°C)	Boiling point (°C)	Tendency to form compounds	Solid solubility in Ti at 20°C
Li	0.53	180	1330	No compounds	negligible
Be	1.85	1280	2500	Forms intermetallics	zero
B	2.47	2030	3700	Forms intermetallics	negligible
Mg	1.74	650	1100	No compounds	negligible
Al	2.70	660	2400	Forms intermetallics	11 at%
Si	2.33	1410	2500	Forms intermetallics	<0.5 at%
Ca	1.54	850	1450	No compounds	negligible
Ti	4.51	1680	3300	-	-

Table 2 Lattice parameters of Ti-Mg deposits from X-Ray diffraction data

Alloy code	Mg (wt%)	a (Å)	c (Å)	c/a	Strongest peak	No. of peaks measured
Ti	0	2.956	4.689	1.586	1011	19
MG28	0.5	2.957	4.698	1.585	0002	19
MG29	1.5	2.960	4.701	1.591	0002	15
MG37	4.0	2.962	4.701	1.587	1011	11
MG32	7.0	2.965	4.754	1.603	1120	8
MG33	15.0	2.999	4.742	1.581	1120	5
MG24	17.0	2.999	4.807	1.602	1120	8
MG25	19.0	2.983	4.804	1.610	1120	6
MG31	25.0	3.010	4.883	1.622	1120	7
MG4	27.0	2.996	4.827	1.611	1120	10
MG20	52.0	3.169	5.009	1.580	0002	9
MG18	60.0	3.154	5.050	1.601	0002	11

References

[1] I.Obinata, Y.Takeuchi and R.Kawanishi, "The titanium-Magnesium System", Metall. 13 (1959), 392-397

[2] H.B.Bomberger, "Titanium-Magnesium Alloys" (Report AFWAL-TR-84-4137, AF Wright Aeronautical Laboratories, 1985).

[3] R.Sundaresan and F.H.Froes, "Development of Titanium-Magnesium alloy System Through Mechanical Alloying", Proceedings of Sixth World Conference on Titanium, ed. P.Lacombe (Les Ulis Cedex, France: Les Edition de Physique, 1988) 931-936.

[4] R.Sundaresan and F.H.Froes, "Mechanical Alloying in the Titanium-Magnesium System", Key Engineering Materials 29-31 (1989), 199-206.

[5] C.Suryanarayana and F.H.Froes, "Nanocrystalline Titanium-Magnesium Alloys Through Mechanical Alloying", J. Mater. Res. 9 (1990) 1880.

[6] C.M.Ward-Close and P.G.Partridge, "The Production of Titanium-Magnesium Alloys by vapour Quenching", Materials Letters, 11, (1991), 295-300.

[7] A.D.McQuillan and M.K.McQuillan, Titanium (London: Butterworth, 1956) 36.

[8] L.Murray, ed., Phase Diagrams of Binary Titanium Alloys, (Metals Park, OH: ASM International, Ohio, 1987) 156.

[9] E.K.Molchanova, Phase Diagrams of Titanium Alloys (Jerusalem: Keterpub, 1965) 125.

[10] C.M.Ward-Close, P.G.Partridge and C.Gilmore, "Precipitation Hardening in Titanium-Magnesium and Titanium-Calcium Alloys", This Conference

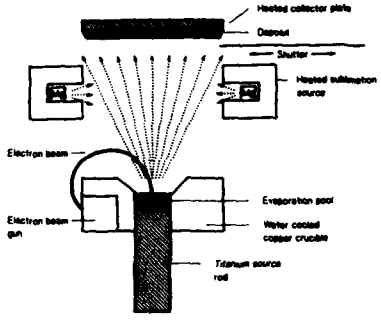


Figure 1-
Schematic diagram showing vapour quenching apparatus

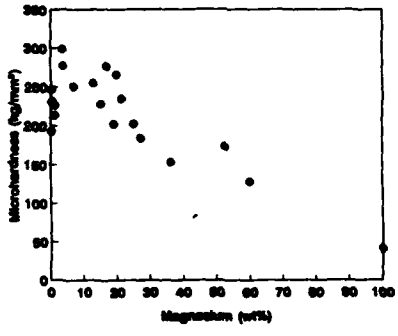


Figure 2-
Microhardness versus magnesium content for as-deposited titanium-magnesium alloys

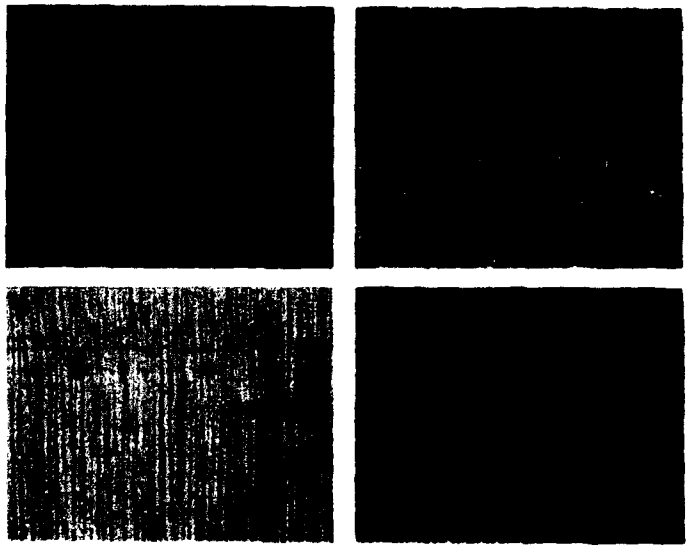


Figure 3-
Polarised light micrographs of (a) as-deposited Mg-free titanium (b) Mg-free titanium annealed 600°C, 0.5 h, in vacuum, (c) as-deposited Ti-4 wt% Mg (d) Ti-4 wt% Mg annealed 600°C, 0.5 h, in vacuum

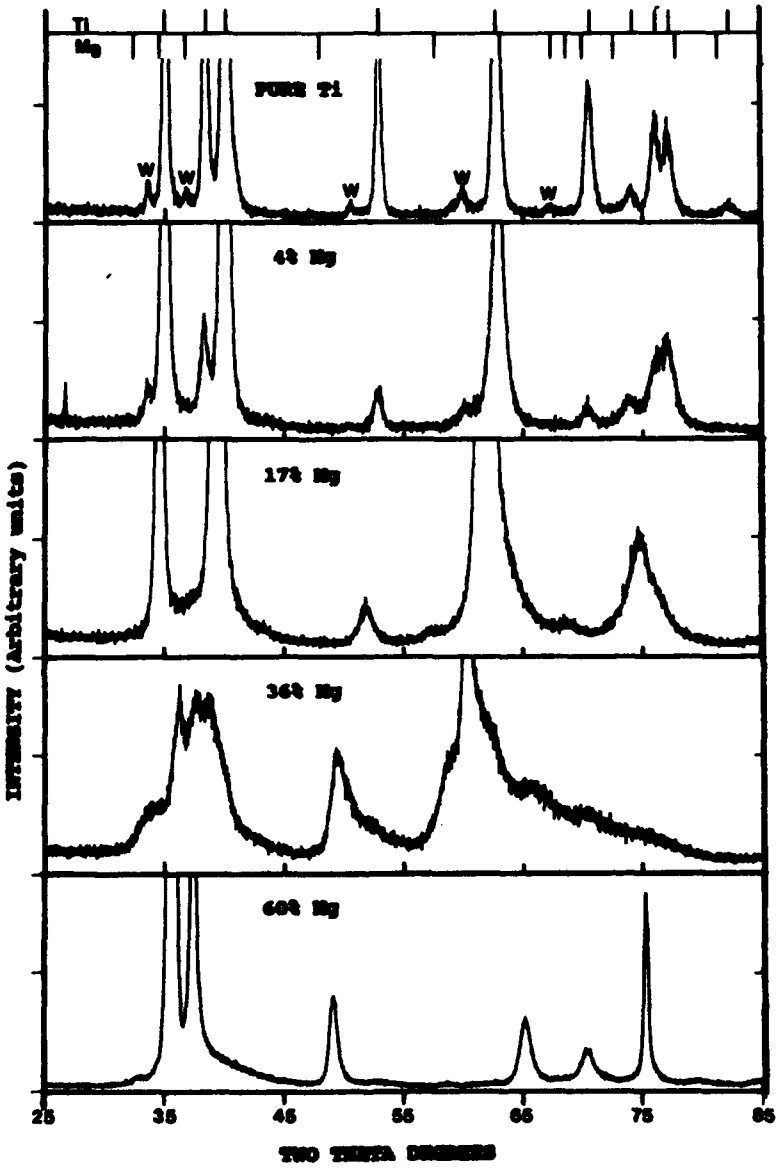


Figure 5-
X-ray diffractometer traces for vapour quenched pure titanium and titanium magnesium alloys

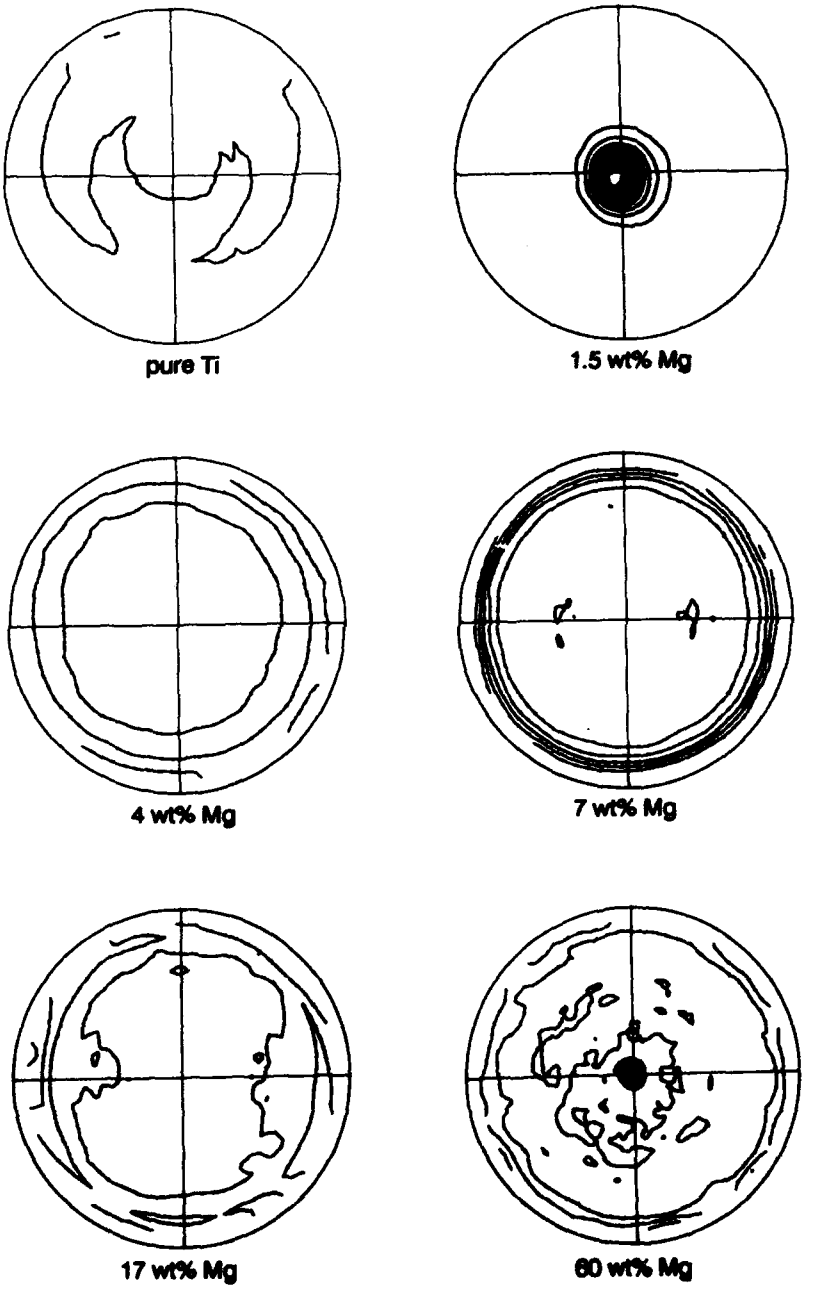


Figure 7-
(0002) pole figures for as-deposited vapour quenched Ti-Mg alloys (X-ray beam normal to substrate)



Figure 4-
Transmission electron micrograph of a Ti-15 wt% Mg alloy

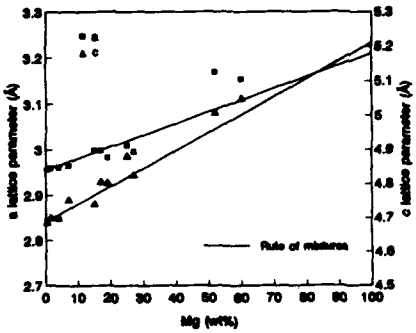


Figure 6-
Lattice parameters versus magnesium content for as-deposited titanium-magnesium alloys

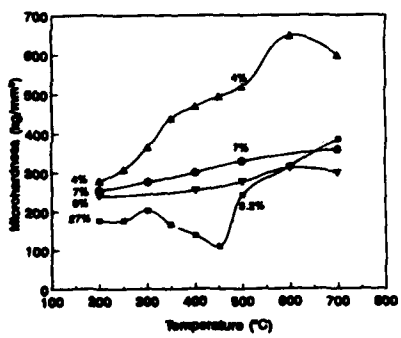


Figure 8-
Microhardness versus isochronal annealing temperature for three vapour quenched Ti-Mg alloys and vapour quenched pure titanium, after 0.5 h anneal in vacuum (figures denote as-deposited magnesium contents and magnesium contents after 500°C anneal - note magnesium loss in 27wt% Mg sample).

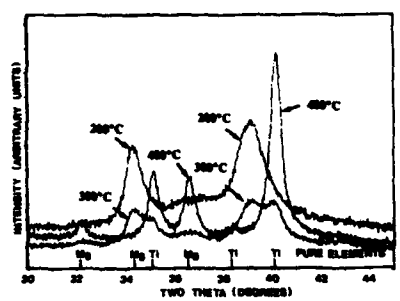


Figure 9-
X-ray diffractometer traces for Ti-27wt% Mg heat treated at 200°C, 300°C and 400°C
(0.5 h in vacuum)

GRAIN GROWTH OF TA6V β PHASE AFTER THERMOMECHANICAL TREATMENTS

Nathalie Côme-Dingremont, Elisabeth Gautier, and André Simon

Laboratoire de Science et Génie des Matériaux Métalliques CNRS UA 159
Ecole des Mines, Parc de Saurupt
54042 Nancy, FRANCE

Abstract

Thermomechanical processing in the β temperature range must be controlled accurately in order to obtain an acceptable final grain size. To study grain size evolution during a complete thermomechanical treatment (deformation, cooling and annealing), we have followed the grain size variations after deformation in the β temperature range, for different strain levels ; and after annealing at the same temperature. The grain size evolution has been established versus the prior strain level, and versus the temperature-time of the annealing. In addition, an analysis was made of the grain size variations during annealing versus deformation level, when the deformation is followed by transformations during cooling to room temperature, and further heating to the annealing temperature. The results are discussed taking into account the stored energy of deformation, and the driving forces for grain boundaries migration.

Introduction

After plastic deformation, materials can undergo large modifications during thermal treatment, such as recovery or recrystallization, by rearrangement and (or) annihilation of the dislocations introduced by plastic deformation. In the case of the pseudo α titanium alloy, TA6Zr5D, it has been observed an important growth of β grains in industrial parts after a thermomechanical treatment carried out in the β field. It has been shown (1) that the exaggerated β grain growth has the main features of static recrystallization. This study has been extended to the TA6V alloy in order to establish the way by which this growth occurs. The deformation has been performed by tensile test in the β temperature range, followed by a thermal treatment generally carried out at the same temperature.

The structural evolutions have been analysed by the variations of β grain size after plastic deformation and after annealing, with the strain level, and with the temperature-time of the annealing. The influence of the phase transformations between the two treatments has also been studied.

Titanium '92
Science and Technology
Edited by F.H. Froes and I. Caplan
The Minerals, Metals & Materials Society, 1993

Experimental Procedure

The TA6V alloy used in this investigation has the chemical composition shown in Table I.

Table I Chemical composition of TA6V alloy

Al wt%	V wt%	Fe wt%	N ppm	O ppm
6.17	3.95	0.15	88	1955

Its β transus temperature is 985°C, and the as-received microstructure is α equiaxed, β transformed. The specimens used are cut from the bar, so that the tensile axis is parallel to the bar axis. All the treatments are performed under secondary vacuum with a thermomechanical simulator DITHEM, which allows to control the main parameters such as heating and cooling rates, strain rate and strain level. The thermomechanical treatments applied on the specimens are schematically given in Figure 1.

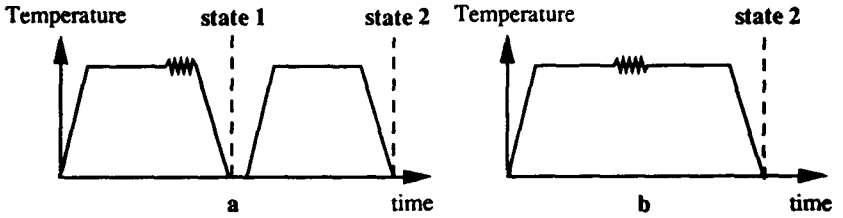


Figure 1 - Schematic representation of the thermomechanical treatments

A constant heating rate of 5°C/s, and cooling rate of 0.5°C/s were chosen for all the heat treatments. Before deformation, specimens are β solution treated at 1015°C for 30 minutes. Then, deformation at various strain levels (< 30 %) is carried out at a strain rate of 10^{-2} s^{-1}. The deformed specimen is either immediatly cooled at room temperature (figure 1a), or is annealed just after deformation (figure 1b). The annealing treatment is mainly performed at 1015°C for 30 minutes. However, for the kinetics study, the annealing temperatures are 1005, 1015 and 1025°C, for various times between 5 and 60 minutes.

The microstructures were observed in a plane containing the tensile axis at different stages of the thermomechanical treatments, at states 1 and 2 as defined Figure 1. Mean β grain sizes correspond to the mean linear intercept measured with an optical microscope at a magnification of 250x.

Results

Macrostructural Observations

We first consider the results from the thermomechanical treatments of Figure 1a. In order to reveal the grain size evolution between states 1 and 2, photographs of samples only deformed, and deformed and annealed are presented Figure 2 at a low magnification.

For state 1, deformed specimens, all the macrostructures show an homogeneous and constant β grain size whatever the degree of deformation. At 30 %, a diffuse aspect can be observed, due to the serration of β grain boundaries. For state 2, whatever the strain level, the grain structure is coarser than the as-deformed specimens. It can be seen that the grain boundaries are recovered

after annealing, and are continuous and generally curved. For the sample deformed to 5 %, very large grains appear in comparison to the non-deformed specimens. Sometimes, only two grains are observed in the diameter of the specimen. When the strain level increases, these very large grains progressively dissapear, and the β grain size is lowered, as can be seen at 30 %. So, these macrostructures reveal that thermal treatment has an important effect on the β grain size of the TA6V alloy.

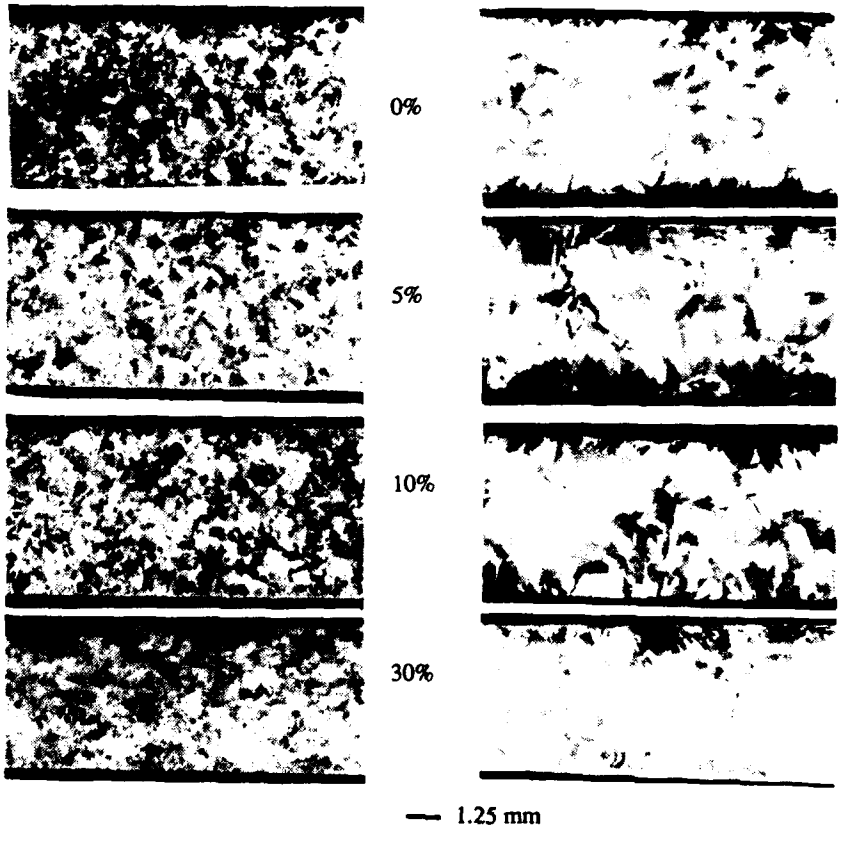


Figure 2 - Macrostructures of the samples only deformed (state 1), and deformed and annealed (state 2)

Grain Size Variations

The variations in mean grain size versus strain level are reported Figure 3.

On this figure the grain size at state 1 is also indicated. The following remarks are relevant :
- all the as-deformed samples exhibit a constant grain size about 330 μm, whatever the strain level between 0 and 30 %.
- for the annealed samples, and for deformation below 5 %, the grain size remains constant, about 600 μm. At 5 %, the β grain size suddenly i. creases, from 600 to 1700 μm. Above this

critical strain value, the grain size slowly decreases as the strain level increases. Nevertheless, the resultant grain size is larger than that at strains below 5 %.

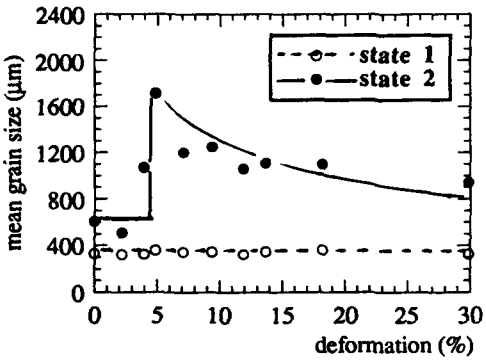


Figure 3 - Variation of the ß grain size versus the degree of previous deformation

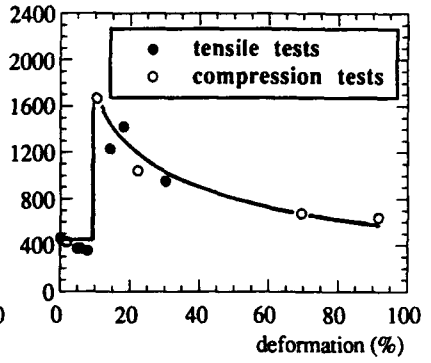


Figure 4 - Variation of the ß grain size versus the degree of previous deformation, without cooling at room temperature after deformation

Effect of Phase Transformations

After deformation, cooling at room temperature involves the phase transformation $\beta \rightarrow \alpha$, and $\alpha \rightarrow \beta$ during subsequent heating for annealing. In order to determine the influence of phase transformations on the grain size evolution during annealing, thermomechanical treatments without cooling after deformation (Figure 1b) have been performed. The results are reported figure 4. Some results have been obtained on compression specimens deformed in the same experimental conditions by Briottet (2).

By avoiding phase transformations, the grain size evolutions are similar to the previous one. Nevertheless, the critical strain is translated towards larger strain levels, about 10 %. Above this value, and again up to 90 %, the largest applied deformation, the mean grain size slowly decreases but still remains larger than that of samples which undergo deformation below 10 %.

Kinetics Study

The kinetics study has been performed for the thermomechanical treatments of Figure 1a. The strain level has been set at 10 %. Three annealing temperatures of the β field 1005, 1015 and 1025°C have been tested. The mean grain size versus annealing time is reported Figure 5.

An S-shape of the grain size/time evolution can be observed. It appears that an incubation period, then a fast growth period, and finally a slowing down period have occured. When the annealing temperature decreases, the incubation period of the phenomenon slightly increases (approximatly 7 minutes at 1005°C against 5 minutes at 1015 and 1025°C). The annealing temperature does not have a significant effect on the kinetics of the grain growth. At 1005°C, the resultant grain size, between 30 and 60 minutes, is larger than that at the other annealing temperatures.

Discussion

Critical Strain Values

We have clearly demonstrated that after deformation and annealing in the β field, the β grain size varies with the degree of deformation previously applied. The grain size evolution exhibits a

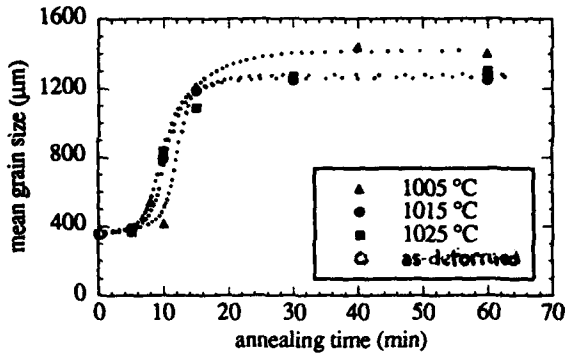


Figure 5 - Kinetics of the β grain growth during annealing at 1005, 1015, and 1025 °C. Previous strain value : 10 %

classical variation observed in static recrystallization process. This graph shows a relatively small critical deformation, approximately 5 %, for which a maximum grain size is revealed (1700 µm). Before this critical strain, the grain size is constant. Above the critical value, a progressive decrease of the grain size is observed with an increasing deformation. Without cooling after deformation the same scheme is again observed, but in this precise case the critical deformation is larger, about 10 %.

For titanium alloys, only the study conducted by J.M. Kempf et al. (1) on TA6Zr5D has reported a similar microstructural evolution after deformation in the β temperature range. These authors have shown that the thermomechanical treatment conditions can modify the critical strain value. A strain rate increase, or a deformation temperature decrease, implys a lower critical strain. So, the variations of the critical deformation are linked with the thermomechanical parameter and thermal treatments parameters. To understand these variations, we establish relationships between the critical strain value and the stored energy due to the high temperature deformation, for the two alloys TA6V and TA6Zr5D. The deformation stored energy which is necessary to initiate the grain growth, has been estimated by the product of the flow stress (at the critical strain) with the critical strain value. These values are given in table II for the two alloys and for different deformation conditions.

As it can be seen, the deformation stored energy necessary to initiate β grain growth takes values near 1 MJ/m^3 (for relatively different treatment parameters). Nevertheless, for two cases, this value is larger : for the TA6Zr5D alloy, a value of 1.5 MJ/m^3 has been obtained when tensile test is performed at 1060°C, at a strain rate of 2.10^{-3} s^{-1}. For the TA6V alloy, a larger value of 1.8 MJ/m^3 is obtained when deformation is realized at 1015°C with a strain rate of 10^{-2} s^{-1} and without cooling after deformation. In Table II, we have only reported the deformation stored energy of the alloys at the minimal deformation for which grain growth occurs. In fact, during deformation or thermal treatments, softening phenomena can occur and then result in a change of dislocations arrangements and of the stored energy.

Moreover, the critical deformation is modified by phase transformations between deformation test and annealing. Then, we assume that grain growth mechanism initiation requires a constant energy E, whatever the deformation conditions. We can express E by the relationship :

$$E = E_{defo} (1 - X) + E_{transfo}$$

Table II Deformation stored energy

	test conditions T (°C)	$\dot{\varepsilon}$ (s^{-1})	σ_f (MPa)	ε_c	$\sigma_f \times \varepsilon_c$ (MJ/m^3)
TA6Zr5D	1010	2.10^{-3}	14	0.07	**0.98**
	1060	2.10^{-3}	10	0.15	**1.5**
		0.15	35	0.03	**1.05**
TA6V	1015	with transfo. 10^{-2}	18	0.05	**0.9**
		without transfo.	18	0.1	**1.8**

with E_{defo} the deformation stored energy, which has been precedently calculated. The term (1-X) express a reduction, in order to take into account a dynamic or static softening phenomenon. $E_{transfo}$ is the energy introduced by phase transformation. This last energy can be considered as being constant for relatively medium cooling rates. We now can discuss the higher values of the deformation energy.

For the TA6Zr5D alloy, all the thermomechanical treatments are performed with cooling at room temperature after deformation ($E_{transfo} \neq 0$). For the thermomechanical treatment carried out at 1060°C, at a strain rate of 2.10^{-3} s^{-1}, the authors note that the β grain boundaries are less serrated than those obtained after the treatment at the same temperature at a faster strain rate of 0.15 s^{-1} (for the same strain level). This has been associated with a dynamic recovery phenomenon. For this reason, X can not be neglected, and the deformation energy must be higher to compensate and finally reach the same total energy E. (We assume that for the deformation rates of 10^{-2} s^{-1} (TA6V) or 0.15 s^{-1} (TA6Zr5D), X is negligible because E doesn't vary).

For the TA6V alloys, the effect of phase transformations is to lower the critical strain value. This implies a decrease of the deformation stored energy from 1.8 MJ/m^3 to 0.9 MJ/m^3. Then, it can be stated that the phase transformations provide an amount of energy which is of the same order of magnitude as the deformation energy. The phase transformation effect on the deformation state has been studied by Gastaldi and Jourdan (3). They have shown that during α → β transformation, strains are introduced at the αβ interface, inside the β grains. The main conclusion of their investigation is that the phase transformation introduces a large deformation energy for recrystallization of titanium. Our results are consistent with this.

Origin of the Grain Boundaries Migration

The kinetics study provides information about grain growth mechanisms. We observe that there is no nucleation of new small grains which are smaller than the initial grain size. Grain size variations result from the prior grain boundaries migration. Then, the mechanism is not the current static recrystallization by nucleation and growth of new grains.

In a general point of view, the grain boundary migration takes its origin from :
- the reduction of the grain boundary curvature
- the dislocation density, due to plastic deformation
- the chemical potentials.

To put forward the origin of the grain boundary migration we can compare our results to the normal grain growth. In this last case, the driving force is the reduction of the grain boundaries curvature. The grain growth law for normal grain growth is

$$D - D_0 = k.t^n$$

with D mean grain size at time t, D_0 initial grain size (in our study D_0 = 100 μm), k a constant dependent on temperature, and n time exponent. In Figure 6 are given the variations of Ln (D - D_0) versus Ln t. For normal grain growth we obtain a linear variation. The slope is the time exponent, and takes a value of 0.5.

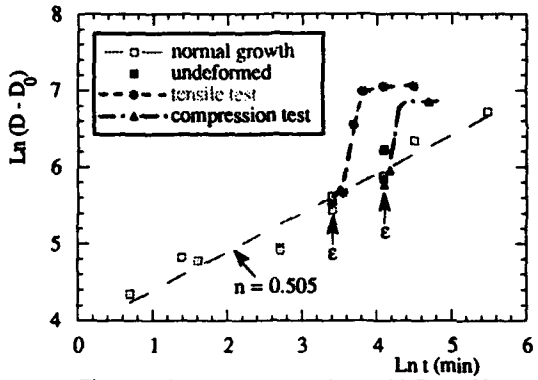


Figure 6 - Ln (D - D_0) versus Ln t, with D_0= 100 μm, t is the annealing time at 1015 °C

This Figure also contains data concerning grain growth of the specimens deformed by tensile or compression tests (2). In order to report these points, we have cumulated time before and after deformation at 1015°C. The deformation is fixed at 10 % in tension and 22 % in compression. We show that if a deformation is applied, a strong deviation from normal grain growth appears. A fast growth happens, followed by another domain of slow growth, compared to normal grain growth. The first deviation from normal growth is observed after a few minutes at the annealing temperature (~ incubation period), and for strain levels larger than the critical strain (not for the underformed sample). Clearly, the observed deviation is linked to the applied deformation. This kind of deviation from normal grain growth has already been observed in abnormal grain growth studies. Heckelmann et al. (4) have shown similar results for two aluminium alloys. However, in their investigation, the abnormal grain size variations are clearly related to the texture.

Concerning our results, it can be stated that :
- the β grain growth could be compared to abnormal growth because the two phenomena proceed by grain boundary migration, without nucleation of new grains. But in our case, a critical strain is necessary.
- the β grain growth could be a static recrystallization process because of the necessary critical deformation to initiate the phenomenon. The major difference is the nature of the nuclei : in our case they can be considered as the prior grains. It is the prior grain boundary which moves, not a subboundary.

In our case, grain growth requires a minimum strain level. Below this level, grain growth is only normal growth, resulting from thermal treatment. The critical strain which is a typical feature of static recrystallization, is in fact the lower deformation level required to activate grain boundaries. As the β grain boundary mobility is linked to plastic deformation heterogeneities, it can then be suggested that for the weak strain level applied (< 30 %), heterogeneities of deformation exist and could be the driving forces for grain boundaries migration.

Most of the time, heterogeneities of deformation have been seen at large levels of deformation and high dislocations density can be observed near prior grain boundaries (5). In that cases, new small grains appear in the vicinity of the serrated grain boundary. Such heterogeneities require higher strain levels than that applied in our study. Another distribution of these heterogeneities could be suggested for smaller strain levels : it means grain to grain. In this last

case dislocations density is relatively uniform inside each grain, but differences exist between grains, involving grain boundary migration.

In our study this last assumption seems to be the more realistic, and leads to explain the grain growth scheme as followed : at or near the critical strain value, the low strain level involves larger heterogeneities. Few grain boundaries are submitted to a large driving force and migrate rapidly towards the much more deformed grains, resulting in a very large grain size. When the strain level increases, the grain to grain heterogeneities are lowered. In this case, the driving force is weaker and more grain boundaries can move. The final grain size is then smaller.

This study allows us to define more precisely the grain growth phenomenon observed for the TA6V and TA6Zr5D alloys as a "static recrystallization by prior grain boundaries migration" mechanism. This mechanism can be compared to that observed by Hamelin and Goux (6) for aluminium bicrystals. They introduce two types of critical strains :

- the critical strain required for nucleation, that means new grains
- the critical strain to involve growth.

This last value is two to four times smaller than the first one, in the case of aluminium single crystal. In comparaison, in our investigation the critical strain level could also be defined as a critical strain to induce grain growth.

Conclusion

Microstructural evolutions in the β field after plastic deformation have received little attention. We have clearly shown that β grain growth happens in titanium alloys TA6V and TA6Zr5D after deformation. The phenomenon proceeds by prior grain boundaries migration. The critical strain value can be predicted depending on the thermomechanical parameters, taking into account the effect of phase transformations.

Aknowledgements

This work has been realized in the framework of the "Groupement Scientifique Titane Traitements Thermomécaniques", supported by CNRS, MRT, DRET-DGA, AEROSPATIALE, FORTECH / AIRFORGE, CEZUS, SNECMA, and TURBOMECA.

References

1. J.M. Kempf et al., "Effect of thermomechanical treatments on TA6Zr5D β grain size evolution", this conference.

J.M. Kempf, "Déformation et recristallisation dans le domaine β de l'alliage TA6Zr5D" (Thesis, INPL Nancy, France 1989).

2. L. Briottet, "Etude de l'évolution statique après déformation à chaud du TA6V et du β-CEZ", (Report of D.E.A, ENSM St-Etienne, 1990).

3. J. Gastaldi, C. Jourdan, "Recrystallization of pure titanium studied by synchroton X-ray topography", (Paper presented at the 7th RISO 1986).

4. I. Heckelmann et al, "Texture development during grain growth", (Paper presented at ICOTOM 9, Avignon, France, 1990).

5. D. Dajno, "Rhéologie globale et structurale des alliages de titane TA6V et BETACEZ dans les domaines α+β et β", (Thesis INPL Grenoble, France, 1991).

6. A. Hamelin, C. Goux, "Contribution à l'étude de la recristallisation de monocristaux et de bicristaux en aluminium pur", Mémoires Scientifiques Revue Metallurgie, LX, 2, (1963), 85-99.

PHASE EQUILIBRIA IN THE SYSTEMS Ti-N, Ti-Zr-N AND Ti-Hf-N AND PROPERTIES OF δ-TiN_{1-x}, δ-$(Ti,Zr)N_{1-x}$ AND δ-$(Ti,Hf)N_{1-x}$

W.Lengauer, R.Täubler, J.Bauer*, J.Debuigne* and P.Ettmayer

Institute for Chemical Technology of Inorganic Materials, University of Technology Vienna, Getreidemarkt 9/161, A-1060 VIENNA, Austria

*Laboratory of Metallurgy and Physical Chemistry of Materials, INSA Rennes, 20, av. des Buttes de Coësmes, F-35043 RENNES, France

Abstract

Phase equilibria studies in the systems Ti-N, Ti-Zr-N and Ti-Hf-N were performed using diffusion couples and arc-melted or hot-pressed buttons. In the Ti-N system diffusion couples were annealed isothermally as well as in a temperature gradient parallel to the diffusion layers. The latter technique also made the non-variant phase reactions, as a function of both temperature and composition, metallographically visible [1,2]. A phase diagram of the Ti-N system is presented.

The Ti-Zr-N and Ti-Hf-N systems were investigated using arc-melted and hot-pressed buttons which were heat treated for homogenization and equilibration. When substituting Ti with Zr the titanium subnitride phases are destabilized and extend only slightly in the ternary Ti-Zr-N system. Phase diagrams of the systems Ti-Zr-N and Ti-Hf-N are presented. Some properties of the refractory fcc phases δ-TiN_{1-x}, δ-$(Ti,Zr)N_{1-x}$ and δ-$(Ti,Hf)N_{1-x}$, such as hardness, color and electrical and thermal conductivities, are given as a function of the [N]/[Ti], [Ti]/[Zr] and [Ti]/[Hf] ratios, respectively.

1. Introduction

The transition metal nitrides TiN, ZrN and HfN are of high technological interest because of their special properties such as high hardness, chemical stability and corrosion resistance, metallic, thermal and electrical conductivities, among others. It is the combination of such properties that makes these materials interesting for applications such as for conductive diffusion barriers in microelectronic devices, gold-colored and highly wear-resistant coatings for jewelery, and in carbonitride-based hard metals (cermets) for cutting tools [3].

Of interest were the effects of the substitution of Ti by Zr or Hf. This is subject of the present paper, in which the phase equilibria of the binary Ti-N system and of the ternaries Ti-Zr-N and Ti-Hf-N are reported. Several material properties of δ-$(Ti,Zr)N_{1-x}$ and δ-$(Ti,Hf)N_{1-x}$ were measured and are included. The properties of TiN were recently reported [4].

Titanium '92
Science and Technology
Edited by F.H. Froes and I. Caplan
The Minerals, Metals & Materials Society, 1993

Information on the systems Ti-Zr-N and Ti-Hf-N is scarce. Complete miscibility of TiN with ZrN as well as of TiN with HfN was reported [5,6,7]. This is an interesting result since the lattice parameters of ZrN and HfN differ from that of TiN by about 6-8%, making the existence of a miscibility gap likely, as in the corresponding systems Ti- Zr-C and Ti-Hf-C [8] where the relative differences in lattice parameters are very similar. In fact, only recently a spinodal decomposition of sputtered δ-(Ti,Zr)N films and a corresponding increase in the microhardness was reported [9,10]. No detailed information exists for the subnitride regions of either system.

2. Sample preparation

Because of the severe loss of N during the arc-melting process, only samples with a N content below about 38at% could be prepared by this technique. Mixtures of powders of Ti, ZrH_2 and nitrides were pressed at room temperature, dehydrogenated in vacuum at 1000°C and arc-melted in an Ar atmosphere (200 mbar). These samples were heat treated for homogenization under Ar for 6-7 d at 1300-1600°C and then equilibrated at 1100°C in silica tubes.

Samples with higher N contents were prepared by hot-pressing mixtures of metal and nitride powders in graphite dies at 2200-2500°C. The mixtures were wrapped in Zr foil as an oxygen getter and a diffusion barrier for carbon. These samples were then heat treated and equilibrated as described above.

Alloys of Ti/Zr and Ti/Hf prepared by arc-melting pressed mixtures of Ti and Zr or Ti and Hf powders were homogenized at 1250-1300°C. These buttons were cut into discs 1-3 mm thick. The samples were nitrided in an autoclave under a N_2 pressure of 5-10 bar at 1100°C and 1300°C for 48 and 14.3 h, respectively.

Binary diffusion couples TiN-Ti were prepared by nitriding Ti sheet in the temperature region of 1000-1300°C, further annealed in silica capsules at various temperatures, and quenched. Furthermore, diffusion couples were also prepared by annealing in a temperature gradient.

Single-phase specimens were prepared by nitriding Ti sheet or slices cut from arc-melted buttons of Ti-Zr and Ti-Hf alloys at a temperature of 1600°C for 500-650 h. These conditions were not sufficient to obtain fully stoichiometric homogeneous single-phase samples. Microscopic investigations of the cross sections of such nitrided samples revealed a zone of oxide precipitations and pores accumulating in the centers of the samples perpendicular to the diffusion path. In order to remove this thin zone the samples were diamond sawed in half and ground to make a plane surface. The sample halves were nitrided once more for 450-650 h at 1600-1650°C to reach near-stoichoimetric composition.

3. Sample characterization

Nitrogen analysis was done using an automated Dumas method [11]. For EPMA the intensities of the $Ti_{K\alpha}$, $Zr_{L\alpha}$ and $Hf_{M\alpha}$ lines were measured. Due to the coincidence of the $Ti_{L\beta}$ and $N_{K\alpha}$ lines [12] nitrogen was determined by difference in ternary alloys. In binary Ti-N samples a recently devised standard calibration method [13] made it possible to correct for the coincidence.

Phase analysis was carried out by X-ray diffraction of the powdered samples using Ni-filtered Cu-K_α radiation. Lattice parameters were either determined by using the five highest diffraction peaks and external Si standardization in an X-ray diffractometer or by the Debye-Scherrer film technique. For metallography the samples were embedded in cold-setting resin, ground, diamond polished and finally polished using an aqueous silica suspension.

4. Measurements of physical properties

Vickers microhardness measurements were made on diamond polished samples at a load of 0.98 N. Standardization was done by calibrating the measurements against a hardened steel standard.

The visible light reflectance of polished samples was measured in a wavelength range of approximately 300-800 nm. The angles between primary beam and the sample surface as well as between the reflected beam and sample were 45° for all samples. Since the angles could not be exactly reproduced and the surface finish was not always the same, the reflectance values can only be given in arbitrary units and the absolute values obtained for different samples cannot be compared to each other.

Thermal diffusivity measurements were made using the laser-flash technique up to 1400°C, for which cylindrical samples of 10 mm in diameter and 0.8-1.5 mm height were used. The reliability of this method is approx. ± 4-5 rel%. The density of these samples was measured at room temperature using $CHBr_3$ as a buoyancy fluid.

Finally, the specific heat was measured using a Netzsch heat flux differential scanning calorimeter in the range of 50-1000°C in steps of 50°C against a sapphire reference.

Electrical conductivity measurements were performed by the method of inductive resistivity.

5. Results and discussion

5.1. The Ti-N system

The temperature ranges in which the subnitride phases in the Ti-N system are stable and the sequence of transformation between them were determined from the microstructural and XRD investigations of temperature-gradient diffusion couples (TGDCs). The non-variant peritectoid formation/decomposition temperatures of the subnitride phases could be detected rather exactly, an example of which is given in Fig. 1. This TGDC shows the formation of η-Ti_3N_{2-x} from the reaction of ε-Ti_2N with α-Ti(N) at 1066°C.

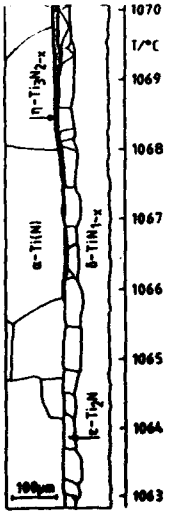


Fig. 1.
Drawing of the microstructure of a temperature-gradient diffusion couple showing the reaction α-Ti(N) + ε-Ti_2N → η-Ti_3N_{2-x} at 1066°C (drawing obtained by tracing the grain boundaries of the microstructure).

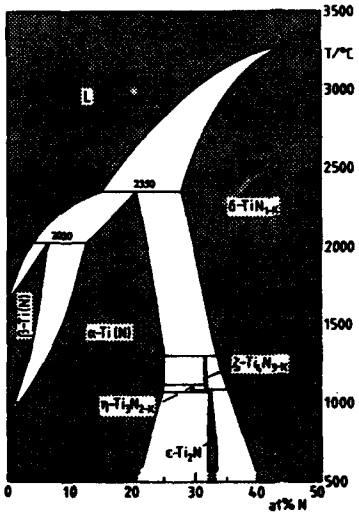


Fig. 2.
Phase diagram of the Ti-N system compiled by Wriedt and Murray [14] with a revised subnitride region [2].

Combined results from metallography and EPMA obtained on isothermal and TGDCs in the Ti-N system were combined to construct a phase diagram for the Ti-N system with a revised subnitride region (Fig. 2).

5.2. The ternary systems Ti-Zr-N and Ti-Hf-N

The results of combined XRD and microstructural phase analyses on arc-melted and hot-pressed samples and diffusion couples for both systems are shown in Fig. 3 and Fig. 4 in isothermal sections at 1100°C. In the Ti-Zr-N system the homogeneity range of δ-(Ti,Zr)N_{1-x} extends to below 30 at% N at [Ti]/[Zr]≈1. No proof of the existence of a miscibility gap in the δ-phase region could be detected, but neither could it be ruled out: The distinct α1/α2 line

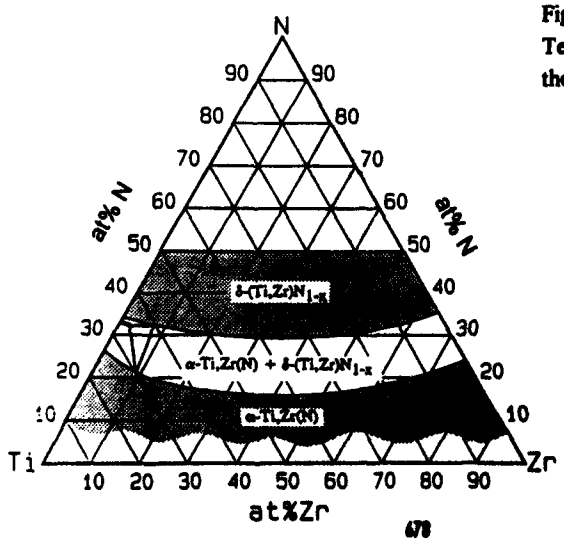


Fig. 3.
Tentative isothermal section of the Ti-Zr-N system at 1100°C

splitting at higher diffraction angles, which is indicative of very homogeneous phases, could not be attained. Whether this is due to the very sluggish metal/metal diffusion or whether it is the result of a spinodal demixing-process cannot unambiguously be decided.

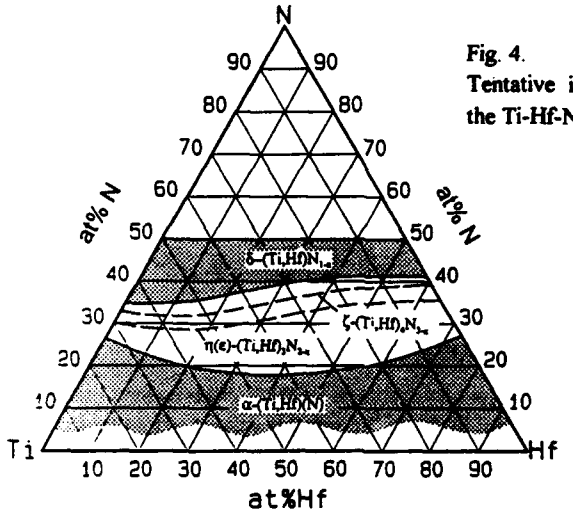


Fig. 4.
Tentative isothermal section of the Ti-Hf-N system at 1100°C

In the diffusion couples (Ti,Zr)/(Ti,Zr)N and (Ti,Hf)/(Ti,Hf)N the diffusion of N into the bulk alloy is accompanied by a shift in the *[Ti]/[Zr]* and *[Ti]/[Hf]* ratios at the diffusion front. This leads to uneven metal distributions even in fully nitrided single-phase alloys as illustrated in Fig. 5. During the diffusion of nitrogen into the starting alloy the phases coexisting at the front tend to adjust their respective compositions in such a way as to come as near as possible to local equilibrium. This is obviously the driving force that leads to this uneven distribution of [Ti]/[Zr] and [Ti]/[Hf]. Apparently, the conodes between adjacent phases do not point ideally to the N corner but are somewhat inclined to that direction.

Since nitrogen diffusion is much faster than the interdiffusion of the metals in the host lattice, the local shifts in composition persist even after the single-phase sample has been fully nitrided. In the Ti-Hf-N system these compositional shifts are not as pronounced, but still do exist.

The ζ-$(Ti,Zr)_4N_{3-x}$ phase extends only slightly from ζ-Ti_4N_{3-x} into the ternary region (up to about 5-6 at% Zr at 31.5 -32.0 at% N). This value for the extent of substitution of Ti by Zr in the ζ-phase was measured by EPMA and was accompanied by an increase of lattice parameters from a=0.29795(1) to a=0.29988(7) nm and from c=2.89655(47) to c=2.92223(55) nm. According to the *Vegard's* rule and assuming a hypothetical Zr_4N_{3-x}, calculated from geometrical relationships between the hexagonal and the fcc cell, the lattice parameters corresponded to a Zr content of 6-7 at%. The extension of the $\alpha+\delta+\zeta$ phase field was also located by microprobe analysis. The conodes in the $\alpha+\delta$ phase field point from a relatively Zr-rich α-phase to a Zr-poor δ-phase on the titanium-rich side and vice versa.

In the Ti-Hf-N system the δ-$(Ti,Hf)N_{1-x}$ phase does not have a homogeneity region as broad as the corresponding phase in the Ti-Zr-N system. A miscibility gap in the δ-$(Ti,Hf)N_{1-x}$ region could not be detected here, either. The solid solutions of the subnitride phases ζ-$(Ti,Hf)_4N_{3-x}$ and η-$(Ti,Hf)_3N_{2-x}$ extend between the corresponding binary subnitrides.

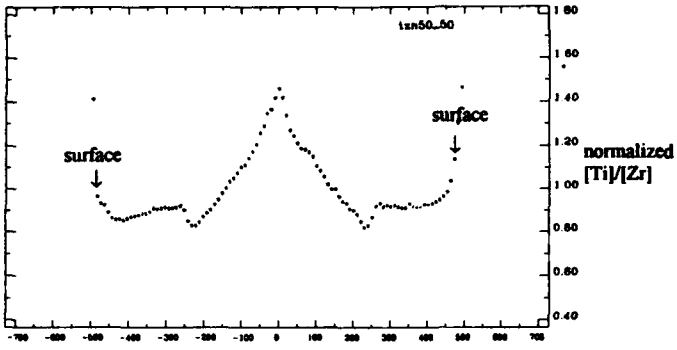


Fig. 5.
Normalized [Ti]/[Zr] ratio calculated from the concentration profiles of single-phase δ-$(Ti,Zr)N_{1-x}$ with [Ti]/[Zr]=5/5 in the starting alloy

5.3. Bulk properties of δ-$(Ti,Zr)N_{1-x}$ and δ-$(Ti,Hf)N_{1-x}$

In both systems an increase in the microhardness of the δ-phase in the ternary region over the binary phases was observed (Fig. 6). Since the samples were prepared by the diffusion couple technique, they were not completely homogeneous. Despite the errors introduced by that effect, fully dense diffusion samples were preferred to hot-pressed samples with a residual porosity of about 1-4%. The extreme increase in the hardness values of the δ-$(Ti,Zr)N_{1-x}$ samples containing only a small amount of the other metal (10 and 90 mol% ZrN, respectively) is probably due to their lower nitrogen content compared to the other samples that were nearly stoichiometric (in δ-TiN_{1-x} the microhardness decreases with increasing nitrogen content).

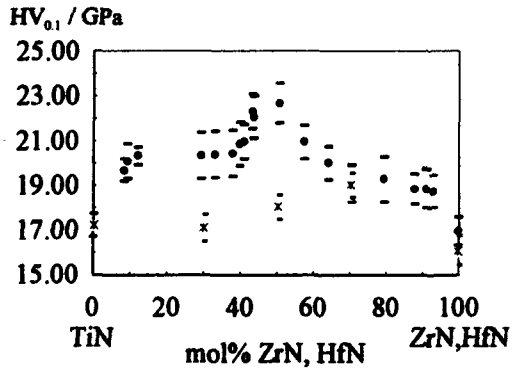


Fig. 6.
Vickers microhardness (load 0.98 N) of δ-$(Ti,Zr)N_{-1}$ (closed circles) and δ-$(Ti,Hf)N_{-1}$ (crosses) as a function of composition

The color of δ-TiN_{1-x} changes considerably within the homogeneity range -- with increasing nitrogen content -- going from metallic gray to brownish-yellow and at last to the golden yellow color of stoichiometric TiN. The reflectance curves, which are given in Fig. 7, quantify these optical results. Very substoichiometric $TiN_{0.67}$ and even $TiN_{0.77}$ show reflectance curves with only a small drop in reflectivity around 360-380 nm. With increasing N content this reflectivity minimum becomes more pronounced and is shifted continuously until it is located at 420 nm in $TiN_{0.96}$, where the entire band reaches from the the lower end of the measurement

range (300 nm) to more than 500 nm. The reflectance minimum at 420 nm corresponds to the selective absorptance of the blue part of the visible spectrum.

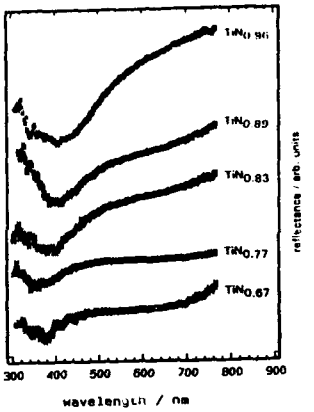


Fig. 7.
Reflectance curves of samples in the homogeneity range of δ-TiN_{1-x}

In Fig. 8 the heat conductivities of nitrided samples are plotted as a function of temperature for δ-$(Ti,Zr)N_{1-x}$ and δ-$(Ti,Hf)N_{1-x}$. The heat conductivity of δ-TiN shows the highest value of all samples prepared by N diffusion at all temperatures. δ-$(Ti,Zr)N_{1-x}$ samples with 7/3 < [Ti]/[Zr] < 3/7 also have high heat conductivities, whereas samples with only a small amount of the other metal and δ-ZrN_{1-x} show quite low conductivities. A comparison of the nitrogen contents reveals that the samples with low heat conductivities also have lower nitrogen contents ([N]/([Ti]+[Zr]) = 0.90-0.94). A comparison of fully dense δ-ZrN_{1-x} samples prepared by diffusional treatment of Zr sheet and hot-pressed δ-ZrN_{1-x} (not shown) leads to an interesting detail: The heat conductivity of the hot-pressed sample is even higher than that of δ-TiN. These results and those for the electrical conductivity lead to the conclusion that heat (and electrical) conductivities are strongly dependent on the N content, especially as the stoichiometric composition is approached.

The results of the electrical conductivity measurements are given in Fig. 9. The comparison between hot-pressed and nitrided samples of δ-$(Ti,Zr)N_{1-x}$ leads to the same results as with heat

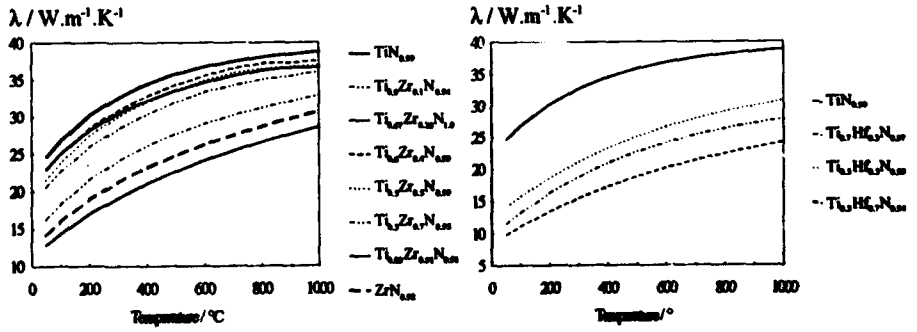


Fig. 8. Heat conductivity as a function of temperature and composition for δ-$(Ti,Zr)N_{1-x}$ (left) and δ-$(Ti,Hf)N_{1-x}$ (right).

conductivity: The samples containing 30-70 mol% ZrN have a relatively high electrical conductivities, whereas the electrical conductivity of hot-pressed ZrN is three times higher than that of a sample made by nitriding Zr sheet. The slightly better conductivity of the nitrided samples with a [Ti]/[Zr] ratio near 1, which are stoichiometric, may be due to the higher purity and the absence of porosity. The *Wiedemann-Franz* law is obeyed with a *Lorenz* number of $L=2.5\text{-}2.7*10^{-8}\ V^2K^{-2}$, indicative of a predominantly electronic transport of both heat and electric current. The metallic behavior of both phases becomes apparent in their conductivity properties.

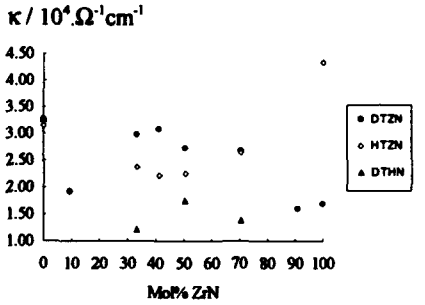


Fig. 9.
Electrical conductivity of hot-pressed (HTZN) and nitrided (DTZN) δ-$(Ti,Zr)N_{1-x}$ and nitrided δ-$(Ti,Hf)N_{1-x}$ (DTHN) as a function of composition

The fact, that both electrical and thermal conductivity are strongly dependent on the nitrogen content is consistent with results obtained in the Ti-N system [5]. The steep increase in both transport properties as the stoichiometric composition is approached, as clearly observed in δ-ZrN_{1-x}, may be explained by the scattering effect of the incomplete metalloid sublattices.

6. References

[1] W.Lengauer, *J. Solid State Chem.* **91**, 279 (1991).

[2] W.Lengauer, *Acta Metall. Mater.* **39**, 2895 (1991).

[3] P.Ettmayer and W.Lengauer, Nitrides, in: *Ullmann's Encyclopedia of Industrial Chemistry*, **Vol. A17**, Verlag Chemie, Weinheim (1991), p 341-361.

[4] W.Lengauer, *J.Alloys Compounds* (1992) in press.

[5] P.Duwez and F.Odell, *J. Electrochem. Soc.* **97(10)**, 299 (1950).

[6] H.Nowotny, F.Benesovsky and E.Rudy, *Monatsh. Chem.* **91**, 348 (1960).

[7] R.Kieffer, H.Nowotny, P.Ettmayer and G.Dufek, *Metall* 7, 701 (1972).

[8] R. Kieffer, H. Nowotny, A. Neckel, P. Ettmayer, L. Usner, *Monatsh. Chem.* **99**, 1020 (1968).

[9] O.Knotek and A.Barimani, *Thin Solid Films* **174**, 51 (1991).

[10] R. A. Andrievski, I. A. Anisimova, V. P. Anisimov, *Thin Solid Films* **205** (1992) in press.

[11] R.Täubler, S.Binder, M.Groschner, W.Lengauer and P. Ettmayer, *Mikrochim. Acta* **107**, 337 (1992).

[12] G. F. Bastin, H. J. M. Heijligers and J. F. M. Pinxter, *Microbeam Analysis* **290** (1980).

[13] W.Lengauer, J.Bauer, A.Guillou, J.-P.Bars, M.Bohn, E.Etchessahar, J.Debuigne and P.Ettmayer, *Mikrochim. Acta* **107**, 303 (1992).

[14] H.A.Wriedt and J.L.Murray, *Bull. Alloy Phase Diagr.* **8**, 378 (1987).

Acknowledgements

The study was supported by the Austrian National Science Foundation under Projekt No. 7370. The thermophysical measurements were performed at the research Centre Seibersdorf, Austria, Department of Engeneering, for which thanks are due to Mr. G. Grol oth.

THE REGULARITIES OF STRUCTURE FORMATION IN PSEUDO-ALPHA-TI ALLOYS

DURING HOT PLASTIC DEFORMATION

Stal Ushkov, Boris Krivitskiy, I.N.Rasuvaeva, V.N.Kopylov

Central Research Institute of Structural Materials "Prometey"
Sankt-Petersburg, 193167, Russia

Abstractt

Pseudo-alpha-Ti alloy was tested on a torsional plastometre in a wide range of temperature and strain rates. The parameters of thermal activation of hot plastic deformation are defined on basis of experimental results; the structure of tested samples was investigated. It is shown, that the obtained results may be considered as a methodological base for regulated structure prediction in titanium semiproducts; and, therefore, for a given combination of physical and mechanical properties as well.

Introduction

As the physico-mechanical properties of metallic materials are defined by their structural condition, appreciably, the investigation of the conformities of the structure building with hot plastic deformation (HPD) is an important technological problem. However, a sufficiently reliable procedure to investigate the structure evolution at the time of HPD in a multi-phase alloy where transformation occurs in several phases at a time during the hot plastic deformation doesn't exist.
The structure formed during HPD is known to depend on the type and the intensity of the dynamic ordering-disordering. Their combination can be represented by Q values, the apparent activation energy (1,2).
The present work aims at an investigation of possible application of the thermodynamic parameter, Q, as an integral parameter for the evaluation of the general conformities of the structure building at the time of HPD of the pseudo-alpha-titanium alloys.

Material and Investigation Procedure

The Q value was defined on the basis of the hot torsion test results. Specimens of 8 x 25 mm size of the pseudo-alpha-titanium alloy containing Al, S,V,C,O_2 and Fe were tested at the strain rate, $\dot{\varepsilon}$, equal to 10^{-2} -10 s^{-1} at 850 - 1150°C. The strain extent, ε, is 0,6-0,7, which corresponds to the steady yield.
The specimens were placed in a furnace heated up to the required temperature for 10 minutes, followed by the torsion at the desired rate at 360°C and a

Titanium '92
Science and Technology
Edited by F.H. Froes and I. Caplan
The Minerals, Metals & Materials Society, 1993

fast cooling in water. The microsection for metallographic analyses was cut from each tested specimens.
At the time of test the tensometric system and a loop oscillograph were applied to record the "moment-torsion angle" machine diagram. The tipical diagrams are shown in Figure 1.

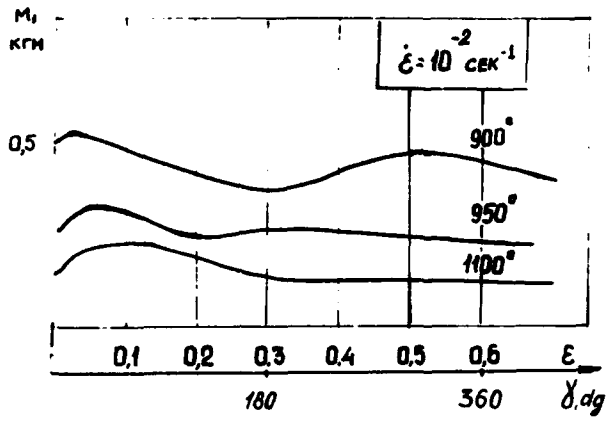


Figure 1 The torsion moment vs torsion angle

The strain resistance was designed for steady state in accordance with the Fijidja-Beckofen equation (3)

$$\sigma = \frac{\sqrt{3}}{2\sqrt{\pi}\, r_o^3} M (3 + m + n) \qquad (1)$$

where M is the torsion moment,
m,n are the coefficients of the strain and rate hardening, respectively,
r_o is the radius of the gauge section of the specimen.
Q value was evaluated by ref. (1,2)

$$Q = R \frac{\ln \dot{\varepsilon}_2/\dot{\varepsilon}_1}{\frac{1}{T_1} - \frac{1}{T_2}} \qquad (2)$$

where R is the gas constant R = 1.986 cal/grad,
$\dot{\varepsilon}$ is defined using the plot on Figure 2.
Figures 2,3 show the results of σ and Q calculation for the investigated range of T and ε.

Test Results

Figure 1 shows the "moment-torsion angle" diagram recorded at the time of the test, which is the base experimental data to calculate σ and Q values. The figure indicates that the torsion moment value vs strain e tent at T=900 and 950°C and $\dot{\varepsilon} = 10^{-2} s^{-1}$ is of n oscillating type. With strain rate increase the relation has a single maximum only, so either the maximum value or the intensity of M reduction as a function of the strain extent decreases as the test rate increases.
At T = 1000 - 1100°C and $\dot{\varepsilon} = 10^{-2} s^{-1}$ when "M-γ" curves arrive to the maximum

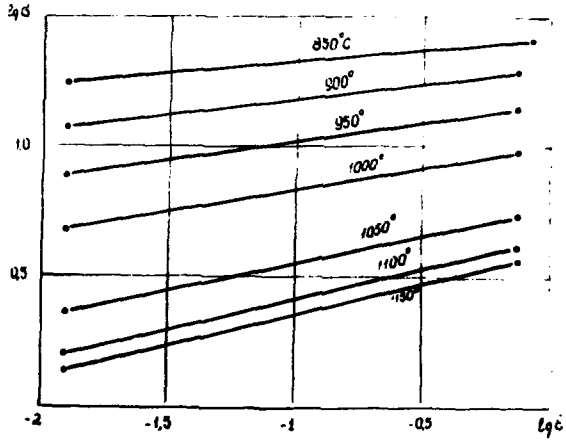


Figure 2 Deformation resistance vs temperature and strain rate.

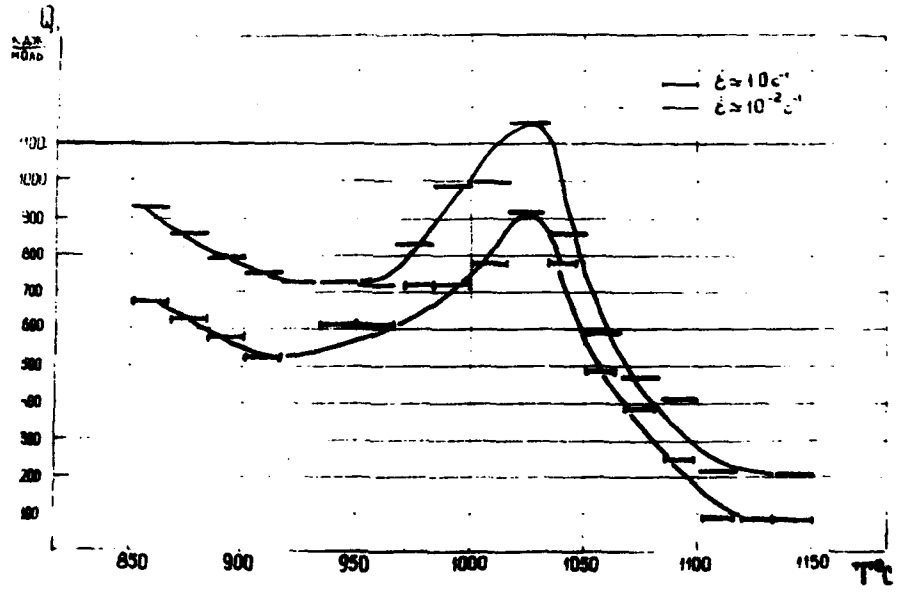


Figure 3 The apparent activation energy Q vs temperature and strain rate.

moment value with strain extent, the plateau of the steady yield is established. The type of the curves is changed, with $\dot{\varepsilon} = 0{,}1\ s^{-1}$ is similar to that of "M - γ" curves obtained at test temperature 900 and 950°C with same rates.

Figure 3 shows the apparent activation energy as function of temperature-strain rate conditions calculated by equation (2). As the represented data

indicate, either the absolute Q values or the type of its variation as a function of the test temperature 1000 - 1100°C and 900 - 950°C differ fundamentally. In the first range (1000 - 1100°C) the values are lower compared to the second range, appreciably, they are equal at both temperatures, in fact, and are small dependent on the strain rate. In the second range the apparent activation energy values is 1 - 2,5 times as high as Q values at 1000 - 1100°C, and at 900°C Q value is a function of the test rate. The metallographic analyses show that the original structure of the investigated alloy is heterogeneous, and consists of large fragments of the parallel α- phase interlaid by the β-phase (Figure 4a).

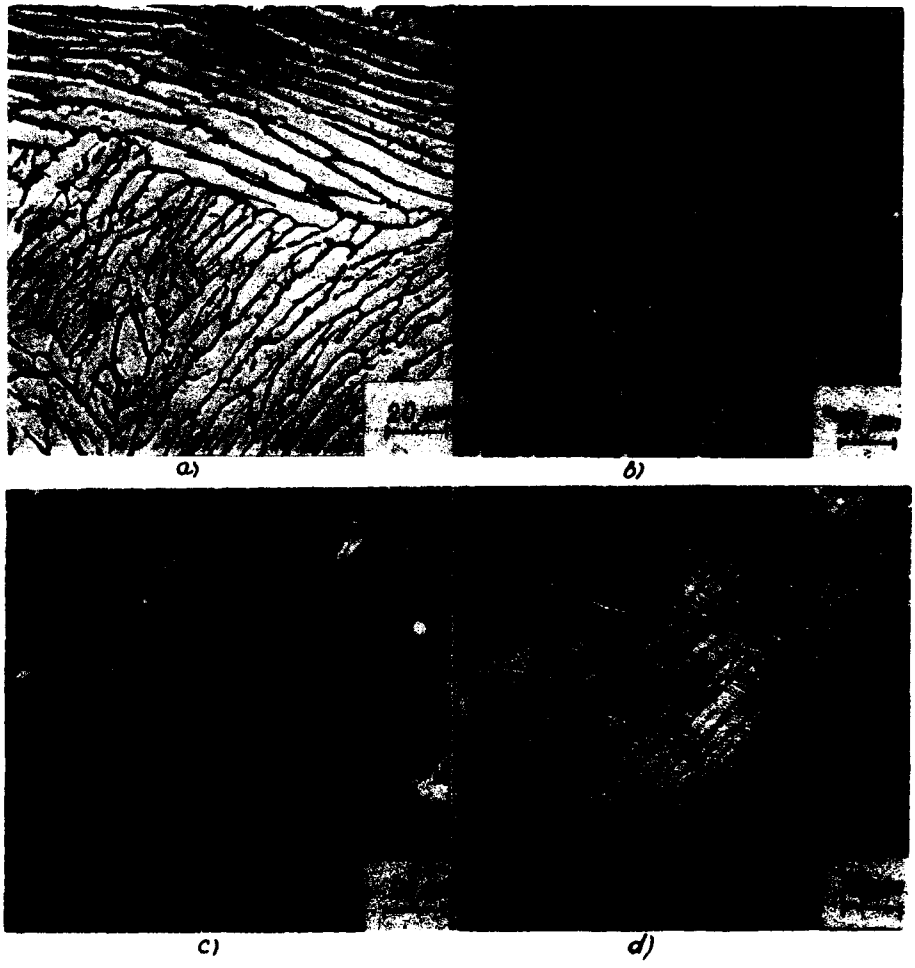


Figure 4 The microstructure of the investigated alloy in original (a) state and after torsion at T = 1000°C, $\dot{\varepsilon} = 10^{-2}\ s^{-1}$(b); T = 950°C, $\dot{\varepsilon} = 10^{-2}\ s^{-1}$(C) and T = 900°C, $\dot{\varepsilon} = 10^{-3} s^{-1}$(d).

The heating of the specimens before the torsion tests results in a natural change of the phase composition which induces α-phase spheroidization, which is the more complete the higher the temperature.

The beta-phase content of the investigated alloy as a function of the heating temperature obtained by a second method with an error about 5% varies as follows: 850°C - 25%, 900°C - 35%, 950°C - 48%, 1000°C - 78%. The temperature of polymorphous transformation (Tpt) is 1050°C. Heating above Tpt results in the formation of the large grains of the beta-phase.

The investigation of the specimen structure after torsion at 1000°C (beta-range) indicated that, at relatively high strain rates ($\dot{\varepsilon} = 1{,}0\ s^{-1}$), the new grains of the beta-phase finer than the grains occured with the heating before test in the gauge section of the specimens.

At 1000°C, when the beta-phase dominates quantitively in the phase composition of the alloy at strain rates of $10^{-2} - 1{,}0\ s^{-1}$, the new finer beta-grains appear. At the same time in the individual grains the a relief appears (Figure 4).

The structural variance at 900°C, when either the alpha-phase is a dominating phase, or the phase correletion is about similar, is complex and different. The heterogeneity of the original structure plays an important role, which results in an appreciable difference of a strain type and, hence, of structural transformations in the fragments of different orientations.

Wigh relatively low strain rate ($\dot{\varepsilon} = 10^{-3} - 10^{-1} s^{-1}$), some fragments and the alpha-grains are characterized by twinning traces, whose quantity increases with strain rate increase.

In some fragments the spheroidization of the alpha-phase plates occurs, which seems to be preceded by the twinning. The twinning traces induced by the strain at 950°C are observed with the rate $\dot{\varepsilon} = 1{,}0\ s^{-1}$ only, at the same time the structure contains round grains of the alpha-phase. With $\dot{\varepsilon} = 10^{1} s^{-1}$ the beta-phase is observed. In the individual alpha-grains the characteristic relief appears.

Discussion of the Results

The comparison of the obtained relations of the appearent activation energy (Figure 3) and the temperature - rate conditions of deformation and results of the metallographic analyses show that the Q value represents qualitively the general conformity of the structure building.

So, in 1000-1050°C range with $\dot{\varepsilon} = 0.01 - 1.0\ s^{-1}$ the Q value is maximum. In this range the structure building seems to be controlled by the dynamic recrystallization of the beta-phase. From the one hand, it is certified by the beta-grain refinement (Figure 4b), from the other hand, by the oscillating nature of the yield curves with $\dot{\varepsilon} = 0.01\ s^{-1}$ and the existance of peaks with $\dot{\varepsilon} = 0.1\ s^{-1}$ (Figure 1).

The strain at 900°C with rate of $10^{-2}\ s^{-1}$ results in the spheroidization of the alpha-phase plated, which is in most cases induced by the twin boundaries The spheroidization is activated by the diffusion mechanism and is characterized by a high energy capacity and high activation energy, respectively (1,5). When the strain rate approaches 1.0 s^{-1} rate range represents naturally progressivaly substituted by the poligonization and twinning, in the individual volumes the recrystalized alpha-grains are observed. This indicates that the reduction of the Q value at 900°C with $10^{-2} - 1.0\ s^{-1}$ rate range represents naturally transition of the processes with higher energy capacity (the alpha-phase spheroidization) to processes of less energy capacity (the polygoniaation and twinning). This is additionally certified by the progress ive disappearance of the assimilations and "peaks" on the yield curves with test rate increase. At 950°C within the investigated rate range at the time of the alpha-phase softening the dynamic recryltallization of the alpha-phase plays an important role. This is certified either by the structural investigation or the type of a yield curve. One can suppose that the processes occuring in the bcc beta-phase of higher selfdiffusion coefficient compared to the alpha-phase (6) determines either the absolute Q values or

its change type in the investigated test rate range, i.e. the small dependence of Q value of test rate at 950°C.

Conclusion

The torsion tests of the specimens of the pseudo-alpha-titanium alloy with corse plate structure were performed at 900 - 1100°C and strain rate of 10^{-2} - 1.0 s^{-1}. The investigation results were applied to calculate the value of the so called, apparent activation energy. It is established that the activation energy represented qualitively the general conformities of the structure building in the investigated temperature-rate range.

References

1. The Diagram of Hot Deformation Structure and Properties of Steess. Handbook, ed. Bernstein, (Russia, Moscow, Metallurgia, 1989).

2. S.Trizerr, R.Otani, The Theory of High Temperature Strength of Materials, (Russia, Moscow, Metallurgia, 1986).

3. V.Bekofen, The Deformation Process, (Russia, Moscow, Metallurgia, 1977).

4. G.V.Sakjanova et al., "Resistance of Deformation and Dynamic Change in the Structure of Two-Phase Ti-Alloys Under Hot Deformation", Titanium 80-4th International Conference on Titanium.(Quioto, Japan, May 80), 849-861.

5. S.S.Gorelick, The Recrystallization of Metals and Alloys,(Russia, Moscow, 1978).

THE Ti-C-N SYSTEM AND PROPERTIES OF Ti(C,N)

S.Binder, W.Lengauer and P.Ettmayer

Institute for Chemical Technology of Inorganic Materials
Technical University of Vienna
Getreidemarkt 9/161, A-1060 Vienna, Austria

Abstract

The hard constituents in *cermet* cutting tools are based on titanium carbonitrides. In order to gain more insight in the Ti-C-N system the phase diagram of the Ti-C-N system was established and single-phase samples of compact carbonitrides were prepared by hot pressing and various of their properties investigated.

Temperature conductivities of titanium carbonitrides were measured in the range 25 - 1400°C by the laser-flash method. Using the specific heats obtained by differential scanning calorimetry, the heat conductivities could be calculated. The nitrides generally had a higher heat conductivity than the carbides. In the region of solid solution between nitride and carbide the heat conductivity decreased steadily with increasing carbon content. Vickers microhardness values at a load of 0.98 N were measured and showed a positive deviation from the addition rule.

Diffusion couples $Ti(C_xN_{1-x})_{1.00}$/liquid Ni were prepared in order to study the interaction between titanium carbonitrides and liquid nickel. By EPMA measurements a quantification of this interaction was possible.

1 Introduction

Although Ti(C,N) is of substantial interest for technological applications in cermets [1] systematic experimental investigations necessary to establish a phase diagram of the Ti-C-N system have not been performed. Stone [2] investigated the metal-rich part of the system and constructed isothermal sections for temperatures between 800 and 1300°C. Teyssandier et al. [3] calculated a complete isothermal section for 1400°C. A number of studies have dealt with the investigation of the thermodynamic properties of $Ti(C_xN_{1-x})_{1.0}$ [4-7]. Generally, there is a lack of information on the physical properties of $Ti(C_xN_{1-x})$. The electrical conductivities have been investigated for several $Ti(C_xN_{1-x})_{1.0}$ compounds [8]. Existing microhardness data scatter considerably [9,10], and no studies on the thermal conductivity could be found in the literature. This study was performed performed in order to establish a phase diagram for the Ti-C-N system, to systematically investigate the

Titanium '92
Science and Technology
Edited by F.H. Froes and I. Caplan
The Minerals, Metals & Materials Society, 1993

properties of $Ti(C_xN_{1-x})_{1.0}$, and to reinvestigate properties for which the literature values are too scattered to be considered as reliable.

2 Experimental

TiC, TiN and Ti powders of various grain sizes were mixed and arc melted under Ar. They were then sealed in silica capsules under Ar, heat treated for two weeks at 1150°C and water quenched.

For the preparation of hot-pressed samples TiC, TiN and Ti powders were mixed in a planetary mill under cyclohexane, dried and filled into the graphite die of the hot press. Between sample powder and graphite a 25μm Zr foil was placed in order to impede carbon diffusion into the samples. After flushing the hot press with Ar the temperature and pressure were increased up to 2500°C and 55 MPa respectively. These conditions were kept constant for 5 minutes, and then the samples were cooled to room temperature. The zirconium carbide scale was completely removed from the samples by grinding with a diamond disc.

$Ti(C_xN_{1-x})_{1.0}$/liquid Ni diffusion couples were prepared by embedding hot-pressed carbonitride pieces in Ni powder in an alumina crucible. Coarse grained alumina was placed onto the bottom of the crucible in order to prevent the nickel melt from sticking to the crucible wall. The samples were heated to 1500°C within 15 minutes in a pure Ar atmosphere. The ramp time at this temperature was 20 min.

Compact hot-pressed carbonitride samples were chosen to make it easier to observe the interaction of molten nickel with the titanium carbonitride than is possible with fine-grained carbonitride and nickel powder mixtures used for cermet production. In addition, EPMA, an exceptionally most powerful quantitative microanalytical technique, can be applied to characterize this interaction. This is impossible when typical cermet starting materials are used [11] because of the restricted lateral resolution.

3 Sample Characterization

The samples were ground with a diamond disk (20μm) followed by SiC paper (2500 mesh). Polishing was performed first with 3μm diamond paste then with an aqueous silica suspension. The Vickers microhardness HV was measured at a load of 0.98 N. Usually about 10-15 indentations were made on each sample, and the mean value and the standard deviation were calculated. Density measurements were made by with $CHBr_3$ as an immersion liquid and a thin steel wire to a suspend the sample. XRD was performed with Ni-filtered Cu-K_α radiation or by use of a secondary graphite monochromator. Fine mortar-ground powders were used as well as compact samples, the latter being mounted on a rotating sample holder.

Chemical analysis was performed for nitrogen and carbon using Dumas gas-chromatography. V_2O_5 was used as a combustion booster. The obtained peak areas of the gas chromatograms were calibrated with standards. A detailed description of the setup and procedure is given in [12].

EPMA was performed at the IFREMER Brest, France, with a CAMECA SX 50 microprobe, equipped with four wavelength-dispersive spectrometers. Samples of $Ti(C_xN_{1-x})_{1.0}$ and Ni-Ti alloys served as standards. Due to the coincidence of the Ti-L_l and the N-K_α lines nitrogen was determined as the balance of the concentrations of carbon, titanium and nickel.

From the hot-pressed samples discs 1mm thick and 5 or 10 mm in diameter were machined with a hollow diamond drill bit. The larger discs were used for thermal diffusivity measurements by the laser-flash method the smaller discs were used for heat capacity measurements by DSC.

4 Results and discussion

4.1 Phase equilibria

Fig.1 shows an isothermal section of the Ti-C-N system at 1150°C based on the analysis of heat-treated arc-melted buttons and heat-treated hot-pressed samples. The phase diagram is consistent with the thermodynamic calculations of Teyssandier et al.[3].

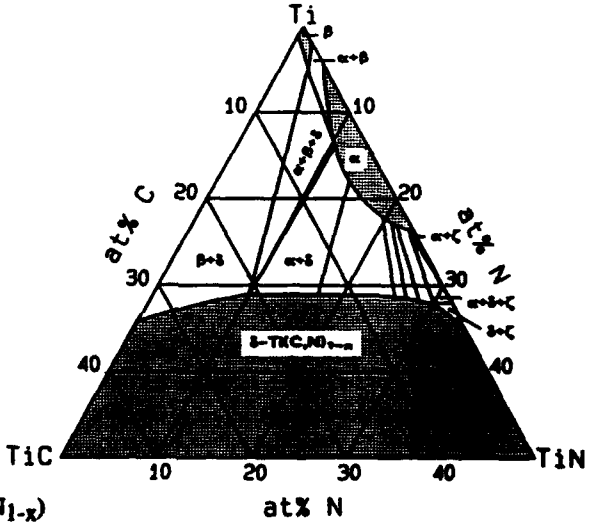


Fig.1
Phase diagram of the
Ti-C-N system (1150°C)

4.2 Properties of δ-Ti(C_xN_{1-x})

4.2.1 Microhardness

The microhardness of $Ti(C,N)_{1.00}$ decreased in a nearly linear manner from TiC to TiN with a small positive deviation from an additive behavior (Fig.2). This positive deviation was also observed in substoichiometric samples $Ti(C,N)_{0.82}$. In the latter case the hardness curve is less steep due to the fact that the hardness decreases in δ-TiC_{1-x} with decreasing C content [13,14] but increases in δ-TiN_{1-x} with decreasing N content [15]. Apparently, the hardness of δ-$Ti(C,N)_{1-x}$ is an almost linear function of both the [C]/([C]+[N]) and the [Ti]/([C]+[N]) ratios.

4.2.2 Thermal diffusivity

Fig.3 shows the thermal diffusivities of stoichiometric $Ti(C_xN_{1-x})$. TiN had the highest thermal diffusivity and it can be seen that a 20% nitrogen replacement by carbon drastically reduced the thermal diffusivity. After this decrease the diffusivity decreased much less with increasing carbon content and the data are within the error limits (about 8%).

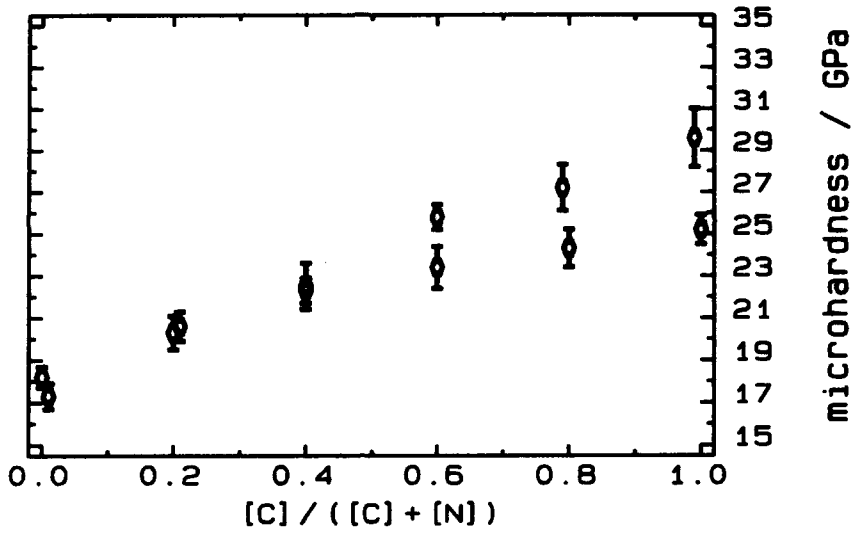


Fig.2
Microhardness $HV_{0.1}$ (load:0.98 N) of $Ti(C_xN_{1-x})_{1.00}$ and $Ti(C_xN_{1-x})_{0.82}$ as a function of the [C]/([C]+[N]) ratio.

The thermal diffusivity of substoichiometric $Ti(C_xN_{1-x})$, i.e. $Ti(C_xN_{1-x})_{0.82}$, was much lower than that of the stoichiometric samples. At high temperatures (T = 500-1400°C) the thermal diffusivity decreased from $TiN_{0.82}$ to $TiC_{0.82}$. At low temperatures the sequence was reversed and $TiC_{0.82}$ had the highest thermal diffusivity.

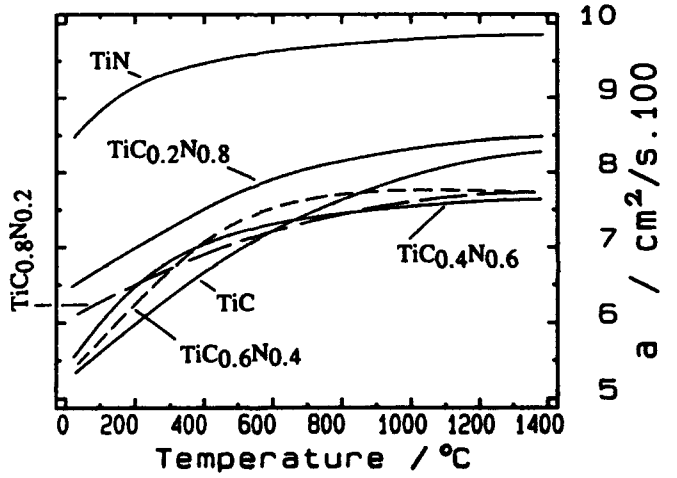


Fig.3
Thermal diffusivity of $Ti(C_xN_{1-x})_{1.0}$

4.2.3 Heat capacity

The molar heat capacity (Fig.4) increased slightly with increasing nitrogen content of $Ti(C_xN_{1-x})_{1.0}$. These samples showed a slightly higher heat capacity than samples with the composition $Ti(C_xN_{1-x})_{0.82}$. The latter showed a marked jump in C_p at 700-800°C which would be indicative of a phase transition in this temperature region. It should be investigated whether this phenomenon is reversible and/or repeatable. XRD patterns of the sample at room temperature did not give any indication of such a phase transition.

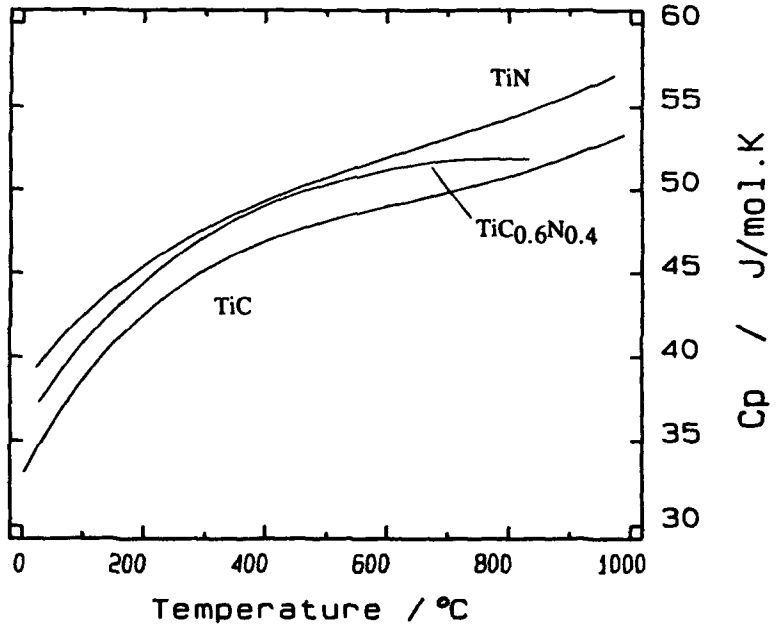


Fig.4

Molar heat capacity of TiC, TiN and $TiC_{0.6}N_{0.4}$

4.2.4 Heat conductivity

The data sets of thermal diffusivity and heat capacity were interpolated and used to calculate the thermal conductivity. It was assumed that in the $Ti(C_xN_{1-x})_{1.00}$ lattice the Ti and C+N sites were 100% occupied. Therefore X-ray densities were taken. The thermal expansion, which would cause a reduction in the density with increasing temperature, was neglected because the error is less than 3%. Fig.5 shows the heat conductivities of $Ti(C_xN_{1-x})_{1.00}$ and $Ti(C_xN_{1-x})_{0.82}$.

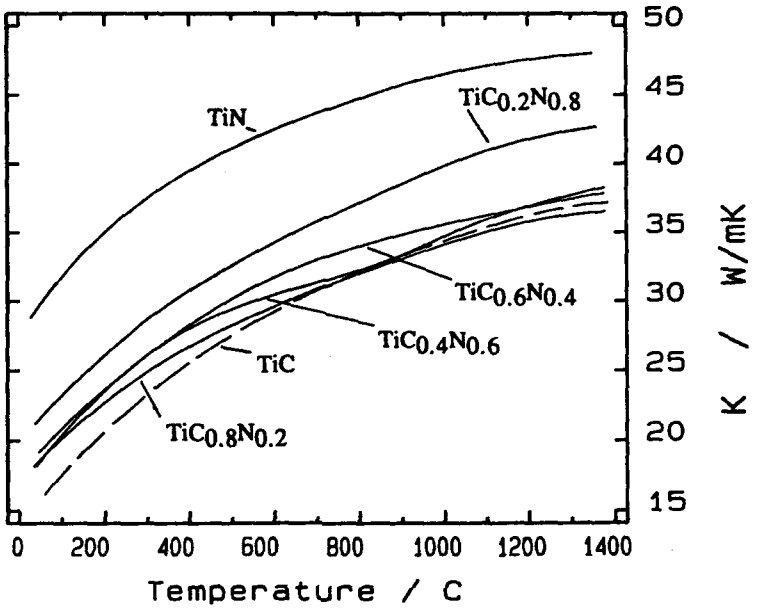


Fig.5
Heat conductivity of $Ti(C_xN_{1-x})_{1.0}$

4.2.5 *Reaction of compact* $Ti(C_xN_{1-x})_{1.0}$ with liquid nickel

Fig.6 shows the micrographs of the 6 different samples that were subjected to the action of liquid nickel. Liquid Ni penetrated along the grain boundaries of the carbonitride where the reaction proceeded to the center of the carbonitride grains. Carbon or TiC is preferentially dissolved by liquid Ni so that the reacted carbonitride contained significantly more nitrogen that the unreacted part. Interestingly, the original grain boundary structure of the carbonitride samples appeared to be retained in the microstructure of the reacted zone. The penetration depth of liquid Ni was the greater the higher the carbon content in the carbonitride. The original carbonitride grains were attacked by the nickel melt in such a way that the crystallites were broken up into smaller carbonitride grains which were significantly richer in nitrogen than the original hot-pressed carbonitride. Often the carbonitride formed via the liquid phase featured rectangular or triangular facetted crystallites. The more nitrogen the carbonitride contained the more globular were the precipitates.

Because Ni reacted more intensively with $Ti(C_xN_{1-x})_{1.0}$ with high carbon contents, the grain boundaries where Ni had penetrated the carbonitride changed structure as a function of the [N]/[C] ratio. At high carbon contents (see $TiC_{0.8}N_{0.2}$ and $TiC_{0.6}N_{0.2}$) the nickel canals were wide and the particles of the reacted carbonitride were located mainly within the nickel phase. The more nitrogen the carbonitride contained the narrower were the nickel intergrain canals and the original carbonitride grains appeared to have a rim with a higher

nitrogen content. This was very pronounced in the $Ti(C_{0.2}N_{0.8})$ sample where the *intergrain* boundary consisted mainly of reacted $Ti(C_xN_{1-x})_{1.0}$ and only of very small Ni canals in comparison to $Ti(C_{0.8}N_{0.2})$, where a large Ni content was observed.

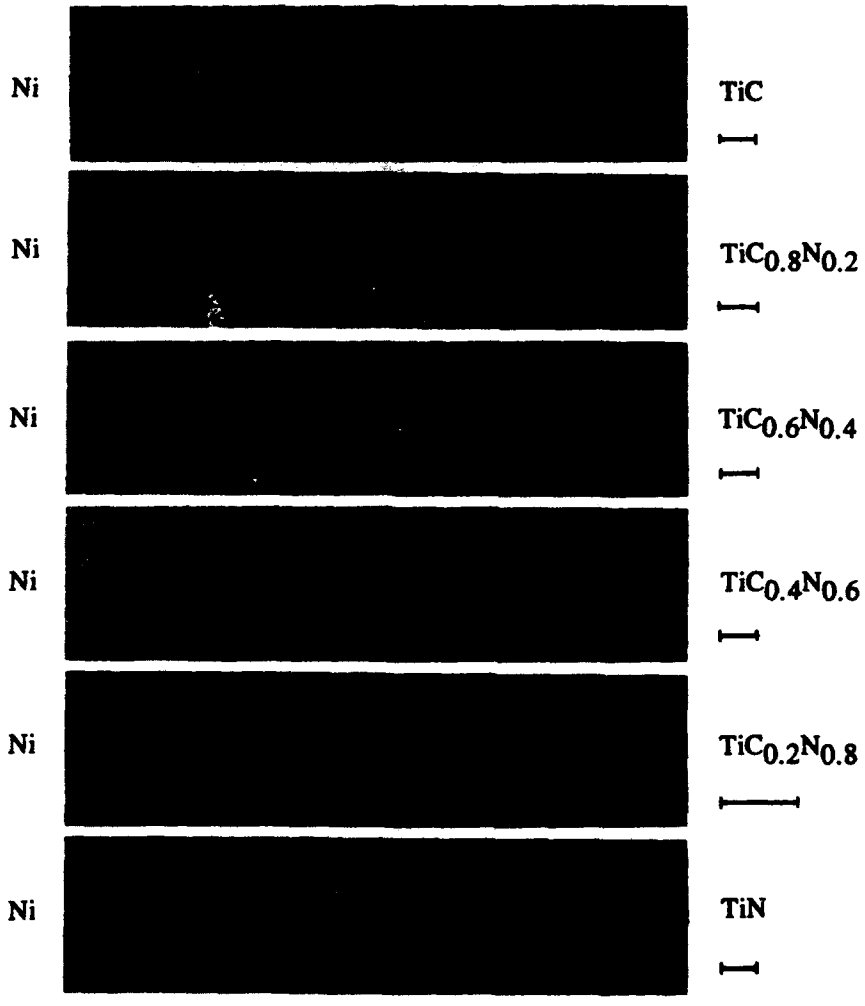
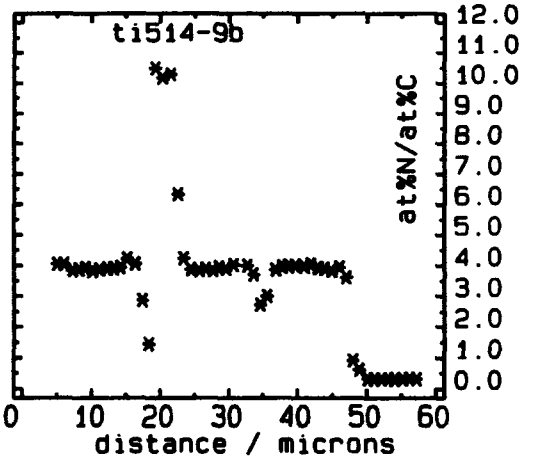


Fig.6
Microstructure of Ni/TiC_xN_{1-x} diffusion couples (the bar corresponds to 20μm).

As a first approach, for the nitrogen-rich carbonitride grades the color change as a function of the carbon/nitrogen ratio could well be used for an optical estimation of the [C]/([C]+[N]) shift upon reaction with Ni. Further quantitative information was obtained by EPMA. For all the investigated $Ni/Ti(C_xN_{1-x})_{1.0}$ diffusion couples the [N]/[C] ratio between the reacted and the unreacted carbonitride phase differed by a factor of 2-2.5. This is shown in Fig.7 for the sample $Ti(C_{0.2}N_{0.8})_{1.00}$.

Fig.7
Microprobe scan across the interface of a Ni/$TiC_{0.2}N_{0.8}$ diffusion couple. The differences in composition between reacted and unreacted carbonitride can be seen.





Acknowledgements
The study was supported by the "Jubiläumsfonds der Oesterreichischen Nationalbank" under project No.3729. The laser-flash and DSC measurements were performed at the Forschungszentrum Seibersdorf for wich the authors would like to thank Mr.G.Groboth. Support via the French-Austrian research contract, project A16, is also gratefully acknowledged. Further thanks are due to Mr.M.Bohn (IFREMER Brest, France) for support during the EPMA measurements.

References

[1] P.Ettmayer, Hardmetals and Cermets, Ann.Rev.Mater.Sci. **19**, 145 (1989)
[2] L.Stone and H.Margolin, Trans.AIME (1953), 1498
[3] F.Teyssandier, M.Ducarroir and C.Bernard, CALPHAD **8** (1984), 233
[4] A.N.Zelikman and N.N.Gorowitz, Zh.Prikl.Khim.23 (1950), 689
[5] P.Grieveson, Proc.Brit.Ceram.Soc.**8** (1967), 137
[6] R.Kieffer, H.Nowotny, P.Ettmayer and M.Freudhofmeier, Monatsh.Chem.**101** (1979) 65
[7] H.Pastor, Mater.Sci Engineer.**A105/106** (1988) 401
[8] E.Barbier and F.Thevenot, in press (1991)
[9] G.D.Bomomolov et al., Izv.Akad.Nauk.SSSR, Neorgan.Mater.7 (1971), 67
[10] R.Kieffer, W.Wruss, K.Constant and H.Habermann, Monatsh.Chem.**106** (1975), 1349
[11] B.Roebuck and M.G.Gee, Proc.12th Plansee Seminar, Reutte, Austria, Vol.2 (1989), 1. ed.by H.Bildstein and H.M.Ortner
[12] R.Täubler, S.Binder, M.Groschner, W.Lengauer and P.Ettmayer, Mikrochim. Acta **107** 337 (1992)
[13] J.-L.Chermant, P.Delavignette, A.Deschanvres, J.Less-Common Met.**21** (1970) 89
[14] H.Holleck, H.Schweitzer, KfK report 6/75-2, Research Centre Karlsruhe, FRG (1975)
[15] W.Lengauer, J.Alloys Compounds, in press (1992)

Relation between Electrical Resistivity and Phase Constitution in Metastable β Ti-Nb Alloys.

Masahiko IKEDA, Shin-ya KOMATSU, Takashi SUGIMOTO, and Kiyoshi KAMEI
Department of Materials Science and Engineering, Faculty of Engineering,
Kansai University, 3-3-35 Yamate-cho, Suita 564, Osaka, JAPAN.

Abstract

For Ti-20 to 50mass%Nb alloys quenched from 1073K, negative temperature dependence of electrical resistivity was investigated in relation to, reverse transformation of α'' martensite and formation and dissociation athermal ω.

Changes of resistivity and its temperature dependence with aging at relatively low temperatures were related to phase transformations revealed by X-ray diffraction.

The resistivity-temperature curve of Ti-40mass%Nb alloy showed a minimum and a maximum between 77 and 350K supporting the previous model for the resistivity change due to athermal ω formation.

For several alloys, values of starting(ω_s) and finishing(ω_f) temperatures of athermal ω formation were estimated from measured resistivity -temperature curves. Both of ω_s and ω_f decreased with Nb content.

The resistivities, especially at 77K, of Ti-30 to 40%Nb alloys remarkably increased with isothermal aging at relatively low temperatures. This behavior was attributed to reverse transformation of α'' to β.

Titanium '92
Science and Technology
Edited by F.H. Froes and I. Caplan
The Minerals, Metals & Materials Society, 1993

1. Introduction

For metastable β Ti alloys, an apparently negative temperature dependence(NTD) of electrical resistivity(ρ) is often observed[1-7].

Namely, the ρ at liquid nitrogen temperature(ρ_{LN}) is larger than that at room temperature(ρ_{RT}) in these cases. Even in cases of apparently positive temperature dependence; $\rho_{LN} < \rho_{RT}$, anomalous changes are often observed on ρ-T curves. These anomalies were qualitatively explained by a completely reversible formation and dissociation of athermal ω with cooling and heating of metastable β phase[4,5].

Ames et al. made the first report about the NTD in metastable β Ti-Nb alloys[1]. Balcerzak et al.[8] reported the formation of α'' orthorhombic martensite in composition range of only a retained β phase reported by Ames et al.[1], and that a solution treatment at relatively low temperature caused the α'' formation.

There are many investigations about NTD in β Ti-Mo, Ti-V system alloys, because the NTD is a good index for existence of metastable β phase and its decomposition[1-5]. However, no report after Ames et al.[1] is found about the NTD in Ti-Nb alloys.

In present work, the ρ and its temperature dependence were related to athermal ω formation and reverse transformation of α''.

2. Experimental procedure

Methods of alloy melting and specimen preparation were same as previous reports[4-7]. Table 1 shows the alloy marks, nominal compositions and chemical analyses.

Table 1 Alloy marks, nominal compositions, chemical analyses and phases*.

Alloy marks	nominal compositions (mass%Nb)	chemical analyses (mass%Nb)	(mass%O)	phases*
T20N	20	19.94	0.099	α''
T25N	25	26.01	0.091	α''
T30N	30	30.21	0.096	$\alpha'' + \beta$
T35N	35	35.40	0.072	$\alpha'' + \beta$
T40N	40	39.83	0.089	β
T45N	45	45.39	0.053	β
T50N	50	50.47	0.092	β

* detected by X-ray diffraction at R.T. after quenching from 1073K.

Specimens were quenched into iced water after solution treatment carried out for 3.6ks at 1073K. Some specimens were isothermally aged at suitable temperatures between 423 and 773K.

In T40N alloy, "isothermal-isochronal" aging was carried out for 1.8ks at every 50K in the temperature range of 323 to 473K. Data were collected for 0.06, 0.18, 0.6 and 1.8ks at each aging temperatures.

The ρ was measured by the same method as previous works[4-7].

Average cooling and heating rates were ca. 0.03K/s in measurement of the temperature dependence of ρ below ca. 400K.

Phase constitutions of the quenched and the aged state were determined by X-ray diffraction.

3. Results and Discussions

3-1. Composition dependence of phase constitution and ρ in quenched specimens.

Phase constitution in as quenched state is also shown in Table 1.

T20N and T25N show reflections only of the orthorhombic α'' martensite. Reflections from the α'' and the β are observed both in T30N and T35N. T40N, T45N and T50N show reflections only from the β phase.

These results coincide with the report of Balcerzak et al.[8].

Fig. 1 shows changes of the ρ with Nb content and phase constitutions

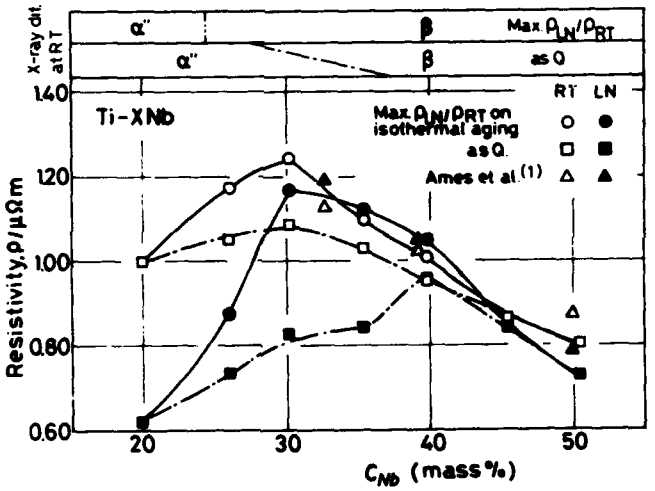


Fig. 1 ρ values in the as quenched state and after isothermal aging state showing maximum ρ_{LN}/ρ_{RT}, compared with phase constitutions.

in two, the as quenched and the aged, states. In the as quenched state, the NTD is observed only in the T40N. All of other alloys show apparently positive temperature dependence of ρ.

Changes of ρ in the as quenched state with composition and the phase constitutions can be specified into following three types; 1) in the case of α'' martensite only, both of ρ_{LN} and ρ_{RT} increase, 2) in $\beta+\alpha''$ structure, ρ_{LN} increases whereas ρ_{RT} decreases, and 3) in β single phase structure, both of ρ_{LN} and ρ_{RT} decrease with increasing Nb content.

Ames et al.[1] observed the NTD and β single phase structure in 32.7 and 39.3%Nb alloys as shown in Fig. 1. These discrepancies in structures and temperature dependence of ρ in the as quenched state should be resulted from the difference in the content of interstitial impurities of specimens and/or, as discussed later, the cooling rate

near M_s point of the α'' martensite.

3-2. Temperature dependence of ρ

Fig. 2 shows the ρ-T curves measured below ca. 400K. All the ρ-T curves showed completely reversible change during measurement without any detectable hysteresis. The ρ values of T20N and T25N, which showed reflections only of α'' martensite, increase almost linearly with elevating temperature. Also in T45N and T50N alloys which showed no reflections except β phase, the gradients of ρ-T curves are positive but very small. In T30N and T35N alloys which have $\beta+\alpha''$ two phases structure, ρ increases parabolically with elevating temperature up to ca. 400K.

In previous works on Ti-Mo system[4], a schematic ρ-T curve was

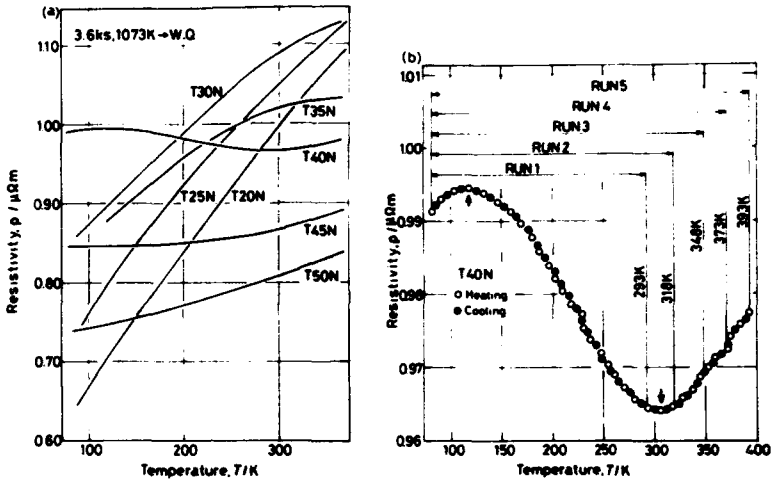


Fig. 2 ρ-T curves of (a) all specimens and (b) of T40N with enlarged ρ axis.

synthesized from ρ-T curves of several alloys of different compositions. However, on an enlarged ρ-T curve of T40N in Fig. 2(b), a maximum and a minimum of ρ are clearly observed at about 120 and 307K, respectively. This fact supports the validity of previous model[4].

Even after heating to 573K[6,7], a shape of ρ-T curve with heating was quite similar to that on cooling, except for shifting to higher ρ values perhaps by the reverse transformation of α'' or the decomposition of β phase accompanied with diffusion.

ω_s and ω_f were estimated from measured ρ-T curves as temperatures at which deviation from linear relation was observed[6]. For T30N and T35N, also for T40N as discussed above, these temperatures were for the β coexisting with α''. Fig. 3 shows ω_s and ω_f as functions of Nb content. M_s[8], A_s and A_f[7] points of α'' are also shown.

The values of ω_s and ω_f decrease with Nb content. Comparing at same composition, the ω_f is always lower than M_s of α'' and the ω_s is higher than extrapolated values of the M_s.

As also shown in the Fig. 3, the composition range, in which the so-called "quenched ω" was observed[8], coincides with the range in which the room temperature situates between ω_s and ω_f. Then, the quenched ω is considered to be the athermal ω which has an enough large volume fraction at room temperature.

3-3. Changes of ρ and X-ray diffraction profiles with isothermal aging

In T20N, ρ and ρ_{LN}/ρ_{RT} decreased with aging at 673 and 773K[7]. This phenomenon suggests that the α'' directly decomposes to α and β accompanied by diffusion without reverse transformation to β.

In T25N, abrupt increases in ρ_{LN}, ρ_{RT} and ρ_{LN}/ρ_{RT}, which were

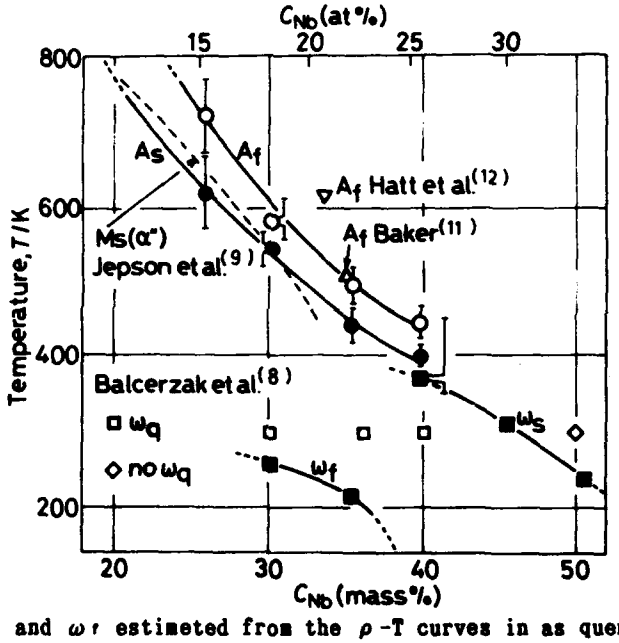


Fig. 3 ω_s and ω_f estimeted from the ρ-T curves in as quenched state, and A_s and A_f of α'' estimated from the ρ change by aging and ρ-T curves up to 573K[7].

immediately followed by decrease, were caused by the shortest aging for 0.06ks at 673 and 773K, though no change in these values was caused by 573K aging[7]. X-ray diffraction also showed an abrupt transformation of α'' to β[7]. This reverse transformation of α'' to β occurred also in alloys up to 35%Nb, but at lower temperatures and more slowly.

Fig. 4 shows, for example, the changes in ρ-T curves and X-ray diffraction profiles of T35N by isothermal aging at 473K. During first stage, in which the increment of ρ_{LN} was larger than that of ρ_{RT}, the ratio of these values (ρ_{LN}/ρ_{RT}) increased and then a ρ maximum appeared in range of 77 to 300K. Apparent NTD was observed between 1.02 and 10.2ks. The temperature of maximum ρ is lowered at first, then the $T_{max.}$ is increased again perhaps by a phase transformation with diffu-

sion. X-ray diffraction shown in Fig. 4(b) reveals that the transformation of α'' to β occurs during the first increase in ρ_{LN}/ρ_{RT}. After complete reversing of α'' to β by 3.6ks, no change in X-ray diffraction profile is detected in the second stage showing decrease of ρ_{LN}/ρ_{RT}.

Similar aging behavior is observed also in T40N, as shown in Fig. 5.

The ρ_{LN}/ρ_{RT} started to increase from 423K aging and showed a maximum during aging at 473K.

Considering previous results on a Ti-15Mo-5Zr alloy[18], the relation between the changes in these ρ values and the characteristics

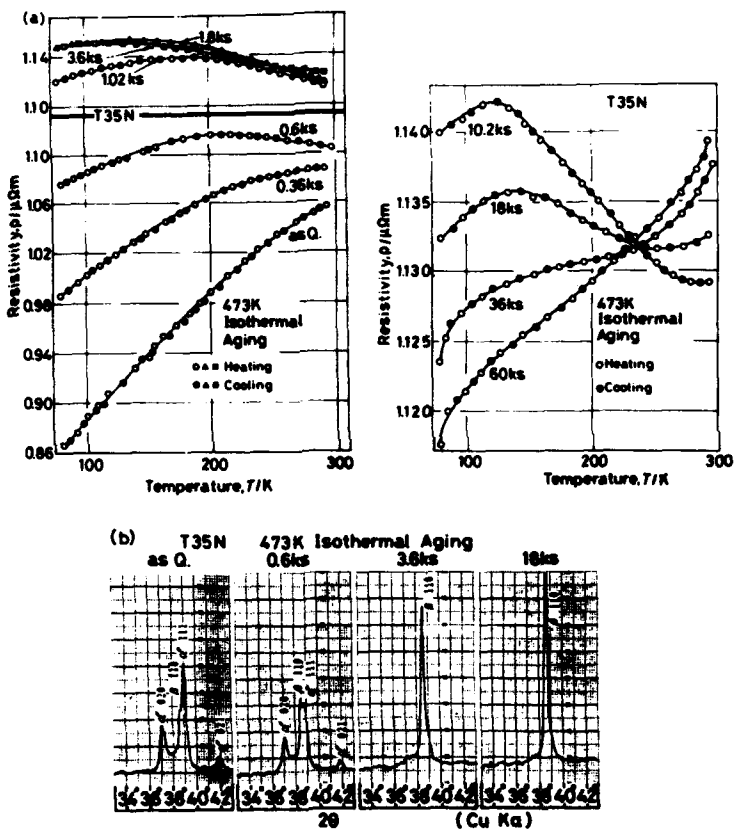


Fig. 4 Changes in ρ-T curves(a) and in X-ray diffraction profiles(b) of T35N by isothermal aging at 473K.

in mode of phase transformation can be assigned as shown in Table 2.

From changes in ρ-T curves with aging up to 3.6ks at 473K shown in Fig. 4(a), it is considered that the ω_f tends to decrease with reverse transforamton of α'' to β[7].

A_s and A_f of α'' in alloys up to 40%Nb were estimated from aging curves and ρ-T curves[7], which have been shown in Fig. 3. The A_s and A_f decrease with Nb content. The A_s and/or A_f can be distinguished from ω_s by complete reversibility of ρ change with temperature and

difference in sign of curvature of ρ-T curves between A_f and ω_e.

Also values of ρ_{RT} and ρ_{LN} on aging of maximum ρ_{LN}/ρ_{RT} have been shown Fig. 1. These values of ρ became closer to values of Ames et al.[1]. This fact suggests that formation of α'' in their[1] specimens was suppressed by some causes, e.g. solutionizing temperature or cooling rate near M_s point etc..

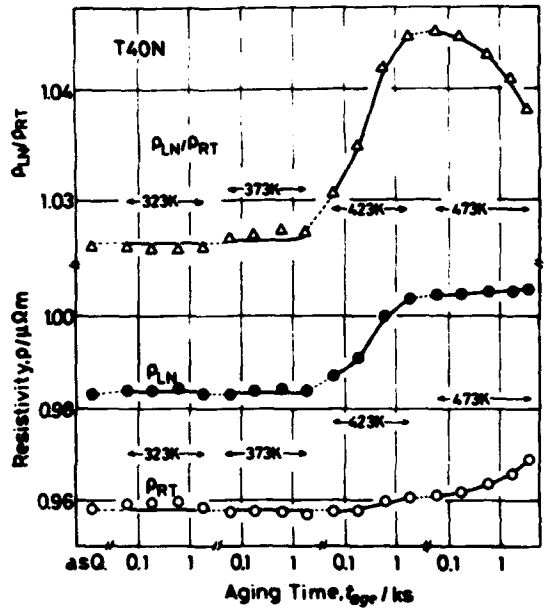


Fig. 5 ρ and ρ_{LN}/ρ_{RT} changes in T40N with aging below 473K.

Table 2 Assignation of direction of isothermal change in ρ and ρ_{LN}/ρ_{RT} for various phase transformations in β type Ti alloys.

	$\alpha'' \rightarrow \beta$	$\beta \rightarrow \begin{matrix}\beta_1+\beta_2 \\ (\beta+\omega_{p.e.}*)\end{matrix}$	$\beta \rightarrow \begin{matrix}\beta+\omega_{eq} \\ \beta+\alpha\end{matrix}$	$\alpha'' \rightarrow \alpha+\beta$
ρ_{LN}	++	+	−	−
ρ_{RT}	+	++	−	−
ρ_{LN}/ρ_{RT}	++	−	−	−

*$\omega_{p.e.}$ means pre-aged ω phase of very small size like G.P. zone in Al alloys.

4. Conclusions

From the X-ray diffraction profiles and measurements of ρ and its temperature dependence in Ti-Nb alloys, the following results were obtained.

1. A tendency toward NTD is lowered by existence of α'' in β.

2. The ω_s and ω_f show a tendency to be lowered with increasing Nb content.
3. So-called quenched ω can be considered as the athermal ω existing at room temperature with enough large volume fraction.
4. In 26 to 40%Nb alloys, increments of ρ_{LN} in initial stage of aging were larger than those of ρ_{RT}. This fact corresponded to the reverse transformation of α'' to β occurring initially by aging at relatively low temperatures.
5. The reverse transformation occurred slowly during aging at low temperatures, e.g. aging of T35N at 473K.

references

1. S.L.Ames, and A.D.McQuillan, "The Resistivity-Temperature-Concentration Relationship in The System Niobium-Titanium," Acta Met., 2(1954), 831-836.

2. J.C.Ho and E.W.Collings, "Anomalous Electrical Resistivity in Titanium-Molybdenum Alloys," Phys. Rev. B, 6(10)(1972), 3727-3738.

3. E.W.Collings, "Anomalous Electrical Resistivity, bcc Phase Stability, and Superconductivity in Titanium-Vanadium Alloys," Phys. Rev. B, 9(10)(1974), 3989-3999.

4. M.Ikeda et al., "Negative Temperature Dependence of Electrical Resistivity in Ti-Mo Binary Alloys," Proceedings of Sixth World Conference on Titanium, ed. P.Lacombe, R.Tricot, and G.Berange, (Societe Francaise de Metallurgie, 1988), 313-318.

5. M.Ikeda et al., "Resistometric Estimation of Temperature Range of Athermal ω Phase Formation in Quenched Ti-V Alloys," J.Japan Inst. Metals, 54(7)(1990), 743-751.

6. M.Ikeda et al., "Temperature Range of Formation of Athermal ω Phase in Quenched β Ti-Nb Alloys," J. Japan Inst. Metals, 52(12)(1988), 1206-1211.

7. M.Ikeda et al.,"Reverse Transformation of α'' and Initial β Decompostition in Quenched Ti-Nb Binary Alloys," J. Japan Inst. Metals, 53(7)(1989), 664-671.

8. A.T.Balcerzak and S.L.Sass, "The Formation of The ω Phase in Ti-Nb alloys," Met. Trans., 3(1972), 1601-1605.

9. K.S.Jepson, A.R.G.Brown, and J.A.Gray, "The Effect of Cooling Rate on The Beta Transformation in Titanium-Niobium and Titanium-Aluminium Alloys," The Science, Technology and Application on Titanium, ed. R.I.Jaffee and N.E.Promisel, (Oxford, Pergamon Press, 1970), 677-690.

10. S.Komatsu, "Aging Phenomena in Titanium Base Alloys," J. Japan Inst. Light Metals, 41(5)(1991), 344-352, Fig. 11.

11. C.Baker, "The Shape-Memory Effect in a Titanium-35wt%Niobium Alloy," Met. Sci. J., 5(1971), 92-100.

12. B.A.Hatt and V.G.Rivlin, "Phase Transformation in Superconducting Ti-Nb Alloys," Brit. J. Appl. Phys., 1(1968), 1145-1149.

THE EFFECT OF ALUMINIUM ON THE PHASE TRANSFORMATIONS IN Ti-19V AND 23V ALLOYS

T.Maeda and H.M.Flower*

Advanced Technology Research Laboratories, Sumitomo Metal Industries Ltd.
Amagasaki 660, Japan
*Department of Materials, Imperial College
London SW7 2BP, U.K.

Abstract

The influence of aluminium, an α former for titanium, in additions up to 10 wt% on the phase transformations in Ti-19 and 23wt%V, metastable β titanium alloys, have been studied in both athermal and isothermal processes. Five wt% of aluminium is necessary to completely suppress the athermal ω phase resulting in the minimum hardness in quenched Ti-19V alloy and, on the contrary, only solid solution hardening with aluminium additions was observed in Ti-23V alloy. In the isothermal process, 3wt% of aluminium addition substantially retards the ageing kinetics in both alloys and results in significantly long incubation times for α phase precipitation in the Ti-23V alloy. Aluminium additions to these alloys also strongly affect the morphology and the size of precipitated α phase.

Introduction

Near β and β titanium alloys are generally defined as the alloys in which martensitic transformation is completely suppressed when quenched from the β phase field, resulting in the retention of metastable β phase at room temperature[1]. The increase of β stability results in better cold workability due to the body centered cubic structure. Furthermore, these alloys can offer excellent strength compared to conventional $\alpha + \beta$ type alloys resulting from the substantial precipitation hardening on subsequent ageing in $\alpha + \beta$ field, which is very attractive especially for aerospace application.

Vanadium, a β -isomorphous element, is preferred to be used in commercial β titanium alloys because of its relatively light weight among β stabilizers and being isomorphous with titanium in β field. Aluminium is a typical α -former and an important element for the development of titanium alloys regardless of alloy type. The combination of these two elements coupled with other minor elements in alloying titanium have yielded a number of commercial near β and β titanium alloys such as Ti-10V-2Fe-3Al and Ti-15V-3Cr-3Sn-3Al. The authors have systematically studied the effects of aluminium on the phase transformations in Ti-11V[2] and 15V[3], in which a martensitic structure and a highly unstable β phase containing a large amount of athermal ω phase were obtained respectively. These works revealed that aluminium strongly influences the phase transformation behaviour in these systems.

Titanium '92
Science and Technology
Edited by F.H. Froes and I. Caplan
The Minerals, Metals & Materials Society, 1993

The purpose of the present paper is to study the effect of aluminium additions up to 10wt% on the β phase stability in athermal and isothermal processes in Ti-19V and 23V alloys, in which the quenched β phase is more stabilized than the above two alloys previously investigate.

Experimental

The alloy compositions examined were Ti-(19, 23)V-(0,3,5,7,10)Al(in wt%) and approximately 25 gramme rod shaped ingots of these compositions were obtained by Ar arc melting using high purity elemental components. All the ingots except 10%Al alloy were hot rolled at 873-973K to 1mm thick sheet. Oxygen and hydrogen contents in the descaled Ti-19V-5Al were 0.094 and 0.005wt% respectively so that similar levels for the other alloys can be expected. Small pieces of 10mm square were cut from the sheet and were solution treated at 1273K for 1.8ks followed by rapid quenching into iced water. Ageing behaviour in the alloys except for 10wt% aluminium was assessed by isothermal ageing between 573 and 873K for periods up to 600ks using conventional electric furnaces. In all the heat treatments, the samples were wrapped in molybdenum foil and sealed in silica capsules evacuated and filled with argon. The phase transformations were characterized by Vickers hardness measurement with 20kg load, microstructure observation using optical microscopy and transmission electron microscopy, X-ray diffractometry and electron diffractometry.

Results

Athermal Processes

All the alloys quenched from β field in both Ti-19 and 23%V systems exhibited single phase β regardless of aluminium concentration according to optical microscopy observations. The hardness and phase condition in quenched samples as functions of the aluminium concentration in the both systems are shown in Figure 1, in which the results on Ti-11%V[2] and 15%V[3] previously investigated by the authors are superimposed. The hardness of binary Ti-19%V alloy is considerably lower than that of the 15%V alloy but still higher than the 23%V alloy which exhibits the lowest hardness in the four binary alloys. Aluminium addition to the 19%V alloy results in the substantial decrease of hardness and attained the minimum at 5wt% and it increases again with the further addition, which is similar to behaviour observed in Ti-15%V alloy[3]. On

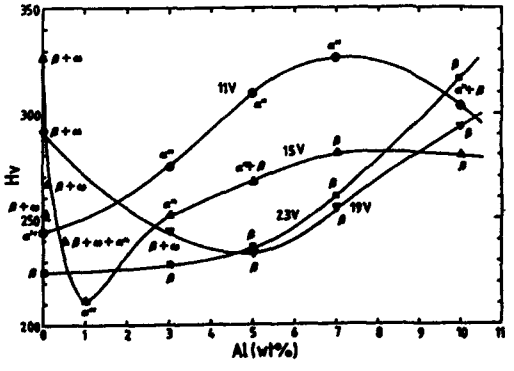


Figure 1-The hardness change with aluminium concentration in quenched Ti-V alloys.

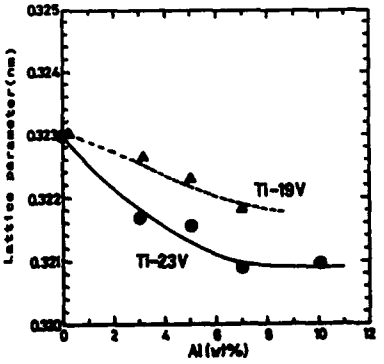


Figure 2- Lattice parameters of quenched β v.s. Al.

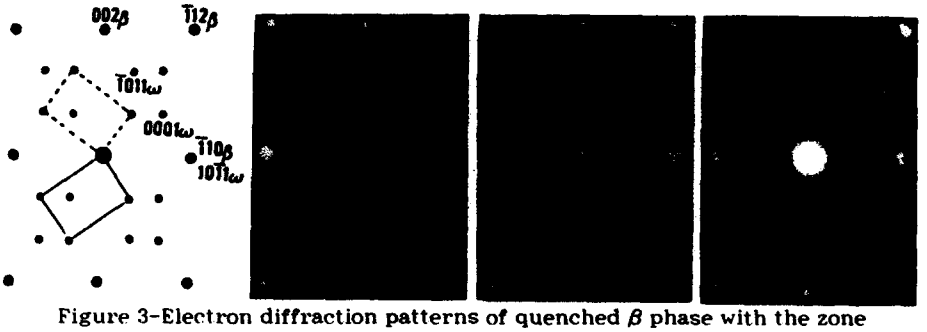


Figure 3-Electron diffraction patterns of quenched β phase with the zone axis [110] β in quenched β phase. (a)19V, (b)19V-3Al, (c)23V

the contrary, this behaviour was not observed in the Ti-23%V alloy in which the hardness simply increases with the aluminium addition and it exceeds the value in Ti-19V alloy at 5wt%. ω phase in the binary Ti-19V alloy was also detected by X-ray diffractometry and the hexagonal lattice parameters were determined to be a=0.464 and c=0.279nm, however it was not detected in the binary Ti-23V alloy. The variation of lattice parameter of quenched β phase with aluminium concentration in both systems is shown in Figure 2. The lattice parameters of quenched β phase decreases with aluminium addition as a result of substitution of titanium atoms by aluminium atoms.

Typical electron diffraction patterns of quenched β phase by TEM, obtained using the [110] β beam orientation, are shown in Figure 3. Distinct spots reflecting ω phase appeared in the binary Ti-19V alloy. These spots became faint with the addition of aluminium or the increase of vanadium by stabilizing the β phase and by suppressing the athermal ω phase, however diffuse streaking still remained even in sufficiently stabilized β phase as in Ti-23V-5Al. The above results indicate that hardness in quenched samples strongly depends on the volume of athermal ω phase present.

Isothermal Processes

Ti-19V System The age hardening behaviour between 573 and 873K in the binary and aluminium containing alloys is shown in Figure 4. The aluminium free alloy exhibits an enormous increase of hardness in early ageing time at the lower temperatures of 573 and 673K. The results show that 3% aluminium addition substantially changes ageing characteristics as in the Ti-15%V alloy[2]. Aluminium addition retards the age hardening response at short ageing times at 573 and 673K. It must be noted, however, that the hardness reaches almost the same level at longer aging times such as 600ks at 573K and 60ks at 673K. Dark field images through TEM in Ti-19V-Al alloys aged at 573K are shown in Figure 5. The binary alloy aged 0.6ks exhibits numerous fine isothermal ω phase reflecting the high hardness. The ω phase was coarsened and changed its morphology to cuboidal form at 600ks without significant decrease in hardness(Figure 5b) . The 3%Al containing alloy aged for 600ks also exhibits ω phase but the morphology is fine and ellipsoidal(Figure 5c) as in the above binary alloy aged for 0.6ks, indicating that aluminium retards the nucleation and the growth of ω phase as in the above athermal process. The 7%Al alloy aged for 600ks exhibits the fine and thin plate-like α phase which is sympathetically nucleated(Figure 5d). These results confirmed that the same hardness level can be achieved with completely different substructures, although the composition of the alloys is different.

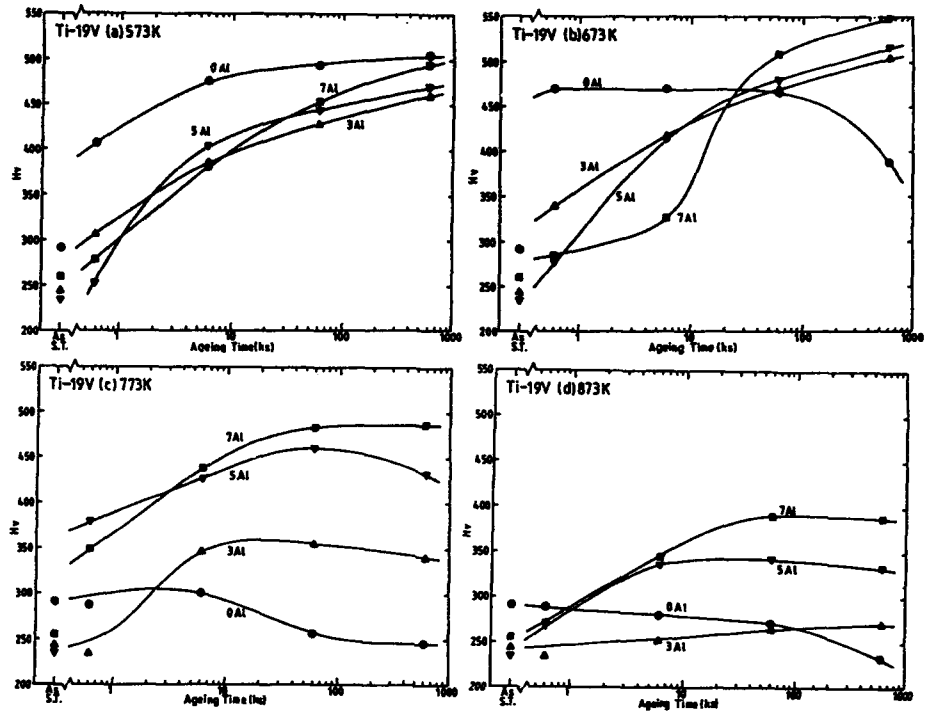


Figure 4-Age hardening curves for Ti-19V-Al alloys at (a)573K (b)673K (c)773K and (d)873K.

The hardness in the binary Ti-19V alloy decreases with longer ageing time at 773 and 873K. On the contrary, significant age hardening occurs in the aluminium containing alloys and the hardness obtained in longer ageing times longer than depends on the aluminium content. TEM micrographs in Ti-19V and Ti-19V-5Al alloys both aged at 773K for 60ks, in which the latter is substantially harder, are shown in Figure 6. The binary alloy shows well coarsened and elongated α phase particles which were formed during the ageing. 5%Al addition to this alloy results in the significant refinement of precipitated α particles, reflecting the higher hardness. These particles became smaller and thinner in proportion to aluminium content.

Ti-23V System Figure 7 shows age hardening response between 573 and 873K in the Ti-23V-Al alloys. The binary alloy exhibits substantial hardening from short ageing times at lower temperatures, e.g., 573 and 673K. However, incubation periods appeared in the other three aluminium containing alloys at all the ageing temperatures examined. Increasing aluminium content progressively increases incubation time at 573 and 673K, although, for a given aluminium content, incubation time decreases with increase in temperature. However, these aluminium contained alloys exhibit substantial hardening in ageing times of 60ks and longer. The TEM micrographs of the Ti-23V and Ti-23V-7Al alloys both aged at 573K for 60ks are shown in Figure 8. In the binary alloy, ω phase is observed in the former with a very high associated hardness as Hv490. In contrast, the two aluminium containing alloys exhibit small α particles nucleated on dislocations which sympathetically nucleate the heterogeneously distributed rafts of α which are associated with some what lower hardness values.

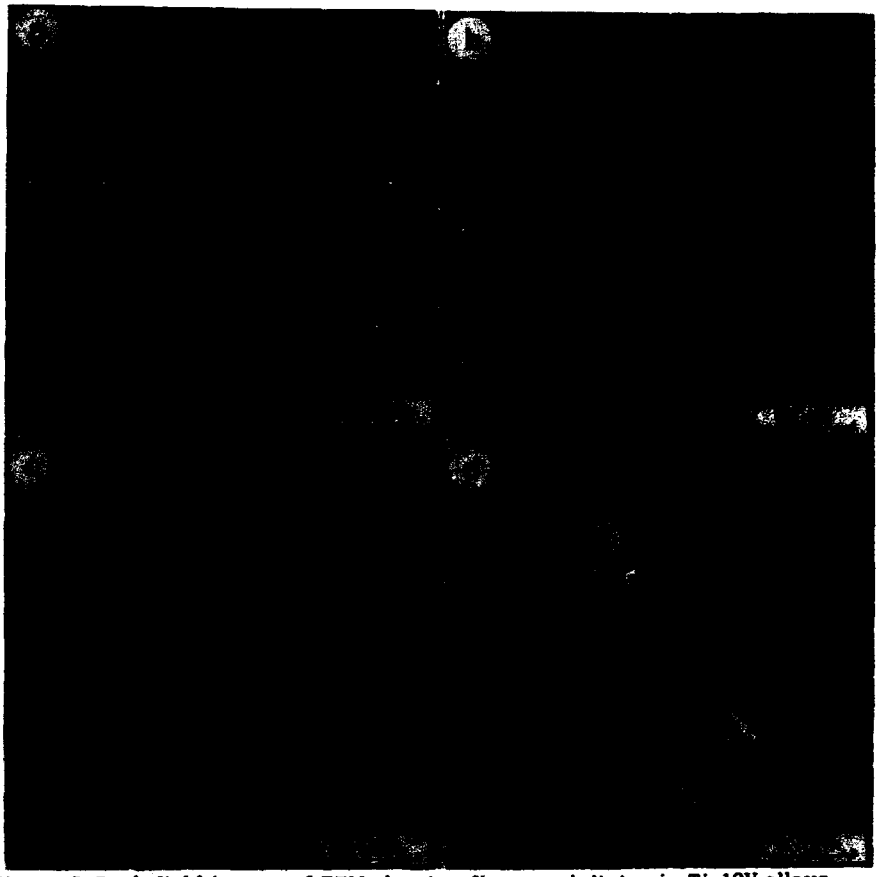


Figure 5-Dark field images of TEM showing fine precipitates in Ti-19V alloys aged at 573K. (a)0wt% for 0.6ks, g=(1$\bar{1}$01) ω, (b)0wt% for 600ks, g=(1$\bar{1}$01) ω (c)3wt%Al for 600ks g=(1$\bar{1}$01) ω, (d)7wt%Al for 600ks g=(01$\bar{1}$2) α.

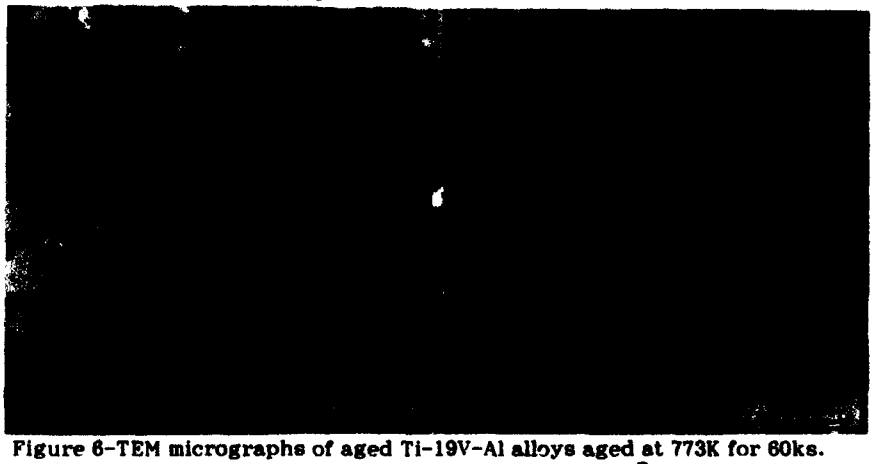


Figure 6-TEM micrographs of aged Ti-19V-Al alloys aged at 773K for 60ks. (a) 0wt% ,(b) 5wt%Al in dark field using two (01$\bar{1}$2) α reflections.

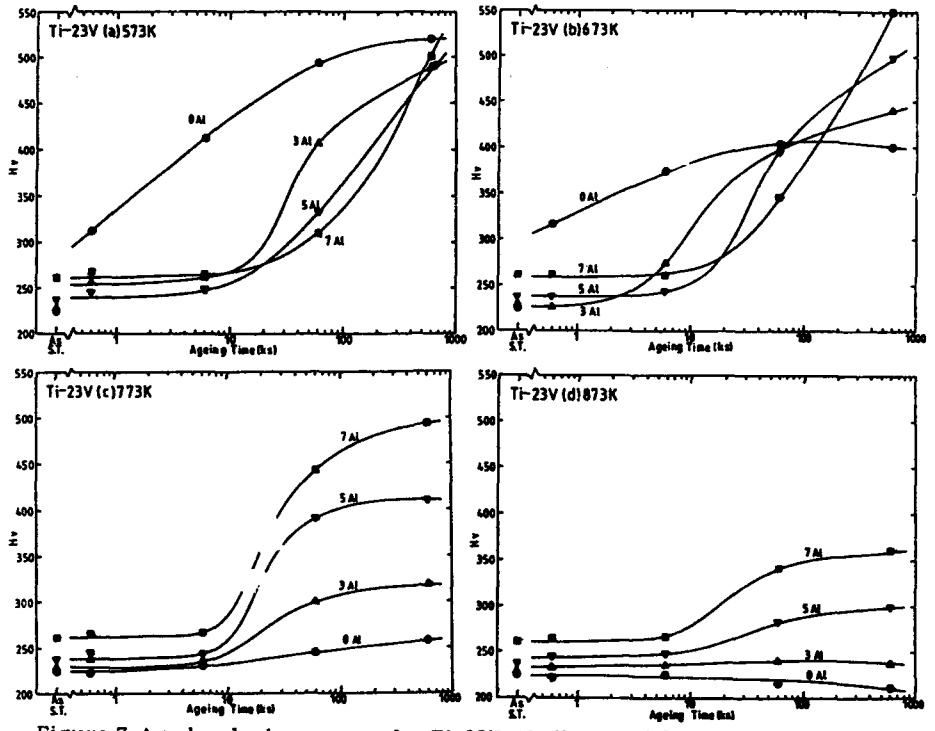


Figure 7-Age hardening curves for Ti-23V-Al alloys at (a)573K (b)673K (c)773K and (d)873K.

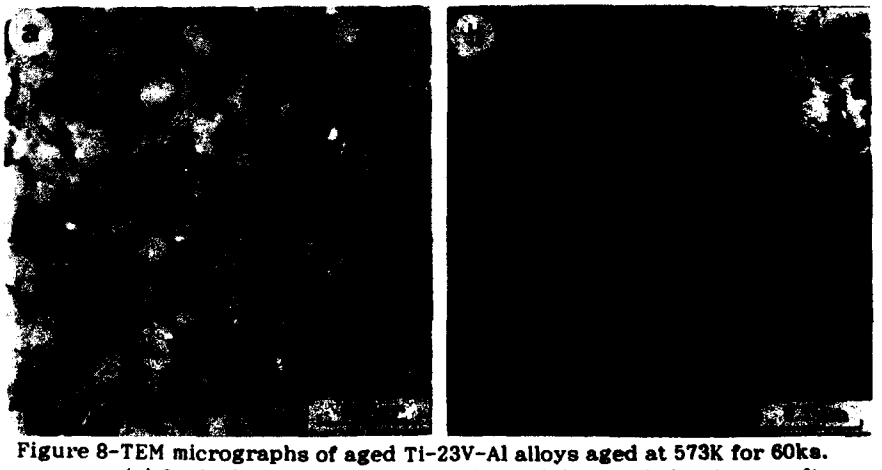


Figure 8-TEM micrographs of aged Ti-23V-Al alloys aged at 573K for 60ks. (a) 0wt% showing isothermal ω phase, (b) 7wt%Al showing α rafts.

At 773 and 873K, it is interesting to note that all the alloys examined exhibit very little age hardening when aged less than 6ks. However, age hardening is more significant in the alloys with higher aluminium concentration when aged 60ks and longer. Figure 9 shows the optical microstructure of the Ti-23V and

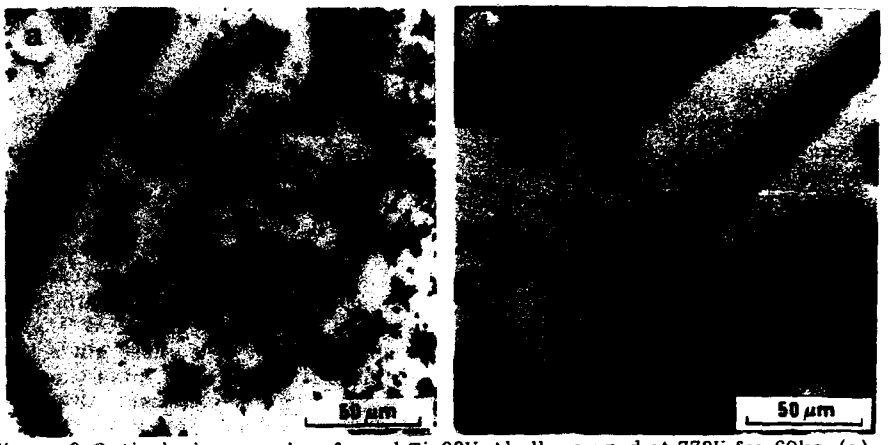


Figure 9-Optical micrographs of aged Ti-23V-Al alloys aged at 773K for 60ks. (a) 0wt%, (b)7wt%Al showing the precipitation free zone and grain boundary.

Ti-23V-3Al alloys both aged at 773K for 60ks, in which the hardness is 245 and 303 respectively. In the binary alloy, α phase precipitates heterogeneously on grain boundaries and as sympathetically nucleated rafts of plates in the β grains. The addition of 3% aluminium produces a higher volume fraction of finer α plates in rafts, which reflects the increase of hardness; however, the precipitation is rather heterogeneous as PFZ and precipitation free grain boundaries are observed. The Ti-23V-7Al alloy aged at 873K for 600ks exhibited blocky α phase which is ordered indicating the formation of $\alpha_2(Ti_3Al)$ phase.

Discussion

Athermal Processes

The hardness of binary Ti-19V alloy is significantly lower than that of the Ti-15V alloy which exhibits the most unstable β phase[3] in the Ti-V system. The quenched β phase in the Ti-19V alloy is still highly unstable and contains a large amount of athermal ω phase, which was confirmed by both X-ray and electron diffractometries. The increase of β stability by further addition of vanadium to 23% resulted in substantial decrease in hardness, reflecting the much lower volume fraction of ω phase in this alloy: it has previously been noted that such low volume fractions may not significantly affect the hardness[4].

The hardness of Ti-19V alloy also decreased as aluminium was added as a result of suppression of athermal ω phase as observed in the Ti-15V alloy[3]. The minimum in hardness with 5% aluminium and the disappearance ω spots with 3% aluminium suggested that 5% aluminium addition completely suppresses athermal ω phase in the Ti-19V alloy. This is consistent with the result on the Ti-20V-6Al alloy[5], in which only diffuse streaks were observed. Since the diffuse streaking was observed in highly stabilized alloys such as Ti-23V-5Al in the present study, this diffuse streaking may be related to other forms of instability of β phase, such as displacement defects[4] rather to the ω phase itself. These results suggest that aluminium addition shows the same effects of increasing the β stability. The decrease and increase in hardness by aluminium addition is interpreted as the competition between the depression of the ω_s temperature and the solid solution hardening of the β phase.

Isothermal Processes

The effects of aluminium on the isothermal ageing characteristics in the alloy systems investigated significantly differs at low(573-673K) and high(773-873K) temperatures. This relates to the different kinetics in precipitation and coarsening of α phase during ageing. The precipitation of α phase occurs via isothermal ω phase in both alloy systems with low aluminium concentration especially at lower ageing temperatures, otherwise α phase directly precipitates from the metastable β phase resulting in the heterogeneous microstructure shown above. The present results showed that aluminium additions to metastable β Ti-V alloys strongly suppress isothermal ω phase formation as well as athermal ω phase, which is consistent with the previous results in Ti-15V-Al[3] and Ti-20V-Al[6] alloys. This effect retards the precipitation of α phase since the formation of α phase through an transition phase ω needs much lower energy compared to one for the direct precipitation from the β phase. Although isothermal ω phase was confirmed in Ti-19V-3Al alloy as shown Figure 5c, the age hardening behaviour is close to those in the alloys with higher aluminium concentration rather than the binary alloy. This is attributed to the volume of ω phase contained is not being sufficient to dominate the total kinetics of isothermal transformation, which is reflected in the changes in the mechanical properties[7].

Acknowledgement

The present work was carried out at Imperial College of Science, Technology and Medicine. The financial support by Sumitomo Metal Industries, Ltd. is greatly acknowledged.

References

1. H.M.Flower, "Microstructural Development in Relation to hot working of Titanium Alloys," Mater. Sci. and Technol., 6(1990),1082-1092.

2. T.Maeda and H.M.Flower, "The Effects of Aluminium on the Phase Transformations in Ti-11%V, " Proc. of The Six World Conference on Titanium, ed. R. Lacomb, R. Tricot and G. Beranger, (Les Editions de Phisique, 1989), 1629-1634.

3. T.Maeda and H.M.Flower, "The Effects of Aluminium on the Phase Transformations in Ti-15%V, " ibid., 1589-1594.

4. J.C.Williams, D.de Fontaine and N.E.Paton, "The ω -Phase as an Example of an Unusual Shear Transformation," Metall. Trans., 4(1973), 2701-2708.

5. S.Hanada and O.Izumi, "Correlation of Tensile Properties, Deformation Modes and Phase Stability in Commercial β -Phase Titanium Alloys," Metall. Trans., 18A(1987), 265-271.

6. J.C.Williams, B.S.Hickman and D.H.Leslie, "The Effect of Ternary Additions on the Decomposition on Metastable Beta-Phase Titanium Alloys," Metall. Trans., 2(1971), 477-484.

7. J.C.Williams, B.S.Hickman and H.L.Marcus, "The Effect of Omega Phase on the Mechanical Properties of Titanium Alloys," Metall. Trans., 2(1971), 1913-1919.

HIGH TEMPERATURE PHASE EQUILIBRIA IN THE

Ti-Al-Ta TERNARY SYSTEM

T. J. Jewett, S. Das and J. H. Perepezko

Department of Materials Science and Engineering
University of Wisconsin-Madison
1509 University Avenue
Madison, WI 53706

Abstract

An investigation of the phase equilibria and the phase stability in the Ti-Al-Ta system has resulted in the refinement of the 1100° C isothermal section. Major revisions include the extension of the binary δ (Al_2Ta) and ϵ (AlTa) phases into the ternary phase field and the establishment of the B2 phase field. Quenching studies have allowed for the construction of a preliminary 1440° C isothermal section. Stable two phase regions in the 1440° C isothermal section include the β (bcc) - σ ($AlTa_2$), σ - α (hcp), σ - δ and δ - η (Al_3Ta) phase fields. The solid-state phase transformations that result in the formation of the ϵ phase were determined by quenching studies and information obtained from differential thermal analysis, x-ray diffraction and electron microprobe analysis. These studies provide a useful lesson on the reaction pathways involved in the approach to phase equilibria in high temperature intermetallic systems. In addition, the kinetics and the microstructural characteristics of the order-disorder, B2 - β, transformation have been studied.

Introduction

As a result of the recent interest in high temperature alloy development, intermetallic compounds including a variety of titanium aluminides have received considerable attention. Work on these systems has been centered on the development of high temperature structural materials. Among the information necessary for the development of such alloys and their processing are accurate data regarding the phase equilibria and phase transitions in the system of interest. One alloy system that has been examined recently is the Ti-Al-Ta ternary system. To date, work on the Ti-Al-Ta system has consisted of several limited studies of various isothermal sections [1-4]. The current work expands upon the previous examinations by providing additional detail on the phase equilibria at 1100° C and 1400° C.

Experimental Procedures

Bulk alloy samples were prepared from Al(99.999%), Ti(99.8%) and Ta(99.98%) by repeated arc-melting in a gettered, argon atmosphere. Bulk samples were homogenized at either 1200° C or 1300° C for periods up to 2 weeks in a gettered, argon atmosphere. The samples were then re-equilibrated for 24 - 72 hours at the temperature of interest in a vertical quench furnace in a purified argon atmosphere, and then quenched into a brine solution with a minimum cooling rate of about 800° C/sec.

The annealed samples, and a number of the as-cast samples, were checked for

Titanium '92
Science and Technology
Edited by F.H. Froes and I. Caplan
The Minerals, Metals & Materials Society, 1993

compositional variation by chemical analysis from several places within the ingots. The ingots were found to contain no gross inhomogeneities and the annealed samples were found to have low interstitial impurities. In general, the oxygen levels were below 1000 wt ppm and the carbon, nitrogen and hydrogen levels were at least an order of magnitude lower. Phase equilibria in the equilibrated samples were determined by optical and scanning electron microscopy (SEM), x-ray diffraction (XRD), electron microprobe analysis (EMPA), transmission electron microscopy (TEM) and differential thermal analysis (DTA).

Results and Discussion

1100° C Isothermal Section

An investigation of the 1100° C isothermal section of the Ti-Al-Ta system has indicated extensive solubility of several phases in the ternary phase field, Figure 1. These include the β (bcc-Ti), B2 (Ti_2AlTa - CsCl structure), α_2 (Ti_3Al-DO_{19}), γ (TiAl-$L1_0$), σ (Ta_2Al-$D8_b$) and η ($Al_3(Ti,Ta)$-DO_{22}) phases. The remaining phases present at this temperature; the α (hcp-Ti), δ (Al_2Ta or Al_3Ta_2 -tentatively identified as a complex bcc with $a_0 \simeq 19.3$ nm [5,6]) and ϵ (TaAl-tentatively identified as a monoclinic [6] phase) exhibit narrower or less extensive solubilities than the aforementioned phases. Due to problems retaining single phase β or B2, in alloys containing greater than about 50 at% Ti and greater than about 20 at% Al, the extent of the β, α and α_2 phase fields into the ternary systems were determined from diffusion couple studies. The resulting diagram closely resembles that of the 1200° C section of the Ti-Al-Nb system [7] and the high temperature Ti-Al-Mo system [8].

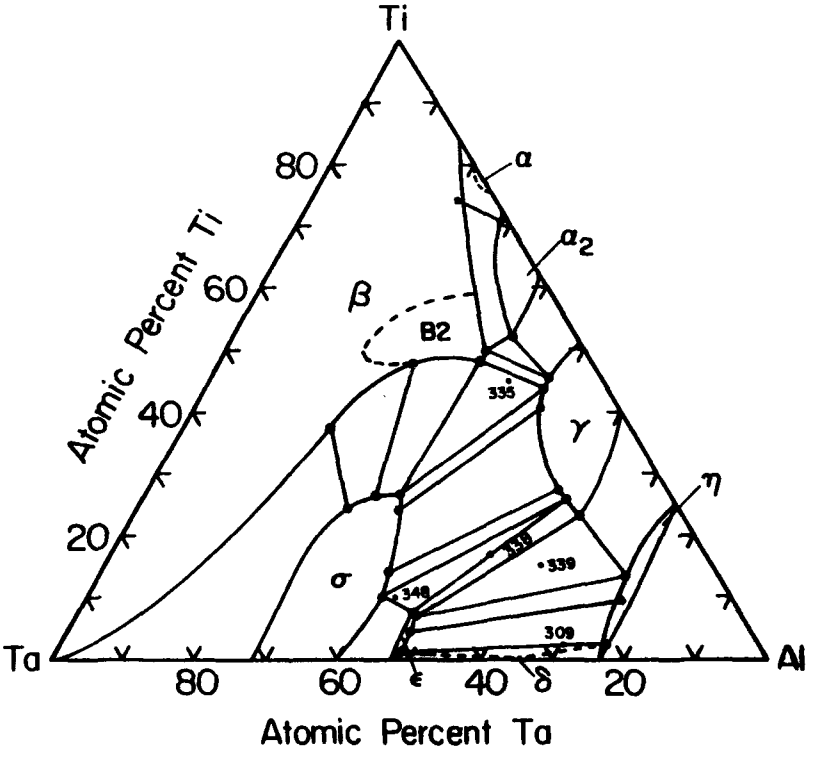


Figure 1 - The 1100° C isothermal section of the Ti-Al-Ta ternary system.

The difficulty in retaining the single-phase β appears to result from the inability to suppress low temperature phase transformations upon cooling. This problem was alleviated in part by using diffusion couples to probe this region of the phase diagram. Sometimes it is not possible to obtain elevated temperature phase equilibria information from bulk annealed samples due to some unavoidable phase transformation(s) during the cooling of the samples. In this case, diffusion couple experiments can play a major role in establishing the tie-lines. The diffusion couple measurements provide a retention of the composition information established during the interface equilibration at high temperature during the annealing treatment. Upon cooling a diffusion couple, this compositional information is retained, even though the structural identity of the phases involved in the high temperature interfacial equilibrium may have undergone alteration to other crystal structures. One point of caution is that the cooling rate of the diffusion couple must be rapid enough so that the size scale of any decomposition is smaller than the electron microprobe sampling size.

The various three-phase fields identified in this isothermal section include the η - δ - ϵ, η - δ - γ, δ - γ - σ and γ - σ - B2 fields. Representative micrographs of the samples from these phase fields are shown in Figure 2. The compositions of the individual phases in each of the three-phase fields were determined by EMPA of the quenched bulk alloy ingots, see Table I. However, the composition of the ϵ phase in the η - δ - ϵ field and the γ phase in the δ - γ - σ field had to be interpolated because the size of these regions was much smaller than the electron probe size.

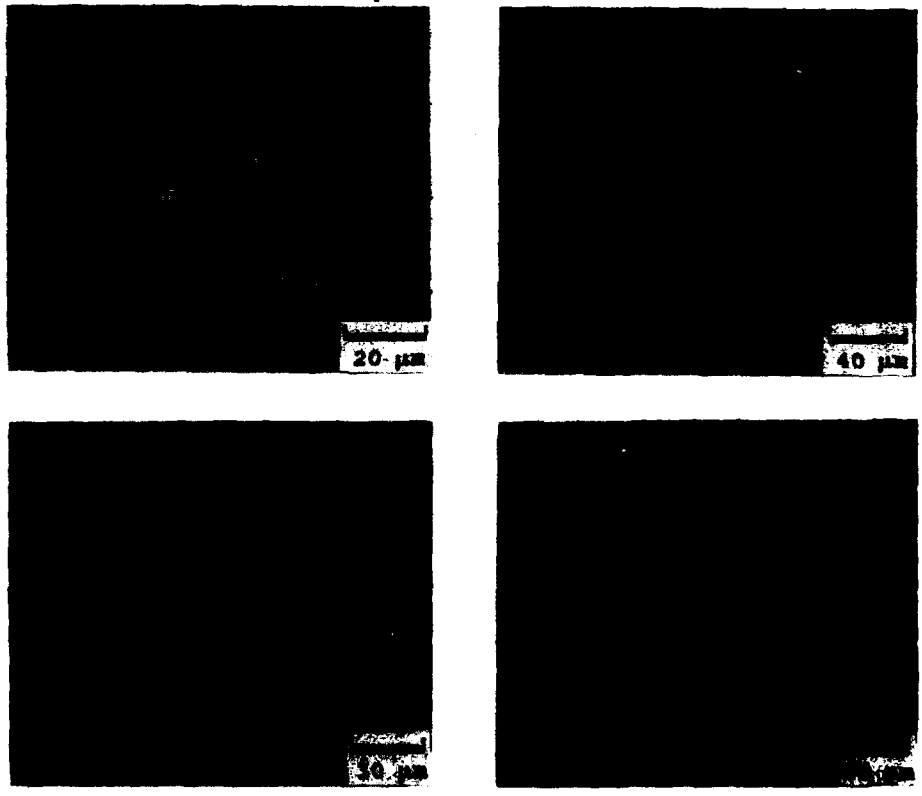


Figure 2 - A) Micrograph of alloy 348 (Ti-43.5Al-46.5Ta), B) micrograph of alloy 339 (Ti-60Al-25Ta), C) micrograph of alloy 309 (Ti-70Al-27Ta), D) Micrograph of alloy 335 (Ti-43Al-12Ta): all annealed for 72 hours at 1100° C and then quenched into brine.

Table I Ingot Composition and Phase Identification at 1100° C with Compositions Given in Atomic Percent.

Sample Number	Composition Ti	Al	Ta	Phase	Phase Composition Ti	Al	Ta
335	45.0	42.9	12.1	σ	27.3	36.3	36.4
				γ	43.7	47.5	8.8
				B2	47.6	37.2	15.2
338	18.0	51.4	30.6	σ	-----	-----	-----
				γ	26.3	60.1	13.6
				ϵ	8.6	48.1	43.3
339	15.1	59.8	25.1	ϵ	7.2	48.1	44.7
				γ	23.2	62.6	14.2
				η	14.0	73.4	12.6
309	3.0	70.0	27.0	ϵ	0.9	49.7	49.4
				η	3.1	77.3	19.6
				δ	-----	-----	-----
348	10.0	43.5	46.5	σ	10.0	41.5	48.5
				γ	25.3	60.2	14.5
				ϵ	7.5	48.0	44.5

Note: The compositions denoted as ----- indicate that the phase regions were smaller than the spot size of the EMPA.

The initial phase equilibria work, involving both diffusion couple and bulk alloy studies, definitely indicated the presence of a ternary phase (B2) near the composition Ti_2AlTa [3]. The extent of the B2 phase field has yet to be fully established at 1100° C. However, work to date has shown that the B2 phase field extends at least to the composition of alloy 345, Ti-30Al-20Ta. A transmission electron micrograph and the selected area electron diffraction patterns (SADP) of the B2 phase present in alloy 203, Ti-33Al-20Ta, are shown in Figure 3. The ternary phase is indicated in the micrograph as B2, the second phase regions are probably α_2. Several diffraction patterns were obtained with the incident electron beam parallel to all the major low index zone axes of the ternary phase. The <001>, <011>, <111> and <012> patterns are shown in Figure 3. These diffraction patterns, except for the <111>, contain superlattice spots as indicated by arrows. From the subsequent analysis it is clear that the crystal structure of the ternary phase is ordered bcc, B2. The <011> SADP of Figure 3 was obtained at a very long exposure time and shows diffuse intensity maxima at $\mathbf{g} = 2/3\langle 211\rangle$ and $\mathbf{g} = 1/3\langle 111\rangle$. The diffuse intensity maxima may arise due to the development of the ordered ω-related phase. The ω-related phase forms as a decomposition product from the B2 phase during aging or cooling. A detailed study on the ordering of the B2 phase in the alloy Ti-33Al-17Ta has been published [9]. Thermal analysis suggests that the ordering of the B2 phase is most likely taking place around 1200° C. No temperature hysteresis was observed for this transformation with the change in heating and cooling rates in DTA experiments. Thermal antiphase boundaries were also observed in the B2 phase, suggesting a solid-state ordering reaction. On the basis of these results, it was inferred that the ordering of the B2 phase is most likely a second-order phase transformation.

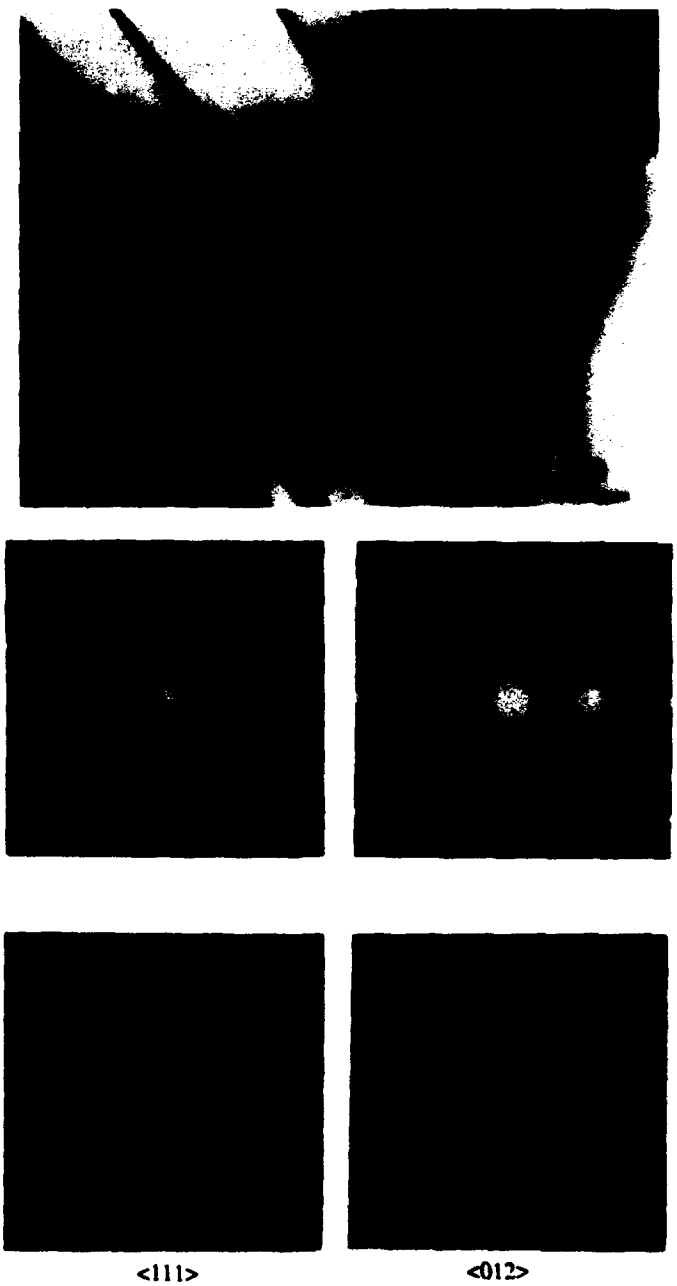


Figure 3 - The transmission electron micrograph of the Ti-33Al-20Ta sample showing the B2 phase and the plate like second phase (probably α_2) along with a set of selected area electron diffraction patterns obtained from the B2 phase.

1440° C Isothermal Section

In attempting to determine the thermal stability of the ϵ (TaAl) phase several alloys were quenched from 1440° C. The choice of this temperature was due in part to experimental data from DTA measurements and in part to furnace temperature limitations. This data was combined with that from several other groups [6,10,11] to produce a composite isothermal section, Figure 4 [12]. This diagram was subsequently adopted by Weaver et al. [13]. The three-phase fields identified at this temperature include the σ - δ - α, the σ - β - α, the δ - η - γ and the η - γ - L.

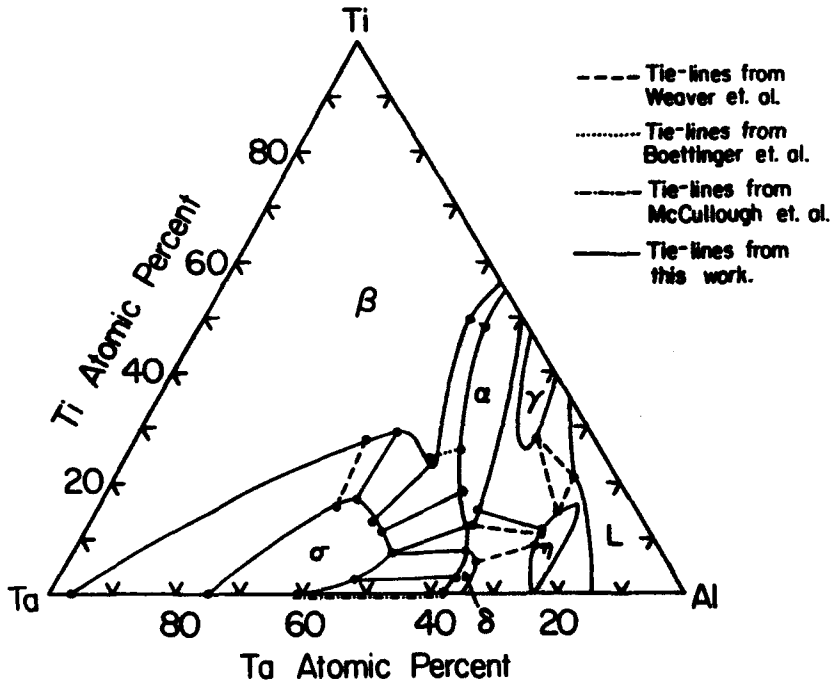


Figure 4 - The 1440° C isothermal section of the Ti-Al-Ta ternary system.

Although only the σ - δ - α and the η - γ - L three-phase fields are identified on the diagram, Figure 4, the other three-phase fields can be extrapolated from the given two -phase tie-lines. The σ - β - α and δ - η - α three-phase fields have been omitted from the diagram due to the possible confusion the extra tie-lines may cause. The σ - β - α three-phase field is bounded by the σ - β and the σ - α two-phase tie-lines determined by this work. X-ray analysis of the quenched sample indicates the presence of β in the sample yielding the σ - α two-phase tie-line, but the β regions were too small to focus on using EMPA. The δ - α - η three-phase field is bounded by the δ - η and the α - η tie-lines given by Weaver et al. [11] and by the σ - α - δ three-phase field from this work.

Another item to note about the 1440° C isothermal section is the absence of the ϵ phase. Work by McCullough et al. [6] indicates that the ϵ phase does not exist at 1440° C, as shown by their σ - δ two phase tie-line. Quenching and DTA studies of the alloys in this region revealed that the solubility of the ϵ phase, into the ternary field, decreases as the temperature is increased from 1100° C, eventually disappearing via a peritectoid reaction. At the same time, the δ phase, which has almost no solubility into the ternary field at 1100° C, steadily extends into the ternary as the temperature increases.

Conclusions

This study has resulted in the establishment of the phase equilibria at 1100° C in the Ti-Al-Ta ternary system. In addition, the phase equilibria of this isothermal section have been shown to be consistent with the high temperature phase equilibria for other chemically similar systems of Ti-Al-M, where M is Nb or Mo. The existence of the δ, B2 and ϵ phases and their solubilities were determined for the 1100° C isothermal section. Initial information of the phase equilibria at 1440° C has allowed a preliminary isothermal section to be constructed. Based on these two sections, it is apparent that alloys in the region of $TiTaAl_2$ undergo significant phase transformations between these temperatures. Knowledge of these reactions and those of other regions of interest in the phase diagram will greatly aid in the processing of such alloys.

Acknowledgements

The authors would like to thank Dr. R Hecht and Dr. M. Maloney of Pratt & Whiney for supplying many of the ingots used in this study, Dr. C. McCullough and Dr. C. Levi of the University of California at Santa Barbara and Dr. Y. L. Tian and Mr. J. C. Mishurda of the University of Wisconsin-Madison for their help and insightful discussions during the course of this research. The support of DARPA (URI/N 0014-K-0753 P.O. VB 38640-0) is gratefully acknowledged.

References

1. A. Raman, Z. Metallkde., 57 (1966), 535.

2. S. Sridharan and H. Nowotny, Z. Metallkde., 74 (1983), 468.

3. S. Das et al., Microstructure/Property Relationships in Titanium Aluminides and Alloys, ed. Y. W. Kim and R. R. Boyer (Warrendale, PA: The Metallurgical Society, 1991), 31.

4. C. McCullough et al., Acta Metall., 39 (1991), 31.

5. D. Miracle, private communication with author, University of California, Santa Barbara, 3 January 1991.

6. C. McCullough, private communication with author, University of California, Santa Barbara, 3-5 January 1991.

7. T. J. Jewett, S. Das and J. H. Perepezko, in preparation.

8. H. Margolin, J. P. Nielson and H. K. Work, "Titanium Phase Diagram Study" (Report DA-30-069-ORD-208, Watertown Arsenal Laboratory, 1954).

9. S. Das and J. H. Perepezko, Light Weight Alloys for Aerospace Applications II, (Warrendale, PA: The Metallurgical Society, 1991), 453.

10. W. J. Boettinger et al., Scripta Mettal. et Mater., 25 (1991), 1993.

11. M. L. Weaver et al. Mat. Res. Soc. Symp. Proc., 213 (1991), 163.

12. T. J. Jewett, S. Das and J. H. Perepezko, "High Temperature Phase Equilibria in the Ti-Al-Ta Ternary System" (Paper Presented at the Fall 1991 TMS Annual Meeting, Cincinatti, OH, 23 October 1991).

13. M. L. Weaver and M. J. Kaufman, Scripta Mettal. et Mater., 26 (1992), 411.

ON THE NATURE OF ORTHORHOMBIC SYMMETRY OF MARTENSITE IN TITANIUM ALLOYS

O.M. Ivasishin and N.S. Kosenko

Institute for Metal Physics
36 Vernadsky str.
252142 Kiev, Ukraine

Abstract

A new explanation of the crystalline lattice symmetry of martensite phases in titanium alloyed by isomorphic β-stabilizing elements is given. Beginning from some critical solute content elastic stresses arising at coherent conjugating in two-dimensionally modulated structure of the martensite, spinodal decomposition were shown to lead to transition from hexagonal to orthorhombic symmetry.

Introduction

In titanium alloys with an increase in the isomorphic β-stabilizing element (Mo,Ta,Re,Nb,W,V) content the $a=b/\sqrt{3}$ relationship between the martensite lattice parameters, which is true for hexagonal lattice, gradually disturbs and splitting of some x-ray diffraction maxima is observed [1]. For instance, the [110] line of hexagonal martensite splits on two lines [200] and [130]. Since the angular positions of the new lines correspond to an orthorhombic lattice, the conclusion about new type of martensite, α''-martensite, which differs from hexagonal α'-martensite by lattice symmetry was made [1]. Attempts were made to explain the transition of hexagonal lattice to orthorhombic by superposition of the ordering on the martensitic transformation [2] or by the influence of impurities [3]. Nevertheless, these explanations were not verified by the experimental results. Another point of view, which has not been proven, consists of the assumption that the α''-martensite is not an independent phase and must be thought as α'-martensite distorted due to the increase of the alloying element content [4].

Titanium '92
Science and Technology
Edited by F.H. Froes and I. Caplan
The Minerals, Metals & Materials Society, 1993

In the current investigation, a new explanation for the nature of the martensite lattice symmetry transition, based on experimental data [5],is given. According to [5], spinodal decomposition of α''-martensite in Ti-Mo and Ti-V alloys takes place on quenching and aging. As a result of decomposition, a modulated structure with periodic distribution (the period is about 2.0-2.5nm) of enriched and depleted in solute regions is formed. The $\alpha'+\alpha''$ transition is explained as the phase transformation of the second order. However,it is considered that the spinodal decomposition occurs in martensite with *orthorhombic* lattice.

Model

The following model of α''-martensite formation is offered in this paper. The high-temperature BCC phase transforms on quenching to *hexagonal* martensite. Beginning from some concentration of the solute (for the Ti-Mo alloys this concentration is about 4 wt% Mo) the transformation takes place within the chemical spinodal. This results in decomposition of martensite on two *hexagonal* phases which differ both from each other and from the matrix by the composition and the specific volume. It was established earlier [6],that elastic stresses arising at coherent conjugation of cubic phases with different lattice parameters can lead to changing of cubic symmetry to tetragonal. The nature of such tetragonality is explained by the tendency of the system to minimize the elastic energy. According to [6], a two-dimensional periodic macrolattice is formed on spinodal decomposition of cubic solid solution. The rods of the two phases (composition C_1 and C_2) with square cross sections and rods of third phase (composition $C_3 = (C_1+C_2)/2$) with rectangular cross sections are forming the macrolattice. Experimental observations [5] allow to suppose that two-dimensional periodic macrolattice also is formed on decomposition of the titanium martensite. All the rods are elongated along the [0001] and have the habit plane $(n_1,n_2,0)$, which varies from (340) to (110) [5] in rhombic coordinates depending upon the duration and temperature of aging. Proceeding from the orientation of the habit of the precipitation [5], the assumption can be put forward that the crystallographic axes $\langle n_1,n_2,0\rangle$ are the directions of composition modulation, while in alloys with cubic lattice the modulations proceed along the cubic directions.

The two-dimensional distribution of concentration in a three-phase complex is described by the function [6] :

$$C(\bar{r}) = C^{m_1,n_2,\alpha_1} + C^{m_1,\bar{n}_2,\alpha_2}, \qquad (1)$$

which is a superposition of the two one-dimensional distributions along the

$[n_1, n_2, o]$ and $[n_1, \bar{n}_2, o]$ directions. Distribution (1) gives three values of concentration only when each of the functions, $C^{[n_1, n_2, o]}$ and $C^{[n_1, \bar{n}_2, o]}$, has two values only, $[C_1 - \bar{C}] / 2$ and $[C_2 - \bar{C}] / 2$. Here the C_1 and C_2 are close to equilibrium values, i.e. they correspond to minima at the free energy curve (Fig. 1) and the $C_3 = [C_1 + C_2]/2$ corresponds to maximum of this curve, i.e. is close to the composition of the initial solid solution. Such a three-phase composition corresponds to free energy minimum of the complex with two-dimensional distribution (1). Nevertheless, this minimum is not absolute since one structural part of the complex has the composition C_3 which is close to the composition of the initial martensite and its metastable state is ensured by competition between elastic and surface energies [6]. Therefore the rods with the composition C_3 have a tendency for secondary decomposition which leads to modulation of the composition along the [0001] axis and to the formation of plates of C_1 and C_2 compositions normal to this direction.

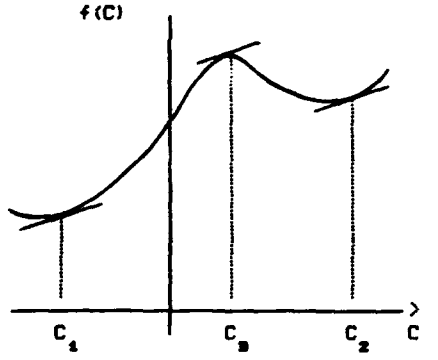


Figure 1. Free energy curve for spinodal decomposition of solid solution.

Theory

As a result of coherent conjugation of spinodal decomposition products, internal stresses (elastic deformations) arise inside the martensite plates. These stresses can significantly change not only the parameters, but symmetry as well of crystalline lattices. We suppose that structural deformation $\varepsilon^{\circ}_{ij}(\bar{r})$ attributed to concentrational inhomogeneities $\Delta C(\bar{r}) = C(\bar{r}) - \bar{C}$ is described by the Vegard rule:

$$\varepsilon^{\circ}_{ij}(\bar{r}) = U_o \, \delta_{ij} \, \Delta C(\bar{r}), \qquad (2)$$

where $U_o = \frac{1}{a} \frac{da}{dc}$ is a concentrational factor of hexagonal lattice expansion in the basal plane. Then the stress tensor corresponding to deformation (2) is as follows:

$$\sigma^{\circ}_{ij}(\bar{r}) = S_{ij\beta m} \varepsilon^{\circ}_{lm}(\bar{r}) = (2K_1 + K_3) U_o \, \delta_{ij} \, \Delta C(\bar{r}), \qquad (3)$$

where $S_{ij\beta m}$ is a tensor of modulus while $K_1 = \frac{1}{3}(C_{11} + C_{12} + C_{13})$ and $K_3 = \frac{1}{3}(C_{33} + 2C_{13})$ are the bulk moduli of the hexagonal crystal.

According to [6], the energy of internal stresses of non-homogeneous solid solution E can be calculated:

$$E = \frac{1}{2}\int \frac{d^3k}{(2\pi)^3} B(\bar{\frac{k}{k}}) |\check{C}(\bar{k})|^2; \qquad \check{C}(\bar{k}) = \int d^3r\, [C(\bar{r})-\bar{C}] \exp[-i\bar{k}\bar{r}]. \quad (4)$$

For an hexagonal crystal, the effective elastic modulus $B(\bar{\frac{k}{k}})$ depends on the boundary orientation $\bar{n}$:

$$B(\bar{\frac{k}{k}}) = B(\bar{n}) = 3KU_o^2[1-3n_i\Omega_{ij}^{-1}(\bar{n})n_j], \quad (5)$$

where $K=(2K_1+K_3)$, $\Omega_{ij}^{-1}(\bar{n})=(B_{imnj}n_m n_n)^{-1}$. It follows from (4) that the deformation of the crystalline lattice is connected with the concentrational distribution (1):

$$\varepsilon_{ij}(\bar{r}) = \frac{KU_o}{2}\int [n_i\Omega_{jl}^{-1}(\bar{n})n_l + n_j\Omega_{il}^{-1}(\bar{n})n_l]\,\check{C}(\bar{k})e^{i\bar{k}\bar{r}}\frac{d^3k}{(2\pi)^3}. \quad (6)$$

If the tensor components $\Omega_{ij}^{-1}(\bar{n})$ from [7] are used, the expression (6) for narrow and long rods with the habit planes $\bar{n} = [n_1,n_2,0]$ and $[n_1,\bar{n}_2,0]$ becomes:

$$\varepsilon_{ij}(\bar{r}) = \frac{KU_o}{C_{11}}\left[\begin{bmatrix} n_1^2 & n_1n_2 & 0 \\ n_1n_2 & n_2^2 & 0 \\ 0 & 0 & 0 \end{bmatrix} C^{[n_1n_2o]} + \begin{bmatrix} n_1^2 & -n_1n_2 & 0 \\ -n_1n_2 & n_2^2 & 0 \\ 0 & 0 & 0 \end{bmatrix} C^{[n_1\bar{n}_2o]}\right]. \quad (7)$$

From (7) the values of lattice parameters for all three stressed phases appearing on martensite decomposition can be easily obtained.

Phase I. Since the depleted phase (composition C_1) satisfy the condition $C^{[n_1n_2o]} = C^{[n_1\bar{n}_2o]} = (C_1-\bar{C})/2$, its lattice is subjected to deformation:

$$\varepsilon_{ij}(I) = \frac{KU_o}{C_{11}}(C_1-\bar{C})\begin{bmatrix} n_1^2 & 0 & 0 \\ 0 & n_2^2 & 0 \\ 0 & 0 & 0 \end{bmatrix} \quad (8)$$

Hence, the phase I will have the following lattice parameters:

$$a_I = \bar{a}[1+\varepsilon_{xx}(I)] = \bar{a} + \frac{K}{C_{11}}(a_I^o-\bar{a})n_1^2,$$

$$b_I = \bar{b}[1+\varepsilon_{yy}(I)] = \bar{b} + \frac{K}{C_{11}}(b_I^o-\bar{b})n_2^2, \quad c_I = \bar{c}, \quad (9)$$

where $a_I^o = b_I^o/\sqrt{3} = \bar{a}[1+U_o(C_1-\bar{C})]$ are the lattice parameters of phase I free from stresses.

Phase II. For the enriched phase (composition C_2) $C^{[n_1n_2o]} = C^{[n_1\bar{n}_2o]} = (C_2-\bar{C})/2$ and therefore lattice parameters of the phase II are:

$$a_{II} = \bar{a} + \frac{K}{C_{11}}(a_{II}^o-\bar{a})n_1^2, \quad b_{II} = \bar{b} + \frac{K}{C_{11}}(b_{II}^o-\bar{b})n_2^2, \quad c_{II} = \bar{c}, \quad (10)$$

where $a^{\circ}_{II}=b^{\circ}_{II}/\sqrt{3}=\bar{a}[1+U_o(C_2-\bar{C})]$ are the lattice parameters of phase II free from stresses.

It should be noted that at $n_1^2 \neq n_2^2$, both phases are orthorhombically distorted since the relationship $a = b/\sqrt{3}$ is not fulfilled.

Phase III. For the phase with intermediate composition $C_3=(C_1+C_2)/2$, two cases are possible:

$$1.\quad C^{[n_1 n_2 o]} = (C_1-\bar{C})/2\,, \quad C^{[n_1 \bar{n}_2 o]} = 0\,.$$

$$2.\quad C^{[n_1 n_2 o]} = 0\,, \quad C^{[n_1 \bar{n}_2 o]} = (C_2-\bar{C})/2\,.$$

The corresponding deformations and lattice parameters are given by:

$$1.\quad a_{III'} = \bar{a} + \frac{K}{2C_{11}}(a^{\circ}_2 - \bar{a})\,n_1^2\,,$$

$$b_{III'} = \bar{b} + \frac{K}{2C_{11}}(b^{\circ}_2 - \bar{b})\,n_2^2\,, \quad c_{III'} = \bar{c}\,, \qquad (11)$$

$$2.\quad a_{III''} = \bar{a} + \frac{K}{2C_{11}}(a^{\circ}_{II} - \bar{a})\,n_1^2\,,$$

$$b_{III''} = \bar{b} + \frac{K}{2C_{11}}(b^{\circ}_{II} - \bar{b})\,n_2^2\,, \quad c_{III''} = \bar{c}\,, \qquad (12)$$

Since the non-diagonal elements of deformation tensors for phase III are non-zero, it is subjected to rhombic distortions and the angle between the $[2\bar{1}\bar{1}0]$ and $[01\bar{1}0]$ directions in the phase III' becomes $90^{\circ}-\beta'$, where:

$$\beta' \approx \varepsilon_{12}(III') = \frac{K}{2C_{11}}\,\frac{(b^{\circ}_2-\bar{b})}{\bar{b}}\,n_1 n_2\,, \qquad (13a)$$

while in the phase III'' it becomes $90^{\circ}+\beta''$, where:

$$\beta'' \approx \varepsilon_{12}(III'') = \frac{K}{2C_{11}}\,\frac{(a^{\circ}_{II}-\bar{a})}{\bar{a}}\,n_1 n_2\,. \qquad (13b)$$

Results

In Table I lattice parameters of the phases calculated from (9-12) at $\bar{n}=[340]$ for Ti-Ta, Ti-Mo (see also Fig. 2), Ti-W and Ti-Nb alloys at different solute concentrations are presented. Elastic moduli of pure Ti were used: C_{11}=162,40; C_{12} = 91,96; C_{13} = 69,00; C_{33} = 180,70 (in HPa) [8]. Unknown values a°_2 and a°_{II} were used as fitting parameters.

Each phase gives a set of lines in X-ray diffraction patterns. The angular position of the lines must differ from those of the hexagonal matrix. For example, calculation shows (Fig. 3) that Bragg angles for [200] and [130]

lines in Ti-Mo alloy differ for each phase and have some angular dispersion around the [110] line of hexagonal α''-martensite. Due to elastic strains each line has certain breadth, therefore they can overlap creating two wide lines instead of the [110] line of initial α'-martensite. The increase of Mo content leads to the shift of these lines relatively to the [110] line, as well as to an increase of their dispersion (breadth) which is observed in actual experiments. In the same way, the $[100]_{\alpha'}$ line splits to $[110]_{\alpha''}$ and $[020]_{\alpha''}$ lines.

It should be emphasized that in calculations of lattice parameters we neglected by the rhombicity of the phase III, which due to elastic interaction, can lead to rhombic distortion of phases I and II also. This can change, to some extent, the diffraction patterns attributed to all three constituents additionaly broadening or even splitting the diffraction maxima. Such complicated

TABLE I. LATTICE PARAMETERS OF MARTENSITE (EXPER.) AND PHASES FORMED ON SPINODAL DECOMPOSITION (CALCUL.).

A L L O Y		Ti-Ta [9]		Ti-Mo [1]		Ti-W [10]		Ti-Nb [1]	
solute content, wt%		30	50	6	8	10	15	15	20
α'(hexagonal) $a=b/\sqrt{3}$		2.950		2.945		2.960		2.940	
α'' (orth) exper.	a	3.060	3.240	2.970	3.000	2.980	3.020	2.980	3.040
	$b/\sqrt{3}$	2.860	2.720	2.890	2.820	2.930	2.860	2.930	2.910
Phase I	a_I	2.889	2.821	2.914	2.875	2.943	2.904	2.934	2.923
	$b_I/\sqrt{3}$	2.860	2.720	2.890	2.820	2.930	2.860	2.930	2.910
	$a^o_I=b^o_I/\sqrt{3}$	2.879	2.769	2.902	2.847	2.936	2.881	2.932	2.916
Phase II	a_{II}	3.060	3.240	2.970	3.000	2.980	3.020	2.980	3.040
	$b_{II}/\sqrt{3}$	3.146	3.466	2.989	3.043	2.996	3.067	3.011	3.118
	$a^o_{II}=b^o_{II}/\sqrt{3}$	3.104	3.356	2.980	3.022	2.988	3.044	2.996	3.080
Phase III' ($\beta<0$)	$a_{III'}$	2.925	2.885	2.930	2.910	2.952	2.932	2.937	2.932
	$b_{III'}/\sqrt{3}$	2.905	2.835	2.918	2.882	2.945	2.910	2.934	2.925
	$a^o_{III'}=b^o_{III'}/\sqrt{3}$	2.879	2.769	2.902	2.847	2.936	2.881	2.932	2.916
Phase III'' ($\beta>0$)	$a_{III''}$	3.005	3.095	2.957	2.972	2.970	2.990	2.960	2.990
	$b_{III''}/\sqrt{3}$	3.048	3.208	2.967	2.994	2.978	3.013	2.976	3.029
	$a^o_{III''}=b^o_{III''}/\sqrt{3}$	3.104	3.356	2.980	3.022	2.988	3.044	2.996	3.080

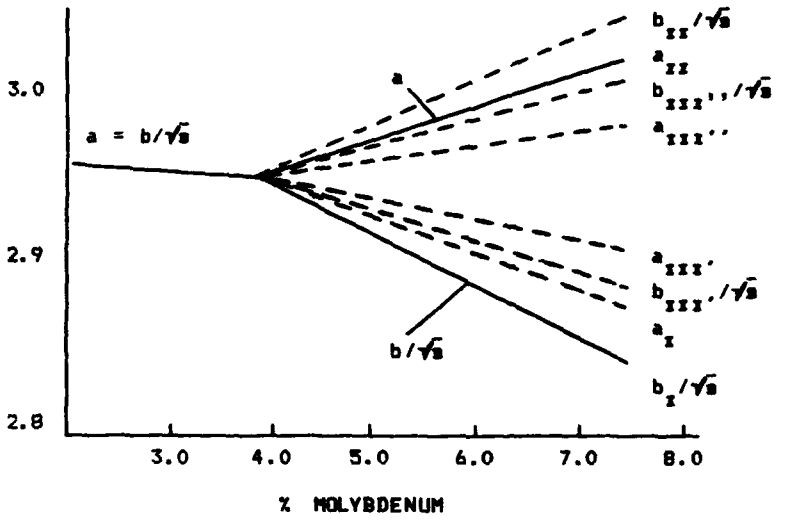


Figure 2. Lattice parameters of martensite (solid lines) [1] and products of its decomposition (dashed lines) as a function of molybdenum content in Ti-Mo alloys.

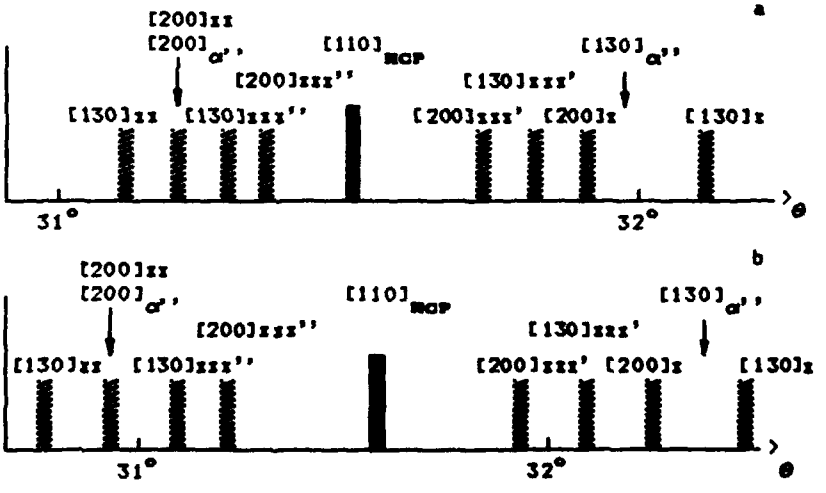


Figure 3. Calculated splitting of the $[110]_{HCP}$ line in Ti-6wt% Mo (a) and Ti-8wt% Mo (b). Experimental data presented by arrows.

diffraction pattern of martensite, in which separate maxima are difficult to resolve, can explain, to our mind, the conclusion on orthorhombic structure of martensite, which was made previously.

Conclusion

Orthorhombic symmetry of the martensite crystalline lattice in some titanium alloys can be attributed to the spinodal decomposition when the periodic structure with the modulation of the composition is formed instead of homogeneous solution. Elastic deformation of coherently conjugated depleted and enriched phases produces the effect of orthorhombicity in the X-ray diffraction patterns. That means that in titanium alloys which did not show the spinodal decomposition, the formation of the orthorhombic α''-martensite must not occur. On the other hand, one can assume that in Ti-Ta, Ti-Nb, Ti-W, and Ti-Re alloys in which the α''-martensite was identified the spinodal decomposition of martensite should take place.

References

1. J. A. Bagariatskii, G. I. Nosova and T. V. Tagunova, "General Features of the Formation of Metastable Phases in Titanium Alloys", Doklady AN SSSR, 122 (1958), 593-599.

2. J. M. Dupony and B. L. Averbach, "Atomic Arrangement in Ti-Mo-solid", Acta metal., 9 (1961), 755-763.

3. L. K. Dolinskaya and L. N. Guseva, Crystalline Structure and Properties of Metallic Systems (Moskow, Nauka, 1978), 226-232

4. S. G. Fedotov, Investigation of Metals and Alloys in Liquid and Solid State (Moskow, Nauka, 1964), 207-240.

5. R. Davis, H. M. Flower and D. R. F. West, "The Decomposition of Ti-Mo Alloy Martensites by Nucleation and Growth and Spinodal Mechanisms," Acta metal., 27 (1979), 1041-1052.

6. A. G. Khachaturyan, Theory of Structural Transformations in Solids. (New York, 1983), 574.

7, A. I. Olemsky and M. M. Chruschov, "Elastic interaction of Concentrational Unhomogeneities in Solid Solutions with the HCP Lattice in Continued Approach" Metallofizika, 12 (1990), 39-43.

8. E. S . Fisher and C. T. Renken, "Single - Crystal Elastic Moduli and HCP -> BCC Transformation in Ti-Zr and Hf," Phys. Rev., 135 (1964), 482-494.

9. K. A. Bywater and J. W. Christian, "Martensitic Transformations in Titanum-Tantalum Alloys", Phil. Mag., 25 (1972), 1249-1273.

10. J. A. Bagariatskii, T. V. Tagunova and G. I. Nosova, Probl. Fiz. Metallov i Metalloved. (Moskow, Metalurgizdat, 1958), 210-234.

PHASE TRANSFORMATION IN COMBINED ALLOYED α -TI ALLOYS AND THEIR EFFECT ON THERMAL EMBRITTLEMENT AND CORROSION MECHANICAL PROPERTIES

Stal Ushkov, Valeriy Rybin, Iliana Rasuvaeva, E.Nesterova, O.Gunbina

Central Research Institute of Structural Materials "Prometey"
Sankt-Petersburg, Russia, 193167

Abstract

The change of mechanical and corrosion-mechanical properties of α- Ti alloys of the Ti-Al, Ti-Al-C, Ti-Al-Zr, Ti-Al-C-Zr, Ti-Al-Si, Ti-Al-Zr-Si systems in dependence of aging time in 400-600°C range was investigated. It is established that aging results in a thermal embrittlement effect, manifested as an impact values reduction and a corrosion-mechanical strength decrease of great extent.

Introduction

It is experimentally established that at 400-600°C titanium Ti-6Al-base α-alloys aging tends to a decrease in ductility and corrosion-mechanical strength characteristics deterioration (1-4). Within this temperature range titanium α-alloys with more than 6-7% of Al display the effects of embrittlement and sharp reduction of corrosion-mechanical properties due to supersaturated solid solution decay with α_2-phase (Ti_3Al) dispersion particles precipitation (1-3). Alloys with less than 6Al and un-alloyed titanium are also exposed to thermal embrittlement at 400-600°C. This effect is of different nature and relates to redistribution of substitution impurities Fe, Ni between body and grain boundaries (4). It is evident to suppose that both processes are reasized to some extent in Ti-6Al base alloy composition. But the way these processes are going in defferent alloys of this type and how each of them affects ductility and corrosion mechanical properties are not clear.
The aim of the present work was to answer this question.

Material and Ex perimental Procedure

Investigations were carried out on Ti-6Al-base alloys, additionally alloyed by 6%Zr or 0.1% C and simultaneously by 6% Zr and 0.1% C. Besides the Ti-6Al-6Zr system alloy, additionally alloyed by 0.5% Si, was studied. Ingots of 10 kg in weight were bar-forged (section 40x40 mm) at 1500...1200°C. Bar forging on rods Ø 12 and 18 mm was performed at 950°C which allowed to obtain

Titanium '92
Science and Technology
Edited by F.H. Froes and I. Caplan
The Minerals, Metals & Materials Society, 1993

the fime-grain polyhedron structure after recrystallization annealing. After it rods were subjected to quenching in water at 900°C followed by aging at 500°C for 10 or 100 hours with air cooling. Impact bending tests were performed on Menage specimens. The low-cycle endurance value in air and corrosion medium was determined according to procedure (5) and evaluated by the number of cycles to failure Np.

Experimental Results

Mechanical Properties. The results of impact toughness KCV measurements and of the number of cycles to failure in corrosion medium Np are pressened in Figure 1 for all tested materials in initial state and after exposure for 10 or 100 hours at 500°C. It is observed that all tested materials are prone to thermal embrittlement which is substantially revealed only after longer exposure for 100 hours. The relative reduction of impact toughness is 25-50% (Figure 1a) for all alloys.

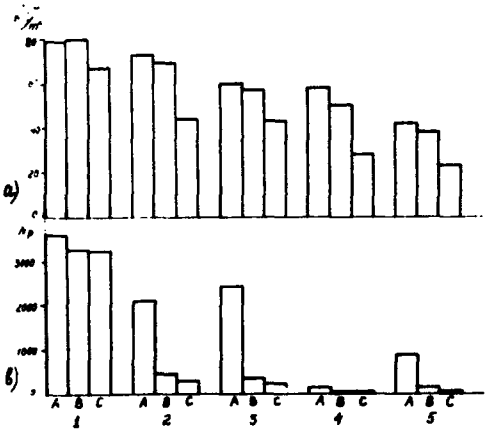


Figure 1 Histograms of changes in mechanisal properties versus aging time: a - impact toughness, b - corrosion-mechanical strength; 1-Ti-6Al; 2-Ti-6Al-6Zr ; 3-Ti-6Al-0,1C; 4- Ti-6Al-6Zr-0,1C. a- quenching in water at 900°C; B - quenching + aging for 10 h at 900°C; C - quenching + aging for 100 h at 500°C.

The effect of aging on corrosion-mechanical strength is considerably dependent on the alloy chemical composition. So, the Np value for Ti-6Al binary alloy is almost constant during the aging process. In ternary Ti-6Al-6Zr and Ti-6Al-0,1C alloys the sharp (for about an order of magnitude) decrease of Np is observed even after 10 hours of exposure at 500°C (Figure 1b). In the alloy combinely alloyed by Zr and C the effect of corrosion-mechanical strength sharp decrease shows itself even in the initial state and is pronouncenly growing in the process of aging. The similar process is observed in Ti-6Al-6Zr-0.5Si alloy, where low-cycle endurance in the corrosion medium also has low values in initial state and after aging.
After impact bending tests in initial, quenched state the main fracture component for all alloys is through bowl transcrystalline failure (Figure 2a). Aging for 500 hours at 500°C leads to a sharp increase in grain-boundary failure fraction in fracture: it achieves 30% for Ti-6Al, Ti-6Al-6Zr, Ti-6Al-0,1C and 50% for Ti-6Al-6Zr-0,1C (Figure 2b). Besides Ti-6Al-6Zr-0,1C -al-

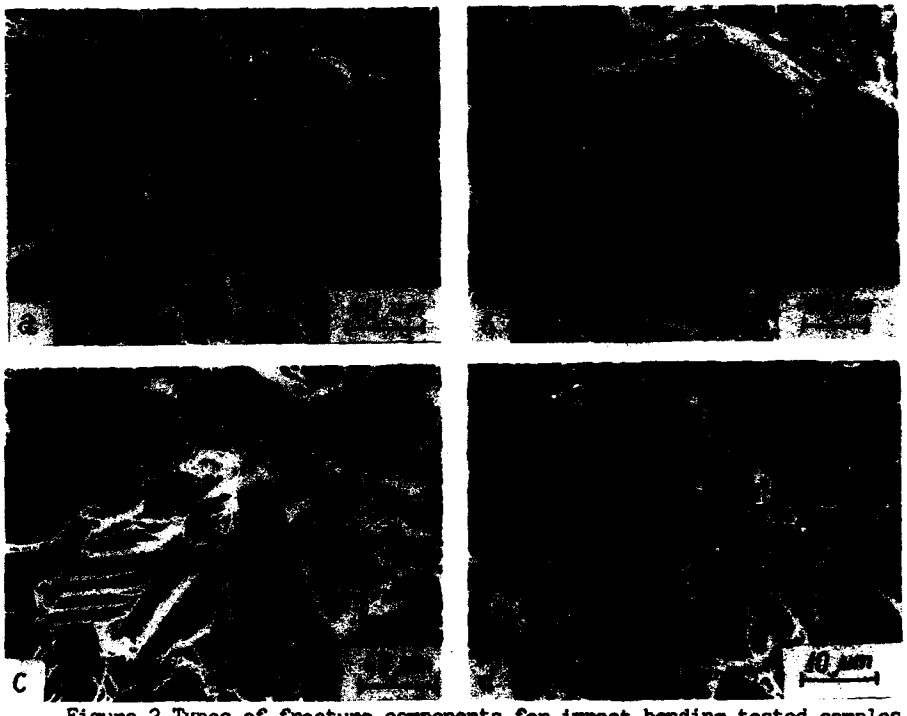


Figure 2 Types of fracture components for impact bending tested samples, a - dimpe transcrystalline failure (Ti-6Al-6Zr alloy, quenching in water at 900°C); b - grain boundary failure (Ti-6Al-6Zr alloy, aging for 100 h at 500°C); c - corrugated fracture (Ti-6Al-6Zr-0,1C alloy, aging at 500°C for 100 h); d - fracture surface of Ti-6Al-6Zr-0,5C alloy (aging at 500°C for 100 h).

loy has an increase in relative fraction of other fracture component-corrugated fracture (Figure 2c) during aging which corresponds to transcrystalline failure along the prism planes $\{10\ \bar{1}0\}$. The recorded changes analyses allow to conclude that thermal embrittlement of binary and ternary alloys is governed by the changes in intercrystalline boundaries state. The effect of thermal embrittlement for the quaternary alloy is of other complicated nature. It is connected with processes occuring in the body and on grain boundaries. The failure surface of Ti-6Al-0,5Si alloy after impact bending tests has a pit type due to micropores nucleation in silicon-seperated impurities (Figure 2d). The pits are not deep with little ligaments between them, in some places quasispallings appear together with pit failure.

The comparative analysis of failure for samples with high and low parameters of low-cyclic endurance in corrosion medium has revealed that failure is alloys taking place in the grain body without any notices of intercrystalline failure. A zone of fatigue crack propagation with peculiar grooves is covering the main part of Ti-6Al alloy specimens in the quenched state, while in the zone of fracture, a tough bowl transcrystalline failure is observed (Figure 3a). In the fracture of Ti-6Al-0,1C (and Ti-6Al-6Zr) alloys fatigue grooves are observed in the crack initiation zone, and then as the crack is developing the areas of spalling and corrugated fractures appear. The fracture surface of Ti-6Al-6Zr-0,1C alloy specimens consists of spalling and

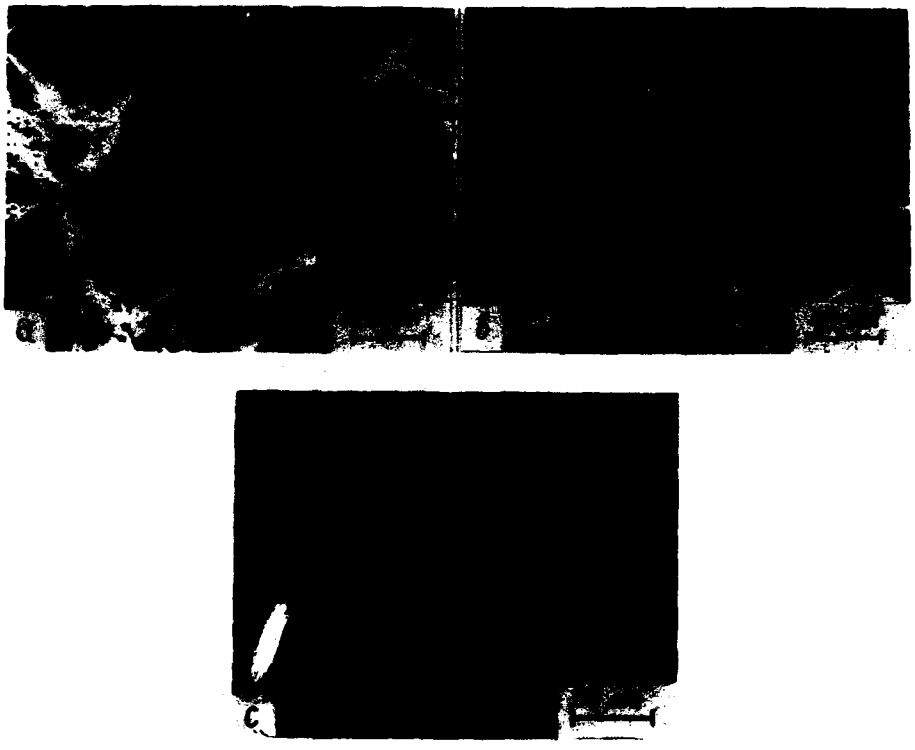


Figure 3 Types of fracture components for low-cycle endurance tested samples in corrosion medium. a - fatigue grooves (Ti-6Al-0,1C alloy, quenching in water at 900°C); b - areas of corrugated fracture and spalling (Ti-6Al-6Zr-0,1C alloy, quenching in water at 900°C); c - review on fracture surface of Ti-6Al-6Zr-0,5Si alloy.

corrugated fracture areas (Figure 3b). Aging at 500°C does not affect the corrosion-mechanical fracture properties of Ti-6Al alloy while in the ternary Ti-6Al-0,1C, Ti-6Al-6Zr alloys and Ti-6Al-6Zr-0,1C quaternary alloy substantial changes are observed: fatigue grooves zone completely disappears while there is a sharp increase in spalling area at corresponding decrease of corrugated fracture area (Figure 4). Revealed changes in failure character allow to conclude that corrosion-mechanical strength characteristics decrease of additionally alloyed by Zr and C alloys is governed by processes occuring in grain bodies and sequently is of different nature as compared to thermal embrittlement effect of these materials. The fracture surface of silicium-containing alloy consists in spalling areas and quasi-spalling areas in equal proportion. A large amount of precipitations is present along the whole fracture surface.

Structural Investigations. These were carried out by optical metallographic methods and transmission electron microscopy, and made it possible to give a detailed expression to the processes resulting from aging in the internal volumes of grains and on the intergranular boundaries of alloys. Microstruc-

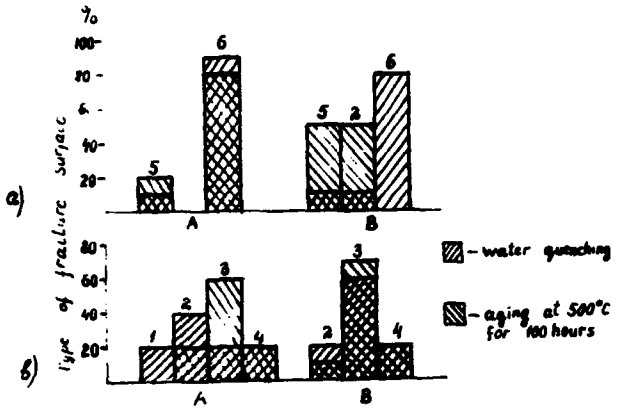


Figure 4 a - impact bending test; b - low-cycle fatigue test. 1 - fatigue grooves, 2 - corrugated fracture, 3 - cleavage (brittle fracture), 4 - zone of fracture, 5 - intergranular fracture, 6 - ductile dimple fracture.

ture of all the Ti-Al-Zr-C system alloys in the initial, quanched state comprises a set of equiaxial grains of α - phase with well-defined, clear boundaries free from any precipitations (Figure 5). After 100 hours of exposure the fine-dispersion grain-boundary particles 1,2-0,3 mkm in dimensions appear on grain-boundaries of these materials. Their crystal lattice was identified by single reflex method (6), as FCC with a = 1,31 nm, which corresponds to the $Ti_2(Fe, Ni)$ intermetallic.

The summary of results obtained from mechanical tests and fractography investigations allows to conclude that thermal embrittlement of Ti-6Al alloy and Ti-6Al base alloys additionaly alloyed α-titanium alloys.

No visible structural changes were detected in the intergranular volumes of Ti-Al-Zr-C system alloy aged at 500°C for 10 and 100 hours. But after longer exposure (for 500-1000 hours) weak superstructural reflexes belonging to α_2- phase are recorded in all materials except binary Ti-6Al alloy. It is presented in Figure 6 where microdiffraction pi cture (a) and its sketch (b) are given. The arrangement of intermediate rows of weak additional reflexes (marked-x in the diagram) precisely in between the rows of the main reflexes in the plane (100) of the reverse lattice of α - phase, taked into account the known relation between α- and α_2- phases parameters: $a\alpha_2 = 2a_\alpha$, $C\alpha_2 = C\alpha$. The α_2- phase precipitations in the tested alloys even after 500 hours of exposure at 500°C are extremely fine dispersional. Due to the fact that it is not possible to detect them neither in bright-field no in dark-field image, one may consider that the formations size does not exceed 1nm.

Structural investigations of silicium-containing alloys have shown that a large anount of rounded precipitations are located chaotically in the grain body and on boundaries even in the quenched state. The quantity and dimensions of precipitations are growing with increase in aging time (Figure 7). Investigations performed with the help of transmission electron microscope allowed to establish that these precipitations have haxagonal lattice with the following parameters: a = 0.36 and 0.70 i.e. are titanium silicides $(TiZr)_6Si_3$, depended by S_2 in literature (7).

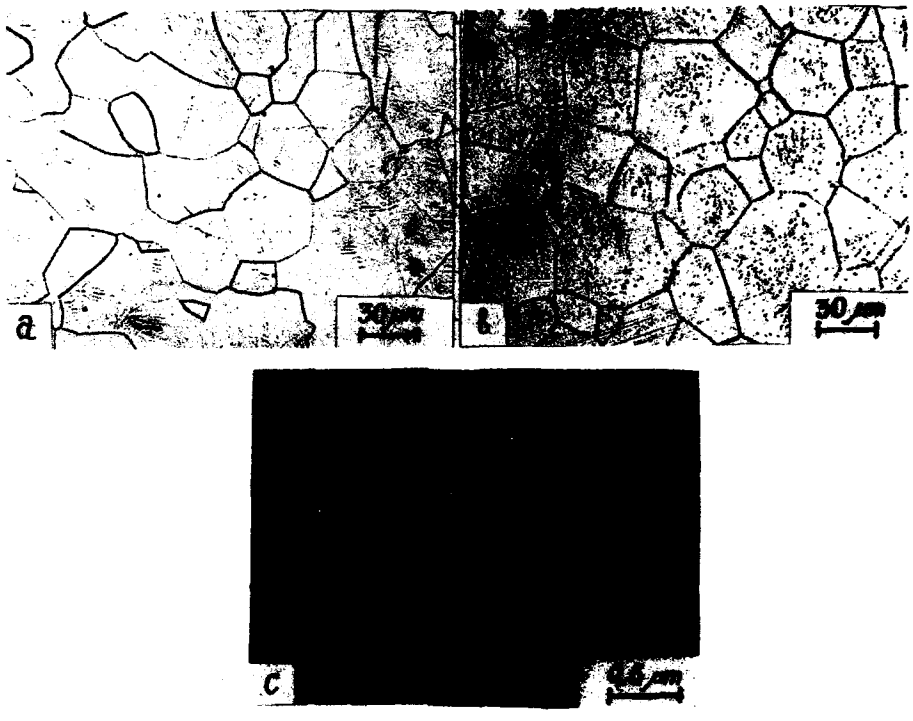


Figure 5 Microstructure of Ti-6Al-6Zr alloy
a - in quenched state; b - after aging for 100 h at 500°C;
c - specific type of grain-boundary precipitations after aging for 100 h at 500°C (transmission electron microscope).

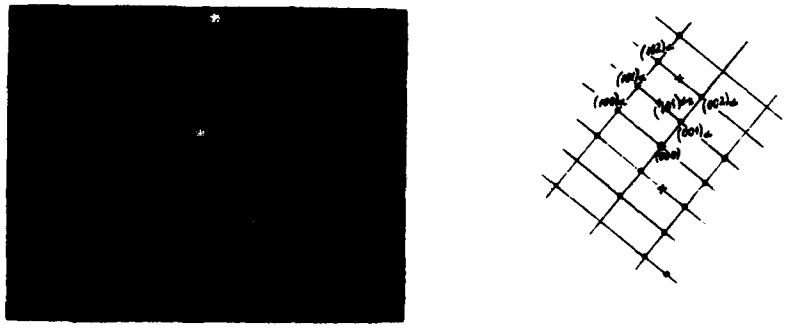


Figure 6 Electronogram and its treatment diagram which bear witness to α_2- phase presence.

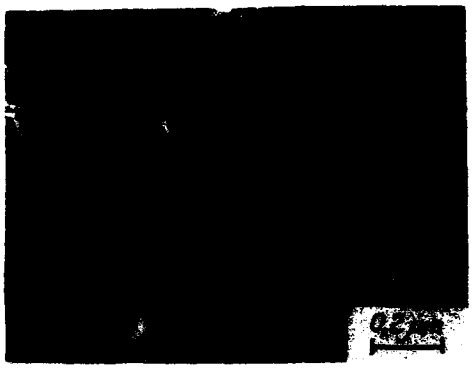


Figure 7 Distinctive view on precipitations in Ti-6Al-6Zr-0,5Si alloy after aging for 1000 hours at 500°C.

Results and Discussion

Metallographical and electron-microscopic analyses results indicate that two simultaneous processes take place at aging of tested alloys. They are diffusion of impurities of eutectoid-generating β-stabilizers on grain boundaries which forms intermetallics $Ti_2(Ni, Fe)$ on α - grainboundaries and the process of ordering resulting in α_2- phase formation in the grain. Earlier (4) it was shown that grain-boundary segregation of Fe,Ni impurities governs a decrease in impact toughness due to cohesion strength decrease of grain boundaries. But, at the same time, additionally experiment we carried out on technically pure titanium has shown that it is not detrimental to the corrosion-mechanical strength: KCV value after exposure for 100 hours at 500°C declined from 32 to 18 kg/m² while the Np value in the corrosion medium remained on 5000 cycles level.

α_2- phase for its pre-precipitations/formation is changing the deformation type and tends to plastic flow concentration in narrow or rare slip bands forming a shear step of substantial height on the surface of the specimen (8-9). α_2- phase precipitations being in the slip band are cut-off many times gibing a rise to their dispersal and causing Al-supersaturation of α-solid solution in the slip bands and of formed shear steps. The bands become chemically active and play the role of anodes in the corrosion medium and under the conditions of passivity fault. Therefore, the α_2- phase precipitations/pre-precipitations/ are responsible for a decrease of corrosion-mechanical characteristics.

Intermetallics Ti_5Si_3 precipitated in silicium containing alloys in large quantities on grain boundaries and inside the grains on low angle boundaries may have an effect on both characteristics mentioned above.

Both processes namely-grain boundary precipitations of intermetallics and ordering are mostly active in the 400-600°C temperature range. The low bound of this range is governed by the diffusion mobility of dissolved atoms while the upper bound in the first case is determined by the eutectoid transformation temperature in Ti-Fe and Ti-Ni systems and by the disorder temperature in the second. These processes kinetics and mechanisms are of great difference.

α_2-phase formation is preceded by arising diffusion of aluminium in the Al-enriched areas being inijtally presented in Ti-Al system alloys.

Mainly α_2- phase formation is a matrix crystal lattice rebuilding due to ordered location of atoms in its ponts, the new phase growth is taking place in coherence with the matrix with a gradual increase of crystal lattice distortion. In this case, there are bo power stimuler to aluminium segregation

to grain boundaries and atoms translation occurs for distances close to interatomic as a result the process is going rather repidly.
Developed grain boundary precipitations of intermetallics are governed by the translation of atoms Fe and Ni-stabilizers found in a form of impurities in solid solution. As this is long-distance translation (50-100 mkm), the process of intermetallics generation is going slower than ordering process.
The difference in the processes kinetics explains the fact that impact toughness value decrease is observed at longer exposures as compared to corrosion-mechanical strength.
In contrast of the process of grain-boundary precipitation the kinetics of ordering process is dependent on the alloying type. Interstitial impurities including carbon considerably accelerate the ordering process. Zirconium beeing more active element than titanium enters into intersolution interaction with aluminium forming the ordered systems of $(Ti,Zr)_3Al$ type at the early stages of aging (3).
One may say that at simultaneous alloying of Ti-6Al base alloy by Zr and C the simula systems development is taking place in the process of semi-finish shed product manufacture resultant in corrosion -mechanical strength decrease in the initail and aged state.
In silicon-containting alloys zirconium is taking part in $(Ti,Zr)_5Si_3$(7) intermetallic development.

Conclusions

1. Ti-6Al binary alloy is subjected to thermal embrittlement at long-term exposures within 400-600°C temperature range.
This effect is not followed by the corrosion-mechanical strength decrease and is of the same nature as thermal embrittlement of low-alloyed titanium α-alloys, i.e. it is governed by a decrease in cohesion strength of grain boundaries due to Fe,Ni substitutional impurities segregation an them followed by $Ti_2(Fe,Ni)$ intermetallic particles precipitation.
2. In Ti-6Al-0,1C and Ti-6Al-6Zr alloys after exposure at 400-600°C the thermal embrittlement is observed as well as corrosion-mechanical strength decrease and these correleting effects are of different nature. The first one is governed by Fe,Ni impruities re-distribution between the body and grain boundaries, while the second effect is realized in accordance with the mechanism of Ti-Al solid solution homogeneous decay at early stages. The separation of mechanisms responsible for a decrease in impact toughness and corrosion-mechanical strength reduction is consistent with the differences in the processes kinetics.
3. Simultaneous alloying of Ti-6Al by 0.1%C and 6%Zr leads to the greater effect of Ti-Al solid solution decay processes on ductility and corrosion-mechanical strength. In this case, the thermal embrittlement of this alloy is governed by the processes occuring on grain boundaries (Fe,Ni segregation and $Ti_2(Fe,Ni)$ intermetallic particles precipitation) as well as Ti-Al solid solution homogeneous decay processes.
4. Ti-6Al-6Zr-0m5Si alloy embrittlement results from $(Ti,Zr)_6Si_3$ intermetallic particles precipitation on low-angle boundaries.

References

1. K.G.Namboodhiri, C.J.McMahon, H.Herman, "Decomposition of the α-Phase in Titanium Rich Ti-Al Alloys", Met.Trans,4,(5) (1973),1323-1328.

2. F.A.Crossly, "Kinetics of Ti_3Al Grain Boundary Precipitation in Ti-Al Alloys", Met.Trans.1(5) (1970),1921-1929.

3. I.V.Gorynin, B.B.Chechulin, I.N.Razuvaeva, Yu.D.Hesin,"On the Interaction between Alloying Elements in Multicomponent Metal Systems",in Titanium, Metal Science and Technology, Proc.3rd Int. Conf. on Titanium, Moscow, 1976,(1978), 541-546.

4. E.V.Nesterova, V.V.Rybin, S.S.Ushkov, G.I.Kolodkina, "Investigations of Low-Alloyed Titanium α-Alloys", F.M.M., 50(6) (1980),1218-1255.

5. V.A Zhukov, L.A.Ivanova, T.K.Marinets, I.N.Razuvaeva, Yu.D.Hesin, "Thermal Stability of Titanium Pseudo- α-Alloys and Evaluation Methods", MiTOM, (12) (1981),37-39.

6. V.V.Rybin, A.S.Rubtsov, E.V.Nesterova, "Method of Single Reflexes (SR) and Its Application for Electron-Microscopic Analyses of Dispersion Phases", Plant Laboratory, (5)(1982),21-26.

7. G.Sridhar, V.V.Kutumbarao, D.S.Sarma, "The Influence of Heat Treatment on the Structure and Properties of a Near -α- Titanium Alloy", Met.Trans. 18A(5) (1987),877-891.

Transformation kinetics of Titanium and Equi-atomic Titanium-Zirconium Solid-Solution by means of isothermal dilatometry

J. DEBUIGNE and E. ETCHESSAHAR

**Laboratoire de Métallurgie et Physico-Chimie des Matériaux,
U.R.A. C.N.R.S.1495
I.N.S.A., 20, avenue des Buttes de Coësmes
F-35043 Rennes Cédex - France.**

Abstract

The kinetics of $\alpha \rightarrow ß$ et $ß \rightarrow \alpha$ transformations are studied by isothermal dilatometry in high vacuum (typically 10^{-6}Pa). For pure Titanium of different grades both the $\alpha \rightarrow ß$ and $ß \rightarrow \alpha$ transitions are very slow but non isothermal except for V.A. Titanium. The phase transition of three Ti-Zr solid solutions of different purities are investigated. The $\alpha \rightarrow ß$ transition is isothermal for the purest alloy but the $ß \rightarrow \alpha$ one is isothermal for the three alloys. These last experimental data follow well a Johnson-Mehl equation and open the discussion upon the mechanisms of these phase transitions.

Introduction

The study of the kinetics of phase transformation is of particular importance when it furnishes quantitative data of easy use in modeling thermal treatments of metals and alloys. Obtaining an analytical expression for the progress of the transformation is a step in the same direction, and in addition, the form of this expression can provide information concerning the possible transition mechanisms. The transition is studied by observation of a physical effect providing numerical values which determine the transformation ratio in an inequivocal manner.

There is renewed interest in the use of dilatometry for observing the transformations undergone by solids. The works of E.J. Mittemeijer et al.(1) is an interesting example of kinetic study using non-isothermal dilatometry and the Johnson-Mehl-Avrani equation. Recently, M.H. Carvalho et al. (2) propose dilatometry in the study of phase transformation in the Ti 6242 alloy (Ti - 6 Al - 2 Sn - 4 Zr - 2 Mo). Although the list is incomplete, several dilatometric studies on titanium and some of its alloys may be mentionned. Cizeron and Lacombe (3) have studied the allotropic transformation of pure industrial titanium and have shown the particular dilatometric behaviour depending on the $\alpha \rightarrow ß$ transformation cycles concerned. Hocheid and al. (4) have studied the transformations of Ti6Al4V. T. Yukawa and al. (5) have studied the precipitation of the ω -phase and the order in Ti-8 Al; Etchessahar (6) and Etchessahar and Debuigne (7,8) using high sensitivy and very-high vacuum dilatometry have studied the transitions in titanium, zirconium and the titanium zirconium solid-solution in isothermal and non isothermal conditions. The metals studied by the latter were of different purities ranging from industrial grade to the zone-melted grade.

Titanium '92
Science and Technology
Edited by F.H. Froes and I. Caplan
The Minerals, Metals & Materials Society, 1993

The influence of the interstitials, particularly nitrogen, has been precisely stated. Fujishiro et al. (9) have studied the phase transformation of industrial titanium and confirmed the characteristics previously published. Loier et al. (10) have studied the transformation of Ti6Al4V by dialatometry under stressed conditions. In this present study, we give the kinetic data obtained by isothermal dilatometry.

Experimental

Apparatus and dilatometric tests

The dilatometer used is an horizontal-axis direct type operating under ultra-high-vacuum. This dilatometric unit was constructed in our Laboratory and has been described in detail (6,11). More recently we studied a special specimen holder for carrying out thermal expansion measurements on thin and flexible metallic ribbons (12-14), for example amorphous alloys prepared by planar flow casting on a copper wheel. This dilatometer allows study of transformation phenomena in materials submitted to different thermal cycles. It also permits study of the phenomena which take place in the course of cumulative annealing ; if the sample is heated to a temperature situated outside transition conditions, equilibrium is established and no length variation with time is observable. By successive steps of temperature change in the phase transition region, fine measurements may be made of the evolution of the sample and the transformation temperatures and possible incubation time.

Materials

The experiments were carried out on three grades of titanium, the composition of which are given in Table I.

TABLE I - Composition of the various grades of titanium (ppm atomic)

	0	N	C	Al	Fe	Ni	Si	Mn	Mg	Zr
T 40	2100	600	900		990		300	< 135	< 20	
Ti E-B	900		280	10	150	50				10
melting	1800			200	250	70				40
Ti	10				70					
Van Arkel	150				100					

The equiatomic Ti-Zr alloys of different impurity levels were studied. The first one, Ti-Zr 1, is of industrial purity level, the other two, Ti-Zr 2 and Ti-Zr 3, were synthesized under very pure argon., starting with bulk metals melted by rf induction on a water cooled copper crucible and then homogenized by long time annealing in an ultra-high-vacuum furnace. The impurity concentrations of the starting metals are given in Table I I for Ti Zr1, provided by CEZUS, the values of impurities content are those of the alloy, for Ti Zr2 and Ti Zr 3 the analysis are concerning the starting metals.

TABLE II - Impurities in the starting materials (ppm atomic)

Samples	Materials	0	N	C	Cr	Hf	Al	Fe	Ni	Zr	Ti
Ti-Zr 1	Ti Zr	3130	500			4000					
Ti-Zr 2	Ti	900		280			10	150	50	10	
	Zr	2250	293	1520	105	102					38
	Ti	100						70			
Ti-Zr 3	Zr	8	8			27	0	2			

Results

Titanium

Titanium dilatograms exhibit well-known features showing clearly the non proportionality between the transformation ratio and dilatation. During cumulative annealing tests, both the $\alpha \rightarrow \beta$ and the $\beta \rightarrow \alpha$ transitions are very slow and non isothermal. After these tests, there is macroscopic deformation of the titanium rods. This macroscopic deformation is a result of the phase transitions and is not due to stress exerted by the push-rod of the dilatometer, these stresses being of extremely small value, less than 10^{-2}N on a sample 8 mm diameter and 35 mm long.

Equi-atomic Titanium-Zirconium Solid-Solution

Recent works (8,15,16) have established the equilibrium diagram with precision. No change in composition occurs at all during the $\alpha \rightarrow \beta$ transition in an equi-atomic solution.

$\alpha \rightarrow \beta$ transition in cumulative annealing

Only the purest alloy, named Ti-Zr 3, shows an isothermal transition and this is of 480 minutes duration.

$\beta \rightarrow \alpha$ transition in cumulative annealing

The transformations are isothermal for the three alloys and the transition temperatures are as follows : 612°C for Ti-Zr 1, 600°C for Ti-Zr 2 and 585° C for Ti-Zr 3, the purest of the three alloys. These transitions are very slow, of from 500 minutes to more than 1000 minutes duration. The Figures 1 to 3 show typical $\beta \rightarrow \alpha$ transformation curves for the three grades of equiatomic Ti-Zr alloy subjected to step heatings. Contrary to what is observed on pure Titanium, experimental results allow us to assume a linear dependence of length change versus the transformation ratio.

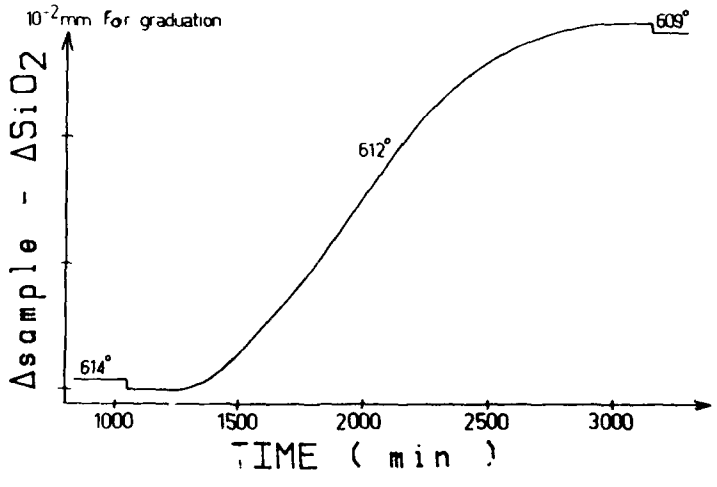


Figure 1 - Dilatometry of $\beta \rightarrow \alpha$ transformation for Ti-Zr 1, 50/50. Isothermal annealing measurement of the difference between the linear expansion of the silica holder and the specimen. Length of the sample : 35 mm

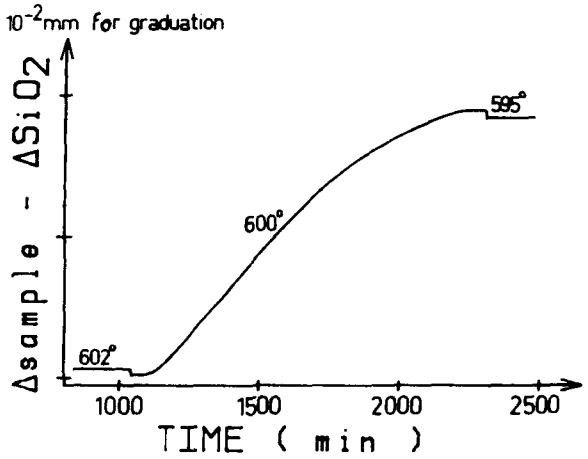


Figure 2 - Dilatometry of ß → α transformation for Ti-Zr 2, 50/50. Length of the sample 19,5 mm

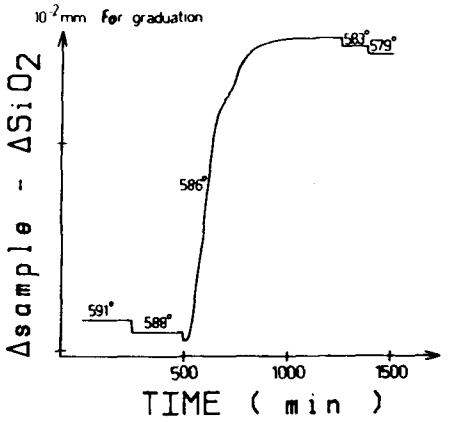


Figure 3 : Dilatometry of ß → α transformation for the purest Ti-Zr, 50/50 alloy. Length of the specimen 9,5 mm

The kinetics of isothermal transition of the equi-atomic titanium-zirconium solid-solution are well represented by equations of the well known Johnson-Mehl type.

$$1 - y = \exp -\left(\frac{t}{\theta}\right)^n$$

where y is the transformation ratio, t the time and θ a constant. This equation was used in the following form :

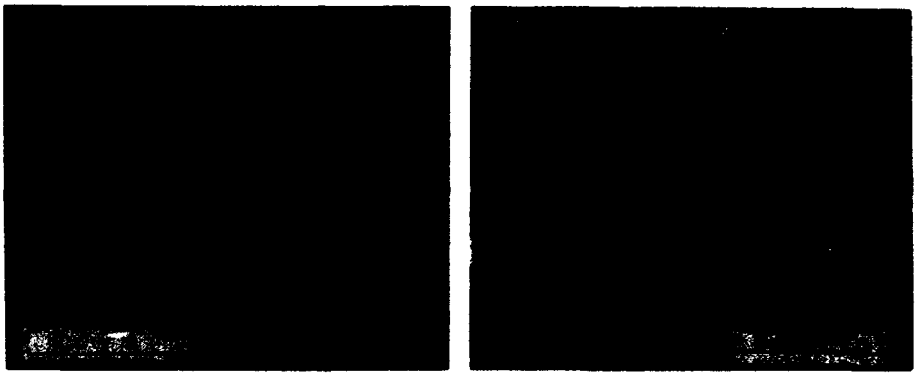
$$\ln [-\ln (1-y)] = n \ln t - n \ln \theta$$

Expressing the time in minutes, the results shown in Table III were obtained :

TABLE III - Coefficients of the Johnson-Mehl equation

Alloy	Transition	Température	n	n ln θ
Ti-Zr 3	$\alpha \rightarrow \beta$	621° C	1,24	6,24
Ti-Zr 1	$\beta \rightarrow \alpha$	612°C	1,80	1,20
Ti-Zr 2	$\beta \rightarrow \alpha$	600° C	1,63	1,02
Ti-Zr 3	$\beta \rightarrow \alpha$	585° C	1,55	7,62

Micrographic sections of Ti-Zr alloys having undergone the ß → α transformation in cumulative annealing are given in Figure 4. It should be noted that the morphology of the α-grains obtained show great similarity with that of the α-grains in Van Arkel titanium having undergone an isothermal ß → α transformation by cumulative annealings. In this Van Arkel titanium, the α-grains are however much larger. Nevertheless, the micrographs in Figure 4 show grains much larger than the needles seen on samples transformed martensitically during nonisothermal heat treatments.



a) b)

Figure 4 - Typical structure of Ti-Zr equi-atomic solid-solution samples after isothermal ß → α transition

a) Ti-Zr 2 alloy b) Ti-Zr 3 alloy

Discussion

Dilatometrics is an old experimental technique but its use provides much data in the study of transformation in solids. It is essential to respect certain requirements, which although quite standard, are not always respected. Particularly, in the study of kinetics, it is necessary to be certain that the length variation of the test sample is proportional to the transformation ratio. There are numerous cases where dilatometry is not the best method of quantitavely checking the progress of a transformation.

Dilatometric study of metals and alloys that are readily oxidized implies the use of a sufficiently good vacuum, limiting the contamination rate by oxygen and nitrogen. In fact, in the case of the IV A metals (Ti, Zr, Hf) contamination of the metal by interstitials is observed in vacuum levels of the order of 10^{-4} Pa ; the increase in oxygen concentration is monitored by measuring the electrical resistivity at low temperature. Thus Renucci (17) has shown that at 1070°C, for 0,5 mm thick samples, the contamination are 19.10^{-6} per hour of annealing at 2.10^{-4} Pa and $2,1.10^{-6}$ per

hour at $1{,}5.10^{-5}$ Pa. Thus in the work of M.H. Carvalho et al. (2) we note a large effect due to contamination by oxygen and, contrary to these authors proposition, outgassing is impossible at higher vacuum levels. Their explanation of the form of the dilatometric curves by outgassing is erroneous ; it is well known (3,6,7,8) that titanium shows very variable dilatometric curves when cycled around its allotropic transformation. The explanation of this phenomenon is more complex than that involving outgassing.

A technique complementary to dilatometry is to measure the electrical resistance during thermal cycling. In fact, the electrical resistivity variation ratio is very generally proportional to the transformation ratio. Numerous works have used this technique, for example those of Cormier et al. (18,19) for pure titanium, of Loïer et al. (10) using dilatometry together with resistivity for Ti6AP4V and of Arias and al. (19) for the Ti-Zr and Zr-Sc alloys. Preliminary results obtained in our laboratory (21) show resistivity variations quite similar to the dilatometric determinations. These results support our assuption of proportionnality between the transformation ratio and dilatation. Jourdan et al (22) showed in their study by synchrotron X-Ray topography the occurence of heterogeneous nucleation during the Titanium $\alpha \rightarrow ß$ transformation. They tested the diffusionless character only in the experiments where no incubation time for the new phase nucleation had been detected.

Conclusion

The transformation kinetics are not affected by Oxygen or Nitrogen contamintion owing to the use of ultrahigh vacuum. The exponents of the Johnson-Mehl equations representing the isothermal kinetics of the $ß \rightarrow \alpha$ transformation, on the one hand, and the microstructures, on the other hand, seem in favour of a mechanism by nucleation and growth. This nucleation takes place essentially at the grain-boundaries, followed by growth after saturation of the nucleation sites. In their works on titanium, Cormier et al. (18,19) have also proposed a mechanism of nucleation and growth for the $ß \rightarrow \alpha$ transition when the cooling rate is not too high. Amongst several propositions still under discussion, it appears to us that our results could be in favour of a mechanism of a slow massive transformation the speed of which would be determined by the diffusion of impurities in the interfaces in movement. Such as a conclusion was also examined by D. Arias et al (23) in their study of $ß \rightarrow \alpha$ transformation in dilate TItanium base alloys. Clarifing this question would require further work.

References

1. E.J. Mittemeijer, A. Van Gent and P.J. Van der Schaaf, Met. Trans. A 17A, 1441-1445 (1986)

2. M.H. Carvalho, H.J. Carvalhinos and J.F. Thomas, Scripta Met. 21, 1417-1422 (1987)

3. G. Cizeron and P. Lacombe, Mém. Sci. Rev. Mét., LVII, 3 (1960)

4. B. Hocheid, R. Klima, C. Beauvais, M. Rapin and C. Roux, Mém. Sci Rev. Mét. 9, 583 (1970)

5. T. Yukama, S. Othani,; T. Nishimma and T. Sakai, in "The Science" Technology and Application of Titanium, 699-710, Pergamon Press, Oxford (1970)

6. E. Etchessahar, Thesis (University of Nantes) (1975), I.N.S.A. Rennes

7. E. Etchessahar and J. Debuigne, C.R. Acad. Sci., Paris, t. 283, série C, 63-66 (1976)

8. E. Etchessahar and J. Debuigne, Mém. Sci. Rev. Met. 3, 195-205 (1977)

9. S. Fujishiro and S. Nadiv, in Titanium '80, 899-906, TMS-AIME, Warendale, PA (1980)

10. C. Loïer, A. Hazotte, G. Thauvin and A. Simon, J. Less-Common Met. 108, 295-312 (1985)

11. E. Etchessahar, D. Ansel and J. Debuigne, Mém. Sci. Rev. Mét. 7/8, 469-474 (1977)

12. M. Harmelin, E. Etchessahar, J. Debuigne and J. Bigot, Thermochim. Acta 130, 177-192(1988)

13. E. Etchessahar, M. Harmelin, and J. Debuigne, Thermochimica Acta 142, 29-47, (1989)

14. E. Etchessahar, M. Harmelin and J. Debuigne, ASTM Symposium ou "Materials Characterization by Thermomechanical Analysis" Philadelphia 1990 STP 1136, A.T. Riga and C.M. Neag, Eds ASTM, Philadelphia, 49-67, (1991)

15. J.P. Auffredic, E. Etchessahar and J. Debuigne, J. Less-Common Met., 84, 49-64 (1982)

16. N. Sauders and B.B. Argent, J. Less-Common Met. 125, L11-L13 (1986)

17. L. Renucci, Thesis, Paris (1968) France

18. M. Cormier, Thesis, University of Laval (1972) Québec, Canada

19. M. Cormier and F. Claisse, J. Less-Common Met. 34, 181-189 (1974)

20. D. Arias, L. Roberti and Y.M. Ruch, Primer Symposio Franco-Argentino Ciencia de Materiales, Mar del Plata (29 sept. - 3 oct. 1986)

21. B. Jounel, D. Ansel and J. Debuigne, (private communication, 1992)

22. C. Jourdan, J. Gastaldi and G. Grange, Acta Metall 36, 11, 2979-2987 (1988)

23. D. Arias and M. Ruch - Sixth World Conference on Titanium - France 1988 - Proceedings, pp. 1669-1674 - Les Editions de Physique (1989).

ON THE TERNARY SYSTEM Ti-V-N

A. GUILLOU, J. BAUER and J. DEBUIGNE

Laboratoire de Métallurgie
U.R.A.- C.N.R.S. 1495
I.N.S.A., 20, avenue des Buttes de Coësmes
35043 RENNES CEDEX

Abstract

The ternary system Ti-V-N has been investigated by means of metallographic, X -Ray and EPMA methods. The system is characterized by two continuous solid solutions : δ Ti N_{1-x} - δ VN_{1-x} and β Ti – α V (at temperatures higher than 882°C). The solubility of the respective second metal in the other binary phases is small. δ ' Ti N_x , Ti_2N, pure α-Ti as well as the nitrogen stabilized α- Ti (26 at% N) dissolve only between 1,5 and 2 at% vanadium. Vanadium subnitride β-V_2N_{1-y} dissolves 5 at% Ti. In vanadium rich samples the banded microstructure frequently observed and corresponding to $V_{32}N_3$ disappears with addition of titanium.

Introduction

In technical titanium TA6V4, aluminium and vanadium are the main additive elements. To understand the behaviour of this alloy under nitriding conditions, i.e., to study the quaternary system Ti-Al-V-N, knowledge of the ternary systems involved is necessary. The systems Ti-Al-N(1) and V-Al-N (2) have already been published. No relevant data were found in the literature on Ti-V-N. This is a first report on the ternary system dealing especially with the solubility of the third element in the binary compounds.

Experimental

The samples were prepared from commercially available pure elements, (Ti : 99,9 %, 100 mesh, VENTRON ; V : 99,7% 325 mesh, MALLET SA) and the corresponding nitrides (TiN : 99,5 % 325 mesh, VN : 99,5 % 325 mesh, both from CERAC). Mixtures of the powders were compacted to pellets in stainless steel dies without the use of binders or lubricants. The pellets, each of a total weight of 2g, were arc melted on a water-cooled copper hearth using a non consumable thoriated tungsten electrode under Ti/Zr gettered high purity

Titanium '92
Science and Technology
Edited by F.H. Froes and I. Caplan
The Minerals, Metals & Materials Society, 1993

argon. To obtain homogeneous samples each melted button was turned over and remelted again. After rapid cooling ($\approx$ 150Ks^{-1}), the samples were cut in several pieces. In order to study the ternary crystallization behavior, one part was examined in the as-cast state. Phase equilibria were furthermore checked at different temperatures. Samples were wrapped in 0.025 mm Mo-foils, put in an alumina boat and annealed under purified argon (10^5 Pa) in a constantan wire wound furnace, employing a Haskins E-270 chromel-alumel temperature controller system.

Annealing conditions were : 1400h at 700 and 400h at 1000°C, and, additionally 3000h at 1000°C, in all cases samples were cooled by withdrawing the furnace.

For metallographic inspection, alloys were mounted in epoxy resin, ground on siliconcarbide paper and diamond wheels and subsequently polished on a nylon cloth using diamond paste of consecutively finer grain sizes (down to 0.25 μm) and finally examined on a Olympus optical microscope under reflected and polarized light.

X-ray powder diffraction patterns at room temperature were prepared from all experimental alloys in the as-cast as well as annealed condition, whereby samples were crushed in steel mortar and ground to fine powders in a B_4C mortar. X-ray Debye-Scherrer (114,59 mm camera) photographs as well as diffractometer readings using Cu Kα radiation were evaluated with respect to the number of observed phases, their structure and unit cell dimensions. Precise lattice parameters and standard deviations were obtained from a least-squares fit evaluation procedure; powder diffraction intensities were calculated employing the LAZY-PULVERIX PC program.
Nitrogen losses during arc-melting cannot be avoided or controlled, therefore, the total nitrogen content of selected samples has been determined. These chemical analyses for nitrogen were performed by means of a Carlo ERBA CHN 1108 Dumas-GC analyzer using tin crucibles giving an exothermic reaction upon injection of oxygen and of V_2O_5 as a flux. As seen by the results, all our samples contained less than 30 at% N. Typical measurements were for example : starting composition 60 at% Ti, 5 % V, 35% N yields after arc melting 67% Ti, 5,6% V, 27,4 % N, or 35% Ti, 20% V, 45 % N gives 46,7 % Ti, 26,6% V, 26,7% N.
It was, however, not only necessary to perform average nitrogen analysis, but also - due to the multiphase character of the studied samples - microchemical analysis. For electron probe microanalysis (EPMA) a Cameca SX 50 microprobe with four crystals was used. For nitrogen analysis the crystal PC1 and for titanium analysis an PET crystal was applied. Vanadium was measured by LiF. Accelerating voltages between 15-25 KV with a beam current of 20-60 nA (in some cases up to 300 nA) were chosen. The measurement time per step was usually 10 sec for the peak maximum and 5 sec for the background. Quantitative nitrogen microprobe analysis in the presence of titanium is a difficult procedure since the N-K_α and Ti_{LI} lines coincide. The amount of overlap is such that both lines superimpose to a single line without fine-structure. Sophisticated procedures have been worked out dealing with peak shape determination (3)

which, however are very time consuming and do not allow a sufficient sample throughput. In this work, the nitrogen content determination was performed on the basis of the classical standardization technique. Strictly single phased titanium nitride standards of following compositions were used : α-Ti(N) 23.2 at% N, ε-Ti_2N 32.8 at%N and δ-TiN_x with 37.0 at% N. Another method was just to count the titanium and vanadium concentrations and define the complement as the nitrogen content. This was allowed since the impurity level of the samples, especially oxygen, was found to be below the detection limit of the microprobe apparatus. These measurements were performed at the "Centre de Microsonde Electronique de l'Ouest" in Brest with the valuable help of M. M. Bohn.

Results

The titanium rich side of the diagram.

Arc melted samples containing 5% vanadium and various amounts of nitrogen showed on metallographic inspection a common feature. The most stable compound, TiN_{1-x} , crystallizes first from the melt in a dentritic form. The dendrites are surrounded by a small band of a second phase. The colour effect of their grains in polarized light is much more intensive than that of the dendrites or that of the matrix, a result of the lower symmetry of the hcp α phase as opposed to the fcc crystal lattice of the nitride and to the bcc symmetry of the ß Ti / αV solid solution. Precipitates of the same colours, presumably parallel to the (111) planes are observed within the dendrites [photo 1].



Photo 1

X-ray diffraction patterns (Debye-Scherrer) confirmed these interpretations. We have identified three phases :

- face centred cubic δ - TiN_{1-x} (Vss) with lattice parameters variing between 4,188 Å and 4,212 Å

- hcp α -Ti (V,N)ss with little change in the lattice parameters : a_o remains near to 2,969 Å and c_o remains between 4,770 and 4,795 Å,
- body centered cubic ßTi with vanadium and nitrogen in solid solution, giving very large smeared X-ray peaks which do not allow a precise parameter determination. In these samples we found a_o in the neighbourhood of 3,24 Å.

On the basis of the binary Ti-N diagram (4) one can explain the crystallization behaviour of the arc melted samples, even if equilibrium conditions are not fullfilled, thus the isopleth at 5 at% V can be regarded as a pseudo-binary system.

By cooling from the melt, primary crystallization of TiN_{1-x} takes place first. The primary axes of the dendrites do not contain detectable amounts of vanadium, but the V-concentration increases with the growth of the crystals up to 1,5 at% V near to the interface δ / α. Nitrogen concentrations in these mischkristalls depend upon the total N-content in the melt and are in good agreement with the proposed phase diagrams. Typical EPMA results were for example : 60 at% Ti 38 at%N or 65 at% Ti 34 at%N, the complement being vanadium.
On further cooling the peritectic reaction L + δ -> α begins, giving the coloured bands around the dendrites. However, cooling is too fast and the reaction is not complete. The hexagonal phase has been analyzed in various samples. Concentrations were : 1,5-2 at% V, 72-75 at% Ti, 26-24 at%N. The highest nitrogen concentration corresponds to the maximum solubility of nitrogen in α-titanium. Even in this nitrogen-stabilized α the solubility of vanadium remains low, as opposed to Al, which is also an α stabilizer and increases the solubility of vanadium in α titanium (5). In pure α titanium the order of magnitude of V-solubility is the same; according to (6) it does not exceed 1,5 at% V.
The bcc matrix shows the largest variations in composition, depending upon the weighed in concentrations on the isopleth 5 at% V. Here we find all vanadium rejected from the other phases. Extreme values were 83 at% Ti, 7 at% V, 10 at% N and 65 at% Ti, 27 at% V, 8 at% N. The maximum solubility of nitrogen in ß titanium is 6 at% N at 2000°C. Addition of vanadium which is a ß stabilizer itself, increases the solubility of N in these alloys.

Annealing at 1000°C.

The evolution of the samples after heat treatment at 1000°C shows the transformation of the substoichiometric δ dendrites to ε -Ti_2N (Vss), the presence of stabilized α and an increased solubility of N in the ß phase.
ε -Ti_2N dissolves less than 2 at% vanadium, α dissolves between 1 and 2 at% V. The lattice parameters remain the same in all samples : a = 4,938 Å, c = 3,036 Å for ε and a = 2,969 Å c = 4,786 Å for α.
The body centered cubic solid solution is still poorly crystallized showing wide X-ray diffraction lines. EPMA measurements showed, beside the understandable variations in the Ti/V contents, a surprisingly high nitrogen concentration between 20 and 25 at%.

Annealing at 700°C .

At this temperature, according to Ti-N phase diagrams (7,8) appears the metastable δ'-Lobier-Marcon phase with ordered vacancies in the nitrogen sublattice. Metallographic inspections allowed us to identify this phase clearly, [photo 2] but only in small quantities, thus precise lattice parameters cannot be given. The vanadium content of this phase is less than 1at%, in spite of the existence of a corresponding δ'-VN_x. There might be a continuous solid solution between these two phases, but at lower temperatures, since δ'-VN_x is not stable above 520°C. In our case δ'-TiN_x appears at the center of the dendrites which crystallized first and are very poor in vanadium. The other dendrites are transformed to ε -Ti_2N with a vanadium content of less than 1 at%. Lattice parameters change little in different samples (a_o from 4,930 to 4,937 Å, c_o from 3,032 to 3,036 Å).
One can still identify the small α -bands around ε -blocks. The vanadium content in α is now less than 2 at%. X-ray imaging [photo 3] shows that the rejected vanadium is concentrated between the α -bands and ε . The ß matrix presents various aspects. In some cases uniform as usual, in other cases with small precipitates polarizing like α. Their compositions are also quite different, varying from 73% Ti, 25% V, 2% N to 58% Ti, 30% V, 12% N.

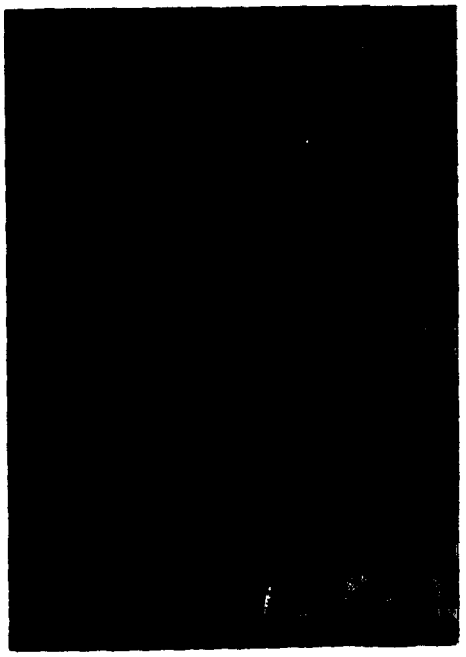


Photo 2



Photo 3

The vanadium rich side

One metallographically very characteristic alloy in the V-N system is the mestastable phase V_{32} N_3 showing a particular, banded microstructure as a result of twinning. One of our samples of the initial composition 90% V 10% N showed this microstructure [photo 4]. EPMA analyses confirmed the $V_{32}N_3$ stoichiometry. By substitution of 5% V by Ti the banded microstructure disappears [photo 5]. The alloy 5% Ti, 85% V, 10% N (initial composition and also the composition observed by EPMA) forms large, homogeneous grains without twinning. Small quantities of titanium are sufficient to prevent the twinning and probably also the ordering of N atoms in this alloy. Other alloys, still on the isopleth 5% Ti, were of two-phase composition, showing the bcc solid solution and the subnitride V_2N_{1-y}. The lattice parameters of the subnitride are slightly increased by titanium incorporation, a = 4,913 Å c = 4,572 Å. A maximum solubility of 5 at% Ti in V_2N_{1-y} has been observed. The lattice parameters of the bcc solid solution were 3,058 Å corresponding to the composition 5 at% Ti, 85 at% V, 10 at% N in all arc melted samples. After annealing at 1000°C the nitrogen concentration decreases slightly in the solid solution. Ti-V-N : 5-85-10 at% and Ti-V-N : 5-80-15 at% present large, homogeneous grains without twinning with V_2N_{1-y} at the grain bounderies. EMPA gives Ti-V-N : 5-86-9 at% for the solid solution and Ti-V-N : 5-66-29 at% for V_2N_{1-y} in very good agreement with respect to the nitrogen concentrations in the two-phase region as described by (9).

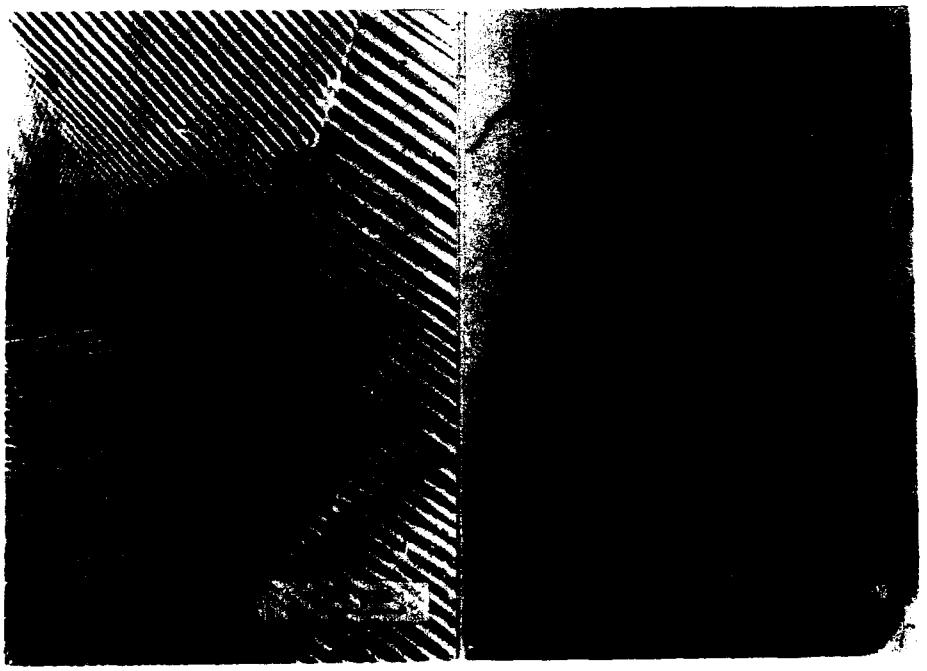


Photo 4

Photo 5

Conclusion

We have measured the solubility of vanadium in arc melted and consecutively annealed Ti-N alloys as well as the solubility of titanium in V-N alloys. These solubilities are small, not exceeding 2 at% vanadium in titanium nitrides under our experimental conditions. Even δ-TiN_X, which presents a complete solid solution with δ-VN_X, dissolves only 2 at% V after arc melting of titanium rich samples. A similar behaviour has been observed in the corresponding Ti-V-C system (10) Technical titanium TA6V4 contains more vanadium, about 4 at %, than the observed solubility limits. This explains why, by nitriding or oxynitriding of TA6V4, vanadium is rejected (11).

References

1. J.C. Schuster and J. Bauer, "The Ternary System Titanium-Aluminium - Nitrogen", Journal of solid state chemistry 53, 260-265 (1984) ; also in "Sixth World Conference on Titanium" France 1988, 1663-1668.

2. J.C. Schuster, J. Bauer and H. Nowotny, "Applications to materials science of phase diagrams and crystal structures in the ternary systems Transition Metal-Aluminium-Nitrogen" *revue de Chimie Minerale*, 22, (1985) 546-554.

3. G.F. Bastin, H.J.M. Heijligers and J.F.M. Pinxter, "Quantitative EPMA of Nitrogen in Ti-N compounds" Microbeam Analysis (D.E. Newburg, Ed) San Francisco Press Inc., 1988, 290-294.

4. W. Lengauer, "The Titanium-Nitrogen System : A Study of Phase Reactions in the Subnitride Region by Means of Diffusion Couples" , Acta metall. mater, vol. 39, n° 12, 2985-2995, 1991

5. E.W. Collings, "The Physical Metallurgy of Titanium Alloys", ASM, Metals Park, OH, 1984, p.62

6. G. Grewal and S. Ankem, "Solubility of Vanadium in α and β Titanium" Metallurgical Transactions A vol. 20A, 334-337, 1989

7. E. Etchessahar, J.P. Bars and J. Debuigne "The Ti-N System : Equilibrium Between the δ, ε and α phases and the Conditions of Formation of the LOBIER and MARCON Metastable Phase" J. of the Less Common Metals, 134, (1987) 123-139

8. E. Etchessahar, Young-Un Sohn, H. Harmelin and J. Debuigne "The Ti-N System, Kinetic, Calorimetric Structural and Metallurgical Investigations of the δ'-$TiN_{0.51}$ Phase" J. of the Less Common Metals 167 (1991) 261-281.

9. O.N. Carlson, J.F. Smith and R.H. Nafziger , "The Vanadium-Nitrogen System : A Review" Metallurgical Transactions A vol. 17A (1986) 1647-1656.

10 E. Rudy, "Ternary Phase Equilibria in Transition Metal-Boron-Carbon-Silicon-Systems", Part V (may 1969) Air Force Material Laboratory, Air Force System Command, Wright-Patterson Air Force Base, Ohio.

11. A. Guillou and J. Debuigne, "Oxynitriding of Titanium and TA6V4 at high Temperature in Dry Air at Low Pressure" Sixth World Conference on Titanium, (France 1988) 1829-1834.

THE EFFECT OF THE β-STABILIZING ELEMENTS AND HEATING/COOLING RATE ON PHASE TRANSFORMATIONS IN MULTICOMPONENT TI-ALLOYS WITH CONSTANT AL CONTENT.

J. Sieniawski and F. Grosman

Silesian Technical University
Department of Mechanics and Technology of Metal Forming
Krasińskiego 8, 40-019 Katowice, Poland

Abstract

Dilatometric studies with heating and cooling rates controlled in the range of 0.004 - 0.08 K/s were performed to evaluate the phase transformation temperatures of the following alloys: Ti-6Al-3Mo, Ti-6Al-3Mo-V, Ti-6Al-2Mo-2Cr and Ti-6Al-5Mo-5V-1Cr-Fe. The values of activation energy of the transformations are similar to those of activation energy of diffusion of the substitutional elements in Ti. Two periods of the $\alpha + \beta \rightarrow \beta$ transformation in the course of heating were revealed: a slow (A^{pw}) and an intensive (A^{pi}) one. To practical applications the intensive period temperature was taken. The equations showing the relationship between the transformation temperature and heating or cooling rate, as well as the content of the β-stabilizing elements have been derived.

Titanium '92
Science and Technology
Edited by F.H. Froes and I. Caplan
The Minerals, Metals & Materials Society, 1993

Introduction

Phase transformations in the titanium alloys containing the elements stabilizing both α-phase (eg. Al) and β-phase (eg. Mo, V, Cr) are rather complicated and still not entirely understood. However, for their important role in the processing of these materials, they require further research to be carried out. Some specific physico-chemical and mechanical properties of these alloys [1-5] in comparison with other construction materials make the studies even more desired.

Taking as an example some selected $\alpha + \beta$ alloys containing different amounts of the β-stabilizing elements (Ti-6Al-3Mo, Ti-6Al-3Mo-1V, Ti-6Al-2Mo-2Cr and Ti-6Al-5Mo-5V-1Cr-1Fe) the phase transformations taking place in the course of continuous cooling and the cooling with an isothermal step within the range of α-phase stability. The temperature ranges of diffusion controlled ($\beta \rightarrow \alpha + \beta$) transformations and the martensitic $\beta \rightarrow \alpha'(\alpha'')$ transformation have been established depending on the cooling rate and the value of the β-phase stability factor K_β [6], and the TTT-curves have been worked out.

Materials and experimental procedures

As a subject of the studies a number of titanium alloys with constant content of Al and with different value (0.3 - 1.2) of the stability factor (K_β were taken. Chemical composition of these alloys is given in Table 1. The following experimental research have been performed to achieve the objectives of the work:

- dilatometric tests;
- x-ray structural analysis to determine the phase composition of the alloys;
- hardness tests;
- microstructure studies using optical and electron microscope.

Dilatometric studies have been performed in argon atmosphere with an absolute dilatometer LS and cylindrical specimens of 4 mm in diameter and 15 mm in length. Phillips PW-1130-00 x-ray diffractometer with a Cu-tube and a Ni filter have been applied to the phase composition studies. As far as the hardness tests are concerned, the Metsuzawa Seiki - Micro SA instrument have been used (Vickers method - 5N/20s load).

Table 1. Chemical composition of the alloys being analyzed

Alloys	Composition (wt %)						Stability factor
	Al	Mo	V	Cr	Fe	Si	K_β
Ti-6Al-3Mo	6.2	3.3	-	-	-	0.3	0.3
Ti-6Al-3Mo-1V	6.2	2.5	1.1	-	-	0.1	0.4
Ti-6Al-2Mo-2Cr	6.3	2.6	-	2.1	0.4	0.25	0.6
Ti-6Al-5Mo-5V-1Cr-1Fe	5.8	5.3	5.1	0.9	0.8	0.15	1.2

The specimens for metallographical studies have been etched with the Kroll's etchant (50% HNO_3 + 40% HF + 10% H_2O) and for the electron microscopy studies a number of thin foils have been prepared.

Results and their analysis

In the first stage of the investigations the $\alpha + \beta \rightarrow \beta$ phase transformation start and finish temperatures were determined using the heating rate V_g = 0.08 K/s. An example of a dillatogramme for Ti-6Al-5Mo-5V-1Cr-1Fe alloy is given in fig.1. In this way the temperatures of the mentioned phase transformation finish have been established which for Ti-6Al-3Mo, Ti-6Al-3Mo-1V, Ti-6Al-2Mo-2Cr and Ti-6Al-5Mo-5V-1Cr-1Fe were 1260, 1224, 1239 and 1153 K, respectively.

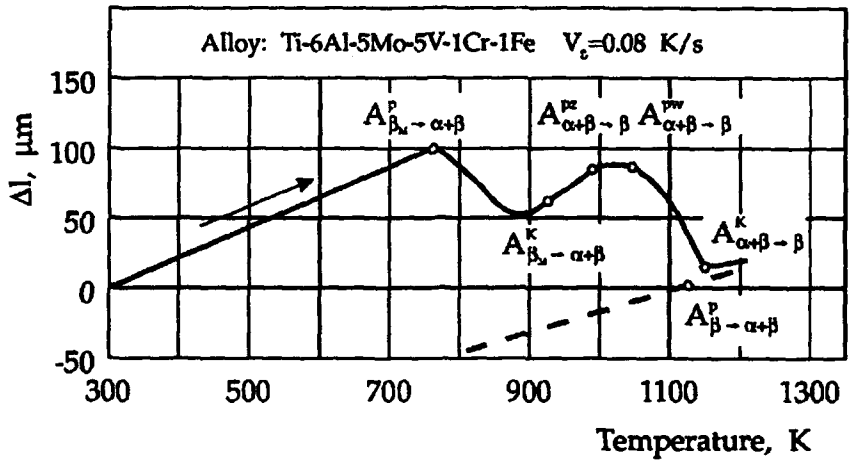


Figure 1 - Dilatogram of a selected alloy

The obtained results served as a basis for the programme of further studies involving continuous and isothermal cooling of the titanium alloys. To obtain the TTT_c-curves the samples of the alloys being studies were first heated to the temperature within their range of β-phase stability with the rate of 0.08 K/s, then annealed for 0.5 h and finally cooled in different media with average cooling rate between 48 - 0.004 K/s within the phase transformation range. As far as the TTT_i-diagrams are concerned, the heating and annealing conditions were the same, but the specimens were cooled in water to the temperature of isothermal annealing. The isothermal annealing was carried out within the temperature range of 559 - 1325 K for 5 to 10^6 s. Two selected examples of TTT_c and TTT_i diagrams for Ti-6Al-3Mo-1V alloy are given in fig.2 and 3.

It was found that during the continuous cooling from the β-stability range, depending on the cooling rate the following transformations of the supercooled metastable β_M phase are possible:

$\beta \rightarrow \alpha'$; $\beta \rightarrow \alpha' + \alpha'' + \alpha$; $\beta \rightarrow \alpha'(\alpha'') + \alpha + \beta_{conc}$; $\beta \rightarrow \alpha + \beta$; β + $TiCr_2(TiFe_2)$.

Moreover, it was noticed that the increase of the content of β-stabilizing elements and thus the increase of the stability factor K_β leads as a rule to decrease martensitic $\beta \rightarrow \alpha'(\alpha'')$ transformation start and finish temperatures at continuous cooling, and that diffusion-controlled transformations tend to shift toward the lower cooling rate (fig.4.). In the case of the increased content of the elements which forms an eutectoid with titanium (eg. Cr, Fe) the eutectoidal transformation was observed at the lowest cooling rate applied (V_{ch} = 0.004 K/s). In the conditions of isothermal annealing the phase composition of the alloys varies quite widely - from martensitic or β_M metastable phase to stable phases being the products of diffusion processes. The following phase transformations, depending on the temperature and the isothermal annealing time may take place: $\beta \rightarrow \alpha + \beta$; $\alpha'(\alpha'') \rightarrow \alpha + \beta$; $\beta_{conc} \rightarrow \omega + \alpha$; $\beta \rightarrow \alpha$ $TiCr_2(TiFe_2)$ and $\alpha' \rightarrow \beta_{conc} + \beta_{conc} \rightarrow \beta_{conc} + \alpha \rightarrow \alpha + \alpha' + \beta_{conc} \rightarrow \alpha + \beta$.

It should be mentioned that the decomposition of the martensitic α' phase, depending on the

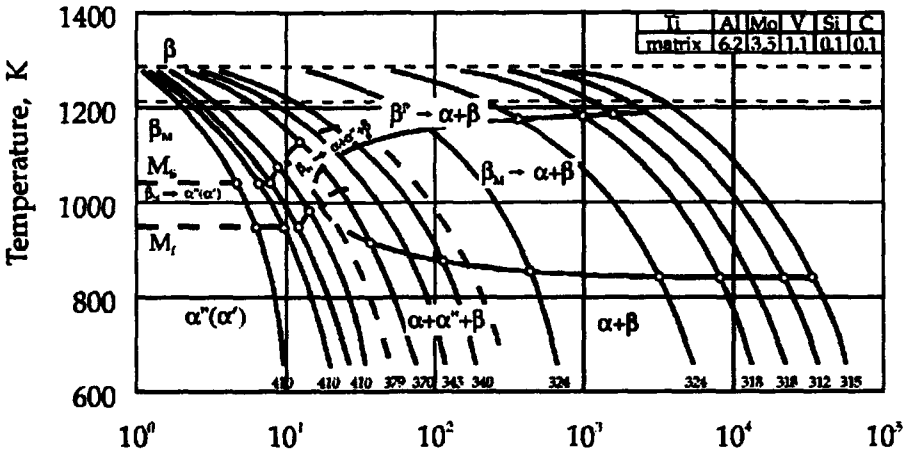


Figure 2 - TTT_c-diagram of Ti-6Al-3Mo-1V ($K_{\beta-0.4}$)

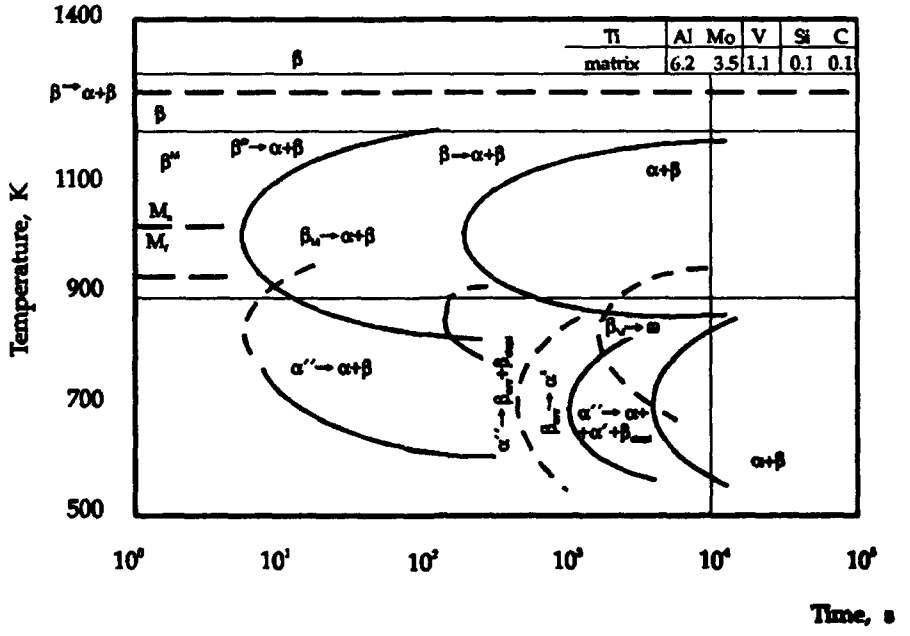


Figure 3 - TTT_t-diagram of Ti-6Al-3Mo-1V alloy ($K_{\beta-0.4}$)

temperature of isothermal annealing can produce either directly stable α and β phases (above 800 K) or the intermediate α'' martensitic phase in the areas of the β-phase enriched with the alloying elements (β_{ann}) which takes place below 700 K and may have a considerable importance in the process of precipitation strengthening of the alloys. Phase transformations in the multicomponent titanium alloys containing Al, Mo, V and Cr at isothermal cooling depend also on the content of the β-stabilizing elements content and vary according to the scheme (fig.5.).

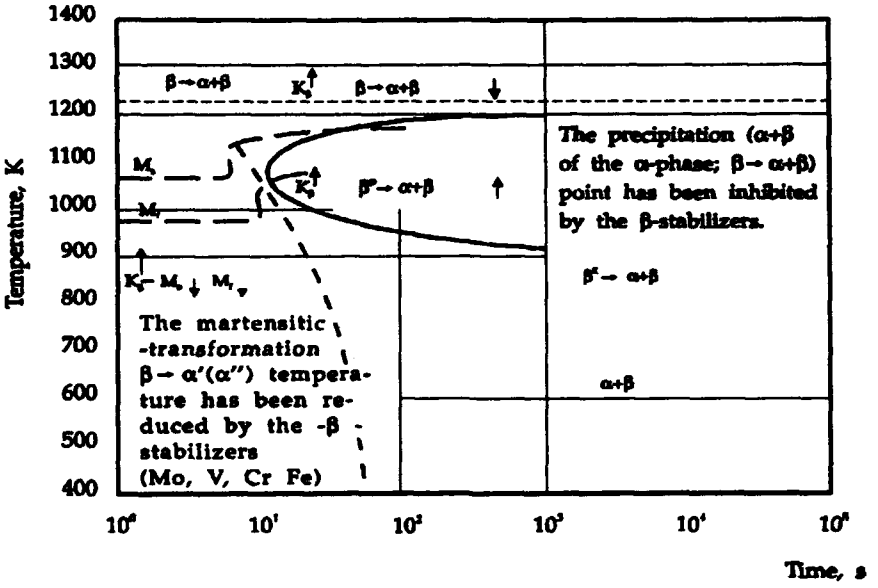


Figure 4 - Effect of β-stability factor (K_β) on the phase transformation in continuous cooling of titanium allouys containing Al, Mo, V and Cr.

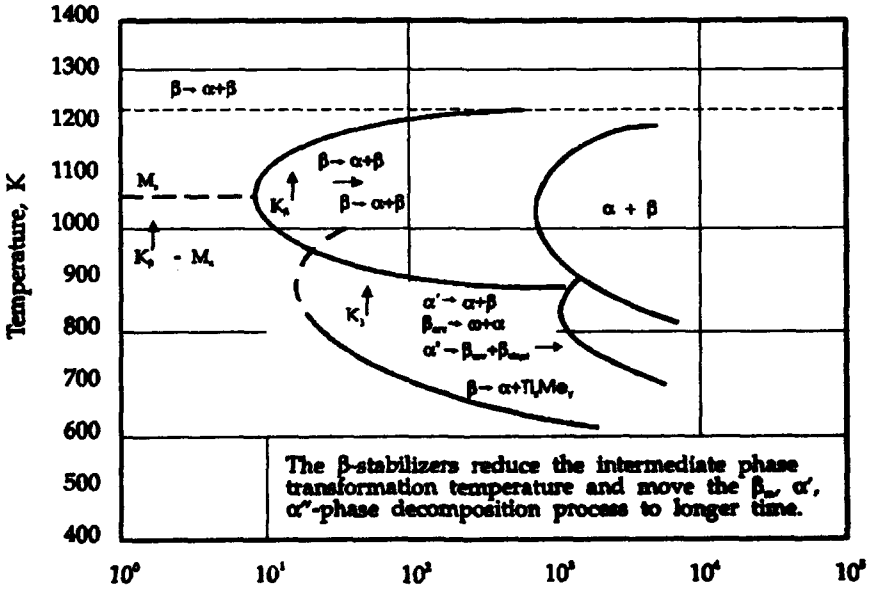


Figure 5 - Effect of β-stability factor (K_β) on the phase transformations in isothermal cooling of titanium alloys containing Al, Mo, V and Cr

Increase of the stability factor K_β impedes the $\beta \rightarrow \alpha + \beta$ transformation which shifts its start toward longer times of annealing, and lowers the temperature of the transformations in the intermediate phases. The $\beta \rightarrow \alpha + \beta$ transformation at higher temperature range (eg. 1150 K) begins in the alloys being studied just after several tens of minutes which is demonstrated by the precipitation of acicular α-phase particles along the primary β-phase grain boundaries. This is followed by the α-phase precipitation process within grains that leads to the formation of colonies of parallel lamellae of the α-phase with various orientations. At lower temperature ranges the transformation starts also as a process of precipitation of the needle-like particles of α-phase along the β-phase grain boundaries; however, in this case the α-phase lamellae are generally smaller in the colonies both at the grain boundaries and within the grains [3].

Conclusions

As a result of the performed studies it was established that the phase composition of Ti-6Al-3Mo, Ti-6Al-3Mo-1V, Ti-6Al-2Mo-2Cr and Ti-6Al-5Mo-5V-1Cr-1Fe alloys changes depending on the content of β-stabilizing elements, cooling rate and the isothermal annealing temperature. During the continuous cooling from the β-phase stability range, depending on the cooling rate, the phase compositions varies from martensitic α'(α'') or metastable β_M-phase structures (in Ti-6Al-5Mo-5V-1Cr-1Fe alloy), via complex structures comprising martensitic and diffusion-produced phases (α, β) to the structures consisting only of stable α and β phases. At the conditions of isothermal cooling the phase composition of the alloys also changes widely - from unstable martensitic α'(α'') or β_M phases to stable α and β phases being the product of diffusion-controlled processes. It should be noticed that the decomposition of the martensitic α' phase, depending on the isothermal annealing temperature may lead either directly to the formation of stable α and β phases (>800 K) or via formation of an intermediate martensitic α''-phase in the areas enriched with the β-stabilizing elements (β_{en}) (<700 K) which may play an important role in the precipitation hardening processes of these alloys. Appropriate selection of the isothermal annealing conditions within the range of the $\beta \rightarrow \alpha + \beta$ phase transformation temperatures makes it possible to control the morphology of the lamellar structure [3] which is of particular importance when these alloys are to be applied in the conditions of heavy dynamic loads and elevated temperature.

References

1. Ulrich Zwicker, Titan und Titanlegierungen (Berlin-New York, Springer Verlag 1974)

2. Andrzej Bylica, Jan Sieniawski, Titanium and Titanium Alloys(in Polish) (Warszawa PWN, 1985)

3. J. Sieniawski, "Lamellae Structure Formation in $\alpha + \beta$ Titanium Alloy" (in Polish), Inżynieria Materiałowa, 1 (1988), 10-14.

4. K.R. Narendrnath and H. Margolin, "The Effect of Matrix Strength on the Fracture Resistance of an Alpha-Beta Titanium Alloy", Metal. Trans., 19A (1988), 2503-2512.

5.F. Grosman and W. Szkliniarz, "Forming of the Structure and Mechanical Properties....." (Paper presented at the 6-th World Conf. on Titanium, France 1988, 1433-1438.

6. J. Sieniawski and F. Grosman, "Wliyanie β-stabiliziruyuszczych elementov i skorosti nagreva i ochlazdenya na fazowye prewraszczenya w splawach titana", (Paper presented at XIII Celoetatne Dni Tepelnego Spracowanya, Bratislava 1990

PHASE TRANSFORMATIONS IN TI–15V–3Cr–3Sn–3Al ALLOY

Wang shihong, Shen guiqin, and Liang youming

Beijing University of Aeronautics and Astronautics
Beijing, 100083, China

Abstract

The T–T–T behaviors of a metastable β–titanium alloy, Ti–15V–3Cr–3Sn–3Al, during isothermal decomposition has been examined using hardness, X–ray diffraction analyses, and optical, Scanning and electron microscopy. The microstructure quenched from above β–transus consists of retained β phase, no ω_a or stress–induced transformation occurs. At isothermal temperature below 450℃, the $\beta \rightarrow \beta+\beta'$ phase separation reaction is observed at early stage of decomposition. The β' formed rate is rather high, at 450℃ –300℃ for time of a few minutes, the coherent metastable β'–phase particles can be detected by TEM. Finally, a TTT diagram is presented and also correlated with the observed hardness changes.

Introduction

Ti–15V–3Al–3Cr–3Sn Alloy (Ti–15–3) is a metastable beta titanium alloy which has high strength and deep hardenability. Usually, it is used in solution treated and aged condition. It is important to understand the structural transformation of this alloy during solution treating and aging, and in particular, the influence of the decomposition of the metastable beta phase on the control of the final properties of the alloy. This paper is based on the research of the isothermal transformation of Ti–15–3 alloy. It summarizes the characterstics of transformation of the metastable beta phase in the temperature range of 300~700℃. During low temperature aging, the $\beta \rightarrow \beta+\beta'$ phase separation reaction occurs extensively. This characteristic has practical significance when determining aging regime of the alloy.

Titanium '92
Science and Technology
Edited by F.H. Froes and I. Caplan
The Minerals, Metals & Materials Society, 1993

Experimental

An ingot of Ti–15–3 alloy of 150 mm in diameter was vacuum consumable–electrode remelted. After heating to the β–phase region, the ingot was forged into a slab, and hot rolled to plate of 6mm thickness. After β–solution annealing, sand blasting and pickling, the plated was cold rolled to 1mm thick sheet. The size of all samples was 10 × 10mm. The composition of the ingot is listed in Table I. The beta transus temperature is about 760℃ ± 5℃, determined by metallographic examination.

Table I Compostion of Ti–15–3 Alloy

Element	V	Al	Cr	Sn	Fe	Si	N	O	Ti
Wt.%	14.42	2.92	2.66	2.66	0.09	0.063	0.0165	0.11	balance

Metallographic samples were heat treated in a tin–bath at 820℃ / 20min. They were transfered to an isothermal furnace and annealed at temperatures of from 300℃ to 700℃, and holding times from 0.5 min to 48h, followed by water quenching. The furnace temperature was controlled to within ± 5℃.

The changes in microstructure after isothermal treatment at different temperaturs was observed. The starting time of metastable β phase transformation was determined by optical microscopy and SEM. The finishing time of transformation was determined by x–ray diffraction analyses. Using these data, the isothermal transformation curves were determinded. The transformation products of low temperature aging were examined by TEM, and their structures were determined by electron diffraction.

To compare transformation characteristics of structures in different aging conditions, this paper analyzes some structures in the direct and pre–cold worked conditions solution treatment.

Finally, the superficial Rockwell hardness of samples was measured after different isothermal treament (Type HR2–45 Superficial Rockwell hardness tester with test load 15kg) to analyze the aging–hardening characteristics.

Results and discussion

1.The characteristics of isothermal transformation in the high temperature region (500~700℃).

Above 500℃, the principal transformation of the metastable β phase is β→α phase. To observe the precipitation process of the secondary α phase (α_s phase), Ti–15–3 alloy specimens were solution treated at 820℃ / 20 min and isothermal annealed at 500, 550, 600 and 700℃ for 0.5 min → 48h, then water quenched. The isothermal treatment at 700℃, which is near the β transus (760 ℃) with less supercooling and driving force of phase transformation, results in a long incubation period. After 30 min, traces of α_s are just visible along prior β grain boundaries. After 4h, the α_s is clearly visible. When the holding time is extended continuously to about 12h, short plates of α_s start forming, but its quantity is still small. After holding for 48h, the quantity of α_s remains unchanged; this means that the transformation has basically The volume fraction of α_s phase is about 22% as determines by x–ray diffraction.

After isothermal treament at 600℃, the rate of formation of α_s increases significantly. After 1

min, α phases are precipitated at prior β grain boundaries. After 15 min, α_g is clearly visible and occurs preferentially at grain boundaries and regularly distributed platelet-like Widmannstatten α formed within grains. Because of the lower transformation temperature, the dimension of α_g decrease clearly, and its dispersion increases. After holding isothermally for 24h, the transformation is completed. The volume fraction of α_g is 41%, which is determined by x-ray diffraction.

The characteristics of isothermal transformation at 500 and 550℃ are similar to that at 600℃. The only difference lies in the kinetics and dispersion of the microstructure. The incubation periods at 550 and 550℃ are 30sec and 1 min respectively. The transformation finish times are all 12h, and the volume fractions of α_g are 50 and 62% respectively. The lower the transformation temperature, the finer the α_g. In addition, in the microstructure of isothermally transformed Ti-15-3 alloy, no precipitation-free-zone or other non-uniform precipitation at grain boundaries were observed. However, these can usually be found in highly alloyed β titanium alloys; for example, the Ti-5V-5Mo-8Cr-3Al alloy (TB2 alloy). In titanium alloys, the nucleation of α_g proceeds auto-catalytically or homogeneously; the former happens in the higher transformation temperature range. The feathered α_g which grew from prior β grain boundaries into the grains, and the Widmannstatten α cluster which formed within the grains, all belong to this case. The homogeneous nucleation of α_g takes place at the expense of transition phases, as the ω phase, and the corresponding transformation temperature is lower, usually below 450℃.

Figure 1 shows the hardening curves of Ti-15-3 alloy during isothermal transformation. It can be seen that the hardening effect is negligible at 700℃, since the quantity of α_g is small, and its size is coarse. The hardening effect at 600℃ is higher, but the peak hardness at 12h is still lower, after that, it enters into overageed condition. However, at 500℃ the hardening effect is obvious, and reaches its peak after 24h. This aging temperature is used in commercial production.

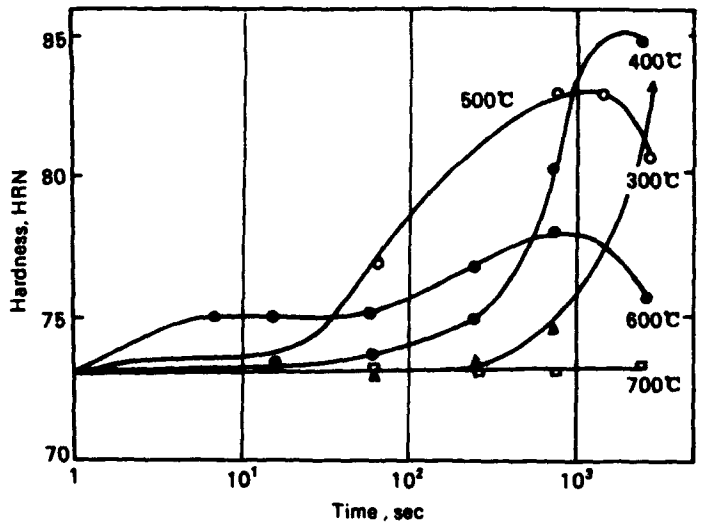


Fig.1 The hardening curves of Ti-15-3 alloy isothermally treated in the temperature region of 300~700℃

2. The charateristics of istothermal transformation in low temperature region (300~450℃).

For the metastable β titanium alloy, the diffusion process slows down below 450℃, and it is difficult to transform the metastable β phase into α phase directly. It must pass through some intermediate transitional phase. The isothermal ω phase is the most frequently encountered

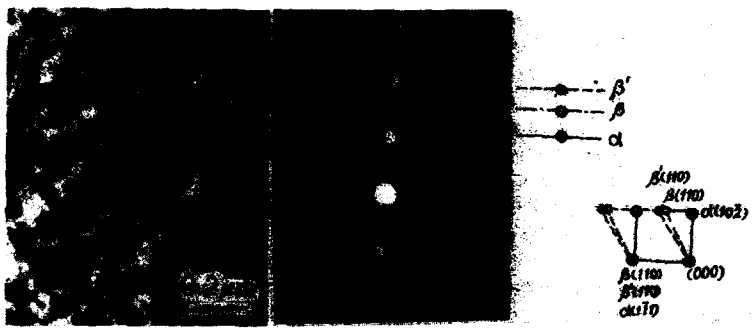
one, for example; in the Ti–10V–2Fe–3Al and β–Ⅲ alloys. The β′ phase is less observed, as in the TB2 alloy. The isothermal ω phase has hcp structure, but the structure of β′ phase is the same as β phase, i.e. bcc structure, but with less alloying element content. Both ω phase and β′ phase have coherent interfaces with the matrix, and their sizes are very fine , usually tens of nm. Under TEM (Figure 2a), the morphology of the precipitates is shown by clusters of speckle–like, contrast. By electron diffraction pattern analysis, these are mixture of two phases,



Fig.2 TEM photographs and diffraction pattern of Ti–15–3 alloy isothermal treated at 400℃ for 12h

i.e.; hexagonal α phase and bcc β′ phase with lattice parameter little different from β phase (Figure 2b). It shows that the β′ transition phase formed before the precipitation of α phase. The sequence of precipitation should be as follows: $\beta \rightarrow \beta' + \beta \rightarrow \beta' + \alpha + \beta$. In order to undrestand the process further, structures of isothermal treatment at 300℃ for different aging times were analyed in more detail. The aging times were 15min, 30 min, 1h, 4h, 12h, and 24h. TEM observation and electron diffraction analysis showed that β′ phase began to form after isothermal holding for 15min. As the isothermal holding time is extened, the size of β′ phase increases continuously, and the β′ phase precipitates assume the form of a crescent. A non–contrast line exists in β′ phase, as a result of a coherent strain field. When the isothermal holding time was extended to 24h, the transformation of β′ to α phase begins. The nucleation of α phase takes place at the expense of β phase, and the α phase assumes the form of colonies which are cluster–like or of snow flake–like with homogeneous distribution. At the same time, long, plate–shaped α phase is present along grain boundaries and sub–grain boundaries (Figure 3). No doubt, β′ phase promotes nucleation of α phase within the grains intensively; therefore, the homogeneity of the aged structure is enhanced. But the β′ phase itself is different from the isothermal ω phase, in that it has no direct contribution to the hardening effect of the alloy. The hardness curves illustrated in Figure 1 show that the $\beta' \rightarrow \alpha$ transformation starts only after isothermal treatment at 300℃ for 24h, causing a significant increase of hardness. At 400℃, this process occurs earlier; after 4h, the hardness increases rapidly, and after 48h the hardness ceases to change.

In order to assess the influence of other heat treatment regimes on the structural transformation mentioned above, structure analysis of specimens in the direct and pre–cold worked conditions after solution treatment has been carried out. After water quenching from solution temperature at 800℃ and aging at 300, 400 and 450 ℃, the $\beta' \rightarrow \beta$ transformation is also observed in the early stage aging, and the transition of $\beta' \rightarrow \alpha$ starts earlier. For example, after aging at 400℃ for 4h, many snow–flake–like structures can be observed by TEM (in Figure 4).



a b

Fig.3 TEM photographs and electron diffration pattern of Ti–15–3 alloy isothermally treated at 300℃ for 24h

(a) precipitation within grain , 50,000x

(b) electron diffraction pattern and indexing from area (a)

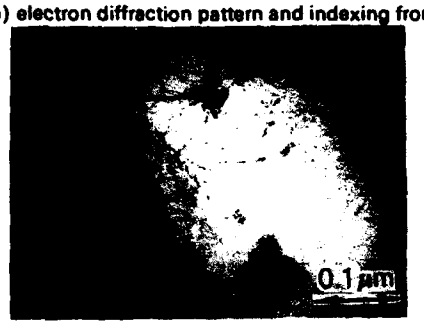
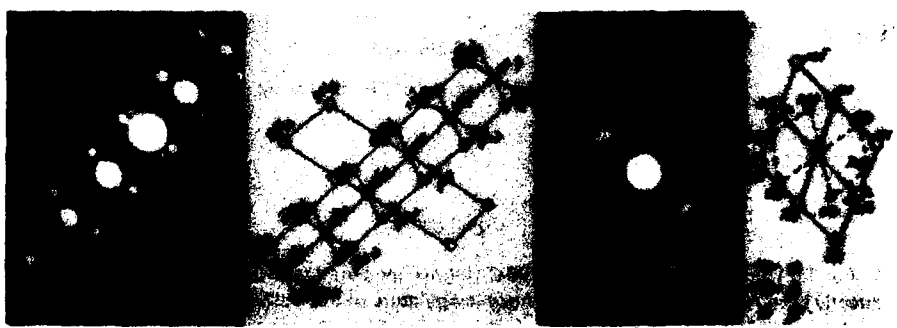


Fig.4 TEM photographs of Ti–15–3 alloy solution treated and aged at 400℃ 4h

As for the pre–cold worked and aged specimens, after annealing (air cooling) from solution temperature and cold working 32 and 78.9% respectively, with a final aging at 450 ℃ for 0.5h, it is surprising to find that in the former case diffraction spots of β' phase appearing in the electron diffraction pattern (Figure 5a), but in the latter case diffracton spot of ω phase is appeared (Figure 5b).



a b

Fig.5 Electron diffraction patterns of Ti–15–3 alloy aged at 450℃, 0.5h after cold worked (a) 78.9% and (b) 32%

This phenomenon, in which two transition phase form in the same alloy during aging at low temperatures, has never been reported here or abroad. According to the theory of phase transformation in titanium alloys, it is generally considered that in near–β titanium alloy, i.e. in lean

β titanium alloys, aged at lower temperatures, the ω phase forms easily; and in rich β titanium alloys the β' transition phase forms preferably. It is not clear whether β' phase and ω phase can appear at the same time, and what relationship exists between these two phase. The content of β stabilising elements of Ti–15–3 alloy is higher than that of near–β titanium alloys, for example, Ti–1023; and is lower than the traditional metastable β titanium alloy, for example, β_c and TB2, since the structure and composition of ω phase is nearer to that of the final equilibrium α phase. The transformation β→ω is more difficult than β→β', and more fluctuations of structure and compostition are neeeded. The experimental results mentioned above show that, in general, during isothermal treatment or solution and aging process of Ti–15–3 alloy, only β→β'→α transformation occurs. However, if the alloy undergoes cold deformation and, especially, sever cold deformation, the β→ω→α transformation can be induced. Figures 5a and 5b show that the ω+α+β and β'+α+β phases coexist respectively. It is confimed, therefore , that both β' phases and ω phases can be the transition phase preceeding the formation of α phase in the same alloy. As to the relationship and condition of transformation between β ' and ω phases, more systematic and deeper study is needed. This will have important theoretical and practical significance.

Based on the above mentioned experimental results, the isothermal transformation curves of Ti–15–3 alloy are determined. Since only limited data have been obtained for the low temperature region, no corresponding curves can be drawn in the Figure 6.

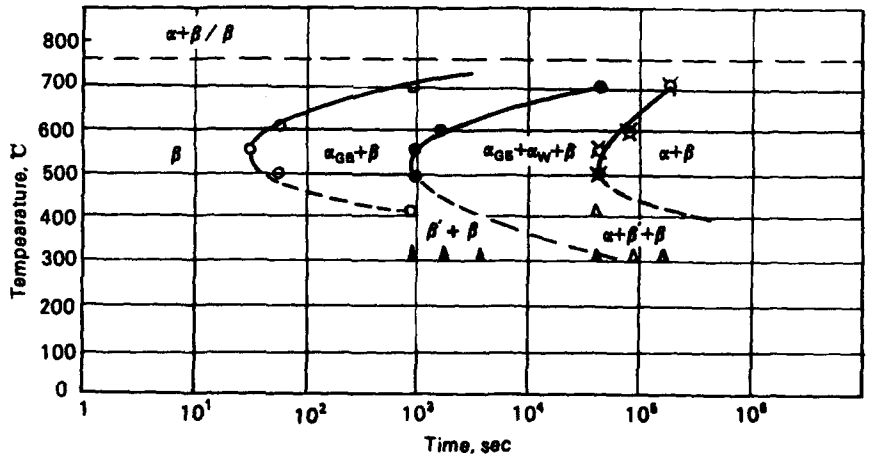


Fig.6 TTT diagram of Ti–15–3 alloy

Conclusions

1. For Ti–15–3 alloy, in the 500~ 700℃ higher temperature region, α_s phase precipitates directly from metastable β phase. The nose temperature of the isothermal transformation curves is about 550℃ . The lower the transformation temperature, the greater the dispersion and homogeneity of α_s phase, the higher the fraction of transformation and the lower the fraction of grain boundary α.
2. Below 450℃, the phase separation reaction β→β'+β occurs first, then transforms gradually to equilibrium α phase.

3. In pre—cold worked and aged condition, ω transition phase can appear in Ti–15–3 alloy. For extended aging times, ω phase transforms to α phase.
4. The hardening effect of α_s precipitates is directly related to the dispresion and transformation quantity, and β' phase itself has no clear hardening effect.

References

1. T.W. Duerig and J.C. Wlliams, " Microstructure and properties of Beta Titanium Alloys" , Beta Titanium Alloys in the 1980's, (Pittsburgh, Pennsylvania, 1984) P.19–67.
2. F.H. Froes, C.F. Yolton and J.A. Hall, " Development and Properties of Ti–15–3", ibid, 209–230.
3. M.Okada, D.Banerijee and J.C. Williams, " Tensile Properties of Ti–15–3 Alloy" , Titanium Science and Technology, (1984.4.3), 1835–1842.

A Study of Grain Growth Behaviour in Titanium Alloys

S.P. Fox

IMI Titanium Ltd., Birmingham, England, UK.

ABSTRACT

The beta grain size of forged and beta heat treated titanium alloys is an important factor in determining the properties of a component. However, the metallurgical factors that affect the beta heat treated grain size are not fully understood. A study of the kinetics of beta grain growth and the effect of processing variables on grain size and growth behaviour has therefore been carried out.

At least two different types of grain growth behaviour have been identified. The most rapid growth corresponds to classical steady state behaviour whilst other types of kinetics can be attributed to some restriction of grain boundary mobility. Both types of behaviour can occur in any given alpha-beta or near alpha alloy and once established, the kinetics are relatively unaffected by subsequent processing.

The possible factors responsible for the observed differences are considered. The results highlight the need for consistent process control.

Acknowledgement

This work has been carried out with the support of the Procurement Executive, Ministry of Defence.

Titanium '92
Science and Technology
Edited by F.H. Froes and I. Caplan
The Minerals, Metals & Materials Society, 1993

Introduction

The beta grain size of forged and beta heat treated titanium alloys has an important influence on the mechanical properties. However, the factors that affect the beta heat treated grain size are not fully understood. A study of the kinetics of grain growth during beta heat treatment has, therefore, been carried out. The effects of alloy composition and temperature have been included. The results are discussed with reference to established theories and mechanisms relating to grain growth.

Experimental Procedures

Three different alloys were included in this study. Near alpha alloys IMI 685 and IMI 829 (the compositions are given in Table I) were considered in most detail as these are commonly used in the beta heat treated condition. Samples of these alloys with various processing histories were selected for this study. The grain growth behaviour in these near alpha alloys was compared with that in the alpha beta alloy IMI 318 (Ti-6Al-4V).

Table I. Alloy Details

Alloy	Beta Transus °C	Nominal Composition
IMI 318	995	Ti - 6Al-4V
IMI 685	1020	Ti - 6Al-5Zr-0.5Mo-0.25Si
IMI 829	1015	Ti - 5.6Al-3.5Sn-3.0Zr-1Nb-0.25Mo-0.3Si

The material was in the form of as-forged 250mm diameter billet slices, except for the IMI 318, where 300mm diameter billet was used.

To determine the grain growth kinetics, heat treatments were carried out at temperatures from 1050°C to 1200°C for various times. After heat treatment, the samples were machined to remove the effect of oxidation and to eliminate the influence of the surface on grain size. The mean grain size was determined by the mean linear intercept technique according to ASTM E112.

Data Analysis

The macro grain size data was plotted as Log_{10} D vs Log_{10}t on the assumption that the general expression for grain growth is appropriate(1).

$$D = at^n \qquad (1)$$

Where D = the mean grain size, a is a temperature dependent constant, t is the time and n is the time exponent obtained from the slope of the Log D vs log t plot. The above relationship is only approximate, (2) but provides a useful basis for comparing behaviour.

If n is independent of temperature and the constant a varies exponentially with temperature according to:-

$$a = a_0 \exp\left(-{}^{Q}/_{RT}\right) \qquad (2)$$

Then a plot of ln D vs ${}^{1}/_{T}$ should produce a straight line of slope $-n{}^{Q}/_{R}$ when Q is the activation energy for grain growth and a_0 is the pre-exponential rate constant. The activation energy Q for grain growth was determined by this approach for selected samples of IMI 685 and IMI 829.

Results

The important results are presented in Figures 1 to 4. Substantial differences in grain size and growth rates are apparent. Three distinct types of grain growth behaviour have been observed. These may be categorised as:-

a). Type 1. Normal growth (Figure 1)

b). Type 2. Slow growth (Figure 2)

c). Type 3. Discontinuous growth (Figures 3 and 4)

a). Type 1.

Normal or type 1 grain growth behaviour was observed in samples of both IMI 685 and IMI 829 (see Figure 1 for example). The data corresponds well with equation 1 and the exponent n is independent of temperature, see Table II. Values of n in the range 0.33-0.37 are in agreement with the literature for normal grain growth in substitutional alloys (1,2). Table II also shows values for the activation energy obtained. Values of 200KJ/mol are typical of those for substitutional diffusion in titanium alloys.

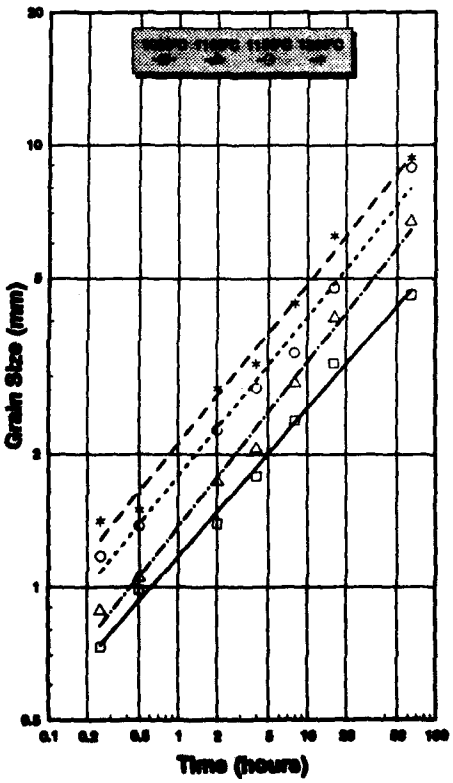


Figure 1. Grain Growth Kinetics Sample IMI685/1

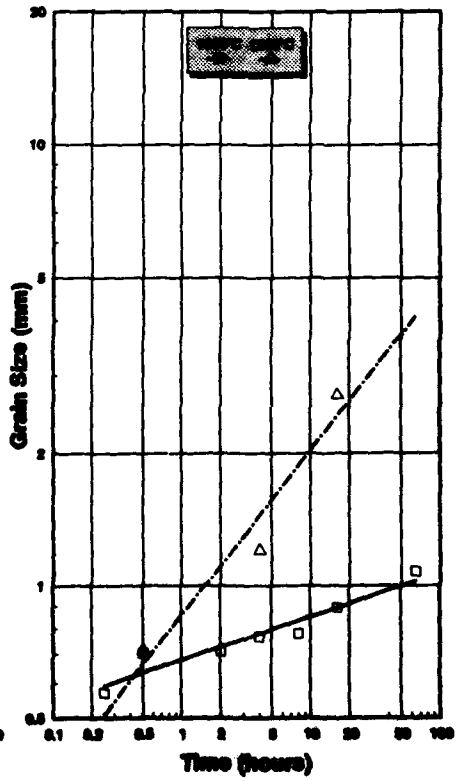


Figure 2. Grain Growth Kinetics Sample IMI829/3

Table II. Normal Grain Growth Exponents and Activation Energies

Temperature	Sample IMI 685/1		Sample IMI 829/1	
	n	R*	n	R
1050	0.33	0.994	0.34	0.989
1100	0.37	0.992	0.35	0.995
1150	0.36	0.989	0.36	0.995
1200	0.35	0.988	0.33	0.989
	Q = 203KJ/mol		Q = 211KJ/mol	

* R = correlation coefficient

b). Type 2.

An example of slow or type 2 grain growth is presented in Figure 2 for sample IMI 685/3. Although at 1050°C the grain size at 0.25hrs is similar to that shown in Figure 1, the growth rate is very much slower. The data approximates to a straight line yielding an exponent of n = 0.10. Additional data is given in Table III.

Limited data at 1200°C suggests a possible change to "normal" behaviour.

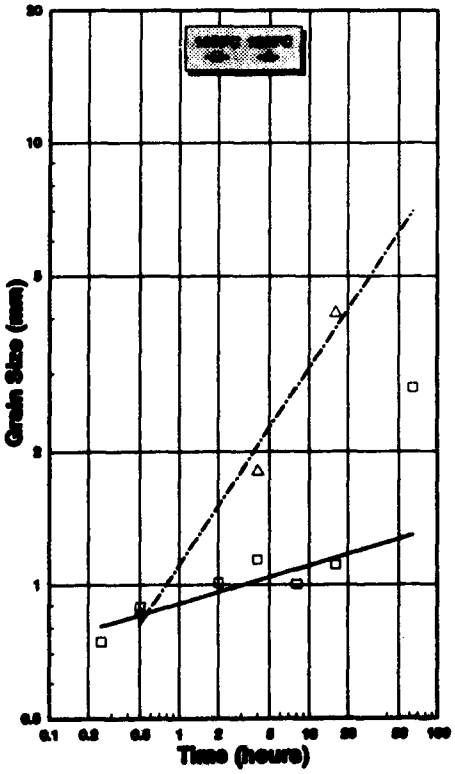


Figure 3. Grain Growth Kinetics Sample IMI685/2

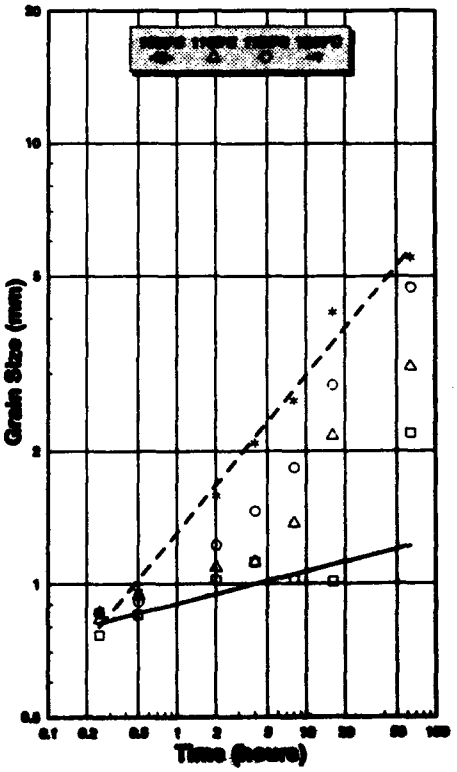


Figure 4. Grain Growth Kinetics Sample IMI810/1

Table III. Grain Growth Data for Growth Type 2 and 3

Growth type	Alloy	Sample Identity	1050°C Exponent	R	1200°C Exponent	R
Type 2	IMI 635	IMI 685/3	0.10	0.916	0.37	0.940+
Type 2	IMI 685	IMI 685/4	0.13	0.916	-	-
Type 2	IMI 829	IMI 829/2	0.07	0.992	-	-
Type 3	IMI 685	IMI 685/2	0.09*	0.762	0.44	0.979+
Type 3	IMI 318	IMI 318/1	0.07*	0.685	0.36	0.984

\+ 3 points only
* Up to 16 hours

c). Type 3.

Discontinuous or type 3 behaviour has been observed in samples of IMI 685 (Figure 3) and IMI 318 (Figure 4). The main features of this type of growth are significant deviation from power law behaviour and an apparent transition to "normal" behaviour at longer times and higher temperatures. This is shown most clearly for IMI 318 in Figure 4. The initial "average" growth rate at 1050°C shown in Figures 3 and 4 is similar to that shown in Figure 2, but displaced to an overall higher grain size. However, between 16 hours and 64 hours, perhaps upon achieving a "critical" grain size,

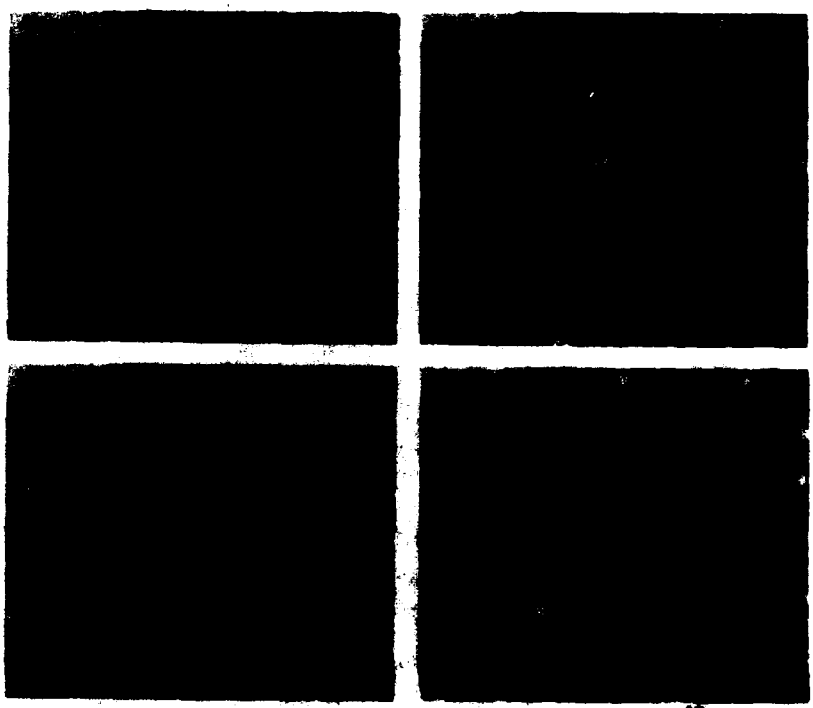
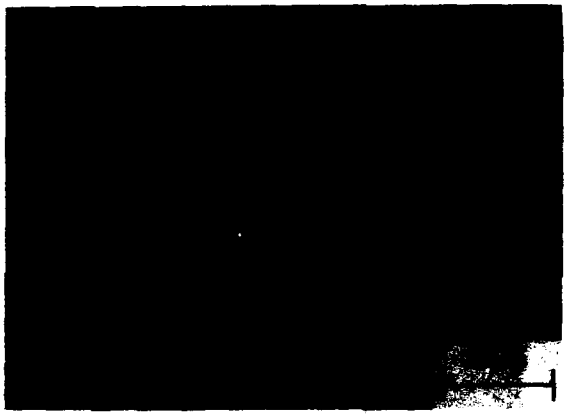


Figure 5. Abnormal Grain Growth in IMI318/1 at 1100°C 10mm

the growth rate increases to a level similar to that for "normal growth". However there is evidence to suggest that this is due to abnormal growth of a few grains. This effect is illustrated in Figure 5. The presence of a few large grains leads to a distorted mean grain size.

On the assumption that type 1 behaviour represents *normal grain growth*, then types 2 and 3 must be due to some restriction of grain boundary mobility. Given that IMI 685 shows all types of behaviour, alloy composition would not appear to be a significant factor in this regard. Precipitation is the most commonly cited reason for grain boundary pinning. Figure 6 shows SEM and TEM micrographs of grain boundaries in IMI 685 cast SC 34199 after treatment at 1050°C for 4h. There is no evidence of precipitates in either case. The TEM micrograph (Figure 6b) shows the grain boundary to one side of the grain boundary alpha. The occasional "particles" in the grain boundary alpha have been identified as beta phase.

a) Back scattered electron micrograph showing clean grain boundaries.



b). Transmission electron micrograph showing grain boundary to one side of the grain boundary alpha. Occasional beta particles are present in the grain boundary alpha

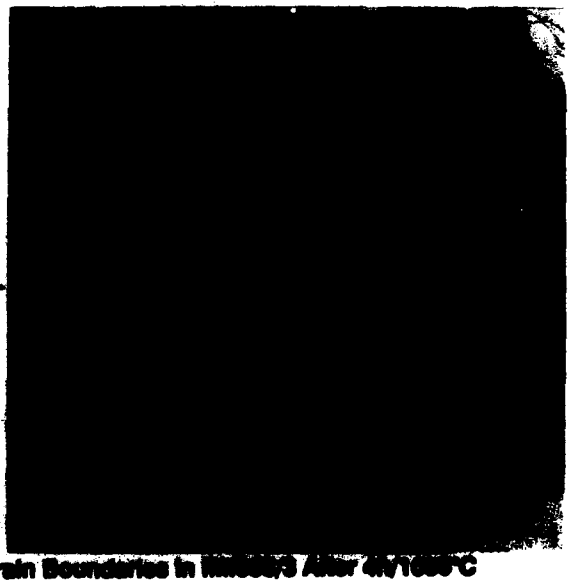


Figure 6. Showing Grain Boundaries in IMI685 After 4h/1050°C

Discussion

As mentioned previously, plotting Log_{10} D vs Log_{10}t is not strictly valid(2). However, it has served to illustrate the variation in beta grain growth behaviour in near alpha and alpha beta titanium alloys.

It was stated earlier that grain growth types 2 and 3 must be due to some restriction of grain boundary mobility. In fact, the abnormal grain growth in type 3 requires a strong restriction to growth (3,4). Four grain boundary pinning mechanisms relating to surface energy, precipitation, solute drag and texture have been recognised.

a). Surface Energy

For the majority of samples, sufficient material was removed to ensure no influence of the surface. This became impractical for the very large grain sizes. However, in all samples the grain size was uniform across the section suggesting little if any influence of the surface.

b). Particle Pinning

The pinning of grain boundaries by precipitates is the most obvious mechanism for restricting grain size and for generating the conditions for abnormal grain growth. No evidence for such mechanism has been found in this instance and whilst this may be regarded as inconclusive, the additional point that there are no known precipitates present in these alloys above the beta transus leads to the conclusion that this mechanism is unlikely.

c). Solute Drag

The normal alloy content is not relevant in this instance given the spread of grain growth behaviour in IMI 685.

Thus to argue this mechanism, some additonal species such as the low solubility elements, chlorine, sulphur and phosphorous must be invoked. The role of these elements in titanium is uncertain and therefore despite the high homologous temperature, solute drag cannot be eliminated.

d). Grain Orientation/Texture

Texture has long been cited as a mechanism for restricting grain growth (1,5). From the theoretical viewpoint, it has been demonstrated that depending on the exact range of orientations present and the size distribution of the different grain populations, all forms of grain growth behaviour can occur (6). Evidence of orientation controlled grain growth in alpha titanium has been reported (7), but there is no information for beta annealed titanium. The texture in beta heat treated titanium alloys is generally assumed to be minimal (8), but this is not always the case (9). Thus it would appear that texture effects should be investigated further.

Whatever the mechanisms involved, it has been shown previously that once a type of grain growth kinetics are established during primary manufacture it is difficult to change them by secondary processing such as rolling or simple forging (10).

The implications of this are that in order to achieve a specific grain size in a final forged and heat treated component it is necessary to obtain the required grain size and growth behaviour in the initial billet. This has been achieved in practice by close process control at all stages of primary manufacture, and in particular by control of reheat and heat treatment practice to minimise grain growth.

Summary/Conclusions

A study of the kinetics of beta grain growth during beta heat treatment has revealed three types of growth kinetics. One corresponds to normal grain growth whilst the other two are due to restriction of grain boundary mobility. Alloy chemistry has been shown to be unimportant in this regard. The implications of the variations in grain growth behaviour for beta heat treated alloys such as IMI 685 and IMI 829 have been discussed. The potential for wide variations in grain size in a beta heat treated component is avoided by close process control at all stages of manufacture.

References

1. F. Haessner, ed., Recrystallisation of Metallic Materials (Dr.Riederer Verlag GmbH, Stuttgart, 1978).

2. P.Ganesan, K. Okazaki and H. Conrad. Met. Trans. 10A (1979), 1021-1029.

3. M. Hillert, Acta Met., 13 (1965), 227-238.

4. D.J. Srolovitz et al., Acta Met., 32 (1984) 1429-1438.

5. J.W. Martin and R.D. Doherty, Stability of Microstructure in Metallic Systems, (Cambridge University Press, 1976) 221.

6. G. Abbruzzeso and K. Lucke, Acta Met., 5 (1986), 905-914.

7. H.J. Bunge, Titanium Science and Technology, Munich, 1984, ed . G. Lutjering, U. Zwicker and W. Bunk (Deutches Gesellschaft fur Metallkunde e.v. 1985) 1713-1719.

8. A. Sommer et al., Titanium and Titanium Alloys., Moscow, 1976, ed. J.C. Williams and A.F. Belov, (Plenum Press 1982) 1683.

9. M.R. Winstone, Sixth World Conference on Titanium, Cannes, 1988, ed., P. Lacombe, R. Tricot and G. Beranger (Les Editions de Physique, 1989) 169.

10. D.F. Neal, Beta Recrystallisation of Near Alpha Titanium Alloys (Report IMI Ti/RDR/7/87, IMI Titanium Ltd, 1987).

GRAIN GROWTH KINETICS IN BETA PHASE OF Ti-6Al-4V ALLOY.

F.J.Gil, P.Tarín* and J.A.Planell.

Dept. Ciencia de los Materiales e Ingeniería Metalúrgica.
E.T.S. Ingenieros Industriales. Universidad Politécnica de Cataluña. Av.Diagonal 647. 08028-Barcelona.

*Dept. de Materiales y Producción Aerospacial.
E.T.S. de Ingenieros Aeronáuticos. Universidad Politécnica de Madrid.

Abstract

The grain growth kinetics of a ß Ti-6Al-4V alloy has been determined by measuring different grain size parameters (perimeter, area, minimum and maximum diameter) as well as the ratio of the grain boundary area per unit volume for different heat treatment temperatures and times. The grain order and activation energy have been also evaluated.

Introduction

It is well established that the driving force for grain growth is the reduction in the energy associated with the decrease in grain boundary area , and it has been proposed that the rate of boundary migration is inversely proportional to the boundary radius of curvature (1). Grain growth takes place due to diffusion when thermal energy is given to the material. This means that the ratio number of grains/unit volume decreases, the size of the grains increases, and both the ratio of grain boundary area/unit volume, and the ratio of stored energy/unit volume, decrease. Consequently a state of higher thermodynamic stability is reached.

This grain growth kinetics at constant temperature and for normal grain growth of single phase metals follows the Arrhenius equation (2-4):

$$D - D_0 = Kt^n \qquad [1]$$

where D is the size of the grain at a certain time, D_0 is the initial grain size, t is the he : treatment time, and K and n are constants which depend on the metal composition and the temperature, but are independent of grain size.

Moreover, if atomic diffusion across the grain boundary is a simple activated process, it can then be shown that K can be written as (2-3):

$$K = K_0 \exp(-E_a/RT) \qquad [2]$$

Titanium '92
Science and Technology
Edited by F.H. Froes and I. Caplan
The Minerals, Metals & Materials Society, 1993

where E_a is the activation energy for the process, T is the temperature in Kelvin and R is the universal gas constant. Therefore, the law of grain growth can be written in terms of both temperature and time:

$$D - D_0 = K_0 \exp(-E_a/RT)t^n \qquad [3]$$

In the present work, the experimental investigation of the grain growth kinetics at different temperatures and times of heat treatment for Ti-6Al-4V alloy in ß phase has been carried out . One of the reasons, usually stated, for avoiding annealing treatments and hot working of the Ti-6Al-4V alloy at temperatures over ß transus is the large grain growth exhibited at such temperatures. The aim of the present work is to quantify the grain growth kinetics when the alloy is heat treated in its ß phase.

Experimental Procedure

Grain growth kinetics have been studied in a Ti-6Al-4V alloy kindly donated by Industrias Quirúrgicas de Levante S.A., which came in cylindrical rods of 13 mm in diameter and 11 cm in length. Discs 6 mm high were cut and 30 specimens were prepared. The chemical composition of this alloys is shown in Table I. The microstructure of the as received material corresponded to the "mill annealed", obtained by forging at 950°C, annealing at 700°C for 2 hours and cooling in air. Fig.1 shows a tranverse cut of the rod. Both the chemical composition and microstructure are in good agreement with the ASTM F136-84 standard (5) for wrought Ti-6Al-4V for surgical applications.

Table I. Chemical composition of the Ti-6Al-4V ELI.

Al	V	Fe	C	O_2	N_2	H_2	Ti
6.1	4.0	0.11	0.021	0.09	0.010	0.0012	Balance



Fig.1. "Mill-annealed" microstructure corresponding to a transverse cut of the rod.

Two specimens were used as reference samples, whilst the others 28 were subjected to different heat treatments above the ß transus temperature of the material. The temperatures used were 1050, 1100, 1150 and 1200°C and the heat treatment times were 5, 10, 15, 20, 30, 60 and 120 minutes at each temperature.

A set of specimens was placed in a tubular furnace with argon atmosphere at a fixed temperature for each experiment and then removed from the furnace according to the time sequence and rapidly quenched in water at 20°C.

The specimens were then metallographically polished and etched with a mixture of HNO_3 and HF acids diluted in water. Metallographic observation was carried out and grain size paramenters (perimeter, area, minimum and maximum diameter) were obtained by Image Analysis with a MIP (Microm Image Processing) equipment. The samples were studied transversally and longitudinally. Fig.2 shows the microstructure of a sample heat treated at 1050°C for 5 minutes.



Fig.2. Martensitic microstructure of a sample heat treated at 1050°C during 5 min.

Experimental Results

The grain size values obtained (perimeter, area, minimum and maximum diameter) are shown in relation to heat treatment time and at each temperature in Figs. 3, 4, 5 and 6 for each growth parameter. The grain size increases as both the heat treatment temperature and the heat treatment time increase. Taking into account that the initial average grain size of the alloy has an area of 24000 μm^2, the final average grain size after 120 minutes of heat treatment increases by a factor of 19 at 1050°C, by a factor of 31 at 1100°C, by a factor of 45 at 1150°C and by a factor of 58 at 1200°C.

These graphs show that rapid grain growth occurs during the first 15 to 20 minutes of heat treatment, but subsequently the grain growth rate decreases.

The grain growth kinetics of the alloy ß Ti-6Al-4V follows the Hillert distribution (6), since the maximum radius is smaller than 1.8 times the value of the average radius. This means that growth takes place in a uniform way in the whole material and that the distribution of sizes obeys an asymptotic law, typical of equilibrium states. Such kinetic behaviour agrees with equation [1], since after taking logarithms, linear equations are obtained with correlation coefficients greater than 0.97. The slope of such straight lines is the growth order n, shown in Table II.

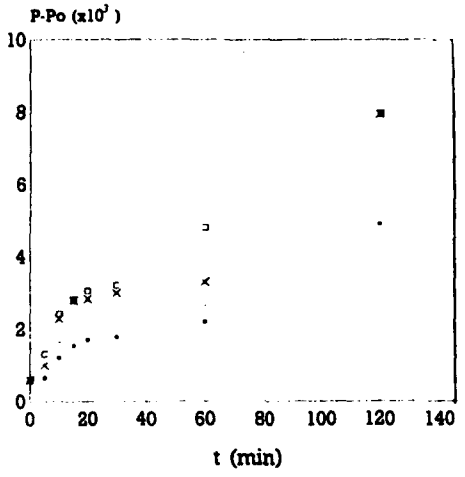


Fig.3. Perimeter (μm) in relation to temperatures and times of heat treatment (min).

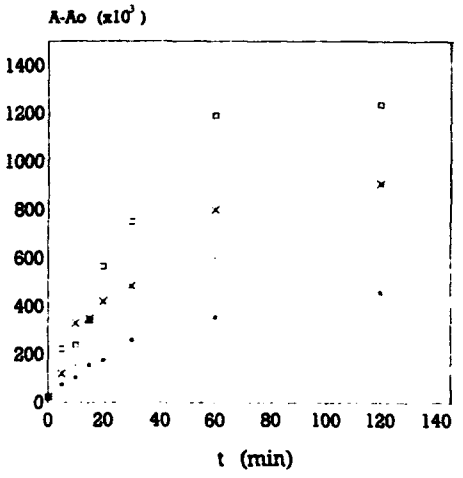


Fig.4. Area (μm^2) in relation to temperatures and times of heat treatment (min).

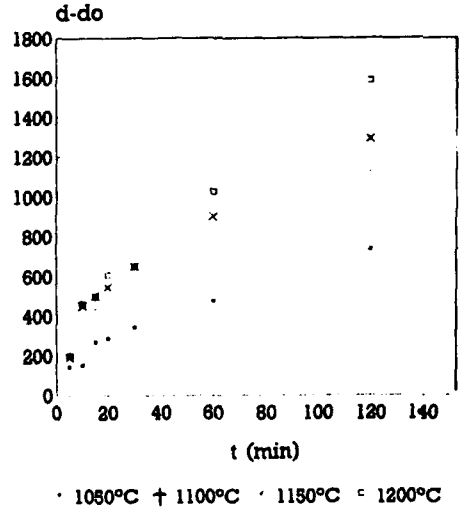


Fig.5. Minimum diameter (μm) in relation to temperatures and times of heat treatment (min).

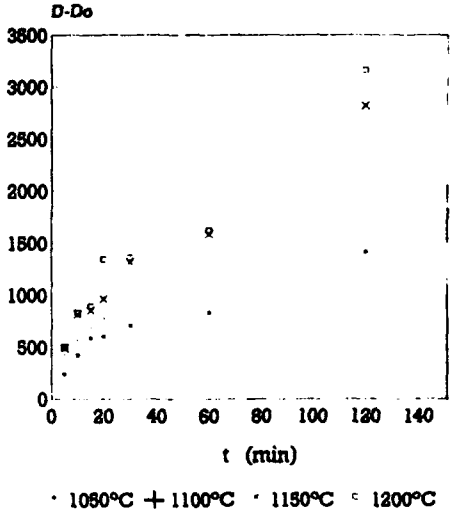


Fig.6. Maximum diameter (μm) in relation to temperatures and times of heat treatment (min).

The activation energy for grain growth, using the different growth parameters, has been calculated from equation [2]. Table III shows the corresponding average values for the different heat treatment times. Such results have been obtained by taking logarithms to equation [3], considering the growth order constant with temperature for growth parameter. The activation energies range between 91 KJ/mol for the maximum diameter and 98 KJ/mol

for the perimeter. The fact that the values are all very similar show that grain growth can be described by a simple activation law.

Table II. Growth order and different heat treatment temperatures for the measured parameters. (r is the lineal correlation coefficient).

T(°C)	Equation	Growth exponent
Perimeter		
1050	$P-P_0 = 2.49t^{0.55}$	0.55 (r=0.99)
1100	$P-P_0 = 2.57t^{0.55}$	0.55 (r=0.97)
1150	$P-P_0 = 2.75t^{0.52}$	0.52 (r=0.98)
1200	$P-P_0 = 2.84t^{0.49}$	0.49 (r=0.98)
Area		
1050	$A-A_0 = 4.46t^{0.59}$	0.59 (r=0.99)
1100	$A-A_0 = 4.67t^{0.59}$	0.59 (r=0.99)
1150	$A-A_0 = 4.75t^{0.63}$	0.63 (r=0.97)
1200	$A-A_0 = 4.82t^{0.65}$	0.65 (r=0.97)
Minimum diameter		
1050	$d-d_0 = 1.75t^{0.53}$	0.53 (r=0.98)
1100	$d-d_0 = 1.97t^{0.52}$	0.52 (r=0.98)
1150	$d-d_0 = 2.02t^{0.54}$	0.54 (r=0.97)
1200	$d-d_0 = 1.97t^{0.59}$	0.59 (r=0.99)
Maximum diameter		
1050	$D-D_0 = 2.11t^{0.50}$	0.50 (r=0.98)
1100	$D-D_0 = 2.20t^{0.55}$	0.55 (r=0.98)
1150	$D-D_0 = 2.33t^{0.53}$	0.53 (r=0.99)
1200	$D-D_0 = 2.28t^{0.60}$	0.60 (r=0.99)

Table III. Activation energies for the different grain size parameters.

Parameter	Equation	Activation energies (KJ/mol)
Perimeter	$K= 10^{7.00}\exp(-98/RT)$	98
Area	$K=10^{10.01}\exp(-97/RT)$	97
Minimum diameter	$K= 10^{6.04}\exp(-94/RT)$	94
Maximum diameter	$K= 10^{6.24}\exp(-91/RT)$	91

The ratio of the grain boundary area per unit volume (Gv) has been determined at each temperature and for each heat treatment time. Assuming that the grains have the ideal shape of a tetrakai-decahedron, the value of Gv can be determined from the mean grain boundary area on a random section from (7):

$$Gv = 3.059/A^{1/2} \qquad [4]$$

Fig.7 shows a steep decrease of Gv with time up to 15 minutes. For longer times a limiting grain size is asymptotically approached.

When the samples were heat treated at higher temperatures (1300°C) or during longer times (more of 120 minutes at 1200°C), abnormal grain growth was observed, as shown in Fig.8. This is a common effect in other metals and alloys. Burke (8) suggested that when a

secondary grain has become considerably larger than its inmediate neighbours, it can grow at their expense, at a level of normal grain growth inhibition which may still prevent the growth of smaller grains since the boundary tension forces at the edge of an exceptionally large grain will be further from equilibrium, and will therefore provide a greater driving force for growth by successive straightening and recurving, than is the case for the (inhibited) smaller grains.

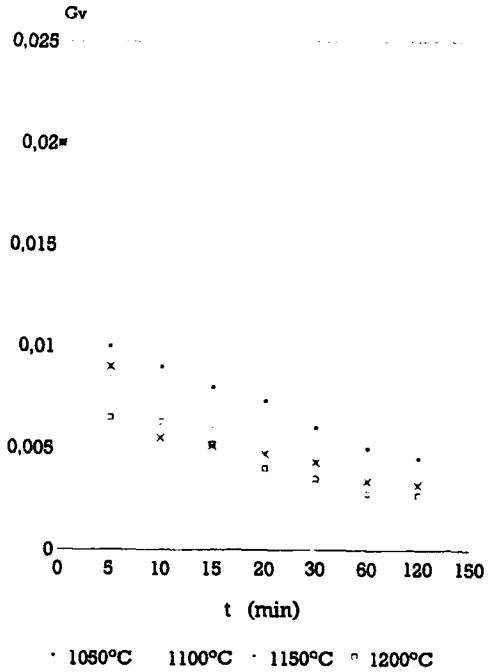


Fig.7. Ratio of the grain boundary area per unit volume at each temperature and for each heat treatment time (min).



Fig.8. Microstructure of a sample heat treated at 1200°C during 120 min.

Discussion

The Figs. 3, 4, 5 and 6 show very rapid grain growth up to 15-20 minutes of heat treatment time, followed by a decreasing grain growth rate. Such decrease can be interpreted in terms of the grain size increase which produces a decrease in the grain boundary area per unit volume ratio. This means that the grain boundary interfacial energy per unit volume decreases and therefore, the driving force for grain growth is lower. The final result is a slower growth kinetics which will eventually decrease to zero when the grain boundary area will not be able to introduce further growth at such heat treatment temperature.

The average value of the growth exponent is 0.56, which is high compared to that of other metals and alloys. Aluminium (99.99%) shows a growth order of 0.1 at 400°C, which increases to 0.3 at 600°C (9); for the austenitic grain of carbon steels (0.8%C), it ranges between 0.1 at 760°C and 0.23 at 980°C (10) and for cartridge brass (70%Cu, 30%Zn) it is 0.2 in the range of 500-700°C (10). In the case of b.c.c. alloys, where the structure is more open and prone to diffusion, the growth order is higher and for α-Fe the values increase from 0.2 at 600°C to nearly 0.5 at 800°C (10) whilst for the ß-brasses the values range from 0.35 at 500°C to 0.60 at 850°C (9, 11).

From the results shown in Table II, it can be noticed that the growth exponent increases with temperature for the area, minimum diameter and maximum diameter parameters, whilst it decreases for the perimeter. Such behaviour seems to indicate that the grains tend to become spheroidized. This means that as the radius of curvature of the grain boundaries increases, the growth rate of the grains decreases since the atomic transfer through the grain boundary varies inversely with the curvature radius (1). In fact when the shape factor of the grains is calculated (ratio between the ideal spherical area calculated with the average diameter and the area experimentally determined), as shown in Table IV, it can be noticed that it tends to increase with both heat treatment temperature and time. Ideally, the shape factor would be one for an equiaxed spheroidized grain structure. Such behaviour confirms that the grains tend to become spherical by reducing their perimeter and by increasing their area and their maximum and minimum diameters in the two dimensional experimental data.

Table IV. Shape factor of the grains.

t/T	1050°C	1100°C	1150°C	1200°C
5	0.68	0.68	0.70	0.70
10	0.69	0.70	0.70	0.70
15	0.70	0.70	0.70	0.72
20	0.71	0.72	0.73	0.74
30	0.71	0.72	0.73	0.75
60	0.73	0.73	0.74	0.76
120	0.73	0.74	0.75	0.77

In general, the maximum value of the growth exponent in the kinetics of normal growth is 0.5. Departures from n=0.5 to higher values have been currently interpreted in terms of solute drag or the effect of texture (12). Although texture is normal in this titanium alloy, it does not seem to play a leading role when normal grain growth is observed. It can be noticed

from the results shown in Table II that the growth exponent for the ß Ti-6Al-4V alloy is slightly higher than 0.5. The physical explanation of such behaviour lies in the diffusion of solute atoms which induces the grain boundary migration. In fact, in the initial mill annealed structure, the solute atoms of aluminium and vanadium are not evenly distributed in the two phases and the transformation to ß phase produces a drag effect at the grain boundaries. The diffusion process which leads to solute depletion at the grain boundaries induces an increase in the rate of growth (13).

The activation energies for grain growth are virtually independent of the grain size parameters used in their determination. The actual values obtained are small when compared to other metallic systems like α-Fe in alpha phase where the value is 239 KJ/mol, or in γ-Fe which is 270 KJ/mol for Cu in Al where it is 136 KJ/mol and for Zn in Cu where it is 171 KJ/mol (10). Therefore, it seems that for Ti-6Al-4V the diffusion through grain boundaries is easier than in the others alloys and consequently, the grain growth will take place faster.

Acknowledgements

The authors are grateful to the CICYT for funding the present work through project MAT90-0755 and to Industrias Quirúrgicas de Levante S.A. for kindly donating the material.

References

1. J.E.Burke, Trans.Am.Inst.Min.Engrs. 180,(1949), 73.
2. P.A.Beck, J.C.Kremer, L.J.Demer and M.L.Holzworth, Trans.Met.Soc.AIME 175, (1948), 372.
3. P.A.Beck. J.Appl.Phys. 19, (1948), 507.
4. I.M.Lifshitz and V.V.Slyozov. J.Phys. Chem. Solids 19, (1961), 35-50.
5. ASTM, Annual Book of ASTM Standards, section 13, Medical devices, vol.13 (01) (Philadelphia, American Society for Testing and Materials. 1986), 28-30.
6. M.Hillert. Acta Metall. 13, (1965), 227.
7. E.E.Underwood. Quantitative Stereology. (Massachustes. Addison Wesley Publishing Co. Reading Mass. 1980), 134.
8. J.E.Burke, Trans. Met.Soc. AIME, 185, (1949) 315.
9. A.G.Guy and J.J.Hren. Elements of Physical Metallurgy. (Massachusets. Addison Wesley Publishing Co. 3rd. edition. 1974), 446-450.
10.R.L.Fullman, American Society for Metals. Seminar Metal Interfaces. 179, (1952), 54.
11.J.C.Fisher and R.L.Fullman. Progress in Metal Physics. (Chalmers Ed. 1952), 97.
12.G.T.Higgins, Met. Sci. 8, (1974), 143-150.
13.B.Ralph, Mat. Sci and Techn. 6, (1990), 1139-1144.

ON THE ORDERING TRANSFORMATIONS

IN Ti_3Al–Nb ALLOY

Li Dong, Zhou Jing, Chang Xin, and Guan Shaoxuan

Institute of Metal Research,Academia Sinica
shenyang 110015, China

Abstract

Study was made of the behaviour of ordering transformation in Ti_3Al-Nb alloy, including the ordering at high temperature, the transformation of high temperature β phase during cooling, and the decomposition of metastable β phase during aging. Results show that the ordered primary α_2 and high temperature β in alloy occurred at 1060℃. The transformation of high temperature β phase proceeded by $\beta \rightarrow \alpha_2+\omega$ decomposition during cooling, and the decomposition of metastable β and ω type proceeded by $(\beta+\omega)_{metastable} \rightarrow (\alpha_2+\beta)_{stable}$ during holding at 700℃.

1. Introducton

A Ti_3Al system containing Nb has received much attention because of the improvement of ductility possible with the addition of Nb. To explain the mechanism of improving ductility Sastry [1] and Strychor[2] have investigated some aspects of the ordering transformation of Ti_3Al-Nb alloys, and pointed out that the behaviour of the ordering transformation has a considerable change with alloy composition and heat treatment. The properties of some alloys have been investigated by the present authors, who found that the ductility and strength of the alloys also show a change within a wide range of compositions and heat treatment. The above experimental results show that there is a close relationship between the mechanical properties and ordering transformation of alloys. The present investigation studied the formation of high temperature ordering phase, the transformation of high temperature ordered β phase during quenching and the decomposition of the β phase during aging and was also carried out to provide a basis for determining a reasonable composition of alloy and heat treatment.

2.Experimental procedure

The buttons were obtained by melting Ti–14Al–21Nb(wt–%)alloy in an argon–filled arc furnace for three times. The buttons were forged at 1250℃, then rolled into bar of 8 mm in diameter at 1100℃. Solution treatment was carried out at 1060℃ for 0.5 h followed by water quenching or air cooling, then the bar was aged at 700℃ for 1 h. The structures, compositions and ordering transformation of phases in the alloy were studied with an X–ray diffractometer and TEM.

Titanium '92
Science and Technology
Edited by F.H. Froes and I. Caplan
The Minerals, Metals & Materials Society, 1993

3. Results and discussion

3.1 Microstructure of solution treated alloy

The microstructure of Ti_3Al-Nb alloy consists of an equiaxed primary $\alpha_2$phase and a transformed β phase after solution treatment (Fig.1). About 40% volume fraction of primary $\alpha_2$phase exists, the transformed β phase forms during water quenching due to the transformation of high temperature β phase.

In the selected area diffraction pattern of the $\alpha_2$phase, the superlattice reflection of DO_{19} structure as shown in Fig.2a and 2b was observed according to the relation of lattice parameters by $a_{\alpha 2} \approx 4a_\alpha$and $c_{\alpha 2} \approx c_\alpha$. In the selected area diffraction pattern of the retained β phase in transformed β microstructure,the characteristic reflections of B2(CsCl) superlattice structure, such as streaking along $<110>_\beta$ directions and faint reflections at $(1/2)<110>_\beta$ positions as shown in Fig.2c and 2d were observed. The above experimental results show that both the primary $\alpha_2$phase and high temperature β phase are ordered structures at room temperature.

3.2 Transformation during cooling

3.2.1 $\beta \rightarrow \alpha_2$ transformation. The electron micrograph of the $\alpha_2$phase showing the morphology of the α_2 plate and substructure arising from the transformation during water quenching is shown in Fig.3a. The selected area diffraction pattern in Fig.3b indicates that the $\alpha_2$phase is ordered The compositions of primary α_2, plate α_2 and retained β phases are given in Table 1. It can be seen that in the water quenched specimen, there are lower Al content and higher Nb content in plate α_2 than in primary α_2. From this information, it can be judged that the plate α_2 forms from β phase during cooling, but not during solution treatment. In addition, it can be seen that there is a higher Al content in plate α_2 than in β. This shows that $\beta \rightarrow \alpha_2$ transformation is accompanied by a change of distribution of Al and Nb atoms in β and $\alpha_2$phases. The composition of selected alloy deviates from M_s in Ti_3Al-Nb diagram, thus it is impossible for nondiffuse martensitic transformation to occur.

3.2.2 $\beta \rightarrow \omega$*transformation.* Fig.4a shows the diffraction pattern of transformed β in a water quenched specimen with a $[110]_\beta$ zone axis. It can be seen that extra weak reflections were observed in the electron diffraction pattern, in addition to reflections of β superlattice structure.When the electron diffraction pattern was indexed [3－6]according to the relation of lattice parameter of $a_\omega \approx a_{\omega-Ti}$ and $c_\omega \approx c_{\omega-Ti}$, the extra reflections correspond to the superlattice structure of " ω type" phase.



Fig.1 Microstructure of Ti_3Al-Nb alloy



Fig.2 Ordered structure occurred in Ti_3Al–Nb alloy at high temperature
(a) bright field of primary α_2; (b) diffraction pattern,$[010]_{\alpha_2}$ zone axis;
(c) dark field,$(110)_\beta$ reflection; (d) diffraction pattern,$[001]_\beta$ zone axis

Table 1 Composition of ordered phases, wt-%

Metal	1060℃, 0.5 h, W.Q.			1060℃, 0.5 h, W.Q.+700℃, 1 h, A.C.		
	Primary α_2	plate α_2	β	primary α_2	plate α_2	β
Al	16.7	13.7	11.7	13.5	16.0	13.1
	16.1	14.2	13.7	14.5	14.5	
Nb	12.4	13.5	20.0	14.3	11.6	24.4
	13.3	14.4	19.0	13.3	13.3	



Fig.3 High temperature $\beta \rightarrow \alpha$ transformation
(a) bright field of structure transformation from β;
(b) diffraction pattern,$[\bar{1}12]_{\alpha_2}$ zone axis

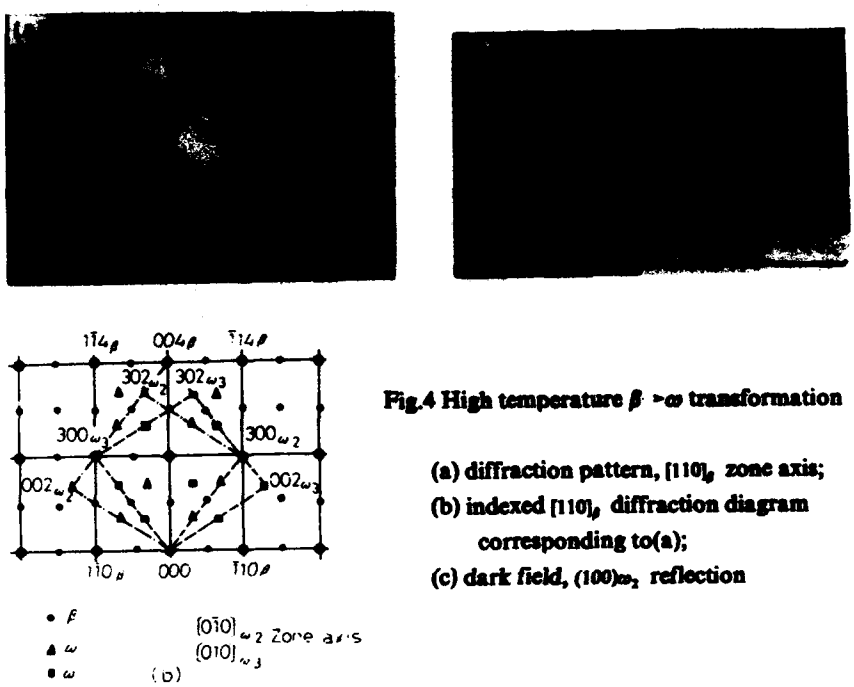


Fig.4 High temperature $\beta \rightarrow \omega$ transformation

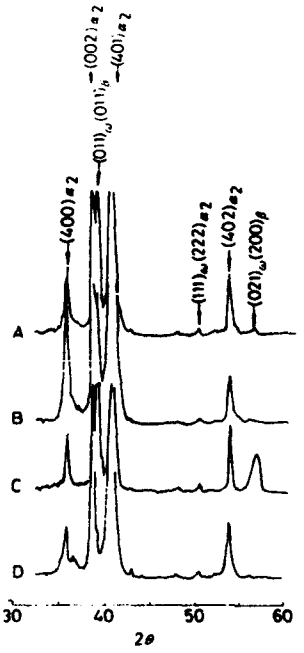
(a) diffraction pattern, $[110]_\beta$ zone axis;
(b) indexed $[110]_\beta$ diffraction diagram corresponding to(a);
(c) dark *field*, $(100)_{\omega_2}$ reflection

3.3 Transformation during aging

As indicated above, β and "ω type" phases exist in the alloy after quenching from 1060℃. Transmission electron microscopic examination proves that the phases resulted from the decomposition of metastable β and "ω type" phases during aging are well defined α_2 (Fig.5a,b) and stable ordered β phase (Fig.5c,d). Fig.6 shows the difference in X-ray diffraction patterns obtained on different heat treated specimens such as solution treatment at 1060℃ / 0.5 h A.C.or W.Q. and aging at 700℃ / 1 h respectively. It can be seen that $(110)_\beta$,$(011)_{\alpha_2}$and $(200)_\beta$,$(021)_{\alpha_2}$reflections obtained on 1060℃ / 0.5 h A.C. or W.Q. specimens are stronger than those obtained on aged specimens, but $(002)_{\alpha_2}$ and $(401)_{\alpha_2}$ reflections obtained on aged specimens are stronger than those obtained on solution treated specimens. The aging process decomposes the metastabe β and "ω type" phases and alters the phase compositions. It can be seen from Table 1 that as compared with solution treated specimens, an increase in Al content and a decrease in Nb content of the plate α_2, and in contrast, a decrease in Al content and an increase in Nb content of the metastable β-phase occur in aged specimens. This change of composition accords with Ti_3Al-Nb diagram. Above experimental results confirm the decomposition of metastable β and "ω type "phases during aging.



Fig.5 Decomposition of metastable β and ω type in aging
(a) dark field, $(200)_{\alpha_2}$ reflection;
(b) diffraction pattern, $[010]_\beta$ zone axis;
(c) dark field using $1/2[1\bar{1}0]_\beta$ superlattice reflection;
(d) diffraction pattern, $[111]_\beta$ zone axis



A – 1060℃,0.5 h, W.Q.

B – 1060℃,0.5 h, W.Q.+ 700℃,1 h,A.C.

C – 1060℃,0.5 h, A.C.

D – 1060℃,0.5 h, A.C.+700℃,1 h,A.C

Fig.6 X – ray diffraction pattern,CuKα

4. Conclusion

The ordered primary α_2 and high temperature β in Ti_3Al – Nb alloy occurred during solution treatment at 1060℃. The transformation of high temperature β phase proceeds by $\beta \succ \alpha_2 +$ "ω type" during cooling, and the decomposition of metastable β and "ω type" goes on according to reaction $(\beta +$ "ω type"$)_{metastable} \succ (\alpha_2+\beta)_{stable}$ during aging at 700℃.

References

1. Sastry S M L,Lipsitt H A. Metall Trans, 1977,8A:1543

2. Strychor R,Williams J C, and Soffa W A. Metall Trans, 1988,19AA:225

3. Prasetyo A, Reynaud F, and Warlimont H. Acta Metall, 1976,24:1009

4. Prasetyo A, Reynaud F, and Warlimont H. Acta Metall, 1976,24:651

5. Banerjee R, Cahn R W. Acta Metall, 1983,31:1721

6. Reynaud P F.J Appl Crystallogr,1976,9:263

POWDER METALLURGY, THERMOCHEMICAL PROCESSING, AND NANOSTRUCTURES

SYNTHESIS OF TITANIUM ALLOYS BY POWDER METALLURGY, NANOSTRUCTURED MATERIALS, AND THERMOCHEMICAL PROCESSING.

Alain Vassel * and F.H. (Sam) Froes **

* ONERA, BP 72, 92322 Chatillon Cedex, France
** IMAP, University of Idaho, Moscow, Idaho 83843-4195, U.S.A.

Abstract

The scientific/technological areas treated in this paper are advanced synthesis/processing methods which allow production of titanium-based materials with reduced cost or increased performance for aerospace and terrestrial systems. Powder metallurgy is discussed under four categories : blended elemental, prealloyed, rapidly solidified and mechanically alloyed products. The advantages to be gained from nanostructured materials are emphasized along with recent work including the titanium aluminides Ti_xAl (x=1or 3). Finally the thermochemical processing technique is reviewed.

Introduction

Reduced cost and enhanced behaviour are desirable goals for all type of structural materials, including titanium-based alloys. And of the six approaches to synthesis of titanium materials covered in this paper, one is concerned mainly with cost reduction, one with cost reduction at an equivalent mechanical behaviour level, and four with enhancing property levels.

The blended elemental (BE) powder metallurgy (PM) approach is designed to produce net or near-net shapes at reduced cost, with some degradation in mechanical behaviour generally being accepted. For the prealloyed (PA) PM technique, reduced cost is again a goal but mechanical properties at least at ingot metallurgy (IM) levels are required, and have been obtained.

The other four synthesis techniques - rapid solidification (RS), mechanical alloying (MA), nanostructured materials, and thermochemical processing (TCP, the use of hydrogen as a temporary alloying element) - are all concerned with enhanced properties at acceptable cost levels. RS and MA lead to constitutional and microstructural effects not possible in IM material. Nanostructures, with extremely small dimensions <100nm, offer novel processing/physical/mechanical properties combinations. Finally, the TCP method allows improved processability, and microstructural refinement leading to enhanced mechanical behaviour particularly in net shape products such as PM parts or castings.

Titanium '92
Science and Technology
Edited by F.H. Froes and I. Caplan
The Minerals, Metals & Materials Society, 1993

Powder metallurgy

Blended elemental

The BE approach is basically a conventional press and sinter method [1,2]. The BE material is currently made from a mixture of "sponge fines" and elemental or master alloy powder. The sponge fines are the small (<150μm) irregular shaped particles of nominally pure titanium which are produced during the conversion of titanium ore to an ingot. Since the commercial conversion processes involve reacting the titanium ores with chlorine, sponge fines normally contain approximately 0.15wt% Cl.

After blending to the desired bulk alloy composition, the powder is cold compacted under vacuum by either a mechanical press or cold isostatic press (CIP) to 85-90% density. The "green" compacts are vacuum sintered at about 1260°C to a density of 95-99%. A further increase in density can be achieved by post sinter hot isostatic pressing (HIP) and densities as high as 99.8% can be obtained from a standard sponge fine blend. The existence of chlorides in the BE material prevents achievement of 100% density.

Recently, a chloride free (<0.001wt%) powder produced by the hydride-dehydride process (HDH) became available and 100% density was achieved in CIP+HIP BE material [3]. As expected, both static and dynamic mechanical properties of BE titanium compacts improve with density. The 99% dense sintered products meet minimum required IM properties in tensile strength, elongation and fracture toughness. However, the small levels of porosity lead to a degradation in fatigue strength. At 99.8% density, the BE fatigue strength is still slightly lower than the lower bound of the IM scatterband. Only the 100% dense BE compacts resulted in fatigue strength equivalent to IM material [3,4,5] (Fig. 1).

The fatigue strength of both 99.8 and 100% material can be improved by innovative heat treatments such as the "broken up" structure treatment (BUS) [4], the TCP method described in a following section [6], and by a technique in which the material is quenched from the beta phase field before HIP'ing [5].

This improvement in density and fatigue has opened the door for use of BE components in critical aerospace applications.

One problem with BE parts is the difficulty in welding owing to the inherent salt content and/or porosity. However, the recently developed BE titanium powder compacts with less than 10ppm chloride should be weldable just like IM material of the same composition.

The most attractive aspect of the BE technology is its relatively low cost. Because of this, several components are already manufactu-

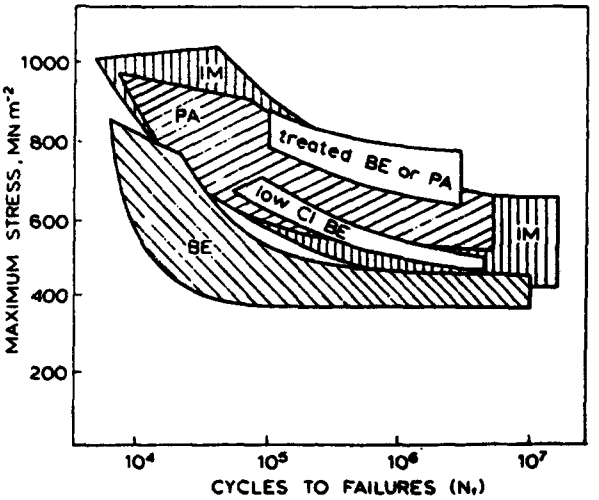


Figure 1 Fatigue data scatterbands of conventional BE, low chloride BE, treated low chloride BE and prealloyed (PA) compacts, compared with wrought Ti-6Al-4V annealed material [2].

red for the aerospace and non aerospace industries.

Prealloyed

For the production of high integrity near-net shapes, clean, spherical, PA powder is generally required [1,2]. However, because of the extreme reactivity of the molten metal, titanium powder cannot be easily produced by the atomization processes routinely practiced for less reactive metals such as aluminium. This has led to the development of a number of processes in which only local melting occurs. Today, only the rotating electrode process using a plasma heat source (PREP) is at a full production status to yield powder that is not contaminated with tungsten [7]. The PSV process (Pulvérisation Sous Vide - Electron Beam Vacuum Atomization) appears promising and it was shown that fatigue properties of PSV compacts are at least as good as those of PREP compacts [8,9]. Other emerging processes which relate more to rapid solidification technology will be discussed in the following section.

Powder consolidation can be achieved by HIP'ing, fluid die compacting, the Ceracon process, vacuum hot pressing and extrusion. A number of techniques are being used to produce complex shapes [2].

Mechanical properties such as ductility and fatigue resistance can be improved by either deforming the powder prior to densification or by compacting the powder at relatively low temperature and high pressure [1,2]. The normal microstructure of PA compacts can also be modified using the BUS or TCP processes previously mentioned.

At the present time, each PA product is made from a single alloy powder composition (for example Ti-6Al-4V). An interesting prospect offered by the PA route is the possibility of mixing different alloy powders in order to obtain compacts with specific properties. For instance, the creep strength of the Ti-6Al-2Sn-4Zr-2Mo alloy can be significantly improved by incorporating 30vol.% of PREP Ti_3Al or TiAl alloy powder (Fig. 2) [10]. Similarly, ductile-phase reinforcement of brittle materials, a concept that has been successful in the toughening of ceramics, is now been explored in the case of intermetallics (Fig. 3) [11]. The toughening ratio K/K_m, where K is the applied stress intensity and K_m is the matrix toughness is given by

$$K/K_m = 1+2\sqrt{2\pi}\,(Cn\sigma_y L/K_m)$$

where C, n, σ_y represent respectively the volume fraction, the strain hardening coefficient and the yield stress of the ductile phase and L is the bridge length. Thus, it has been shown that the fracture toughness of a Ti_3Al base material (Ti-25Al-10Nb-4Mo, at.%) which is only 8MPa$\sqrt{m}$ can be increased up to 21MPa$\sqrt{m}$ by adding 20vol.% of 100µm particles of a tough Ti-15Al-23Nb (at.%) alloy [12].

Recently, the use of PA powders has been demonstrated in the field of metal matrix composites. Innovative PM processes have been employed to obtain an homogeneous dispersion of 10 to 20.vol% of ceramic particles (SiC, TiC, TiB_2) in different titanium alloy matrices with a resultant improvement in hardness, stiffness and high temperature tensile strength [13,14].

Also, a "powder cloth" process has been used for the fabrication of continuous fibre-reinforced titanium aluminide composites [15]. The advantage of this process is that a variety of matrix compositions can be used especially those which are not easy to obtain in the form of rolled foil due to their low deformability.

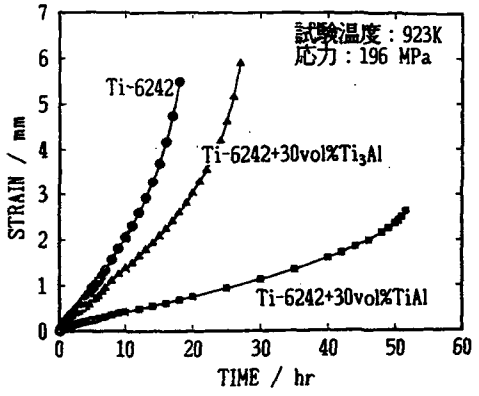


Figure 2 Creep elongation versus time of Ti-6242 alloy reinforced with Ti_3Al and TiAl [10].

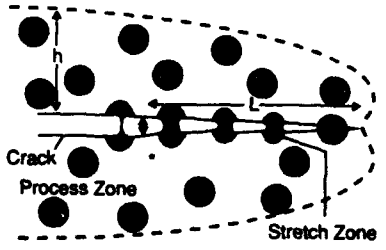


Figure 3 The toughening of brittle materials reinforced with a ductile phase [11].

Rapid solidification

Rapid solidification (RS) results in significant undercooling of the melt and leads to refinement of microstructural features and constitutional effects such as formation of metastable supersaturated solid solutions, crystalline and quasicrystalline intermediate phases, and metallic glasses [16-21]. A number of techniques have been used to produce RS titanium alloys including melt spinning and gas atomization.

Conventional alloys. A study of the Ti-6Al-4V alloy showed that the β grain size dramatically decreases at very high solidification rates. As a consequence, the α phase which subsequently forms on annealing changed from the normal lenticular morphology to a more fatigue- resistant globular shape [24].

Rare earths. At high enough solidification rates, rare-earth elements can be retained in solid solution at levels approaching 1at.% [22,23,25], and can subsequently result in a uniform dispersion of second phase particles.

Erbium is the rare-earth element which has been studied most extensively as an addition to RS titanium alloys [26,27]. A comparison of the dispersoid distribution and coarsening in a series of rare-earth containing titanium alloys indicated that alloys with Dy, Er, La and Nd had the highest resistance to coarsening at 800°C [22]. The stability of the dispersoids has been shown to be excellent as long as the alloy remains in the α phase field. However, coarsening is significant in the β phase field due to increased diffusivity [28]. The highest volume fraction of dispersoids was reported in melt-spun and aged Ti-24Al-10Cr-8Er alloys, offering good potential for enhancement in elevated temperature strength [29].

The possibility of developing new high temperature/high strength titanium alloys through the dispersion of rare earth oxide particles was evaluated within the framework of a collaborative European programme. The work showed that although the REP was capable of achieving a fine dispersion of Y_2O_3, this technique was not suitable for eliminating the pre-existing macro-segregation of Y_2O_3. Hardening through Y_2O_3 dispersion was significant when it was not offset by the grain size effect. The consolidation through HIP avoiding the recrystallization enhances the high tempera-

ture strength and the hardening by Y_2O_3 dispersion becomes very effective [30].

Mechanical properties of dispersoid containing RS alloys are improved due to grain refinement, solid-solution hardening and Orowan strengthening. Consistently lower steady-state creep rates were also observed in these alloys [28,31]. Thus, there appears to be some advantage to RS processing of dispersoid containing alloys but not to the same extent as in the aluminium system, where a much higher volume fraction of second phase particles are formed.

Metalloids. Addition of boron to titanium decreases the density and increases the elastic modulus. RS processing of Ti-B alloys results in non-equilibrium supersaturated solid solutions (containing as much as 10at.% boron, as opposed to 0.5at.% under equilibrium conditions) and uniformly distributed, high aspect-ratio TiB needles [32]. In addition to solid-solution strengthening, the hardness of boron containing RS titanium alloys can be increased by as much as 20-40% by ageing from the as-quenched state.

Solid solubilities of carbon, silicon and germanium in titanium also can be increased by RS processing. Subsequent annealing produces fine, spherical dispersoids in these systems contributing to high strength and acceptable levels of ductility.

Eutectoid formers. RS processing of the eutectoid formers (e.g. Ni, Co, Cu, Fe, Cr, Si and W) leads to minimization/avoidance of segregation, refinement of the microstructure, and a change in the kinetics of decomposition behaviour of the supersaturated solid solution obtained [33]. Unfortunately, most eutectoid transformation temperatures are below 900°C and the stability of the eutectoid products is not high. However, eutectoid forming alloys offer good potential as high strength and transformation hardenable alloys for intermediate temperature applications, provided that ductility problems can be overcome. Work on the Ti-1Al-8V-5Fe alloy has shown that it can be aged to very high strength levels (>1400MPa yield strength) while maintaining acceptable ductility, and could have applications for example in landing gears [34].

Intermetallics. RS processing offers the potential for improved ductility in these intermetallics by disordering, grain refinement and development of fine dispersoid particles [35]. When these fine dispersoids are oxides, an additional gain in ductility can result from deoxidation of the matrix.

Ti_3Al (α_2)

The solid solubility of erbium and other rare earth elements in Ti_3Al has been increased by rapid solidification [36] leading to a uniform distribution of fine Er_2O_3 particles which restrict the motion of grain boundaries so that consolidation below the β transus temperature does not significantly increase the grain size relative to as-rapidly solidified powder. In some cases, consolidation of dispersion modified alloys results in a refinement of the grain size. Grain refinement and chemical homogeneity of RS Ti_3Al-Nb-Er_2O_3 alloys lead to room temperature ductility improvements relative to IM alloys. However, the elevated temperature (815°C) tensile ductility of consolidated Ti_3Al-Nb based alloys is markedly reduced in alloys containing Er_2O_3 dispersoid particles. This is probably due to grain boundary segregation of erbium and associated elevated temperature grain boundary decohesion [37]. To date there has been no dramatic advantage noted for RS of the α_2-type alloys.

TiAl (γ)

Alloys in the 49-55at.% Al composition range solidify by a peritectic reaction so that chemical homogeneity is a problem in IM alloys. RS TiAl base alloys are chemi-

cally much more homogeneous and microstructurally much finer than IM alloys [38].

The tensile yield strength of RS and consolidated binary TiAl alloys is consistently higher than equivalent IM alloys over the temperature range 20-900°C [39].

Ternary alloy additions (Co, Cr, Fe, Ge, Mn, Ni, V, W) have a dramatic effect upon the strength and ductility of RS TiAl based alloys [40,41]. Additions of Co, Fe, Ni and W result in the greatest hardening of TiAl alloys while additions of Cr, Mn and V enhance the ductility of RS Ti-48at.% Al alloys [41]. The maximum room temperature tensile ductility is 3.5% as compared with 1% in a binary Ti-48at.% Al alloy.

It appears that there may be some advantages to RS processing of the TiAl base composition in addition to the net shape possibility offered by the RS/PM approach for this very difficult to work composition.

Mechanical alloying

Like rapid solidification, mechanical alloying (MA) is another non-equilibrium processing technique that has been developed in recent years to produce entirely novel compositions in order to improve material performance. This process consists of repeated welding, fracturing and rewelding of powder particles in a dry, high-energy ball charge. There is much to be gained from the mechanical alloying of titanium alloys. The whole process takes place in the solid state ; it is possible to increase the solid solubility limits of alloying elements and form metastable crystalline and amorphous phases. Also, alloys produced from virtually immiscible components can be obtained [42].

Addition of magnesium to titanium can reduce the density and potentially produce very light alloys with a high specific strength. Attempts to make Ti-Mg alloys have met with only limited success because magnesium, with its boiling point well below the melting point of titanium, cannot be retained in the molten titanium metal using conventional melting methods. Besides, the solid solubility of magnesium in α-titanium is very small under equilibrium conditions (0.5wt% at 650°C). It has been shown that a non- conventional method such as rapid solidification did not improve the situation any further [43]. Hence, mechanical alloying has been tried and this led to the production of a f.c.c. nanocrystalline solid solution containing approximately 2.5 to 3wt% magnesium [44]. *In-situ* hot stage experiments revealed that this structure is quite stable and does not coarsen appreciably at least up to 500°C.

Although considerable work has been done to develop alloys based on the intermetallics Ti_3Al and TiAl through both ingot metallurgy and rapid solidification/powder metallurgy routes, it has yielded only limited success. A study was undertaken to evaluate the effects of mechanical alloying on Ti_3Al-based alloy systems, both with and free of rare-earth element additions [42]. Screening experiments were carried out and the Ti-25Al-10Nb-3V-1Mo (at.%) alloy was chosen for a detailed investigation. It is worth mentioning that due to a careful experimental procedure, the oxygen pick-up during mechanical alloying was only about 200 to 300ppm (wt.%). Figure 4 shows a comparison of the microstructures of HIP compacts from the rapidly solidified and mechanically alloyed products. Even after HIP'ing at a higher temperature, the MA material exhibits a fine grain size, a small dispersoid size and the absence of dispersoid-free zones. The observation of a high density of dislocations and stacking faults in the MA product can be easily rationalized in terms of the large amount of plastic deformation experienced by the individual powder particles during the milling operation. The continued presence of the deformation structure after annealing at 1200°C suggests that this microstructure is extremely stable and omens well for strength retention up to very high temperatures.



Figure 4 TEM micrographs showing the size and distribution of dispersoids in rapidly solidified (RS) and mechanically alloyed (MA) products. (a) RS Ti_3Al + 2wt.% Er alloy HIP'ed at 850°C and (b) MA Ti-25Al-10Nb-3V-1Mo + 2wt.% Er alloy HIP'ed at 1000°C [42].

Nanostructured materials

Nanostructured materials exhibit at least one dimension in the nanometer range, generally <100nm. Because of their novel combinations of mechanical and physical properties, they have received considerable attention in the past few years [45-47]. The nanostructures can be one-dimensional (layered), two dimensional (fibrous) or three dimensional (crystallites). The vast majority of the work conducted to date has been on the third type and is the only type produced in the titanium system.

A schematic representation of a nanostructured crystallite material is shown in Figure 5 [48]. The large fraction of atoms located in the grain boundary regions allow unusual combinations of physical and mechanical behaviour. Production of nanostructured materials has concentrated on gas condensation methods but chemical and mechanical methods have also been used [47]. For the titanium system, the majority of the nanostructured material has been produced by mechanical alloying and magnetron sputtering methods.

As described in the previous section, MA of titanium and magnesium results in the formation of 10-15nm sized grains containing about 3wt.% (6at.%) magnesium.

Nanostructured grains of 6-8nm size were produced in a Ti-10at.%Cu alloy by MA [49]. These grains were found to be very stable which was attributed to grain growth suppression due to segregation of Cu atoms to grain boundaries. Also, na-

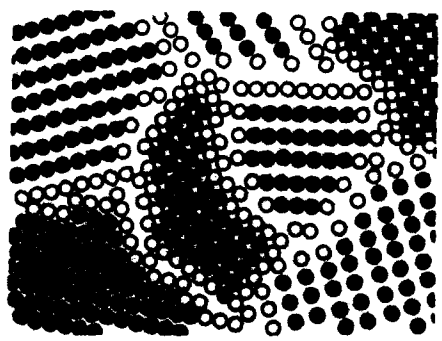


Figure 5 Schematic representation of a nanostructured material. Atoms in normal lattice position (black circles) and atoms that are "relaxed" at grain boundaries (white circles).

nostructures have been found in the Ti-Ni system when fabricated by either MA [50] or magnetron sputtering [51].

In the case of intermetallics, the very fine grain size offers an intriguing way for exploration of these normally brittle materials. A number of papers have reported on formation of nanostructured grains (<15nm) in Ti_3Al-Nb alloys (Fig. 6) [52-54].



Figure 6 Electron micrograph of nanostructured grains in MA Ti-24Al-11Nb (at.%) alloy [53].

The magnetron sputtering method was used to produce an amorphous TiAl condensate which crystallized to a 10nm grain size on annealing [55]. This material displays a two times increase in hardness over conventional TiAl and an inverse Hall-Petch relationship (Fig. 7). This behaviour is considered to be unrelated to a pore density effect.

In an equiatomic TiAl alloy, MA produces a lamellar structure which is followed by grain size refinement to about 20nm, and finally amorphization [56]. The decrease in grain size with MA time in TiAl was also demonstrated by Frefer et al. [57].

Work by Valiez has indicated that after extremely high deformation a nanostructured TiAl can be produced which exhibits a 5% room temperature ductility, considerably higher than in material with a conventional grain size [58].

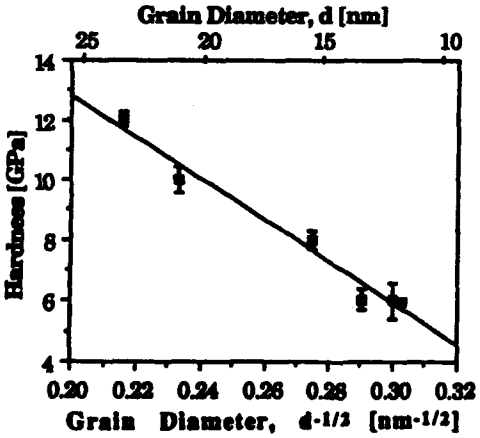


Figure 7 Inverse Hall-Petch relationship in nanostructured TiAl [55].

Thermochemical processing

Thermochemical processing (TCP), that is the use of hydrogen as a temporary alloying element, has been developed to enhance both hot workability and final mechanical properties [59]. In this process, hydrogen is added to the titanium alloy by simply holding the material at a relatively high temperature in a hydrogen environment. The presence of hydrogen then allows the titanium alloy to be processed at lower stresses/lower temperatures, because of the increased amount of β phase. Further, the subsequent removal of hydrogen produces novel fine microstructures with improved mechanical properties. The hydrogen is simply removed by a vacuum annealing treatment to levels below which no detrimental effects occur.

TCP is particularly amenable to near-net shapes, such as powder metallurgy products and castings, since this treatment does not rely on working the material to modify the microstructures. However, the technique can also be applied to IM products.

TCP can be applied to a wide range of titanium-based alloys, due to their high hydrogen solubility, although the vast majority of the work reported to date has been on the Ti-6Al-4V alloy, the most commonly used titanium alloy for both aerospace and non-aerospace applications.

Hydrogen-assisted processing

A comprehensive study of the effects of hydrogen on the forgeability of wrought Ti-6Al-4V was conducted by Kerr et al. [60] and it was shown that peak flow stresses displayed a minimum at 0.3-0.4wt.% hydrogen content. It was suggested that the reduction in flow stress was a result of the increased proportion of the β phase, stabilized by hydrogen. At hydrogen contents higher than 0.4wt.%, it was proposed that the flow stress increased due to the presence of hydrides in the microstructure.

At the present time, TCP is not being used commercially to improve the processability of wrought titanium alloys. Only laboratory-scale studies are in progress.

The use of TCP in the consolidation of titanium alloy powders was investigated by Kao et al. [61]. Two types of powders with quite different morphologies were studied : a spherical rotating electrode process (REP) powder and an angular hydride-dehydride (HDH) powder. It was determined that the presence of hydrogen enhanced processability rather than any differences in particle size or shape.

Early work demonstrated that hydrogenated powder did not lose hydrogen during hot isostatic pressing (HIP) in an evacuated mild steel can. The dehydriding after compaction causes void formation due to the much larger specific volume of the hydrides compared to the parent matrix (+17.2%). Consequently, it is critical that the product after dehydriding be subjected to further compacting, such as HIP, forging or extrusion to close cracks and voids and thus provide the necessary integrity of the material [62].

Modification of microstructure and properties

One of the few contributions to understanding of the microstructure development during TCP is the work of Mahajan et al. [63]. It is clear that at sufficient levels, the addition of hydrogen can give rise to an eutectoid reaction $\beta \rightarrow \alpha$ + hydride. When the material is dehydrogenated below the eutectoid temperature, the hydride decomposes to a mixture of fine α and spheroidized β phase ; the lower the dehydrogenation temperature, the finer the microstructure. Thus, TCP can be used to control the microstructure and improve the mechanical performance of different products.

In powder material, thermochemical processing of low chloride BE and PA compacts resulted in a refined microstructure and a substantial enhancement of fatigue behaviour (Fig. 1).

The inferior fatigue performance of Ti-6Al-4V castings compared to IM material is due to the presence of a continuous grain boundary α phase and a coarse α plate structure (Fig. 8a). The TCP treatment eliminates the thick grain boundary α and the large α plate colonies (Fig. 8b) [64]. As a consequence, both the strength level and the fatigue limit are greatly improved.

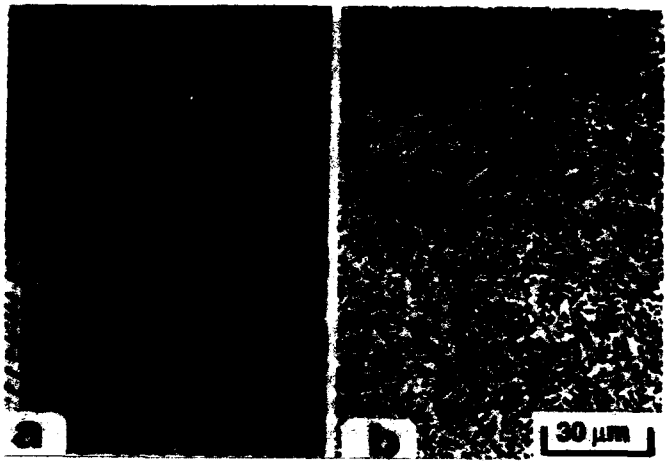


Figure 8 The refinement in microstructure of cast Ti-6Al-4V given a TCP treatment. (a) as-cast and (b) after TCP [64].

Conclusions and future thoughts

The six synthesis techniques discussed in this paper all offer either cost or performance advantages for titanium based materials.

The low cost BE/PM method is showing some growth but at a slow rate.

The PA/PM approach offers cost advantages at equivalent performance levels to IM material but there are virtually no flying applications.

The RS method for production of titanium alloys has yet to demonstrate the advantages which occur in other systems, such as aluminium, using this approach. Specifically, the volume fraction of second phase dispersoid particles is always <5% in the titanium system while it can be >30% for RS aluminium alloys. However, it may be that very difficult to process intermetallics, such as TiAl (γ), may be produced net shape using RS material.

The MA approach is at an early stage of development in the titanium system but advantages in terms of producing alloys which (i) are impossible to make by fusion methods and (ii) with higher volume fractions of dispersoids than possible using the RS method, are apparent. A stumbling block here may be maintaining acceptable levels of cleanliness.

Nanostructured titanium-based materials are also only of recent interest. However, the novel property levels, particularly enhanced ductility, are very interesting especially for the normally brittle intermetallics.

The TCP method offers clear processing and final mechanical property advantages, especially fatigue initiation resistance in near net shapes such as powder parts and castings. Some semi-commercial use of TCP in processing of difficult to fabricate alloys has been reported, and one casting house in the USA has extensively evaluated the technique. However, wide spread use is still to come.

The bottom line is that, as always, acceptance of new materials and processes is extremely slow. And unless clearly defined substantial cost or performance improvements are present, along with a new system which demands these new techniques, this transition from laboratory to production will not speed up.

Acknowledgements

The authors recognize useful discussions with C. Suryanarayana, A. Frefer and G.H. Chen.

References

[1] F.H. Froes, D. Eylon, Titanium Science and Technology, vol.1 (DGM, Germany, 1985), 267.
[2] F.H. Froes, D. Eylon, International Materials Reviews, 35 (1990), 161.
[3] S. Abkowitz, D. Rowell, J. of Metals, 38 (1986),36.
[4] D. Eylon, F.H. Froes, Progress in Powder Metallurgy, vol. 42 (MPIF, Princeton, 1986), 625.
[5] M. Hagiwara et al., ISIJ International, 31 (1990), 922.
[6] R.G. Vogt et al., Titanium Net Shape Technologies (TMS Publications, 1984), 145.
[7] E.J. Kosinski, Progress in Powder Metallurgy, vol. 38 (MPIF, Princeton, 1983), 491.
[8] J. P. Herteman, D. Eylon, F.H. Froes, Powder Metallurgy International, 17 (1985), 116.
[9] M. Marty, H. Octor, C. Renon, A. Walder, La Recherche Aérospatiale, No 3 (1979), 165.
[10] M. Hagiwara, S. Emura, J. Takahashi, this conference.
[11] S.M.L. Sastry, R.J. Lederich, T.C. Peng, J. of Metals, 40 (1988), 11.
[12] M.J. Blackburn, M.P. Smith, U.S. Patent 4,927,458 , Sep. 1988.
[13] S. Abkowitz, S. Abkowitz, 1990 Int. Conf. on Titanium Products and Applications, vol. 2 (T.D.A., Dayton, 1990), 700.
[14] A. Vassel, M. Marty, French Patent 90 16350, Dec. 1990.
[15] R.A. MacKay, P.K. Brindley, F.H. Froes, J. of Metals, 43 (1991), 23.
[16] F.H. Froes, R.G. Rowe, Rapidly Solidified Alloys and Their Mechanical and Magnetic Properties (MRS, Pittsburgh, 1986), 309.
[17] F.H. Froes, D. Eylon, eds. Titanium Rapid Solification Technology (TMS, Warrendale, 1986).
[18] T.R. Anantharaman, C. Suryanarayana, Rapidly Solidified Metals - A Technological Overview (Aedermannsdorf, Switzerland : Trans. Tech. Publ., 1987).
[19] F.H. Froes, R.G. Rowe, Sixth World Conference on Titanium, vol. 2 (Les Editions de Physique, Les Ulis, France, 1989), 801.
[20] C. Suryanarayana, F. H. Froes, J. of Metals, 42 (1990), 22.
[21] C. Suryanarayana, F. H. Froes, R.G. Rowe, Int. Mater. Rev., 36 (1991),85.
[22] S.M.L. Sastry, P.J. Meschter, J.E. O'Neal, Met. Trans. A, 15A (1984), 1451.
[23] S. Naka, M. Marty, H. Octor, J. Mat. Sci., 22 (1987), 887.
[24] T.F. Broderick et al., Met. Trans. A, 15A (1984), 1951.
[25] D.G. Konitzer, R. Kirchheim, H.L. Fraser, Rapidly Solidified Metastable Materials (Elsevier, New-York,1984), 381.
[26] D.G. Konitzer, B.C. Muddle, H.L. Fraser, Scripta Met., 17 (1983), 963.
[27] D.G. Konitzer et al., Acta Met., 34 (1986), 1269.
[28] M.F.X. Gigliotti et al., as ref. [16], 343.
[29] A.G. Jackson et al., Mater. Sci. Eng., 98 (1988), 239.
[30] T. Khan et al., this conference.
[31] S.M.L. Sastry, T.C. Peng, L.P. Beckerman, Met. Trans. A, 15A (1984), 1465.
[32] S.M.L. Sastry, T.C. Peng, R.J. Lederich, Mechanical Behavior of Rapidly Solidified Materials (TMS, Warrendale, 1986), 207.
[33] S. Krishnamurthy, F.H. Froes, Int. Mater. Rev., 34 (1989), 297.

[34] F.H. Froes et al., Bull. Mater. Sci. (India), 12 (1989), 293.
[35] F.H. Froes, C. Suryanarayana, D. Eliezer, J. of Iron and Steel Inst. of Japan, 31 (1991), 1235.
[36] J.A. Sutliff, R.G. Rowe, as ref. [16], 371.
[37] R.G. Rowe, as ref. [19], 979.
[38] S.C. Huang, E.L. Hall, M.F.X. Gigliotti, as ref. [19], 1109.
[39] S.C. Huang, Scripta Met., in press.
[40] D. Vujic, Z.X. Li, S.H. Whang, Met. Trans. A, 19A (1998), 2445.
[41] E.L. Hall, S.C. Huang, High Temperature Ordered Metallic Alloys III (MRS, Pittsburgh, 1989), 693.
[42] C. Suryanarayana, R. Sundaresan, F.H.Froes, Proceedings of the Conference on Structural Applications of Mechanical Alloying, (ASM, Materials Park, 1990),193.
[43] R. Sudaresan, F.H. Froes, Key Eng. Mater., 29 (1989), 199.
[44] C. Suryanarayana, F.H. Froes, J. Mater. Res., 5 (1990), 1880.
[45] H. Gleiter, Progress in Materials Science, 33 (1990), 223.
[46] F.H. Froes, C. Suryanarayana, J. of Metals, June 1989, 12.
[47] R.W. Siegel, Materials Science and Technology, vol. 15, Processing of Metals and Alloys (VCH Weinheim,1991).
[48] R. Birringer, U. Herr, H. Gleiter, Suppl. Trans. Japan Inst. Met., 27 (1986), 43.
[49] Y.R. Abe, W.L. Johnson, paper presented at the "International Symposium on Mechanical Alloying", Kyoto, Japan, May 1991, Proceedings to be published 1992.
[50] W. Schlump, H. Grewe, New Materials by Mechanical Alloying (DGM, Germany, 1988), 307.
[51] R.S. Averback et al., Appl. Phys. Letters, 57 (1990), 1745.
[52] E. Bonneti et al., Mat. Sci. and Tech., 6 (1990), 1258.
[53] G.H. Chen, C. Suryanarayana, F.H. Froes, work in progress, University of Idaho, Moscow, Idaho.
[54] T. Christman, M. Jain, Scripta Met. et Mat., 25 (1991), 767.
[55] H. Chang et al., as ref. [54], 1161.
[56] J.H. Ahn et al., as ref. [49].
[57] A. Frefer, C. Suryanarayana, F.H. Froes, this conference proceedings.
[58] R.Z. Valiez, private communication to F.H. Froes, January 1991.
[59] F.H. Froes, D. Eylon, C. Suryanarayana, J. of Metals, 42 (1990), 26.
[60] W.R. Kerr et al., Titanium'80 Science and Technology, vol. 4 (TMS, Warrendale, 1980), 2477.
[61] W.H. Kao et al., Progress in Powder Metallurgy, vol. 37 (MPIF, Princeton, 1982), 289.
[62] C.F. Yolton, F.H. Froes, U.S. Patent 4,219,357 , Aug. 1980.
[63] Y. Mahajan, S. Nadiv, W.R. Kerr, Scripta Met., 13 (1979), 695.
[64] C.F. Yolton, D. Eylon, F.H. Froes, Sixth World Conference on Titanium, vol. 3 (Les Editions de Physique, Les Ulis, France, 1989), 1641.

A SPRAY-REACTION PROCESS FOR PRODUCTION OF TITANIUM POWDER

Hiroshi KAMETANI* and Hidenori SAKAI**

*NKR Co.Ltd., NKF Bldg. 2-11, Kanda Nishiki-cho, Chiyoda-ku, Tokyo 101, Japan, and Lecturer, Faculty of Science, Science University of Tokyo, Tokyo, Japan.
**Technical Research Center, Kokan Mining Co.Ltd., 6-2, Ohgimachi, Kawasaki-ku, Kawasaki 210, Japan.

Abstract

A process for producing Ti powder from $TiCl_4$ was studied on a laboratory scale. The process consisted of a spray-reaction and successive leaching. The spray-reaction involved spraying a falling stream of molten Mg at a rate of about 100 g/min with a jet of preheated $TiCl_4$ gas at a stoichiometric ratio, thereby inducing instantaneous reduction of $TiCl_4$ on the surface of the atomized Mg droplets. The reaction product was then leached in dilute HCl solution. The residual Ti powder was ground, sieved to pass a 75 μm screen, and leached again. The total yield of Ti was around 90%, 70 to 80% of which was recovered as the product. The median diameter of the Ti product ranged from about 10 to 40 μm. The oxygen content was around 0.25%. A flowsheet of the process is presented.

1 INTRODUCTION

Titanium and its alloys have a low density, a high melting point, and excellent mechanical and corrosion-resisting properties, and they are widely used as construction materials in the aircraft, machine, and chemical industries. There is also a great potential demand for low-cost titanium powder for use in powder metallurgy, because the cost of raw material for the production of various parts can be reduced by near-net-shape forming [1].

At present, titanium powder is produced using the Hunter Process, but production is limited by the fact that fine powder suitable for powder metallurgy is restricted to the portion obtained by screening the main process product. A number of studies are, therefore, aimed at methods for the production of titanium powder, such as Hydride De-Hydride (HDH) and the Rotating Electrode Processes. Because the starting material used in these studies is sponge titanium produced by the Kroll and Hunter Processes, high production costs are inevitable.

In order to produce titanium powder directly from titanium tetrachloride, efforts have been made to develop a new process which is comprised of a spray-reaction and successive leaching. This paper presents experimental results obtained by fundamental studies at our laboratory.

Titanium '92
Science and Technology
Edited by P.H. Frose and I. Caplan
The Minerals, Metals & Materials Society, 1993

2 SPRAY SYSTEM

Most spray systems can be divided into one-fluid spray systems and two-fluid spray systems [2]. One-fluid spray systems, using various types of hollow-cone pressure nozzles and rotating nozzles, are widely used for spray drying [2], and for spray-decomposition for the production of ferric oxide from pickle solutions [3]. These nozzles of complex construction are not suitable for molten metals at high temperatures. The metallurgical applications of two-fluid spray systems include spray-atomization, spray-deposition, and spray-reaction. There have been a number of studies of spray-atomization [4-8] and some of spray-deposition in recent years [9,10], but there has been only one study for spray-reaction [11]. The spray-reaction involves spraying a falling stream of a liquid reactant with a jet of a gaseous reactant, thereby inducing an instantaneous reaction on the surface of the atomized liquid droplets. The spray-reaction process was originally applied to the oxidation of molten white metal (cuprous sulfide) with oxygen, aiming at a continuous furnace in place of a copper convertor [11].

The reduction of titanium tetrachloride gas (above b.p.: 136°C) with molten magnesium (above m.p.: 651°C) is represented by,

$$TiCl_4(g) + 2\,Mg(l) = Ti(c) + 2\,MgCl_2(l) \qquad (1)$$

In the spray-reaction, molten magnesium is sprayed with tetrachloride gas at a stoichiometric ratio, i.e., Mg : $TiCl_4$ = 2 : 1 in mole and 1 : 3.902 in weight. The amount of titanium produced (47.90 g, 1 mole) is nearly the same as that of magnesium exhausted (48.62 g, 2 moles), namely Ti : Mg = 1 : 1.015.

3 EXPERIMENTAL

3.1 Spray-reaction

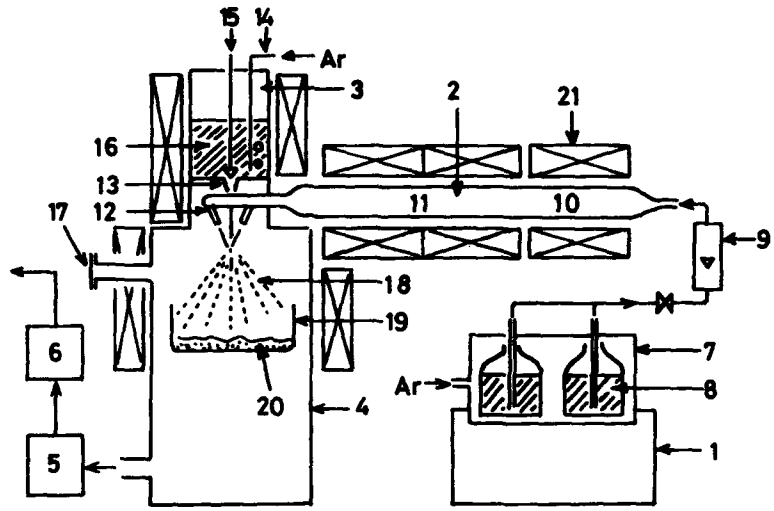
Apparatus

The apparatus used for spray-reaction experiments is shown in Figure 1 in schematic form. The apparatus consisted of 4 sections, namely a glovebox for feeding the liquid tetrachloride, a tubular transparent quartz vessel with a gas nozzle, a cylindrical magnesium vessel, and a cylindrical reaction chamber. A cooler and a gas washer were attached to treat the outlet gas from the reaction chamber.

The glovebox contained an air tight pressure vessel. Two bottles each containing 2 kg of the liquid tetrachloride were placed in the pressure vessel. The tetrachloride was fed under pressure through a flowmeter into the quartz vessel. The tubular part of the quartz vessel (4 cm diameter and 1 m length) consisted of an evaporator and a preheater. The tubular part was heated with three furnaces to evaporate the liquid tetrachloride and to preheat the chloride gas up to 600°-800°C. A 4-lance-type gas nozzle (2 mm diameter) was attached to the end of the quartz vessel.

The magnesium vessel (11 cm diameter and 45 cm height) was mounted on top of the reaction chamber. The vessel was fitted with an Ar blow pipe to measure the head of the molten contents, a magnesium nozzle (1.5 mm diameter and 4 cm length) at the bottom, and a stopper for plugging the nozzle. The magnesium nozzle was surrounded by the gas nozzle. One kg of magnesium was melted in the vessel at 750°C.

The upper half of the reaction chamber (25 cm diameter and 80 cm height) was heated to about 650°C. The chamber was lowered during heating, and raised during cooling, to compensate for expansion and contraction, and so



1: Glovebox, 2: Quartz vessel, 3: Mg vessel, 4: Reaction chamber, 5: Gas cooler, 6: Gas washer, 7: Pressure vessel, 8: Liquid TiCl , 9: Flowmeter, 10: Evaporator, 11: Preheater, 12: Gas nozzle, 13: Mg nozzle, 14: Blow pipe, 15: Stopper, 16: Molten Mg, 17: Peeping window, 18: Spray cone, 19: Bath, 20: Reaction prpduct, 21: Furnaces.

Fig. 1 Illustration of apparatus for spray experiment

maintain the gas nozzle at a constant height. A bath was placed in the chamber about 30 cm below the gas nozzle to recover the reaction product.

The magnesium vessel, the reaction chamber, and the bath were made of stainless steel, which was slightly corroded by unreacted tetrachloride. Contaminants in the product due to this corrosion were analysed, but no attempt was made to reduce them.

Procedure

After the temperature of each furnace had risen to a set value, the liquid tetrachloride in the bottle was fed to the top level of the flowmeter (this was to minimize the time lag due to feeding). The stopper of the magnesium nozzle was lifted. After the downward stream of molten magnesium had been observed through a peeping window in the wall of the reaction chamber, the tetrachloride was fed at half of the full rate for the first 20 s. In accordance with a smooth increase in chloride gas pressure in the quartz vessel, the feed rate was then gradually increased to the full rate. The head of residual magnesium in the vessel was checked regularly. When it had decreased to zero, feeding of the tetrachloride was stopped.

3.2 Leaching

Leaching was carried out in two steps using two conventional agitated vessels, each fitted with electrodes for measurement of pH and suspension potential, and a temperature controller. The pH of the solution in each vessel was controlled at a value of about 3 by the automatic addition of 2 N HCl solution.

Experiments were conducted in the following steps:
First leaching: The products (Ti powder and aggregates, $MgCl_2$, and unreacted Mg) were collected in the bath. At the end of an experiment, the bath and its contents were removed from the chamber and leached with dilute HCl solution at about 50°C. After the products separated, the bath was removed. Leaching continued until the demand for HCl was satisfied.
Screening: After decantation, the residue was screened to separate it into the >150, 150-75, and <75 μm screen size portions, and each portion was wet-weighed.
Grinding: The portions larger than 75 μm were ground to pass a 75 μm screen using a small vibrating mill.
Second leaching: The original <75 μm portion and the ground material were separately leached again, washed with deionized water and dried in Ar at about 80°C.

4 EXPERIMENTAL RESULTS

4.1 Spray experiment

Experiments were conducted with a charge of 1 kg of magnesium and with a charge of 4 kg of the tetrachloride. The flow rate of magnesium varied, run by run, in the range 90 to 110 g/min, and the duration of the experiment varied correspondingly from 11 to 9 min. The feed rate of liquid tetrachloride was increased from one third of the stoichiometric ratio in the initial runs to the full rate, i.e., 390 g/min. Various difficulties were encountered during the course of our experiments, concerning irregular evaporation of the liquid chloride due to bumping, blocking of the magnesium and gas nozzles, sealing up between quartz and stainless steel, measurement of gas pressure, leaching conditions and other aspects. These were gradually overcome through improvements in the apparatus and procedure.

A spray experiment began by lifting the stopper to allow the downward flow of molten magnesium. The liquid chloride was then fed and increased to the stoichiometric rate, as the chloride was fed the gas pressure rose to a level of 0.4 to 0.6 atm. As the spray-reaction took place, a bright orange spray cone was observed. Not more than a few seconds later, the reaction chamber was filled with white smoke, and the bright orange changed to orange shimmers. The experiment continued in a stable state for about 10 min. When the head of residual magnesium decreased to zero and the orange shimmers vanished, feeding of the chloride was stopped. The gas pressure then decreased to zero as the residual liquid in the quartz vessel evaporated off.

4.2 Leaching

After the spray experiment, the apparatus was cooled in Ar. The products in the bath were clearly separated into two layers, an upper transparent layer of $MgCl_2$ and a bottom gray layer of Ti powder and unreacted magnesium. There was a rise in temperature at the beginning of the first leaching, due to exothermal dissolution of $MgCl_2$. The duration of the first leaching was dependent upon the nature of the products, especially the aggregate phase of Ti particles. It usually required 30 to 40 h.

The grinding of Ti particles in the portions larger than 75 μm after screening was very easily accomplished, because the particles consisted of aggregates of smaller spherical particles. The second leaching usually required 4 to 7 h.

4.3 Cone temperature

The temperature of the spray cone could be measured by inserting a thermocouple through the peeping window during the reaction. Measurement at a chloride feed rate of 120 cm^3/min gave a value of about 1000°C, which is

about 400°C higher than the temperature before spraying. However, this measurement is dangerous, since a "stalagmite" of Ti particles grew upwards very rapidly from the protective stainless tube. The second measurement at the same feed rate recorded 1200°C, at which point the run was interrupted by the stalagmite growth reaching the gas nozzle and blocking the jet stream. Extrapolation of the recorded curve gave a temperature of about 1300°C. The cone temperature varied mainly with the temperature of the chloride gas.

4.4 Ti powder produced

Yield

Precise estimation of the yield was difficult, because there was a time lag between Mg and $TiCl_4$ feed, as previously noted. The amount of $TiCl_4$ left in the bottles after the experiment could not be used in the calculation, because an amount of $TiCl_4$ remained evaporating in the evaporator. Furthermore, the distribution of Ti particles in the spray cone meant that not all products fell into the bath. Yield was, therefore, estimated from the amount of Ti powder recovered from the bath, plus that recovered from the reaction chamber, compared with the amount of $TiCl_4$ in the outlet gas recovered in the cooler. In this way, the total yield of Ti powder was estimated at about 90%, of which 80 to 90% was recovered from the bath, regardless of the feed ratio of Mg to $TiCl_4$.

The amount of unreacted magnesium in the product could be calculated from the amount of HCl added during leaching. About 90% of the magnesium reacted at the stoichiometric ratio.

Particle size

The distribution of Ti particles in the three screen size portions, <75, 150-75, and >150 μm, was in most cases around 30-60%, 30-50%, and 10-20%, respectively, by using wet weighing. The distribution seemed to be dependent upon the cone temperature, that is, aggregation of Ti particles by collision in the spray cone would proceed more rapidly at a higher cone temperature, resulting in an increase in coarse aggregated particles. The final products recovered were around 40-60%, 60-40%, and a few % for the original <75 μm portion, the ground material (also <75 μm), and the remainder which did not pass the screen, respectively. The median diameter and specific surface area were roughly 10 and 40 μm, and 0.5 and 0.05 m^2/g, for the original <75 μm portion and the ground material, respectively.

Most of the fine Ti particles were roundish in shape, while the coarse particles were aggregates of fine particles, some containing twisted strings, showing that the particles were formed under a half-melt condition, as shown in Figure 2.



Fig. 2 Photograph (SEM) of Ti particles

Impurities

A major impurity in the products was the oxygen content. In the early experiments, the content was as high as 1%, however this was reduced to about 0.25% by improving the apparatus and procedure. The latter value seemed to be a lower limit for the present apparatus on a small scale. The magnesium, chlorine, and hydrogen contents ranged from 0.4 to 0.6%, 0.01 to 0.02%, and 1.0 to 1.2%, respectively. Other metal contents, iron, nickel, and chromium, which originated from corrosion of the reaction chamber, fell in a wide range, in the order 0.1 to 0.5%. These levels could be reduced by using a corrosion-resistant material in place of stainless steel.

5. DISCUSSION

5.1 Spray-atomization and spray-reaction

There have been a number of studies on spray-atomization of molten metals with an inert gas [4-15]. The size and distribution of atomized metal particles are dependent upon the design of the nozzles and various spray conditions. The latter include the gas speed and impingement angle of the lance, the mass flow ratio of the liquid to the gas, the surface tension of the molten metal, and the density and kinetic viscosity of the gas and the molten metal. Effects of these factors can be inferred from previous papers on spray-atomization. Two apparent differences, however, are that the reaction takes place on the surface of metal droplets and that the tetrachloride gas is exhausted in the course of the reaction.

As for the spray reduction of $TiCl_4$, the mass flow ratio of the liquid (Mg) to the gas ($TiCl_4$) is determined by the stoichiometric ratio given by Eq. (1), i.e., 100 : 390.2. Therefore, gas speed is the only variable which affects formation of the spray state. The gas speed is dependent upon the volume and pressure of the gas, and upon the lance diameter for the 4-lance-type gas nozzle used. The gas volume is a constant, about 46 dm^3 at the standard state, and increases to 164 dm^3 at 700°C, for 100 g of Mg to be sprayed. The gas speed and gas pressure then are determined by the lance diameter and the gas temperature.

The surface tension of molten magnesium in an inert gas is known (569 dyne/cm at the melting point). However, nothing is known about the surface tension for molten magnesium on which a reaction is taking place. Reported values of the median diameter for metal particles formed by spray-atomization fall in the wide range of 40 to 300 μm, while those for Ti particles in this study are in the range 10 to 40 μm. Although the size of Ti particles will not be the same as that of the atomized magnesium droplets, the latter low values suggest that the surface tension is being lowered by the surface reaction. Thus, calculation of particle size using equations proposed for spray-atomization may give false indications when applied to spray-reactions.

For the design of the gas nozzle, the impingement angle (the angle between the axes of lance) is of greatest importance [8]; a value below 30 is generally adopted. A special design is needed which avoids smearing of the gas nozzle with ultrafine Ti particles by minimizing irregular eddy streams in the vicinity of the gas nozzle.

5.2 Reaction in spray cone

Spray-reaction is a special reaction which takes place in a gas stream with an initial speed of about 10^2 m/s and approaches the end within a short time less than 0.1 s. Analysis of the reaction mechanism involves two aspects. One is that of chemical engineering which relates to the nature of a jet stream and the formation of atomized droplets and a spray cone, and the other relates to the heterogeneous reaction which takes place on the

surface of the disintegrating droplets. These two aspects are inseparably related, that is, the atomization and the reaction occur simultaneously. It is, therefore, very difficult to make a model for the reaction in the spray cone. A tentative reaction model has been presented elsewhere [12]. Only a brief explanation is given here.

In the jet stream with a subsonic speed, the partial pressure of $TiCl_4$ may decrease due to entrainment of the surrounding gas (Ar), before the reaction takes place. The falling stream of molten magnesium meets the gas jet in the vicinity of the impingement point, where the atomization and the reaction begin to take place simultaneously, and a spray cone is formed. The gas speed relative to droplets is very high. The reaction rate increases very rapidly as the magnesium stream is atomized into fine particles, and the rate would be expected to be dependent upon the partial pressure of $TiCl_4$. The rapid reaction may continue for about 10 cm in the upper part of the cone. For the angle of the spray-atomization cone, a value of about 74° has been estimated from droplet velocity vectors [10].

The speed of magnesium droplets, including Ti particles and molten $MgCl_2$ formed, is accelerated by the gas stream, and then reaches a maximum speed. The reaction rate decreases with a decrease in the partial pressure of $TiCl_4$ and a decrease in unreacted magnesium. It seems that the rate is not hindered by the reaction products. The gas speed decelerates, firstly with an increas in the cross-sectional area of the cone, and secondly through gas exhaustion due to the reaction. In the lower part of the cone, the particles continue to fall with a gradual decrease in speed, and the reaction approaches the end. The total height of the cone necessary to complete the reaction (about 90%) seems to be from 20 to 40 cm. The reaction rate may be very slow below this height.

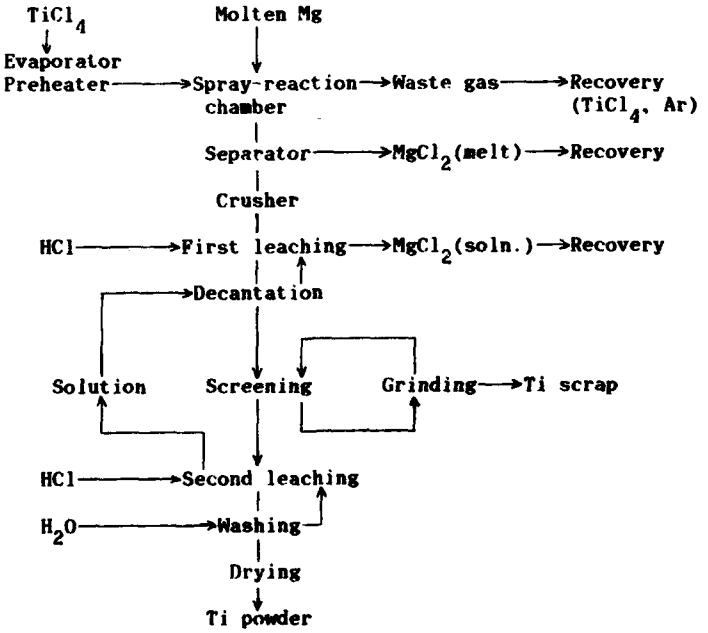


Fig. 3 Flowsheet of the spray-reaction process

5.3 Spray-reaction process

It has been shown that the spray-reaction process has a satisfactory yield of Ti powder and a very large production capacity. Even the rate of 100g Ti/min, produced by the laboratory scale appaaratus used in this study, amounts to a few tons per a month, which is quite high considering the present state of development. Figure 3 shows the flowsheet of the spray-reaction process. When the spray-reaction in the flowsheet is replaced with the conventional magnesium reduction, the proposed process is almost the same as the Kroll Process in the earliest stage of development.

The lance-type gas nozzle used in this study would be replaced with a concentric annulus-type gas nozzle for large scale production.

6. Summary

Experiments on the use of a spray-reaction for direct production of titanium powder by reduction of titanium tetrachloride with magnesium are described. The results obtained have encouraged us to continue the study. Efforts have been made to develop the spray-reaction process to a semi-commercial scale.

REFERENCES

1. F.H.Froes,et al.,"Potential of Titanium Metallurgy," First International SAMPE Metals Conference,Aug.(1987),240-254.
2. J.H.Perry,ed., Chemical Engineers' Handbook(New York,NY:McGraw-Hill,Inc. 1950),838-841, 1170-1175.
3. C.M.Brown,"High Purity Iron Oxide from Spent Hydrochloric Acid Pickle Liquor," Continuous Processing and Process Control,49(1966),93-104.
4. H.Lubenska,"Correlation of Spray Ring Data for Gas Atomization of Liquid Metals," J.Metals, 22(1970),45-49.
5. J.Brucesee and G.H.Johnston:"Interaction between Nitrogen Jet and Liquid Lead and Tin," Powder Metallurgy,21(1978),119-133.
6. A.Unal,"Liquid Break-up in Gas Atomization of Fine Aluminium Powder," Metall. Trans.B, 20B(1989),61-69.
7. A.Unal,"Flow Separation and Liquid Rundown in Gas Atomization Process," ibid.,20B(1989),613-622.
8. A.Unal,"Influence of Gas Flow on Performance of Confined Atomization Nozzles," ibid.20B(1989),833-843.
9. S.P.Bewlay and B.Cantor,"Modeling of Spray Deposition," Metall. Trans.B, 21B(1990),899-912.
10. S.P.Bewlay and B.Cantor,"Modeling of Spray Deposition," Metall.Trans.B, 21B(1990),899-912.
11. H.Kametani and C.Yamauchi,"Method for Production of Copper Particles," Japan Pat.,No.899418,Feb.1978, and USA Pat.,No.3980470,Sept.1976.
12. H.Kametani,"A Reaction Model for Spray-Reaction of $TiCl_4$ Gas with Molten Mg," Presented at the Annual Meeting of MMIJ, March,1992, Tokyo, Japan,p.353.

Y_2O_3-DISPERSED $\alpha+\beta$ AND NEAR-α TITANIUM ALLOYS PREPARED BY P/M PROCESSING

T. Khan [1], D.F. Neal [2], M.J. Hill [3], M.J. Weaver [4],
F. Schwartz [5], B. Champin [6] and S. Naka [1]

1 : ONERA, 29, Av. de la Division Leclerc, 92322 Châtillon CEDEX, France,
2 : IMI Titanium Ltd., PO BOX 704, Witton, Birmingham, B6 7UR, UK,
3 : Rolls Royce plc, Derby, DE2 8BJ, UK,
4 : DRA (RAE), Pyestock, Farnborough, GU14 OLS, UK,
5 : SNECMA, BP. 81, 91003 Evry CEDEX, France,
6 : CEZUS, BP. 33, 73400 Ugine, France.

Abstract

In the present work, the possibility of developing new high temperature/high strength titanium alloys through the dispersion of rare earth oxide particles was evaluated. The work shows that although the REP, which is an industrially viable P/M technique, was capable of achieving a fine dispersion of Y_2O_3, this technique was not suitable for eliminating the pre-existing macro-segregation of Y_2O_3. This is due to the fact that the small superheat provided by this technique cannot overcome the large difference in melting points between Ti and Y_2O_3. Hardening through Y_2O_3 dispersion was significant when it was not offset by the grain size effect, i.e. at lower temperatures and in tensile tests rather than in creep tests. Very small grain sizes observed in the extruded alloys due to the recrystallization contribute to the strengthening at lower temperatures but counteract the effect of the dispersion at higher temperatures and in creep tests. The consolidation through HIP avoiding the recrystallization improves the high temperature strength and the hardening by the Y_2O_3 dispersion becomes very effective. It was found that in order to avoid the strong embrittlement induced by the presence of Y_2O_3, macro-segregation must be avoided.

Introduction

The quest for higher operating temperatures in aeroengines has incited work on new light weight materials and novel processing techniques. The potential of conventional titanium alloys which are widely used in the modern aircraft compressors is limited to a temperature of about 600°C. It has also become apparent mainly through the alloy development work accomplished by IMI that with the advent of the IMI834 alloy we have almost reached the upper limit of utilization of conventional titanium alloys [1].

The present work was therefore directed toward the development of new high temperature/high strength titanium alloys through the dispersion of rare earth oxide particles. This type of strengthening mechanism was not effective in alloys produced by conventional Ti ingot metallurgy due to the difficulties encountered in controlling the proper dispersion parameters (particle size and inter-particle spacing). Rapid solidification processing was, however, found to be useful in resolving most of these difficulties, as shown by various U.S. works [2].

Since a moderate cooling rate of about 10^3-$10^4 Ks^{-1}$ during solidification was found to be sufficient for obtaining a fine and homogeneous dispersion of Y_2O_3 particles during previous

Titanium '92
Science and Technology
Edited by F.H. Froes and I. Caplan
The Minerals, Metals & Materials Society, 1993

work [3,4] and because most of the powder particles obtained by the REP (Rotating Electrode Process) are solidified at such cooling rates, this technique which is a commercially viable industrial process was used for the present alloy development work.

Within the aeroengine companies participating in this programme, there were two requirements for high strength/high temperature titanium alloys; an $\alpha+\beta$ type high strength alloy for use in the intermediate temperature range (450-550°C) and a near α-type alloy which could push the temperature capability beyond 600°C.

The present work was implemented in the following inter-related stages : 1) Choice of alloy systems, 2) Ingot/electrode production, 3) Powder production (REP), 4) Powder consolidation, 5) Microstructure/mechanical property evaluation.

Choice of alloy systems

The composition of the the near α titanium matrix was determined by IMI after a considerable amount of experimental work and by taking into account its thermal stability. As for the $\alpha+\beta$ base matrix, the composition of the IMI550 alloy was chosen. In both cases, Y_2O_3 was selected as the dispersed phase, as in the previous experiments undertaken at ONERA [3,4]. However, in this programme, it was decided to directly incorporate Y_2O_3 instead of yttrium. The idea behind this approach was to maintain the initial oxygen content of the titanium matrix, which is necessary to preserve the initial strength level of the base alloy. It is also worth noting that it is possible, according to a theoretical prediction [5], to reduce the coarsening rate to some extent even in the β-phase field if a titanium-rare earth alloy contains oxygen in excess after the formation of rare earth oxide It should be emphasized here that the dispersed oxide particles coarsen very rapidly in the β-phase field inspite of their remarkable size stability in the α-phase field during hot consolidation [3,4,6] or even after severe cold rolling followed by annealing [7].

Processing route

1. Ingot/electrode production

1.1. $\alpha+\beta$ alloys. For $\alpha+\beta$ alloys, the base alloy ingot (148Kg) manufactured at CEZUS was used. By forging this ingot, two bar products were prepared. Eight electrodes of the base alloy for REP were directly cut and machined from one of the two bar products. An alloy ingot containing 2vol.%Y_2O_3 was produced by double melting at CEZUS using its consumable electrode melting facilities. On the electrode corresponding to the second bar product, about 200 small holes (ϕ=12mm, depth=50mm) were bored by machining. Addition of Y_2O_3 was made by regularly distributing Y_2O_3 powder into these small holes. After duoble melting, the ingot was thermomechanically processed into two bars of ϕ=50mm. Nine REP electrodes were finally prepared by machining these bars.

1.2. Near α alloys. Both the base alloy and the Y_2O_3 containing alloy were prepared by double melting at IMI using its consumable electrode facilities. Electrodes for this operation were made using a blend powder technique. The ingots obtained for both alloys were transformed by extrusion at 1170°C to bars of ϕ=50mm. From these bars, ten REP electrodes were machined for the base alloy, and twenty for the Y_2O_3 containing alloy.

2. Powder production

Powder production was carried out at ONERA using its REP facilities. The REP equipment at ONERA comprises essentially : an airtight chamber operating under inert gas (Ar+He) atmosphere, a spindle which permits an alloy electrode (anode) to rapidly rotate and a tungsten cathode device which allows suitable arc-melting of the alloy electrode. The diameter of the electrode was always 41mm, and the spindle rotating rate was 17100rpm. The particle size distribution determined after sieving showed that the most frequent particle diameter is around 125-160μm and the majority of the powder particles possess a diameter below 200μm. In the present study, all the particles below 200μm diameter were used for

alloy consolidation after controlling the oxygen content and they constituted a single batch.

3. Powder consolidation

The consolidation was carried out primarily through extrusion but occasionally, hot isostatic pressing (HIP) was also used. Mild steel cans containing alloy powder were degassed under secondary vacuum for two hours and then sealed by electron beam welding. Extrusion was carried out using a press of 250 tons. Consolidation by HIP was performed at 920°C or 950°C under 2000bars.

Results and discussion

1. Microstructural analysis

The ingots containing Y_2O_3, prepared both by CEZUS and IMI, showed a heavy segregation presumably due to the strong differnce in melting points between Y_2O_3 and the base alloys. In the Y_2O_3 containing $\alpha+\beta$ alloy produced by CEZUS, the chemical analysis revealed that the average level of Y_2O_3 content was about 0.76%. Two thirds of Y_2O_3 were apparently lost probably during melting. In the Y_2O_3 containing near α alloy produced by IMI, the chemical analysis showed that the Y_2O_3 content was of about 2%, indicating that the yttria loss was avoided through the blended powder technique.

The microstructure of the alloys obtained after consolidating of the REP powder by extrusion shows a significant Y_2O_3 segregation, at an optical microscopy scale. The observed segregation is characterized by the presence of very large (often larger than 20μm) Y_2O_3 particles, either isolated or clustered (Fig.1). This is certainly due to the non-dissolution of Y_2O_3 during REP. Indeed, in the as-REP powder, Y_2O_3 particles or agglomerates were frequently observed in numerous powder particles, independent of the powder particle size.

In order both to understand why Y_2O_3 was not dissolved during REP and to find how to remedy this difficulty, three types of experiments were conducted, by using arc-melting facilities (with water-cooled Cu hearth) : (1) re-melting of the near α+2%Y_2O_3 alloy by using the non-consumed part of the REP electrode, (2) melting of the cold-consolidated mixture of Ti with Y_2O_3 (2%) (Ti sponge + Y_2O_3 powder), (3) melting of the Ti-1.84Y alloy with TiO_2.The first experiment was undertaken to determine whether the superheat during melting played a role in achieving a complete dissolution of Y_2O_3. It should be noted that the melting point of titanium alloys is around 1650°C while that of Y_2O_3 is around 2400°C. The second experiment was done in order to understand how and why the segregation occurs in the system through a simplified approach. The third experiment was undertaken in order to find

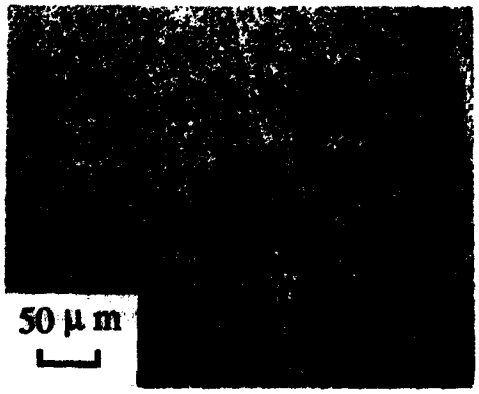


Fig.1 Macro-segregation observed after consolidation of the REP'ed powder by extrusion.

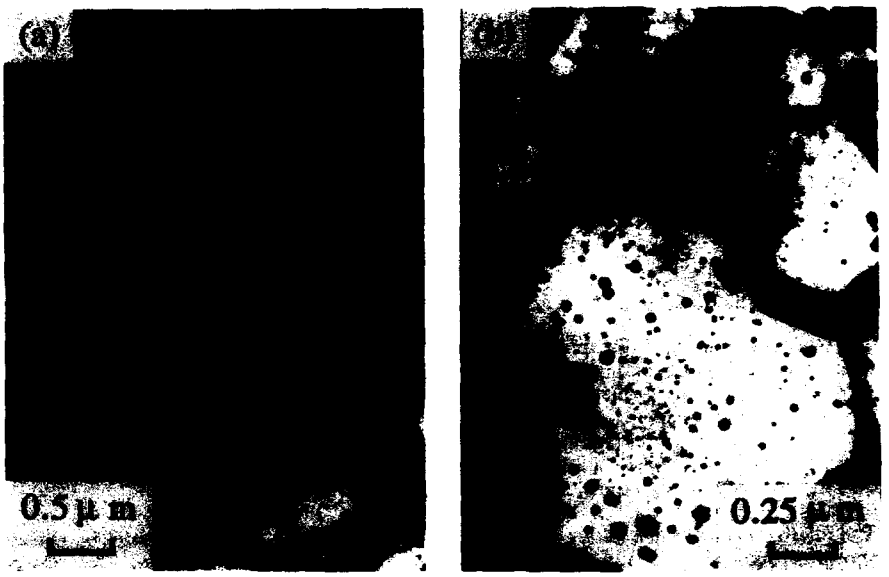


Fig.2 Observed Y_2O_3 dispersion : (a) $\alpha+\beta$ alloy, (b) near α alloy.

out whether the addition of Y and TiO_2 was more efficient than the direct addition of Y_2O_3. All these experiments indicated that both the degree of superheat and the heating time are two important factors affecting the complete dissolution of Y_2O_3, which is a prerequisite for obtaining the segregation-free P/M titanium alloys. These experiments also suggested that the incorporation of Y_2O_3 should have been achieved by the following steps : (1) near α (or $\alpha+\beta$) + TiO_2, (2) addition of yttrium. It is worth noting that the melting point of TiO_2 is around 1850°C and that of Y around 1500°C.

Despite the presence of the macro-segregation, transmission electron microscopy revealed a fine and rather homogeneous dispersion of Y_2O_3 (Fig.2) in the as-extruded state in both the yttria containing alloys indicating that a part of the oxide was dissolved in the molten alloys during REP. Because of the presence of a fairly homogeneous and fine dispersion, it was decided to conduct mechanical tests on these materials in order to evaluate its strengthening effect.

2. Mechanical properties

2.1. $\alpha+\beta$ alloys. The results of the tensile tests carried out on the $\alpha+\beta$ alloys (Y_2O_3 free and Y_2O_3 containing alloys) are presented in Table 1. This table includes the values specified as "minimum values" by SNECMA for the cast and forged IMI550 alloy as well as the values obtained on the wrought small diameter IMI550 bars. In this table, we can clearly see that in the whole temperature range, the Y_2O_3 containing alloy shows a slight strength increment of 30-60MPa, compared to the Y_2O_3 free alloy, while the presence of Y_2O_3 induces a decrease in both the elongation to rupture (EL) and reduction in area (RA). The strengths of both the Y_2O_3 containing and Y_2O_3 free alloys are higher than the minimum values specified by SNECMA. However, when compared to the values obtained on the wrought small diameter IMI550 bar, only the Y_2O_3 containing alloy is significantly stronger than the wrought alloy up to 400°C.

The results of creep tests conducted on the Y_2O_3 containing alloy are shown in Table 2. This table also includes the results obtained on the Y_2O_3 free alloy as well as minimum values specified by SNECMA for the wrought IMI550 alloy. Contrary to the case for the tensile

Table 1 Results of the tensile tests carried out on the α+β alloys.

Alloy	T (°C)	UTS (MPa)	0.2% PS (MPa)	EL (%)	RA (%)
IMI550 + Y_2O_3	20	1235	*	6.2	11
IMI550	20	1190	1185	14.2	33
minimum SNECMA	20	1100 to 1280	960	9	20
IMI550 small ϕ bar	20	1200	1050		
IMI550 + Y_2O_3	400	875	800	10.3	32
IMI550	400	835	740	17	60
minimum SNECMA	400	680	520		
IMI550 small ϕ bar	400	850	700		
IMI550 + Y_2O_3	500	780	690	14.2	42
IMI550	500	745	670	20.4	75
IMI550 small ϕ bar	500	800	600		

strength, the addition of Y_2O_3 was found to provide no significant improvement in creep strength. The reason for this may be the lack of sufficiently effective dispersion of Y_2O_3. Indeed, because of the macro-segregation observed in the as-extruded bar stock, the volume fraction of dispersed small Y_2O_3 particles is probably much less than the nominal value (0.76%). Note also that the two P/M alloys exhibit a poorer creep resistance, considering the minimum value specified by SNECMA. This is probably because of the small grain size (1-5μm) observed in the P/M alloys after extrusion.

Table 2 Results of the creep tests carried out on the α+β alloys alloys.

Alloy	T (°C)	Applied stress (MPa)	Time for 0.2% elongation (h)
IMI550 + Y_2O_3	400	600	200
IMI550 + Y_2O_3	400	600	55
IMI550	400	600	171
minimum SNECMA	400	480	100
IMI550 + Y_2O_3	450	280	85
IMI550 + Y_2O_3	450	280	75
IMI550	450	280	165
minimum SNECMA	450	280	140
IMI550 + Y_2O_3	500	240	8
IMI550	500	240	5
minimum SNECMA	500	240	20

2.2. Near α alloys. The results of the mechanical tests on both the Y_2O_3 free and Y_2O_3 containing alloys are shown in Table 3 and Table 4. In tensile tests (Table 3), the Y_2O_3 containing alloy shows a 0.2% yield stress of 1252MPa at room temperature and its strength increment is of 130MPa, compared to that of the Y_2O_3 free alloy. The elongation to rupture of the Y_2O_3 containing alloy is however very low, compared to that of the Y_2O_3 free alloy (2.1% vs. 13%). This embrittlement may be caused by the Y_2O_3 macro-segregation. The strength increment due to the Y_2O_3 dispersion diminishes with increasing temperature. Addition of Y_2O_3 provides an improvement in ultimate tensile strength (UTS), up to about

Table 3 Results of the tensile tests carried out on the near α alloys.

Alloy	T (°C)	UTS (MPa)	0.2% PS (MPa)	EL (%)
Near α base alloy	20	1122	1122	13
	400	836	776	12
	500	737	674	41
	520	685	633	23
	600	530	390	52
	650	340	244	198
Y_2O_3 containing near α alloy	20	1252	1252	2.1
	400	891	860	6.5
	500	783	737	12
	520	746	678	14
	600	519	425	26
	650	322	240	160

550°C. At 650°C, both alloys have a low strength (about 240MPa for the 0.2% yield stress) and a very large elongation to rupture(160-200%), showing a "superplastic" like behaviour.

Addition of Y_2O_3 gives a limited improvement in creep resistance at lower temperatures, but seems to decrease creep resistance at high temperatures (Table 4). The transition temperature is arround 550°C, similar to the tensile test results. The creep strength of both the Y_2O_3 free and Y_2O_3 containing alloys is quite low at 600 and 650°C.

All these results indicate that the dispersion does not provide any real benefit. The poor high temperature strength of these alloys is thought to be related to the very fine grain size resulting from recrystallization during extrusion.

In order to improve the high temperature mechanical properties by preventing recrystallization, we attempted to consolidate alloy powders through HIP. The results of the tensile tests undertaken on HIP products are shown in Table 5. Initially, HIP was performed at 920°C at 2000bars. By comparing these results with those of the extruded alloy (See Table 3), it was found that the HIP alloy is much stronger than the extruded one at 650°C (472MPa vs. 286MPa for the 0.2% yield stress). It is also clear that the increment in yield stress due to the

Table 4 Results of the creep tests carried out on the near α alloys.

Alloy	T (°C)	Applied stress (MPa)	Time for 1% elongation (h)	Time for 10% elongation (h)
Near α base alloy	500	100	1131	-
	550	100	47	405
	600	100	3.2	32
	650	100	0.5	5.7
Y_2O_3 containing near α alloy	500	100	1246	-
	550	100	65	675
	600	100	2.0	24
	650	100	0.3	3.6

Table 5 Results of the tensile tests carried out on the Y_2O_3 containing near α alloy. (HIP products)

Alloy	T (°C)	UTS (MPa)	0.2% PS (MPa)	EL (%)
Y_2O_3 containing near α alloy HIP'ed at 920°C	650	485	472	0.3
Y_2O_3 containing near α alloy HIP'ed at 950°C	650	518	510	0.9
Y_2O_3 free near α alloy HIP'ed at 920°C	650	479	424	8

Y_2O_3 addition is significant (472MPa vs. 424MPa). The problem, however, is with the brittleness of the HIP Y_2O_3 containing product (elongation to rupture : 0.3%). Fractographic examination showed decohesion of the powder particle boundaries in the Y_2O_3 containing material, while the fracture surface of the Y_2O_3 free alloy showed normal ductile features. HIP was also performed at 950°C at 2000bars in order to verify whether the HIP temperature had any influence on the ductility. Indeed, there may be some micro-porosities left within the material, if the HIP temperature is too low. However, the result of the tensile test could not clearly confirm this explanation; the elongation to rupture showed only a slight improvement (0.3% after HIP at 920°C ⇒ 0.9% after HIP at 950°C). It is finally worth citing the work of Gigliotti et al. [8] which showed a similar ductility loss at high temperatures due to dispersion of Er_2O_3.

Conclusions

The following overall conclusions can be drawn from this investigation.

1) Although the REP process, which is an industrially viable P/M technique, was capable of achieving a microscopical dispersion of Y_2O_3, it was not suitable for eliminating any pre-existing macro-segregation of Y_2O_3. This is due to the fact that the small superheat provided by this technique cannot overcome the large difference in melting points between Ti and Y_2O_3.

2) Incorporation of Y through the blend powder technique is certainly the most appropriate route for preparing Y_2O_3 containing Ti alloy ingot destined to the REP powder production, although the complete suppression of the macro-segregation still seemed to be difficult.

3) A moderate hardening through Y_2O_3 dispersion is observed when it is not offset by the grain size effect, i.e. at lower temperatures and in tensile tests rather than in creep tests. Very small grain sizes observed in the extruded alloys due to the recrystallization contribute to the strengthening at lower temperatures but counteract the effect of the dispersion at higher temperatures and in creep tests. The consolidation through HIP avoiding the recrystallization improves the high temperature strength and also renders the hardening by Y_2O_3 dispersion very effective.

4) The embrittlement due to the presence of Y_2O_3 was quite significant; it is therefore essential to avoid the macro-segregation of Y_2O_3. Further effort in this direction is necessary for the development of rare earth oxide dispersion hardened titanium alloys.

Acknowledgements

This work was conducted under the contract (MA1E-0054-C) of the Euram programme. The authors are very grateful to Dr. Schmidt of the Commission of the European Communities for his permanent encouragement to the progress of the present study. Thanks are also due to the members of staff of each partner who participated in this collaborative work.

References

1. P.A. Blenkinsop, "High Temperature Titanium Alloys", in Proc. Conf. on "Designing with Titanium", Bristol, The Institute of Metals, 1986, 191.
2. Proceedings of the Conference on "Titanium - Rapid solidification Technology", Ed. F.H. Froes and D. Eylon, New orleans, TMS, 1986.
3. S. Naka, M. Marty and H. Octor, "Oxide-Dispersed Titanium Alloys Ti-Y Prepared with the Rotating Electrode Process", J. Mater. Sci., 22 (1987) 887.
4. S. Naka, H. Octor, M. Marty and A. Lasalmonie, "Microstructure and Mechanical Properties of Oxide Dispersed Titanium Alloys Ti-Y and Ti-Al-Y Obtained by Powder Metallurgy Processing", in Proc. Conf. on "Designing with Titanium", Bristol, The Institute of Metals, 1986, 64.
5. D.G. Konitzer, J.P.A. Lofvander, S.A. Court, R. Kirchheim and H.L. Fraser, "Theoretical and Experimental Determinations of the Thermal Stability of Rare Earth Oxide Particles in Rapidly Solidified Titanium Alloys", Acta Metall., 36 (1988) 1595.
6. F.H. Froes and R.G. Rowe, "Rapidly Solidified Titanium - A Review", in Proc. Conf. on "Titanium - Rapid solidification Technology", Ed. F.H. Froes and D. Eylon, New orleans, TMS, 1986, 1.
7. S. Naka, H. Octor, E. Bouchaud and T. Khan, "Reprecipitation Observed in Y_2O_3 Dispersed Titanium during Heat Treatment after Cold Rolling", Scripta Metall., 23 (1989) 501.
8. M.F.X. Gigliotti, G.E. Wasielewski and R.G. Rowe, "Microstructural Development and High Temperature Mechanical Characterization of a Dispersoid-containing Titanium Alloy", in Proc. 6th World Conf. on Titanium, Ed. P. Lacombe, R. Tricot and G. Béranger, Cannes, Les Editions de Physique, 1988.

TENSILE AND FRACTURE TOUGHNESS PROPERTIES OF P/M Ti-1.3Al-8V-5Fe AND DERIVATIVES

C. F. Yolton
Crucible Materials Corporation
Crucible Research
Pittsburgh, PA 15230

L. M. Orsborn
LTV Aerospace and Defense
Aircraft Division
Dallas, TX 75265

Abstract

Ti-1.3Al-8V-5Fe is a metastable beta titanium alloy which can be heat treated to very high strengths by solution treating and aging. Strengths over 1400 MPa (203 Ksi) have been reported with acceptable ductility. This alloy is segregation prone in ingot form, but can be readily made via powder metallurgy. Components can then be made by consolidation of the powder by hot isostatic pressing or other means. A baseline and derivatives were investigated to determine the effects of additional beta stabilizers and reduced oxygen on strength and toughness. Microstructure, hardness, tensile properties and toughness are reported on five derivatives.

Introduction

Research over the years has demonstrated the potential in reducing part cost through the use of powder metallurgy (PM) and near net shape processing(1,2). This potential is a result of being able to decrease the amount of purchased raw material and by reducing the amount of labor expended in machining, inspecting and handling of parts. To date these incentives have not appeared sufficiently attractive to lure applications into production.

To add incentive, LTV and Crucible have embarked on a joint program to develop a titanium alloy that takes advantage of the PM process to achieve superior properties. Most of the alloys reported on in the past have been ingot metallurgy (IM) alloys that have been converted to powder. Little attempt was made to capitalize on the benefits of a faster cooling rate. Rapid solidification enables much wider variety of alloys because of being able to solidify solutions of metals that would be impossible in IM technology because of solute segregation during solidification.

A case for Ti-1.3Al-8V-5Fe (Ti-1-8-5) (3,4) can be made on this basis. This alloy was developed in the 1950s by the Mallory-Sharon Titanium Corp (now RMI). It exhibited high strength, but was eventually abandoned because of its tendency for segregation of iron. In the past few years PM techniques have shown the ability to eliminate this problem. The objective of this study was to improve the ingot metallurgy and wrought properties of this alloy through composition modifications possible only through powder metallurgy techniques.

Ti-1-8-5 is a metastable beta alloy that can be heat treated to very high strengths. Ultimate strengths of over 1540 MPa (220Ksi) have been demonstrated (5). Like other beta alloys, it also exhibits good fracture toughness, deep hardenability, and excellent corrosion resistance. With this strength and its density, it becomes attractive in airframes in competition with high strength steels (6, 7). Landing gear components have been specifically identified as a potential area for trade studies.

Figure 1 shows a prototypical landing gear as part of a short takeoff and vertical landing (STOVL) transport concept. Traditionally, high strength steel would be employed in a strength range of 1750 MPa (250 Ksi). A weight analysis projected each gear to weigh 713 Kg (1573 lbs) in steel and, assuming all parts could be converted, 554 Kg (1223 lbs) in a hypothetical titanium alloy with a strength of 1680 MPa (240 Ksi). The reduction in gear weight, however, could also be used to reduce the rest of the airframe by hundreds of additional pounds.

Titanium '92
Science and Technology
Edited by F.H. Froes and I. Caplan
The Minerals, Metals & Materials Society, 1993

Experimental Procedure

Powder Production

Powders for this study were produced by inert gas atomization. Though this technology is not currently commercial, it does have potential for lowering powder costs over current methods. Inert gas atomization produces powder direct from melted metal, instead of from bar that has been reduced from ingots. Melting stock was made by a single consumable arc melting (20 lbs) ingots using titanium sponge, master alloy and high purity iron. Atomization was accomplished in an apparatus illustrated in Figure 2. This unit employs a water cooled, skull furnace and a nonconsumable electrode for melting. As power is added to the furnace, an arc is drawn and the top of the metal charge begins to melt. Additional power melts progressively more of the charge. Since the sides of the crucible are cooled, the molten metal is always surrounded by a container of its own alloy. When the molten portion reaches the bottom of the furnace, it flows through the hole in the bottom and through a ring of gas nozzles. As the stream is broken up by the gas jets, it is cooled and solidifies into small spherical particles.

Mechanical properties were determined from compacts of the powders. The compacts were made by canning the powder in pure titanium containers and hot isostatically pressing (HIP) under 103 MPa (15 Ksi) at 788°C (1450°F) for four hours. Tensile and fracture toughness specimens were cut from the rectangular blocks and tested according to ASTM E 8 and E 399, respectively.

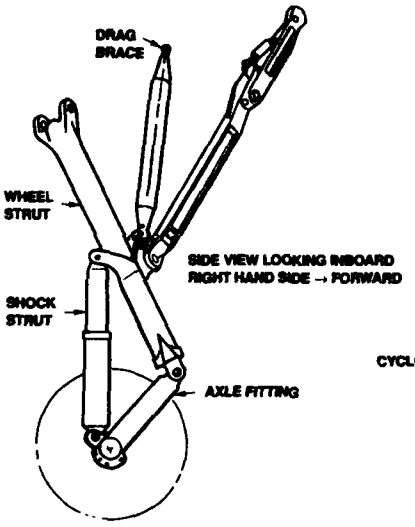


Figure 1. Prototypical STOVL Landing Gear for Material Trade Studies

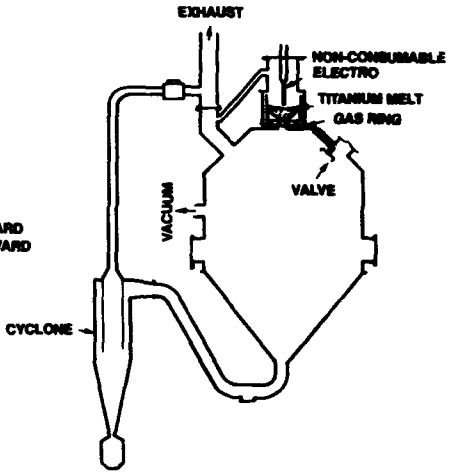


Figure 2. Inert Gas Atomization Furnace Used to Manufacture the Titanium Powders

Alloy Selection and Preparation.

The emphasis for study centered on the weight fractions of beta stabilizers vanadium and iron. Particular interest centered on the potential for additional iron in solution, made possible through the PM approach. Patents of the basic Ti-1-8-5 alloy cite high oxygen as one of its strengthening agents and yet it is also one of the three gaseous interstitial elements (others nitrogen and hydrogen) that lead to lower toughness. This study evaluates the substitution of additional metal alloying elements for a reduction of oxygen and the effects on the strength and fracture toughness combination. Properties of derivatives were compared with those of a standard, nominal composition.

Results and Discussion

Powder Characterization.

Table I shows the nominal composition and the actual weight fractions along with the beta transus for each alloy. Particle size distributions were determined and are shown in Table II. Surfaces exhibited subtle dendritic features that became progressively more pronounced with increasing beta stabilizer content.

Table I. Chemical Composition of Ti-1-8-5 and Derivatives Alloys

Alloy	Weight Percent							Beta Transus	
	Al	V	Fe	C	N	O	H	°C	°F
Ti-1-8-5 Standard O	1.4	8.2	5.0	0.047	0.010	0.227	0.0053	765	1410
Ti-1-8-5L Low O	1.5	7.8	5.1	0.018	0.014	0.398	0.0096	800	1575
Ti-1-5-8	1.2	5.2	7.8	0.020	0.010	0.127	0.0065	727	1340
Ti-1-8-8	1.3	8.3	7.6	0.028	0.011	0.147	0.0049	727	1340
Ti-1-5-10	1.3	5.4	10.5	0.020	0.007	0.130	0.066	700	1290
Ti-1-10-10	1.3	10.2	9.8	0.026	0.009	0.110	0.0055	693	1280

Table II. Particle Size Distribution of Alloy Powders in Percent Undersize

Alloy	Standard Mesh						
	35	45	60	80	100	200	325
Ti-1-8-5 Standard O	100	78	37	19	13	3	1
Ti-1-8-5L Low O	100	78	44	28	21	7	2
Ti-1-5-8	100	87	63	39	29	4	1
Ti-1-8-8	100	84	63	41	33	7	1
Ti-1-5-10	100	85	67	45	34	6	1
Ti-1-10-10	100	92	69	40	29	3	1

As Figure 3 shows, this dendritic structure was evident in the particle microstructure, which is consistent with evidence from previous studies of other beta titanium powders (7). Again, the dendritic appearance became progressively more pronounced with increasing beta stabilizer content. Grain size increased with increasing particle size because of the slower cooling rates experienced by the larger droplets.

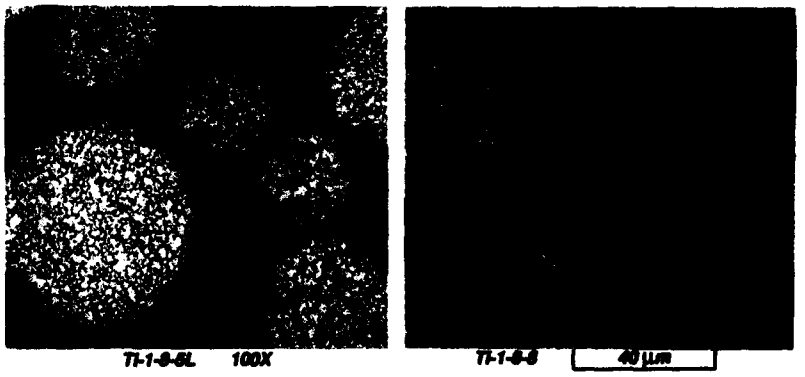


Figure 3. Particle Microstructures Show Increasing Dendritic Features

Compact Microstructure.

A comparison of compact microstructures was made with the corresponding prior particle microstructure. Because the HIP temperature was above the beta transus, considerable grain growth occurred. Grain size increased, in general, from less than 20 micrometers to 75-100 micrometers during consolidation. The greater the solute fraction, the smaller the amount of growth. Figure 4 shows the microstructure of Ti-1-8-5L and Ti-1-8-8, which was representative of the higher beta alloys. The Ti-1-8-5L microstructure exhibits partial recrystallization while the others showed relatively large recrystallized, equiaxed beta with traces of alpha in the grain interiors. This alpha could have precipitated during the relatively slow cool down from the HIP temperature.

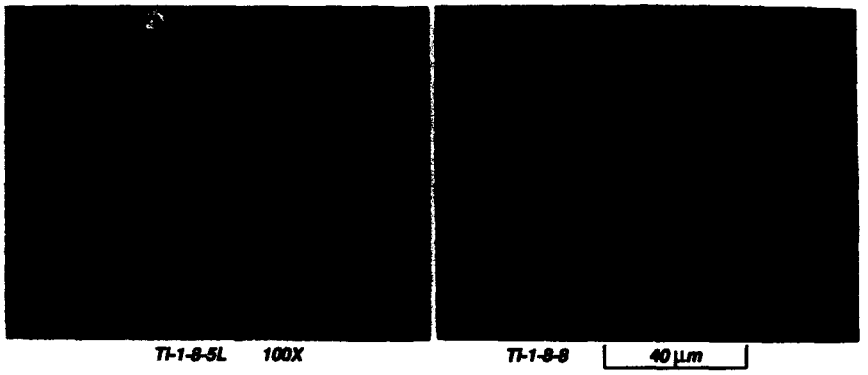


Figure 4. Compact Microstructures After HIP

Mechanical Properties.

Initial tests were conducted on compacts with a uniform heat treatment. All compacts were solution treated at 704°C (1300°F) for one hour, water quenched and aged at 482°C (900°F) for four hours. For the higher beta derivatives, the beta transus was below the solution-treating temperature. Tensile bars were cut from the compacts and test results are shown in Table III. These strength levels were lower than the baseline Ti-1-8-5, as were the ductilities, particularly in the higher beta content alloys.

Table III. Tensile Properties of PM Ti-1-8-5 and Derivative Alloy Compacts with Standard and Reduced Oxygen

Alloy	Tensile Strength MPa	(Ksi)	Yield Strength MPa	(Ksi)	Elongation %	Modulus GPa	(Msi)
Ti-1-8-5 Standard O	1394	(202)	1346	(195)	4.8	110	16.1
Ti-1-8-5L Low O	1297	(188)	1276	(185)	4.8	110	15.9
Ti-1-5-8	1132	(164)	1111	(161)	5.8	106	15.3
Ti-1-8-8	1228	(178)	1214	(176)	3.3	112	16.2
Ti-1-5-10	1021	(148)	1021	(148)	1.0	100	14.5
Ti-1-10-10	1104	(160)	1090	(158)	0.5	104	15.0

Averages of 2 tests
Heat treatment 704° (1300°F) 1 hour, WQ, 482°C (900°F), 4 hours

The next experiment was to tailor the solution treatment to the alloy and perform a hardness study to determine the optimum aging parameters. New solution temperatures were selected below the alloy's beta transus and are shown in Table IV. Samples were held at temperature for one hour and water quenched, followed by aging at three temperatures, 427°C (800°F), 482°C (900°F) and 538°C (1000°F) for various periods.

Table IV. Tensile Properties of PM Ti-1-8-5 and Derivative Alloy Compacts with Reduced Oxygen and Individualized Heat Treatments

Alloy	Solution Temperature	Aging Cycle	Tensile Strength MPa	(Ksi)	Yield Strength MPa	(Ksi)	Elongation %
Ti-1-8-5L	710°C (1310°F)	427°C (800°F) 32 Hrs	1504	(218)	1484	(215)	1.5
		482°C (900°F) 4 Hrs	1428	(207)	1346	(195)	4.7
Ti-1-5-8	671°C (1240°F)	427°C (800°F) 32 Hrs	1428	(207)		pf	1.6
		482°C (900°F) 32 Hrs	1249	(181)	1187	(172)	7.8
Ti-1-8-8	671°C (1240°F)	427°C (800°F) 32 Hrs	1456	(211)	1394	(202)	1.5
		482°C (900°F) 32 Hrs	1290	(187)	1228	(178)	7.8
Ti-1-5-10	643°C (1190°F)	427°C (800°F) 32 Hrs	1242	(180)		pf	1.6
		482°C (900°F) 8 Hrs	1166	(169)	1166	(169)	3.1
Ti-1-10-10	616°C (1140°F)		not tested				

One test for each condition
Solution temperature soak for 1 hour
pf – premature fracture

To determine the best aging conditions for mechanical properties, a hardness study was conducted. Aging treatments were made at three temperatures: 426°C (800°F), 482°C (900°F) and 537°C (1000°F) and at varying periods. Figure 5 shows the aging response curves.

Examination of the hardness curves shows a progressive sluggishness in hardening with increased beta stabilizer. Solution treated hardness, on the other hand, shows a progressive increase. Apparently, the added solute significantly changed the precipitation kinetics of alpha. Since the HIP cycle was performed above the beta transus for most of the alloys, it is possible this excursion may have caused undesirable, localized precipitation of alpha at grain boundaries during the cool down. A concentration of alpha at grain boundaries is known to drastically reduce ductility and would rob grain interiors of needed alpha for precipitation strengthening. However, previous work on Ti-1-8-5 (8) showed little difference in tensile properties of material with HIP temperatures above and below the beta transus.

The increase in solution treated hardness is presumed to be a result of solid solution strengthening. However, the increasing amount of solute progressively stabilized the beta phase, and therefore, decreased the response of the alloys to aging. For example, the Ti-1-8-5L alloy developed a maximum hardness of 440 DPH at 482°C (900°F) after one hour, the other alloys reached a maximum hardness of only 410-420 DPH after aging up to 48 hours at the same temperature.

Microstructures of the solution-treated condition are shown in Figure 6. Since the solution-treatment temperatures were below the beta transus temperature, relatively coarse primary alpha was formed. In the Ti-1-8-5L alloy, the alpha tended to form in the unrecrystallized regions of the microstructure, while in the higher beta derivatives, the alpha formed more uniformly throughout their recrystallized structure.

Microstructures of the alloys in the aged condition, shown in Figure 7, confirmed the hardness data. They exhibited a decreasing amount of precipitated alpha with increasing beta solute after similar aging cycles.

The aging response curves were reviewed and selected heat treatments were duplicated on larger samples of the corresponding alloys from which tensile specimens were cut and tested. Table IV shows the results of the tests for the conditions indicated. Aging temperatures of 427°C (800°F) and 482°C (900°F) were selected to develop maximum strength in the alloys. As indicated in the table, the 427°C (800°F) aging temperature developed the highest strengths, but the ductilities were low. Better combinations of strength and ductility were obtained by aging at 482°C (900°F). The alloy Ti-1-8-5L developed the best combination of strength and ductility. The Ti-1-5-8 and the Ti-1-8-8 alloys had similar ductilities, but with strengths that were over 138 MPa (20 Ksi), lower. The Ti-1-5-10 and Ti-1-10-10 alloys had relatively low strength and ductility in all age conditions.

Oxygen Concentration Effects on Toughness.

Fracture toughness tests were performed on samples containing standard and reduced levels (0.398 and 0.227 respectively) of oxygen in a Ti-1-8-5 nominal alloy to determine the trade-off of added metal alloying with lower oxygen. Results of the tensile and fracture toughness tests are presented in Table V. Though the reduced oxygen did provide an increase in toughness, it also allowed a drop in strength. Additional heat treatments of the standard oxygen also showed modest improvements in toughness.

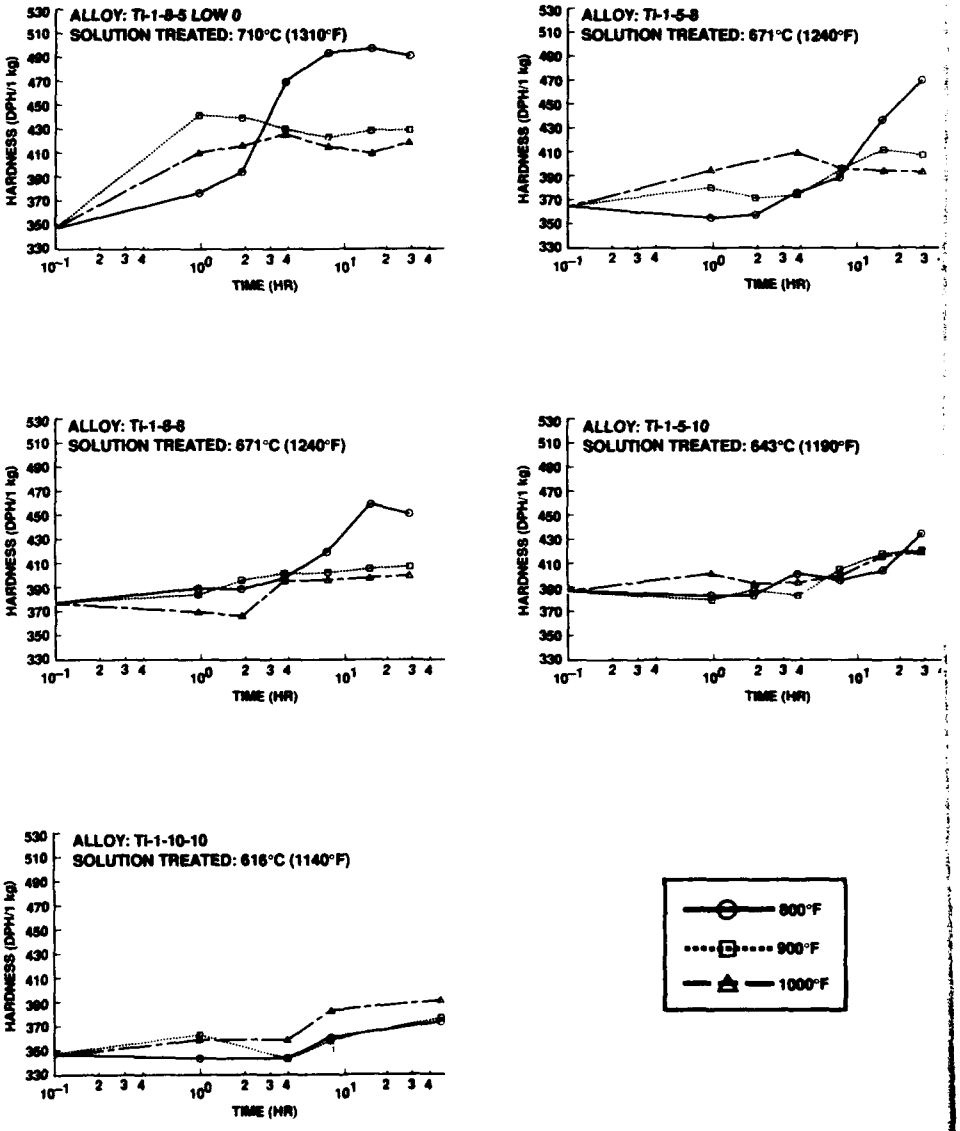


Figure 5. Aging Response of Ti-1-8-5 Derivative Alloys

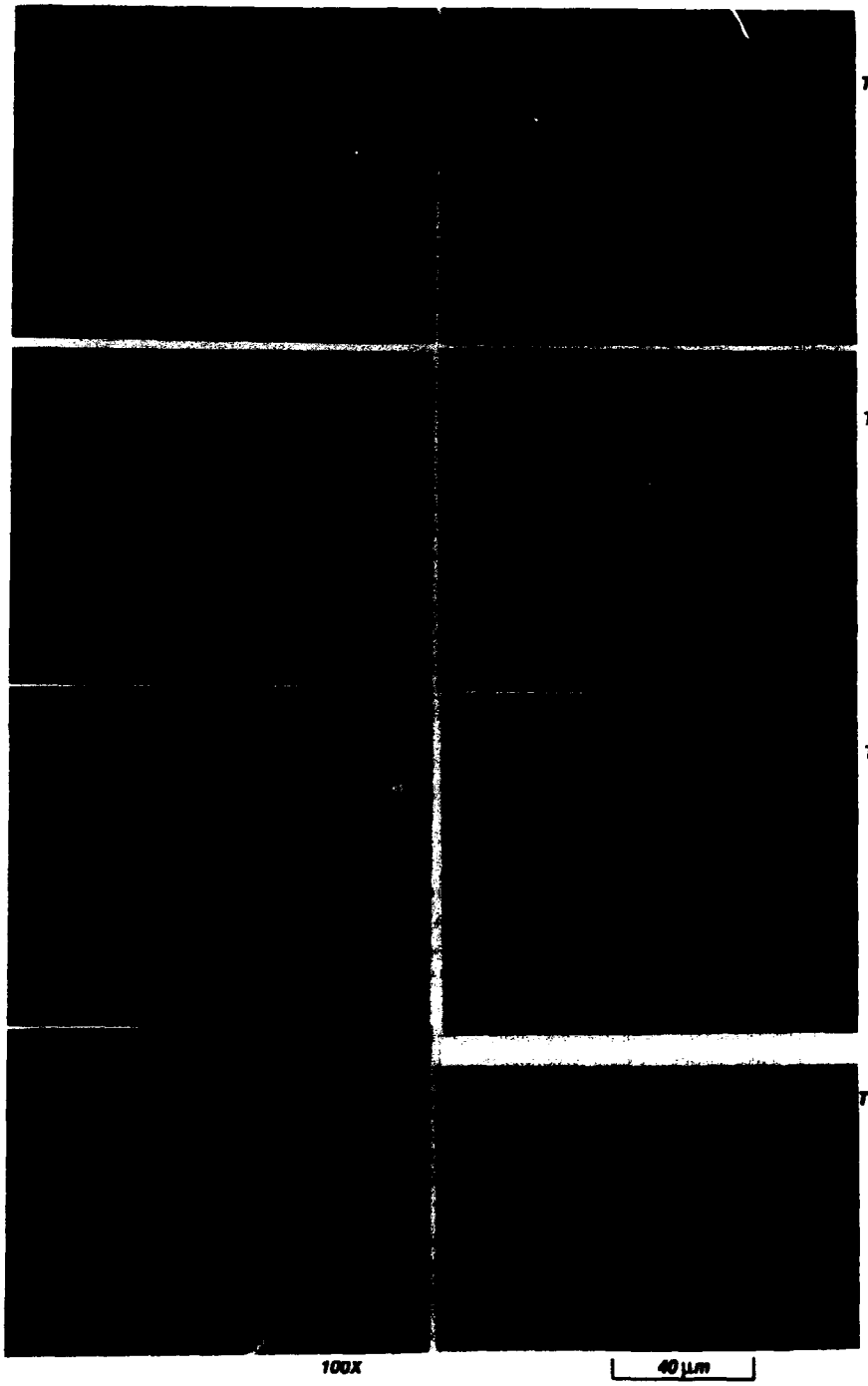


Figure 6. Solution-Treated Microstructures

Figure 7. Aged Microstructures

Table V. Fracture Toughness of PM Ti-1-8-5 Alloy Compacts with Reduced and Standard Oxygen Content

Heat Treatment	Oxygen Content %	Tensile Strength MPa	(Ksi)	Yield Strength MPa	(Ksi)	Elongation %	Fracture Toughness, K_Q GPa $\sqrt{m}$	(Ksi $\sqrt{in}$)
704°C (1300°F) 1 Hr, WQ 482°C (900°F) 4 Hrs	0.398	1396	(202)	1346	(195)	4.8	22.4	(20.4)
744°C (1375°F) 1 Hr, WQ 537°C (1000°F) 4 Hrs	0.398	1360	(197)	1352	(196)	1.8	24.8	(26.5)
788°C (1450°F) 1 Hr, WQ 482°C (900°F) 8Hrs	0.398	1414	(205)	1400	(203)	3.3	27.5	(25.1)
704°C (1300°F) 1 Hr, WQ 482°C (900°F) 4 Hrs	0.227	1297	(188)	1276	(185)	4.8	29.0	(26.4)

Conclusions

Toughness and ductility are relatively low for the Ti-1-8-5 derivatives in the high strength aged condition. The strength of Ti-1-8-5 has not been improved by these composition changes, but much more work needs to be done with heat treatments before definite conclusions, can be drawn. Either the beta stabilizers must be reduced or the percentage of alpha stabilizers must be increased to cause an effective aging response.

No definitive conclusions can be made regarding the suspected detrimental effects on ductility and toughness after consolidation above the beta transus. If consolidation must be accomplished below the beta transus for the desired properties, the alloy composition must be selected with this limitation in mind.

In general, the strength/toughness product was not noticeably improved by either the oxygen reduction or by heat treatments in the baseline Ti-1-8-5 nominal composition.

Acknowledgement

This work was jointly supported by LTV Aerospace and Defense Company, Aircraft Division, and by Crucible Materials Corporation, Crucible Research.

References

1. V. C. Petersen, V .K. Chandhok, and J. H. Moll, *Manufacturing Process for the Hot Isostatic Pressing of Large Titanium PM Shapes*, AFML-TR-85-4120, December, 1985.
2. R. H. Witt, *Near-Net Shape HIP of Complex Titanium Parts*, final report to contract N00019-80-C-0034, Department of the Navy, Naval Air Systems Command, Washington, DC, January 1989.
3. U. S. Patent 2,884,323, Mallory-Sharon Titanium Corporation, Niles, Ohio.
4. U. S. Patent 2,819,959, Mallory-Sharon Titanium Corporation, Niles, Ohio.
5. J. L. Shannon, "Ti-1Al-8V-5Fe," *Aerospace Structural Metals Handbook*, Belfour Stulen Inc., Traverse City, MI, 1968.
6. C. F. Yolton and J. H. Moll, "Review and Status of Titanium Materials Produced from Spherical Prealloyed Powder," *Modern Developments in Powder Metallurgy*, Volumes 18-21, Metal Powder Industries Federation, Princeton, NJ, 1988.
7. C.F. Yolton, "P/M Beta Titanium Alloys for Landing Gear Application," *Progress in Powder Metallurgy*, Volume 42, Metal Powder Industries Federation, Princeton, NJ, 1986.
8. C. F. Yolton and J. H. Moll, "Evaluation of a High Strength Rapidly Solidified Beta Titanium Alloy," presented at the 1987 Annual P/M Conference.

SYNTHESIS OF TITANIUM ALUMINIDES USING A COMBINED MECHANICAL ALLOYING AND THERMOCHEMICAL PROCESSING APPROACH

D.K. Mukhopadhyay, C. Suryanarayana, and F.H. (Sam) Froes

Institute for Materials and Advanced Processes (IMAP)
College of Mines, University of Idaho, Moscow, ID 83843, U.S.A.

Abstract

Synthesis of Ti_3Al, TiAl and Al_3Ti intermetallic compounds in the Ti-Al system have been attempted by mechanical alloying of $TiH_{1.924}$ and Al powders, followed by annealing. Results of X-ray diffraction analysis of the material during processing and following annealing are reported. The intermetallics TiAl and Al_3Ti were successfully formed, but not Ti_3Al.

Introduction

In recent years there has been considerable interest in the development of intermetallics based on the Ti-Al system, including Ti_3Al, TiAl and Al_3Ti. All the three intermetallics have the potential for use in elevated temperature applications, especially in the aerospace industry, due to their attractive combination of properties such as low density, high temperature strength, modulus retention, and high resistance to oxidation. Commercialization is however, proving to be very difficult because of the extremely low ductility of these intermetallic compounds. Chemistry modifications and microstructural control have been extensively investigated to alleviate this problem[1,2], with limited success.

In the present work a combined thermochemical processing(TCP)[3,4] and mechanical alloying(MA) approach[5,6,7] was used to synthesize the three intermetallics. Table I lists the crystal structure data of the different phases involved. Mechanical alloying allows intimate mixing(alloying) while use of TCP contributes both microstructure refinement and a brittle phase. Mechanical alloying has been generally employed for systems with at least one ductile component. However, recently it was used to explore the possibility of producing equiatomic TiAl intermetallic compound through mechanical alloying of a mixture of two brittle compounds, Al_3Ti and TiH_2, blended in an appropriate ratio[8]. Davis and Koch also used two brittle powders, Si and Ge and formed a Si-Ge solid solution by MA [9].

Titanium '92
Science and Technology
Edited by F.H. Froes and I. Caplan
The Minerals, Metals & Materials Society, 1993

Table I : Crystal Structure Data of the Phases Involved

Phase	Pearson symbol	Space group	Lattice parameters a(nm)	c(nm)	c/a
Ti	hP2	$P6_3/mmc$	0.295	0.4686	1.588
Al	cF4	Fm3m	0.4049	-	-
TiH_2(<20°C)	tI6	I4/mmm	0.3202	0.4279	1.336
TiH_2(>20°C)	cF12	Fm3m	0.4454	-	-
$TiH_{1.924}$(<20°C)	tI*	-	0.4468	0.4400	0.985
$TiH_{1.924}$(>20°C)	cF*	-	0.4448	-	-
Ti_3Al	hP8	$P6_3/mmc$	0.5775	0.4638	0.080
TiAl	tP4	P4/mmm	0.3976	0.4049	1.018
$Al_{23}Ti_9$	tI*	-	0.3843	3.3465	8.708
Al_3Ti	tI32	I4/mmm	0.3875	3.3835	8.732

* Suggests that the number of atoms is not clearly determined in the crystal structure.

The present study is an extension of the previous work [8], again using the combined MA and TCP method of synthesis. In this program the formation of the three intermetallic compounds Ti_3Al, TiAl and Al_3Ti has been attempted from $TiH_{1.924}$ and Al powders.

Experimental Procedure

Titanium Hydride($TiH_{1.924}$, -100 mesh,>99% pure) and elemental Al(-100 mesh, >99% pure) powders were blended in proportions of 3:1, 1:1 and 1:3 ratios to produce the Ti_3Al, TiAl, and Al_3Ti intermetallic compounds.

Mechanical alloying (MA'ing) was carried out at room temperature in a Spex 8000 shaker mill for times ranging from 30h to 35h. The milling balls are made of 52100 steel balls of diameter 3/16 in. About 10gms of powder and 100gms of balls were charged for each run. The container was sealed in a glove box in an argon atmosphere. In all cases MA was carried out without process control agents (PCA's). The MA'd powders were removed from the canister in the argon filled glove box and x-ray diffraction studies were conducted using a monochromatic Cu K_α radiation at 40 kV and 15 mA settings in a Philips x-ray diffractometer . The MA'd powders were subsequently annealed at a temperature of 620°C, and the phase changes occurring as a result of the elevated temperature exposure were followed. The phases were analyzed by comparing the peak positions and intensities with those listed in the JCPDS files.

Results

In all the cases it is observed that with an increase in MA time, the peaks broadened and the intensities decreased. The hydrogen content of the materials studied, under various conditions, is shown in Table II.

Table II : H_2 analysis

Compositions	Conditions	H_2 Content (wt%)
3 $TiH_{1.924}$ + Al	MA 20h	1.65
3 $TiH_{1.924}$ + Al	MA 20h 620°C, 10 days	0.92
$TiH_{1.924}$ + Al	MA 16.5h	1.58
$TiH_{1.924}$ + Al	MA 16.5h; 620°C, 7 days	0.77
$TiH_{1.924}$ + 3 Al	MA 20h	1.30
$TiH_{1.924}$ + 3 Al	MA 20h; 620°C, 2 days	0.062

Ti_3Al: Fig.1 shows the x-ray diffraction patterns of the powders MA'd up to 30h. It is observed that the Al peaks disappear after 15h of MA suggesting formation of a solid solution of Al in $TiH_{1.924}$ has occurred. An amorphous phase appeared after 30h of MA. The powder MA'd for 20h was annealed at 620°C for 10 days. Fig.2 shows the x-ray diffraction pattern of this material. The pattern shows the formation of complex compound(s) which could not be matched to the data for Ti_3Al.

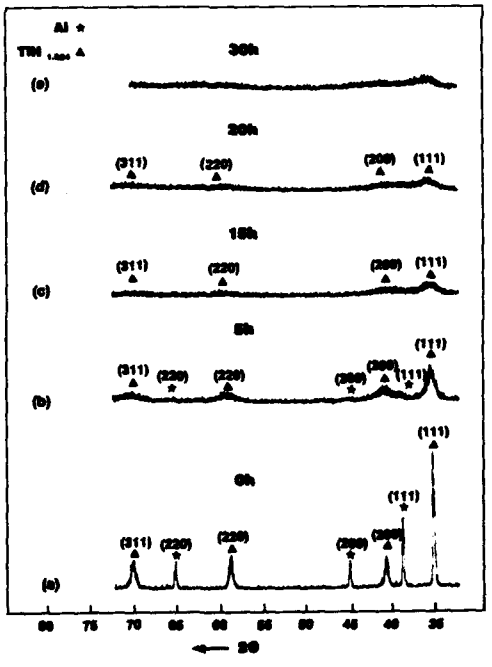


Fig.1 : XRD shows the effect of MA in the powders of composition 75 at% $TiH_{1.924}$ + 25 at% Al

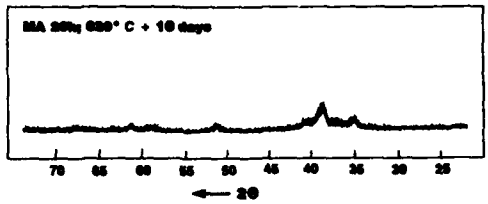


Fig.2 : XRD of the powder MA'd for 20h and annealed at 620°C for 10 days showing the formation of complex compound which does not match with Ti_3Al.

TiAl: Fig.3 shows the x-ray diffraction patterns of the powders MA'd up to 30h. It is observed that the Al peaks almost disappeared after 16.5h of MA'ing and the titanium hydride peaks shift to higher angles indicating formation of a solid solution of Al in titanium hydride. After 30h, the pattern appears amorphous. The powder MA'd for 16.5h, which was solid solution of Al in titanium hydride, was annealed at 620°C for 7days and 100% formation of TiAl was achieved (Fig.4).

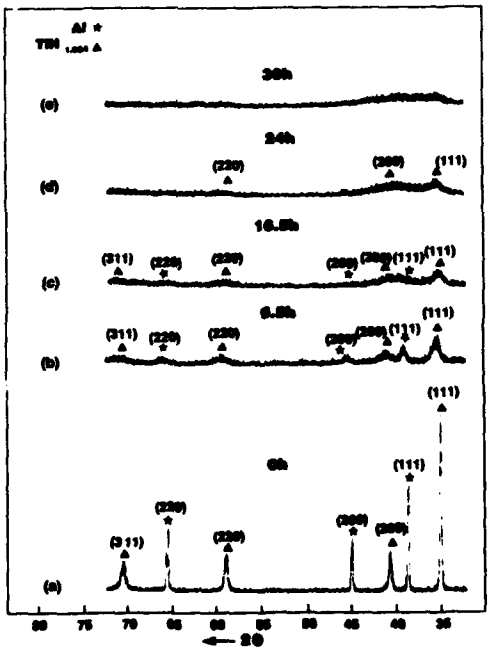


Fig.3 : XRD shows the effect of MA in the powders of composition 50 at% $TiH_{1.924}$ + 50 at% Al.

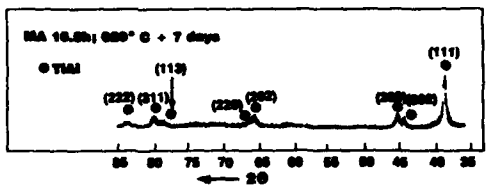


Fig.4 : XRD of the powder MA'd for 16.5h and annealed at 620°C for 7 days showing the formation of TiAl.

Al_3Ti: Fig.5 shows the x-ray diffraction patterns of the powders MA'd up to 35h. With an increase in MA time, the peaks broadened and the intensities decreased. At 35h, all the peaks became very broad but no change in the position of the peaks was observed suggesting no alloy formation by MA. The powder MA'd for 20h was annealed at 620°C for 2 days and 100% formation of Al_3Ti was achieved (Fig.6). The lattice parameters of the Al_3Ti phase obtained are a=0.3898nm and c=3.3526nm, compared to the JCPDS data of a=0.3875nm, c=3.3835nm. The intensity of the peaks, showed minor differences compared to the JCPDS data.

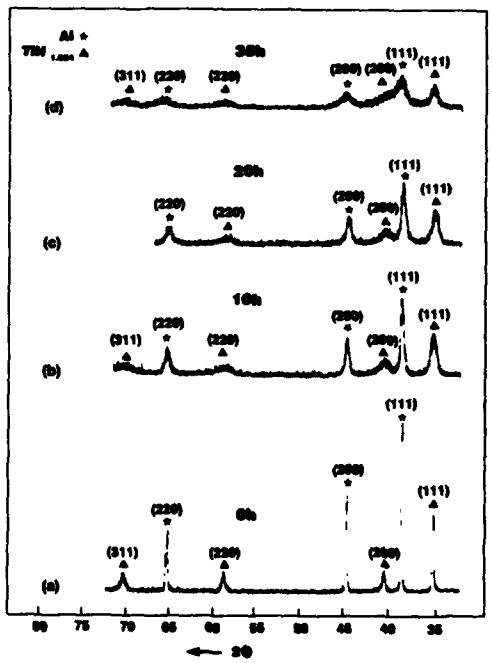


Fig.5 : XRD shows the effect of MA in the powders of composition 25 at% $TiH_{1.924}$ + 75 at% Al.

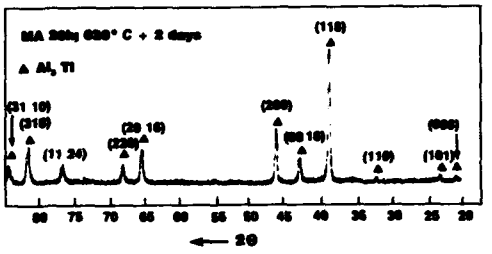


Fig.6 : XRD of the powder MA'd for 20h and annealed at 620°C for 2 days showing formation Al_3Ti.

Discussion

In both the cases of Ti_3Al and TiAl, MA resulted in a slight shift of the $TiH_{1.924}$ peaks towards higher angles along with disappearance of the Al lines. This indicates the formation of a solid solution of Al in $TiH_{1.924}$. Titanium hydride has an fcc structure similar to Al, but the cell is slightly larger than that of Al. Hence, dissolution of Al in $TiH_{1.924}$ shrinks the titanium hydride cell causing the peak shift towards higher angles. However no peak shift was observed in the case of Al_3Ti suggesting no alloy formation by MA. Again amorphous phases were obtained in both the cases of Ti_3Al and TiAl after longer milling time. But in the case of Al_3Ti, the amorphous phase was not observed even after long milling time. Murty et al.[10] reported the amorphization in Ti-Al system occurs in the 10-75% Al range using MA of blended elemental powders. It is likely that the presence of hydrogen in the present work prevented amorphization in the Al_3Ti boundary compositions.

Ti_3Al was not formed even after heat treatment probably due to the presence of a large amount of H_2 which might prohibit the formation of Ti_3Al. Results of heat treatment in the case of both the equiatomic compound and Al_3Ti, shows 100% formation of TiAl and Al_3Ti respectively. Some of the peak intensities in the present work are a little different from the JCPDS data, probably due to the presence of H_2 causing slight changes in the atomic arrangement.

In addition to the demonstration of successful formation of the two intermetallics TiAl and Al_3Ti, it has also been shown that the use of the extremely brittle $TiH_{1.924}$ allows effective alloying to occur without PCA's. Since $TiH_{1.924}$ is brittle, sticking problems are avoided even in the case of the 75%Al+25%$TiH_{1.924}$ mixture. Significantly, the titanium aluminides produced by this process, should have less contamination compared to the situation where PCA's are used.

Conclusions

Successful synthesis of the intermetallic compounds TiAl and Al_3Ti was achieved by mechanical alloying mixtures of $TiH_{1.924}$ and Al powders in the appropriate ratio and subsequent annealing at elevated temperature. No PCA's were used during the MA process, reducing the level of contamination. Synthesis of Ti_3Al was not

accomplished using the same technique as for the other intermetallics, rather complex compound(s) were formed. The reason for this is not clear and further work, including dehydrogenation studies, are needed to define why Ti_3Al did not form.

Acknowledgements

The authors would like to acknowledge Alcoa for the supply of Al powder for this program. In addition the assistance of Mrs. Susan Goetz in manuscript preparation is appreciated.

References

1. F.H. Froes, C. Suryanarayana and D. Eliezer, "Production, characteristics, and commercialization of Titanium Aluminides", ISIJ International, 31 (1991), 1235-1248.

2. F.H. Froes, C.Suryanarayana, and D. Eliezer, "Synthesis, properties and applications of titanium aluminides", J. Mater.Sci., 27, 1992, (in press).

3. F.H. Froes and D.Eylon, "Thermochemical processing(TCP) to improve the behavior of titanium alloys - Temporary alloying with hydrogen", Hydrogen effects in Material behavior, eds. A.W. Thompson and N.R. Moody,(Warrendale, PA:TMS,1990), 261-284.

4. F.H. Froes, D.Eylon and C.Suryanarayana, "Thermochemical processing of titanium alloys", JOM, no.3, 42 (1990), 26-29.

5. P.S. Gilman and J.S. Benjamin, "Mechanical alloying", Ann. Rev. Mater. Sci, 13 (1983), 279-300.

6. R. Sundaresan and F.H. Froes, "Mechanical alloying of light metals", Metal Powder Rep., 44 (1989), 195-200.

7. C. Suryanarayana, F.H. Froes, "Light metal synthesis by mechanical alloying", Mater. Sci. Forum, 88-90 (1992), 445-452.

8. C. Suryanarayana, R. Sundaresan, and F.H. Froes, "TiAl formation by mechanical alloying", Mater. Sci. and Engg., A150 (1992), 117-121.

9. R.M Davis, B. McDermott and C.C. Koch, "Mechanical alloying of brittle materials", Met. Trans. A, 19A (1988), 2867-2874.

10. B.S. Murty, M.D. Naik, M. Mohan Rao and S. Ranganathan, "Glass-forming range in Al-Ti system by mechanical alloying" Mater. Sci. Forum, (in press).

EFFECTS OF HYDROGEN ON MICROSTRUCTURE AND PHASE STABILITY OF ALPHA-2 BASE TITANIUM ALUMINIDE CASTINGS

M. Saqib, L. S. Apgar*, D. Eylon*, and I. Weiss

Department of Mechanical and Materials Engineering,
Wright State University, Dayton, OH 45435, USA

*Graduate Materials Engineering
University of Dayton, Dayton, OH 45469, USA

Abstract

Changes in microstructure, volume fraction, and distribution of phases in Ti–25Al–10Nb–3V–1Mo (at%) castings with up to 0.35 wt% hydrogen were investigated. Hydrogen was introduced into the material by thermochemical processing at temperatures ranging between 1200°F to 1800°F. Changes in the microstructure and phases were examined using optical and electron microscopy, and x-ray diffraction. Ti–25Al–10Nb–3V–1Mo castings show a microstructure consisting of α_2, B2, and orthorhombic phases. The α_2 phase displays an equiaxed Widmanstaten and cellular morphology. The B2 phase was observed mainly along the α_2 cell boundaries. Some of the Widmanstaten plates also contain very fine orthorhombic (O) phase in a plate-like morphology. The presence of hydrogen did not change the morphology of the α_2 and B2 phases in the alloy. However, hydride precipitation and an increased volume fraction of orthorhombic phase were observed. This paper discuss the formation of hydride precipitates and the stability of the orthorhombic phase.

Introduction

The interaction of hydrogen with Ti alloys has been a subject of interest in recent years for several reason. The beneficial effects of hydrogen on the processessability [1,2], include lower processing loads, and temperatures, and higher ductility at elevated temperature. In castings the use of hydrogen as a temporary alloying element provides a processing route to modify the cast structure [3,4]. A study of the interaction of hydrogen with α_2 (Ti_3Al) and γ(TiAl) base titanium aluminide alloys is of particular interest since these are potential candidates for hydrogen-fueled flight vehicles [5]. Therefore, material degradation due to hydrogen embrittlement as well as thermal decomposition of metastable phases is of great concern. The Ti–25Al–10Nb–3V–1Mo (at. %) alloy, can have varying amounts of α_2, β, ω, ω-related metastable phases and O phase. The microstructure and volume fraction of the phases depends largely upon the prior thermal and/or thermomechanical history. Introduction of hydrogen to the alloy affects the stability of the phases present. Previous studies have shown that hydrogen stabilises the β phase in both $\alpha+\beta$ and $\alpha_2+\beta$ alloys [6,7]. The open lattice of the β phase holds large quantities of hydrogen on interstitial sites, without forming hydrides. However, hydrides can form in the β phase in material exposed to large amount or high pressures of hydrogen [8]. Charging hydrogen by electrochemical method is known to stabilise the O phase in Ti–25Al–10Nb–3V–1Mo alloys [9]. The presence of 0.31 to 0.45 wt.% hydrogen in $\alpha_2+\beta$ alloys results in the formation of hydrides in the α_2 phase [10]. This paper deals with changes in microstructure, distribution and volume fraction of the phases in Ti–25Al–10Nb–3V–1Mo alloy exposed to hydrogen at constant temperatures and pressure.

Titanium '92
Science and Technology
Edited by F.H. Froes and I. Caplan
The Minerals, Metals & Materials Society, 1993

Experimental Procedures

Hydrogen–charging

Cast Ti–25Al–10Nb–3V–1Mo alloy (Table I) was HIP'd at 2150°F/40ksi/6hr. Specimens (0.25" x 0.25" x 1.75") were machined by EDM. To avoid oxidation during hydrogen–charging, the specimens were wrapped in three layers; CP titanium, stainless steel and another layer of CP titanium foil. Before exposing to hydrogen, the chamber was pumped to a pressure of less than 5 mm Hg. The specimens were placed in the chamber and heated to the desired temperature. High purity hydrogen gas (containing less than 500 ppm of oxygen) was introduced at 3 psi positive pressure. After completion of the hydrogen–charging for a desired time, the chamber was tilted to slide the specimens to a cooler zone, in order to minimise hydrogen pick up during the cool down period. The

Table I: CHEMISTRY OF THE CAST ALLOY (WT.%) Balance = Ti

Al	Nb	V	Mo	Fe	Si	C	Mg	Ta	O	H	N
14.0	20.2	3.1	1.9	<0.1	<0.3	0.023	<0.05	<0.2	0.07	0.002	.09

Table II: TEMPERATURES/TIME FOR HYDROGEN CHARGING

I.D. No.	A2	A3	A4	A5	A6	A9
Temp/Time (°F/hr)	1200/20	1400/20	1600/20	1800/20	1800/2+1600/4 + 1400/6+1200/6	1800/10 + 1200/10
Conc. of H (ppm by wt)	3200	1850	1600	1250	3500	3500

temperatures and times used for the hydrogen–charging are given in Table II.

Material Characterisation

Specimens were characterized in the as HIP and HIP+ more hydrogen–charged conditions. The concentration of hydrogen after HIP was determined to be <25 ppm by wt. The concentration of hydrogen after different hydrogen–charging cycles is given in Table II. The β transus temperature of this alloy was determined to be between 1950 and 2000°F [11].

Microstructure and identity of the phases was studied by optical microscopy and x–ray diffraction. Specimens for optical microscopy were etched with Kroll's reagent. Specimens for x–ray diffraction were prepared by mechanical polishing on 800 grit SiC paper. Without etching, to avoid the formation of etch induced orthorhombic phase [12]. To determine the significance of cold working induced by mechanical polishing, selected specimens were prepared by electropolishing without mechanical polishing. No significant differences in x–ray diffraction peaks were observed. The grain size of the material (1 mm) as compared to x–ray beam size (12.5 mm) was fairly small and the diffraction peaks were recorded from an area representative of the material. The intensity of the peaks for transverse, longitudinal, and 45° sectioned material was reproducible to about $\pm$ 10% indicating little effect of texture on the peak intensities. The volume fraction of the phases could not be determined because of the overlap of the diffraction peaks from different phases present in the material.

TEM foils were prepared primarily by electrolytic polishing. Some specimens were also prepared using an alternate method of core drilling and ion milling, to determine if there are any artifacts introduced by electrolytic polishing. TEM was performed to reveal the morphology of the phases. Crystal structure and orientation relationships between the different phases were determined by selected area electron diffraction (SAD). Convergent beam electron diffraction was used to differentiate between the α_2 and O phases [13].

Results and Discussion

As–HIP Material

Following HIP at 2150°F/40ksi/6hrs the material consisted of α_2(Ti_3Al), B2 (Ti_2AlNb) and orthorhombic phases. x–ray diffraction peaks corresponding only to these phases are present in the spectrum, shown in Figure 1. The spectrum does not show the presence of any additional phase.

Low magnification optical micrograph of the alloy in as–HIP condition (Figure 2) reveals inhomogeneous microstructure. The microstructure displays Widmanstaten network of α_2 phase with varying size, in addition, a cellular morphology of α_2 phase is also observed at some locations.

TEM examination of the as–HIP specimens confirmed the presence of α_2, B2 and O phases. Figures 3a and 3b show bright field images from regions of α_2 phase with a Widmanstaten network morphology and cellular morphology, respectively. Micrographs from the regions with a Widmanstaten morphology does not reveal the presence of any phase other than α_2 in the inter–phase regions. Regions with cellular morphology show presence of B2 phase at α_2/α_2 boundaries. At certain locations between two lenticular α_2 grains, a finer transformed microstructure of α_2 and B2 phases are also observed

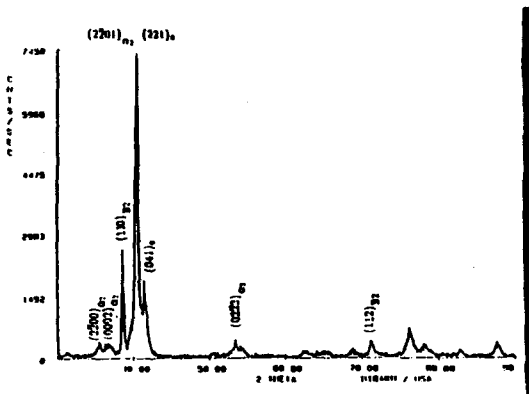


Figure 1: X–ray diffraction spectrum from Ti–25Al–10Nb–3V–1Mo alloy, cast and HIP (2150°F/40ksi/6hrs).

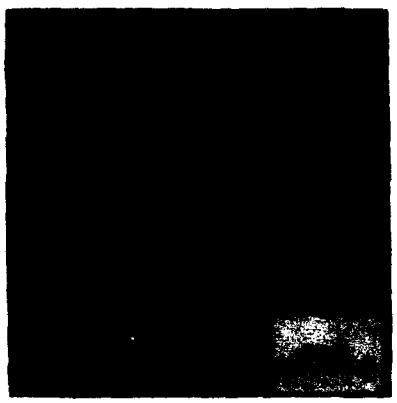


Figure 2: Optical micrograph from Ti–25Al–10Nb–3V–1Mo alloy, cast and HIP (2150°F/40ksi/6hrs).

(A in Figure 3b). The B2 phase at the α_2/α_2 boundaries was often connected to small grains of retained B2 phase as shown in Figure 3c. The general orientation relationship between α_2 and B2 phases is given as:

$$(0001)_{\alpha_2} \parallel (1\bar{1}0)_{B2}, \quad [2\bar{1}\bar{1}0]_{\alpha_2} \parallel [111]_{B2}$$

Some of the α_2 needles present in the Widmanstaten type network show formation of orthorhombic phase in plate morphology. Example of such microstructure is shown in Figure 3d. The orientation relationship between the α_2 phase and the orthorhombic phase is given as [13]:

$$(10\bar{1}0)_{\alpha_2} \parallel (110)_{orth}, \quad [0001]_{\alpha_2} \parallel [00i]_{orth}$$

Hydrogen–charged Material

Optical Microscopy

The microstructure of material charged with hydrogen was highly inhomogeneous. The hydrogen concentration of the alloy varied from 1250 to 3500 ppm by weight (Table II), but the microstructure produced by different hydrogen–charging cycles was similar at the optical level. Figures 4a and 4b show an example of the microstructure obtained from a specimen charged with hydrogen at 1200°F for 20hrs. The microstructure displaysdisplays light contrast regions surrounded by areas of darker contrast coarse

Widmanstaten network. The size of the light contrast regions in Figure 4a vary, but in general it is smaller than the prior β grain size. Furthermore, the size and shape of the light contrast region or regions showing coarse Widmanstaten network (dark contrast)

bears no relationship to the prior β grain boundaries. Where as in the as HIP specimens, the regions of darker contrast are generally observed at the prior β grain boundaries (Figure 2). This difference in microstructure is probably because the HIP temperature is above the β transus (1950–2000°F [11]) and the hydrogen–charging temperature is below



Figure 3: TEM micrographs from Ti–25Al–10Nb–3V–1Mo alloy, cast and HIP (2150°F/40ksi/6hrs) (a) from area showing Widmanstaten network (b) showing cellular morphology, (c) B2 in α_2/α_2 boundary connected to small grain of B2 (d) higher magnification showing fine scale phase separation in the α_2 lath.

the β transus of the alloy. The coarse α_2 laths in the hydrogen–charged material are a result of coarsening reaction at the hydrogen–charging temperature. The reason of the inhomogeneity in the microstructure in the hydrogen charged specimens is not clearly understood. However, it may not be related to concentration of hydrogen in the material, since similar inhomogeneous microstructures were also observed in HIP specimens following vacuum annealing in similar temperature range [14].



Figure 4: Optical micrograph from Ti–25Al–10Nb–3V–1Mo alloy, cast and HIP (2150°F/40ksi/6hrs) and charged with 3200 ppm hydrogen using conditions A2 (see Table II), (a) low magnification (b) higher magnification.

X–ray Diffraction

The x–ray diffraction spectra from the hydrogen–charged material show the presence of α_2, B2 and orthorhombic phases. Figure 5 shows an x–ray spectrum obtained from a specimen containing 3500 ppm hydrogen. Notice that the intensity of the $(110)_{B2}$ and $(112)_{B2}$ peaks are higher when compare to the same peaks from as HIP specimen (Figure 1). The most intense peak from the orthorhombic phase; $(221)_{ortho}$, overlaps with the $(2\bar{2}01)$ diffraction peak of the α_2 phase. However, the second highest peak from the orthorhombic phase i.e. $(041)_{ortho}$ is more intense in hydrogen–charged specimens as

compared to as–HIP specimens. X–ray diffraction spectra from other hydrogen–charged specimens using different aging times and temperatures showed peaks with maximum differences in peak intensities of about ± 10%. This difference could be due to a true difference in the volume fraction of the phases present in the material, or due to some texture effect caused by grain orientation.

Peaks from the TiH_2 phase, most commonly observed titanium hydride in titanium aluminide base alloys overlap with other peaks in x–ray spectra. Any extra peaks corresponding to any other hydrides of titanium or niobium were absent. The three most intense peaks expected from TiH_2 phase are $(110)_{TiH_2}$, $(101)_{TiH_2}$ and $(211)_{TiH_2}$. Unfortunately these three peaks overlap with the $(2\bar{2}01)_{\alpha_2}$, $(2\bar{2}00)_{\alpha_2}$, and $(112)_{B2}$ x–ray diffraction peaks. Therefore, the presence or absence of the TiH_2 phase could not be established.

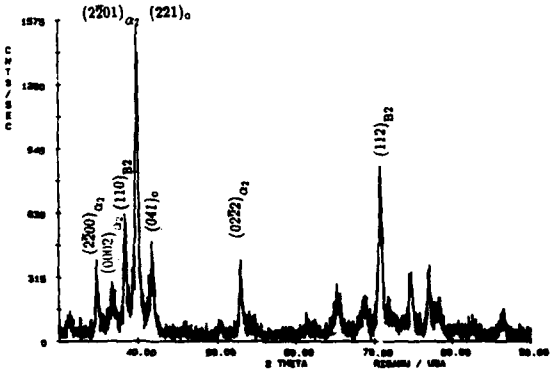


Figure 5: X–ray diffraction spectrum obtained from a specimen containing 3500 ppm hydrogen (condition A6).

Transmission Electron Microscopy

The local variation in the microstructure shown in the optical micrographs (Figure 4) was also observed in TEM micrographs. The inhomogeneity of the microstructure made it difficult to establish whether the variation in the TEM microstructures observed in different hydrogen–charged material is related to the difference in hydrogen concentration or merely reflects local variation. as observed in the optical micrographs. Microstructural features presented here are typical of all the hydrogen–charged material.

Figure 6a shows a low magnification bright field image from a specimen hydrogen–charged using conditions A5 (Table II). The micrograph shows a Widmanstaten type network similar to the one observed in the optical micrograph of Figure 4. Higher magnification of the same area is shown in Figure 6b. The micrograph reveals a fine scale phase separation by formation of parallel plates of O and α, inside the needles. Microdiffraction taken from the fine plates in the needles (50nm) show either 2mm or a 6mm symmetry in the diffraction patterns obtained from $[0001]_{\alpha_2} \parallel [001]_{orth}$. Such phase separation was also observed in the as–HIP specimens, (Figure 3d), and was shown to consistent with the formation of α_2+O, as was previously observed [15]. In hydrogen–charged material such phase separation was observed in almost all the needles of the Widmanstaten network, where as in the as–HIP material very few needles displayed such phase separation. The presence of hydrogen promotes the α_2 to α_2+O transformation. Therefore a higher quantity of O phase is reflected in the x–ray diffraction spectra obtained from the specimens charged with hydrogen.

Another important feature noticeable in Figure 6a, is the rim around most of the α_2 needles. Microdiffraction from the rim–area is shown in Figure 6c. The diffraction pattern shows a 2mm pattern symmetry consistent with [001] diffraction pattern from O phase, instead of 6mm pattern symmetry expected from $[0001]_{\alpha_2}$ diffraction pattern. The diffraction pattern from other orientations are also consistent with orthorhombic phase.

Formation of orthorhombic phase at the α_2 phase boundaries has been reported earlier in Ti–25Al–10Nb–3V–1Mo alloy hydrogen–charged by electro–chemical method [11].

No other phases were observed in the α_2 + O plates present in the needles as shown in Figure 6b. The diffraction patterns corresponding to Figure 6b do not show any streaking [16]. Nearly half of the needles present in the microstructure show a similar α_2 + O plate morphology. The rest had a typical microstructure similar to the one shown in Figure 7a. The areas marked as A and B correspond to α_2 + O in plate morphology and O phase in the rim areas, respectively. Notice the very fine planer precipitates (2nm) which are present in both areas A and B. The fine precipitates can be seen more clearly in the higher magnification micrograph as shown in Figure 7b. In the α_2 + O plates the fine precipitates are parallel to the length of the α_2 and O plates. The diffraction pattern taken from the area in Figure 7b, after tilting the foil to $[001]_{orth}$ is shown in Figure 7c. Notice streaking in the diffraction pattern in [110] direction ([110] direction in orthorhombic phase is equivalent to direction perpendicular to $(10\bar{1}0)$ plane in α_2 phase). The crystallographic plane of α_2 or O phase on which these planer precipitates are present is perpendicular to the direction of streaking. Formation of fine planer precipitates (80nm) on $\{10\bar{1}0\}$ planes of α_2 phase have been reported earlier and were identified as hydride phase [10]. The very fine precipitates observed in this study are probably also the hydride phase. However, the lower thickness of the precipitates in this study, (2nm) cause streaking in the diffraction patterns without any extra diffraction spots, which makes conclusive identification of the precipitates impossible at the present time.



Figure 6: TEM information from Ti–25–Al–10Nb–3V–1Mo alloy, cast and HIP (2150°F/40ksi/6hrs) and charged with 1250 ppm hydrogen (condition A5), (a) low magnification bright field image of Widmanstaten network (b) Higher magnification of a needle in the Widmanstaten structure. (c) Microdiffraction pattern from the area marked A in Figure 6b. (m denotes the mirror axes).

The as–HIP material contained regions of α_2 laths in cellular morphology with B2 phase at lath boundaries. The B2 phases in α_2/α_2 boundaries was often connected to small grains of retained B2 phase (Figure 3c). Regions of similar morphology were observed in hydrogen–charged material. Although the morphology is similar, the images and the diffraction pattern corresponding to some of such areas show the presence of orthorhombic phase. Figure 8a show a representative micrograph. The corresponding diffraction pattern after tilting the foil to [110] of B2 phase shows spots from [01] of orthorhombic phases (Figure 8b). The orientation relationship of the two phase in such areas generally follows the relationship:

$$(001)_{B2} \parallel (100)_{orth} \quad , \quad [110]_{B2} \parallel [001]_{orth}$$

The presence of thin plates in the bright field image and streaking along [110] direction of O phase is consistent with presence of similar precipitates as the ones observed in (α_2 + O) and O phase rim regions (Figure 7b). TEM micrographs from certain locations show the presence of orthorhombic phase in B2 matrix with absence of streaking in the diffraction patterns due to finer hydride precipitates. Figures 9a and 9b show an example of such microstructure and the corresponding diffraction pattern, respectively.



Figure 7: TEM information obtained from Ti–25Al–10Nb–3V–1Mo alloy cast and HIP (2150°F/40ksi/6hrs) and charged with 3500 ppm hydrogen (condition A9), (a) α_2 +O and O phase rim areas showing the presence of find hydride precipitates (b) Higher magnification image of the area marked B in figure 7a (c) diffraction pattern corresponding to Figure 7b after tilting to $[001]_{orth}$.



Figure 8: TEM information from Ti–25Al–10Nb–3V–1Mo alloy, cast and HIP (2150°F/40ksi/6hrs) and charged with 3500 ppm hydrogen (condition A6), (a) area similar to Figure 3c before hydrogen–charging, shows the presence of O phase and fine planer precipitates in B2 matrix, (b) diffraction pattern corresponding to Figure 8a.

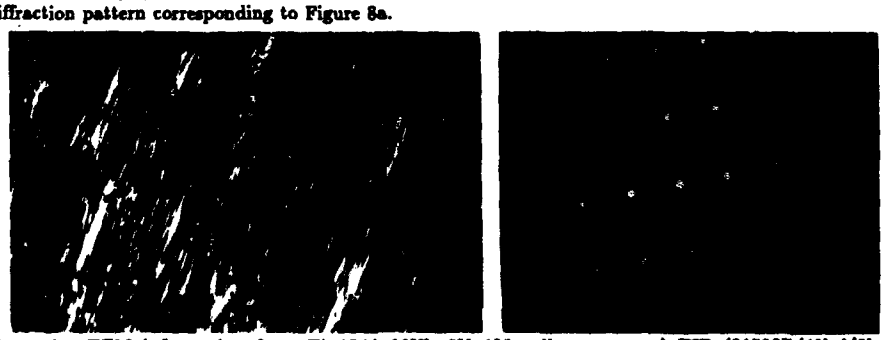


Figure 9: TEM information from Ti–25Al–10Nb–3V–1Mo alloy, cast and HIP (2150°F/40ksi/6hrs) and charged with 1600 ppm hydrogen (condition A2), (a) Bright field image from B2 phase showing presence of O phase in B2 matrix, (b) diffraction pattern corresponding to area in Figure 9a after tilting to [110] of B2, the extra weaker spots are consistent with [101] of O phase.

Conclusions

1. The microstructures produced following HIP at 2150°F/40ksi/6hrs of Ti–25Al–10Nb –3V–1Mo alloy at and after subsequent hydrogen–charging are highly non– homogeneous.
2. Introduction of hydrogen to the material increases the volume fraction of B2 and orthorhombic phases.
3. Formation of orthorhombic phase and planer precipitates of hydride phase were observed in the specimens after charging with hydrogen. Only B2 phase was present in these areas prior to hydrogen–charging.

References

1. B.A. Kolachev, et.al., "Evaluation of the Beneficial Effect of Hydrogen on Deformability of Titanium Alloy)ST4," Kusechno–Shtampovochnoye Proisvodstvo, Nr.1, January 1975, pp. 79–82, USAF Foreign Technology Division Translation, FTD–ID (RS) I–2347–75.
2. U. Zwickev et.al., "Process for Improving Workability of Titanium Alloys," US Patent No. 2892,742, June 1959.
3. R.G. Vogt, F.H. Froes, D. Eylon and L. Levin, "Thermo–Chemical Treatment (TCT) of Titanium Alloy Net Shapes," in Titanium Net Shape Technologies, ed. by F.H. Froes and D. Eylon, TMS, Warrendale, PA, 1984, pp. 145–153.
4. F.H. Froes and D. Eylon, "Thermochemical Processing (TCP) of Titanium Alloys by Temporary Alloying with Hydrogen," in Hydrogen Effects on Materials Behavior, ed. by A.W. Thompson and N.R. Moody, TMS, Warrendale, PA, 1990, pp. 261–283.
5. T.M. Ronald, "Materials Challenge for the National Aero*Space Plane," presented at NASP 2nd Workshop, Publication 1004, published by NASA Langley Research Center, November 1988, pp. 5–17.
6. W.R. Kerr, "The Effect of Hydrogen as a Temporary Alloying Element on the Microstructure and Tensile Properties of Ti–6Al–4V, Met. Trans., Vol. 16A, June 1985.
7. L. Steele, D. Eylon and F.H. Froes, "Microstructural Control of Titanium Aluminide Powder Compacts by Thermochemical Treatment," in Advances in Powder Metallurgy, Vol. 3, ed. by T.G. Gasbarre and W.F. Jandeska, MPFF/APMI, Princeton, NJ, 1989, pp. 509–529.
8. "Hydrogen Interaction with Titanium: Summary," presented at NASP 2nd Workshop, Publication 1004, published by NASA Langley Research Center, November 1988.
9. E. Manor and D. Eliezer, "Hydrogen Effects in Titanium Alloys Stabilised by Nb, V and Mo," Scripta Met. et Mater., Vol. 24, 1990, pp. 124–134.
10. N.S. Stoloff, "Hydrogen Embrittlement of Intermetallics," presented at NASP 2nd Workshop, Publication 1004, published by NASA Langley Research Center, November 1988, pp. 84–91.
11. Interim Report for Period October 1980)January 1982, "R&D on Composition and Processing of Titanium Aluminide Alloys for Turbine Engines," AFWAL–TR82–4086, 1982, pg. 11.
12. K. Muraleedharan, S.V. Negender Naidu and D. Banerjee, "Orthorhombic Distortion of the α_2 Phase in Ti_3Al–Nb Alloys: Artifacts and Facts," Scripta Met Vol. 24, 1990, pp. 27–32.
13. D. Banerjee, A.K. Gogia, T.K. Nandi and V.A. Joshi, "A New Orthorhombic Phase in a Ti_3Al–Nb Alloy," Acta Metall., 36, 1988, pp. 871–882.
14. Final Report, "Property Improvement of Titanium Aluminide Casting," EMTEC–CT–8/TR–90–8, 1991, pp. 156–162.
15. M.J. Kaufman, "Phase Relations in Ti_3Al–Nb system," AFWAL Technical Report 88–4113, July 1988.
16. G. Thomas and M.J. Goringe in Transmission Electron Microscopy of Materials, published by John Wiley & Son, 1979, pp. 139–222.

CHANGES IN MICROSTRUCTURE AND PHASE MORPHOLOGY DURING VACUUM ANNEALING OF Ti-25Al-10Nb-3V-1Mo-H ALLOY

M. Saqib, L. S. Apgar*, D. Eylon*, and I. Weiss

Department of Mechanical and Materials Engineering,
Wright State University, Dayton, OH 45435, USA

*Graduate Materials Engineering, University of Dayton,
300 College Park, Dayton, OH 45469-0240, USA

Abstract

Ti-25Al-10Nb-3V-1Mo (at. %) titanium aluminide castings with up to 0.35 wt. % hydrogen were vacuum annealed at 1200° F for 48 hours in an attempt to remove hydrogen from the material. Changes in the microstructure, volume fraction and morphology of the phases during vacuum annealing were examined using optical microscopy, transmission electron microscopy, and x-ray diffraction. The hydrogen containing material consisted of α_2, B2, orthorhombic, and hydride phases. Higher volume fraction of the orthorhombic phase was observed in the Ti-25Al-10Nb-3V-1Mo castings with hydrogen as compared to the as- cast alloy. Following annealing, the hydrogen level was found to be less than 0.0025 wt. %. Transmission electron microscopy of the vacuum annealed specimens did not reveal the presence of hydride precipitates, however, the high volume fraction of the orthorhombic phase was found to be stable during vacuum annealing. The stability of the hydride precipitates and the morphology of the α_2, B2 and orthorhombic phases are discussed in this paper.

Introduction

The utilization of hydrogen as a temporary alloying element in titanium alloy net-shape castings provides many benefits. It offers a method to modify microstructure and change volume fraction of phases without thermomechanical processing, in order to improve mechanical properties of castings. Such effects are well documented for various $\alpha_2 + \beta$ [1] and $\alpha + \beta$ alloys [2]. Alloying with hydrogen has also been proved advantageous in improving hot workability [3, 4] and during forging of titanium alloys.

One of the main limitation of using hydrogen as a temporary alloying element in net-shape castings is the removal of hydrogen. Hydrogen has to be completely removed before utillizing the casting in service, otherwise severe embrittlement of the material may occur. Therefore, hydrogen charging is always followed by vacuum annealing for hydrogen removal. The process of hyddrogen removal can limit the maximum allowable section thickness in castings. In the thicker sections the diffusion distances for complete removal of hydrogen may be large, consequently the vacuum annealing times may be very long, rendering the thermochemical process uneconomical for such castings.

The introduction of hydrogen to the material changes the stability of the different phases present to different extent. In α_2 + B2 alloys, hydrogen is known to stabilizes the B2 phase[5] and distort the lattice of α_2 to forms Orthorhombic (O) phase [6]. The maximum solubility limit of hydrogen in α_2 phase is about 16 at.% at 1250°F, with decreasing temperature the solubility de-

Titanium '92
Science and Technology
Edited by F.H. Froes and I. Caplan
The Minerals, Metals & Materials Society, 1993

creases to almost zero and all the hydrogen present in the α_2 phase reacts to form hydride precipitates [7]. Compared to the α_2 phase, the B2 phase has higher solubility and diffusivity of hydrogen and can accommodate larger quantities of hydrogen without forming hydrides. However, the presence of large concentration of hydrogen or the introduction of hydrogen at high pressure can form hydride precipitates in B2 phase [8].

Microstructural and phase changes during the second step of the thermochemical processing, i.e. vacuum annealing of the hydrogen-charged material are particularly important since the microstructural refinement accompanying dissociation of hydrides and the removal of hydrogen was found to be a major contributing factor in improvement of mechanical properties in several $\alpha + \beta$ alloys. Eutectoid decomposition of the β phase to $\alpha + TiH_2$ is believed to be responsible for the formation of ultra fine transformation products during vacuum annealing of some hydrogen-charged titanium alloys [9]. Microstructural refinement and an increase in amount of B2 phase after the removal of hydrogen from hydrogen-charged Ti-24Al-10Nb alloy has also been reported [1]. However, the resultant microstructure was very sensitive to cooling rate following hydrogen-charging. Hydrogen-charging above the β-transus temperature and air cooling followed by the removal of hydrogen is shown to produce very fine α_2 needles and an increase in amount of B2 phase. For treatment where hydrogen-charging was followed by furnace cooling, no change in the colony size of α_2 phase was observed following vacuum annealing. This paper deals with the changes in microstrcture and volume fraction of the phases during hydrogen-charging and subsequent vacuum annealing of Ti-25Al-10Nb-3V-1Mo-H castings.

Experimental Procedures

Hydrogen-charging

Ti-25Al-10Nb-3V-1Mo cast blocks were HIP'd at 2150°F/40ksi/6 hrs. Specimens 0.25" x 0.25" x1.75" were machined by EDM. The specimens were wrapped in three layers, CP-titanium, stainless steel, and an other layer of CP-titanium foil, to avoid oxidation during hydrogen-charging. Before introduction of hydrogen, the chamber was pumped to a pressure < 5mm of Hg. The specimens were placed in the chamber and heated to the desired temperature. High purity hydrogen gas (containing less than 500 ppm of oxygen) was introduced at 3psi positive pressure. After completion of hydrogen-charging for desired time, the chamber was tilted to slide the specimens to cooler zone, in order to minimize hydrogen pick up during cool down.

Vacuum Annealing

Selected hydrogen-charged specimens were vacuum annealed at 1200°F for 48 hrs. The specimens were wrapped in CP titanium foil to avoid oxidation. The pressure during vacuum annealing was 12 to 18 millitorr and the out gassing rate was 5 to 8 millitorr per minute at the annealing temperature.

Material Characterization

Specimens were characterized in as-HIP, HIP+ hydrogen-charged and after vacuum annealing. The chemical composition in the as-cast condition is given in reference 13. In the as-HIP state, the concentration of hydrogen was determined to be <25 ppm by wt. The specimens containing the maximum amount of hydrogen after hydrogen charging, 3500ppm and 5200ppm (conditions A2, A6 and A9 in reference 13) were selected for vacuum annealing at 1200°F for 48 hrs. Analysis of these specimens after vacuum annealing showed presence of < 50 ppm of hydrogen.

The microstructure and identity of the phases was studied by optical microscopy and x-ray diffraction, respectively. The specimens for optical microscopy were polished and etched with Kroll's reagent. Specimens for x-ray diffraction were prepared by mechanical polishing on 800 grit SiC paper with no acid etching in order to avoid the formation of etch-induced O phase [10]. To determine the significance of cold working induced by mechanical polishing, selected specimens were prepared by electropolishing without mechanical polishing. No significant differences in x-ray diffraction peaks were observed. The grain size of the material (1 mm) as compared to x-ray beam size (12.5mm) was fairly small and the diffraction peaks were recorded from an area representative of the material. The intensity of the peaks for transverse, longitudinal, and 45° sectioned material was reproducible to about ± 10% indicating some effect

of texture on the peak intensities. Determination of volume fraction of the phases was not attempted because of the overlap of the the diffraction peaks from different phases and variation in the peak intensity due to texture effect.

TEM foils were prepared primarily by electrolytic polishing. Some specimens were also prepared using an alternate method of core drilling and ion milling, to determine if there are any artifacts introduced by electrolytic polishing, but no significant differences were found. TEM was performed to reveal the morphology of the phases. Crystal structure and orientation relationships between the different phases were determined by selected area electron diffraction. Convergent beam electron diffraction was used to differentiate between the α_2 and O phases.

Results and Discussion

X-ray Diffraction

Figures 1a, 1b and 1c show x-ray diffraction spectra from as HIP (2150°F/40ksi/6hrs), HIP + hydrogen charged (3200ppm) and hydrogen-charged+vacuum annealed conditions, respectively.

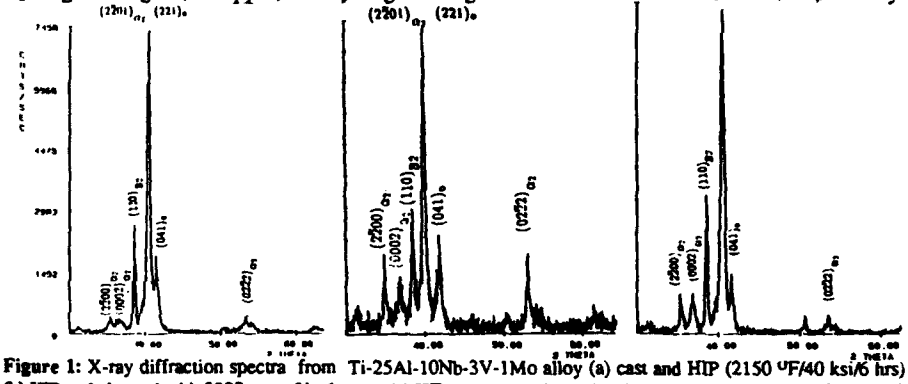


Figure 1: X-ray diffraction spectra from Ti-25Al-10Nb-3V-1Mo alloy (a) cast and HIP (2150 °F/40 ksi/6 hrs) (b) HIP and charged with 3200ppm of hydrogen, (c) HIP, hydrogen-charged and vacuum annealed at 1200°F for 48 hrs.

X-ray diffraction peaks corresponding to α_2 (Ti_3Al), B2 (Ti_2AlNb) and orthorhombic phases are present in all the specimens. The spectra do not show the presence of any additional phases. Comparison of the relative intensity of the $(110)_{B2}$ and $(112)_{B2}$, $(2\bar{2}01)_{\alpha_2}/(221)_{ortho.}$, and $(041)_{ortho.}$ in Figures 1a, 1b and 1c, indicates an increase in amount of B2 and orthorhombic phases in hydrogen-charged specimens as compared to as-HIP specimens. However, quantitative estimation of the increase was not attempted. The presence or absence of the most commonly observed hydride in titanium alloys, TiH_2 could not be established from the x-ray diffraction spectra. The three most intense peaks expected from TiH_2 phase are $(110)_{TiH_2}$, $(101)_{TiH_2}$ and $(211)_{TiH_2}$. Unfortunately these three peaks overlap with the $(2\bar{2}01)_{\alpha_2}$, $(2\bar{2}00)_{\alpha_2}$, and $(112)_{B2}$ x-ray diffraction peaks. Any extra peaks corresponding to any other hydrides of titanium or niobium are absent.

The x-ray diffraction spectra from the other hydrogen-charged specimens also showed same x-ray diffraction peaks with a maximum of +/- 10% differences in peak intensities. The reason for this difference could be due to a true difference in the volume fraction of the phases present in the material or due to some texture effect caused by orientation of the grains in the specimens.

X-ray diffraction spectrum from the vacuum annealed specimen (Figure 1c) shows a considerable drop in the relative intensities of the peaks corresponding to orthorhombic and B2 peaks, as compared to similar peaks in the spectrum from hydrogen-charged specimen (figure 1b). Which indicates a drop in the volume fraction of B2 and orthorhombic phases during vacuum annealing. However, the diffraction peak intensities from B2 and orthorhombic phases are higher in the vacuum annealed condition as compared to the spectrum from the as-HIP specimen, indicating presence of higher volume fraction of the above mentioned phases in the vacuum annealed state as compared to as HIP state. Same trend in the relative peak intensities in the spectra from other vacuum annealed specimens was also followed.

Optical microscopy

Low and high magnification optical micrograph of the alloy following charging with 3200 ppm hydrogen are presented in Figure 2a and 2b, respectively. The photomicrographs reveals that the microstructure is inhomogeneous. The microstructure displays Widmanstaten network of varying size. The microstructure displays light contrast regions marked as A, which at higher magnification reveals fine Widmanstaten network. The lighter regions are surrounded by areas of darker contrast marked B, consisting of coarser Widmanstaten network. Microstructure from the other hydrogen charged specimens in which, the hydrogen concentration of the alloy varied from 1250 to 3500ppm by weight, also revealed a similar morphology. The size of the light and dark contrast. The coarse α_2 laths in the as-HIP material are broken up to form shorter α_2 laths during hydrogen-charging treatment. The coarser α_2 laths marked A in Figure 2b are a result of coarsening at hydrogen-charging temperature. The reason of the inhomogeneity in the microstructure in the hydrogen-charged specimens is not understood. However, it may not be related to concentration of hydrogen in the material, since similar inhomogeneous microstructures were also observed following HIP + vacuum annealing treatment [11].

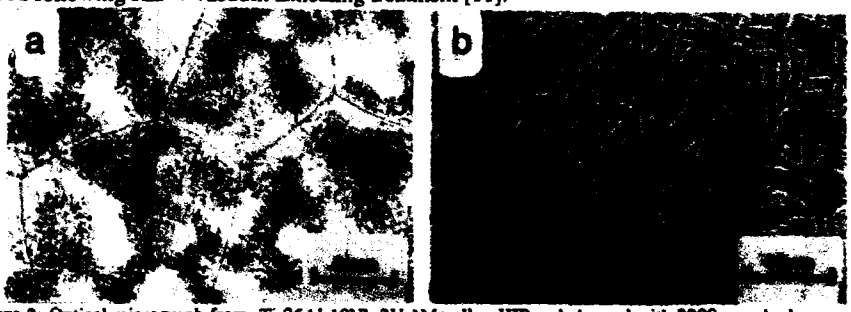


Figure 2: Optical micrograph from Ti-25Al-10Nb-3V-1Mo alloy HIP and charged with 3200 ppm hydrogen, (a) lower hagnification, (b) higher magnification.

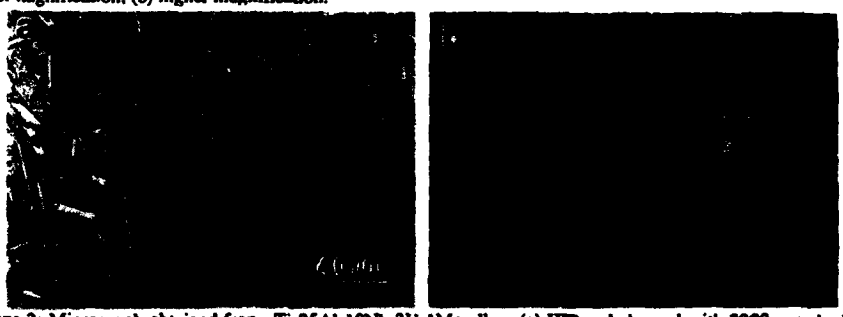


Figure 3: Micrograph obtained from Ti-25Al-10Nb-3V-1Mo alloy, (a) HIP and charged with 3200 ppm hydrogen followed by vacuum annealing at 1200°F for 48 hrs.(b) HIP and charged with 3500 ppm hydrogen followed by vacuum annealing at 1200°F for 48 hrs.

Photomicrograph from the material after charging with 3200 ppm hydrogen and vacuum annealing is presented in Figure 3a. Comparison of the two micrographs in Figure 2b and 3a show that there is no apparent change in the morphology or distribution of the phases during vacuum annealing. Photomicrographs from other vacuum annealed specimens for example conditions A6 (Figure 3b) also show microstructure similar to its respective hydrogen-charged conditions.

Transmission Electron Microscopy

Hydrogen-charged Material The local variation in the microstructure shown in the optical micrographs (Figure 2a) was also observed in TEM micrographs. Due to this inhomogeneity in the microstructure it was difficult to establish whether the variation in the TEM microstructure observed in different hydrogen-charged material is related to difference in hydrogen concentration or merely reflects the local variation, similar to the one observed in the optical micrographs. Few

examples of the microstructures observed after hydrogen-charging are presented here. Further details are available in an other paper presented at this conference [13].

Figure 4a shows a low magnification bright field image from a specimen hydrogen-charged using conditions A5 (Table-1). The micrograph shows a Widmanstaten type network similar to the one observed in the optical micrograph (Figure 2b). Higher magnification of the needles in the Widmanstaten network is shown in Figure 4b. The micrograph reveals a fine scale phase separation by formation of parallel plates, inside the needle. The microdiffraction from the fine plates (50nm) show either 2mm or a 6mm symmetry in the diffraction patterns obtained from $[0001]_{\alpha 2}$ // $[001_{orth.}$. Such phase separation was also observed in the as-HIP specimens and was shown to consistent with the formation of α_2 + O plates, parallel to the observation of other researchers [13]. In hydrogen charged material such phase separation was observed in almost all the needles of the Widmanstaten network, where as in the as-HIP material very few needles displayed such phase separation. The presence of hydrogen promotes α_2 to α_2 + O transformation. Which is consistent with a higher quantity of O phase being reflected in the x-ray diffraction spectra from the specimens charged with hydrogen.

An other important feature noticeable in Figure 4a, is the rim around most of the needles. Microdiffraction patterns from the rim-area are consistent with orthorhombic phase. Formation of orthorhombic phase at the boundaries of α_2 phase has been reported earlier in Ti-25Al-10Nb-3V-1Mo alloy hydrogen-charged by electro-chemical method [6].

Nearly half the needle in the widmanstaten network exhibited very fine plates (2nm) in-the α_2 and O phase. The diffraction pattern corresponding to such areas show streaking in directions perpendicular to $\{10\bar{1}0\}$ plane of the α_2 phase and equivalent direction in the O phase. Formation of fine planer precipitates (80nm) on $\{10\tilde{1}0\}$ planes have been reported earlier and were identified as hydride phase. [7]. However insufficient thickness of the precipitates observed in this study restrain positive identification of the precipitates at the present time.

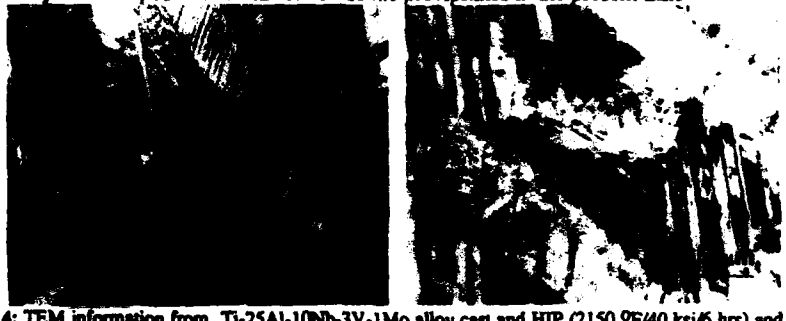


Figure 4: TEM information from Ti-25Al-10Nb-3V-1Mo alloy cast and HIP (2150 ^{o}F/40 ksi/6 hrs) and charged with hydrogen, (a) low magnification bright field image of the widmanstaten network (b) Higher magnification of needles in the widmanstaten network area.

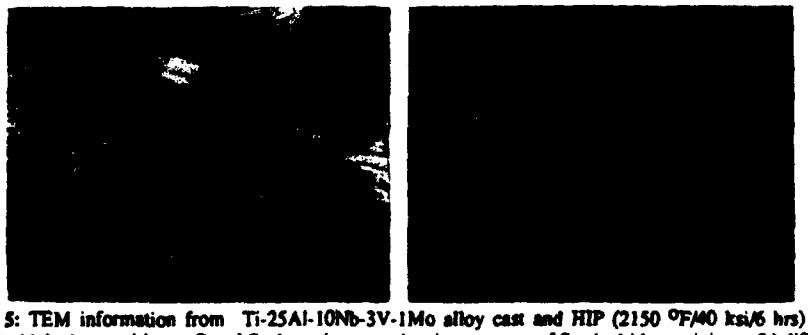


Figure 5: TEM information from Ti-25Al-10Nb-3V-1Mo alloy cast and HIP (2150 ^{o}F/40 ksi/6 hrs) and charged with hydrogen, (a) α_2 +O and O-phase rim areas showing presence of fine hydride precipitates (b) diffraction pattern corresponding to area A in Figure 5a after tilting to $[001]_{orth.}$.

The regions of B2 phase between the α_2 laths grown in cellular morphology were observed in the as HIP material. These regions were often connected with inter-granular retained B2 phases. The B2 phase usually contained high density of dislocations [14]. Precipitation of a second phase in the B2 matrix was not observed in the as HIP condition [14]. The images and diffraction pattern corresponding to the B2 phase in some of the areas in hydrogen-charged specimens show the presence of O phase. Figure 6(a) show a representative micrograph. The corresponding diffraction pattern after tilting the foil to [110] of B2 phase shows spots from [001] of O phases (Figure 6b). The presence of thin plates in the bright field image and streaking along [110] direction of O phase is consistent with presence of similar precipitates as the ones observed in (α_2 + O) and O-phase-rim regions (Figure 5).

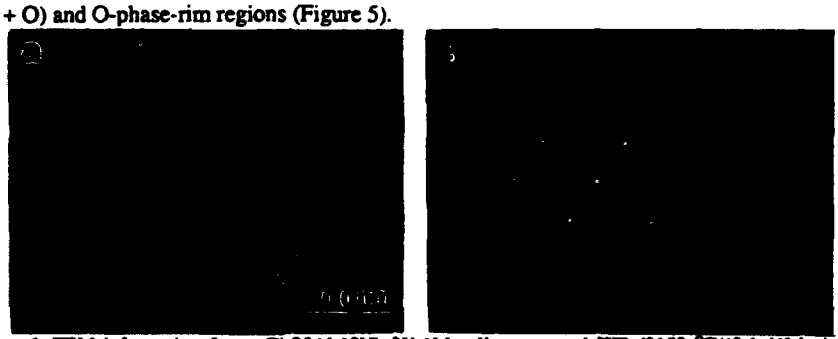


Figure 6: TEM information from Ti-25Al-10Nb-3V-1Mo alloy cast and HIP (2150 ^{o}F/40 ksi/6 hrs) and charged with 1250 ppm hydrogen, (a) B2 phase (dark contrast) showing the presence of O phase and fine planer hydride precipitates in B2 matrix, (b) diffraction pattern corresponding the area marked B in Figure 6(a).

Vacuum Annealed Material

A lower magnification TEM micrograph of the material after hydrogen charging and vacuum annealing is shown in Figure 7a. The microstructure confirms the microstructure observed in SEM micrograph (Figure 3b). The microstructure consists of larger size needles and fine transformed structure. Higher magnification image is shown in Figure 7b. The microstructure shows fine lamellar structure of α_2 and O phases. The orientation relationship between the α_2 phase and orthorhombic phase was consistent with:

$$(10\bar{1}0)_{\alpha_2} \parallel (110)_{orth.} \ , \ [0001]_{\alpha_2} \parallel [001]_{orth.}$$

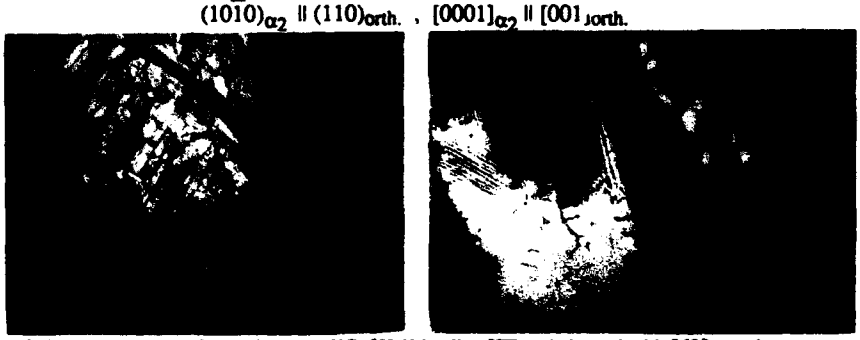


Figure 7: TEM micrographs from Ti-25Al-10Nb-3V-1Mo alloy HIP and charged with 3600 ppm hydrogen and vacuum annealed at 1200° F for 48 hours, (a) lower magnification, (b) higher magnification.

The above mentioned orientation relationship is consistent with the observations of others [12, 15], and has been observed previously in as-HIP and after hydrogen charging [13]. Such phase morphology was observed in at least half of the coarse needles observed by TEM. The transformation of $\alpha_2 \rightarrow \alpha_2$ + O in the needles was observed in fewer needles as compared to hydrogen-containing alloy, but much higher as compared to the as-HIP specimens. The α_2 needles did not contain the fine planar hydride precipitates observed in the hydrogen-charged

specimens. In addition to this phase separation most of the coarse needles contained a moderate quantity of faults shown in Figure 8a and 8b. The symmetric fringe contrast in bright field image (Figure 8a) and asymmetric fringe contrast in dark field image is consistent with stacking faults. Higher magnification image of fine transformed structure similar to the one shown in area marked B in Figure 7a, is presented in Figure 9a. The diffraction patterns from the different phases present in the fine transformed structure are shown in Figures 9b,9c and 9d. These diffraction patterns are consistent with O, B2 and α_2 phases respectively. The diffraction patterns from other directions (not shown here) confirm the above mentioned phase identification. The orientation between α_2 and B2 phases was observed to follow the relationship:

$$(0\bar{0}01)_{\alpha_2} \parallel (1\bar{1}0)_{B2} \ , \ [2\bar{1}\bar{1}0]_{\alpha_2} \parallel [111]_{B2}$$

The orientation relationship between the B2 and Orthorhombic phase followed the relationship:

$$(001)_{B2} \parallel (100)_{orth.} \ , \ [110]_{B2} \parallel [001]_{orth.}$$

The transformation of $\alpha_2 \rightarrow \alpha_2 + O$ in the needles as seen in the coarse needles (Figure 7b), and in hydrogen coontaining alloy, Figure 4b, was absent in the finer transformed α_2 needles.

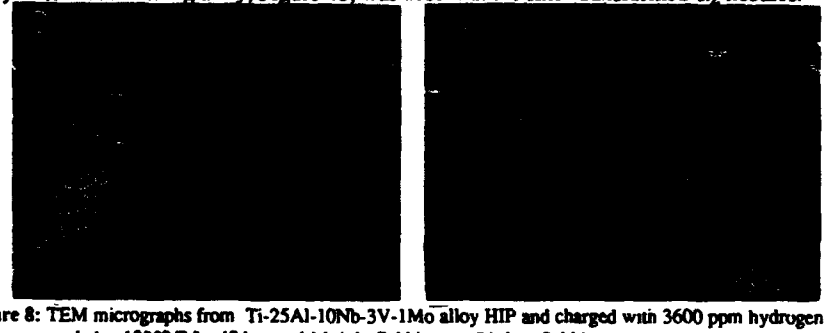


Figure 8: TEM micrographs from Ti-25Al-10Nb-3V-1Mo alloy HIP and charged with 3600 ppm hydrogen and vacuum annealed at 1200° F for 48 hours, (a) bright field image, (b) dark field image.

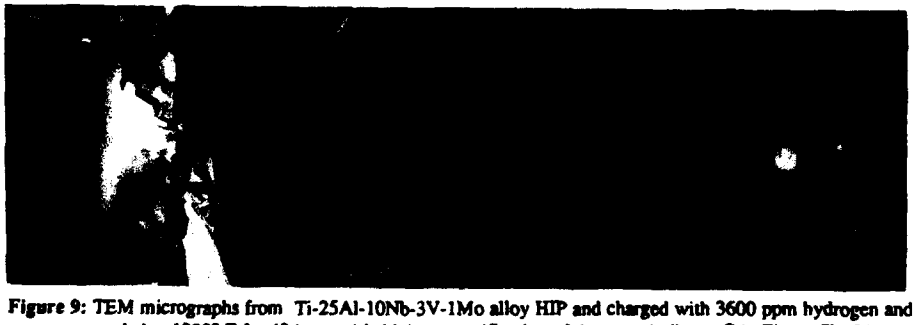


Figure 9: TEM micrographs from Ti-25Al-10Nb-3V-1Mo alloy HIP and charged with 3600 ppm hydrogen and vacuum annealed at 1200° F for 48 hours, (a) higher magnification of the area similar to C in Figure 7b, (b), and (c) are diffraction patterns from areas D and E, respectively in Figure 9a.

TEM micrograph from a region with B2 phase is shown in Figure 10. Such region before vacuum annealing contained precipitates of O phase and occasionally fine planar hydride precipitates. Following vacuum annealing of specimen containing 3200ppm hydrogen, the B2 phase contained moderate quantity of stacking faults (Figure 10a and 10b). The B2 phase did not contain any fine planar precipitate. Presence of O phase in B2 matrix as observed in the hydrogen-containing material was absent in the vacuum annealed alloy. The B2 phase contained high number of stacking faults probably left behind by dissociated hydride precipitates or O phase.

Conclusions

1. Introduction of hydrogen to the material increases the volume fraction of B2 and orthorhombic phases, and form very fine planer precipitate in all the phase present in the material.

Increase in the volume fraction of O phase is caused by precipitation of O phase in the matrix of B2 and promotion of α_2 to (α_2 + O) transformation in needles of Widmanstaten structure and formation of O-phase rim around the needles.

2. The concentration of hydrogen the Ti-25Al-10Nb-3V-1Mo-H alloy could be reduced from 3500 ppm to < 25 ppm by vacuum annealing at 1200°F for 48 hrs.

3. A drop in the volume fraction of the B2 and O phases is observed during vacuum annealing of the hydrogen-containing specimens. However, the volume fraction of these phases remains higher than the specimens before hydrogen-charging (as-HIP condition).



Figure 10: TEM micrographs from Ti-25Al-10Nb-3V-1Mo alloy cast and HIP (2150 °F/40 ksi/6 hrs) and charged with 3200 ppm hydrogen and vacuum annealed at 1200°F for 48 hrs., (a) Bright field image from B2 phase in ~[110], (b) Dark field image using $(110)_{B2}$ diffraction spot.

References

1. W. U. Yang Chu and A. W. Thompson, "Effect of Hydrogen as a Temporary β Stabilizer on Microstructure and Brittle Fracture Behavior in Titanium Aluminide Alloys", Met. Trans. A, Vol 22A, 1991, pp 71-81.
2. W.R. Kerr, "The Effect of Hydrogen as a Temporary Alloying Element on the Microstructure and Tensile Properties of Ti-6Al-4V, Met. Trans., Vol. 16A, 1985, pp 1077-1087.
3. B.A. Kolachev, et.al., "Evaluation of the Beneficial Effect of Hydrogen on Deformability of Titanium Alloy-ST4," Kuzechno-Shtampovochnoye Proizvodstvo, Nr.1, January 1975, pp. 79-82, USAF Foreign Technology Division Translation, FTD-ID (RS) I-2347-75.
4. U. Zwickev et.al., "Process for Improving Workability of Titanium Alloys," US Patent No. 2892,742, June 1959.
5. L. Steele, D. Eylon and F.H. Froes, "Microstructural Control of Titanium Aluminide Powder Compacts by Thermochemical Treatment," in Advances in Powder Metallurgy, Vol. 3, ed. by T.G. Gasbarre and W.F. Jandeska, MPFF/APMI, Princeton, NJ, 1989, pp. 509-529.
6. E. Manor and D. Eliezer, "Hydrogen Effects in Titanium Alloys Stabilized by Nb, V and Mo," Scripta Met. et Mater., Vol. 24, 1990, pp. 124-134.
7. N.S. Stoloff, "Hydrogen Embrittlement of Intermetallics," presented at NASP 2nd Workshop, Publication 1004, published by NASA Langley Research Center, November 1988, pp. 84-91.
8. "Hydrogen Interaction with Titanium: Summary," presented at NASP 2nd Workshop, Publication 1004, published by NASA Langley Research Center, November 1988.
9. F.H. Froes and D. Eylon, "Thermochemical Processing (TCP) of Titanium Alloys by Temporary Alloying with Hydrogen," in Hydrogen Effects on Materials Behavior, ed. by A.W. Thompson and N.R. Moody, TMS, Warrendale, PA, 1990, pp. 261-283.
10. K. Muraleedharan, S.V. Negender Naidu and D. Banerjee, "Orthorhombic Distortion of the α_2 Phase in Ti_3Al-Nb Alloys: Artifacts and Facts," Scripta Met Vol. 24, 1990, pp. 27-32.
11. Final Report, "Property Improvement of Titanium Aluminide Casting," EMTEC-CT-8/TR-90-8, 1991, pp. 156-162.
12. M.J. Kaufman, "Phase Relations in Ti_3Al-Nb system," AFWAL Technical Report 88-4113, July 1988.
13. M. Saqib, L. S. Apgar, D. Eylon and I. Weiss, "Effects of Hydrogen on the Microstructure and Phase Stability of α_2 Base Titanium Aluminide Castings", Proceedings of this Conference.
14. M. Saqib, L. S. Apgar, D. Eylon and I. Weiss, "Effects of HIP Processing on the Microstructure and Phase Relations in α_2 Base Titanium Aluminides", to be published in Mater. Science and Engineering, 1992.
15. D. Banerjee, A. K. Gogia, T. K. Nandi, and V. A. Joshi; "A New Orthorhombic Phase in a Ti_3Al-Nb alloy", Acta Metallurgica Vol. 36, No. 4, pp. 871-882, 1988.

IMPROVEMENT IN MECHANICAL PROPERTIES OF α+β TYPE TITANIUM ALLOYS BY MICROSTRUCTUAL CONTROL USING THERMOCHEMICAL PROCESSING

M. Niinomi*, B. Gong**, T. Kobayashi* and Y. Ohyabu***
*Department of Production Systems Engineering, Toyohashi University of Technology, Tempaku-cho, Toyohashi 441, Japan.
**Graduate School of Toyohashi University of Technology, Tempaku-cho, Toyohashi 441, Japan (Present : Department of Physics, Northeast University of Technology, Shenandoah 110006, China).
***Graduate School of Toyohashi University of Technology, Toyohashi 441, Japan.

Abstract

Hydrogen behavior and microstructual modification of Ti-6Al-4V alloys during Thermochemical Processing (TCP) were investigated. The newly proposed and conventional TCP were conducted in order to refine the microstructure of Ti-6Al-4V and Ti-5Al-2.5Fe alloys. Tensile properties and fracture toughness were measured on the TCP Ti-6Al-4V and Ti-5Al-2.5Fe materials. Newly proposed Below Transus Hydrogenation (BTH) TCP was found to be effective in achieving good balance of strength and elongation in Ti-6Al-4V and Ti-5Al-2.5Fe alloys. Fracture toughness of the TCP Ti-6Al-4V alloys were fairly low.

Introduction

Hydrogenation and dehydrogenation processes (TCP) has been reported to be highly effective in improving tensile and fatigue strength of titanium alloys with coarse microstructure because of microstructual refinement by TCP [1-3].

Various types of TCP have been reported up till now. For example, HVC (Hydrovac) [1], CST (Constitutional Solution Treatment) [4], βQ-HDH (Hydrogenation / Dehydrogenation of Beta Quenched Materials) [5], and HTH (High Temperature Hydrogenation) [6]. Strength of titanium alloys are considerably increased by these TCP while ductility is, in general, decreased. The decrease in ductility was attributed to β grain growth and the formation of continuous grain boundary α phases caused by heating the alloys into the β region during TCP.

Titanium '92
Science and Technology
Edited by F.H. Froes and I. Caplan
The Minerals, Metals & Materials Society, 1993

Therefore, the authors proposed a TCP where the alloys were always treated below the hydrogenated β transus temperature, that is, BTH (Below Transus Hydrogenation). The effect of BTH on the microstructual refinement of rolled Ti-6Al-4V alloys with microstructures of coarse equiaxed α and Widmanstätten α, respectively, and forged Ti-5Al-2.5Fe alloys [7] with microstructure of coarse elongated α were investigated. Ti-5Al-2.5Fe alloy is expected as implant material [7]. The hydrogenation of Ti-6Al-4V alloys with coarse equiaxed α and Widmanstätten structures were examined and the mechanism of microstructural refinement of the alloys mentioned above were studied. The tensile properties and fracture toughness of BTH treated Ti-6Al-4V and Ti-5Al-2.5Fe alloys were also investigated and compared with those of other TCP treated materials.

Experimental procedures

The materials used in this study were rolled plates of Ti-6Al-4V alloy with a thickness of 2.5×10^{-2} m and forged bars of Ti-5Al-2.5Fe alloy with a diameter of 6.0×10^{-2} m. The chemical compositions of these alloys are given in Table I. Specimens for tensile and fracture toughness tests were machined from these plates and bars. The longitudinal direction of the specimens was parallel to the rolling direction of the plates and parallel to

Table I Chemical Compositions of Ti-6Al-4V and Ti-5Al-2.5Fe Alloys Used in the Present Study (mass%).

Alloy	Al	V	Fe	C	N	O	H
Ti-6Al-4V	5.96	4.09	0.15	0.010	0.093	0.0034	0.005
Ti-5Al-2.5Fe	4.99	< 0.01	2.37	0.01	0.016	0.100	0.0023

the forging direction of the bars. The starting microstructures of Ti-6Al-4V alloy plates contain both coarse equiaxed α (the as received structure), and coarse Widmanstätten α which were obtained by β treatment of the as - received material. The starting microstructure of the Ti-5Al-2.5Fe bars consisted of elongated α grains which was the as-forged structure.

The test specimens were subjected to various TCP treatments which are schematically shown in Figure 1. TCP 4 and 5 (BTH) are the newly proposed TCP in the present study. Hydrogenation temperatures for TCP 4 and 5 are 1053K and 1023K, respectively. TCP 1, TCP 2 and TCP 3 treatments [1] [5] [6] were also carried out for comparison with TCP 4 and TCP 5 treatments.

Hydrogenation was done in a stream of hydrogen gas at one atmosphere (0.1MPa) except for TCP 1 treatment. Hydrogen source of hydrogenation in TCP 1 was Ti hydrides put in the

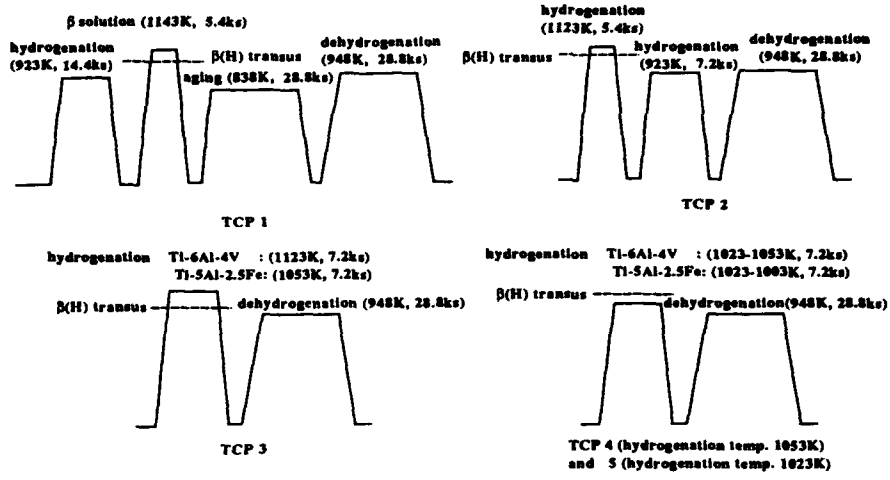


Figure - 1 Schematic drawings of conventional TCP ; TCP 1 , 2 and newly proposed TCP ; TCP 4 and 5.

furnace. Dehydrogenation was performed in a vacuum furnace at a temperature of 948 K for 28.8 ks. The hydrogen content after hydrogenation was at round 1 mass%. The hydrogen content after TCP was less than 0.0020 mass%.

Specimens following TCP treatment were machined into tensile samples with a gage size of (ϕ 4 x 20) x 10^{-2} m and static fracture toughness specimens with a size of (10 x 10 x 55) x 10^{-2} m. Static fracture toughness specimens were precracked to obtain ao / W (ao: initial crack length and W : specimen width) of about 0.6, according to ASTM E399. Tensile tests were carried out at a cross head speed of 8.3 x 10^{-6} m / sec using an Instron machine. Static fracture toughness tests were carried out using DC electrical potential method. Small samples with a reduced size of (ϕ1.2 x 10) x 10^{-2} m were also used to investigated the hydrogenation process and the microstructual changes occuring during the TCP treatment. Microstructures were characterized using a light microscope and TEM. The phase compositions of the hydrogenated samples were identified by X-ray and TEM diffraction analysis.

Experimental results and discussion

Hydrogenation of Ti-6Al-4V alloys

Relationships between hydrogen content and hydrogenation time at various hydrogen flow rates at 923K, in Ti-6Al-4V alloys having coarse Widmanstätten α structure (transformed β) are shown in Figure 2. Hydrogen content was found to saturate over a certain hydrogenation temperature in every flow rate. The time needed for reaching hydrogen saturation content was

increased with increasing hydrogen flow rate. Small difference in the time between flow rate of 12.3 ml / sec and over 12.3 ml / sec was detected. Same results were observed in Ti-6Al-4V alloy with coarse equiaxed α structure.

Microcracking occurred in samples treated at the hydrogen flow rate of over 12.3 ml / sec when the starting microstructure was coarse Widmanstätten α. However, microcracking never occurred in the samples with starting microstructure of coarse equiaxed α.

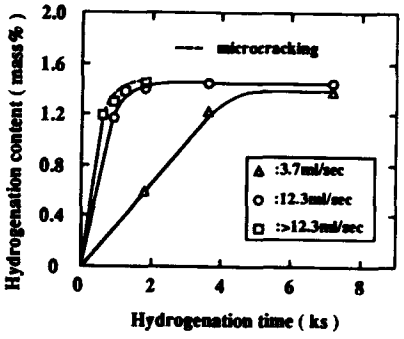


Figure - 2 Hydrogenation of β transformed Ti-6Al-4V alloy hydrogenated at 923K at hydrogen flow rates of 3.7ml/sec , 12.3ml/sec and >12.3ml/sec

Microstructure of as-received and TCP treated Ti-6Al-4V

Microstructures of various TCP treated Ti-6Al-4V alloy with starting microstructure of equiaxed α are shown in Figure 3. Considerable microstructual refinement is obtained in every TCP treatment when compared to that of the as-received structure. Continuous grain boundary α phase can be seen in TCP 1, 2 and 3 treated specimens although considerably finer α+β microstructure is produced. The grain boundary α phase is eliminated

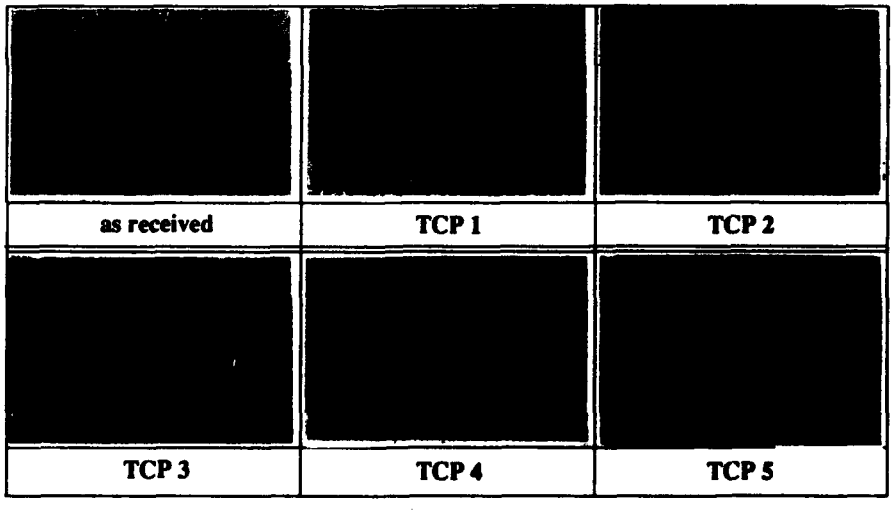


Figure - 3 Microstructures of as received and various TCP treated Ti-6Al-4V alloys.

in the microstructures of the BTH (TCP 4 and 5) treated specimens. Coarse Widmanstätten α structure was also considerably refined by every TCP applied. Prior β grain size of specimens with coarse Widmanstätten α structure was found to increase following TCP 1, 2 and 3 treatments.

TEM and X-ray analysis

The identified phases and lattice parameters of the as-hydrogenated Ti-6Al-4V alloy having equiaxed α structure, using X-ray and TEM diffraction pattern analysis are shown in Table II. Primary α, hydrogenated β phase ; β (H), and δ hydride with fcc structure are identified in the alloy hydrogenated at 923K. The martensite phase ; α"(H) with orthorhombic structure was identified in alloys hydrogenated at 1023K and 1123K which are the temperaturs below and above the β(H) transus temperature, respectively. The mechanism of microstructural refinement obtained in samples following TCP 3, 4 and 5 treatments are related to the following reaction occuring during the hydrogenation and dehydrogenation steps ;

Table II Phase Compositions and Lattice Parameters of As Received and Hydrogenated Ti-6Al-4V Alloys.

Alloy condition		Phase and lattic parameter		
As - received		α	β	
		a=0.2942 b=0.4690 c/a=1.594	a=0.3236	
Hydrogenated at	923K	α a=0.2950 b=0.4708 c/a=1.596	β(H) a=0.3331	δ a=0.4414
	1023K	β(H)	α"(H) a= 0.2964 b=0.5040 c=0.4744	α
	1123K	α"(H)	β(H)	

δ is the hydride with fcc structure.
α"(H) is the martensite with orthorhombic structure.

during hydrogenation

TCP 3 (HTH) $\alpha + \beta \longrightarrow \alpha''(H) + \beta(H)$ (1)

TCP 4 and 5 (BTH) $\alpha \longrightarrow \alpha_{fine}$ (2)

$\beta(H) \longrightarrow \alpha''_{fine}$ (3)

Refinement of the primary α phase and the formation of fine α" during cooling from hydrogenation temperature to room temperature were ovserved by TEM of the as - hydrogenated alloys following TCP 4 and 5 treatment, and are indicated below.

during dehydrogenation

TCP 3 (HTH) $\alpha'' \longrightarrow (\alpha + \beta)_{fine}$ (4)

$\beta(H) \longrightarrow (\alpha + \beta)_{fine}$ (5)

TCP 4 and 5 (BTH) $\beta(H) \longrightarrow (\alpha + \beta)_{fine}$ (6)

α and α'' $\longrightarrow$ α_{fine} (7)

Mechanical properties of TCP Ti-6Al-4V and Ti-5Al-2.5Fe all

Yield strength and elongation of various TCP treated Ti-6Al-4V alloy with starting microstructures of coarse equiaxed α and Widmanstätten α, respectively are shown in Figure 4. The values of the as-received and transformed β, materials with microstructures of coarse equiaxed α and Widmanstätten α, respectively are also shown in Figure 4.

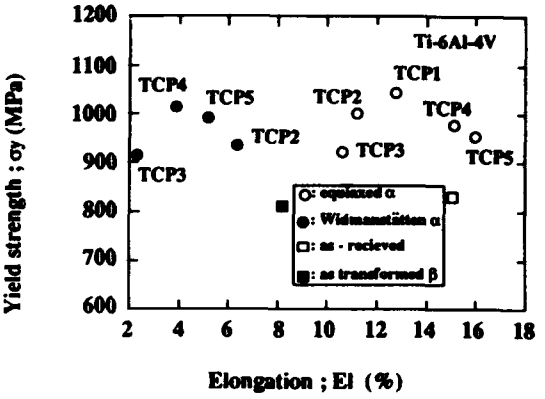


Figure - 4 Tensile properties of various TCP treated Ti-6Al-4V alloys.

The yield strength of TCP treated Ti-6Al-4V alloy with equiaxed α starting microstructure is higher than that of the as-received material, while the elongation of TCP 4 and 5 treated material is greater, and those of TCP 1, 2 and 3 treated alloy are smaller than that of the as-received material. TCP 4 and 5 treated alloy exhibit good balance of strength and elongation.

The yield strength of TCP treated Ti-6Al-4V alloy with Widmanstätten α starting microstructure is greater than that of material with transformed β structure while

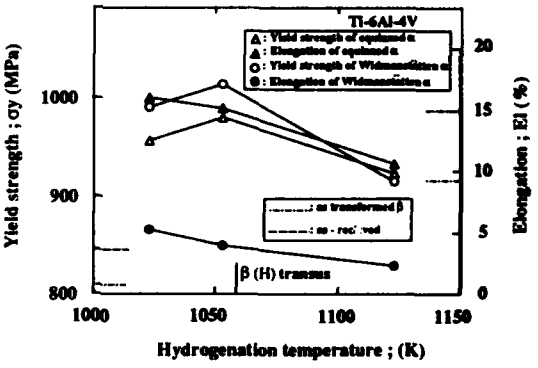


Figure - 5 Effect of hydrogenation temperature during TCP on yield strength and elongation of TCP treated Ti- 6Al-4V alloys.

the elongation are smaller than for material with as transformed β structure. However, TCP 4 and 5 treated alloys exhibited much greater strength and relatively greater elongation. The yield strength and elongation of TCP treated Ti-6Al-4V alloys with starting microstructures of equiaxed α and Widmanstätten α, respectively are shown in Figure 5 for different hydrogenation temperatures. Both elongation and yield strength are smaller when the alloys are hydrogenated in the β (H) region, 1123K.

The effect of hydrogenation temperature on yield strength and elongation of TCP treated Ti-5Al-2.5Fe alloy are shown in Figure 6. A trend similar to that of Ti-6Al-4V alloys can be observed for Ti-5Al-2.5Fe alloy. Microstructual refinement of Ti-5Al-2.5Fe alloys was also found to be possible by TCP treatment. Considering that greater yield strength has been achieved by the hydrogenation at the temperature just below the β (H) transus temperature and elongation has been smaller by the hydrogenation in the β (H) region in both Ti-6Al-4V and Ti-5Al-2.5Fe alloys, the newly proposed TCP, BTH was found to be an effective process for achieving good balance of strength and elongation.

Fracture toughness of TCP treated Ti-6Al-4V alloy

Yield strength, σy, and fracture toughness, Jic, of various TCP treated Ti-6Al-4V alloy with equiaxed α and Widmanstätten α starting microstructures, respectively are shown in Figure 7. Jic of TCP treated alloy is smaller than that of alloys with as-received microstructure. However, a decrease in Jic of alloys with Widmanstätten α starting microstructure by TCP is more pronounced when compared with alloy with equiaxed α starting microstructure .

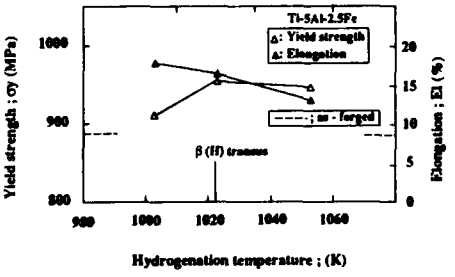


Figure -6 Effect of hydrogenation temperature during TCP on yield strength and elongation of TCP treated Ti-5Al-2.5Fe alloys.

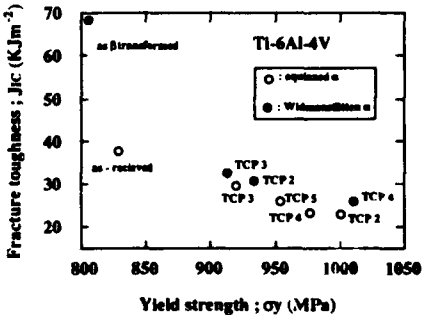


Figure - 7 Relationship between fracture toughness , Jic, and yield strength of various TCP treated Ti-6Al-4V alloys.

Conclusions

Hydrogen behavior and microstructual changes during TCP treatment were investigated in Ti-6Al-4V alloy. The newly proposed and conventional TCP treatment were conducted for

refining the microstructure of Ti-6Al-4V and Ti-5Al-2.5Fe alloys. Tensile and fracture toughness tests were carried out on the TCP treated alloys. The following results were obtained.

(1) Hydrogen absorption of Ti-6Al-4V alloy in a stream of hydrogen gas at a pressure of one atmosphere (0.1MPa) is influenced by hydrogenation temperature, time and flow rate.

(2) Ti-6Al-4V alloy with Widmanstätten α starting microstructure is sensitive to microcracking during hydrogenation comparing with that with coarse equiaxed α starting microstructure when the hydrogen flow rate is over 12.3 ml / sec.

(3) The phase compositions of as-hydrogenated Ti-6Al-4V alloy were well identified using X-ray and TEM techniques.

(4) The newly proposed TCP where the alloy is hydrogenated below the hydrogenated β transus temperature, air cooled to room temperature and dehydrogenated at lower temperature, BTH, is effective for refining the microstructures of Ti-6Al-4V and Ti-5Al-2.5Fe alloys. Good balance of yield strength and elongation is achieved by BTH.

(5) Fracture toughness value of TCP Ti-6Al-4V alloy is fairly small compared with that of the alloy without TCP.

References

[1] W. R. Kerr : " The Effect of Hydrogen as a Temparay Alloying Element on Microstructure and Tensile Properties of Ti-6Al-4V ", Metall. Trans. A, 16A (6) (1985), 1077-1087.

[2] F. H. Froes, D. Eylon and C. Suryanarayana: " Thermochemical Processing of Titanium Alloys ", JOM, 42 (3) (1990), 26-29.

[3] D. H. Kohn and P. Ducheyvè: "Microstructual Refinement of β - sintered and Ti-6Al-4V Porous-coated by Temporary Alloying with Hydrogen ", J. Materials Science, 26 (1991), 534-544.

[4] J. Stinson, R. G. Vogt and D. Eylon and F. H. Froes: " Improvement of HCF Properties in Ti-6Al-4V Castings via Thermochemical Treatment ", High Integrity Castings , ed. C. V. White, D. Eylon and F. H. Froes, (ASM INT, 1988), 3-8.

[5] L. Levin, R. G. Vogt, D. Eylon and F. H. Froes: " Fatigue Resistance Improvement of Ti-6Al-4V by Thermochemical Treatment ", Proc. of 5th Int. Conf. on Titanium, (1988), 2107-2114 .

[6] D. Eylon, C.F.Yolten and F. H. Froes: " Property Enhancement of Titanium Alloys by Microstructure Modification ", Proc. of 6th world Conf. on Titanium, (1984), 1523-1528.

[7] M. Merget and F. Aldinger: "Influence of Technological Parameters on the Fatigue Strength of Ti5Al2.5Fe - A New Material for Endoprostheses" Proc. 5th Int. Conf. of Titanium, (1984), 1393 - 1400.

THE EFFECT OF HYDROGEN ALLOYING ON WORKABILITY OF TITANIUM ALLOYS

Boris Alexandrovitch Kolatchev,
Professor, Moscow Aviation Manufacture Institute, Stoopino City, Pobeda Avenue, 14-64, Moscow Region, USSR;
Alexander Vassilyevitch Malkov,
Professor, Moscow Aviation Manufacture Institute, Stoopino City, Pervomayskaya St., 53-37, 142800, Moscow Region, USSR;
Igor Andreyevitch Vorobyov,
Chief Designer of the Normal Production Association, Kovalyhynskaya St., 77-59, 603155, Nizhny Novgorod, USSR;
Vyatcheslav Anatolyevitch Volodin,
President and Director General, Normal Production Association, Dzerzhinskogo St., 24G-19, 603005, Nizhny Novgorod, USSR;
Anatoly Vassilyevitch Mitin,
President and Director of the USSR State Research Institute for Standardization, Moscow Region, USSR

Abstract

This investigation is concerned with ductility improvement of Titanium alloys by introduction of hydrogen. The effect of hydrogen in lowering the β-transus temperature, the phase proportions and hydrogen assisted deformation mechanism are con-

Titanium '92
Science and Technology
Edited by F.H. Froes and I. Caplan
The Minerals, Metals & Materials Society, 1993

sidered. The mechanical properties of dehydrogenated materials were found to be compatible with the properties of the original material.

Introduction

Hydrogen induced ductility was accidentally discovered in West Germany by Zwiecker and Schleicher in 1950's. At that time, American and Soviet investigators were concerned with hydrogen embrittlement of rods in contrast to German scientists who actually introduced hydrogen into ingots prior to primary processing to improve workability. The method of enhancing the workability of titanium alloys as suggested by Zwiecker and Schleicher was patented in the USA in 1959 [1]. In 1970, V.K. Nosov started his work at the Moscow Aviation Manufacture Institute on the impact of hydrogen on the manufacturability of titanium alloys. The initial results described the favourable effect of hydrogen on ductility improvement in titanium alloys containing large amounts of Aluminum and were published in 1972 [2]. In subsequent works [3-5], the term "hydrogen plasticization" was introduced to denote this effect. The present investigation is concerned with microstructural modification and associated changes in mechanical properties of titanium alloys treated with hydrogen.

Results and discussion

Yiels strength of Ti-3Al-4.5Mo-4.5V (BT16 alloy) (upsetting cylindrical specimens 16 mm diameter, 20 mm length) with different hydrogen contents is given in Figure 1. At temperatures between 200 to 800 °C the yield strength decreases with increasing hydrogen content.

Similar reduction of yield stress of material with hydro-

gen at hot forming temperatures was observed for all titanium alloys [6]. This was observed in tensile and upsetting tests. The hydrogen plasticization effect was found to be most pronounced in the case of titanium alloys containing an α_2 phase.

The effect of hydrogen on the strain to initiate cracks, ε_{kp}, for Ti-3Al-4.5Mo-4.5V different temperatures is shown in Figure 2, and reveals the beneficial effect of hydrogen on ductility. The plasticity, ε_{kp}, increases with hydrogen content for test carried out at temperatures between 500-600 °C. High plastic strains are observed for material with hydrogen concentrations of 0.1 and 0.5% at room temperature while lower strains are observed for hydrogen levels of 0.005 and 0.3 to 0.4%. The lowest ε_{cr} was observed at 400 °C because of instability of β-phase.

The decrease in flow stress of hydrogenated material is most significant at temperatures at which the structure shows the same amounts of α and β phases. Figure 3 shows that the temperature at which maximum ductility is observed is shifted to lower temperatures with increasing hydrogen for BT3-1 alloy - Ti-Al 5.5-7.0%, Mo 2.0 - 3.0%, Cr 0.8 - 2.3%, Si 0.15 - 0.40%, Fe - 0.2 - 0.7%. The strain rate sensitivity index, m, defined by the equation: $\sigma = K\dot{\varepsilon}^m$ (where σ is stress, K is constant, $\dot{\varepsilon}$ is strain rate), is larger than 0.3 for material with hydrogen [7,8]. It is also worthwhile to note that when testing hydrogenated material at temperatures in the β-phase range, the yield stress was found to increase with hydrogen content. This effect can be viewed as a solution hardening of β alloys due to hydrogen.

Hydrogen plasticization at low temperatures increases the strain to initiate cracks without a significant decrease in

flow stress. Low temperature hydrogen plasticisation was observed for the first time in 1970 for β titanium alloys Ti - Al 2.3 - 3.6%, Mo 6.8 - 8.0%, Cr 9.5 - 11.5% (BT 15) and Ti - Mo 11%, Zr 5.5%, Sn 4.5% (β-III), as shown in Figure 4. Material with hydrogen content of about 0.003% shows upset strain to initiate the first crack of about 60%. However, specimens with hydrogen contents above 0.1% were flattened to a thin pancake with sharp edges with no traces of cracks on the surface. No distinguishable decrease of yield stress was observed.

The improvement of hot ductility of titanium by hydrogen was rationalized in terms of superplasticity behaviour [7]. For hydrogenated material the superplasticity temperature was lowered by 100 to 150 °C. The hydrogen plasticization can be observed at strain rates which are about 1 to 2 orders of magnitude higher than those of unhydrogenated material.

According to V.K.Nosov [6,8], high temperature hydrogen plasticization is maximized at temperature range where the α and β phases contribute to the total deformation in the same way. The hydrogen reduces this temperature range to lower values, thus effecting the evolution of the dynamic hardening and softening processes during hot formation.

Low temperature hydrogen plasticization can be attributed to the increase in the quantity of the β phase, to the reduced resistance to glide and multiplication of dislocations and formation of additional dislocation glide and twinning systems.

Depletion of the beta phase with respect to beta stabilizer elements due to addition of hydrogen to α and β alloys was experimentally discovered by A.A.Ilyin et al. [11]. The reduction in the amount of β phase stabilizing element in two phase $\alpha + \beta$ titanium alloys, when hydrogen is introduced, follows

immediately from the analysis of isothermal cross sections of the ternaries, Titanium - beta stabilizer - hydrogen, taking into account the observation of increasing the β phase quantity in this type of alloys by hydrogen [3].

The second cause for low temperature hydrogen plasticization, i.e. increased dislocation mobility when hydrogen is introduced was shown experimentally [12,13], for some titanium alloys including Ti - 6Al - 4V. When loaded directly in an electron microscope, it was observed that hydrogen introduced into the system gives rise to sharp increase in dislocation mobility under constant stress [13]. Further, a significant increase in dislocation density was observed. Suggestion that additional gliding and twinning occurred due to hydrogen needs to be confirmed experimentally.

The following illustrates the application of hydrogen plasticization for the production of titanium alloy bolts. Ti - Al 1.6 - 3.0%, Mo 4.5 - 5.5%, V 4.0 - 5.0% BT 16 alloy bolts with diameter up to 12 mm are produced by cold heading. When manufacturing bolts with smaller diameter, one has to adhere strictly to the microstructure and rod surface finish requirements to avoid rejections, whereas 12 mm diameter bolts and those with larger diameters are manufactured by hot heading.

The above observations indicate that reversible alloying of BT 16 alloy with hydrogen allows temperature reduction of the hot heading process from the current 800 to 850 °C to 700 - 750 °C by addition of a 0.3% hydrogen as shown in Figure 1. Besides, at large hydrogen concentrations, coarse grains are formed which affect mechanical properties. The above recommendations are based on experimental data. BT 16 bolts, with 16 mm diameter rods with 0.3% hydrogen, were processed at 750,

700 and 600 °C which are about 100 to 200 °C less than those used in industry. Under all heading temperatures, the bolt head was fully formed with no observable defects.

The headed bolts were heat treated for two hours at 810 °C, followed by water quenching and the final heat treatment consisted of a 12 hour vacuum ageing at 570 to 590 °C. Vacuum ageing not only resulted in increased strength due to the decomposition of the beta and formation of the alpha phase, but also reduction in the hydrogen to level of 0.003 to 0.004%.

Using the low temperature hydrogen plasticization effect, bolts upto 16 mm dia. were manufactured from the BT 16 alloy by means of cold heading. After hardening and vacuum ageing, the mechanical properties of the cold headed bolts were as required.

Conclusions

1. Hydrogen enhanced ductility was found to occur in two different temperature ranges of 20-100 and above 400 °C.

2. A microstructure consists of equal amounts of α and β phases and appears to be ideal for high temperature hydrogen plasticization. Under these conditions, considerable reduction in flow stress is also observed.

3. Hydrogen induced enhancements in strain to crack initiation were also observed at room temperature, but without any significant change in flow stress.

4. High temperature hydrogen plasticization can be employed in order to improve the hot working of titanium alloy while the low temperature plasticization can replace hot forming with cold forming.

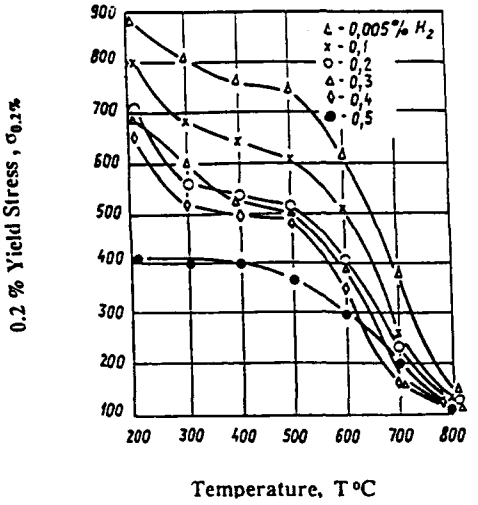


Fig. 1. Effect of Temperature on the Yield Strength σ_{02}, of BT16 Alloy as determined by upsetting of cylindrical specimens with different hydrogen contents

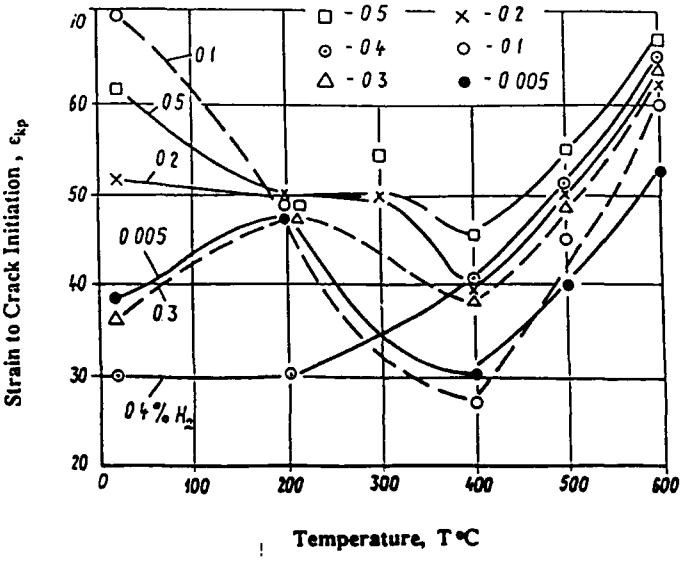


Fig. 2. Effect of Temperature on the strain to crack formation determined by upsetting cylindrical specimens of BT16 alloy with different hydrogen content.

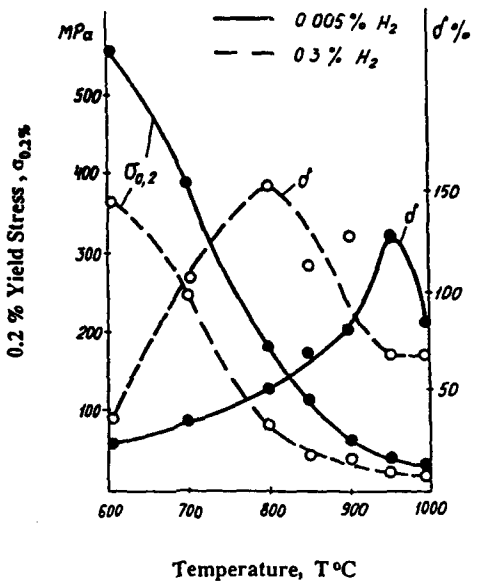


Fig. 3. The effect of temperature on tensile yield stress and elongation, d, of BT3-1 alloy with the strain rate $\varepsilon = 1.4 \times 10^{-3}\ s^{-1}$ [6]. - 0.005% H_2

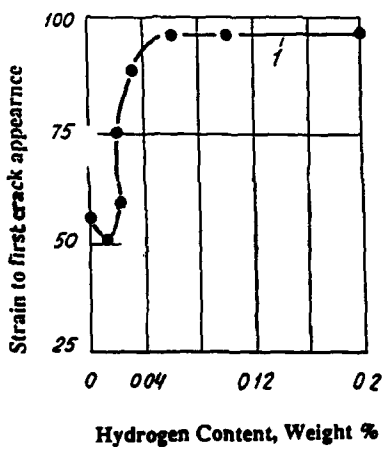


Fig. 4.The effect of hydrogen on strain to first appearance of crack when heading β III alloy at room temperature .

References

1. U.Zwiecker and V.Schleicher "A Way to Increase the Deformability of Titanium Alloys subject to Hot Working" (USA patent No. 2892742, cl. 148-11,5,1959).

2. B.A.Kolatchev et al. "Hydrogen Impact on Technological Plasticity of Titanium Alloys", Izv. vusov. Tsvetn. Met., 4, 1(972), 137-142.

3. B.A.Kolatchev, V.A.Livanov and A.A.Bukhanova, "Mechanical Properties of Titanium and its Alloys", Metallurgia, M,(1974), 554.

4. B.A.Kolatchev, V.A.Livanov and V.K.Nosov "Hydrogen Impact on Deformability of Titanium Alloys with Different Phase Composition", (paper presented at Titan. Metallovedenie i tekhnologia, Tr. 3 Mezhd. Konf. po titanu. M. VILS., 1978), 61-68.

5. B.A.Kolatchev and V.K.Nosov "Hydrogen Plasticization in Hot Deforming of Titanium Alloys", (paper presented at Titanium Science and Technology, Proceed. 5th Intl. Conf. Munich, Oberussel, 1985) (1), 625-632.

6. V.K.Nosov and B.A.Kolatchev "Hydrogen Plasticization Under Hot Deforming of Titanium Alloys", M. Metallurgia, (1976),117.

7. B.A.Kolatchev and V.K.Nosov "Hydrogen Plasticization of Titanium Alloys Under Hot Deformation", Izv. vusuv. Tsvetn. Metallurgia., 5, (1983) 92-96.

8. B.A.Kolatchev and V.K.Nosov "Hydrogen Plasticization and Superplasticity of Titanium Alloys", Fizika metallov i metallovedenie. (57), 2, (1984) 288-297.

11. A.A.Ilyin et al. "Effect of Hydrogen on Alloying Element Distribution Between Alpha and Beta Phases in VT23 Titanium Alloy", FKHMM., 1, (1987) 112-114.

12. B.A.Kolatchev "Hydrogen Embrittlement in Metals", M. Metallurgia, (1985) 217.

13. D.S.Shih, J.M.Robertson and H.K.Birnbaum "Hydrogen Embrittlement of Titanium", Acta. Metall., (36) 1, (1988).

STUDY ON EFFECTS OF HVC TREATMENTS ON IMPROVEMENT OF SUPERPLASTIC BEHAVIOR OF Ti−10V−2Fe−3Al

Du Zhongquan, Wang Gaochao, Chen Yuxiu, Wei Chunlei
Nanchang Institute of Aeronautical Technology,
Nanchang, Jiangxi, 330034, China
Zhang Zhifang
Research Institute of Aeronautical Materials,
Beijing, 100095, China

Abstract

In this paper, an attempt has been made to investigate the effects of hydrovac (HVC) treatment on the superplastic behavior of Ti−10V−2Fe−3Al alloy (Ti−10−2−3). In order to find out the optimal rigimes for HVC treatments to refine the microstructure of Ti−10−2−3, three test regimes have been chosen and an orthogonal test layout has been determined.

The results have shown that after HVC treatments, the microstructure of Ti−10−2−3 bars have been significantly refined, which lead to a large increase in elongation. The optimal strain rate at 750℃ is faster on an order of magnitude than that from the available data source.

Introduction

Titanium and titanium alloys always exhibit strong affinity to hydrogen. For example, it is possible to dissolve hydrogen in pure titanium as much as 60 at % (3 wt %) at 600℃. Most of the hydrogen can be removed in vacuum.

In order to avoid the embrittlement caused by the remaining hydrogen, the hydrogen content in titanium and titanium alloys should generally be restricted to 100～150ppm. [3,4]

Hydrogen can be used as a temporary alloying element in titanium and titanium alloys. Hydrogen decreases the β transus temperature in titanium and its alloys, which is helpful in stabilizing the b. c. c. structure, making it easy to hot−work the material. In the process of annealing treatment the β −phase dissolves and new phases form, which can significantly refine the microstructure of titanium alloys and improve their superplastic deformation.

Ti−10−2−3 is one of the newly developed Ti−base structural alloys, characterized by high−strength, high−toughness and deep−hardenability, and it is an ideal substitute for 30CrMnSiA−as high−strength steel for aero−space use. The aim of this paper is to investigate the effects of HVC treatments on structure refinement of Ti−10−2−3, and subsequently the improvement of superplastic behavior.

Titanium '92
Science and Technology
Edited by F.H. Froes and I. Caplan
The Minerals, Metals & Materials Society, 1993

Material and Experimental Procedures

Material

Ti－10－2－3 rolled bars used in these experiments were provided by the Shanghai Iron & Steel Research Institute. Table 1 shows the chemical composition. These bars were cogged at 850℃, rolled from ϕ 43mm to ϕ 25mm and then from ϕ 25mm to ϕ 12mm at a final rolling temperature 800～830℃. The material prepared is "β－rolled"because the final rolling temperature just above the β－transus temperature. The original microstructure of the "β－rolled"material is composed of coarse equiaxed grains with an average size of about 18μm.

Table 1 Chemical Composition of "β－rolled"

alloying element	V	Fe	Al	Si	C	N	H	O	Ti
Content (wt %)	9.46	1.98	3.08	0.02	0.03	0.019	0.0023	0.085	bal.

Specimen geometry

The specimen geometry is shown in Figure 1. It is designed in order to compare the results obtained with those available in the reference [1].

Experimental procedures

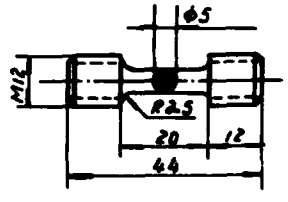


Figure 1－Sketch of a Tensile Specimen

Hydrogenation was performed in an open－hearth type hydrogen treatment furnace, in which the hydrogen level was controlled by regulating the temperatures and the holding time.

Solution treatment and annealing were carried out in a heat treatment furnace. Two dehydrogenation processes were used; dehydrogenation in a furnace full of argon (for short "argon－dehydrogenation") and dehydrogenation in vacuum (for short "vacuum－dehydrogenation").

The vacuum－dehydrogenation process was carried out in a specially designed apparatus, at a vacuum of 9×10^{-3} Torr at 600℃.

The hydrogen concentration was measured using a MHS－806 type hydrogen analyzer.

Tensile experiments were carried out on the vacuum dehydrogenated material using a tensile test machine, equipped with a split－type high－temperature furnace, where the temperature fluctuation ranges within +5～－5℃. An X－－－Y recorder was

used to record the forces and displacements. This machine was also fitted with a patented device to meet the requirements of constant strain rate tensile test.

HVC conditions

Three HVC conditions were selected as shown in Table 2.

Table 2 HVC Conditions

Operation	1	2	3
hydrogenation	750℃×4h	700℃×4h	700℃×2h
solid solution treatment	700℃×1h		
annealing	600℃×8h		
argon—dehydrogenation	600℃×16h		
vacuum—dehydrogenation	600℃×10h		

Results

Results of HVC treatments

Table 3 shows the changes of hydrogen contents and grain sizes in Ti—10—2—3 specimens before and after the three HVC treatments.

Table 3 Changes of hydrogen contents and grain sizes before and after the HVC treatments

Regime		1	2	3
hydrogen content (ppm)	before hydrogenation	23	23	23
	after hydrogenation	2489	2783	2651
	argon—dehydrogenated	1475	1640	1580
	vacuum—dehydrogenated	282	344	312
grain size (μm)	before hydrogenation	18	18	18
	vauum—dehydrogenated	4	1	2

Microstructural changes during the HVC treatment

Figure 2 shows the microstructural changes occurring during the HVC treatment #1 (Table 2). The changes in the micro—structures are somewhat similar to those deserved following treatments #2 and #3.

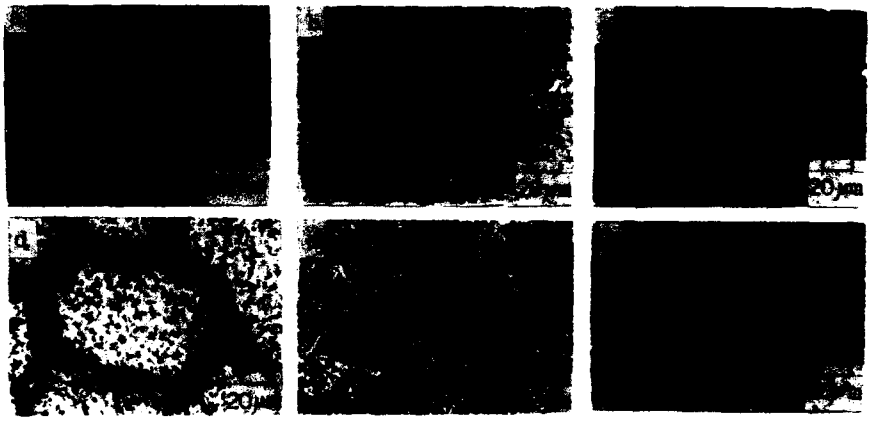


Figure 2 Microstructural changes during HVC treatment (Table 2) a) starting structure; b) hydrogenated, [H]:2783 ppm; c) solution treated; d)annealed; e) argon—dehydrogenated, [H]:1640 ppm; f) vacuum—dehydrogenated, [H]: 344 ppm, d=4μm

Orthogonal tests

The orthogonal layout of $L_9(3^4)$ was adopted to investigate the effects of strain rate ($\dot{\varepsilon}$), temperature (t)and grain size (d)on the elongation(δ)(see Table 4).

Table 4 Orthogonal test arrangement and their results

Factor / level / No.	A		B		C		elongation (%)				max. flow stress σ_m (MPa)
		$\dot{\varepsilon}$ (s^{-1})		t (℃)		d (μm)	δ_1	δ_2	$\bar{\delta}$	error (%)	
1	A_1	2.9×10^{-4}	B_1	700	C_3	4	313	300	307	2	52.8
2	A_1	2.9×10^{-4}	B_2	750	C_4	18	372	321	347	2	39.7
3	A_1	2.9×10^{-4}	B_3	800	C_1	1	328	320	324	1	16.5
4	A_2	8.0×10^{-4}	B_1	700	C_4	18	177	176	177	0.3	84.4
5	A_2	8.0×10^{-4}	B_2	750	C_1	1	418	432	425	2	45.5
6	A_2	8.0×10^{-4}	B_3	800	C_2	4	380	393	387	2	36.8
7	A_3	2.7×10^{-3}	B_1	700	C_1	1	326	327	327	0.3	78.6
8	A_3	2.7×10^{-3}	B_2	750	C_3	4	499	562	531	6	45.4
9	A_3	2.7×10^{-3}	B_3	800	C_4	18	268	277	272	2	43.6

The variance analysis of the above listed results (Table 4) is shown in Table 5.

Table 5 Variance analysis of orthogonal test results in Table 4

deviation source	sum of squares of deviation	degree of freedom	average sum of squares of deviation	F_r	significance
A	$s_A=289$	2	$\bar{s}_A=145$	3.08	Fair
B	$s_B=2276$	2	$\bar{s}_B=1138$	24.21	High
C	$s_C=1756$	2	$\bar{s}_C=878$	18.68	High
error	$s_E=520$	11	$\bar{s}_E=47$		
$F_{0.1}(2,11)=2.86$,		$F_{0.05}(2,11)=3.98$,		$F_{0.01}(2,11)=7.21$	

logσ/logε̇ curves

Here σ is the flow stress and m is the strain rate sensitivity index of flow stress ($\sigma=K\dot{\varepsilon}^m$).

Figures 3 and 4 show the logσ/log $\dot{\varepsilon}$ and m/log$\dot{\varepsilon}$ curves for d=4μm and d=1μm respectively.

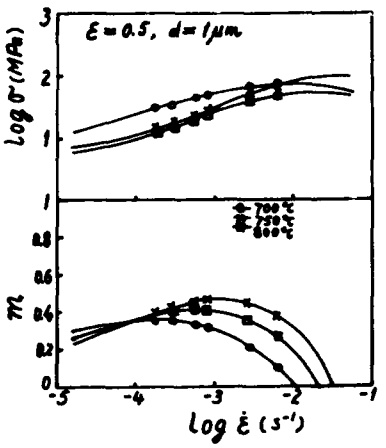


Figure 3—logσ/logε̇ and m/logε̇ curves for d=1μm

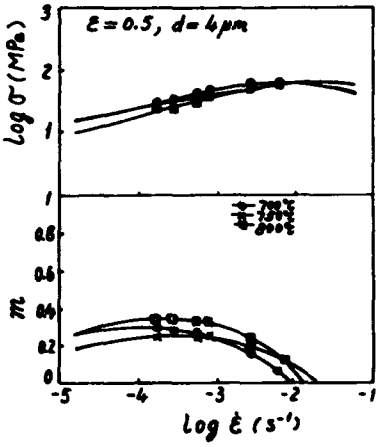


Figure 4—logσ/logε̇ and m/logε̇ curves for d=4μm

Discussion

Table 3 shovs that, the hydrogen content gradually increases as the hydrogenation temperature decreases and the time prolongs although only a fairly little increase at-

tainable because the hydrogen partial pressure can only be kept around one atmosphere in the open—hearth type furnace. It is for the same reason which leads to less marked effectiveness of the argon—dehydrogenation in reducing hydrogen concentration, therefore, vacuum—dehydrogenation was used.

Figure 2 demonstrates microstructure development in a specimen HVC treated. By comparing the microstructure from the argon—dehydrogenation treatment (Figure 2e)to that of the vacuum—dehydrogenation treatment (Figure 2f), there appears to be a minor difference i. e. the vacuum—dehydrogenated material shows somewhat more homogeneous microstructure.

Moreover, HVC—treated specimens show optimal superplastic deformation condition of 750℃ and $2.7\times10^{-3}s^{-1}$(d=4μm)(see Table 4). For the non—HVC—treated "β—rolled" material (d=5μm) the optimal superplastic deformation condition was found to be at 750℃ and $1.71\times10^{-4}\,s^{-1}$. [1]
Temperature and grain size are of great importance to the superplastic behavior of Ti—10—2—3. The strain rate test in the range $2.9\times10^{-4}\sim2.7\times10^{-3}s^{-1}$ has less effect on the superplastic behavior (Table 5).

Figure 5 shows logσ/logε and m/logε curves taken from reference [1]. The non—HVC—treated "β—rolled" material has a grain size of about 5μm. From a comparison among Figure 3~5, it is observed that the m—values of the HVC—treated material have been increased and the max. flow stress decreased. This can be attributed, besides the refined grains, to the possible increase (especially in the β—phase) in grain boundary slipping caused by higher hydrogen concentration and, therefore, easing the superplastic deformation.

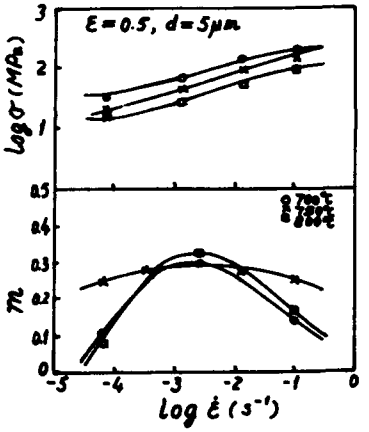


Figure 5—logσ/logε and m/logε curves (d=5μm) [1]

Conclusions

1. HVC treatment can be used to reduce the grain sizes of Ti—10—2—3 from 18μm to less than 4μm which proves to be a new way to refine the microstructure to

prepare andvantageous conditions for superplastic deformation.

2. The argon－dehydrogenation is far less effective in lowering hydrogen contents in Ti－10－2－3 than vacuum dehydrogenation.

3. The grain size is of great importance for the superplastic behavior of Ti－10－2－3. As the grain size decreases from 18μm to 4μm, the elongation increases from 177～327% to 300～562%. The optimal superplastic deformation condition is 750℃ and $2.7\times10^{-3}s^{-1}$.

4. The hydrogen remained in the material plays a role to activate and improve slipping along grain boundaries, which is helpful to plastic deformation. For this reason the optimal strain rate for HVC－treated Ti－2－3 is higher on an order of magnitude than that for non－HVC－treated one at the same temperature, which undoubtedly, means a great deal to production practices.

References

[1] Du Zhongquan, Wang Gaochao, Chen Yuxiu, "Superplastic Mechanical Behavior of Ti－10－2－3 Alloy" (China Aeronautical Scientific－Technical Report HJB 890753, 1989)

[2] Wang Gaochao, Chinese Patent CN 88211517.0

[3]F. H. Froes and D. Eylon, "Thermomechanical Processing(TCP) of Titanium Alloys by Temporary Alloying with Hydrogen" (Proceedings of the 7th International Conference on Hydrogen Effects on Material Behavior, 1989)

[4]W. R. Kerr, P. R. Smith et al., " Hydrogen as an alloying element in Titanium (Hydrovac)", Titanium' 80, 2477～2486

High Pressure Hydrogenation for Ti-6Al-4V Castings:

S.E. Hsu, C.P. Chang, S.G. Kao,
W.P. Sun and S.T. Thun

Materials R&D Center, CSIST
P. O. Box 90008-8, Lung-Tan, Taiwan, R. O. C.

ABSTRACT

A newly developed High Pressure Hydrogenation (H P H) process was used in CSIST to improve the mechanical properties of the Ti-6Al-4V investment castings. This HPH process is a modified Thermo Chemical Treatment (TCT) by temporarily alloying the Ti-6Al-4V with hydrogen at a rather high pressure(up to 5 atm). The benifits of this process as compare to the conventional TCT are in two fold : 1. decreasing both hydrogenation temperature and time, 2. controlling the hydrogen content precisely. Both microstructure and mechanical properties are improved after hydrogen removal.

Titanium '92
Science and Technology
Edited by F.H. Froes and I. Caplan
The Minerals, Metals & Materials Society, 1993

Introduction

Since 1970's, to refine titanium casting's microstructure by temporary hydrogen alloying has interested a lot of researchers to invest in this topic which is summarized in the literature (1).

In general, hydrogen was added to titanium alloy around 1.4 wt% (24) under 1 atm hydrogen pressure at different temperatures.An intermediate treatment may be added to it, such as aging or cooling to room temperature. Finally, a dehydrogenation step was held between 700 to 815 oC under vacuum. This treatment, refined the alpha plus beta microstructure of the worked piece and results a 10 to 17 % increase in strength over cast + HIP specimen.

Although there is no limit on the possible pressure of hydrogen atmosphere for such a microstructure refining process, it is difficult to control hydrogen concentration at higher hydrogen pressure. When hydrogen concentration is over 1.4% for Ti (5) and 0.75% for Ti-64 (6), the complication involving the delta phase and other low temperature phases exists. Since the delta phase is very brittle, there are chances that the delta involved transformation may cause undisirable result.

It is pointed out that the optimal hydrogenation temperature is 850 oC (6), because the hydrogen concentrations of 0.71 to 0.85 wt% are indiffused and beta transformation is achieved. Futher more, eutectoid decomposition with the hydrogen concentration in the range 0.5 to 0.8 wt% will yield the finest microstructure.

But what the effects of higher hydrogen pressure on this microstructure refining process are the interest of the author. In this experiment,the authors first measured the hydrogen absorption rate under hydrogen pressure from 1 to 5 atm. Using this information, we tried to control the hydrogen absorption and followed by grain refining process.

Experiment

An apparatus which was set up includes a tube furnace, a vacuum system, and a hydrogen supply system with a flow meter control. The temperature variation of the furnace is controlled within + - 5 oC. The working chamber is a stainless tube, 65 mm dia. x 620 mm long, which was pumped and flushed with hydrogen twice, then, pumped down to 10 -5 torr before the furnace was raised to the hydrogenation temperature.At the entrance the furnace, titanium sponge was used to absorb the possible existing contaminations. The hydrogen pressure is controlled by the flow meter system within +0.06 to -0.01 atm of the preset value. A digital readout clearly showed the hydrogen pressure in the chamber to +-0.01 atm. The hydrogen absorption was measured according to the pressure drop of the closed chamber during a 5 min period. After the pressure drop value was recorded, the hydrogenvalve was opened and the chamber was refilled

with hydrogen to the preset pressure. Figure 1 shows the pressure drop vs the time at different hydrogen pressure in the chamber at 850 oC. These samples were 3 x 60 x 60 mm pieces cut from Ti-64 castings. The furnace cooling rate was 10 oC/min between 850 to 650 oC and the hydrogen pressure is normally maintained at 1 atm to avoid dehydrogenation. A thicker specimen 13 x 58 x 43 mm were hydrogenized under 3 atm of hydrogen to measure the thickness effect on the dopping rate. The results were presented in Figure 2.

The hydrogenation, intermediate treatment, the dehydrogenation procedures and the designations of these samples are listed in Table I.

Based on the measurements of A2-0, samples A2-1 to A2-4 were prepared to find out the presented phases. X-ray was used for this examination. The as-cast specimen A0, and the vacuum heat treated specimen A0-1 are used as reference materials.Simplified results of x-ray were also given in Table I.

Samples for calculating the hydrogen concentration were A2-4, A3-1,A4-1 and A5-1; they were 3 x10 x10 mm ones and weighted to the third decimal point before and after the hydrogenation. Note that the hydrogenation time was selected according to the curves in Figure 1,at the end of the flatter region. Table II exhibits these information.

In order to compare the microstructure variation under different treatment, some samples were intermediately treated. Optical microscope was used to examine the microstructure.

Results and Discussion

The pressure drop measurements, plotted in Figure 1,indicated the hydogen absorption was very fast at the begining, followed by a near constant rate region and then decreased to nil.The higher the hydrogen pressure, the faster the abseption rate is. The constant rate region ended around 40, 60, 90 and 120 min for hydrogen pressure of 5, 4, 3 and 2 and 2 atmospheres. However, the hydrogen saturation time is lengthened for thicker specimen as indicated in figure 2. With higher hydrogen pressure,the time required for hydrogenation is shortened.

The X-ray diffraction pattern for specimen A0, was predominately alpha phase with only a small amount of beta. Sample A0-1, appeared with more beta phase. Half an hour at 850 oC,under 2 atm hydrogen,the A2-1 specimen presented only the beta phase. For A2-2, 60 min at this situation, it was a predominante beta phase with very small amount of delta. while in A2-3 specimen, the amount of delta phase increased as the hydrogenation time increased to 90 min. Sample A2-4 became very brittle and it could be easily pulverized into powder for x-ray differaction. The x-ray results indicated that only the delta phase existed. Although it is possible that hydrogen will diffuse into specimen during the time of

cooling which was held under 1 atm of hydrogen,note that all these samples experienced the same treatment but came out with different microstructures. The simplest explaination is that they have a different start point. In other words, under 2 atm hydrogen, 30,60,90 and 120 min have resulted different microstructure phases.

Therefore, it is a clear indication that to prolong the hydrogenation time will transform the alpha + beta structure to beta, from beta to beta + delta and finally to the predominant delta phase.

In Table II, the hydrogen concentrations for these samples were very close to each other at 3.05 +- 0.05 wt%. They should be : : delta phase. Indeed, each one of them was so brittle that they cracked during cooling to room temperature. However, samples dehydrogenized before cooling to room temperature showed no cracks.

The microgrophs in Figure 3 show the microstructure variation before and after the treatment. Fig 3(a) represents the as-cast material. From Fig 3(b) to (e),they clear indicate that microstructure refining is not evident unless the intermediate treatment were given at 650 oC.

It is the same temperature at the nose of the eutectoid decomposition T-T-T curves for Ti-6Al-4V - 1.35H (7). Since the alpha-beta transition temperature for Ti-64 is around 800 oC, delta phase will transform to low temperature phases through the eutectoid decomposition.

The mechanical properties test results are listed in Table III, which indicates a 40% improvement in tensile strength from as-casted to HTH treated but the ductility decreased from 9% to 3%. Since the sample is treated along the same path as A4-3, the microstructure is mainly submicron sized alpha phase and little beta. The reason for the low ductility is going to be investigated.

Conclusions

The high pressure hydrogenation (HPH) method is developed for improving themechanical properties of the castings. Up to this moment, it is sure chat the hydrogen pressure up to 5 atmospheres can be applied for this purpose.

It is found that the specimens doped hydrogen for different time period have different microstructure phases. The phases changed from as-casted alpha + beta , to beta, to beta + delta, and finally, delta dominated.

The specimen can be hydrogenized to 3.05 +- 0.05wt% of hydrogen depending on the combination of the hydrogenation pressure and time .

The tensile strength is improved to 167 KSI, which is 40 % over the as-casted value. However,the ductility is decreased to only 3% which needs futher investigation.

References

1. D. Eylon, F.H. Froes and W.J. Barice, "Effects of Treatments on Mechanical Properties of Titanium Alloy Castings, " SAMPE QUARTERLY, Jan (1989), p.42- 45.
2. R.G. Vogt. F.H. Froes, D. Eylon and L. Levin, "Therwo-Chemical Treatment (TCT) of Titanium Alloy Net Shapes," in Titanium Net Shape Technologies, edited by F. H. Froes and D. Eylon, The Metallurgical Society, Warrendate, PA (1984), p.145-154.
3. R.J. Smickley and L.E. Dardi, "Microstructure Refinement of Cast Titanium," U.S.Patent 4,505,764 (March 19,1985)
4. C.F. Yolton, D. Eylon, and F.H. Froes, "Microstructure Modification of Titanium Alloy Products by Temporary Alloying with Hydrogen, " Sixth World Conference on Titanium, ed. P. Lacombe, R. Tricot and G. Beranger (Les Ulis Cedex: Les Editions de Physique, 1988),p.1641.
5. T. B.Massalski, editor in-chief, "Binary Alloy Phase Diagrams", American Society for Metals, (1986)
6. D. H. Kohn and P. Ducheyne, " Microstructural refinement of beta-sintered and Ti-6Al-4V porous-coated by temperary alloying with hydrogen", J. Mat. Sci. 26 (1991) p.534-544.
7. W.R. Kerr, P.R. Smith,M.E. Rosenblum, F.J. Gurney, Y.R. Mahajan and L.R. Bidwell in "Titanium '80 Science and Technology", Proceedings of the 4th International Confierence of Titanium, Kyoto ,May 1980. p.2477.

Table III Results of the tensile tests.

		Y.S.(KSI)	T.S.(KSI)	Elong.(%)	R.A.(%)
As-casted	1	119	133	8.8	12.5
	2	119	131	9.3	17.6
HIPped	1	114	123	9.8	22.5
	2	112	122	11.0	27.1
HPH	1	166	175	2.8	6.3
	2	168	180	3.3	6.7

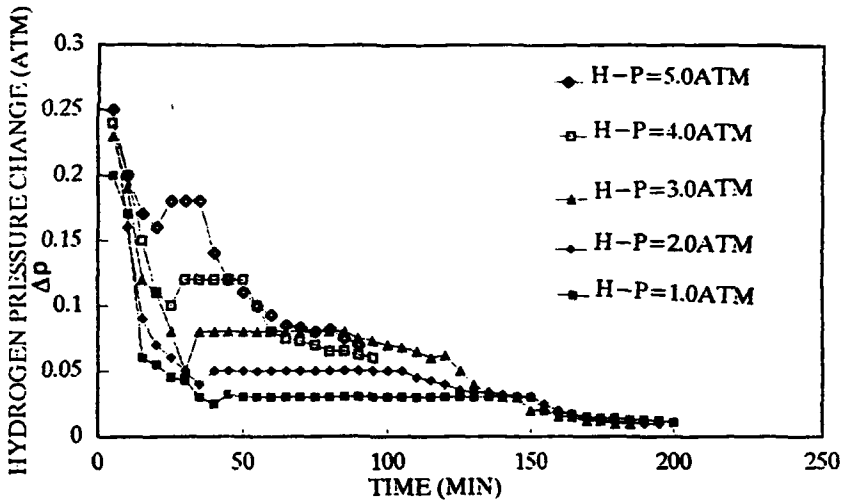


Fig. 1 The hydrogen pressure drop for every 5 min period is plotted against time, at 850 oC, under 5 different hydrogen pressure.

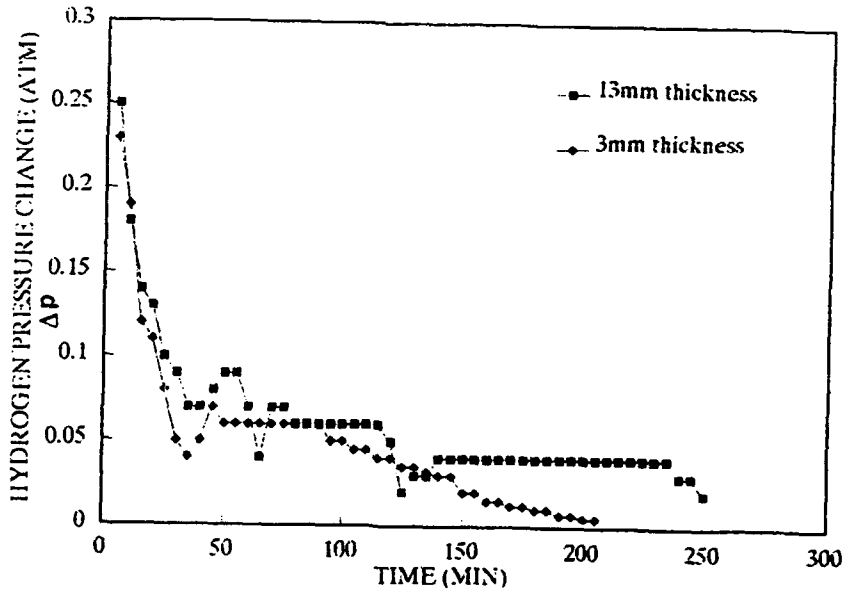


Fig. 2 The comparison of the hydrogen pressure drop between two specimens of different thickness, at 850 oC, 3 atm hydrogen.

Table I Specimen preparation precedures and X-ray results

Design-tion	Hydrogenation temp./time oC / min	Intermediate treatment # oC / min	Dehydrogena-tion temp. oC	Note *	X-Ray result @
AO				as-cast	A/B (10/1)
AO-1		850 / 60		vacuum	A/B (10/4)
A2-1	850 / 30			FC, H	B
A2-2	850 / 60			FC, H	B/D (20/1)
A2-3	850 / 90			FC, H	B/D (10/1)
A2-4	850 / 120			FC, H	D
A2-5	850 / 120		760	FC, V	A/B (10/2)
A2-6	850 / 120	750 / 60		FC, H	D/B (10/5)
A2-7	850 / 120	650 / 60	650	FC, V	A
A3-1	850 / 90			FC, H	D
A4-1	850 / 60			FC, H	D
A4-2	850 / 60	750 / 60	750	FC, V	A/B (20/5)
A4-3	850 / 60	650 / 60	650	FC, V	A/B (10/1)
A5-1	850 / 40			FC, H	D
A5-2	850 / 40	650 / 60		FC, H	

All intermediate treatments were done under 1 atmosphere hydrogen.
* FC (furnace cool):cooling rate between 850 to 650 oC is 10 oC/min.
@ For X-ray results: A (alpha), B (beta), D (delta)
(10/1) represent the relative intensity for major peak

Table II The hydrogen concentration of samples treated under different hydrogen pressure at 850 oC

Designa-tion	Initial wt. (gm)	Weight after hydrogenation(gm)	Hydrogen (gm)	content %
A2-4	1.556	1.605	0.049	3.05
A3-1	1.252	1.292	0.040	3.09
A4-1	1.255	1.295	0.040	3.08
A5-1	1.357	1.399	0.042	3.00

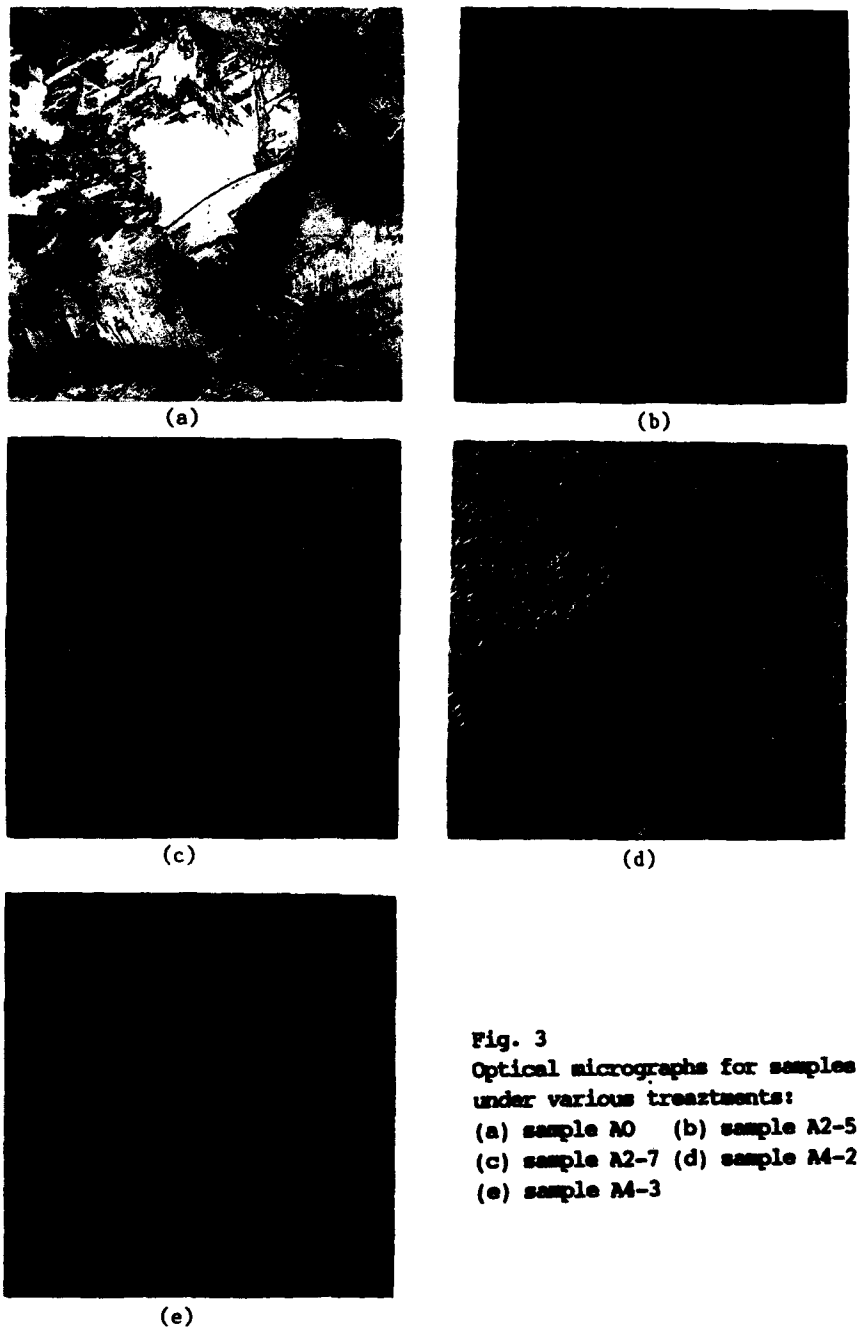


Fig. 3
Optical micrographs for samples under various treaztments:
(a) sample A0 (b) sample A2-5
(c) sample A2-7 (d) sample A4-2
(e) sample A4-3

PROPERTY ENHANCEMENT OF α-β TITANIUM ALLOYS

BY BLENDED ELEMENTAL P/M METHOD

Masuo Hagiwara, Yoshinari Kaieda, Yoshikuni Kawabe
and Shin Miura*

National Research Institute for Metals
1-2-1 Sengen, Tsukuba, Ibaraki, 305 Japan

*Chichibu Research Laboratory, Showa Denko K.K.,
1505 Shimokagemori, Chichibu, Saitama, 369-18 Japan

Abstract

A variety of α-β type titanium alloys were produced by the new blended elemental (BE) P/M method, in which water-quench stage is added before final HIP'ing. A fine two phase microstructure was obtained in near α type alloys. In contrast, in highly β-stabilized alloys, this method produced a massive grain boundary α phase. Tensile, smooth axial high and low cycle fatigue, and creep tests were performed with emphasis on relating composition/processing/microstructure to these mechanical properties.

Introduction

Blended elemental(BE) titanium powder metallurgy(P/M) is considered to be one of the most attractive net shape technologies[1]. However, mechanical properties, particularly fatigue strength, are inferior to those of prealloyed P/M and ingot metallurgy(IM) materials due to microstructual formation of α-platelet colonies and a massive grain boundary(GB) α phase[2,3]. In addition, the presence of residual porosity attributed to the chloride salts inherited in the titanium powder leads to a degradation in fatigue strength even with chloride level as low as 0.016 wt pct[4]. Therefore, both microstructure modification and the use of extra low chlorine(ELCL) powder are necessary to obtain better mechanical properties.

The authors have developped a microstructure-controllable new BE P/M method, in which as-sintered preform is subjected to quench from the β phase region. The Ti-6Al-4V produced by this new method using ELCL titanium powder exhibited fine α-β two phase microstructure with much less GB α phase and showed considerably higher high cycle fatigue strength over conventionally processed counterpart[4].

Besides well known Ti-6Al-4V, there are other types of α-β alloys which are superior in certain specific properties such as high temperature capability and fracture-related properties. The application of the new BE P/M method to these

Titanium '92
Science and Technology
Edited by F.H. Froes and I. Caplan
The Minerals, Metals & Materials Society, 1993

alloys will produce alloys possessing superior certain specific properties combined with the improvements in other properties, particularly fatigue strength. From this point of view, a variety of α-β alloys were produced applying this new method on relating composition/processing/microstructure to mechanical properties.

Experimental procedure

α-β alloys produced are shown in Table 1. ① Ti-5.5Al-3.5Sn-3Zr-0.3Mo-1Nb-0.3Si (IMI829) is an established, creep resistant near α type alloy, in use as compressor disks and blades in Rolls Royce engine[5]. The use temperature limit of about 600℃ is the highest at this moment. ② Ti-6Al-5Zr-0.5Mo-0.25Si(IMI685), which is a precursory alloy of IMI829, has good creep resistance and thermal stability up to about 520℃ and is used extensively by aero-engine manufactures in Europe[6]. ③ Ti-6Al-2Sn-4Zr-2Mo and ④ Ti-6Al-2Sn-4Zr-2Mo-0.1Si have remained the most widely used high temperature alloys with a service temperature of 470℃ especially in US manufactured engines[7]. The addition of Si was found to significantly increase the creep properties. ⑤ Ti-6Al-2.7Sn-4Zr-0.4Mo-0.45Si(Ti-1100) offers roughly a 55℃ creep advantage over beta processed Ti-6242S[8]. ⑥ Ti-6Al-4V is used as a baseline alloy for comparison. ⑦ Ti-5Al-2Cr-1Fe was developed in Japan, which possesses good heat treatment response and can attain high strength both at room and high temperatures [9]. ⑧ Ti-4.5Al-5Mo-1.5Cr(Corona 5) is a high strength alloy developed for applications requiring high fracture toughness[10]. ⑨ Ti-5Al-2.5Fe[11], which was developed in Germany for medical applications, can be classified as a moderate to high strength alloy comparable in mechanical properties to Ti-6Al-4V.

Processing steps are shown in Fig.1. The ELCL titanium powder(-100mesh,0~1800ppm) were used. Alloying elements were added using master alloy powder. The oxygen content of a HIP'ed Ti-6Al-4V compact was 2500ppm. The high temperature tensile tests were performed in a vacuum at a cross head speed of 0.1mm/min. The smooth axial fatigue tests were performed in air at an R-ratio of 0.1 in the load-control mode and a frequency of 80Hz. The creep and strain-controlled low cycle fatigue tests were done in air.

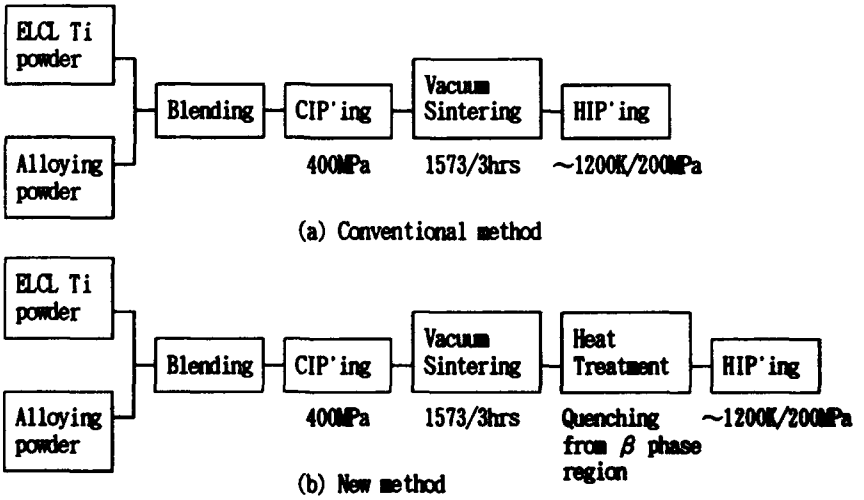
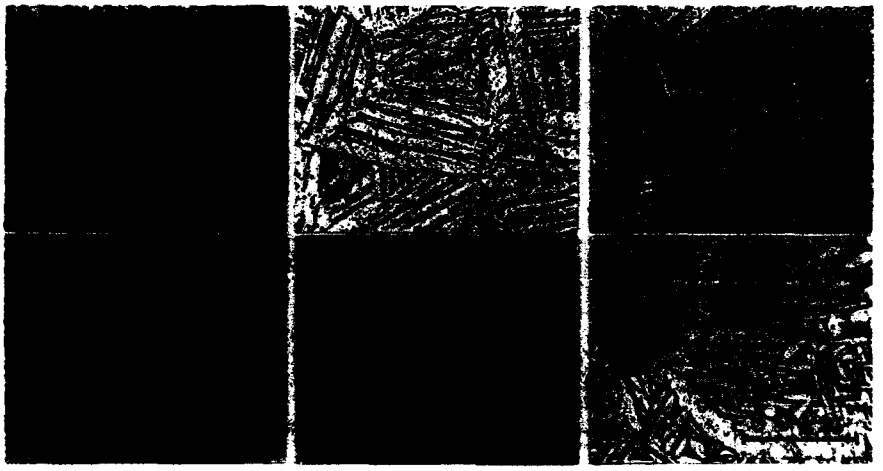


Fig.1 - Processing steps for fabrication of EE P/M titanium compacts.

Results and discussion

Microstructures

Some typical microstructures of ELCL BE P/M α-β titanium alloys are shown in Fig. 2. When these alloys were produced by the conventional BE P/M method, each alloy displays a coarse colony microstructure of similarly aligned alpha-platelets with massive GB α phase. The new BE P/M method is successfull in producing fine microstructures. However, it should be noted that the degree of fineness has a dependence on alloy composition. In alloys such as ⑦ Ti-5Al-2Cr-1Fe,⑧ Ti-4.5Al-5Mo-1.5 Cr and ⑨ Ti-5Al-2.5Fe which contain higher amounts of beta-stabilizing elements, a distinct GB α phase can be seen in the microstructure. In particular, Fe-containing alloys(⑦ and ⑨) exhibit very massive GB α phase morphology. It is known that Fe, Co and Ni have more rapid diffusivities in Ti than other β-stabilizing elements such as V, Nb and Mo[12], which means that the nucleation and growth kinetics of the α phase are faster in Fe,Co and/or Ni containing alloys. The existence of Fe in the alloy constitution would therefore be responsible for the very massive α phase morphology.



③ Ti-6Al-2Sn-4Zr-2Mo ⑤ Ti-1100 ⑦ Ti-5Al-2Cr-1Fe

Fig.2 - Microstructures of α-β titanium alloys produced by conventional(top photographs) and new(bottom photographs) BE P/M methods.

Room temperature mechanical properties

The room temperature tensile properties of various BE P/M titanium alloys are summarized in Table 1. Fig.3 illustrates the relationship between ultimate tensile strength(UTS) and elongation for these alloys. It is seen that the new BE P/M method generally leads to higher strength and ductility over those for corresponding conventional alloys. It is also seen that, irrespective of the fabrication methods, alloys which contain relatively higher β-stabilizing elements such as Ti-5Al-2Cr-1Fe possess a good combination of strength and ductility. Contrary to this, near α type alloys such as IMI829 and IMI685 exhibit considerably lower ductility, although higher tensile strength can be attained in these alloys.

Table 1 - Summary of room temperature mechanical properties of extra low chlorine blended elemental P/M α-β titanium alloys.

Alloy	Method	0.2%YS MPa	UTS MPa	El (%)	RA (%)	σ_f at 10^7 (MPa)
① Ti-5.5Al-3.5Sn-3Zr-0.3 Mo-1Nb-0.3Si(IMI829)	Conv	941	1019	4	8	
	New	960	1039	9	23	
② Ti-6Al-5Zr-0.5Mo- -0.25Si(IMI685)	Conv	911	1000	14	24	
	New	970	1058	12	25	
③ Ti-6Al-2Sn-4Zr-2Mo	Conv	892	980	15	31	412
	New	990	1088	15	26	647
④ Ti-6Al-2Sn-4Zr-2Mo -0.1Si	Conv	970	1058	18	27	
	New	1020	1117	13	18	
⑤ Ti-6Al-2.7Sn-4Zr-0.4Mo 0.45Si(Ti-1100)	Conv	887	971	11	13	420
	New	1003	1088	10	23	530
⑥ Ti-6Al-4V	Conv	833	921	14	36	412
	New	862	951	15	42	588
Ti-6Al-4V(Ingot Met)		862	970	13	24	598
⑦ Ti-5Al-2Cr-1Fe	Conv	941	1000	18	40	
	New	951	1029	19	42	549
⑧ Ti-4.5Al-5Mo-1.5Cr (Corona 5)	Conv	921	1009	19	40	
	New	931	1019	20	45	549
⑨ Ti-5Al-2.5Fe	Conv	882	970	18	35	441
	New	1009	1069	17	36	588

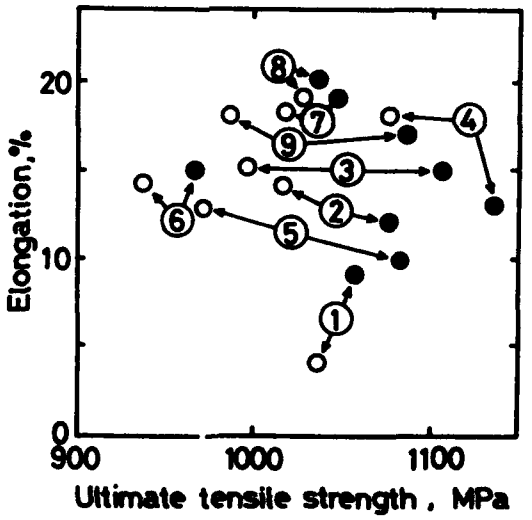


Fig.3 - Relatioship between ultimate tensile strength(UTS) and elongation for α-β titanium alloys produced by conventional(open circles) and new (solid circles) BE P/M methods.

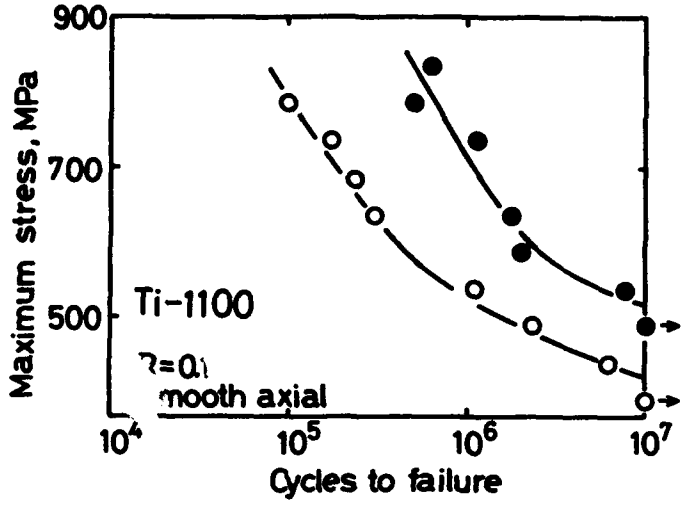


Fig.4 - Smooth axial fatigue data for ⑤Ti-6Al-2.7Sn-4Zr-0.4Mo-0.45Si(Ti-1100) produced by conventional(open circles) and new(solid circles) BE P/M methods.

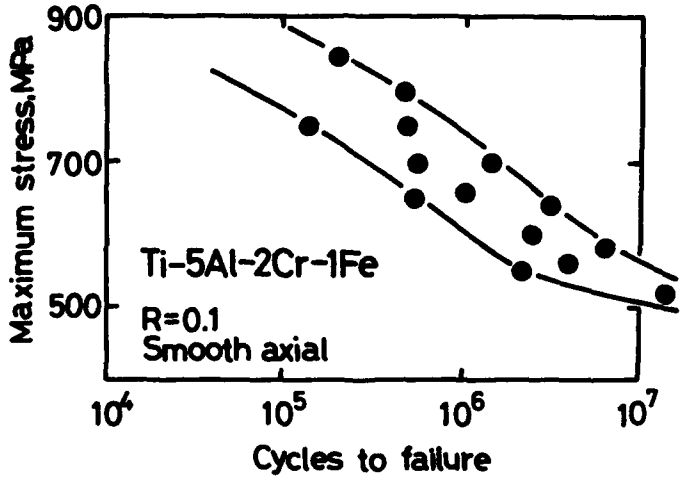


Fig.5 - Smooth axial fatigue data for ⑨Ti-5Al-2Cr-1Fe produced by new BE P/M method.

Fig.4 shows the fatigue test data for ⑤ Ti-6Al-2.7Sn-4Zr-0.4Mo-0.45Si(Ti-1100). The new method resulted in a substantially improved fatigue strength in the whole cycle range with very little scatter in test data. The new method also resulted in an improved fatigue strength in other alloys. However, a large test data scatter was observed especially in Fe-containing alloys such as ⑦ Ti-5Al-2Cr-1Fe and ⑨ Ti -5Al-2.5Fe when produced by the new method, as shown in Fig.5. The concurrent

observation of the initiation facet and the underlying microstructure[13] revealed that, for specimens whose fatigue data lie in or is close to the lower bound of the scatter band, the fatigue initiation was associated with the cracking along the boundary between GB α and an adjacent colony.

Fig.6 summarizes the relationship between fatigue ratio S at 10^7 cycle and Mo equivalent for α-β alloys. This Mo equivalent is used as a measure of the degree of β phase stability of each alloy[14]. The S value of the conventional BE P/M alloy is almost equal irrespective of alloy composition. This constancy would stem from the fact that the colony size and thus slip length is almost the same in each of alloys. On the other hand, the S value of the new BE alloy changes with alloy composition. The highest S values are obtained in alloys such as Ti-6Al-2Sn-4Zr-2Mo and Ti-6Al-4V. In alloys with higher beta-stabilizer contents, the new BE P/M method has only a marginal effect on fatigue strength due to the formation of the microstructural heterogeniety such as GB α phase.

High temperature mechanical properties of near α type BE P/M alloys

It was found that there is a good correlation between the UTS and Al equivalent value for each alloy. As shown in Fig.7, the UTS at RT and 773K(500℃) increased with increasing Al equivalent value. The results of creep tests done on ③ Ti-6Al-2Sn-4Zr-2Mo(Fig.8) and ⑥ Ti-6Al-4V(Fig.9) revealed that the fine α-β two phase microstructure produced by the new BE P/M method exhibites superior creep characteristics over colony microstructure of conventionally processed alloys. Fig.10 shows strain-controlled, low cycle fatigue data for ③ Ti-6Al-2Sn-4Zr-2Mo tested at 500℃. It is obvious that the BE P/M alloys possess significantly higher low cycle fatigue strength over currently used Fe-based heat resistant alloys. It is also seen that the new BE P/M alloys have clear advantage in low cycle fatigue strength over conventional counterparts. These findings demonstrate that the new BE P/M method can give rise to improved balance of mechanical properties ,especially low cycle fatigue and creep, compared with those for conventional BE P/M alloys when applied to near α type α-β alloys.

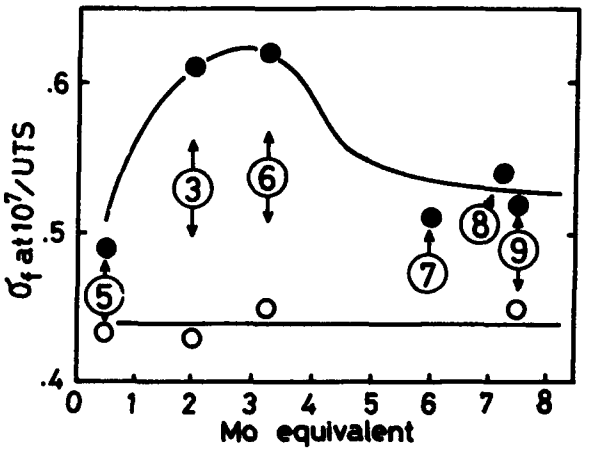


Fig.6 - Relationship between fatigue ratio at 10^7 cycle and Mo equivalent for titanium alloys produced by conventional(open circles) and new(solid circles) BE P/M methods.

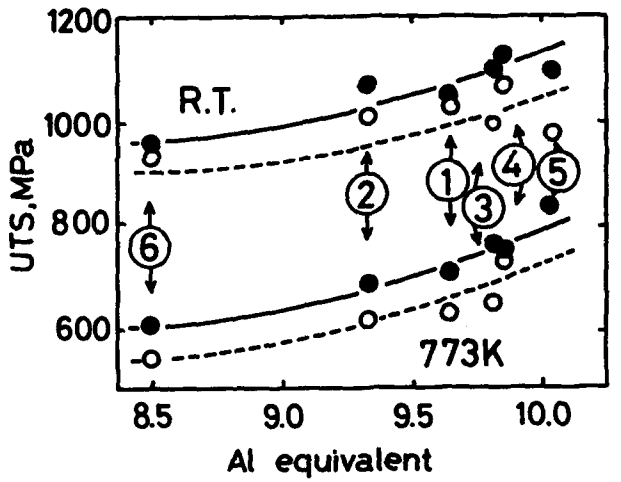


Fig.7 - Relationship between UTS and Al equivalent for α-β alloys produced by conventional(open circles) and new(solid circles) BE P/M methods.

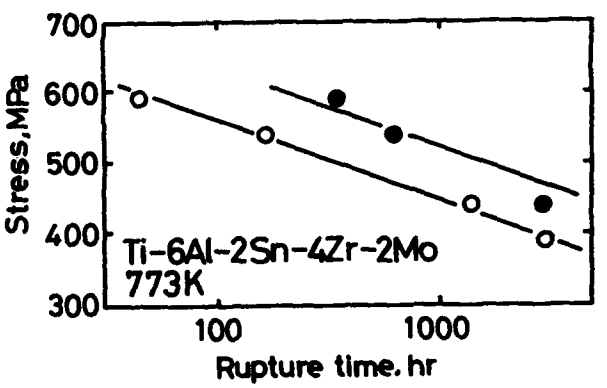


Fig.8 - Creep data for Ti-6Al-2Sn-4Zr-2Mo produced by conventional(open circles) and new(solid circles) BE P/M methods.

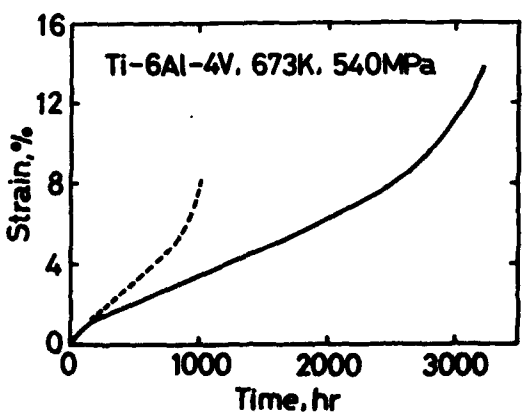


Fig.9 - Creep curves for Ti-6Al-4V produced by conventional (broken line) and new (solid line) BE P/M methods.

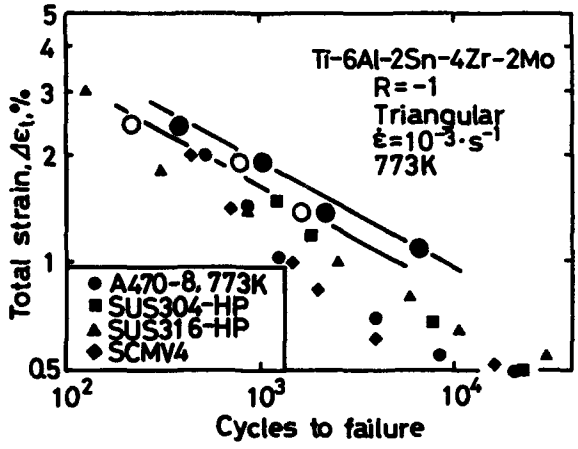


Fig.10 - Low cycle fatigue data at 773K(500℃) for Ti-6Al-2Sn-4Zr-2Mo produced by conventional(open circles) and new(solid circles) BE P/M methods.

Conclusion

A variety of titanium alloys were produced by the BE P/M methods. Alloy composition was found to have a strong effect on the microstructure. In near α type α-β alloys such as Ti-6Al-2Sn-4Zr-2Mo, the new BE method created a fine two phase microstructure and resulted in an improved high cycle fatigue strength. In contrast, in β-rich α-β alloys such as Ti-5Al-2Cr-1Fe and Ti-5Al-2.5Fe, this new method produced a massive grain boundary alpha(GBα) phase and a large scatter in fatigue test data. The formation of GBα was more pronounced in Fe-containing alloys. The lower fatigue data were associated with the fatigue crack initiation at the boundary between GBα and adjacent colony. High temperature mechanical tests done on near α type alloys revealed that the new BE P/M method can give rize to improved creep resistance and low cycle fatigue strength over conventional BE P/M alloys.

References

1) Titanium Net Shape Technologies,ed.by F.H.Froes and D.Eylon (1984),[TMS-AIME]
2) D.Eylon: J. Mater.Sci.,14(1979),p.1914
3) D.Eylon: Metall Trans.A,10A(1979),p.311
4) M.Hagiwara,Y.Kaieda and Y.Kawabe: Proc. of 1986 Int. Conf.on Titanium Products and Applications,(1986),p.850 [TDA]
5) S.Fujishiro,F.H.Froes,T.Matumoto and D.Eylon: Titanium, Science and Technology ed,G.Lutjering, U. Zwicker and W.Bunk (1985),p.593[DGM]
6) D.Eylon and J.A.Hall: Metall Trans.A,8A(1977),p.981
7) D.F.Neal and P.A.Blenkinsop: Titanium'80,ed H.Kimura et al.,(1980),p.1287[AIME]
8) P.Bania: Proc.6th World Conf.on Titanium,(1989),p.825[Les Edition de Physique]
9) Z.Takao,H.Kusamichi,S.Tokuda.K.Miyamoto and Y.Fukuhara: The Sciece,Technology and Application of Titanium,ed,R.I.Jaffee et al.,(1970),p.891[Pergamon Press]
10) F.H.Froes and W.T.Highberger: J.Met.,32(1980),P.57
11) J.Breme: Proc.6th World Conf.on Titanium,(1989),p.57[Les Edition de Physique]
12) J.E.Wert and N.E.Paton: Metall Trans.,A,14A(1983),p.2535
13) W.R.Kerr,D,Eylon and J.A.Hall: Metall.Trans.A,7A(1976),p.1477
14) R.I.Jaffee: Trans.TMS-AIME, 230(1964),p.541

Fabrication of Ti-Ni-Cu Shape Memory Alloys by Spontaneous Reaction Synthesis and Directed Hot Extrusion Forming

M. T. Yeh, H. P. Kao and S. E. Hsu

Materials R&D Center, CSIST
P. O. Box No. 90008-8-8 Lung-Tan, Taiwan, R. O. C.

Abstracts

Spontaneous reaction synthesis (SRS), combustion synthesis or self-propagating high temperature synthesis (SHS) has been well known as a kind of novel, rapid and less contaminative modern technique used to fabricating Ti-Ni shape memory alloy. Some previous researches proved that the chemical compositions and properties of SMA can be precisely controlled by this way [1,2,3,4].
In this paper, we investigated to synthesize $Ti_{100-x}Ni_{x-y}Cu_y$ (x= 49.8 $\sim$ 50.2, y= 0,5,10) ternary SMA by the similar exothermic reaction:

$$(100-x)Ti + (x-y)Ni + y\,Cu \rightarrow Ti_{100-x}Ni_{x-y}Cu_y + \triangle H.$$

A special combination type reactor has been designed in this investigation. So, the compacted pillarlike reactant of mixed powders once ignited by a heating coil in SRS area and rapidly became melting product which could be immediately shifted to hot extrusion forming (HEF) area in the same reactor and was forged through a hot extrusion die to becoming ingot. Then, the ingot was conducted by a sequent conventional materials processing: hot swaging, cold drawing, hot rolling, cold rolling and adequate heat treatment became wire or plate type products.
All these SRS + HEF SMA products reveal excellent shape memory effect (SME), pseudoelasticity (PE) and damping capacity which have been proven by a series of material inspection and testing. It is mean that the SRS + HEF technique is really a convenient and effective producting method to Ti-Ni-Cu SMA.

Titanium '92
Science and Technology
Edited by F.H. Froes and I. Caplan
The Minerals, Metals & Materials Society, 1993

Introduction

Near equiatomic Ti-Ni shape memory alloy is a very interesting and versatile material, because it simultaneously has some very practical characteristics,ie, high strength, fair ductility, good corrosion resistance, high damping capacity, pseudoelasticity (due to stress induced martensitic tranformation)and shape memory effect (due to thermal elastic martensitic transformation), more and more applications of this alloy have been developed continuously.However, conventional vacuum melting method of producting Ti-Ni SMA usually gives poor reproductivity, and is easily to be contaminated by impurity elements, oxygen and carbon which most come from crucible during melting process. These not only degrade the properties of the material but also result in the shift of martensitic transformation temperature (about 10℃/0.1 atomic percent) [5]. It is the reason why we want to develop the process of spontaneous reaction synthesis (SRS) in the controlled atmospheres to product Ti-Ni SMA. The crucibleless feature of SRS can prevent most contamination problems and the powder metallurgy procedure of SRS lets the preparation of alloy's components easier. Those are very helpful to obtaining more uniform and controlled chemical compositions, specially in the more complicated ternary SMA. Otherwise, the primary product after SRS is porous, necessitating subsequent remelting in a VAR furnace which is a rather expensive facility comparing with the SRS reactor. For the cost down and the procedure simplify reasons, a combination type reactor was designed by us.There are two major parts inside the reactor chamber, as shown in the Figure 1 , right side is the RSR area and left side is the hot extrusion forming (HEF) area. At first, the compacted pillarlike reactant of mixed powders was put in SRS area and preheated,then was ignited by a heating coil, SRS reaction occured rapidly and violently, as the reacted product still keeping in melting condition, it was shifted to HEF area and was forged through a hot extrusion die immediately. So, we could effectively vanish most porosities and get a approach theoretic density ingot.
Sequentially, we tried to demostrate whether the SRS + HEFed ingots can be readily fabricated into the final alloy products which possessing expected SME, PE and high damping capacity characteristics. Otherwise, we want to know except Ti-Ni binary SMA if the Ti-Ni-Cu ternary SMA also can be successfully fabricated by this SRS + HEF's method.

Experimental Procedure

The powders used in this investigation were 99.5% purities titanium powder (below 100 microns), 99.9% purities nickel powder (below 10 microns) and 99.5% purities copper power (below 80 microns). The powders were blended at $Ti_{100-x}Ni_{x-y}Cu_y$ (x=49.8～50.2, y=0,5,10) stoichiometry and subsequently tumbled thoroughly in a cylindrical container to achieve homogeneity using a mechanical shaker, then, pressed into pillar shape by CIP. Each pillarlike pellet weighed approximately 300g with a green density 65±3%. The pellets were put in the SRS area of special designed combination type reactor and preheated to 500℃～700℃ under argon atmospheres, then ignited by a 1100℃ molybdenum spiral. After violent reaction, the melting pellet was shifted immediately to the HEF area of reactor and forged through a hot extrusion die became ingot. Schematic representation of the all procedures of this SRS + HEF's method is shown in the Figure 2. The ingots were taken out the reactor chamber and conducted by a sequent conventional materials processing: hot swaging, cold drawing, hot rolling, cold rolling and adequate heat treating became wire or plate type final products.

Differential Thermal Analyzer (DTA) and Differential Scanning Calorimeter (SDC) were used to measure the transformation temperatures and reacting energy of the SMA products. The shape memory effect (SME) of SMA products was compared by a bending test as shown in the Figure 4 and the pseudoelasticity (PE) of SMA products was compared by a three points bending test as shown in the Figure 5 . In addition, we used internal friction measuring equipment by inversed pendulum method and accelerator and oscilloscopes by timing logarithmic decreasement method to measure the damping capacity of SMA products.

Results and Discussion

SRS and HEF procedure

The preheating temperature of pellets before SRS had better be set up as high as possible, so that, the pellets can be thoroughly melted after SRS and let us have enough time to complete the HEF procedure in the latter step. Otherwise, the SRS reaction might be interrupted and the semi-melted products are not easily be pressed through the hot extrusion die. According to the DTA chart, the reasonable preheating temperature to different composition's SMA have been found out, e.g. 600℃ to near equiatomic Ti-Ni SMA, 550℃ to Ti rich Ti-Ni SMA and 650℃~700℃ to Ti-Ni-Cu series SMA.

Alloy Properties

Martensitic Transformation Temperatures. Under the same composition condition, we found the martensitic transformation temperature of SMA by SRS method is higher than that of SMA by conventional vacuum melting method about 10℃, as Figure 3 shown. We believe that the lower temperature rapid reaction and crucibleless process of SRS make the contamination chance of SMA much lower than the conventional vaccum melting method and result in the increase of martensitic transformation temperature.

Shape Memory Effect (SME). The results of shape memory effect of $Ti_{50}Ni_{50}$, $Ti_{50}Ni_{45}Cu_5$ and $Ti_{50}Ni_{40}Cu_{10}$ wires by bending test are shown in Figure 4. All of those exhibit good enough SME.

Pseudoelastisity (PE). After 25%, 35% and 45% cold drawing and subsequent fix feature heat treatment at 400℃ for one hour, the $Ti_{49.8}Ni_{45.2}Cu_5$ alloy was drawn to 0.018" diameter wires which can be used as orthodontic arch. The results of the three points bending test are shown in Figure 5, these arches exhibit three different loading value pseudoelasticity curves: soft, medium and hard, all reveal excellent PE characteristics.

Damping Capacity. One set of the results of internal friction and timing logarithmic decreasement damping measurement of $Ti_{49.8}Ni_{50.2}$ alloy are shown in Figure 6. The alloy exhibits high damping capacity specially around its martensitic phase transformation temperature. The similar results also present in the $Ti_{50}Ni_{45}Cu_5$ and $Ti_{50}Ni_{40}Cu_{10}$ alloy's cases. We believe that the very high density of matensitic twin interfaces exsisting inside the SMA and the large hysteresis loss between parent and martensite phases when interfaces moving both result in the high damping capacity of SMA.

Conclusions

The SRS + HEF technique has been proven as a very convinient and effective producting method to Ti-Ni SMA even Ti-Ni-Cu ternary SMA. All of the SMA products reveal expected excellent SME, PE and high damping capacity.

Reference

1. A. D. Bratchikov et al., Sov. Powd. Metall. Met. Ceram., 19(1980),p.5.
2. V. I. Itin et al., Sov. Powd. Metall. Met. Ceram., 22(1983),p.156.
3. H. C. Yi and J. J. Moore, Scripta Metall., 22(1988),p.1989.
4. James W. McCauley, Ceram. Eng. Sci. Pro., 11(1990),p.1151.
5. M. T. Yeh, H. P. Kao and S. E. Hsu, Unpublished Research, MR&DC, CSIST.

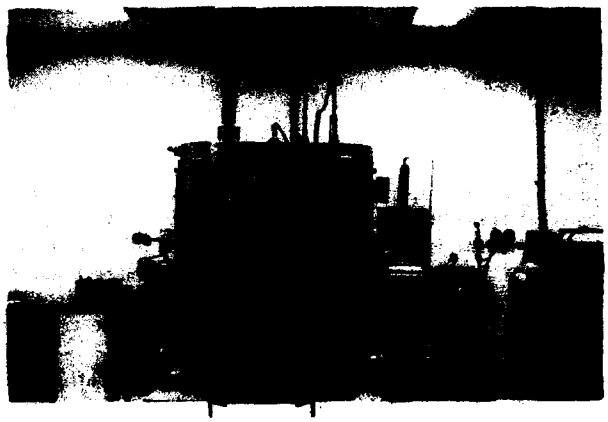


Figure 1. The specially designed combinational type reactor. Right side: RSR area. Left side: HEF area.

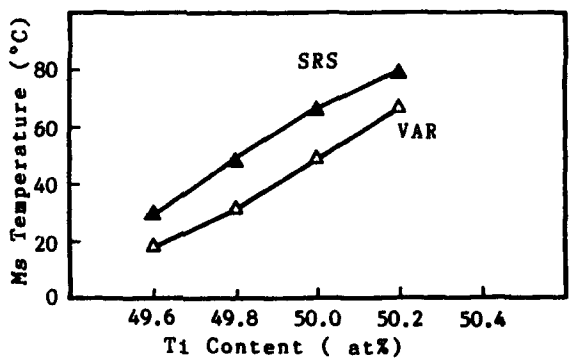


Figure 3. Comparision of the change of martensitic transformation temperatures of SMA with titanium contents between SRS procedure and VAR procedure.

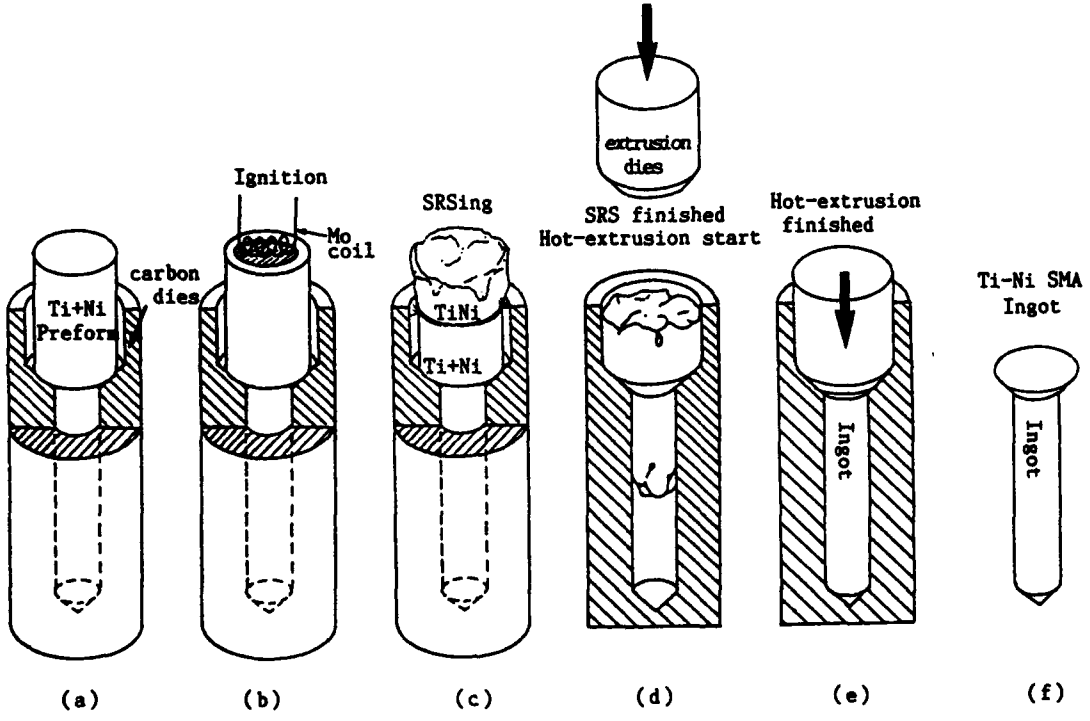
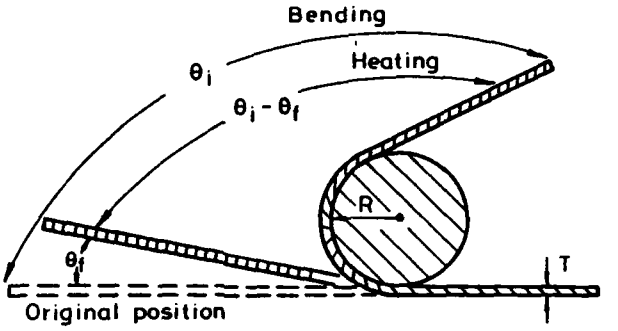


Figure 2. Schematic representation of the all procedures of SRS + HEF.



$$R_{SME} = \frac{\theta_i - \theta_f}{\theta_i}$$

$$\varepsilon_S \doteq \frac{T}{2R}$$

T: specimen thickness
(or diameter = 1mm)
R: deformed diameter
(R = 10mm)

SME test of Ti-Ni SMA wires:

Specimen	M_s °C	A_f °C	SME (Heat to 120°C)
$Ti_{50}Ni_{50}$	68	110	100%
$Ti_{50}Ni_{45}Cu_5$	62	90	98%
$Ti_{50}Ni_{40}Cu_{10}$	60	90	98%

Figure 4. (a) Schematic representation of the bending test used to measure the shape memory effect.
(b) The results of shape memory effect test.

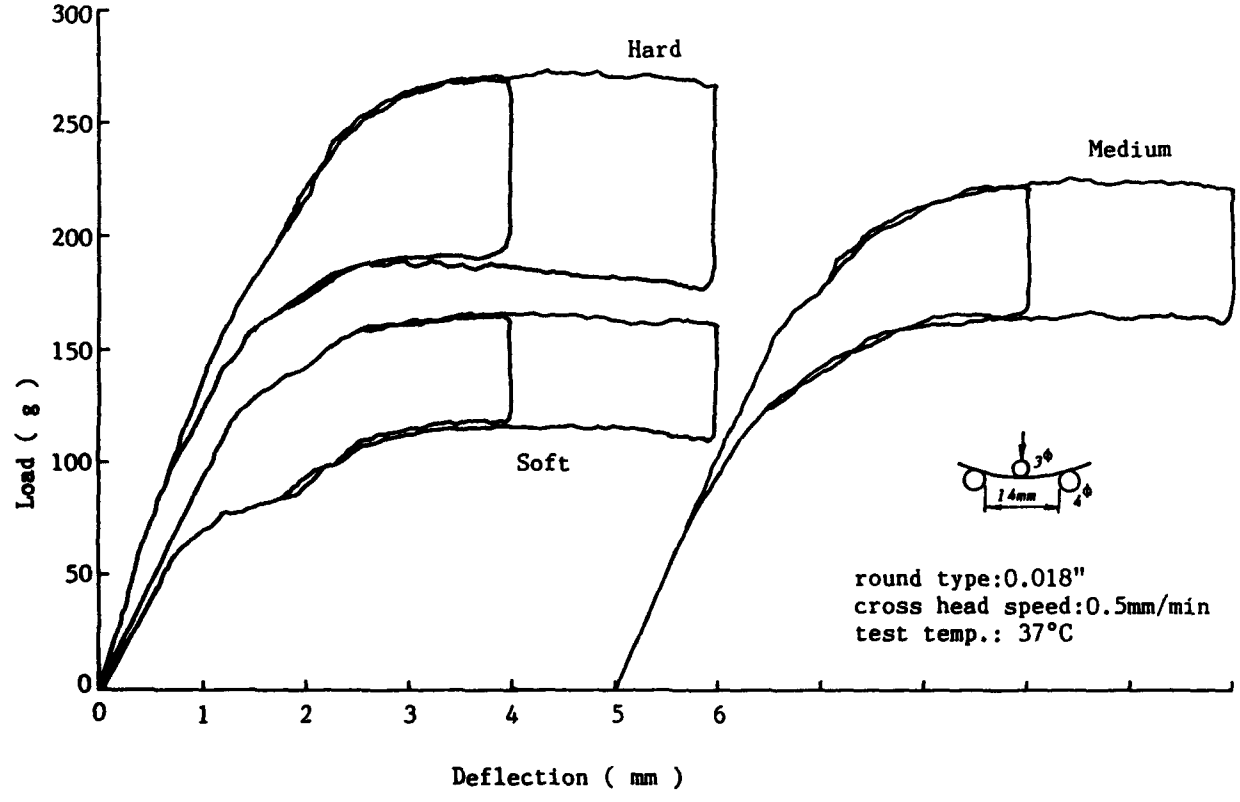
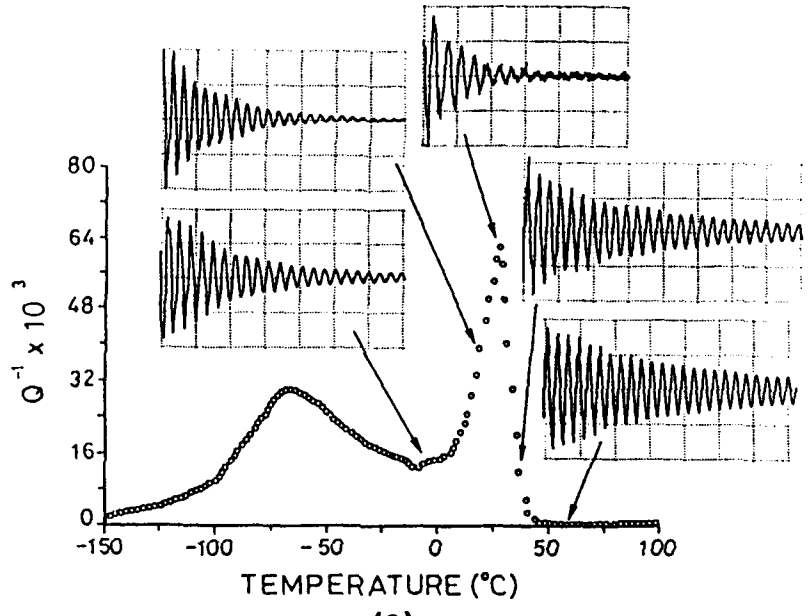


Figure 5. The results of three points bending test of $Ti_{49.8}Ni_{45.2}Cu_5$ wires after 25%, 35% and 45% cold drawing seperately.



(a)

Temperature(°C)	-5	20	28	36	60
Phase	B19	B19+B2	B19+B2	B19+B2	B2
#I.F. ($Q^{-1}x10^3$)	14.5	39.6	62.2	11.0	0.5
* $\zeta = \frac{1}{2\pi}\ln\frac{An}{An+1}$	0.021	0.036	0.059	0.012	0.009
* Natural Frequency (Hz)	165	163	160	167	172

#Invesed Torsion Pendulum Method * Logarithmic Decreasement Method

(b)

Figure 6. (a)Schematic representation of internal friction and timing logarithmic decreasement damping measurement of $Ti_{49.8}Ni_{50.2}$ alloy.
(b)The results of damping measurement.

NANOSTRUCTURE FORMATION

IN A MECHANICALLY ALLOYED Ti-24Al-11Nb ALLOY

GUO-HAO CHEN, C.SURYANARAYANA AND F.H.(SAM) FROES

Institute for Materials and Advanced Processes
University of Idaho
Moscow, ID 83843-4195 (U.S.A.)

Abstract

Mechanical alloying of the Ti-24Al-11Nb(at%) alloy has been carried out on both blended elemental and prealloyed powders and the structural evolution has been investigated as a function of milling time using x-ray diffraction and transmission electron microscopy techniques. During the early stages of milling the blended elemental powder formed a titanium(hcp) solid solution, which was followed by the partial formation of a B2(bcc) phase and an amorphous phase, and finally only an fcc phase was present after continued milling. The prealloyed powder which consisted entirely of the B2(bcc) phase in the as-received condition transformed completely into an amorphous phase and then totally to an fcc phase with increasing milling time. Formation of nanostructure grains was observed in both the types of powder.

Introduction

Recently there have been a number of investigations on the structure and properties of nanocrystalline materials [1,2], which are polycrystalline materials with a grain size of typically 10-100 nm (1 nm = 10^{-9} m). Because of the fineness of the grain size, a large fraction of the atoms resides in the grain boundaries and confer beneficial properties on these materials. Two important consequences of the small grain size of the nanocrystalline materials are (a) enhanced strength due to the Hall-Petch effect, at least down to a critical size below which dislocation mobility is greatly retarded, and (b) an increase in elevated temperature deformation rate (by Coble diffusional creep), due to the decreased grain size and increased grain boundary diffusivity. Thus, in comparison with a conventional polycrystalline material, nanocrystalline materials are expected to plastically deform more easily even at low temperatures.

Mechanical alloying (MA) was developed during the late sixties and has been used to produce several commercial nickel- and iron-base oxide-dispersion-strengthened alloys [3,4]. Recently, the application of the technique has been extended to the synthesis of a variety of equilibrium and non-equilibrium phases in a number of alloy systems, particularly those based on aluminum and titanium [5-7]. It has been shown clearly that during MA the grain size decreases

Titanium '92
Science and Technology
Edited by F.H. Froes and I. Caplan
The Minerals, Metals & Materials Society, 1993

continuously with milling time reaching nanometer levels [8,9], indicating that MA is an effective method of producing nanometer-sized grains.

Titanium aluminides (both α_2-Ti_3Al and γ-TiAl) are attractive structural materials in the aerospace industry due to their low density, high specific strength, elevated temperature strength and modulus retention, and excellent creep resistance [10,11]. However, a serious handicap in using these intermetallics is their generally low ambient temperature ductility. Refinement of grain size, addition of ternary/quaternary alloying elements, and innovative heat treatments have been used to increase the ductility. Amongst these approaches, addition of alloying elements, particularly of niobium, has proven to be beneficial. Niobium produces the B2 phase having an ordered bcc(CsCl-type) structure and increases the ductility due to an increased number of slip systems. Accordingly, there have been several investigations in recent years to define the constitution, microstructure and properties of ternary Ti-Al-Nb alloys [12-15].

Since MA is known to produce nanometer-sized grains, if the B2 phase can be synthesized in Ti-Al-Nb alloys by MA, then potentially these two effects can be used together to maximize ductility. The present paper reports on the structural evolution and synthesis of nanostructures in blended elemental and prealloyed ternary Ti-Al-Nb alloys by MA.

Experimental Procedure

Titanium(-100 mesh, >99.4% pure), aluminum(-100 mesh, >99.7% pure), and niobium(-20 mesh, >99% pure) were mixed to yield an average starting composition corresponding to Ti-24at%Al-11at%Nb. (This composition will be referred to as Ti-24-11). Prealloyed Ti-24-11 powder(150 μm average diameter) rapidly solidified by the Plasma Rotating Electrode Process(PREP) was also used in this investigation.

Mechanical alloying was carried out at room temperature in a Spex 8000 mixer mill for times up to 24 h. The grinding medium was hardened 52100 steel balls of diameter 3/16 in. and the powder-to-ball weight ratio was always maintained at 1:10. About 2 wt% stearic acid was used as a process control agent. Forced air cooling during milling prevented excessive temperature rise of the powder.

A small quantity of the mechanically alloyed powder was removed from the canister periodically and the structure evolution was examined by x-ray diffraction using Cu Kα radiation at 40 kV and 15 mA settings in a Philips x-ray diffractometer. The phases present were identified by comparing the peak positions and intensities with those listed in the JCPDS files. The mechanically alloyed powder was also examined in a transmission electron microscope(TEM). Powders were heat treated in glass tubes sealed under vacuum and the phase changes were followed using the x-ray diffraction and TEM techniques.

Results

The results obtained will be presented under the two categories of blended elemental and prealloyed material.

Blended Elemental Ti-24-11

Fig. 1 shows the x-ray diffraction patterns of the blended elemental (BE) Ti-Al-Nb powders as a function of time. In the as-mixed condition the peaks due to α-Ti (hcp), Al (fcc) and Nb (bcc) with the expected lattice parameters

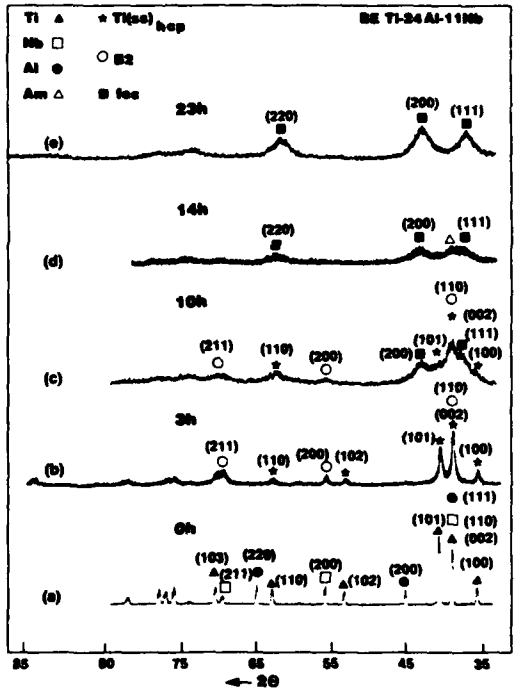


Fig. 1. X-ray diffraction patterns of blended elemental Ti-24Al-11Nb powders as a function of milling time.

present. With increasing milling time the peaks broaden and their intensities decrease. In addition, alloying takes place leading to the formation of some stable and metastable phases. After 3 h of milling, the Ti(Al) (hcp) solid solution [$Ti(Al)_{s.s.}$] and the B2 (bcc) phase with a = 0.330 nm were observed. Continued milling led to the formation of a mixture of amorphous and fcc phases, and the end product of milling beyond 23 h was only the fcc phase with a = 0.421 nm. Thus, the sequence of phases formed with milling time can be summarized as:

$$BE\ (Ti+Al+Nb) \xrightarrow{3h} Ti(Al)_{s.s.}+B2 \xrightarrow{10h} Ti(Al)_{s.s.}+B2+fcc \xrightarrow{14h} Am+fcc \xrightarrow{23h} fcc$$

The crystal size of the powder as a function of milling time was evaluated from the broadening of the x-ray reflections using the Scherrer formula [16]. Fig. 2 shows a plot obtained for both BE and prealloyed Ti-24-11. Values for pure titanium are also shown for comparison. The crystal size decreases exponentially with milling time and reaches nanometer levels in about 10 h. A transmission electron micro-graph showing the nanostructure formation in BE Ti-24-11 can be seen in Fig. 3; the crystal size is about 15 nm.

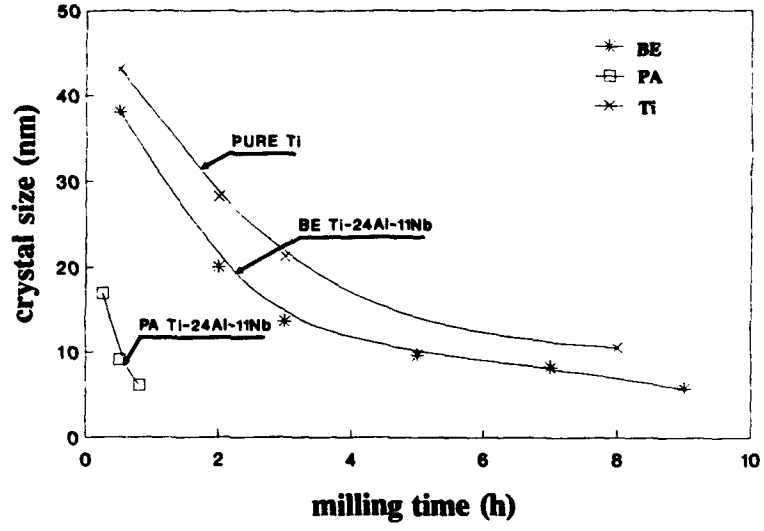


Fig. 2. Crystal size as a function of milling time in pure titanium, blended elemental, and prealloyed Ti-24Al-11Nb powders.

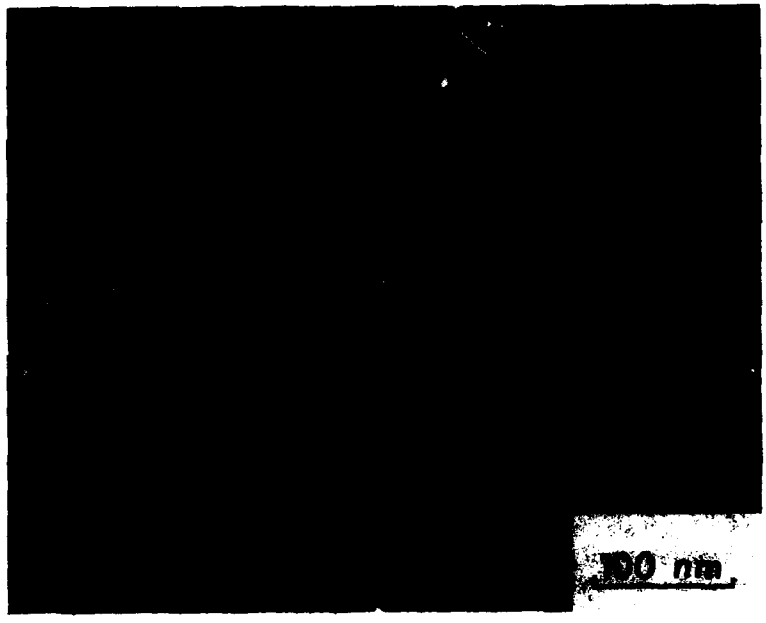


Fig. 3. Transmission electron micrograph showing 15 nm size fcc crystals in blended elemental Ti-24Al-11Nb after 14 h MA.

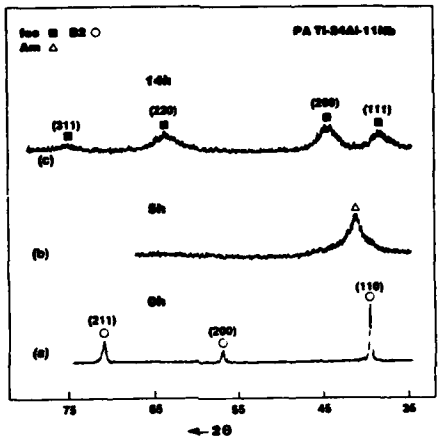


Fig.4. X-ray diffraction patterns of the prealloyed Ti-24Al-11Nb powders as a function of milling time.

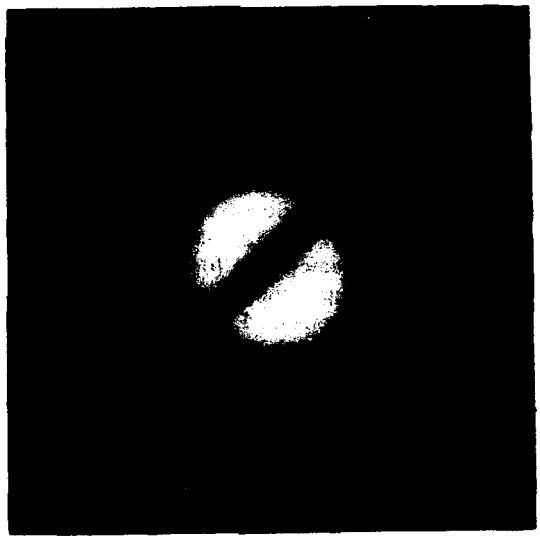


Fig.5. Electron diffraction pattern of the amorphous phase in mechanically alloyed prealloyed Ti-24Al-11Nb after 5 h MA.

Prealloyed Ti-24-11

Fig. 4 shows the x-ray diffraction patterns of prealloyed (PA) Ti-24-11 as a function of milling time. The as-received powder has a B2 (bcc) structure with a = 0.324 nm. The powder contained predominantly the amorphous phase, with a small amount of the B2 phase, after 1 h of milling. A fully amorphous phase was obtained after 5 h of milling; confirmed by electron diffraction (Fig. 5). With further milling time, the amorphous phase eventually transformed fully to an fcc phase with a = 0.423 nm. The gradual reduction in crystal size with milling time for the PA Ti-24-11 is shown in Fig. 2. The phases formed in the PA Ti-24-11 can thus be summarized as:

$$\text{PA (Ti-24-11)B2} \xrightarrow{8h} \text{Am} \xrightarrow{14h} \text{fcc}$$

Discussion

Clear differences have been noted in the structural evolution in the BE and PA Ti-24-11 powders. These differences pertain essentially to the nature of phases produced and the times required for their formation. However, the end product in both cases is the fcc phase.

Mechanical alloying is a solid-state process involving repeated fracture, cold welding and further fragmentation. Due to the heavy deformation involved, the powder particles form lamellae with a small interlamellar spacing and thus the diffusion distances are significantly reduced. This, coupled with the high diffusivity due to the presence of crystalline defects, facilitates alloy formation.

The Ti-Al-Nb ternary equilibrium diagram indicates that B2 is the equilibrium phase in the composition range of interest [12]. Thus, the prealloyed powder shows the presence of only the B2 phase in the as-received condition. However, in the BE powder, the Ti(Al) or perhaps Ti(Al,Nb) solid solution forms in the early stages of milling. This and the B2 phase were observed after 3 h. But 100% conversion to the B2 phase did not occur even after milling for longer times, perhaps due to the slow kinetics of the B2 phase formation. Continued milling of the BE material, to total 10 h, resulted in the formation of a mixture of three phases: $Ti(Al)_{s.s.}$, B2 and fcc, suggesting that the solid solution has probably partially transformed into the fcc phase. Further milling to total 14 h led to the amorphization of the B2 phase, and the preexisting $Ti(Al)_{s.s.}$ has now completely transformed into the fcc phase. In contrast, the B2 phase of the as-received PA Ti-24-11 directly transformed fully into the amorphous phase after 5 h of milling. The amorphous phase in both the BE and PA cases transformed into the fcc phase on continued milling. Thus, the phase observed at the last stages of milling (14 h in PA and 23 h in BE powders) is fcc.

Since the B2 phase in Ti-Al-Nb alloys is known to confer ductility to Ti-24-11 type alloys [17], it is significant that we have synthesized this phase by mechanical alloying starting from elemental powders. The B2 phase has a CsCl-type ordered structure, in which the Ti atoms are at the cube corners of the bcc unit cell, while the (Al+Nb) average atom occupies the body-centered position. Since the atomic scattering factor of titanium is very close to that of the average (Al+Nb) atom, the superlattice reflections of the B2 phase (those for which h+k+l is odd) cannot be observed in the X-ray diffraction patterns. Neutron scattering experiments, currently under progress, will confirm whether the B2

phase produced by MA is in the disordered or in the ordered state.

From the phase formation sequence in both the BE and PA powders, it appears that the B2 phase becomes amorphized with subsequent transformation into an fcc phase. It also appears that in the BE powders, Ti, Al and Nb alloy together to form a solid solution with a hcp structure which also subsequently transforms into the fcc phase. Thus, the fcc phase can form either by the transformation of the hcp phase (perhaps due to introduction of stacking faults) or by crystallization of the amorphous phase. The lattice parameter of this fcc phase remains constant and does not change either with the alloy composition or time of milling and has been found to be extremely stable. Even after annealing the powder containing the fcc phase for one month at 600°C, the fcc phase was still present without any change in the lattice parameter and without decomposing into any other phase(s).

The high thermal "stability" of the fcc phase suggests that this phase is probably formed and stabilized by impurity elements, e.g. nitrogen. An earlier investigation [18] suggested that the fcc phase in mechanically alloyed Ti-Al alloys could be titanium nitride. However, the nitrogen content in our powders has been analyzed to contain a maximum of 5 wt%, even at the longest milling times, when the powder was loaded into the canister in air, and much less (0.3 wt%) when the powder was loaded into the canister in a glove box under a protective argon atmosphere. Complete conversion to the fcc phase was observed to form in both the cases. If TiN or (Ti,Al)N were present it would be anticipated that the nitrogen content would be at least 11wt%, which is not compatible with our results. Clearly further investigations of this phase are necessary.

Irrespective of the origins of the formation of the fcc phase, it is important to note that we achieved our goal of nanostructure synthesis in this alloy. A similar result, based on x-ray diffraction data alone, was also reported earlier [19]. The B2 and the fcc phases in both the BE and PA powders had a grain size of only a few nanometers although with increasing milling time, this B2 phase transformed into an amorphous phase and eventually to an fcc phase. By stopping the milling at an appropriate time, the nanocrystalline B2 phase can be produced by mechanical alloying starting from either BE or PA powders. By optimizing the composition, e.g. Ti-25Al-25Nb, it was possible to get 100% of the B2 phase [20]. Such an alloy is expected to show much higher ductilities than obtained in this alloy class to date when processed by conventional techniques, and work is now being conducted to verify this assumption. If the fcc phase observed in this alloy is not a nitride, it may also have good ductility since it is cubic and it has nanometer-sized grains. This is yet another avenue for profitable exploitation.

Conclusions

Based on the results presented above, the following conclusions can be drawn:

1. Mechanical alloying of blended elemental Ti-24Al-11Nb powders led initially to the formation of a solid solution, partial formation of a B2 (bcc) phase, an amorphous phase, and at still longer times fully an fcc phase.

2. Mechanical alloying of prealloyed Ti-24Al-11Nb powder, which started with the B2 structure, amorphized completely and then transformed totally to an fcc phase.

3. The B2 and fcc phases produced had a nanometer-size grain structure.

Acknowledgements

The authors would like to acknowledge useful discussions with Dr. Garrett Hyde of Bureau of Mines, Washington, DC, and George Vivian of Bureau of Mines, Idaho Falls. The work reported in this paper was supported by the Interior Department's Bureau of Mines under Contract No. J0134035 through DOE Idaho Field Office Contract No. DE-AC07-76ID01570.

References

1. H. Gleiter, Prog. Mater. Sci., 33 (1989) 223.
2. C. Suryanarayana and F.H. Froes, Metall. Trans., A23 (1992) 1071.
3. J.S. Benjamin and T.S. Volin, Metall. Trans., 5 (1974) 1929.
4. F.H. Froes and J.J. deBarbadillo (eds.), Structural Applications of M hanical Alloying, ASM International, Materials Park, OH, 1990.
5. C.C. Koch, in Processing of Metals and Alloys, (ed.) R.W. Cahn, vol.15 of Materials Science and Technology - A Comprehensive Treatment, VCH Verlagsgesellschaft, Weinheim, Germany, 1991, p.193.
6. C. Suryanarayana and F.H. Froes, Mater. Sci. Forum, 88-90 (1992) 445.
7. C. Suryanarayana, R. Sundaresan and F.H. Froes, as Ref. 4, p.193.
8. H.J. Fecht, E. Hellstern, Z. Fu and W.L. Johnson, Metall. Trans., A21 (1990) 2333.
9. C. Suryanarayana and F.H. Froes, J.Mater. Res., 5 (1990) 1880.
10. Y-W. Kim, in High Temperature Ordered Intermetallic Alloys IV, (eds.) L.A. Johnson, D.P. Pope and J.O.Stiegler, Mater. Res. Soc., Pittsburgh, PA, 231 (1991) 777.
11. F.H. Froes, C. Suryanarayana and D. Eliezer, ISIJ Internat., 31 (1991) 1235.
12. R. Strychor, J.C. Williams and W.A. Soffa, Metall. Trans., A19 (1988) 225.
13. D. Banerjee, A.K. Gogia, T.K. Nandy and V.A. Joshi, Acta Metall., 36 (1988) 871.
14. J.H. Perepezko, Y.A. Chang, L.E. Seitzman, J.C. Lin, N.R. Bonda, T.J. Jewett and J.C. Mishurda, in High Temperature Aluminides and Intermetallics, (eds.) S.H. Whang, C.T. Liu, D.P. Pope and J.O.Stiegler, TMS, Warrendale, PA, 1990, p. 19.
15. C. Suryanarayana and D.S. Lee, Scripta Metall. Mater., 26 (1992) 919.
16. B.D. Cullity, Elements of X-ray Diffraction, Addison-Wesley Pub. Co., Inc., Reading, MA, second ed., 1978.
17. R.G. Rowe, as Ref. 14, p. 375.
18. W. Guo, S. Martelli, F. Padella, M. Magini, N. Burgio, E. Paradiso and U. Franzoni, Mater. Sci. Forum, 88-90 (1992) 139.
19. T. Christman and M. Jain, Scripta Metall. Mater., 25 (1991) 767.
20. Guo-Hao Chen, C. Suryanarayana and F.H. Froes, Scripta Metall. Mater., 25 (1991) 2537.

COMPLEX PROCESSING OF LOW-GRADE SPONGY TITANIUM INTO HIGH EFFECTIVE POWDERY PRODUCTS

V.S.Ustinov, V.M.Anokhin, V.V.Voleinik,
V.A.Drozdenko, V.M.Prozorov
Titanium Institute, Ukraine

Abstract

Titanium Institute has developed the complex system of low-grade spongy titanium processing into the powder products based on two technologies: electrolysis with the soluble anode and mechanochemical grinding. Articles manufactured of electrolytic and mechanochemical powders are characterized by high strength, corrosive resistance, can be welded and treated on machine tools and are biologically neutral.

Introduction

When producing spongy titanium by magnesium-thermic reduction the substantial part in the product is composed by the low-grade material, which is unfit by its properties to using in the charge for melting the ingots of production alloys. This low-grade spongy titanium is used at present mainly in ferrous metallurgy for alloying and deoxydation of steel and melting high-percent ferrotitanium parallel with off-grade waste of titanium alloys. Such use of the product, in which the content of titanium makes up 96-98%, cannot be recognized as effective. Titanium Institute has developed and successfully uses at the pilot metallurgical plants the complex system of processing this product into titanium powders, powders of refractory titanium compounds and their products, said system being based on three original technologies: electrolytic refining, mechanochemical grinding, plasma method. There can also be used the technology of hydrogenation-grinding-dehydrogenation which allows to convert the excess quantities of the most large-sized fractions of spongy titanium.

Electrolysis with soluble anode

The initial material is divided into 3 fractions: -70+25; -25+5 and -5 mm. The basic method of processing -70+25 mm and -25+5 mm fraction of spongy titanium is electrolysis. The process is

Titanium '92
Science and Technology
Edited by F.H. Froes and I. Caplan
The Minerals, Metals & Materials Society, 1993

carried out at 993-1053 K in the molten mixtures of sodium and potassium chlorides containing 1.4-2.8% of dissolved titanium in the form of titanium dichloride and titanium trichloride. Electrolysis is followed by grinding cathode precipitate consisting of crystalline titanium aggregations and solidified electrolyte (about 50% by mass), its leaching in the solutions of hydrochloric acid, washing from salts residues with water, additional disintegration in titanium mills, wet screening, and completed with drying the powders more coarse than 0.18 mm and packing the products.

The technology of electrolysis developed in the late sixties and in the early seventies (1) was subsequently improved on the base of using the principles of developed process of the volumetrical electrochemical refining (2), that allowed without the supplementary expenditures to increase the output of electrolytic cell and the quality of products even when using for preparation of electrolyte the crude salt instead of high-purity salt used before.

Initially during assembly of the electrolytic cell, spongy titanium of -70+25 mm fraction is charged into the anode containers while the material of -25+5 mm fraction is charged once a day in the course of electrolysis. Usually when the duration of cyc lic process is 90-120 days mass relation of two said fractions after electrolytic refining makes up from 1:2 to 1:3. At the relation 1:2 in the raw material part of coarse -70+25 mm fraction is processed by hydrogenation.

Mechanical processing

The process of mechanochemical processing of low-grade spongy titanium of less than -5 mm fraction is based on the presentation of spongy titanium as the product of "incomplete sintering" of the particles formed during magnesium-thermic reduction of titanium tetrachloride. In order to separate ferric inclusions there are introduced into the system the operations of magnetic separation and acidic treatment at 353 K in 1% or 3% solutions of hydrochloric acid, classification, re-grinding of -1 mm fraction in the ball mills and division into narrow fractions. The technology is economically effective, without waste and low-power intensive (3).

Properties of powders

Table I reveals the content of the major impurities in electrolytic and mechanochemical titanium powders. Hardness index is established only for coarse and average electrolytic powders (not more than 100-155 HB) and for higher grades of coarse and average mechanochemical powders (up to 180 HB). Besides that, in the electrolytic powders there is limited the content of silicon (up to 0.02-0.04%), carbon (up to 0.01-0.03%), while in mechanochemical ones - hydrogen (up to 0.1-0.9%).

Some technological properties of mechanochemical and electrolytic powders of -0.63+0.18 and -0.18 mm fraction that are basically used when producing structural articles are presented in Table II.

Table I. MAIN IMPURITIES CONTENT IN ELECTROLYTIC AND MECHANOCHEMICAL TITANIUM POWDERS

Powders group by particle size (fraction, mm)	Powder type	Powder grade	Impurities fraction of total mass,%			
			Fe	Cl	H	O
Coarse (-3+1; -5+0.63; -1+0.63 mm)	Electrolytic	ПТЭК-I ПТЭК-2	0.02-0.10	0.05-0.08	0.015-0.04	0.04-0.08
	Mechanochemical	ПТХ-I ПТХ-2	0.3-0.8	0.06-0.08	0.05-0.08	0.10-0.30
Medium (-1+0.18-0.63 +0.18 -0.45+0,08 mm	Electrolytic	ПТЭС-I ПТЭС-0 ПТЭС-2	0.02-0.10	0.03-0.08	0.02-0.04	0.04-0.08
	Mechanochemical	ПТХ-3 ПТХ-4 ПТХ-5	0.3-1.0	0.07-0.12	0.05-0.12	0.10-0.45
Fine (-0.18 mm)	Electrolytic	ПТЭМ-I ПТЭМ-2	0.02-0.20	0.05-0.15	0.02-0.05	0.10-0.30
	Mechanochemical	ПТХ-6 ТПАТ	0.08-1.9	0.09-0.20	0.08-0.30	0.5-1.00
Dispersed (-0.08 mm)	Electrolytic	ТПЭ-I ТПЭ-2	0.9-1.2	0.10-0.15	not detected	not detected
	Mechanochemical	ПТХ-7 ТПЭ-I ТПЭ-2	0.9-1.8	0.09-0.15	0.08-0.20	not detected

Table II Powders Technological Properties

Fraction mm	Powder type	Apparent density g/cm^3	Tap density g/cm^3	Flow s	Specific surface m^2/2
-0.63 +0.18	Mechano-chemical	0.75-1.20	0.80-1.40	none	0.05-0.07
	Electrolytical	1.40-1.70	1.60-1.95	none	0.03-0.05
-0.18	Mechano-chemical	0.70-1.10	0.80-1.50	none	0.15-0.21
	Electrolytical	1.75-1.80	1.75-2.00	37-40	0.12-0.17

Bulk density, density of shaking and flowability are increased by 6-15% if the powder was subjected to additional disintegration or spinning in the ball mill (4).

Electrolytic powders are the most qualitative of all titanium powders; they possess the greatest ductility, are characterized by lower shrinkage during sintering and allow to produce more dense products. By their mechanical properties and chemical composition they are close to the high-grade spongy titanium.

Application of powders

Production of structural parts. Properties of the parts manufactured of electrolytic powders are close to the properties of the parts of cast metal of BTI-0 grade. Breaking strength limit makes up 350-450 MPa and elongation constitutes 10-15%. When alloying with aluminium and molybdenum powders ultimate strength increases approximately twice at retaining ductility. During testings the parts withstand vibration with the frequency up to 1000 Hz and single impacts with acceleration up to 100 g. Electrolytic titanium powders are used for production of bushings, flanges, covers, sleeves, breakers, etc. Moreover, the cost of parts is decreased by 40-45% as compared with their production from the tube or rod of BTI-0 alloy. Each ton of processed powder saves 2-5 tons of titanium rolled stock and labour productivity of the worker at the plants of titanium powder metallurgy is 1.3-1.5 times higher than when manufacturing parts of cast metal (1,4).

Mechanochemical powders of -1+0.25 mm fraction are used for production of the articles only in those cases when high requirements for ductility are not imposed. Particularly, there is organized large-scale production of titanium rings of Rashig rings type (diameter - 15,25,50 and 80 mm, height - 15,25,50 and 70 mm respectively). In chemical industry in a number of productions rectifying and distilling towers are of titanium with

the packing of such titanium rings. Replacement of ceramic rings by titanium ones allowed to increase their strength and, respectively, service life between the repairs of the towers, as well as to increase the output of the latter (3).

Production of charges and corrosion-resisting compositions. The major mass of fine and dispersed titanium powders is used not for production of sintered products, but as the components of charge in manufacturing refractory compounds, fractional materials, metallopolymer anticorrosive compositions and magnitoabrasive materials. Using the method of self-extending high-temperature synthesis (SHS-process) one can produce titanium carbide containing 79.2-79.60% of titanium, 18.12-19.42% of fixed carbon and 0.18-0.28% of free carbon (5) with economical efficiency. Moreover, the best results are achieved when using titanium powders more fine than 0.1 mm. Anticorrosive titanopolymer compositions are prepared by using epoxide resin of ED-20 and ED-16 type and titanium powder of less than 0.25 mm size in relation 1:1. Plastifier is dimethyl phthalate or dibutyl phthalate, hardener - polyethylene polyamine. Thickness of coating - about 1.0-1.5 mm. This anticorrosive coating (6) has a number of advantages: high stability in the most corrosive media of chemical industry, for example, in solutions of nitric, sulphuric and acetic acids, high adhesion to concrete and steel, higher mechanical strength and ductility. Up to the present time over a million square meters of the surface of various equipment and constructions has been protected with such a composition at the least cost price as compared with other coatings (4).

Tabletted powders. Mechanochemical powders of the coarse fractions are used mainly in the form of tablets from 20 up to 100 mm in diameter and of 20-30 mm height in ferrous metallurgy. Thus only part of low-grade spongy titanium not conversed into the powders of average or fine fractions is supplied to ferrous metallurgy. Besides that due to high density of tabletted titanium and relatively small size of tablets burning loss during their use is approximately 1.5 time lower than during the direct use of spongy titanium. Dosage and mechanization of tablets introduction into the molten steel is easily carried out. In practice of ferrous metallurgy of a number of European companies there are by now widely used during several years tabletted mechanochemical titanium powders, produced by pilot plants of Titanium Institute.

Titanium articles of higher purity. One of the most perspective trends of application of coarse electrolytic powders may be electronics, particularly, production of targets for various purposes. When carrying out electrolysis at a special condition from the low-grade spongy titanium there is possible production of material, in which after melting the fraction of total mass of a sum of the most harmful impurities (Cl, Fe, Cr, Si, P, Na, K, Ca, Mg) makes up less than 0.1%. Titanium Institute is ready to cooperate with the foreign companies interested in development and application of similar materials that, apparently, could be also used as one of the components for producing super conductors of Ti-Nb alloys and alloys with Ti-Ni shape memory as well as for production of TiN, $TiSi_2$ and other high-purity compounds.

Titanium Hydride production. At present at the pilot plants of Titanium Institute there is produced titanium hydride as serial large-sized powder of ПТЭК-I grade with the fraction of hydrogen total mass 3.7-3.9% (3).

Electrolytic titanium hydride shows high purity and is rather effectively used as hydrogen generator, particularly, for annealing of clock filaments (7) and as an addition agent for the charge of various metals powders, which activates the process of sintering. Ground titanium hydride can be used as raw material for production of solid materials - carbides, borides, nitrides and silicides of titanium (8).

Porous sintered articles. Usage of both electrolytic and magnesium-thermic powders of various fractions for manufacturing porous articles is rather effective. There is developed and assimilated the technology of manufacturing the articles in the form of tubes, disks, sleeves, rings and beakers, recommended for application in the chemical, textile, metallurgical and other branches of industry (1,3,4).

Porous elements are used as filtering elements in various constructions of cartridge filter and aerators in the units of regeneration and beneficiation by flotation and in the units of biological cleaning of waste water (9). They are used as filtering elements in Bush filters and drain units, as gas absorbers fire obstacles and moisture and oil separators. The elements can be welded by argon-arc, resistance and diffusion welding and treated by metal-cutting machine tools. In spite of high cost as compared with traditional materials titanium elements are used with great economic efficiency thanks to high strength (from 1-4 MPa during testing of large-sized pipe filters by hydraulic pressure up to 60 MPa during axial compression for the filters of acetylene pressure regulators), exceeding resistance to corrosion, biological inertness, low density (2.3-3.1 g/cm^3), the possibility of repeated many times regeneration, safe keeping of the properties of filtered solutions, decrease of filtered materials losses, the possibility of increasing velocity and pressure during filtration and aeration.

Depending on size of initial powder and parameters of compression the permeable materials from electrolytic or mechanochemical titanium powders have the main diameter of pores from 25 up to 250 mu, 30-50% porosity, minimum coefficient of permeability as to various groups from 0.5 up to 45 Pm^2.

Production of titanium compound powders by plasma technology. Use of original plasma technology allows to convert some dispersed products of spongy titanium processing into the powders of titanium compounds - TiN, TiCN.

Particularly, titanium nitride powder is a new material having no analogues as to complex of attributes: particles size, content of impurities and specific surface value. If the size of polydispersed particles is 0-20 mu, the specific surface constitutes 1-5 m^2/g (existing types of powdery TiN possess either very high - more than 30 m^2/g, or very low specific surface - 0.05-0.1 m^2/g). Fraction of total mass of nitrogen in nitride

makes up 16-19%, of oxygen - less than 1.5%, of hydrogen -less than 0.3%; the content of other impurities may not exceed their concentration in the powders of ПТЭК-I grade.

Thus, at complex processing of low-grade spongy titanium there is created practically wasteless technology for manufacturing various products. At the same time it is to be noted that revealed requirements of domestic market as to some types of products are still behind the development of production.

Titanium Institute being both development institution and a producer of the main part of titanium powder production can offer titanium powders and their products for realization at the foreign market. On order of interested companies it can carry out research work on development of technology and manufacturing products with the given properties as well as organizing their output and supply.

References

1. Ustinov V.S. et al., Powder Metallurgy of Titanium (M.: Metallugia, 1981), 248.

2. Voleinik V.V. "About Volumetric Electrochemical Refinement of Transaction Metals and Their Metal-Like Compounds", Electro chemistry,XVII, vol11 (1981), 1613-1620.

3. Olesov Yu. et al., Titanium Hydrometallurgy (M.: Metallurgia, 1983), 120.

4. Vorobiov B.Ya. et al., Production of Articles from Titanium Products (Kiev: Technika, 1976), 174.

5. Processes of Combustion in Chemical Technology and Metallurgy (Chernogolovka: OIHV AN USSR, 1975), 35-39.

6. Vazhenin S.F. et al., Titanium for Equipment of Food Industry (Kiev: Technika, 1973), 120.

7. Olesov Yu.G. et al., "Testing of Apparatus and Process Flow Diagram of Titanium Hydrogenation on a Pilot-Commercial Scale", Non-Ferrous Metals, 9 (1970), 48-51.

8. Antonova M.N. et al.,"Investigations of Titanium Carbides and Carbohydrides of Intermediate Composition", Refractory Carbides, (Kiev: Naukova Dumka, 1970).

9. Anokhin V.M. et al., "Usage of Porous Titanium Articles in the System of Water Preparation and Effluents Cleaning", Industrial Power Engineering, 4 (1986), 21-23.

CHARACTERISTICS OF HIGH PURITY TITANIUM POWDER BY HDH PROCESS

E. Fukasawa, R. Murayama, and W. Kagohashi

Toho Titanium Co, Ltd., 3-3-5 Chigasaki, Chigasaki-shi, Kanagawa-ken, Japan

1.INTRODUCTION

Recently, the powder metallurgy(P/M) of titanium has been considered as a cost effective processing with emphasis on near-net shape[1-2].
Among titanium P/M techniques, the blended elemental(BE) method has been reported in many applications because of its flexibility of alloy composition and economic advantage[3-4]. In many applications, the quality of titanium powder as a starting material is very critical. Especially, oxygen and chlorine as impurities in the titanium powder can strongly influence mechanical qualities of P/M parts. In order to meet the demand for high quality powder, an extra low impurity titanium powder has been needed.
We have developed an extra low chlorine and low oxygen titanium powder by the hydride-dehydride(HDH) process which is highly optimized under high quality control.
In this paper, the above titanium powder was evaluated about its characteristics such as flowability, compressibility, green strength and so on.

2.EXPERIMENTAL PROCEDURE

2.1 Materials

The powders used were produced commercially by the mentioned HDH process. Chemical compositions of the powders studied are tabulated in Table 1.

Table 1. Chemical compositions and bulk densities of the titanium powders used.

	Chemical Composition(wt%)							Bulk Density
Type	Ti	Fe	Cl	O	H	C	N	(g/cm^3)
TC-150	bal.	0.02	<0.002	0.11	0.01	0.01	0.01	1.8
TC-151	bal.	0.04	<0.002	0.20	0.01	0.01	0.01	1.7
TC-152	bal.	0.07	<0.002	0.29	0.02	0.01	0.01	1.5

Titanium '92
Science and Technology
Edited by F.H. Froes and I. Caplan
The Minerals, Metals & Materials Society, 1993

In Table 1, Type TC-150 is a typical high purity titanium powder having an extra low chlorine and low oxygen content. This oxygen content is close to that of sodium reduced titanium sponge fine. Type TC-151 and TC-152, having higher oxygen content, were especially produced to compare with TC-150 in characteristics of hardness of powder particles, compressibility of powders, and green strength. The oxygen content level of TC-151 had seemed to be typical as a standard HDH powder before TC-150 appeared.
A sieve analysis and flow rate of the titanium powders used are listed in Table 2. Also, Figure 1 shows SEM micrograph of the powder(TC-150).

Table 2. Sieve analysis and flow rate of the powders used.

Type	Weight Percent Retained(wt%) +150	-150+106	-106+75	-75+45	-45μm	Flow Rate (seconds/50gs)
TC-150	0.1	33.3	32.3	29.5	5.0	41
TC-151	0.2	37.6	33.1	24.8	4.3	-
TC-152	0.2	32.0	33.7	24.2	9.9	-

As described in Table 2, these powders have a similar particle distribution. Also powder particles of TC-150 are angular in shape like other HDH powders.

2.2 Methods

As fundamental characteristics of the powders, flowability, compressibility, green strength and densification by sintering were investigated. The hardness of the powder particle itself was also measured in order to confirm its effect on these characteristics. Each characteristic was measured by the following procedure:

(1)Flowability of powder

Flowability was determined by Carr's method[5]. Along the method, flowability of the powder(TC-150) was totally evaluated by using four properties, angle of repose, compression rate, angle of spatula and coefficient of uniformity. Each property was measured by using an all-in-one type apparatus, as shown in Figure 2.

(2)Hardness of powder particles

Micro-Vickers hardness of powder particles was measured. Each measurement was carried out by pressing the central portion of twenty powder particles ranging from -150+106μm diameter, molded in a resin. The hardness was determined by averaging the twenty-particles hardness measured.

(3)Compressibility of powders

Compressibility was evaluated in accordance with The Japan Society of Powder and Powder Metallurgy standard (JSPM1-64), "Compressibility Test of Metal Powders," by the use of floating die pressing at given pressures of 98MPa to 686MPa. Compressibility was expressed as relative density of the theoretical. In this method, the green compact is cylindrical and has a diameter and height of 11.3mm, respectively. When pressing the powders, a die wall lubrication(lubricant, zinc stearate) was adopted.

(4)Green strength

Green strength was evaluated by the Rattler test which provides information on the abrasion resistance of a green compact and the ability to retain its shape(edge stability). The Rattler test is specified in JSPM4-69, "Method for Determination of Green Strength by Rattler Test,"[6] using five green compacts pressed at same given pressure. In the test, the green strength is reported as weight loss(%). The green compacts were pressed at 294 MPa to 686MPa of applied pressures as the compressibility test above.

(5)Densification by sintering

Sintered densities were measured by sintering green compacts in a vacuum at 1300°C for two hours. The green compacts were pressed from 98 MPa to 490MPa by a die pressing. Densification by sintering was expressed as sintered density with green density.

3.RESULTS AND DISCUSSION

3.1 Flowability of powder

Table 3 lists results of flowability evaluation. Consequently, the flowability of TC-150 is fairly good. This means that this powder requires no special attention in its handling.

Table 3. Flowability of the high purity titanium powder(TC-150).

Angle of Repose (degree)	Compression Rate(%)	Angle of Spatula (degree)	Coefficient of Uniformity	Flowability
40	17	48	2	**fairly good**

3.2 Hardness of powder particles

Figure 3 gives hardness of powder particles adopted. As shown in Figure 3, the higher the oxygen content in the powder, the higher linearly the hardness.
It is well known that oxygen in commercially pure titanium has a strong effect on hardness of the titanium itself. Kusamichi et al. reported that oxygen as an impurity in titanium could affect approximately twice in content(ppm) as strong as iron[7]. According to this result, increase of the hardness in Figure 3 can be explained mainly by the effect of oxygen in the powders. About work hardening of the particles, there was no evidence because of no significant change in hardness after annealing the powders in an inert gas at 670°C for ten hours.
As a result, TC-150 containing 0.11wt% oxygen is a softer powder. This will reflect good effects on other characteristics, for example, compressibility.

3.3 Compressibility of powders

Figure 4 shows the comparison of compressibility among three kinds of powders used. Through 98MPa to 688MPa of compacting pressure, TC-150 showed better compressibility. At 495MPa, the relative density of TC-150 was 86% of the theoretical. This compressibility will be close to that of sodium reduced titanium sponge fine.

Generally, the compressibility of a powder is influenced by several factors, inherent hardness of the metal, particle shape, internal porosity, particle size distribution, and so on. Among three powders used, the most affecting factor will be the inherent hardness of the titanium particles. As described above, the inherent hardness of TC-150 particle is lower. Therefore, the powder would be more compressible during pressing.

3.4 Green strength

Figure 5 illustrates the effect of compacting pressure on green strength of the compacts. As TC-150 gave weight loss of less than 1% at 490MPa, it would be satisfactory to maintain size and shape during handling prior to sintering.
Because the strength of green compacts results mainly from mechanical interlocking of particle surface irregularities, particle shape will be the most important factor contributing to green strength. Accordingly, in comparison with the powders having different oxygen content, no significant difference in green strength was seen.

3.5 Densification by sintering

Figure 6 gives sintered densities versus compacting pressures. With increase in the compacting pressure, the sintered densities also increased similar to the green densities. At 490 MPa, the sintered density was 4.1g/cm^3.From this result, it will be understood that TC-150 can reach higher density after sintering in a vacuum only.
In order to increase the sintered density of the TC-150, fine powder(-45μm) was added to the TC-150. The fine powder had also an extra low chlorine(<0.002wt%) and low oxygen(0.23wt%). Figure 7 shows the effect of the fine powder addition on the sintered densities of the mixtures. As illustrated in the figure, the sintered density increased considerably by adding the fine powder. In particular, adding the fine powder up to 30wt% resulted in remarkable increase of the density. At 30wt% of the fine powder addition, the sintered density was 94% of theoretical density. On the other hand, the green density of the mixed powder decreased significantly with the addition of the fine powder. At 100wt% of the fine powder, the green density was only 80% of the theoretical. However, up to 30wt% of the addition, the green density was decreased slightly. The green density of the mixture was about 85% at 30wt% of the addition.
Though there are numerous variables that can affect sintered density, the better compressibility of TC-150 will reflect this characteristics also.

4. CONCLUSIONS

(1)The high purity titanium powder including the extra low chlorine and low oxygen is being produced commercially by the HDH process.
(2)The powder(TC-150) gives satisfactory flowability and green strength.
(3)This powder is more compressible than other HDH powders. By using this powder as a starting material, denser green and sintered compacts can be obtained.

REFERENCES

(1)F.H.Froes and D.Eylon, "Titanium Net Shape Technologies," TMS-AIME Publications, Warredale, PA (1984), pp.1-299.

(2)F.H.Froes and J.E.Smugeresky, "Powder Metallurgy of Titanium Alloys," TMS-AIME Publications, Warrendale, PA (1980), pp.1-308.

(3)M.Hagiwara, Y.Kaieda, and Y.Kawabe, "Improvement of Mechanical Properties of Blended Elemental ∂-ß Titanium Alloys by Microstructural Modification," Proceedings of the 1986 International Conference on the Titanium Products and Applications, TDA, OH, (1987), pp.850-858.

(4)M.Hagiwara, Y.Kaieda, and Y.Kawabe, "The Relationship of Chlorine level /Microstructure/Mechanical Properties for Blended Elemental P/M Ti-6Al-4V Compacts," Proceedings of Sixth World Conference on Titanium, Cannes, France, (1988), pp.673-678.

(5)R.L.Carr, "Evaluating Flow Properties of Solids." Chemical Engineering, Jan. 18, (1965), pp.163-168.

(6)The Japan Society of Powder and Powder Metallurgy standard, "Method for Determination of Green Strength by Rattler Test," JSPM1-69, (1985), pp.8-9.

(7)H.Kusamichi et al., "Study on Impurities in Commercially Pure Titanium," Kobe Steel Technical Report, 14, (1964), pp.173-188.

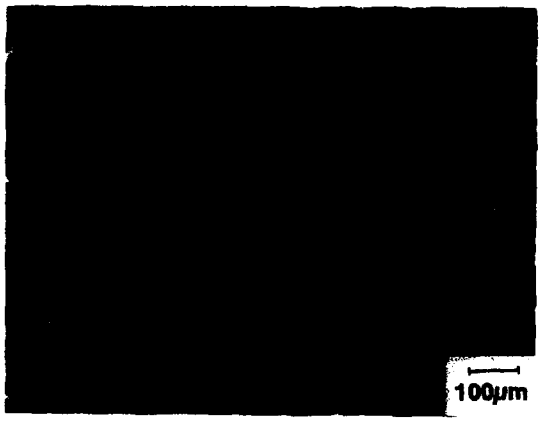


Fig.1 Scanning electron micrograph of the powder(TC-150).

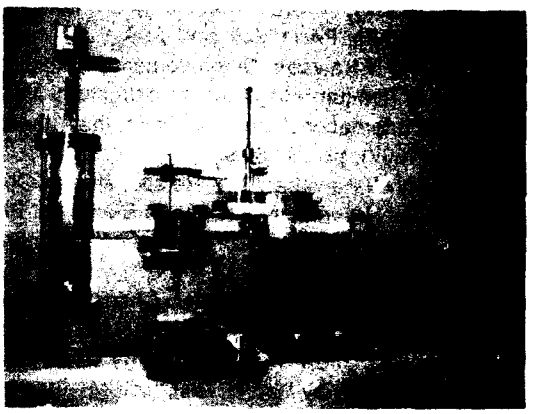


Fig.2 All-in-one type apparatus for flowability evaluation.

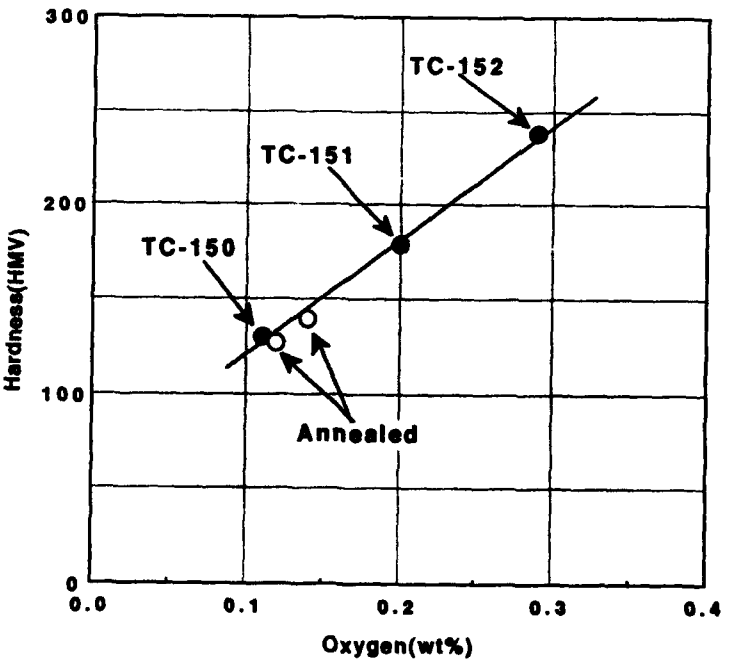


Fig. 3 Hardness of particles versus oxygen contents in powders.

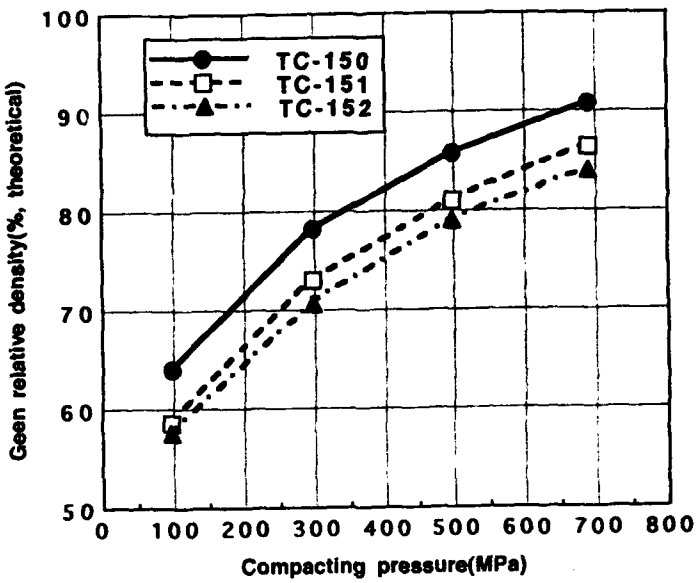


Fig. 4 Comparison of compressibility among the powders used.

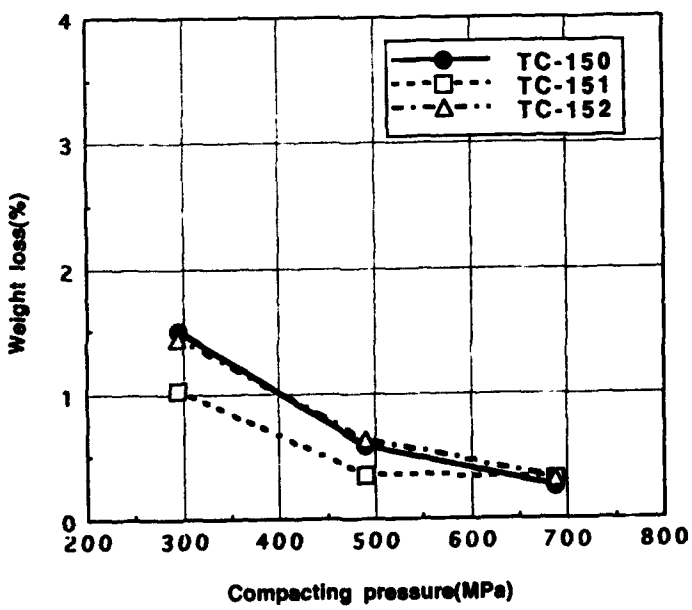


Fig. 5 Effect of compacting pressure on green strength of the compacts.

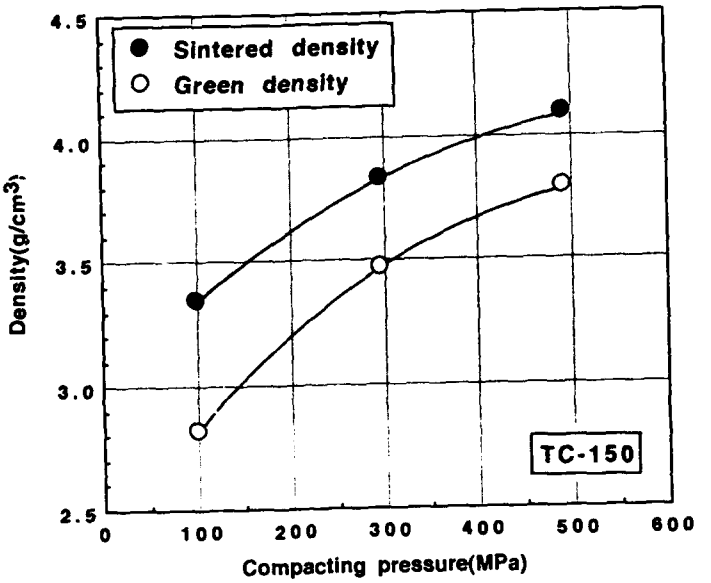


Fig.6 Effect of compacting pressure on sintered densities.

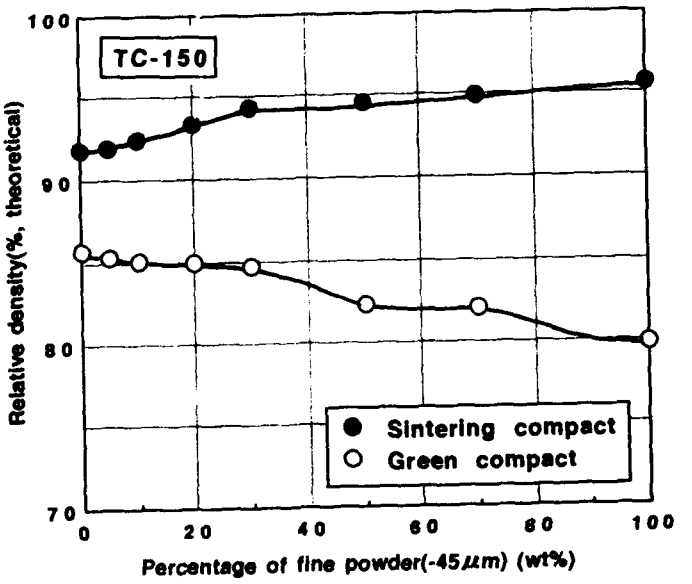


Fig.7 Effect of fine powder addition on sintered densities.

FABRICATION AND STUDY OF AN ODS β TITANIUM ALLOY

BY MECHANICAL ALLOYING

Régis Baccino, Didier Brenet, Frédéric Moret

CEREM / Laboratoire de Génie des Matériaux
CEA / CENG - 85X - 38041 Grenoble Cedex

Abstract

This study of the Y_2O_3 dispersion strengthening of a β titanium alloy by mechanical alloying has shown that the technique is sufficiently mastered to lead to the desired microstructure but that the chosen metallurgical base (Ti-Mo-Al) is not favourable. The direct introduction of yttrium is probably better to reduce oxygen content.

Mechanical alloying of titanium alloys

β titanium alloys have good forming capabilities and high mechanical properties at room temperature but a poor creep resistance at high temperature. Oxide dispersion strengthening of these alloys by mechanical alloying is interesting for weight reduction in aeronautic turbomachines (1).

The dispersion of rare earths oxides (Er, La, Ce, Y) in titanium alloys by rapid solidification processes (precipitation from the supersaturated matrix) has been the object of numerous recent works (2) and of an European project (BRITE EURAM 0275). A few works were concerned by improving the dispersion and the stability of rare earths oxides by mechanical alloying (3)(4) but none of them was aimed towards the dispersion of oxide powders by this technique.

Conventional elaboration and properties of alloys in Ti-Mo-Al system

Ti-Mo-Al system

Ti-Mo-Al system has been studied by Hida and Weissmann in 1976 (5). The Ti-14%Mo-9%Al (wt%) composition allows hardening by precipitation of Ti_3Al phase while avoiding brittle phases ω and β_2 (fig.1). Starting from a laminated alloy, Hida and Weissmann reported the existence of an optimal compromise between yield strengh and ductility after staged thermal treatments inducing Ti_3Al precipitation (at room temperature, yield strength=1500 MPa,

Titanium '92
Science and Technology
Edited by F.H. Froes and I. Caplan
The Minerals, Metals & Materials Society, 1993

elongation=4%, after thermal treatment: 960°C/30 mn - water quench - 800°C/30 mn - water quench - 600°C/24 h - water quench).

Mechanical properties

Samples of Ti-14%Mo-9%Al (wt%) have been cast by CEZUS or densified by HIP or HIP plus extrusion after rotating electrode atomization of the cast alloy. Thermal treatments suggested by Hida and Weissmann have been applied to the ingots, the HIP densified and the extruded samples.

The microstructures observed by S.E.M. and the obtained compositions appeared to be equivalent to those announced by these authors. The materials having not been milled, the oxygen content was lower than 2000 wt. ppm.

Mechanical properties have been measured at room temperature on cylindrical samples (4 mm in diameter).

None of the processing conditions allowed us to obtain any ductility. Fractography showed that the rupture was both intergranular and intragranular. No microstructural anomaly linked to the rupture was detected. These zero ductilities were also observed on the milled materials described in the following paragraph.

The lack of information on the precise conditions of the primary material elaboration used by Hida and Weissmann could constitute an interpretation of the difference between our results and those described by these authors.

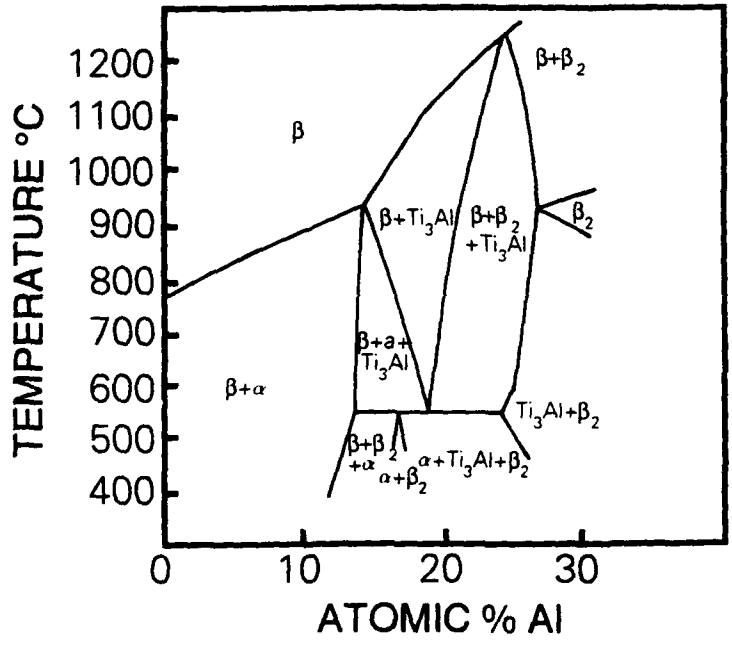


Figure 1 - Pseudo-binary equilibrium diagram (Ti-7 at.%Mo)-Al

Experimental study of the mechanical alloying of Ti-Mo-Al alloys + Y_2O_3

Processing conditions

Initial powders were either in elemental form (rotating electrode atomized Ti, Mo CERAC, Al PECHINEY, Y_2O_3 CERAC) or in pre-alloyed form (rotating electrode process).

Milling has been studied either with an orbital mill, a ball mill or an attritor. All of the operations, milling, handling and canning of the powders have been performed in an argon glove box with controlled residual oxygen pressure. A milling additive such as cyclohexane (0.5 wt%) or stearic acid (1 wt%) has been used.

Table I: Analysis of the elements whose content is modified by mechanical alloying (as-milled Ti-14%Mo-9%Al powders - before hot degassing).

Analysis (wt%)	H	O	C
Ball mill	0.099	0.28	0.55
Attritor	-	0.36	0.95

H, O and C contents of the as-milled powders (Table I) are directly connected to the quantities of milling additive. So, the elaboration doesn't bring any other contamination. In particular, the iron content doesn't vary perceptibly.

The development of the mechanical alloying operation is concerned with different parameters of the process (milling energy, masses and dimensions ratios between beads and powder, initial powders nature, milling duration, evolution of the efficiency of the additive, level of homogeneity wanted for the repartition of the alloy constituants). Only ball mill and attritor processing of elemental powders allowed us to obtain a permanent milling rate leading to homogeneous powders.

After milling, X-rays diffraction showed the presence of pure phases Ti, Mo, and Al. The phases α-Ti, β-Ti, Ti_3Al and the carbides only appeared after the 950°C/10 hours degassing. This vacuum degassing reduces hydrogen content down to 30 ppm.

After canning, powders were densified by hot isostatic pressing at 1100°C (β domain) or 940°C (β + Ti_3Al domain) or extruded after pre-heating at 940°C.

Microstructures

Without oxides additions, the observed phases after densification are β-Ti, Ti_3Al and carbides, (mainly TiC). TiC phase is found within grain boundaries of the β-Ti matrix. Some massive precipitates are also observed. Ti_3Al precipitation is both inter- and intragranular. In the alloy heated in the β+Ti_3Al domain, fine Ti_3Al polyhedric precipitates (2-5 μm) appear inside the grains.

The main differences in the observed structures between the samples are linked to the milling conditions.

The attritor, more energizing, gives a more homogeneous structure (finer grains and TiC precipitates).

The stearic acid additive (1 wt%) favours an extremely fine grain size of about 10 μm compared to 30 μm with 0.5 wt% cyclohexane. The higher content of TiC in the case of stearic acid explains the better anchoring of the grain boundaries.

In all cases, these grain sizes are conserved during the thermal treatments.

Under identical processing conditions, oxide addition doesn't modify the obtained microstructures. TEM observations of the densified material show a dispersed oxide in the form of 20-100 nm spherical precipitates with 200-300 nm spacing (fig.2).

Conclusions

- Under the different processing conditions that we have experienced (casting, powder metallurgy by HIP or extrusion, HIP after milling), the Ti-14%Mo-9%Al (wt%) alloy has never shown any ductility contrarily to the results reported by Hida and Weissmann. These results could be specific of the laminated material used by these authors.
- The Ti-14%Mo-9%Al (wt%) β-alloy with and without 20-100 nm Y_2O_3 dispersoids reinforcement (1 vol%) has been successfully produced by attritor or ball mill mechanical alloying, followed by extrusion.
- The growth of β-Ti, Ti_3Al and carbides phases doesn't occur during milling but during the subsequent thermal treatments.
- A decrease of dissolved oxygen content may be obtained by directly introducing the rare earth instead of the oxide.
- The processing parameters, in particular the milling mode, the quantity and the nature of the additive, have a major influence on the microstructure through the dispersion and the quantity of carbides that they impose.

Acknowledgements

This work has been done with DRET support under the contract n°88/125.

References

1. Y. Honnorat, (Paper presented at the 6th World Conf. on Titanium, Cannes, France, 6-9 June 1988), IV
2. M.F.X. Gigliotti, G.E. Wasielewski, and R.G. Rowe, (Paper presented at the 6th World Conf. on Titanium, Cannes, France, 6-9 June 1988), II, 861
3. R. Sundaresan, F.H. Froes, (Paper presented at "Modern Developments in Powder Metallurgy", Orlando, 5-10 June 1988), 429
4. R. Sundaresan, A.G. Jackson, F.H. Froes, (Paper presented at the 6th World Conf. on Titanium, Cannes, France, 6-9 June 1988), II, 855
5. M. Hida, S. Weissmann, Metall. Trans. A, 6A (1976), 1541
6. T. Hamajima, S. Weissmann, Metall. Trans. A, 6A (1976), 1536

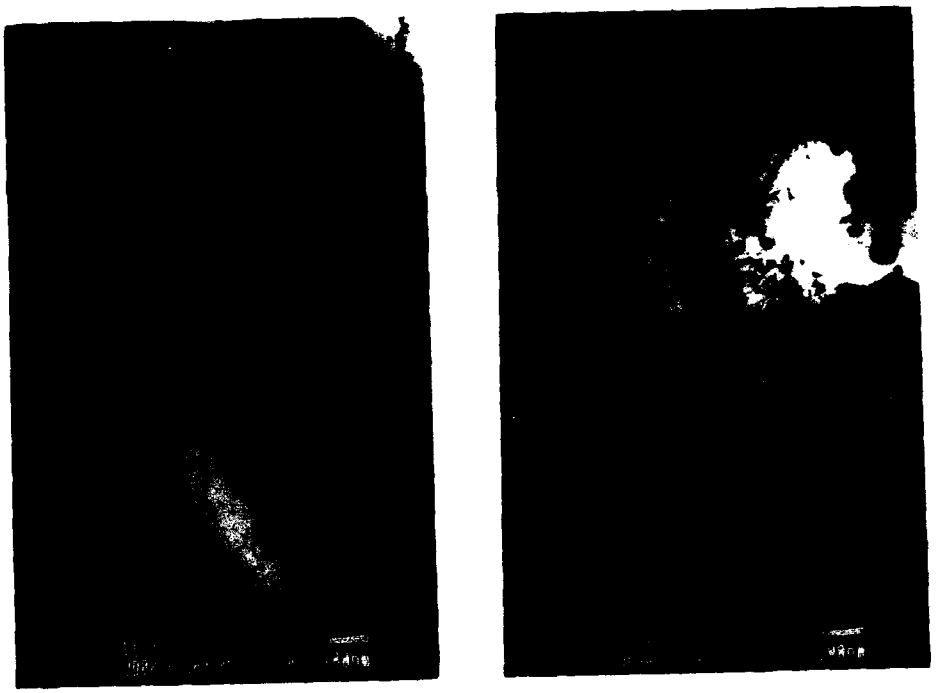


Figure 2 - TEM observation of a Ti-14%Mo-9%Al (wt%) extruded rod.
Distribution of Y_2O_3 dispersoids.

SYNTHESIS OF γ-TiAl BY MECHANICAL ALLOYING OF ELEMENTAL POWDERS

ABDULBASET FREFER, C.SURYANARAYANA and F.H. FROES

Institute for Materials and Advanced Processes
University of Idaho
Moscow, ID 83843-4195 (U.S.A.)

Abstract

Titanium powders with 50 and 55 at.% aluminum, were mechanically alloyed in a SPEX 8000 mill to synthesize the γ-TiAl intermetallic. The phase evolution was followed by x-ray and electron diffraction techniques. With increasing milling time a solid solution of aluminum in titanium, an amorphous phase and an f.c.c. phase formed. Formation of TiAl was obtained by subsequent heat treatment of the amorphous powder at 615°C. The small (nanostructure) grain size should exhibit enhance ambient temperature ductility.

Introduction

Interest in developing low-density and high temperature structural materials has been continuously growing during the past few years in order to find optimum materials for use in aerospace applications [1]. Titanium aluminides (TiAl and Ti_3Al) are attractive for this purpose since they possess low density, high temperature strength and high corrosion and oxidation resistance. However, at ambient temperature they suffer from inadequate ductility [2]. Emphasis in recent times has concentrated on TiAl because its density (3.9 g/cm^3) is even lower than that of Ti_3Al (4.2 g/cm^3), and it also has high oxidation resistance [2]. In order to improve the ductility of these intermetallics alloy additions, reduction in grain size, and microstructural modifications have been tried but with limited success[2].

Mechanical alloying (MA) is a technique which can be employed to refine the grain size through high energy ball milling [3]. In addition, MA leads to the formation of both stable and metastable phases including supersaturated solid solutions, intermetallic compounds and amorphous phases [3-5].

There have been some attempts earlier to produce the TiAl (γ) intermetallic compound by MA of blended elemental powders. Watanabe et al. [6,7] investigated the effect of ball size on the final constitution of the product in the Ti-Al system. It was reported that milling with small diameter balls (4.76 mm) always led to the formation of an amorphous phase. However,

Titanium '92
Science and Technology
Edited by F.H. Froes and I. Caplan
The Minerals, Metals & Materials Society, 1993

milling with larger diameter balls (19.1 mm) resulted in the formation of the titanium aluminide intermetallic. Tokizane et al. [8] were able to produce the TiAl compound by vacuum hot pressing the MA powder. Formation of TiAl was reported by Burgio et al. [9] in a Ti-60 at.% Al powder mixture.

Amorphous phase formation was reported in MA Ti-Al powders in the range of 10 to 75 at.% Al [6,7,9-13]. It has also been reported that an fcc phase formed in these alloys after the formation of the amorphous phase [9,14,15].

This paper discusses preliminary results obtained on MA Ti-50 and 55 at.% Al. powders including the synthesis of TiAl by crystallization of the amorphous phase, and formation of the fcc phase. An extremely small (nanostructure) TiAl grain size produced from the amorphous phase is likely to exhibit increased ambient temperature ductility compared to material with a more conventional grain size.

Experimental Procedure

Elemental Ti powder (-100 mesh size and 99.4% purity) and Al powders (-325 mesh size and 99.7% purity) were blended together to produce the nominal compositions Ti-50 at.% Al and Ti-55 at.% Al. About 1% stearic acid was added to the powder mix as a process control agent (PCA). The powder mixture and stainless steel balls with a powder to ball weight ratio of 1:10, were loaded into a steel container in air and milled in a Spex 8000 mill. The milling medium was 3/16" diameter hardened 52100 steel balls. Forced air cooling during milling prevented an excessive increase of the temperature of the powder.

The MA powder was taken out of the container periodically to follow the progress of alloying. The milled powder was characterized by x-ray diffraction using Cu K_α radiation at 40 kV and 15 mA. Transmission electron microscopy (TEM) and scanning electron microscopy (SEM) techniques were also used. The milled powder was also heat treated at various temperatures by sealing the powder in glass or silica tubes under vacuum to follow the structural changes which occurred.

Further, to improve intimate mixing and to avoid formation of a thick crust at the bottom, the vial was inverted (through 180°) every 30 min.

Results

Figure 1 shows the x-ray diffraction patterns of the milled Ti-50 at.% Al powder as a function of time. In the as-mixed powder (Figure 1a), all the expected Ti and Al peaks can be seen, with the fcc Al (111) peak overlapping the hcp Ti (002) peak. After 5 h of milling (Figure 1b) the peaks showed a decrease in intensity and broadening of all the reflections. Only a small amount of Al appears to be present at this stage. A slight change in the position of the titanium reflections indicates that some aluminum is dissolved in titanium forming a titanium solid solution [$Ti(Al)_{ss}$]. From the variation of lattice parameters with Al content [16] in these alloys, it was estimated that about 10 at.% Al had dissolved in the Ti. With continued milling (to 10 h) an amorphous phase (Am) formed (Figure 1c) and with further

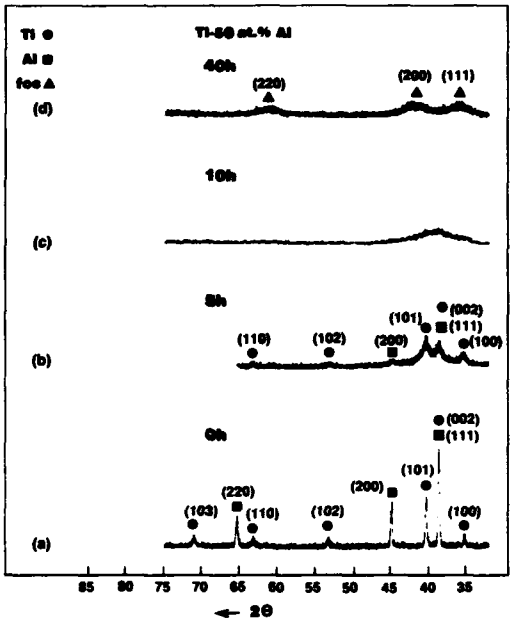


Fig 1. X-ray diffraction patterns of Ti-50 at.% Al powder mix MA'd for different milling times. (a) as-mixed powder, (b) MA for 5 h showing the presence of free aluminum and $Ti(Al)_{s.s.}$ phases, (c) MA for 10 h showing the amorphous phase and (d) MA for 40 h showing the f.c.c. phase.

milling formation of an fcc phase is observed after 30 h (Figure 1d). No further changes in the x-ray diffraction patterns were observed even up to 100 h of milling. The sequence of phase formation in the Ti-55 at.% Al alloy was identical to that in the Ti-50 at.% Al powder.

Thus, the sequence of phase formation in both Ti-50 and 55 at.% Al powders can be represented as:

$$(Ti + Al) \xrightarrow{5\ h} Ti(Al)_{s.s.} + Al \xrightarrow{9\ h} Am \xrightarrow{30\ h} f.c.c.$$

The particle size of the powder continuously decreased with milling time (Figure 2).



Fig 2. SEM micrographs showing a reduction in particle size with increasing milling time for Ti-50 at. % Al.

Confirmation of the formation of the amorphous and fcc phases in these powders was achieved from electron diffraction patterns (Figures 3 and 4).

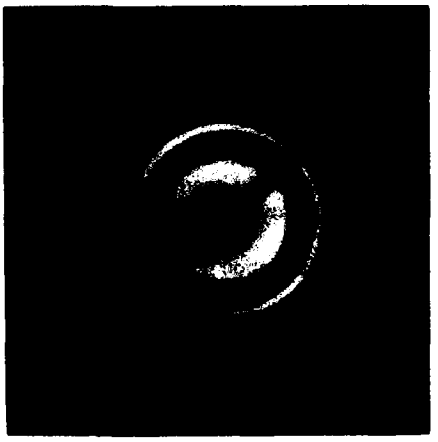


Fig 3. Electron diffraction pattern of the amorphous phase obtained in Ti-50 at. % Al powder mix MA'd for 10 h.

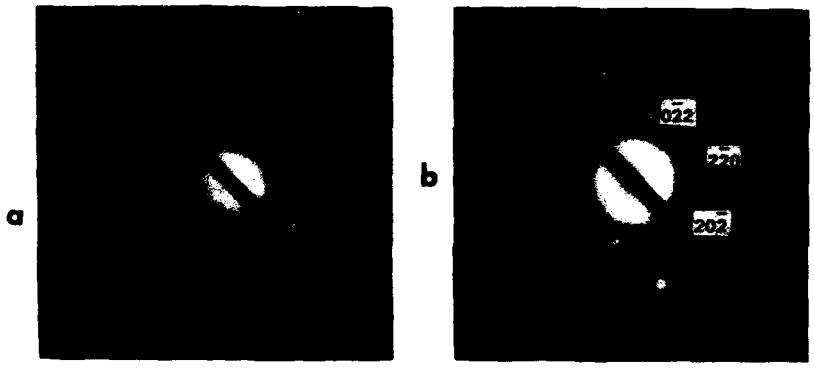


Fig 4. Electron diffraction patterns of the f.c.c. phase in MA'd Ti-50 at.% Al powder. (a) polycrystalline and (b) single crystal diffraction patterns. The foil normal in (b) is [111].

The MA powder milled to 10 h, showing the amorphous phase in both compositions, was annealed for 1 week at 615°C to determine whether crystallization leads to the formation of the TiAl phase. Figures 5(a) and (b) show the obtained x-ray diffraction patterns indicating that the predominant phase is TiAl, even though significant amounts of the Ti_3Al phase are also present. From a ratio of the intensities of the peaks corresponding to these two phases, it was calculated that the heat treated Ti-50 at.% Al powder contained 37% Ti_3Al phase. The amount of the Ti_3Al phase in the Ti-55 at.% Al powder was not determined, but from the x-ray pattern, it appears to be very small. From this trend it is suggested that Ti-60 at.% Al powder should give 100% of the TiAl phase.

Figure 5(c) shows the x-ray pattern of Ti-50 at.% Al powder MA'd for 50 h, which contained the fcc phase. After heat treatment at 900°C for 48 h the fcc phase continued to be present, but the reflections became sharper, presumably due to stress relief and grain coarsening in the powder.

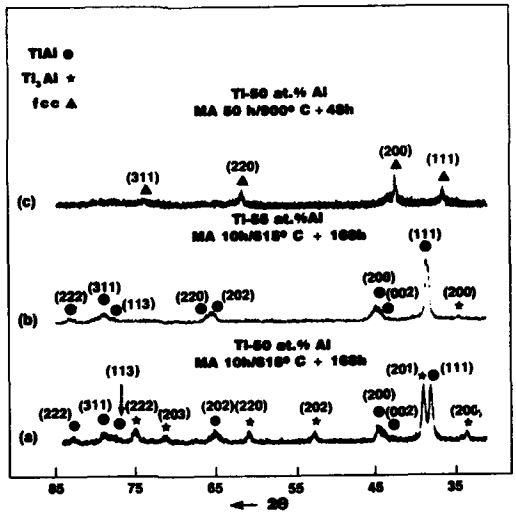


Fig 5. X-ray diffraction pattern of (a) Ti-50 at. % Al powder MA'd for 10 h and heat treated for 168 h at 615°C showing the presence of TiAl and Ti_3Al. (b) Ti-55 at. % Al powder MA'd for 10 h and heat treated for 168 h at 615°C. Only TiAl intermetallic peaks can be seen. (c) Ti-50 at. % Al powder MA'd for 50 h and heat treated for 48 h at 900°C. Only sharpening of the f.c.c. phase peaks is observed.

Discussion

The Amorphous Phase

Several investigators have reported on the formation of an amorphous phase in MA Ti-Al powders [6,7,9,11-14], even though the composition range for formation of this phase appears to be different depending on the type of mill used and milling intensity. The two conditions required for solid-state amorphization, (i) negative heat of mixing and (ii) anomalously high diffusivity of one of the components, are satisfied in the Ti-Al system and thus it is not surprising that an amorphous phase formed in the present work. Since MA leads to considerable grain refinement, often resulting in the formation of nanometer-sized grains, the continuous decrease in grain size and introduction of lattice defects destabilizes the crystalline structure and can lead to amorphization. In fact, Ahn et al. [13] reported that in the Ti-50 at. % Al alloy, the crystal size was less than 20 nm just prior to amorphization. On the other hand, Murty et al. [12] suggested that amorphization in their Ti-Al alloys started when the strain in the titanium, the relatively slow-diffusing species, reached a maximum value.

The TiAl Phase

The γ-TiAl phase could be synthesized in our investigation only after heat treating the amorphous powder. In earlier investigations, other workers reported that the TiAl phase could

be produced either by vacuum hot pressing [8] the MA'd powder or by using larger diameter steel balls for the milling[6,7], or by heat treatment at 600°C [17]. Production of γ-TiAl by use of large steel balls has been rationalized based on the relative contribution of frictional forces and impact forces. Smaller balls with intense frictional action would yield an amorphous phase while the larger milling balls with higher impact energy would yield the intermetallics [6,7]. On the other hand, it has been clearly shown in the present investigation that crystallization of the amorphous phase, produced by MA, can also lead to the synthesis of the TiAl phase.

Production of the γ-TiAl phase directly by MA was not achieved; only on heat treating the powder with a proper choice of the temperature. Attempts to control the grain size of the intermetallic in the nanometer range by carrying out the crystallization at a sufficiently low temperature will be conducted in further studies. Amorphous phases have been used as precursors for the production of nanocrystalline microstructures in earlier work [18].

A significant amount (37%) of Ti_3Al phase is detected in the Ti-50 at.% Al powder and a much smaller amount in the Ti-55 at.% Al powder. Even though the accepted Ti-Al equilibrium diagram suggests that the γ-TiAl phase is stable at room temperature in the composition range of 48-55 at.% Al [19], it is possible that during MA, a small quantity of the ductile Al sticks to the mill container walls and steel balls and thus the actual Al content in the powder is less than the starting composition. A further increase in Al (to 60 at.%) to compensate for the loss of Al may produce 100% of the TiAl phase; this experiment is currently in progress.

The FCC Phase

The formation of an fcc phase in MA Ti-Al and Ti-Al-Nb alloys has been reported earlier [9-11,15], and a detailed discussion of its possible origin was also presented [14]. It was suggested [15] that the fcc phase may be titanium nitride. This hypothesis gets support from the present study and other work from the following observations:

(i) the fcc phase forms more readily (and faster) when the powder is milled in air rather than under a protective argon atmosphere [20].

(ii) the fcc phase formed is very stable and does not decompose even on annealing for 48 h at 900°C.

(iii) the lattice parameter of the fcc phase remains constant with milling time and is not a function of the alloy composition.

This behavior can be rationally explained if the phase formed is very stable. According to the binary Ti-N diagram [21], TiN forms when the nitrogen content is at least 11 wt.%. However, chemical analysis of the Ti-50 at.% Al powder milled for 30 h indicated the presence of only 3.34 wt.% nitrogen (and 0.13 wt.% oxygen), too low for the powder to contain only the titanium nitride phase. It is possible that the nitrogen content required to form a (Ti,Al) nitride is lower than 11 wt.%, and this idea is being pursued.

Conclusions

Based on the results presented above, the following conclusions can be drawn:

1. With increasing milling time, the blended elemental Ti-50 and 55 at.% Al powders resulted in the sequential formation of a solid solution of Al in Ti, an amorphous phase, and at long times an fcc phase.

2. Heat treatment of the amorphous powder in both compositions led to the formation of the equilibrium intermetallics TiAl and Ti_3Al. The 50 at.% Al powder contained 37% Ti_3Al, while the Al-rich powder contained very little Ti_3Al.

3. Based on the available data, the fcc phase is suggested to be (Ti,Al) nitride .

References

1. F.H. Froes, C. Suryanarayana, and D. Eliezer, ISIJ International, **31** (1991) 1235.
2. Y-W. Kim, JOM, 41 (July 1989) 24.
3. C.C. Koch, in Processing of Metals and Alloys, (ed.) R. W. Cahn, vol. 15 of Materials Science and Technology - A Comprehensive Treatment, VCH Verlagsgesellschaft, Weinheim, Germany, (1991) 193.
4. C.C. Koch, Annu. Rev. Mater. Sci., **19** (1989) 121.
5. P. H. Shingu, K.N. Ishihara and J. Kuyama "Non-equilibrium alloy phases produced by mechanical alloying", A Report from Proceedings of the Thirty fourth Japan Congress on Materials Research.", Kyoto, Japan, 1991.
6. R. Watanabe, H. Hashimoto and Y.H. Park, in "Advances in Powder Metallurgy," compiled by L.F. Pease III and R.J. Sansoucy, Metal Powder Industries Federation, Princeton, NJ, **6** (1991) 119.
7. Y.H. Park, H. Hashimoto and R. Watanabe, Mater. Sci. Forum, 88-90 (1992) 155.
8. M. Tokizane, K. Ameyama and H. Sugimoto, in "Solid State Powder Processing," (eds.) A.H. Clauer and J.J. deBarbadillo, TMS, Warrendale, PA, 1990, p. 67.
9. N. Burgio, W. Guo, M. Magini, F. Padella, S. Martelli, and I. Soletta, Structural Applications of Mechanical Alloying, F.H. Froes and J.J. deBarbadillo (eds.), Amer. Soc. Mater., Materials Park, OH, (1990) 175.
10. E. Bonetti, G. Cocco, S. Enzo and G. Valdre, Mater. Sci. and Technol., **6** (1990) 1258.
11. G. Cocco, I. Soletta, L. Battezzati, M. Baricco, S. Enzo, Phil. Mag. B, **61** (1990) 473.
12. B.S. Murty, M.D. Naik, M. Mohan Rao and S. Ranganathan, Materials Forum, **16** (1992) 19.
13. J.H. Ahn, H.S. Chung, R. Watanbe and Y.H. Park, Mater. Sci. Forum, 88-90 (1992) 347.
14. C. Suryanarayana, Guo-Hao Chen, Abdulbaset Frefer and F.H. Froes, Materials Science and Engineering A, 1992. (*In press*).
15. W. Guo, S. Martelli, F. Padella, M. Magini, N. Burgio, E. Paradiso and U. Franzoni, Mater. Sci. Forum, 88-90 (1992) 139.
16. W.B. Pearson, "A Handbook of Lattice Spacings and Structures of Metals and Alloys", Pergamon Press, Oxford, UK, vol. 2, 1967.
17. R.C. Benn, P.K. Mirchandani, A.S. Watwe, Modern Developments in Powder Metallurgy, Metal Powder Industries Federation, **18-21** (1988) 479.
18. C. Suryanarayana and F.H. Froes, Paper to be presented at "Recrystallization '92", San Sebastian, Spain, 1992.
19. J.L. Murray, Metall. Trans. A., **19A** (1988) 243.
20. Guo-Hao Chen, C. Suryanarayana and F.H. Froes, To be presented at the Seventh World Conference on Titanium, San Diego, CA, June-July 1992.
21. A.E. Palty, H. Margolin, and J.P. Nielsen, Trans. ASM, **46** (1954) 312.

PHASE AND STRUCTURE TRANSFORMATIONS IN TITANIUM ALLOYS UNDER THERMOHYDROGENOUS TREATMENT

A. A. Ilyn, B. A. Kolachev, A. M. Mamonov

Aviation Technology Institute, Moscow, Russia

Abstract

The hydrogen dopping influence of phase composition, structure, morphology and chemical composition of phases in titanium alloys of different classes were investigated in this article. The term of thermal hydrogenous treatment as a new direction of titanium alloys technology was entered. The opportunities of structure managing and raising of mechanical and exploitation properties complex of titanium alloys with the help of thermohydrogen treatment were shown.

Hydrogen which is enough powerful β-stabilizer has the appreciable influence at phase and structural transitions in titanium alloys. This influence is developed in decreasing of $\alpha+\beta/\beta$ transition temperature (t_t), increasing of β-phase quantity at the given temperature, alloying elements redistribution between α and β-phases, the lattice period change of α and β-phases, and as follows of volume effect of allotropic transition $\beta \rightleftarrows \alpha$, β-phase stability increasing and ω-phase formation suppression, the hydrides and α_2-phase precipitation and martensite transformation beginning and ending temperatures decreasing. Fig. 1 illustrates the hydrogen influence at $\alpha+\beta/\beta$ transformation temperature t_t for some titanium alloys.

The transformation temperature t_t decreasing is usually the more expressed β-stabilizer content in alloy. For some Ti alloys (Ti-5Al; Ti-5Al-2.5Sn; Ti-6Al-4V; Ti-3Al-5Mo-5V; Ti-7.5 Al-11Zr-0.6Mo-1Nb-0.3Si; Ti-6Al-2Zr-1Mo-1V) we had constructed the vertical sections which are illustrating their phase composition variation with the hydrogen content raising. The Fig. 2 gives the example of such sections for Ti-6Al-4V (VT6) and Ti-7.5Al-11Zr-0.6Mo-1Nb-0.3Si (VT18) alloys.

For α-alloys (Ti-5Al; Ti-5Al-2.5Sn) the advent of hydrogen leads to β-phase appearance at comparatively low temperatures (250-270 °C); in $\alpha+\beta$ alloys Ti-6Al-4V (VT6) and Ti-3Al-5Mo-5V (VT16) hydrogen leads to raising of β-phase quantity; in pseudo α-alloys with the high content of Al (Ti-8Al-11Zr-0.6

Titanium '92
Science and Technology
Edited by F.H. Froes and I. Caplan
The Minerals, Metals & Materials Society, 1993

Mo-1Nb) hydrogen at its high contents allows to α_2-phase precipitation. The all alloys at high content of hydrogen the hydrides precipitate.

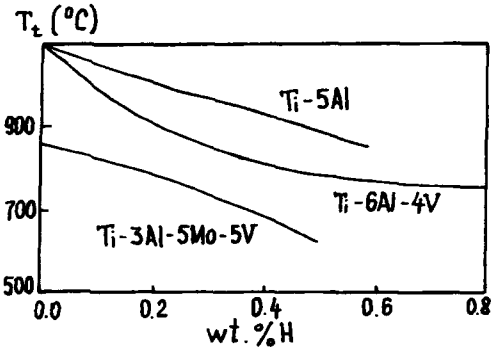


Figure 1 - Hydrogen influence at $\alpha+\beta/\beta$ transformation for some titanium alloys

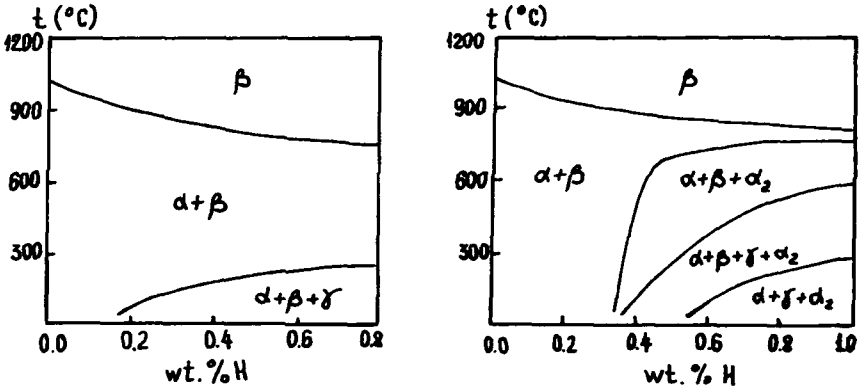


Figure 2 - The hydrogen influence at phase equilibrium in Ti-6Al-4V (a) and Ti-7.5Al-11Zr-0.6Mo-1Nb-0.3Si (b) alloys

The increasing of β-phase quantity in $\alpha+\beta$ titanium alloys is accompanied by its leaning with β-stabilizers. Experimentally [4,3] this effect was detected in VT23 (Ti-4.5Al-4.5V-2Mo-1Cr-0.6Fe) and VT18 (Ti-7.5Al-11Zr-0.6Mo-1Nb-0.3Si) alloys (Fig.3).

But the decreasing of dopping degree of β-phase in biphase $\alpha+\beta$ titanium alloys with the hydrogen advent into these alloys is the consequence of triad systems Ti-β-stabilizer - hydrogen isothermal sections alloying for the set experimental low of β-phase quantity raising for this type alloys with the hydrogen advent [2]. This section diagram is shown in Fig. 4. This diagram may be extended to complex-dopping alloys with the account of β-stabilizers influence by Mo equivalent and taking into account the comparatively low influence of β-stabilizers at Al solubility in α-phase. The hydrogen dopping in tita-

nium alloys leads to β-phase quantity increasing in accordance to $\alpha_1 C_1/\alpha_1\beta_1$; $\alpha_2 C_2/\alpha_2\beta_2$; $\alpha_3 C_3/\alpha_3\beta_3$ till the alloy goes over to one-phase β-region, where β-phase quantity is 100 %. But the β-stabilizers content in β-phase must decrease; this content is defined by β_1 ; β_2 ; β_3 ; b points. The supposition that β-phase composition is constant or that β-stabilizers content in β-phase with the hydrogen dopping of alloys leads to contradiction to experiments.

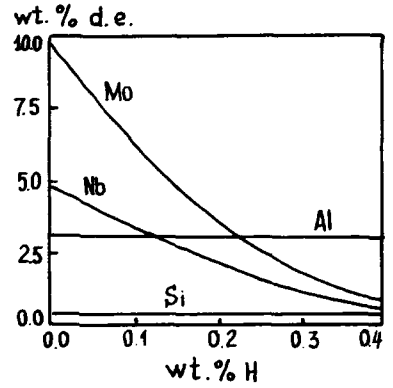


Figure 3 - The hydrogen influence at dopping elements in β-phase in VT18U alloys at 650 °C

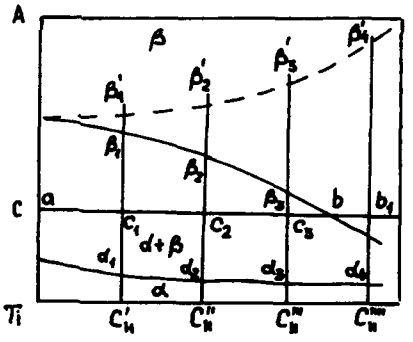


Figure 4 - The isothermal section of Ti-β-stabilizer-hydrogen diagram

For some $\alpha + \beta$ titanium alloys, for example Ti-12V, hydrogen decreasing the volume effect of $\alpha \rightleftarrows \beta$ transformation which is near zero at some hydrogen concentrations (Fig. 5). This effect is combined with the fact that hydrogen concentrates in β-phase. In nonhydronized metal the β-phase atomic volume is latter than of α-phase one. The hydrogen dopping of metal leads to β-phase atomic volume increasing, and α-phase atomic volume changes slightly because of comparatively low hydrogen solubility in it. This fact allows us to manage the phases morphology because the transition volume effect determinates the crystals shape [1].

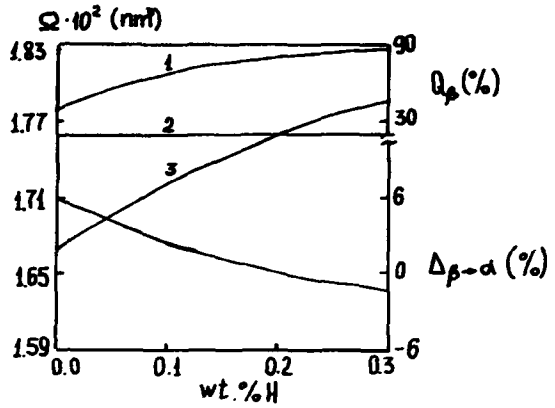


Figure 5 - Hydrogen influence at β-phase quantity, Q_β (1), atomic volumes, Ω_α (2), and β-phase (3) and volume effect, Δ of $\beta \rightarrow \alpha$ transformation (4) in annealed Ti-12V alloys [3].

The hydrogen influence at transformations taking place in titanium alloys under different cooling conditions may be introduced as cooling rate-hydrogen containing diagram. At these diagrams the phase composition of alloys with different hydrogen containing after cooling temperature with different rates. In Fig. 6 such a diagram is given as an example for VT6 alloy (Ti-6Al-4V) after heating till β-region.

At the diagram V_{cr} corresponds to the cooling rates below which the initial stages of β-phase decomposition are observed, and the unequilibrium compositions of β and α''-phases (β_u and α''_u) form as a result. This appears in X-rays lines expansion. V_{cr} corresponds to the cooling rates supplying comparatively equilibrium compositions of α and β-phases (α_e and β_e). Such diagrams were constructed by us for VT20 (Ti-6Al-2Zr-1Mo-1V); VT18 (Ti-7.5Al-11Zr-0.6Mo-1Nb-0.3Si); VT23 (Ti-4.5Al-4.5V-2Mo-1Cr-0.6Fe) alloys. For these diagrams the next three laws are characteristic: a) hydrogen decreases the critical cooling rates of quenching; b) hydrogen helps the rhombic martensite to formate; the rhombic distortion degree of martensite being increased with the hydrogen content raising; c) the hydrogen dissolution in α''-phase causes the $\alpha'' - \beta$ phase transition [5].

The ω-phase formation suppressing in β-titanium alloys was plotted out in our early papers [5] and was confirmed in [6]. Hydrogen decreases the thermal hardening effect of pseudo β-titanium alloys and when its concentration is high transfers them into thermal dishardened alloys class [5].

The hydrogen influence at phase and structural transitions in titanium alloys laws being pointed above were a base of new direction of titanium alloys technology, named thermohydrogenous treatment [3, 5, 10]. The thermohydrogenous treatment is based on reversible hydrogen dopping of titanium alloys, because it is necessary to finish it with vacuum annealing to

decrease hydrogen content in metal till safe concentrations where hydrogenous brittleness of titanium alloys development during their work is excluded.

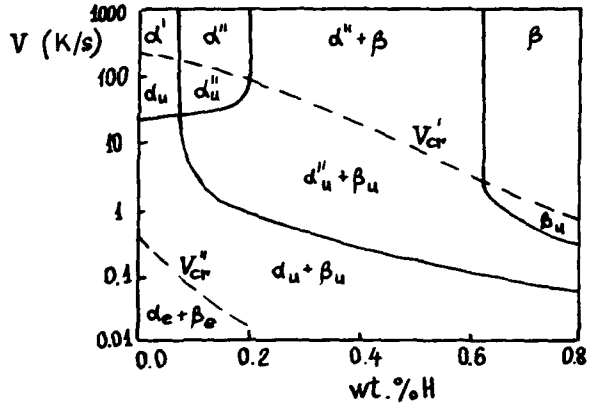


Figure 6 - Phase composition of VT6 alloy (Ti-6Al-4V) with the different hydrogen containing after cooling from β-region with different rates

Thermohydrogenous treatment (THT) allows to solute the next tasks [3, 11]:
a) to transfer the wrought plate structure into fine grain globular one, that leads to cyclic endurance and plasticity increasing;
b) to manage the α-phase morphology and quantity at aging with positive mechanical properties change;
c) to transfer the thermally dishardened pseudo α-alloys into thermally hardened class;
d) to increase $\alpha+\beta$-alloys penetration hardness.

The microstructure fining of casting titanium alloys by their temporary hydrogen dopping was discussed earlier [7-9, 12]. The investigations of this problem are made in USA, Japan, China, Russia. The developed technology, that is hydrogenation of casted metal and its vacuum annealing (named "hydrovac") allows to fine the internal structure of micrograin and to increase the mechanical properties complex.

The other opportunities of thermohydrogenous treatment are known. For example, the reversive hydrogen dopping makes in VT18U alloy the unique heterogeneous structure, where α-phase presents as two solid solutions with different chemical specification, this state being conservated till high temperatures (800-850 °C). Pseudo α of enriched concentration is gathered of initial α-phase, and α-phase of enpoored concentration is formed during hydrogen stabilized β-solid solution decomposition. The low quantities of β- and α_2-phases are present in thermohydrogenous treated alloy structure. Such structure formes, for example, as a result of THT regime: alloy hydrogen saturation till 0.5-0.8 %, that results in β-phase quantity

increasing; cooling till room temperature with the aid of β-phase eutectoid decomposition, vacuum annealing. This structure state leaded to hardness characteristics raising of VT18U alloy sheets at room and enraised temperature (Table 1) as a result of disperse hardening.

Table 1 - The Mechanical Properties of VT18U Alloy Sheet

Testing temperature, °C	Heat treatment	σ_t, MPa	$\sigma_{0.2}$, MPa	δ %	The final hydrogen concentration
20	supplied state	1050	970	6.5	0.0033
	vacuum annealed (T=900 °C, 1 h, V=2K/s)	1020	960	8.2	0.003
	THT (0.8 % H)	1170	1090	3.3	0.004
	THT (0.6 % H)	1150	1080	3.9	0.004
700	supplied state	540	470	21.0	0.003
	vacuum annealed (T=900 °C, 1 h)	560	480	20.9	0.003
	THT (0.8 % H)	690	610	17.4	0.004
	THT (0.6 % H)	670	590	20.1	0.004
800	supplied state	290	210	32.3	0.003
	vacuum annealed (T=900 °C, 1 h)	300	210	30.4	0.003
	THT (0.8 % H)	400	320	28.3	0.004
	THT (0.6 % H)	370	300	30.7	0.004

The opportunity of penetrated hardening raising of titanium alloys by means of thermohydrogenous treatment is communicated with critical cooling rate decreasing when they are dopped with hydrogen. For example, the dopping of VT23 alloy by 0.2 mass. % of hydrogen the critical cooling rate decreases from 400 till 0.4 K/s, and 0.8 mass. % of hydrogen decreases the critical cooling rate for VT23 alloy till 0.3 K/s. The decreasing of critical cooling rate allows to use more soft quenching regimes for stress and warping of semies and details.

The thermohydrogenous treatment may be combined with the earlier hot deformation of titanium alloys with the using of hydrogenous plastification. The development THT regimes of VT18U alloy blades combined with hydrogenous plastification supply the more high mechanical properties at normat temperature (σ_t=1240 MPa, $\sigma_{0.2}$=1170 MPa, δ=9-11 %, σ_{-1}=455 MPa) than after standard blades production technology (σ_t=960-975 MPa, δ=10-14 %).

As it could be clear of saying before, we are sure that thermohydrogenous treatment is more general titanium alloys heat treatment technology than "hydrovac" process.

References

1. J. W. Christian. "Transformation in metals and alloys" (Sec. edition. Part I. Equilibrium and general kinetic theory. Pergamon Press. Oxford e. a., 1975), 806 p.
2. B. A. Kolachev, V. A. Livanov, A. A. Buchanova. "Mechanical properties of titanium and its alloys". (Moscow, Metallurgiya, 1974.
3. B. A. Kolachev, A. A. Ilyn, A. M. Momonov. "Thermohydrogen treatment of titanium alloys". Metalloobednenie i obrabotka titanovykh i jaroprochnykh splavov. (Moscow, VILS, 1991, 132-142.
4. A. A. Ilyn, et al. "Redistribution of alloying elements between α and β phases in VT23 alloys. Phisiko-khimicheskaya mekhanika materialov, N 1, 1987, 112-114.
5. A. A. Ilyn. "Phase and structural transformation in titanium alloys with hydrogen". Izvestiya vuzov: Tsvetnaya metallurgiya, N 1, 1987, 96-101.
6. A. A. Ilyn, S. B. Belova, Kobuilkin A. N. Izvestiya vuzov: Tsvetnaya metallurgiya, N 6, 1986, 112-114.
7. B. A. Kolachev, Nosov V. K., U. A. Lebedev. "Reversible hydrogen alloying of titanium alloys". Izvestiya vuzov: Tsvetnaya metallurgiya, N 3, 1985, 104-110.
8. W. R. Kerr. "The effect of hydrogen as a temporary alloying element on the microstructure and tensile properties of Ti-6Al-4V." Met. Trans, 16a, (1-6), 1985, 1077-1087.
9. San Tohan. "Improvement of mechanical properties of precise titanium castings". Metals and Technology, 59 (5), 1989, 18-21.
10. I. S. Polkin, B. A. Kolachev. "Phase transformation, thermal and thermodynamical processing of titanium alloys." Sixth World Conference on Titanium, Cannes.
11. B. A. Kolachev, A. A. Ilyn. "About of thermohydrogen treatment of titanium alloys". The thermal, chemical and laser treatment of steels and titanium alloys. Perm. USSR, 1989, 97-101.
12. R. Y. Smickly, L. D. Dardy. "Microstructure reduction of cast titanium". USA Pat. 4505764.

THE EFFECT OF POROSITY ON THE VISCOPLASTIC RESPONSE OF SINTERED Ti-6Al-4V

M. da Silva & K.T. Ramesh
Department of Mechanical Engineering
The Johns Hopkins University
Baltimore, MD 21218

Abstract

Fully dense and porous samples Ti-6Al-4V were tested by compression and torsion. Stress-strain curves were obtained for homogeneous deformations at high strain rates (between 10^2-10^4 s^{-1}). In addition, quasistatic compression tests were performed on the fully dense and porous metals. The results show that the porosity affects the degree of strain hardening and the rate sensitivity in compression; the pores have negligible effect on the strain hardening behavior during shearing deformation.

Introduction and Background

The unique mechanical and physical properties of titanium alloys have led to their widespread use in the design of advanced components. However the extreme difficulty of machining titanium alloys has spurred considerable interest in alternate manufacturing methods such as powder metallurgy which offer significant advantages when combined with conventional production processes. Modeling of sintered powder metals undergoing manufacturing processes requires a knowledge of the constitutive law which is complicated by the evolution of porosity with the deformation. Since the volume does not remain constant during deformation, conventional plasticity theories which are suitable for pore-free metals are inapplicable.

The complexity of the microstructure and the presence of residual porosity are major factors influencing the mechanical behavior of porous metals. In the case of the Ti-6Al-4V alloy variations in the microstructure have been observed to strongly influence the mechanical properties both at low and high rates of deformation. This effect is observed as scatter in the reported data on the yield strength, strain hardening and strain rate sensitivity and is not discussed here.

The residual porosity is the other major factor influencing the mechanical behavior of sintered metals. The effect of porosity on the mechanical behavior of sintered metals has been a subject of interest both theoretically and experimentally for a number of researchers. Again, the data in the literature shows a great deal of scatter; this is due to the fact that besides the pore-content many other factors such as pore shape, size, orientation and distribution strongly influence the mechanical response. A comprehensive set of references is available in Haynes [1].

Titanium '92
Science and Technology
Edited by F.H. Froes and I. Caplan
The Minerals, Metals & Materials Society, 1993

The progressive densification of porous materials has been described by various methods ranging from micromechanical modeling to simple phenomenological modeling. Some of the more rigorous analytical approaches to the constitutive modeling of porous metals have been largely motivated by the problem of void nucleation and growth in ductile fracture (e.g. Rice & Tracey[2]). Gurson[3] developed approximate yield criteria and flow rules for porous ductile materials and studied the role of the hydrostatic stresses in yielding and void growth. Numerical studies of deformation in two dimensional models of porous metals with cylindrical pores and an elastic plastic matrix have been presented by Needleman[4]. Further numerical studies (e.g. by Mear[5]) have examined yield phenomena in a cubic array of spherical pores. Using a different approach (formulating the problem in strain space) Kim[6] studied the response of porous materials under general three dimensional loading conditions where these materials may exhibit strong coupling between volumetric and deviatoric effects.

The plastic deformation and densification of sintered porous compacts has led to studies of the applicability of the theory of plasticity to the modeling of porous materials. The plastic deformation of conventional isotropic metals is incompressible and hence simple classical rate-independent plasticity theories such as J_2 - flow can be readily applied, but these are inapplicable in the case of porous materials. Thus for the porous material a different set of yield criteria and flow rules are required; the yield criteria should reduce to the von Mises criterion as the porosity tends to zero. A natural choice for the yield function includes dependence on the hydrostatic and deviatoric components of the Cauchy stress as shown below,

$$F = F(I, J_2, \rho) = \alpha(\rho)\, I^2 + \beta(\rho)\, J_2^2$$

where I represents the trace of the Cauchy stress, J_2 is the second invariant of the deviatoric stress tensor, and where α, β are constitutive functions of the current density ρ. This approach was independently proposed by Kuhn et al.[7] and Green[8]. Shima and Oyane [9] successfully utilized similar relations to describe the behavior of porous (sintered) copper, by experimentally evaluating the functions $\alpha(\rho)$ and $\beta(\rho)$ through simple tension and compression tests. Corapceioglu & Uz [10] reviewed the model mentioned above and compared the expressions obtained for the functions α and β by various authors. Haynes [1] presents results on the effect of porosity on the yield strength, plastic deformation and work hardening of porous metals. Besides these results, data exists for copper [9], iron [11] and tungsten (Shipman[12]) under quasistatic axial and torsional loading; Bourcier et al. [13] reported data for porous Ti-6Al-4V under quasistatic tension.

However modeling of the dynamic behavior of porous metals at high rates has not been extensively studied (aside from the work done by Duffy [14] and a few others). This paper presents an investigation of the dynamic behavior of porous Ti-6Al-4V in compression and shear. Since the dynamic response of these materials is of interest, the primary experimental facilities used are the Kolsky compression and torsion bars[15]. Using standard procedures, flow stress measurements are made from the recorded stress-strain histories. In addition to the high rate testing, the quasi-static behavior (in compression) of the fully dense and porous metals is determined.

Material Description

The titanium alloy chosen for this work is the two phase (α+β) material Ti-6Al-4V, which is the most widely used of the commercially available titanium alloys. The presence of α-stabilizers (*Al*) and β-stabilizers (*V*) makes Ti-6Al-4V a two phase alloy supporting a mixture of α, retained β and transformed β phases which may exist in different forms, ranging from lanticular to equiaxed

or combinations of such structures. When this alloy is cooled from the β-region, α begins to form below the β-transus (954°C). The α phase forms in plates morphology, with a crystallographic relationship to the β phase in which it forms. Besides the annealing temperature, the cooling rate also affects the microstructure.

The sintered material (obtained from Industrial Materials Technology, Inc.) was vacuum sintered at 1177°C for 4 hours and then HIPed (Hot Isostatically Pressed). The powders were manufactured by the HDH (Hydride/Dehydride) process utilizing material which was further refined through vacuum arc melting. The sintered metal was heat treated at 920°C for 1 hour and furnace cooled; a micrograph of the resulting microstructure is shown in Fig. 1. The slowly cooled, Widmanstatten microstructure is apparent, as is the residual porosity. The structure consists of transformed β and plate-like α. The α phase occupies more than 90% of the matrix and thus is the majority phase. The manufacturer provided porosity estimates of approximately 8% obtained by fluid immersion testing.

Experimental Procedure

A technique for the measurement of the properties of materials undergoing homogeneous deformations at high rates was developed by Kolsky[15] and has since become the most widely used testing procedure for dynamic property measurements at strain rates of the order of 10^2-10^4 s^{-1}.

The Kolsky compression bar is a device that is used to subject small samples to nearly homogenous compressive deformations at strain rates of 10^2-10^4 s^{-1}. The instrument consists of two long metal bars that are designed to remain elastic throughout the test. These bars sandwich a small cylindrical specimen. One end of the incident bar is impacted by a projectile fired from a gas gun and the compressive pulse generated by the impact propagates down the incident bar into the specimen. After several reverberations within the specimen, a transmitted pulse is sent into the transmitter bar and a reflected pulse back into the incident bar. Conventionally, strain gages placed on the incident and transmitter bars are used to measure the pulses propagating in the bars. The reflected pulse provides a measure of the strain rate imposed on the specimen, and the transmitted pulse provides a measure of the stress state within the sample. The strain gage signals thus provide the histories of the strain rate and stress within the sample; by combining the two signals it is possible to obtain the stress-strain relation for the specimen material under moderately high rates.

Assuming that we have homogenous deformation a simple analysis (Lindholm [16]) yields the mean specimen stress and mean strain rate in terms of the strain in the incident bar ε_R and that in the transmitter bar ε_T as follows;

$$\overline{\sigma}_s = \frac{EA_b}{2A_s}\varepsilon_T$$

and

$$\dot{\overline{\varepsilon}}_s = \frac{2c_o}{l_o}\varepsilon_R$$

where A_b and c_o represent the bar cross-section area and the bar velocity respectively, and E is the Young's modulus of the bars. The strain rate is then integrated to obtain the strain history of the specimen. Eliminating time from these recorded histories by cross-correlation gives us the specimen stress-strain curve at the observed high strain rate.

A similar technique to the Kolsky compression bar has been adapted to the study of materials undergoing nearly homogenous shearing deformation at high strain rates. This adaptation uses a torsional pulse rather than a compressive pulse, and the specimen is a thin walled tube rather than a short cylinder. The device consists of two long bars that sandwich a short tubular specimen with a thin walled tube making up the gage section and circular flanges which are attached to the bars using epoxy. Both bars are instrumented with foil strain gages for measuring shear strain. In operation, a torque is applied to a short section of the input bar; the rest of the bar is restrained from rotation using a friction clamp. When the friction clamp is suddenly released (by breaking a pre-notched bolt), a torsional pulse propagates down the bar.

The torsional pulse arrives at the specimen, and is partly transmitted and partly reflected. The transmitted pulse directly gives the stress history of the specimen, while the reflected pulse provides a direct measure of the nominal shear rate within the sample after the deformation becomes homogenous. Using relations analogous to those for the compression bar the nominal shear stress and nominal shear rate sustained by the specimen can be obtained from the recorded strain gage signals (Hartley et al.[17]) . The shear rate is then integrated over time to give the specimen shear strain γ; hence a torsion bar test can provide a complete shear stress-shear strain curve at a high strain rate.

Specimen Preparation

The micrograph of the sintered Ti-6Al-4V shows the presence of α plates with intergranular β in the plane of the section. The fully dense Ti-6Al-4V was heat treated to generate a similar microstructure to that which exists in the matrix of the porous metal. The heat-treatment required in this case consists of solution treating at 1100°C for one hour, and furnace cooling.

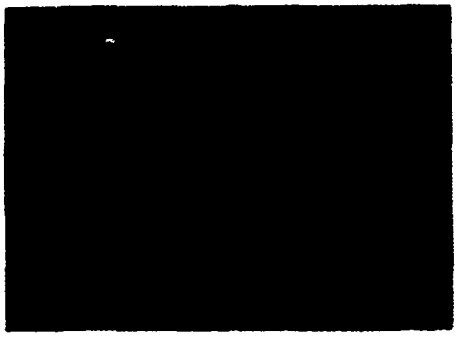


Fig. 1. Micrograph of Sintered Ti-6Al-4V

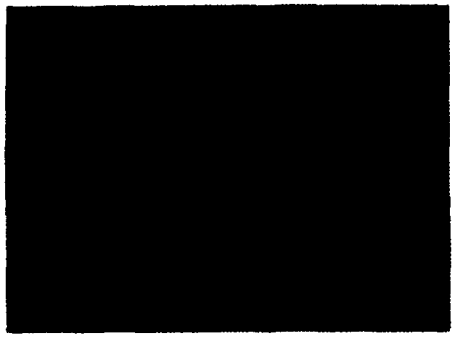


Fig. 2. Micrograph of Fully Dense Ti-6Al-4V

After the heat treatment both the fully dense material and the matrix of the porous Ti-6Al-4V possess similar microstructures (Fig. 1 & 2) which consists of the distinctive Widmanstatten structure of α-plates with some intergranular β phase. In order to further characterize the microstructures, the microhardness, grain sizes and phase compositions were measured. Vickers microhardness measurements yielded an average value of 419VH for the fully dense heat-treated metal and 412VH in the matrix of the sintered metal. The microstructures are also governed to some extent by the size of the grains present. In both microstructure the plate-like α-grains have lengths between 20-100 μm and aspect ratios varying from 2 to 10. The grain sizes measured in the fully dense and porous metals are comparable (10-15 μm across and 20-100 μm in length). Further

characterization of the microstructures is done by comparing the composition of individual phases in the fully dense and porous metals with the help of an electron microprobe; the results indicate that the microstructures are equivalent and contain greater than 90% of the α-phase and less than 10% of the β-phase.

Other important features of the microstructure are the volume fraction, size and aspect ratio of the pores. An image processing system was developed for quantitative analysis of the microstructure of the porous Ti-6Al-4V. It is sufficient to measure the areal pore fraction in order to obtain the pore volume fraction present in the solid. The mean pore area fraction or relative porosity obtained is approximately 7.6%, which is close to the value of 8% obtained from fluid immersion tests. In measuring the size and shape of the pores present, the image analysis software attempts to fit an ellipse to each pore and then sizes the pore using the major and minor axes of the fitted ellipse. Using this method the measured values of the major and minor axes yield a mean aspect ratio of 2.0 for the pores with the mean major axis length equal to 9.46 μm and the mean minor axis equal to about 4.71 μm.

Results and Discussion

The porous metal and the fully dense Ti-6Al-4V are subjected to quasistatic compression at strain rates betweeen 10^{-4}-10^{-3} s^{-1}. In the case of the porous metal true constitutive information cannot be inferred directly due to the compressibility effects of the pores. Thus another strain measure (such as radial strain) or the evolution of the porosity as a function of compression must be known before we can obtain the true stress - true strain constitutive information.

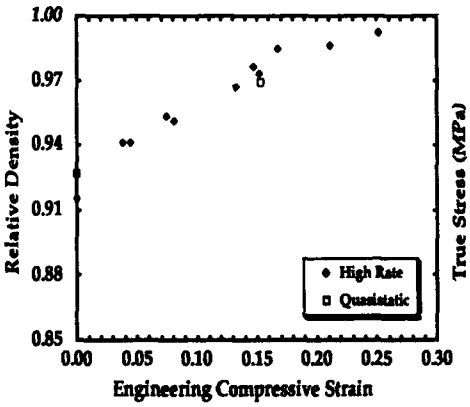


Fig. 3. Density Evolution with Compressive Strain

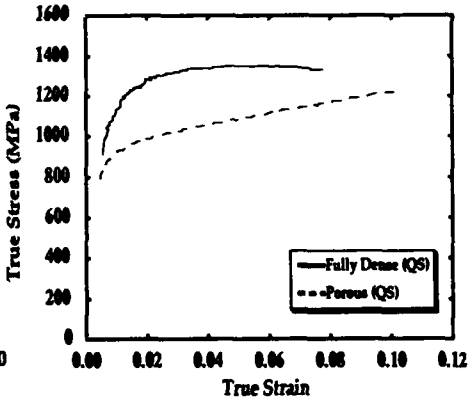


Fig. 4. True Stress-Strain in Quasistatic Compression

In order to obtain the evolution of the material porosity with compressive strain several specimens are strained at a nominally constant strain rate (2000 s^{-1}) to various amounts of plastic strain. The relative density is then measured employing Archimedes's principle and the procedure outlined by Bourcier et al.[13]. The evolution of the relative density of the porous material as a function of the compressive strain is shown in Fig. 3. Similar measurements are made on the porous metal deformed under quasistatic compression; the final density is also plotted in Fig. 3. The results show that the effect of strain rate on the compaction is negligible. The behavior of the density evolution curve is similar to that observed in porous copper [9] and porous iron [11]. However the

difference is that these results [9,11] are from quasistatic tests rather than dynamic tests.

Using this evolution information, and consequently knowing the plastic compressibility of the porous metal, the true stress and true strain values can now be computed from the measured load and axial displacements during both the dynamic and quasistatic tests. These represent effective global properties for the porous metal. All the data presented henceforth represents true constitutive behavior.

Fig. 4 depicts the true stress-strain curves for the porous and fully dense metals at a strain rate of $10^{-4}s^{-1}$. The softening effect of the pores is apparent in terms of the yield strength. The fully dense metal is seen to exhibit a small degree of hardening as compared to the porous metal. Another important feature noticeable in Fig. 4 is that the stress-strain curve for the fully dense metal reaches a peak value at a strain of about 8%. Subsequent to the peak an inhomogenous deformation develops, eventually leading to failure of the specimen by shearing at an angle (approx. 35-45°) to the vertical axis.

In comparison, the porous metal is able to sustain large strains (as large as 20%) under compression without developing any evidence of inhomogeneous flow. This increased stability of the deformations under compression is due to the greater degree of strain hardening; the presence of the pores results in a greater ease of accommodation of the deformations within the material.

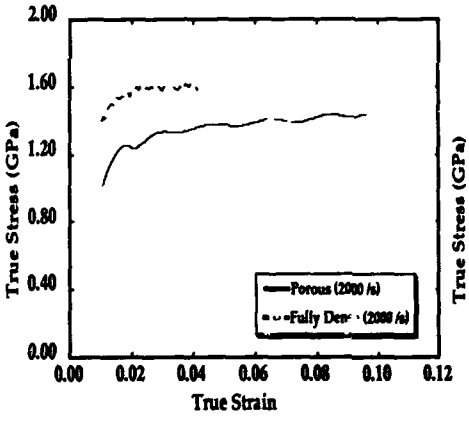


Fig. 5. Dynamic Response of Porous and Fully Dense Ti-6Al-4v

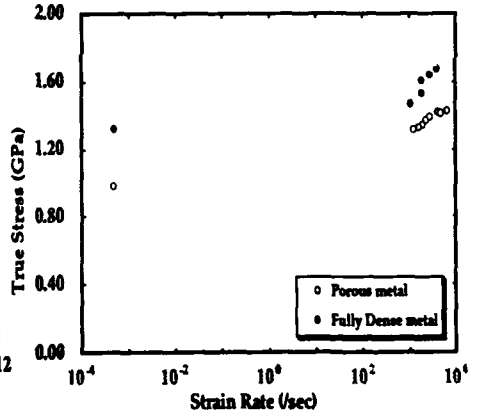


Fig. 6. Rate Sensitivity of Porous and Fully Dense Ti-6Al-4V

The behavior observed during dynamic compressive deformations is qualitatively similar to that obtained during quasistatic compression; the true stress-strain curve for the porous material is compared (Fig. 5) with that for the fully dense material during dynamic compression at a strain rate of $2.0x10^{3}s^{-1}$. Again, the porous material is generally weaker than the fully dense alloy, and there is again a strong difference in strain-hardening. Further, the same instability develops during dynamic deformations of the fully dense microstructure, while the porous material can sustain large compressive strains even at high strain rates without failure. The highest engineering strain obtained in tests on the porous metal was 20%; even at these strains there is no indication of any

macroscopic inhomogeneous deformation or other incipient "failure."

The porous material is subjected to dynamic compression over a range of strain rates from $10^3 s^{-1}$ to $7x10^3 s^{-1}$ and this information is used to plot a rate-sensitivity diagram at constant strain, for the porous and fully dense metals (Fig. 6). Note that the difference in the magnitude of the flow stresses for the porous and fully dense materials is clearly a function of the chosen strain, since the porous material exhibits strong hardening. Some interesting distinctions are apparent in the response of the two materials. First, over the lower range of rates the porous material appears to be more rate-sensitive than the fully dense alloy, so that at the high rates the softening effect of the pores is weaker than observed during quasistatic deformations. Note that this is true at ' 'tant strain, so that the compaction due to strain remains the same. Second, the sharp upturn in th. high-

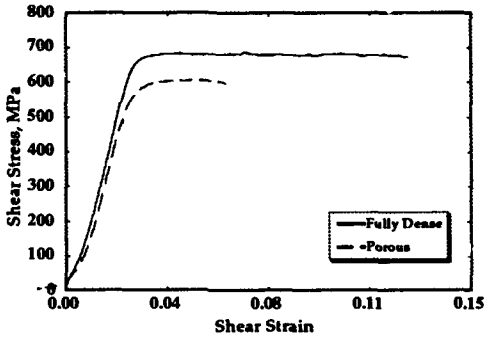


Fig. 7. Dynamic Shearing of Porous and Fully Dense Ti-6Al-4V at 400 s^{-1}

rate flow stress observed in the fully dense metal is not seen in the high-rate behavior of the porous metal, suggesting that the changes in "structure" that affect the flow stress are quite different in the two cases.

In order to integrate the above results into a typical constitutive model the response under a wider range of stress states is required. In this spirit, the porous and fully dense Ti-6Al-4V are subjected to dynamic shearing deformations between 10^2-$10^3 s^{-1}$ using the torsional Kolsky bar. The shear stress-shear strain curves for the fully dense and porous metal at a nominal shear rate of $400 s^{-1}$ are shown in Fig. 7.

In shear, both the fully dense and porous materials exhibit behavior that is close to perfectly plastic. In the case of the fully dense metal it is expected that the response be similar to that observed under compressive deformations and the recorded shear stress level can be predicted by the Von-Mises criterion. In the case of the porous metal the observed shear response can be explained if under shearing deformations the voids do not change in size but only in shape. This implies no change in the porosity during deformation. Thus macroscopic compressibility effects which are observed in compression (strain hardening) are not observed in shear. However as in compression, the weakening effect of the voids is apparent from the lower measured shear stress level.

A through crack was observed in the wall of the gage section of the porous metal shear specimens after deformation (at $400 s^{-1}$). A narrow region along the crack was examined with

the help of an SEM and some evidence of void linkage and large localized deformations in the grains close to the crack flanks is observed. These large local deformations are observed in the fully dense shear specimen as well and is probably evidence of flow localization.

Conclusions

The Kolsky compression and torsion bars and a screw driven quasistatic testing machine are effective instruments with which to investigate the effect of material porosity on the mechanical response of Ti-6Al-4V. A process of heat treatment is used to generate similar microstructures in the fully dense metal and in the matrix of the porous Ti-6Al-4V. Under quasistatic compression the porosity is seen to reduce the yield strength. At high rates the porosity is seen to affect the strain rate sensitivity (at constant strain) significantly. Further the compaction of the porous metal is observed to be relatively rate independent. Another noticeable effect of the porosity during compression is that the porous metal has a much higher degree of hardening due to the compressibility of the pores which provides a stabilizing influence in uniaxial compression by suppressing the localized deformation observed in the fully dense metal. In shearing deformations, due to the absence of any hydrostatic components of stress the compressibility effects (and consequently strain hardening) of the pores are not observed although their presence is still observable through the reduction in strength of the porous metal.

References

1. Haynes, R., (1981), *The Mechanical Behavior of Sintered Metals*, Freund London.
2. Rice, J.R., & Tracey, D.M., (1969), *J. Mech. Phys. Solids*, Vol. 17, pp. 201-217.
3. Gurson, A.L., (1977), *Jour. of Eng. Matls. and Tech.*, pp. 2-15.
4. Needleman, A., (1972), *Journ. of App. Mech.*, pp. 964-970.
5. Mear, M.E., (1990), *Mech. of Matls.* , Vol.9, pp. 33-48.
6. Kim, K.T., (1988), *Int. J. of Solids and Struct.*, Vol. 24, No.9, pp. 937-945.
7. Kuhn, H.A. & Downey, C.L., (1971), *Int. Jour. Powder Metall.*, Vol.7, (1), pg. 15.
8. Green, R.J., (1972), *Int. Jour. Mech. Sci.*, Vol.14, pp. 215-224.
9. Shima, S. & Oyane, M., (1976), *Int. Jour. Mech. Sci.*, Vol. 18, pp. 285-291.
10. Corapcioglu, Y. & Uz, T., (1978), *Powder Tech.*, Vol.21, pp. 269-274, 1978.
11. Kim, K.T., et al., (1990), *Private Communication.*
12. Shipman, F.H., et al., (1975), *Tech. Report No. 75-79*, Terra-Tek, Salt Lake City.
13. Bourcier, R.J., et al., (1986), *Acta Metall.*, 34, pp. 2443-2453.
14. Duffy, S.F., (1988), *Mech. of Matls.*, Vol.7, pp. 245-254.
15. Kolsky, H., (1949), *Proc. Phys. Soc. London*, Vol. 62B, pp. 676-700.
16. Lindholm, U.S., (1964), *J. Mech. Phys. Solids*, Vol. 12, pp. 317-335.
17. Hartley, K.A. et al., (1985), *ASM Metals Handbook*, Vol. 8, pp. 218-228.